

**Design, Functionalization, Synthesis and Evaluation
of New Chiral Stationary Phases for (U)HPLC and
Their Implementation in Drug Analysis,
(Enantio)Purification and Structural Elucidation**

Dissertation

der Mathematisch-Naturwissenschaftlichen Fakultät
der Eberhard Karls Universität Tübingen
zur Erlangung des Grades eines
Doktors der Naturwissenschaften
(Dr. rer. nat.)

vorgelegt von
Christian Michael Geibel
aus Trier

Tübingen
2022

Gedruckt mit Genehmigung der Mathematisch-Naturwissenschaftlichen Fakultät der
Eberhard Karls Universität Tübingen.

Tag der mündlichen Qualifikation:

22.08.2022

Dekan:

Prof. Dr. Thilo Stehle

1. Berichterstatter:

Prof. Dr. Michael Lämmerhofer

2. Berichterstatter:

Jun.-Prof. Dr. Matthias Gehring

Gewidmet meinen Eltern Michaela und Thomas
und meiner Schwester Natascha

Table of Contents

List of Abbreviations	1
Summary	4
Zusammenfassung	5
List of Publications	7
Author Contributions.....	11
Contributions to Meetings and Conferences	23
1 Introduction	24
1.1 Chirality	25
1.1.1 What is Chirality?.....	25
1.1.2 Different Entities of Chirality	25
1.1.3 Pharmaceutical, Toxicological and Clinical Background of Chirality	26
1.2 High Performance Liquid Chromatography (HPLC)	29
1.2.1 Chiral Selectors	31
1.2.2 Van Deemter Analysis	34
1.3 Stationary Phases	37
1.3.1 Silica Gel as Chromatographic Support.....	37
1.3.2 Silica Surface Chemistry and Functionalization.....	39
1.4 Mass Spectrometry (MS)	42
1.4.1 LC-MS Hyphenation	42
1.5 Nuclear Magnetic Resonance (NMR) Spectroscopy	44
1.5.1 Solid-State NMR (SS-NMR)	45
2 Aim of This Work.....	47
Table of Figures	48
References.....	49
3 Results and Discussion.....	54
3.1 Accepted Manuscripts – Part One: Development of Chiral Stationary Phases.....	54
3.1.1 Publication I: Evaluation of superficially porous particle based zwitterionic chiral ion exchangers against fully porous particle benchmarks for enantioselective ultra-high performance liquid chromatography	54
3.1.2 Publication II: Thiol-ene photo-click immobilization of a chiral chromatographic ligand on silica particles	84

3.1.3	Publication III: Controllable organosilane monolayer density of surface bonding using silatranes for thiol functionalization of silica particles for liquid chromatography and validation of microanalytical method for elemental composition determination	102
3.1.4	Publication IV: Study of microheterogeneity of silatrane-based silica surface bonding chemistry and its optimization for the synthesis of chiral stationary phases for enantioselective liquid chromatography	124
3.2	Accepted Manuscripts – Part Two: Application of Chiral Stationary Phases	134
3.2.1	Publication V: Towards enantioselective ultrahigh performance liquid chromatography–mass spectrometry-based metabolomics of branched-chain fatty acids and anteiso-fatty acids under reversed-phase conditions using sub-2-µm amylose- and cellulose-derived chiral stationary phases	134
3.2.2	Publication VI: High Plasticity of the Amicetin Biosynthetic Pathway in Streptomyces sp. SHP 22-7 Led to the Discovery of Streptocytosine P and Cytosaminomycins F and G and Facilitated the Production of 12F-Plicacetin	164
3.2.3	Publication VII: DoE Optimization Empowers the Automated Preparation of Enantiomerically Pure [¹⁸F]Talazoparib and its <i>In Vivo</i> Evaluation as a PARP Radiotracer	243
3.2.4	Publication VIII: Discovery and Evaluation of Enantiopure 9H-pyrimido[4,5-<i>b</i>]indoles as Nanomolar GSK-3β Inhibitors with Improved Metabolic Stability	297
3.2.5	Publication IX: Addressing a Trapped High-Energy Water: Design and Synthesis of Highly Potent Pyrimidoindole-Based Glycogen Synthase Kinase-3β Inhibitors	358
	Danksagung	405

List of Abbreviations

2D-NMR	=	Two-dimensional nuclear magnetic resonance
°		Degree, 1/360 of a full rotation, 1° = 0.0175 rad
°C	=	Degree Celsius or degree centigrade, relative temperature scale with 0°C = 273.15 K
ACHSA	=	<i>trans</i> -2-aminocyclohexanesulfonic acid
CDA	=	Chiral derivatization agent
CDCl ₃	=	Deuterated chloroform
CSP	=	Chiral stationary phase
D	=	Dexter (lat.: right), stereodescriptor (Fischer projection) used for amino acids and sugars
Da	=	Dalton, atomic mass unit
DNA	=	Deoxyribonucleic acid
DMSO-d ₆	=	Dimethylsulfoxide, sixfold deuterated
e.g.	=	Exempli gratia (lat.), abbreviation for “for example”
EMA	=	European Medicines Agency
ESI	=	Electrospray ionization
et al.	=	Et alii (masculine), et aliae (feminine) or et alia (neutral); lat.: and co-workers or and co-authors
Fig.	=	Figure
FPP	=	Fully porous particle(s)
GC	=	Gas chromatography
H	=	Theoretical plate height
<i>h</i>	=	Reduced theoretical plate height
HETP	=	Height equivalent to a theoretical plate
HILIC	=	Hydrophilic interaction liquid chromatography
HPLC	=	High performance liquid chromatography
IC	=	Ion exchange chromatography
i.e.	=	Id est (lat), abbreviation for “it is” or “that is”
IUPAC	=	International Union of Pure and Applied Chemistry

K	=	Kelvin, absolute temperature scale, SI unit for temperature
L	=	Laevus (lat.: left), stereodescriptor (Fischer projection) used for amino acids and sugars
lat.	=	Latin
LC	=	Liquid chromatography
m	=	Meter, SI unit for length
m ²	=	Square meter, SI unit for area
m ³	=	Cubic meter, SI unit for volume
MAS	=	Magic angle spinning
min	=	Minutes, unit for time, 1 min = 60 s
mL	=	Milliliter, unit for volume, 1 mL = 1*10 ⁻⁶ m ³
mm	=	Millimeter, unit for length, 1 mm = 1*10 ⁻³ m
mmol	=	Millimole, unit for the amount of a substance, 1 mmol = 1*10 ⁻³ mol
mol	=	Mole, SI unit for the amount of a substance
<i>m/z</i>	=	Mass to charge ratio
MRI	=	Magnetic resonance imaging
MS	=	Mass spectrometer or mass spectrometry
NMR	=	Nuclear magnetic resonance
NP	=	Normal phase
ppm	=	Parts per million
PO	=	Polar organic
QD	=	Quinidine, IUPAC: (S)-[(2 <i>R</i> ,4 <i>S</i> ,5 <i>R</i>)-5-ethenyl-1-azabicyclo[2.2.2]octan-2-yl]-(6-methoxyquinolin-4-yl)methanol
QN	=	Quinine, IUPAC: (R)-[(2 <i>S</i> ,4 <i>S</i> ,5 <i>R</i>)-5-ethenyl-1-azabicyclo[2.2.2]octan-2-yl]-(6-methoxyquinolin-4-yl)methanol
<i>R</i>	=	Rectus (lat.: right), stereodescriptor (Cahn-Ingold-Prelog) used for absolute configuration
rad	=	Radian, SI unit for measuring angles
Resp.	=	Respectively
RNA	=	Ribonucleic acid
RP	=	Reversed phase

s	=	Seconds, SI unit for time
S	=	Sinister (lat.: left), stereodescriptor (Cahn-Ingold-Prelog) used for absolute configuration
SEC	=	Size exclusion chromatography
SFC	=	Supercritical fluid chromatography
SI	=	International System of Units
SPP	=	Superficially porous particle(s) (synonym: coreshell particle(s))
SS-NMR	=	Solid state nuclear magnetic resonance
TLC	=	Thin layer chromatography
TMS	=	Tetramethylsilane
u	=	Velocity of mobile phase
UHPLC	=	Ultra-high performance liquid chromatography
UV	=	Ultraviolet
v	=	Reduced linear velocity of mobile phase
VEGF	=	Vascular endothelial growth factor
vs.	=	Versus
ZWIX	=	Zwitterionic weak ion exchanger
Å	=	Ångström, unit for length, $1 \text{ Å} = 1 \cdot 10^{-10} \text{ m}$
α	=	Descriptor for the differentiation of isomers, α refers to the first carbon atom
β	=	Descriptor for the differentiation of isomers, β refers to the second carbon atom
μm	=	Micrometer, unit for length, $1 \text{ mm} = 1 \cdot 10^{-6} \text{ m}$
μmol	=	Micromole, unit for the amount of a substance, $1 \text{ mmol} = 1 \cdot 10^{-6} \text{ mol}$

Summary

Chiral liquid chromatography is a field of utmost importance for a wide range of academic and industrial applications. Drug development, environmental analysis, laboratory-based diagnostics, or structure elucidation among others, strongly rely on chiral liquid chromatography nowadays. For this reason, this cumulative thesis describes the development and applications of chiral stationary phases for enantioselective (ultra-)high performance liquid chromatography ((U)HPLC). In the first part of the thesis, new chiral stationary phases (CSPs) based on anion-exchange and zwitterionic ion exchange chiral selectors were developed. The following goals were achieved during the work on this thesis: Various silica particles were evaluated for their kinetic performance optimization for enantioselective UHPLC and a deep insight into a variety of interactions between analyte and stationary phase was gained [Publication I]. The bonding chemistry and its generation by thermic or UV-driven radical starter was evaluated and systematically optimized by introducing a solvent-free photo-click immobilization strategy resulting in low-bleeding, "platform-type" stationary phases [Publication II]. Furthermore, the functionalization of bare silica, which can be seen as the starting point of the production of a CSP-based HPLC column, was varied and optimized for fast separations by the reduction of mass transfer resistance using silatranes and thus forming thin, homogeneous monolayer of thiol functionalization in a multiple-step [Publication III] and in a single-step approach [Publication IV].

The second part of the thesis focuses on the application of enantiomer separation. This includes the elaboration of the following aspects: Since chiral methods are becoming increasingly important in the fields of metabolomics and lipidomics, a guide for the chiral analysis of branched short-chain fatty acids based on polysaccharide columns was developed [Publication V]. Furthermore, the chirality of previously unknown natural compounds was elucidated [Publication VI]. A protocol for the enantiopurification of a radiotracer was established [Publication VII]. Knowledge about chiral HPLC was used for both analytical and preparative separation in the development of potential new drugs [Publications VIII and IX]. In summary, extensive research on the design, functionalization, synthesis, and evaluation of chiral stationary phases and their scope of applications has been performed.

Zusammenfassung

Das Feld der chiralen Flüssigchromatographie ist von herausragender Bedeutung für eine Vielzahl akademischer und industrieller Anwendungen. Die Entwicklung neuer potenzieller Arzneistoffe, Umweltanalytik, laborgestützte Diagnostik und Strukturaufklärung sind nur einige der Bereiche, aus denen die chirale Flüssigchromatographie heute nicht wegzudenken ist. Aus diesem Grund gibt die vorliegende kumulative Dissertation einen Überblick sowohl über die Entwicklung als auch über die Anwendung chiraler stationärer Phasen für die enantioselektive (Ultra-)Hochleistungsflüssigchromatographie ((U)HPLC). Im ersten Teil dieser Dissertation wurden neue chirale stationäre Phasen (CSPs) basierend auf Anionentauschern und zwitterionischen Ionentauschern entwickelt. Folgende Ziele konnten dabei erreicht werden: Verschiedene Silikapartikel wurden bezüglich ihrer kinetischen Leistung für enantioselektive UHPLC optimiert. Dabei wurde ein detaillierter Einblick in die zahlreichen Interaktionsprozesse zwischen Analyt und stationärer Phase gewonnen [Publikation I]. Die Anbindungschemie und deren Entstehung durch chemische Radikalstarter (thermisch oder UV-initiiert) wurde verglichen und systematisch optimiert. Hier wurde eine neue, lösemittelfreie, UV-initiierte Immobilisierungsstrategie eingeführt, welche zu wenig blutenden, sogenannten „Plattform-Typ“-Phasen führt [Publikation II]. Die Funktionalisierung von Silika, welche als Ausgangspunkt für die Entwicklung CSP-basierter HPLC-Säulen gelten kann, wurde verändert und für schnelle Trennungen optimiert. Dies wurde durch eine Verringerung des Widerstands gegen den Massentransfer erreicht. Dazu wurden Silatrane verwendet, welche einen dünnen, homogenen Film an Thiolgruppen auf der Oberfläche der Silikapartikel formen. Hierzu wurde erst ein mehr- [Publikation III] und anschließend ein einstufiges Verfahren eingeführt [Publikation IV].

Der zweite Teil der vorliegenden Dissertation handelt von der Anwendung chiraler Trennmethode. Folgende Aspekte wurden dabei ausgearbeitet: Da die Anwendungsfelder der Metabolomik und Lipidomik nach immer mehr chiralen Trennmethode verlangen, wurde ein Leitfaden zur Trennung verzweigter kurzkettiger Fettsäuren basierend auf Polysaccharidsäulen entwickelt [Publikation V]. Des Weiteren wurde die Chiralität von vorher unbekanntem Naturstoffen aufgeklärt [Publikation VI]. Ein Protokoll zur enantiomerenreinen Aufreinigung eines Radiotracers konnte entwickelt und angewandt werden [Publikation VII]. Das Wissen über chirale HPLC-Trennungen sowohl im analytischen als auch im präparativen Maßstab wurde ferner in der Entwick-

lung neuer Wirkstoffkandidaten angewandt [Publikationen VIII und IX]. Zusammenfassend lässt sich sagen, dass eine umfassende Forschungsarbeit in dem Gebiet der Planung, Funktionalisierung, Synthese und Evaluierung chiraler stationärer Phasen sowie ihren breiten Anwendungsbereichen durchgeführt wurde.

List of Publications

Part One: Development of Chiral Stationary Phases

Publication I – Accepted (June 10, 2019)

Geibel, C., Dittrich, K., Woiwode, U., Kohout, M., Zhang, T., Lindner, W., Lämmerhofer, M., **Evaluation of superficially porous particle based zwitterionic chiral ion exchangers against fully porous particle benchmarks for enantioselective ultra-high performance liquid chromatography.** *Journal of Chromatography A* **2019**, *1603*, 130-140. DOI: 10.1016/j.chroma.2019.06.026

Publication II – Accepted (April 14, 2020)

Geibel, C., Dittrich, K., Wolter, M., Lämmerhofer, M., **Thiol-ene photo-click immobilization of a chiral chromatographic ligand on silica particles,** *Journal of Chromatography A* **2020**, *1622*, 461133. DOI: 10.1016/j.chroma.2020.461133

Publication III – Accepted (July 17, 2021)

Geibel, C., Theiner, J., Wolter, M., Kramer, M., Lindner, W., Lämmerhofer, M., **Controllable organosilane monolayer density of surface bonding using silatranes for thiol functionalization of silica particles for liquid chromatography and validation of microanalytical method for elemental composition determination,** *Journal of Chromatography A* **2021**, *1653*, 462418. DOI: 10.1016/j.chroma.2021.462418

Publication IV – Accepted (May 9, 2022)

Geibel, C., Kramer, M., Lämmerhofer, M., **Study of microheterogeneity of silatrane-based silica surface bonding chemistry and its optimization for the synthesis of chiral stationary phases for enantioselective liquid chromatography,** *Journal of Chromatography A* **2022**, *1674*, 463138. DOI: 10.1016/j.chroma.2022.463138

Part Two: Application of Chiral Stationary Phases

Publication V – Accepted (December 24, 2021)

Geibel, C., Zhang, L., Serafimov, K., Gross, H., Lämmerhofer, M., **Towards enantioselective ultrahigh performance liquid chromatography–mass spectrometry-based metabolomics of branched-chain fatty acids and anteiso-fatty acids under reversed-phase conditions using sub-2- μm amylose- and cellulose-derived chiral stationary phases**, *Chirality* **2022**, 34(3): 484-497. DOI: 10.1002/chir.23413

Publication VI – Accepted (February 27, 2022)

Aryal, N., Chen, J., Bhattarai, K., Hennrich, O., Handayani, I., Kramer, M., Straetener, J., Wommer, T., Berscheid, A., Peter, S., Reiling, N., Brötz-Oesterhelt, H., **Geibel, C.**, Lämmerhofer, M., Mast, Y., Gross, H., **High Plasticity of the Amicetin Biosynthetic Pathway in *Streptomyces* sp. SHP 22-7 Led to the Discovery of Streptocytosine P and Cytosaminomycins F and G and Facilitated the Production of 12F-Plicacetin**, *Journal of Natural Products* **2022**, 85, 3, 530–539. DOI: 10.1021/acs.jnatprod.1c01051

Publication VII – Accepted (October 21, 2021)

Bowden, G., Stotz, S., Kinzler, J., **Geibel, C.**, Lämmerhofer, M., Pichler, B., Maurer, A., **DoE Optimization Empowers the Automated Preparation of Enantiomerically Pure [^{18}F]Talazoparib and its *In Vivo* Evaluation as a PARP Radiotracer**, *Journal of Medicinal Chemistry* **2021**, 64, 21, 15690-15701. DOI: 10.1021/acs.jmedchem.1c00903

Publication VIII – Accepted (October 16, 2020)

Andreev, S., Pantsar, T., El-Gokha, A., Ansideri, F., Kudolo, M., Bublitz Anton, D., Sita, G., Romasco, J., **Geibel, C.**, Lämmerhofer, M., Ines Goettert, M., Tarozzi, A., Laufer, S., Koch, P., **Discovery and Evaluation of Enantiopure 9H-pyrimido[4,5-b]indoles as Nanomolar GSK-3 β Inhibitors with Improved Metabolic Stability**, *International Journal of Molecular Sciences* **2020**, 21(21), 7823. DOI: 10.3390/ijms21217823

Publication IX – Accepted (July 2, 2021)

Andreev, S., Pantsar, T., Tesch, R., Kahlke, N., El-Gokha, A., Ansideri, F., Grätz, L., Romasco, J., Sita, G., **Geibel, C.**, Lämmerhofer, M., Tarozzi, A., Knapp, S., Laufer, S., Koch, P., **Addressing a Trapped High-Energy Water: Design and Synthesis of Highly Potent Pyrimidoindole-Based Glycogen Synthase Kinase-3 β Inhibitors**, *Journal of Medicinal Chemistry* **2022**, 65, 2, 1283-1301. DOI: 10.1021/acs.jmed-chem.0c02146

Further publications (not included in this thesis)

Accepted (March 11, 2021)

Wolter, M., Chen, X., Woiwode, U., **Geibel, C.**, Lämmerhofer, M., **Preparation and characterization of poly(3-mercaptopropyl)methylsiloxane functionalized silica particles and their further modification for silver ion chromatography and enantioselective high-performance liquid chromatography**, *Journal of Chromatography A* **2021**, 1643, 462069. DOI: 10.1016/j.chroma.2021.462069

Accepted (July 16, 2021)

Karongo, R., Ge, M., **Geibel, C.**, Horak, J., Lämmerhofer, M., **Enantioselective multiple heart cutting online two-dimensional liquid chromatography-mass spectrometry of all proteinogenic amino acids with second dimension chiral separations in one-minute time scales on a chiral tandem column**, *Analytica Chimica Acta* **2021**, 1180, 338858. DOI: 10.1016/j.aca.2021.338858

Accepted (February 23, 2022)

Dimitrov, T., Anli, C., Moschopoulou, A. A., Kronenberger, T., Kudolo, M., **Geibel, C.**, Schwalm, M. P., Knapp, S., Zender, L., Forster, M., Laufer, S., **Development of novel urea-based ATM kinase inhibitors with subnanomolar cellular potency and high kinome selectivity**, *European Journal of Medicinal Chemistry* **2022**, 235, 114234. DOI: 10.1016/j.ejmech.2022.114234

Accepted (May 19, 2022)

Wolter, M., **Geibel, C.**, Olfert, M., Su, M., Bicker, W., Kramer, M., Lindner, W., Lämmerhofer, M., **Development and chromatographic exploration of stable-bonded crosslinked amino silica against classical amino phases**, *Journal of Separation Science* **2022**, Accepted Author Manuscript, DOI: 10.1002/jssc.202200268

Author Contributions

Part One: Development of Chiral Stationary Phases

Publication I

Evaluation of superficially porous particle based zwitterionic chiral ion exchangers against fully porous particle benchmarks for enantioselective ultra-high performance liquid chromatography. *Journal of Chromatography A* **2019**, *1603*, 130-140. DOI: 10.1016/j.chroma.2019.06.026

Christian Geibel

Investigation, methodology, formal analysis, data curation, visualization, writing – original draft, writing – review & editing

Kristina Dittrich

Investigation, data curation, writing – review & editing

Ulrich Woiwode

Investigation, data curation, writing – review & editing

Michal Kohout

Investigation, writing – review & editing

Tong Zhang

Resources, writing – review & editing

Wolfgang Lindner

Writing – review & editing

Michael Lämmerhofer

Conceptualization, methodology, supervision, writing – review & editing, resources

Publication II

Thiol-ene photo-click immobilization of a chiral chromatographic ligand on silica particles, *Journal of Chromatography A* **2020**, 1622, 461133. DOI:

10.1016/j.chroma.2020.461133

Christian Geibel

Investigation, methodology, formal analysis, data curation, visualization, writing – original draft, writing – review & editing

Kristina Dittrich

Investigation, data curation, writing – review & editing

Marc Wolter

Investigation, writing – review & editing

Michael Lämmerhofer

Conceptualization, methodology, supervision, writing – review & editing, resources

Publication III

Controllable organosilane monolayer density of surface bonding using silatranes for thiol functionalization of silica particles for liquid chromatography and validation of microanalytical method for elemental composition determination, *Journal of Chromatography A* **2021**, 1653, 462418. DOI: 10.1016/j.chroma.2021.462418

Christian Geibel

Investigation, methodology, formal analysis, data curation, visualization, writing – original draft, writing – review & editing

Johannes Theiner

Investigation, methodology, writing – review & editing

Marc Wolter

Investigation, writing – review & editing

Markus Kramer

Investigation, writing – review & editing

Wolfgang Lindner

Methodology, writing – review & editing

Michael Lämmerhofer

Conceptualization, methodology, supervision, writing – review & editing, resources

Publication IV

Study of microheterogeneity of silatrane-based silica surface bonding chemistry and its optimization for the synthesis of chiral stationary phases for enantioselective liquid chromatography, *Journal of Chromatography A* **2022**, 1674, 463138. DOI: 10.1016/j.chroma.2022.463138

Christian Geibel

Investigation, methodology, formal analysis, data curation, visualization, writing – original draft, writing – review and editing

Markus Kramer

Investigation, writing – review and editing

Michael Lämmerhofer

Conceptualization, methodology, supervision, writing – review & editing, resources

Part Two: Application of Chiral Stationary Phases

Publication V

Towards enantioselective ultrahigh performance liquid chromatography–mass spectrometry-based metabolomics of branched-chain fatty acids and anteiso-fatty acids under reversed-phase conditions using sub-2- μ m amylose- and cellulose-derived chiral stationary phases, *Chirality* **2022**, *34*(3): 484-497. DOI:

10.1002/chir.23413

Christian Geibel

Investigation, methodology, formal analysis, data curation, visualization, writing – original draft, writing – review and editing

Li Zhang

Investigation, data evaluation

Kristian Serafimov

Investigation, data evaluation, writing, proofreading

Harald Gross

Supervision of analysis of natural products

Michael Lämmerhofer

Conceptualization, methodology, supervision, writing – review & editing, resources

High Plasticity of the Amicetin Biosynthetic Pathway in *Streptomyces* sp. SHP 22-7 Led to the Discovery of Streptocytosine P and Cytosaminomycins F and G and Facilitated the Production of 12F-Plicacetin, *Journal of Natural Products* 2022, 85, 3, 530–539. DOI: 10.1021/acs.jnatprod.1c01051

Niraj Aryal

Fermentation, extraction, isolation, 2D-structural elucidation of 10 substances, precursor-directed feeding, conceptualization

Junhong Chen

Fermentation, extraction, isolation, 2D-structural elucidation of 10 substances, precursor-directed feeding, conceptualization

Keshab Bhattarai

Fermentation, extraction, isolation, 2D-structural elucidation of 10 substances, precursor-directed feeding, conceptualization

Oliver Hennrich

Fermentation, preparation of bacterial culture

Ira Handayani

Fermentation, preparation of bacterial culture

Markus Kramer

2D-structural elucidation of 10 substances, conceptualization

Jan Straetener

Realization of bioassays (antifungal/antibacterial/antimycobacterial/cytotoxicity)

Tatjana Wommer

Realization of bioassays (antifungal/antibacterial/antimycobacterial/cytotoxicity)

Anne Berscheid

Realization of bioassays (antifungal/antibacterial/antimycobacterial/cytotoxicity)

Silke Peter

Realization of bioassays (antifungal/antibacterial/antimycobacterial/cytotoxicity)

Norbert Reiling

Realization of bioassays (antifungal/antibacterial/antimycobacterial/cytotoxicity)

Heike Brötz-Oesterhelt

Realization of bioassays (antifungal/antibacterial/antimycobacterial/cytotoxicity)

Christian Geibel

3D-structural elucidation of 2 substances

Michael Lämmerhofer

3D-structural elucidation of 2 substances

Yvonne Mast

Fermentation, preparation of bacterial culture

Harald Gross

2D-structural elucidation of 10 substances, precursor-directed feeding, conceptualization, resources, writing

DoE Optimization Empowers the Automated Preparation of Enantiomerically Pure [¹⁸F]Talazoparib and its *In Vivo* Evaluation as a PARP Radiotracer, *Journal of Medicinal Chemistry* **2021**, *64*, *21*, 15690-15701.

DOI: 10.1021/acs.jmedchem.1c00903

Gregory D. Bowden

Study design, synthesis (organic synthesis and radiosynthesis), analysis of the (radio)chemical DoE data, writing – original draft

Sophie Stotz

Study design, in vitro and in vivo experiments and data analysis, writing – original draft

Johannes Kinzler

Writing – review & editing

Christian Geibel

Establishing of the protocol for the chiral analysis, writing – review & editing

Michael Lämmerhofer

Establishing of the protocol for the chiral analysis, writing – review & editing

Bernd J. Pichler

Study design, writing – review & editing

Andreas Maurer

Study design, writing – original draft

Discovery and Evaluation of Enantiopure 9H-pyrimido[4,5-b]indoles as Nanomolar GSK-3 β Inhibitors with Improved Metabolic Stability, *International Journal of Molecular Sciences* **2020**, 21(21), 7823. DOI: 10.3390/ijms21217823

Stanislav Andreev

Planning of syntheses, synthesis of most compounds, interpretation of results, writing of the manuscript (original draft), proofreading of the manuscript

Tatu Pantsar

In-silico experiments, molecular modelling, writing of the manuscript (original draft), design of figures, proofreading of the manuscript

Ahmed El-Gokha

Planning of syntheses, synthesis of compounds, writing of the manuscript (original draft), proofreading of the manuscript

Francesco Ansideri

Determination of IC₅₀-values

Mark Kudolo

Determination of metabolic stability

Déborá Bublitz Anton

Determination of cell toxicity

Giulia Sita

Determination of intracellular kinase inhibition, determination of neuroprotective effects of certain compounds, data evaluation

Jenny Romasco

Determination of intracellular kinase inhibition, determination of neuroprotective effects of certain compounds, data evaluation

Christian Geibel

Determination of chiral purity, data evaluation, proofreading of manuscript

Michael Lämmerhofer

Supervision and coordination of the determination of chiral purity

Márcia Ines Goettert

Coordination of determination of cytotoxicity of certain compounds

Andrea Tarozzi

Coordination of determination of intracellular kinase inhibition and neuroprotective effects of certain compounds

Stefan A. Laufer

Initiation, supervision and coordination

Pierre Koch

Initiation, supervision and coordination, writing of original draft, proofreading

Addressing a Trapped High-Energy Water: Design and Synthesis of Highly Potent Pyrimidoindole-Based Glycogen Synthase Kinase-3 β Inhibitors, *Journal of Medicinal Chemistry* **2022**, 65, 2, 1283-1301. DOI: 10.1021/acs.jmedchem.0c02146

Stanislav Andreev

Planning of syntheses, synthesis of most compounds, coordination of non-synthetic experiments, interpretation of results, writing of the manuscript (original draft), proof-reading of the manuscript

Tatu Pantsar

In-silico experiments, molecular modelling, writing of the manuscript (original draft), design of figures, proofreading of the manuscript

Roberta Tesch

Performance of co-crystallization experiments, data evaluation

Niclas Kahlke

Synthesis of test compounds

Ahmed El-Gokha

Planning of syntheses, synthesis of test compounds

Francesco Ansideri

Determination of IC₅₀-values

Lukas Grätz

Determination of binding affinities, data evaluation

Jenny Romasco

Determination of intracellular kinase inhibition, determination of neuroprotective effects of certain compounds, data evaluation

Giulia Sita

Determination of intracellular kinase inhibition, determination of neuroprotective effects of certain compounds, data evaluation

Christian Geibel

Determination of chiral purity, data evaluation

Michael Lämmerhofer

Supervision and coordination of the determination of chiral purity

Andrea Tarozzi

Coordination of determination of intracellular kinase inhibition and neuroprotective effects

Stefan Knapp

Coordination and supervision of co-crystallization experiments, X-ray crystallography

Stefan A. Laufer

Initiation, supervision and coordination

Pierre Koch

Initiation, supervision and coordination, writing of original draft, proofreading

Contributions to Meetings and Conferences

12th Balaton Symposium on High-Performance Separation Methods 2019

Siófok, Hungary, September 11–September 13, 2019

Poster Presentation:

Zwitterionic Chiral Ion-Exchangers: a Comparison of Different Particle Morphologies Against Fully Porous Particle Benchmark and Implementation in UHPLC Methods

Christian Geibel, Kristina Dittrich, Ulrich Woiwode, Michal Kohout, Tong Zhang, Wolfgang Lindner, Michael Lämmerhofer

Awarded with a poster award

30. Doktorandenseminar Hohenroda 2020

Hohenroda, Germany, January 11–January 14, 2020

Oral Presentation

Comparing different particle morphologies against a benchmark – can state of the art zwitterionic chiral ion-exchangers be improved?

Christian Geibel, Kristina Dittrich, Ulrich Woiwode, Michal Kohout, Tong Zhang, Wolfgang Lindner, Michael Lämmerhofer

Jahrestagung der Deutschen Pharmazeutischen Gesellschaft (DPHG) 2021

Online Conference, September 28–October 01, 2021

Poster Presentation:

Controlling a crucial step in stationary phase synthesis: homogeneous monolayer functionalization of silica particles for liquid chromatography using silatranes

Christian Geibel, Marc Wolter, Markus Kramer, Michael Lämmerhofer

1 Introduction

Operating in the field of analytical chemistry requires knowledge in different chemical subdisciplines that exceeds instrument-related proficiency. For this reason, an overview on related topics is crucial, leads to a better understanding and by this a more satisfactory result. The work on which this thesis is based includes several different projects, all of which are linked and have certain methods or topics in common. Chirality, the handedness of molecules, is a structural feature inherent to most biomolecules (proteins, carbohydrates, nucleic acids, neurotransmitters, etc.) and many drugs. For this reason, it has to be considered in bioanalysis and drug analysis to obtain a full picture of molecular composition. To this end, in this work enantiomers were separated due to their handedness or enantiopure compounds were used as building blocks for the synthesis of chiral stationary phases. In all projects, high performance liquid chromatography (HPLC) was the analytical tool of choice for the separation and identification of compounds, in some cases combined with mass spectrometric (MS) methods for a more detailed characterization. Chiral stationary phases for the use in HPLC were synthesized, with silica as basis material. Furthermore, nuclear magnetic resonance (NMR) measurements were carried out for the characterization of functionalized silica gel, among others. The introduction of this thesis gives an overview of the central aspects of the topics and analytical methods that links all of the projects.

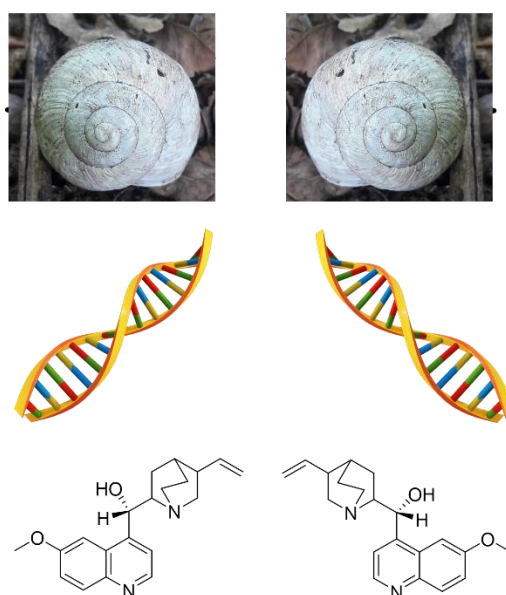
1.1 Chirality

1.1.1 What is Chirality?

The word “chirality” is etymologically derived from the Greek word χείρ (cheir = hand) [1] and describes the handedness of an entity. In chemistry, this refers to the symmetry characteristic of an ion or molecule that is not superimposable with its mirror image [2], despite having an identical two-dimensional composition and sum-formula. When taking the third dimension into account, it becomes evident that enantiomers do not have the same spatial orientation of the atoms and functional groups. This difference in spatial arrangement can be built around one central atom, referred to as a stereo-center – but it can also be built around an axis or a plane (in general referred to as elements of chirality) [3] or can occur as helical chirality [2]. Enantiomers show the same chemical and physical properties in an achiral surrounding (with the exception of their ability to rotate plane-polarized light) but can show very different biological activities.

1.1.2 Different Entities of Chirality

Chirality can be seen in different scales. Even subatomic elementary particles like neutrinos or electrons exhibit chirality [4]. In the living world, chirality can be found everywhere, in the helical twist of our genetic storage media, the DNA, in the winding of polysaccharides, in receptors in the bodies of humans and animals and in macroscopic entities like in snail shells [5] (Fig. 1). Even non-chiral, symmetrical molecules can develop chirality in a supramolecular level, e.g., by crystallization on an asymmetric core [6]. In this work, chirality was mainly given attention to on a molecular or supramolecular, helical level.



The universe is an asymmetrical entity. I am inclined to believe that life as it is manifested to us must be a function of the asymmetry of the universe or of the consequence of this fact.
- Louis Pasteur

The universe is an asymmetrical entity. I am inclined to believe that life as it is manifested to us must be a function of the asymmetry of the universe or of the consequence of this fact.
- Louis Pasteur

Fig. 1: Chirality is occurring everywhere in natural systems, from elementary particles over molecules and living systems to galaxies. At the top: Snail shell as macroscopic example for chirality in nature (own photography). Underneath: DNA helix as example for supramolecular chirality. Below: Quinine (1*S*, 3*R*, 4*S*, 8*S*, 9*R*) and quinidine (1*S*, 3*R*, 4*S*, 8*R*, 9*S*) as example for molecular chirality. At the bottom: Quotation on asymmetry by L. Pasteur (1900) [7].

1.1.3 Pharmaceutical, Toxicological and Clinical Background of Chirality

Even though the source of homochirality in nature is widely discussed up to now [8], the fact that enantiomeric purity is pivotal to the impact of substances such as drugs, amino acids, sugars or other natural and synthetic product is undisputed. This is valid for both, the human body (which is in the focus in pharmaceutical and medical sciences) and the flora and fauna (which is addressed in ecotoxicology, biology, life sciences and others). In pharmaceutical sciences, a distinction is made between eutomer and distomer when either two different effects or two different peculiarities of the same effect are observed when different enantiomers are used [9, 10]. The term “eutomer” here refers to the enantiomer causing the desired effect, while “distomer” describes the less effective, non-effective or even toxic enantiomer. A mixture of both the eu- and distomer must be avoided, as the to-be-taken dose of the drug rises with a higher

percentage of non-effective distomer. This can lead to a decreased ratio of desired to adverse effects (in comparison to the pure eutomer) or the toxic effects of the distomer can cause irritation or serious pathophysiological or pathological alterations in the individual. This effect can be drawn back to the fact that the receptors themselves are chiral. As they are proteins, the receptors are built of proteinogenic amino acids, of which almost all (with glycine being an exception) are chiral. Biological systems are in most cases highly chiral, not only amino acids but also sugars and some fatty acids are chiral, giving rise to the enantioselective response. Highly ordered, nature strictly sticks to homochiral laws. A person that would vary from this rule could not survive – a (hypothetical) person, being for example able to digest only L-configured sugars cannot live in a world dominated by D-sugars.

The variation of enantioselective response between eutomer and distomer can vary from only a lower desired activity of the distomer (e.g. (*R*)-pantoprazole [11]) over an antagonistic activity (e.g. (*R*)-citalopram [12] or anticonvulsive barbiturates [13, 14]) to toxic effects. An example for a toxic distomer is thalidomide, with (*R*)-thalidomide being the sleep inducing eutomer, (*S*)-thalidomide being the VEGF inhibiting (and therefore embryotoxic) distomer (note that the labels eu- and distomer refer here to the original scope of application as sedative drug, not its today's scope of application as VEGF inhibitor). Unfortunately, even enantiopure (*R*)-thalidomide can transform via acid catalyzed tautomerization *in vivo* into its distomer [15, 16].

On a sidenote, “chiral switching” can be a method for pharmaceutical companies to (I) effect to claim patents for, e.g., enantiopure compound while patents for the racemate are still pending [17], (II) to truly improve their product by only selling the eutomer or (III) to present an old drug as a new product (e.g., by patenting the eutomer after the patent for the racemate expires) [18]. The approval of enantiopure (*S*)-Zopiclon by the European Medicines Agency (EMA) in April 2021 marks an event worth mentioning, as it is an example for the use of the “chiral switching” technique. In addition, numerous further drugs are marketed as both chiral and enantiopure compounds (e.g., ketamine and esketamine, cetirizine and levocetirizine and others).

The above-mentioned reasons clarify the need of reliable separation techniques for pharmaceuticals. A racemate of drugs should be treated as a desired product with a purity of only 50% – a value that is far from acceptable.

As a matter of course, pharmaceutical analysis also benefits largely from the achievements in chiral analysis. From a clinical point of view, some chiral substances can be exploited as biomarkers for either an already prevailing pathological condition or as predictive marker in pathophysiological conditions. Physiologically, mainly L-amino acids occur in mammals with elevated D-amino acid levels being in most cases a biomarker for pathological or pathophysiological changes (e.g., D-Asp in β -amyloid as marker for Alzheimer's disease or in elastin as biomarker for arteriosclerosis or D-Ser in α -crystallin as marker for cataract [19]). Furthermore, elevated amounts of D-amino acids or racemic α -methyl fatty acids can hint towards a defective peroxisome function [20]. Compounds over the whole range of -omics can occur naturally in healthy patients with physiological health status in one stereoform and in pathophysiological states in the respective other, whether amino acids in metabolomics, branched fatty acids in lipidomics, or others. Here, reliable and powerful chiral separation techniques can lead to an (optimally) early and easy detection of pathological or subpathological status by analysis of chiral biomarkers. This opens the opportunity for new diagnoses or serves as support and validation for clinical analyses. By this, the patient profits by the early and reliable knowledge about his/her status and the healthcare professional can react, e.g., by starting a therapy.

1.2 High Performance Liquid Chromatography (HPLC)

The first use of chromatographic methods can be dated back to the beginning of the 20th century, when the Russian biologist Mikhail Tsvet first used this technique to separate plant-based pigments [21], resulting in a bouquet of different colors. This gave this particular separation technique its name. Chromatography is borrowed from the Greek words χρώμα (chroma, “color”) and γράφειν (graphein, “to write”). Nowadays, separation in modern laboratories cannot be imagined without chromatography – be it planar chromatography like thin layer chromatography (TLC), gas chromatography (GC), supercritical fluid chromatography (SFC) or liquid chromatography (LC). This thesis focuses mainly on the latter, therefore a detailed description of the first mentioned techniques is not considered.

High performance liquid chromatography (HPLC) or ultra-high performance liquid chromatography (UHPLC) systems are able to transport the mobile phase and the analyte with a pressure up to 400 bar (HPLC) respectively 1200 bar (UHPLC) over the column filled with the stationary phase. By interaction with that, the analyte mixture can be separated, e.g., according to its polarity. (U)HPLC systems can be used in different modes depending on the mixture of substances to be separated. In this case, both the mobile phase composition and the surface of the stationary phase usually differ from another mode. Examples of commonly used modes are (to name but a few):

- Normal phase (NP): The stationary phase typically shows polar behavior, whilst the mobile phase is highly nonpolar.
- Reversed phase (RP): The stationary phase is typically nonpolar, the mobile phase polar (preferred mode, e.g., for hyphenation to mass spectrometry (MS)).
- Polar organic (PO): Closely related to NPLC; mobile phase is polar, but non-aqueous, stationary phase is typically polar like in NPLC.
- Hydrophilic interaction liquid chromatography (HILIC): Closely related to NPLC, mobile phase is usually aqueous and polar organic, leading to a water layer on the (typically polar) stationary phase
- Size-exclusion chromatography (SEC): The mobile phase composition can vary; molecules or particles are separated by their Stoke’s radius.
- Ion exchange chromatography (IC): The interaction between stationary phase and analyte will be increased by the immobilization of counterions on the stationary phase. Retention and separation can be increased by this.

Chiral LC or enantioseparation in LC requires a chiral auxiliary. This chiral auxiliary can be added to the mobile phase as enantiopure substance or can be immobilized on silica or other polymeric support material to obtain a chiral stationary phase (CSP). Over the last decades, a vast amount of different chiral selectors for chiral stationary phases was developed, such as polysaccharides [22], cyclodextrins [23], antibiotics such as teicoplanin or vancomycin [24], crown ethers [25], chiral ligands [26] or ion exchangers [27], all of them applicable in a more or less versatile way.

Nevertheless, some analytes must be derivatized before injection for several reasons. Here, either a direct or an indirect method for separation can be chosen. Enantiomers can be separated indirectly after their derivatization with a chiral derivatization agent (CDA) to form a pair of diastereomers on an achiral stationary phase using an achiral mobile phase [28]. Precolumn derivatization (as indirect approach) with chiral derivatizing agents (such as Marfey's reagent, 1-fluoro-2,4-dinitrophenyl-5-L-alanine amide) is one such example and can be beneficial for the separation of e.g., chiral amino acids. The chromophoric label introduced via the CDA can increase both the retention and separation, and show the pleasant effect of transferring non-UV-detectable substances into UV-detectable substances. However, this indirect approach also shows disadvantages that make it less desirable; a derivatization step is prone to both error and racemization of the product, potentially leading to wrong results. Furthermore, the analyte must comprise a functionality that can be easily derivatized; if this is lacking, this indirect method is hardly possible. In addition, the chiral derivatization agent must be available in a high enantiomeric purity. In case of direct enantiomer separation by CSPs transient diastereomeric complexes between an enantiomerically pure chiral selector and the two opposite enantiomers which can have different complex stabilities. They lead to distinct retention times for the two enantiomers. Also, in the direct approach achiral derivatization can be performed – both for the sake of improved enantioseparation (for example with Fmoc (9H-fluoren-9-ylmethoxy)carbonyl chloride), benzyl chloroformate, AQC (6-aminoquinolyl-N-hydroxy-succinimidylcarbamate) or Sanger's reagent (1-fluoro-2,4-dinitrobenzene)), but also for better UV-detectability, lowered limit of detection in MS, higher retention or for the masking of detrimental functional groups (for example cysteine side chain protection with iodoacetamide). For the direct approach, two possibilities are feasible: Either a chiral, enantiopure selector can be added to the mobile phase (with the price of very high consumption of the chiral

additive and by this high costs for every run) or the chiral, enantiopure selector can be applied on the surface of the stationary phase. The latter approach is the favored by far, as it is easier to use, reproducible and highly reliable. Chiral selectors are either coated or covalently immobilized on the silica. Immobilized selectors open the gate to a vast spectrum of possible modes in which they can be used, as they are often compatible with many solvents. Coating of selectors, however, is a comparably easy and fast way of chiral stationary phase (CSP) production that shows high reproducibility [29, 30]. Yet, many selectors are unfortunately restricted to only a small number of solvents with which they are compatible; coated polysaccharide columns can be run in NP mode (using a mixture of alcohol and alkane), PO (using a mixture of alcohol and acetonitrile) or SFC mode. Running with intermediate polar solvents like dioxane or ethyl acetate or running in reversed phase mode with polar solvents can destroy the column by eluting the selector [28]. In the case of polysaccharides, this problem can be overcome by immobilization instead of coating. But the price to be paid is a decreased chiral recognition due to detrimental influence on the helicity during immobilization process [31]. As the choice of the correct selector is compulsory for a satisfactory separation, the available selector types are presented in detail in the following subchapter.

1.2.1 Chiral Selectors

Nowadays, a vast choice of chiral selectors have been immobilized (usually on silica) and are available as CSPs. They can be divided in different subgroups, the most important of which will be briefly presented here.

Biopolymer-derived chiral selectors comprise among others proteins and polysaccharide CSPs, the latter of which was introduced by *Okamoto et al.* in 1984 [22]. Those selectors are based on either amylose or cellulose as helical backbone and usually derivatized threefold per monomer. As they exhibit multiple stereocenters as well as supramolecular chirality displayed as helicity, polysaccharide based columns reveal exceptional enantioseparation abilities [28]. Synthetic polymer chiral selectors contain for example poly(triphenylmethacrylate). Their enantiorecognition principles are comparable with those of polysaccharide CSPs [28].

Macrocyclic selectors include cyclofructans, cyclodextrins, crown-ether and antibiotics. Cyclofructans are oligosaccharides first described in 1989 [32] and consist of (at

least) six D-fructanofuranose monomers, which are β -(2 \rightarrow 1)-linked [33, 34]. By this, they form a crown-ether core inside of the fructane ring and show comparable separation mechanisms as crown-ether CSPs regarding amines [35]. Crown-ether CSPs are built up of a cyclic ring of polyethers that usually carries some further derivatization moieties in its periphery. *Sousa et al.* introduced this class of CSP in 1978 using 18-crown-6 derivatives [28, 36] (here, 18 stands for the ring size and 6 for the oxygen atoms) for the complexation of chiral ammonium salts. It was known for several years that cyclic polyether can form complexes with either alkali metal ions or ammonia [37] (hence the name, since the ligand carries the complexation agent as a “crown”). This explains its application scope mainly for chiral compounds carrying a primary amino group, such as amino acids and their derivatives [28, 38]. The working pH-range must be chosen carefully – to avoid a dissolution of silica, a pH above the isoelectric point should be chosen, which is at roughly pH = 2 [39]. However, a low pH (< pH = 3.5) is needed because the primary amino group must be protonated for the complexation, as a positive charge is necessary. Furthermore, 18-crown-6-ether carrying free carboxylic acid moieties slowly lose their ability to complexation at a pH higher than 3.5 – at least towards alkaline metal ions [40].

Cyclodextrins form a further subclass of macrocyclic selectors. They were introduced in 1984 by *Armstrong et al.* [41] and are composed of 6–8 glucose units connected via α -1,4-linkage [28]. Those cyclodextrins form a cone that has a hydrophobic inside, as it contains mainly carbon, and hydrophilic edges, originating from the hydroxy moieties [28]. The analyte can enter this truncated cone. Preferably lipophilic molecules are complexed in reversed-phase mode [28, 42], resulting in enantioseparation for chiral molecules. A comparable approach of enantioseparation can be seen in the subclass of macrocyclic antibiotics. Like cyclodextrins, they were introduced by the working group of *Armstrong* 10 years after cyclodextrins, in 1994 [24]. The first CSP from this group was based on vancomycin, an antibiotic produced by the bacterium *Amycolatopsis orientalis*, followed by the antibiotics teicoplanin and ristocetin A in the following years [28].

Donor-acceptor phases, chiral ion exchangers as well as ligand exchangers respectively chelating agents can be considered as low molecular mass selectors. The latter were developed by *Davankov et al.* in 1968 [43] and are based on the formation of a complex between a selector molecule, a chelated central metal ion (in this case Cu(II))

and a selectand. A necessity of the application is the ability of both the selector and the selectand to form complexes with the central ion. This technique is mainly used for the chiral resolution of amino acids and α -hydroxycarboxylic acids [28].

Chiral donor-acceptor selectors are synthetic, neutral, low-molecular mass molecules. They mainly interact with the analyte by non-ionic weak interactions, such as hydrogen bonding, π - π -interactions, dipole-dipole interactions or steric interactions and are often described as "Pirkle-type" phases [28]. Since the previously described typical interactions are disturbed by polar solvents, those phases are mainly used in normal phase mode. As this class of chiral selector is of low molecular weight in comparison with, e.g., cyclodextrins or macrocyclic antibiotics, a higher surface loading on silica can be achieved, which can be beneficial for the separation abilities of the CSPs [44].

As last class of chiral selectors, chiral ion exchangers will be briefly introduced here. All beneficial characteristics of Pirkle-type selectors can be observed in this subclass of selectors, since they are small molecules that exhibit all possibilities of interactions as donor-acceptor selectors, but they are amended by their ability to form ionic interactions, thus strong respectively long-range interdependence between themselves and a charged analyte. Derivatives from natural occurring alkaloids from *Cinchona pubescens*, quinine and quinidine, were introduced by *Lämmerhofer and Lindner* in 1996 as anion exchanger [27]. Slightly acidic conditions of the mobile phase (as are also commonly used to prevent deprotonation of residual silanols) are sufficient for the protonation of the quinine (QN) or quinidine (QD) moiety, as it exhibits a basic nitrogen in the quinuclidine moiety. As anion exchanger, it forces anions (like deprotonated acids) to be retained. By the spatial arrangement of the alkaloid and by its Pirkle-type features (like its ability to form hydrogen bonds or π - π -interaction), enantiodiscrimination can be achieved. When a reversal of the elution order is desired, QN and QD based CSPs can be used as complementary stationary phases. About 20 years later, a cation exchanger on the basis of *trans*-2-aminocyclohexanesulfonic acid (ACHSA) for the separation of chiral bases was published in 2007 [45]. It acts accordingly, but as cation exchanger it retains protonated bases. Virtually at any pH, *trans*-2-aminocyclohexanesulfonic acid is deprotonated, the protonation of the analyte can be achieved by pH adjustment of the mobile phase. A combination of both phases, the QN or QD-based anion exchanger phase and the ACHSA-based cation exchanger phase, led to a zwitterionic weak ion exchanger (ZWIX) phase in 2008 [46]. Denoted as ZWIX(+) for

QN-based and ZWIX(-) for QD-based selectors, it widens the applicability of this selector class on underivatized biomolecules such as amino acids, but can also be used for bases and acids [28]. The presence of both charges leads to attractive and repulsive forces which can have a beneficial effect on the peak shape. Preferentially, those columns should be driven in either reversed-phase or polar organic mode with added buffer. The corresponding buffer counterion can act as a competitor for the analyte, increase desorption, and thereby sharpen the peaks and increase the efficiency of the column.

1.2.2 Van Deemter Analysis

To reliably specify the separation ability in chromatographic systems, the height equivalent to a theoretical plate (HETP) can be determined by the application of the van Deemter equation (Eq. 1). It was derived by the Dutch physicist and engineer Jan Jozef van Deemter in 1956 [47] and describes the impact of different factors of HETP in dependence on the velocity of the mobile phase, i.e. on peak broadening and thus on the performance of a chromatographic system.

$$HETP = H = A + \frac{B}{u} + C * u \quad (\text{Eq. 1})$$

Here, u describes the velocity of the mobile phase. The term “A” refers to the Eddy-diffusion and is the only term in the equation that is independent from the mobile phase’s velocity. It describes the occurrence of peak broadening by eddies that are appearing as the analyte paths around the particles. Those eddies are characterized by a short reversal in flow direction when changing from laminar into turbulent flow [48] inside the column. Since each molecule of the analyte encounters a different number of particles as it travels through the column, each molecule is struck by a different number of eddies. Therefore, variable times are needed when passing through the column – the result is peak broadening. The A-term is an indicator for the packing quality; a tightly packed bed translates into a low A-term. Whether a narrow particle size distribution of the silica particles used is beneficial for the A-term is still debated [49-52], while it seems clear that small fines (dust-like particles) negatively influence the packing quality [49, 51].

The second term in the van Deemter equation is the “B-term” or the longitudinal dispersion. It is a peak broadening effect resulting from molecular movement along a

concentration gradient. The dispersion takes place in longitudinal direction, meaning in and counter the direction of flow. The B-term is lower in viscous liquids and furthermore dependent on the temperature, as high temperature (I) increases the Brownian molecular movement (and by this the diffusion, that enhances the dispersion effect) and (II) mostly decreases the viscosity of liquids. Furthermore, it is a time-dependent factor: The shorter the analyte stays on the column, the less it has to suffer from longitudinal dispersion. The term is dependent on the reciprocal value of the flow rate – it decreases when the flow rate increases. For fast separations at high flow rates, the B-term hardly carries weight, but its impact becomes evident at low flow rates. This is the reason why the optimum flow rate must be evaluated by recording H/u curves and why the optima are not at the lowest possible flow rate.

While longitudinal diffusion is negligible at high flow rates, the “C-term” (or resistance towards mass transfer) shows its greatest effect here. It describes the attaining of an equilibrium between the mobile and the stationary phase in a chromatographic system and by this the spreading of the molecules between the immiscible phases. It can be divided into several parts, all having impact on the overall C-term. C_s and C_m refer to a delay in reaching local equilibria [53]; The mass transfer resistance on the particle surface (written as C_s) is the delay of analyte exchange in the pores of the stationary phase, generally averaged over the particles [53-55], while the mass transfer resistance in the mobile phase (C_m) corresponds to the averaged delay of analyte exchange in the interstitial space (or between adjacent flow vectors) [53, 55]. Another term, C_{ads} , describes the kinetics of the adsorption and desorption process of the analyte on the stationary phase surface. In general, it can be neglected in non-chiral reversed phase chromatography due to very fast kinetics; however, this is not the case in enantioselective chromatography, predominantly due to very slow desorption kinetics [56, 57]. In addition, the C-term is contingent on the way, the analyte has to pass inside the mobile phase: A shorter way enhances the kinetics and favors a lower C-term. This can be reached by (I) using superficially porous particles or (II) small particle diameters or (III) potentially forming a thin and homogeneous layer of functionalization respectively selector on the silica surface (for detailed explanations, see respective subchapters 1.3.1 and 1.3.2). A low C-term is of crucial interest for both academia and industry, as it is one key for the achievement of superfast separations, which are desperately needed to meet the needs of new separation technologies such as two-

dimensional LC, or to achieve the highest possible throughput in, e.g., clinical or toxicological analyses. A very low C-term decouples the column efficiency as much as possible from the restraints it is forced in by the fast flow rate.

To gain a better comparability for different columns, the indication of reduced values is useful. Here, the flow rate is given as reduced linear velocity v . The calculation of the linear velocity (in mm/s) from the flow rate (in mL/min) compensates for different column inner diameter, amongst others. This can be done when the external porosity is known. If this is not the case, literature values of 0.35-0.40 can be estimated [58]. The transformation to a reduced linear velocity requires information about the linear velocity u_e , the particle diameter d_p , and the diffusion coefficient D_m . According to [59], it can be written as

$$v = \frac{u_e * d_p}{D_m} \quad (\text{Eq. 2})$$

H , as introduced in Eq. 1, can be transformed into its reduced form, h , by simply dividing H by the particle diameter [60]. In this way, an H/u curve can be transformed into a reduced h/v -plot, which is independent from the column's particle size. The terms A, B and C described above translate into their reduced forms a , b and c in this way. The idea of a reduced plate height h was first introduced by *Giddings et al.* [61] and later on used by *Knox* and co-workers [62]. Unlike van Deemter, he developed a formula for the comparison of columns that was not derived from physical models but adapted to experimental data [63] (Eq. 3).

$$h = av^n * \frac{b}{v} * cv \quad (\text{Eq. 3})$$

Due to flow anisotropy effects, it is proposed here that n can have values between 0.2 and 0.5 [60], but is assumed to have a value of 1/3 [60, 63]. The van Deemter equation, however, neglects flow anisotropy and therefore reflects a case in which $n = 0$. Both the van Deemter and the (reduced) Knox equation are very useful tools for comparing the performance of different columns.

1.3 Stationary Phases

1.3.1 Silica Gel as Chromatographic Support

The majority of columns used in LC are silica based [64, 65]. Therefore, it is worthwhile to discuss this material in more detail. Silica gel is the support for the selector that is bonded on its functionalized surface, forming the chromatographic bed. Over the last decades, silica has proven itself as suitable material to meet the requirements of supports for stationary phases. It shows high physical stability [65], which is of utmost importance when using columns with a pressure up to 1200 bar and makes silica highly versatile also over a high temperature range [66]. Moreover, the production of silica results in highly controllable particles in terms of particle size, pore size, and particle morphology due to highly efficient and useful material science techniques such as the Stöber process [67]. Those techniques also open the possibility to produce cost-effective materials. Over the years, silica particles manufacturing capabilities changed as both boundaries of the possibilities were pushed forward, and new needs were met. This applies to all three properties mentioned.

The first HPLC columns used particles with a size of 5–10 μm [64, 68], with a tendency to decrease over time. By reducing the particle size, the density of the chromatographic bed can be increased. This in turn leads to a higher number of particles in the column and by this to an overall higher surface and more possible immobilization sites for selectors. In contrast, there is a higher backpressure when using smaller particles. *Darcy's law* describes the fact that the backpressure increases proportionally to a decreasing particle diameter. With the introduction of modern UHPLC systems in 2004, pumps could deliver pressures up to 1200 bars and reliably switch valves under high pressure. This made the use of sub-2- μm particles feasible and quickly gained acceptance in the pharmaceutical industry [69]. Nowadays, particles with a size of 3 μm and lower (depending on the application) are state of the art.

Whilst particles tended to grow smaller over time, the particle morphology also changed. Today, four major morphologies are used: Monoliths, non-porous, fully porous, and superficially porous particles. As monoliths and non-porous particles were not used in this thesis, the main focus will be on the latter two morphologies. Fully porous particles (FPP) have pores through the whole particle, making it fully accessible for the analyte. This increases both the specific surface area as well as the porosity

and permeability, but detrimentally influences the mass transfer resistance (“C-term”). Although they have been around since the 1960s [70], it was the work by *Kirkland et al.* that led to the commercial success of superficially porous particles (SPP) in 2006 [71, 72]. Here, particles with an inner non-permeable core of 1.7 μm and a porous shell of 0.5 μm were used. These particles led to numerous advantages, including a factor of 2 to 3 lower backpressure than comparable FPPs, which had to be smaller in size [71]. Furthermore, virtually all terms affecting the van Deemter equation are improved with SPP. Eddy-diffusion (“A-term”) is reduced [73], most likely due to a more homogeneously packed chromatographic bed. This is the case as they display a smaller particle size distribution while concomitantly showing a higher particle density by reason of the solid core [74] or of the higher particle roughness, leading to a more homogeneous distribution of shear forces while packing [49]. The latter is explicable by the fact that SPP do not absorb shear forces as easy as FPP by deforming [49]. Longitudinal diffusion (“B-term”) is decreased by roughly 20% in SPP [75] based on the hindrance by the solid core and the lower permeability mediated by it. As the diffusion pathways inside the particles are significantly smaller in SPP, mass transfer resistance (“C-term”) can drastically be reduced [73], leading to a virtually doubled efficiency of SPP in comparison to FPP [76].

Apart from their size and morphology, FPP and SPP can also be characterized by their pore size. The choice of the correct pore size is crucial in size exclusion chromatography but can also exhibit a large impact in other chromatographic modes. Small pores generally lead to a higher number of pores per m^2 and by this to a higher specific surface area, thus more area to be loaded with selector molecules. For small particles ($\sim < 1,000$ Da), generally up to 10 \AA in diameter, pores smaller than 120 \AA are sufficient because the pore size should be at least roughly 4-10 times higher than the particle’s hydrodynamic diameter [68, 77]. Accordingly, higher pore sizes should be chosen for larger particles, e.g., 300 \AA for a molecular weight of up to 50,000 Da [68] or short to medium sized peptides, and very large pore sizes such as 1,000 \AA or more for biomolecules [77] like monoclonal antibodies. Wider pores exhibit generally lower resistance to mass transfer and thus a lower C-term, but suffer from dramatically decreased mechanical pressure stability [78]. This effects both the acceptable packing pressure and by this the highest operating pressure and can be a limiting factor concerning separation speed.

1.3.2 Silica Surface Chemistry and Functionalization

Understanding of the surface chemistry of silica particles is a key to their successful functionalization. Knowledge about and effective exploitation of it can result in both an optimized (high) amount of functionalization agent and selector on the silica surface and a possibly low detrimental interaction of the unfunctionalized part of the surface with the analytes. Silica gel has a hydrophilic surface due to its silanol moieties and is usually derivatized with hydrophobic moieties. On the inside, silica gel resembles quartz – at least from a strictly chemical and non-crystallographic point of view – as it is solely built from Si-O-Si bonds. The possible forms that silica gel can present on its surface are shown in Fig. 2 a).

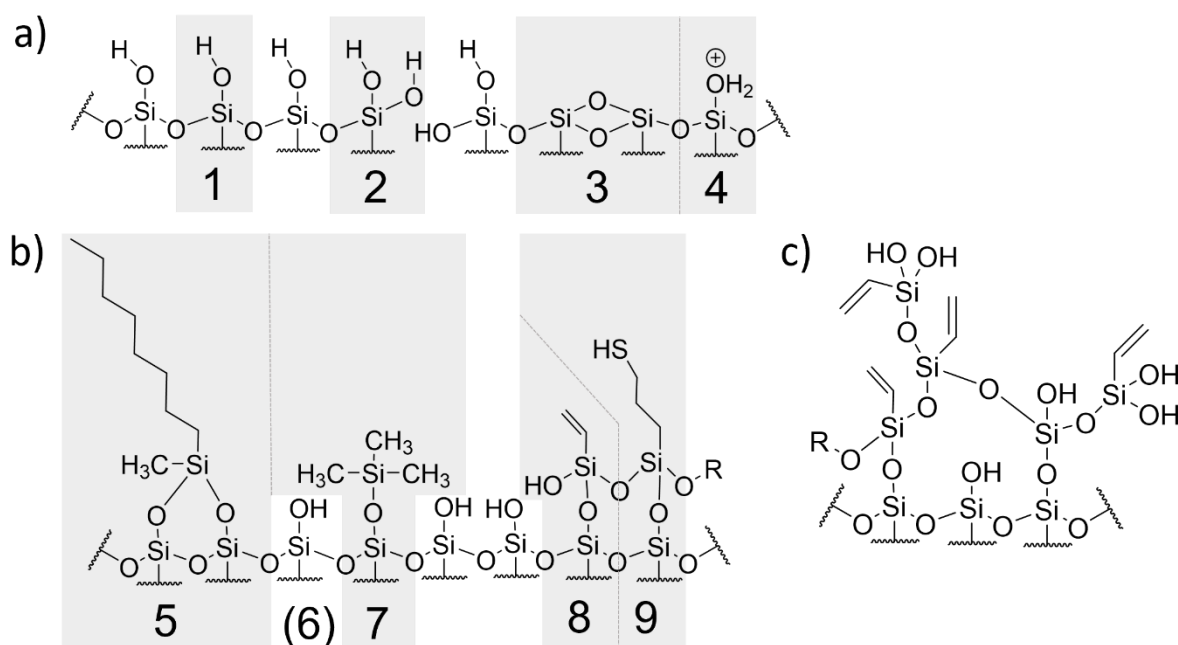


Figure 2: a) Depicts the different entities of surface chemistries on a bare silica particle. b) Shows typical functionalization resp. derivatization forms of silica. c) Indicates a non-optimal, chaotic surface functionalization with detrimental effect on the column performance.

Number 1 shows the usually most abundant form on the silica surface, the terminal vicinal silanol groups. Since they prevail on the surface, they determine most of the silica's surface characteristics [79, 80]. Due to their polarity, they are responsible for silica's hydrophilicity. Furthermore, silica tends to be weakly acidic, and exhibits pK_a -values slightly lower than 3 [80, 81] when being vicinal. They can interact with each other either directly or via water molecules. Isolated silanols, however, have pK_a -values of roughly 10 [80, 81], comparable to weakly acidic aromatic alcohols such as phenol. Geminal silanols, as shown in number 2, carry two hydroxyl moieties on the

same silicon atom. They can occur as convex or concave silanols, with the pK_a values of the former being comparable to those of vicinal silanols and those of the latter being ~ 9 [80]. The remarkable difference in acidity for different spatial forms of geminal silanols can be explained by a better stabilized silanolate (thus by a better stabilized negative charge) in convex silanols. Number 3 depicts siloxane bridges. Those siloxanes can occur during the production of silica, when temperatures around $\sim 400\text{--}500^\circ\text{C}$ are elevated. In a calcination process, the silica surface loses silanols, resulting in siloxane bridges [82, 83]. As they decrease the polarity and deny accessibility to the silica's surface due to missing silanols, they can be seen as pernicious and should be avoided. Generally, their formation can be reversed by rehydroxylation, a process in which the calcinated silica particles are refluxed in water or diluted aqueous hydrochloric acid [82, 83]. A protonated silanol species, SiOH_2^+ , can be seen at number 4. It plays a minor role at neutral pH, as it virtually does not appear. At pH 2, however, it covers $\sim 18\%$ of the silica surface [84]. Lower pH would even increase its amount, but would lead to a dissolution of the gel, as the particles are only stable at pH higher than their isoelectric point, which lies around $\text{pH} = 2$ [39]. The protonated silanol species can have an impact on the functionalization, as it shows very high acidity of pK_a between -2 and -5 [85, 86].

Fig. 2 b) shows typical surface chemistries of functionalized stationary phases. Number 5 demonstrates a C8 chain, bivalently bond to the silica surface, as it is used in RP-columns. The bivalent bonding is supposed to increase the mechanic and hydrolytic stability of the alkyl chain and prevent the column from excessive bleeding, leading both to a lower background noise (especially in MS measurements) and a higher column lifetime. Number 6 depicts an underivatized surface silanol. The general chemistry of this has been discussed above; however, demonstrating that free silanols are present in functionalized silica gel is critical because only about 50% of silanols (4 of available $8 \mu\text{mol}$ silanol per m^2 silica surface) can be functionalized [87, 88]. Those can develop unfavorable interactions with the analyte due to their protic ionic character (which can be suppressed by the addition of acid in the mobile phase). Endcapping, as shown in number 7, decreases their adverse effect on the separation. Small molecules are generally used for endcapping, as they have only little spatial hindrance by their adjacent (usually larger) selectors. Here, a trimethylsilyl endcapping is shown exemplarily. Nevertheless, even using very small endcapping agents and optimal

conditions, a “full” endcapping of more than 50% of the terminal silanols cannot be achieved due to steric hindrance. Number 8 and 9 are functionalized in preparation for a thiol-ene click reaction. Both display a short alkyl linker (C2 for 8, C3 for 9) with a terminal double bond (vinyl, 8) or thiol (9) moiety. They can easily be armed with a selector carrying the respective (thiol or vinyl) counterpart by a radical mediated reaction. Number 8 is bivalently bond, number 9 trivalently (if R does not correspond to a proton). This makes both agents resistant towards bleeding.

Fig. 2 c) depicts a non-optimal surface functionalization carrying a vinyl moiety. Here, the formation of a homogeneous monolayer failed in favor of an oligomeric thick film. This impacts negatively on the mass transfer resistance, as the paths of the analyte inside the functionalization film are long, leading to slow and hindered adsorption and desorption mechanisms.

1.4 Mass Spectrometry (MS)

The use of mass spectrometry as a detector is virtually indispensable in a wide range of science and especially in analytical chemistry. It allows to derive essential information on the analyte or the composition of a mixture. A vast variety of different mass spectrometers and different modes in which they can be driven lead to an enormous choice of possible ways for analyzing a compound. As the use of mass spectrometry was only of minor but not negligible interest of the work underlying this thesis at hand, it will only be discussed briefly and superficially to give an overview of this technique. A very detailed approach of this technique is beyond the scope of the introduction of this thesis.

In general, MS can be seen as a very sensitive selector, capable of reliable measurements at very low concentrations – which is of great importance in trace analysis or -omics, in forensics, and structural elucidation, amongst others. The m/z values obtained from the analysis provide information about the analyte and its charge or ionization. Furthermore, its elemental composition (based on the isotopic pattern) can be estimated. Mass spectrometry can be used both for qualification and quantification of analytes. In either case, the analyte needs to be ionized. For the generation of ions, several different ionization methods are available, which differ in their ability to ionize (soft vs. hard ionization methods), to produce single or multiple charged ions, or to produce in-source fragments of the molecule. As the soft ionization method electrospray ionization (ESI) can be set to produce only few in-source fragments [89] and is suitable for rather polar components [90], it is frequently the ionization method of choice in metabolomics. The following mass filter can be set to transfer only ions displaying a distinct m/z value to the detector. In MS^2 or MS^n experiments, the parent compound can be fragmented, and these fragments – when ionized – can be analyzed. A specific fragmentation pattern can in turn contain information about the parent compound.

1.4.1 LC-MS Hyphenation

The hyphenation of MS with chromatographic methods is usually needed for the analysis of highly complex samples. Here, either gas chromatographic (GC), liquid chromatographic (LC), supercritical fluid chromatographic (SFC), or other methods can be used for the hyphenation with an MS system. All those techniques allow a more

precise statement on the sample as not only the m/z value but also the retention behavior is taken into account. In addition, the right choice of the chromatographic system can, e.g., result in a separation of stereoisomers. These would lead to the same m/z value and the same specific fragmentation pattern in MS *without* prior separation. Hence, they would be misinterpreted as only one analyte. Ion chromatograms, which result from a hyphenated LC-MS run, are three dimensional; for every peak in the two-dimensional chromatogram (intensity versus retention time), a third dimension, namely a mass spectrum, is added. This causes a higher amount of generated information and makes the hyphenation of chromatographic with mass spectrometric methods a very powerful tool.

1.5 Nuclear Magnetic Resonance (NMR) Spectroscopy

Nuclear magnetic resonance spectroscopy is a very important non-destructive tool for the structural elucidation of analytes. It is indispensable for synthesis control, for structural elucidation of unknown analytes [91] such as natural products [92, 93], or for understanding the interplay between analytes and receptors in biological systems [94], to name but a few. NMR-technique is also omnipresent in everyday medical, clinical practice as imaging device in magnetic resonance imaging (MRI) systems which allow non-invasive imaging of tissue hidden deep inside the body. The importance of NMR can also be seen in the list of Nobel Prize winners who have worked on NMR techniques – between 1944 and 2003, seven NMR scientists were awarded a Nobel Prize in physics, chemistry or medicine [95].

NMR spectroscopy takes advantage of the fact that nuclei with an odd number of protons and/or neutrons display a nuclear spin momentum. Nuclei with even numbers of protons and neutrons, such as ^{12}C , have no nuclear spin momentum and are therefore not accessible for NMR spectroscopy. By applying a magnetic field to NMR-active nuclei, they will be separated into different energy level with always a slightly higher number of protons in the energetic lower level, according to the Boltzmann distribution. When irradiated with energetic electromagnetic radiation, the nuclei absorb the energy and are transferred to a higher energy level. This absorption is measured. It is necessary to do this under the specific resonance conditions for the core to be measured. As every chemically and magnetically different core absorbs at (slightly) different frequencies, this can be exploited for the analysis of the analyte. The difference in absorption is the chemical shift, usually stated as ppm. As tetramethylsilane (TMS) shows a high symmetry and 4 magnetically equal carbons as well as 12 magnetically equal hydrogens, it is usually used as standard for ^1H and ^{13}C NMR measurements and marks a chemical shift of 0 ppm. All other analytes are measured in reference to this. For carbon NMR, only the NMR-active isotope ^{13}C is detected because the most abundant isotope, ^{12}C , is NMR inactive (see above). Despite ^{13}C being only ~1.1% of the natural occurring carbon, the amount is sufficient for NMR spectroscopy. Usually, NMR measurements are performed in liquid state, solved in deuterated solvent such as CDCl_3 or DMSO-d_6 . This is important for the suppression of the solvent peak. When most of the (NMR-active) hydrogen is substituted by NMR-inactive deuterium, the solvent shows only minor peaks. Nevertheless, they are visible due to incomplete

deuteration and hydrogen-deuterium exchange. Hydrogen, with only one proton being the smallest NMR-active nucleus, needs comparably low energetic electromagnetic irradiation. Since no further nuclei are excited by this, a direct relative quantification of the analyte by the signal is possible. For all other nuclei, a decoupling frequency must be irradiated to suppress the ^1H signal. For this reason, a reliable quantification cannot be performed with nuclei other than ^1H – at least not without prolonged relaxation times [96, 97].

For coupling experiments, where not only the nucleus but also its surroundings can be determined, different modes of higher complexity are used. Especially in the analysis of either unknown biomolecules or large proteins, where the three-dimensional structure has not yet been elucidated, NMR experiments with more than one dimension (mostly two dimensions) are performed. Here, conclusions about the chemical structure can be drawn by interpreting the visible spin-spin couplings, which can either show coupling via chemical bonds or spatial couplings that give an impression of the three-dimensional structure. This spatial structural behavior of, e.g., proteins, which can be determined in solution in liquid state by 2D-NMR [98], can also be determined by solid-state NMR (SS-NMR) [99].

1.5.1 Solid-State NMR (SS-NMR)

Solid-state NMR transfers the pleasant proficiencies of liquid state NMR to solid entities. This technique can be used to obtain information about the chemical structure of crystallized or (under chosen circumstances) insoluble substances as well as about the surface of macroscopic particles. In stationary phase design, this is especially useful as it can give an impression of the surface of the silica particles. For characterizing both the quantity and quality of functionalization, a combination of ^{13}C - and ^{29}Si -SS-NMR is especially beneficial. The quantity is usually measured as immobilized functionalization agent on the silica surface by silicon functionalities as a measure of free silanols [100] (here a combination of SS-NMR and elemental analysis (EA) is useful). Its quality is measured by its number of chemical bonds respectively silicon functionalities. Unfortunately, solid-state NMR has a significantly lower resolution than liquid-state NMR for many reasons, including the reduced ability for nuclei to rotate and align rapidly, resulting in broad peaks [101]. This low resolution leads to the necessity of comparably high amounts of samples that are needed for a reasonable spectrum. The

resolution of the system can be drastically increased by applying the so-called magic angle spinning (MAS) NMR spectroscopy [101]. As shown by *Andrew et al.* in 1958 [102] (and independently shown by *Lowe et al.* in the following year [103]), detrimental anisotropic effects in solid state (which do not occur in liquid state due to faster isotropic tumbling [104]) can effectively be suppressed by spinning the probe at an angle of 54.74° to the magnetic field [101, 105]. Often another technique is used in combination with MAS-SS-NMR measurements: Cross polarization (CP) can transfer the polarization (or: magnetization) from one nucleus to another [105]. For example, since ^1H nuclei are usually highly abundant in samples, they can be used as vehicle to transfer the magnetization to the less abundant nuclei (like ^{13}C or ^{29}Si), thereby increasing their signal. The sensitivity can be significantly increased by these techniques.

2 Aim of This Work

The driving force and motivation of this thesis was to find new routes in stationary phase synthesis and to improve already established routes, with chiral liquid chromatography as the target of optimization. Hence, the first logic step as starting point was to understand the interactions between the analyte and the stationary phase. By accurately naming and precisely describing the interactions that lead to peak broadening and thus loss in performance, it became clearer which parameters should be addressed to systematically improve the stationary phase. Based on the results of this first project, both the bonding chemistry as well as the functionalization of silica were improved to obtain better performing columns. Constantly increasing demands as, e.g., faster separations with the goal of subminute separations, lower bleeding or higher pressure and temperature stability are imposed on chromatographic methods and thus also on chromatographic hardware, with the column being the heart of a chromatographic system. To meet the requirements for reliable, versatile and ultrafast separations, the synthesis of stationary phases has been systematically improved in this work. This is of course valid for both achiral and chiral methods, but with gaining knowledge about, e.g., chiral biomarkers in the fields of -omics and the implementation of chiral methods in multidimensional LC, the need for fast and reliable chiral methods is especially high.

Since the knowledge gained about chiral separations is not intended to serve as isolated discipline and end in itself but can be used as a problem-solving tool in many related disciplines, several side-projects were performed in this work. Chiral separation techniques helped in the structural elucidation of unknown compounds and the chiral purification of new drug candidates. In addition, these techniques were exploited for the enantiopurification of a radiotracer that is highly useful in cancer therapy. The fact that numerous related projects were completed and problems solved once again demonstrates the importance of chiral chromatographic methods and the dovetailing of (chiral) HPLC analytics with a variety of related (sub)disciplines. It would be desirable if this thesis could act as a meaningful piece in the big puzzle of science and understanding, and contain answers to previously open questions.

Table of Figures

Fig. 1: Chirality is occurring everywhere in natural systems, from elementary particles over molecules and living systems to galaxies. At the top: Snail shell as macroscopic example for chirality in nature (own photography). Underneath: DNA helix as example for supramolecular chirality. Below: Quinine (1*S*, 3*R*, 4*S*, 8*S*, 9*R*) and quinidine (1*S*, 3*R*, 4*S*, 8*R*, 9*S*) as example for molecular chirality. At the bottom: Quotation on asymmetry by L. Pasteur (1900) [7]. 26

Figure 2: a) Depicts the different entities of surface chemistries on a bare silica particle. b) Shows typical functionalization resp. derivatization forms of silica. c) Indicates a non-optimal, chaotic surface functionalization with detrimental effect on the column performance..... 39

References

- [1] R. Bentley, Chiral: A confusing etymology, *Chirality*, 22 (2010) 1-2.
- [2] G.P. Moss, Basic terminology of stereochemistry (IUPAC Recommendations 1996), *Pure Appl. Chem.*, 68 (1996) 2193-2222.
- [3] B. Testa, P.-A. Carrupt, J. Gal, The so-called “interconversion” of stereoisomeric drugs: An attempt at clarification, *Chirality*, 5 (1993) 105-111.
- [4] F. Devínsky, Chirality and the Origin of Life, *Symmetry*, 13 (2021) 2277.
- [5] M. Liu, L. Zhang, T. Wang, Supramolecular Chirality in Self-Assembled Systems, *Chem. Rev.*, 115 (2015) 7304-7397.
- [6] T. Matsuura, H. Koshima, Introduction to chiral crystallization of achiral organic compounds: Spontaneous generation of chirality, *J. Photochem. Photobiol. C: Photochem. Rev.*, 6 (2005) 7-24.
- [7] P. Debré, in: Louis Pasteur, The Johns Hopkins University Press, Baltimore, MD, USA, 1998, pp. 78.
- [8] D.G. Blackmond, The Origin of Biological Homochirality, *Cold Spring Harb Perspect Biol*, 11 (2019) a032540.
- [9] P.A. Lehmann F, J.F. Rodrigues de Miranda, E.J. Ariëns, Stereoselectivity and Affinity in Molecular Pharmacology, in: E. Jucker (Ed.) *Progress in Drug Research/Fortschritte der Arzneimittelforschung/Progrés des recherches pharmaceutiques*, Birkhäuser Basel, Basel, 1976, pp. 101-142.
- [10] M. Eichelbaum, Side effects and toxic reactions of chiral drugs: A clinical perspective, in: G.H. Degen, J.P. Seiler, P. Bentley (Eds.) *Toxicology in Transition*, Springer Berlin Heidelberg, Berlin, Heidelberg, 1995, pp. 514-521.
- [11] H. Cao, M.W. Wang, L.X. Sun, T. Ikejima, Z.Q. Hu, W.H. Zhao, Pharmacodynamic comparison of pantoprazole enantiomers: inhibition of acid-related lesions and acid secretion in rats and guinea-pigs, *J. Pharm. Pharmacol.*, 57 (2005) 923-927.
- [12] C. Sánchez, The Pharmacology of Citalopram Enantiomers: The Antagonism by R-Citalopram on the Effect of S-Citalopram, *Basic Clin. Pharmacol. Toxicol.*, 99 (2006) 91-95.
- [13] H. Downes, R.S. Perry, R.E. Ostlund, R. Karler, A study of the excitatory effects of barbiturates, *J. Pharmacol. Exp. Ther.*, 175 (1970) 692-699.
- [14] E.J. Ariëns, Stereochemistry: A source of problems in medicinal chemistry, *Med. Res. Rev.*, 6 (1986) 451-466.
- [15] T. Eriksson, S. Björkman, B. Roth, Å. Fyge, P. Höuglund, Stereospecific determination, chiral inversion in vitro and pharmacokinetics in humans of the enantiomers of thalidomide, *Chirality*, 7 (1995) 44-52.
- [16] R.L. Smith, S.C. Mitchell, Thalidomide-type teratogenicity: structure–activity relationships for congeners, *Toxicol. Res.*, 7 (2018) 1036-1047.
- [17] G.T. Tucker, Chiral switches, *Lancet*, 355 (2000) 1085-1087.
- [18] G. Hancu, A. Modroiu, Chiral Switch: Between Therapeutical Benefit and Marketing Strategy, *Pharmaceuticals*, 15 (2022) 240.
- [19] M. Morvan, I. Mikšik, Recent Advances in Chiral Analysis of Proteins and Peptides, *Separations*, 8 (2021).
- [20] C. Argyriou, M.D. D'Agostino, N. Braverman, Peroxisome biogenesis disorders, *Transl. Sci. Rare Dis.*, 1 (2016) 111-144.
- [21] E.P. Altova, I. Hargittai, Mikhail S. Tsvet—pioneer of chromatography—150 years from his birth, *Struct. Chem.*, (2021).
- [22] Y. Okamoto, M. Kawashima, K. Hatada, Chromatographic resolution. 7. Useful chiral packing materials for high-performance liquid chromatographic resolution of enantiomers: phenylcarbamates of polysaccharides coated on silica gel, *J. Am. Chem. Soc.*, 106 (1984) 5357-5359.
- [23] D.W. Armstrong, T.J. Ward, R.D. Armstrong, T.E. Beesley, Separation of Drug Stereoisomers by the Formation of β -Cyclodextrin Inclusion Complexes, *Science*, 232 (1986) 1132-1135.

- [24] D.W. Armstrong, Y. Tang, S. Chen, Y. Zhou, C. Bagwill, J.-R. Chen, Macrocyclic Antibiotics as a New Class of Chiral Selectors for Liquid Chromatography, *Anal. Chem.*, 66 (1994) 1473-1484.
- [25] Y. Machida, H. Nishi, K. Nakamura, H. Nakai, T. Sato, Enantiomer separation of amino compounds by a novel chiral stationary phase derived from crown ether, *J. Chromatogr. A*, 805 (1998) 85-92.
- [26] V.A. Davankov, S.V. Rogozhin, Ligand chromatography as a novel method for the investigation of mixed complexes: stereoselective effects in α -amino acid copper(II) complexes, *J. Chromatogr. A*, 60 (1971) 280-283.
- [27] M. Lämmerhofer, W. Lindner, Quinine and quinidine derivatives as chiral selectors I. Brush type chiral stationary phases for high-performance liquid chromatography based on cinchonan carbamates and their application as chiral anion exchangers, *J. Chromatogr. A*, 741 (1996) 33-48.
- [28] M. Lämmerhofer, Chiral recognition by enantioselective liquid chromatography: mechanisms and modern chiral stationary phases, *J. Chromatogr. A*, 1217 (2010) 814-856.
- [29] C. Fernandes, J. Teixeira, M.M.M. Pinto, M.E. Tiritan, Strategies for Preparation of Chiral Stationary Phases: Progress on Coating and Immobilization Methods, *Molecules*, 26 (2021) 5477.
- [30] B. Chankvetadze, Recent trends in preparation, investigation and application of polysaccharide-based chiral stationary phases for separation of enantiomers in high-performance liquid chromatography, *Trends Anal. Chem.*, 122 (2020) 115709.
- [31] J. Shen, T. Ikai, Y. Okamoto, Synthesis and application of immobilized polysaccharide-based chiral stationary phases for enantioseparation by high-performance liquid chromatography, *J. Chromatogr. A*, 1363 (2014) 51-61.
- [32] M. Kawamura, T. Uchiyama, T. Kuramoto, Y. Tamura, K. Mizutani, Formation of a cyclinulooligosaccharide from inulin by an extracellular enzyme of *Bacillus circulans* OKUMZ 31B, *Carbohydr. Res.*, 192 (1989) 83-90.
- [33] P. Sun, C. Wang, Z.S. Breitbach, Y. Zhang, D.W. Armstrong, Development of New HPLC Chiral Stationary Phases Based on Native and Derivatized Cyclofructans, *Anal. Chem.*, 81 (2009) 10215-10226.
- [34] E.A. Agathokleous, I.J. Stavrou, C. Kapnissi-Christodoulou, Comparison of cyclofructan-, cyclodextrin-, and polysaccharide-based chiral stationary phases for the separation of pharmaceuticals, *Anal. Bioanal. Chem.*, 414 (2022) 1323-1333.
- [35] R. Berkecz, G. Némethi, A. Péter, I. Ilisz, Liquid Chromatographic Enantioseparations Utilizing Chiral Stationary Phases Based on Crown Ethers and Cyclofructans, *Molecules*, 26 (2021) 4648.
- [36] L.R. Sousa, G.D.Y. Sogah, D.H. Hoffman, D.J. Cram, Host-guest complexation. 12. Total optical resolution of amine and amino ester salts by chromatography, *J. Am. Chem. Soc.*, 100 (1978) 4569-4576.
- [37] C.J. Pedersen, Cyclic polyethers and their complexes with metal salts, *J. Am. Chem. Soc.*, 89 (1967) 2495-2496.
- [38] R. Berkecz, I. Ilisz, A. Misicka, D. Tymecka, F. Fülöp, H.J. Choi, M.H. Hyun, A. Péter, HPLC enantioseparation of β 2-homoamino acids using crown ether-based chiral stationary phase, *J. Sep. Sci.*, 32 (2009) 981-987.
- [39] S.-H. Wu, C.-Y. Mou, H.-P. Lin, Synthesis of mesoporous silica nanoparticles, *Chem. Soc. Rev.*, 42 (2013) 3862-3875.
- [40] P.J. Dutton, T.M. Fyles, S.J. McDermid, Synthesis and metal ion complexation behavior of polycarboxylate 18-crown-6 ethers derived from tartaric acid, *Can. J. Chem.*, 66 (1988) 1097-1108.
- [41] D.W. Armstrong, W. DeMond, Cyclodextrin Bonded Phases For the Liquid Chromatographic Separation of Optical, Geometrical, and Structural Isomers, *J. Chromatogr. Sci.*, 22 (1984) 411-415.
- [42] D.W. Armstrong, L.W. Chang, S.C. Chang, X. Wang, H. Ibrahim, G.R. Reid†, Iii, T.E. Beesley, Comparison of the Enantioselectivity of β -Cyclodextrin vs. Heptakis-2,3-O-dimethyl- β -cyclodextrin LC Stationary Phases, *J. Liq. Chromatogr. Relat. Technol.*, 20 (1997) 3279-3295.
- [43] V.A. Davankov, A.V. Semechkin, Ligand-exchange chromatography, *J. Chromatogr. A*, 141 (1977) 313-353.

- [44] E.R. Francotte, Enantioselective chromatography as a powerful alternative for the preparation of drug enantiomers, *J. Chromatogr. A*, 906 (2001) 379-397.
- [45] C.V. Hoffmann, M. Lämmerhofer, W. Lindner, Novel strong cation-exchange type chiral stationary phase for the enantiomer separation of chiral amines by high-performance liquid chromatography, *J. Chromatogr. A*, 1161 (2007) 242-251.
- [46] C.V. Hoffmann, R. Pell, M. Lämmerhofer, W. Lindner, Synergistic Effects on Enantioselectivity of Zwitterionic Chiral Stationary Phases for Separations of Chiral Acids, Bases, and Amino Acids by HPLC, *Anal. Chem.*, 80 (2008) 8780-8789.
- [47] J.J. van Deemter, F.J. Zuiderweg, A. Klinkenberg, Longitudinal diffusion and resistance to mass transfer as causes of nonideality in chromatography, *Chem. Eng. Sci.*, 5 (1956) 271-289.
- [48] J.E. Meisner, R.F. Rushmer, Eddy Formation and Turbulence in Flowing Liquids, *Circ. Res.*, 12 (1963) 455-463.
- [49] F. Gritti, D.S. Bell, G. Guiochon, Particle size distribution and column efficiency. An ongoing debate revived with 1.9 μ m Titan-C18 particles, *J. Chromatogr. A*, 1355 (2014) 179-192.
- [50] F. Gritti, T. Farkas, J. Heng, G. Guiochon, On the relationship between band broadening and the particle-size distribution of the packing material in liquid chromatography: Theory and practice, *J. Chromatogr. A*, 1218 (2011) 8209-8221.
- [51] C. Dewaele, M. Verzele, Influence of the particle size distribution of the packing material in reversed-phase high-performance liquid chromatography, *J. Chromatogr. A*, 260 (1983) 13-21.
- [52] D. Cabooter, A. Fanigliulo, G. Bellazzi, B. Allieri, A. Rottigni, G. Desmet, Relationship between the particle size distribution of commercial fully porous and superficially porous high-performance liquid chromatography column packings and their chromatographic performance, *J. Chromatogr. A*, 1217 (2010) 7074-7081.
- [53] F. Gritti, G. Guiochon, Mass transfer kinetics, band broadening and column efficiency, *J. Chromatogr. A*, 1221 (2012) 2-40.
- [54] S. Golshan-Shirazi, G. Guiochon, Comparison of the various kinetic models of non-linear chromatography, *J. Chromatogr. A*, 603 (1992) 1-11.
- [55] S. Deridder, G. Desmet, New insights in the velocity dependency of the external mass transfer coefficient in 2D and 3D porous media for liquid chromatography, *J. Chromatogr. A*, 1227 (2012) 194-202.
- [56] F. Gritti, G. Guiochon, Mass transfer mechanism in chiral reversed phase liquid chromatography, *J. Chromatogr. A*, 1332 (2014) 35-45.
- [57] O.H. Ismail, A. Ciogli, C. Villani, M. De Martino, M. Pierini, A. Cavazzini, D.S. Bell, F. Gasparrini, Ultra-fast high-efficiency enantioseparations by means of a teicoplanin-based chiral stationary phase made on sub-2 μ m totally porous silica particles of narrow size distribution, *J. Chromatogr. A*, 1427 (2016) 55-68.
- [58] P. Gzil, N. Vervoort, G.V. Baron, G. Desmet, General Rules for the Optimal External Porosity of LC Supports, *Anal. Chem.*, 76 (2004) 6707-6718.
- [59] C. Horvath, H.-J. Lin, Band spreading in liquid chromatography: General plate height equation and a method for the evaluation of the individual plate height contributions, *J. Chromatogr. A*, 149 (1978) 43-70.
- [60] J.H. Knox, Practical Aspects of LC Theory, *J. Chromatogr. Sci.*, 15 (1977) 352-364.
- [61] J.C. Giddings, Evidence on the Nature of Eddy Diffusion in Gas Chromatography from Inert (Nonsorbing) Column Data, *Analytical Chemistry*, 35 (1963) 1338-1341.
- [62] G.J. Kennedy, J.H. Knox, The Performance of Packings in High Performance Liquid Chromatography (HPLC) I. Porous and Surface Layered Supports, *J. Chromatogr. Sci.*, 10 (1972) 549-556.
- [63] U. Tallarek, E. Bayer, G. Guiochon, Study of Dispersion in Packed Chromatographic Columns by Pulsed Field Gradient Nuclear Magnetic Resonance, *J. Am. Chem. Soc.*, 120 (1998) 1494-1505.
- [64] E.M. Borges, Silica, Hybrid Silica, Hydride Silica and Non-Silica Stationary Phases for Liquid Chromatography, *J. Chromatogr. Sci.*, 53 (2014) 580-597.

- [65] S. Bocian, B. Buszewski, Residual silanols at reversed-phase silica in HPLC – a contribution for a better understanding, *J. Sep. Sci.*, 35 (2012) 1191-1200.
- [66] C.R. Adams, High Temperature Stability of Silica-Base Gels, *J. Phys. Chem.*, 67 (1963) 313-318.
- [67] W. Stöber, A. Fink, E. Bohn, Controlled growth of monodisperse silica spheres in the micron size range, *J. Colloid Interface Sci.*, 26 (1968) 62-69.
- [68] K.K. Unger, R. Skudas, M.M. Schulte, Particle packed columns and monolithic columns in high-performance liquid chromatography-comparison and critical appraisal, *J. Chromatogr. A*, 1184 (2008) 393-415.
- [69] L. Nováková, L. Matysová, P. Solich, Advantages of application of UPLC in pharmaceutical analysis, *Talanta*, 68 (2006) 908-918.
- [70] I. Halasz, C. Horvath, Micro Beads Coated with a Porous Thin Layer as Column Packing in Gas Chromatography. Some Properties of Graphitized Carbon Black as the Stationary Phase, *Anal. Chem.*, 36 (1964) 1178-1186.
- [71] J.J. DeStefano, T.J. Langlois, J.J. Kirkland, Characteristics of Superficially-Porous Silica Particles for Fast HPLC: Some Performance Comparisons with Sub-2- μm Particles, *J. Chromatogr. Sci.*, 46 (2008) 254-260.
- [72] J.J. Kirkland, S.A. Schuster, W.L. Johnson, B.E. Boyes, Fused-core particle technology in high-performance liquid chromatography: An overview, *J. Pharm. Anal.*, 3 (2013) 303-312.
- [73] S. Fekete, D. Guillarme, M. Dong, Superficially Porous Particles: Perspectives, Practices, and Trends, *LCGC N. Am.*, 32 (2014) 420-433.
- [74] K. Broeckhoven, D. Cabooter, G. Desmet, Kinetic performance comparison of fully and superficially porous particles with sizes ranging between 2.7 μm and 5 μm : Intrinsic evaluation and application to a pharmaceutical test compound, *J. Pharm. Anal.*, 3 (2013) 313-323.
- [75] M. Catani, O.H. Ismail, F. Gasparrini, M. Antonelli, L. Pasti, N. Marchetti, S. Felletti, A. Cavazzini, Recent advancements and future directions of superficially porous chiral stationary phases for ultrafast high-performance enantioseparations, *Analyst*, 142 (2017) 555-566.
- [76] F. Gritti, G. Guiochon, Theoretical investigation of diffusion along columns packed with fully and superficially porous particles, *J. Chromatogr. A*, 1218 (2011) 3476-3488.
- [77] B.M. Wagner, S.A. Schuster, B.E. Boyes, T.J. Shields, W.L. Miles, M.J. Haynes, R.E. Moran, J.J. Kirkland, M.R. Schure, Superficially porous particles with 1000Å pores for large biomolecule high performance liquid chromatography and polymer size exclusion chromatography, *J. Chromatogr. A*, 1489 (2017) 75-85.
- [78] I. Novák, B. Buszewski, C. Garaj, D. Berek, Influence of pore structure of silica packing on HPLC column characteristics, *Chem. Papers*, 44 (1990) 31-43.
- [79] J. Nawrocki, The silanol group and its role in liquid chromatography, *J. Chromatogr. A*, 779 (1997) 29-71.
- [80] G. Busca, Catalytic materials based on silica and alumina: Structural features and generation of surface acidity, *Prog. Mater. Sci.*, 104 (2019) 215-249.
- [81] C. Sögaard, J. Funehag, Z. Abbas, Silica sol as grouting material: a physio-chemical analysis, *Nano Converg.*, 5 (2018) 6.
- [82] V. Dugas, Y. Chevalier, Surface hydroxylation and silane grafting on fumed and thermal silica, *J. Colloid Interface Sci.*, 264 (2003) 354-361.
- [83] L.T. Zhuravlev, The Surface Chemistry of Amorphous Silica. Zhuravlev Model, *Colloids Surf. A: Physicochem. Eng. Asp.*, 173 (2000) 1-38.
- [84] Y. Duval, J.A. Mielczarski, O.S. Pokrovsky, E. Mielczarski, J.J. Ehrhardt, Evidence of the Existence of Three Types of Species at the Quartz–Aqueous Solution Interface at pH 0–10: XPS Surface Group Quantification and Surface Complexation Modeling, *J. Phys. Chem. B*, 106 (2002) 2937-2945.
- [85] X. Liu, J. Cheng, X. Lu, R. Wang, Surface acidity of quartz: understanding the crystallographic control, *Phys. Chem. Chem. Phys.*, 16 (2014) 26909-26916.
- [86] M. Sulpizi, M.-P. Gaigeot, M. Sprik, The Silica–Water Interface: How the Silanols Determine the Surface Acidity and Modulate the Water Properties, *J. Chem. Theory Comput.*, 8 (2012) 1037-1047.

- [87] K.K. Unger, *Porous Silica - its properties and use as support in column liquid chromatography*, Elsevier, Amsterdam, 1979.
- [88] H. Engelhardt, C. Blay, J. Saar, *Reversed Phase Chromatography – the Mystery of Surface Silanols*, *Chromatographia*, 62 (2005) s19-s29.
- [89] J. Xue, X. Domingo-Almenara, C. Guijas, A. Palermo, M.M. Rinschen, J. Isbell, H.P. Benton, G. Siuzdak, *Enhanced in-Source Fragmentation Annotation Enables Novel Data Independent Acquisition and Autonomous METLIN Molecular Identification*, *Anal. Chem.*, 92 (2020) 6051-6059.
- [90] Z. Lei, D.V. Huhman, L.W. Sumner, *Mass spectrometry strategies in metabolomics*, *J. Biol. Chem.*, 286 (2011) 25435-25442.
- [91] M. Elyashberg, *Identification and structure elucidation by NMR spectroscopy*, *Trends Anal. Chem.*, 69 (2015) 88-97.
- [92] W.F. Reynolds, Chapter 29 - *Natural Product Structure Elucidation by NMR Spectroscopy*, in: S. Badal, R. Delgoda (Eds.) *Pharmacognosy*, Academic Press, Boston, 2017, pp. 567-596.
- [93] K.R. Westphal, M.I. Werner, K.A. Nielsen, J.L. Sørensen, V. Andrushchenko, J. Winde, M. Hertz, M.A. Jensen, M.L. Mortensen, P. Bouř, T.E. Sondergaard, R. Wimmer, *Characterization of Eight Novel Spiroleptosols from Fusarium avenaceum*, *Molecules*, 24 (2019).
- [94] O. Cala, F. Guillièrè, I. Krimm, *NMR-based analysis of protein–ligand interactions*, *Anal. Bioanal. Chem.*, 406 (2014) 943-956.
- [95] C. Boesch, *Nobel prizes for nuclear magnetic resonance: 2003 and Historical perspectives*, *J. Magn. Reson. Imaging*, 20 (2004) 177-179.
- [96] D.A.L. Otte, D.E. Borchmann, C. Lin, M. Weck, K.A. Woerpel, *¹³C NMR spectroscopy for the quantitative determination of compound ratios and polymer end groups*, *Org. Lett.*, 16 (2014) 1566-1569.
- [97] T.H. Mareci, K.N. Scott, *Quantitative analysis of mixtures by carbon-13 nuclear magnetic resonance spectrometry*, *Anal. Chem.*, 49 (1977) 2130-2136.
- [98] K. Wüthrich, *Protein structure determination in solution by NMR spectroscopy*, *J. Biol. Chem.*, 265 (1990) 22059-22062.
- [99] J. Hoffmann, J. Ruta, C. Shi, K. Hendriks, V. Chevelkov, W.T. Franks, H. Oschkinat, K. Giller, S. Becker, A. Lange, *Protein resonance assignment by BSH-CP-based 3D solid-state NMR experiments: A practical guide*, *Magn. Reson. Chem.*, 58 (2020) 445-465.
- [100] M. Luhmer, J.B. d'Espinose, H. Hommel, A.P. Legrand, *High-resolution ²⁹Si solid-state NMR study of silicon functionality distribution on the surface of silicas*, *Magn. Reson. Imaging*, 14 (1996) 911-913.
- [101] S.E. Ashbrook, P. Hodgkinson, *Perspective: Current advances in solid-state NMR spectroscopy*, *J. Chem. Phys.*, 149 (2018) 040901.
- [102] E.R. Andrew, A. Bradbury, R.G. Eades, *Nuclear Magnetic Resonance Spectra from a Crystal rotated at High Speed*, *Nature*, 182 (1958) 1659-1659.
- [103] I.J. Lowe, *Free Induction Decays of Rotating Solids*, *Phys. Rev. Lett.*, 2 (1959) 285-287.
- [104] F. Nardelli, S. Borsacchi, L. Calucci, E. Carignani, F. Martini, M. Geppi, *Anisotropy and NMR spectroscopy*, *Rend. Lincei Sci. Fis. Nat.*, 31 (2020) 999-1010.
- [105] B. Reif, S.E. Ashbrook, L. Emsley, M. Hong, *Solid-state NMR spectroscopy*, *Nat. Rev. Methods Primers*, 1 (2021) 2.

3 Results and Discussion

3.1 Accepted Manuscripts – Part One: Development of Chiral Stationary Phases

3.1.1 Publication I: **Evaluation of superficially porous particle based zwitterionic chiral ion exchangers against fully porous particle benchmarks for enantioselective ultra-high performance liquid chromatography**

Christian Geibel^a, Kristina Schmitt^a, Ulrich Woiwode^a, Michal Kohout^b, Tong Zhang^c,
Wolfgang Lindner^{d,e}, Michael Lämmerhofer^{a,*}

^a Institute of Pharmaceutical Sciences, Pharmaceutical (Bio-)Analysis, University of Tübingen, Auf der Morgenstelle 8, 72076 Tübingen, Germany

^b Department of Organic Chemistry, University of Chemistry and Technology, Prague, Czech Republic

^c Chiral Technologies Europe, 160 Boulevard Gonthier d'Andernach, 67400 Illkirch-Graffenstaden, France

^d Lindner Consulting GmbH, Ziegelofengasse 37, 3400 Klosterneuburg, Austria

^e Institute of Analytical Chemistry, University of Vienna, Waehringerstrasse 38, 1090 Vienna, Austria

* Corresponding author. E-mail address: michael.laemmerhofer@uni-tuebingen.de (M. Lämmerhofer)

Journal of Chromatography A **2019**, 1603, 130-140.

DOI: 10.1016/j.chroma.2019.06.026

Authors of Elsevier articles retain the right to include it in a thesis
or dissertation without further permission.

© 2019 Elsevier B.V.



Evaluation of superficially porous particle based zwitterionic chiral ion exchangers against fully porous particle benchmarks for enantioselective ultra-high performance liquid chromatography

Christian Geibel^a, Kristina Dittrich^a, Ulrich Woiwode^a, Michal Kohout^b, Tong Zhang^c, Wolfgang Lindner^{d,e}, Michael Lämmerhofer^{a,*}

^a Institute of Pharmaceutical Sciences, Pharmaceutical (Bio-)Analysis, University of Tübingen, Auf der Morgenstelle 8, 72076 Tübingen, Germany

^b Department of Organic Chemistry, University of Chemistry and Technology, Prague, Czech Republic

^c Chiral Technologies Europe, 160 Boulevard Gonthier d'Andernach, 67400 Illkirch, Graffenstaden, France

^d Lindner Consulting GmbH, Ziegelofengasse 37, 3400 Klosterneuburg, Austria

^e Institute of Analytical Chemistry, University of Vienna, Waehringerstrasse 38, 1090 Vienna, Austria



ARTICLE INFO

Article history:

Received 4 May 2019

Received in revised form 10 June 2019

Accepted 10 June 2019

Available online 14 June 2019

Keywords:

Chiral stationary phase

Core-shell particle

Fully porous particle

Chiral separation

Effective medium theory

Kinetic performance

Kinetic plot

ABSTRACT

Zwitterionic chiral ion-exchange selectors (ZWIX) obtained by conjugation of quinine and 2-aminocyclohexanesulfonic acid via a carbamate bond were immobilized on three different silica particle types, viz. 120 Å 3 μm fully porous particles (FPP), 200 Å 3 μm FPP and 160 Å 2.7 μm superficially porous particles (SPP). Selector densities were determined by elemental analysis and the porosities of packed columns measured by inverse size exclusion chromatography with polystyrene standards. Liquid chromatographic tests with a set of chiral zwitterionic, acidic and basic analytes showed that the surface chemistry was successfully transferred to the distinct particle morphologies. The chromatographic performance of the three columns was evaluated by acquiring van Deemter curves. The results showed that the column packed with the SPP particles gives the best performance and kinetic plots further demonstrated that they represent the most favorable compromise in terms of speed, efficiency and pressure drop. Sub-minute separations could be accomplished at much lower pressure drop on the core-shell column, e.g. 2-amino-2-phenylbutyric acid was baseline separated in less than 15 s on a 5 cm long column. The Maxwell effective medium theory with second order approximation was applied to calculate effective diffusion in the mesoporous zones of SPP and FPP, which allowed eventually to deconvolute the individual peak dispersion contributions (h_a , h_b , $h_{c,m}$, $h_{c,s}$, $h_{c,ads}$). The efficiency gain of the 160 Å SPP column compared to the 120 Å FPP (benchmark) column was mainly due to lower eddies (h_a), smaller c -term accounting for slow adsorption-desorption kinetics in enantioselective chromatography ($h_{c,ads}$), and also due to lower stationary mass transfer resistance ($h_{c,s}$). Enhanced effective diffusion (D_{eff}) in the SPP column contributed to a lower longitudinal diffusion (h_b). In contrast, the mobile phase mass transfer coefficient was similar in the two columns leading to comparable $h_{c,m}$ contributions. This study discloses some options for improvement of the efficiency of ZWIX-type chiral columns such as replacing narrow pore (120 Å) by wide pore (200 Å) particles, substituting FPP by SPP and reducing the selector density on the surface.

© 2019 Elsevier B.V. All rights reserved.

1. Introduction

Enantioselective liquid chromatography (LC) is an analytical technology which is of major importance in drug discovery, pharmaceutical research, food chemistry, agricultural and envi-

ronmental sciences. For its implementation, both the choice of a chiral selector as well as the choice of a certain particle design is crucial when deciding for a column to separate chiral analytes. A large variety of chiral stationary phases (CSPs) utilized nowadays for this purpose were developed in the late 1980s and early 1990s [1], and are based on chiral selectors comprising proteins [2], polysaccharides [3], macrocyclic antibiotics [4], cyclodextrins [5], cyclofructans [6], chiral crown ethers [7,8], synthetic selectors with donor-acceptor capabilities (e.g. Whelk-O1 CSP) [9], chiral lig-

* Corresponding author.

E-mail address: michael.laemmerhofer@uni-tuebingen.de (M. Lämmerhofer).

and exchange selectors [10], and chiral ion-exchangers e.g. derived from cinchonan carbamates [11,12].

Since enantiomer separation usually requires resolution of only two peaks per chromatogram, there has been a great deal to make these separations faster. For long time this was most conveniently achieved by operating chiral columns with supercritical or subcritical fluids as eluents (SFC) [13]. This is still an established methodology in pharmaceutical industry for fast screening [13]. As early as mid 1990s, nonporous silica particles (1.5 μm) were evaluated as support for CSPs. Due to a low surface area and a low total porosity of such columns, separations in subminute time scale could be achieved [14–16]. Plate numbers, however, were lower than expected (ca. 70,000 per m) probably due to instrumentation that was not optimized for such columns and suboptimal packing. The advent of UHPLC technology in 2004 and the introduction of sub-2 μm fully porous silica particles (FPP) paved the way to fast LC in subminute time scale. However, its realization and implementation in enantioselective LC took until 2010 [17]. Further works on CSPs based on sub-2 μm for enantioselective UHPLC followed [18–23] and meanwhile sub-2 μm particle based CSPs are commercially available (e.g. polysaccharide CSPs) [24].

Since 2006, promoted by Kirkland and co-workers [25,26] reengineered core-shell particles experienced a renaissance. So-called core-shell or superficially porous particles (SPP) consist of an impermeable core and a porous shell. The particles designed by Kirkland et al., and used herein, had a solid core with 1.7 μm diameter and a 0.5 μm thick shell, which results in 2.7 μm superficially porous particles [26]. Those particles showed a favorable performance regarding the efficiency-speed-backpressure compromise [27]. The gain in efficiency of SPP was reported to be due to lower A-term [28], also, a decreased longitudinal diffusion (B-term) by roughly 20% [25], and a reduced mass transfer resistance (C-term) due to shortened diffusion pathways inside the particles [28]. First chiral core-shell particle CSPs based on quinine/quinidine carbamate derived chiral anion exchangers were reported in 2011 [29]. Subsequently, polysaccharide [30–32], macrocyclic antibiotics [6,33,34], cyclodextrin [33,35], cyclodextran [6,33] based SPP CSPs were reported. Much of the most recent work in this field was devoted to the evaluation of the performance gain of chiral SPP columns [20,36,37], addressing the question which of the modern particles performs better SPP or sub-2 μm FPP [6,38] as well as deconvolution of the peak dispersion contributions in these modern particles [37,38]. Furthermore, it was shown in a series of articles that chiral LC and SFC separations can be performed in sub-minute and even subsecond time scales with these modern “chiral” particles [39–41] which facilitates their implementation in 2D LC analysis concepts [42–44].

In spite of the proven benefit, various chiral selectors of commercially available chiral columns have not yet been evaluated on modern particle designs. This includes zwitterionic chiral ion-exchangers (ZWIX) obtained by merging cinchonan carbamates (quinine or quinidine) with 2-aminocyclohexanesulfonic

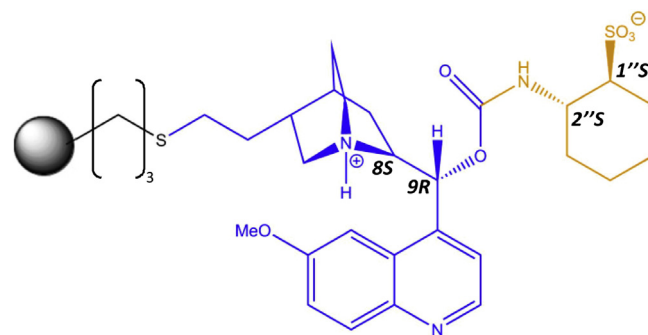


Fig. 1. Structure of the zwitterionic ion exchange CSP (ZWIX(+)). The selector is assembled from a quinine carbamate chiral anion-exchange moiety (blue coloured) and a (1*S*,2*S*)-*trans*-2-aminocyclohexanesulfonic acid cation exchange site (For interpretation of the references to colour in this figure legend, the reader is referred to the web version of this article.).

acid (ACHSA). As this ZWIX selector features both cationic and anionic chiral moieties in its structure, it enables separation of zwitterionic, acidic and basic chiral analytes with short analysis times due to both attractive and repulsive electrostatic forces acting simultaneously [12]. In this work, a benchmark 120 Å 3 μm FPP ZWIX(+) column (in which the chiral selector is assembled from quinine carbamate and (S,S)-ACHSA) (Fig. 1) is compared to a 3 μm FPP column with wider pores (200 Å) as well as to a 2.7 μm SPP column with 160 Å pores (solid core is 1.7 μm). The latter particle morphology turned out as the best compromise in terms of efficiency, speed and column back pressure in a recent study on quinine carbamate based weak anion-exchange CSPs [37]. Wide pore SPP CSP with 160 Å pore size exhibited a lower mass transfer resistance (C-term) over 90 Å SPP CSP. Thus, in this work these three silica particle morphologies with comparable particle diameter were evaluated against each other based on van Deemter analysis and kinetic performance evaluation, respectively, to address the scientific question to what extent the two new alternative particle morphologies can provide better chromatographic performances. Kinetic plots have been generated and a temperature dependency study was carried out besides determination of permeability parameters and porosities.

2. Experimental

2.1. Materials

Zwitterionic ion-exchange CSPs, with structure as shown in Fig. 1, were synthesized by immobilizing the zwitterionic chiral selector (denoted as ZWIX(+)), which was obtained from (1*S*,2*S*)-*trans*-2-aminocyclohexanesulfonic acid and quinine, on three distinct types of silica particles according to the procedure described in ref [12]. Specifications of the CSPs and corresponding

Table 1
Summary and characteristics of tested ZWIX(+) CSPs and columns, respectively.

CSP	d_p ¹	pore size ²	specific surface area	selector coverage ³		column dimensions	porosities			permeability	
	[μm]			[$\mu\text{m}^2/\text{g}$]	[$\mu\text{mol}/\text{g}$]		[$\mu\text{mol}/\text{m}^2$]	[L x ID mm]	ε_t	ε_e	ε_i
ZWIX(+) FPP, 3 μm , 120 Å	3.2	125	337	215 ⁴	0.64 ⁴	150 × 3	0.648	0.369	0.279	8.61	150
ZWIX(+) FPP, 3 μm , 200 Å	2.9	212	210	142	0.67	150 × 3	0.714	0.378	0.335	8.69	135
ZWIX(+) SPP, 2.7 μm , 160 Å	2.7	156	77	86	1.12	50 × 3	0.553	0.391	0.162	6.18	190

¹ Particle size as determined by silica supplier.

² Modal pore size as specified by silica supplier.

³ Selector coverage calculation based on nitrogen amount determined by elemental analysis.

⁴ Surface coverage as specified for experimental prototypes of ZWIX phases (see Ref. [12]).

columns are summarized in Table 1. Further materials and analytes as specified in Supplementary [45,46].

2.2. Instrumentation

For the LC experiments, a UHPLC system of the Agilent 1290 Infinity series from Agilent Technologies (Waldbronn, Germany) was used. The system featured a binary pump, an autosampler, a thermostatted column compartment (TCC) and a diode array detector (DAD). To reduce extra-column volume, the flow cell of the DAD was replaced by a Max-Light ultralow dispersion cartridge flow cell with a volume of 0.6 μl . Furthermore, needle seat assembly was replaced by ultralow dispersion needle seat assembly (1 μl injected). Capillaries from autosampler to TCC and from TCC to DAD were replaced by MavelX capillaries from Idex Corporation (Lake Forest, Illinois, USA) with an inner diameter of 0.075 mm each and a length of 350 mm (autosampler to TCC) and 250 mm (TCC to DAD), ensuring minimal dead volumes right before and after the column. Extra column volume was measured isocratically with a zero dead-volume union instead of a column and was determined to be 11 μl . The extra-column peak variance was 13 μl^2 determined by the second moment method.

2.3. Determination of permeability parameters

The column permeability coefficient K_V was calculated by Darcy's law according to Eq. (1a) [47]

$$K_V = \frac{u_s \cdot \eta \cdot L}{\Delta P} \quad (1a)$$

In this equation, u_s indicates the superficial velocity, calculated by $u_s = \frac{F}{\pi r^2}$ (with F being the volumetric flow rate), η stands for the dynamic viscosity. The determination of the permeability was carried out with the final optimized mobile phase consisting of methanol and 50 mM formic acid as well as 25 mM ammonia as additives. As dynamic viscosity of methanol, a value of $\eta = 0.544$ mPa·s at 30 °C was assumed. ΔP was determined by subtracting the system backpressure, measured with zero-dead volume union, from the backpressure observed with installed column.

The Kozeny-Carman constant K_C was calculated in accordance to ref [38] with porosity data from inverse size exclusion chromatography (ISEC) (see Suppl.) by equation 1b

$$K_C = \frac{\varepsilon_e^3}{(1 - \varepsilon_e)^2} \cdot \frac{d_p^2}{K_V} \quad (1b)$$

2.4. Van Deemter analysis

For the sake of determination of the performance of each column, separation of 2-amino-2-phenylbutyric acid (APBA) was carried out. Column performance was tested for different mobile phases and temperatures to identify optimal chromatographic conditions (see Suppl., Table S1 for details). Volumetric flow rates for the recording of van Deemter curves ranged between 0.015 ml/min and 2.5 ml/min, always taking care that a maximum pressure of 800 bar was not exceeded. For definitions see Supplementary.

2.5. Determination of A-, B- and C-term

The individual coefficients of the van Deemter equation (see Suppl., Eq. S6a), i.e. eddy dispersion (A-term), longitudinal dispersion (B-term), and mass transfer resistance (C-term), were determined by curve fitting using Origin (OriginPro 2018). Additionally, the contribution of longitudinal diffusion to peak broadening was determined independently, using an approach in which H_B was derived at very small flow rates, as reported by

Andrés et al. [47]. The increase in peak broadening at very low linear velocities is basically a result of the B-term contribution while mass transfer resistance is more or less neglectable. For the B-term determination, the three slowest flow rates of the H/u curve recording have been chosen (0.05 ml/min, 0.025 ml/min as well as 0.015 ml/min). The plate height equivalent of the B-term decreases inversely proportional to the linear flow rate u_0 (calculated from elution time of unretained tracer by $u_0 = L/t_0$) [47] in accordance to Eq. (2).

$$H = H_B + H_A \text{ with } H_B = \frac{2 \cdot D_{eff}}{u_0} \cdot (1 + k) \quad (2)$$

Since k (phase retention factor) was known, D_{eff} , the effective diffusion coefficient in the packed bed, could be obtained from the slope of a plot of H vs $1/u_0$ at the three slowest flow rates (with the intercept providing an approximation of H_A). D_{eff} in turn is related to the molecular diffusion coefficient in free solution D_m , via the coefficient γ_{eff} (effective longitudinal diffusion) ($D_{eff} = \gamma_{eff} \cdot D_m$) [47].

2.6. Kinetic plots

For a more holistic characterization of the columns, kinetic plots have been constructed from data acquired during H/u curve recording [47]. The Poppe plot provides a way of creating a column length independent way to generate a kinetic plot. To do so, the plate time calculated from void time of the column (t_0) divided by the plate number (N) (t_0/N) was plotted against N, using the following two equations [48]:

$$N = \frac{\Delta P}{\eta} \cdot \left(\frac{K_V}{u_s H} \right) \quad (3)$$

$$\frac{t_0}{N} = \frac{\varepsilon_t H}{u_s} \quad (4)$$

In this, ΔP is defined as the highest possible (acceptable) pressure drop and was set herein to 800 bar. The total porosity (as shown in Table 1) is defined as ε_t , u_s is defined as the superficial linear velocity.

2.7. Deconvolution of individual peak dispersion contributions by effective medium theory

The second order effective medium theory (EMT) expression, as described by Deridder and Desmet was used to calculate the C_m and C_s mass transfer terms which are related to mass transfer resistance in the interstitial space and the particle space. However, as discussed by Gritti and Guiochon [49] as well as Cavazzini and coworkers [21,50], in enantioselective chromatography the slow mass transfer kinetics of adsorption and desorption cannot be neglected and significantly contribute to peak dispersion as well so that the van Deemter equation in reduced terms reads as follows (Eq. (5)).

$$h = h_a + h_b + h_{c,m} + h_{c,s} + h_{c,ads} \quad (5)$$

In a more explicit form this equation can be written as Eq. (6).

$$h = h_a + \frac{2\gamma_{eff}(1+k')}{v_i} + 2 \frac{k'^2}{(1+k')^2} \frac{v_i}{\alpha} \frac{1}{Sh_m} \frac{1}{1-\varepsilon_e} + 2 \frac{k'}{(1+k')^2} \frac{v_i}{\alpha} \frac{1}{Sh_{part}} \frac{D_m}{D_{pz}} + h_{c,ads} \quad (6)$$

wherein Sh_m and Sh_{part} , respectively, are dimensionless numbers which represent the mobile zone and particle zone mass transfer coefficients (known as Sherwood numbers), α is a (particle) shape factor (6 for a spherical particle), D_{pz} is the diffusion coefficient

in the porous zone and k' is the zone retention factor. The exact definitions and calculations, respectively, of these parameters can be found in [47].

The determination of the h_b term was described above. The h_a term can be independently determined by coupling theory of eddy dispersion as discussed by Gritti and Guiochon [49]. For sake of simplicity, it was estimated herein with the non-retained marker TTBB by applying Eq. (6) assuming that $h_{c,ads}$ is 0 due to absence of stationary phase interactions allowing the deconvolution of the a-term contribution. For the retained APBA enantiomers, the y-intercept from the B-term determination (a_0) (eq. 2) was combined with the slope of the a-term curve of TTBB (a_1) to assess roughly the a-term by $h_a = a_0 + a_1 \cdot v$. The $h_{c,m}$ and $h_{c,s}$ terms (3rd and 4th term in Eq. (6)) were calculated by the corresponding expressions of the general plate height model in Eq. (6) proposed first by Lapidus and Amundson as described in detail by Desmet and coworkers [47]. Porous particle diffusion coefficient (D_{part}) and porous zone diffusion coefficient (D_{pz}) in fully porous and superficially porous particles, respectively, were determined in accordance to Desmet and coworkers [47,51,52] following the Maxwell EMT model using second order effective medium theory expression. Thus, the diffusion inside the particle D_{part} was obtained by Eq (7).

$$D_{part} = \frac{\alpha_{part}(1 - \varepsilon_e)}{\varepsilon_T(1 + k) - \varepsilon_e} D_m \quad (7)$$

To solve this equation, the relative permeability of spherical particles α_{part} must be known which is related to the polarizability constant β_1 by Eq. (8).

$$\alpha_{part} = \frac{1 + 2\beta_1}{1 - \beta_1} \quad (8)$$

In the following, the 2nd order accuracy expression was used for β_1 (Eq. 53a in [52] with $B = 2 \cdot \gamma_{eff} \cdot (1 + k')$) (Eq. (9)).

$$\beta_1 = \frac{(\varepsilon_e - 1)(4 + B\varepsilon_T) + \sqrt{(4 + B\varepsilon_T)^2(1 - \varepsilon_e)^2 + 8\varepsilon_e \zeta_2 (B\varepsilon_T - 2)^2}}{4\varepsilon_e \zeta_2 (B\varepsilon_T - 2)} \quad (9)$$

As discussed by Andrés et al, the EMT theory allows to deconvolute the effect of the porous and impermeable zones in core-shell particles [47]. Thus, the diffusion coefficient in the mesoporous zone of the core-shell particle (D_{pz}) can be calculated by Eq. (10).

$$D_{pz} = \frac{2 + \rho^3}{2} D_{part} \quad (10)$$

wherein ρ is the core to particle diameter. For the deconvolution of the c_s -term of Eq. (6), the Sherwood number of the stationary phase particles is needed. It adopts a value of 10 for fully porous particles and can be calculated by Eq. (11) for core-shell particles.

$$Sh_{part} = \frac{4}{3} \cdot \frac{1 - \rho^3}{\frac{2}{15} - \frac{2}{3}\rho^3 + \frac{6}{5}\rho^5 - \frac{2}{3}\rho^6} \quad (11)$$

The dimensionless mobile zone mass transfer coefficient (Sherwood number Sh_m) was calculated in accordance to ref [51] by Eq. (12) and represents a simplification for random packed beds which is only valid within the range of $0.35 < \varepsilon_e < 0.44$ and $1 < v_i < 250$.

$$Sh_m = \frac{13}{(1 + 2.1 \cdot v_i)} + 8.6 \cdot v_i^{0.21} \quad (12)$$

3. Results and discussion

3.1. Column properties characterization and comparison

All CSPs were synthesized according to published protocols [12] and slurry packed into stainless columns. Column proper-

ties are summarized in Table 1. It can be seen that the actual modal particle diameters (as provided by the silica suppliers) were within a narrow range (2.7–3.2 μm) and the actual modal pore size distributions were close to their nominal values. An important characteristic of the CSPs is their selector coverage. When comparing the selector coverages, it is striking that the SPP column has a higher selector density on the surface (see Table 1, selector coverages in $\mu\text{mol}/\text{m}^2$), but the total selector content grafted per unit mass is much lower than for the two FPP CSPs. The lower specific surface area of the superficially porous particles is readily explainable by the particular particle morphology with their thin porous layer covering a non-penetrable core (in this case: core 1.7 μm , shell: 0.5 μm) [37]. A higher surface density of selector on SPP vs corresponding FPP CSPs has also been reported in other studies [53]. One possible explanation for this finding is that pores deep inside FPP are difficult to reach by the selector during surface modification reaction and as a result the bonding density is on average (as measured by elemental analysis) significantly lower than in SPP materials which do not have pores buried deeply inside the particle because this space is occupied by the impermeable core. Taking into account that a superficially porous particle shows a higher density due to its solid core, the higher selector coverage per area unit while at the same time showing a lower selector coverage per mass unit is easily explainable.

Porosities were determined by ISEC (see Suppl.). All columns show external porosities ε_e in the range of 0.37 to 0.39 which conforms to the literature values (0.35 – 0.40) [54]. As anticipated, the 200 Å pore-sized FPP CSP exhibits the highest internal porosity ε_i (particle porosity). Due to the impermeable core, the particle porosity of the SPP CSP is significantly lower (0.162 compared to 0.335 for the 200 Å FPP CSP). For the same reason, the total porosity is much lower for the SPP CSP (0.553 vs 0.714 for the comparable 200 Å FPP CSP) which should lead to considerably smaller void volume and along with the lower total surface area in the column to much faster separations.

The permeability factors K_v of the three columns lie in narrow margins, as expected from their similar particle diameter. While the two FPP CSP columns showed identical permeabilities, the SPP ZWIX column exhibited a slightly lower K_v , which could indicate a more homogeneously therefore more densely packed bed. Particle size distributions of the Halo SPP 2.7 μm material are narrower than of common 3 μm particles and the modal diameter is slightly smaller [26]. The Kozeny-Carman constant K_C (Table 1) indicates the highest flow resistance of the SPP column and the lowest resistance of the wide pore FPP column.

3.2. Comparison of retention and selectivity characteristics

The commercial Chiralpak ZWIX(+) is supplied with a test chromatogram of 2-amino-2-phenylbutyric acid (APBA) obtained using acetonitrile/methanol/water (49/49/2; v/v/v) with 50 mM formic acid and 25 mM diethylamine. Since reduced plate heights with these conditions were slightly lower than theoretically expected optimal values, it was decided to firstly optimize the mobile phase before starting the column comparison. A variety of conditions were screened employing the 5 cm long SPP ZWIX(+) column and the results are given in Supplementary Table S1. Replacement of diethylamine by ammonia, omitting water and substituting the acetonitrile/methanol mixture for entirely methanolic conditions provided a slight but significant improvement of both efficiencies and peak symmetries. With this optimized mobile phase (methanol containing 50 mM FA and 25 mM ammonia) plate numbers of around 132,000 per m could be achieved at 0.5 ml/min and was used for further experiments.

First, for the characterization of the surface chemistry of the new wide pore FPP and SPP CSPs and thereof in comparison to the

Table 2
Summary of chromatographic data on different ZWIX(+) type CSPs for various chiral analytes.

	ZWIX(+) 2.7 μm , SPP 160 Å			ZWIX(+) 3 μm , FPP 200 Å			ZWIX(+) 3 μm , FPP 120 Å		
	k_1	α	R	k_1	α	R	k_1	α	R
APBA	0.42	1.45	2.54	0.32	1.50	3.05	0.72	1.53	4.70
Tryptophan	1.39	1.47	3.25	0.94	1.25	1.40	2.53	1.65	6.87
Ac-Phe	0.33	1.37	1.74	0.09	1.26	0.63	0.33	1.49	2.91
DNP-Me-Leu	0.90	1.22	1.71	0.17	1.25	0.97	1.12	1.26	3.07
DNP-Pro	1.52	1.19	0.86	0.34	1.18	0.61	1.85	1.26	1.73
Fmoc-Phe	0.96	1.44	3.14	0.26	1.31	1.84	1.16	1.48	4.86
DNB-Leu	0.46	7.04	13.30	0.17	5.07	10.07	0.63	8.02	26.22
Mefloquine	0.49	6.33	8.79	0.92	2.75	10.76	1.26	11.09	19.16

Ac, acetyl; DNB, *N*-(3,5-dinitrobenzoyl); DNP, *N*-(2,4-dinitrophenyl); Fmoc, *N*-[(9H-Fluoren-9-ylmethoxy)carbonyl]; APBA, 2-amino-2-phenylbutyric acid. Conditions: Mobile phase, methanol containing 50 mM FA +25 mM NH_3 ; T, 30 °C, flow rate, 0.5 mL/min.

Table 3
Chromatographic results and column performance of ZWIX(+) chiral stationary phases for the test compound APBA. N_{max}/m corresponds to the plate number per m at optimal flow rate. Column dimensions: 150 x 3 mm (both 3 μm FPP), 50 x 3 mm (2.7 μm SPP), 30 °C.

CSP	APBA							
	$N_{\text{max},1}/m$	$N_{\text{max},2}/m$	$H_{\text{min},1}$ [μm]	$H_{\text{min},2}$ [μm]	$h_{\text{min},1}$ [l]	$h_{\text{min},2}$ [l]	$u_{\text{opt},1}$ [mm/s]	
FPP, 3 μm , 120 Å	71,507	73,747	13.98	13.56	4.37	4.24	0.96	
FPP, 3 μm , 200 Å	77,893	78,013	12.84	12.82	4.43	4.42	2.18	
SPP, 2.7 μm , 160 Å	141,540	143,960	7.07	6.95	2.62	2.57	0.90	

Table 4
Summary of determined values for A-, B- and C-terms as well as reduced values.

CSP	peak	A-term ^a [μm]	B-term ^a [mm^2s^{-1}]	B-term ^b [mm^2s^{-1}]	C-term ^a [ms]	reduced values		
						a	b	c
						ZWIX(+) FPP, 3 μm , 120 Å	1	11.33 ± 0.43
	2	10.32 ± 0.37	1.72 ± 0.07	0.72 ± 0.01	2.05 ± 0.056	3.22 ± 0.12	1.16 ± 0.05	0.30 ± 0.01
ZWIX(+) FPP, 3 μm , 200 Å	1	10.61 ± 0.27	1.80 ± 0.05	0.95 ± 0.01	0.842 ± 0.038	3.66 ± 0.09	1.22 ± 0.04	0.15 ± 0.01
	2	10.09 ± 0.23	1.88 ± 0.04	1.00 ± 0.01	0.979 ± 0.032	3.48 ± 0.08	1.27 ± 0.03	0.17 ± 0.01
ZWIX(+) SPP, 2.7 μm , 160 Å	1	6.46 ± 0.40	1.22 ± 0.07	1.06 ± 0.02	0.690 ± 0.044	2.39 ± 0.15	0.82 ± 0.05	0.14 ± 0.01
	2	5.96 ± 0.38	1.30 ± 0.07	1.06 ± 0.03	0.835 ± 0.042	2.21 ± 0.14	0.88 ± 0.05	0.17 ± 0.01

^a Determined by curve fitting in accordance to Van Deemter eq.

^b Determined by measurement of H at very low flow rates.

120 Å, 3 μm FPP ZWIX(+) CSP, the thermodynamics-related parameters (retention factor k , separation factor α) of the three ZWIX CSPs were evaluated for a diverse set of chiral acidic, basic and zwitterionic test compounds (Table 2). Retention factors of the wide pore 200 Å FPP ZWIX material are significantly lower than of the corresponding 120 Å FPP CSP due to a lower specific surface area available in the column. The same is valid for the SPP ZWIX column which has even lower interaction surface, yet the effect is partly compensated for by a higher selector density. On the other hand, it becomes evident that the separation factors are to a large extent similar on the three ZWIX phases which are based on different particle morphologies. It indicates a successful transfer of the surface chemistry to different silica particles. Exemplary chromatograms of enantiomer separations of a chiral zwitterionic compound (APBA), a chiral acid (FMOC-Phe), and a chiral base (mefloquine) on the three distinct ZWIX CSPs are given in Fig. 2.

3.3. Comparison of kinetic performance

H/u curves of zwitterionic APBA were recorded for the three columns with the optimized mobile phase (see section 3.2) and the results are shown in Fig. 3a and in reduced coordinates in Fig. 3b (see Table 3 and 4 for calculated performance parameters and Van Deemter coefficients, respectively). Here, it can be seen that the benchmark column (3 μm FPP with 120 Å pore size, blue symbols) shows the highest plate heights and therefore the lowest efficiencies. Upon increasing the pore size of the FPP CSP to 200 Å the effective diffusion coefficient in the porous bed is significantly elevated which leads to a slight increase of the B-term and a strong

reduction of the C-term (i.e. a flatter H/u curve) (Table 4). The maximal theoretical plate number of the wide pore FPP was nearly the same, yet the optimum was observed at much higher linear flow velocities (Table 3).

A further improvement in chromatographic efficiencies was observed for the 160 Å 2.7 μm SPP CSP (core-shell particle CSP). The H/u curves for the separation of APBA, indicate clearly a better performance of the tested SPP column over the other columns. H_{min} is with 6.9 μm (for peak 2 at a linear velocity of 0.90 mm/s) almost bisected (41% lower) in comparison to FPP 200 Å (12.8 μm for peak 2 at a linear velocity of 2.18 mm/s) and 44% lower in comparison to the benchmark column (13.6 μm for peak 2 at a linear velocity of 0.96 mm/s). Thus, the maximal plate numbers were nearly doubled with SPP in spite of the similar particle diameter. Minimal reduced theoretical plate heights in the order of 2.6 could be achieved (Table 3). The gain in performance with this particle type over the benchmark (120 Å 3 μm FPP CSP) is a combined effect of a lower A-term (eddy dispersion), presumably due to a better packed bed, slightly lower B-term (due to the impermeable core) and in particular a (more than factor 2) lower C-term (wider pores, better effective diffusion) (Table 4).

The above discussion focused on the efficiency of the columns and the flow velocity dependency of the major contributions to peak dispersion. Kinetic plots on the other hand may provide additional information on the relationship between efficiencies and speed taking the back pressure into account. A column length-independent Poppe plot (plate time t_0/N vs N) was generated assuming a maximum pressure drop of 800 bar (Fig. 4). The vertical asymptote indicates the theoretically maximal feasible plate

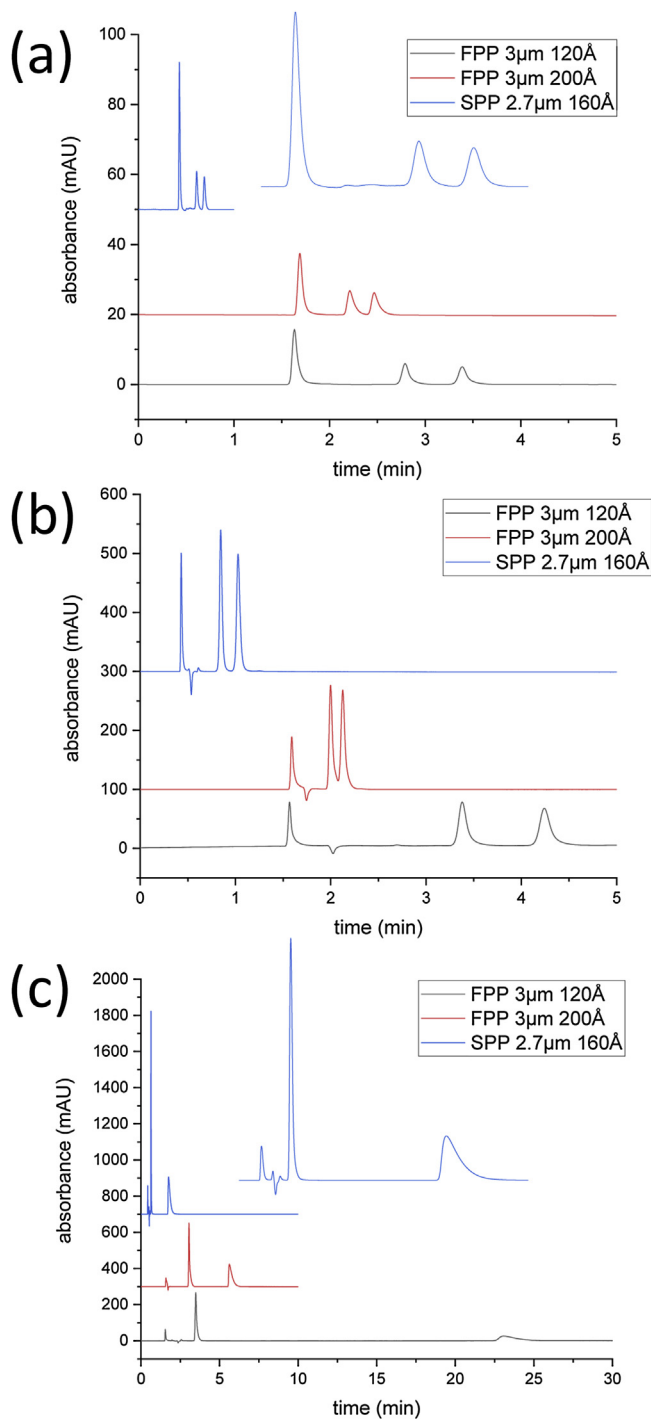


Fig. 2. Exemplary chromatograms obtained on the different columns showing enantiomer separations of (a) zwitterionic analyte APBA, (b) acidic analyte Fmoc-Phe, and (c) basic analyte mefloquine. Benchmark 120 Å 3 µm FPP (black, bottom), 200 Å 3 µm FPP (red, middle), and 160 Å 2.7 µm SPP (blue, top). For column dimensions, see Table 1. All chromatograms were recorded at a linear velocity of 3.0 mm/s; mobile phase, methanol with 50 mM formic acid and 25 mM ammonia as additives; temperature, 30 °C (For interpretation of the references to colour in this figure legend, the reader is referred to the web version of this article.).

number on a column under these constraints. Since it is particle diameter dominated, all three curves overlap in this range. On the other hand, the horizontal asymptote provides information on the kinetic performance in the C-term dominated region. It is evident that the wide pore FPP CSP can perform separations faster than the benchmark (120 Å 3 mm FPP ZWIX CSP) at equal performance and

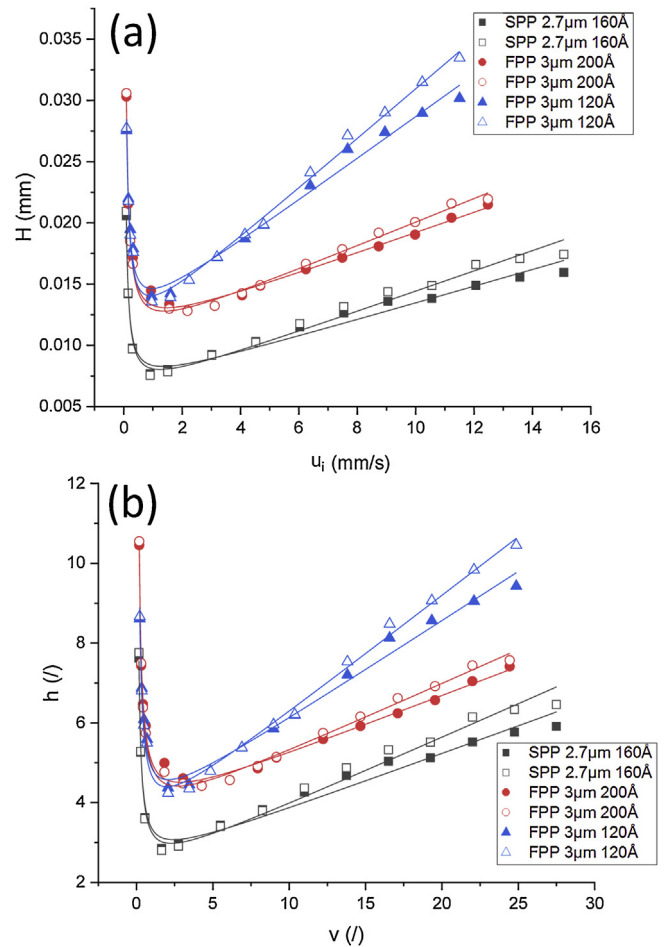


Fig. 3. Van Deemter curves generated with the three tested columns. Analyte was APBA. (a) H/u curves and (b) h/v curves (van Deemter in reduced coordinates). Open signs indicate the first eluted peak, filled signs stand for the second eluted peak. Separation took place at 30 °C with methanol plus 50 mM formic acid and 25 mM ammonia as additives. 120 Å 3 µm FPP benchmark (blue), 200 Å 3 µm FPP (red), 160 Å 2.7 µm SPP (black) (For interpretation of the references to colour in this figure legend, the reader is referred to the web version of this article.).

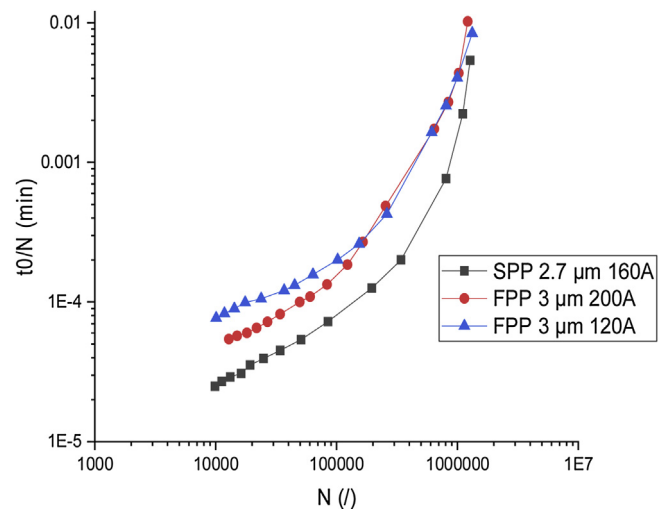


Fig. 4. Kinetic (Poppe) plots for the three tested columns. 120 Å 3 µm FPP benchmark (blue), 200 Å 3 µm FPP (red), 160 Å 2.7 µm SPP (black) (For interpretation of the references to colour in this figure legend, the reader is referred to the web version of this article.).

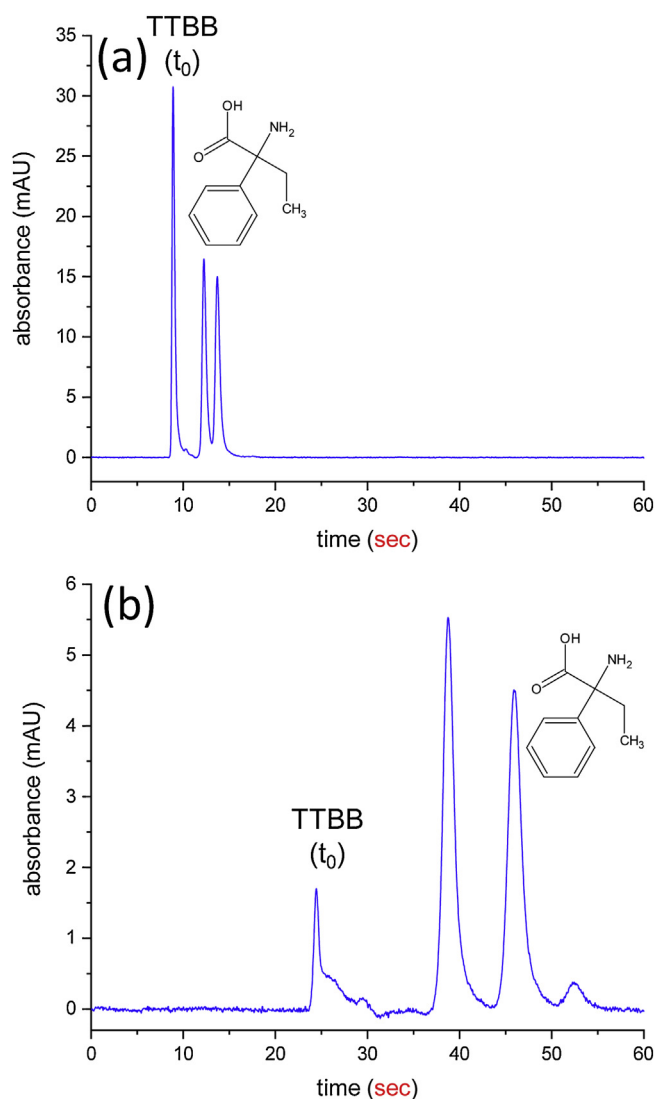


Fig. 5. Fast (sub-minute) enantiomer separations on (a) 160 Å 2.7 μm SPP ZWIX column and (b) 120 Å 3 μm FPP benchmark. Conditions: (a) Column dimension, 50 × 3 mm ID; temperature, 30 °C; flow rate, 1.5 ml/min; ΔP = 339 bar (incl. system back pressure). (b) Column dimension, 150 × 3 mm; temperature, 30 °C; flow rate, 2.0 ml/min; ΔP = 793 bar (incl. System back pressure). Mobile phase, MeOH + 50 mM formic acid + 25 mM NH₃.

the 160 Å 2.7 μm SPP CSP outperforms both of the tested FPP CSPs in this regard. Fast separations in sub-minute time frame can be readily accomplished, even on a short 5 cm column. APBA enantiomers could be resolved in about 15 s on the SPP column (Fig. 5a). However, also on the 120 Å 3 μm FPP column sub-minute separations are possible (Fig. 5b). In conclusion, the superficially porous particle containing column outperformed the FPP columns in terms of speed and exhibit interesting properties for fast separations as required in high-throughput applications and 2-dimensional separations.

3.4. Temperature dependency of column performance

The 2.7 μm 160 Å SPP column was more thoroughly investigated by a temperature dependency study of the column performance. The optimized mobile phase was used which was composed of methanol with 50 mM FA and 25 mM ammonia. To evaluate the temperature dependence of the A-, B- and C-terms, four different H/u curves were recorded with varying temperatures from 10 to

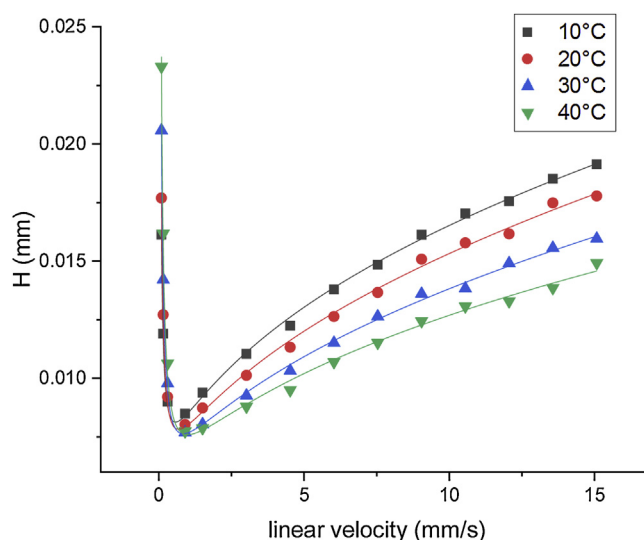


Fig. 6. H/u curves (fitted by Knox model) of second eluted peak acquired at different temperatures. All curves were recorded with APBA with methanol + 50 mM formic acid and 25 mM ammonia as additives. As column, SPP 2.7 μm 160 Å was used.

40 °C in 10K steps under otherwise identical conditions. Results are shown in Fig. 6.

It can be seen in Fig. 6 that the H/u curves are shifted to a lower y-offset thus leading to higher plate numbers with increase in column temperature as expected. A closer look indicates that H_{min} gets smaller by raising the temperature. Surprisingly, u_{opt} does not change to higher flow rates. To decipher those effects, A-, B-, and C-terms were estimated by curve fitting (Table 5). It documents that the B-term increases by a factor of more than 2 by rising the temperature from 10 to 40 °C. However, this is counteracted by a decrease of the C-term (factor 1.35) due to more efficient diffusional mass transfer in the mobile and stationary phase and accelerated adsorption/desorption rate constants at higher temperature. Interestingly, the A-term is decreased as well (factor 1.27) when the temperature is raised from 10 to 40 °C. This effect can be explained by enhanced radial diffusion which compensates for flow inhomogeneities between distinct tortuous flow paths (Fig. 7).

3.5. Deconvolution of individual peak dispersion contributions by effective medium theory (EMT)

The deconvolution of peak dispersion contributions in achiral and enantioselective LC was described in a number of studies [21,25,38,47,49,55]. We previously adopted the EMT approach, described in refs [47,52,56] for enantioselective anion-exchange LC [37].

The splitting into the distinct peak dispersion contributions started with the determination of the h_b term. Usually peak parking is used to determine effective diffusion D_{eff} in presence of the packing and the B-term, respectively. However, in the current situation the parked peak eluted right after the solvent front after mobilization of the analyte zone which made it error-prone. For this reason, D_{eff} was obtained from measurement of plate heights at very small flow rates. The three lowest flow rates were employed for this purpose. C-term contributions are negligible at such conditions, and hence plots of H vs $1/u_0$ allowed the calculation of D_{eff} from the slope in accordance to eq. 2. h_b was then calculated by the expression of the 2nd term of Eq. (6). A considerable difficulty arises for the independent measurement of the a-term. Recently, Gritti and Guiochon discussed the approximation of the h_d term by coupling theory of eddy dispersion [49]. For sake of simplicity, Catani et al. suggested to approximate this contribution by measur-

Table 5

Summary of determined values for A-, B- and C-terms and corresponding reduced values depending on the temperature. All values recorded on ZWIX(+) SPP, 2.7 μm , 160 \AA (all data for the first eluted peak of APBA by curve fitting in accordance to Van Deemter eq.).

Temperature [$^{\circ}\text{C}$]	A-term	B-term	C-term	a	b	c
	[μm]	[mm^2s^{-1}]	[10^{-4}s]	/	/	/
10	7.87 ± 0.48	0.67 ± 0.09	8.16 ± 0.53	2.92 ± 0.18	0.45 ± 0.06	0.17 ± 0.01
20	7.12 ± 0.42	0.89 ± 0.08	7.73 ± 0.47	2.64 ± 0.16	0.60 ± 0.05	0.16 ± 0.01
30	6.46 ± 0.40	1.22 ± 0.07	6.89 ± 0.44	2.39 ± 0.15	0.82 ± 0.05	0.14 ± 0.01
40	6.18 ± 0.32	1.51 ± 0.05	6.03 ± 0.35	2.29 ± 0.12	1.02 ± 0.04	0.12 ± 0.01

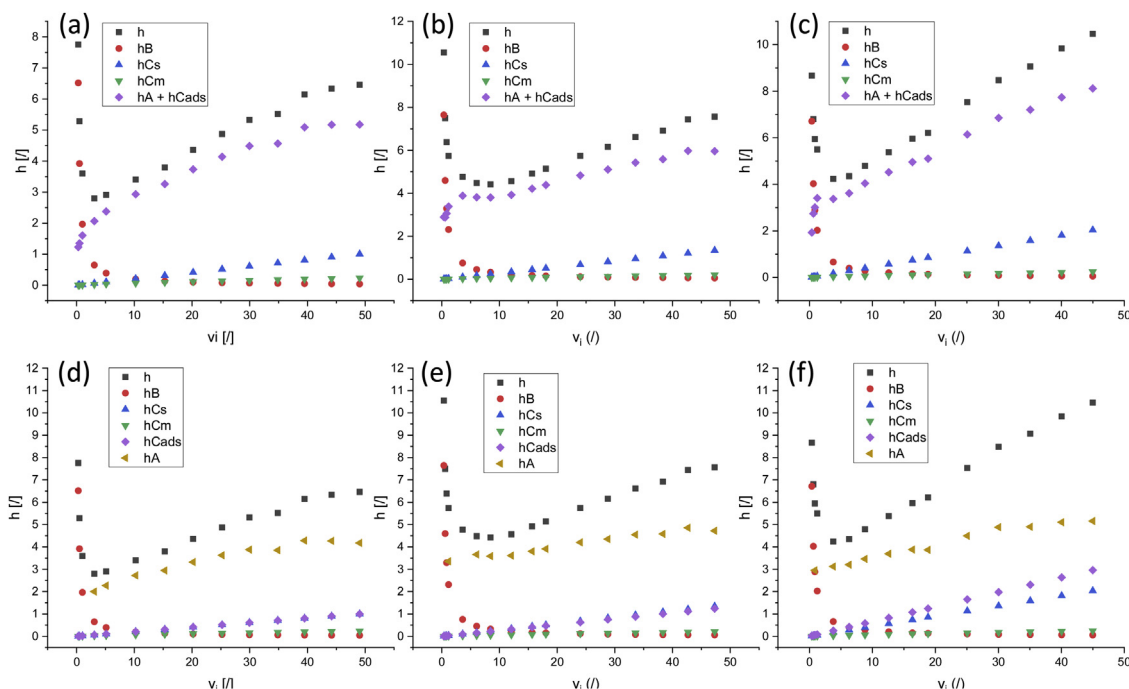


Fig. 7. Van Deemter curves and deconvoluted contributions to peak dispersion of 2nd eluted peak of APBA on various ZWIX CSP columns. (a–c) with combined h_a and $h_{c,ads}$, and (d–f) deconvoluted h_a and $h_{c,ads}$. (a,d) 160 \AA 2.7 μm SPP, (b,e) 200 \AA 3 μm FPP, (c,f) 120 \AA 3 μm FPP. For corresponding coefficients see Table 6.

ing an achiral compound, devoid of interaction with the stationary phase and thus of c_{ads} contribution, eluted on the same column by otherwise same conditions [25]. We herein approximate h_a by combining results from two different experiments: The y-intercept from the B-term determination (a_0) for the respective enantiomer combined with the slope from the flow dependency curve of h_a for the non-retained TTBB (a_1), deconvoluted by Eq. (6) omitting the last c_{ads} term, may be regarded as a reasonable approximation for h_a by $h_a = a_0 + a_1 \cdot v$. Here it was assumed that the analyte molecules (APBA enantiomers) which are of similar size are subject of similar eddy dispersion that, in its reduced form, mainly depends on packing irregularities. The mobile and stationary phase mass transfer were calculated by the third and fourth term of Eq. (6). Here, the major difficulty exists in the estimation of β_1 (Eq. (8)) because it requires the use of a best fit value for ζ_2 (three point geometrical parameter) which depends strongly on the exact geometry of the bed that is not really known [57]. When D_{part} is large, the effect of ζ_2 is very small, but when D_{part} becomes very small (like common in enantioselective LC), an exact knowledge of the value of ζ_2 (typically in the range between 0.2 and 0.3) is more important for an accurate estimation of D_{part} [57]. Herein a ζ_2 value of 0.2 was used. With these estimates, $h_{c,m}$ and $h_{c,s}$ were calculated. It was pointed out by Gritti and Guiochon [49] and Cavazzini et al. [50] that the rate constant of adsorption-desorption is very small in enantioselective chromatography as compared to RP and is therefore not negligible as mass transfer resistance term. Thus, $h_{c,ads}$ was considered as well and obtained by subtraction of the other 4 already determined zone

dispersion contributions from the observed reduced plate height h in accordance to Eq. (5). The parameters used for the calculations and the results (D_{eff} , D_{pz} , D_{part} , and individual coefficients of van Deemter equation) are summarized in Table 6.

It can be seen that the effective diffusion coefficient D_{eff} in presence of the packed bed increases with the pore size of the underlying silica particles. It translates into b-terms in the order of 2.0 to 2.7 for APBA enantiomers being generally slightly lower for the SPP column (see Table 6). The mobile phase mass transfer coefficients c_m are relatively similar for the three columns which is not surprising considering the narrow range of external porosity values. A key parameter for the mass transfer coefficient in the stationary phase c_s is the effective diffusion coefficient in the mesoporous zone of the stationary phase D_{pz} . As can be seen from Table 6 this property significantly increases with the pore size when the two FPP ZWIX columns are compared. As a consequence, the stationary phase mass transfer coefficient is factor 1.6 lower on the 200 \AA wide pore compared to 120 \AA FPP ZWIX column. However, it is striking that D_{pz} of the SPP ZWIX column is significantly lower than for the 120 \AA narrow pore FPP, in spite of its pore size (160 \AA) between the two FPP ZWIX columns. While this appears counter-intuitive, it may be explained by the much higher selector density of the SPP ZWIX CSP (factor 1.5 compared to the FPP ZWIX CSPs) (see Table 1). The different particle morphology might also play a role. Surprisingly, the c_s -coefficient is even lower than the one of the 200 \AA FPP ZWIX column. The reason for that, most probably, are the much shorter diffusion paths in the SPP ZWIX CSP due to the solid

Table 6
Summary of column specific and peak dependent parameters used for the approximation of the peak dispersion contributions. For explanation, see footnotes (data reported for peak 2 obtained with APBA only; for TTBB and first peak of APBA see Suppl. Material).

#NAME?		2.7 μm 160 Å SPP	3 μm 200 Å FPP	3 μm 120 Å FPP
Column parameter				
d_{core}^1	[m]	1.70E-06	0.00E+00	0.00E+00
ρ^2	[/]	0.63	0.00	0.00
ε_e^3	[/]	0.391	0.378	0.369
ε_T^3	[/]	0.553	0.714	0.648
ε_i^3	[/]	0.162	0.335	0.279
k''_0	[/]	1.169	1.642	1.710
D_m^4	[m ² /s]	7.13E-10	7.13E-10	7.13E-10
ζ_2	[/]	2.00E-01	2.00E-01	2.00E-01
Sh_{part}^5	[/]	22.67	10.00	10.00
φ	[/]	0.81	0.40	0.54
APBA, peak 2				
γ_{eff}^6	[/]	0.442	0.491	0.340
D_{eff}^6	[m ² /s]	3.15E-10	3.50E-10	2.42E-10
k^7	[/]	0.603	0.476	1.101
k^{*7}	[/]	1.267	1.785	2.689
K	[/]	0.746	1.189	2.027
β_1^8	[/]	-0.417	-0.013	-0.105
α_{part}^8	[/]	0.117	0.960	0.715
D_{pz}^9	[m ² /s]	1.15E-10	6.30E-10	3.24E-10
D_{part}^9	[m ² /s]	1.02E-10	"= D_{pz} "	"= D_{pz} "
D_{pz}/D_m	[/]	0.161	0.884	0.455
D_{part}/D_m	[/]	0.143	"= D_{pz}/D_m "	"= D_{pz}/D_m "
b	[/]	2.006	2.732	2.510
c_m	[/]	0.0048	0.0043	0.0054
c_s	[/]	0.0205	0.0284	0.0454
c_{ads}	[/]	0.0204	0.0262	0.0658
k_p	[/]	3.860	2.360	5.238
$k_{\text{ads}}(D_m)$	[s ⁻¹]	1447	1200	643
$k_{\text{ads}}(D_{\text{pz}})$	[s ⁻¹]	233	1061	292

¹ d_{core} = diameter of the impermeable core (in FPP = 0).

² ρ = ratio core/particle diameter (not available for FPP).

³ ε_e = external porosity, ε_T = total porosity, ε_i = internal porosity.

⁴ D_m = molecular diffusion coefficient.

⁵ Sh_{part} = Sherwood number.

⁶ γ_{eff} = effective longitudinal diffusion, D_{eff} = effective diffusion coefficient.

⁷ k = phase retention factor, k^* = zone retention factor.

⁸ β_1 = polarizability constant, α_{part} = relative particle permeability.

⁹ D_{pz} = porous zone diffusion coefficient, D_{part} = intraparticle diffusion coefficient (in FPP, $D_{\text{pz}} = D_{\text{part}}$).

impermeable core (1.7 μm in diameter) and the thin mesoporous shell (0.5 μm thick) (core-to-particle ratio = 0.63). The mass transfer coefficient accounting for slow adsorption-desorption kinetics c_{ads} follows the same trends as described for the stationary phase mass transfer term (c_s). The narrow pores in the 120 Å FPP ZWIX CSPs have a detrimental effect on the exchange kinetics. The specific particle morphology of SPP ZWIX CSP appears to compensate for the higher selector density which was assumed to have a negative effect on the adsorption-desorption kinetics. To get a deeper insight into the dependency of the c_{ads} mass transfer resistance term on the rate constant of adsorption-desorption we adopt a model described previously by Gritti and Guiochon. They suggested a reduced coefficient c_{ads} derived from the Laplace transformation of the general rate model of chromatography (Eq. (13)) [49].

$$c_{\text{ads}} = 2 \frac{\varepsilon_e}{1 - \varepsilon_e} \frac{1}{1 - \varepsilon_i} \left(\frac{k'}{1 + k'} \right)^2 \left(\frac{k_p}{1 + k_p} \right)^2 \frac{1}{k_{\text{ads}}} \frac{D_m}{d_p^2} \quad (13)$$

with k_p is

$$k_p = \frac{1 - \varepsilon_i K}{\varepsilon_i} \quad (14)$$

wherein K is the mobile-stationary phase distribution coefficient which can be obtained by $k = \varphi \cdot K$ (φ is the phase ratio). After having obtained c_{ads} from the above deconvolution process, k_{ads} was calculated by Eq. (13) and (14). Values of k_{ads} for 2nd eluted enantiomer of APBA of 0.64 and $1.20 \times 10^3 \text{ s}^{-1}$ were obtained for 120 Å and 200 Å FPP CSPs, respectively, and $1.45 \times 10^3 \text{ s}^{-1}$ for the 160 Å

SPP CSP. From these results it appears that the rate constants are mainly dependent on the pore size which is most probably not true. From former experiments we know that the efficiency of CSPs is significantly altered with the selector density. In Eq. (13), the rate constants ($k_{\text{ads}}(D_m)$) are calculated with the free solution diffusion coefficient D_m . In fact, however, the practically relevant diffusion coefficient is the one measured in the mesoporous zone of the particles D_{pz} and should be preferably used in Eq. (13). Recalculation of the adsorption-desorption rate constant using D_{pz} , yields $k_{\text{ads}}(D_{\text{pz}}) = 2.92 \times 10^2$, 10.61×10^2 and $2.33 \times 10^2 \text{ s}^{-1}$ for 120 Å FPP CSP, 200 Å FPP CSP and 160 Å SPP CSP, respectively, for the 2nd eluted enantiomer of APBA. Now we see that the narrow pore FPP particles yield much slower exchange kinetics (factor 3.6). On the other hand, the much lower rate constant for the 160 Å SPP CSP compared to the 200 Å FPP CSP can be readily explained by the higher surface density of chiral selector. Overall, it becomes evident that the adsorption-desorption rate constants are very small for the present affinity type zwitterionic ion-exchange materials. This is in line with the discussion by Gritti and Guiochon that chiral chromatography is associated with a very slow adsorption-desorption kinetics with k_{ads} roughly between a few hundreds to a few thousands s^{-1} [49].

4. Conclusions

A benchmarking study with zwitterionic chiral ion exchangers (ZWIX) was carried out using commercially available narrow pore 3 μm fully porous particles (FPP) and CSPs based on two new par-

ticle types 200 Å 3 μm FPP and 160 Å 2.7 μm superficially porous particles (SPP). A comparison of separation factors revealed that the surface chemistry could be successfully transferred to the new particle types. Although some minor differences existed, the separation factors were largely comparable on the distinct ZWIX CSPs. The comparison of the columns with the optimized mobile phase showed a clear superiority of the SPP particles over FPP in terms of separation efficiencies. With H_{min} at 7.56 μm, the SPP column outperformed the benchmark by a 44% lower H_{min} (13.56 μm) and was 41% better than the second experimental column (200 Å 3 μm FPP with H_{min} at 12.82 μm).

Van Deemter curves were recorded for APBA as test analyte on the different columns. To gain a deeper insight into the peak dispersion contributions, the effective medium theory was applied to deconvolute individual C-term contributions. The improved performance of the 160 Å SPP CSP over the 120 Å FPP benchmark CSP was found to be a combined effect of i) a lower reduced a -term contribution: it seems that the core-shell particles are easier to pack and provide a more homogenous bed, ii) a slightly lower b -term, which is beneficial, especially in the low flow regime, due to an decreased effective diffusion coefficient (D_{eff}), iii) a factor 2.2 reduced c_s -term due to significantly shorter diffusion paths, and iv) a factor 3.2 lower C_{ads} -term also because only a fraction of the particle contributes to this dispersion increment.

In general, our data confirm that chiral recognition processes are associated with slow exchange kinetics due to a number of simultaneous multiple analyte-selector interactions and steric factors as well as peculiar dynamics of the process. While this slow association-dissociation of such molecular recognition is intrinsic to chiral recognition systems and cannot be overcome easily, the current work reveals some possibilities to improve the efficiency of ZWIX-type chiral columns such as replacing narrow pore (120 Å) by wide pore (200 Å) particles, substituting FPP by SPP and reducing the selector density on the surface.

Acknowledgement

We are grateful to Pilar Franco from Chiral Technologies Europe and T. Onishi from Daicel Corporation for packing prototype columns.

Appendix A. Supplementary data

Supplementary material related to this article can be found, in the online version, at doi:<https://doi.org/10.1016/j.chroma.2019.06.026>.

References

- [1] M. Lämmerhofer, Liquid chromatographic enantiomer separation with special focus on zwitterionic chiral ion-exchangers, *Anal. Bioanal. Chem.* 406 (2014) 6095–6103.
- [2] J. Hermansson, Liquid chromatographic resolution of racemic drugs using chiral α 1-acid glycoprotein column, *J. Chromatogr. A* 298 (1984) 67–78.
- [3] Y. Okamoto, M. Kawashima, K. Hatada, Useful chiral packing materials for high-performance liquid chromatographic resolution of enantiomers: phenylcarbamates of polysaccharides coated on silica gel, *J. Am. Chem. Soc.* 106 (1984) 5357–5359.
- [4] D.W. Armstrong, Y. Tang, S. Chen, Y. Zhou, C. Bagwill, J.-R. Chen, Macrocyclic antibiotics as a new class of chiral selectors for liquid chromatography, *Anal. Chem.* 66 (1994) 1473–1484.
- [5] D. Armstrong, T.J. Ward, R.D. Armstrong, T. Beesley, Separation of drug stereoisomers by the formation of B-cyclodextrin complexes, *Science* 232 (1986) 1132–1135.
- [6] D. Spudeit, M.D. Dolzan, Z. Breitbach, W.E. Barber, G. Mücke, D. Armstrong, Superficially porous particles vs. Fully porous particles for bonded high performance liquid chromatographic chiral stationary phases: isopropyl cyclofructan 6, *J. Chromatogr. A* 1363 (2014) 89–95.
- [7] Y. Machida, H. Nishi, K. Nakamura, H. Nakai, T. Sato, Enantiomer separation of amino compounds by a novel chiral stationary phase derived from crown ether, *J. Chromatogr. A* 805 (1998) 85–92.
- [8] M.H. Hyun, J. Sung Jin, W. Lee, Liquid chromatographic resolution of amino acids and their derivatives on a new chiral stationary phase based on crown ether, *J. Chromatogr. A* 822 (1998) 155–161.
- [9] W.H. Pirkle, C.J. Welch, B. Lamm, Design, synthesis, and evaluation of an improved enantioselective naproxen selector, *J. Org. Chem.* 57 (1992) 3854–3860.
- [10] V. Davankov, S.V. Rogozhin, Ligand chromatography as a novel method for the investigation of mixed complexes: stereoselective effects in α -Amino acid copper(II) complexes, *J. Chromatogr. A* 60 (1971) 280–283.
- [11] M. Lämmerhofer, W. Lindner, Quinine and quinidine derivatives as chiral selectors I. Brush type chiral stationary phases for high-performance liquid chromatography based on cinchonan carbamates and their application as chiral anion exchangers, *J. Chromatogr. A* 741 (1996) 33–48.
- [12] C.V. Hoffmann, R. Pell, M. Lämmerhofer, W. Lindner, Synergistic effects on enantioselectivity of zwitterionic chiral stationary phases for separations of chiral acids, bases, and amino acids by HPLC, *Anal. Chem.* 80 (2008) 8780–8789.
- [13] S. Khater, M.-A. Lozac'h, I. Adam, E. Francotte, C. West, Comparison of liquid and supercritical fluid chromatography mobile phases for enantioselective separations on polysaccharide stationary phases, *J. Chromatogr. A* 1467 (2016) 463–472.
- [14] U. Woiwode, S. Neubauer, M. Kaupert, W. Lindner, M. Lämmerhofer, Trends in enantioselective high performance liquid chromatography, special issue on recent developments in HPLC and UHPLC, Supplement to LCGC Europe/LCGC North America 30 (2017) 34–42.
- [15] V. Piette, M. Lämmerhofer, K. Bischoff, W. Lindner, HPLC Enantioseparation of N-protected amino acids using non-porous silica modified by a quinine carbamate as chiral stationary phase, *Chirality* 9 (1997) 157–161.
- [16] T. Welsch, C. Schmidtkunz, B. Müller, F. Meier, M. Chlup, A. Köhne, M. Lämmerhofer, W. Lindner, A comprehensive chemoselective and enantioselective 2D-HPLC set-up for fast enantiomer analysis of a multicomponent mixture of derivatized amino acids, *Anal. Bioanal. Chem.* 388 (2007) 1717–1724.
- [17] G. Cancelliere, C. Alessia, I. D'Acquarica, F. Gasparrini, J. Kocergin, D. Misiti, M. Pierini, H. Ritchie, P. Simone, C. Villani, Transition from enantioselective high performance to ultra-high performance liquid chromatography: a case study of a brush-type chiral stationary phase based on sub-5-micron to sub-2-micron silica particles, *J. Chromatogr. A* 1217 (2009) 990–999.
- [18] D. Kotoni, A. Ciogli, C. Molinaro, I. D'Acquarica, J. Kocergin, T. Szczerba, H. Ritchie, C. Villani, F. Gasparrini, Introducing enantioselective ultrahigh-pressure liquid chromatography (eUHPLC): theoretical inspections and ultrafast separations on a new Sub-2-μm Whelk-O1 stationary phase, *Anal. Chem.* 84 (2012) 6805–6813.
- [19] F. Ai, Y. Wang, H. Chen, Y. Yang, T.T. Yang Tan, S.-C. Ng, Enantioselective separation of dansyl-dl-amino acids and some racemates on "click" functionalized native α -cyclodextrin based sub-2 μm columns, *Analyst* 138 (2013) 2289–2294.
- [20] C. Barhate, M.F. Wahab, Z. Breitbach, D. Bell, D. Armstrong, High efficiency, narrow particle size distribution, sub-2 μm based macrocyclic glycopeptide chiral stationary phases in HPLC and SFC, *Anal. Chim. Acta* 898 (2015) 128–137.
- [21] O.H. Ismail, C. Alessia, C. Villani, M. De Martino, M. Pierini, A. Cavazzini, D. Bell, F. Gasparrini, Ultra-fast high-efficiency enantioseparations by means of a teicoplanin-based Chiral Stationary Phase made on sub-2 μm totally porous silica particles of narrow size distribution, *J. Chromatogr. A* 1427 (2016) 55–68.
- [22] S. Rocchi, A. Rocco, J. Pesek, M. Matyska, D. Capitani, S. Fanali, Enantiomers separation by nano-liquid chromatography: use of a novel sub-2 μm vancomycin silica hydride stationary phase, *J. Chromatogr. A* 1381 (2015) 767–772.
- [23] D. Ibrahim, A. Ghanem, Sub-2 μm silica particles in chiral separation, in: J.U.V. Marcelo Ruben, Andres Pagnola, Guillermo Marrugo (Eds.), *New Uses of Micro and Nanomaterials*, IntechOpen, Hungary, 2018, pp. 55–72.
- [24] D. Patel, M.F. Wahab, D. Armstrong, Z. Breitbach, Advances in high-throughput and high-efficiency chiral liquid chromatographic separations, *J. Chromatogr. A* 1467 (2016) 2–18.
- [25] M. Catani, O.H. Ismail, F. Gasparrini, M. Antonelli, L. Pasti, N. Marchetti, S. Felletti, A. Cavazzini, Recent advancements and future directions of superficially porous chiral stationary phases for ultrafast high-performance enantioseparations, *Analyst* 142 (2017) 555–566.
- [26] J.J. DeStefano, T.J. Langlois, J.J. Kirkland, Characteristics of superficially-porous silica particles for fast HPLC: some performance comparisons with Sub-2-μm particles, *J. Chromatogr. Sci.* 46 (2008) 254–260.
- [27] R. Hayes, A. Ahmed, T. Edge, H. Zhang, Core-shell particles: preparation, fundamentals and applications in high performance liquid chromatography, *J. Chromatogr. A* 1357 (2014) 36–52.
- [28] S. Fekete, D. Guillaume, M.W. Dong, Superficially porous particles: perspectives, practices, and trends, *LCGC North America* 32 (2014) 420–433.
- [29] R. Reischl, L. Hartmanová, M. Carozzo, M. Huszar, P. Frühauf, W. Lindner, Chemoselective and enantioselective analysis of proteinogenic amino acids utilizing N-derivatization and 1-D enantioselective anion-exchange chromatography in combination with tandem mass spectrometric detection, *J. Chromatogr. A* 1218 (2011) 8379–8387.
- [30] K. Lomsadze, G. Jibuti, T. Farkas, B. Chankvetadze, Comparative high-performance liquid chromatography enantioseparations on

- polysaccharide based chiral stationary phases prepared by coating totally porous and core-shell silica particles, *J. Chromatogr. A* 1234 (2012) 50–55.
- [31] S. Rocchi, S. Fanali, T. Farkas, B. Chankvetadze, Effect of content of chiral selector and pore size of core-shell type silica support on the performance of amylose tris(3,5-dimethylphenylcarbamate)-based chiral stationary phases in nano-liquid chromatography and capillary electrochromatography, *J. Chromatogr. A* 1363 (2014) 363–371.
- [32] L. Bezhitashvili, A. Bardavelidze, A. Mskhiladze, M. Gumustas, S. Ozkan, A. Volonterio, T. Farkas, B. Chankvetadze, Application of cellulose 3,5-dichlorophenylcarbamate covalently immobilized on superficially porous silica for the separation of enantiomers in high-performance liquid chromatography, *J. Chromatogr. A* 1571 (2018) 132–139.
- [33] D.C. Patel, Z.S. Breitbach, M.F. Wahab, C.L. Barhate, D.W. Armstrong, Gone in seconds: praxis, performance, and peculiarities of ultrafast chiral liquid chromatography with superficially porous particles, *Anal. Chem.* 87 (2015) 9137–9148.
- [34] Y. Min, Z. Sui, Z. Liang, L. Zhang, Y. Zhang, Teicoplanin bonded sub-2 μm superficially porous particles for enantioseparation of native amino acids, *J. Pharm. Biomed. Anal.* 114 (2015) 247–253.
- [35] D. Spudeit, Z. Breitbach, M.D. Dolzan, G. Micke, D. Armstrong, Superficially porous particle based hydroxypropyl-cyclodextrin stationary phase for high-efficiency enantiomeric separations, *Chirality* 27 (2015) 788–794.
- [36] D. Patel, Z. Breitbach, J. Yu, K. Nguyen, D. Armstrong, Quinine bonded to superficially porous particles for high-efficiency and ultrafast liquid and supercritical fluid chromatography, *Anal. Chim. Acta* 963 (2017) 164–174.
- [37] K. Schmitt, U. Woiwode, M. Kohout, T. Zhang, W. Lindner, M. Lämmerhofer, Comparison of small size fully porous particles and superficially porous particles of chiral anion-exchange type stationary phases in ultra-high performance liquid chromatography: effect of particle and pore size on chromatographic efficiency and kinetic performance, *J. Chromatogr. A* 1569 (2018) 149–159.
- [38] O.H. Ismail, L. Pasti, A. Ciogli, C. Villani, J. Kocergin, S. Anderson, F. Gasparrini, A. Cavazzini, M. Catani, Pirkle-type chiral stationary phase on core-shell and fully porous particles: are superficially porous particles always the better choice toward ultrafast high-performance enantioseparations? *J. Chromatogr. A* 1466 (2016) 96–104.
- [39] N. Khundadze, S. Pantsulaia, C. Fanali, T. Farkas, B. Chankvetadze, On our way to sub-second separations of enantiomers in high-performance liquid chromatography, *J. Chromatogr. A* 1572 (2018) 37–43.
- [40] C. Alessia, O.H. Ismail, G. Mazzocanti, C. Villani, F. Gasparrini, Enantioselective ultra high performance liquid and supercritical fluid chromatography: the race to the shortest chromatogram, *J. Sep. Sci.* 41 (2018) 1307–1318.
- [41] O.H. Ismail, G.L. Losacco, G. Mazzocanti, A. Ciogli, C. Villani, M. Catani, L. Pasti, S. Anderson, A. Cavazzini, F. Gasparrini, Unmatched kinetic performance in enantioselective supercritical fluid chromatography by combining latest generation Whelk-O1 chiral stationary phases with a low-dispersion in-house modified equipment, *Anal. Chem.* 90 (2018) 10828–10836.
- [42] U. Woiwode, R.J. Reischl, S. Buckenmaier, W. Lindner, M. Lämmerhofer, Imaging peptide and protein chirality via amino acid analysis by chiral \times chiral two-dimensional correlation liquid chromatography, *Anal. Chem.* 90 (2018) 7963–7971.
- [43] U. Woiwode, S. Neubauer, W. Lindner, S. Buckenmaier, M. Lämmerhofer, Enantioselective multiple heartcut two-dimensional ultra-high-performance liquid chromatography method with a Coreshell chiral stationary phase in the second dimension for analysis of all proteinogenic amino acids in a single run, *J. Chromatogr. A* 1562 (2018) 69–77.
- [44] C.L. Barhate, E.L. Regalado, N.D. Contrella, J. Lee, J. Jo, A.A. Makarov, D.W. Armstrong, C.J. Welch, Ultrafast chiral chromatography as the second dimension in two-dimensional liquid chromatography experiments, *Anal. Chem.* 89 (2017) 3545–3553.
- [45] T. Teerlink, Derivatization of posttranslationally modified amino acids, *J. Chromatogr. B, Biomed. Appl.* 659 (1994) 185–207.
- [46] I.S. Krull, Z. Deyl, H. Lingemann, General strategies and selection of derivatization reactions for liquid chromatography and capillary electrophoresis, *J. Chromatogr. B, Biomed. Appl.* 659 (1994) 1–17.
- [47] A. Andrés, K. Broeckhoven, G. Desmet, Methods for the experimental characterization and analysis of the efficiency and speed of chromatographic columns: a step-by-step tutorial, *Anal. Chim. Acta* 894 (2015) 20–34.
- [48] F. Gritti, G. Guiochon, The current revolution in column technology: how it began, where is it going? *J. Chromatogr. A* 1228 (2012) 2–19.
- [49] F. Gritti, G. Guiochon, Mass transfer mechanism in chiral reversed phase liquid chromatography, *J. Chromatogr. A* 1332 (2014) 35–45.
- [50] A. Cavazzini, M. Remelli, F. Dondi, A. Felinger, Stochastic theory of multiple-site linear adsorption chromatography, *Anal. Chem.* 71 (1999) 3453–3462.
- [51] S. Deridder, G. Desmet, New insights in the velocity dependency of the external mass transfer coefficient in 2D and 3D porous media for liquid chromatography, *J. Chromatogr. A* 1227 (2012) 194–202.
- [52] G. Desmet, S. Deridder, Effective medium theory expressions for the effective diffusion in chromatographic beds filled with porous, non-porous and porous-shell particles and cylinders. Part I: theory, *J. Chromatogr. A* 1218 (2011) 32–45.
- [53] S. Felletti, C. De Luca, O.H. Ismail, L. Pasti, V. Costa, F. Gasparrini, A. Cavazzini, M. Catani, On the effect of chiral selector loading and mobile phase composition on adsorption properties of latest generation fully- and superficially-porous Whelk-O1 particles for high-efficient ultrafast enantioseparations, *J. Chromatogr. A* 1579 (2018) 41–48.
- [54] P. Gzil, N. Vervoort, G.V. Baron, G. Desmet, General rules for the optimal external porosity of LC supports, *Anal. Chem.* 76 (2004) 6707–6718.
- [55] F. Gritti, G. Guiochon, Mass transfer kinetics, band broadening and column efficiency, *J. Chromatogr. A* 1221 (2011) 2–40.
- [56] F. Gritti, I. Leonadis, J. Abia, G. Guiochon, Physical properties and structure of fine core-shell particles used as packing materials for chromatography, *J. Chromatogr. A* 1217 (2010) 3819–3843.
- [57] S. Deridder, G. Desmet, Calculation of the geometrical three-point parameter constant appearing in the second order accurate effective medium theory expression for the B-term diffusion coefficient in fully porous and porous-shell random sphere packings, *J. Chromatogr. A* 1223 (2012) 35–40.

Supplementary Material

Evaluation of superficially porous particle based zwitterionic chiral ion exchangers against fully porous particle benchmarks for enantioselective ultra-high performance liquid chromatography

Christian Geibel ^a, Kristina Dittrich ^a, Ulrich Woiwode ^a, Michal Kohout ^b, Tong Zhang ^c, Wolfgang Lindner ^{d,e}, Michael Lämmerhofer ^{a,*}

^a Institute of Pharmaceutical Sciences, Pharmaceutical (Bio-)Analysis, University of Tübingen, Auf der Morgenstelle 8, 72076 Tübingen, Germany

^b Department of Organic Chemistry, University of Chemistry and Technology, Prague, Czech Republic

^c Chiral Technologies Europe, 160 Boulevard Gonthier d'Andernach, 67400 Illkirch-Graffenstaden, France

^d Lindner Consulting GmbH, Ziegelofengasse 37, 3400 Klosterneuburg, Austria

^e Institute of Analytical Chemistry, University of Vienna, Waehringerstrasse 38, 1090 Vienna, Austria

*Author for correspondence:
Prof. Dr. Michael Lämmerhofer
Pharmaceutical (Bio-)Analysis
Institute of Pharmaceutical Sciences
University of Tübingen
Auf der Morgenstelle 8
72076 Tübingen, Germany
T +49 7071 29 78793, F +49 7071 29 4565
E-mail: michael.laemmerhofer@uni-tuebingen.de

1.1 Material

Tetrahydrofuran (THF) as well as methanol were HPLC-grade and were supplied by Sigma Aldrich (Munich, Germany). Acetonitrile was also HPLC-grade and was supplied by Fisher Chemical (Schwerte, Germany). Ultra-pure water was taken from the Elga PureLab Ultra purification system (Elga LabWater, Celle, Germany). Ammonia (4M solution in methanol), diethylamine as well as formic acid were purchased from Sigma Aldrich. All test substances were racemic. *N*-(9-fluorenylmethoxycarbonyl)phenylalanine (Fmoc-Phe) was obtained from Fluka Chemicals (Buchs, Switzerland). 2-Amino-2-phenylbutyric acid (APBA), tryptophan (Trp), *N*-acetylphenylalanine (Ac-Phe), *N*-(3,5-dinitrobenzoyl)leucine (DNB-Leu) were purchased from Sigma Aldrich. *N*-(2,4-dinitrophenyl)-*N*-methyl-leucine (DNP-Me-Leu) and *N*-(2,4-dinitrophenyl)proline (DNP-Pro) were derivatized in-house according to known synthesis protocols [1, 2]. Mefloquine as well as the void volume marker 1,3,5-tri-*tert*-butylbenzene (TTBB) were supplied by Sigma Aldrich.

1.2 Inverse size-exclusion chromatography

Inverse size-exclusion chromatography (ISEC, see chapter 2.3) was carried out with the "ReadyCal Kit" with twelve polystyrene standards from Sigma Aldrich. Peak molecular weights were 370, 1,306, 3,470, 8,680, 17,600, 34,800, 66,000, 130,000, 277,000, 552,000, 1,210,000 and 2,520,000 Da.

ISEC was the method of choice to determine the porosity of the investigated columns. To do so, twelve polystyrene standards were divided into three samples. Each sample contained four different polymer standards which were dissolved in THF at concentrations of 0.5 mg/ml (2,520,000 Da and 1,210,000 Da) or 1.0 mg/ml. TTBB served as void volume marker with a concentration of 1 mg/ml. Mobile phase was THF, injection volume was 0.5 μ l. Flow rate was adjusted to 0.05 ml/min at a column temperature of 30 °C and detection occurred at 254 nm. Each polymer mixture sample was measured three times. ISEC plots were acquired by plotting the polymer's peak molecular weight against the difference of elution volumes and extra column

volume [3]. By doing so, one can perceive two distinguishable parts of the plot – a steeper and a flatter part. While the former represents the excluded polymers, the latter one typifies the polymers that penetrated deeper into the stationary phase's pores. V_e , the interstitial volume, can be ascertained by firstly performing a linear regression of each of the former mentioned two parts and secondly finding the intersection point of those lines [4]. Equations S1 and S2 show the calculation of the total porosity (ε_t) and the external porosity (ε_e). V_0 indicates the void volume of TTBB, V_e stands for the external volume. V_{col} is the empty column's geometrical volume, calculated as $V_{col} = \pi r^2 L$ (with r being the column's radius and L being its length).

$$\varepsilon_t = \frac{V_0}{V_{col}} \quad (\text{Eq. S1})$$

$$\varepsilon_e = \frac{V_e}{V_{col}} \quad (\text{Eq. S2})$$

As the total porosity (ε_t) is a sum of the internal porosity (ε_i) and the external porosity (ε_e), ε_i can be calculated by equation S3

$$\varepsilon_i = \varepsilon_t - \varepsilon_e \quad (\text{Eq. S3})$$

1.3 Van Deemter analysis

The efficiency of each column was determined by calculating the height equivalent of a theoretical plate (HETP, in the equations written as H) from the column's length (L) and the theoretical plate number N by equation S4.

$$H = \frac{L}{N} \quad (\text{Eq. S4})$$

Interstitial linear velocities u_i , used to construct van Deemter plots, were calculated by equation S5,

$$u_i = \frac{4 \cdot F}{\pi \cdot d_c^2 \cdot \varepsilon_e} \quad (\text{Eq. S5})$$

with F being the flow rate, d the inner diameter of the column and ε_e the external porosity as determined by inverse size exclusion chromatography (see above).

The contributions to peak dispersion in the tested columns were evaluated by use of the van Deemter equation (equation S6).

$$H = A + \frac{B}{u_i} + C \cdot u_i \quad (\text{Eq. S6a})$$

or in reduced coordinates

$$h = a + \frac{b}{v} + c \cdot v \quad (\text{Eq. S6b})$$

wherein the A-term represents the eddy dispersion, B the longitudinal diffusion, and C the mass transfer resistance (a, b, c the corresponding reduced terms), and $h = \frac{H}{d_p}$, (Eq. S7) with d_p being the particle diameter.

The reduced linear velocity v is the dimensionless parameter of the linear velocity u_i and was calculated according to equation S8.

$$v = u_i \cdot \frac{d_p}{D_m} \quad (\text{Eq. S8})$$

D_m is the bulk diffusion coefficient. For small molecules, it is convenient to calculate it by the Wilke - Chang equation [5] (see equation S9):

$$D_m = \frac{7.4 \cdot 10^{-12} \cdot \sqrt{\Psi \cdot M \cdot T}}{\eta \cdot V_A^{0.6}} \quad (\text{Eq. S9})$$

In this equation, Ψ indicates the solvent constant, M stands for the molecular weight of the mobile phase, T for the temperature (absolute temperature), η indicates the solvent's viscosity and V_A the molar volume of the analyte.

1.4 Alternative A-term determination

On the basis of the work of Gritti and Guiochon [6], an alternative way of the determination of the A-term was carried out. The advantage of this kind of determination is the independence of different compounds. A calculation can be obtained for every single peak without the aid of the data derived from the void volume marker. However, as some of the parameters used for the calculation are only approximations and were not estimated precisely, the whole determination can only be seen as a rough approximation and will therefore only be mentioned in the supplementary. Apart from that, the work from Gritti and Guiochon gives a holistic and detailed overview of the different parts of the Eddy-diffusion.

The trans-channel Eddy-diffusion ($=H_{Eddy, TS}$) describes the velocity differences between neighboring particles [7]. As the particles that are building channels amongst each other are very close to each other in a packed column, it can be assumed that wall effects are contributing largely to the behavior of the mobile phase flow through the packed bed. Concluding, the mobile phase will not flow in a sharp zone but will form an arrow-like form with a tip in the middle of the adjacent particles. This leads to Taylor-diffusion in which the diffusion takes place against the concentration gradient [6]. According to [6], eq. 53, the trans-channel Eddy-diffusion for a column with the external porosity of $\epsilon_e = 0.4$ can be calculated by equation S10a

$$\frac{H_{Eddy,TS}}{d_P} = \frac{1}{\frac{1}{0.9} + \frac{1}{0.0045v}} \quad (\text{Eq. S10a})$$

Or solved to $H_{Eddy, TS}$

$$H_{Eddy,TS} = \frac{1}{\frac{1}{0.9} + \frac{1}{0.0045v}} \cdot d_P \quad (\text{Eq. S10b})$$

Both with v being the reduced interstitial linear velocity.

The short range inter-channel Eddy-diffusion ($=H_{Eddy, IT}$) results from differences of trans-channel Eddy-diffusions. As a not fully homogenous particle size distribution leads to denser and less dense parts in a packed bed, the free spaces between particles are not showing the same size [6, 7]. However, these differences in size lead to differences in Eddy-diffusion, which in turn can be calculated (according to ref. [6], eq. 54) as

$$\frac{H_{Eddy,IT}}{d_P} = \frac{1}{\frac{1}{0.5} + \frac{1}{0.13v}} \quad (\text{Eq. S11a})$$

Or

$$H_{Eddy,IT} = \frac{1}{\frac{1}{0.5} + \frac{1}{0.13v}} \cdot d_P \quad (\text{Eq. S11b})$$

A further contribution to the Eddy-dispersion is the so-called trans-channel Eddy-dispersion ($=H_{Eddy, TC}$), which in turn can be divided into flow and diffusion trans-channel Eddy-dispersion (henceforth referenced to as $H_{Eddy, TC, flow}$ and $H_{Eddy, TC, diffusion}$). Both effects take into account that wall effects play a role in Eddy-dispersion. While $H_{Eddy, TC, flow}$ deals with the fact that the analyte can move easier through the bed when having the maximum distance to the column wall (therefore in the radial center of the column), $H_{Eddy, TC, diffusion}$ reflects the passive diffusion of the ana-

lyte through the packed bed. According to [6], eq. 59, $H_{Eddy, IT, flow}$ can be calculated by equation S12.

$$H_{Eddy,TC,flow} = 2 \cdot \frac{p}{q} \cdot L \cdot \omega_{\beta,c}^2 \quad (\text{Eq. S12})$$

Here, L is the length of the column, $\omega_{\beta,c}$ is the relative difference in velocity between the wall of the column and its center and p and q are integers that are related to the polynomial order which has to be used to calculate the flow homogeneity between a columns wall and its center [6]. As both the polynomial order as well as $\omega_{\beta,c}$ could only be estimated and was not precisely determined in our case, $H_{Eddy, TC, flow}$ can only be treated as an approach to the true value of this parameter. Both Gritti and Guiochon [6] and Farkas et al. [8] worked with columns with 4.6 mm inner diameter. While Gritti and Guiochon [6] propose a polynomial order of $n = 8$ with $p = 8$ and $q = 225$, Farkas et al. [8] is calculating with a polynomial order of 4 to 6. The latter describes his work to be performed in strictly laminar flow with Reynolds numbers below 0.1. We decided to assume that the polynomial order of $n = 8$ might also serve for our columns with 3 mm inner diameter to be able so estimate the value of $H_{Eddy, TC, flow}$. Further, just as in ref. [6], a value of 1.5% for $\omega_{\beta,c}$ has been assumed.

Gritti and Guiochon propose the following equation for calculation of $H_{Eddy, TC, diffusion}$ (see ref. [6], eq. 60):

$$H_{Eddy,TC,diffusion} = \frac{d_p}{\frac{q}{2p \cdot m_l \cdot \omega_{\beta,c}^2} + \frac{\epsilon_t(D_{eff} + 0.5\epsilon_e \gamma_r D_m \nu)^{(1+k)}}{\epsilon_e C_m m_r^2 D_m \nu}} \quad (\text{Eq. S13})$$

Herein, m_l is the ratio of the column length to the particle diameter, m_r is the ratio of the inner column radius to the particle diameter, ϵ_t is the total porosity, ϵ_e is the external porosity, D_{eff} is the effective diffusion coefficient, D_m is the bulk molecular diffusion coefficient, γ_r is the coefficient related to the contribution of eluent convection to the radial dispersion, k is the retention factor and C_m is the Aris-Taylor coefficient. While most of the parameters could be calculated, some had to be estimated. γ_r has been used with the same value as in ref. [6] ($\gamma_r = 0.3$) and also C_m was taken from ref. [6]. As two reference values for C_m were given, it was decided to use $2.7 \cdot 10^{-7}$, as the values for k were small (see ref. [6], Fig. 6).

The total Eddy-dispersion was calculated by eq. S14

$$H_{Eddy} = H_{Eddy,TS} + H_{Eddy,IT} + H_{Eddy,TC,flow} + H_{Eddy,TC,diffusion} \quad (\text{Eq. S14})$$

Results for ZWIX SPP 2.7 μ m, 50x3mm can be found in Table S3. For the results of all columns in reduced form (accomplished by dividing each H_{Eddy} term by the particle diameter), see Figure S4. A comparison with the a-term obtained by deconvolution as described in the main document shows that the a-term in the first approach is probably a bit overestimated while the c_{ads} -term a bit underestimated. The real a-term however remains difficult to be established accurately due to many assumptions made in the above A-term determination in accordance Gritti and Guiochon [6].

Table S1a. Screening of mobile phase conditions (Analyte, 2-amino-2-phenylbutyric acid; column, ZWIX(+) 2.7 μm , SPP 160 \AA , 50 x 3 mm ID)

Organic modifier	Additive	Concentration [mM]	Temperature [°C]	Retention factor k peak 1	Retention factor k peak 2	Selectivity α	Resolution Rs		
MeOH/ACN/H ₂ O (49/49/2)	FA + DEA	50/25	30	0.78	1.03	1.37	2.61		
			40	0.85	1.12	1.31	2.56		
	FA + NH ₃	50/25	30	0.77	1.05	1.37	2.66		
			40	0.78	1.04	1.34	2.54		
			30	0.94	1.30	1.38	3.02		
			40	0.96	1.31	1.36	2.95		
MeOH/ACN (80/20)	FA + DEA	20/10	30	0.56	0.81	1.44	2.72		
			40	0.58	0.82	1.41	2.65		
	FA + NH ₃	20/10	30	0.58	0.84	1.44	2.75		
			40	0.58	0.83	1.42	2.74		
			MeOH	20/10	30	0.52	0.76	1.45	2.62
					40	0.52	0.75	1.43	2.54
MeOH	FA + NH ₃	50/25	30	0.42	0.61	1.45	2.54		
			40	0.42	0.61	1.43	2.34		
			25/12.5	30	0.49	0.71	1.46	2.59	
				40	0.49	0.70	1.44	2.49	

FA = formic acid, DEA = diethylamine, NH₃ = ammonia
Flow rate = 0.5 mL/min

Table S1b. Screening of mobile phase conditions (Analyte, 2-amino-2-phenylbutyric acid; column, ZWIX(+) 2.7 μ m, SPP 160 \AA , 50 x 3 mm ID)

Organic modifier	Additive	Plate number N per 50 mm column		Plate number N per m		Peak symmetry		
		peak 1	peak 2	peak 1	peak 2	peak 1	peak 2	
MeOH/ACN/H ₂ O (49/49/2)	FA + DEA	4870	4975	97400	99500	0.43	0.53	
		5814	5768	116280	115360	0.56	0.50	
	FA + NH ₃	4986	5240	99720	104792	0.68	0.66	
		5228	5318	104564	106358	0.56	0.56	
		5070	5202	101395	104048	0.57	0.48	
		5143	5224	102853	104480	0.49	0.44	
MeOH/ACN (80/20)	FA + DEA	5408	5596	108160	111920	0.56	0.52	
		5526	5690	110520	113800	0.61	0.64	
	FA + NH ₃	5119	5645	102385	112893	0.64	0.58	
		5555	5775	111108	115494	0.59	0.67	
		FA + DEA	5313	5454	106260	109080	0.51	0.56
			5124	5582	102480	111640	0.68	0.53
MeOH	FA + NH ₃	6633	6594	132663	131880	1.06	0.79	
		6095	6168	121903	123351	0.79	0.84	
	FA + NH ₃	5331	5609	106612	112174	0.59	0.71	
		5368	5667	107356	113334	0.49	0.75	

FA = formic acid, DEA = diethylamine, NH₃ = ammonia
Flow rate = 0.5 mL/min

Suppl. Table S2.

Summary of column specific and peak dependent parameters used for the approximation of the peak dispersion contributions. For explanation, see footnotes

		2.7 μ m 160A SPP	3 μ m 200A FPP	3 μ m 120A FPP
column parameter				
d_{col}^1	[m]	3.00E-03	3.00E-03	3.00E-03
d_p^1	[m]	2.70E-06	2.90E-06	3.20E-06
d_{core}^1	[m]	1.70E-06	0.00E+00	0.00E+00
ρ^2	[/]	0.63	0.00	0.00
ϵ_e^3	[/]	0.391	0.378	0.369
ϵ_T^3	[/]	0.553	0.714	0.648
ϵ_r^3	[/]	0.162	0.335	0.279
k''^0	[/]	1.169	1.642	1.710
D_m^4	[m ² /s]	7.13E-10	7.13E-10	7.13E-10
ζ_2	[/]	2.00E-01	2.00E-01	2.00E-01
Sh_{part}^5	[/]	22.67	10.00	10.00
ϕ	[/]	0.81	0.40	0.54
void volume marker (TTBB)				
γ_{eff}^6	[/]	0.854	0.859	0.763
D_{eff}^6	[m ² /s]	6.09E-10	6.12E-10	5.44E-10
k^7	[/]	0	0	0
k'^7	[/]	0.414	0.886	0.756
β_1^8	[/]	-0.351	-0.238	-0.321
α_{part}^8	[/]	0.221	0.423	0.270
D_{pz}^9	[m ² /s]	6.67E-10	5.58E-10	4.36E-10
D_{part}^9	[m ² /s]	5.93E-10	= D_{pz}	= D_{pz}
D_{pz}/D_m	[/]	0.935	0.783	0.611
D_{part}/D_m	[/]	0.832	= D_{pz}/D_m	= D_{pz}/D_m
b	[/]	2.415	3.240	2.678
c_m	[/]	0.0023	0.00231	0.0019
c_s	[/]	0.00389	0.00655	0.0134
APBA, peak 1				
γ_{eff}^6	[/]	0.505	0.485	0.368
D_{eff}^6	[m ² /s]	3.60E-10	3.46E-10	2.62E-10
k^7	[/]	0.417	0.317	0.718
k'^7	[/]	1.005	1.484	2.016

K	[/]	0.516	0.791	1.321
β_1^8	[/]	-0.414	-0.078	-0.163
α_{part}^8	[/]	0.122	0.782	0.579
D_{pz}^9	[m ² /s]	1.51E-10	6.17E-10	3.50E-10
D_{part}^9	[m ² /s]	1.34E-10	= D_{pz}	= D_{pz}
D_{pz}/D_m	[/]	0.212	0.865	0.491
D_{part}/D_m	[/]	0.188	= D_{pz}/D_m	= D_{pz}/D_m
b	[/]	2.025	2.411	2.218
C_m	[/]	0.004	0.004	0.005
C_s	[/]	0.016	0.034	0.054
C_{ads}	[/]	0.016	0.005 ¹⁰	0.049
k_p	[/]	2.671	1.570	3.414
$k_{\text{ads}}(D_m)$	[s ⁻¹]	1230	4283	820
$k_{\text{ads}}(D_{\text{pz}})$	[s ⁻¹]	261	3707	402

¹ d_{col} = column diameter, d_p = particle diameter, d_{core} = diameter of the impermeable core (in FPP = 0)

² ρ = ratio core/particle diameter (not available for FPP)

³ ϵ_e = external porosity, ϵ_T = total porosity, ϵ_i = internal porosity (particle porosity)

⁴ D_m = molecular diffusion coefficient,

⁵ Sh_{part} = Sherwood number

⁶ γ_{eff} = effective longitudinal diffusion, D_{eff} = effective diffusion coefficient

⁷ k = phase retention factor, k' = zone retention factor

⁸ β_1 = polarizability constant, α_{part} = relative particle permeability

⁹ D_{pz} = porous zone diffusion coefficient, D_{part} = intraparticle diffusion coefficient (for FPP columns, $D_{\text{pz}} = D_{\text{part}}$)

Table S3a.

Values for A-term calculation according to chapter 1.4. Table S3a shows flow independent constants, flow dependent values and results can be found in table S3b. Results are shown exemplarily for ZWIX(+) 2.7 μm , 160 \AA SPP only.

L [m]	p n = 8	q n = 8	$\omega^*\beta, c$	ml (length/dp)	et	$\epsilon\epsilon$	D_{eff} [m ² /s] (peak 1)	D_{eff} [m ² /s] (peak 2)	D_m [m ² /s]	γ_r	k	C_m	mr (diameter/dp)
0.05	8	225	0.015	18500	0.553	0.391	3.60E-10	3.15E-10	7.13E-10	0.3	0.417	2.70E-07	1.11E+03

Table S3b.

Values and results for A-term calculation according to chapter 1.4.

peak 1 flow rate [ml/min]	v	k	H Eddy, TS [m]	H Eddy, IT [m]	H Eddy, TC, flow [m]	H Eddy, TC, diffusion [m]	H Eddy [m]	H Eddy [μm]
2.5	27.499	0.341	2.94E-07	1.18E-06	8.00E-07	7.07E-07	2.99E-06	2.99
2.25	24.749	0.356	2.68E-07	1.17E-06	8.00E-07	7.04E-07	2.94E-06	2.94
2	21.999	0.372	2.41E-07	1.15E-06	8.00E-07	7.01E-07	2.89E-06	2.89
1.75	19.249	0.383	2.13E-07	1.13E-06	8.00E-07	6.97E-07	2.84E-06	2.84
1.5	16.500	0.369	1.85E-07	1.09E-06	8.00E-07	6.93E-07	2.77E-06	2.77
1.25	13.750	0.384	1.56E-07	1.05E-06	8.00E-07	6.86E-07	2.70E-06	2.70
1	11.000	0.394	1.27E-07	1.00E-06	8.00E-07	6.76E-07	2.60E-06	2.60
0.75	8.250	0.408	9.63E-08	9.21E-07	8.00E-07	6.59E-07	2.48E-06	2.48
0.5	5.500	0.417	6.50E-08	7.94E-07	8.00E-07	6.30E-07	2.29E-06	2.29
0.25	2.750	0.430	3.30E-08	5.63E-07	8.00E-07	5.57E-07	1.95E-06	1.95
0.15	1.650	0.435	1.99E-08	4.05E-07	8.00E-07	4.82E-07	1.71E-06	1.71
0.05	0.550	0.441	6.66E-09	1.69E-07	8.00E-07	2.89E-07	1.26E-06	1.26
0.025	0.275	0.442	3.34E-09	9.01E-08	8.00E-07	1.80E-07	1.07E-06	1.07
0.015	0.165	0.445	2.00E-09	5.55E-08	8.00E-07	1.20E-07	9.78E-07	0.98

peak 2 flow rate [ml/min]	v	k	H Eddy, TS [m]	H Eddy, IT [m]	H Eddy, TC, flow [m]	H Eddy, TC, diffusion [m]	H Eddy [m]	H Eddy [μm]
2.5	27.499	0.341	2.94E-07	1.18E-06	8.00E-07	7.10E-07	2.99E-06	2.99
2.25	24.749	0.356	2.68E-07	1.17E-06	8.00E-07	7.07E-07	2.94E-06	2.94
2	21.999	0.372	2.41E-07	1.15E-06	8.00E-07	7.04E-07	2.89E-06	2.89
1.75	19.249	0.383	2.13E-07	1.13E-06	8.00E-07	7.00E-07	2.84E-06	2.84
1.5	16.500	0.369	1.85E-07	1.09E-06	8.00E-07	6.97E-07	2.78E-06	2.78
1.25	13.750	0.384	1.56E-07	1.05E-06	8.00E-07	6.90E-07	2.70E-06	2.70
1	11.000	0.394	1.27E-07	1.00E-06	8.00E-07	6.81E-07	2.61E-06	2.61
0.75	8.250	0.408	9.63E-08	9.21E-07	8.00E-07	6.67E-07	2.48E-06	2.48
0.5	5.500	0.417	6.50E-08	7.94E-07	8.00E-07	6.41E-07	2.30E-06	2.30
0.25	2.750	0.430	3.30E-08	5.63E-07	8.00E-07	5.73E-07	1.97E-06	1.97
0.15	1.650	0.435	1.99E-08	4.05E-07	8.00E-07	5.03E-07	1.73E-06	1.73
0.05	0.550	0.441	6.66E-09	1.69E-07	8.00E-07	3.12E-07	1.29E-06	1.29
0.025	0.275	0.442	3.34E-09	9.01E-08	8.00E-07	1.99E-07	1.09E-06	1.09
0.015	0.165	0.445	2.00E-09	5.55E-08	8.00E-07	1.34E-07	9.91E-07	0.99

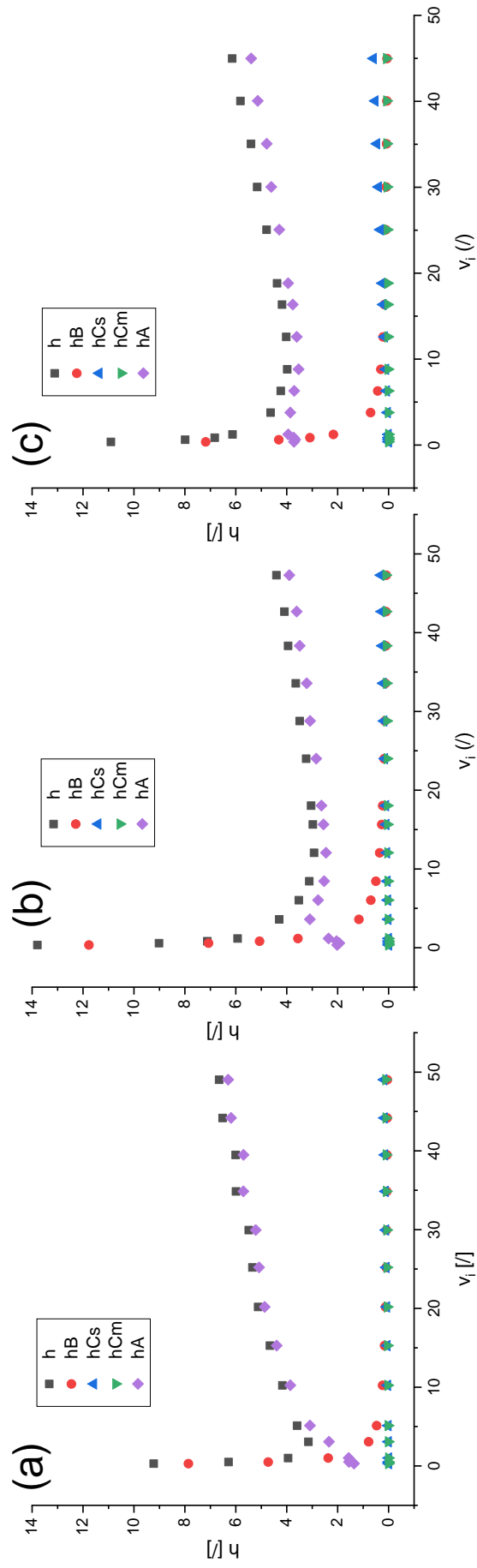


Figure S1. Van Deemter curves and deconvoluted contributions to peak dispersion of void volume marker TTBB on various ZWIX CSP columns. (a) 160Å 2.7μm SPP, (b) 200Å 3μm FPP, (c) 120Å 3μm FPP. For corresponding coefficients see Suppl. Table S2.

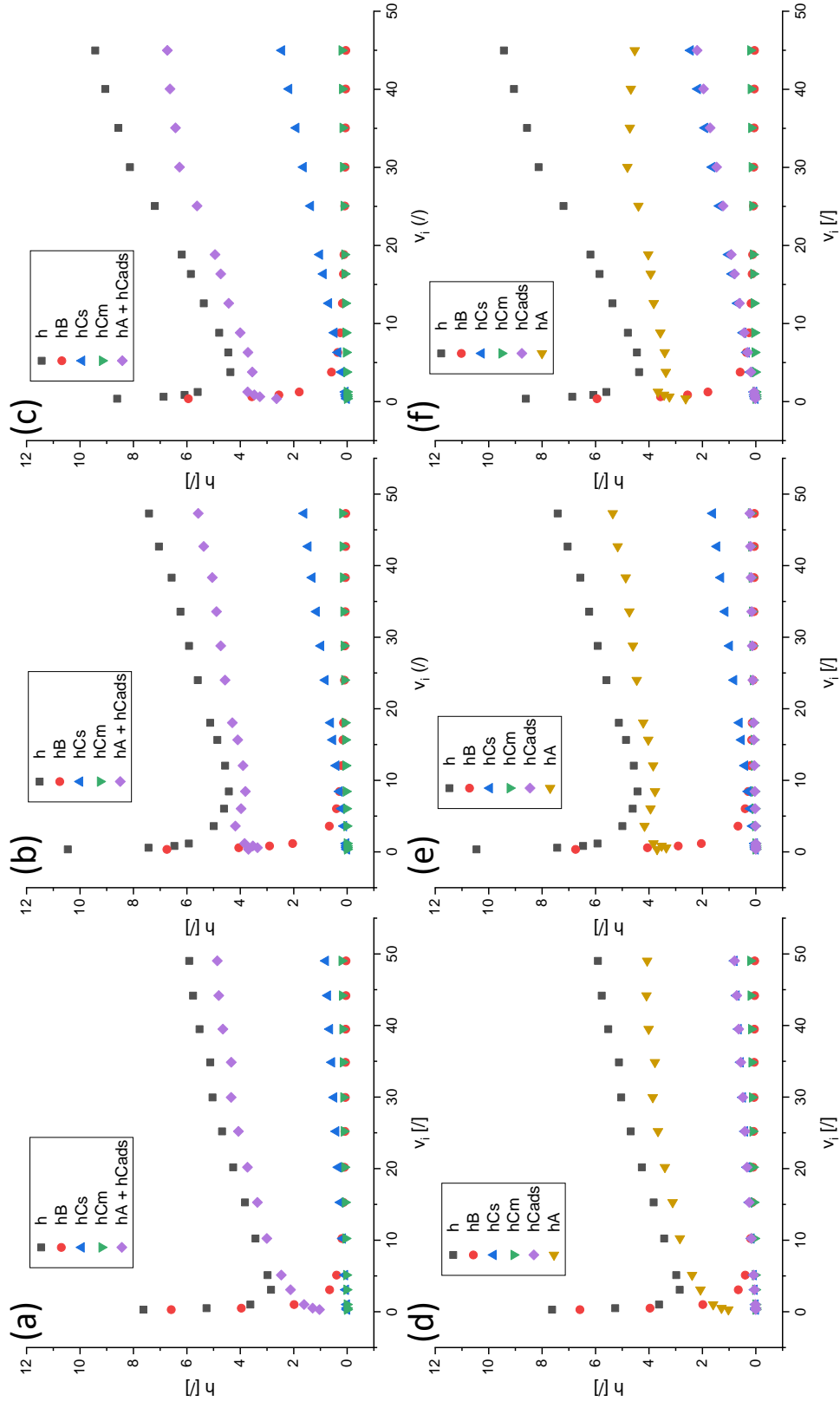


Figure S2. Van Deemter curves and deconvoluted contributions to peak dispersion of 1st eluted peak of APBA on various ZWIX CSP columns. (a-c) with combined h_a and $h_{c,ads}$ and (d-f) deconvoluted h_a and $h_{c,ads}$: (a,d) 160Å 2.7µm SPP, (b,e) 200Å 3µm FPP, (c,f) 120Å 3µm FPP. For corresponding coefficients see Suppl. Table S2.

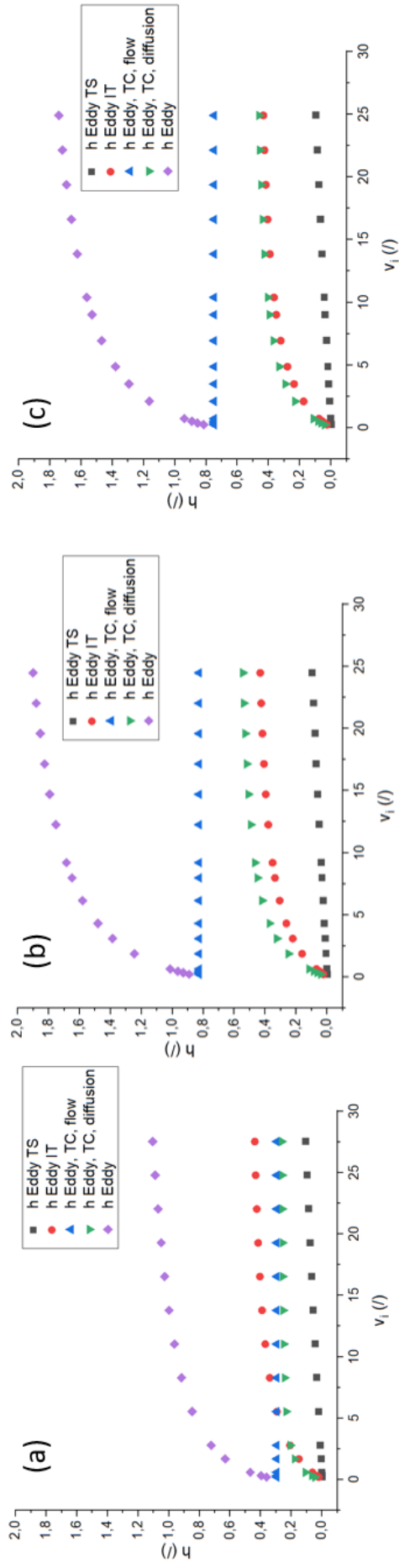


Figure S3. Results from alternative A-term calculations as described in chapter 1.4. (a) 160Å 2.7µm SPP, (b) 200Å 3µm FPP, (c) 200Å 3µm FPP. h Eddy (purple rhomb) is the sum of the four different graphs. All data are for the first eluting peak. Explanation and calculation can be found in chapter 1.4.

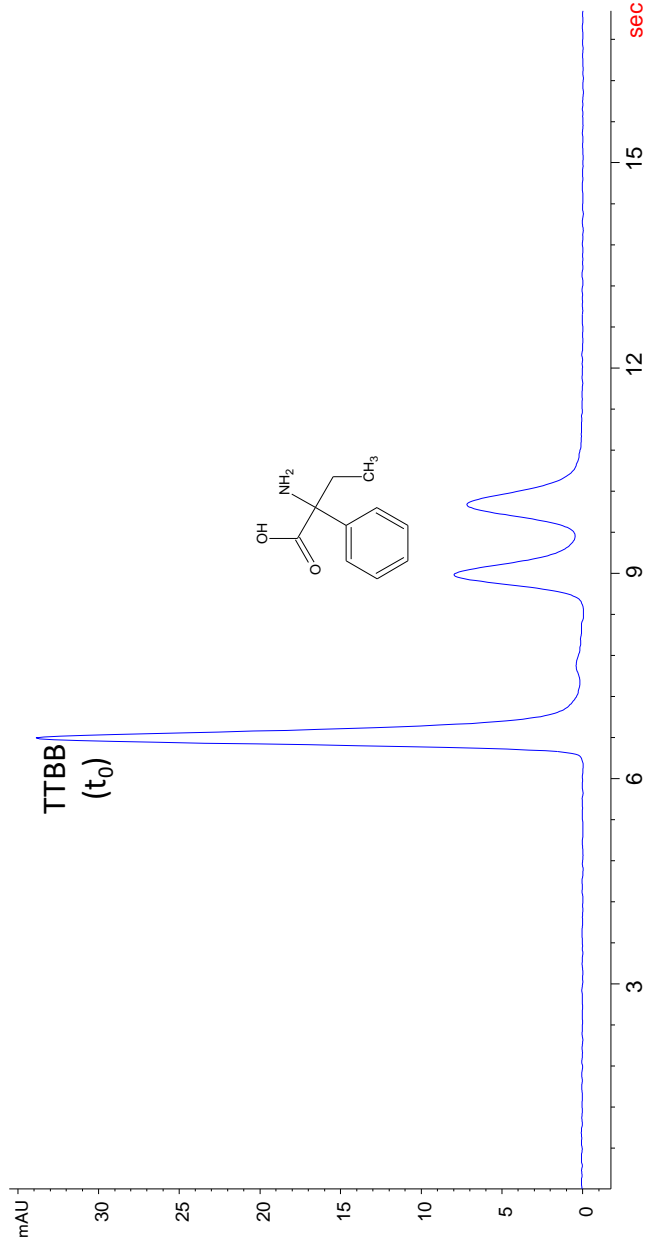


Figure S4. Subminute enantiomer separation of ABPA on ZWIX(+) 160 Å 2.7 µm SPP (Halo) at 40°C. Column dimension, 50 x 3 mm ID; column temperature, 40°C; eluent, MeOH + 50 mM formic acid + 25 mM NH₃; flow rate, 2.0 ml/min; ΔP = 549 bar (incl system back pressure).

- [1] T. Teerlink, Derivatization of posttranslationally modified amino acids, *J. Chromatogr. B Biomed. Appl.*, 659 (1994) 185-207.
- [2] I.S. Krull, Z. Deyl, H. Lingemann, General strategies and selection of derivatization reactions for liquid chromatography and capillary electrophoresis, *J. Chromatogr. B Biomed. Appl.*, 659 (1994) 1-17.
- [3] O.H. Ismail, L. Pasti, A. Ciogli, C. Villani, J. Kocergin, S. Anderson, F. Gasparrini, A. Cavazzini, M. Catani, Pirkle-type chiral stationary phase on core-shell and fully porous particles: Are superficially porous particles always the better choice toward ultrafast high-performance enantioseparations?, *J. Chromatogr. A*, 1466 (2016) 96-104.
- [4] A. Andrés, K. Broeckhoven, G. Desmet, Methods for the experimental characterization and analysis of the efficiency and speed of chromatographic columns: A step-by-step tutorial, *Anal. Chim. Acta*, 894 (2015) 20-34.
- [5] C.R. Wilke, P. Chang, Correlation of diffusion coefficients in dilute solutions, *AIChE Journal*, 1 (1955) 264-270.
- [6] F. Gritti, G. Guiochon, Mass transfer kinetics, band broadening and column efficiency, *J. Chromatogr. A*, 1221 (2011) 2-40.
- [7] A. Daneyko, A. Höltzel, S. Khirevich, U. Tallarek, Influence of the Particle Size Distribution on Hydraulic Permeability and Eddy Dispersion in Bulk Packings, *Analytical Chemistry*, 83 (2011) 3903-3910.
- [8] T. Farkas, M. J. Sepaniak, G. Guiochon, Radial Distribution of the Flow Velocity, Efficiency and Concentration in a Wide HPLC Column, *AIChE Journal*, 43 (1997) 1964-1974.

3.1.2 Publication II: **Thiol-ene photo-click immobilization of a chiral chromatographic ligand on silica particles**

Christian Geibel^a, Kristina Dittrich^a, Marc Wolter^a, Michael Lämmerhofer^{a,*}

^a Institute of Pharmaceutical Sciences, Pharmaceutical (Bio-)Analysis, University of Tübingen, Auf der Morgenstelle 8, 72076 Tübingen, Germany

* Corresponding author. E-mail address: michael.laemmerhofer@uni-tuebingen.de (M. Lämmerhofer)

Journal of Chromatography A **2020**, 1622, 461133.

DOI: 10.1016/j.chroma.2020.461133

Authors of Elsevier articles retain the right to include it in a thesis or dissertation without further permission.

© 2020 Elsevier B.V.



Thiol-ene photo-click immobilization of a chiral chromatographic ligand on silica particles

Christian Geibel, Kristina Dittrich, Marc Wolter, Michael Lämmerhofer*

Institute of Pharmaceutical Sciences, Pharmaceutical (Bio-)Analysis, University of Tübingen, Auf der Morgenstelle 8, 72076 Tübingen, Germany

ARTICLE INFO

Article history:

Received 7 March 2020

Revised 9 April 2020

Accepted 14 April 2020

Available online 19 April 2020

Keywords:

Chiral stationary phase

Chiral separation

Chiral ion-exchanger

Thiol-ene click reaction

Photoreaction

Photoinitiator

ABSTRACT

This work reports procedures for the immobilization of vinyl ligands on silica particles by UV-initiated thiol-ene radical addition reaction (photo-click immobilization). *tert*-Butylcarbamoyl quinine was the functional ligand (ene component) for the synthesis of chiral stationary phases. Two distinct surface chemistries were evaluated. In one approach, the ligand was directly attached to 3-mercaptopropyl-silica triggered by radicals generated by UV irradiation from a photoinitiator. In another approach, the ligand was immobilized onto vinyl silica via poly(3-mercaptopropyl-methylsiloxane) (PMPMS) as crosslinker by a photoinitiated double click reaction in which functionalization with chiral ligand and crosslinking to vinylsilica occurred simultaneously in one synthesis step. PMPMS-bonded CSPs were prepared from suspension (slurry method) or solventless after coating of the polythiol onto the vinylsilica surface (film method). Optimization by a design of experiment approach showed that the reaction time is the prime variable to optimize the surface coverage of chiral selector which also increased with PMPMS concentration. When the film formation of the latter approach was assisted by a minute volume of toluene during photo-click immobilization, selector coverage could be significantly increased to $0.73 \mu\text{mol}/\text{m}^2$ in a 2 h synthesis compared to $0.44 \mu\text{mol}/\text{m}^2$ by the solventless film method and $0.47 \mu\text{mol}/\text{m}^2$ by the slurry method under otherwise comparable conditions. The solvent assistance improved the chromatographic efficiency of the film method and resulted equal minimal reduced plate height of 2.6 as the slurry method for a chiral probe (Fmoc-Phe). The mass transfer resistance was around factor 2 smaller with the solvent-assisted film method as compared to the film approach without toluene, presumably due to a more homogenous distribution of the thin polymer film owing to lower dynamic viscosity in presence of toluene.

© 2020 Elsevier B.V. All rights reserved.

1. Introduction

Immobilization of chromatographic ligands on silica surfaces allows flexible tailoring of the selectivity of stationary phases for various HPLC applications. Simple, well controllable and quantitative reactions are favourable for this purpose. Thiol-ene and thiol-yne click chemistries raised significant interest for this purpose [1,2]. The gain in popularity of thiol click reactions in the past decade was somehow stimulated by the enormous popularity of Huisgen azide-yne 1,3-dipolar cycloaddition. What its application for the immobilization of chromatographic ligands is concerned, thiol click reactions are not a new chemistry. It has already been utilized in the late 1980s and beginning of 1990s for the immobilization of chiral selectors with vinyl groups to thiol-modified silica gels [3–6]. Known as radical addition reaction they were typically per-

formed by using 2,2'-azobis(2-methylpropionitrile) (AIBN) as radical initiator and thermal initiation of the addition reaction. It has been widely exploited for the synthesis of stationary phases for chiral separation, reversed-phase type, ion-exchange type, mixed-mode stationary phases, hydrophilic interaction liquid chromatography (HILIC) and ionic-liquid stationary phases [7–19]. This immobilization strategy was also extended to thiol-yne addition reaction [1,20,21].

Instead of thermal initiation of the addition reaction, UV initiated thiol-ene and thiol-yne reactions have attracted some attention. These photo-initiated variants have been exploited for instance in sensor sciences to modify surfaces because it allows convenient, spatially controlled micropatterning [22–24]. Thiol-ene photopolymerization has become quite popular for preparation of polysilsesquioxane (POSS)-based monolithic capillary columns in UV-transparent fused-silica capillaries [25–30]. It is a straightforward approach to obtain a functionalized monolithic capillary column in a single step within a few minutes with dedicated

* Corresponding author.

E-mail address: michael.laemmerhofer@uni-tuebingen.de (M. Lämmerhofer).

surface chemistry through incorporation of a functional monomer and tailored macropore structure via porogenic solvents. Besides these straightforward and simple single step approaches, functionalized monolithic capillary columns have also been prepared via two-step photo-initiated reactions in which a reactive POSS-based monolith was formed in the first step which was functionalized e.g. by photo-initiated thiol-yne click reaction e.g. for reversed-phase (RP) and strong cation-exchange (SCX) [31] or for boronate affinity chromatography [32]. While photo-initiated click addition or polymerization reaction were quite popular for the preparation of monolithic capillary columns, this reaction type was rarely used for particle functionalization. Yet, a recent study used photo-click reaction for the synthesis of functional silanes which were subsequently immobilized to silica particles by a conventional silanization reaction [33]. A direct photo-initiated thiol-ene or thiol-yne immobilization of chromatographic ligands on silica has not been reported.

In this study, we present the results of such a direct photo-click immobilization of a chromatographic ligand. The chiral selector *tert*-butylcarbamoylquinine (tBuCQN) which carries a vinyl group serves as a model ene component for immobilizing ligands on thiol-silica via photoinitiated click addition reaction. Thiol-ene and thiol-yne addition reactions were classified as click reactions because these chemical transformations proceed with high yields under mild reaction conditions, can tolerate water and oxygen (although oxygen may consume some radicals and oxidize the thiol component to disulfide), are adoptable for a wide range of starting materials, selectively react with each other (almost) without side reactions, and reactions can be performed in water or various organic solvents [34]. 3-Mercaptopropyl-modified silica (brush-type) and poly(3-mercaptopropyl-methylsiloxane) (PMPMS), respectively, represented the thiol component whereby the latter was crosslinked to vinyl-modified silica during the photoclick reaction. A number of distinct synthesis approaches (Fig. 1) were compared to each other with regard to selector coverages and chromatographic performances. Synthesis conditions were systematically optimized with regard to reaction time, educt concentrations in the reaction mixture and type of initiation.

2. Experimental

2.1. Materials

Spherical silica particles Kromasil 5 μm , 200 \AA (200 m^2/g) and 100 \AA (300 m^2/g), were supplied by Eka Chemicals (Bohus, Sweden). The chiral selector *tert*-butylcarbamoylquinine (tBuCQN) was synthesized as described elsewhere [35,36]. 2,2-Dimethoxy-2-phenylacetophenone (DMPA) and 4-dimethylaminopyridine (DMAP) were obtained from Sigma Aldrich (Munich, Germany). Vinyltrimethoxysilane, 3-mercaptopropylmethyltrimethoxysilane and poly(3-mercaptopropyl)methylsiloxane (PMPMS, homopolymer, [102783-03-9], viscosity 75–150 cSt.) were supplied by ABCR Chemicals (Karlsruhe, Germany). Test compounds *N*-[(9H-fluoren-9-ylmethoxy)carbonyl]-phenylalanine (Fmoc-Phe), *N*-acetylphenylalanine (Ac-Phe), *N*-carbobenzoxy-phenylalanine (Z-Phe) and 2-(2,4-dichlorphenoxy)propanoic acid (dichlorprop) were obtained by Sigma Aldrich or synthesized in-house according to ref. [37,38]. Empty stainless steel columns (all with a dimension of 50 \times 3 mm) were supplied by Bischoff Chromatography (Leonberg, Germany).

2.2. Instrumentation

The chromatographic experiments were conducted on an Agilent 1290 Infinity series liquid chromatographic system from Agilent Technologies (Waldbronn, Germany). The system consisted of a binary pump, a thermostatted column compartment (TCC), a diode array detector (DAD) and an autosampler. To obtain a minimal extra-column volume and minimize extra-column peak dispersion, the system was equipped with an ultralow dispersion kit. This included a Max-Light ultralow dispersion cartridge flow cell (inner volume 0.6 μL) and an ultralow dispersion needle seat assembly (1 μL injected). MarvelX capillaries from IDEX Corporation (Lake Forest, Illinois, USA) were installed from autosampler to TCC (350 mm length \times 0.075 mm inner diameter) and from TCC to DAD (250 mm \times 0.075 mm). Subsequent to packing, columns were washed overnight with methanol at a flow rate of 0.5 mL/min. The

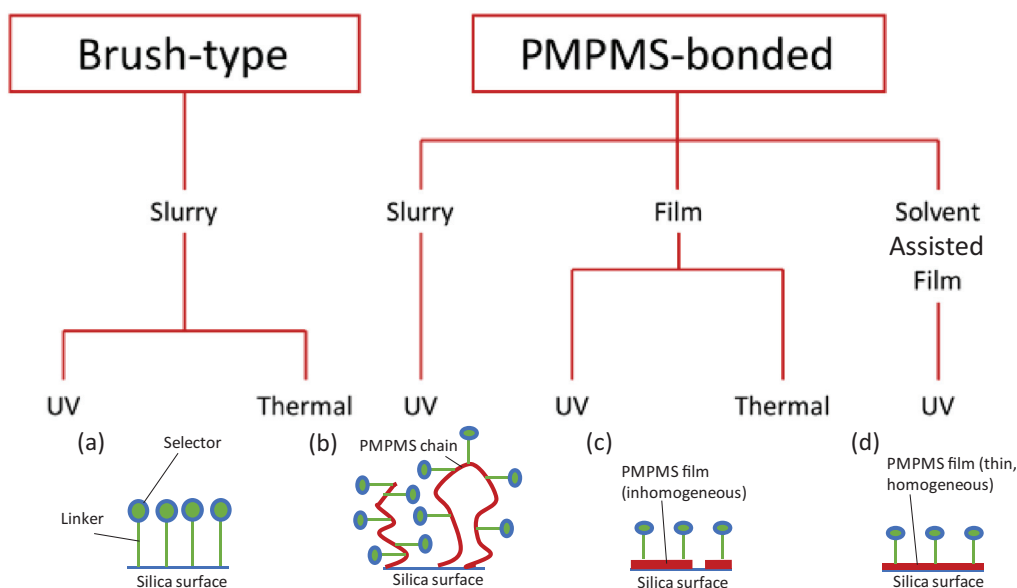


Fig. 1. Schematic overview of the employed synthesis strategies. CSP morphology on top, reaction method in the middle panel, and type of initiation of the radical addition reaction at the bottom. Schemes of resulting tentative surface morphologies: (a) Brush-type, (b) PMPMS-bonded slurry method, (c) PMPMS-bonded film method, and (d) PMPMS-bonded solvent-assisted film method.

flow rate was varied between 0.015 and 2.5 mL/min for generation of Van Deemter curves, always taking care that the maximum pressure of 800 bar was not exceeded. The column temperature was kept constant at 25 °C. With isocratic conditions, extra-column volume was determined to be 13 μL with an extra-column peak variance of 7 μL^2 (determination was carried out by second moment method with Fmoc-phenylalanine as sample, flow rate of 0.5 mL/min, and a column temperature of 25 °C). Columns were slurry packed with a smartline pneumatic pump, model 1950, from Knauer (Berlin, Germany). Data analysis was performed by using ChemStation Offline Software (Rev. B.04.03 [16], 2010) from Agilent Technologies. For data acquisition OpenLab CDS ChemStation Online Software (Rev. C.01.03 [37], 2011) from Agilent Technologies was utilized. For systematic optimization by design of experiments (DoE) approach, MODDE Pro-Ver. 12.1.0.5491 from Sartorius Stedim (Umeå, Sweden) was used.

2.3. Chiral stationary phase (CSP) synthesis

2.3.1. Synthesis of vinylsilica

18.26 g of silica particles (5 μm , pore size 200 Å) were dispersed in 200 mL toluene and heated to reflux while stirring with a mechanical stirrer. The first 50 mL of toluene were distilled off to remove traces of water. Vinyltrimethoxysilane (6 μmol per m^2 ; 3.36 mL) and 5 mol% of the catalyst 4-dimethylaminopyridine were added. Before the reaction was started, the reaction flask was flushed with nitrogen for 10 min. Reaction took place by refluxing under nitrogen atmosphere for 16 h. The product was repeatedly washed with boiling toluene and boiling methanol, three times each. After drying of the vinylated silica gel, it was subjected to elemental analysis. Results were as follows: C: 2.19 ± 0.02 wt%, H: 0.52 ± 0.00 wt%, N: 0.02 ± 0.00 wt%, S: 0.00 ± 0.00 wt%, corresponding to 1.82 $\mu\text{mol}/\text{m}^2$ immobilized vinyl groups (for sake of simplicity the initial specific surface area of the unmodified silica as specified by the supplier was used in all calculations).

2.3.2. Synthesis of thiol-modified silica

10.01 g of silica particles (5 μm , pore size 100 Å) were dispersed in toluene. After distilling off the water-containing azeotrope of toluene and water, 3-mercaptopropylmethyltrimethoxysilane (5.5 μmol per m^2 ; 2.98 mL) and 10 mol% of 4-dimethylaminopyridine were added. After flushing the system with nitrogen for 10 min, the reaction was held under reflux and under nitrogen atmosphere. Reaction time was 7 h. Subsequently, the product was washed with boiling methanol and boiling toluene, three times each. After drying the modified silica gel was subjected to elemental analysis. Results were as follows: C: 3.85 ± 0.02 wt%, H: 0.92 ± 0.01 wt%, N: 0.00 ± 0.00 wt%, S: 2.15 ± 0.03 wt%, corresponding to 2.23 $\mu\text{mol}/\text{m}^2$ immobilized thiol (related to the initial specific surface area).

2.3.3. Photoreactions

Film-type reactions as well as solvent assisted film-type reactions were carried out in a round bottom flask (Duran Glastechnik, Wertheim/Main, Germany) consisting of borosilicate glass, the volume of the vessel was 250 mL. The reactions following the slurry method were carried out in a three neck flask, volume, material and supplier were likewise (Duran Glastechnik, Wertheim/Main, Germany) equipped with a mechanical stirrer and reflux condenser. The glass has a negligible UV-absorption in the range from 310 nm upwards. The UV lamp (Ultra Vitalux, 300 W, from Osram, Munich, Germany) has a radiant power of 13.6 W in the UV-A spectrum (315 – 400 nm) and 3.0 W in the UV-B spectrum (280 – 315 nm). PMPMS was only partly soluble in methanol and formed a homogenous emulsion in methanol. The average molecular weight of PMPMS is 4000 – 7000 g/mol, containing 1 active

thiol group per monomer and a monomeric molecular weight of roughly 343 g/mol, resulting in 12 – 20 active thiol groups per mol.

For the film method, a solid, thin layer on the inside of the round bottom flask was irradiated with UV-light. No co-solvent or diluent (non-solvent) was added.

2.3.4. Photo-click immobilization of chromatographic ligand

The distinct synthesis procedures are schematically outlined in Fig. 1 and can be generally divided into (PMPMS) polymer-bonded and brush-type phases. The thermally initiated immobilization reactions were described previously, for the PMPMS-bonded stationary phase in ref. [39] and for the brush-type phase in ref. [35]. Amongst the photo-click immobilization reactions via polythiol (PMPMS) polymer layer three distinct variants were evaluated: i) a slurry method, ii) a film method, and iii) a solvent-assisted film method.

For the slurry method, 0.136 mmol tBuCQN were dissolved in 10 mL of degassed methanol. 0.5 g of vinylated silica were added and the suspension was stirred with a mechanical stirrer. The system was flushed with nitrogen and 0.226 mmol PMPMS were added. After 10 min, DMPA (0.0136 mmol) was added to the reaction mixture and the thiol-ene click reaction was initiated by UV irradiation with a UV lamp (Ultra Vitalux, 300 W, from Osram, Munich, Germany). The UV lamp was positioned in a distance of 15 cm to the reaction flask (angle to upright flask: 180°). A Dimroth cooler prevented loss of methanol by evaporation due to the heat generated by the UV lamp. The reaction mixture was exposed to UV light for certain reaction times as specified in Table 1. Afterwards, the UV lamp was switched off and the product was washed with boiling toluene and boiling methanol three times each. Finally, it was dried at 60 °C overnight.

For the (solvent-less) film method, the same quantities of reactants were added to 20 mL of methanol. After dispersing the vinylsilica in methanol, methanol was completely removed by slow evaporation, resulting in a thin film of PMPMS and other reactants on the silica surface. Irradiation with UV light as well as washing was carried out the same way as described above for the slurry method.

For the solvent assisted film method the synthesis procedure was the same as for the solvent-less film method. However, the reaction was performed in presence of a small amount of less volatile toluene. Instead of dispersing vinylsilica in methanol, it was dispersed in a mixture of 20 mL methanol and the amount of toluene as stated in Table 1 (CSPs # 21 and 22). Afterwards, methanol was completely removed while taking care that the toluene was not evaporated but remained in the reaction mixture. Apart from this, the synthesis protocol was the same as described above.

For comparison, the tBuCQN selector was also immobilized on 3-mercaptopropyl-modified silica yielding typical brush-type CSPs. For this sake, the slurry method as described above was chosen for comparison with some slight modifications. Most importantly, vinylsilica was replaced by 3-mercaptopropylsilica and PMPMS was omitted from the reaction mixture. Five batches were synthesized with identical quantities of educts (tBuCQN, DMPA) in the reaction mixture as described above for the slurry method. Reaction times of 30, 60, 120 and 420 min were examined. The fifth synthesis batch was carried out by thermal initiation with AIBN as radical starter as described previously [35].

All methods have been carried out with distinct quantities of reactants as specified in Table 1 along with the results of the surface coverages.

2.3.5. Oxidation of CSP # 22

An aliquot of CSP # 22 (1 g) was suspended in 10 mL methanol and 0.9 mL formic acid 99%. To this suspension, 3.4 mL performic

Table 1
Summary of the starting conditions and results for CSP synthesis.

CSP #	Reaction conditions						Results ^a				
	Reaction type	Initiation	Reaction time [min]	Initial weight	Amount of added	Coverage	Coverage [$\mu\text{mol}/\text{m}^2$] ^b		Ratio	Yield [%]	
				[$\mu\text{mol}/\text{m}^2$]	Sulfur (PMPMS)	[$\mu\text{mol}/\text{m}^2$] ^b added toluene	tBuCQN	Sulfur		S/SO ^c	tBuCQN
1	Brush-type ^d	T	420	–	–	–	1.14	–	–	–	–
2	Brush-type ^e	UV	30	1.36	–	–	0.19 ± 0.001	2.14 ± 0.010	11.16	14.0	–
3	Brush-type ^e	UV	60	1.36	–	–	0.21 ± 0.002	2.12 ± 0.039	10.05	15.4	–
4	Brush-type ^e	UV	120	1.36	–	–	0.20 ± 0.002	2.15 ± 0.018	10.68	14.7	–
5	Brush-type ^e	UV	420	1.36	–	–	0.41 ± 0.007	1.90 ± 0.065	4.64	30.1	–
6	film	UV	120	1.36	2.26	–	0.44 ± 0.001	1.20 ± 0.018	2.73	32.4	53.2
7	slurry	UV	120	1.36	2.26	–	0.47 ± 0.002	1.18 ± 0.030	2.51	34.6	52.2
8	film	UV	60	1.36	2.26	–	0.35 ± 0.010	1.15 ± 0.055	3.31	25.6	51.1
9	slurry	UV	60	1.36	2.26	–	0.29 ± 0.014	0.55 ± 0.011	1.91	21.0	24.2
10	film	UV	30	1.36	2.26	–	0.34 ± 0.008	1.13 ± 0.056	3.31	25.0	50.0
11	slurry	UV	30	1.36	2.26	–	0.14 ± 0.010	0.48 ± 0.008	3.33	10.6	21.3
12	film	UV	60	2.72	2.26	–	0.21 ± 0.003	0.52 ± 0.058	2.48	7.7	22.9
13	film	UV	60	1.36	1.70	–	0.34 ± 0.004	0.88 ± 0.047	2.59	24.9	51.6
14	film	UV	60	2.72	1.70	–	0.22 ± 0.010	0.45 ± 0.009	2.10	8.1	26.5
15	film	UV	60	1.36	3.40	–	0.42 ± 0.002	1.48 ± 0.055	3.55	30.6	43.5
16	film	UV	60	2.72	3.40	–	0.36 ± 0.000	0.84 ± 0.014	2.34	13.1	24.6
17	slurry	UV	231	1.36	2.26	–	0.20 ± 0.003	1.02 ± 0.011	5.20	14.7	45.1
18	slurry	UV	388	1.36	2.26	–	0.25 ± 0.000	1.23 ± 0.021	4.93	18.4	54.4
19	film	UV	376	1.36	2.26	–	0.62 ± 0.007	1.97 ± 0.078	3.18	45.6	87.2
20	film	UV	706	1.36	2.26	–	0.66 ± 0.007	2.05 ± 0.020	3.11	48.5	90.7
21	solvent assisted film ^f	UV	120	1.36	2.26	2 mL	0.61 ± 0.005	1.89 ± 0.042	3.10	44.9	83.6
22	solvent assisted film ^f	UV	120	1.36	2.26	1 mL	0.73 ± 0.007	2.11 ± 0.192	2.89	53.7	93.4
23	film, thermal ^g	T	120	1.36	2.26	–	0.50	1.23	2.46	36.8	54.4
24	film, thermal ^g	T	240	1.36	2.26	–	0.55	1.39	2.53	40.4	61.5
25	film, thermal ^g	T	480	1.36	2.26	–	0.57	1.75	3.07	41.9	77.4

^a results based on elemental analysis.

^b specific surface area (as stated by the manufacturer): 200 Å FPP = 200 m²/g, 100 Å = 300 m²/g.

^c S = sulfur, SO = selector = tBuCQN.

^d thermally initiated brush-type material on 5 μm , 120 Å FPP was used as benchmark.

^e brushtype phases were synthesized on 5 μm 100 Å particles.

^f solvent assisted film was carried out with additional toluene on particles.

^g no standard deviation available, as the thermal CSPs were only determined once.

acid (obtained by incubation of formic acid 99% with hydrogen peroxide solution 30%, 95:5 (v/v) in an ice bath for 30 min) were dropwise added under ice cooling and mechanical stirring. After 6 h reaction at room temperature, the modified oxidized silica gel was washed with a mixture of water/methanol (50:50, v/v) until a neutral pH was obtained. After multiple washing steps with hot methanol the material was dried at 60 °C under vacuum.

2.3.6. Column packing

All CSPs were slurry packed with the same slurry medium and transport (push) solvent. As transport solvent, HPLC-grade methanol was used. Slurry medium for all CSPs was isopropanol with 10% acetic acid. Concentration was 300 mg CSP in 10 mL slurry medium. The pressure was kept constant at 800 bars and packing was performed for 1 h.

3. Results and discussion

3.1. Synthesis procedures

Vinyl ligands are commonly immobilized on thiol-silica by thermally initiated thiol-ene click chemistry using AIBN as radical initiator. The reaction of tBuCQN with 3-mercaptopropyl-silica by this thiol-ene click immobilization leads to a brush-type CSP (CSP # 1) and serves as reference in this work [35,36]. The surface coverage with tBuCQN is typically around 1 $\mu\text{mol}/\text{m}^2$ but can be adjusted by the relative concentration of tBuCQN in the reaction mixture resulting in a controlled selector coverage [40].

The above reaction involves the refluxing of a suspension of silica particles (slurry) i.e. the boiling of organic solvent over sev-

eral hours. From this viewpoint, photoinitiation appeared attractive as it can be performed at ambient temperature i.e. no boiling of organic solvents is needed which may be a safety argument in larger synthesis batches. The idea of using photo-click immobilization was partly also driven by reports that UV-initiated radical addition reactions may occur with short reaction times [41]. Another driving force to use photoreactions may be thermal instability of reaction components which was, however, not the case in this work. For the current photoclick immobilization reaction, the photoinitiator represents a key component. A popular photoinitiator is DMPA (Fig. 2a). DMPA breaks down upon UV light irradiation at its absorption maximum at roughly 330 nm [42] and forms two radicals (namely a benzaldehyde and a (dimethoxy)methylbenzene radical) that can start the reaction by transferring the radical either to the double bond (of the functional ligand; ene component), or to the thiol group of the thiol reactant. Both radical products from the UV-triggered decomposition of DMPA can act as starting agents for the radical addition reaction. After photochemical formation of a thiyl radical, the subsequent hydrothiolation reaction on the C=C bond yields an intermediate carbon-centered radical with following chain transfer to another molecule of thiol [41]. This thiol-ene click reaction gives a product with an anti-Markovnikov configuration (Fig. 2a). Thermal and photoinitiated reactions lead to the same products, yet radical initiators are typically different (azo initiators in case of thermal initiation).

Two generally distinct chemical approaches were pursued. In one approach (PMPMS-bonded), the functional ligand tBuCQN was immobilized via a polythiol film of PMPMS on vinylsilica (Fig. 2b), similar to a procedure introduced by Zimmermann et al. with ther-

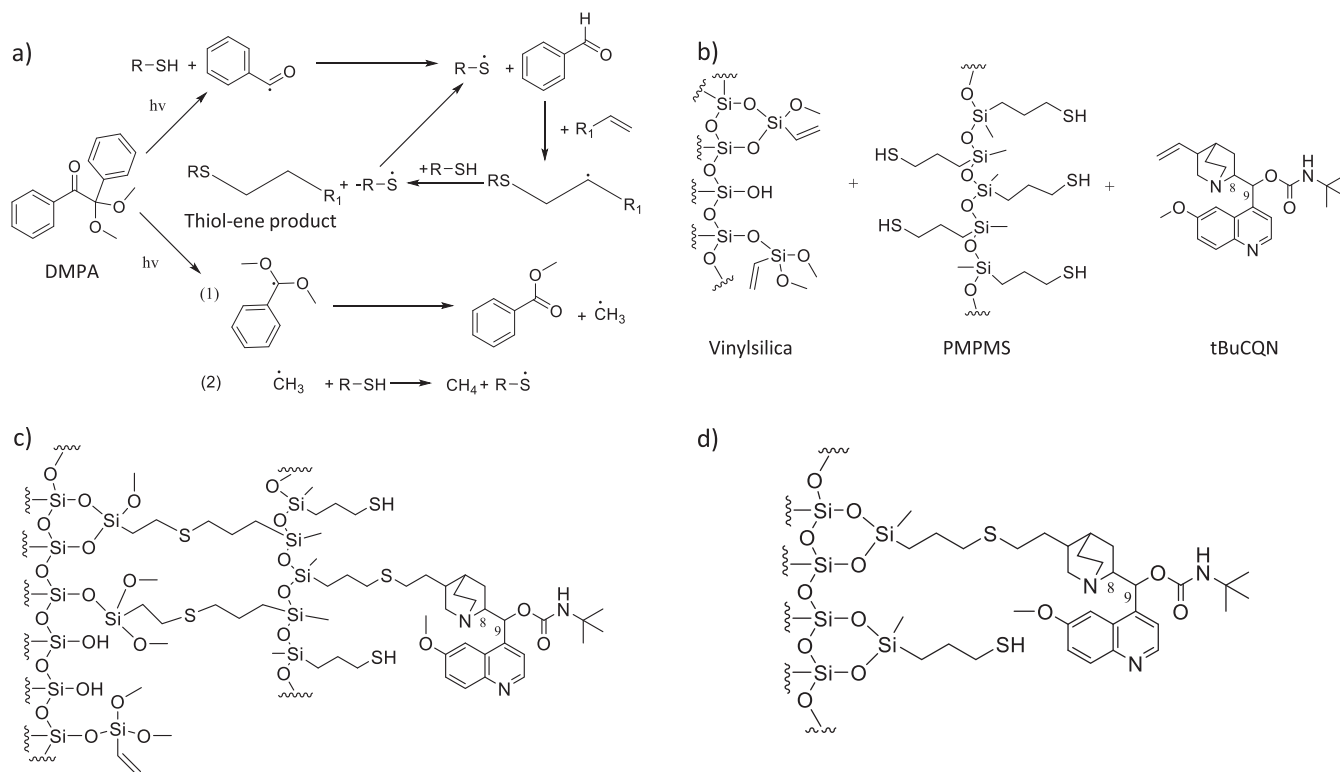


Fig. 2. Reaction scheme of the thiol-ene photo-click immobilization. a) UV irradiation-triggered decomposition of the radical photoinitiator 2,2-dimethoxy-2-phenylacetophenone (DMPA) and the propagation to the target molecule. b) Reactants of the PMPMS-bonded approach (vinylized silica particles, crosslinker poly(3-mercaptopropyl)methylsiloxane, PMPMS, functional ligand *tert*-butylcarbamoquinine, tBuCQN, i.e. the chiral selector). c) Surface chemistry of the resultant PMPMS-bonded CSPs. d) Surface structure of the brush-type CSPs.

mal initiation [43]. Evidently, the two ene components, chiral selector and vinyl groups on the silica surface, are competing for the thiyl radicals formed by UV irradiation from PMPMS. The reaction product is shown in Fig. 2c. In the second approach a brush-type bonding is obtained by immobilization of the ligand tBuCQN on thiol-silica in a methanolic slurry. Fig. 2d shows the structure of the brush-type CSP as resulting from photoinitiated thiol-ene click reaction (CSPs # 2 – 5) as well as in the benchmark obtained by thermal initiated reaction (CSP # 1).

3.2. Brush-type CSP by photoclick immobilization

First, brush-type photo-clicked CSPs were prepared by an approach resembling the common synthesis procedure of thermally initiated brush-type CSP. Thus, a slurry of thiol-silica in methanol containing $1.36 \mu\text{mol}/\text{m}^2$ tBuCQN and DMPA was treated with UV light. The reaction time was investigated as experimental variable and the reaction was carried out at ambient temperature in a vented fume hood under stirring. It can be seen in Table 1 that after 30 min a selector coverage of $0.19 \mu\text{mol}/\text{m}^2$ resulted (CSP # 2) corresponding to a 14% yield only. As reaction time was extended, the selector coverage increased (cf. CSPs # 2 – 5) reaching $0.41 \mu\text{mol}/\text{m}^2$ (30% yield) after 7 h, corresponding to an equal reaction time used for the synthesis of the thermally initiated brush-type reference CSP. It is evident that under chosen conditions the surface coverage is lower by UV irradiation. The lower reaction temperature can be one of the contributing factors for the lower surface coverage with photo-click reaction. There are certainly several ways to optimize this type of reaction, however, a different approach was then pursued, viz. photo-click immobilization via PMPMS.

3.3. Optimization of polythiol-bonded photo-click CSP synthesis

A fractional factorial design has been chosen to find optimal reaction conditions for the optimization of the PMPMS-bonded CSP synthesis. Three distinct approaches were evaluated: i) A slurry method: the vinylsilica was suspended in methanol in which the PMPMS was finely dispersed. tBuCQN and DMPA were dissolved in this reaction mixture and the radical addition reaction initiated by UV irradiation of the suspension. ii) A (solvent-less) film method: the same reaction mixture as in i) was prepared, but before reaction the solvent (MeOH) was completely evaporated. Thereby, the liquid PMPMS formed a thin film on the vinylsilica surface and the photo-reaction proceeded in this thin film that contained the selector and radical initiator. iii) A solvent-assisted film method: In this approach, a small amount of toluene was added to the reaction mixture prepared like in approach i). The methanol in the slurry was completely evaporated while the toluene remained in the reaction mixture. It should support the formation of a more homogenous film of the reaction mixture as well as accelerate reaction kinetics due to lower dynamic viscosity and higher diffusivity of the thiyl radicals in the solvent film.

In the course of the optimization of the reaction conditions, different synthesis batches were prepared, varying in synthesis method (slurry method, film method and solvent-assisted film method), reaction time, and initial concentration of educts as well as initiation type (UV irradiation vs temperature) (see Table 1). The optimization was assisted by DoE software MODDE to find the best compromise in terms of selector coverage, yield and chromatographic performance. Tentative surface morphologies are depicted in Fig. 1a-d. The brush-type phase has relatively regularly ordered and oriented homogeneously distributed selector moieties attached to the silica surface (Fig. 1a). In the PMPMS-bonded slurry method

the polythiol may be attached to the surface as a chain or loop on which the selector moieties are attached (Fig. 1b). In the film methods the PMPMS is bonded horizontally and selector moieties are attached to this polymer film. Since the PMPMS is poorly soluble in methanol it may form an inhomogeneous film or patches on the surface which might be less favorable (Fig. 1c). PMPMS on the other hand is well soluble in toluene. The resultant polymer film is thus deemed to be more homogeneous (Fig. 1d).

3.3.1. Comparison of synthesis procedures

Three different synthesis strategies have been tested for the PMPMS-bonded reaction procedure, slurry and film method as well as solvent-assisted film method. Only the general procedure was varied, while other variables were kept identical. For the following comparison of the different synthesis methods, CSP # 6, 7, 21 and 22 are taken into account. Selector coverages (in $\mu\text{mol}/\text{m}^2$) were calculated from the nitrogen content of elemental analysis assuming a specific surface area of $200 \text{ m}^2/\text{g}$ (as stated by the silica manufacturer i.e. for sake of simplicity the calculations were based on the initial surface area of the silica). One has to consider that as an inevitable consequence of ligand immobilization, the pore space and consequently specific surface area of the parent silica particles may change significantly, especially when polymeric ligands and cross-linkers are employed like herein, and hence the reported values have to be regarded as approximations of the true surface coverage. However, they should adequately reflect the relative trends which are of interest here. Reaction mixtures were charged with the same initial amount of selector ($1.36 \mu\text{mol}/\text{m}^2$) and PMPMS ($2.26 \mu\text{mol}/\text{m}^2$). As can be seen from Table 1, for a 120 min reaction time film and slurry methods afforded essentially the same selector coverages (0.44 vs $0.47 \mu\text{mol}/\text{m}^2$) as well as sulfur loadings (1.20 vs $1.18 \mu\text{mol}/\text{m}^2$) which corresponds to around 34% yields for selector bonding and around 53% yields for PMPMS immobilization (cf. CSP # 6 and 7). At identical reaction times, the surface coverages of selector and sulfur could be increased to 0.61 and $0.73 \mu\text{mol}/\text{m}^2$ (tBuCQN) as well as 1.89 and $2.11 \mu\text{mol}/\text{m}^2$ (sulfur) (corresponding to yields in the order of 45–54% and 84–93% for tBuCQN and PMPMS, respectively) in presence of 2 and 1 mL toluene, respectively, by the solvent-assisted film method (cf. CSP # 21 and 22). The thermally initiated film method provided coverages of 0.50 and $1.23 \mu\text{mol}/\text{m}^2$ for selector and sulfur, respectively, at the same reaction time (120 min) corresponding to 34 and 54% yields (CSP # 23). This is quite comparable to the UV-initiated film method (CSP # 1). On contrary, the UV-initiated brush-type CSP # 4 showed by a factor of ~ 2 lower immobilization yields.

For evaluation of the chromatographic performance of these newly synthesized CSPs, Fmoc-Phe served as test compound. The *S*-enantiomer was always stronger retained than the *R*-enantiomer. The results of the chromatographic parameters on the different CSPs are summarized in Table 2 along with test conditions. For a deeper insight into peak dispersion contributions in dependence of synthesis parameters, we recorded for each column a Van Deemter (H/u) curve and the coefficients for Eddy diffusion (A-term), longitudinal diffusion (B-term) and mass transfer resistance (C-term) derived by curve fitting using the Van Deemter equation are given in Table 2. It is quite interesting to note that retention factors were systematically lower with the slurry method compared to the film method in spite of similar selector and thiol coverages (cf. CSP # 6 - 11 in Tables 1 and 2). Separation factors are comparable (~ 1.5). The slurry method gives on average slightly better chromatographic efficiency as can be seen from higher theoretical plate numbers ($N_{1, \text{opt}}/m$) and lower reduced plate height at optimal flow rate h_{min} . The coefficients of the Van Deemter equation clearly reveal a significantly lower mass transfer resistance (C-term) for the slurry method, most probably due to the lower selector coverage, while the A-terms are relatively similar (cf. CSP 6 and 7 in Table 2).

On the other hand, it is worthwhile to note that the higher selector coverage of the CSPs # 21 and 22 prepared with the solvent-assisted film method is not associated with higher C-term. It seems that the solvent added during the photo-click reaction reduces the dynamic viscosity of the PMPMS film and enhances the diffusivity of the reactants (PMPMS, selector and UV irradiation-triggered radicals) during reaction. The solvent appears to improve both the reaction rates and morphology of the surface coating, possibly leading to a more homogenous, thinner film compared to thick irregular patches without solvent. The results in terms of C-term are comparable to the ones of the thermally initiated film approach (CSP # 23 - 25) although the latter have a lower selector coverage.

3.3.2. Effect of reaction time

The solvent-assisted film approach gave the best results in the above described initial tests. However, further optimization experiments with regard to surface coverage, enantioselectivity and chromatographic efficiency focused on film and slurry methods to keep the reaction process simple and avoid the additional influence of the reaction solvent. To figure out the influence of the reaction time on the selector coverages, film and slurry synthesis strategies have been tested with different reaction times between 30 min and 2 h. Results regarding selector and sulfur coverages can be found in Table 1 and corresponding chromatographic performance data in Table 2. Fig. 3 visualizes the major trends in graphical form. Here, it can be seen that the increase in selector and sulfur coverage with reaction time is steeper for the slurry method than the film approach (Fig. 3a and 3b). It mainly tells us that in case of the slurry method the faster bonding rate of PMPMS onto the surface limits the overall selector immobilization efficiency. At 30 min and 1 h reaction time, selector coverages are significantly higher for the film method due to more reactive sulfhydryls on the silica surface (Fig. 3a and 3b). After 3 h of reaction, the selector coverage was, however, comparable as stated above. Also, the ratio of sulfur-to-selector is very similar (Fig. 3c). Fig. 3d shows that the retention factors are plateauing at two distinct levels for film (higher k of around 2.4) and slurry method (lower k at around 1) with little variation in dependence on reaction time. Since plate numbers drop with reaction time, also resolution is smaller with 3 h reaction in case of the film method (Fig. 3e and 3f). Fig. 3f again confirms that chromatographic efficiencies are significantly higher for the slurry method which might have something to do with the specific morphology of the PMPMS film or chains.

3.3.3. Effect of reactants' concentration

The initial quantities of reactants and their ratio to each other represent crucial factors for the optimization of the photo-click immobilization process with regard to surface coverage, enantioselectivity and chromatographic efficiency. Consequently, initial amounts of tBuCQN as well as PMPMS in the starting reaction mixture were systematically altered along with reaction time. In order to understand the change of the response (viz. here the tBuCQN surface coverage) in dependence on the investigated factors, a DoE approach using a screening design was utilized. tBuCQN and PMPMS in the reaction mixture and reaction time were continuous variables in the design and the synthesis method (slurry and film approach) were considered as discrete variables. A fractional factorial design Resolution IV was employed. Due to a limited number of experiments a model with linear terms only was evaluated and the coefficients as well as statistical parameters are given in Suppl. Material. The resultant model gives useful trends of the different factors, however, does not have predictive quality which was not the goal of this screening design (note, the inclusion of quadratic terms and model derivation by PLS rather than MLR improved the predictive quality but statistical parameters could

Table 2
Summary of the chromatographic results.

CSP #	Reaction conditions		Coverage		Chromatographic results ^a							
	Reaction type	Initiation	Reaction time [min]	tBuCQN [$\mu\text{mol}/\text{m}^2$]	k_1	α_{opt}^b	R^c	$N_{1, \text{opt}}/\text{m}^2$	h_{min}	A [10^{-3} mm]	B [10^{-3} mm ² s ⁻¹]	C [10^{-3} s]
1	Brush-type ^{d, e}	T	420	1.14	3.40	1.54	4.47	61,753	3.24	8.66 ± 1.64	0.76 ± 0.17	7.84 ± 0.29
2	Brush-type	UV	30	0.19 ± 0.001	0.56	1.52	1.65	86,640	2.31	7.22 ± 0.74	2.21 ± 0.13	3.88 ± 0.08
3	Brush-type	UV	60	0.21 ± 0.002	0.49	1.52	1.22	81,900	2.44	3.39 ± 1.10	3.29 ± 0.20	6.87 ± 0.13
4	Brush-type	UV	120	0.20 ± 0.002	0.33	1.52	1.05	75,500	2.65	4.64 ± 1.72	2.68 ± 0.45	5.38 ± 0.26
5	Brush-type	UV	420	0.41 ± 0.007	1.61	1.32	1.46	73,880	2.71	7.30 ± 0.61	2.48 ± 0.11	5.95 ± 0.07
6	film	UV	120	0.44 ± 0.001	0.73	1.46	1.22	61,375	3.26	7.64 ± 0.65	2.32 ± 0.11	7.65 ± 0.09
7	slurry	UV	120	0.47 ± 0.002	0.14	1.52	0.75	76,546	2.61	9.30 ± 2.12	1.87 ± 0.31	3.33 ± 0.56
8	film	UV	60	0.35 ± 0.010	0.62	1.48	1.24	64,055	3.12	9.1 ± 0.96	2.09 ± 0.17	6.60 ± 0.11
9	slurry	UV	60	0.29 ± 0.014	0.18	1.51	0.80	74,087	2.70	9.00 ± 1.64	2.60 ± 0.39	3.40 ± 0.34
10	film	UV	30	0.34 ± 0.008	0.58	1.52	1.51	69,909	2.86	7.28 ± 2.69	6.51 ± 0.48	4.36 ± 0.31
11	slurry	UV	30	0.14 ± 0.010	0.14	1.47	0.45	92,374	2.17	4.59 ± 2.61	3.76 ± 0.98	3.54 ± 0.76
12	film	UV	60	0.21 ± 0.003	0.19	1.52	0.58	54,656	3.66	9.04 ± 2.71	4.07 ± 0.58	7.73 ± 0.89
13	film	UV	60	0.34 ± 0.004	0.50	1.50	1.32	75,227	2.66	7.66 ± 0.48	1.72 ± 0.08	4.60 ± 0.07
14	film	UV	60	0.22 ± 0.010	0.17	1.48	0.60	80,758	2.48	8.03 ± 2.78	2.20 ± 0.41	3.89 ± 0.74
15	film	UV	60	0.42 ± 0.002	0.62	1.50	1.17	55,398	3.61	9.00 ± 0.85	2.72 ± 0.14	7.90 ± 0.12
16	film	UV	60	0.36 ± 0.000	0.41	1.55	1.12	61,975	3.23	7.00 ± 1.07	2.74 ± 0.19	6.02 ± 0.12
17	slurry	UV	231	0.20 ± 0.003	0.33	1.38	1.00	60,320	2.82	7.72 ± 4.89	3.13 ± 1.27	5.89 ± 0.62
18	slurry	UV	388	0.25 ± 0.000	0.52	1.32	0.80	82,040	2.44	4.89 ± 2.00	2.49 ± 0.37	6.19 ± 0.28
19	film	UV	376	0.62 ± 0.007	1.08	1.40	0.59	32,240	6.20	15.49 ± 1.53	1.78 ± 0.20	36.41 ± 0.78
20	film	UV	706	0.66 ± 0.007	0.90	1.42	0.47	24,620	8.12	23.1 ± 4.40	1.33 ± 0.50	65.96 ± 3.72
21	solvent assisted film ^f	UV	120	0.61 ± 0.005	0.70	1.44	1.95	76,500	2.61	8.85 ± 0.86	3.50 ± 0.12	3.56 ± 0.10
22	solvent assisted film ^g	UV	120	0.73 ± 0.007	0.92	1.41	1.81	57,780	3.46	12.26 ± 1.03	2.94 ± 0.18	4.55 ± 0.12
23	film, thermal ^{d, g}	T	120	0.50	0.74	1.51	3.00	37,620	5.32	21.59 ± 1.04	1.96 ± 0.52	4.61 ± 0.13
24	film, thermal ^{d, g}	T	240	0.55	0.75	1.52	3.92	66,340	3.01	9.38 ± 0.72	2.87 ± 0.13	4.00 ± 0.10
25	film, thermal ^{d, g}	T	480	0.57	1.07	1.50	4.68	67,560	2.96	8.01 ± 0.26	2.86 ± 0.45	4.14 ± 0.36

^a mob. ph. MeOH/Ac/NH₄Ac (98/2/0.5, v/v/w).

^b index "opt" stands for results at optimum flow rate.

^c R at a linear flow rate of 5.89 mm/s.

^d column length for CSPs 1 and 23 - 25: 150 mm.

^e commercial brush-type material on 5 μm , 120 Å FPP was used as benchmark.

^f solvent assisted film was carried out with additional toluene on particles.

^g results for coverages of CSP 23 - 25 taken from Schmitt et al. [39].

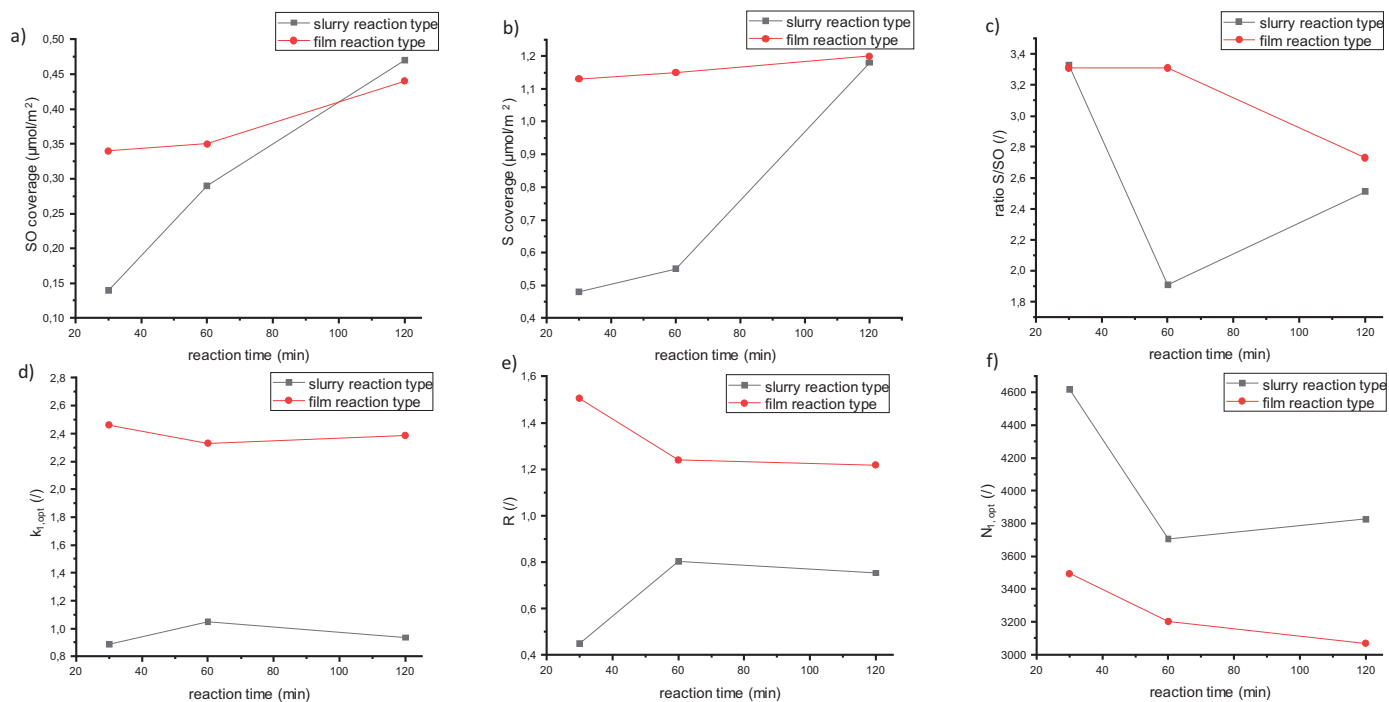


Fig. 3. Effect of reaction time on surface coverages of tBuCQN selector (SO) (a), sulfur (S) coverage (b), sulfur (S)/selector (SO) ratio (c), retention factor k_1 at optimal flow velocity (d), resolution (e), column plate number (at optimal flow velocity) ($L = 5$ cm) (f) for slurry and film method. The data correspond to CSPs # 6 - 11.

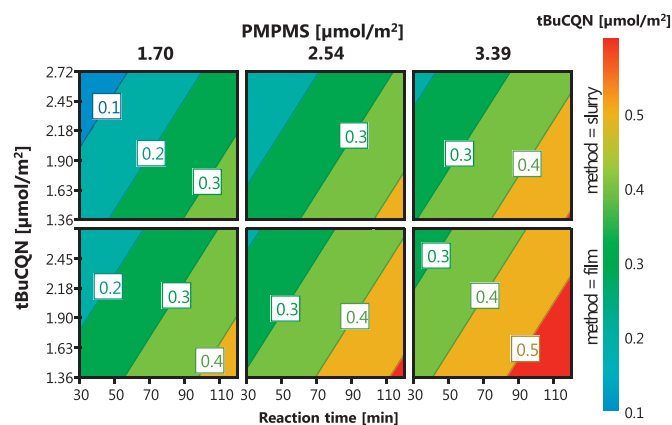


Fig. 4. DoE optimization for the synthesis of the chiral stationary phase considering 4 factors, tBuCQN and PMPMS concentrations, reaction time and synthesis approach (film as well as slurry method). The top panels show the response surfaces (tBuCQN coverage) for the slurry method, the bottom panels for the film method.

not be comprehensively evaluated). Response surfaces for the linear model are depicted in Fig. 4. They show that the surface coverage increases with reaction time and PMPMS amount in the reaction mixture. On contrary, the model also reveals that a higher selector concentration in the reaction mixture leads to lower surface coverage, which is a bit counterintuitive at first glance. It may, however, be explained by increasing modification of the thiols of PMPMS by the selector so that these thiols are not available for surface grafting anymore. From this viewpoint this result also makes sense because of the competitive nature of reactions taking place. An initial weight ratio of 2.5 of sulfur (PMPMS) and selector seems to be most promising with the chosen conditions.

3.4. Chromatographic performance

A summary of the chromatographic performance of the synthesized CSPs is given in Table 2. In general, the main goal of the development of a useful CSP is to obtain sufficient enantioselectivity and good chromatographic performance, i.e. low plate height. This does not necessitate a high selector coverage. However, a certain concentration of chiral selector is needed. As can be seen from Table 2, the average separation factor of all synthesized columns is $1.47 (\pm 0.06)$ which corresponds to an RSD of 4.4% while selector coverages and retention factors show variances of 43.7% and 93.5% RSD, respectively. Even the CSP with the lowest selector coverage (CSP # 11) having grafted $0.14 \mu\text{mol}/\text{m}^2$ of tBuCQN only gives a separation factor of 1.47. The chromatographic efficiency seems to depend on several factors, amongst others on the method of immobilization but to some extent also on the surface coverage. It is interesting to note that the C-term is smaller for the slurry method as compared to the film method in the experiments of direct comparison (CSP # 6 vs 7, 8 vs 9, and 10 vs 11). Overall, reduced plate heights in the order of 2 to 4 are decent but can be certainly further improved. In particular, column packing may need systematic optimization, as can be deduced from the A-terms (see Table 2).

Fig. 5 depicts a comparison of test chromatograms of Fmoc-Phe-obtained with CSPs prepared by distinct approaches. Note that Fig. 5a) as well as Fig. 5c) were recorded with a 150 mm long column while all other chromatograms were recorded with 50 mm long columns. All columns were based on $5 \mu\text{m}$ particles. The mobile phase for all chromatograms was methanol/acetic acid/ammonium acetate (98/2/0.5, v/v/w), and all chromatograms were recorded at the optimal linear velocity of 0.88 mm/s. It can be seen that the brush-type phase synthesized by thermally initiated

click reaction (CSP # 1) gives symmetrical peaks with reduced minimal plate height h_{min} of 3.24 and 61,753 plates/m (Fig. 5a). The corresponding photo-clicked brush-type CSP with the same 7 h reaction time (CSP # 5) produced 73,890 plates/m and provided a h_{min} of 2.71. The peak width at half height looks better which may be related to the significantly lower selector coverage (0.40 and $1.14 \mu\text{mol}/\text{m}^2$ for CSP # 5 and 1, respectively). Peak widths at the basis are, unfortunately, a bit unfavorable for the photo-initiated brush phase and may indicate a sub-optimal column packing. Optimization of column packing may overcome this problem but was not performed in this work because CSPs were synthesized in small quantities only. Another option for improving the peak shape is to oxidize residual thiols and thioethers (vide infra). Figs. 5c) to 5e) show test chromatograms of the thermally initiated (CSP # 23) and UV-initiated film synthesis method (CSP # 6) as well as UV-initiated slurry approach (CSP # 7). In spite of comparable selector coverages of $0.47 (\pm 0.03) \mu\text{mol}/\text{m}^2$, chromatographic parameters are significantly different. For example, the slurry method furnished columns with much less retention (as mentioned above). The chromatographic efficiency increased from 37,620/m (h_{min} 5.32) for CSP # 23 (thermal initiation, film), to 61,375/m (h_{min} 3.26) for CSP # 6 (UV initiation, film) to 76,546/m (h_{min} 2.61) for CSP # 7 (UV initiation, slurry). The UV-initiated solvent-assisted film method (Fig. 5f, CSP # 21) gave slightly better performance in terms of peak width at half height compared to the approach without toluene (Fig. 5d, CSP # 6) (76,500 plates/m; h_{min} 2.61).

The lower selector coverages of the CSPs synthesized by photo-click immobilization in combination with the employed standard mobile phase (methanol/acetic acid/ammonium acetate, 98/2/0.5, v/v/w) led to small retention factors. However, simple dilution of this mobile phase with MeOH to reduce the ionic strength and counterion concentration of the mobile phase afforded a significantly weaker eluent and appropriate retention factors (Fig. 6). A 1:20 and 1:40 (v/v) diluted mobile phase provided baseline separations of Fmoc-Phe-on CSP # 7 prepared by UV-initiated slurry method (Fig. 6b and c) and allowed to adjust largely equivalent separations to the brush-type benchmark on CSP # 6 prepared by UV-initiated film method (Fig. 6d–f). The diluted mobile phases render elution conditions better compatible with mass spectrometry and electrospray ionization, respectively.

The chromatographic data in Table 2 were derived from experiments with the same mobile phase. Due to distinct retention factors perfect comparability may be compromised. Thus, CSPs prepared by UV- and thermally initiated click immobilization by film approach (CSP # 10 and 24, respectively) were compared using isoelutropic conditions, i.e. equal retention factor adjusted by mobile phase dilution, with regard to their Van Deemter curves (Fig. 7). It can be seen that CSP # 24 (thermally initiated film method) shows slight superiority in terms of chromatographic efficiency. The mass transfer resistance term (C-term) is slightly smaller for the thermally initiated method. This might be caused by the inability of the UV light rays to penetrate deeply into the pores of the silica to start the immobilization process. Especially when applying the film method, diffusion of the radicals and the photoinitiator's decomposition products that are formed on the better accessible outer surface of the silica into the pores is limited due to poor diffusivity in the viscous polymer film. Hence, at ambient temperature the selector bonding to the vinyl silica surface inside the pores is inefficient and the surface might be chemically more heterogeneous as compared to reaction at higher temperature of the thermally initiated process. However, both columns show a comparable minimum in reduced plate height (3.83 for CSP # 10, 3.01 for CSP # 24 (both for isoelutropic conditions, values for reduced plate height with undiluted mobile phase: 2.86 for CSP # 10, 3.01 for CSP # 24)).

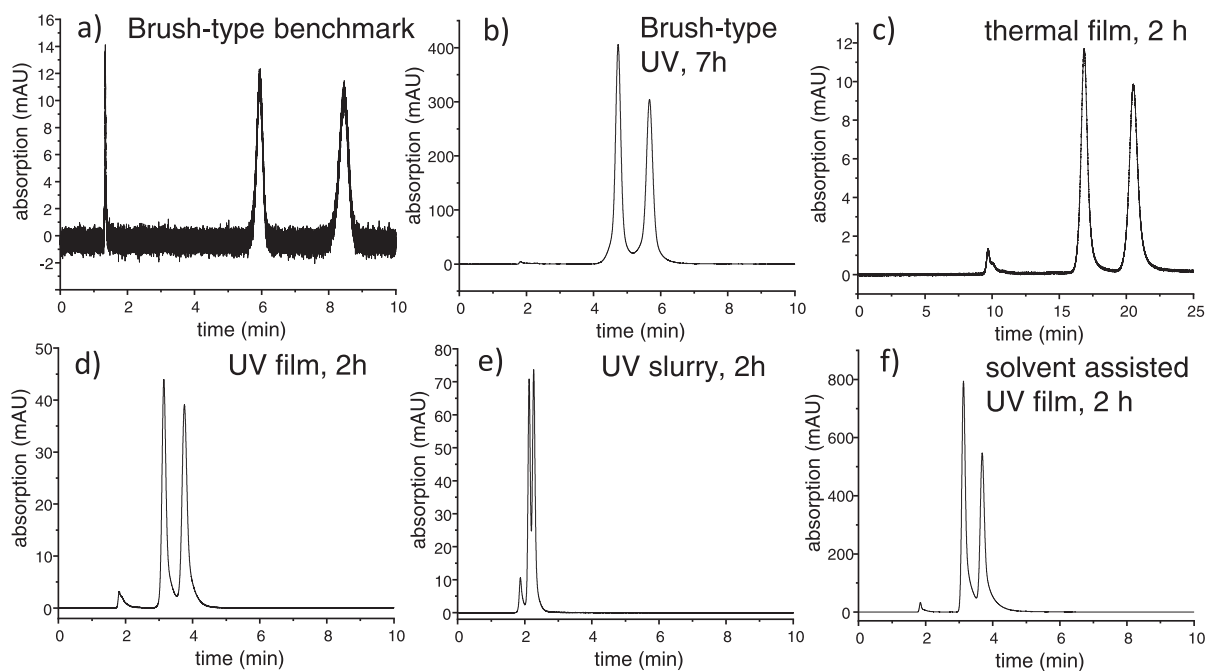


Fig. 5. Representative chromatograms for the distinct synthesis approaches. (a) Brush-type benchmark obtained by thermally initiated thiol-ene click immobilization (CSP # 1). (b) UV-initiated brush-type CSP (CSP # 5), (c) thermally initiated PMPMS-bonded film method (2 h reaction time) (CSP # 23), (d) UV-initiated PMPMS-bonded film method (2 h reaction) (CSP # 6), (e) UV-initiated PMPMS-bonded slurry method (2 h) (CSP # 7), (f) solvent-assisted UV-initiated PMPMS-bonded film method with 2 mL toluene (CSP # 21). All chromatograms were recorded with methanol/acetic acid/ammonium acetate (98/2/0.5, v/v/w) as mobile phase and Fmoc-Phe-as analyte. Flow rate for all chromatograms is 0.15 ml/min. Column length 150 mm (a,c) and 50 mm (b,d,e,f), respectively.

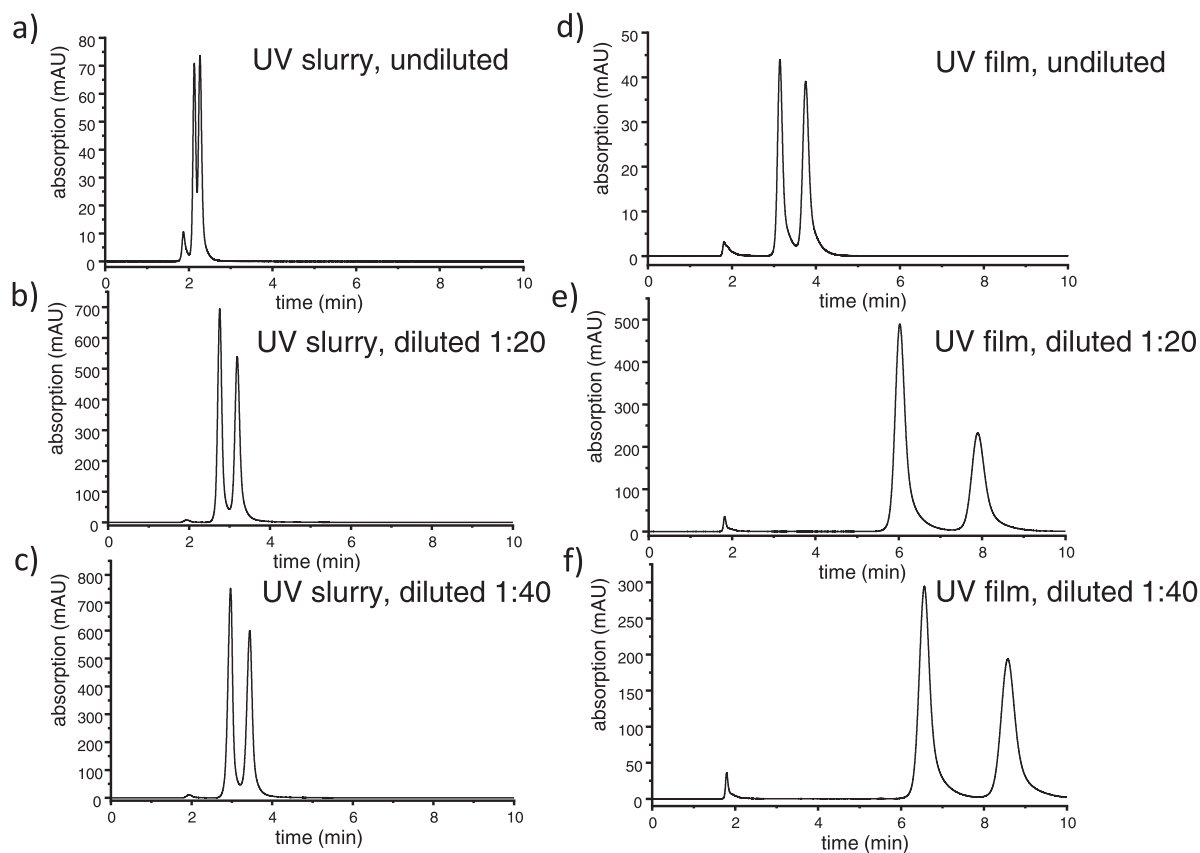


Fig. 6. Effect of ionic strength (mobile phase dilution) on separation of Fmoc-Phe on PMPMS-bonded CSP synthesized by UV-initiated slurry method (CSP # 7) (a,b,c) and by UV-initiated film method (CSP # 6) (d,e,f) (reaction time 120 min for both). Eluents, methanol/acetic acid/ammonium acetate (98/2/0.5, v/v/w) (a,d), 1:20 diluted (b,e) and 1:40 diluted mobile phase (c,f). Flow rate for all chromatograms was 0.15 ml/min, detection at 254 nm.

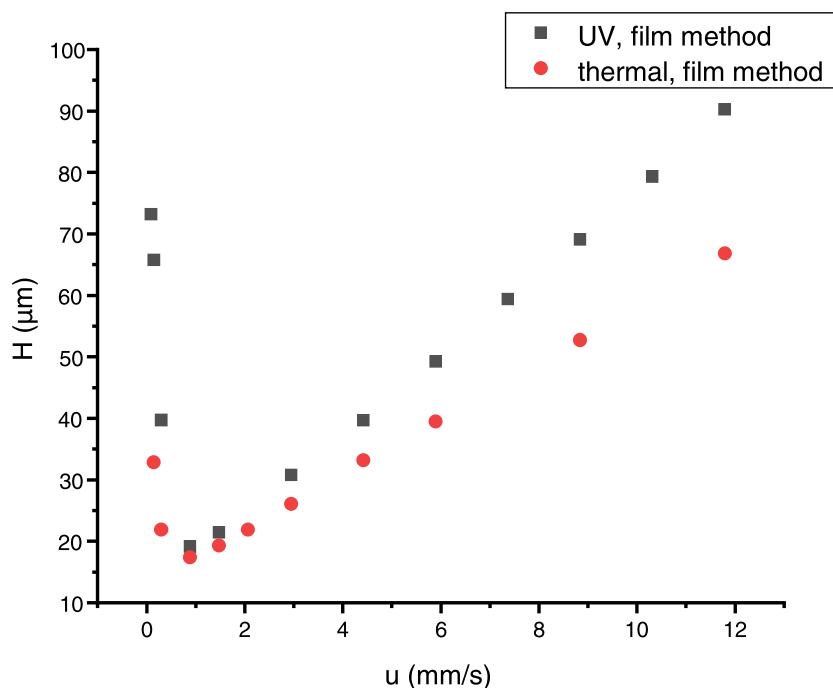


Fig. 7. Comparison of efficiencies (Van Deemter curves) of PMPMS-bonded CSPs prepared by UV-initiated (CSP # 10) and thermally initiated film method (CSP # 24) at isoelutropic conditions. Mobile phase was methanol/acetic acid/ammonium acetate (98/2/0.5, v/v/w) for thermally initiated CSP, and (99.74/0.26/0.065, v/v/w) for UV-initiated CSP.

As indicated above, oxidation of the surface to modify residual thiols into sulfonic acid groups and thioethers into sulfones is a simple strategy to improve peak shapes. It seems that the presence of sulfonate groups minimizes secondary interactions which

translates into more symmetrical peaks as is documented by a comparison of non-oxidized and oxidized CSP # 22 (see Fig. 8). The solvent-assisted photoclick synthesized non-oxidized CSP # 22 shows an ugly peak asymmetry as the material is a bit sticky during column packing (Fig. 8a). In contrast, the oxidized CSP # 22 obtained by treatment with performic acid shows perfect peak symmetry (Fig. 8b).

Overall, the thermal immobilization methods seem to be superior than photo-click immobilization in the current version. However, photochemical methods might become an interesting alternative to the thermal methods, if some specific limitations as outlined in the Conclusions (vide infra) can be addressed successfully.

4. Conclusions

In this work, we presented the proof-of-principle of thiol-ene photo-click immobilization of a chiral vinyl ligand on silica particles. Distinct approaches of linking chemistries were evaluated comprising brush-type bonding of the ligand to thiol silica and its bonding to vinylsilica via a polythiol crosslinker. Brush-type photo-click immobilization yielded lower selector coverages as compared to polythiol-mediated photo-click immobilization. Photoclick immobilization of the selector via coated polythiol film yielded about the same surface coverage as compared to the approach in which all reactants including polythiol were suspended in the slurry of vinyl-silica. In spite of similar selector coverages, the former showed stronger retention of a chiral acidic probe. A solvent-assisted film approach with toluene allowed to enhance yields of the immobilization reaction to ~90% for thiol and ~50% for selector. Separation factors achieved with the distinct approaches were relatively constant (1.47 ± 0.6), but retention factors differed significantly when identical mobile phases were applied. Resultant phases with low coverage and low retention, respectively, required adjustment of the ionic strength in the mobile phase. Overall, useful CSPs were obtained but the procedure has certainly some room for further improvements. For example, the photoinitiator should be fine-tuned. Its absorbance maximum should not overlap with

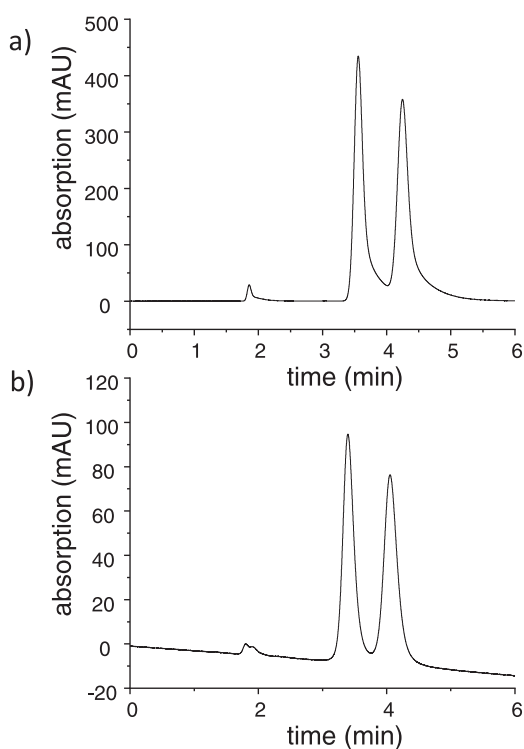


Fig. 8. Comparison of peak symmetry obtained with (a) non-oxidized CSP # 22, and (b) oxidized CSP # 22. Conditions: (a) Mobile phase, methanol/acetic acid/ammonium acetate (98/2/0.5, v/v/w), and (b) with isoelutropic conditions, i.e. mobile phase of (a) diluted with methanol (50:50; v/v); flow rate, 0.15 mL/min (a and b).

absorbance bands of the selector, so that the UV light is more efficiently exploited for generation of radicals. It is expected that reaction rates can then be accelerated. The light source might be another factor for optimization and the transmittance of the reaction vessel should also be considered. To what extent the UV light permeates the silica particles is unclear. However, it is known that toluene and xylene make porous silica translucent which could be beneficial in terms of local radical concentrations inside the pores. The solvent-assisted film approach has some potential for further optimization in this regard. While the application of temperature may be favourable in terms of homogeneity of the coated film, the UV-initiated process at ambient temperature is regarded a mild and safe process, worth to be considered as alternative.

Declaration of Competing Interest

The authors declare that they have no known competing financial interests or personal relationships that could have appeared to influence the work reported in this paper.

Supplementary materials

Supplementary material associated with this article can be found, in the online version, at [doi:10.1016/j.chroma.2020.461133](https://doi.org/10.1016/j.chroma.2020.461133).

CRedit authorship contribution statement

Christian Geibel: Investigation, Methodology, Formal analysis, Data curation, Visualization, Writing - original draft, Writing - review & editing. **Kristina Dittrich:** Investigation, Data curation, Writing - review & editing. **Marc Wolter:** Investigation, Writing - review & editing. **Michael Lämmerhofer:** Conceptualization, Methodology, Supervision, Writing - review & editing, Resources.

References

- [1] X. Liang, A. Shen, Z. Guo, The application of thiol-ene/yne radical click chemistry in surface modification and functionalization, in: A. Lowe, C. Bowman (Eds.), *Thiol-X Chemistries in Polymer and Materials Science*, Royal Society of Chemistry, 2013, pp. 286–308.
- [2] L.F. Ribeiro, J.C. Masini, F. Svec, Use of thiol functionalities for the preparation of porous monolithic structures and modulation of their surface chemistry: a review, *Trends Anal. Chem.* 118 (2019) 606–624.
- [3] C. Rosini, C. Bertucci, D. Pini, P. Altemura, P. Salvadori, Cinchona alkaloids for preparing new, easily accessible chiral stationary phases. I. 11-(10,11-Dihydro-6'-methoxycinchonan-9-ol)-thiopropylsilylated silica, *Tetrahedron Lett.* 26 (1985) 3361–3364.
- [4] E. Veigl, B. Böhs, A. Mandl, D. Krametter, W. Lindner, Evaluation of silica gel-based brush type chiral cation exchangers with (S)-N-(3,5-dinitrobenzoyl)tyrosine as chiral selector: attempt to interpret the discouraging results, *J. Chromatogr. A* 694 (1995) 151–161.
- [5] A. Tambute, L. Siret, A. Begos, M. Caude, Improvement of the enantioselectivity of tyrosine-derived chiral stationary phases: direct resolution of 1,2-amino-alcohols (β -blockers), *Chirality* 4 (1992) 36–42.
- [6] M. Lämmerhofer, W. Lindner, Quinine and quinidine derivatives as chiral selectors. I. Brush type chiral stationary phases for high-performance liquid chromatography based on cinchonan carbamates and their application as chiral anion exchangers, *J. Chromatogr. A* 741 (1996) 33–48.
- [7] J. Horak, W. Lindner, Investigations on the chromatographic behavior of hybrid reversed-phase materials containing electron donor-acceptor systems: I. Contribution of sulfur-aromatic interactions, *J. Chromatogr. A* 1043 (2004) 177–194.
- [8] R. Nogueira, M. Lämmerhofer, W. Lindner, Alternative high-performance liquid chromatographic peptide separation and purification concept using a new mixed-mode reversed-phase/weak anion-exchange type stationary phase, *J. Chromatogr. A* 1089 (2005) 158–169.
- [9] B. Preinerstorfer, W. Bicker, W. Lindner, M. Lämmerhofer, Development of reactive thiol-modified monolithic capillaries and in-column surface functionalization by radical addition of a chromatographic ligand for capillary electrochromatography, *J. Chromatogr. A* 1044 (2004) 187–199.
- [10] A. Shen, Z. Guo, L. Yu, L. Cao, X. Liang, A novel zwitterionic hilic stationary phase based on "thiol-ene" click chemistry between cysteine and vinyl silica, *Chem. Commun.* 47 (2011) 4550–4552.
- [11] E.J. Carrasco-Correa, M. Ferri, U. Woiwode, Y. Ma, J.M. Herrero-Martinez, G. Ramis-Ramos, W. Lindner, M. Lämmerhofer, Zwitterionic codeine-derived methacrylate monoliths for enantioselective capillary electrochromatography of chiral acids and chiral bases, *Electrophoresis* 39 (2018) 2558–2565.
- [12] M. Kohout, S. Wernisch, J. Tuma, H. Hettegger, J. Picha, W. Lindner, Effect of different immobilization strategies on chiral recognition properties of cinchona-based anion exchangers, *J. Sep. Sci.* 41 (2018) 1355–1364.
- [13] M. De Martino, G. Bencivenni, A. Mazzanti, S. Menta, O.H. Ismail, R. Sabia, A. Ciogli, 3,5-Dinitrobenzoyl-9-amino-9-deoxy-9-epiquinine as pirkle-anion exchange hybrid-type chiral selector in high-performance liquid chromatography, *Chromatographia* 80 (2017) 751–762.
- [14] L. Qiao, H. Li, Y. Shan, S. Wang, X. Shi, X. Lu, G. Xu, Study of surface-bonded dicationic ionic liquids as stationary phases for hydrophilic interaction chromatography, *J. Chromatogr. A* 1330 (2014) 40–50.
- [15] A.F.G. Gargano, T. Leek, W. Lindner, M. Lämmerhofer, Mixed-mode chromatography with zwitterionic phosphopeptidomimetic selectors from UGI multicomponent reaction, *J. Chromatogr. A* 1317 (2013) 12–21.
- [16] L. Qiao, A. Dou, X. Shi, H. Li, Y. Shan, X. Lu, G. Xu, Development and evaluation of new imidazolium-based zwitterionic stationary phases for hydrophilic interaction chromatography, *J. Chromatogr. A* 1286 (2013) 137–145.
- [17] A. Shen, X. Li, X. Dong, J. Wei, Z. Guo, X. Liang, Glutathione-based zwitterionic stationary phase for hydrophilic interaction/cation-exchange mixed-mode chromatography, *J. Chromatogr. A* 1314 (2013) 63–69.
- [18] Q. Wang, Y. Long, L. Yao, L. Xu, Z.-G. Shi, L. Xu, Preparation, characterization and application of a reversed phase liquid chromatography/hydrophilic interaction chromatography mixed-mode C18-DTT stationary phase, *Talanta* 146 (2016) 442–451.
- [19] C. Xiong, J. Yuan, Z. Wang, S. Wang, C. Yuan, L. Wang, Preparation and evaluation of a hydrophilic interaction and cation-exchange chromatography stationary phase modified with 2-methacryloyloxyethyl phosphorylcholine, *J. Chromatogr. A* 1546 (2018) 56–65.
- [20] T.T.H. Dao, M. Guerrouache, B. Carbonnier, Thiol-yne click adamantane monolithic stationary phase for capillary electrochromatography, *Chin. J. Chem.* 30 (2012) 2281–2284.
- [21] E.P. Shields, S.G. Weber, A liquid chromatographic charge transfer stationary phase based on the thiol-yne reaction, *J. Chromatogr. A* 1591 (2019) 1–6.
- [22] P. Jonkheijm, D. Weinrich, M. Köhn, H. Engelkamp, P.C.M. Christianen, J. Kuhlmann, J.C. Maan, D. Nüsse, H. Schroeder, R. Wacker, R. Reinbauer, C.M. Niemeyer, H. Waldmann, Photochemical surface patterning by the thiol-ene reaction, *Angew. Chem. Int. Ed.* 47 (2008) 4421–4424.
- [23] C. Wendeln, S. Rinnen, C. Schulz, H.F. Arlinghaus, B.J. Ravoo, Photochemical microcontact printing by thiol-ene and thiol-yne click chemistry, *Langmuir* 26 (2010) 15966–15971.
- [24] E. Melnik, P. Muellner, O. Bethge, E. Bertagnoli, R. Hainberger, M. Lämmerhofer, Streptavidin binding as a model to characterize thiol-ene chemistry-based polyamine surfaces for reversible photonic protein biosensing, *Chem. Commun.* 50 (2014) 2424–2427.
- [25] H. Zhang, J. Ou, Z. Liu, H. Wang, Y. Wei, H. Zou, Preparation of hybrid monolithic columns via "One-Pot" photoinitiated thiol-acrylate polymerization for retention-independent performance in capillary liquid chromatography, *Anal. Chem.* 87 (2015) 8789–8797.
- [26] C. Kip, C. Demir, A. Tuncel, One pot synthesis of carboxyl functionalized-polyhedral oligomeric siloxane based monolith via photoinitiated thiol-methacrylate polymerization for nano-hydrophilic interaction chromatography, *J. Chromatogr. A* 1502 (2017) 14–23.
- [27] Y. Wang, S. Ma, Y. Chen, L. Zhang, J. Ou, Y. Shen, M. Ye, Thiol-radical-mediated polymerization for preparation of POSS-containing polyacrylate monoliths in capillary liquid chromatography, *Talanta* 190 (2018) 62–69.
- [28] C. Kip, S. Liu, X. Fu, A. Tuncel, M. Lämmerhofer, In-situ photopolymerized C4-functionalized organosilicon monoliths for reversed-phase protein separation in nano-liquid chromatography, *Talanta* 198 (2019) 330–336.
- [29] Y. Wang, S. Ma, L. Zhang, N. Zhang, Y. Li, J. Ou, Y. Shen, M. Ye, Fast fabrication of a hybrid monolithic column containing cyclic and aliphatic hydrophobic ligands via photo-initiated thiol-ene polymerization, *J. Sep. Sci.* 42 (2019) 1332–1340.
- [30] M. Li, X. Lei, Y. Huang, Y. Guo, B. Zhang, F. Tang, X. Wu, Ternary thiol-ene photopolymerization for facile preparation of ionic liquid-functionalized hybrid monolithic columns based on polyhedral oligomeric silsesquioxanes, *J. Chromatogr. A* 1597 (2019) 167–178.
- [31] H. Zhang, S. Ma, Y. Yao, Y. Li, Y. Li, J. Ou, M. Ye, Y. Wei, Facile preparation of multi-functionalized hybrid monoliths via two-step photo-initiated reactions for two-dimensional liquid chromatography-mass spectrometry, *J. Chromatogr. A* 1524 (2017) 135–142.
- [32] M.B. Espina-Benitez, J. Randon, C. Demesmay, V. Dugas, Development of a new in-line coupling of a miniaturized boronate affinity monolithic column with reversed-phase silica monolithic capillary column for analysis of cis-diol-containing nucleoside compounds, *J. Chromatogr. A* 1597 (2019) 209–213.
- [33] X. Wang, J. Peng, H. Peng, J. Chen, H. Xian, R. Ni, S. Li, D. Long, Z. Zhang, Preparation of two ionic liquid bonded stationary phases and comparative evaluation under mixed-mode of reversed phase/ hydrophilic interaction/ ion exchange chromatography, *J. Chromatogr. A* 1605 (2019) 460372.
- [34] A.V. Bordoni, M.V. Lombardo, A. Wolosiuk, Photochemical radical thiol-ene click-based methodologies for silica and transition metal oxides materials chemical modification: a mini-review, *RSC Adv.* 6 (2016) 77410–77426.
- [35] A. Mandl, L. Nicoletti, M. Lämmerhofer, W. Lindner, Quinine- versus carbamoylated quinine-based chiral anion exchangers: a comparison regarding enantioselectivity for N-protected amino acids and other chiral acids, *J. Chromatogr. A* 858 (1999) 1–11.

- [36] N. Maier, L. Nicoletti, M. Lämmerhofer, W. Lindner, Enantioselective anion exchangers based on cinchona alkaloid-derived carbamates: influence of C8/C9 stereochemistry on chiral recognition, *Chirality* 11 (1999) 522–528.
- [37] T. Teerlink, Derivatization of posttranslationally modified amino acids, *J. Chromatogr. B Biomed. Sci. Appl.* 659 (1994) 185–207.
- [38] I.S. Krull, Z. Deyl, H. Lingemann, General strategies and selection of derivatization reactions for liquid chromatography and capillary electrophoresis, *J. Chromatogr. B Biomed. Sci. Appl.* 659 (1994) 1–17.
- [39] K. Schmitt, M. Lämmerhofer, Optimization of the surface modification process of cross-linked polythiol-coated chiral stationary phases synthesized by a two-step thiol-ene click reaction, *J. Sep. Sci.* 41 (2018) 1338–1345.
- [40] P. Levkin, N. Maier, W. Lindner, V. Schurig, A practical method for the quantitative assessment of non-enantioselective versus enantioselective interactions encountered in liquid chromatography on brush-type chiral stationary phase, *J. Chromatogr. A* 1269 (2012) 270–278.
- [41] A.B. Lowe, Thiol-ene “click” reactions and recent applications in polymer and materials synthesis, *Polym. Chem.* 1 (2010) 17–36.
- [42] N.F. Ayub, S. Hashim, J. Jamaluddin, N. Adrus, New UV LED curing approach for polyacrylamide and poly(N-isopropylacrylamide) hydrogels, *New J. Chem.* 41 (2017) 5613–5619.
- [43] A. Zimmermann, J. Horak, A. Sievers-Engler, C. Sanwald, W. Lindner, M. Kramer, M. Lämmerhofer, Surface-crosslinked poly(3-mercaptopropyl)methylsiloxane-coatings on silica as new platform for low-bleed mass spectrometry-compatible functionalized stationary phases synthesized via thiol-ene click reaction, *J. Chromatogr. A* 1436 (2016) 73–83.

1 **Supplementary Material**

2
3 **Thiol-ene photo-click immobilization of a chiral chromatographic ligand on silica**
4 **particles**

5
6 Christian Geibel ^a, Kristina Dittrich ^a, Marc Wolter ^a, Michael Lämmerhofer ^{a,*}

7
8 ^a Institute of Pharmaceutical Sciences, Pharmaceutical (Bio-)Analysis, University of Tü-
9 bingen, Auf der Morgenstelle 8, 72076 Tübingen, Germany

10
11 *Author for correspondence:

12 Prof. Dr. Michael Lämmerhofer

13 Pharmaceutical (Bio-)Analysis

14 Institute of Pharmaceutical Sciences

15 University of Tübingen

16 Auf der Morgenstelle 8

17 72076 Tübingen, Germany

18 T +49 7071 29 78793, F +49 7071 29 4565

19 E-mail: michael.laemmerhofer@uni-tuebingen.de

Table S1a. Summary of the chromatographic results with diluted mobile phase.

CSP #	reaction type	reaction time [min]	starting conditions			initial weight [$\mu\text{mol}/\text{m}^2$]	dilution factor of mob. phase ²
			tBuCQN	PMPMS	tBuCQN		
1	film	120	0.136	0.226	1.36	2.26	no dilution 01:20 01:40
2	slurry						no dilution 01:20 01:40

¹ all initial weights based on 0.5 g vinylated silica

² dilution was performed with methanol to obtain lower amounts of additives

26

27

28

29

30

31

32

33

Table S1b. Summary of the chromatographic results with diluted mobile phase (continuation)

chromatographic results ³											
CSP #	dilution factor of mob. phase ²	k_1	α_{opt}^4	R_{opt}^4	$R_{5.89mm/s}^5$	$N_{1, opt}^4$	$N_{1, opt}/m^4$	h_{min}	A [$10^{-3}mm$]	B [$10^{-3}mm^2 s^{-1}$]	C [$10^{-3}s$]
1	no dilution	0.73	1.46	2.39	1.22	3069	61375	3.26	7.64 ± 0.65	2.32 ± 0.11	7.65 ± 0.09
	01:20	2.31	1.45	3.51	1.97	2810	56200	3.56	12.14 ± 1.39	2.43 ± 0.25	6.68 ± 0.16
	01:40	2.66	1.42	3.53	2.02	2865	57300	3.49	11.71 ± 1.12	2.62 ± 0.20	6.18 ± 0.13
2	no dilution	0.14	1.52	0.94	0.75	3827	76546	2.61	9.30 ± 2.12	1.87 ± 0.31	3.33 ± 0.56
	01:20	0.42	1.53	2.05	1.30	3278	65560	3.05	7.50 ± 0.73	2.90 ± 0.13	5.02 ± 0.85
	01:40	0.53	1.46	2.01	1.28	2920	58400	3.43	10.95 ± 0.43	3.29 ± 0.77	4.53 ± 0.49

³ mob. ph. MeOH/Ac/NH₄Ac (98/2/0.5, v/v/w) or diluted as stated

⁴ index "opt" stands for results at optimum flow rate

⁵ R at a linear flow rate of 5.89 mm/s

34

35

36

37

38

39

40

41

42

Table S2. Summary of the statistic parameters of the selector coverage prediction versus the observed results

SO coverage	Coeff. SC	Standard Error	P	Conf. Int. (\pm)
Constant	619,202	480,811	1.35E-01	117,651
time	210,695	536,969	0,00776799	131,392
initial weight SO	-128,383	404,345	0,0191948	989,405
initial weight linker	131,014	536,968	0,0504793	131,392
method (DF = 1)				
film	794,366	404,345	0,0970777	989,405
slurry	-794,366	404,345	0,0970777	989,405

N = 11, DF = 6, R2 = 0.846, RSD = 11.01

red = values higher than p = 0.05

43

44

45

46

47

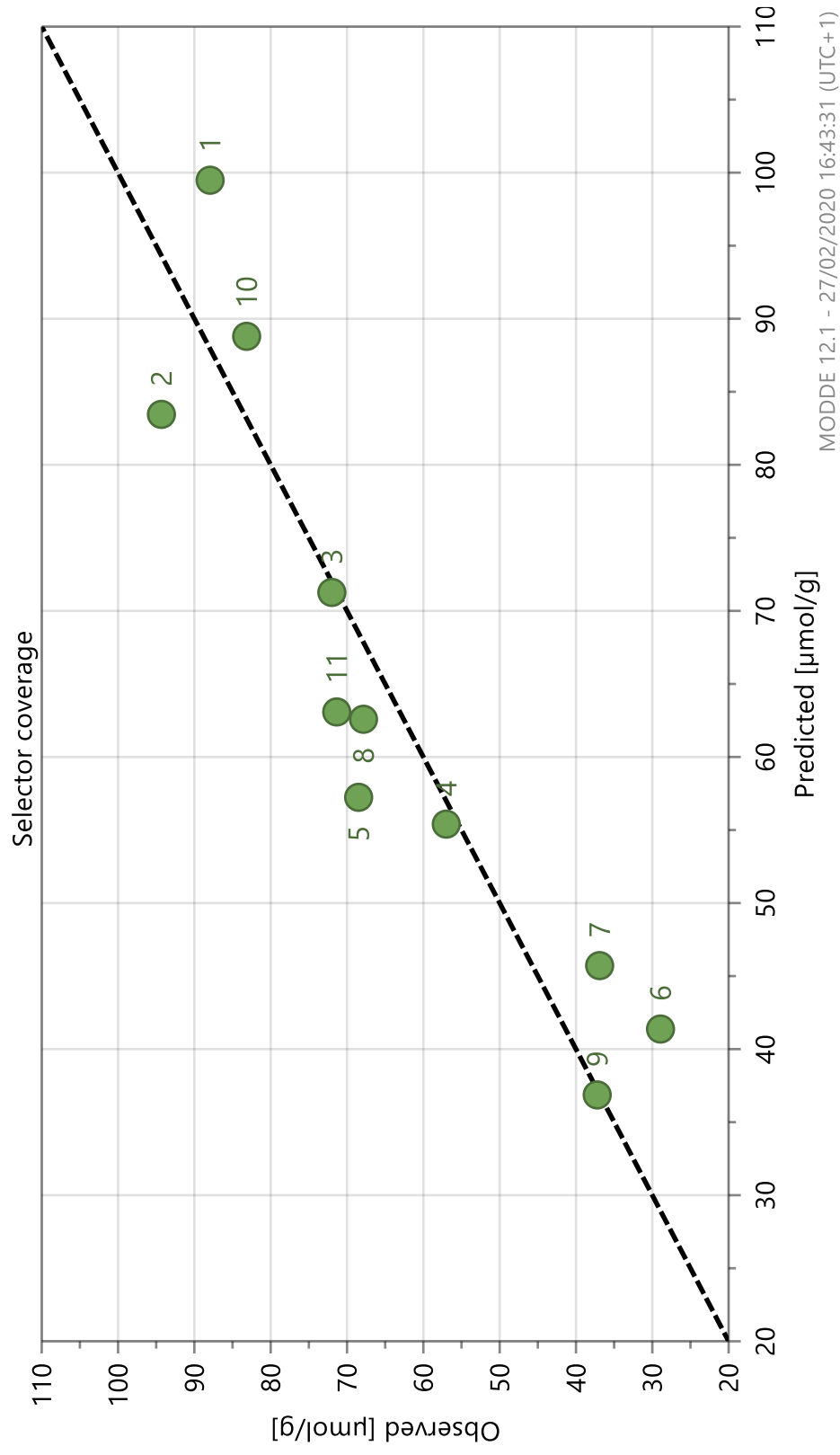
48

49

50

51

Observed vs. predicted selector coverage



52

53 **Figure S1.** Observed vs predicted selector coverage as calculated by MODDE Pro Ver. 12.1.0.5491 from Sartorius Stedim (Umeå,

54 Sweden). Note that the numbers refer to the CSPs 6 – 16 from table 1 and 2.

3.1.3 Publication III: **Controllable organosilane monolayer density of surface bonding using silatranes for thiol functionalization of silica particles for liquid chromatography and validation of microanalytical method for elemental composition determination**

Christian Geibel^a, Johannes Theiner^b, Marc Wolter^a, Markus Kramer^c,
Wolfgang Lindner^d, Michael Lämmerhofer^{a,*}

^a Institute of Pharmaceutical Sciences, Pharmaceutical (Bio-)Analysis, University of Tübingen, Auf der Morgenstelle 8, 72076 Tübingen, Germany

^b Mikroanalytisches Laboratorium, University of Vienna, Währinger Strasse 42, 1090, Vienna, Austria

^c Institute of Organic Chemistry, University of Tübingen, Auf der Morgenstelle 18, 72076 Tübingen, Germany

^d Institute of Analytical Chemistry, University of Vienna, Währingerstrasse 38, 1090 Vienna, Austria

* Corresponding author. E-mail address: michael.laemmerhofer@uni-tuebingen.de (M. Lämmerhofer)

Journal of Chromatography A **2021**, 1653, 462418.

DOI: 10.1016/j.chroma.2021.462418

Authors of Elsevier articles retain the right to include it in a thesis
or dissertation without further permission.

© 2021 Elsevier B.V.



Controllable organosilane monolayer density of surface bonding using silatranes for thiol functionalization of silica particles for liquid chromatography and validation of microanalytical method for elemental composition determination

Christian Geibel^a, Johannes Theiner^b, Marc Wolter^a, Markus Kramer^c, Wolfgang Lindner^d, Michael Lämmerhofer^{a,*}

^a Institute of Pharmaceutical Sciences, Pharmaceutical (Bio-)Analyses, University of Tübingen, Auf der Morgenstelle 8, Tübingen 72076, Germany

^b Mikroanalytisches Laboratorium, University of Vienna, Währingerstrasse 42, Vienna 1090, Austria

^c Institute of Organic Chemistry, University of Tübingen, Auf der Morgenstelle 18, Tübingen 72076, Germany

^d Institute of Analytical Chemistry, University of Vienna, Währingerstrasse 38, Vienna 1090, Austria

ARTICLE INFO

Article history:

Received 7 May 2021

Revised 15 July 2021

Accepted 17 July 2021

Available online 22 July 2021

Keywords:

Silica gel functionalization

Chiral stationary phase

Thiol-ene click reaction

Self-assembled monolayer

Solid-state NMR

Elemental analysis validation

ABSTRACT

The present work systematically investigates a new strategy for the functionalization of silica gel using alkyl silatrane chemistry instead of alkylsilanes for synthesis of chromatographic stationary phases. In this work, silica was chemically modified for further functionalization by a thiol-ene click reaction. Thus, 3-mercaptopropylsilatrane (MPS) was used which is capable to form self-assembled monolayers (SAM) on top of silanol surfaces in a controlled manner as previously shown for silicon wafers. The utility of this chemistry for stationary phase synthesis in liquid chromatography was not evaluated yet. Hence, silica surface modifications using MPS were studied in comparison to established 3-mercaptopropyltrimethoxysilane (MPTMS) chemistry. First, the employed elemental analysis method was validated and it showed excellent intra-day and inter-day precisions (typically less than 5% RSD). It could be shown that the reaction kinetics of MPS was roughly 35-times faster than with MPTMS. After 30 min reaction time with MPS, the thiol content reached 74% of the maximal coverage. Due to controlled chemistry with MPS, which does not lead to oligomeric siloxane network at the silica surface, the ligand coverage was lower. However, multiple silanization cycles with MPS led to a dense surface coverage (around $4 \mu\text{mol m}^{-2}$). ^{29}Si cross polarization/magic angle spinning (CP/MAS) solid-state NMR revealed distinct $T^1/T^2/T^3$ ratios for MPS and MPTMS materials with up to 80% T^3 (indicative for trifunctional siloxane linkage) for MPS and around 20% T^3 for MPTMS. This indicates a more homogeneous, thinner monolayer film of MPS on the silica surface, as compared to an irregular thick oligomeric siloxane network with MPTMS. Bonding of quinine carbamate as chiral selector afforded an efficient chiral stationary phase (CSP) for chromatographic enantiomer separation. Separation factors were comparable to MPTMS-bonded CSP, however, chromatographic efficiency was much better for the MPS-bonded CSP. H/u curves indicated a reduced mass transfer resistance by roughly factor 3 for MPS- compared to MPTMS-bonded CSP. This confirms better chromatographic performance of surfaces with homogeneous monolayer compared to network structures on the silica surface which suffer from poor stationary phase mass transfer.

© 2021 Elsevier B.V. All rights reserved.

1. Introduction

Dedicated surface functionalization of silica particles is a crucial step in the development of stationary phases for the diverse retention principles in liquid chromatography [1]. In a variety of

chromatographic modes, e.g. octadecylsilica, direct surface modification by a single silanization reaction of silica silanols with mono-, di- and trifunctional alkoxy- or chloro-alkylsilanes is a preferred approach [2,3]. For other separation principles, e.g. affinity and enantioselective LC, it is convenient to attach first a reactive anchor to the silica surface by a vinylization reaction and couple the affinity ligand or chiral selector in a second step to the reactive particles. Numerous publications have shown the advantage of either thiol or vinyl moieties as reactive groups for further surface

* Correspondence author.

E-mail address: michael.laemmerhofer@uni-tuebingen.de (M. Lämmerhofer).

functionalization [4–12]. Correspondingly, the thiol-ene click reaction has gained great popularity for dedicated functionalization of stationary phases. Surface coverage and density of the ligand on the silica surface, orientation and chemical environment, accessibility of the ligand's binding site for the analytes play a major role for both thermodynamic and kinetic properties of the stationary phase. Hence, a good control over the surface functionalization steps of the porous silica particles is mandatory as it can have a major influence on the overall chromatographic performance of the resulting column. Uncontrolled functionalization may lead to non-ordered and imperfect layers on the silica surface with associated negative characteristics such as inaccessibility of thiol groups for the thiol-ene click reaction and suboptimal kinetic performance in liquid chromatography.

It is evident that the first stage of silica surface modification is a critical step in stationary phase synthesis. Considering the great importance, however, only a limited number of articles focused on the study of organo-silane monolayer formation on silica surface [3,13]. It is common understanding nowadays that di- and trifunctional silanes under anhydrous conditions lead to monomeric phases similar to monofunctional silanes [3]. With trifunctional silanes and presence of water in the reaction mixture silane polymerization may occur and these silane polymers may subsequently attach to the silica surface affording polymeric phases. If the synthesis is carried out with trifunctional silanes and humidified silica which carries a water monolayer on the surface, the silane polymerization occurs parallel to the silica surface giving a dense self-assembled monolayer of polysiloxane coating (horizontal polymerization) [3,13]. It can be distinguished from the more random vertical polymerization that results from solution polymerization and subsequent multipoint attachment with some silane groups not directly attached to the silica surface [13]. Horizontal polymerization provides higher density and due to its well-ordered regular surface structure and good accessibility of the chromatographic ligand should provide better chromatographic characteristics and higher stability.

In this work, we address a new way of functionalization of silica particles by silatrane chemistry and compare this with the well-established functionalization via trialkoxysilanes. In particular, 3-mercaptopropylsilatrane (MPS) is used as reactive component for the silanization in comparison to 3-mercaptopropyltrimethoxysilane (MPTMS) as benchmark trialkoxysilane (see Fig. 1a). Due to the transannular dative bond between silicon and nitrogen, silatranes are more stable towards hydrolysis than their respective trialkoxysilanes, at least in neutral aqueous solution [14], which makes the handling of the substance more convenient. In presence of acid, the reactivity of the silatrane will be higher due to the increased proton affinity in comparison to their trialkoxysilane analogues [14], mainly because of the pentacoordination of silicon due to the dative N→Si bond [15]. The resistance to hydrolytic degradation of the silatrane inhibits the formation of a heterogeneous siloxane network on the surface in favour for a thin, homogenous monomolecular layer [16]. This in turn might be of great advantage for the functionalization of silica particles with narrow pores (e.g. 100 Å and smaller) avoiding blockage of the pores by polysiloxane network structure. Moreover, silatrane derivatives are straightforward to synthesize from its respective silane counterparts. To our knowledge, this is the first study on the silatrane based functionalization of silica particles for application in liquid chromatography. In this work, we demonstrate the synthesis, reaction kinetics, surface chemistry as elucidated by solid-state NMR, characterization by elemental analysis and liquid chromatography of MPS functionalized silica particles in comparison to MPTMS-bonded silica after functionalization with a quinine carbamate chiral selector.

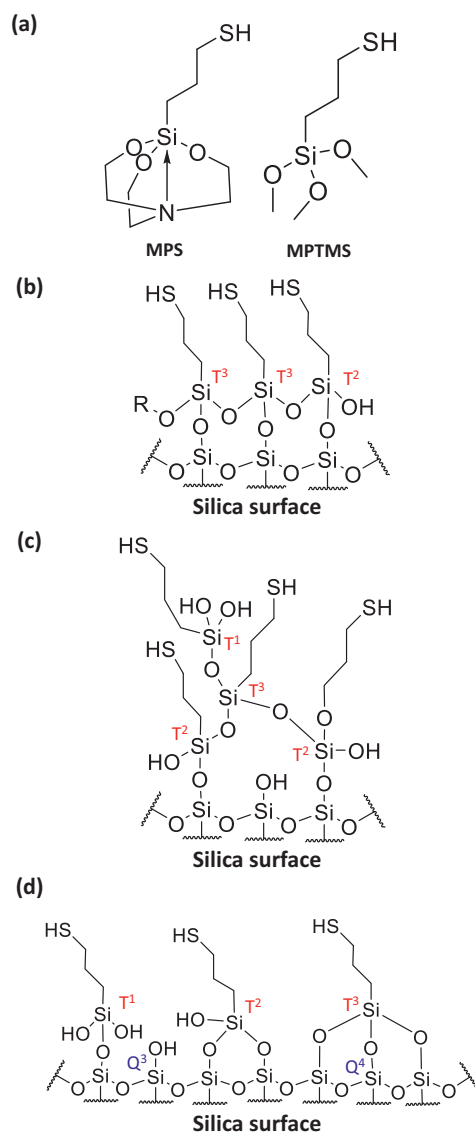


Fig. 1. Silanization agents for silica particles and tentative surface morphologies. (a) 3-mercaptopropylsilatrane (MPS) as new functionalization agent of silica surfaces on the left hand side and commonly used 3-mercaptopropyltrimethoxysilane (MPTMS) on the right hand side. (b) Controlled dense monolayer surface structure obtained by MPS-based silanization of silica surface, (c) uncontrolled irregular oligomeric siloxane structure postulated by silanization with MPTMS [17], and (d) possible monomeric siloxane bondings in accordance to what is typically claimed by the literature for trifunctional silanes reacted under anhydrous conditions such as expected for the present MPTMS silanization. For explanation, see text.

2. Experimental

2.1. Materials

Spherical silica particles (Kromasil, 3 μm, 100 Å, specific surface area 300 m²/g) were supplied by Eka Chemicals (Bohus, Sweden), superficially porous silica particles (SPP) (Halo Sil 2.7 μm, 90 Å, specific surface area 125 m²/g) were supplied by Advanced Materials Technologies (Wilmington, DE, USA). 3-Mercaptopropyltrimethoxysilane was obtained from ABCR Chemicals (Karlsruhe, Germany). *tert*-Butylcarbamoylquinine was synthesized in-house, using quinine from Buchler (Braunschweig, Germany) and *tert*-butyl isocyanate as well as dibutyltin dilaurate from Sigma Aldrich (Munich, Germany). Sodium hydroxide, anhydrous toluene, 4-dimethylaminopyridine (DMAP),

N-[(9H-fluoren-9-ylmethoxy)carbonyl]-phenylalanine (Fmoc-Phe), azobis(isobutyronitrile) (AIBN), tri-*tert*-butylbenzene (TTBB), 2,2'-dipyridyl disulfide (DPDS), 2-mercaptoethanol, formic acid (FA, analytical grade), acetic acid (AA, analytical grade), ammonium acetate and acetonitrile (ACN, HPLC grade) were also purchased from Sigma Aldrich. MilliQ water was purified by using an Elga Pure-Lab Ultra Purification System (Celle, Germany). All empty stainless steel columns were supplied by Bischoff Chromatography (Leonberg, Germany) and had the dimensions of 50 mm × 3 mm i.d.. Porosity determination was carried out by inverse size-exclusion chromatography (ISEC) using the "ReadyCal Kit Polystyrene" by PSS Polymer Standards Service GmbH (Mainz, Germany) with twelve distinct molecular weights (370, 1,306, 3,470, 8,680, 17,600, 34,800, 66,000, 130,000, 277,000, 552,000, 1,210,000 and 2,520,000 Da).

2.2. Instrumentation

All columns were packed using a Smartline pneumatic pump, model 1950, supplied by Knauer (Berlin, Germany). ISEC measurements as well as H/u-curve recordings were conducted on an Agilent 1290 Infinity series liquid chromatographic system from Agilent Technologies (Waldbronn, Germany), equipped with a binary pump, a thermostatted column compartment, a UV diode array detector and an autosampler. The detector was equipped with a Max-Light ultralow dispersion cartridge flow cell with an inner volume of 0.6 µL. Furthermore, to reduce the extra column volume an ultralow dispersion needle seat assembly and connecting capillaries with 0.075 mm inner diameter (autosampler to column compartment, 350 mm length; column compartment to detector, 250 mm length) were installed. For elemental analysis, the elemental analyser EA 3000 CHNS-O from EuroVector SpA (Milan, Italy) was used. Solid-state NMR spectra were acquired on a Bruker Avance III HD 300 XWB spectrometer and soluble samples on a Bruker Avance III HDX 400 spectrometer (Bruker, Rheinstetten, Germany). Data were processed with Bruker TopSpin 4.0.8 software.

2.3. Solid-state NMR

Double bearing zirconia rotors were used for ¹³C as well as for ²⁹Si cross polarization (CP)/magic angle spinning (MAS) NMR analysis. Thereby, the spinning rate was set to 8000 Hz for ¹³C-NMR and 4000 Hz for ²⁹Si-NMR experiments. The 90° proton pulse was set to 2.5 µs for ¹³C and 3.3 µs for ²⁹Si, the CP contact time was 2 ms for ¹³C and 5 ms for ²⁹Si and the relaxation delay 2 s for both nuclei.

2.4. Elemental analysis

For the determination of the C/H/N/S content of the modified silica gel, 3 to 4 mg of the particles were filled into a tin capsule and left to be oxidized by the elemental analyser. Standard parameters for C/H/N/S-analysis were applied. Analytes CO₂, H₂O, N₂ and SO₂ were generated by flash combustion and micro-Dumas-reduction and online separated by gas chromatography using helium (quality 5.0) as carrier gas. The products were detected using a thermal conductivity detector (TCD).

Quantification was done using peak areas and calibrating relative to sulphanylamide and 2,5-bis(5-*tert*-butyl-2-benzo-oxazol-2-yl) thiophene (BBOT) standards analysed repeatedly during the same analysis run. Only NIST-certified reference material was used. Blank values for C, H and N were registered for empty tin vials. A zero blank for S was defined as qualification proof. The linearity of sensitivity was verified as replicates at 2 to 10 mg sample weight did not show any mass correlation in the analysis results.

2.4.1. Preparation of quality control (QC) sample

For the preparation of the QC sample by adsorptive bonding of a thiolated quinine carbamate selector with a targeted selector coverage of 100 µmol/g, 300 mg bare silica and 47.2 mg 10,11-dihydro-11-[(2-hydroxyethyl)thio]-9-[N-(*tert*-butyl)carbamoyl]-cinchonan-9-ol were added to a 10 mL round bottom flask together with 2 mL of toluene and 3 mL of methanol. The mixture was sonicated for 30 min, after which it was gently stirred overnight (~ 18 h). Afterwards, the solvent was removed by rotary evaporation. The product was then dried in a vacuum oven (-700 mbar, 60 °C) for two days before it was subjected to elemental analysis. Bare silica as negative control was dried in a vacuum oven (-700 mbar, 60 °C) for two days and subjected to elemental analysis as well.

2.5. Silanization (synthesis of thiol silicas)

2.5.1. Synthesis of 3-mercaptopropyl-modified SPP silica for validation of EA

Halo Sil 2.7 µm, 90 Å (1.5 g) was dried at 60 °C under reduced pressure and then suspended in 75 mL toluene. 30 mL of toluene were distilled off to remove water azeotropically. Afterwards, 450 µL MPTMS (1.5 mmol/g silica) and 20 mg of DMAP (0.1 mmol/g silica) were added. The reactor was flushed with nitrogen for 10 min and left stirring at 110 °C under reflux. Afterwards, the slurry was filtered using a glass funnel (porosity 5). Washing steps with boiling toluene and boiling methanol were performed 3 times each. Subsequently, the silica gel was dried in a drying oven at 60 °C under atmospheric pressure for 15 h and afterwards at 60 °C in a vacuum oven.

2.5.2. Synthesis of 3-mercaptopropylsilatrane (MPS)

For the synthesis of 3-mercaptopropylsilatrane (MPS), the procedure of Ref. [17] was followed with slight modifications. Anhydrous toluene was used as solvent. Equimolar amounts of 3-mercaptopropyltrimethoxysilane (MPTMS) and triethanolamine (17.76 mmol each, corresponding to 3.3 mL MPTMS and 2.36 mL triethanolamine) were dissolved in 30 mL toluene. After adding 5 mg NaOH, the solution was heated to reflux for 30 h. Subsequently, the mixture was left cooling down to room temperature and slowly dropped into n-hexane in a beaker inducing crystallization. After complete crystallization, the white crystals were dried for three days at 60 °C in vacuum. ¹H-NMR showed a purity of 96%. ¹H-NMR [CDCl₃, 400 MHz]: δ (ppm) = 0.47 (m, 2H), 1.31 (t, J = 7.99 Hz, 1H), 1.70 (m, 2H), 2.49 (q, J = 7.65 Hz, 2H), 2.78 (t, J = 5.82 Hz, 2H), 3.74 (t, J = 5.82 Hz, 2H). ¹³C-NMR: δ (ppm) 57.75 (CH₂), 51.12 (CH₂), 30.47 (CH₂), 28.37 (CH₂), 15.73 (CH₂). ²⁹Si-NMR: δ (ppm) -67.01 (RSiO₃). NMR data for MPTMS gave the following values: ¹H-NMR [CDCl₃, 400 Hz]: δ (ppm) 0.73 (m, 2H), 1.31 (t, J = 7.93 Hz, H), 1.70 (m, 2H), 2.52 (q, J = 7.44 Hz, 2H), 3.55 (s, 9H). ¹³C-NMR: δ (ppm) 50.57 (CH₃), 27.57 (CH₂), 27.45 (CH₂), 8.23 (CH₂). ²⁹Si-CP/MAS-NMR: δ (ppm) -42.52 (RSiO₃).

2.5.3. Determination of reaction kinetics

For the determination of the reaction kinetics of MPS in comparison to MPTMS, the reaction with both silanes was carried out under comparable conditions. 5 g bare silica gel (3 µm, 100 Å) was dispersed in 15 mL anhydrous toluene. After adding of 10 mg DMAP and 8 mmol of MPS (or MPTMS, respectively), the reaction vessel was heated to reflux under mechanical stirring. The mixture was allowed to react for 7 h. After 30 min, 1, 2 and 4 h, samples (1 mL) were drawn, having a total of 5 measuring time points per reaction. All samples were washed with boiling toluene and boiling methanol three times each and dried overnight at 60 °C in a vacuum oven. The samples were subsequently subjected to elemental analysis (C/H/N/S).

Table 1
Validation of elemental analyses method: Intra-day and inter-day precisions.

	coverage [$\mu\text{mol}/\text{m}^2$]	intra-day precision												inter-day precision			
		σ [%]												σ [%]			
		day 1				day 2				day 3							
		C	H	N	S	C	H	N	S	C	H	N	S	C	H	N	S
low range (tBuCQN-TP-SPP) ³	0.00 ± 0.00^1	2.25	5.88	-	3.70	0.55	21.10	-	1.37	0.32	0.00	-	3.22	0.66	6.15	-	2.50
	0.11 ± 0.00^1	1.18	5.75	3.96	2.24	1.05	7.53	3.91	0.67	0.59	2.71	3.21	0.70	0.59	4.40	8.81	1.48
	0.13 ± 0.00^1	1.63	1.17	3.45	0.31	1.28	1.14	1.34	1.88	0.93	0.00	4.25	1.72	1.21	1.78	2.73	1.11
	0.16 ± 0.01^1	0.45	3.40	2.37	2.24	0.26	1.16	2.16	0.87	0.52	1.19	4.33	2.06	0.40	2.68	4.57	1.61
	0.18 ± 0.00^1	0.62	1.89	3.14	2.05	0.00	1.89	0.49	0.92	0.46	1.15	1.89	1.78	0.53	2.95	3.51	0.98
high range (tBuCQN-TP-FPP) ³	0.22 ± 0.00^1	0.88	2.96	2.42	1.89	0.24	1.10	0.60	0.73	0.49	0.00	1.90	0.32	0.35	3.46	3.01	1.35
	0.56 ± 0.01^2	0.75	0.75	3.77	1.56	n.a.	n.a.	n.a.	n.a.	n.a.	n.a.	n.a.	n.a.	n.a.	n.a.	n.a.	n.a.
	0.67 ± 0.01^2	0.92	1.84	4.22	0.94	n.a.	n.a.	n.a.	n.a.	n.a.	n.a.	n.a.	n.a.	n.a.	n.a.	n.a.	n.a.
	0.88 ± 0.03^2	1.64	3.12	7.37	3.01	n.a.	n.a.	n.a.	n.a.	n.a.	n.a.	n.a.	n.a.	n.a.	n.a.	n.a.	n.a.
	1.85 ± 0.05^2	1.30	2.29	9.75	3.01	n.a.	n.a.	n.a.	n.a.	n.a.	n.a.	n.a.	n.a.	n.a.	n.a.	n.a.	n.a.
	2.36 ± 0.06^2	0.81	1.56	3.53	2.92	n.a.	n.a.	n.a.	n.a.	n.a.	n.a.	n.a.	n.a.	n.a.	n.a.	n.a.	n.a.
	0.95 ± 0.02^2	0.79	0.56	0.73	2.19	n.a.	n.a.	n.a.	n.a.	n.a.	n.a.	n.a.	n.a.	n.a.	n.a.	n.a.	n.a.
	1.10 ± 0.02^2	0.65	0.94	0.50	2.19	n.a.	n.a.	n.a.	n.a.	n.a.	n.a.	n.a.	n.a.	n.a.	n.a.	n.a.	n.a.
	1.21 ± 0.04^2	0.60	0.53	0.29	3.98	n.a.	n.a.	n.a.	n.a.	n.a.	n.a.	n.a.	n.a.	n.a.	n.a.	n.a.	n.a.
	1.24 ± 0.01^2	0.45	0.55	1.52	0.70	n.a.	n.a.	n.a.	n.a.	n.a.	n.a.	n.a.	n.a.	n.a.	n.a.	n.a.	n.a.
quinidine sulfate (adsorbed to silica)	0.07 ± 0.00^1	0.71	1.38	1.58	0.71	0.56	1.81	2.22	0.15	1.70	3.23	0.52	1.96	0.21	1.27	-	0.94
	0.13 ± 0.00^1	0.29	1.18	1.43	0.16	1.08	1.24	1.85	1.49	0.50	5.83	2.12	0.73	0.13	2.90	14.31	1.76
	0.40 ± 0.00^1	0.39	1.83	0.72	0.69	0.51	2.25	0.42	1.65	0.26	3.30	0.82	0.35	0.09	2.72	7.56	0.63
	0.59 ± 0.00^1	0.37	1.01	0.13	0.62	0.89	1.87	1.14	0.00	2.58	2.43	1.80	0.97	1.33	1.35	5.99	1.31
	1.18 ± 0.01^1	0.99	1.10	0.66	0.58	0.24	0.27	0.58	0.18	0.27	0.78	0.19	0.33	0.68	0.51	2.47	2.36

¹ selector coverage referred to nitrogen content

² selector coverage referred to sulfur content

³ SPP, superficially porous particles; FPP, fully porous particles

2.5.4. Optimization of MPS-based surface functionalization

To further optimize the surface functionalization, different conditions for the hydrolysis step were tested. Hydrolysis was carried out with MeOH/H₂O (80/20; v/v) + 0.1% (v/v) FA, MeOH/H₂O (50/50; v/v) + 0.1% (v/v) FA, MeOH/H₂O (20/80; v/v) + 0.1% (v/v) FA, MeOH/0.1 M HCl (50/50; v/v) and isopropanol/H₂O (20/80; v/v) + 0.1% (v/v) FA, each of those experiments was conducted in reflux for four hours. Furthermore, multiple alternate hydrolysis/re-functionalization cycles with MPS were performed with up to four cycles to see if the sulfur loading can be further increased.

2.6. Preparation of chiral stationary phases

Further modification of the thiol functionalized silica was performed with *tert*-butylcarbamoylquinine (tBuCQN) as selector, synthesized according to the protocol published in Ref. [18]. The immobilization of the chiral selector tBuCQN on thiol silicas followed the protocol reported by Maier et al. [19,20].

2.6.1. Stationary phase synthesis by thiol-ene click reaction for validation of EA

Five samples of CSP with defined tBuCQN selector amount on 3-mercaptopropyl-modified SPP were synthesized. Thus, 250 mg of the MPTMS modified silica gel and 6.62, 13.24, 19.86, 26.48 and 39.72 mg tBuCQN, respectively, were suspended in 50 mL methanol. Together with 10 mol% AIBN (related to the ene component tBuCQN), the mixture was held under reflux for 8 h while being gently stirred. Washing steps with boiling toluene and boiling methanol while filtering through a glass funnel, porosity 5, were performed three times each. Subsequently, the slurry was left for drying overnight in a drying oven (60 °C, atmospheric pressure) and subsequently for 24 h at 60 °C in a vacuum oven. The results of the elemental analysis are summarized in Table 1.

2.6.2. Thiol-ene click reaction of tBuCQN and thiol functionalized silica

For the loading of the modified silica gel with selector, 1 g of the modified silica gel (either modified with MPTMS or MPS, respectively) was suspended in 10 mL methanol. After adding 255 mg (0.6 mmol) tBuCQN and 5 mg azobis(isobutyronitrile), the suspension was heated to reflux under mechanical stirring for 7 h. Afterwards, the mixture was left cooling down to room temperature, transferred to a glass filter funnel (porosity 5) and washed with boiling toluene and boiling methanol, three times each. To finalize the synthesis, the product was dried in a vacuum oven at 65 °C overnight.

2.7. Inverse size exclusion chromatography (ISEC) for porosity determination

To get a deeper insight on the particle's surface morphology, the determination of both the internal and external porosity of the stationary phase, in this case bare silica, MPS-functionalized as well as MPTMS-functionalized silica was conducted. To do so, a polymer kit with defined molecular weights of 12 different polymers was used. Those polymers were divided into three samples and diluted with THF to a concentration of 1.0 mg/mL (except for 2,520,000 Da and 1,210,000 Da: 0.5 mg/mL). Void volume marker was tri-*tert*-butylbenzene (TTBB, concentration: 1 mg/mL), mobile phase was 100% THF. The flow rate was set at 0.05 mL/min, injection volume was 0.5 μL , detection wavelength was 254 nm and the column temperature was set to 30 °C. After measuring each sample in triplicates, the cubic root of the polymer's molecular weight was plotted against the elution volume (adjusted for the extra column volume) [21]. Accordingly, two specifiable lines are visible after linear regression, which indicate the excluded (steeper line) and included polymers (flatter part). By finding the intersection between both regression lines, the interstitial (or external) volume (V_e) can be defined [22]. V_0 stands for the void volume (elution volume of TTBB), V_{col} is the geometrical volume of the empty, unpacked column which can be calculated by $V_{col} = \pi r^2 L$ (r = radius,

\bar{L} = length). From those values, the porosities can be derived. External (ε_e) and total porosity (ε_t) were determined by Eq. (1a) and (1b).

$$\varepsilon_e = \frac{V_e}{V_{col}} \quad (\text{Eq. 1a})$$

$$\varepsilon_t = \frac{V_0}{V_{col}} \quad (\text{Eq. 1b})$$

The internal porosity can be calculated from the difference of the total porosity and the measured external porosity by (Eq. (2)):

$$\varepsilon_i = \varepsilon_t - \varepsilon_e = \frac{V_0}{V_{col}} - \frac{V_e}{V_{col}} \quad (\text{Eq. 2})$$

2.8. H/u curve recording and mass transfer resistance comparison

H/u curves were recorded using *N*-[(9H-fluoren-9-ylmethoxy)carbonyl] (Fmoc) protected phenylalanine as analyte. For the MPTMS-bonded CSP the mobile phase was methanol/acetic acid/ammonium acetate (98/2/0.5, v/v/w). For the MPS-bonded CSP the mobile phase was adjusted to isoelectronic conditions by diluting the above-mentioned mobile phase with methanol. Flow rates ranged from 0.015 mL/min to 2.5 mL/min. Sixteen (16) data points were recorded. The total pressure was kept under the packing pressure of 800 bar during the measurements. A-, B-, and C-term were calculated by non-linear regression using the Van Deemter model.

2.9. Determination of reactive thiol groups on the silica surface by DPDS-assay

Reactive and accessible sulfhydryl groups on the silica surface were determined by performing a thiol-disulfide exchange reaction with 2,2'-dipyridyl disulfide (DPDS) [10,23,24]. For this purpose, typically, 10 mg of thiol-functionalized silica particles were suspended in 1 mL 0.1 M DPDS solution (in ACN) within a micro centrifuge tube which was impervious to light. After vigorous shaking for 3 h the tubes were centrifuged and the supernatant was diluted with ACN in a ratio of 1 to 10. Subsequently, pyridine-2-thiol and 1,2-dihydropyridine-2-thione formed in the course of the disulfide exchange reaction were quantified by RP-HPLC-UV/Vis. 2-Mercaptoethanol was used as calibrant for the preparation of the calibration function due to its known thiol group content.

3. Results and discussion

3.1. Validation of elemental analysis

Elemental analysis (EA) of the bonded silica materials was carried out for the determination of the surface coverage of sulfur. Typical measurement uncertainties of microanalytical EA of organic surface bondings on inorganic materials such as modified silica particles are scarcely reported. In this research the validity of the results is greatly relying on the validity of the EA data. In order to get an idea about the reliability of EA for this purpose, in particular in the low surface concentration range which is of relevance in the course of a kinetics study of silatrane in comparison to alkoxy-silane chemistry, a series of thiol-modified silicas with distinct controlled 3-mercaptopropyltrimethoxysilane modification was synthesized and the intra-assay and inter-day precision of EA determined. The results are summarized in Table 1.

It can be seen that the repeatability of the elemental analysis is mostly exceptional in spite of the low content of the determined elements on the inorganic silica backbone. Intra-day precisions for carbon (which was present in a range between 1.7 and 14%) were less than 2.6% RSD, for hydrogen (determined in the range between

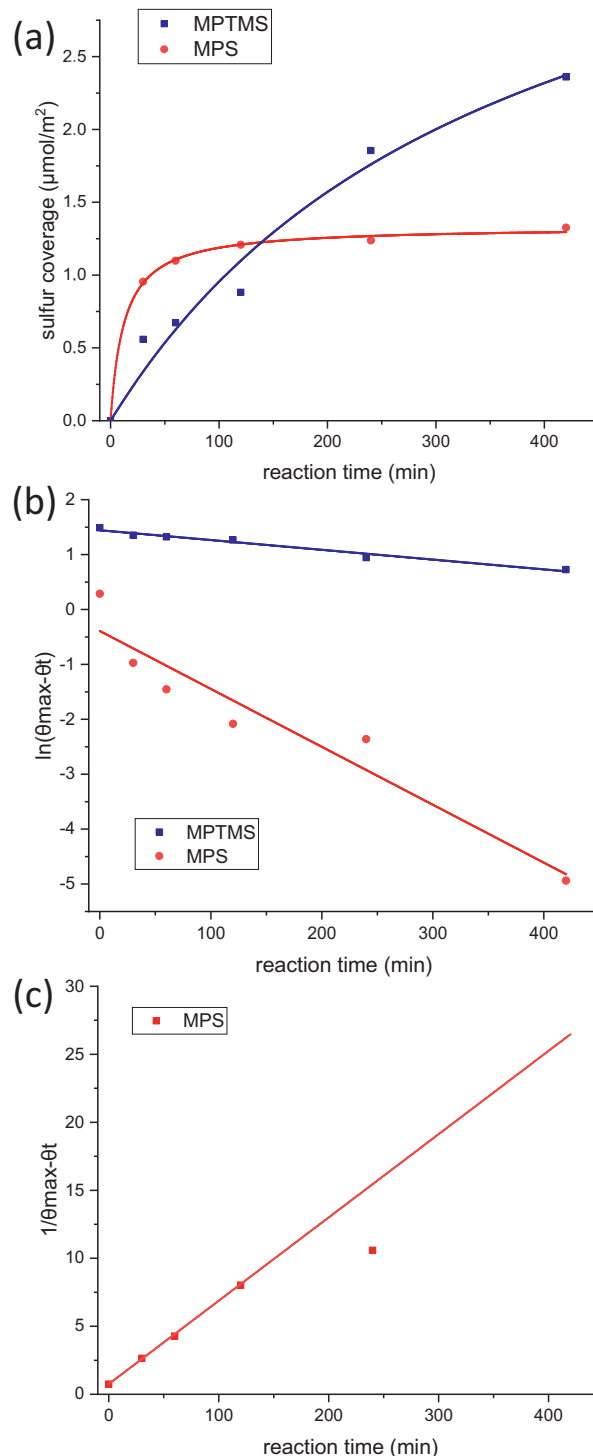


Fig. 2. Reaction kinetics of MPS and MPTMS silanization. (a) Sulfur coverage plotted in dependence on the reaction time. (b) Linearized form. For the determination of the rate constant k , a linearization of the obtained data was performed. Linearization was done by subtracting the sulfur coverage at a given reaction time t , θ_t from the maximum sulfur coverage θ_{max} followed by a logarithmic calculus. Plotting this result versus the reaction time allows to derive k from the slope, which in turn gives access to the half-time. (c) Plot of $1/(\theta_{max} - \theta_t)$ against reaction time for the determination of k and reaction half-time, as MPS seems to show second order kinetics.

Table 2
Validation of elemental analysis method: accuracy.

	target coverage $\mu\text{mol}/\text{m}^2$	theoretically expected				experimental				accuracy				precision (intra-day)			
		[%]				[%]				[%]				RSD [%]			
		C	H	N	S	C	H	N	S	C	H	N	S	C	H	N	S
QC Bare Silica	0	0.00	0.24	0.00	0.00	0.76 ± 0.01	0.62 ± 0.01	< 0.03	0.01 ± 0.00	-	-	-	-	1.3	1.6	-	< 0.1
QC	100	3.12	0.99 ¹	0.42	0.32	3.35 ± 0.07	0.82 ± 0.01	0.40 ± 0.01	0.28 ± 0.00	107.3 ± 2.2	82.8 ± 1.0	95.2 ± 2.4	87.3 ± 0.0	2.1	1.2	2.5	< 0.1

¹ values for H adjusted for hydrogen values in bare silica**Table 3**
Overview on the results of the elemental analysis of the MPTMS-derivatized silica and the first cycle of the MPS-derivatized silica.

reaction type	time [min]	C %	H %	N %	S %	N $\mu\text{mol}/\text{m}^2$	S $\mu\text{mol}/\text{m}^2$	N $\mu\text{mol}/\text{g}$	S $\mu\text{mol}/\text{g}$	k min^{-1}	$t_{1/2}$ min
MPTMS	30	1.33 ± 0.004	0.68 ± 0.068	0.00 ± 0.000	0.54 ± 0.015	0.00	0.56	0	167	0.0018 ± 0.00015	389 ± 32
	60	1.58 ± 0.004	0.71 ± 0.073	0.00 ± 0.000	0.65 ± 0.005	0.00	0.67	0	202		
	120	1.90 ± 0.011	0.72 ± 0.070	0.00 ± 0.000	0.85 ± 0.002	0.00	0.88	0	265		
	240	3.28 ± 0.012	0.88 ± 0.035	0.00 ± 0.000	1.78 ± 0.010	0.00	1.85	0	556		
	420	4.00 ± 0.002	0.94 ± 0.009	0.01 ± 0.001	2.27 ± 0.024	0.03	2.36	9	708		
MPS	30	4.07 ± 0.035	1.0 ± 0.019	0.46 ± 0.005	0.92 ± 0.016	1.10	0.95	331	286	0.057 ± 0.0024	11 ± 1
	60	4.38 ± 0.081	1.04 ± 0.041	0.51 ± 0.003	1.06 ± 0.020	1.22	1.10	367	330		
	120	4.49 ± 0.050	1.06 ± 0.009	0.52 ± 0.001	1.16 ± 0.043	1.24	1.21	371	362		
	240	4.76 ± 0.055	1.10 ± 0.015	0.59 ± 0.001	1.19 ± 0.056	1.41	1.24	422	371		
	420	4.98 ± 0.011	1.11 ± 0.004	0.63 ± 0.002	1.28 ± 0.028	1.49	1.33	447	398		

0.4 and 2%) less than 8%, for nitrogen (present in a range between 0 and 1.5%) less than 10% and for sulfur (analyzed in a range of 0.5 and 3.7%) less than 4%. Corresponding inter-day precisions were < 1.3% (C), < 7% (H), < 15% (N), and < 2.5% (S).

Table 2 shows the validation results of accuracy determined as % recovery for the different elements of the prepared quality control (QC) material. Accuracies range from $95 \pm 2\%$ (for N) over $107 \pm 2\%$ (for C), to $87 \pm 0\%$ (for S) and are all in the acceptable range of up to $\pm 15\%$ bias. For H, the bias is a bit larger but still within $\pm 20\%$ (accuracy $82.8 \pm 1.0\%$); however, H is anyway usually not considered in surface coverage determination. Especially for nitrogen, which is usually used to determine the selector loading (when the selector contains nitrogen) we observe high accuracy ($\sim 5\%$ bias). The results also document that the sulfur determination is valid and reliable enough for the quantification of the functionalization yield in the present work with sulfur-containing MPS.

It can be concluded that the elemental analysis on the inorganic backbone gives, in spite of low elemental percentages, highly reliable values with satisfactory intra-day and inter-day precision as well as accuracy within common acceptance limits and is therefore suitable to determine surface bonding densities and selector coverages, respectively, reliably over a wide range.

3.2. Silanization

3.2.1. Reaction kinetics of surface silanization

Two identical synthesis batches but once with MPTMS and once with MPS as silanization reagent were run for the study of the reaction kinetics of the two distinct silanes. A sample was taken in regular time intervals (0.5, 1, 2, 4, 7 h reaction time). The results of the EA are summarized in Table 3. MPTMS derivatization gave higher final sulfur coverages after 7 h reaction time reaching about $700 \mu\text{mol}$ sulfur per g silica. In sharp contrast, MPS derivatization reacts much faster; after 30 min a surface coverage of $286 \mu\text{mol}/\text{g}$ could be reached (vs $168 \mu\text{mol}/\text{g}$) corresponding to a 70% higher coverage than with MPTMS. However, after 120 min of reaction time no further increase of the sulfur content

was found with MPS (see Fig. 2). A maximal surface coverage of approximately $400 \mu\text{mol}/\text{g}$ resulted with MPS as compared to the $700 \mu\text{mol}/\text{g}$ with MPTMS. This is surprising but could be explained by a controlled monolayer formation with MPS (Fig. 1b), while on contrary an uncontrolled oligomeric siloxane surface structure may be formed with MPTMS (Fig. 1c). In fact, this is in agreement with findings of surface modification on silicon wafers with these two reagents under anhydrous conditions. Surface roughness was found to be 4-fold higher with MPTMS-modified samples than that of MPS [17]. However, as discussed in the introduction, in the literature it is claimed that trifunctional silanes react under nonaqueous conditions to give monomeric bondings (Fig. 1d). In our opinion, the structure shown in Fig. 1c is more likely to be formed in comparison to the one depicted in Fig. 1d. On the one hand, oligomeric structures and thicker layer were shown to occur for MPTMS on the surface of silicon wafers [17]. Traces of water in the reaction mixture may lead to the formation of complex oligomeric structures which then, due to hindered accessibility to the surface silanols, slowly attach to the surface. So the slow reaction kinetics itself may be an indication for the formation of oligomeric siloxane aggregates on the silica surface as schematically depicted in Fig. 1c. Furthermore, high sulfur loadings in combination with low T^3 signals in ^{29}Si CP/MAS solid-state NMR (*vide infra*) are in support of a chaotic, oligomeric structure instead of an ordered, perforated, monomolecular layer (as shown in Fig. 1d) when using MPTMS (see Table 3 for EA and Fig. 4 for NMR results).

Next, the reaction kinetics was determined. The reaction rate follows a second order kinetics according to Eq. (3a)

$$\text{Rate} = \frac{d[AB]}{dt} = k[A][B] \quad (\text{Eq. 3a})$$

wherein [A], [B] and [AB] are the surface silanol, MPS or MPTMS and product concentrations, respectively, and k the reaction rate constant. Since silanols and reactants are present in about the same concentration, which allows to simplify the situation to the integral form of the rate law according to Eq. (3b).

$$\frac{1}{[A]_t} = \frac{1}{[A]_0} + kt \quad (\text{Eq. 3b})$$

$[A]_0$ is the silanol concentration at the start of the reaction and is, assuming a stoichiometric reactivity between silanol and MPS in accordance to Fig. 1b, equivalent to the maximal thiol surface coverage θ_{max} . $[A]_t$ is the free silanol concentration at time t and can thus be written as $\theta_{max} - \theta_t$ (with θ_t being the coverage of silica with MPS or MPTMS). If this is the case, a plot of $1/(\theta_{max} - \theta_t)$ versus t should give a straight line with a positive slope k .

On the other hand, for the determination of the reaction rate constants, a pseudo first-order kinetics could be assumed, e.g. if not all silanols are accessible and thus the reagent is in reasonably large excess, in accordance to Ref. [17]. In this case, the concentration of the reagent can be assumed as constant and the reaction rate depends on the concentration of available silanols $[A]$. The general differential form of the rate law for (pseudo) first order kinetics can be written as Eq. (3c)

$$\text{Rate} = -\frac{d[A]}{dt} = k[A] \quad (\text{Eq. 3c})$$

or in its integral form

$$\ln [A]_t = \ln [A]_0 - kt \quad (\text{Eq. 3d})$$

$[A]_0$ and $[A]_t$ can be again substituted by θ_{max} and $\theta_{max} - \theta_t$, respectively. A plot of $\ln(\theta_{max} - \theta_t)$ versus t will yield a straight line with the slope $-k$.

To solve this equation for the rate constant k , a value for the maximum sulfur coverage must be derived. This is readily possible by applying a Langmuir isotherm model which gives access to θ_{max} (Eq. 4).

$$\theta_t = \frac{\theta_{max} \cdot K \cdot C_t}{1 + K \cdot C_t} \quad (\text{Eq. 4})$$

wherein C_t refers to the equilibrium concentration of MPS or MPTMS at time t for this chemisorption process (i.e. reactant not bound to silica) and K to the equilibrium constant. Having determined k from Eq. (3b) to (3d) the half-life of the reaction can be calculated by Eq. (5)

$$t_{1/2} = \frac{\ln(2)}{k} \quad (\text{Eq. 5})$$

The non-linear fit afforded surface coverages θ_{max} of $4.4 \pm 1.1 \mu\text{mol}/\text{m}^2$ ($1329 \pm 318 \mu\text{mol}/\text{g}$) for the functionalization with MPTMS and $1.33 \pm 0.02 \mu\text{mol}/\text{m}^2$ ($340 \pm 5 \mu\text{mol}/\text{g}$) for its silatrane counterpart with satisfactory quality of fit (R^2 value of 0.966 for MPTMS and 0.998 for MPS). It is evident from Fig. 2a that the plateau is reached much faster with MPS. Apparently, the excess of MPS was too low to validly assume a pseudo first order kinetics which on the other hand seems to be valid for MPTMS. The linearization, as shown in Fig. 2b, shows a poor model fit for MPS. For this reason, a linearization for a second order kinetics was assumed. Here, $1/(\theta_{max} - \theta_t)$ was plotted against time. By doing so, rate constants k of 0.0018 min^{-1} for MPTMS (from pseudo 1st order model) vs 0.061 min^{-1} for MPS (from 2nd order model) have been calculated corresponding to a reaction half-life of 389 min for the former and only 11 min for the latter (Table 3). Thus, the functionalization with MPS can be performed roughly 35 times faster than with MPTMS. On the other hand, the maximal surface coverage with MPS is lower than with MPTMS, but this is not necessarily a disadvantage as separation factors do not increase linearly with selector coverages.

3.2.2. Thiol silica surface chemistry and phase characterization by ^{29}Si and ^{13}C CP/MAS solid state NMR

If we look at the EA results of Table 3, it is striking that in case of MPS silanization approach a nitrogen coverage equivalent to the sulfur surface concentration is obtained after the reaction. This could indicate an incomplete, only mono- or bivalent bonding of the MPS to the silica particles with a residual tri-

ethanolamine residue on the silane (see Fig. 3, reaction product A). Hence, an acidic hydrolysis step of the modified silica particles with MeOH/water (80/20, v/v) containing 0.1% (v/v) FA was subsequently carried out to cleave the triethanolamine moiety (see Fig. 3, B). A second cycle of silanization and hydrolysis was then carried out with MPS (Fig. 3, C). To better understand the surface chemistry, CP/MAS solid-state NMR spectra were acquired and the modified silica gels also subjected to EA (Table 4a). It can be seen that the first hydrolysis cycle (H1 in Table 4a) did not alter the sulfur coverage while the nitrogen was largely hydrolytically cleaved. The second silanization cycle (F2) brought a significant increase in sulfur content (from 1.31 to 3.98 $\mu\text{mol}/\text{m}^2$) and a similar nitrogen content as in the first silanization cycle. It appears that a dense layer of 3-mercaptopropyl-functionalities is obtained on the silica surface, approximating the maximal surface coverage that, according to text books [25], can be achieved by small silanes (note, ca. 4 out of 8 μmol silanols per m^2 silica surface modifiable by small silanes). After hydrolytic cleavage, again the majority of the nitrogen was removed from the modified silica without loss of sulfur (see Table 4a).

In order to gain deeper insights into the surface chemistry of the silica particles, ^{29}Si and ^{13}C CP/MAS NMR spectra were recorded in solid state. A single spectrum of the final MPTMS-derivatized silica gel as well as of every step of the MPS derivatization was acquired to monitor the functionalization process thoroughly. The ^{29}Si spectrum of MPTMS-derivatized silica gel shows signals for mono-, bi- and trifunctional siloxane bond (referred to as T¹, T² and T³) [26] (see Fig. 4a). MPS-derivatized silica (after the first silanization cycle and before hydrolysis) also showed all three possible bonding forms, but with notably less intensity for the signal corresponding to monofunctional siloxane bond (see Fig. 4b). Apparently, a bivalent bonding is favored when working in the absence of water, as the triethanolamine moiety is not cleaved from the silane under these conditions. Aqueous acidic treatment with methanol/water (80/20) containing 0.1% formic acid and subsequent treatment with MPS as well as hydrolysis in a second cycle of MPS derivatization led to a total loss of the T¹ signal and a tremendous rise of T³ signal (see Fig. 4c). It may indicate a homogenous thin polysiloxane monolayer on the silica surface as depicted in Fig. 1b. The high thiol surface coverage of this material with around 4 $\mu\text{mol}/\text{m}^2$ sulfur and the high T³/T² ratio disprove a monomeric surface bonding like shown in Fig. 1d and typically expected for anhydrous reaction conditions according to literature reports [3]. Furthermore, a second set of signals corresponding to Si of the silica surface can be found. The signal at -100 ppm corresponds to Si of free (isolated, vicinal and vicinal-bridged) silanols (Q³), a weak shoulder at -95 ppm indicates presence of some geminal silanols (Q²), and the signal at -110 ppm is due to quaternary Si of the siloxane network (Q⁴). Unfortunately, CP/MAS NMR spectroscopy does not allow to derive direct quantitative information from these signal intensities in a strict manner. For this reason, we considered direct MAS NMR which unfortunately requires long measurement times and is not practical for a larger set of samples. Exemplarily, we show in the Suppl. Material the comparison of ^{29}Si solid-state MAS NMR spectra acquired with and without CP. The latter was acquired with high-power decoupling (HPDec) (see Suppl. Fig. S4). It turned out that the T²/T³ ratio, which is primarily of interest for our interpretation, was fairly the same with and without CP while the ratio between Q and Q/T signals was varied. Due to missing protons in the Q⁴ bulk material and thus missing CP the major difference is visible for that signal. Hence, the relative T-signal intensities of the ^{29}Si CP/MAS NMR spectra may also give a meaningful trend for the relative presence of the distinct (mono-, di- and trifunctional) siloxane bonding states at least from a semi-quantitative viewpoint and relative comparisons of the same signals in different materials.

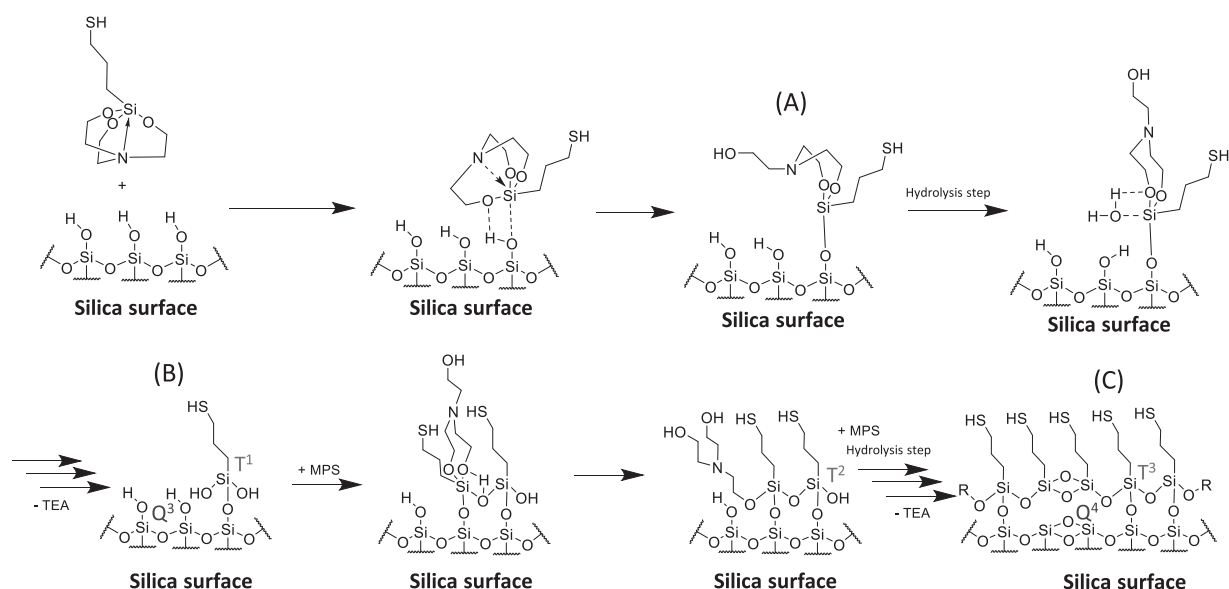


Fig. 3. Proposed reaction scheme of silanization of the silica surface by MPS. The proposed self-assembled monolayer (SAM) attached to vicinal silanols in the drawing represents an idealized view but may be interrupted and restarted at Si-O-Si moieties of the silica or bridged via double siloxane bonds of the organosilane layer on top of the silica surface.

Table 4

Overview on sulfur and nitrogen coverage (determined by elemental analysis) and percentage of T¹, T² and T³ (determined by solid state NMR).

reaction cycle	S %	N %	T ¹ %	T ² %	T ³ %	total sulfur ² [$\mu\text{mol}/\text{m}^2$]	free thiol ³ [$\mu\text{mol}/\text{m}^2$]	free thiol % of total sulfur
(a) twofold MPS-functionalization/hydrolysis cycles (hydrolysis performed with MeOH/H₂O (80/20; v/v) + 0.1% (v/v) FA)								
F1 ¹	1.28	0.63	5	55	40	1.33	n.a.	n.a.
H1 ¹	1.26	0.10	-	59	41	1.31	n.a.	n.a.
F2	3.83	0.75	-	18	82	3.98	n.a.	n.a.
H2	3.96	0.20	-	37	63	4.12	n.a.	n.a.
(b) fourfold MPS-functionalization/hydrolysis cycles (hydrolysis performed with MeOH/H₂O (20/80; v/v) + 0.1% (v/v) FA)								
F1	1.34	0.51	7	63	30	1.39	0.73	53
H1	1.32	0.03	1	43	56	1.38	1.05	76
F2	2.26	0.42	5	51	44	2.35	0.97	41
H2	2.31	0.06	4	42	54	2.40	1.13	47
F3	2.94	0.35	3	43	54	3.06	1.13	37
H3	2.75	0.07	5	46	49	2.86	1.43	50
F4	3.61	0.34	5	48	47	3.75	1.37	37
H4	3.44	0.08	2	41	57	3.58	1.85	52

¹ F stands for functionalization cycle, H for hydrolysis cycle

² as determined by elemental analysis

³ as determined by DPDS assay

3.2.3. Proposed reaction scheme

As previously suggested for silicon wafers [27,28], the reaction is induced by the attachment of silatrane to a silanol group of the silica surface. The high-field shift for ²⁹Si in the ²⁹Si-CP/MAS-NMR spectrum for MPS indicates a higher electron density at the silicon, due to the dative bond from N to Si. This leads to an increased proton affinity of silatranes in comparison to the silane analogues [14,15]. This high proton affinity of the oxygen drives the protonation of the silatrane by the silanol hydrogen, thus weakening the transannular N→Si bond. This in turn weakens the electron density on the silicon, favoring the nucleophilic attack of the hydroxyl oxygen at the silicon atom which drives the attachment to the silica surface. By formation of an Si-O-Si bond on the silica surface, the intramolecular Si-O bond will be cleaved, displacing the hydroxyl proton from the silica surface. The subsequent step needs an acidic aqueous hydrolysis, following a similar mechanism as described above, leading finally to an (ideally) triethanolamine-cleaved 3-mercaptopropylsilane residue bearing two silanol moieties [29]. Those free silanols can act as active centers for cleav-

age of the triethanolamine moiety of the following MPS molecule, leading ideally to the final product C shown in Fig. 3.

3.2.4. Optimization of the surface bonding

A number of factors were considered for further optimization of the surface and bonding chemistry, respectively: (i) more repetitive cycles of silanization and hydrolysis, and (ii) hydrolysis conditions. Furthermore, rehydroxylation of the silica particles prior to surface modification was examined as well but did not bring any differences which let us assume that a rehydroxylation step was already carried out by the silica supplier (see Suppl. Material Fig. S2 and S3 as well as Suppl. Table S1 for more details).

Two cycles of MPS-modification of silica revealed high sulfur densities, higher than typically reached with MPTMS (~3 $\mu\text{mol}/\text{m}^2$). As mentioned above, with small silanes like trimethylsilane, usually only roughly half of the silanol groups can be functionalized [30] leading to a maximal surface coverage of around 4 $\mu\text{mol}/\text{m}^2$ [25,31]. To further explore the limits of surface coverage, a synthesis approach with more cycles was performed. Four cycles of alter-

Table 5
Evaluated hydrolysis strategies and their impact on nitrogen and sulfur content

hydrolysis strategy	before hydrolysis		after hydrolysis		change in %	
	N [$\mu\text{mol}/\text{m}^2$]	S [$\mu\text{mol}/\text{m}^2$]	N [$\mu\text{mol}/\text{m}^2$]	S [$\mu\text{mol}/\text{m}^2$]	of N	of S
MeOH/H ₂ O (20/80; v/v) + 0.1% (v/v) FA	1.21	1.39	0.07	1.38	94.2	-0.7
MeOH/H ₂ O (50/50; v/v) + 0.1% (v/v) FA	1.49	1.33	0.20	1.42	86.6	6.8
MeOH/H ₂ O (80/20; v/v) + 0.1% (v/v) FA	1.49	1.33	0.24	1.31	83.9	-1.5
MeOH/0.1 M HCl (50/50; v/v)	1.49	1.33	0.21	1.44	85.9	8.3
Isopropanol/H ₂ O (20/80, v/v) + 0.1% (v/v) FA	1.49	1.33	0.13	1.42	91.3	6.8

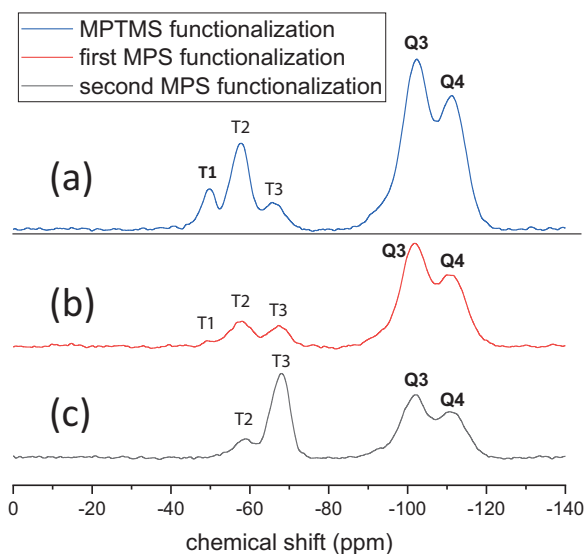


Fig. 4. ²⁹Si CP/MAS solid-state NMR spectra of MPTMS and MPS functionalization. (a) MPTMS functionalization for comparison. (b) After first cycle of MPS modification before hydrolysis step. (c) After second cycle of MPS derivatization and after subsequent hydrolysis step. Noteworthy is the remarkable shift towards trivalent bond (T³) and the complete loss of monovalent bond (T¹). Note, percentages of each signal corresponding to the different bonding states for MPS as obtained by deconvolution can be found in Table 4a.

nate MPS functionalization and hydrolysis were conducted. Since the hydrolysis of the triethanolamine residue was not fully complete with the previously used conditions (MeOH/water (80/20, v/v) + 0.1% (v/v) FA), a higher water content was employed (MeOH/water (20/80, v/v) + 0.1% (v/v) FA). Every sample was investigated by CP/MAS solid state NMR (see Fig. 5 for ¹³C CP/MAS NMR) as well as by EA. The results are summarized in Table 4b. It can be seen that the first silanization reaction yielded the same sulfur coverage as in the first synthesis batch described above (1.39 vs 1.33 $\mu\text{mol}/\text{m}^2$). It documents excellent reproducibility of the reaction. On the other hand, the higher water content during the hydrolysis step indeed led to slightly better hydrolysis yield. However, the increase in sulfur with each cycle of silanization was lower and only after four cycles reached the levels of the two-cycle approach with lower water content during hydrolysis (Table 4a). Besides, also the relative percentage of T³ signal corresponding to trifunctional siloxane bonding was slightly lower, but again approached the level of the two-step method after 4 cycles.

Finally, five different hydrolysis strategies were compared in terms of their ability to cleave the triethanolamine moiety from the surface of the functionalized silica. Results are presented in Table 5. None of the hydrolysis protocols led to a significant loss of the sulfur coverage (< 10% in all cases). The hydrolysis efficiency for the triethanolamine moiety increased with the aqueous content in the reaction mixture (94.2% with 80% water, 86.6% with 50% water, 83.9% with 20% water). Exchange of 0.1% FA by 0.1 M HCl as well as replacement of methanol by 2-propanol as wetting agent did not make a significant difference (Table 5).

In summary, the protocol with 80% MeOH and 0.1% FA was favorable both in view of a high sulfur coverage and high trifunctional siloxane bonding. As silatranes show a high proton affinity [14,15], a low amount of water in the reaction vessel might be sufficient and beneficial for the formation of the MPS monolayer.

3.2.5. ISEC for porosity determination

Silanization with MPTMS can easily lead to uncontrolled oligomeric bonding layer as schematically depicted in Fig. 1c. If this occurs excessively, the narrow pores of the silica particles might become partly inaccessible. For this reason, it was tested whether ISEC has the potential to provide information on the film thickness and pore accessibility in MPTMS- and MPS-modified silica. Complete characterization of the pore structure of plain silica particle column, MPTMS- and MPS-modified silica column might give indirectly some idea about the pore structure (total, external and internal porosities) in these columns. Especially the internal porosity, which indicates the porosity inside the particles (and therefore the size of the pores), could lead to useful information. The thinner the film inside the pores, the higher the internal porosity. Bare silica shows an internal porosity of 0.323 ± 0.0075 . While the functionalization with MPTMS reveals an internal porosity of 0.307 ± 0.0059 , MPS provided a slightly higher value of 0.316 ± 0.0046 (see Table 6). Although the difference is minor and not really significant from a strict statistical viewpoint, there might be a slight trend recognizable from these ISEC data following the expectations.

3.3. Thiol functionalization

3.3.1. Thiol functionalization by thiol-ene click reaction

The thiolated silica material can be conveniently functionalized for chromatographic purposes by thiol-ene click reaction with chromatographic ligands bearing a vinyl-group. As a model system we explore here the attachment of a chiral *tert*-butylcarbamoylquinine selector which has been thoroughly described recently so that plenty of data are available for comparison. The reaction scheme is depicted in Fig. 6. This thiol-ene click reaction relies on radicals generated by a radical initiator and the availability of reactive sulfhydryls.

As elemental analysis provides no information concerning the chemical state of the determined sulfur, the proportion of free reactive thiol groups on the silica surface was analyzed by a LC-UV assay based on a thiol-disulfide exchange reaction using 2,2'-dipyridyldisulfide (DPDS). Here, the reaction of thiols with DPDS leads to the generation of equimolar amounts of pyridine-2-thiol which is quickly converted into its tautomeric thione form shifting the equilibrium to the product side [23,24]. Hence, the formed pyridine-2-thiol and its tautomer were quantified by RP-HPLC-UV/Vis using 2-mercaptoethanol as calibrant. The sulfhydryl content of the prepared silica particles determined in this manner is given in Table 4b along with EA data, total sulfur coverage, and percentage of free reactive sulfhydryls related to the total sulfur content. It can be seen that with each silanization cycle the sulfhydryl surface concentration is increased. It is furthermore

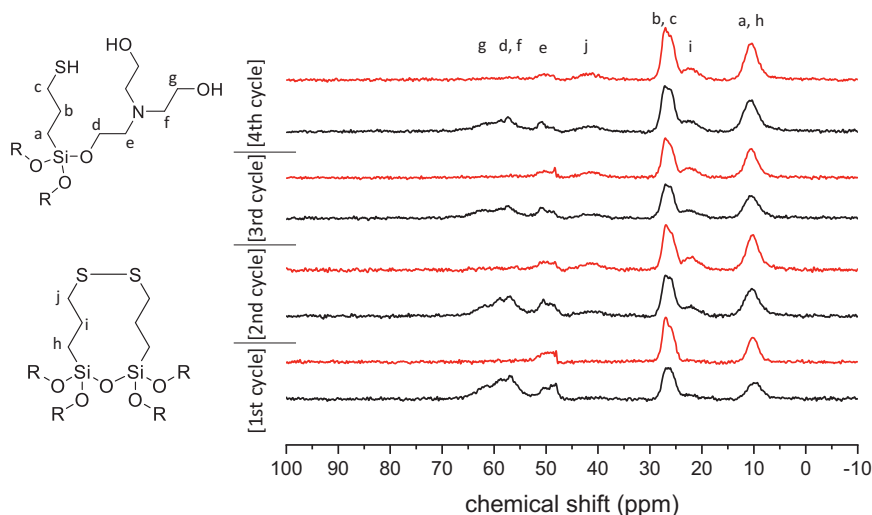


Fig. 5. ^{13}C CP/MAS solid-state NMR spectra of four cycles of MPS functionalization and hydrolysis. Functionalization is colored in black, hydrolysis in red. Note, that the triethanolamine signals (broad peak at ~ 57 ppm) appears at every functionalization and disappears almost completely after every hydrolysis. Further notable are the signals at roughly 23 ppm and 41 ppm. They first appear after the second functionalization cycle and then do not vanish again throughout all further steps. This might indicate disulfide bridges formed between neighbored 3-mercaptopropyl moieties.

Table 6
Results of ISEC and chromatographic evaluation

	bare Silica	MPTMS-functionalized ²	MPS-functionalized (2 cycles) ³
ε_e	0.344 ± 0.0022	0.347 ± 0.0042	0.349 ± 0.0025
ε_i	0.323 ± 0.0075	0.307 ± 0.0059	0.316 ± 0.0046
ε_t	0.668 ± 0.0053	0.653 ± 0.0017	0.665 ± 0.0021
selector coverage [$\mu\text{mol}/\text{m}^2$]	-	1.14	0.25
k_1	-	5.33	5.04
α	-	1.60	1.57
R_s	-	5.28	6.62
$N \text{ m}^{-1}$	-	56140	96560
h_{red}	-	6.33	3.45
$h_{red, uopt}$	-	3.56	3.43
A [μm]	-	6.91	7.40
B [$\text{cm}^2 \text{ s}^{-1}$]	-	1.86	2.18
C term (peak 1) [ms]	-	3.06	1.14
C term (peak 2) [ms]	-	3.40	1.12

¹ determined at a linear flow rate of 2.82 mm/s (= 0.5 mL/min), as shown in Fig. 7a

² mobile phase for chromatographic measurements: methanol/acetic acid/ammonium acetate (98/2/0.5, v/v/w)

³ mobile phase for chromatographic measurements: mobile phase as used for MPTMS, diluted with 97% methanol

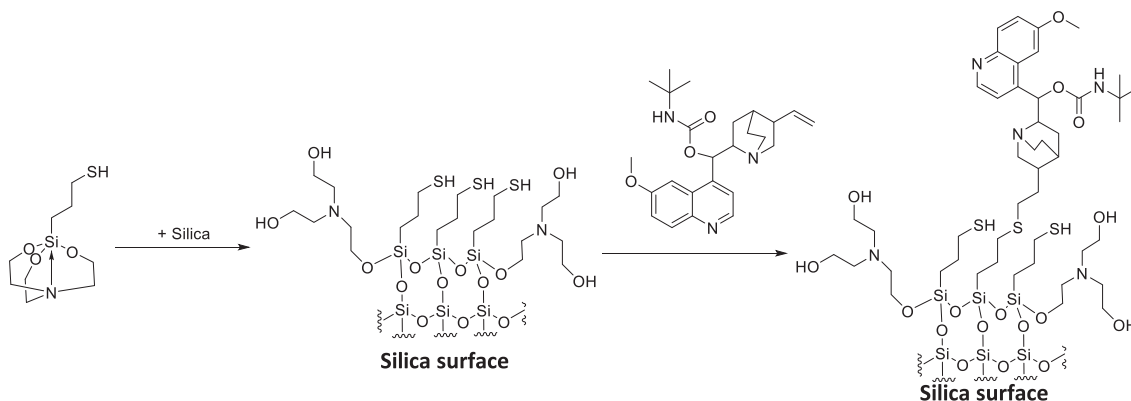


Fig. 6. Reaction scheme of thiol functionalization for enantioselective liquid chromatography by thiol-ene click reaction.

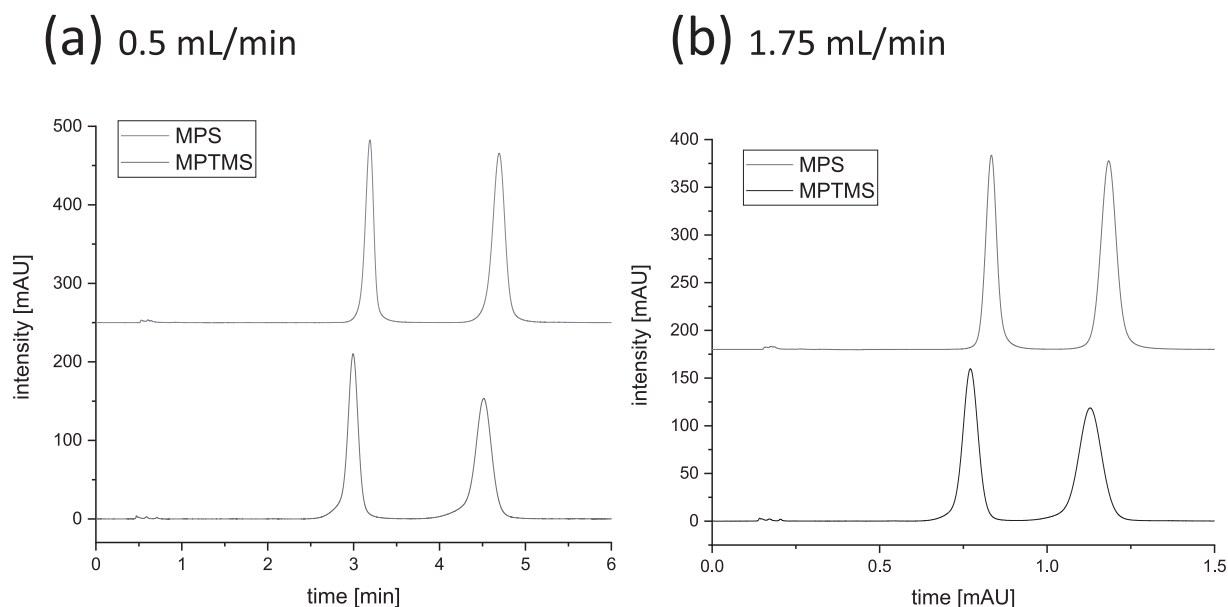


Fig. 7. Exemplary chromatograms for the enantiomer separation of Fmoc-Phe on MPTMS-bonded tBuCQN-CSP (black traces) and MPS-bonded tBuCQN-CSP (2 silanization/hydrolysis cycles) (red traces). All columns were of the dimensions 50×3 mm (L \times i.d.), $T = 25$ °C, flow rate: 0.5 mL/min (a) and 1.75 mL/min (b). Mobile phase: (MPTMS-bonded tBuCQN-CSP, black trace) methanol/acetic acid/ammonium acetate (98/2/0.5, v/v/w), (MPS-bonded tBuCQN-CSP, red trace) 3% of mobile phase specified for MPTMS-bonded CSP diluted with methanol. Plate numbers are in (a) (0.5 mL/min): MPS: Peak 1: 94,900 N/m, Peak 2: 96,560 N/m; MPTMS: Peak 1: 56,150 N/m, Peak 2: 52,690 N/m and in (b) (1.75 mL/min): MPS: Peak 1: 56,300 N/m, Peak 2: 57,440 N/m; MPTMS: Peak 1: 25,320 N/m, Peak 2: 23,210 N/m

striking that the sulfhydryl concentration is significantly higher after the hydrolysis step in each cycle, although the total sulfur content is slightly decreased. At first glance this finding is surprising. However, it may be ascribed to the reducing nature of formic acid which itself can be oxidized to carbon dioxide. If we look at the percentages of sulfur which are available as sulfhydryls and therefore reactive for thiol-ene click reaction we must notice that with increasing thiol density the fraction of disulfides is increasing so that one cannot fully exploit the significant gain of thiol ligands with each silanization cycle. Only around 50% of thiol ligands are available as free thiols for thiol-ene click reaction (after the last hydrolysis step) while this percentage was still 76% after the first silanization/hydrolysis cycle (see Table 4b).

For this reason, the selector coverage for the MPS-bonded CSP approach by thiol-ene click reaction was much lower than expected. Thiols seem to get further inactivated during the radical-initiated thiol-ene click reaction of the selector due to disulfide formation of sterically favorable 3-mercaptopropyl residues which are close enough for disulfide bridge formation of adjacent surface thiols. Thus, only $0.25 \mu\text{mol}$ tBuCQN ligand per m^2 on an MPS-modified silica material with a sulfur content of $3.76 \mu\text{mol}/\text{m}^2$ were immobilized (resp. $4.12 \mu\text{mol}/\text{m}^2$ before selector immobilization, see H2 in Table 4a). Thus, the MPS based column had eminently lower selector coverage than its MPTMS counterpart while showing higher sulfur loadings (selector, $1.14 \mu\text{mol}/\text{m}^2$; sulfur, $1.86 \mu\text{mol}/\text{m}^2$). A reduction step of disulfides with tris(2-carboxyethyl)phosphine prior to selector bonding did not bring about a significant increase of selector coverage (0.33 instead of $0.25 \mu\text{mol}/\text{m}^2$). The fact, that not all sulfur atoms and not even all reactive sulfhydryls (as determined by DPDS assay) are available for immobilization supports the hypothesis that disulfide bridges were formed during the functionalization supported by their close proximity in the polymeric surface bonding.

3.4. Chromatographic evaluation

Columns packed with the two types of tBuCQN silica particles, viz. MPTMS- and MPS-bonded (2 silanization/hydrolysis cy-

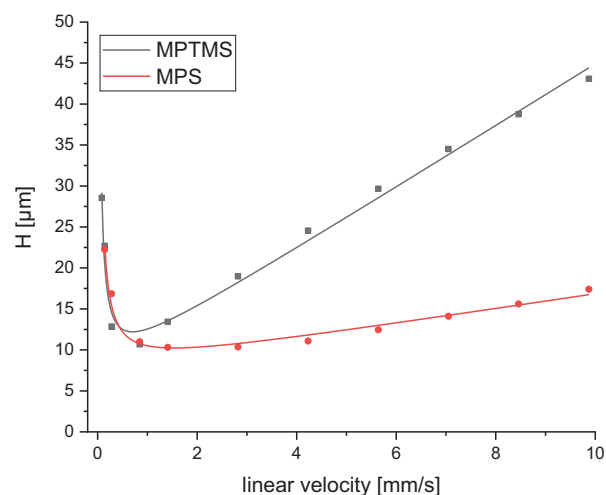


Fig. 8. H/u curves for the enantiomer separation of Fmoc-Phe on MPTMS-bonded tBuCQN-CSP (black curve), MPS-bonded tBuCQN-CSP (2 silanization/hydrolysis cycles) (red curve). All columns were of the dimensions 50×3 mm (L \times i.d.), $T = 25$ °C, mobile phase: (MPTMS-bonded CSP) methanol/acetic acid/ammonium acetate (98/2/0.5, v/v/w), (MPS-bonded CSP) 3% of mobile phase used for MPTMS-bonded CSP diluted with methanol. Note, column packing was not fully optimized specifically for each type of column, however, the fact that both A-terms and h_{red} at u_{opt} are comparable for MPS- and MPTMS-bonded CSPs indicates that their packing quality is comparable and does not significantly bias this comparison.

cles as shown in Table 4a), were chromatographically evaluated. The results are summarized in Table 6 and representative chromatograms are depicted in Fig. 7. For the chromatographic evaluation of the MPS-derived CSPs, isoelutropic conditions (in terms of ionic strength) have been adjusted by dilution of the initial mobile phase (methanol/acetic acid/ammonium acetate; 98/2/0.5, v/v/w), used for the chromatographic test of the MPTMS-bonded CSP, with MeOH to obtain comparable conditions. MPTMS-bonded CSP (with selector coverage of $1.14 \mu\text{mol}/\text{m}^2$) showed an enantioselectivity of 1.60 while the corresponding MPS-bonded CSP with $0.25 \mu\text{mol}/\text{m}^2$

selector coverage exhibited a separation factor of 1.57. It is evident that the selector coverage has only a minor effect on enantioselectivity enabling comparable results (see Table 6). At a flow rate of 0.5 mL/min (linear flow velocity of 2.82 mm/s), the resolution was superior for the MPS-bonded CSP column than the MPTMS-bonded CSP by around 25% (6.62 vs 5.28). Under optimal linear flow velocity of each CSP (0.25 mL/min for MPS- and 0.15 mL/min for MPTMS-bonded CSP), reduced plate height h_{red} were virtually identical.

Furthermore, Van Deemter curves were recorded under isoelutotropic conditions for the distinct CSPs to evaluate the effect of the bonding layer structure on the mass transfer (Fig. 8). In terms of resistance to mass transfer, MPS-functionalized silica clearly outperforms its MPTMS functionalized counterpart. While the MPTMS-bonded CSP could achieve a C-term of 3.06 ms for the first eluted peak (3.40 ms for the second eluted peak), MPS-bonded CSP showed a C-term of 1.14 ms for the first eluted peak (1.12 ms for the second eluted peak). This corresponds to a reduced mass transfer term by factor of 3 for the MPS-bonded CSP compared to the MPTMS-bonded CSP which may be indicative for a more homogeneous thinner surface bonding structure for the MPS-based bonding as schematically illustrated in Fig. 1b and c. It can be explained by a more strongly hindered pore diffusion and/or slower exchange rate in the organosilane layer network to which selector moieties are attached in case of the MPTMS-bonded CSP. Unfortunately, it is difficult to measure surface roughness and bonding thickness inside silica pores to proof this hypothesis. However, it was experimentally proven for flat sensor surfaces [17] and it can be assumed that this advantage is transferable to the silica surfaces of porous silica particles. The experimental results and findings in this paper point into this direction. Consequently, it can be concluded that the new silatrane surface bondings are promising for future chromatographic materials due to their regularity, greater homogeneity and controllable film thickness.

4. Conclusion

Silica surface modification by silanization with functional silatrane, e.g. 3-mercaptopropylsilatrane (MPS) is a promising strategy for the development of functionalized silica materials. Although the silatrane chemistry is generally around for decades, its implementation for silica gel modification represents a new approach. Using elemental analysis, which was thoroughly validated to document its suitability for this research and proved excellent intra-day and inter-day precision, as well as solid-state NMR we could verify the surface chemistry of a dense homogeneous polysiloxane monolayer on top of the silica surface by a high percentage of T³ signal in ²⁹Si CP/MAS solid-state NMR, indicative for a large fraction of trifunctional siloxane bonding. Of great interest is the fast reaction kinetics, which was roughly 35 times faster for the functional silatrane than its respective silane and can lead to faster and denser functionalization films on the silica surface. This very dense functional polymer layer approaches surface coverages commonly assumed as the theoretical maximum limit for the functionalization of silanols on silica (4 μmol/m²). The price to pay for the high sulfur density and high regularity in case of 3-mercaptopropylsilatrane was the high propensity for formation of disulfide bridges, which makes a certain fraction of thiols inaccessible for further reaction and derivatization, respectively. On the other hand, multiple reaction cycles of silanization and hydrolysis (of triethanolamine residues) are required for ending up with a dense polysiloxane layer on the silica surface. Low aqueous hydroorganic mixture with formic acid was favourable in the hydrolysis step. The thinner homogeneous monomolecular film of the MPS functionalization agent in the presented strategy turned out to be superior to the non-ordered, heterogeneous MPTMS-derived

thicker layer. The MPS-bonded chiral stationary phase based on quinine carbamate revealed explicitly lowered resistance to mass transfer, as indicated by a factor 3 lower C-term, compared to corresponding MPTMS-based material making this functionalization chemistry a promising strategy for the optimization of stationary phases in liquid chromatography. This may be of particular interest for fast separations, in which the C-term is often limiting the performance of a column. The present work paves the way for further research on other functional silica materials and shows the potential of using silatrane as powerful functionalization agents in liquid chromatography.

Declaration of Competing Interest

The authors declare that they have no known competing financial interests or personal relationships that could have appeared to influence the work reported in this paper.

Supplementary materials

Supplementary material associated with this article can be found in the online version at doi:10.1016/j.chroma.2021.462418.

CRediT authorship contribution statement

Christian Geibel: Investigation, Methodology, Formal analysis, Data curation, Visualization, Writing – original draft, Writing – review & editing. **Johannes Theiner:** Investigation, Methodology, Writing – review & editing. **Marc Wolter:** Investigation, Writing – review & editing. **Markus Kramer:** Investigation, Writing – review & editing. **Wolfgang Lindner:** Methodology, Writing – review & editing. **Michael Lämmerhofer:** Conceptualization, Methodology, Supervision, Writing – review & editing, Resources.

References

- [1] P. Žuvela, M. Skoczylas, J.J. Liu, T. Bączek, R. Kalisz, M.W. Wong, B. Buszewski, Column characterization and selection systems in reversed-phase high-performance liquid chromatography, *Chem. Rev.* 119 (2019) 3674–3729.
- [2] B. Buszewski, S. Bocian, G. Rychlicki, M. Matyska, J. Pesek, Determination of accessible silanols groups on silica gel surfaces using microcalorimetric measurements, *J. Chromatogr. A* 1232 (2012) 43–46.
- [3] M. Pursch, L. Sander, K. Albert, Peer reviewed: understanding reversed-phase LC with solid-state NMR, *Anal. Chem.* 71 (1999) 733A–741A.
- [4] X. Liang, A. Shen, Z. Guo, The application of thiol-ene/ylene radical click chemistry in surface modification and functionalization, in: *Thiol-X Chemistries in Polymer and Materials Science*, The Royal Society of Chemistry, 2013, pp. 286–308.
- [5] C. Rosini, C. Bertucci, D. Pini, P. Altemura, P. Salvadori, Cinchona alkaloids for preparing new, easily accessible chiral stationary phases. I. 11-(10,11-Dihydro-6'-methoxy-cinchonan-9-OL)-tiopropylsilanized silica, *Tetrahedron Lett.* 26 (1985) 3361–3364.
- [6] C. Geibel, K. Dittrich, M. Wolter, M. Lämmerhofer, Thiol-ene photo-click immobilization of a chiral chromatographic ligand on silica particles, *J. Chromatogr. A* 1622 (2020) 461133.
- [7] M. Lämmerhofer, W. Lindner, Quinine and quinidine derivatives as chiral selectors I. Brush type chiral stationary phases for high-performance liquid chromatography based on cinchonane carbamates and their application as chiral anion exchangers, *J. Chromatogr. A* 741 (1996) 33–48.
- [8] A. Shen, Z. Guo, L. Yu, L. Cao, X. Liang, A novel zwitterionic HILIC stationary phase based on “thiol-ene” click chemistry between cysteine and vinyl silica, *Chem. Commun.* 47 (2011) 4550–4552.
- [9] M. De Martino, G. Bencivenni, A. Mazzanti, S. Menta, O.H. Ismail, R. Sabia, A. Cogli, 3,5-Dinitrobenzoyl-9-amino-9-deoxy-9-epiquinine as pirkle-anion exchange hybrid-type chiral selector in high-performance liquid chromatography, *Chromatographia* 80 (2017) 751–762.
- [10] M. Wolter, X. Chen, U. Woiwode, C. Geibel, M. Lämmerhofer, Preparation and characterization of poly(3-mercaptopropyl)methylsiloxane functionalized silica particles and their further modification for silver ion chromatography and enantioselective high-performance liquid chromatography, *J. Chromatogr. A* 1643 (2021) 462069.
- [11] Q. Wang, Y. Long, L. Yao, L. Xu, Z.-G. Shi, L. Xu, Preparation, characterization and application of a reversed phase liquid chromatography/hydrophilic interaction chromatography mixed-mode C18-DIT stationary phase, *Talanta* 146 (2016) 442–451.

- [12] X. Yao, T.T.Y. Tan, Y. Wang, Thiol–ene click chemistry derived cationic cyclodextrin chiral stationary phase and its enhanced separation performance in liquid chromatography, *J. Chromatogr. A* 1326 (2014) 80–88.
- [13] M.J. Wirth, H.O. Fatunmbi, Horizontal polymerization of mixed trifunctional silanes on silica. 2. Application to chromatographic silica gel, *Anal. Chem.* 65 (1993) 822–826.
- [14] J.K. Puri, R. Singh, V.K. Chahal, Silatranes: a review on their synthesis, structure, reactivity and applications, *Chem. Soc. Rev.* 40 (2011) 1791–1840.
- [15] A. Yoshikawa, M.S. Gordon, V.F. Sidorkin, V.A. Pestunovich, Proton affinities of the silatranes and their analogues, *Organometallics* 20 (2001) 927–931.
- [16] C.J. Huang, Y.Y. Zheng, Controlled silanization using functional silatrane for thin and homogeneous antifouling coatings, *Langmuir* 35 (2019) 1662–1671.
- [17] T.J. Lee, L.K. Chau, C.J. Huang, Controlled silanization: high molecular regularity of functional Thiol groups on siloxane coatings, *Langmuir* 36 (2020) 5935–5943.
- [18] A. Mandl, L. Nicoletti, M. Lämmerhofer, W. Lindner, Quinine versus carbamoylated quinine-based chiral anion exchangers. A comparison regarding enantioselectivity for N-protected amino acids and other chiral acids, *J. Chromatogr. A* 858 (1999) 1–11.
- [19] N.M. Maier, L. Nicoletti, M. Lämmerhofer, W. Lindner, Enantioselective anion exchangers based on cinchona alkaloid-derived carbamates: influence of C8/C9 stereochemistry on chiral recognition, *Chirality* 11 (1999) 522–528.
- [20] P. Levkin, N.M. Maier, W. Lindner, V. Schurig, A practical method for the quantitative assessment of non-enantioselective versus enantioselective interactions encountered in liquid chromatography on brush-type chiral stationary phase, *J. Chromatogr. A* 1269 (2012) 270–278.
- [21] O.H. Ismail, L. Pasti, A. Ciogli, C. Villani, J. Kocergin, S. Anderson, F. Gasparini, A. Cavazzini, M. Catani, Pirkle-type chiral stationary phase on core–shell and fully porous particles: are superficially porous particles always the better choice toward ultrafast high-performance enantioseparations? *J. Chromatogr. A* 1466 (2016) 96–104.
- [22] A. Andrés, K. Broeckhoven, G. Desmet, Methods for the experimental characterization and analysis of the efficiency and speed of chromatographic columns: a step-by-step tutorial, *Anal. Chim. Acta* 894 (2015) 20–34.
- [23] B. Preinerstorfer, W. Bicker, W. Lindner, M. Lämmerhofer, Development of reactive thiol-modified monolithic capillaries and in-column surface functionalization by radical addition of a chromatographic ligand for capillary electrochromatography, *J. Chromatogr. A* 1044 (2004) 187–199.
- [24] R. Nogueira, M. Lämmerhofer, N. Maier, W. Lindner, Spectrophotometric determination of sulfhydryl concentration on the surface of thiol-modified chromatographic silica particles using 2,2'-dipyridyl disulfide reagent, *Anal. Chim. Acta* 533 (2005) 179–183.
- [25] K.K. Unger, *Porous Silica – its Properties and Use as Support in Column Liquid Chromatography*, Elsevier, Amsterdam, 1979.
- [26] C. Hellriegel, U. Skogsberg, K. Albert, M. Lämmerhofer, N.M. Maier, W. Lindner, Characterization of a chiral stationary phase by HR/MAS NMR spectroscopy and investigation of enantioselective interaction with chiral ligates by transferred NOE, *J. Am. Chem. Soc.* 126 (2004) 3809–3816.
- [27] S. Sok, M.S. Gordon, A dash of protons: a theoretical study on the hydrolysis mechanism of 1-substituted silatranes and their protonated analogs, *Comput. Theor. Chem.* 987 (2012) 2–15.
- [28] D. Chachkov, R. Ismagilova, Y. Vereshchagina, Mechanism of reactions of 1-substituted silatranes and germatranes, 2,2-disubstituted silocanes and germocanes, 1,1,1-trisubstituted hyposilatranes and hypogermatranes with alcohols (methanol, ethanol): DFT study, *Molecules* 25 (2020) 2803.
- [29] Y.-T. Tseng, H.-Y. Lu, J.-R. Li, W.-J. Tung, W.-H. Chen, L.-K. Chau, Facile functionalization of polymer surfaces in aqueous and polar organic solvents via 3-mercaptopropylsilatrane, *ACS Appl. Mater. Interface* 8 (2016) 34159–34169.
- [30] H. Engelhardt, C. Blay, J. Saar, Reversed phase chromatography – the mystery of surface silanols, *Chromatographia* 62 (2005) s19–s29.
- [31] K.K. Unger, S. Lamotte, E. Machtejevas, Chapter 3, *Column Technology in LC*, in S. Fanali, P. Haddad, C. Pool, P. Shoemakers, and D. Lloyd (editors), *Handbook of Separation Science: Liquid Chromatography*, Vol.1, Chapter 3 (2013) 41–86.

Supplementary Material

Controllable organosilane monolayer density of surface bonding using silatranes for thiol functionalization of silica particles for liquid chromatography and validation of microanalytical method for elemental composition determination

Christian Geibel ^a, Johannes Theiner ^b, Marc Wolter ^a, Markus Kramer ^c, Wolfgang Lindner ^d, Michael Lämmerhofer ^{a,*}

^a Institute of Pharmaceutical Sciences, Pharmaceutical (Bio-)Analysis, University of Tübingen, Auf der Morgenstelle 8, 72076 Tübingen, Germany

^b Mikroanalytisches Laboratorium, University of Vienna, Währingerstrasse 42, 1090, Vienna, Austria

^c Institute of Organic Chemistry, University of Tübingen, Auf der Morgenstelle 18, 72076 Tübingen, Germany

^d Institute of Analytical Chemistry, University of Vienna, Währingerstrasse 38, 1090 Vienna, Austria

*Author for correspondence:
Prof. Dr. Michael Lämmerhofer
Pharmaceutical (Bio-)Analysis
Institute of Pharmaceutical Sciences
University of Tübingen
Auf der Morgenstelle 8
72076 Tübingen, Germany
T +49 7071 29 78793, F +49 7071 29 4565
E-mail: michael.laemmerhofer@uni-tuebingen.de

1. ^{29}Si -NMR of functionalization agents

To be able to determine the electron density on the silicon atom of the two used functionalization agents, ^{29}Si -NMR spectra were recorded (details for synthesis: see main document). Fig. S1 shows the spectra of MPS (a) and MPTMS (b), indicating a high-field shift for MPS in comparison with MPTMS. Due to the dative bond, a higher electron density is present at the silicon in MPS.

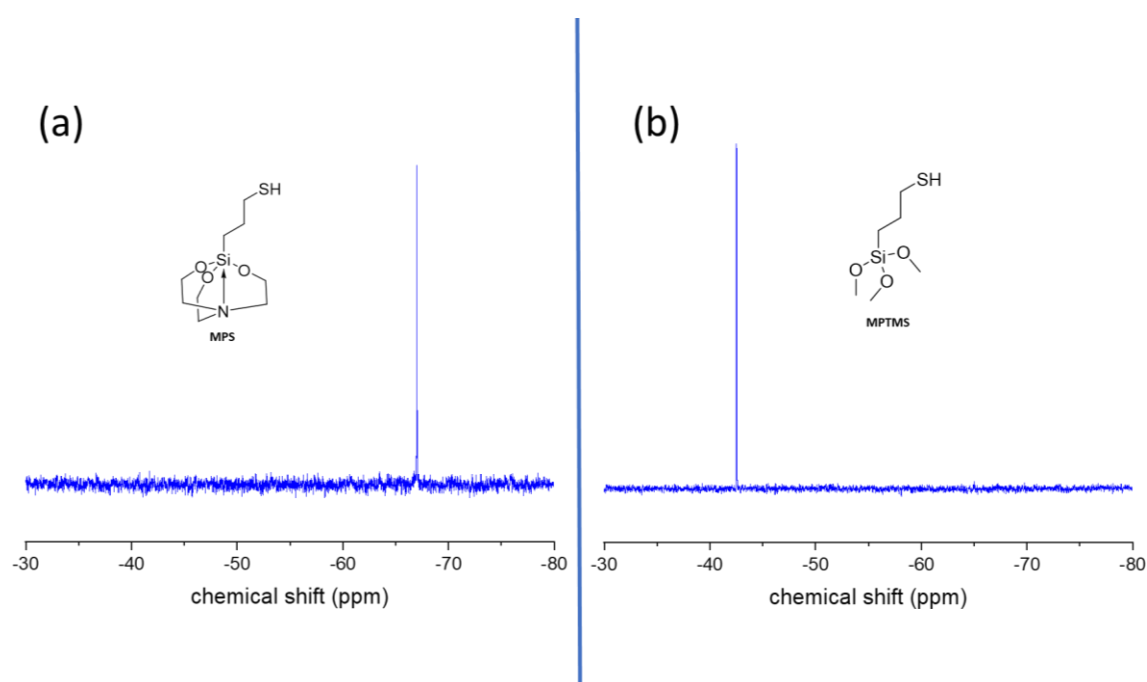


Fig. S1: ^{29}Si -NMR spectra of MPS (a) and MPTMS (b)

2. Rehydroxylation

The silanization with MPS requires free silanols. As the silica production process undergoes a calcination step at temperatures above $\sim 400 - 500\text{ }^\circ\text{C}$, silica will not only be dehydrated i.e. desorbing its physisorbed water, but will also lose silanols due to a condensation reaction, i.e. it will be dehydroxylated leading to elevated levels of surface siloxane groups [1-4]. For this reason, a rehydroxylation step prior to silanization was evaluated for increasing the surface

coverage already after the first silanization cycle. To do so, bare silica gel was heated to reflux in 0.1 M HCl for 3 hours and subsequently dried at 60 °C in vacuum overnight. Afterwards, functionalization with MPS was carried out as described in the main document. The dried material was subjected to elemental analysis and CP/MAS solid state NMR. EA showed comparable results for both nitrogen and sulfur coverage. As in this case, trivalent silane bondings were present even at a lower percentage than without hydroxylation, this strategy was abandoned.

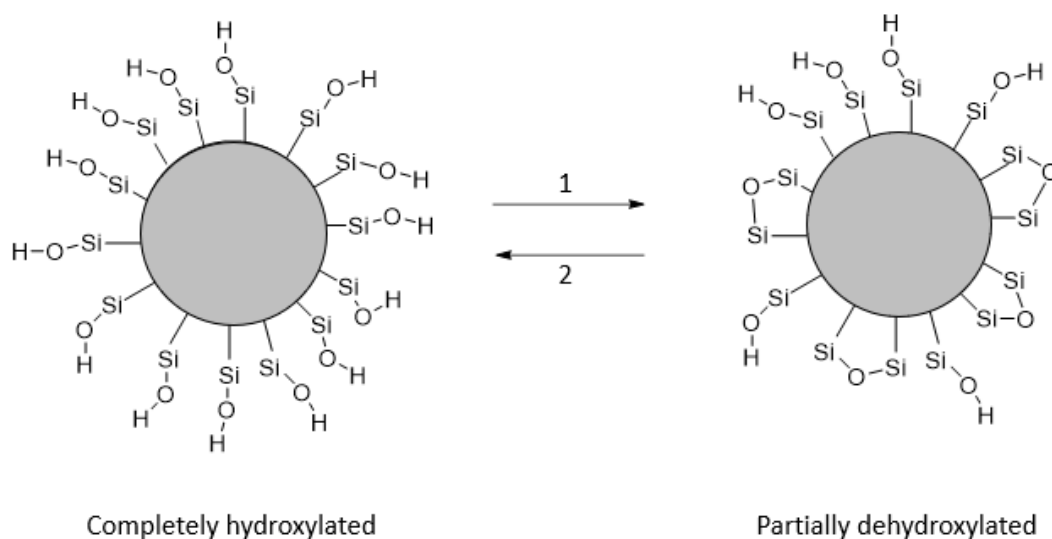


Fig. S2: Shown is a completely hydroxylated silica particle (left) and a partially dehydroxylated silica particle (right). The Si-O-Si groups on the right side are not available for a functionalization with MPS. 1 describes the act of dehydroxylation under the influence of heat while losing water in a condensation reaction. 2 describes the rehydroxylation with aqueous 0.1 M HCl in reflux for 3 hours.

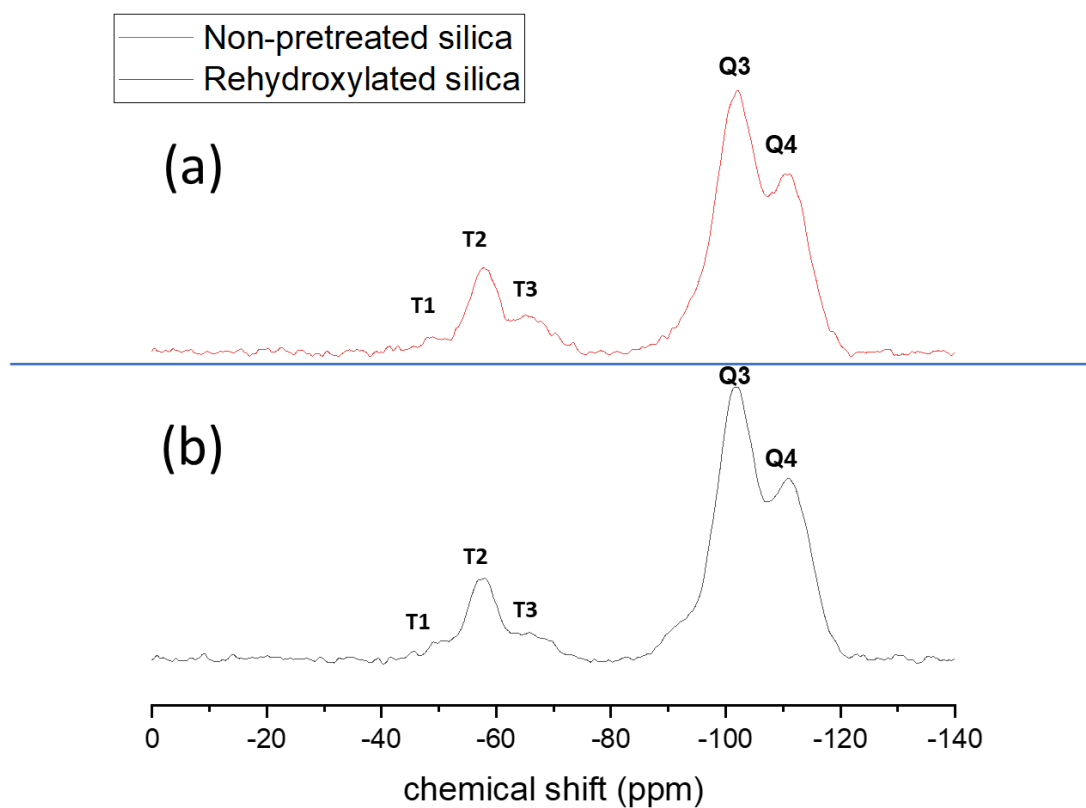


Fig. S3: ^{29}Si CP/MAS solid-state NMR spectra of a) non-pretreated silica and b) rehydroxylated silica after functionalization with MPS.

Table S1: Elemental analysis results of non-pretreated and rehydroxylated silica after MPS functionalization

	C %	H %	N %	S %
Non-pretreated silica	4.98	1.11	0.63	1.28
Rehydroxylated silica	4.34	1.11	0.53	1.21

3. ^{29}Si CP/MAS vs HPDec/MAS solid state NMR

Cross-polarization (CP) in combination with magic angle spinning (MAS) is a common technique for enhancing sensitivity in solid-state NMR spectroscopy. By transferring the proton-spin polarization to less sensitive carbon (^{13}C) or silicon (^{29}Si) nuclei (both having low abundance and lower gyromagnetic ratio) through heteronuclear dipolar coupling by adjusting Hartmann-Hahn conditions, the signal-to-noise ratio can be greatly improved and measurement times can be reduced. Unfortunately, this technique does not allow accurate quantification of the different ^{29}Si signals by their integrals. However, we assumed that the integrals within the T signal groups allow to derive some rough trends.

To support this assumption, spectra obtained by ^{29}Si CP/MAS NMR were compared to those of MAS NMR. In high-power decoupled (HPDec) MAS NMR, only heteronuclear dipolar coupling effects are suppressed. The resulting spectra are shown in Fig. S4. It is clearly visible that Q-signals, especially Q^4 , are not comparable. As Q^4 is not bearing a proton (as hydroxyl moiety) bonded to the measured silicon, the signal-suppressing effect in cross-polarization mode is much stronger on Q^4 than on Q^3 [5]. T signals on the other hand seem to be fairly well comparable (Fig. S4). While CP/MAS gave a ratio of 4.8/46.0/49.2 ($\text{T}^1/\text{T}^2/\text{T}^3$), HPDec/MAS measurement resulted in a ratio of 0/45.5/54.5 ($\text{T}^1/\text{T}^2/\text{T}^3$). T^1 was not detectable in HPDec/MAS, as it disappeared in the noise in the absence of cross-polarization. Apart from that fact, the results are pretty well comparable – showing a ratio of 48.3/51.7 (T^2/T^3 in CP/MAS) vs. 45.5/54.5 (T^2/T^3 in HPDec) taking only T^2 and T^3 into account. This indicates that CP/MAS can be used for a rough estimation of the bonding state from relative T-signals which are of relevance for this work. The percentages of T units obtained by deconvolution from the spectra of solid-state NMR given in Table 4 of the main document should be regarded as an estimation rather than accurate quantification to indicate some trends.

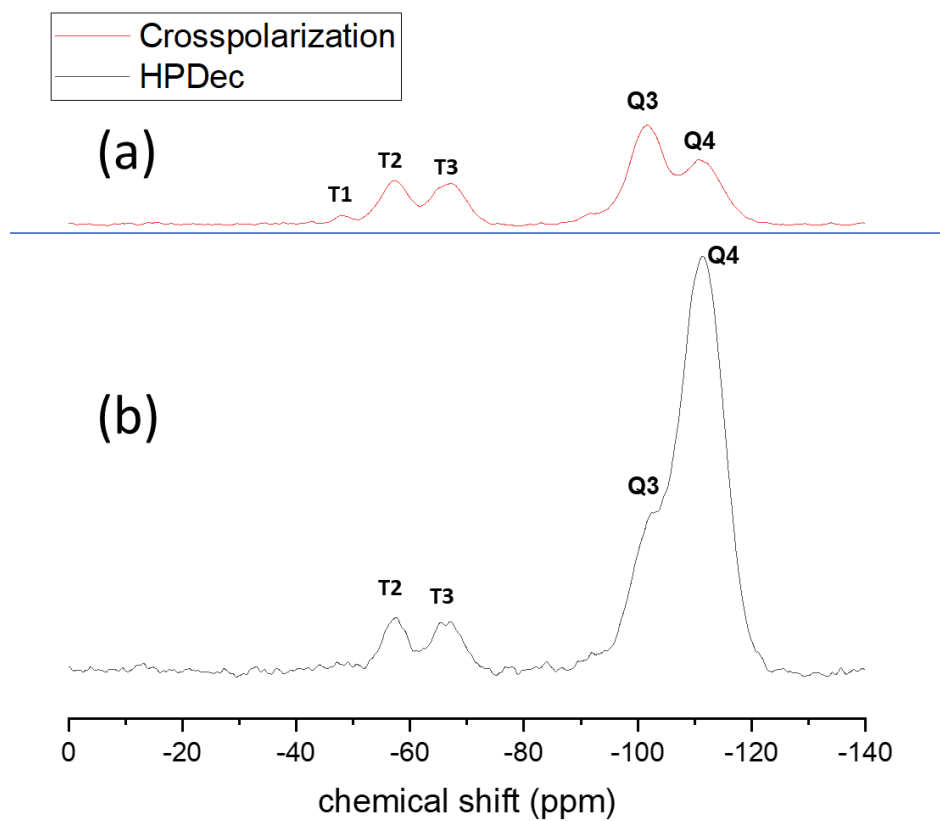


Fig. S4: Solid-state NMR spectra of the same MPS-functionalized silica gel, a) recorded with ^{29}Si CP/MAS solid-state NMR, b) recorded with HPDec/MAS solid-state NMR

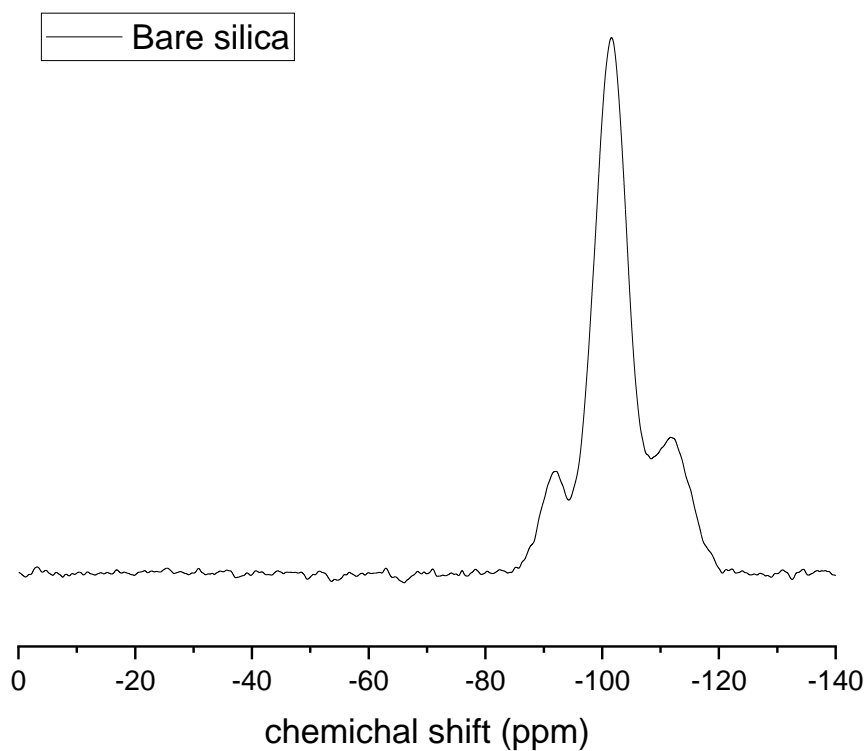


Fig. S5: Solid-state ^{29}Si CP/MAS-NMR spectrum of bare silica used as starting material for all experiments.

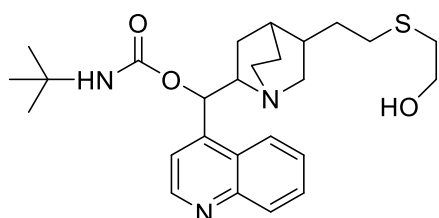


Fig. S6: Structure used for the synthesis of the adsorptively bound thiolated quinine carbamate silica gel which served as quality control (QC) standard

References:

- [1] E.F. Vansant, P. Van Der Voort, K.C. Vrancken, Chapter 3 The surface chemistry of silica, in: E.F. Vansant, P. Van Der Voort, K.C. Vrancken (Eds.) *Studies in Surface Science and Catalysis*, Elsevier, 1995, pp. 59-77.
- [2] L.T. Zhuravlev, The Surface Chemistry of Amorphous Silica. Zhuravlev Model, *Colloid Surface A*, 173 (2000) 1-38.

- [3] V. Dugas, Y. Chevalier, Surface hydroxylation and silane grafting on fumed and thermal silica, *J Colloid Interface Sci*, 264 (2003) 354-361.
- [4] H.E. Bergna, Colloid Chemistry of Silica, in: *The Colloid Chemistry of Silica*, American Chemical Society, 1994, pp. 1-47.
- [5] I.G. Shenderovich, D. Mauder, D. Akcakayiran, G. Buntkowsky, H.-H. Limbach, G.H. Findenegg, NMR Provides Checklist of Generic Properties for Atomic-Scale Models of Periodic Mesoporous Silicas, *J. Phys. Chem. B*, 111 (2007) 12088-12096.

3.1.4 Publication IV: **Study of microheterogeneity of silatrane-based silica surface bonding chemistry and its optimization for the synthesis of chiral stationary phases for enantioselective liquid chromatography**

Christian Geibel^a, Markus Kramer^b, Michael Lämmerhofer^{a,*}

^a Pharmaceutical (Bio-)Analysis, Institute of Pharmaceutical Sciences, University of Tübingen, Auf der Morgenstelle 8, Tübingen 72076, Germany

^b Institute of Organic Chemistry, University of Tübingen, Auf der Morgenstelle 18, Tübingen 72076, Germany

* Corresponding author. E-mail address: michael.laemmerhofer@uni-tuebingen.de (M. Lämmerhofer)

Journal of Chromatography A **2022**, 1674, 463138.

DOI: 10.1016/j.chroma.2022.463138

Authors of Elsevier articles retain the right to include it in a thesis or dissertation without further permission.

© 2022 Elsevier B.V.



Study of microheterogeneity of silatrane-based silica surface bonding chemistry and its optimization for the synthesis of chiral stationary phases for enantioselective liquid chromatography



Christian Geibel^a, Markus Kramer^b, Michael Lämmerhofer^{a,*}

^a Pharmaceutical (Bio-)Analysis, Institute of Pharmaceutical Sciences, University of Tübingen, Auf der Morgenstelle 8, Tübingen 72076, Germany

^b Institute of Organic Chemistry, University of Tübingen, Auf der Morgenstelle 18, Tübingen 72076, Germany

ARTICLE INFO

Article history:

Received 10 March 2022

Revised 7 May 2022

Accepted 9 May 2022

Available online 13 May 2022

Keywords:

Silica gel functionalization

Chiral stationary phase

Thiol-ene click reaction

Self-assembled monolayer

Solid-state NMR

ABSTRACT

The present work systematically investigates the chemical microheterogeneity as part of the optimization of a single-step surface bonding chemistry of 3-mercaptopropylsilatrane (MPS) on mesoporous silica gel in comparison to the state-of-the-art silane chemistry with 3-mercaptopropyltrimethoxysilane (MPTMS). MPS functionalization turns out to be a favourable chemistry for the further use in thiol-ene click reactions such as the immobilization of chiral selectors, herein *tert*-butylcarbamoylequinine (tBuCQN), for the synthesis of chiral stationary phases (CSPs). MPS has higher reactivity than MPTMS and prefers the formation of trifunctional siloxane bondings unlike MPTMS which favours difunctional siloxane bonds to silica, as investigated by solid-state cross-polarization/magic angle spinning (CP/MAS) NMR (²⁹Si and ¹³C nuclei). Reaction conditions (ternary mixtures of methanol, water and toluene; with and without acid; prewetting of silica; HCl pretreatment of silica) were evaluated with the aim to find conditions which promote the formation of a horizontal siloxane polymer layer on top of the silica surface. Silanization reaction times could be reduced to 2 h. The ²⁹Si NMR signal corresponding to trifunctional siloxane bonding could be increased to 60% with no T1 signal that refers to monofunctional siloxane bonding in spite of water in the ternary reaction mixture. Furthermore, no significant disulfide bridges were formed in this approach, leading to high selector loadings. The thiol and selector coverage reached up to 4.6 and 1.4 μmol/m², respectively. With the preferred CSP, the enantioselectivity could be increased for a chiral probe (Fmoc-Phe) and the mass transfer resistance (C-term) bisected compared to the corresponding CSP prepared from benchmark MPTMS-modified silica (2.54 vs 5.72 ms). It is demonstrated that the fine-tuning of the microstructure on the silica surface can have a significant influence on enantioselectivity and mass transfer kinetics of the resultant CSPs.

© 2022 Elsevier B.V. All rights reserved.

1. Introduction

Porous silica gel is the most widely used substrate of stationary phases in liquid chromatography (LC) [1]. For the majority of chromatographic modalities, it requires a derivatization of the silica surface for its adaptation and chemical functionalization to introduce chromatographic ligands for dedicated interactions with specific analytes, such as alkyl bondings for reversed-phase LC [2], hydrophilic interaction LC (HILIC) [3,4], mixed-mode LC [5] or chiral selectors for enantioselective LC [6–11]. Having precise control over the surface functionalization chemistry is the key for obtaining a stationary phase with dedicated selectivity, optimal efficiency and

adequate adsorption capacity. This can be achieved by both providing a reactive platform for a high selector loading and reducing detrimental effects arising from non-functionalized silanols as well as uncontrolled structural and morphological heterogeneities.

Bonded silica phases are commonly synthesized by derivatization of silanols with mono-, di-, and trifunctional (chloro or alkoxy) silanes through silanization reaction [1]. Depending on the conditions, the synthesis of alkyl-bonded phases leads to (i) monomeric bonding from monofunctional silanes, (ii) monomeric bonding utilizing trifunctional silanes (leading usually to a mixture of mono- and trifunctional siloxane bonds), (iii) polymeric bonded phases from trifunctional silanes in the presence of water by polymerization in solution and subsequent attachment of the polymer to the silica surface, and (iv) surface polymerization on humidified silica leading to dense self-assembled monolayers (SAM) of alkylsilanes on the silica surface [2]. Polymeric phases are assumed to have

* Corresponding author.

E-mail address: michael.laemmerhofer@uni-tuebingen.de (M. Lämmerhofer).

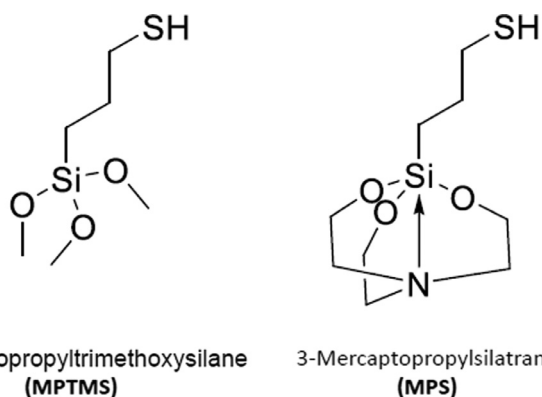


Fig. 1. 3-Mercaptopropyltrimethoxysilane (MPTMS) as state-of-the-art silanization agent and 3-mercaptopropylsilatrane (MPS) as newly introduced silane agent.

better hydrolytic stability owing to attachment of the silane layer by multiple bonds [2,12]. In some studies, it was distinguished between vertical and horizontal polymerization for the latter two types of polymer bondings [12]. Horizontal polymerization refers to a perfect SAM in which an extended Si-O-Si polymer layer is formed parallel to the silica substrate, obtained with trifunctional silanes under anhydrous reaction conditions with silica having a monolayer of water adsorbed to the surface [12]. In contrast, vertical polymerization is achieved through irregular attachment of preformed oligomeric siloxane structures (aggregates) to the silica surface due to polymerization of trifunctional silanes in solution by presence of water in the reaction mixture [12]. It leads to more heterogeneous surface layers since not all siloxanes are directly attached to the silica surface, but some oligomer chains are extending into the vicinity of the silica surface or are forming a micro-heterogeneous siloxane network with mass transfer limitations owing to restricted diffusional mass-transfer through these network channels. The better homogeneity and low film thickness of surface layers obtained by horizontal polymerization appear advantageous, as both factors may contribute positively to the mass transfer resistance term in LC.

To this end, we have recently introduced a new silica surface functionalization strategy using silatranes [13]. Silatranes are more reactive than corresponding silanes and have been shown to form thinner monolayers as well as smooth, and stable coatings on planar microchip surfaces [14]. The silatrane chemistry can be easily adapted for functionalization with either a terminal thiol- or vinyl moiety for immobilization of chromatographic ligands and chiral selectors, respectively, by thiol-ene click reaction, which has gained great popularity for the synthesis of functionalized stationary phases in LC [15–18]. We utilized 3-mercaptopropylsilatrane (MPS, see Fig. 1) for the functionalization of silica with terminal thiols to obtain a reactive surface for immobilization of a chiral selector [13]. MPS can be conveniently synthesized from 3-mercaptopropyltrimethoxysilane (MPTMS, see Fig. 1). Silatranes are easy to handle as they are stable towards hydrolytic decomposition in neutral aqueous solutions [19] but decompose quickly in the presence of acid. The increased proton affinity in comparison to silanes [19] is the key to their fast kinetics (up to 35 times faster than the respective silane [13]) and their ability to form self-assembling monolayers [20]. The pentacoordination forming a dative N→Si bond is the main reason for this enhanced reactivity, as the electron density on both the silicon and the oxygen will be increased [21]. In fact, using MPS and multiple silanization/hydrolysis cycles a more homogeneous organo-silane monolayer was obtained as verified by solid-state NMR [13]. The chiral stationary phase synthesized from this thiol silica showed improved efficiency with factor of ~ 3 lower mass transfer term. However, the multiple cy-

cles of silanization/hydrolysis made this procedure lengthy and unpractical.

To overcome this limitation, we present in this work an efficient one-step silanization approach using ternary mixtures of methanol, toluene and water which yields a similar polymeric siloxane bonding (SAM) as confirmed by solid-state NMR and affords enhanced mass transfer as compared to MPTMS silanization, approaching the performance of the material synthesized by previously reported multicycle silanization with MPS [13].

2. Experimental

2.1. Materials

3-Mercaptopropyltrimethoxysilane was supplied by ABCR Chemicals (Karlsruhe, Germany). Silica particles (spherical silica, Kromasil, 3 μm, 100 Å, specific surface area: 300 m²/g) were obtained by Eka Chemicals (Bohus, Sweden). Quinine was supplied by Buchler (Braunschweig, Germany), dibutyltin dilaurate by Sigma Aldrich (Munich, Germany). *tert*-Butylcarbamoylquinine (tBuCQN) was synthesized in-house following established procedures [22,23]. Toluene (both anhydrous and technical grade), methanol (both technical and HPLC grade), 4-dimethylaminopyridine (DMAP), *N*-[(9H-fluoren-9-ylmethoxy)carbonyl]-phenylalanine (Fmoc-Phe), azobis(isobutyronitrile) (AIBN), tri-*tert*-butylbenzene (TTBB), formic acid (FA, analytical grade), acetic acid (AA, analytical grade), sodium hydroxide and ammonium acetate were supplied by Sigma Aldrich. Ultrapure water was obtained by purification using an Elga PureLab Ultra Purification System (Celle, Germany). Empty stainless steel columns (all 50 mm length x 3 mm inner diameter) were supplied by Bischoff Chromatography (Leonberg, Germany).

2.2. Instrumentation

Slurry packing of all columns was performed using a Smart-line pneumatic pump, model 1950, supplied by Knauer (Berlin, Germany). H/u-curves were recorded on an Agilent 1290 Infinity series liquid chromatographic system from Agilent Technologies (Waldbronn, Germany). The UHPLC system was equipped with a UV-DAD detector with a Max-Light ultralow dispersion cartridge flow cell (inner volume 0.6 μL), an autosampler, a binary pump and a thermostatted column compartment. Extra-column volume and unwanted peak dispersion was reduced using capillaries with 0.075 mm inner diameter (autosampler to column compartment, 350 mm length; column compartment to detector, 250 mm length) and an ultralow dispersion needle seat assembly. Elemental analysis was conducted on an elemental analyser, type EA 3000 CHNS-O from EuroVector SpA (Milan, Italy). NMR spectra were acquired on a Bruker Avance III HD 300 XWB spectrometer (solid-state) and on a Bruker Avance III HDX 400 spectrometer (liquid state) (Bruker, Rheinstetten, Germany), NMR spectra were processed with Bruker TopSpin 4.0.8 software.

2.3. Solid-state NMR

¹³C and ²⁹Si solid-state NMR were performed using cross polarization (CP)/magic angle spinning (MAS) technique. Double bearing zirconia rotors were spun at 8000 Hz for both experiments. CP contact time was set to 2 ms (¹³C) or 5 ms (²⁹Si), 90° proton pulse was set to 2.5 μs (¹³C) or 3.3 μs (²⁹Si), relaxation delay was 2 s (both nuclei).

2.4. Synthesis of 3-mercaptopropylsilatrane

The synthesis of 3-mercaptopropylsilatrane (MPS) was carried out as described in Ref. [13]. Thus, 17.76 mmol of

both 3-mercaptopropyltrimethoxysilane (MPTMS, 3.3 mL) and triethanolamine (2.36 mL) were dissolved in 30 mL anhydrous toluene together with 5 mg sodium hydroxide and refluxed for 30 h. After cooling to room temperature, the mixture was slowly dropped into n-hexane for crystallization. Subsequently, the resulting product was dried at 60 °C *in vacuo*. Purity (according to ¹H-NMR) was 96%. ¹H-NMR [CDCl₃, 400 MHz]: δ (ppm) = 0.47 (m, 2H), 1.31 (t, *J* = 7.99 Hz, 1H), 1.70 (m, 2H), 2.49 (q, *J* = 7.65 Hz, 2H), 2.78 (t, *J* = 5.82 Hz, 2H), 3.74 (t, *J* = 5.82 Hz, 2H). ¹³C-NMR: δ (ppm) 57.75 (CH₂), 51.12 (CH₂), 30.47 (CH₂), 28.37 (CH₂), 15.73 (CH₂). ²⁹Si-NMR: δ (ppm) -67.01 (RSiO₃). NMR data for MPTMS: ¹H-NMR [CDCl₃, 400 Hz]: δ (ppm) 0.73 (m, 2H), 1.31 (t, *J* = 7.93 Hz, H), 1.70 (m, 2H), 2.52 (q, *J* = 7.44 Hz, 2H), 3.55 (s, 9H). ¹³C-NMR: δ (ppm) 50.57 (CH₃), 27.57 (CH₂), 27.45 (CH₂), 8.23 (CH₂). ²⁹Si-CP/MAS-NMR: δ (ppm) -42.52 (RSiO₃).

2.5. Single step silanization of silica by two distinct functionalization strategies

Ternary mixtures of toluene, methanol, and aqueous fraction (either water or water plus formic acid) were prepared, and the silanization reaction was carried out in this mixture. 50 mL of an aqueous-methanolic binary mixture was prepared and 5 mL of toluene were added. After mixing until no phase separation was visible, 5 mL were removed and used as reaction solvent for the silanization of 300 mg dried silica gel. Together with 0.48 mmol MPS (or MPTMS, respectively), and 1 mg DMAP, the mixture was refluxed for either 30 min, 2 h or 7 h. In further experiments, the reaction time was kept constant at 2 h, and the relative percentages of methanol, toluene and acid in the mixture were varied. The composition of the evaluated reaction solvents are summarized in Table 1. Afterwards, a washing step with boiling toluene and boiling methanol (three times each) was performed in a glass filter funnel (porosity 5). After drying of the silica at 65 °C overnight in a vacuum oven (~ -750 mbar), it was subjected to elemental analysis and solid state NMR.

2.6. Preparation of chiral stationary phases

The chiral tBuCQN selector was immobilized by thiol-ene click reaction as described in Refs. [13,23,24]. Briefly, 1 g of the thiol functionalized silica gel (either by modification with MPTMS or MPS, respectively) was suspended in 10 mL methanol together with 255 mg (0.6 mmol) tBuCQN. Furthermore, 5 mg of azobis(isobutyronitrile) as radical initiator were added and refluxed under mechanical stirring for 7 h. Washing with boiling toluene and boiling methanol (three times each) was performed afterwards in a glass filter funnel (porosity 5). Finally, the silica gel was dried at 65 °C in vacuum (~ -750 mbar) overnight.

2.7. Effect of pre-wetting of silica gel

300 mg of silica gel (dried at 65 °C at ~ -750 mbar overnight) and 5 mL dry toluene (over molecular sieve, afterwards distilled azeotropically) were left stirring with a mechanical stirrer. Subsequently, a certain amount of water (1, 2, 4 and 8 μmol/m² silica gel) containing 0.1% formic acid was added to the mixture. Due to its insolubility in toluene, the water molecules form a surface layer on silica. Different amounts were added to obtain different degrees of saturation, e. g. monomolecular or polymolecular aqueous layers on the particles. After 10 min, the equilibrium was supposed to be adjusted. Then, 0.48 mmol (120 mg) MPS and 1 mg DMAP as catalyst were added. The mixture was subsequently heated to reflux for 2 h. The product was washed and dried and subjected to both elemental analysis and solid state NMR.

Table 1 Summary of elemental analysis and solid-state NMR data of the different single-step 3-mercaptopropyl-silicas (TPS)

TPS no.	functionalization agent	reaction time H	reaction mixture ¹											pretreatment ²	
			(v/v/v)												
			C	H	S	N	S	T1	T2	T3	MeOH	Water	Toluene		FA added ³
1	MPS	7	5.50 ± 0.06	1.19 ± 0.02	4.40 ± 0.08	0.05 ± 0.00	4.57	-	37.0	63.0	73	18	9	0.1%	x
2		2	4.58 ± 0.02	1.10 ± 0.03	3.46 ± 0.00	0.05 ± 0.00	3.60	-	51.2	48.8	73	18	9	0.1%	x
3		0.5	2.82 ± 0.01	0.85 ± 0.02	1.91 ± 0.04	0.04 ± 0.01	1.99	7.0	59.8	33.2	73	18	9	0.1%	x
4	MPS	2	4.00 ± 0.02	0.94 ± 0.01	3.08 ± 0.06	0.02 ± 0.00	3.20	6.1	58.2	35.7	82	9	9	0.1%	x
5			5.27 ± 0.02	1.15 ± 0.00	3.96 ± 0.07	0.08 ± 0.00	4.12	-	51.8	48.2	86	5	9	0.1%	x
6			4.18 ± 0.04	0.98 ± 0.00	3.23 ± 0.01	0.02 ± 0.00	3.36	6.4	55.4	38.2	86	9	5	0.1%	x
7			4.11 ± 0.08	0.93 ± 0.01	2.84 ± 0.09	0.03 ± 0.00	2.95	3.3	54.1	42.6	91	5	5	0.1%	x
8			2.50 ± 0.02	0.78 ± 0.00	1.76 ± 0.02	0.02 ± 0.00	1.83	-	50.1	49.9	73	18	9	-	x
9	MPTMS	2	3.07 ± 0.01	0.82 ± 0.01	2.38 ± 0.06	0.00 ± 0.00	2.47	9.2	71.3	19.5	73	18	9	0.1%	x
10			3.29 ± 0.08	0.86 ± 0.02	2.53 ± 0.09	0.00 ± 0.00	2.63	14.9	67.1	18.0	86	5	9	0.1%	x
11	MPS	2	4.71 ± 0.02	1.06 ± 0.02	3.63 ± 0.11	0.08 ± 0.01	3.77	-	39.2	60.9	73	18	9	-	✓

¹ 5 mL of the below listed solvent was used for the functionalization of 300 mg silica.

² silica gel marked with tickmark was pretreated with aqueous HCl, pH = 2, for 15 min.

³ FA = formic acid.

2.8. Acidic silica pretreatment

Silanol groups on the silica surface are known to have an acidic character [25]. By the addition of a stronger acid and a protonation of the terminal silanol groups the impact on the surface acidity on the reaction speed of the MPS-film formation was determined. To do so, 150 mg silica gel were gently stirred in 20 mL aqueous hydrochloric acid (pH = 2) at room temperature for 15 min. As silica becomes instable at pH-values under ~ 2 , lower pH values could not be tested. Thus obtained silica was not washed, but just dried by filtration through a glass filter funnel (porosity 5). Afterwards, it was dried in a vacuum oven overnight (at 65 °C, ~ -750 mbar). Then, MPS and 3 mL from the acid-free solvent (50 mL methanol/water (80/20) + 5 mL toluene) were used to perform a functionalization for 2 h. Washing was performed as previously described, samples were subjected to elemental analysis and solid-state NMR.

2.9. H/u curve recording and mass transfer resistance comparison

N-[(9H-Fluoren-9-ylmethoxy)carbonyl] (Fmoc) protected phenylalanine was used as a chiral probe to record the H/u curves. The H/u curve of the MPTMS-bonded CSP, which served as benchmark, was recorded with methanol/acetic acid/ammonium acetate (98/2/0.5, v/v/w) as mobile phase, and the H/u curves of the MPS-bonded CSPs were recorded under isoeluotropic conditions. This was achieved by diluting the mobile phase mentioned before by methanol. Flow rates ranged from 0.015 to 1.75 mL/min, taking care that the maximum back pressure of 800 bar was not exceeded. Injection volume was 1 μ L, column temperature 25 °C. The van Deemter equation (non-linear fit) was used for the calculation of A-, B- and C-terms. In addition to the newly synthesized CSPs, the most promising column from Ref. [13] obtained by multistep MPS-silanization chemistry was analyzed by recording a H/u curve for comparison.

3. Results and discussion

3.1. One-step MPS functionalization

The MPS silanization of silica with commonly employed non-aqueous conditions (toluene reflux) reported in our former publication exhibited faster reaction kinetics, but lower surface coverage compared to MPTMS silanization [13]. A dense horizontal siloxane polymer layer parallel to the silica surface, as claimed in the literature for planar microchip surfaces [14], was not formed by a single step approach. Elemental analysis allowed to calculate a surface coverage for sulfur of 1.33 μ mol/m² and an equimolar amount of nitrogen, which indicated a surface bonding as shown in Fig. 2, structure (I). This structure was confirmed by ¹³C-CP/MAS solid-state NMR (see Fig. 2a). Subsequent acidic hydrolysis of the triethanolamine residue linked to the surface-bound silane enabled to remove it (see Fig. 2b) and subsequent reaction cycles gave rise to surface coverages of up to 4 μ mol/m² sulfur and silane, respectively, indicating a dense monolayer as also confirmed by ²⁹Si-CP/MAS solid-state NMR [13]. Unfortunately, the multi-cycle synthesis approach resulted in increased oxidation of thiols to disulfide bonds with adjacent silanes (structure (II) in Fig. 2). As this strategy showed the benefits of improved chromatographic efficiency (factor 3 lower C-term), but suffered from a tedious synthetic process, the goal of this study was to develop a one-step strategy that can benefit from the advantages of the MPS chemistry but does not suffer from lengthy multi-cycle synthesis procedures.

It is evident that the removal of the triethanolamine moiety needs some water. Therefore, ternary mixtures of toluene,

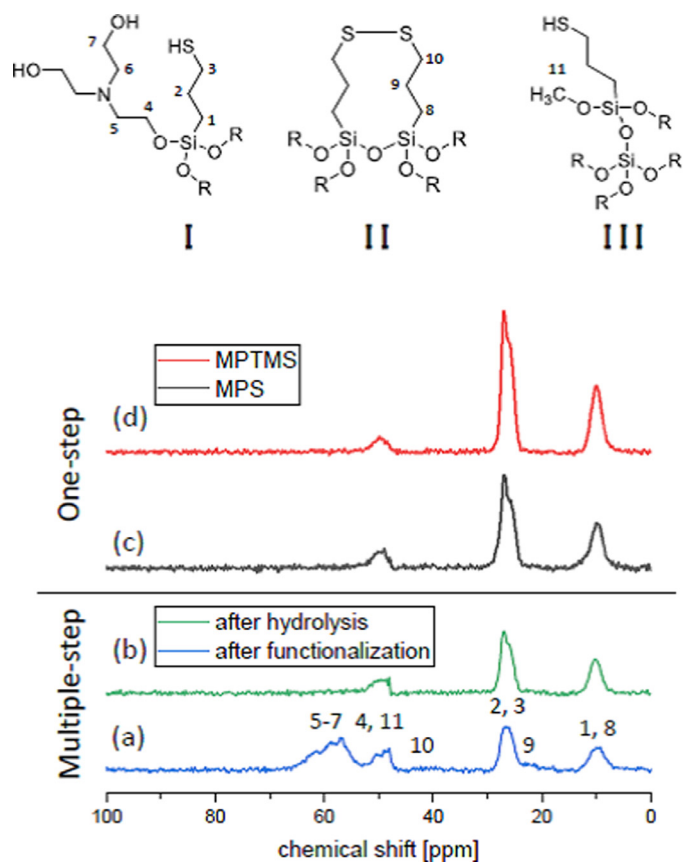


Fig. 2. ¹³C solid-state CP/MAS NMR spectra for multiple-step (a,b, both precursors of TPS no. 12) and for one-step silanization approach with MPS (black, TPS no. 8) (c) and MPTMS (red, TPS no. 9) (d). (a) After first functionalization cycle with MPS silanization (blue) and (b) after subsequent hydrolysis (green)). All on 3 μ m 100 Å FPP and signal assignments as indicated by structure (I), (II), and (III). Note the absence of signals for the triethanolamine moiety (peaks 4–7) in (b–d), and disulfide bridges (8–10) in every spectrum.

methanol and aqueous solvent fraction (either water or water containing some formic acid) were evaluated as solvents for the MPS functionalization reaction. Both solvent composition and reaction time were optimized (Table 1). Thus, 5 mL of toluene added to 50 mL of a binary mixture of methanol and water (80/20; v/v) containing 0.1% formic acid (FA) induced a phase separation, which disappeared after vigorous stirring, indicating that this mixture is highly saturated with toluene [26]. In further experiments, the reaction time was kept constant, and the amount of methanol, toluene and acid were varied. All silica gels functionalized with MPS by this one-step procedure showed a very low amount of nitrogen (< 0.1%) in elemental analysis (Table 1) and missed the broad signals between ~ 55 and 65 ppm in the ¹³C-CP/MAS solid-state NMR (see Fig. 2), indicating a total loss of the triethanolamine moiety. Interestingly, this is also valid for the experiment lacking the addition of formic acid. As silatrane exhibit a high proton affinity [19,21], an acid is necessary to catalyze the reaction of self-assembling monolayer formation. Furthermore, as proposed in Ref. [13], acidic treatment is needed to cleave triethanolamine moieties. It appears as the acidic silanol moieties on the surface of the silica particles (pK_a-values between 3 and 6 depending on their chemical nature [25]) are able to fulfil both of these needs. Fig. 2 shows that no disulfide bridges were formed during the functionalization process, neither using MPS (Fig. 2c) nor with MPTMS (Fig. 2d) in the one-step approach, as peaks 9 and 10 are not occurring (peak 8 is hardly distinguishable from peak 1). Both peaks are visible in the multi-step approach (Fig. 2a and b), especially after mul-

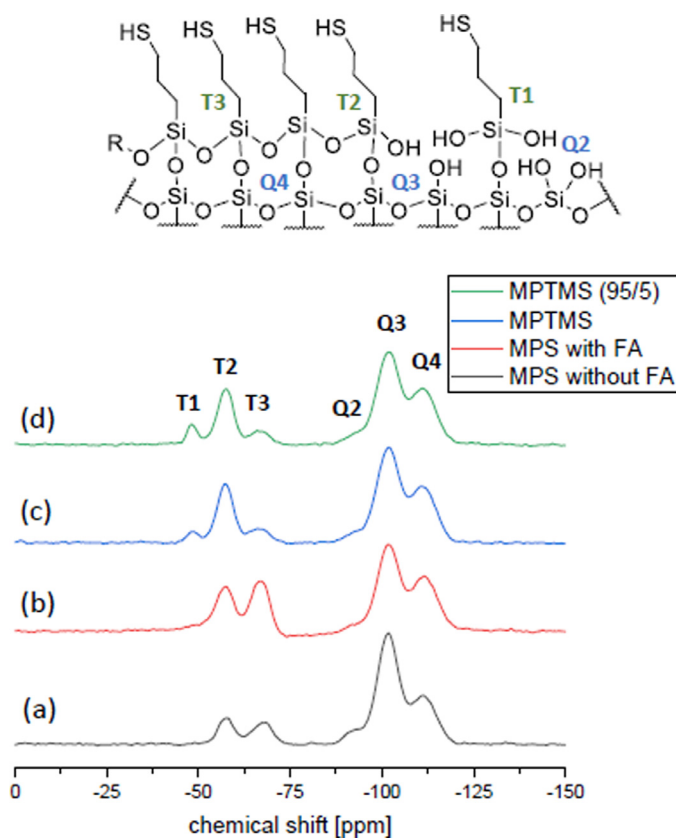


Fig. 3. ^{29}Si solid-state CP/MAS NMR spectra for (a,b) MPS- and (c,d) MPTMS-functionalized silica. Reaction solvent: Methanol/water/toluene 73/18/9 (v/v/v) (a–c) and 86/5/9 (v/v/v) (d), (a) without (TPS no. 8) and (b) with formic acid (TPS no. 2), (c) (TPS no. 9) and (d) with formic acid (TPS no. 10). Note the vanishing of T1 signal in both MPS spectra. Signal assignments as indicated. Monofunctional siloxane bond are referred to as T1 (at -48 ppm), bifunctional siloxane bond as T2 (-57 ppm) and trifunctional siloxane bond as T3 (-66 ppm). Q2 indicates germinal silanols, Q3 (-100 ppm) stands for free, isolated or vicinal silanols, Q4 (-110 ppm) indicates quarternary siloxanes.

multiple cycles (see Ref. [13]). It is furthermore striking, that a peak at ~ 50 ppm arose. This peak could be elucidated to be a methoxy moiety [27,28]. As shown by Bayer et al. [27], the use of methanol as solvent for the functionalization can lead to a reaction with methanol.

Reaction times were varied between 0.5 and 7 h and as can be seen in Table 1. The sulfur content per m^2 determined by elemental analysis increased from $1.99 \mu\text{mol S}/\text{m}^2$ at 0.5 h, over $3.60 \mu\text{mol S}/\text{m}^2$ after 2 h, to $4.57 \mu\text{mol S}/\text{m}^2$ after 7 h reaction time. The bonding states of the silanes can be conveniently obtained from the ^{29}Si -CP/MAS solid-state NMR spectra of the corresponding materials (Fig. 3). The Q-signals in Fig. 3 refer to the silica backbone and the T-signals represent the silane bonding states. Due to cross polarization a direct quantitative information cannot be derived from the individual signals. However, a comparison of CP/MAS solid-state NMR and high-power decoupled (HPDec)/MAS solid-state NMR in our previous publication showed that the results are comparable in particular within the T-group signals thus giving a rough estimation of the relative quantities of the siloxane bonding states [13]. Table 1 depicts that the T1-signal (corresponding to mono-functional siloxane bond) disappears after 2 h (50% T3 and $3.6 \mu\text{mol}$ sulfur per m^2), while the T3-signal (corresponding to trifunctional siloxane bond which is the most stable bonding chemistry of trifunctional silanes) increases with reaction time (63.0% T3, $4.57 \mu\text{mol}$ sulfur/ m^2). While there is only a modest gain in surface coverage from 2 to 7 h reaction time, the bonding state

does still change significantly and 7 h reaction seems favourable in terms of stability of the surface bonding.

As roughly $8 \mu\text{mol}/\text{m}^2$ silanol groups are expected to be available on the silica surface and about 50% can be derivatized with small silanes [1,29,30], we assumed that the reaction was virtually complete after 7 h. For convenience, 2 h reaction time was used in further experiments because the gain in surface coverage is minimal with longer reaction at significant expense of time.

The findings of the optimization study (Table 1) can be summarized as follows: (i) The most significant effect was exerted by omission of the formic acid which led to significantly lower surface coverage, viz. 1.83 instead of $3.60 \mu\text{mol}/\text{m}^2$ with 0.1% FA, (ii) the water content (between 5 and 20% of the binary MeOH/water mixture containing 0.1% FA) had a minor effect on the thiol surface coverage (between 3.2 and $4.1 \mu\text{mol}/\text{m}^2$), (iii) less toluene in the reaction mixture, in particular with low water content, was accompanied by lower sulfur surface coverage, and (iv) the T3 signal intensity depended mainly on the reaction time, increased from 33% at 0.5 h to 63% at 7 h, while it was between 35 and 50% for all experiments with 2 h reaction time. Besides it was striking that omission of the formic acid, had little effect on the siloxane bonding states (with 2 h reaction time T2/T3 ratio around $50/50$ with and without formic acid; compare Fig. 3a and b) while it had a significant effect on the surface coverage as mentioned above.

Thiol silica phases were also prepared with MPTMS under the same reaction conditions for comparison. It is striking that they showed significantly lower amounts in both sulfur content (2.47 and $2.63 \mu\text{mol}/\text{m}^2$ with MPTMS compared to 3.60 and $4.12 \mu\text{mol}/\text{m}^2$ for MPS with 20 and 5% water, respectively, in the binary MeOH/water mixture containing 0.1% FA) and also lower T3 signal intensities ($\sim 19\%$ T3 with MPTMS compared to $\sim 48\%$ T3 with MPS) (Table 1). From these results it can be hypothesized that oligomeric siloxane structures (aggregates) are formed in solution with MPTMS which slowly attach to the silica surface due to sterically hindered reaction (Fig. 4a). MPS reacts faster and forms patches of horizontal siloxane polymer on the silica surface resembling the structure shown in Fig. 4b as compared to a surface with vertical polymerization, schematically shown in Fig. 4c.

3.2. Effect of pre-wetting of silica gel

In the literature it is reported that for alkyl-bonded phases favourable horizontal polymerization can be achieved by the formation of a self-assembling monolayer of trialkoxysilanes on prewetted silica gel having attached a monolayer of water molecules [3,12]. On the contrary, vertical polymerization with irregularly surface-detached siloxane chains results from silanization reaction with trifunctional silanes and water in the reaction mixture [12]. Such irregularities may lead to loss in chromatographic performance of the resultant stationary phase, primarily due to enhanced mass transfer resistance. Furthermore, the sulfur content determined by elemental analysis does not reflect the derivatizable sulfur on top of the silica gel [13]. Disulfide bonds reduce the number of reactive thiols for the subsequent selector bonding. Although it is not fully clear which bonding state (and which further conditions) favour disulfide formation, it is assumed that the flexible siloxane polymer chains readily allow disulfide bond formation while a horizontal polymer restricts this possibility. A visualization of these phenomena is given in Fig. 4. The ratio of selector-to-sulfur can be used as indicator for the availability of sulfur, thus for the amount of reactive thiol moieties. The higher the amount of immobilized selector, the more sulfur is available in reactive form for derivatization. Both MPTMS and MPS without added FA (TPS no. 8 and 10, see Table 2) show similarly high values of 0.48 and 0.47 , respectively. On the contrary, the material from MPS with acid (TPS no. 1) as well as MPS in multiple

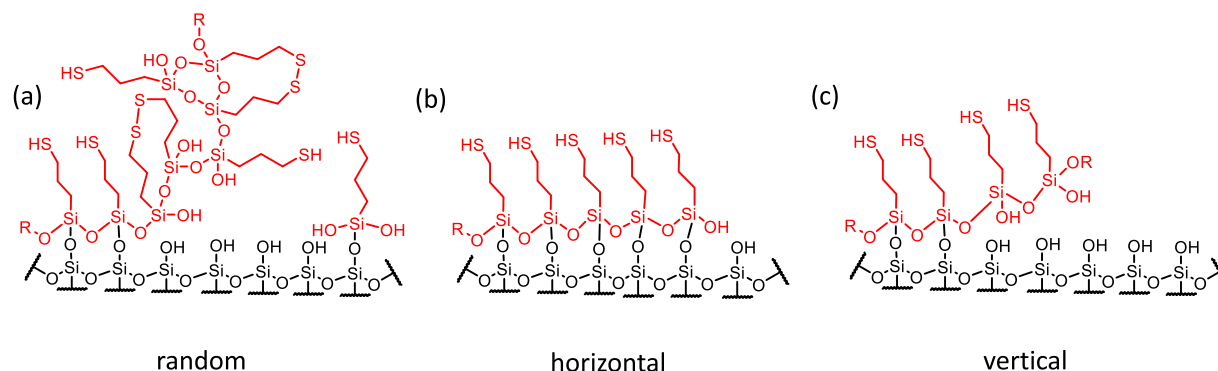


Fig. 4. Tentative structures of (a) random, (b) horizontal and (c) vertical polymerization. The siloxane polymer chain is shown in red. Horizontal polymerization leads to a thin, homogeneous layer of the functionalization agent. Vertical polymerization, on the other hand, leads to a sloughing of the polysiloxane polymer chain during polymerization and to a prolongation in the surrounding solution. This can also lead to detrimental disulfide bridges.

Table 2

Overview on the evaluated stationary phases including C-term.

TPS no.	functionalization agent	reaction time [h]	S ¹ $\mu\text{mol}/\text{m}^2$	selector $\mu\text{mol}/\text{m}^2$	ratio selector/sulfur	T1 %	T2 %	T3 %	Acid added ²	k1 ⁵	α ⁵	C-term [ms] ⁵	
												peak 1	peak 2
10	MPTMS ³	2	2.17	1.05	0.48	14.9	67.1	18.0	✓	4.10	1.65	5.04	5.72
1	MPS	7	3.48	1.42	0.41	-	37.0	63.0	✓	4.14	1.57	8.39	9.07
8	MPS	2	1.66	0.78	0.47	-	50.1	49.9	x	3.99	1.77	2.36	2.54
12	MPS	multiple cycles ⁴	3.76	0.25	0.07	-	37.0	63.0	-	4.20	1.66	1.09	1.09

¹ sulfur content after immobilization of selector differs slightly from content after functionalization.

² when 0.1% formic acid were added to the reaction mixture (see Table 1), the phase is marked with a tickmark.

³ MPTMS-CSP was functionalized in MeOH/water (95/5) + 0.1% FA + 5 mL toluene, all MPS-CSP in MeOH/water (80/20) + 0.1% FA + 5 mL toluene. For explanation, see text.

⁴ MPS-based CSP with 2 cycles of functionalization/hydrolysis as described in Ref. [13] was tested.

⁵ H/u curves recorded with MeOH/AA/NH₄Ac (98/2/0.5, v/v/w) for TPS-10, diluted with MeOH for all other phases (42% MeOH for TPS-1, 56% MeOH for TPS-8, 95.5% MeOH for TPS-12 derived CSP).

step approach (TPS no. 12) reveal lower values (0.41 and 0.07, respectively) while at the same time they exhibit higher sulfur content. This leads to the hypothesis that more disulfide bridges are formed in the latter two thiol materials (TPS no. 1 and 12). Two reasons can be responsible for this effect: (i) the sloughing of the polymeric chain described above and shown in Fig. 4a, or (ii) disulfide bridge formation between two neighbouring mercaptopropyl-strands (only in case of dense surface layers possible). Analogy to the literature let us assume that the above performed single step reaction conditions with water in the reaction mixture lead to vertical polymerization. On the contrary, a pre-wetting of silica and a subsequent functionalization in dry toluene is supposed to afford horizontal polymerization.

To this end, a series of experiments was performed in which silica was prewetted with distinct amounts of water (1, 2, 4 and 8 $\mu\text{mol}/\text{m}^2$) and subsequent silanization reaction performed in toluene with MPS. For all water layer thicknesses, elemental analysis showed a poor coverage of sulfur (1.03–1.34 $\mu\text{mol}/\text{m}^2$). Since all solid-state NMR experiments gave about the same results, solely those of prewetting with 8 $\mu\text{mol}/\text{m}^2$ are described hereafter. No T1 signal (for monofunctional siloxane bonding) was visible in the ²⁹Si-CP/MAS NMR spectra. On the other hand, increased T3 signal intensities (for trifunctional siloxane bonding) were found besides a significant T2 signal (difunctional siloxane bond) (see Fig. 5a). However, the ¹³C-CP/MAS-NMR spectrum in Fig. 5b showed both a strong signal for triethanolamine residues (I) and disulfide bridges (II) (for structures (I) and (II) see Fig. 2). These results resemble the experiments of silanization with MPS in toluene without water (first step of multi-cycle approach) as reported previously [13]. It appears that the triethanolamine residues prevent the further reaction and formation of a horizontal siloxane polymer layer. This strategy was therefore abandoned. Indirectly it can be concluded that the above MPS silanization reaction with water and formic

acid in the reaction mixture that yielded high sulfur loadings is likely to favour vertical polymerization.

3.3. Acidic pretreatment

In an attempt to increase the reaction kinetics and shorten the reaction time with silatrane for silanization, acidic pretreatment of the silica gel with aqueous HCl, pH = 2 was envisioned. The pretreatment leads to a protonation of the acidic silanol groups and by this to a shift in pK_a from slightly under 3 [25] to lower than -2 in quartz [31], respectively, (calculated) -5 [32], depending on the literature used. According to Ref. [33], protonated silanol (SiOH₂⁺) is virtually not apparent at neutral pH, but rises to a relative density of roughly ~ 18 % at pH = 2. It was expected to increase the proton availability and catalyse the reaction at the silica surface. The short acidic pretreatment indeed gave rise of T3 signal intensity in the ²⁹Si-CP/MAS NMR spectrum. When comparing pretreated and non-pretreated thiol-modified silica gel functionalized under otherwise identical conditions, it becomes evident that a significantly higher number of trifunctional siloxane bonds were formed (60.9% vs 49.9% T3 signal) (Fig. 6a and 6b, respectively). It shows in a 2 h reaction a high surface coverage (3.77 $\mu\text{mol}/\text{m}^2$) and elevated levels of stable trifunctional siloxane bonding (60.9% T3) comparable to the material obtained by MPS silanization with formic acid and 7 h reaction time (63.0% T3, 4.57 $\mu\text{mol}/\text{m}^2$ sulfur). A short pretreatment of the silica gel can thus save a significant amount of time in the functionalization process.

3.4. Chromatographic evaluation

Four thiol silicas were chosen for immobilization of a tBuCQN selector and subsequent chromatographic evaluation, one functionalized with MPTMS (MPS no. 10), two one-step functionalized with

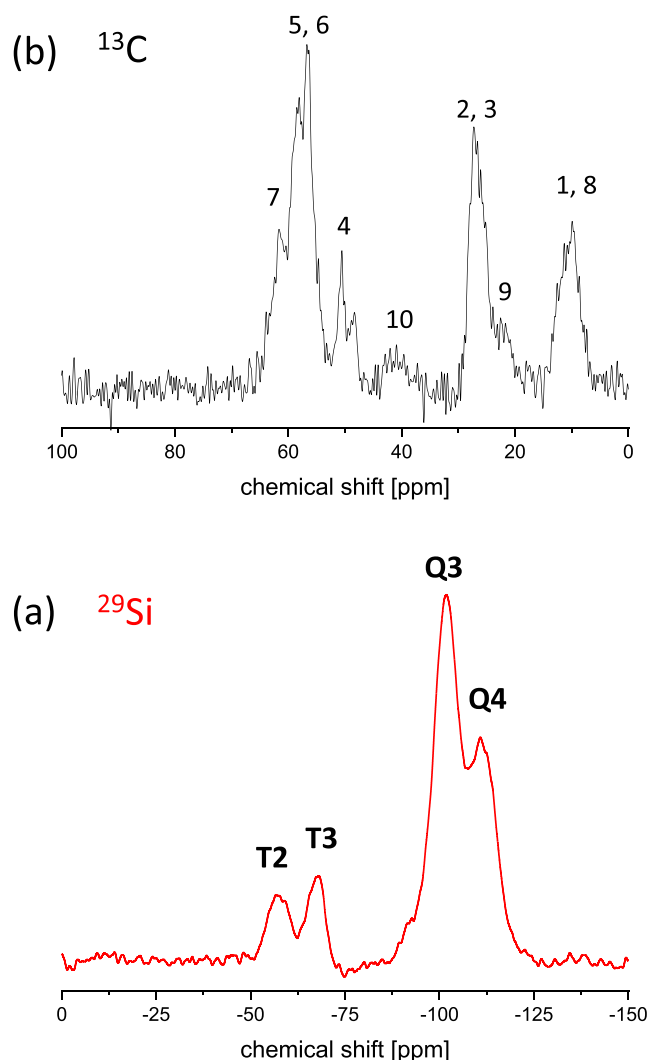


Fig. 5. Solid-state CP/MAS NMR spectra of the MPS-modified material obtained from prewetted silica. (a) ^{29}Si NMR spectrum (for assignment of signals see Fig. 3), and (b) ^{13}C NMR spectrum (for assignment of signals see Fig. 2).

MPS (one with formic acid MPS no. 1, one without MPS no. 8) and one multiple-step functionalized MPS. No. 12, from the previous study comprising two cycles of functionalization with MPS and subsequent hydrolysis, as described in Ref. [13]. Using Fmoc-Phe as test compound, H/u curves for the CSP prepared from MPTMS phase was recorded using methanol/acetic acid/ammonium acetate (98/2/0.5, v/v/w) as mobile phase. For all other phases, the mobile phase was adjusted with methanol (MPS no. 1: 42% methanol, MPS no. 8: 56% methanol, multiple-step MPS-column no. 12: 95.5% methanol; remaining part to 100% above mobile phase) to obtain isoelutotropic conditions. Exemplary chromatograms obtained with a flow rate of 0.5 mL/min are shown in Fig. 7. H/u curves are depicted in Fig. 8, and selected chromatographic data are summarized in Table 2.

The comparison of the separation factors of these CSPs obtained under isoelutotropic conditions reveals that the new surface bonding chemistry using MPS-silanization without formic acid in the reaction mixture provides the highest enantioselectivity ($\alpha = 1.77$) (Table 2 and Fig. 7a). In spite of much higher thiol and selector coverage for the corresponding CSP prepared from MPS-modified silica obtained with formic acid in the reaction medium, its enantioselectivity for Fmoc-Phe was significantly lower ($\alpha = 1.57$) (Fig. 7b). Also, the corresponding MPTMS-based CSP exhibited

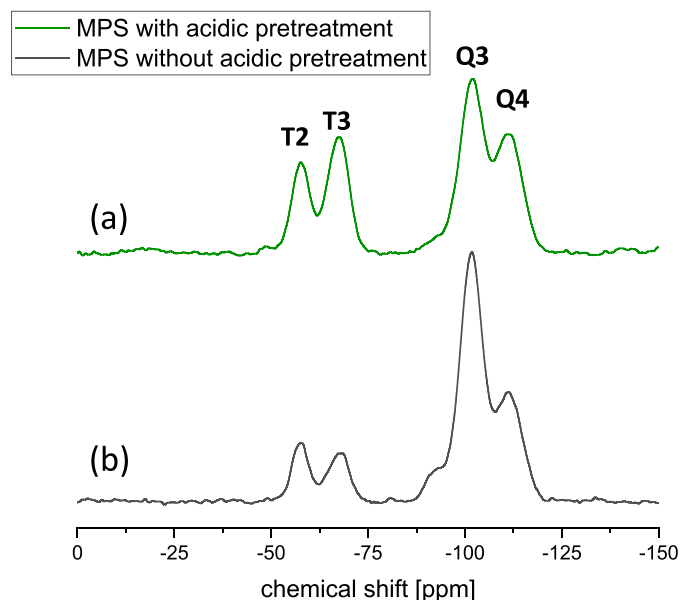


Fig. 6. Solid-state ^{29}Si -CP/MAS NMR spectra for MPS functionalization with (a) and without (b) acidic silica pretreatment ($\text{HCl}_{(\text{aq})}$, pH = 2). Reaction solvent, methanol/water/toluene (73/18/9; v/v/v) (material TPS no. 11).

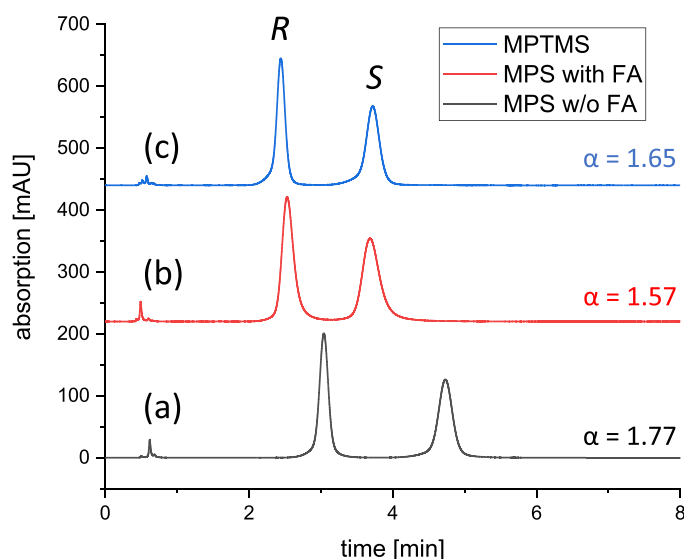


Fig. 7. Representative chromatograms of different columns prepared from different thiol-silicas. (a) MPS no. 8, (b) MPS no. 1, and (c) MPS no. 10. All chromatograms were recorded at a flow rate of 0.5 mL/min. Mobile phase: methanol/acetic acid/ammonium acetate (98/2/0.5; v/v/w) for (a), dilution of mob. ph. (a) with 42% methanol for (b), dilution of mobile phase (a) with 56% methanol for (c). Detection wavelength: 254 nm.

lower enantioselectivity ($\alpha = 1.65$) (compare Fig. 7a and c) and the same is observed for the MPS-based CSP from the previous study obtained by multiple MPS-silanization/hydrolysis cycles ($\alpha = 1.66$) (Table 2). Evidently there is no correlation between selector coverage and separation factor and the tBuCQN-CSP prepared from MPS-silanization without formic acid in the reaction medium achieved the best results, possibly due to free, unhindered access to the binding sites as a result of a more homogeneous surface bonding or less non-specific interactions with the surface.

The H/u curves in Fig. 8 reveal a worse chromatographic efficiency for the CSP made from MPS-silanized silica with formic acid (red trace, circles) as compared to the MPTMS-based benchmark column (black trace, squares). The former has a high thiol

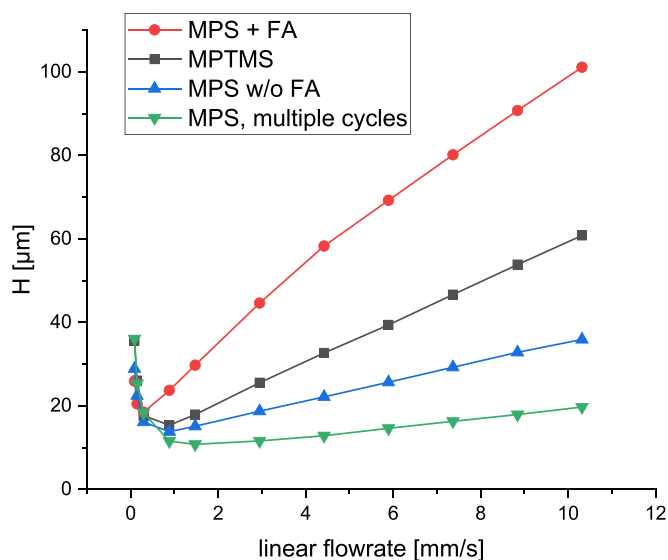


Fig. 8. H/u curves of tBuCQN-CSPs based on MPTMS- (black squares; MPS no. 10) and MPS-functionalized silicas (MPS. no 1, red circles; MPS no. 8, blue upward triangles) as well as multi-cycle MPS-functionalized silica (two silanization/hydrolysis cycles) from Ref. [13] (MPS no. 12, green downward triangles). All H/u curves were recorded under isoelectrostatic conditions, as specified in caption of Fig. 7).

and selector coverage which appears to be unfavorable for the kinetic performance of the CSP yielding a C-term of 9.07 ms for peak 2 of FMOOC-Phe as compared to 5.72 ms on the MPTMS-based CSP (Table 2). On the other hand, the CSP made from the MPS-modified silica obtained by reaction without formic acid (TPS no. 8) exhibits a significantly better performance than the MPTMS-based benchmark CSP (TPS no. 10). The kinetic performance is greatly enhanced as can be derived from the much lower C-term (2.52 ms compared to 5.72 ms for the benchmark) (Table 2). While the selector-to-thiol ratio is relatively constant throughout the CSPs synthesized in this work (slightly below 0.5) (see Table 2, CSPs made from TPS no. 10, 1, and 8), the selector coverage varies significantly. While the lower selector coverage can be a confounding factor contributing itself to a better chromatographic performance [34], the surface bonding structure exerts an effect as well as it decides how the selector is exposed to the surface and freely accessible by the analytes or subject to hindered accessibility by a siloxane network. Although the excellent kinetic performance (lowest C-term of 1.09 ms) of the CSP based on MPS-modified thiol-silica prepared by multiple silanization/hydrolysis cycles could not be fully reached, the best performing single-step MPS-based CSP (TPS no. 8) came close. Since its synthesis is easier and much faster (2 h silanization) as well as it furthermore exhibited even better enantioselectivity, it can be concluded that this single-step silanization procedure with MPS has significant advantages for CSP preparation by thiol-ene click reaction.

4. Conclusions

This work presents an advanced procedure for functionalization of silica particles using 3-mercaptopropylsilatrane. The resulting thiol silica represents a flexible reactive particle platform for synthesis of various functionalized materials from heterogeneous catalysts to chiral stationary phases. The refined procedure of this work can be performed in a single step and overcomes the previous tedious multi step synthesis approach while delivering a material with similar favourable performance. By the use of ternary solvent mixtures containing water, both the thiol functionalization and hydrolysis of triethanolamine residues, which other-

wise block the progress of the reaction, can be carried out in one step. Furthermore, it appears that detrimental formation of disulfide bridges, being a major drawback in the earlier multi-cycle silanization/hydrolysis procedure, could be successfully overcome in this work. It was demonstrated herein that the fine-tuning of the microstructure on the surface may have a significant influence on enantioselectivity and mass transfer kinetics of the resultant CSPs. The C-term was more than bisected in comparison to the state-of-the-art functionalization agent MPTMS. The separation factor was significantly improved for the evaluated chiral probe, in spite of the same chiral selector as the benchmark. Reduced monofunctional siloxane bonds and increased trifunctional siloxane bonds were shown elsewhere to result in more stable bonding chemistry which is certainly favourable for expensive chiral columns. Concluding, this work shows the applicability of silatrane as powerful functionalization agents for silica-based materials and introduces a new, time-efficient silanization method with 3-mercaptopropylsilatrane using easily mixable ternary mixtures of water, methanol and toluene for synthesis of reactive silica materials for convenient further functionalization by popular thiol-ene click chemistry.

Declaration of Competing Interest

The authors declared no conflicts of interest.

CRediT authorship contribution statement

Christian Geibel: Investigation, Methodology, Formal analysis, Data curation, Visualization, Writing – original draft, Writing – review & editing. **Markus Kramer:** Investigation, Writing – review & editing. **Michael Lämmerhofer:** Conceptualization, Methodology, Supervision, Writing – review & editing, Resources.

References

- [1] K.K. Unger, *Porous Silica - Its Properties and use as Support in Column Liquid Chromatography*, Elsevier, Amsterdam, 1979.
- [2] M. Pursch, L. Sander, K. Albert, Peer reviewed: understanding reversed-phase LC with solid-state NMR, *Anal. Chem.* 71 (1999) 733A–741A.
- [3] P. Jandera, P. Janás, Recent advances in stationary phases and understanding of retention in hydrophilic interaction chromatography. A review, *Anal. Chim. Acta* 967 (2017) 12–32.
- [4] G. Qing, J. Yan, X. He, X. Li, X. Liang, Recent advances in hydrophilic interaction liquid chromatography materials for glycopeptide enrichment and glycan separation, *TrAC Trends Anal. Chem.* 124 (2020) 115570.
- [5] K. Zhang, X. Liu, Mixed-mode chromatography in pharmaceutical and biopharmaceutical applications, *J. Pharm. Biomed. Anal.* 128 (2016) 73–88.
- [6] M. Lämmerhofer, Chiral recognition by enantioselective liquid chromatography: mechanisms and modern chiral stationary phases, *J. Chromatogr. A* 1217 (2010) 814–856.
- [7] B. Chankvetadze, Recent trends in preparation, investigation and application of polysaccharide-based chiral stationary phases for separation of enantiomers in high-performance liquid chromatography, *TrAC Trends Anal. Chem.* 122 (2020) 115709.
- [8] I. Ilisz, A. Bajtai, W. Lindner, A. Péter, Liquid chromatographic enantiomer separations applying chiral ion-exchangers based on Cinchona alkaloids, *J. Pharm. Biomed. Anal.* 159 (2018) 127–152.
- [9] J.H. Zhang, S.M. Xie, L.M. Yuan, Recent progress in the development of chiral stationary phases for high-performance liquid chromatography, *J. Sep. Sci.* 45 (2022) 51–77.
- [10] A. Cavazzini, N. Marchetti, R. Guzzinati, M. Pierini, A. Ciogli, D. Kotoni, I. D'Acquarica, C. Villani, F. Gasparrini, Enantioseparation by ultra-high-performance liquid chromatography, *TrAC Trends Anal. Chem.* 63 (2014) 95–103.
- [11] D.C. Patel, M.F. Wahab, D.W. Armstrong, Z.S. Breitbach, Advances in high-throughput and high-efficiency chiral liquid chromatographic separations, *J. Chromatogr. A* 1467 (2016) 2–18.
- [12] M.J. Wirth, H.O. Fatunmbi, Horizontal polymerization of mixed trifunctional silanes on silica. 2. Application to chromatographic silica gel, *Anal. Chem.* 65 (1993) 822–826.
- [13] C. Geibel, J. Theiner, M. Wolter, M. Kramer, W. Lindner, M. Lämmerhofer, Controllable organosilane monolayer density of surface bonding using silatrane for thiol functionalization of silica particles for liquid chromatography and validation of microanalytical method for elemental composition determination, *J. Chromatogr. A* 1653 (2021) 462418.

- [14] T.J. Lee, L.K. Chau, C.J. Huang, Controlled silanization: high molecular regularity of functional thiol groups on siloxane coatings, *Langmuir* 36 (2020) 5935–5943.
- [15] X. Liang, A. Shen, Z. Guo, The application of thiol-ene/yne radical click chemistry in surface modification and functionalization, in: *Thiol-X Chemistries in Polymer and Materials Science*, The Royal Society of Chemistry, 2013, pp. 286–308.
- [16] C. Geibel, K. Dittrich, M. Wolter, M. Lämmerhofer, Thiol-ene photo-click immobilization of a chiral chromatographic ligand on silica particles, *J. Chromatogr. A* 1622 (2020) 461133.
- [17] A. Shen, Z. Guo, L. Yu, L. Cao, X. Liang, A novel zwitterionic HILIC stationary phase based on “thiol-ene” click chemistry between cysteine and vinyl silica, *Chem. Commun.* 47 (2011) 4550–4552.
- [18] M. Lämmerhofer, W. Lindner, Quinine and quinidine derivatives as chiral selectors I. Brush type chiral stationary phases for high-performance liquid chromatography based on cinchonane carbamates and their application as chiral anion exchangers, *J. Chromatogr. A* 741 (1996) 33–48.
- [19] J.K. Puri, R. Singh, V.K. Chahal, Silatranes: a review on their synthesis, structure, reactivity and applications, *Chem. Soc. Rev.* 40 (2011) 1791–1840.
- [20] C.J. Huang, Y.Y. Zheng, Controlled silanization using functional silatrane for thin and homogeneous antifouling coatings, *Langmuir* 35 (2019) 1662–1671.
- [21] A. Yoshikawa, M.S. Gordon, V.F. Sidorkin, V.A. Pestunovich, Proton affinities of the silatranes and their analogues, *Organometallics* 20 (2001) 927–931.
- [22] A. Mandl, L. Nicoletti, M. Lämmerhofer, W. Lindner, Quinine versus carbamoylated quinine-based chiral anion exchangers. A comparison regarding enantioselectivity for N-protected amino acids and other chiral acids, *J. Chromatogr. A* 858 (1999) 1–11.
- [23] N.M. Maier, L. Nicoletti, M. Lämmerhofer, W. Lindner, Enantioselective anion exchangers based on cinchona alkaloid-derived carbamates: Influence of C8/C9 stereochemistry on chiral recognition, *Chirality* 11 (1999) 522–528.
- [24] P. Levkin, N.M. Maier, W. Lindner, V. Schurig, A practical method for the quantitative assessment of non-enantioselective versus enantioselective interactions encountered in liquid chromatography on brush-type chiral stationary phase, *J. Chromatogr. A* 1269 (2012) 270–278.
- [25] G. Busca, Catalytic materials based on silica and alumina: structural features and generation of surface acidity, *Prog. Mater. Sci.* 104 (2019) 215–249.
- [26] L.S. Mason, E.R. Washburn, The ternary system methyl alcohol, toluene and water, *J. Am. Chem. Soc.* 59 (1937) 2076–2077.
- [27] E. Bayer, K. Albert, J. Reiners, M. Nieder, D. Müller, Characterization of chemically modified silica gels by ²⁹Si and ¹³C cross-polarization and magic angle spinning nuclear magnetic resonance, *J. Chromatogr. A* 264 (1983) 197–213.
- [28] T. Zumbink, A. Demiroglou, H.P. Jennissen, Analysis of affinity supports by ¹³C CP/MAS NMR spectroscopy: application to carbonyldiimidazole- and novel tresyl chloride-synthesized agarose and silica gels, *J. Mol. Recognit.* 8 (1995) 363–373.
- [29] K.K. Unger, S. Lamotte, E. Machtejevas, S. Fanali, P.R. Haddad, C.F. Poole, M.L. Riekkola, Chapter 3 - column technology in liquid chromatography, in: *Liquid Chromatography*, Second Ed, Elsevier, 2017, pp. 39–89.
- [30] H. Engelhardt, C. Blay, J. Saar, Reversed phase chromatography – the mystery of surface silanols, *Chromatographia* 62 (2005) s19–s29.
- [31] X. Liu, J. Cheng, X. Lu, R. Wang, Surface acidity of quartz: understanding the crystallographic control, *Phys. Chem. Chem. Phys.* 16 (2014) 26909–26916.
- [32] M. Sulpizi, M.P. Gaigeot, M. Sprik, The silica–water interface: how the silanols determine the surface acidity and modulate the water properties, *J. Chem. Theory Comput.* 8 (2012) 1037–1047.
- [33] Y. Duval, J.A. Mielczarski, O.S. Pokrovsky, E. Mielczarski, J.J. Ehrhardt, Evidence of the existence of three types of species at the quartz–aqueous solution interface at pH 0–10: XPS surface group quantification and surface complexation modeling, *J. Phys. Chem. B* 106 (2002) 2937–2945.
- [34] S. Felletti, C. De Luca, O.H. Ismail, L. Pasti, V. Costa, F. Gasparrini, A. Cavazzini, M. Catani, On the effect of chiral selector loading and mobile phase composition on adsorption properties of latest generation fully- and superficially-porous Whelk-O1 particles for high-efficient ultrafast enantioseparations, *J. Chromatogr. A* 1579 (2018) 41–48.

3.2 Accepted Manuscripts – Part Two: Application of Chiral Stationary Phases

3.2.1 Publication V: **Towards enantioselective ultrahigh performance liquid chromatography–mass spectrometry-based metabolomics of branched-chain fatty acids and anteiso-fatty acids under reversed-phase conditions using sub-2- μ m amylose- and cellulose-derived chiral stationary phases**

Christian Geibel¹, Li Zhang¹, Kristian Serafimov¹, Harald Gross²,
Michael Lämmerhofer^{1,*}

¹ Institute of Pharmaceutical Sciences, Pharmaceutical (Bio-)Analysis, University of Tübingen, Auf der Morgenstelle 8, 72076 Tübingen, Germany

² Institute of Pharmaceutical Sciences, Pharmaceutical Biology, University of Tübingen, Auf der Morgenstelle 8, 72076 Tübingen, Germany

* Corresponding author. E-mail address: michael.laemmerhofer@uni-tuebingen.de (M. Lämmerhofer)

Chirality **2022**, 34(3): 484-497. DOI: 10.1002/chir.23413

This is an open access article under the terms of the Creative Commons Attribution License, which permits use, distribution and reproduction in any medium, provided the original work is properly cited.

© 2022 The Authors. *Chirality* published by Wiley Periodicals LLC.

Towards enantioselective ultrahigh performance liquid chromatography–mass spectrometry-based metabolomics of branched-chain fatty acids and *anteiso*-fatty acids under reversed-phase conditions using sub-2- μm amylose- and cellulose-derived chiral stationary phases

Christian Geibel¹ | Li Zhang¹ | Kristian Serafimov¹ | Harald Gross²  | Michael Lämmerhofer¹ 

¹Institute of Pharmaceutical Sciences, Pharmaceutical (Bio-)Analysis, University of Tübingen, Tübingen, Germany

²Institute of Pharmaceutical Sciences, Pharmaceutical Biology, University of Tübingen, Tübingen, Germany

Correspondence

Michael Lämmerhofer, Pharmaceutical (Bio-)Analysis, Institute of Pharmaceutical Sciences, University of Tübingen, Auf der Morgenstelle 8, 72076 Tübingen, Germany.

Email: michael.laemmerhofer@uni-tuebingen.de

Funding information

BMBF German-Indonesian cooperation project NAbUnAk, Grant/Award Number: 16GW0124K

Abstract

Branched-chain fatty acids (BCFAs) are mostly saturated fatty acids with one or more methyl, seldom ethyl, branches in the alkyl chain. They are derived from branched-chain amino acids, ruminant-derived food, or biosynthetic side products of acetyl-CoA carboxylase. They possess *iso*- (branching at penultimate carbon) and *anteiso*-fatty acid structure (branching at antepenultimate carbon) or are branched at any other position of the carbon chain. Except for *iso*-fatty acids, BCFAs are chiral. They are commonly analyzed by GC-MS, while there is a lack of enantioselective LC-MS methods. In this work, we present a methodology for targeted enantioselective UHPLC-ESI-MS/MS metabolomics of BCFAs. It makes use of precolumn derivatization with 1-naphthylamine and reversed-phase elution conditions. A homologous series of short BCFA analytes with distinct chain lengths (having up to eight carbon atoms), branching type (methyl or ethyl), and position of branching (2, 3, and 4, *anteiso* and *iso*) has been systematically studied on six commercially available polysaccharide UHPLC columns. Chiralpak IB-U exhibited the highest and broadest enantioselectivity while IH-U maintained enantioselectivity also for BCFAs with chirality distant from the carboxylic function (i.e., with other branching than in 2-position). The method was used to assign the absolute configuration of a 4-methylhexanoic acid side chain of a natural product from *Streptomyces* sp. SHP 22-7. The potential of the corresponding UHPLC-ESI-QTOF-MS/MS assay for analyzing stereoselectively BCFAs and other short organic acids by untargeted analysis in human urine was further elucidated in a preliminary proof-of-principle test.

[This article is part of the Special Issue: A Special Issue to Celebrate the 80th Birthday of Professor Yoshio Okamoto. See the first articles for this special issue previously published in Volumes 33:12, 34:1, and 34:2. More special articles will be found in this issue as well as in those to come.]

This is an open access article under the terms of the Creative Commons Attribution License, which permits use, distribution and reproduction in any medium, provided the original work is properly cited.

© 2022 The Authors. Chirality published by Wiley Periodicals LLC.

KEYWORDS

bacterial fatty acids, chiral separation, lipidomics, natural products, organic acids, polysaccharide CSPs

1 | INTRODUCTION

Silica-based polysaccharide chiral stationary phases (CSPs) obtained by coating of cellulose and amylose esters and carbamates onto wide-pore silica, as introduced by Okamoto in 1984, have revolutionized the field of liquid chromatographic chiral separation.^{1,2} They paved the way towards efficient analytical and preparative enantiomer separations with wide applicability scope for chiral compounds.³ Various mechanistic studies greatly contributed to the understanding of the chiral recognition mechanism of these CSPs.^{4–7} Several incremental steps of advancement of this stationary phase technology further improved the performance of these CSPs, comprising the development of solvent-resistant immobilized versions of the polysaccharide CSPs^{8–10} and very recently the introduction of sub-2- μm UHPLC column technology (Figure 1). Although polysaccharide CSPs provide often higher enantioselectivity in normal-phase mode, their applicability in reversed-phase (gradient) elution mode makes them also an attractive choice for enantioselective bioanalysis, including metabolomics, using UHPLC-ESI-MS/MS.¹¹ They have shown potential also in uncommon applications like constitutional isomer separations in lipidomics.¹² Herein, we extend the scope to an application relevant in metabolomics, namely, to the enantiomer and constitutional isomer separation of alkyl-substituted short-chain alkanolic acids by LC-UV and LC-MS, which has been up to now the domain for GC enantiomer separation.

The analysis of such short-chain fatty acids has significant impact in microbiomics,^{13,14} food chemistry,^{15,16} and clinical analysis of inherited metabolic diseases.^{17,18}

Short-chain fatty acids may be branched. They are typically derived from branched-chain amino acids valine (Val), leucine (Leu), and isoleucine (Ile). Their transamination to α -ketoacids, decarboxylation, and chain elongation leads to branched (short)-chain fatty acids, B(S) CFAs. If the methyl branching is derived from the former two amino acids (Val and Leu), it is located on the penultimate carbon of the alkyl chain yielding nonchiral *iso*-fatty acids (*i*FAs). In contrast, *anteiso*-fatty acids (*a*FAs), which are derived from Ile, have the methyl branching at the antepenultimate carbon of the alkanolic acid chain, and are therefore chiral.^{15,16} Traditionally, they have been analyzed as fatty acid methyl esters by GC-FID or GC-MS,¹⁶ yet chiral separation and distinction between enantiomeric forms was rarely in the main focus of such research. Only few studies have been carried out taking the chirality of the *a*FAs into account. In general, it was reported that the *S*-*a*FAs are mostly dominating but the *R*-enantiomers can also be found in food (e.g., ruminants such as meat and milk, as well as fish).^{15,19,20} Furthermore, *a*FAs with significant *R*-enantiomer content have been detected in *vernix caseosa*, which is a biofilm that covers newborns.²¹

BCFAs can also result from other metabolic processes. Acetyl-CoA carboxylase initiates fatty acid synthesis through carboxylation of acetyl-CoA to malonyl-CoA which proceeds by iterative addition of two carbon units by the fatty acid synthetase affording straight-chain fatty acids. As a side reaction, acetyl-CoA carboxylase can carboxylate propionyl-CoA to methylmalonyl-CoA and butyryl-CoA to ethyl-malonyl-CoA which can be converted to methyl-branched and ethyl-branched fatty acids by fatty acid synthase

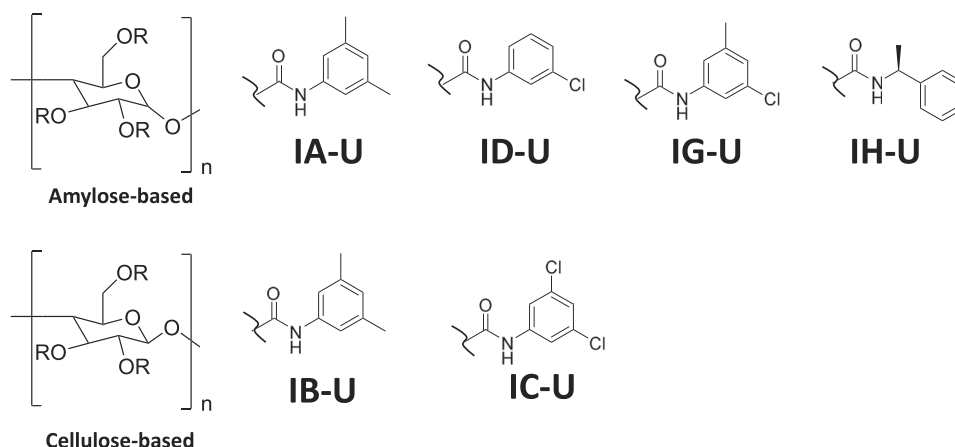


FIGURE 1 Polysaccharide-based UHPLC columns tested in this work. Depicted is the backbone on the left side, the residue on the right side

reaction.²² Enoyl-CoA Hydratase Domain-Containing Protein 1 can decarboxylate those side products of acetyl-CoA carboxylase and prevents them from use for fatty acid synthesis.²² Deficiency of this enzyme can lead to enhanced levels of BCFAs with branchings at various positions along the fatty acid chain (i.e., positions 2, 4, 6, 8, 10, 12, 14, and 15 of the C16 chain). To our knowledge, the absolute configuration of such derived branched fatty acids, on the other hand, has not been described yet.

Phytanic acid ((3*SR*,7*R*,11*R*)-3,7,11,15-tetramethylhexadecanic acids diastereomeric mixture; derived catabolically from chlorophyll) and pristanic acid ((2,6*R*,10*R*,14)-tetramethylpentadecanoic acid; from diet or α -oxidation of phytanic acid) are another group of BCFAs. Like other BCFAs, they cannot be metabolized in mitochondria but in peroxisomes. It involves reversal of the 2*R*- to 2*S*-fatty acyl-CoA esters by the enzyme α -methyl acyl-CoA racemase.²³ This enzyme is also responsible for the inversion of (*R*)- to (*S*)-ibuprofenoyl-CoA ester.²³ α -Methyl acyl-CoA racemase was shown to be overexpressed in several cancers like glioblastoma and prostate cancer.^{24–26} It also plays a major role in several diseases with peroxisomal disorders, like Refsum disease, Zellweger syndrome, and α -methylacyl-CoA racemase deficiency.²⁷

In any case, a robust and reliable method for the chiral separation is the key to both structural characterization and clinical diagnostics. In the past, the chiral separation of BCFAs has been mostly accomplished by enantioselective GC with cyclodextrin-based chiral columns and EI-MS detection.^{15,19–21,28,29} EI-MS detection has the advantage that the resultant MS spectra provide information on the branching position. On the other hand, enantioselective LC separations were rarely reported for BCFAs. In one study, 2-arylpropionic acids were separated on polysaccharide CSPs by normal-phase mode after derivatization of the carboxylic group with 1-naphthylamine, and also, 2-methylbutyric acid was included in this study as test compound.³⁰ When enantioselective LC is used with ESI-MS detection, reversed-phase or polar organic phase conditions are required. Furthermore, it is of utmost importance to have a full separation of the structural isomers, because commonly employed collision-induced dissociation does not fragment the fatty acid side chain. For this reason, structural isomers cannot be distinguished by MS2 spectra, and no selective ion transitions for LC-tandem-MS isomers exist. Since recently, chiral UHPLC columns are available of polysaccharide CSPs and have also shown exceptional performance for enantioselective lipidomics of oxylipins¹¹ and 3-hydroxy fatty acids.³¹ Due to their high efficiency, it is expected that moderate energy

differences for *R*- and *S*-adsorbates of BCFAs are sufficient for baseline separations. Thus, herein, we evaluate the UHPLC versions of the polysaccharide-based CSPs for the enantiomer separation of BCFAs by LC-UV and LC-MS.

First, we report on a wide screening of different α -branched and *a*FAs being separated under reversed-phase conditions on six different sub-2- μ m polysaccharide CSPs after derivatization with 1-naphthylamine. The goal was to derive structure–retention and structure–enantioselectivity relationships as well as to find a single chiral column and generic mobile phase elution conditions which allow enantiomer separations of a wide range of chiral BCFAs as is the quest in a metabolomics approach. Enantiomer elution orders were determined on the distinct chiral column for two model compounds, one with α -branching and another one with branching and chirality in position 4. The potential of the developed method to assign absolute configurations was documented for a BCFA of a natural product isolated from *Streptomyces* sp. SHP 22-7. Finally, the potential of the developed method for enantioselective metabolomics is elucidated with human urine as a matrix focusing on testing of assay specificity for isomers, effect of chain length on retention, and clinically relevant organic acid analysis by the same method. When abbreviations of BCFAs are used in this work, they follow the recommendations of Liebisch et al.³² The abbreviations *a*FA and *i*FA refer to *anteiso*- and *iso*-fatty acid.

2 | EXPERIMENTAL

2.1 | Materials

Racemic 2-methylbutyric acid, 2-methylpentanoic acid, 2-methylhexanoic acid, 2-ethylhexanoic acid, 3-methylpentanoic acid, 4-methylhexanoic acid, 4-methyloctanoic acid and 4-ethyloctanoic acid, enantiopure (*S*)-2-methylbutyric acid, and the derivatization agent 1-naphthylamine and *N*-ethyl-*N'*-(3-dimethylaminopropyl)carbodiimide (EDC) were supplied by Sigma Aldrich (Merck, Munich, Germany), (*R*)-2-methylbutyric acid from Activate Scientific (Prien am Chiemsee, Germany), enantiopure (*R*)- and (*S*)-4-methylhexanoic acid from Chemspace (Riga, Latvia).

2.2 | Instrumentation

All LC-UV runs were performed on an Agilent 1260 LC system from Agilent Technologies (Waldbronn, Germany). The system was equipped with a quaternary

pump, a degasser, an autosampler, and a UV-DAD detector. All used chiral columns were from Daicel (Osaka/Tokyo, Japan) and purchased via Chiral Technologies Europe (Illkirch, France). They had the dimensions of 3.0×100 mm (i.d. \times l.) and were packed with $1.6\text{-}\mu\text{m}$ fully porous particle-based Chiralpak IA-U, IB-U, IC-U, ID-U, IG-U, and IH-U. Separations with reversed-phase chromatography were carried out on YMC-Triart C18 RP (2.1×100 mm, i.d. \times l., $1.9\ \mu\text{m}$). High-resolution mass spectrometry analysis was carried out using an Agilent 1290 series LC system from Agilent Technologies (Waldbronn, Germany) equipped with a binary pump, thermostated column compartment, an HTC-xt PAL (CTC Analytics AG, Zwingen, CH) autosampler, and a TripleTOF 5600+ mass spectrometer with a TurboIonSpray Source from SCIEX (Concord, Ontario, Canada).

2.3 | Derivatization

Unless otherwise stated, precolumn derivatization was performed using 0.31 mmol branched-chain alkanic acid, 0.42 mmol 1-naphthylamine, and 0.42 mmol EDC in 1 ml 2-propanol while shaking at 30°C for 16 h. Subsequently, the product was dried in a high-performance evaporator (Genevac EZ2, Ipswich, UK) and reconstituted in mobile phase to obtain a nominal concentration of 1 mg/ml (related to the starting organic acid).

2.4 | Monitoring of racemization

To test for racemization during the derivatization process, different derivatization conditions were employed using (*S*)-2-methylbutyric acid and analyzed for variations in the enantiomeric excess in dependence on the conditions. The reaction time was varied from 4 , 8 , 16 , 24 , and 32 h while two distinct solvents were tested as well (2-propanol and methanol) (other conditions as described above). The reaction was carried out at 30°C in a 2 ml Eppendorf tube on a thermoshaker at 1500 rpm. After the derivatization, the samples were dried and dissolved in mobile phase. The degree of racemization was monitored using a Chiralpak IC-U column with ACN + 0.1% (v/v) acetic acid/water + 0.1% (v/v) acetic acid ($35/65$; v/v) as mobile phase. Monitoring of the racemization was performed via LC-UV. Chromatographic runs were performed at a flow rate of 0.2 ml/min. The column temperature was held constant at 10°C during the entire run. The autosampler was kept at 4°C . Injection volume was $5\ \mu\text{l}$.

2.5 | Absolute configuration determination in natural products

The developed method was applied to assign the absolute configuration in a previously undescribed natural compound, isolated from the bacterium *Streptomyces* sp. SHP 22-7, carrying a chiral BCFA moiety as a side chain connected via an amide bond to a nucleoside backbone. For the determination of the configuration of the alkyl branching, 1.18 mg of 4-methylhexanoic acid containing natural compound was hydrolyzed using 1 ml 6N HCl at 110°C overnight. After a twofold liquid-liquid extraction using 0.5 ml hexane twice, the free 4-methylhexanoic acid was first dried under a nitrogen stream and subsequently derivatized with 1-naphthylamine as described in Section 2.3. The retention times of this sample was compared with enantiomeric and racemic standards to determine the absolute configuration.

2.6 | Detection of BCFAs in urine

First morning urine (midstream, nil by mouth) was collected from a healthy volunteer by informed consent and desalted using Oasis Prime HLB 3cc RP cartridges from Waters (Milford, MA, USA). To do so, $3 \times 300\ \mu\text{l}$ of urine were injected onto the cartridge without pre-equilibration. Washing was performed with 2×1.5 ml of methanol/water ($5/95$; v/v), and elution was performed with acetonitrile (3×1.5 ml). After drying of the eluate in a centrifugal high-performance evaporator, the samples were derivatized by adding 1 ml of a mixture of 0.42 mmol 1-naphthylamine and 0.42 mmol EDC in an Eppendorf tube. After shaking for 16 h at 30°C and drying of the product in a high-performance evaporator, the dried product was reconstituted in $900\ \mu\text{l}$ mobile phase. LC-MS analysis was performed on the TripleTOF 5600+ QTOF mass spectrometry system using data-dependent acquisition mode (IDA). Measurements were performed on a Chiralpak IB-U and IC-U column using a gradient of A: water + 0.1% acetic acid, and B: acetonitrile + 0.1% acetic acid (0.00 min: 20% B, 10.00 min: 90% B, 10.01 min: 20% B), flow rate: 0.4 ml/min, column temperature: 10°C . Injection volume was $10\ \mu\text{l}$. The autosampler was kept at 4°C . Ion source parameters were as follows: nebulizer gas (GS1) 30 psi, heater gas (GS2) 20 psi, curtain gas (CUR) 30 psi, declustering potential (DP) 100 V, source temperature (TEM) 450°C , and ion source voltage $+5500$ V (positive mode).

Data acquisition was performed in IDA mode with a full-scan experiment (accumulation time of 250 ms) followed by MS/MS for the four most abundant precursor ions with unit resolution precursor isolation width and a

threshold of 100 cps (accumulation time of 100 ms each). The collision energy (CE) in MS2 was 30 V with a collision energy spread (CES) of 20 V. The total cycle time summed up to 700 ms, which yielded a minimum of 10 points per peak with an average peak width at the base of 7 sec. The MS instrument was run in high sensitivity mode achieving a TOF-MS resolution of 30,000 (FWHM at m/z 829.5393) and a MS/MS resolution of 15,000 (FWHM at m/z 397.2122). Full-scan mass spectra were acquired from m/z 70 to 1000 in positive ion mode. Mass calibration was performed before every run via the Calibrant Delivery System (Sciex, Ontario, Canada). The analytical system was controlled by the Analyst 1.7 TF software (Sciex, Ontario, Canada).

3 | RESULTS AND DISCUSSION

3.1 | Precolumn derivatization

In preliminary tests, racemic 2-methylbutyric acid and 4-methylhexanoic acid were selected as test compounds to evaluate the ability of four CSPs (Chiralpak IA-U, IB-U, IC-U, and IG-U) to separate their enantiomers by various RP-type gradient elution conditions with ACN and MeOH as modifiers which remained, however, unsuccessful. For this reason, a precolumn derivatization strategy of the carboxylic acid was selected. The introduction of an aromatic moiety along with hydrogen donor-acceptor functionality, such as 1-naphthylamide, supports chiral recognition and improves detection properties in UV but also MS detection (positive ESI mode becomes possible instead of less sensitive negative ESI; SRM transitions can be conveniently built from precursor ion and signature fragment ion of the naphthylamide moiety, *vide infra*). EDC coupling was used for activation of the carboxylic acid. To test for the risk of racemization of 2-alkylalkanoic acids during derivatization, the *S*-enantiomer of 2-methylbutyric acid was derivatized under different conditions (changing reaction time, solvent, among others) to check whether enantiomeric excess alters with such changes in derivatization conditions. Regardless of conditions, the enantiomeric excess was not changing but randomly fluctuating at 98.3% \pm 0.3%. It was concluded that there is no significant racemization in the course of derivatization.

3.2 | Column screening

Currently, six different UHPLC columns packed with sub-2- μ m polysaccharide-type CSPs differing in the biopolymer backbone (amylose or cellulose) and carbamate

residue (methyl, chlorine, or mixed methyl/chlorine substituted aromatic group as well as α -methylbenzyl) are commercially available (see Figure 1). They have been evaluated systematically in the reversed-phase mode herein to gain a holistic overview on their chiral recognition capability for alkyl BSCFAs. Reversed-phase mode was selected because hydrophobic interactions close to the stereogenic center of the alkyl side chain with the polysaccharide selectors were supposed to be of importance to induce chiral distinction between enantiomers and also for its compatibility with ESI-MS. All columns were first screened by gradient elution with acetonitrile as organic modifier at a column temperature of 10°C (Figure 2). All targeted compounds were eluted, and it can be derived from these gradient separations that the IB-U column seems to have the greatest potential and that the distinct columns behave quite differently. In the next step, isocratic elution conditions were adjusted (Figure 3). An overview of the separation factors achieved under isocratic conditions is given in Figure 4. The detailed results are summarized in Tables S1–S6 and key findings discussed below.

Amylose-based Chiralpak IA-U and cellulose-based IB-U both carry three 3,5-dimethylphenylcarbamate moieties per saccharide unit (see Figure 1) which define a binding cleft for analyte insertion.⁴ Through their distinct backbone helicity (cellulose with its $\beta(1 \rightarrow 4)$ glycosidic bonds is nearly linear [left-handed 3/2 helical confirmation]³³ while amylose has stronger left-handed 4/3 helicity due to $\alpha(1 \rightarrow 4)$ glycosidic bonds⁴), the spatial dimensions of their binding clefts are significantly different, explaining their differences in chiral recognition capability for the BCFAs. As a matter of consequence, 2-methylbutyric acid could be barely baseline separated on amylose-based IA-U (resolution of 1.52), while cellulose-based IB-U achieved a resolution of 6.56 for the same compound (see Figure 3). The situation is similar for the majority of the other compounds. Overall, it appears that under the chosen reversed-phase conditions, cellulose-based CSP is superior to the helical amylose-based CSP. Furthermore, the substituents on the phenylcarbamate residue exert also a major influence on the separation performance of the CSP. Generally, bis-substitution appears to have an advantage over mono-substitution; of all CSPs, the mono-chloro-substituted ID-U shows the worst enantioselectivity (Figure 3). The aromatic substituents govern the electron density of the aromatic ring and on the H-donor and -acceptor moieties of the amide group: halo substitution decreases the e-density of the aromatic moiety and increases the H-donor acidity, while methyl substitution increases the e-density of the phenyl ring and on the carbonyl H-acceptor moiety.⁶ Their effects on

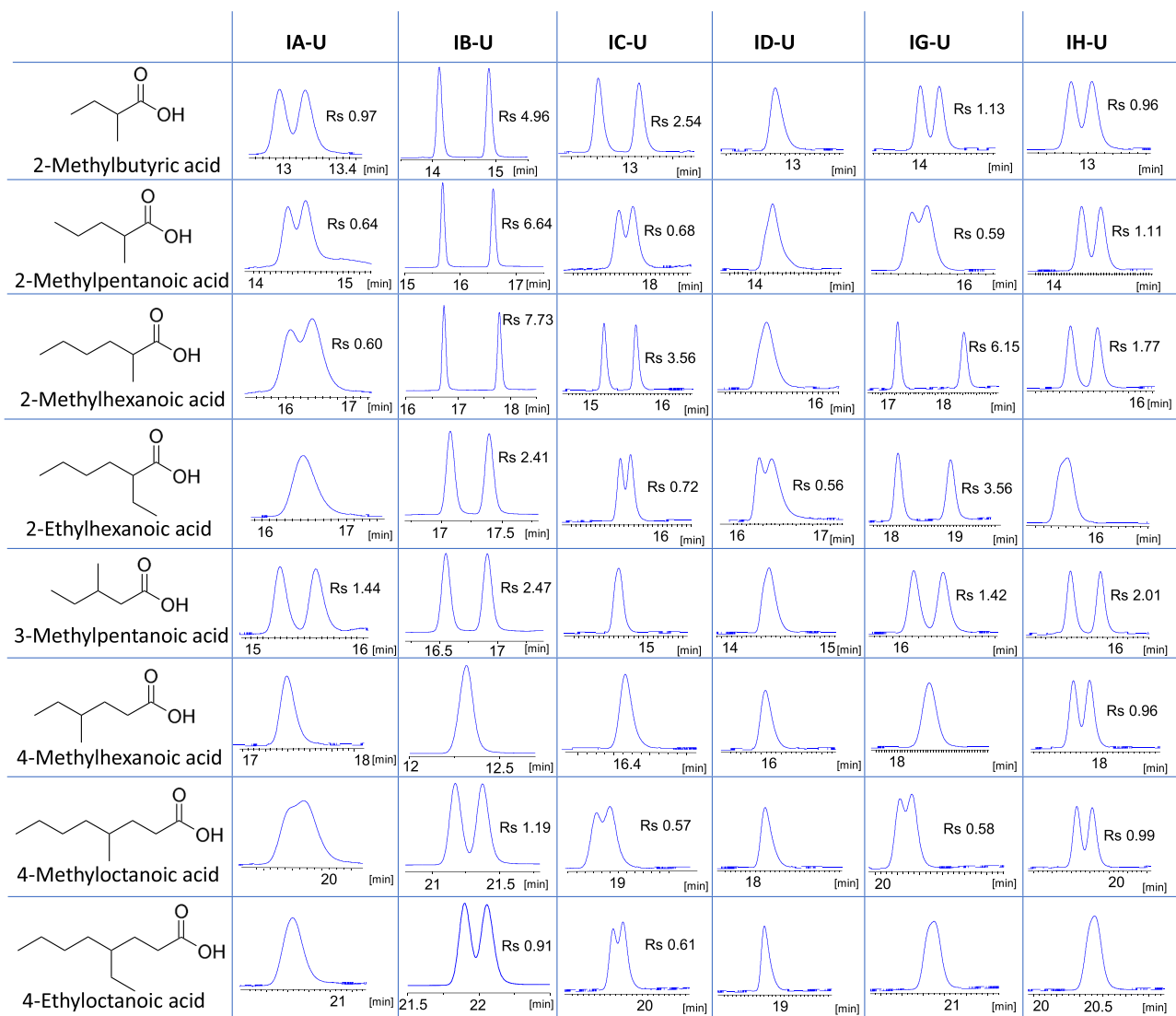


FIGURE 2 Chromatograms of the enantiomer resolution of 1-naphthylamides of racemic BCFAs using gradient UHPLC.

Chromatographic conditions: mobile phase: A: water + 0.1% acetic acid, B: ACN + 0.1% acetic acid; gradient profile: 20% to 90% B in 20 min, 90% to 10% B 20–20.01 min, 10% B 20.01–24 min; flow rate: 0.3 ml/min; column T: 10°C; injection volume: 1 μ l; detection: UV 215 nm

enantioselectivity are hard to rationalize and deconvolute from steric interactions, but it becomes evident that 3,5-dimethyl- (IB-U) is favorable over 3,5-dichloro- (IC-U), 3-chloro- (ID-U), and 3-chloro-5-methylphenylcarbamate (IG-U) (Figures 2 and 3). The latter (IG-U) shows some unexpected high α values for selected analytes (FA 6:0;2Me and FA 6:0;2Et) (Figure 4A). The structural pattern of the pendant side chain of IH-U differs substantially from the others, as it has another chiral element in its aralkyl moiety ((*S*)- α -methylbenzylcarbamate) which may significantly alter the space effects in the binding cavity besides the electronic nature in the aromatic structure. It appears to have a lower enantioselectivity than IB-U, but it maintains it even if the chirality is further away than in 2-position to the carboxylic function.

Overall, it can be clearly concluded that the Chiralpak IB-U column should be advantageous for an enantioselective metabolomics study because of its broadest and mostly highest enantioselectivity. IH-U is also of interest because it seems to maintain enantioselectivity also for chiral analytes exhibiting a stereocenter farther away from the carboxylic group. Tested substances with a methyl branching up to C4 position in the alkane chain were included in this work. IG-U shows inconsistent trends but seems to have a different chiral recognition mechanism as supported by the reversal of the elution order for 2-methylbutyric acid (vide infra). In general, although the separation factors are partly small, close to baseline separations can be achieved with α of around 1.05 or larger due to the high efficiencies of the sub-2 μ m UHPLC columns.

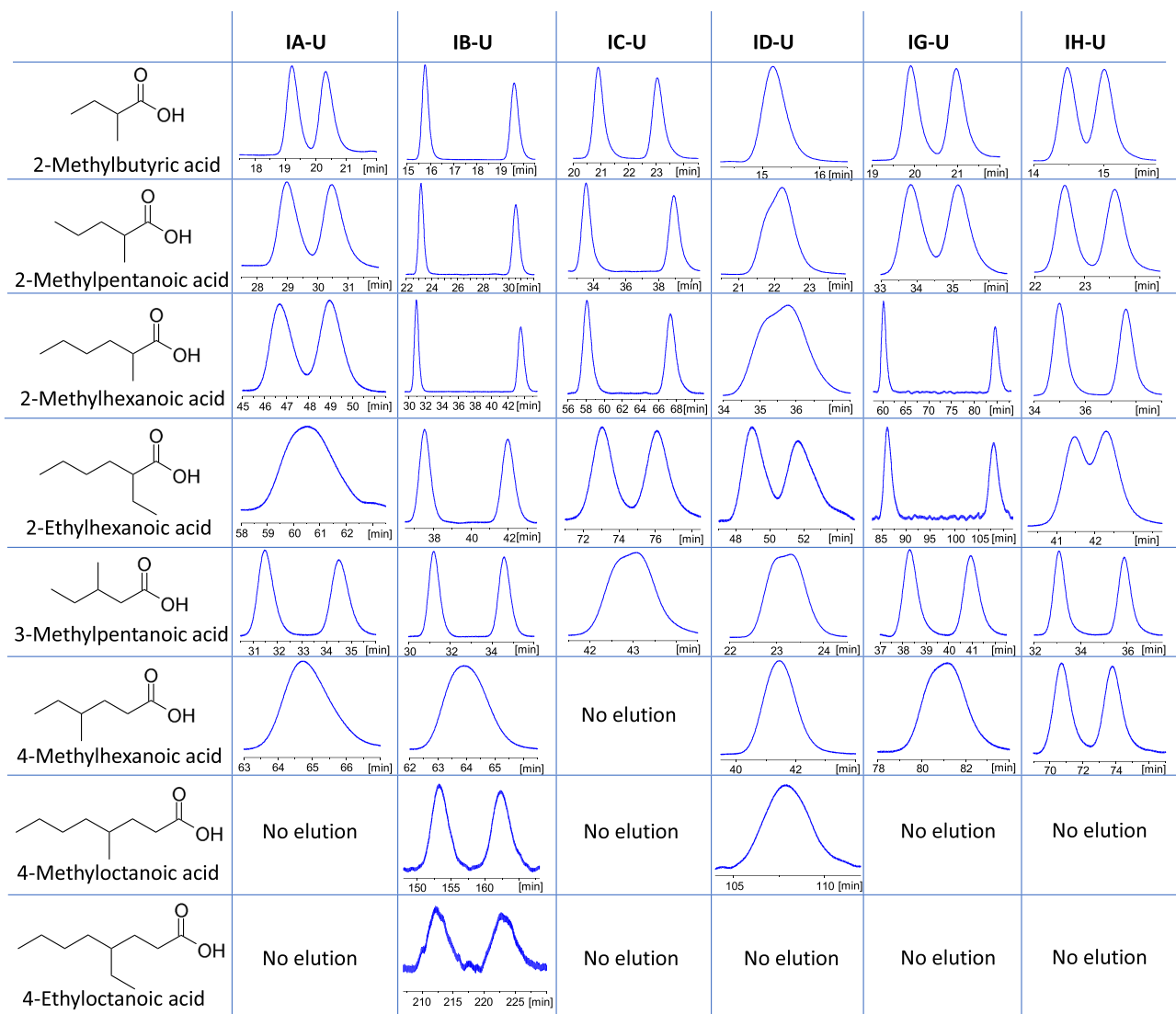


FIGURE 3 Isocratic UHPLC enantiomer separations of the 1-naphthylamide derivatives of different BCFAs and α FAs on various polysaccharide columns. Conditions: mobile phase, acetonitrile-0.1% acetic acid (IC-U, ID-U: 35% ACN; IA-U, IG-U, IH-U: 40% ACN; IB-U: 45% ACN); flow rate, 0.2 ml/min; column temperature, 10°C

3.3 | Impact of mobile phase, column temperature, and flow rate

The effect of organic modifier type, column temperature, and flow rate was investigated on IB-U. Replacement of acetonitrile by methanol as organic modifier led to a drastic decrease in the theoretical plate numbers by a factor of around 3–10 and hence also resolution (Table S7). It indicates that the naphthylamide group interacts with the aromatic moiety of the selector by π - π interactions. Because they are effectively balanced by acetonitrile which has itself π electrons that can compete with such strong interactions, this organic modifier provides high efficiencies (up to 15,000 to 25,000 plates per 10-cm column). On contrary, peaks are very broad

with methanol (always <4000 plates per column). This dramatic loss can be explained by worse desorption kinetics when using methanol. Because acetonitrile also provided higher separation factors, acetonitrile was the organic modifier of choice affording much higher resolutions. The effect was virtually the same on the other columns.

Column temperature effects were tested at 10°C and 40°C. Because efficiencies were not significantly increasing with higher temperature, but separation factors declining, resolution was significantly lower for all analytes at 40°C when using acetonitrile. It was previously reported that resolution and performance suffers from higher temperatures on polysaccharide phases and can even lead to a reversal of elution order.⁵ Hence, 10°C

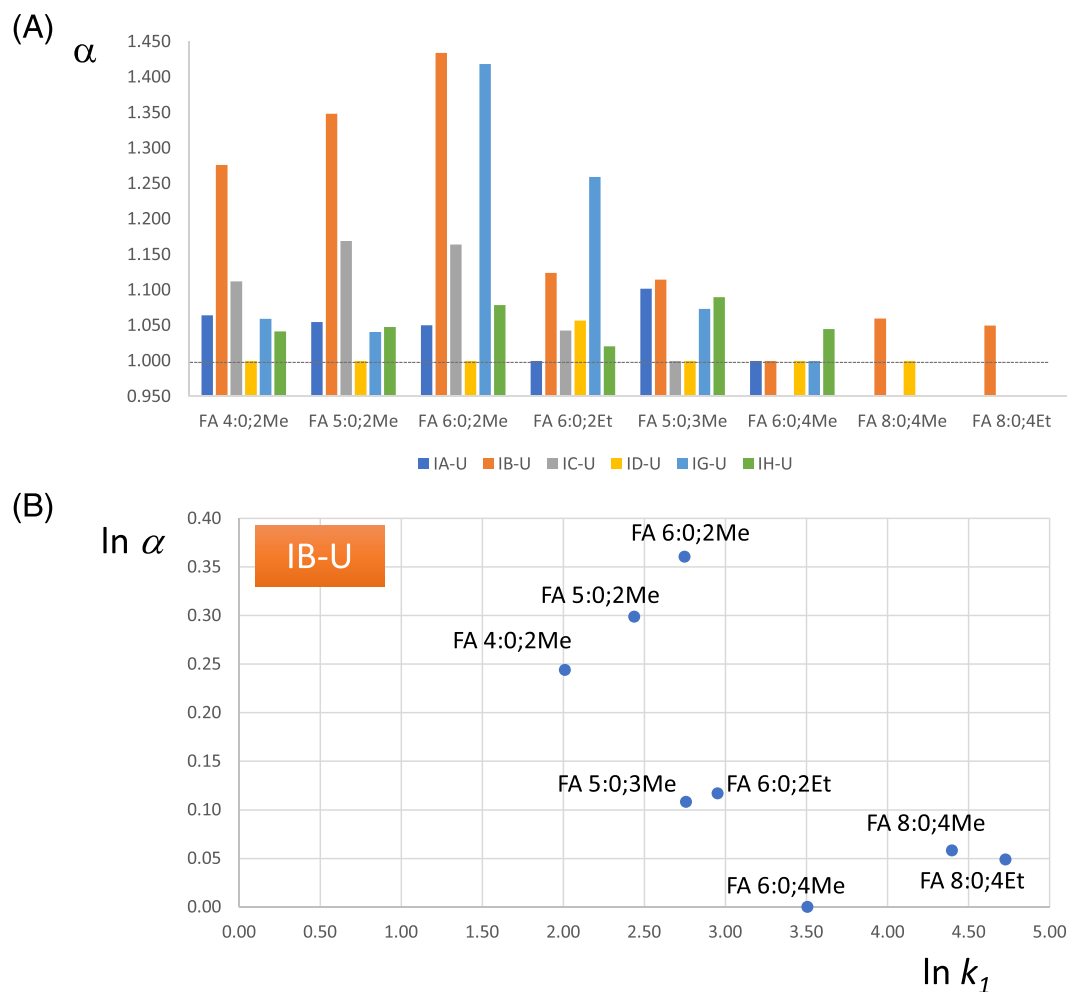


FIGURE 4 (A) Separation factors of isocratic column screening and (B) retention and enantioselectivity increments in dependence on structural factors of analytes (code: FA, fatty acid followed by carbon and double bond number; then position of branching and substituent at branching point)

was maintained as column temperature in further experiments.

Unfortunately, a proper H/u curve could not be recorded with the chosen conditions (10°C) due to pressure limitations (recommended by the supplier not to exceed 60 MPa). At 40°C and acetonitrile as organic modifier, the increase of the flow rate from 0.2 to 0.5 ml/min led to a loss of efficiencies and resolution, indicating that 0.2 ml/min is closer to the minimum of the van Deemter curve.

Acetonitrile as organic modifier, a column temperature of 10°C and a flow rate of 0.2 ml/min were adopted as optimal conditions for isocratic separations. Due to the high theoretical plate numbers ($\sim 150,000$ to $250,000$ per meter) on the sub- $2\text{-}\mu\text{m}$ particle chiral columns, close to baseline separations could be achieved with separation factors of 1.05 under these conditions.

3.4 | Structure–retention and structure–enantioselectivity relationships for BCFA enantiomer separations

In general, retention factors roughly increase with increasing carbon chain lengths as expected for RP-type separations on all columns (Figures 4B and S1). Branching reduces retention. The closer the branching to the naphthylamide moiety, the shorter the retention time. The farther remote the branching from the naphthylamide moiety, the stronger the retention but α values decline significantly. For the bulkier ethyl substituent compared with the methyl side chain, the additional carbon in the former analyte leads to a slight increase in retention.

The impact of chain length and branching on separation factors is less consistent on the different columns (Figures 4A and S1). 2-Methyl-branched series lead to

increased α values with increasing carbon number in case of IB-U and IH-U columns, but the opposite trend is observed for IA-U. A bulkier ethyl branching leads to a decrease in α value compared with methyl branching on the IB-U column. Separation factors further decline for chirality being farther away from the functional group that represents the prime interaction site, for example, 4-methylhexanoic acid and 4-methyloctanoic acid. For IC-U, the separation factor reaches a maximum for FA 5:0;2Me in the series of 2-methyl-branched alkanolic acids and drops significantly with increase of bulkiness of the branching (Et vs. Me) and shift of the branching position (from carbon 2 to 3). The IG-U column exhibits surprisingly high α values for 2-methyl- and 2-ethylhexanoic acid which seemingly do not follow the common trends.

When comparing the enantiomer separation of three investigated α FAs (FA 4:0;2Me, FA 5:0;3Me, and FA 6:0;4Me), it is hard to derive a general trend. The enantiomer separation is better on IA-U for 3-methylpentanoic acid than 2-methylbutanoic acid. For 4-methylhexanoic acid, the enantiomer separation is completely lost. This appears to be different on IB-U; here, a clear trend can be observed. The longer the chain of the α FA, the worse the separation.

3.5 | Enantiomer elution orders on different columns

Above discussion focused on the separation of the enantiomers on the different chiral columns. Of prime importance from a chiral recognition point of view and for practical reasons, for example, the assignment of absolute configurations of analyte enantiomers, are the enantiomer elution orders that were determined for the selected analytes, 2-methylbutyric acid and 4-methylhexanoic acid. Single enantiomers and racemate were injected into all columns that gave a satisfactory separation. The results are shown in Figure 5. For 2-methylbutyric acid, on all cellulose-based columns, the *S*-enantiomer eluted first. In amylose-based columns, ID-U showed no enantioseparation, while on IA-U and IH-U, also, the *S*-enantiomer eluted first. In sharp contrast, on IG-U, a reversal of the elution order was observed with *R*-enantiomer being the first eluted peak. This offers some flexibility for selecting the column with preferred elution order. 4-Methylhexanoic acid could be resolved only on the IH-U column, and the elution order was reversed compared 2-methylbutyric acid, that is, the *S*-enantiomer was stronger retained (Figure 5F). It further indicates the complexity of the chiral recognition

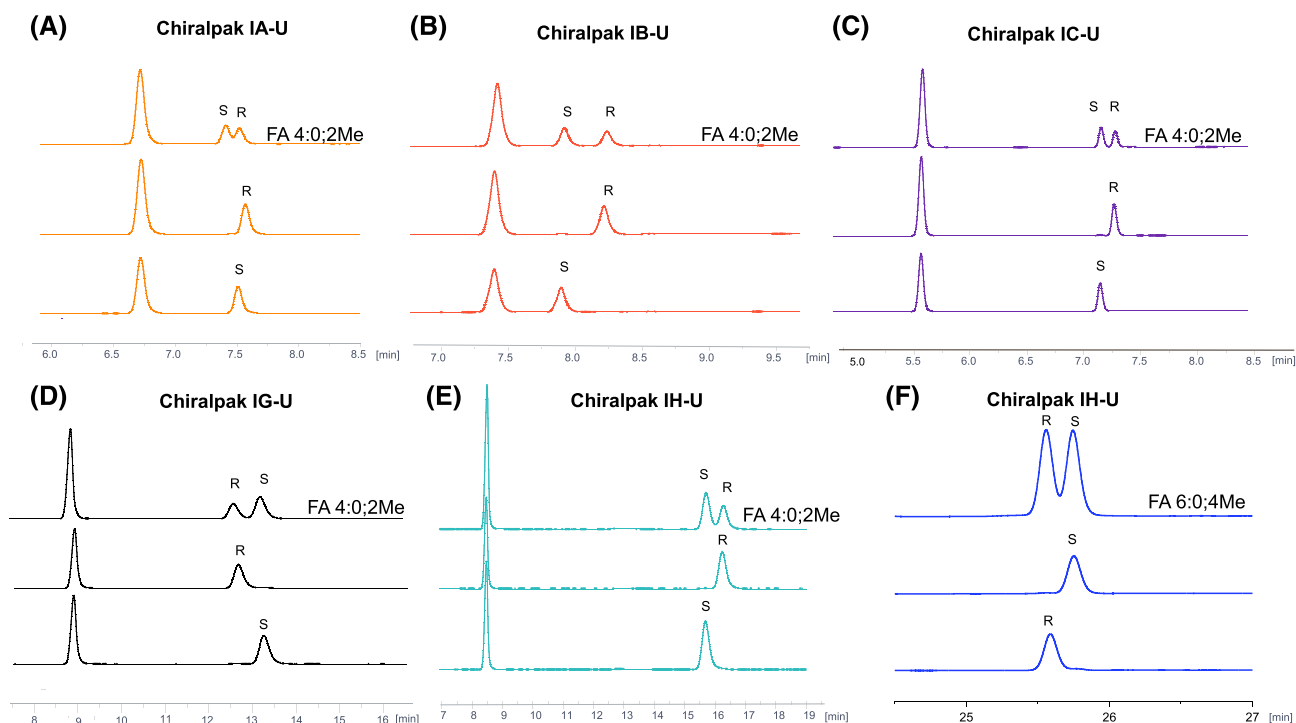


FIGURE 5 Determination of the enantiomer elution order of 1-naphthylamide of 2-methylbutyric acid on all tested columns (except for ID-U, no separation observed). Conditions: gradient run applied for IA-U, IB-U, IC-U: mobile phase A: water + 0.1% acetic acid, B: ACN + 0.1% acetic acid. 0.00 min: 20% B, 20.00 min: 90% B, 20.01 min: 20% B, isocratic runs applied for IG-U (40% B) and IH-U (35% B), for all columns: flow rate: 0.3 ml/min, detection wavelength: 215 nm

process for this type of analytes which makes a prediction and extrapolation to nontested structures hardly possible.

3.6 | Separation of *a*FA and *i*FA constitutional isomers

*a*FAs and *i*FAs are bacterial BCFAs with methyl branching at the antepenultimate and penultimate carbon of the alkyl chain, respectively, as discussed above.¹⁵ They are derived from Ile and Leu, respectively, and bacteria use them for adjusting membrane fluidity, with similar effects as PUFAs for mammals. Because they represent constitutional isomers and ESI-MS with collision-induced dissociation cannot distinguish them in LC-MS/MS analysis, due to lack of fragmentation in the side chain (vide infra), they need to be chromatographically separated from each other. To test for the capability of the chiral polysaccharide CSPs to resolve such isomeric forms by LC, exemplarily racemic samples of 2-methylpentanoic acid and 3-methylpentanoic acid (*a*FA) as well as the achiral 4-methylpentanoic acid (*i*FA) were further analyzed on Chiralpak IB-U (Figure 6A) and IG-U column (Figure 6B) as well as RP C18 (Figure 6C). As shown in Figure 6, the polysaccharide CSPs exhibit much better selectivity between the constitutional isomers than C18, besides allowing enantiomer separation of the chiral methyl-alkanoic acid. While the enantiomer separation is better on the IB-U column, the simultaneous separation of constitutional isomers favors the IG-U column. However, it has to be emphasized that no specific attempts were made to further optimize the separation between the second eluted peak of 2-methylpentanoic acid and the first eluted peak of 3-methylpentanoic acid on the IB-U column. The orthogonality plot in Figure S2 underpins the complementary retention profiles on RP and chiral column (IB-U) and furthermore reveals that retention factors are significantly lower on IB-U compared with C18.

This finding documents the versatility of the polysaccharide columns not only for the separation of enantiomers but also for the separation of constitutional isomers which cannot be distinguished by ESI-MS/MS with CID.

3.7 | Potential application areas

3.7.1 | Determination of configurations of BCFA constituents in natural compounds

Bacterial lipopeptides and other natural compounds contain often fatty acid side chains as constituents. Oftentimes, these fatty acid side chains are branched (*a*FA and

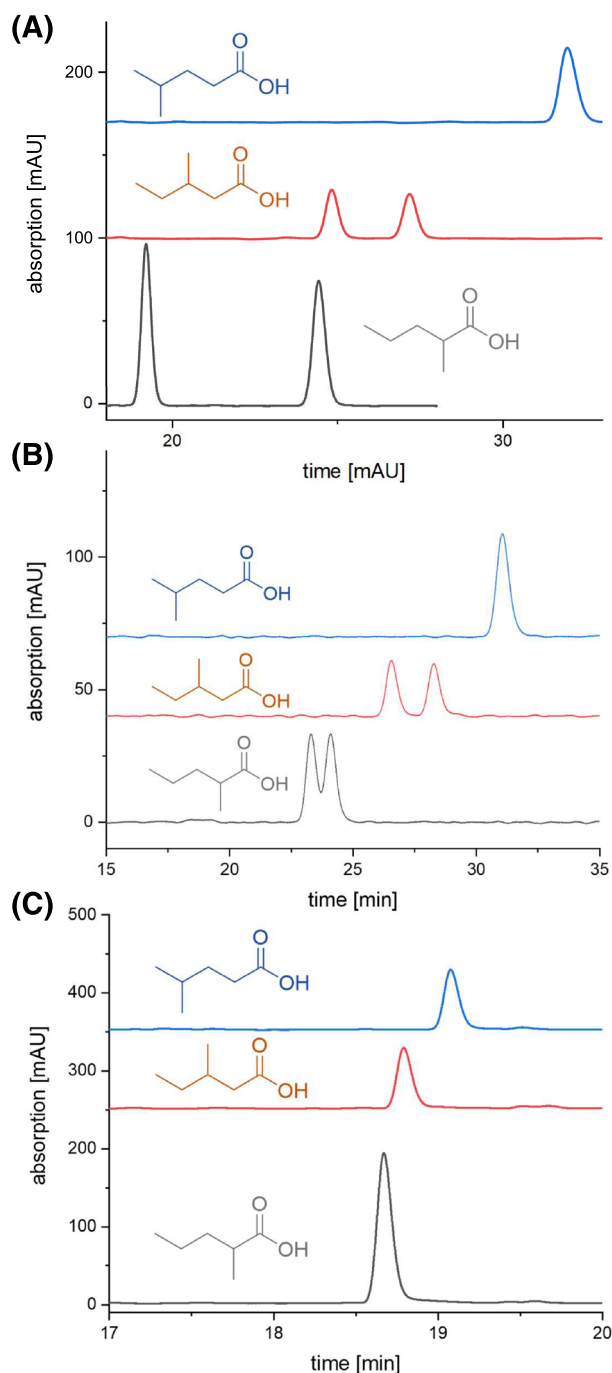


FIGURE 6 Overlay of chromatograms showing the selectivity of (A) Chiralpak IB-U, (B) IG-U, and (C) RP C18 (YMC-Triart C18 RP) for *anteiso*-, *iso*-, and 2-methyl-branched fatty acid constitutional isomers exemplified for methylpentanoic acid using an isocratic run. Mobile phase: water/acetonitrile (60/40; v/v) + 0.1% acetic acid, flow rate: 0.3 ml/min, temperature: 10°C, detection wavelength: 215 nm

*i*FA, e.g., in teicoplanin), potentially derived from branched-chain amino acids Ile and Leu, respectively. In the course of the full structural elucidation, it is necessary to determine the position of the branching and the

absolute configuration if they are chiral. The above results document the suitability of the developed method using polysaccharide CSPs. Here, the practical applicability is demonstrated by a natural compound having a 4-methylhexanoic acid side chain which was released by HCl hydrolysis from a newly derived natural compound isolated from *Streptomyces* sp. SHP 22-7. The structure elucidation by NMR showed it has a 4-methylhexanoic acid side chain, corresponding to an α FA with unknown configuration at this point. Sample preparation involving 1-naphthylamine derivatization and injection to the Chiralpak IH-U column, along with racemic and enantiomeric authentic standards revealed *S*-configuration for this α FA, like in the Ile side chain. The correct absolute configuration assignment was further verified by spiking experiments (see Figure 7). Spiking of the racemate to the sample of the hydrolysate of the natural compound clearly indicated a scalemic mixture with a larger amount of *S*-enantiomer (second eluted peak; Figure 7B), thereby proving the correct assignment of the absolute configuration.

3.7.2 | Analysis of organic acids and short-chain fatty acids in urine

Another potential field of application is in clinical analysis of urine samples. In order to assess the method's

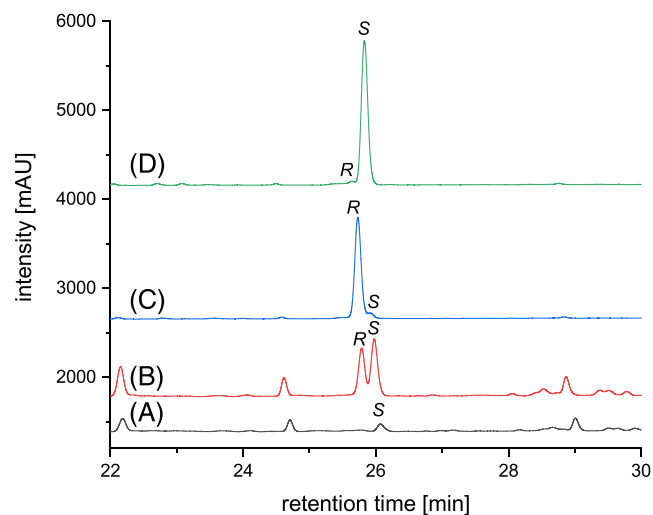


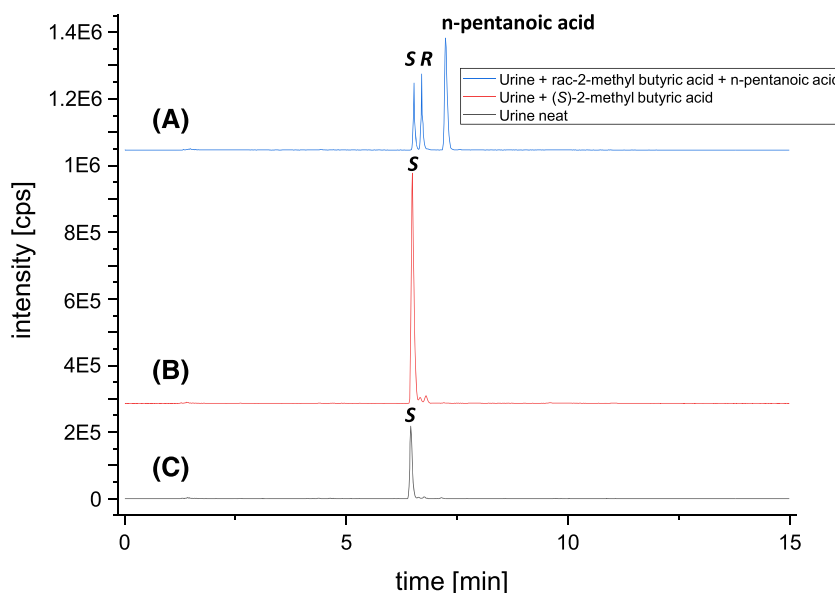
FIGURE 7 Assignment of the absolute configuration of the 4-methylhexanoic acid side chain of a natural compound. (A) Real sample (hydrolyzed natural product after derivatization with 1-naphthylamine) and real sample spiked with (B) racemic, (C) (*R*-), and (D) (*S*-) 4-methylhexanoic acid standards. Conditions: column: Chiralpak IH-U; mobile phase A: water + 0.1% acetic acid, B: ACN + 0.1% acetic acid, 0.00 min: 20% B, 20.00 min: 90% B, 20.01 min: 20% B, flow rate: 0.3 ml/min, detection wavelength: 215 nm

performance in a biological matrix, urine sample was collected from a healthy volunteer and analyzed by UHPLC-QTOF-MS after precolumn derivatization with 1-naphthylamine. Chromatographic runs were performed on IB-U and IC-U in gradient elution mode with acetonitrile and distinct gradient times (5, 10, and 15 min) have been evaluated. As can be seen in Figure S3, for IB-U even the shortest 5-min gradient provided full baseline resolution of the enantiomers. With IC-U, the 15- and 10-min gradients allowed a sufficient separation of the 2-methylbutyric acid enantiomers, while with 5-min gradient time baseline resolution was lost. Although IB-U provided better enantioselectivity, IC-U was evaluated for the enantioselective analysis of 2-methylbutyric acid in human urine. As can be seen in Figure 8, the urine sample shows one major peak and a couple of smaller ones in the EIC chromatogram. Retention times indicated that the major peak is (*S*)-2-methylbutyric acid (confirmed by spiking of standards into the urine sample), as expected when α -methyl acyl-CoA racemase activity is normal. Several isomeric species in the urine can interfere with enantiomer separation of 2-methylbutyric acid, and hence, assay specificity in urine was tested by injection of standards of *n*-pentanoic acid and isovaleric acid. Indeed, this indicated that the other peaks in the EIC chromatogram of Figure 8 correspond to isomeric (*R*)-2-methylbutyric acid, isovaleric acid, and *n*-pentanoic acid. Although these isomeric compounds are reasonably well resolved from the 2-methylbutyric acid enantiomers indicating good assay specificity by LC-MS with this chiral column (IC-U) for isovaleric acid (Figure S4), a further improvement of resolution, for example, by optimizing gradient time and steepness, temperature, and other factors, should be accomplished before this method is applied for clinical studies, which was beyond the current goal.

While a fast-scanning high-resolution QTOF-MS instrument was used herein, the achiral derivatization concept enables the use of highly sensitive triple quadrupole instrument with SRM acquisition. The naphthylamine moiety yields a highly abundant signature fragment ion of m/z 144.0805 (Figure S5) which can be used to build conveniently sensitive ion transitions from precursor ions of a target list and the signature fragment ion, even if no standards are available for measuring product ion spectra. On the other hand, it becomes clear that the fatty acid side chain, which does not get fragmented by collision-induced dissociation, does not give any characteristic fragment ion, and thus MS cannot distinguish between isomeric alkanolic acids; it needs selective chromatography.

Because the measurements of the urine sample were done in untargeted profiling mode (by data-dependent

FIGURE 8 Extracted ion chromatogram of (A) a mixture of racemic 2-methylbutyric acid and *n*-pentanoic acid spiked to human urine, (B) urine sample spiked with (*S*)-2-methylbutyric acid, and (C) neat urine sample. Conditions: mobile phase A: water + 0.1% acetic acid, B: acetonitrile + 0.1% acetic acid, flow rate: 0.4 ml/min, column temperature: 10°C, column: Chiralpak IC-U. Gradient profile: 0.00 min: 20% B, 10.00 min: 90% B, 10.01 min: 20% B. All analytes were detected as 1-naphthylamide derivatives by ESI-QTOF-MS, EIC generated from m/z 228.1383 \pm 0.02



acquisition), also other organic acids were detected. Plots of the homologous branched- and straight-chain alkanolic acid series reveal a peculiarity (see Figure S6). While *n*-alkanoic acids are lying on a straight line in the plot of m/z versus t_R values, formic acid is considerably deviating from this trend. It is stronger retained than acetic acid which indicates that there is either an additional interaction possible with the formamide group or alkyl chains lead to some steric collisions and shorter retention.

The method could be also very useful for general organic acid analysis in urine which is an important application in clinical analysis.¹⁸ A number of organic acids were detected (see Figure S6), but this is beyond the goal of the current study. Its further extension and validation will be reported elsewhere.

4 | CONCLUSIONS

Polysaccharide-based CSP technology introduced by Okamoto in 1984 evolved now into a highly powerful UHPLC column technology which has great potential not only in pharmaceutical analysis but due to broad enantioselectivity, reversed-phase gradient elution capability, electrospray-MS compatibility, and high efficiencies for bioanalysis comprising the fields of enantioselective metabolomics and lipidomics. This work proves the versatility of polysaccharide columns in the field of branched fatty acid analysis in reversed-phase elution mode. Besides enantiomers, the novel UHPLC column technology has also great potential for constitutional isomers separation and can be extended to clinically relevant organic acid analysis. Precolumn

derivatization using 1-naphthylamine not only drives retention and isomer selectivity on the polysaccharide CSPs but also improves detection sensitivity. In this way, the acids showed both a higher retention time by the introduction of π - π interactions and a proper visibility in UV absorption. Furthermore, this work gives an overview on the separation abilities of six commercially available polysaccharide-based UHPLC columns. The practical applicability of the developed method could be proven by both the analysis of the BCFA side chain of a newly isolated natural product and the untargeted stereoselective UHPLC-ESI-QTOF-MS/MS profiling of BCFAs in human urine. The methodology holds great promise to be further extended and applied in clinical analysis.

ACKNOWLEDGMENTS

H.G. gratefully acknowledges the funding received from the BMBF German-Indonesian cooperation project NAbUnAk (16GW0124K).

DATA AVAILABILITY STATEMENT

The data that support the findings of this study are available in the Supporting Information of this article.

ORCID

Harald Gross <https://orcid.org/0000-0002-0731-821X>
Michael Lämmerhofer <https://orcid.org/0000-0002-1318-0974>

REFERENCES

- Okamoto Y, Kawashima M, Yamamoto K, Hatada K. Useful chiral packing materials for high-performance liquid chromatographic resolution. Cellulose triacetate and tribenzoate

- coated on macroporous silica gel. *Chem Lett.* 1984;13(5): 739-742.
- Okamoto Y, Kawashima M, Hatada K. Chromatographic resolution. 7. Useful chiral packing materials for high-performance liquid chromatographic resolution of enantiomers: phenylcarbamates of polysaccharides coated on silica gel. *J Am Chem Soc.* 1984;106(18):5357-5359.
 - Ikai T, Okamoto Y. Structure control of polysaccharide derivatives for efficient separation of enantiomers by chromatography. *Chem Rev.* 2009;109(11):6077-6101.
 - Yamamoto C, Yashima E, Okamoto Y. Structural analysis of amylose tris(3,5-dimethylphenylcarbamate) by NMR relevant to its chiral recognition mechanism in HPLC. *J Am Chem Soc.* 2002;124(42):12583-12589.
 - Matarashvili I, Kobidze G, Chelidze A, et al. The effect of temperature on the separation of enantiomers with coated and covalently immobilized polysaccharide-based chiral stationary phases. *J Chromatogr A.* 2019;1599:172-179.
 - Chankvetadze B. Recent developments on polysaccharide-based chiral stationary phases for liquid-phase separation of enantiomers. *J Chromatogr A.* 2012;1269:26-51.
 - Chankvetadze B. Recent trends in preparation, investigation and application of polysaccharide-based chiral stationary phases for separation of enantiomers in high-performance liquid chromatography. *Trends Anal Chem.* 2020;122:115709.
 - Francotte E, Huynh D. Immobilized halogenophenylcarbamate derivatives of cellulose as novel stationary phases for enantioselective drug analysis. *J Pharm Biomed Anal.* 2002; 27(3):421-429.
 - Franco P, Zhang T. Common approaches for efficient method development with immobilised polysaccharide-derived chiral stationary phases. *J Chromatogr B Biomed Appl.* 2008;875(1): 48-56.
 - Zhang T, Franco P. Analytical and preparative potential of immobilized polysaccharide-derived chiral stationary phases. In: Subramanian G, ed. *Chiral Separation Techniques: A Practical Approach*. 3rd ed. Wiley-VCH; 2006:99-134.
 - Cebo M, Fu X, Gawaz M, Chatterjee M, Lämmerhofer M. Enantioselective ultra-high performance liquid chromatography-tandem mass spectrometry method based on sub-2 μ m particle polysaccharide column for chiral separation of oxylipins and its application for the analysis of autoxidized fatty acids and platelet releasates. *J Chromatogr A.* 2020;1624: 461206.
 - Li P, Lämmerhofer M. Isomer selective comprehensive lipidomics analysis of phosphoinositides in biological samples by liquid chromatography with data independent acquisition tandem mass spectrometry. *Anal Chem.* 2021;93(27): 9583-9592.
 - Silva YP, Bernardi A, Frozza RL. The role of short-chain fatty acids from gut microbiota in gut-brain communication. *Front Endocrinol.* 2020;11:25.
 - Han J, Lin K, Sequeira C, Borchers CH. An isotope-labeled chemical derivatization method for the quantitation of short-chain fatty acids in human feces by liquid chromatography-tandem mass spectrometry. *Anal Chim Acta.* 2015;854:86-94.
 - Eibler D, Abdurahman H, Ruoff T, Kaffarnik S, Steingass H, Vetter W. Unexpected formation of low amounts of (R)-configured anteiso-fatty acids in rumen fluid experiments. *PLOS One.* 2017;12(1):e0170788.
 - Wang DH, Wang Z, Brenna JT. Gas chromatography chemical ionization mass spectrometry and tandem mass spectrometry for identification and straightforward quantification of branched chain fatty acids in foods. *J Agric Food Chem.* 2020; 68(17):4973-4980.
 - Gallagher RC, Pollard L, Scott AI, Huguenin S, Goodman S, Sun Q. Laboratory analysis of organic acids, 2018 update: a technical standard of the American College of Medical Genetics and Genomics (ACMG). *Genet Med.* 2018;20(7): 683-691.
 - Mouskeftara T, Virgiliou C, Theodoridis G, Gika H. Analysis of urinary organic acids by gas chromatography tandem mass spectrometry method for metabolic profiling applications. *J Chromatogr A.* 2021;1658:462590.
 - Thurnhofer S, Hottinger G, Vetter W. Enantioselective determination of anteiso fatty acids in food samples. *Anal Chem.* 2007; 79(12):4696-4701.
 - Hauff S, Hottinger G, Vetter W. Enantioselective analysis of chiral anteiso fatty acids in the polar and neutral lipids of food. *J Lipids.* 2010;45(4):357-365.
 - Hauff S, Vetter W. Exploring the fatty acids of vernix caseosa in form of their methyl esters by off-line coupling of non-aqueous reversed phase high performance liquid chromatography and gas chromatography coupled to mass spectrometry. *J Chromatogr A.* 2010;1217(52): 8270-8278.
 - Dewulf JP, Paquay S, Marbaix E, Achouri Y, Van Schaftingen E, Bommer GT. ECHDC1 knockout mice accumulate ethyl-branched lipids and excrete abnormal intermediates of branched-chain fatty acid metabolism. *Biol Chem.* 2021; 297(4):101083.
 - Kong G, Lee H, Tran Q, et al. Current knowledge on the function of α -methyl acyl-CoA racemase in human diseases. *Front Mol Biosci.* 2020;7:153.
 - Lee H, Kim M, Kim S-H, et al. Alpha-methylacyl-CoA racemase (AMACR), a potential new biomarker for glioblastoma. *Front Oncol.* 2020;10:550673.
 - Zhou M, Chinnaiyan AM, Kleer CG, Lucas PC, Rubin MA. Alpha-methylacyl-CoA racemase: a novel tumor marker overexpressed in several human cancers and their precursor lesions. *Am J Surg Pathol.* 2002;26(7):926-931.
 - Cooney MM, Thompson CL, Lin P-Y, et al. Detection of alpha-methylacyl-CoA racemase (AMACR), a biomarker of prostate cancer, in patient blood samples using a nanoparticle electrochemical biosensor. *J Clin Oncol.* 2012;30(30_suppl):41.
 - Ferdinandusse S, Rusch H, van Lint AEM, Dacremont G, Wanders RJA, Vreken P. Stereochemistry of the peroxisomal branched-chain fatty acid α - and β -oxidation systems in patients suffering from different peroxisomal disorders. *J Lipid Res.* 2002;43(3):438-444.
 - Dregus M, Schmarr H-G, Takahisa E, Engel K-H. Enantioselective analysis of methyl-branched alcohols and acids in rhubarb (*Rheum rhabarbarum* L.) stalks. *J Agric Food Chem.* 2003;51(24):7086-7091.

29. Barbeni M, Allegrone G, Cisero M, Guarda PA. GC and NMR enantiodiscrimination of 2-methyl substituted aliphatic acids via diastereomeric esterification with (*R*)-pantolactone. *Flavour Fragr J.* 1992;7(3):163-167.
30. Islam MF, Adhikari S, Paik M-J, Lee W. Liquid chromatographic enantiomer separation of 1-naphthylamides of chiral acids using several amylose- and cellulose-derived chiral stationary phases. *Arch Pharm Res.* 2017;40(3):350-355.
31. Karongo R, Jiao J, Gross H, Lämmerhofer M. Direct enantioselective gradient reversed-phase ultra-high performance liquid chromatography tandem mass spectrometry method for 3-hydroxy alkanolic acids in lipopeptides on an immobilized 1.6 μm amylose-based chiral stationary phase. *J Sep Sci.* 2021;44(9):1875-1883.
32. Liebisch G, Fahy E, Aoki J, et al. Update on LIPID MAPS classification, nomenclature, and shorthand notation for MS-derived lipid structures. *J Lipid Res.* 2020;61(12):1539-1555.
33. Lämmerhofer M. Chiral recognition by enantioselective liquid chromatography: mechanisms and modern chiral stationary phases. *J Chromatogr A.* 2010;1217(6):814-856.

SUPPORTING INFORMATION

Additional supporting information may be found in the online version of the article at the publisher's website.

How to cite this article: Geibel C, Zhang L, Serafimov K, Gross H, Lämmerhofer M. Towards enantioselective ultrahigh performance liquid chromatography–mass spectrometry-based metabolomics of branched-chain fatty acids and *anteiso*-fatty acids under reversed-phase conditions using sub-2- μm amylose- and cellulose-derived chiral stationary phases. *Chirality.* 2022;34(3):484-497. doi:10.1002/chir.23413

Supplemental Material

Towards enantioselective ultra-high performance liquid chromatography-mass spectrometry-based metabolomics of branched chain fatty acids and *anteiso*-fatty acids under reversed phase conditions using sub-2 μ m amylose- and cellulose-derived chiral stationary phases

Christian Geibel¹, Li Zhang¹, Kristian Serafimov¹, Harald Gross², Michael Lämmerhofer^{1,*}

¹ Institute of Pharmaceutical Sciences, Pharmaceutical (Bio-)Analysis, University of Tübingen, Auf der Morgenstelle 8, 72076 Tübingen, Germany

² Institute of Pharmaceutical Sciences, Pharmaceutical Biology, University of Tübingen, Auf der Morgenstelle 8, 72076 Tübingen, Germany

*Author for correspondence:

Prof. Dr. Michael Lämmerhofer

Pharmaceutical (Bio-)Analysis

Institute of Pharmaceutical Sciences

University of Tübingen

Auf der Morgenstelle 8

72076 Tübingen, Germany

T +49 7071 29 78793, F +49 7071 29 4565

E-mail: michael.laemmerhofer@uni-tuebingen.de

**Suppl. Table
S1.**

IA-U

particle size	1.6 μ m	HPLC	injection	1 μ L
fully porous	A	Agilent 1260	wavelength	215 nm
length [mm]	100 mm		flow rate	adjusted
ID [mm]	3 mm			

10°C ACN - 40%	Flow [mL/min]	Retention time [min]		Retention factor k		Selectiv- ity α	Resolu- tion R	Plate number N	
		peak 1	peak 2	peak 1	peak 2			peak 1	peak 2
FA 4:0;2Me	0.2	19.21	20.33	9.313	9.912	1.064	1.515	11932	11059
FA 5:0;2Me	0.2	28.98	30.46	14.553	15.351	1.055	1.387	11908	12629
FA 6:0;2Me	0.2	46.70	48.96	24.065	25.279	1.050	1.318	11843	12889
FA 6:0;2Et	0.2	60.53	60.53	31.489	31.489	1.000	1.000	4783	-
FA 5:0;3Me	0.2	31.47	34.49	15.893	17.512	1.102	2.448	11972	10914
FA 6:0;4Me	0.2	64.71	64.71	33.732	33.732	1.000	1.000	11311	-
FA 8:0;4Me	0.2	no elution							
FA 8:0;4Et	0.2	no elution							

Suppl. Table S2.

IB-U

particle size	1.6 μ m	HPLC	injection	1 μ L
fully porous	A	Agilent 1260	wavelength	215 nm
length [mm]	100 mm		flow rate	adjusted
ID [mm]	3 mm			

10°C ACN - 45%	Flow [mL/min]	Retention time [min]		Retention factor k		Selectiv- ity α	Resolu- tion R	Plate number N	
		peak 1	peak 2	peak 1	peak 2			peak 1	peak 2
FA 4:0;2Me	0.2	15.77	19.61	7.463	9.524	1.276	6.557	14708	14368
FA 5:0;2Me	0.2	23.15	30.57	11.427	15.407	1.348	8.948	16516	16865
FA 6:0;2Me	0.2	30.92	43.54	15.597	22.369	1.434	10.695	15854	15848
FA 6:0;2Et	0.2	37.53	41.96	19.143	21.520	1.124	3.790	18869	18002
FA 5:0;3Me	0.2	31.21	34.57	15.751	17.554	1.114	3.273	15765	16891
FA 6:0;4Me	0.2	63.92	63.92	33.308	33.308	1.000	1.000	8057	-
FA 8:0;4Me	0.2	153.19	162.27	81.230	86.100	1.060	1.968	18655	18606
FA 8:0;4Et	0.2	212.18	222.69	112.889	118.533	1.050	1.836	25263	21011

Suppl. Table S3.

IC-U

particle size	1.6 μ m	HPLC	injection	1 μ L
fully porous	A	Agilent 1260	wavelength	215 nm
length [mm]	100 mm		flow rate	adjusted
ID [mm]	3 mm			

10°C ACN-35%	Flow [mL/min]	Retention time [min]		Retention factor k		Selectiv- ity α	Resolu- tion R	Plate number N	
		peak 1	peak 2	peak 1	peak 2			peak 1	peak 2
FA 4:0;2Me	0.2	20.90	23.03	10.217	11.363	1.112	3.065	16155	15532
FA 5:0;2Me	0.2	33.57	38.93	17.019	19.894	1.169	4.914	17635	17580
FA 6:0;2Me	0.2	58.11	67.34	30.194	35.144	1.164	5.010	18524	18444
FA 6:0;2Et	0.2	73.05	76.09	38.209	39.844	1.043	1.505	20945	22313
FA 5:0;3Me	0.2	43.08	43.08	22.121	22.121	1.000	1.000	7234	-
FA 6:0;4Me	0.2	no elution							
FA 8:0;4Me	0.2	no elution							
FA 8:0;4Et	0.2	no elution							

Suppl. Table S4.

ID-U

particle size	1.6 μ m	HPLC Agilent 1260	injection	1 μ L
fully porous	A		wavelength	215 nm
length [mm]	100 mm		flow rate	adjusted
ID [mm]	3 mm			

10°C ACN - 35%	Flow [mL/min]	Retention time [min]		Retention factor k		Selectivity α	Resolution R	Plate number N	
		peak 1	peak 2	peak 1	peak 2			peak 1	peak 2
FA 4:0;2Me	0.2	15.18	15.18	7.148	7.148	1.000	1.000	6072	-
FA 5:0;2Me	0.2	22.21	22.21	10.922	10.922	1.000	1.000	3028	-
FA 6:0;2Me	0.2	35.79	35.79	18.211	18.211	1.000	1.000	2996	-
FA 6:0;2Et	0.2	48.97	51.65	25.287	26.726	1.057	1.027	6808	5218
FA 5:0;3Me	0.2	23.32	23.32	11.517	11.517	1.000	1.000	3461	-
FA 6:0;4Me	0.2	41.45	41.45	21.250	21.250	1.000	1.000	6756	-
FA 8:0;4Me	0.2	107.90	107.90	56.916	56.916	1.000	1.000	9585	-
FA 8:0;4Et	0.2	no elution							

Suppl. Table S5.

IG-U

particle size	1.6 μ m	HPLC	injection	1 μ L
fully porous	A	Agilent 1260	wavelength	215 nm
length [mm]	100 mm		flow rate	adjusted
ID [mm]	3 mm			

10°C	Flow [mL/min]	Retention time [min]		Retention factor k	Selectivity α	Resolution R	Plate number N	
		peak 1	peak 2				peak 1	peak 2
ACN -40%								
FA 4:0;2Me	0.2	19.90	20.98	9.683	1.059	1.634	15196	15621
FA 5:0;2Me	0.2	33.84	35.14	17.162	1.041	1.189	15484	15756
FA 6:0;2Me	0.2	60.16	84.57	31.294	1.419	11.488	17449	19241
FA 6:0;2Et	0.2	86.10	107.94	45.217	1.259	7.518	17918	17637
FA 5:0;3Me	0.2	38.29	40.95	19.551	1.073	2.274	17930	18431
FA 6:0;4Me	0.2	81.23	81.23	42.604	1.000	1.000	7946	-
FA 8:0;4Me	0.2	no elution						
FA 8:0;4Et	0.2	no elution						

Suppl. Table S6.

IH-U

particle size	1.6 μ m	HPLC	injection	1 μ L
fully porous	A	Agilent 1260	wavelength	215 nm
length [mm]	100 mm		flow rate	adjusted
ID [mm]	3 mm			

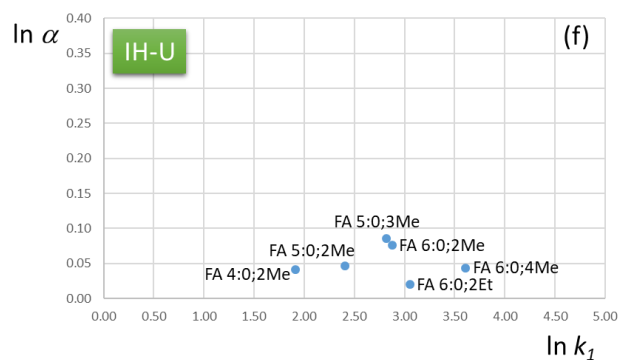
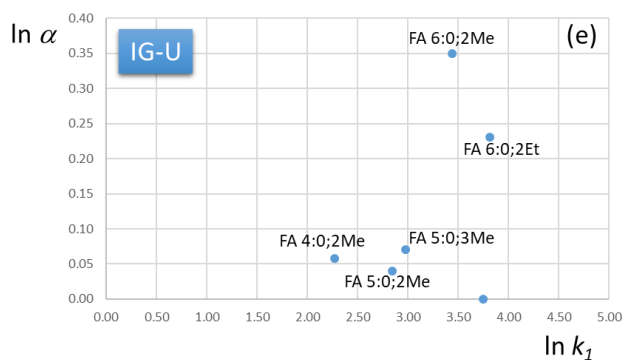
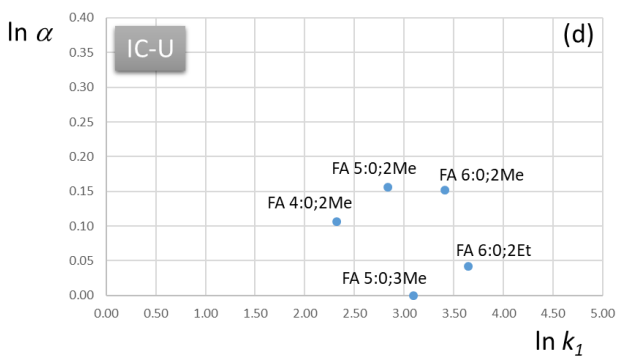
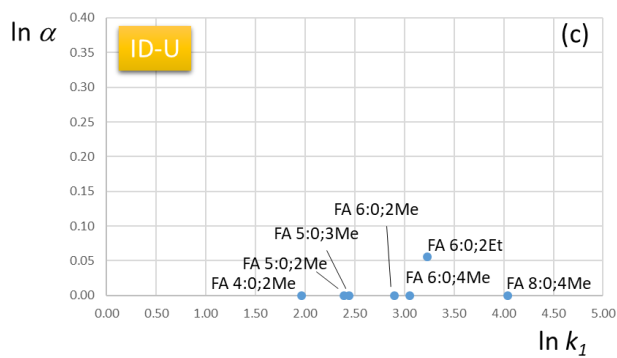
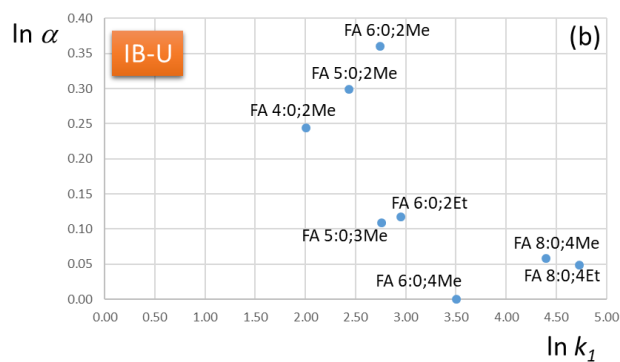
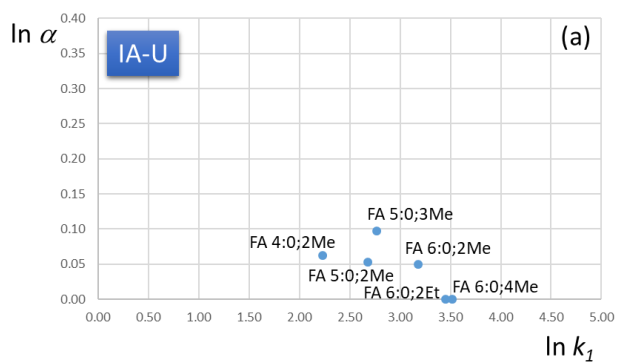
10°C ACN - 40%	Flow [mL/min]	Retention time [min]		Retention factor k		Selectiv- ity α	Resolu- tion R	Plate number N	
		peak 1	peak 2	peak 1	peak 2			peak 1	peak 2
FA 4:0;2Me	0.2	14.49	15.01	6.776	7.058	1.042	1.145	16807	16039
FA 5:0;2Me	0.2	22.60	23.59	11.130	11.665	1.048	1.484	19088	18709
FA 6:0;2Me	0.2	34.99	37.60	17.780	19.181	1.079	2.612	20656	21325
FA 6:0;2Et	0.2	41.49	42.30	21.269	21.706	1.021	0.634	18343	15724
FA 5:0;3Me	0.2	33.07	35.87	16.749	18.252	1.090	2.929	20468	20895
FA 6:0;4Me	0.2	70.70	73.79	36.950	38.610	1.045	1.731	26103	25912
FA 8:0;4Me	0.2	no elution							
FA 8:0;4Et	0.2	no elution							

Suppl. Table S7. Effect of organic modifier content, temperature and flow rate on the enantiomer separation of branched alkanolic acids derivatized by 1-naphthylamine on Chiralpak IB-U. All runs isocratic with either ACN + 0.1% AA/water + 0.1% AA (45/55; v/v) or MeOH + 0.1% AA/water + 0.1% AA (70/30; v/v).

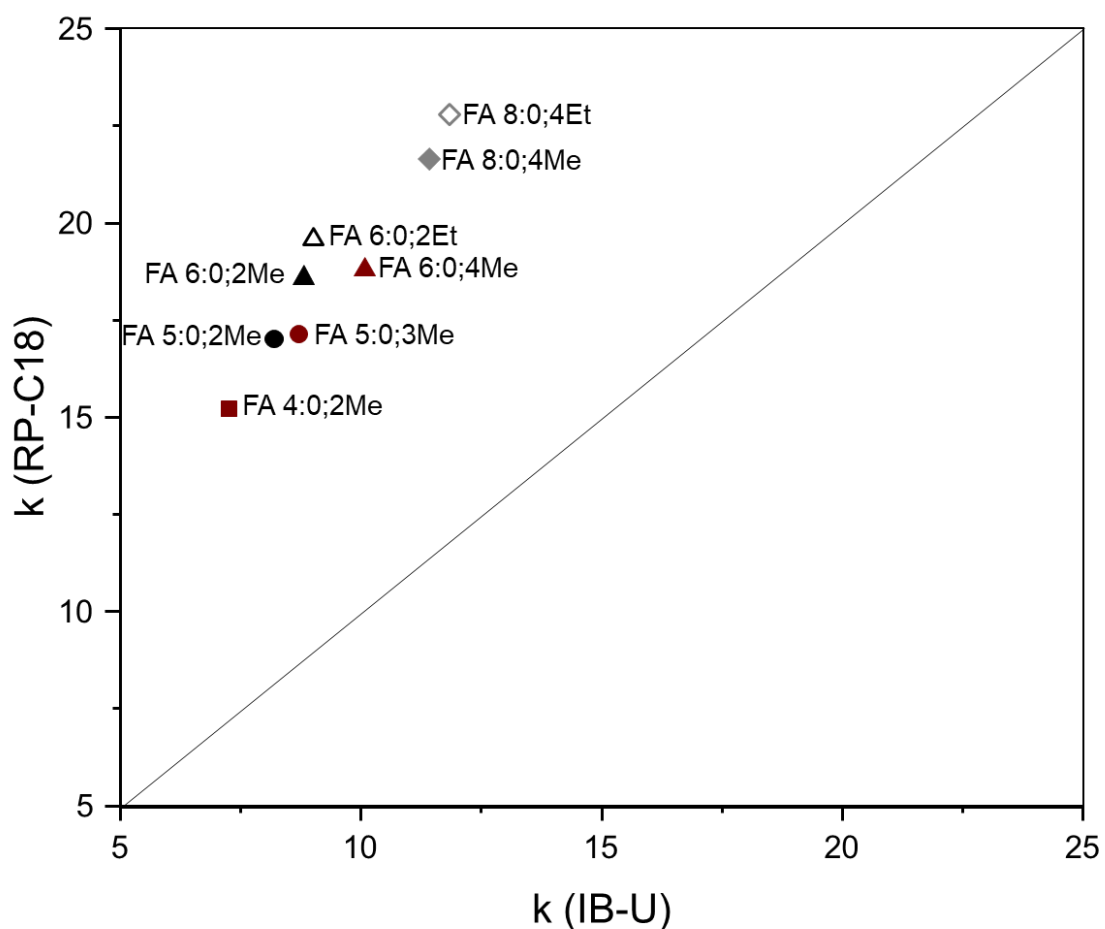
	10°C, 0.2 mL/min							
	ACN				MeOH			
	k_1	α	N_2	R_s	k_1	α	N_2	R_s
FA 4:0;2Me	5.29	1.29	14,368	6.56	10.96	1.10	654	0.61
FA 5:0;2Me	8.24	1.36	16,865	8.95	17.11	1.16	1,208	1.27
FA 6:0;2Me	11.34	1.44	15,848	10.70	22.22	1.28	901	1.89
FA 6:0;2Et	13.97	1.13	18,002	3.79	24.32	1.14	1,123	1.13
FA 5:0;3Me	11.45	1.12	16,891	3.27	21.66	1.16	1,511	1.34

	40°C, 0.2 mL/min							
	ACN				MeOH			
	k_1	α	N_2	R_s	k_1	α	N_2	R_s
FA 4:0;2Me	3.93	1.18	14,401	4.04	5.00	1.10	1,160	0.70
FA 5:0;2Me	5.80	1.23	17,726	5.90	6.58	1.15	1,578	1.19
FA 6:0;2Me	8.47	1.27	17,234	7.22	8.81	1.21	2,062	1.96
FA 6:0;2Et	10.16	1.08	18,355	2.27	9.28	1.07	2,445	0.60
FA 5:0;3Me	7.33	1.07	18,028	2.06	8.00	1.11	1,635	0.94

	40°C, 0.5 mL/min							
	ACN				MeOH			
	k_1	α	N_2	R_s	k_1	α	N_2	R_s
FA 4:0;2Me	3.54	1.17	12,764	3.45	2.95	1.10	3,724	1.17
FA 5:0;2Me	5.18	1.22	13,179	4.90	3.90	1.15	3,386	1.69
FA 6:0;2Me	7.57	1.26	13,692	6.10	5.49	1.21	3,426	2.43
FA 6:0;2Et	9.22	1.07	13,694	1.89	5.69	1.07	2,283	0.65
FA 5:0;3Me	6.55	1.07	13,559	1.63	4.88	1.10	3,364	1.20

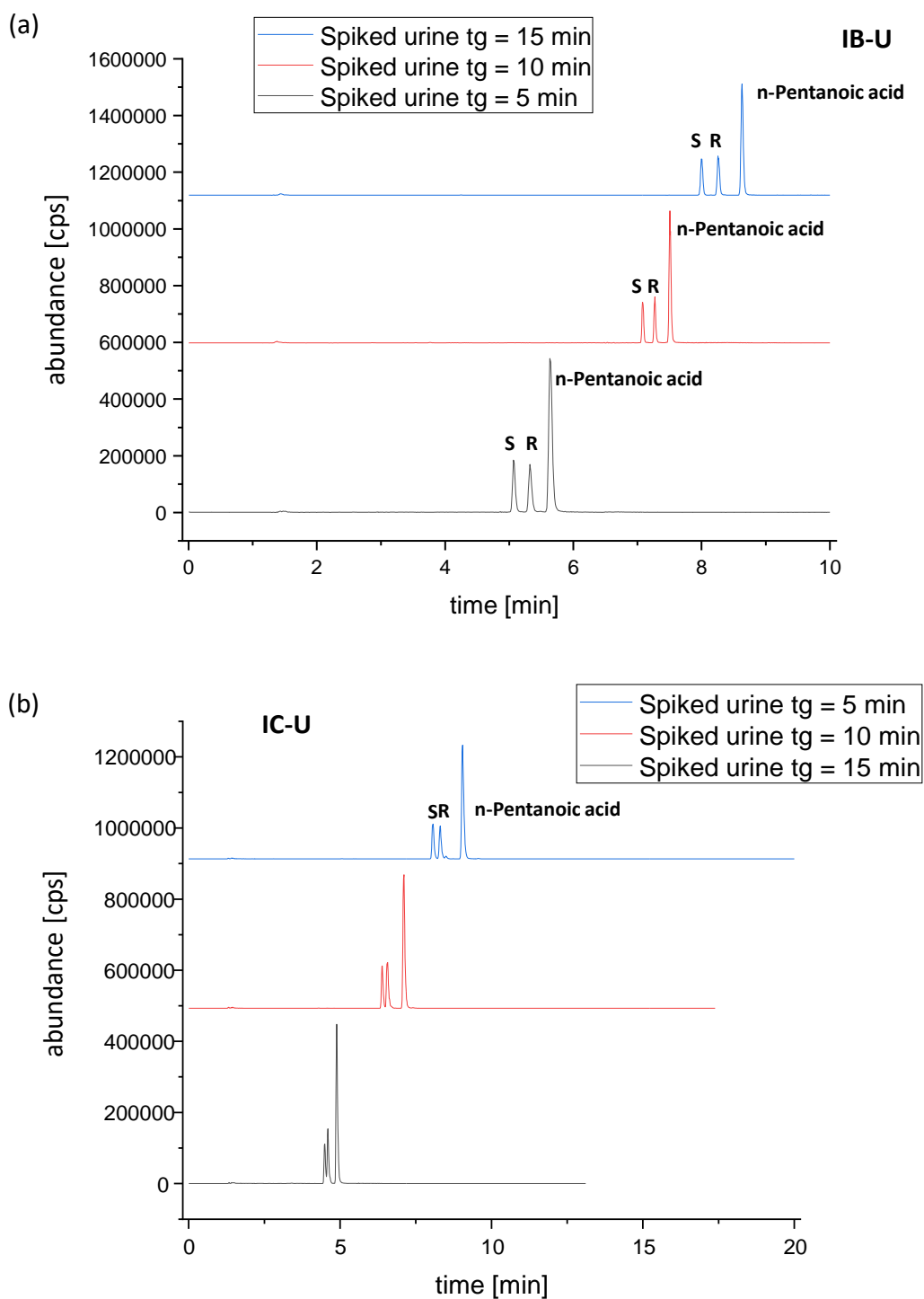


Suppl. Fig. S1. Retention and enantioselectivity increments for branched chain fatty acids on various polysaccharide-type UHPLC columns. Conditions as specified in Suppl. Table S1 – S6.

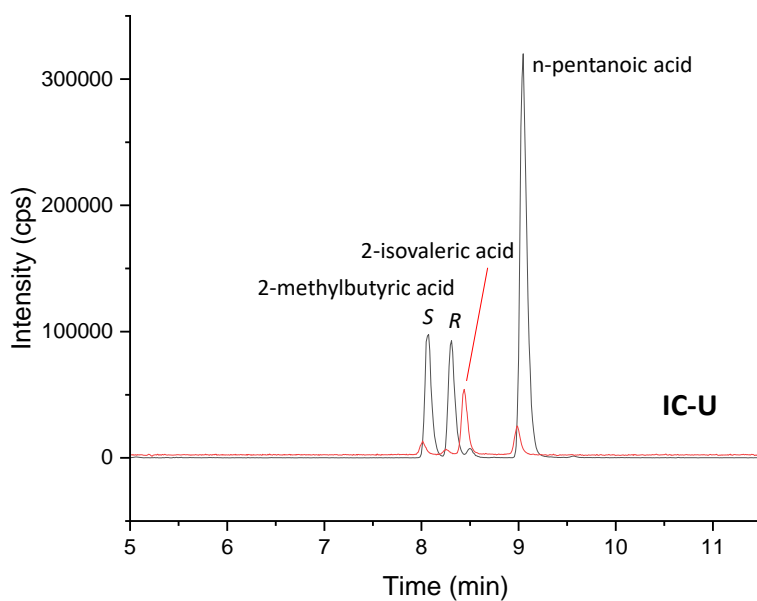


Suppl. Fig. S2. Orthogonality plot of retention factors on RP C18 vs IB-U. Mobile phases: A: water + 0.1% acetic acid, B: acetonitrile + 0.1% acetic acid. Gradient: 0.00 min: 20% B, 20.00 min: 90% B, 20.01 min: 20% B, injection volume: 1 μ L, linear flow rate: 1.8 mm/s, column temperature: 10°C, detection wavelength: 215 nm. Used columns: Chiralpak IB-U (100 x 3.0 mm, 1 x i.d., 1.6 μ m) and YMC-Triart C18 RP (100 x 2.1 mm 1 x i.d., 1.9 μ m).

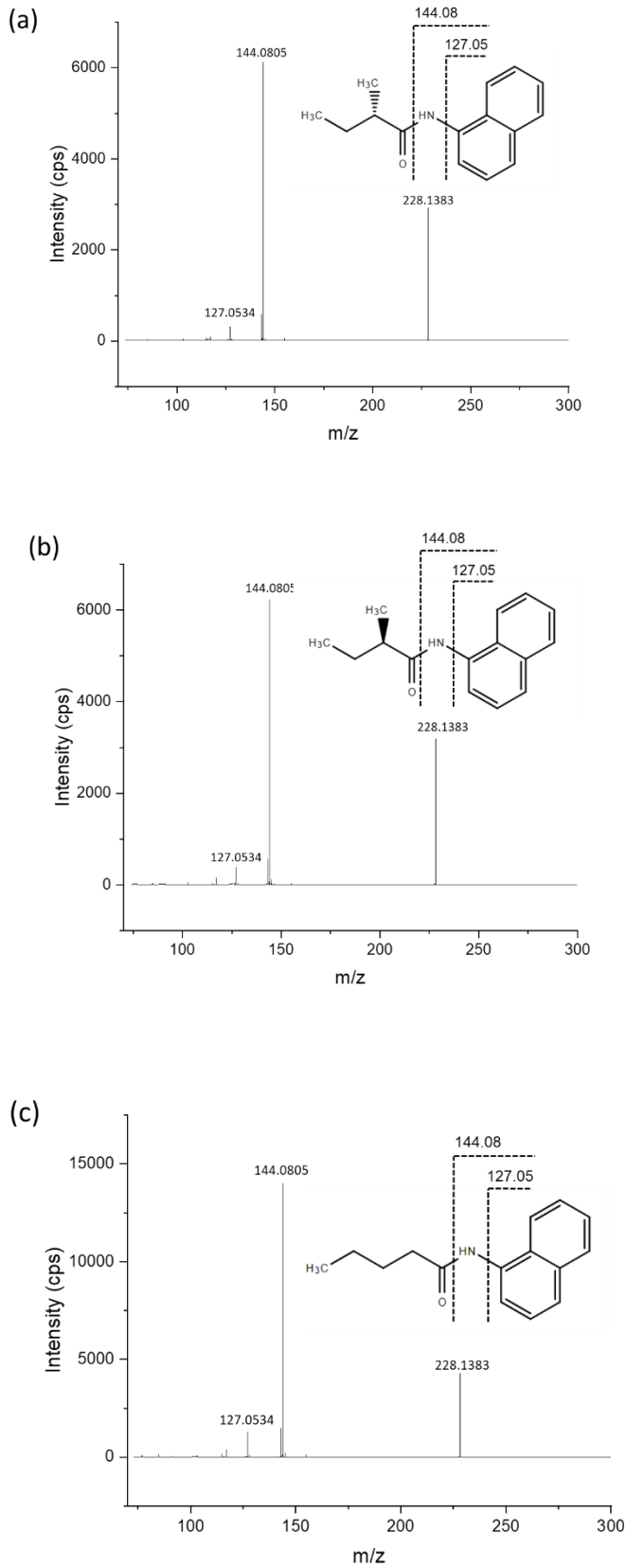
Open signs: ethyl branched FAs, filled signs: methyl branched FAs. Square: butyric acid, circle: pentanoic acid, triangle: hexanoic acid, rhomb: octanoic acid. Red: *anteiso*-FAs, black: branched in α -position (except FA 4:0;2Me, as this is *anteiso*), grey: branched in position four (except FA 6:0;4Me, as this is *anteiso*).



Suppl. Fig. S3. Optimization of gradient time (tg) for analysis of 2-methylbutyric acid in human urine on Chiralpak IB-U (a) and IC-U (b) using UHPLC-ESI-QTOF-MS. Conditions: mobile phase A: water + 0.1% acetic acid, B: acetonitrile + 0.1% acetic acid, flow rate: 0.4 mL/min, column temperature: 10°C. Gradient profile: 0.00 min: 20% B, in 5, 10, and 15 min to 90% B, respectively; column temperature, 10°C; flow rate, 0.4 mL/min.

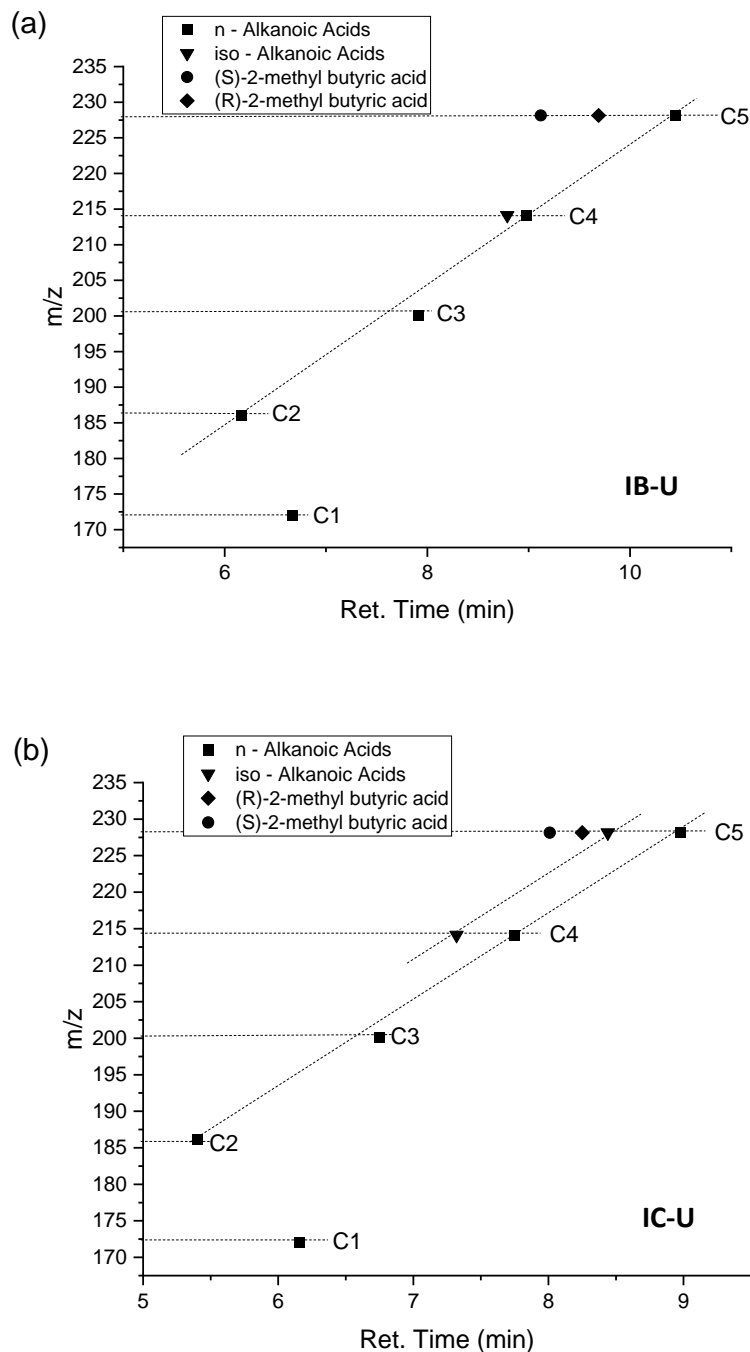


Suppl. Fig. S4. Chromatograms showing an overlay of human urine spiked with racemic 2-methylbutyric acid and n-pentanoic acid (black trace) and isovaleric acid standard (Sigma Aldrich) (red trace). It can be seen that the isovaleric acid standard contains also significant amount of impurities of the other isomeric forms (*S*)- and (*R*)-2-methylbutyric acid as well as n-pentanoic acid (valeric acid). Conditions as specified in Suppl. Fig. S3 (15 min gradient time).



Suppl. Fig. S5. MS2 spectra of (a) (S)-2-methylbutyric acid, (b) (R)-2-methylbutyric acid, and (c) n-pentanoic acid obtained from urine sample spiked with racemic 2-methylbutyric acid and n-

pentanoic acid as shown in Suppl. Fig. S4 (black trace). It can be seen that alkanolic acid side chains do not fragment and hence these isomeric substances cannot be distinguished by HR-MS.



Suppl. Fig. S6. Retention pattern of homologous branched- and straight-chain fatty acids on Chiralpak IB-U (a) and IC-U (b) detected by UHPLC-ESI-QTOF-MS in human urine with precolumn derivatization using 1-naphthylamine. Conditions as specified in Suppl. Fig. S3. Analytes: C1,

formic acid; C2, acetic acid; C3, propionic acid; C4, iso- and n-butyric acid; C5, 2-methylbutric acid, iso- and n-valeric acid.

3.2.2 Publication VI: **High Plasticity of the Amicetin Biosynthetic Pathway in *Streptomyces* sp. SHP 22-7 Led to the Discovery of Streptocytosine P and Cytosaminomycins F and G and Facilitated the Production of 12F-Plicacetin**

Niraj Aryal[†], Junhong Chen[†], Oliver Hennrich[‡], Ira Handayani[§], Markus Kramer[⊥], Jan Straetener[‡], Tatjana Wommer[‡], Anne Berscheid[‡], Heike Brötz-Oesterhelt^{‡,||}, Norbert Reiling^{□,◦}, Silke Peter^{||,±}, Christian Geibel[^], Michael Lämmerhofer[^], Yvonne Mast^{#,||}, Harald Gross^{†,||,*}

[†] Pharmaceutical Institute, Department of Pharmaceutical Biology, University of Tübingen, 72076 Tübingen, Germany

[‡] Department of Microbiology/Biotechnology, Interfaculty Institute of Microbiology and Infection Medicine, Tübingen (IMIT), Cluster of Excellence 'Controlling Microbes to Fight Infections', University of Tübingen, 72076 Tübingen, Germany

[§] Research Center for Biotechnology, the National Research and Innovation Agency of Indonesia (RC Biotechnology BRIN) Jl.Raya Bogor Km.46, Cibinong, 16911, Bogor; West Java, Indonesia

[⊥] Institute of Organic Chemistry, University of Tübingen, 72076 Tübingen, Germany

^{||} German Center for Infection Research (DZIF), partner site Tübingen, 72076 Tübingen, Germany

[□] Microbial Interface Biology, Research Center Borstel, Leibniz Lung Center, Parkallee 22, 23845 Borstel, Germany

[◦] German Center for Infection Research (DZIF), partner site Hamburg-Lübeck-Borstel-Riems, Hamburg, Germany

[±] Institute of Medical Microbiology and Hygiene, University of Tübingen, Tübingen, Germany

[^] Pharmaceutical Institute, Department of Pharmaceutical Analysis and Bioanalysis, University of Tübingen, 72076 Tübingen, Germany

[#] Department Bioresources for Bioeconomy and Health Research, Leibniz Institute DSMZ-German Collection of Microorganisms and Cell Cultures, 38124 Braunschweig, Germany

^{*} Corresponding author. E-mail address: harald.gross@uni-tuebingen.de (H. Gross)

Reprinted with permission from *Journal of Natural Products* **2022**, 85, 3, 530–539.

DOI: 10.1021/acs.jnatprod.1c01051

Copyright 2022 American Chemical Society.

High Plasticity of the Amicetin Biosynthetic Pathway in *Streptomyces* sp. SHP 22-7 Led to the Discovery of Streptcytosine P and Cytosaminomycins F and G and Facilitated the Production of 12F-Plicacetin

Niraj Aryal, Junhong Chen, Keshab Bhattarai, Oliver Hennrich, Ira Handayani, Markus Kramer, Jan Straetener, Tatjana Wommer, Anne Berscheid, Silke Peter, Norbert Reiling, Heike Brötz-Oesterhelt, Christian Geibel, Michael Lämmerhofer, Yvonne Mast, and Harald Gross*



Cite This: *J. Nat. Prod.* 2022, 85, 530–539



Read Online

ACCESS |



Metrics & More

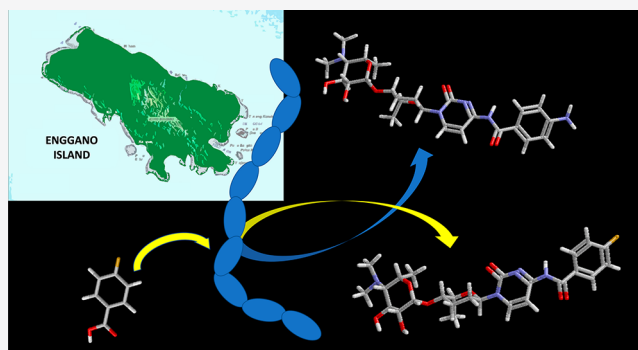


Article Recommendations



Supporting Information

ABSTRACT: A chemical reinvestigation of the Indonesian strain *Streptomyces* sp. SHP 22-7 led to the isolation of three new pyrimidine nucleosides, along with six known analogues and zincphyrin. The structures of the new compounds (**6**, **7**, **10**) were elucidated by employing spectroscopic techniques (NMR, MS, CD, and IR) as well as enantioselective analyses of methyl branched side chain configurations. Application of the precursor-directed feeding approach led to the production and partial isolation of nine further pyrimidine analogues. The new compounds **6**, **7**, and **11** and three of the known compounds (**2–4**) were found to possess antimycobacterial and cytotoxic properties.



Within the framework of a previous campaign in which Indonesian microbial biodiversity was scrutinized for bioactive natural products, the mangrove-derived strain *Streptomyces* sp. SHP 22-7 was prioritized due to its antibacterial activity toward Gram-positive bacteria. The bioactivity could readily be assigned to the production of amicetin (Figure S1).¹

Amicetin, originally isolated in the early 1950s from *Streptomyces vinaceusdrappus* and *S. fasciculatis*,^{2a,b} represents the founding member of a large family of pyrimidine nucleoside antibiotics. Structurally, these compounds share a disaccharide pyrimidine nucleoside motif, termed cytosamine, in which the sugar amosamine (4,6-dideoxy-4-dimethylamino-D-glucose) is linked to amicetose, which is in turn bonded to a cytosine nucleus (Figure 1). The amino group of the amosamine moiety is commonly dimethylated. Deviating from this standard motif, the amosamine moiety can be solely monomethylated^{2c} or completely absent, and position 3' of amicetose can be in rare cases additionally hydroxylated. However, the highest degree of molecular diversity within this compound class is given by the acylation of the amino group (NH₂-7) of cytosine with a huge variety of aminobenzoic or aliphatic carboxylic acids.^{2d} Several members of the amicetin family exhibit antiviral and antibiotic activity.^{3a} The latter effect is mediated by inhibition of protein synthesis through binding to the ribosomal P-site, ultimately inhibiting prokaryotic

translation.³ Furthermore, also the corresponding biosynthetic gene cluster (BGC) was identified and proven by heterologous expression.⁴

In follow-up studies with the strain SHP 22-7, the amicetin BGC and its specific regulation were further investigated.^{5,6} Both during the molecular MS networking approach¹ and during the regulator-overexpression studies⁶ it became apparent that SHP 22-7 produces a plethora of potentially new pyrimidine nucleoside analogues.

Thus, we herein report the isolation and the structure elucidation of three structurally new pyrimidine nucleosides (**6**, **7**, and **10**) and their evaluation in bioassays. In addition, we exploited the flexibility of the biosynthetic pathway and complemented the study with a precursor-directed feeding approach, leading to several new amicetin derivatives including halogenated versions.

Special Issue: Special Issue in Honor of William H. Gerwick

Received: November 6, 2021

Published: March 9, 2022



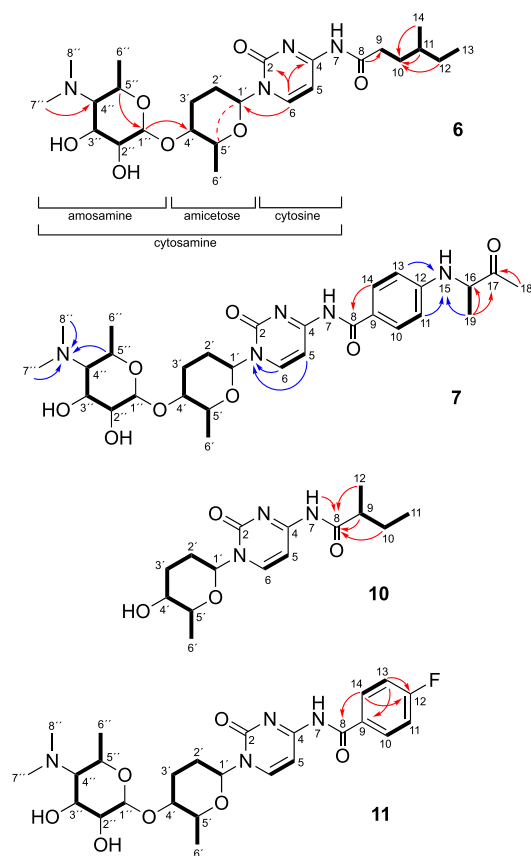


Figure 1. Key NMR correlations of compounds **6**, **7**, **10**, and **11**. Bold lines indicate ^1H – ^1H -COSY or ^1H – ^{13}C -HSQC-TOCSY correlations, while red arrows and dashed lines show key ^1H – ^{13}C -HMBC and ^1H – ^1H -NOESY cross correlations, respectively. Blue arrows represent key ^1H – ^{15}N HMBC correlations.

RESULTS AND DISCUSSION

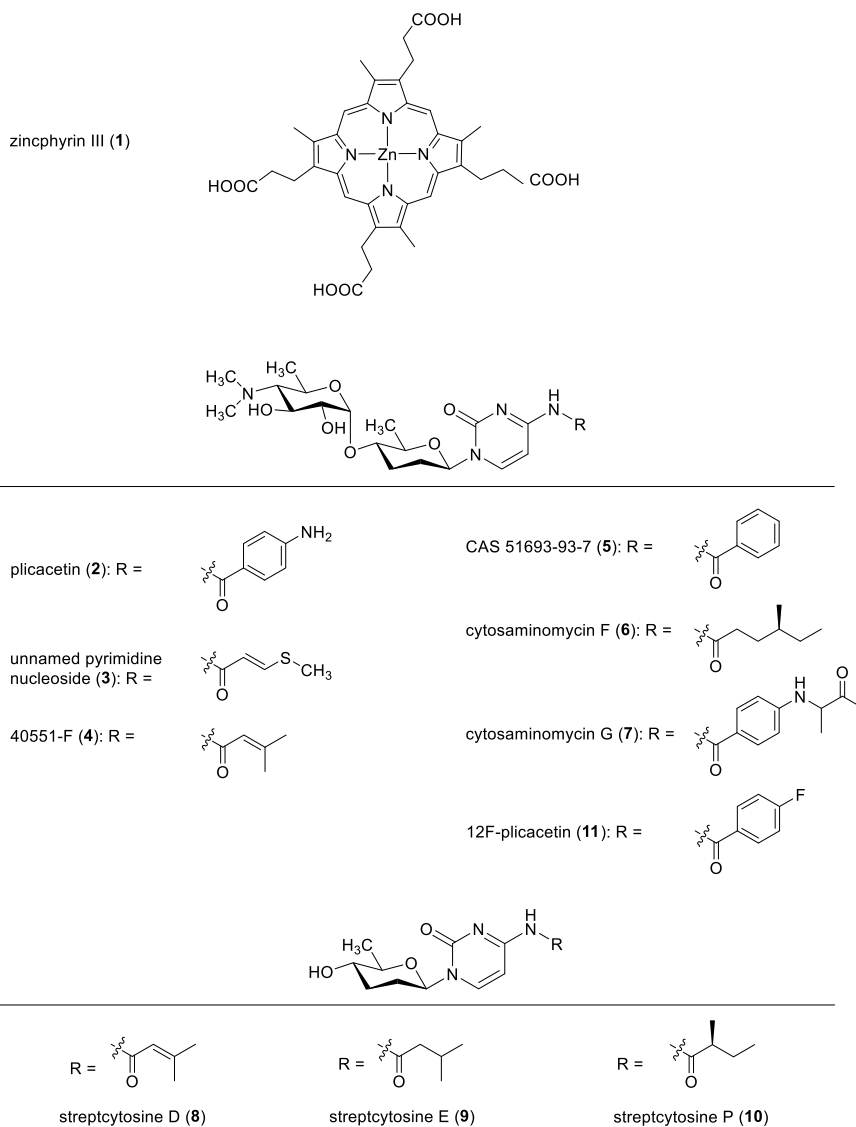
Target Compound Identification by HR-LC-MS/MS-Based Dereplication. The new derivatives were produced in a heterogeneous complex mixture and in small quantities. Therefore, in order to identify the new amicetin congeners, an MS-guided fractionation approach was applied. During the MS/MS fragmentation process, amicetins split off the monosaccharide amosamine and the disaccharide amicitose/amosamine, producing the characteristic fragments m/z 174.11 and 288.18, respectively (Figure S1). Consequently, employing HR-LC-MS/MS, we focused on fractions exhibiting the above-mentioned fragmentation pattern.

Isolation and Structural Analysis of Natural Nucleoside Antibiotics. In order to obtain sufficient amounts for structure elucidation and biological testing, repeated batches were cultivated, and the whole broth was extracted with EtOAc. Chromatographic separation of the crude extract using Sephadex LH20, C_{18} reversed phase vacuum liquid chromatography (VLC), SPE, and HPLC led to the identification and isolation of 10 compounds. One thereof was recognized as zincphyrin III (**1**),⁷ while the remaining compounds **2**–**10** were identified as cytosine-type nucleoside derivatives. The known compounds thereof were verified by comparison of their spectral data with those previously reported,^{2,8} while the structures of the new pyrimidine nucleosides **6**, **7**, and **10** were elucidated by extensive NMR spectroscopic and mass spectrometric experiments.

The HR-ESI-MS spectra of **6** gave molecular ions consistent with the formula $\text{C}_{25}\text{H}_{42}\text{N}_4\text{O}_7$ and required seven degrees of unsaturation. Initial evaluation of the ^1H and ^{13}C NMR spectra already supported the hypothesis that **6** was a cytosine derivative, similar to compounds **2**–**5**. Briefly, the ^1H NMR spectrum of **6** exhibited two aromatic protons at δ_{H} 7.48 and 8.11 (Table 1), which were connected to carbons at δ_{C} 98.4 and 146.3 (Table 2), respectively, and are typical of the CH-5 and CH-6 resonances of a cytosine unit.² Further ^1H – ^{13}C -HMBC cross correlations substantiated this assumption. In addition, the ^1H NMR spectrum of **6** displayed typical resonances for the two sugar units amicitose and amosamine as in plicacetin (**2**) (Tables 1, 2, and S2). The two major spin systems of the disaccharidic moiety were delineated from the combined analysis of the ^1H – ^1H -COSY and ^1H – ^{13}C -HSQC-TOCSY spectrum of **6**. For each sugar moiety, a continuous spin system from H-1' through H₃-6' and from H-1'' through H₃-6'' could be observed (Figure 1). The HMBC correlation H-1''/C-5'' and the ^1H – ^1H -NOESY-based through-space interaction of H-1' with H-5', respectively, proved both sugar moieties to be cyclic. Furthermore, the HMBC spectrum of **6** demonstrated coupling between two magnetically equivalent lower field methyl groups at δ_{H} 2.46 (CH₃-7'' and CH₃-8'') and carbon C-4', which proved that a $\text{N}(\text{CH}_3)_2$ moiety is attached to the hexose residue, thereby completing the structure of amosamine.

The connectivity of the established compound fragments resulted from long-range couplings in the HMBC spectrum of the anomeric proton H-1'' of amosamine with C-4' of amicitose, whereas the anomeric carbon C-1' of the latter sugar showed a heteronuclear correlation with H-6 of the cytosine unit. Subtraction of the C, N, and O atoms accounted for by the cytosamine residue ($\text{C}_{18}\text{N}_4\text{O}_6$) from the molecular formula of **6** showed that the remaining partial structure of the molecule had to contain one oxygen and seven carbon atoms. The DEPT135 and ^1H – ^{13}C -HSQC NMR data showed that two CH₃, three CH₂, one CH, and one amide carbonyl were involved. From the ^1H – ^1H -COSY and ^1H – ^{13}C -HSQC-TOCSY spectrum, the complete spin system of the side chain formed by C-9 through C-14 could be readily delineated (Figures 1 and S28–S30). The methylene proton resonances of atom 9 were in turn correlated in the HMBC spectrum to the amide carbonyl carbon C-8. Taken together, the above evidence suggested the presence of 4-methyl hexanoic acid. The remaining amidic linkage between the fatty acid and the cytosamine residue followed by deduction, but was also corroborated by MS/MS and by IR (1673 cm^{-1}) data. Thus, the skeletal structure of **6** was assigned and recognized as a cytosaminomycin analogue. Being the sixth member of this compound subfamily,^{2d,8c} the metabolite was named cytosaminomycin F.

With the planar structure of **6** determined, the configuration of the sugar moieties and the chiral center at C-11 required resolution. Since cytosaminomycin F (**6**) was obtained together with its analogues from strain SHP 22-7, it was assumed that these building blocks will be biosynthesized by the same pathway and therefore possess the same absolute configuration. This hypothesis was supported by NOESY data, which showed that **6** shared the same relative configuration with **2**. In addition, the experimental ECD curve showed a negative Cotton effect at 222 nm (ϵ –5.00) and three positive effects at 204 (ϵ +4.15), 262 (ϵ +4.05), and 299 (ϵ +2.83) nm, which were comparable in wavelength and ϵ -values with CD



spectra of established analogues, particularly with cytosaminomycin E.^{8c} Thus, in combination with the NOESY data, these data demonstrated that the absolute configuration of the disaccharide was 1'R, 4'S, 5'R, 1''R, 2''R, 3''S, 4''R, 5''R. In order to determine the absolute configuration at C-11, a small sample of **6** was hydrolyzed with 6 N HCl to its fragments and derivatized with 1-naphthylamine. These were analyzed by chiral HPLC and compared with the retention times of authentic standards. Employing this workflow, the 4-methyl hexanoic acid unit of **6** was shown to possess an S-configuration, thus completing the 3D structure of cytosaminomycin F (**6**).

The molecular formula of **7** was determined to be C₂₉H₄₁N₅O₈ by HR-ESI-MS. Comparison of the ¹H and ¹³C NMR spectral data with those of **6** (Tables 1 and 2) revealed that compound **7** contains also the cytosamine substructure. However, two aromatic resonances ($\delta_{\text{H}}/\delta_{\text{C}}$ 6.64, d, 8.7 Hz/114.4 and 7.82, d, 8.7 Hz/131.5) were indicative for the presence of a *para*-amino benzoic acid at NH-7. The remaining unassigned fragment consisting of C₄H₇O₁ was identified as butan-2-one using the following information. The ¹H–¹³C-HSQC-TOCSY and ¹H–¹H-COSY spectrum provided evidence that H-16 was directly bonded to H₃-19 (Figure 1). ¹H–¹³C-HMBC correlations from H₃-19 and H₃-18 to the

keto-carbonyl C-17 (δ_{C} 212.3) allowed the acetyl group to be located at C-16. The attachment of the butanone moiety at C-16, via an aza-ether linkage to NH-15, was corroborated by ¹H–¹⁵N-HMBC correlations from H-11, H-13, and H₃-19 to N-15. The NOESY data, which showed cross correlations of H-1'/H-5', H-4'/H-1'', H-2''/H-4'', and H-3''/H-5'', proved that the relative configuration of the sugar units of **7** was the same as that of **2**. A stereoanalysis of C-16 was not undertaken since chiral standards were not commercially available. For **7**, the trivial name cytosaminomycin G is proposed.

Compound **10** had a molecular formula of C₁₅H₂₃N₃O₄, as deduced from its HR-ESI-MS spectrum, indicating six ring double bond equivalents. In the ¹H and ¹³C NMR spectra, resonances for amosamine were absent; however COSY and HMBC NMR data established firmly the presence of the amicosylcytosine unit. The remaining substructure (C₅H₉O) required the assignment of two CH₃, one CH₂, one CH, and one C=O group. From the COSY spectrum, the spin system –CH₃–CH–CH₂–CH₃– could be deduced, which ranges from atom 9 to 12 (Figure 1). HMBC correlations between carbonyl atom C-8 and H-9/H₂-10/H₃-12 showed that C-8 was directly bonded to CH-9, establishing thereby the partial structure 2-methylbutanoic acid. The latter substructure could be linked to the cytosine unit via NH-7 by cross-peaks between

Table 1. ¹H NMR Data for Compounds 6, 7, 10, and 11 (δ in ppm, J in Hz)

moiety	no.	6 ^{a,c}	7 ^{a,d}	10 ^{b,d}	11 ^{a,c}
cytosine	5	7.48, d (7.5)	7.58, d (7.4)	7.26, d (7.5)	7.59, d (7.6)
	6	8.11, d (7.5)	8.12, d (7.4)	8.07, d (7.5)	8.18, d (7.6)
side chain	7		10.79, brs ^b	10.85, s	
	9	2.45, dd		2.55, m	
	10	1.47, m	7.82, d (8.7)	1.37, m	8.05, dd (5.3, 8.7) ^e
		1.71, m		1.55, m	
	11	1.39, m	6.64, d (8.7)	0.82, t (7.4)	7.28, dd (8.7, 8.7) ^e
	12	1.20, m		1.04, d (6.6)	
	13	0.90, t (7.5)	6.64, d (8.7)		7.28, dd (8.7, 8.7) ^e
	14	0.92, d (6.8)	7.82, d (8.7)		8.05, dd (5.3, 8.7) ^e
	15		6.84, d (7.3) ^b		
	16		4.17, m		
	18		2.17, s		
amicetose	1'	5.76, m	5.77, dd (10.8, 2.3)	5.62, dd (10.8, 2.2)	5.79, m
	2'	1.64, m	1.65, m	1.66, m	n.o. ^f
		2.37, m	2.15, m	1.88, m	2.18, m
	3'	1.64, m	1.68, m	1.52, m	1.66, m
		2.15, m	2.38, m	2.00, m	2.39, m
	4'	3.40, m	3.41, m	3.11, m	3.43, m
	5'	3.74, dq (9.1, 6.1)	3.75, m	3.38, dq (9.1, 6.1)	3.75, m
6'	1.36, d (6.1)	1.36, d (6.4)	1.20, d (6.1)	1.37, d (6.1)	
amosamine	1''	4.91, m	4.92, d (3.7)		4.91, d (3.8)
	2''	3.42, dd (9.5, 3.8)	3.41, m		3.43, m
	3''	3.87, m	3.87, t (9.6)		3.88, m
	4''	2.13, m	2.13, t (10.1)		2.16, m
	5''	3.82, m	3.83, m		3.83, m
	6''	1.24, d (6.2)	1.24, d (6.4)		1.25, m
	7''	2.46, s	2.47, s		2.48, s
	8''	2.46, s	2.47, s		2.48, s

^aRecorded in *d*₄-MeOH. ^bRecorded in *d*₆-DMSO. ^c400 MHz. ^d700 MHz. ^eBesides regular homonuclear ¹H–¹H-coupling, the protons of the fluorine-substituted aromatic ring being located in *ortho* and *meta* position to the fluorine, further exhibit heteronuclear ¹H–¹⁹F-coupling. ^fn.o.: not observed.

NH-7 and C-8 in the corresponding ¹H–¹³C HMBC spectrum. Compound 10 was thus similar to streptocytosine C^{8a} and differed solely by the fact that its side chain is saturated instead of bearing a double bond. Being the 16th member of the streptocytosine compound family,^{8a,c} 10 was consequently named streptocytosine P. The relative stereochemistry of the sugar portion was based on the close similarity of ¹H and ¹³C NMR shifts between 8, 9, and 10 (Tables 1, S7, and S8) and confirmed by NOESY correlations. Furthermore, the ECD spectrum of 10 was similar to that of 6 (Figures S35 and S69), thereby establishing the absolute configuration for the sugar portion. For the elucidation of the absolute configuration of the chiral center at C-9, chiral HPLC upon derivatization of the hydrolysis products was applied in a similar fashion to that conducted with 6 and showed atom 9 of 10 to be *S*-configured.

Precursor-Directed Feeding Study. The diversity of pyrimidine nucleosides is generated by the variation of either the sugar units (mono vs disaccharide, extra-hydroxylation, demethylation) or the side chain, that gets attached to NH-7 by an amide bond by highly promiscuous acyltransferases. Considering the metabolite spectrum obtained (compounds 2–10), the latter mechanism appears to be dominant in strain SHP 22-7. Based on the discovery of the amicetin biosynthetic gene cluster and deletion experiments,⁴ the acyltransferases AmiF and transacylase AmiR were identified as responsible for the amidic fusion of *p*-aminobenzoic acid to NH-7 and the

amidic attachment of terminal side chains, respectively. With the exception of the deoxy-sugar biosynthesis cassette *amiABCDE*, the complete *ami* gene cluster is also present in the strain SHP 22-7 (Figure S82). Both transferase encoding genes, *amiF* and *amiR*, are present therein and show a very high level of identity (>99%) to their orthologues in *S. vinaceusdrappus* NRRL 2363 (Table S11). The obtained compounds are in line with the biosynthetic knowledge, accumulated so far, except for compound 7. Here, it is striking that the linkage between the *p*-aminobenzoic acid and its terminal side is provided by an amine instead of the commonly observed amide bond. To the best of our knowledge, such a terminal amine linkage was not observed before in the amicetin compound family. However, *p*-amino benzoic acid condensates, within of the frame of the bacterial folate pathway, physiologically with dihydropteroate-diphosphate and the help of the enzyme dihydropteroate synthase (DHPS) via an amine bridge.⁹ Likewise, it can be envisioned that a 1-methyl-2-ketopropanone-1-pyrophosphate precursor, in interaction with a DHPS-like enzyme, leads to the targeted side chain moiety given in 7. It is noteworthy to mention that the *ami* gene cluster of SHP 22-7 contains no obvious additional candidate gene nearby, encoding such a protein, but the corresponding gene can be still located elsewhere in the genome.

We hypothesized that we could exploit the extensive substrate flexibility of AmiF and AmiR to generate optimized

Table 2. ^{13}C NMR and ^{15}N NMR Data for Compounds 6, 7, 10, and 11 (δ in ppm)

moiety	no.	6 ^{b,c}	7 ^{b,c}	10 ^{b,d}	11 ^{a,c}	
cytosine	1		168.4, tN ^{d,e}			
	2	157.5, qC	157.4, qC	154.0, qC	157.3, qC	
	3		n.o. ^{d,e,i}			
	4	164.3, qC	164.8, qC	162.5, qC	164.8, qC	
	5	98.4, CH	98.7, CH	95.8, CH	98.8, CH	
	6	146.3, CH	145.8, CH	145.4, CH	146.4, CH	
	7		n.o. ^{d,e}	147.6, NH ^f		
	side chain	8	176.2, qC	168.6, qC	177.3, qC	168.1, qC
		9	36.0, CH ₂	12.1, qC	41.8, CH	131.1, qC, d, ⁴ J _{C,F} = 3.0 Hz
		10	32.6, CH ₂	131.5, CH	26.5, CH ₂	132.1, CH, d, ³ J _{C,F} = 9.4 Hz
		11	35.4, CH	114.4, CH	11.4, CH ₃	116.8, CH, d, ² J _{C,F} = 22.4 Hz
		12	30.3, CH ₂	155.0, qC	16.8, CH ₃	165.7, qC, d, ¹ J _{C,F} = 250.9 Hz ^g
		13	11.6, CH ₃	114.4, CH		116.8, CH, d, J _{C,F} = 22.4 Hz
		14	19.3, CH ₃	131.5, CH		132.1, CH, d, J _{C,F} = 9.4 Hz
		15		85.4, NH ^{d,e}		
		16		59.2, CH		
		17		212.3, qC		
		18		25.4, CH ₃		
		19		17.3, CH ₃		
amicetose		1'	84.7, CH	84.6, CH	82.1, CH	84.7, CH
		2'	30.8, CH ₂	31.0, CH ₂	29.8, CH ₂	31.1, CH ₂
		3'	27.7, CH ₂	27.7, CH ₂	31.4, CH ₂	27.7, CH ₂
		4'	75.0, CH	75.0, CH	69.6, CH	75.0, CH
		5'	78.5, CH	78.5, CH	78.5, CH	78.5, CH
		6'	19.1, CH ₃	19.1, CH ₃	18.2, CH ₃	19.2, CH ₃
amosamine		1''	96.2, CH	96.1, CH		96.2, CH
	2''	74.7, CH	74.6, CH		74.6, CH	
	3''	70.2, CH	70.2, CH		70.2, CH	
	4''	71.9, CH	71.8, CH		71.9, CH	
	5''	67.4, CH	67.4, CH		67.3, CH	
	6''	19.7, CH ₃	19.6, CH ₃		19.6, CH ₃	
	7''	42.4, CH ₃	42.3, CH ₃		42.3, CH ₃	
	8''	42.4, CH ₃	42.3, CH ₃		42.3, CH ₃	
N		18.4, tN ^{d,e,h}				

^a100 MHz. ^b175 MHz. ^cRecorded in *d*₄-MeOH. ^dRecorded in *d*₆-DMSO. ^e41 MHz. ^f71 MHz. ^gShift value was not observed in the ^{13}C NMR experiment but extractable from the corresponding ^1H - ^{13}C -HMBC NMR experiment. The indicated $^1J_{\text{C,F}}$ coupling constant value was read out from a data set, recorded in *d*₆-DMSO, in which C-12 was detectable. ^hTertiary amine. ⁱn.o.: not observed.

or clickable¹⁰ new-to-nature analogues by feeding either fatty acids or benzoic acid analogues within the framework of a precursor-directed feeding approach.¹¹ In order to determine an optimal feeding time point, a growth curve was established and the production rate was monitored. These time course studies indicated that nucleoside production coincided with the start of the exponential log phase; that is, it begins approximately 40 h after inoculation, reaches its maximum at about 90 h, and is then followed by an ongoing but fluctuating production (Figure S83). Thus, the precursors were added before production starts, typically 32 h after inoculation, while the harvest time point was scheduled for 96 h after inoculation. Forty-three commercially available precursors were fed to small-scale cultures, extracted, and analyzed by HR-LC-MS and MS². As depicted in Figures 2 and S84–S93, 10 out of 43 tested precursors were incorporated into the pyrimidine nucleoside backbone and led to the corresponding plicacetin congeners. The successful examples consisted foremost of halogenated benzoic acid derivatives, while none of the linear fatty acids were accepted. Notably, precursor 1a enhanced the production of analogue 5 approximately 10-fold, while the other accepted precursors led to the production of the

expected new-to-nature pyrimidine nucleosides. However, the majority of the new derivatives were only produced in minute amounts. One derivative, 12-fluoro-plicacetin (11), could be obtained in amounts sufficient for NMR analysis and bioassay testing upon large-scale cultivation and feeding of precursor 4c.

The molecular formula C₂₅H₃₃FN₄O₇ of 11 was ascertained by HR-ESI-MS. Furthermore, the structure of 11 was verified by NMR. Its ^{13}C NMR spectrum was nearly superimposable with the one obtained for plicacetin (2), except for the resonances belonging to the aromatic moiety (Figure S72). Beside a downfield shift of C-12 from 155.0 to 165.7 ppm, a typical $J_{\text{C,F}}$ coupling constant pattern over 1–4 bonds¹² was observed (Table 2), hinting at the successful incorporation of a fluorobenzene moiety in 11. The detection of a characteristic resonance at δ_{F} at -107.7 in the ^{19}F NMR spectrum¹² of 11, together with ^1H - ^1H -COSY correlations between H-10/H-14 and H-11/H-13 in combination with HMBC cross-peaks between qC-8/H-14, H-14/qC-12, H-13/qC-12, and H-13/qC-9, provided final evidence for the presence of a *para*-substituted fluorobenzene residue (Figure 1).

Biological Activity. Pyrimidine nucleosides have been reported to be strongly active against various Gram-positive

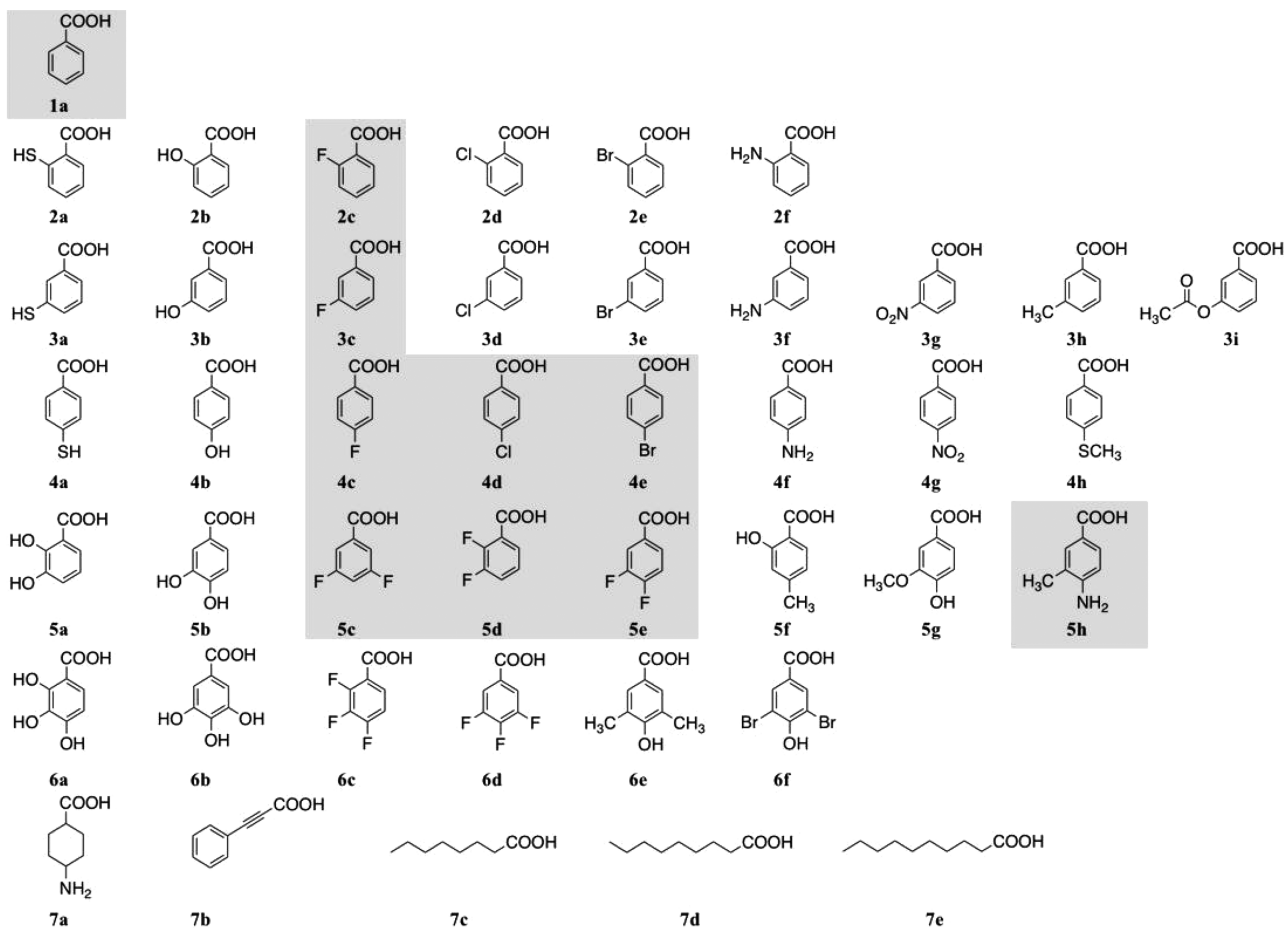


Figure 2. Overview of the precursors, supplemented to cultures of SHP 22-7. Gray-shaded structures represent precursors that were incorporated into the pyrimidine nucleoside backbone, leading to the corresponding plicacetin derivatives.

Table 3. Biological Activities of the Isolated Pyrimidine Nucleosides

organism	compound									
	2	3	4	6	7	8	9	10	11	
Antibacterial Assays, MIC [$\mu\text{g}/\text{mL}$]										
<i>C. albicans</i> Tü01	>32	>32	>32	>32	>32	>32	>32	>32	>32	>32
<i>C. glabrata</i> Tü04	>32	>32	>32	>32	>32	>32	>32	>32	>32	>32
Antibacterial Assays, MIC [$\mu\text{g}/\text{mL}$]										
<i>E. faecium</i> BM4147-1	>32	>32	>32	>32	>32	>32	>32	>32	>32	>32
<i>S. aureus</i> ATCC 29213	>32	16	>32	>32	>32	>32	>32	>32	>32	>32
<i>K. pneumoniae</i> ATCC 12657	>32	>32	>32	>32	>32	>32	>32	>32	>32	>32
<i>A. baumannii</i> 09987	>32	>32	>32	>32	>32	>32	>32	>32	>32	>32
<i>P. aeruginosa</i> ATCC 27853	>32	>32	>32	>32	>32	>32	>32	>32	>32	>32
<i>E. aerogenes</i> ATCC 13048	>32	>32	>32	>32	>32	>32	>32	>32	>32	>32
<i>E. coli</i> ATCC 25922	>32	>32	>32	>32	>32	>32	>32	>32	>32	>32
<i>B. subtilis</i> 168	32	8	32	>32	>32	>32	>32	>32	>32	>32
<i>S. aureus</i> NCTC 8325	>32	16	>32	>32	>32	>32	>32	>32	>32	>32
<i>M. smegmatis</i> mc ² 155	2	4	4	16	2	>32	>32	>32	>32	8
Antitubercular Assays, MIC ₉₅ [μM]										
<i>M. tuberculosis</i>	16	8	32	n.d. ^a	32	n.d.	n.d.	n.d.	n.d.	64
<i>In Vitro</i> Translation Assay, IC ₅₀ [$\mu\text{g}/\text{mL}$]										
	12.0	1.0	1.6	9.5	13.0	n.d.	n.d.	n.d.	n.d.	n.d.
Cytotoxicity Assays, IC ₅₀ [$\mu\text{g}/\text{mL}$]										
HeLa cell line	16–32	1–2	2–4	>64	16–32	>64	>64	>64	>64	>64

^an.d.: not determined.

bacteria and mycobacteria since the 1960s.^{2,3,8} Since they demonstrated instabilities and cytotoxicity, they were not

developed further as a drug. Nevertheless, they are considered as a tractable lead structure that can be optimized for

selectivity, stability, and potency and serve foremost as antitubercular agents. Consequently, all compounds that could be obtained in sufficient amounts were subjected to a cytotoxicity and antimicrobial screening. In antifungal assays no activity could be observed. Overall, the tested compounds were at best weakly active against a panel of human pathogenic bacteria (Table 3). However, the known compounds plicacetin (2), the unnamed pyrimidine nucleoside (3),^{8d} and 40551-F (4)^{8e} as well as the new compounds 6, 7, and 11 were found to be active toward mycobacteria. In the case of the known pyrimidine nucleosides and to a lesser extent compound 7, this activity was accompanied by cytotoxicity (Table 3). Complementary to the *in vivo* assays, the compounds were further tested, employing an *in vitro* translation assay (IVTA). Unexpectedly, the binding to the ribosomal target did not correlate necessarily with the whole cell activity. This can be demonstrated by compound 4, which exhibited comparably strong inhibition in the IVTA, but displayed weak or moderate activity against *M. tuberculosis* and *M. smegmatis*, respectively. In contrast, 7 showed only a weak effect in the IVTA and weak activity against *M. tuberculosis* but a potent activity against *M. smegmatis*. Thus, it appears that inhibition of translation is possibly not the only mode of action by which pyrimidine nucleosides mediate their activity against mycobacteria.

EXPERIMENTAL SECTION

General Experimental Procedures. Optical rotation values were measured on a Jasco P-2000 polarimeter, using a 3.5 mm × 10 mm cylindrical quartz cell. UV spectra were taken on a PerkinElmer Lambda 25 UV/vis spectrometer. ECD spectra were conducted using a Jasco J-720 spectropolarimeter. Infrared spectra were obtained employing a Jasco FT/IR 4200 spectrometer, interfaced with a MIRAcle ATR device (ZnSe crystal). 1D and 2D NMR spectra were acquired on either a 400 MHz Bruker AVANCE III HD (400, 100, 40.56, and 376.5 MHz for ¹H, ¹³C, ¹⁵N, and ¹⁹F isotopes, respectively), a 600 MHz Bruker Avance III HDX (600 and 150 MHz for ¹H and ¹³C), or a 700 MHz Avance III HDX (700, 175, and 70.97 MHz for ¹H, ¹³C, and ¹⁵N isotopes) NMR spectrometer, equipped with a 5 mm broadband SMART, Prodigy BBO-cryo, or Prodigy TCI cryo probe head, respectively. All spectra were recorded in either *d*₄-MeOH ($\delta_{\text{H}}/\delta_{\text{C}}$ 3.31/49.0) or *d*₆-DMSO ($\delta_{\text{H}}/\delta_{\text{C}}$ 2.50/39.5), respectively, and referenced to the residual solvent signals or the internal offset for ¹⁵N assigned by the instrument manufacturer. ¹⁹F NMR chemical shifts were calculated relative to CF₃COOH (δ_{F} −76.55). High-resolution mass spectra were acquired on an HR-ESI-TOF-MS Bruker maXis 4G mass spectrometer. HPLC was performed with a Waters system, consisting of a Waters 1525 pump with a built-in degasser, a Waters 996 photodiode array detector, and a Rheodyne 7725i injector, operated by the software Millennium32. For LC-MS analysis, an 1100 Series Agilent HPLC system was fitted with a G1322A degasser, a G1312A binary pump, a G1329A autosampler, and a G1315A diode array detector. The Agilent HPLC components were connected with an ABSCIEX 3200 QTRAP LC/MS/MS mass spectrometer. All solvents were purchased as HPLC or LC-MS grade, respectively. Steam sterilization of medium components and waste was performed at 121 °C for 15 min at 2.1 bar using a Systec VX-150 autoclave, equipped with air exhaust filtration.

Bacterial Strains. Strain SHP 22-7 was collected and isolated by one of the authors (I.H.) from a mangrove soil sample obtained from Enggano Island, Indonesia, and subsequently genome sequenced.^{1,5} For the bioassay experiments, all ATCC strains were provided by the American Type Culture Collection, while *A. baumannii* 09987 was obtained from the University of Bonn, Germany, and *Bacillus subtilis* 168 was provided by Prof. Hamoen, University of Amsterdam, The Netherlands, respectively.

Cultivation of SHP 22-7. For production of the nucleoside antibiotics, strain SHP 22-7 was grown in 200 mL of NL 410

preculture medium, consisting of glucose (10 g L⁻¹), glycerol (10 g L⁻¹), oatmeal (5 g L⁻¹), soy flour (10 g L⁻¹), yeast extract (5 g L⁻¹), Bacto casamino acids (5 g L⁻¹), CaCO₃ (1 g L⁻¹), and distilled water (pH was adjusted to 7.0 with NaOH) in 1 L Erlenmeyer flasks (with steel springs) on an orbital shaker (180 rpm) at 28 °C. After 3 days of cultivation, 200 mL of preculture was transferred to 2 L of main culture medium NL 300, consisting of mannitol (20 g L⁻¹), cotton seed (20 g L⁻¹), and distilled water (pH adjusted to pH 7.5 with NaOH). Cultures were grown for 4 days at 28 °C in 5 L Erlenmeyer flasks (with steel springs) on an orbital shaker (180 rpm). In total, a volume of 26 L of SHP 22-7 culture has been used for the isolation of compounds 1–10.

Extraction and Isolation. Portions of 2 L of the culture broth were extracted with the same volume of ethyl acetate for 3 h at RT. Samples were centrifuged at 4,000 rpm for 15 min. The upper organic phase was dried *in vacuo*. The crude extract was subjected to open column chromatography employing Sephadex LH20 as stationary phase and MeOH as mobile phase, yielding five subfractions. LC-MS profiling of these fractions indicated the presence of compound 1 (1.9 mg) in the first fraction and that the third fraction contained compounds with the targeted fragmentation pattern. The separation of this fraction was performed by RP-HPLC using a linear gradient of 50:50 to 100:0 MeOH–H₂O (0.1% TFA) over a period of 30 min, followed by isocratic elution at 100% MeOH for an additional 10 min (Phenomenex C₁₈ Luna, 10 × 250 mm, 5 μm; 2 mL/min flow rate; UV monitoring at 215 nm). It is noteworthy to mention that initially the aqueous phase contained 0.1% trifluoroacetic acid. However, this solvent system led to rapid degradation of the nucleosides. Therefore, either purified H₂O or a 1 M phosphate buffer was used as aqueous solvent. RP-HPLC separation of the three obtained subfractions (Phenomenex Omega-polar, 250 × 10.0 mm, 5 μm; isocratic elution with MeOH–H₂O (65:35), 2 mL/min) yielded compounds 2 (44.0 mg), 3 (4.1 mg), 4 (4.9 mg), 5 (2.5 mg), 6 (9.2 mg), 7 (13.9 mg), 8 (5.9 mg), 9 (8.4 mg), 10 (11.3 mg), and upon feeding 11 (3.7 mg). In case of contamination with lipids, the same conditions were applied, using a Phenomenex C₅ column (250 × 4.6 mm).

Zincphyrin III (1): reddish-pink powder (Figure S2); ¹H NMR and ¹³C NMR data, see Table S1; HRESIMS *m/z* 715.1754 [M – H][−] (calcd for C₃₆H₃₆N₄O₈⁶⁴Zn, 715.1746; Δ +1.1 ppm) (Figure S3).

Plicacetin (2): amorphous, white opaque powder; [α]_D²⁵ +92.3 (c 0.95, MeOH); UV (MeOH) λ_{max} (log ϵ) 255 (4.36), 326 (4.67) nm; FT-IR (ATR) ν_{max} 3352, 3228, 2928, 1648, 1603, 1482, 1253, 1180, 1026 cm^{−1}; ¹H NMR and ¹³C NMR data, see Table S2; HRESIMS *m/z* 518.2602 [M + H]⁺ (calcd for C₂₅H₃₆N₃O₁₁, 518.2615; Δ −2.5 ppm).

Unnamed pyrimidine nucleoside (3): amorphous, white opaque powder; [α]_D²³ +95.1 (c 0.41, MeOH); UV (MeOH) λ_{max} (log ϵ) 255 (4.16), 313 (4.59) nm; FT-IR (ATR) ν_{max} 3362, 2924, 1653, 1569, 1490, 1137, 1087, 1023 cm^{−1}; ¹H NMR and ¹³C NMR data, Table S3; HRESIMS *m/z* 499.2215 [M + H]⁺ (calcd for C₂₂H₃₅N₄O₇S, 499.2226; Δ −2.2 ppm).

40551-F (4): amorphous, white opaque powder; [α]_D²³ +100.6 (c 2.46, MeOH); UV (MeOH) λ_{max} (log ϵ) 263 (4.34), 303 (4.06) nm; FT-IR (ATR) ν_{max} 3419, 2924, 1674, 1443, 1189, 1132 cm^{−1}; ¹H NMR and ¹³C NMR data, see Table S4; HRESIMS *m/z* 481.2657 [M + H]⁺ (calcd for C₂₃H₃₇N₄O₇, 481.2662; Δ −1.0 ppm).

CAS 51693-93-7 (5): amorphous, white opaque powder; ¹H NMR and ¹³C NMR data, see Table S5; HRESIMS *m/z* 503.2497 [M + H]⁺ (calcd for C₂₅H₃₅N₄O₇, 503.2506; Δ −1.8 ppm).

Cytosaminomycin F (6): amorphous, white opaque powder; [α]_D²² +75.3 (c 0.76, MeOH); UV (MeOH) λ_{max} (log ϵ) 204 (4.49), 248 (4.33), 298 (3.95) nm; ECD (MeOH) λ_{max} ($\Delta\epsilon$) 204 (+4.15), 222 (−5.00), 262 (+4.05), 299sh (+2.83) nm; FT-IR (ATR) ν_{max} 3383, 2925, 1673, 1201, 1133, 1026 cm^{−1}; ¹H NMR and ¹³C NMR data, see Tables 1 and 2; HRESIMS *m/z* 511.3119 [M + H]⁺ (calcd for C₂₅H₄₃N₄O₇, 511.3132; Δ +1.8 ppm).

Cytosaminomycin G (7): amorphous, white opaque powder; [α]_D²³ +92.3 (c 0.59, MeOH); UV (MeOH) λ_{max} (log ϵ) 255 (4.31), 332 (4.59) nm; FT-IR (ATR) ν_{max} 3317, 2967, 2926, 2868, 1653, 1603, 1482, 1253, 1181, 1034 cm^{−1}; ¹H NMR and ¹³C NMR data, see

Tables 1, 2, and S6; HRESIMS m/z 588.3035 $[M + H]^+$ (calcd for $C_{29}H_{42}N_5O_8$, 588.3033; Δ +0.3 ppm).

Streptocytosine D (8): amorphous, white opaque powder; $[\alpha]_D^{23}$ +33.3 (c 0.30, MeOH); UV (MeOH) λ_{max} ($\log \epsilon$) 264 (4.27), 300 (3.92) nm; FT-IR (ATR) ν_{max} 2928, 2868, 1674, 1636, 1489, 1202, 1132, 1054 cm^{-1} ; 1H NMR and ^{13}C NMR data, see Table S7; HRESIMS m/z 308.1610 $[M + H]^+$ (calcd for $C_{15}H_{22}N_3O_4$, 308.1610; Δ 0.0 ppm).

Streptocytosine E (9): amorphous, white opaque powder; $[\alpha]_D^{23}$ +50.0 (c 0.24, MeOH); UV (MeOH) λ_{max} ($\log \epsilon$) 214 (4.45), 248 (4.32), 300 (3.94) nm; 1H NMR and ^{13}C NMR data, see Table S8; HRESIMS m/z 310.1766 $[M + H]^+$ (calcd for $C_{15}H_{24}N_3O_4$, 310.1767; Δ -0.3 ppm).

Streptocytosine P (10): amorphous, white opaque powder; UV (MeOH) λ_{max} ($\log \epsilon$) 211 (4.52), 248 (4.33), 292 (4.09) nm; ECD (MeOH) λ_{max} ($\Delta\epsilon$) 206 (+8.86), 223 (-12.49), 263 (+8.75), 298 (+7.47) nm; FT-IR (ATR) ν_{max} 2924, 2871, 1672, 1491, 1183, 1134, 1056 cm^{-1} ; 1H NMR and ^{13}C NMR data, see Tables 1 and 2; HRESIMS m/z 310.1766 $[M + H]^+$ (calcd for $C_{15}H_{24}N_3O_4$, 310.1767; Δ -0.3 ppm).

12-F-Plicacetin (11): amorphous, white opaque powder; $[\alpha]_D^{23}$ +47.4 (c 0.97, MeOH); UV (MeOH) λ_{max} ($\log \epsilon$) 259 (4.15), 305 (3.85) nm; FT-IR (ATR) ν_{max} 3361, 2921, 2850, 1682, 1655, 1489, 1202, 1136, 1023 cm^{-1} ; 1H NMR and ^{13}C NMR data, see Tables 1 and 2; HRESIMS m/z 521.2413 $[M + H]^+$ (calcd for $C_{25}H_{33}FN_4O_7$, 521.2412; Δ +0.2 ppm).

Enantioselective HPLC-MS Analysis of the Branched Fatty Acid Side Chains of Compounds 6 and 10. For the determination of the absolute configuration of the side chains of 6 and 10, both compounds were subjected to the same sample preparation procedure. The compounds were dissolved in 6 N HCl and heated to 110 °C overnight. With this hydrolysis step, the chiral carboxylic acids 2-methyl butyric acid of 10 and 4-methyl hexanoic acid of 6, respectively, were cleaved from the nucleoside backbone. After hydrolysis, a liquid–liquid extraction step of the branched short-chained fatty acids was performed with hexane. The organic layer was collected and dried, and the residue was directly employed for derivatization. As derivatization agent, 1-naphthylamine was used in combination with 1-ethyl-3-(3-dimethylaminopropyl)carbodiimide (EDC), dissolved in 2-propanol. Derivatization was allowed to proceed while shaking at 25 °C for 12 h. After drying of the product, it was reconstituted in the respective mobile phase.

The analytical standards, *rac*-2-methyl butyric acid, (*S*)-2-methyl butyric acid, and *rac*-4-methyl hexanoic acid, were supplied by Sigma-Aldrich (Merck, Munich, Germany), (*R*)-2-methyl butyric acid was from Activate Scientific (Prien am Chiemsee, Germany), and (*S*)-4-methyl hexanoic acid and (*R*)-4-methyl hexanoic acid were supplied by Chemspace (Riga, Latvia).

HPLC-UV analysis was performed on an Agilent 1260 LC-system from Agilent Technologies (Waldbronn, Germany) equipped with a quaternary pump, a degasser, an autosampler, and a UV-DAD detector.

HPLC-MS analysis was performed on an Agilent 1290 LC-system with an API 4000 QQQ MS system from AB Sciex (Toronto, Ontario, Canada) and an HTC PAL autosampler from CTC Analytics (Zwingen, Switzerland). For data acquisition an MS² product ion scan was performed for both compounds with the following settings: declustering potential: 100.0 V, entrance potential: -10.0 V, collision energy: -30.0 V, collision cell exit potential: 36.0 V, collision gas: 4 psi, curtain gas: 30 psi, ion source gas 1: 30 psi, ion source gas 2: 20 psi, ionspray voltage: 5500.0 V, temp: 450 °C. Measurements were performed in multiple reaction monitoring mode, using the following transitions: m/z 228.138 \rightarrow 144.080 (2-methyl butyric acid); m/z 256.160 \rightarrow 144.080 (4-methyl hexanoic acid).

Both chiral columns (Chiralpak IB-U and IH-U, 100 \times 3 mm, 1.6 μm fully porous particles) were obtained from Daicel (Tokyo, Japan). HPLC-UV measurements for 2-methyl butyric acid on Chiralpak IB-U were performed in normal phase, using hexane–isopropanol (95/5; v/v) as mobile phase. Flow rate was set to 1 mL/min, and column temperature was held constant at 25 °C. Detection wavelength was

215 nm. MS measurements for this compound were conducted on the same column but in reversed phase gradient elution mode with water + 0.1% acetic acid (A) and acetonitrile + 0.1% acetic acid (B) in isocratic mode (55/45). Column temperature was set to 10 °C, and flow rate was 0.2 mL/min. HPLC-UV measurements for 4-methyl hexanoic acid on Chiralpak IH-U were performed in reversed phase gradient elution mode with water + 0.1% acetic acid (A) and acetonitrile + 0.1% acetic acid (B). The gradient was as follows: 0 min 20% B, 30 min 90% B, 30.01 min 20% B, 36 min 20% B. Flow rate was set to 0.2 mL/min, and column temperature was held constant at 25 °C. Detection wavelength was 215 nm. MS measurements for this compound were conducted with the following gradient: 0 min 20% B, 37.50 min 90% B, 37.51 min 20% B, 45 min 20% B. Flow rate was set to 0.2 mL/min, and column temperature was held constant at 10 °C.

The IH-U column showed an elution order of R before S for 4-methyl-N-1-naphthylhexanamide and hence proved that the hydrolysis product of 6 is S-configured (Figures S79 and S80). On the IB-U column an elution order of S before R was determined for 2-methyl-N-1-naphthylbutanamide. Injection of the sample and co-injections with enantiomeric standards established an S-configuration for the hydrolysis product of 10 (Figure S81).

Antifungal Assay. The minimal inhibitory concentration (MIC) of pure compounds against different *Candida* clinical isolates was determined by broth microdilution using the direct colony suspension method with an inoculum of $(0.5\text{--}2.5) \times 10^5$ CFU/mL, according to the recommendations of the European Committee on Antimicrobial Susceptibility Testing (EUCAST).¹³ Caspofungin was used as reference antifungal agent. MIC testing was performed in sterile 96-well microdilution plates using MOPS-buffered RPMI 1640 medium supplemented with glucose to a final concentration of 2%, pH 7.0. MICs were read after incubation of the microplates at 37 °C for 48 h.

Antibacterial Assay. The MIC was determined in cation-adjusted Mueller-Hinton medium that contains casein, beef extract, and starch by using a 2-fold serial dilution method according to the standards and guidelines of the Clinical and Laboratory Standards Institute.¹⁴ In brief, a 2-fold serial dilution of the test compound was prepared in microtiter plates and seeded using a final test concentration of bacteria of 5×10^5 CFU/mL. After the overnight incubation at 37 °C, the MIC was determined as the lowest compound concentration preventing visible bacterial growth. The strain panel included representative species of nosocomial pathogens, known as “ESKAPE” bacteria. Specifically, the following strains were used: *Enterococcus faecium* BM 4147-1, *Staphylococcus aureus* ATCC 29213, *Klebsiella pneumoniae* ATCC 12657, *Acinetobacter baumannii* 09987, *Pseudomonas aeruginosa* ATCC 27853, and *Enterobacter aerogenes* ATCC 13048. *Bacillus subtilis* 168, *Escherichia coli* ATCC 25922, and *Mycobacterium smegmatis* mc² 155 ATCC 700084 were used as further reference strains.

Antibacterial Assay against *Mycobacterium tuberculosis*. *M. tuberculosis* (Mtb) strain H37Rv (ATCC 25618) carrying an mCherry-expressing plasmid (pCherry10)¹⁵ was cultured in 7H9 complete medium (BD Difco; Becton Dickinson) supplemented with oleic acid–albumin dextrose–catalase (OADC, 10%; BD), 0.2% glycerol, and 0.05% Tween80. At mid log phase ($OD_{600} = 0.4$) cultures were harvested and frozen in aliquots at -80 °C as previously described.¹⁶ Frozen aliquots of mCherry-Mtb H37Rv were thawed and centrifuged (3700g, 10 min). Supernatants were discarded, and bacteria were thoroughly resuspended in 7H9 medium (10% OADC) in the absence of glycerol and Tween80 by use of a syringe and a 26-gauge syringe needle. Compounds were tested in triplicates (2×10^5 bacteria, volume 100 μL) for their antitubercular activity in 2-fold serial dilutions starting from 64 μM using 96-well flat clear-bottom black polystyrene microplates (Corning CellBIND, New York, USA) as recently described.¹⁷ Bacterial growth was measured as relative light units (RLU) from the fluorescence intensity obtained at an excitation wavelength of 575 nm and an emission wavelength of 635 nm (Synergy 2, BioTek Instruments, VT, USA) after 7 days of culture at 37 °C. Obtained values were normalized to RLU values of the solvent control (DMSO-treated bacteria set to 100%), and a MIC₉₅ value of each compound was determined. MIC₉₅ was defined as the minimum

concentration of the compound required to achieve a reduction in fluorescence by 95%. Obtained MIC values were validated by a visual resazurin microtiter assay¹⁸ by adding 30 μ L of 0.02% resazurin (Cayman) solution to each well followed by another 20 h of culture without agitation (data not shown).

In Vitro Translation Assay. An *in vitro* translation assay was performed to assess the potency of the compounds on bacterial translation in a cell-free system. The assay is based on S30 extracts prepared from logarithmically growing *E. coli* MRE600,¹⁹ an RNase I deficient strain, according to a procedure described by Zubay.²⁰ For the assay, the pET14b-luc plasmid was constructed by integrating the gene encoding firefly (*Photinus pyralis*) luciferase into the pET14b (Novagen) vector. In the pET14b-luc plasmid, the luciferase is transcribed from a phage T7 promoter, allowing the selective detection of bacterial translation inhibitors by measuring luminescence. Inhibitors of bacterial transcription do not affect the assay because transcription is performed by the phage T7 RNA polymerase. Apart from the S30 extract and the pET14b-luc plasmid, the reaction mixture contained the following supplements: T7 RNA polymerase (182 U/mL, Thermo Scientific), 2.5 mM ATP, 0.5 mM GTP, 0.5 mM UTP, 0.5 mM CTP, 20 amino acids (0.04 mM each), an ATP regenerating system (creatine phosphokinase/phosphocreatine), 3.2% (w/v) polyethylene glycol 600, 8 mM putrescine, and 2 mM DTT in an appropriate buffer system (40 mM triethylamine pH 7.5, 140 mM potassium acetate, 8 mM magnesium acetate, 20 mM ammonium acetate, 1.4 mM spermidine). *In vitro* translation reactions were performed for 2 h at 25 °C. After addition of the substrate luciferin, chemiluminescence was recorded in a multiplate reader (SPARK, TECAN). The IC₅₀ was determined as the concentration that led to 50% reduction of luminescence compared to an untreated control.

Cytotoxicity Assay. The cytotoxicity test against the HeLa human cervical carcinoma cell line was performed in RPMI cell culture medium supplemented with 10% fetal bovine serum using the 7-hydroxy-3H-phenoxazin-3-one-10-oxide (resazurin) assay. A 2-fold serial dilution of the test compounds was prepared in duplicates in a microtiter plate and seeded with trypsinized HeLa cells to a final cell concentration of 1×10^4 cells per well. After 24 h of incubation at 37 °C, with 5% CO₂ and 95% relative humidity, resazurin was added at a final concentration of 200 μ M, and cells were again incubated overnight. Cell viability was assessed by determining the reduction of resazurin to the fluorescent resorufin. Fluorescence was measured in a TECAN M200 reader at an excitation wavelength of 560 nm and an emission wavelength of 600 nm in relation to an untreated control.

■ ASSOCIATED CONTENT

SI Supporting Information

The Supporting Information is available free of charge at <https://pubs.acs.org/doi/10.1021/acs.jnatprod.1c01051>.

Spectroscopic data (HRESIMS, IR, UV, 1D and 2D NMR spectra), enantioselective analyses, bioinformatics analyses, and biological assay details (PDF)

■ AUTHOR INFORMATION

Corresponding Author

Harald Gross – Pharmaceutical Institute, Department of Pharmaceutical Biology, University of Tübingen, 72076 Tübingen, Germany; German Center for Infection Research (DZIF), partner site Tübingen, 72076 Tübingen, Germany; orcid.org/0000-0002-0731-821X; Phone: +49-7071-2976970; Email: harald.gross@uni-tuebingen.de; Fax: +49-7071-295250

Authors

Niraj Aryal – Pharmaceutical Institute, Department of Pharmaceutical Biology, University of Tübingen, 72076 Tübingen, Germany

Junhong Chen – Pharmaceutical Institute, Department of Pharmaceutical Biology, University of Tübingen, 72076 Tübingen, Germany

Keshab Bhattarai – Pharmaceutical Institute, Department of Pharmaceutical Biology, University of Tübingen, 72076 Tübingen, Germany

Oliver Hennrich – Department of Microbial Bioactive Compounds, Interfaculty Institute of Microbiology and Infection Medicine, Tübingen (IMIT), Cluster of Excellence ‘Controlling Microbes to Fight Infections’, University of Tübingen, 72076 Tübingen, Germany

Ira Handayani – Research Center for Biotechnology, National Research and Innovation Agency of Indonesia (RC Biotechnology BRIN), 16911 Bogor, West Java, Indonesia

Markus Kramer – Institute of Organic Chemistry, University of Tübingen, 72076 Tübingen, Germany

Jan Straetener – Department of Microbial Bioactive Compounds, Interfaculty Institute of Microbiology and Infection Medicine, Tübingen (IMIT), Cluster of Excellence ‘Controlling Microbes to Fight Infections’, University of Tübingen, 72076 Tübingen, Germany

Tatjana Wommer – Department of Microbial Bioactive Compounds, Interfaculty Institute of Microbiology and Infection Medicine, Tübingen (IMIT), Cluster of Excellence ‘Controlling Microbes to Fight Infections’, University of Tübingen, 72076 Tübingen, Germany

Anne Berscheid – Department of Microbial Bioactive Compounds, Interfaculty Institute of Microbiology and Infection Medicine, Tübingen (IMIT), Cluster of Excellence ‘Controlling Microbes to Fight Infections’, University of Tübingen, 72076 Tübingen, Germany; orcid.org/0000-0003-1585-8715

Silke Peter – Institute of Medical Microbiology and Hygiene, University of Tübingen, 72076 Tübingen, Germany; German Center for Infection Research (DZIF), partner site Tübingen, 72076 Tübingen, Germany

Norbert Reiling – Microbial Interface Biology, Research Center Borstel, Leibniz Lung Center, 23845 Borstel, Germany; German Center for Infection Research (DZIF), partner site Hamburg-Lübeck-Borstel-Riems, 20095 Hamburg, Germany; orcid.org/0000-0001-6673-4291

Heike Brötz-Oesterhelt – Department of Microbial Bioactive Compounds, Interfaculty Institute of Microbiology and Infection Medicine, Tübingen (IMIT), Cluster of Excellence ‘Controlling Microbes to Fight Infections’, University of Tübingen, 72076 Tübingen, Germany; German Center for Infection Research (DZIF), partner site Tübingen, 72076 Tübingen, Germany; orcid.org/0000-0001-9364-1832

Christian Geibel – Pharmaceutical Institute, Department of Pharmaceutical Analysis and Bioanalysis, University of Tübingen, 72076 Tübingen, Germany

Michael Lämmerhofer – Pharmaceutical Institute, Department of Pharmaceutical Analysis and Bioanalysis, University of Tübingen, 72076 Tübingen, Germany; orcid.org/0000-0002-1318-0974

Yvonne Mast – German Center for Infection Research (DZIF), partner site Tübingen, 72076 Tübingen, Germany; Department of Bioresources for Bioeconomy and Health Research, Leibniz Institute DSMZ-German Collection of Microorganisms and Cell Cultures, 38124 Braunschweig, Germany

Complete contact information is available at:

<https://pubs.acs.org/10.1021/acs.jnatprod.1c01051>

Notes

The authors declare no competing financial interest.

ACKNOWLEDGMENTS

We like to thank Dr. D. Wistuba and her team (Mass Spectrometry Department, Institute for Organic Chemistry, University of Tübingen, Germany) for HR-MS measurements. Thanks are also due to L. Niwinski (Research Center Borstel, Leibniz Lung Center Borstel, Germany), to A. Heyne (Pharmaceutical Institute, University of Tübingen, Germany), and to Leo Endres (Institute for Microbiology and Infection Medicine, University of Tübingen) for performing the antitubercular assays, for supporting the compound isolation process, and for validating the T7 translation assay, respectively. We gratefully acknowledge the funding received from the BMBF German–Indonesian cooperation project NAbAUnAk (16GW0124K) and the Baden-Württemberg-Stiftung (BWST_WSF-035). I.H. is grateful for the RISET-Pro scholarship program from the Indonesian Ministry for Research and Technology (World Bank Loan No. 8245-ID). N.A. is thankful for his Ph.D. scholarship (grant PKZ 91609054), generously provided by the German Academic Exchange Service (DAAD). H.B.-O. and S.P. acknowledge funding by the German Center for Infection Research (DZIF, TTU 09.818), and A.B. and T.W. support by the BMBF (Gram-NEG design). The authors H.G. and H.B.-O. gratefully acknowledge financial support from the German Research Foundation (DFG), TRR261, project ID 398967434.

DEDICATION

Dedicated to Dr. William H. Gerwick, University of California at San Diego, for his pioneering work on bioactive natural products.

REFERENCES

- (1) Handayani, I.; Saad, H.; Ratnakomala, S.; Lisdiyanti, P.; Kusharyoto, W.; Krause, J.; Kulik, A.; Wohlleben, W.; Aziz, S.; Gross, H.; Gavriilidou, A.; Ziemert, N.; Mast, Y. *Mar. Drugs* **2021**, *19*, 316.
- (2) (a) Flynn, E. H.; Hinman, J. W.; Caron, E. L.; Woolf, D. O., Jr. *J. Am. Chem. Soc. USA* **1953**, *75*, 5867–6871. (b) Stevens, C. L.; Nagarajan, K.; Haskell, T. H. *J. Org. Chem.* **1962**, *2*, 2991–3005. (c) Evans, J. R.; Weare, G. *J. Antibiot.* **1977**, *30*, 604–606. (d) Shiomi, K.; Haneda, K.; Tomoda, H.; Iwai, Y.; Omura, S. *J. Antibiot.* **1994**, *47*, 782–786.
- (3) (a) Carrasco, L.; Vázquez, D. *Med. Res. Rev.* **1984**, *4*, 471–512. (b) Shammas, C.; Donarski, J. A.; Ramesh, V. *Magn. Reson. Chem.* **2007**, *45*, 133–141. (c) Serrano, C. M.; Reddy, H. R. K.; Eiler, D.; Koch, M.; Tresco, B. I. C.; Barrows, L. R.; VanderLinden, R. T.; Testa, C. A.; Sebahar, P. R.; Looper, R. E. *Angew. Chem., Int. Ed.* **2020**, *59*, 11330–11333. (d) Nelli, M. R.; Heitmeier, K. N.; Looper, R. E. *Acc. Chem. Res.* **2021**, *54*, 2798–2811.
- (4) Zhang, G.; Zhang, H.; Li, S.; Xiao, J.; Zhang, G.; Zhu, Y.; Niu, S.; Ju, J.; Zhang, C. *Appl. Environ. Microbiol.* **2012**, *87*, 2393–2401.
- (5) Handayani, I.; Ratnakomala, S.; Lisdiyanti, P.; Fahrurrozi, F.; Kusharyoto, W.; Alanjary, M.; Ort-Winklbauer, R.; Kulik, A.; Wohlleben, W.; Mast, Y. *Microbiol. Resour. Announc.* **2018**, *7*, e01317–18.
- (6) Krause, J.; Handayani, I.; Blin, K.; Kulik, A.; Mast, Y. *Front. Microbiol.* **2020**, *11*, 225.
- (7) (a) Toriya, M.; Yaginuma, S.; Murofushi, S.; Ogawa, K.; Muto, N.; Hayashi, M.; Matsumoto, K. *J. Antibiot.* **1993**, *46*, 196–200. (b) Anttila, J.; Heinonen, P.; Nenonen, T.; Pino, A.; Iwai, H.; Kauppi, E.; Saliymani, R.; Baumann, M.; Saksi, J.; Suni, N.; Haltia, T. *Biochim. Biophys. Acta Bioenergetics* **2011**, *1807*, 311–318. (c) Nguyen, H. T.; Pham, V. T. T.; Nguyen, C. T.; Pokhrel, A. R.; Kim, T.-S.; Kim, D.; Na, K.; Yamaguchi, T.; Sohng, J. K. *Appl. Microbiol. Biotechnol.* **2020**, *104*, 713–724.
- (8) (a) Bu, Y.-Y.; Yamazaki, H.; Ukai, K.; Namikoshi, M. *Mar. Drugs* **2014**, *12*, 6102–6112. (b) Aksoy, S. C.; Uzel, A.; Bedir, E. *J. Antibiot.* **2016**, *69*, 51–56. (c) Xu, C.-D.; Zhang, H.-J.; Ma, Z.-J. *J. Nat. Prod.* **2019**, *82*, 2509–2516. (d) Kate, A. S.; George, S. D.; Sonawane, S.; Periyasamy, G. Patent, WO 2013/144894, 2013. (e) Tomoda, H.; Koyama, N.; Kanamoto, A.; Hashimoto, J.; Kozono, I. Patent, WO 2019/044941, 2019.
- (9) Yun, M.-K.; Wu, Y.; Li, Z.; Zhao, Y.; Waddell, M. B.; Ferreira, A. M.; Lee, R. E.; Bashford, D.; White, S. W. *Science* **2012**, *335*, 1110–1114.
- (10) (a) Guo, H.; Schmidt, A.; Stephan, P.; Raguz, L.; Braga, D.; Kaiser, M.; Dahse, H.-M.; Weigel, C.; Lackner, G.; Beemelmans, C. *ChemBioChem* **2018**, *19*, 2307–2311. (b) Moschny, J.; Lorenzen, W.; Hilfer, A.; Eckenstaler, R.; Jahns, S.; Enke, H.; Enke, D.; Schneider, P.; Benndorf, R. A.; Niedermeyer, T. H. *J. Nat. Prod.* **2020**, *83* (83), 1960–1970.
- (11) (a) Thiericke, R.; Rohr, J. *Nat. Prod. Rep.* **1993**, *10*, 265–289. (b) Kirschning, A.; Taft, F.; Knobloch, T. *Org. Biomol. Chem.* **2007**, *5*, 3245–3259.
- (12) (a) Weigert, F. J.; Roberts, J. D. *J. Am. Chem. Soc. USA* **1971**, *93*, 2361–2369. (b) Pretsch, E.; Bühlmann, P.; Badertscher, M. *Spektroskopische Daten zur Strukturaufklärung organischer Verbindungen*; Springer Spektrum Press: Berlin, 2019. (c) Berger, S.; Braun, S.; Kalinowski, H.-O. *NMR-Spektroskopie von Nichtmetallen, Band 4, ¹⁹F-NMR-Spektroskopie*; Georg Thieme Press: Stuttgart, 1994.
- (13) Arendrup, M. C.; Meletiadis, J.; Mouton, J. W.; Lagrou, K.; Hamal, P.; Guinea, J.; Subcommittee on Antifungal Susceptibility Testing (AFST) of the ESCMID European Committee for Antimicrobial Susceptibility Testing (EUCAST). *Method for the determination of broth dilution minimum inhibitory concentrations of antifungal agents for yeasts*. EUCAST Definitive Document E.DEF 7.3.2; April 2020. Accessed under https://www.eucast.org/astoffungi/methodsinantifungalsusceptibilitytesting/susceptibility_testing_of_yeasts/.
- (14) Patel, J. B.; Cockerill, F. R.; Bradford, P. A.; Eliopoulos, G. M.; Hindler, J. A.; Jenkins, S. G.; Lewis, J. S.; Limbago, B.; Miller, L. A.; Nicolau, D. P.; Powell, M.; Swenson, J. M.; Turnidge, J. D.; Weinstein, M. P.; Zimmer, B. L. *Methods for Dilution Antimicrobial Susceptibility Tests for Bacteria that Grow Aerobically. Approved Standard*, Vol. 35, 10th ed.; Clinical and Laboratory Standards Institute, USA, 2015.
- (15) Zelmer, A.; Carroll, P.; Andreu, N.; Hagens, K.; Mahlo, J.; Redinger, N.; Robertson, B. D.; Wiles, S.; Ward, T. H.; Parish, T.; Ripoll, J.; Bancroft, G. J.; Schaible, U. *J. Antimicrob. Chemother.* **2012**, *67*, 1948–1960.
- (16) Reiling, N.; Homolka, S.; Walter, K.; Brandenburg, J.; Niwinski, L.; Ernst, M.; Herzmann, C.; Lange, C.; Diel, R.; Ehlers, S.; Niemann, S. *mBio* **2013**, *4*, e00250–13.
- (17) Jumde, R. P.; Guardigni, M.; Gierse, R. M.; Alhayek, A.; Zhu, D.; Hamid, Z.; Johannsen, S.; Elgaher, W. A. M.; Neusens, P. J.; Nehls, C.; Haupenthal, J.; Reiling, N.; Hirsch, K. H. *Chem. Sci.* **2021**, *12*, 7775–7785.
- (18) Franzblau, S. G.; DeGroot, M. A.; Cho, S. H.; Andries, K.; Nuermberger, E.; Orme, I. M.; Mdluli, K.; Angulo-Barturen, I.; Dick, T.; Dartois, V.; Lenaerts, A. *J. Tuberculosis* **2012**, *92*, 453–488.
- (19) Wade, H. E.; Robinson, H. K. *Biochem. J.* **1966**, *101*, 467–79.
- (20) Zubay, G. *Annu. Rev. Genetics* **1973**, *7*, 267–287.

High Plasticity of the Amicetin Biosynthetic Pathway in *Streptomyces* sp. SHP 22-7 Led to the Discovery of Streptcytosine P and Cytosaminomycins F and G and Facilitated the Production of 12F-Plicacetin

SUPPORTING INFORMATION

Table of Contents

Spectral Data

Figure S1	Characteristic MS/MS fragments of pyrimidine nucleosides
Figure S2	Pink-reddish color of 1
Figure S3	HR-ESI-MS spectrum (negative mode) of 1
Figure S4	400 MHz ¹ H NMR spectrum of zincphyrin III (1) in <i>d</i> ₆ -DMSO
Figure S5	100 MHz ¹³ C NMR spectrum of zincphyrin III (1) in <i>d</i> ₆ -DMSO
Table S1	Tabulated NMR data of zincphyrin III (1), recorded in <i>d</i> ₆ -DMSO
Figure S6	400 MHz ¹ H NMR spectrum of plicacetin (2) in <i>d</i> ₄ -MeOH
Figure S7	100 MHz ¹³ C NMR spectrum of plicacetin (2) in <i>d</i> ₄ -MeOH
Table S2	Tabulated NMR data of plicacetin (2), recorded in <i>d</i> ₄ -MeOH
Figure S8	FT-IR spectrum of plicacetin (2)
Figure S9	HR-ESI-MS spectrum of unnamed pyrimidine nucleoside (3)
Figure S10	400 MHz ¹ H NMR spectrum of unnamed pyrimidine nucleoside 3 in <i>d</i> ₆ -DMSO
Figure S11	100 MHz ¹³ C NMR spectrum of unnamed pyrimidine nucleoside 3 in <i>d</i> ₆ -DMSO
Table S3	Tabulated NMR data of unnamed pyrimidine nucleoside 3 (<i>d</i> ₆ -DMSO)
Figure S12	FT-IR spectrum of unnamed pyrimidine nucleoside 3
Figure S13	HR-ESI-MS spectrum of 40551-F (4)
Figure S14	400 MHz ¹ H NMR spectrum of 40551-F (4) in <i>d</i> ₄ -MeOH
Figure S15	100 MHz ¹³ C NMR spectrum of 40551-F (4) in <i>d</i> ₄ -MeOH
Figure S16	400 MHz edited ¹ H- ¹³ C HSQC NMR spectrum of 40551-F (4) in <i>d</i> ₄ -MeOH
Figure S17	400 MHz ¹ H- ¹ H COSY NMR spectrum of 40551-F (4) in <i>d</i> ₄ -MeOH
Figure S18	400 MHz ¹ H- ¹³ C HMBC NMR spectrum of 40551-F (4) in <i>d</i> ₄ -MeOH
Table S4	Tabulated NMR data of 40551-F (4), recorded in <i>d</i> ₄ -MeOH
Figure S19	FT-IR spectrum of 40551-F (4)
Figure S20	HR-ESI-MS and HR-ESI-MS/MS spectrum of CAS 51693-93-7 (5)
Figure S21	400 MHz ¹ H NMR spectrum of CAS 51693-93-7 (5) in <i>d</i> ₄ -MeOH
Figure S22	100 MHz ¹³ C NMR spectrum of CAS 51693-93-7 (5) in <i>d</i> ₄ -MeOH
Figure S23	400 MHz ¹ H- ¹ H-COSY NMR spectrum of CAS 51693-93-7 (5) in <i>d</i> ₄ -MeOH
Table S5	Tabulated NMR data of CAS 51693-93-7 (5), recorded in <i>d</i> ₄ -MeOH

Figure S24	400 MHz ^1H NMR spectrum of cytosaminomycin F (6) in d_4 -MeOH
Figure S25	175 MHz ^{13}C NMR spectrum of cytosaminomycin F (6) in d_4 -MeOH
Figure S26	600 MHz DEPT135 spectrum of cytosaminomycin F (6) in d_4 -MeOH
Figure S27	700 MHz edited ^1H - ^{13}C -HSQC spectrum of cytosaminomycin F (6) in d_4 -MeOH
Figure S28	700 MHz ^1H - ^1H COSY spectrum of cytosaminomycin F (6) in d_4 -MeOH
Figure S29	700 MHz ^1H - ^{13}C -HSQC-TOCSY spectrum of cytosaminomycin F (6) in d_4 -MeOH
Figure S30	Detail region of the ^1H - ^{13}C -HSQC-TOCSY spectrum of 6 and its interpretation
Figure S31	600 MHz ^1H - ^{13}C HMBC spectrum of cytosaminomycin F (6) in d_4 -MeOH
Figure S32	700 MHz ^1H - ^1H NOESY spectrum of cytosaminomycin F (6) in d_4 -MeOH
Figure S33	Visualization and interpretation of the NOESY data of 6
Figure S34	FT-IR spectrum of 6
Figure S35	CD spectrum of 6 in MeOH
Figure S36	400 MHz ^1H NMR spectrum of cytosaminomycin G (7) in d_4 -MeOH
Figure S37	100 MHz ^{13}C NMR spectrum of cytosaminomycin G (7) in d_4 -MeOH
Figure S38	400 MHz ^1H NMR spectrum of cytosaminomycin G (7) in d_6 -DMSO
Figure S39	100 MHz ^{13}C NMR spectrum of cytosaminomycin G (7) in d_6 -DMSO
Figure S40	400 MHz DEPT135 NMR spectrum of cytosaminomycin G (7) in d_6 -DMSO
Figure S41	400 MHz edited ^1H - ^{13}C HSQC NMR spectrum of 7 in d_6 -DMSO
Figure S42	400 MHz ^1H - ^1H COSY NMR spectrum of cytosaminomycin G (7) in d_6 -DMSO
Figure S43	400 MHz ^1H - ^{13}C HSQC-TOCSY NMR spectrum of 7 in d_6 -DMSO
Figure S44	400 MHz ^1H - ^{13}C HMBC NMR spectrum of cytosaminomycin G (7) in d_6 -DMSO
Figure S45	400 MHz ^1H - ^{15}N HSQC NMR spectrum of cytosaminomycin G (7) in d_6 -DMSO
Figure S46	400 MHz ^1H - ^{15}N HMBC NMR spectrum of cytosaminomycin G (7) in d_6 -DMSO
Table S6	Tabulated NMR data of cytosaminomycin G (7), recorded in d_6 -DMSO
Figure S47	FT-IR spectrum of cytosaminomycin G (7)
Figure S48	400 MHz ^1H NMR spectrum of streptcytosine D (8) in d_6 -DMSO
Figure S49	100 MHz ^{13}C NMR spectrum of streptcytosine D (8) in d_6 -DMSO
Table S7	Tabulated NMR data of streptcytosine D (8), recorded in d_6 -DMSO
Figure S50	FT-IR spectrum of streptcytosine D (8)
Figure S51	400 MHz ^1H NMR spectrum of streptcytosine E (9), recorded in d_6 -DMSO
Figure S52	100 MHz ^{13}C NMR spectrum of streptcytosine E (9), recorded in d_6 -DMSO
Table S8	Tabulated NMR data of streptcytosine E (9), recorded in d_6 -DMSO
Figure S53	400 MHz ^1H NMR spectrum of streptcytosine P (10) in d_4 -MeOH
Figure S54	100 MHz ^{13}C NMR spectrum of streptcytosine P (10) in d_4 -MeOH
Figure S55	400 MHz DEPT135 and 100 MHz ^{13}C NMR spectrum of 10 in d_4 -MeOH
Figure S56	400 MHz edited ^1H - ^{13}C -HSQC NMR spectrum of 10 in d_4 -MeOH
Figure S57	400 MHz ^1H - ^1H -COSY NMR spectrum of streptcytosine P (10) in d_4 -MeOH
Figure S58	400 MHz ^1H - ^{13}C -HSQC-TOCSY NMR spectrum of 10 in d_4 -MeOH
Figure S59	400 MHz ^1H - ^{13}C -HMBC NMR spectrum of streptcytosine P (10) in d_4 -MeOH
Table S9	Tabulated NMR data of streptcytosine P (10), recorded in d_4 -MeOH
Figure S60	700 MHz ^1H NMR spectrum of streptcytosine P (10) in d_6 -DMSO
Figure S61	175 MHz ^{13}C NMR spectrum of streptcytosine P (10) in d_6 -DMSO
Figure S62	700 MHz edited ^1H - ^{13}C -HSQC NMR spectrum of 10 in d_6 -DMSO
Figure S63	700 MHz ^1H - ^{15}N -HSQC NMR spectrum of streptcytosine P (10) in d_6 -DMSO

Figure S64 700 MHz ^1H - ^1H -COSY NMR spectrum of streptcytosine P (**10**) in d_6 -DMSO
Figure S65 700 MHz ^1H - ^{13}C -HMBC NMR spectrum of streptcytosine P (**10**) in d_6 -DMSO
Figure S66 700 MHz ^1H - ^1H -NOESY NMR spectrum of streptcytosine P (**10**) in d_6 -DMSO
Figure S67 Visualization and interpretation of the NOESY data of **10**
Figure S68 FT-IR spectrum of streptcytosine P (**10**)
Figure S69 CD spectrum of streptcytosine P (**10**) in MeOH

Figure S70 400 MHz ^1H NMR spectrum of 12F-plicacetin (**11**) in d_4 -MeOH
Figure S71 100 MHz ^{13}C NMR spectrum of 12F-plicacetin (**11**) in d_4 -MeOH
Figure S72 Superimposed ^{13}C NMR spectra of **11** and **2** in d_4 -MeOH
Figure S73 400 MHz edited ^1H - ^{13}C -HSQC NMR spectrum of **11** in d_4 -MeOH
Figure S74 400 MHz ^1H - ^1H COSY NMR spectrum of 12F-plicacetin (**11**) in d_4 -MeOH
Figure S75 400 MHz ^1H - ^{13}C -HSQC-TOCSY NMR spectrum of **11** in d_4 -MeOH
Figure S76 400 MHz ^1H - ^{13}C -HMBC NMR spectrum of 12F-plicacetin (**11**) in d_4 -MeOH
Figure S77 ^{19}F -NMR spectrum of **11** in d_4 -MeOH
Figure S78 FT-IR spectrum of 12F-plicacetin (**11**)

Enantioselective HPLC-MS Analysis of the Branched Fatty Acid Side Chains of **6** and **10**

Figure S79 HPLC-UV enantiomer separation for **6-I**
Figure S80 HPLC-UV enantiomer separation for **6-II**
Figure S81 HPLC-MS enantiomer separation for **10**
Table S10 Chromatographic parameters

Bioinformatics and Genetic Data

Figure S82 Synteny analysis of the amicetin biosynthetic gene cluster
Table S11 Detailed overview about the *ami* locus in strain SHP 22-7

Precursor Feeding Biosynthesis Approach

Figure S83 Growth- and production curve
Figure S84 Precursor directed biosynthesis feeding study with precursor **1a**.
Figure S85 Precursor directed biosynthesis feeding study with precursor **2c**.
Figure S86 Precursor directed biosynthesis feeding study with precursor **3c**.
Figure S87 Precursor directed biosynthesis feeding study with precursor **4c**.
Figure S88 Precursor directed biosynthesis feeding study with precursor **4d**.
Figure S89 Precursor directed biosynthesis feeding study with precursor **4e**.
Figure S90 Precursor directed biosynthesis feeding study with precursor **5c**.
Figure S91 Precursor directed biosynthesis feeding study with precursor **5d**.
Figure S92 Precursor directed biosynthesis feeding study with precursor **5e**.
Figure S93 Precursor directed biosynthesis feeding study with precursor **5h**.

Bioassays

Figure S94 Cell-free assay specific for bacterial translation inhibitors

Figure S1. Characteristic MS/MS fragments of pyrimidine nucleosides.

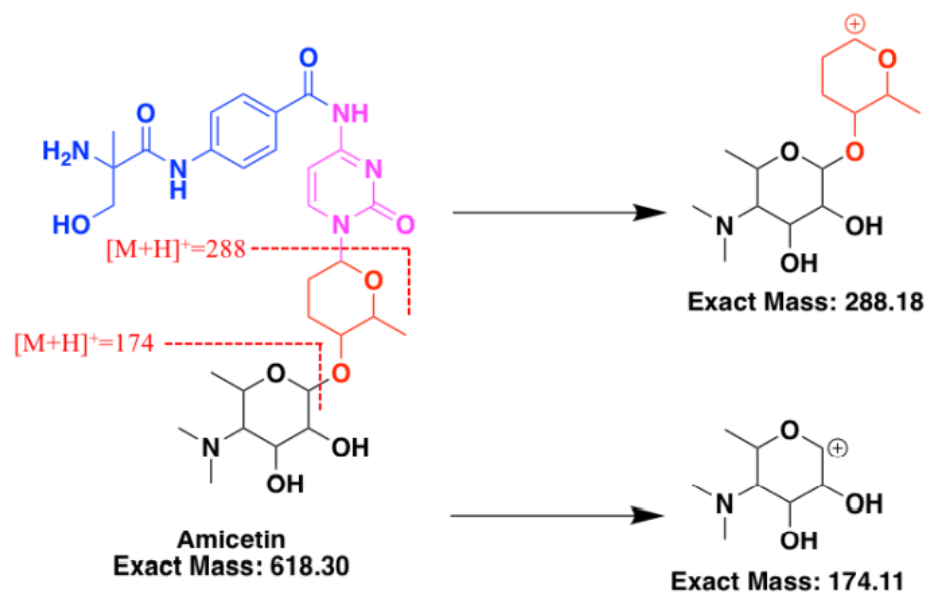


Figure S2. Pink-reddish color of **1**.



Figure S3. HR-ESI-MS spectrum (negative mode) of zincphyrin III (**1**).

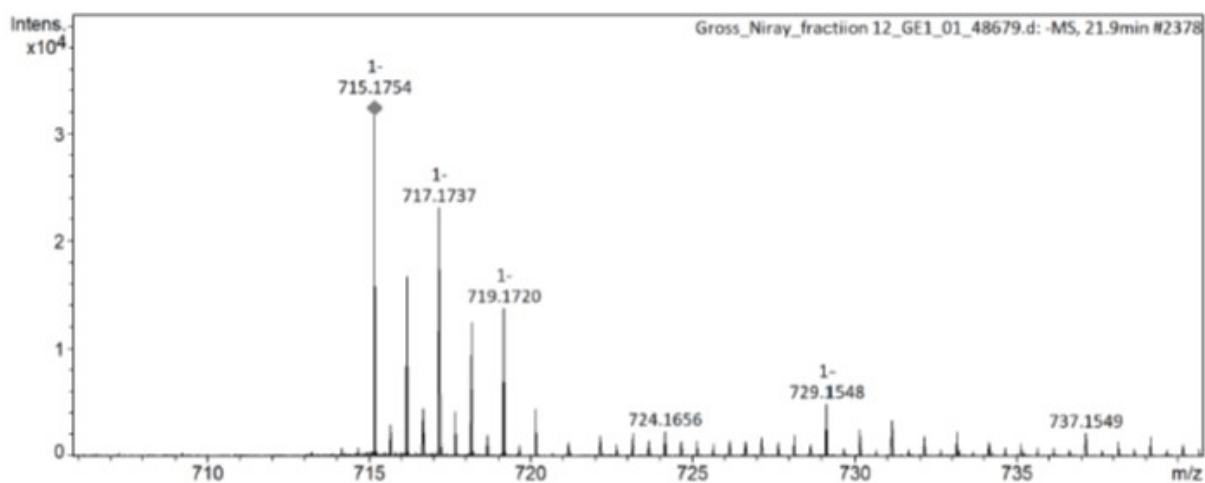


Figure S4. 400 MHz ^1H NMR spectrum of zincphyrin III (**1**) in d_6 -DMSO.

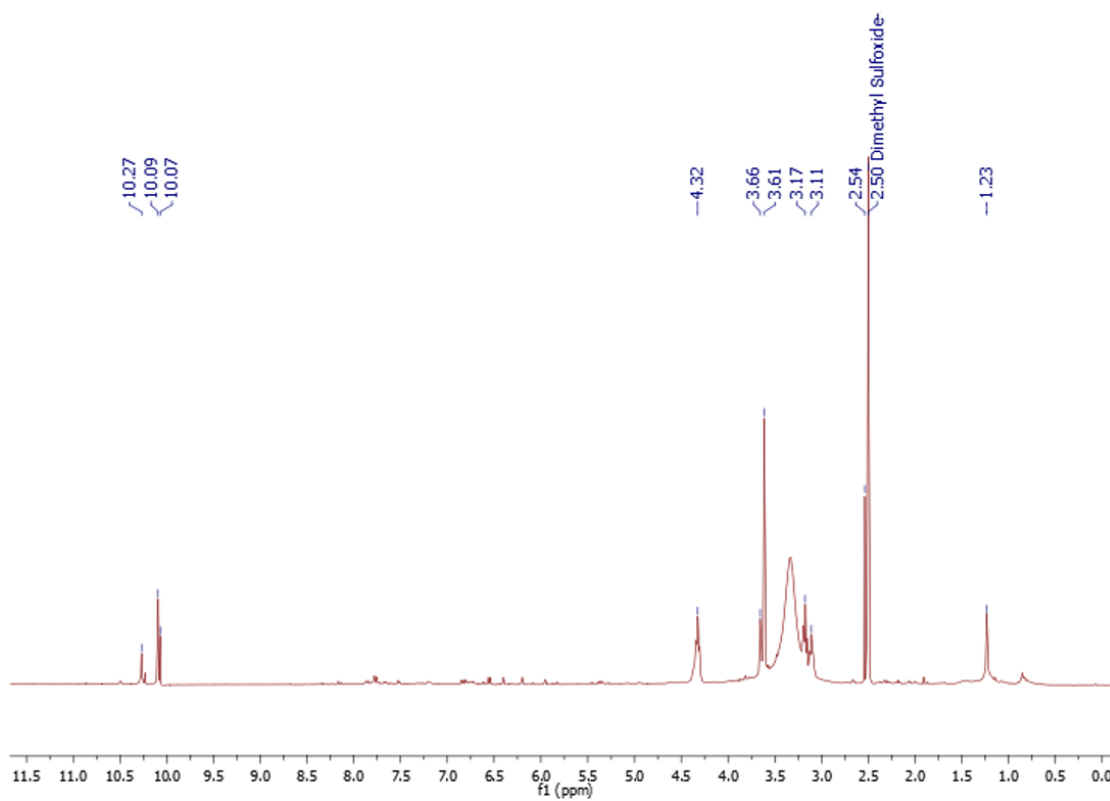


Figure S5. 100 MHz ^{13}C NMR spectrum of zincphyrin III (**1**) in d_6 -DMSO.

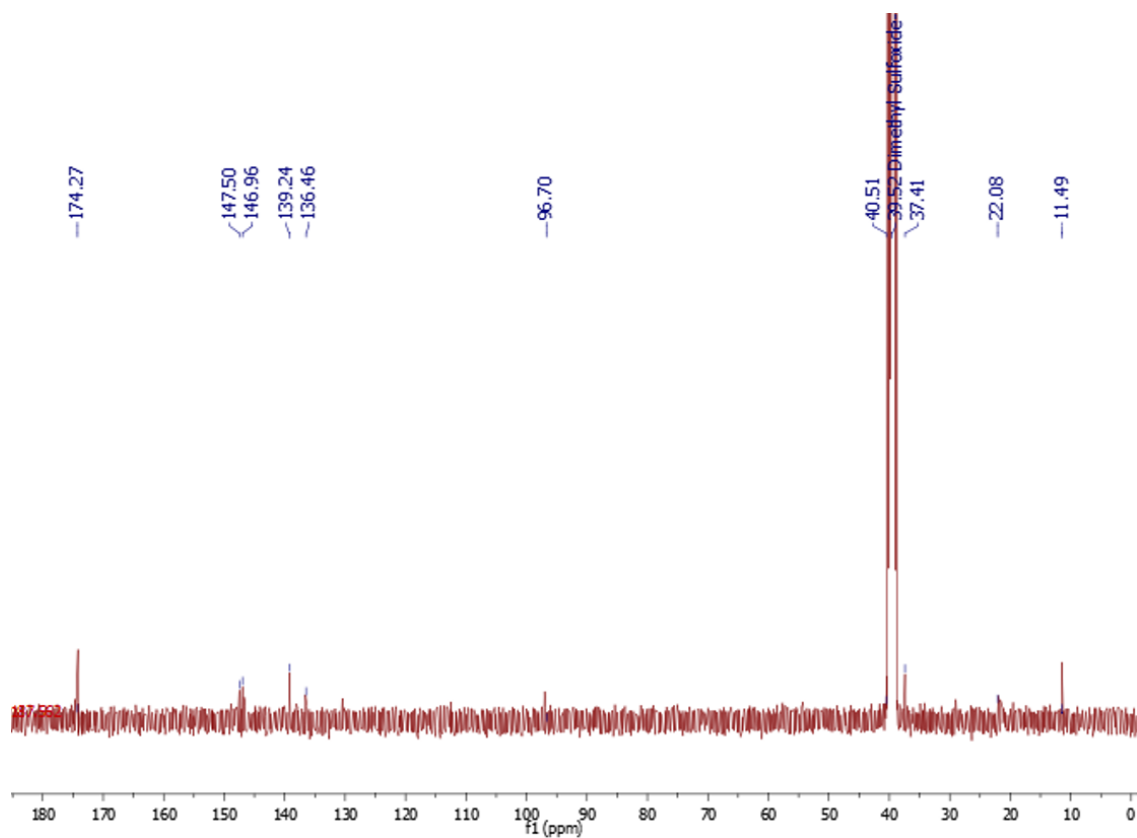
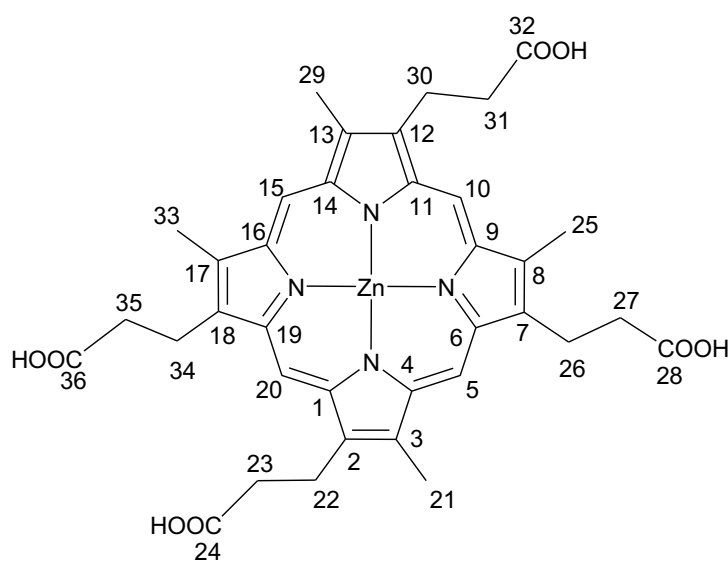


Table S1. ^1H and ^{13}C NMR data of zincphyrin III (**1**), recorded in d_6 -DMSO.

no.	δ_{H}	δ_{C}
1		147.5, qC
2		139.2, qC
3		136.5, qC
4		147.0, qC
5	10.09, s ^a	96.7, CH
6		147.5, qC
7		139.2, qC
8		136.5, qC
9		147.0, qC
10	10.27, s ^a	96.7, CH
11		147.0, qC
12		139.2, qC
13		136.5, qC
14		147.5, qC
15	10.09, s ^a	96.7, CH
16		147.0, qC
17		136.5, qC
18		139.2, qC
19		147.5, qC
20	10.07, s ^a	96.7, CH
21	3.61, s	11.5, CH ₃
22	4.32, m	22.1, CH ₂
23	3.17, m	37.4, CH ₂
24		174.3, qC
25	3.66, s	11.5, CH ₃
26	4.32, m	22.1, CH ₂
27	3.17, m	37.4, CH ₂
28		174.3, qC
29	3,66, s	11.5, CH ₃
30	4.32, m	22.1, CH ₂
31	3.17, m	37.4, CH ₂
32		174.3, qC
33	3.61, s	11.5, CH ₃
34	4.32, m	22.1, CH ₂
35	3.17, m	37.4, CH ₂
36		174.3, qC



^asignals are interchangeable

Figure S6. 400 MHz ^1H NMR spectrum of plicacetin (**2**) in d_4 -MeOH.

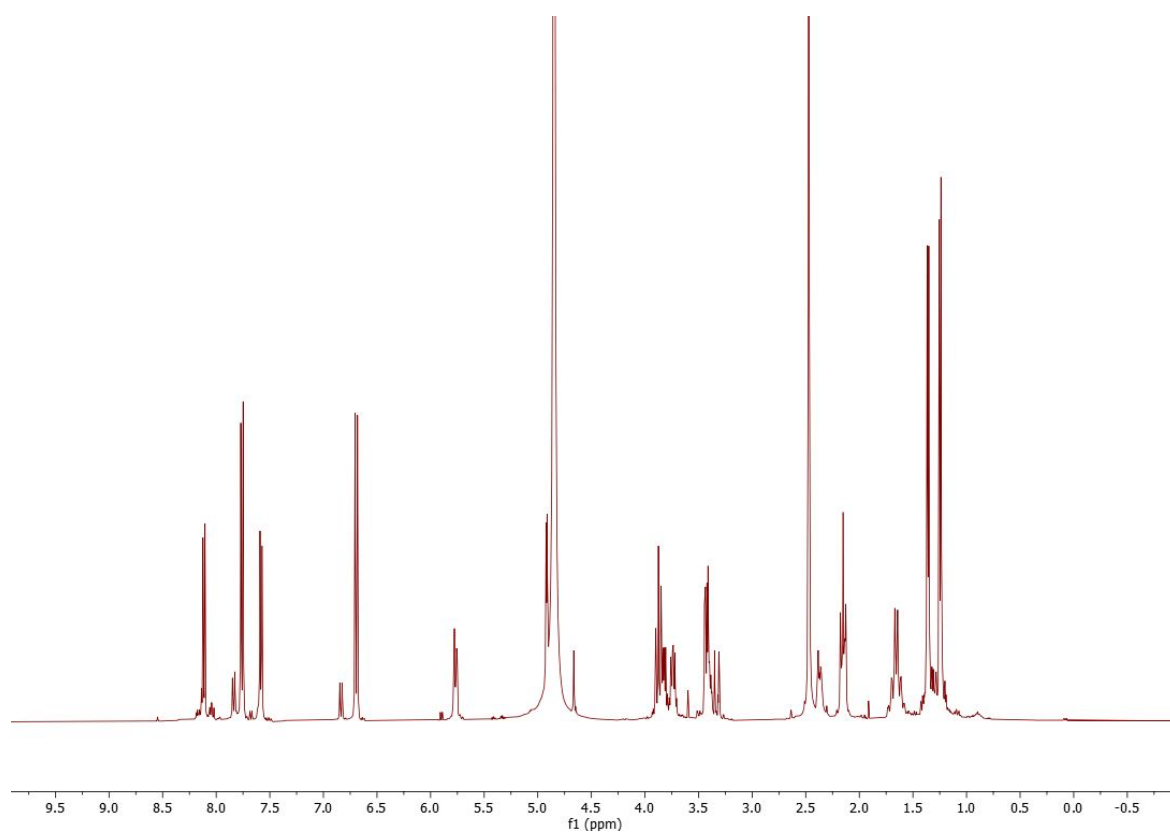


Figure S7. 100 MHz ^{13}C NMR spectrum of plicacetin (**2**) in d_4 -MeOH.

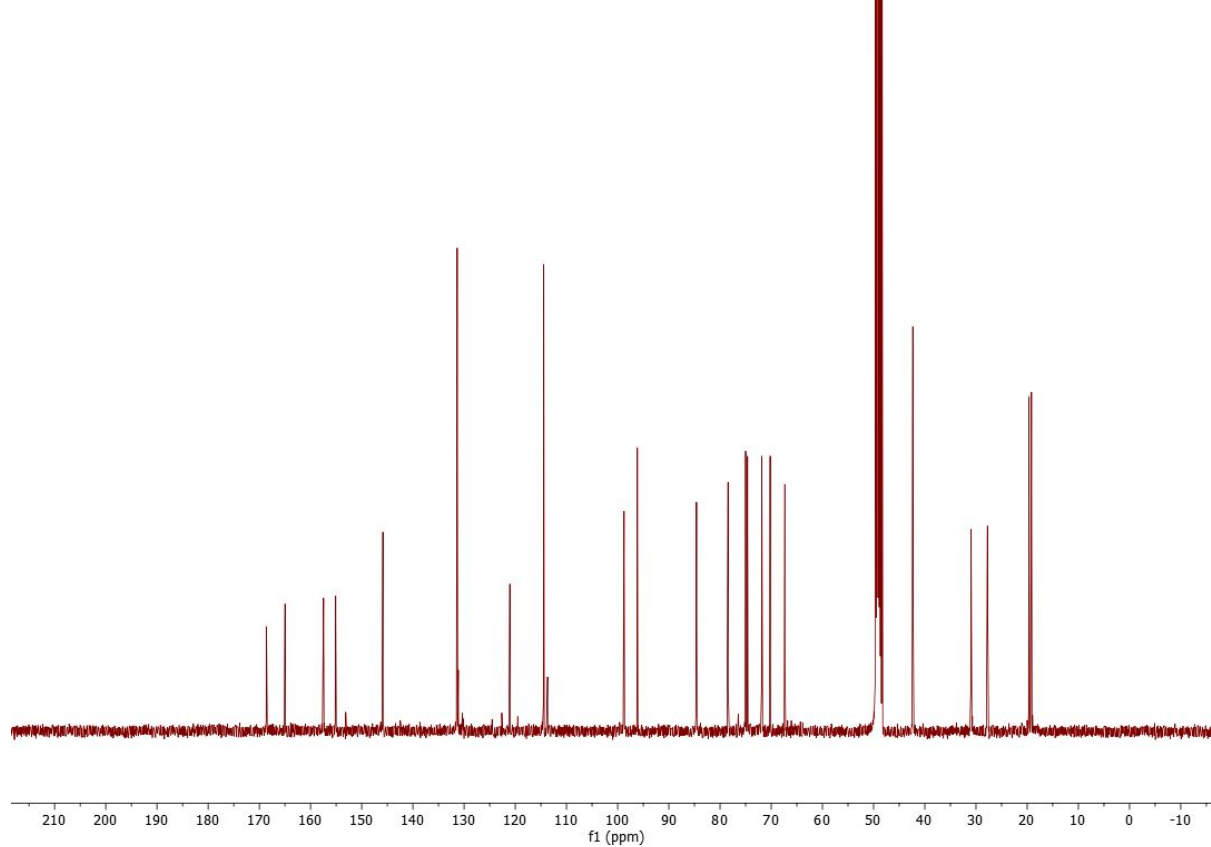


Table S2. ^1H and ^{13}C NMR data of plicacetin (**2**), recorded in d_4 -MeOH.

moiety	no.	δ_{H}	δ_{C}
cytosine	2		157.4, qC
	4		164.8, qC
	5	7.59, d (7.4)	98.7, CH
	6	8.11, d (7.4)	145.8, CH
side chain	8		168.6, qC
	9		121.0, qC
	10	7.76, d (8.7)	131.5, CH
	11	6.69, d (8.7)	114.4, CH
	12		155.0, qC
	13	6.69, d (8.7)	114.4, CH
amicetose	1'	5.76, dd (10.8, 2.3)	84.6, CH
	2'	1.65, m	31.0, CH ₂
		2.15, m	
	3'	1.65, m	27.7, CH ₂
		2.38, m	
	4'	3.41, m	75.0, CH
5'	3.75, m	78.4, CH	
6'	1.36, d (6.4)	19.1, CH ₃	
amosamine	1''	4.92, d (3.7)	96.1, CH
	2''	3.41, m	74.6, CH
	3''	3.87, t (9.6)	70.2, CH
	4''	2.13, t (10.1)	71.8, CH
	5''	3.83, m	67.4, CH
	6''	1.24, d (6.4)	19.6, CH ₃
	7''	2.47, s	42.3, CH ₃
	8''	2.47, s	42.3, CH ₃

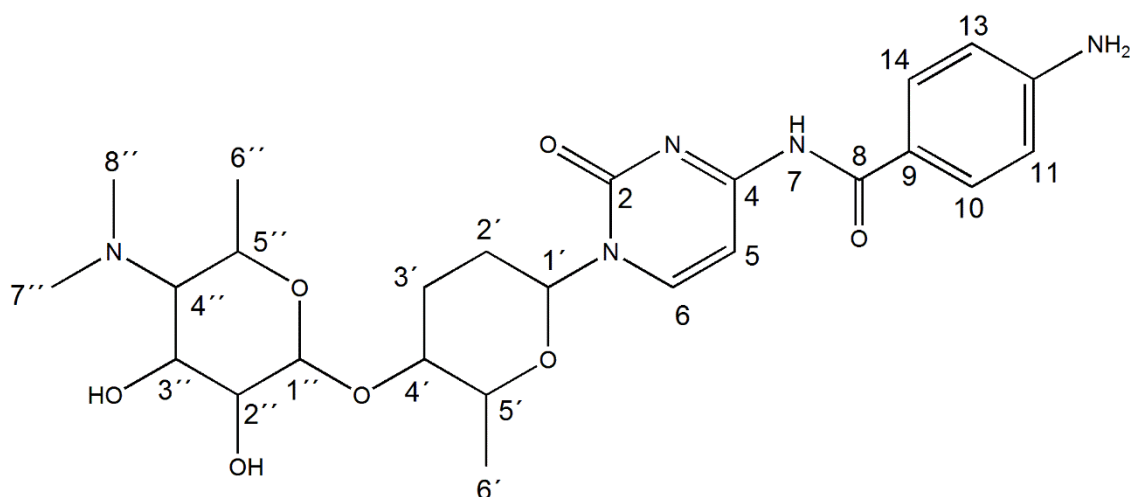


Figure S8. FT-IR spectrum of plicacetin (2).

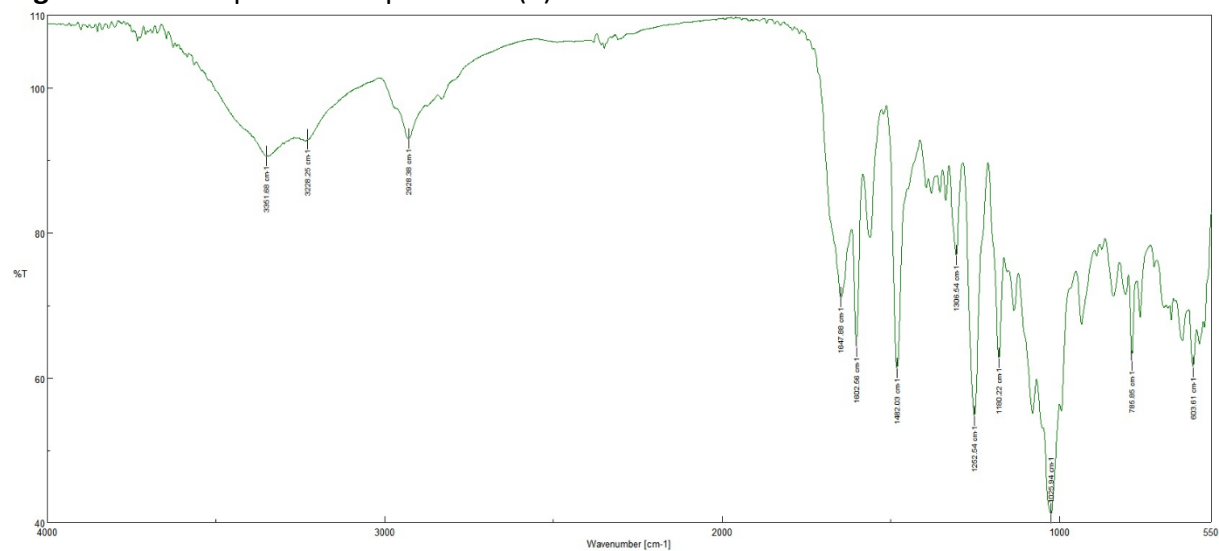


Figure S9. HR-ESI-MS/MS spectrum of unnamed pyrimidine nucleoside (3).

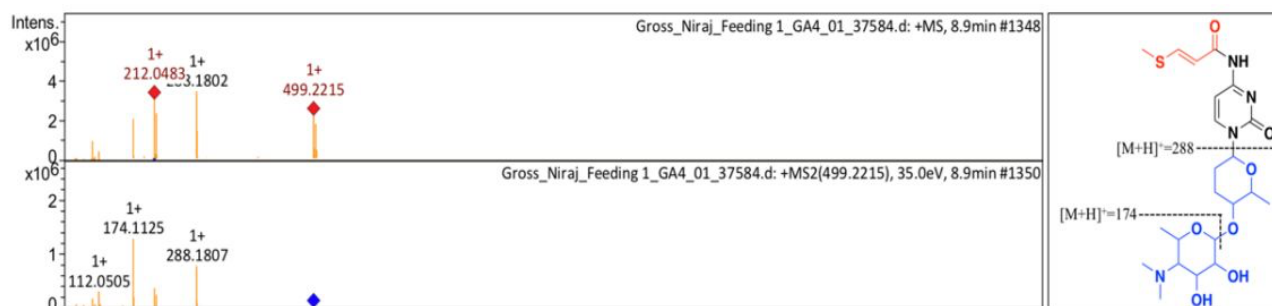


Figure S10. 400 MHz ^1H NMR spectrum of unnamed pyrimidine nucleoside **3** in d_6 -DMSO.

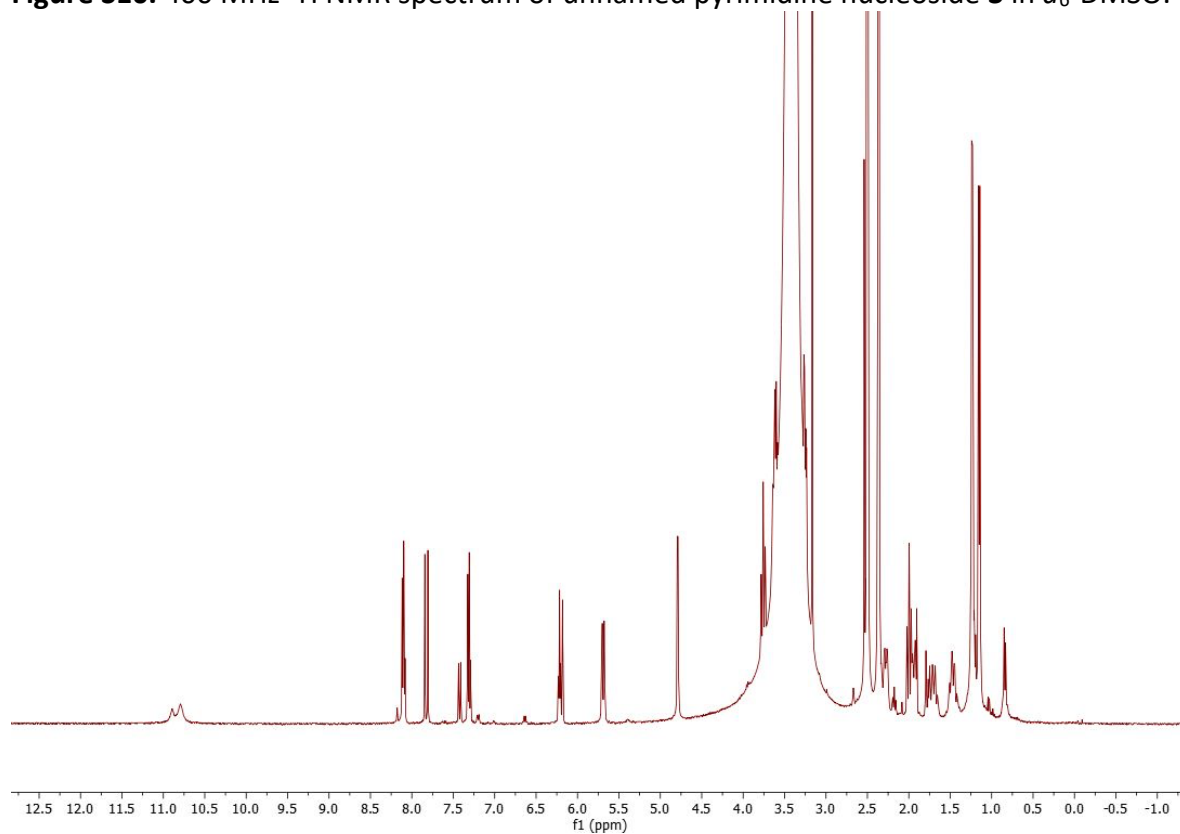


Figure S11. 100 MHz ^{13}C NMR spectrum of unnamed pyrimidine nucleoside **3** in d_6 -DMSO.

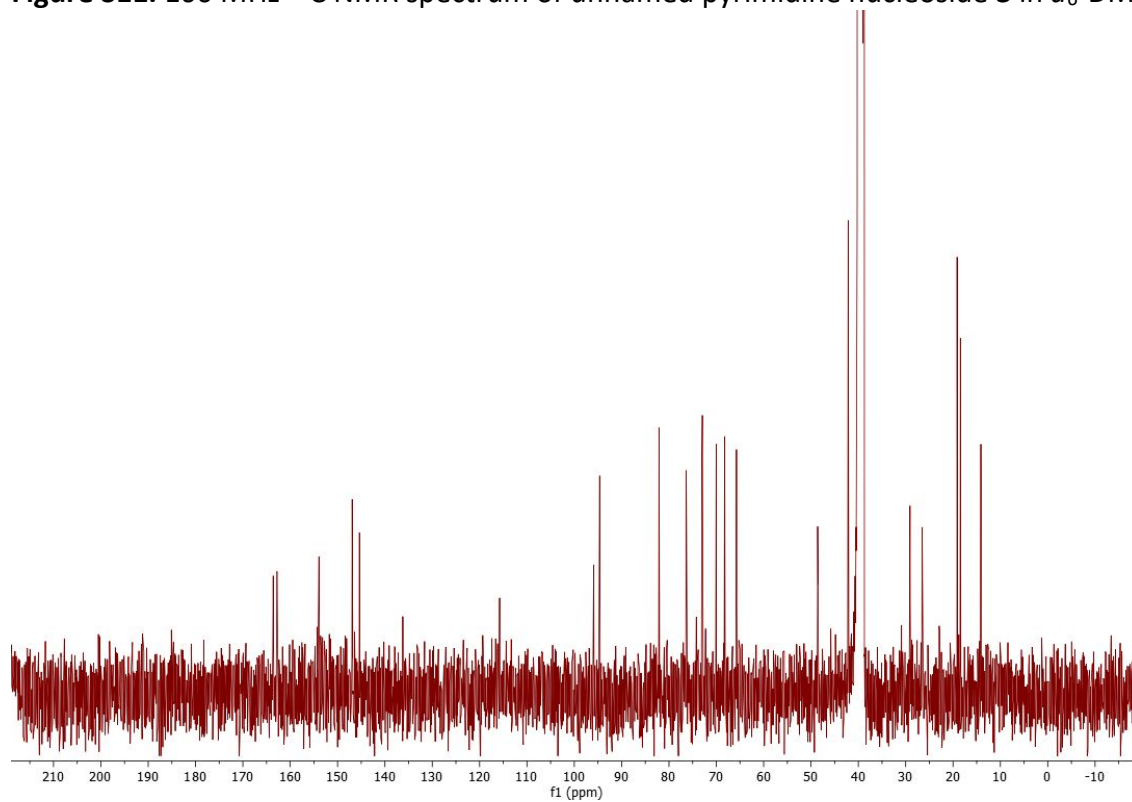


Table S3. ^1H and ^{13}C NMR data of unnamed pyrimidine nucleoside (**3**), recorded in d_6 -DMSO.

moiety	no.	δ_{H}	δ_{C}
cytosine	2		153.9, qC
	4		162.8, qC
	5	7.32, d (7.4)	95.9, CH
	6	8.11, d (7.4)	145.5, CH
	7	10.79, s	
side chain	8		163.6, qC
	9	6.22, d (14.7)	115.8, CH
	10	7.82, d (14.7)	146.9, CH
	12	2.36, s	14.1, CH ₃
amicetose	1'	5.69, dd (10.8, 2.3)	82.2, CH
	2'	1.70, m	29.5, CH ₂
		1.93, m	
	3'	1.40, m	26.1, CH ₂
		2.30, m	
	4'	3.25, m	73.1, CH
	5'	3.63, m	76.4, CH
6'	1.23, d (6.1)	18.4, CH ₃	
amosamine	1''	4.79, d (3.7)	94.7, CH
	2''	3.41, m	72.9, CH
	3''	3.87, t (9.6)	68.3, CH
	4''	2.13, t (10.1)	70.1, CH
	5''	3.83, m	65.7, CH
	6''	1.15, d (6.2)	19.1, CH ₃
	7''	2.37, s	42.2, CH ₃
	8''	2.37, s	42.2, CH ₃

Figure S12. FT-IT spectrum of unnamed pyrimidine nucleoside **3**.

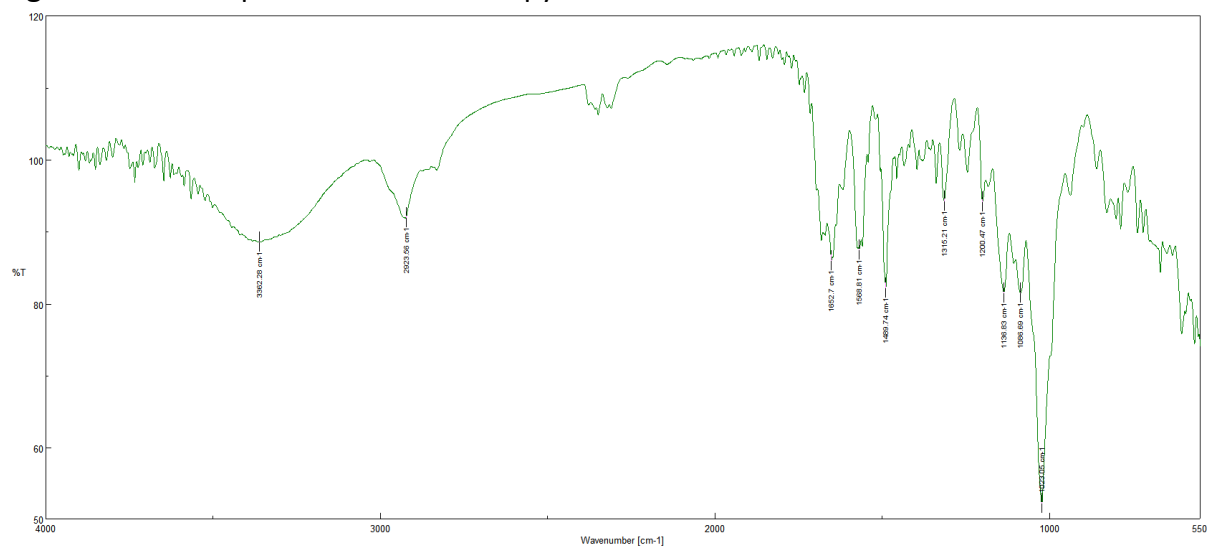


Figure S13. HR-ESI-MS and MS/MS spectrum of 40551-F (**4**).

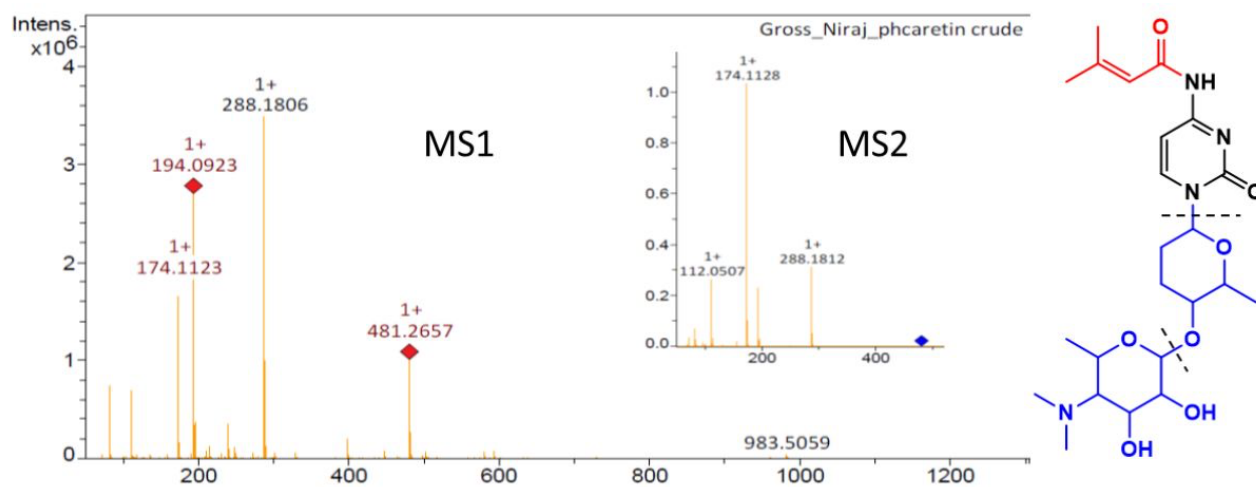


Figure S14. 400 MHz ¹H NMR spectrum of 40551-F (**4**) in d₄-MeOH.

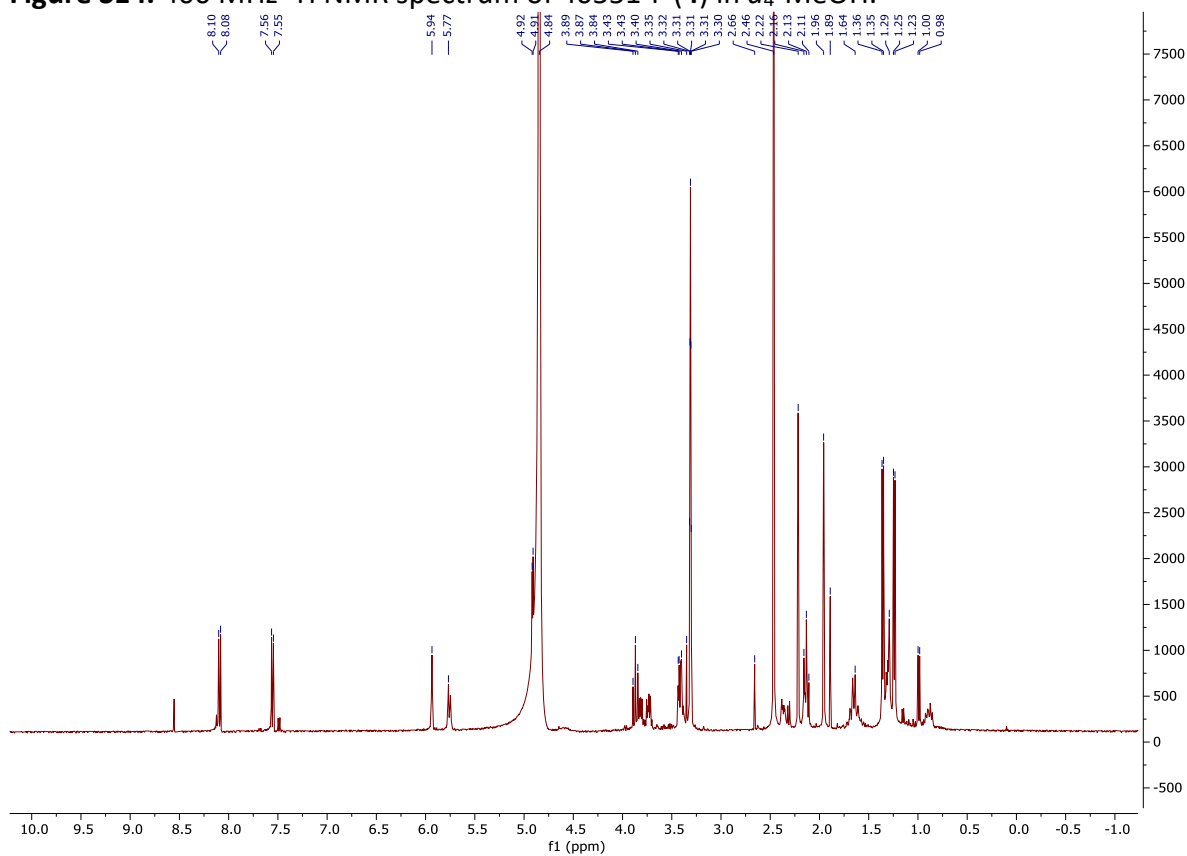


Figure S15. 100 MHz ^{13}C NMR spectrum of 40551-F (**4**) in d_4 -MeOH.

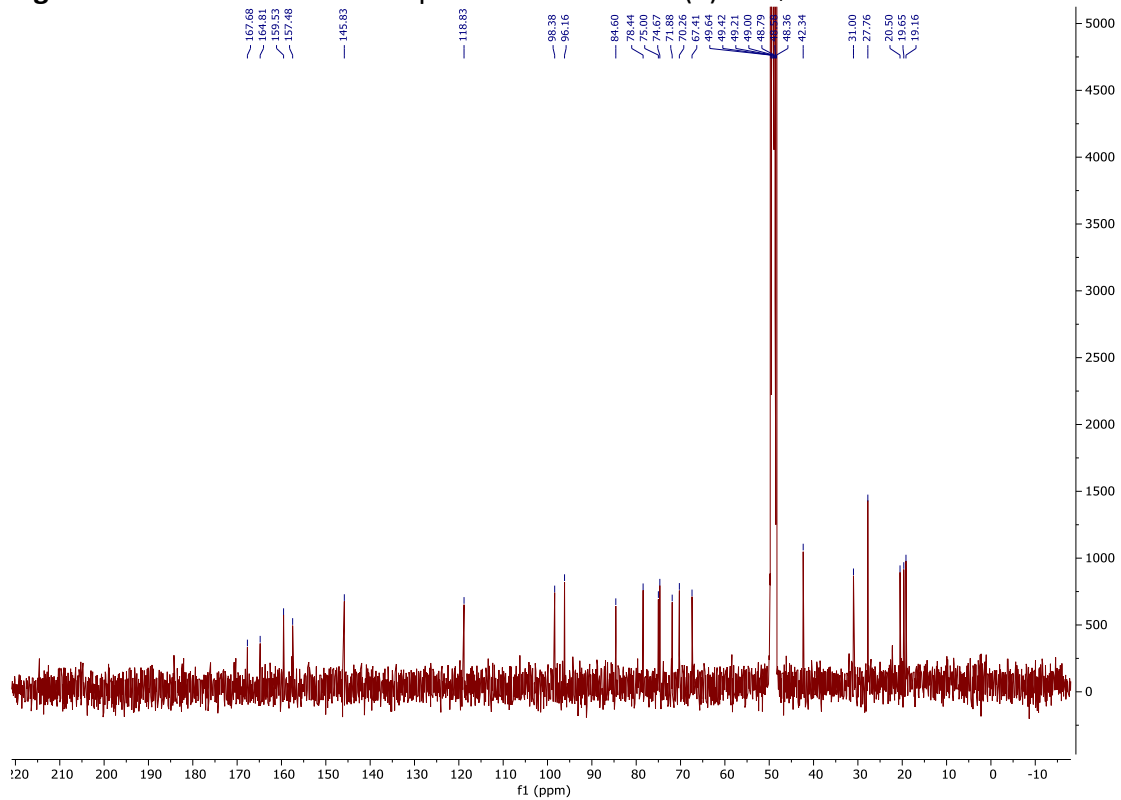


Figure S16. 400 MHz edited ^1H - ^{13}C HSQC NMR spectrum of 40551-F (**4**) in d_4 -MeOH.

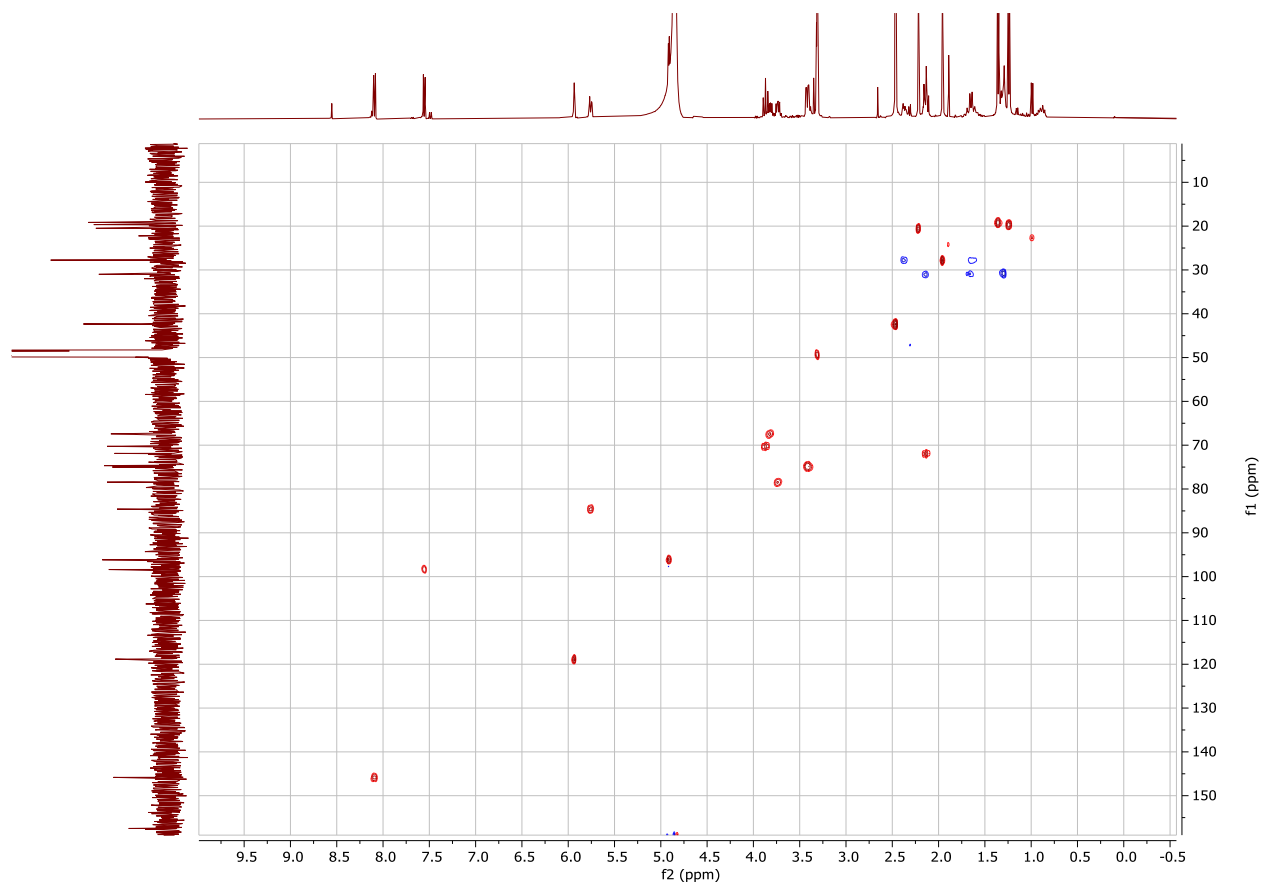


Figure S17. 400 MHz ^1H - ^1H COSY NMR spectrum of 40551-F (**4**) in d_4 -MeOH.

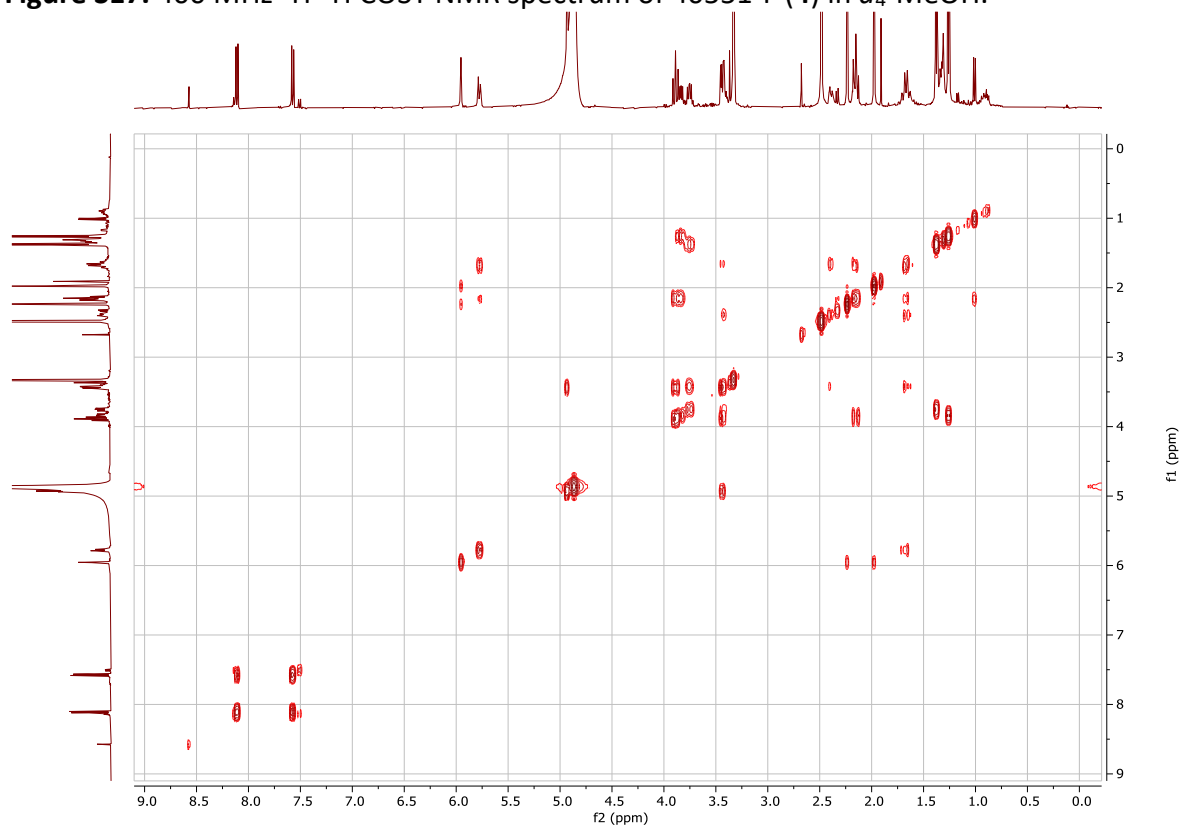


Figure S18. 400 MHz ^1H - ^{13}C HMBC NMR spectrum of 40551-F (**4**) in d_4 -MeOH.

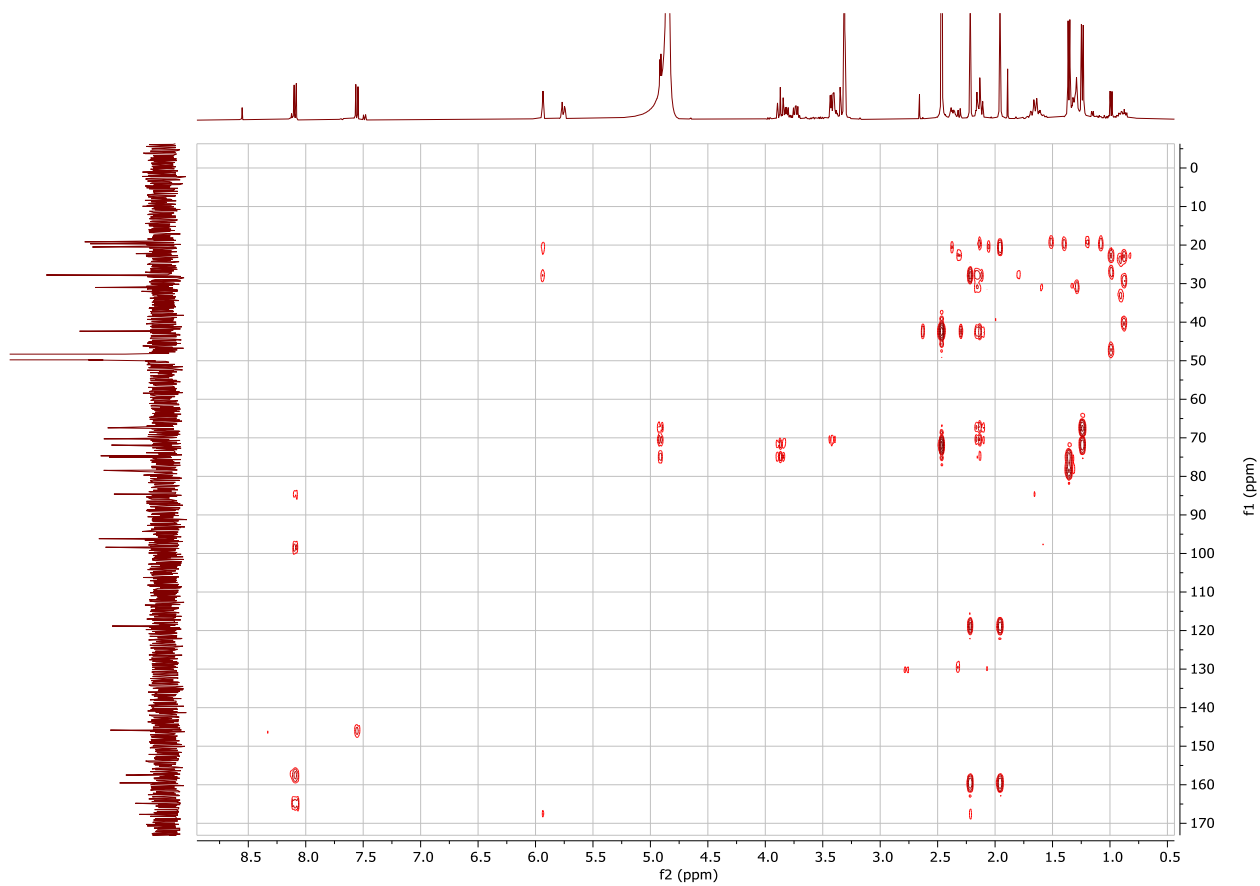


Table S4. ^1H and ^{13}C NMR data of 40551-F (**4**), recorded in d_4 -MeOH.

moiety	no.	δ_{H}	δ_{C}
cytosine	2		157.5, qC
	4		164.5, qC
	5	7.55, d (7.6)	98.4, CH
	6	8.09, d (7.6)	145.8, CH
	7	8.55, s	NH
side chain	8		167.8, qC
	9	5.94, t (1.2)	118.8, CH
	10		159.5 qC
	11	2.22, d (1.2)	20.5, CH ₃
	12	1.96, d (1.2)	27.7, CH ₃
amicetose	1'	5.76, dd (9.9, 2.0)	84.6, CH
	2'	1.65, m	31.0, CH ₂
		2.38, m	
	3'	1.66, m	27.7, CH ₂
		2.14, m	
	4'	3.42, m	75.0, CH
5'	3.74, m	78.4, CH	
6'	1.36, d (6.1)	19.2, CH ₃	
amosamine	1''	4.91, d (3.8)	96.2 CH
	2''	3.42, m	74.7, CH
	3''	3.87, t (9.8)	70.3, CH
	4''	2.13, t (10.1)	71.9, CH
	5''	3.83, m	67.4, CH
	6''	1.24, d (6.2)	19.7, CH ₃
	7''	2.46, s	42.3, CH ₃
	8''	2.46, s	42.3, CH ₃

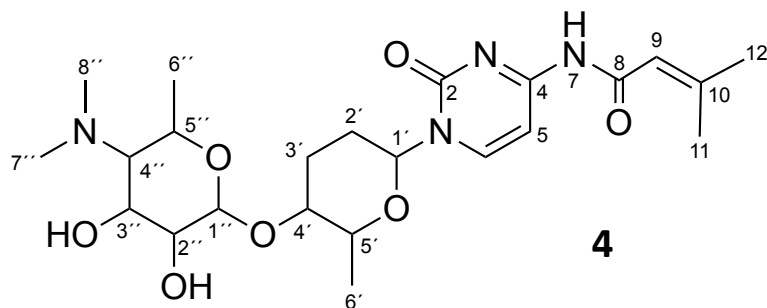


Figure S19. FT-IR spectrum of 40551-F (4).

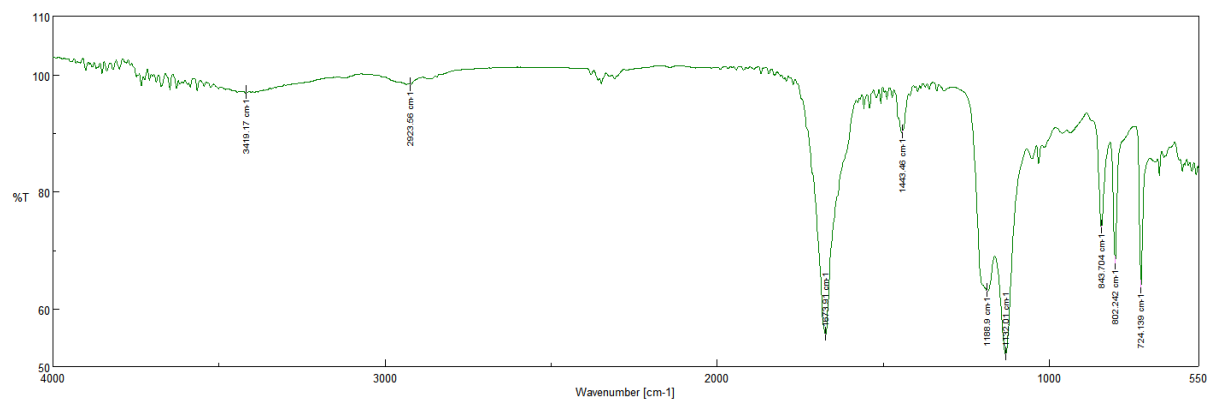


Figure S20. HR-ESI-MS and HR-ESI-MS/MS spectrum of CAS 51693-93-7 (**5**).

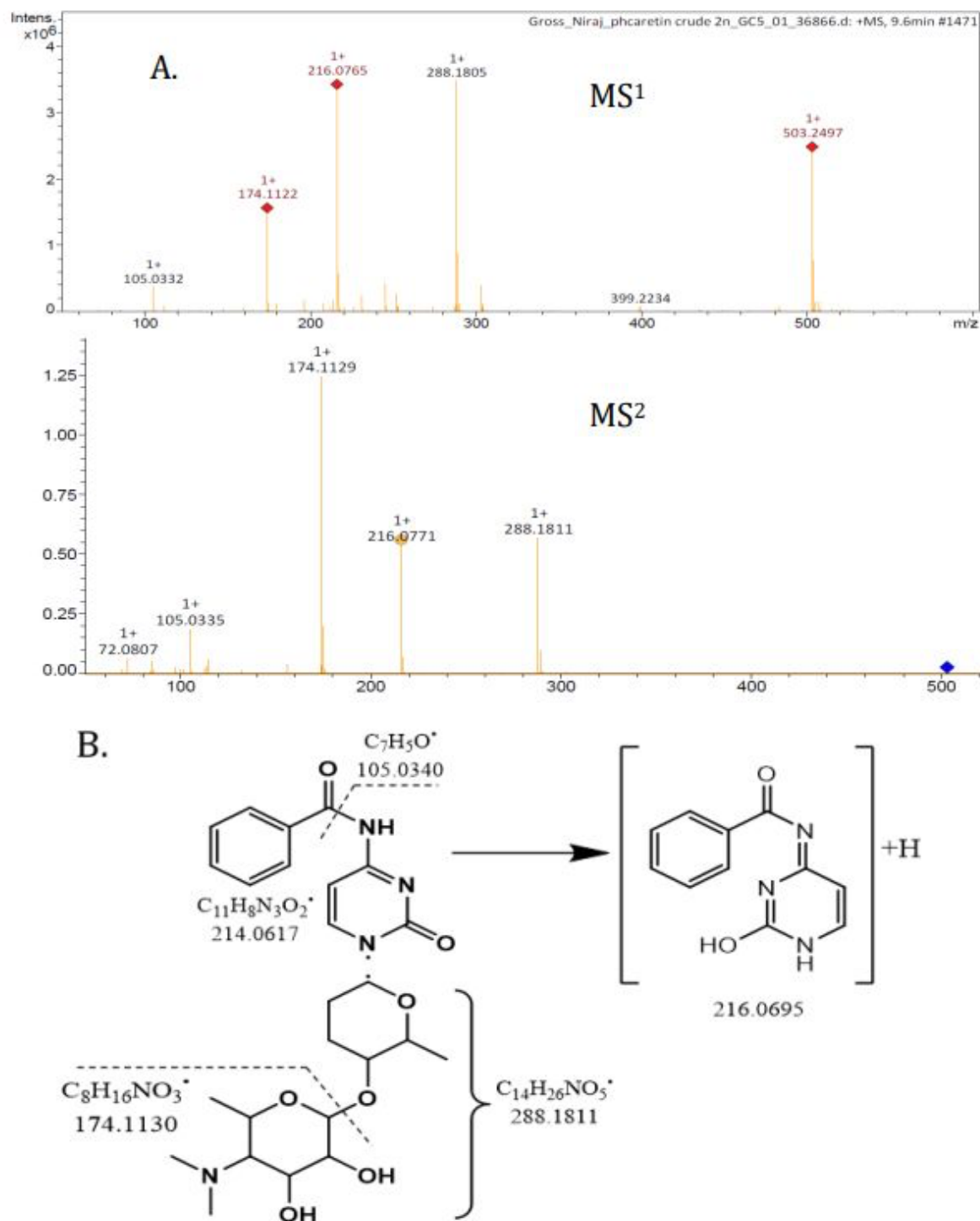


Figure S21. 400 MHz ^1H NMR spectrum of CAS 51693-93-7 (**5**) in d_4 -MeOH.

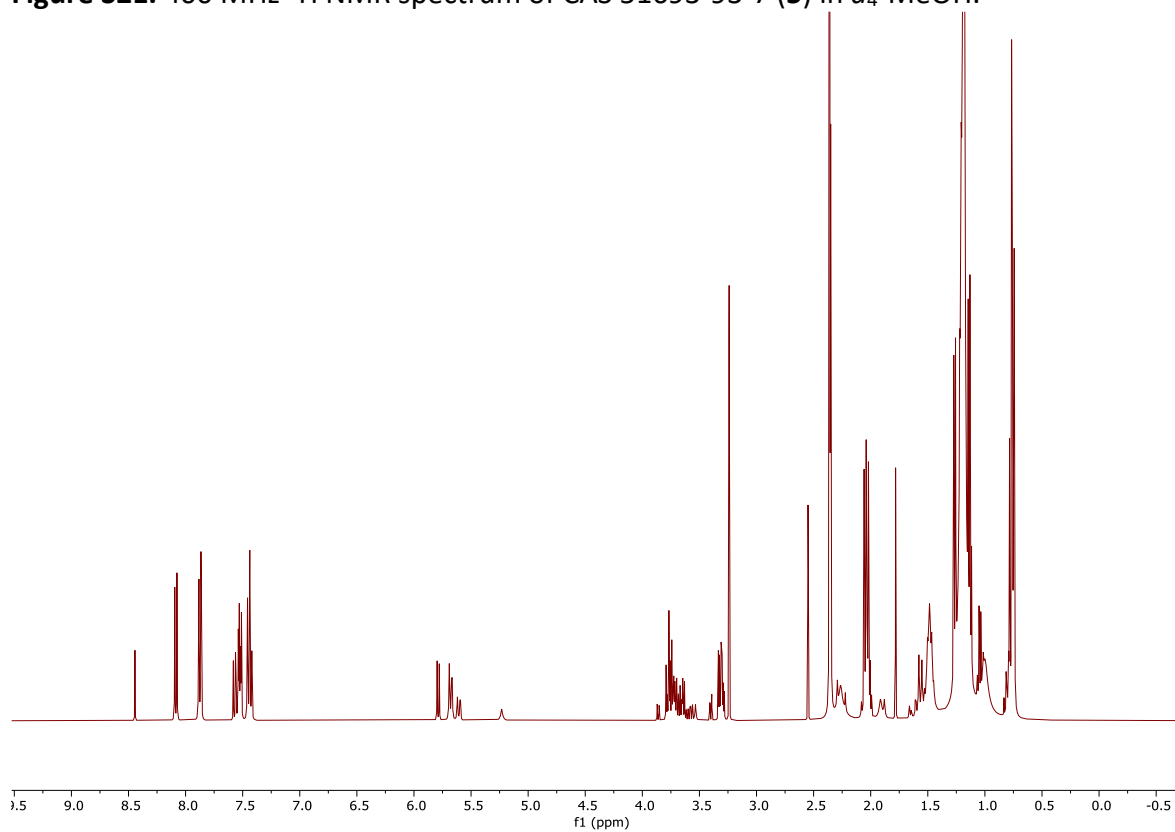


Figure S22. 100 MHz ^{13}C NMR spectrum of CAS 51693-93-7 (**5**) in d_4 -MeOH.

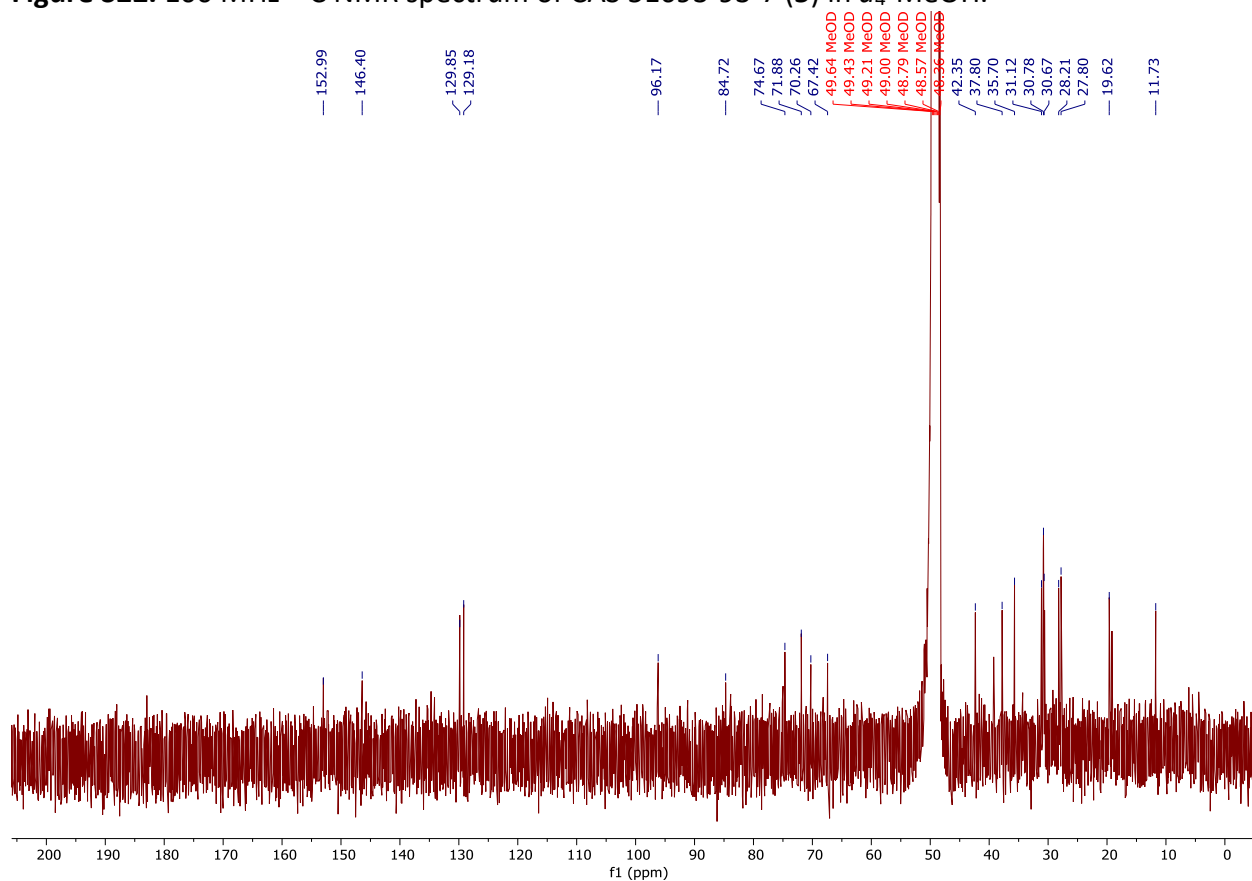


Figure S23. 400 MHz ^1H - ^1H COSY NMR spectrum of CAS 51693-93-7 (**5**) in d_4 -MeOH.

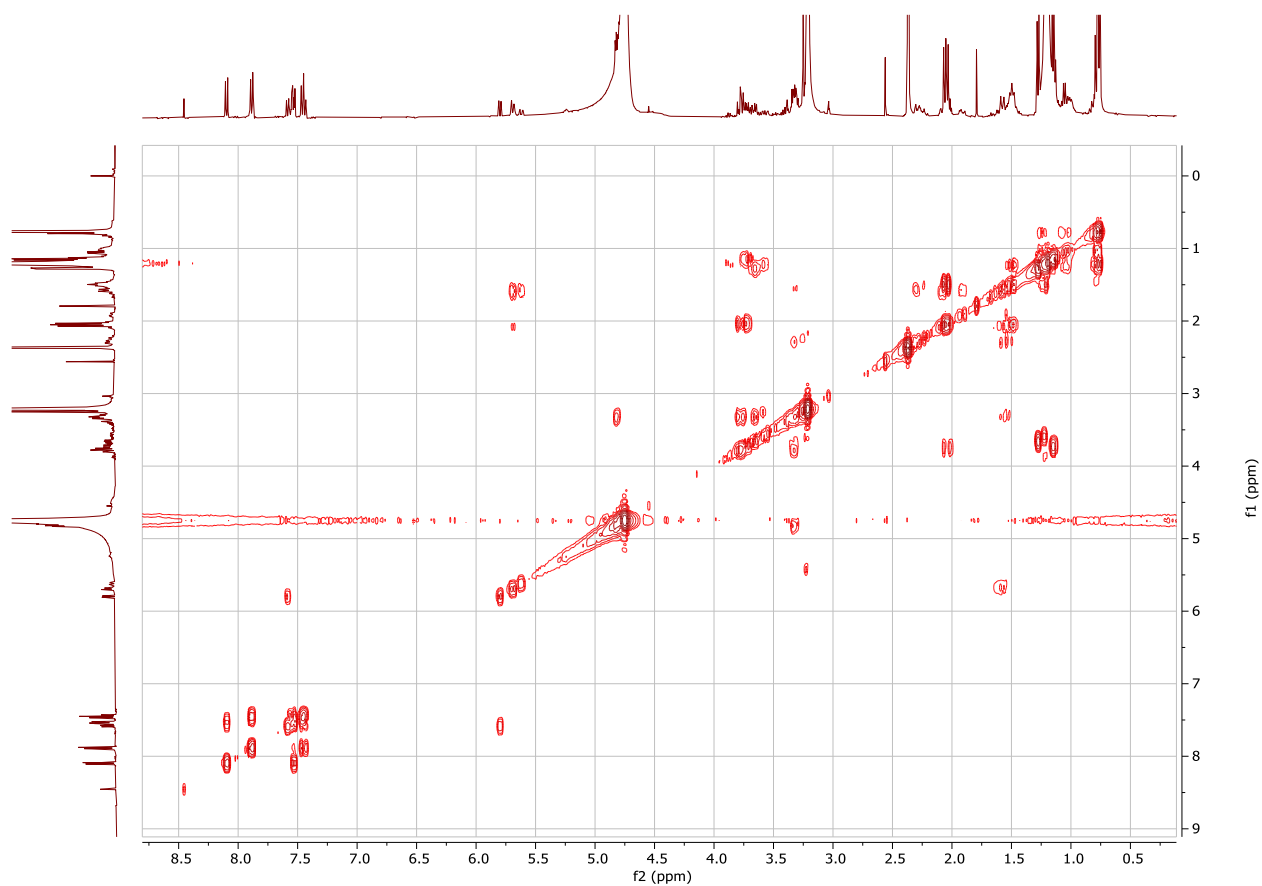


Table S5. ^1H and ^{13}C NMR data of CAS 51693-93-7 (**5**) in d_4 -MeOH.

moiety	no.	δ_{H}	δ_{C}
cytosine	2		qC, n.o.
	4		qC, n.o.
	5	7.53, d (7.5)	CH, n.o.
	6	8.09, d (7.5)	146.4, CH
	7	8.44, s	NH
side chain	8		qC, n.o.
	9		qC, n.o.
	10	7.88, dd (8.2, 1.5)	129.9, CH
	11	7.44, brt	129.2, CH
	12	7.54, m	CH, n.o.
	13	7.44, brt	129.2, CH
amicetose	1'	5.68, m	84.7, CH
	2'	2.04, m	31.1, CH ₂
	3'	2.30, m	27.8, CH ₂
	4'	3.30, m	75.0, CH
	5'	3.66, m	78.5, CH
	6'	1.26, d (6.1)	19.1, CH ₃
amosamine	1''	4.82, m	96.2 CH
	2''	3.32, m	74.7, CH
	3''	3.77, m	70.3, CH
	4''	2.04, m	71.9, CH
	5''	3.73, m	67.4, CH
	6''	1.14, d (6.1)	19.6, CH ₃
	7''	2.35, s	42.4, CH ₃
	8''	2.36, s	42.4, CH ₃

n.o.: not observed.

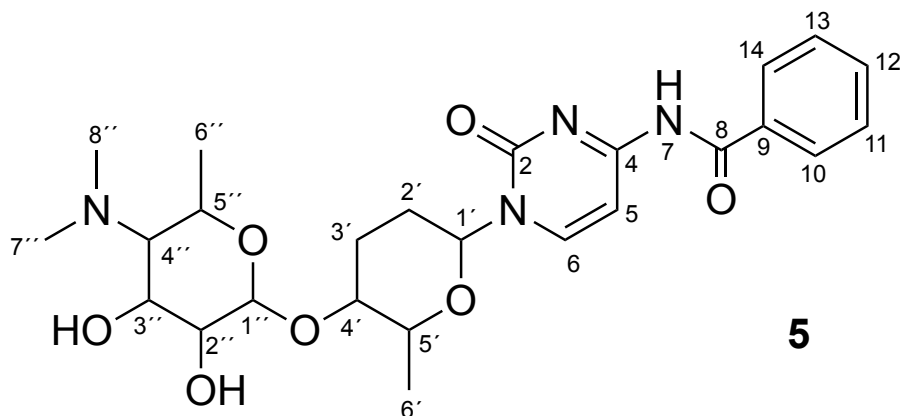


Figure S24. 400 MHz ^1H NMR spectrum of cytosaminomycin F (**6**) in d_4 -MeOH.

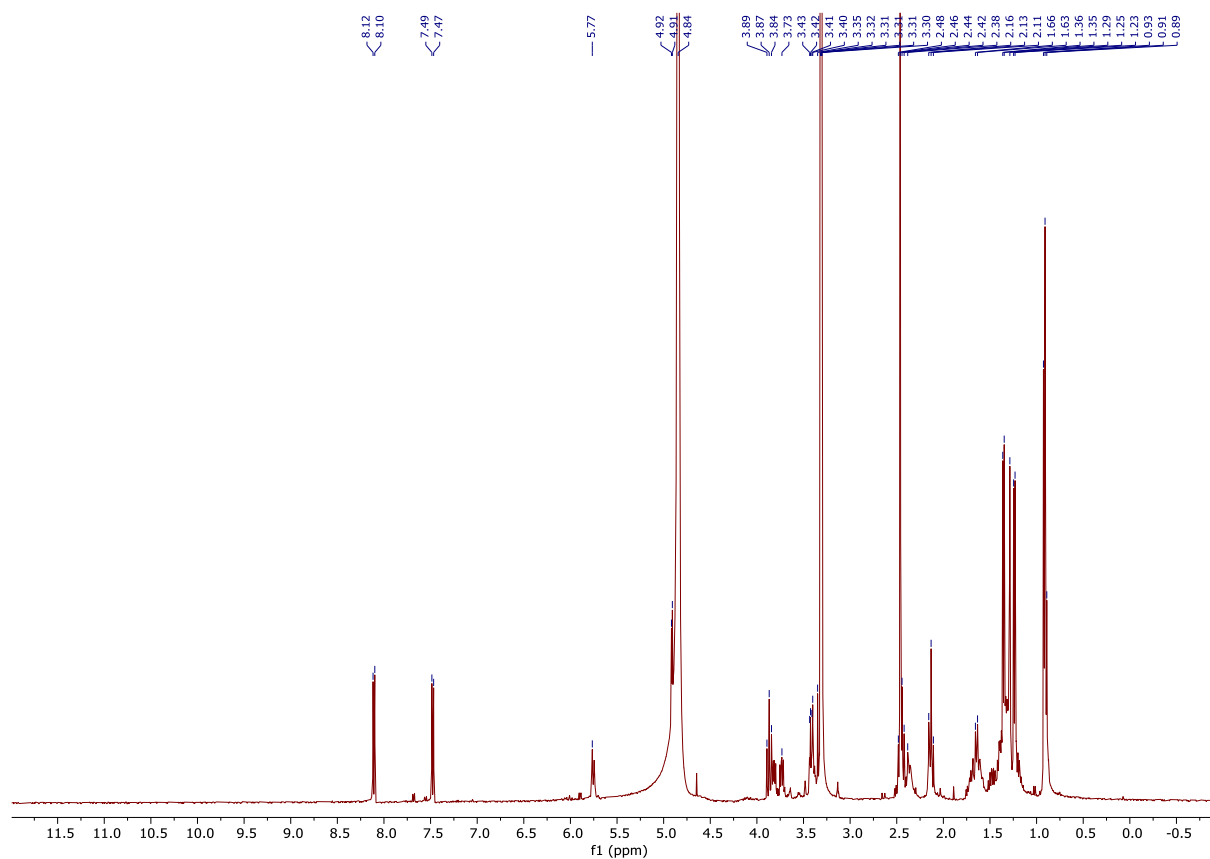


Figure S25. 150 MHz ^{13}C NMR spectrum of cytosaminomycin F (**6**) in d_4 -MeOH.

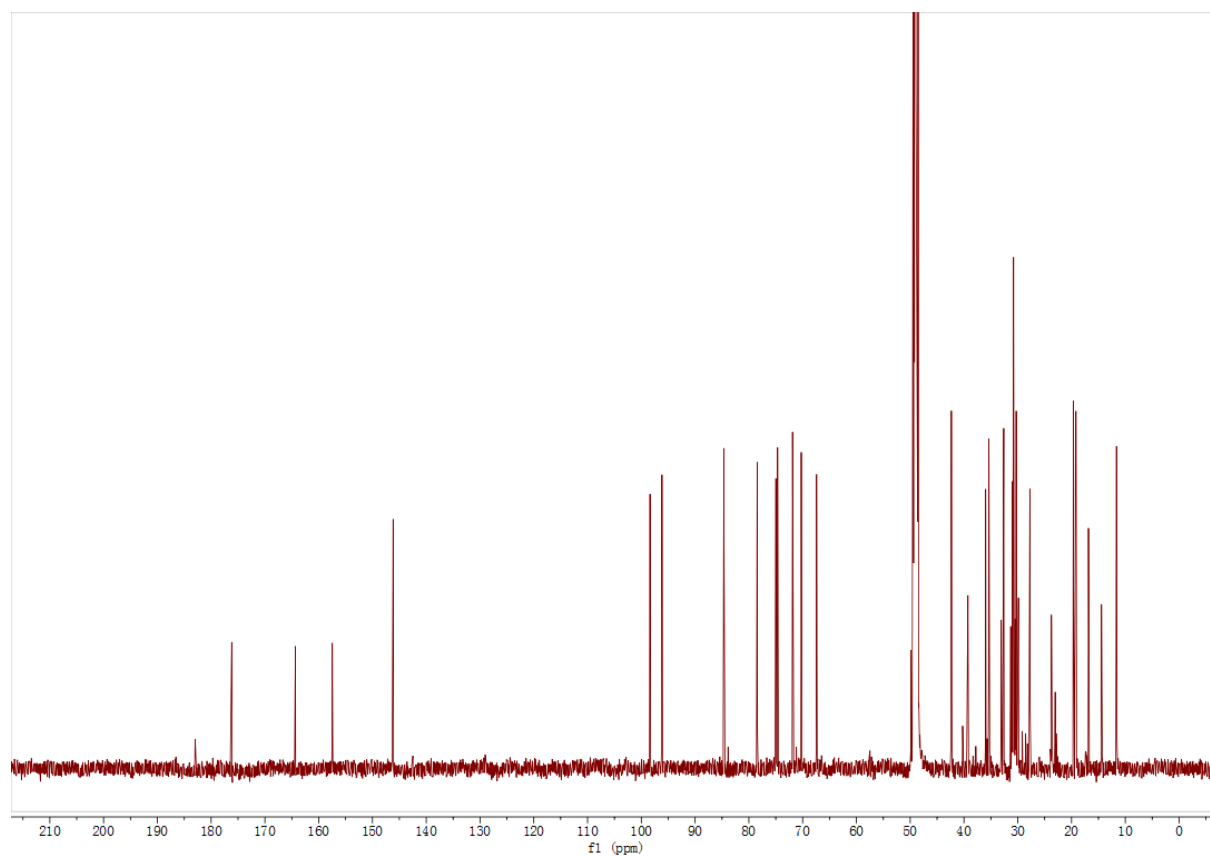


Figure S26. 600 MHz DEPT135 NMR spectrum of cytosaminomycin F (**6**) in d_4 -MeOH.

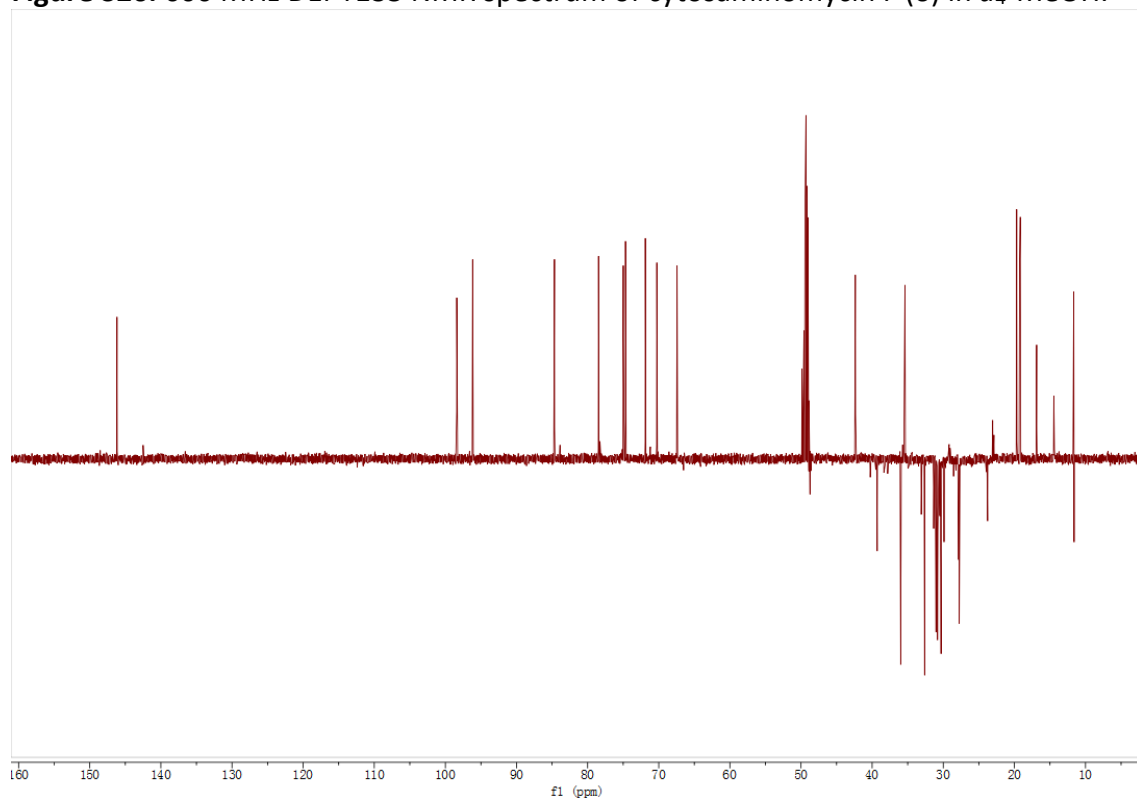


Figure S27. 700 MHz edited ^1H - ^{13}C HSQC NMR spectrum of **6** in d_4 -MeOH.

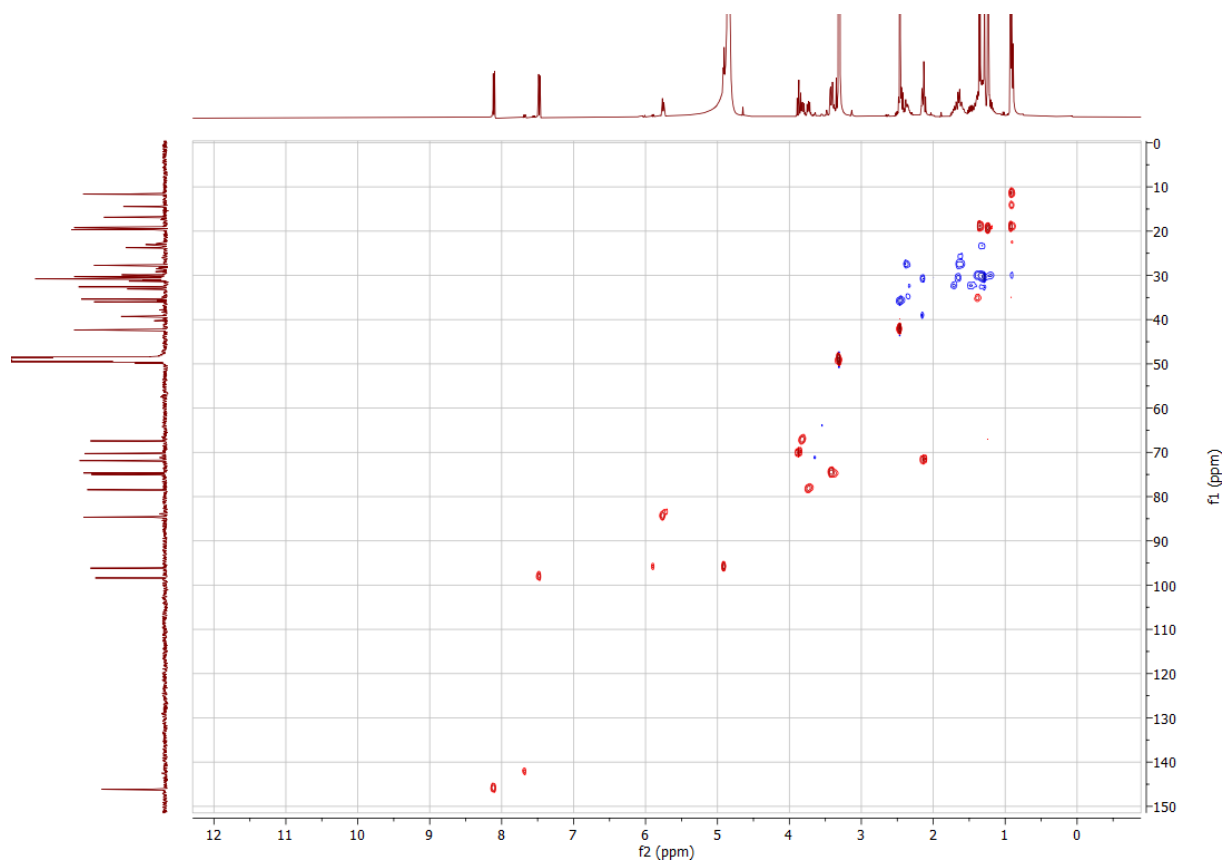


Figure S28. 700 MHz ^1H - ^1H COSY NMR spectrum of cytosaminomycin F (**6**) in d_4 -MeOH. Bold lines in the insert visualize the observed correlations.

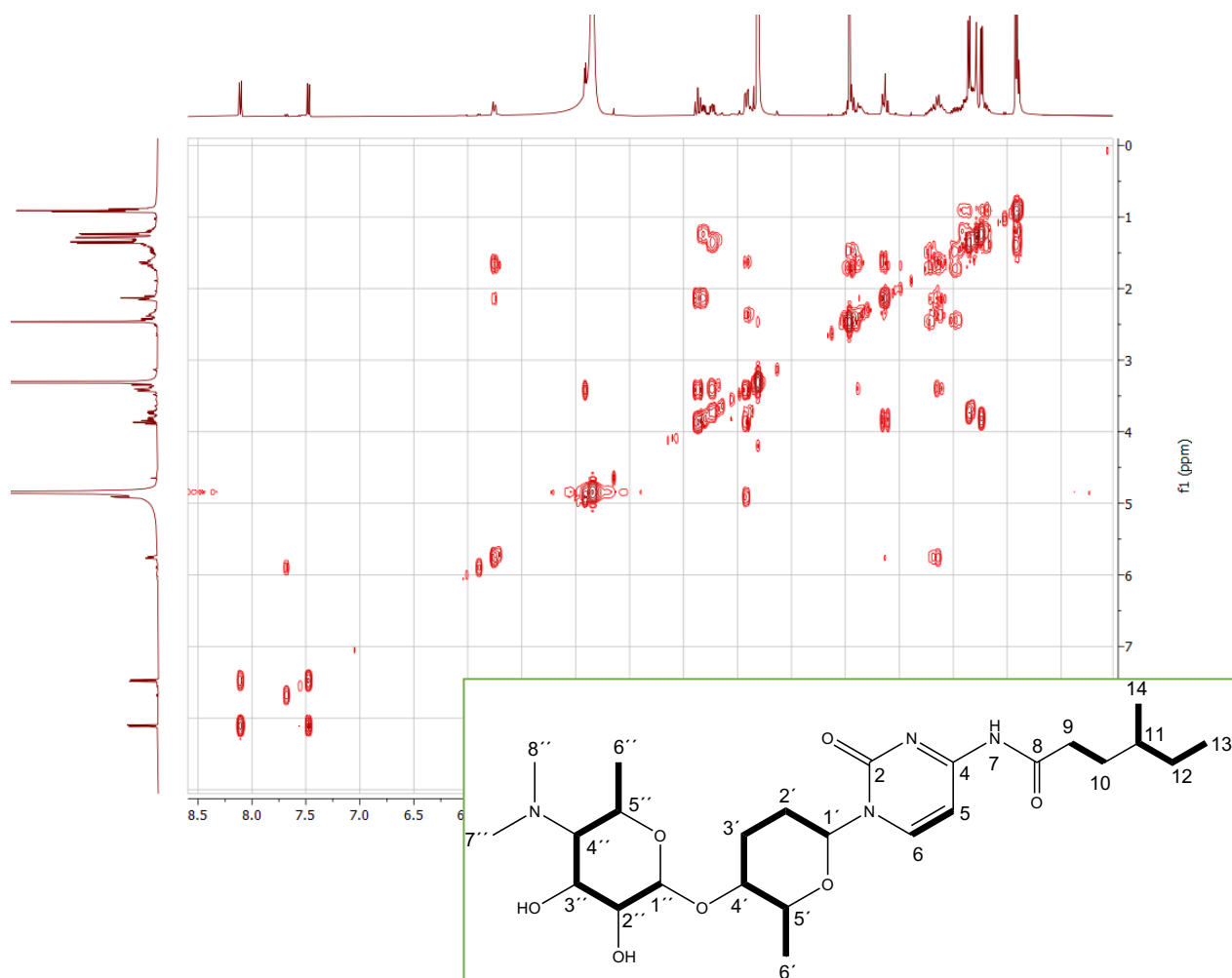


Figure S29. 700 MHz ^1H - ^{13}C HSQC-TOCSY NMR spectrum of cytosaminomycin F (**6**) in d_4 -MeOH. The inserts are showing, color-code-assisted, three out of four spin systems given in **6**.

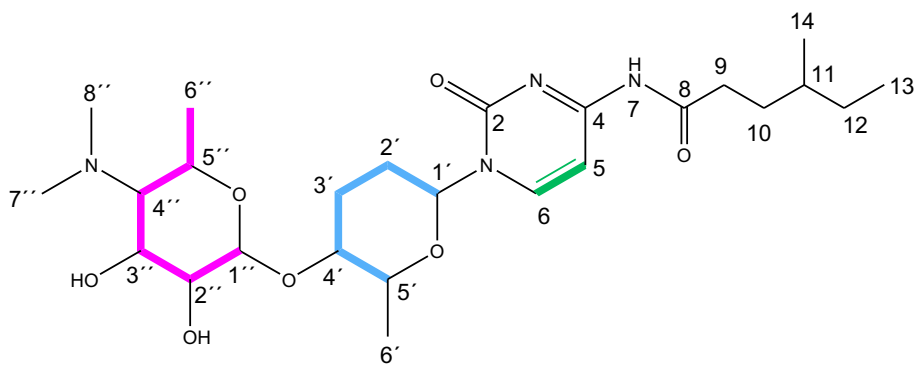
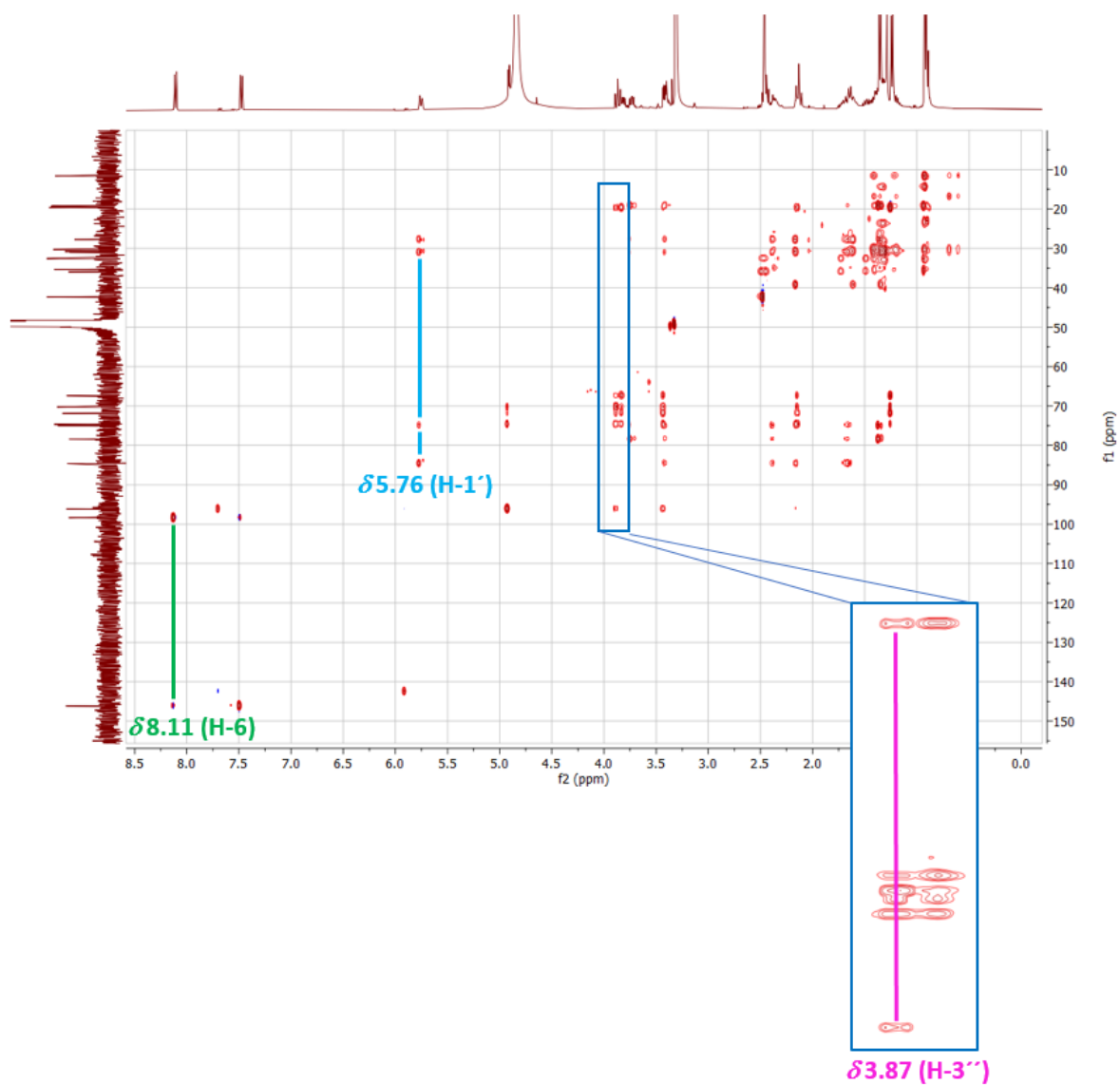


Figure S30. Detail region (δ_H 0.7 - 2.6 / δ_C 7.6 - 53.0) of the 700 MHz 1H - ^{13}C HSQC-TOCSY NMR spectrum of cytosaminomycin F (**6**) in d_4 -MeOH. The insert is visualizing the observed complete spin system of the side chain of **6** by bold blue lines.

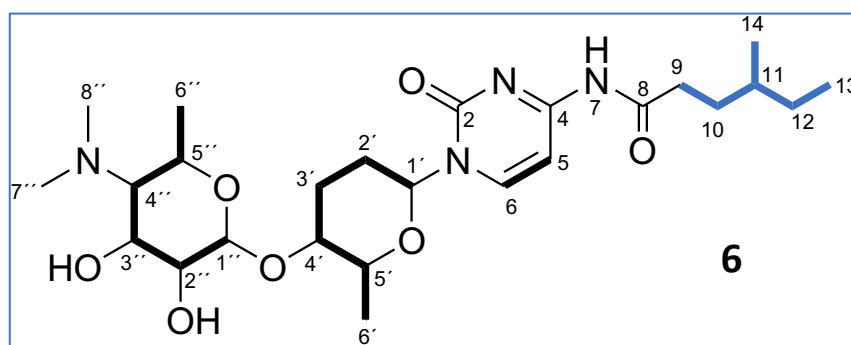
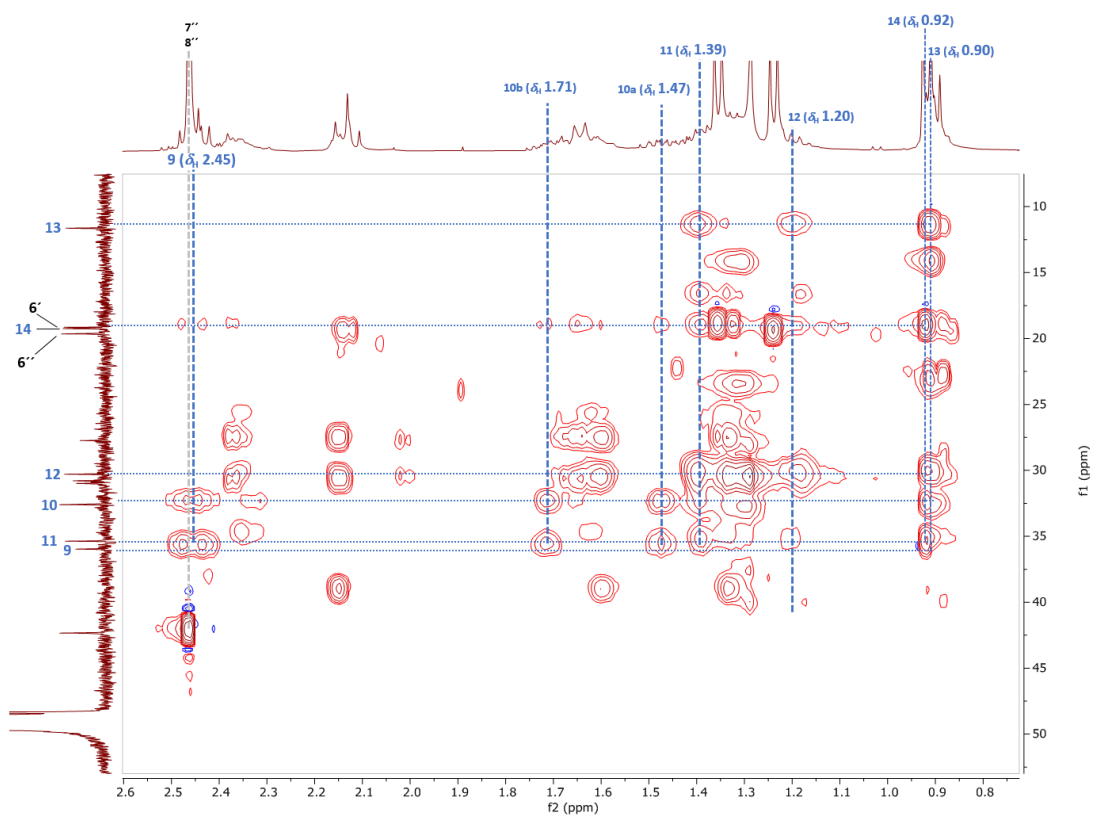


Figure S31. 600 MHz ^1H - ^{13}C HMBC NMR spectrum of cytosaminomycin F (**6**) in d_4 -MeOH.

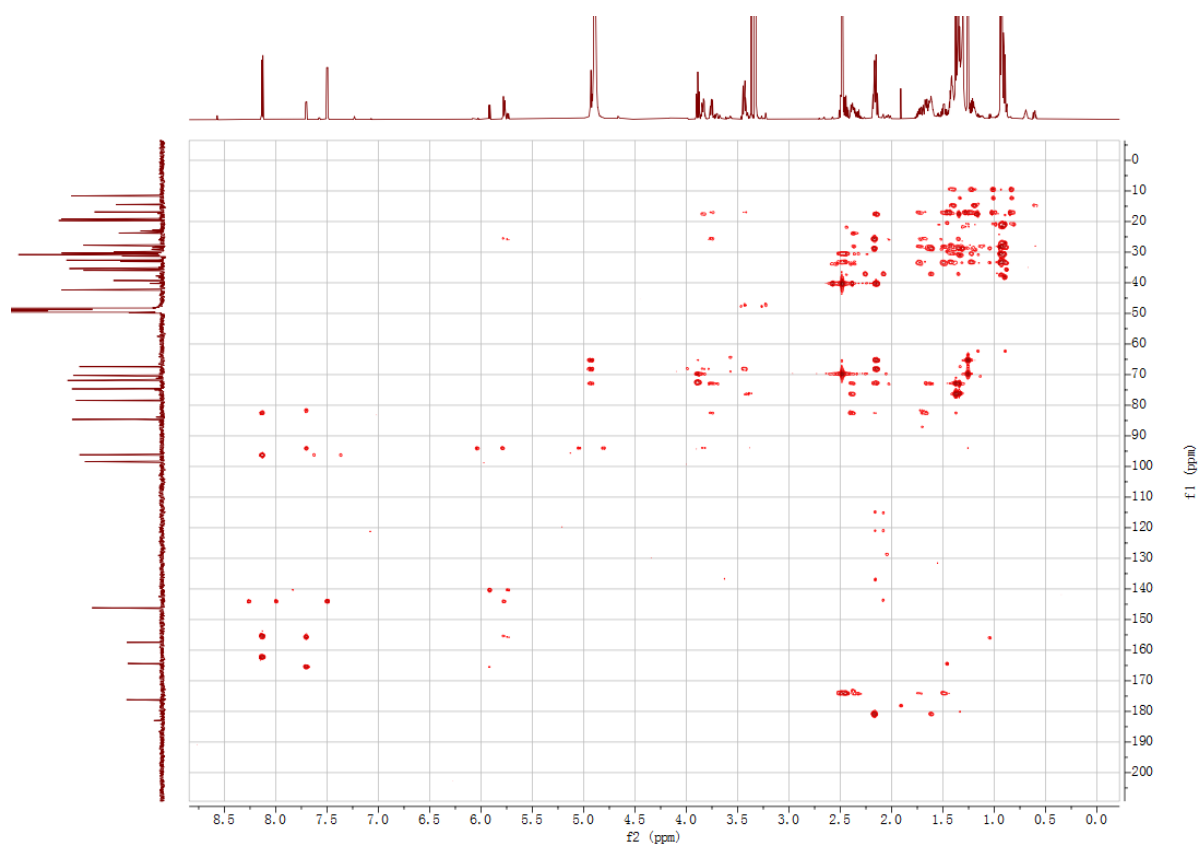


Figure S32. 700 MHz ^1H - ^1H NOESY NMR spectrum of cytosaminomycin F (**6**) in d_4 -MeOH.

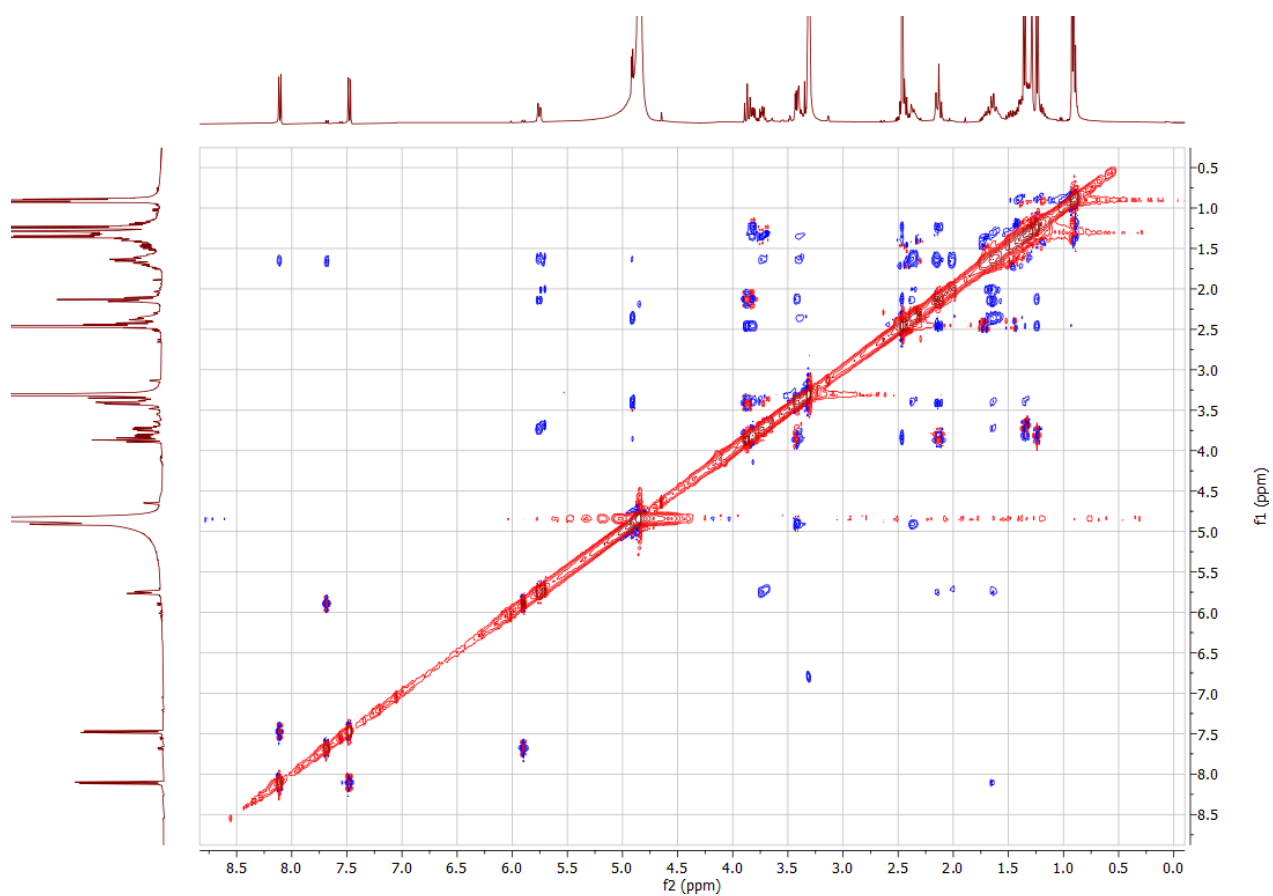


Figure S33. Interpretation of the NOESY correlations. Shown are minimized 3D structures of compound **6** from two different perspectives. The upper one highlights the through space interactions (as dashed lines) of amicitose, cytosine and the side chain, while the one at the bottom visualizes the NOE contacts given in the amosamine unit.

Color Code: **Yellow:** NOEs at the upper face of the sugar moiety
Orange: NOEs at the lower face of the sugar moiety
Blue: NOE's of the cytosine portion and the sidechain

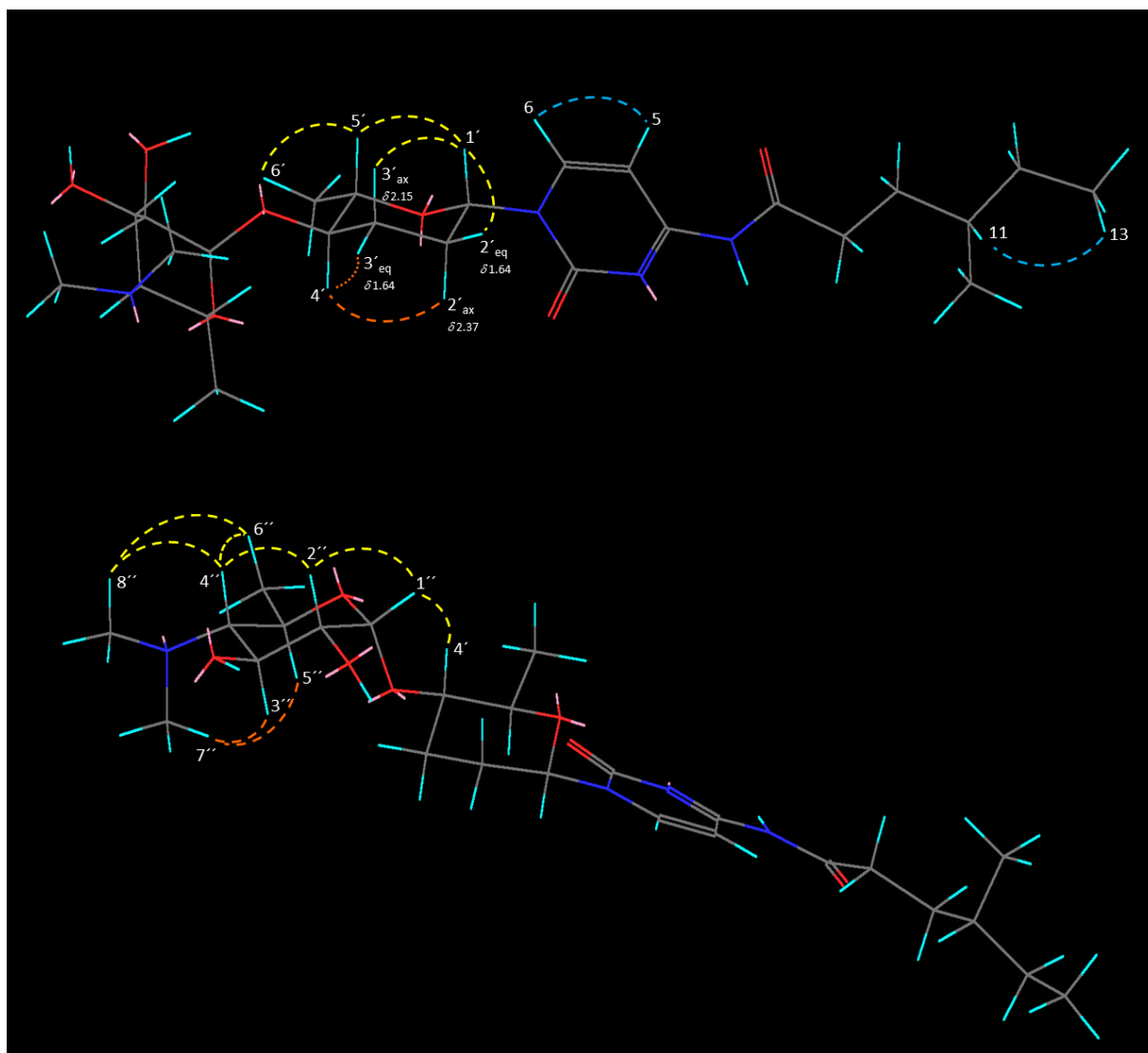


Figure S34. FT-IR spectrum of **6**.

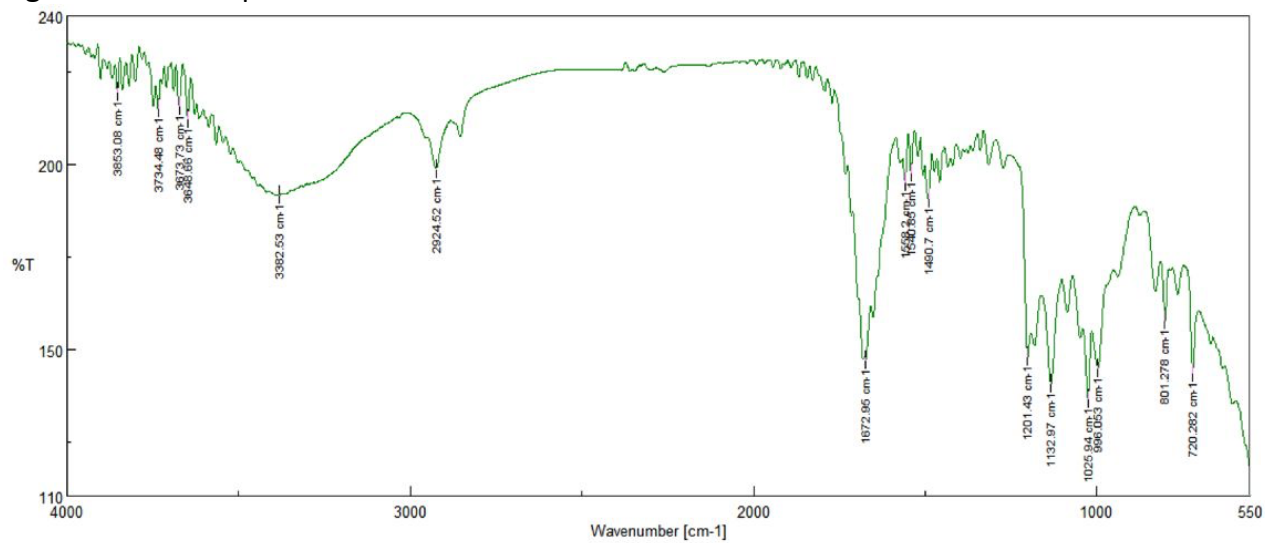


Figure S35. CD spectrum of **6** in MeOH (conc = 0.2 mg/mL).

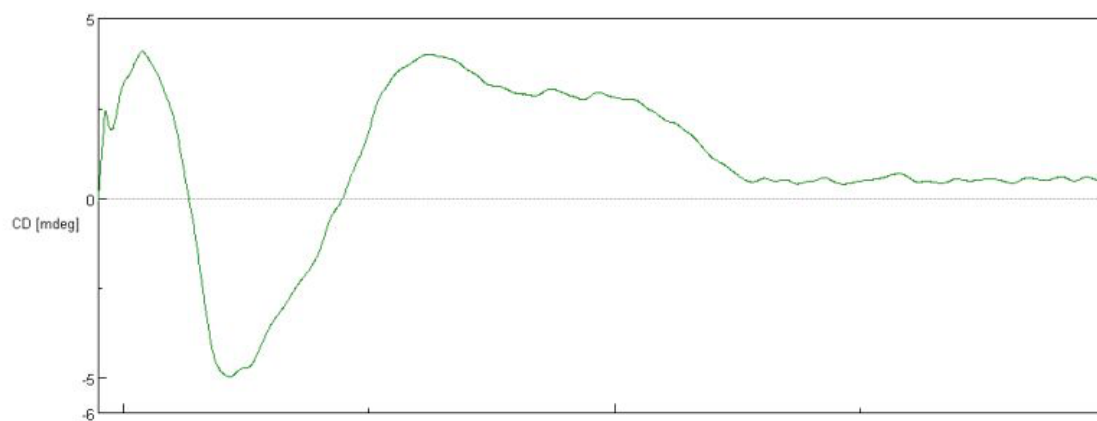


Figure S36. 400 MHz ^1H NMR spectrum of cytosaminomycin G (**7**) in d_4 -MeOH.

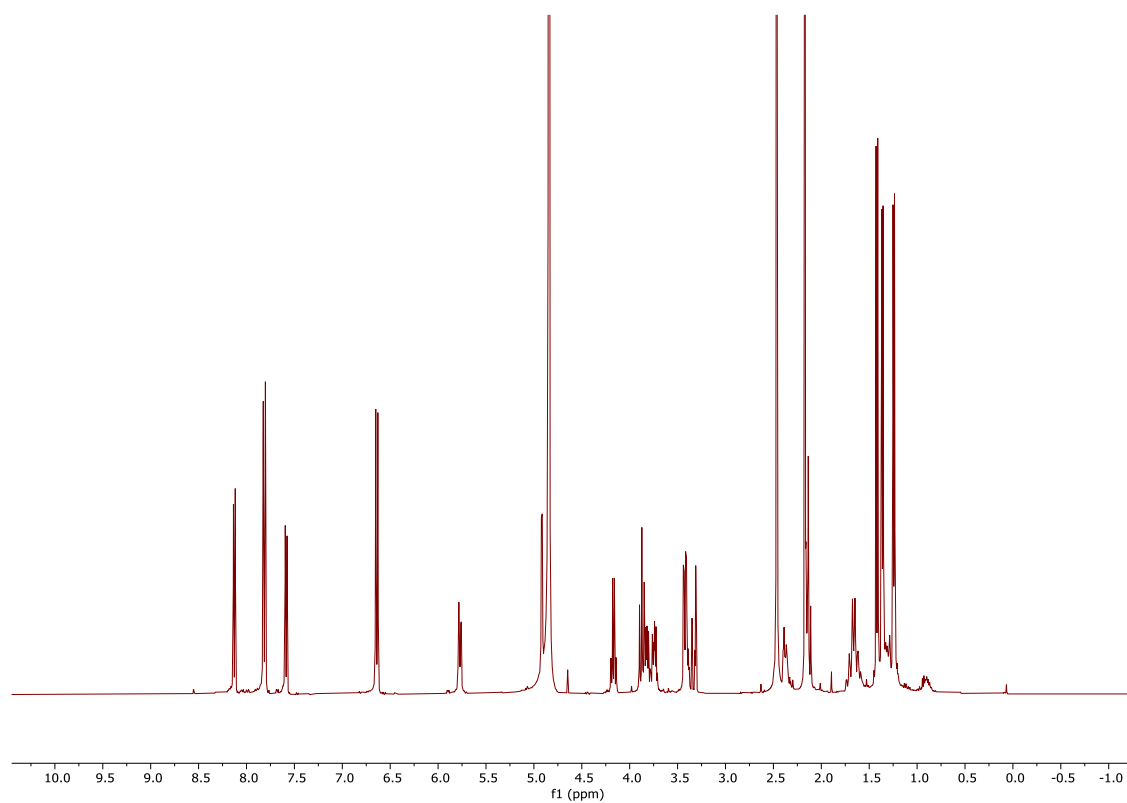


Figure S37. 100 MHz ^{13}C NMR spectrum of cytosaminomycin G (**7**) in d_4 -MeOH.

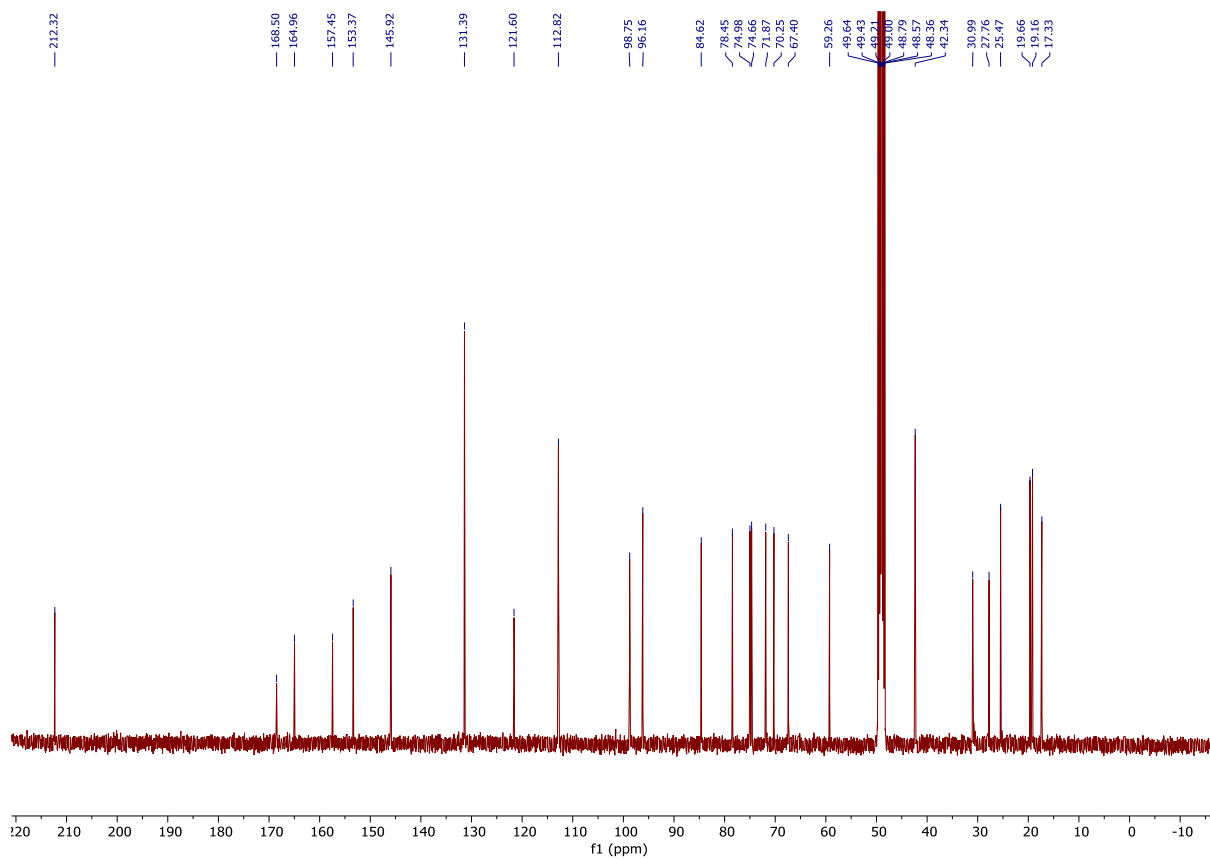


Figure S38. 400 MHz ^1H NMR spectrum of cytosaminomycin G (**7**) in d_6 -DMSO.

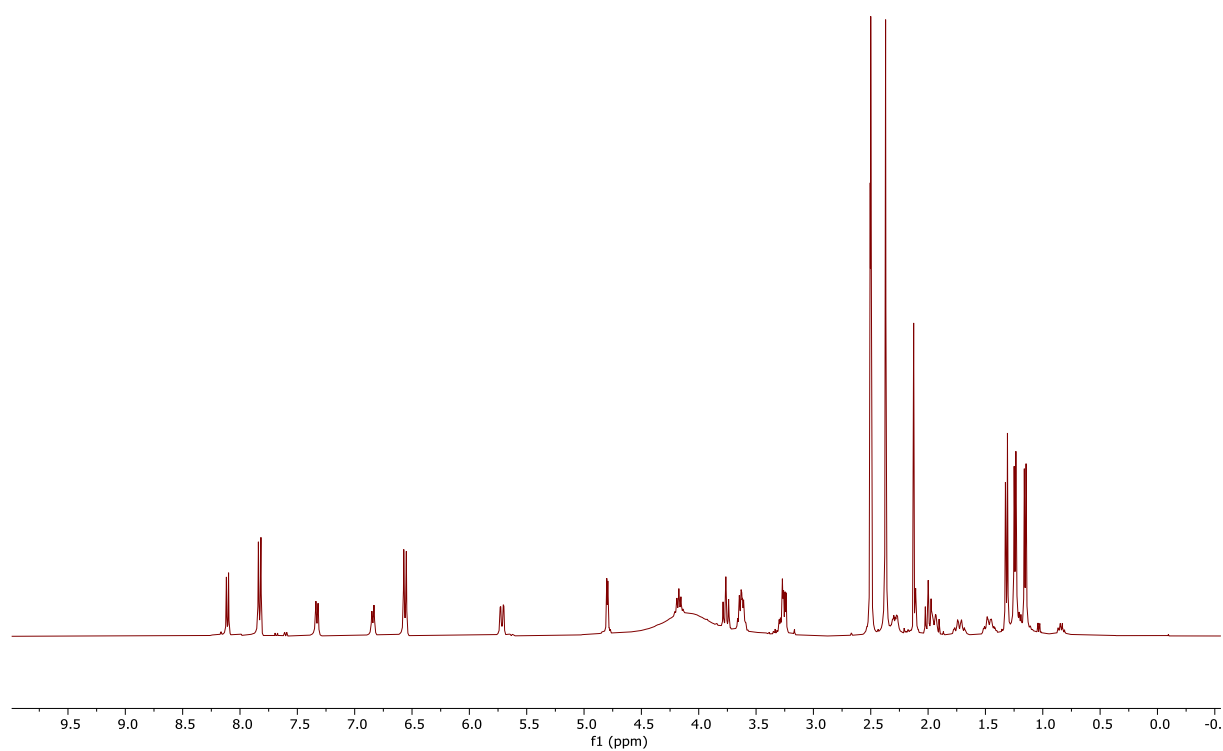


Figure S39. 100 MHz ^{13}C NMR spectrum of cytosaminomycin G (**7**) in d_6 -DMSO.

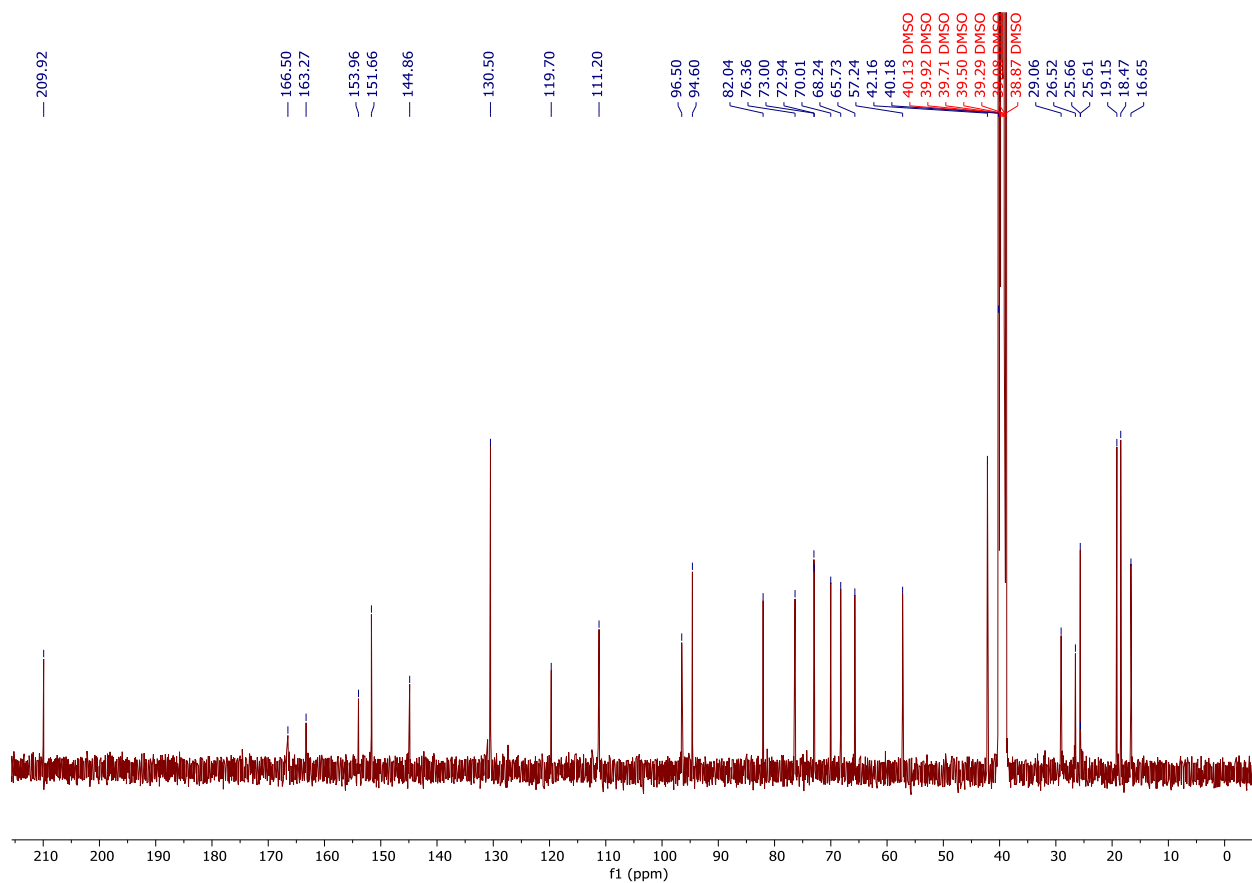


Figure S40. 400 MHz DEPT135 NMR spectrum of cytosaminomycin G (**7**) in d_6 -DMSO.

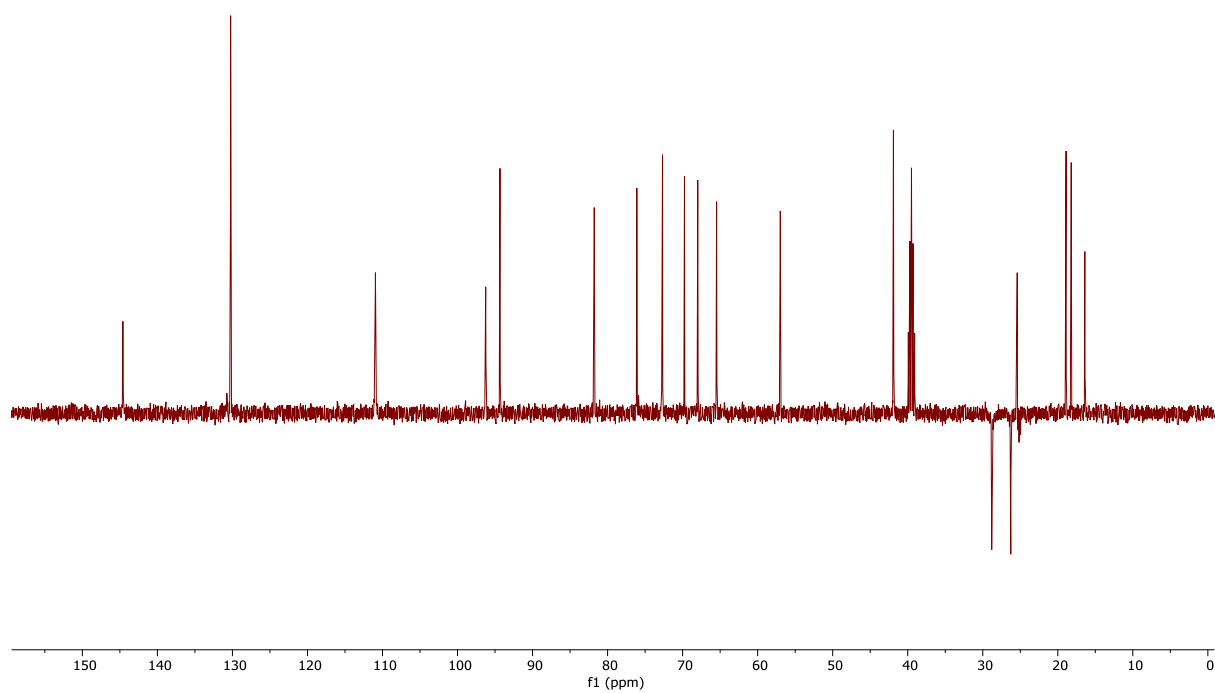


Figure S41. 400 MHz edited ^1H - ^{13}C HSQC NMR spectrum of **7** in d_6 -DMSO.

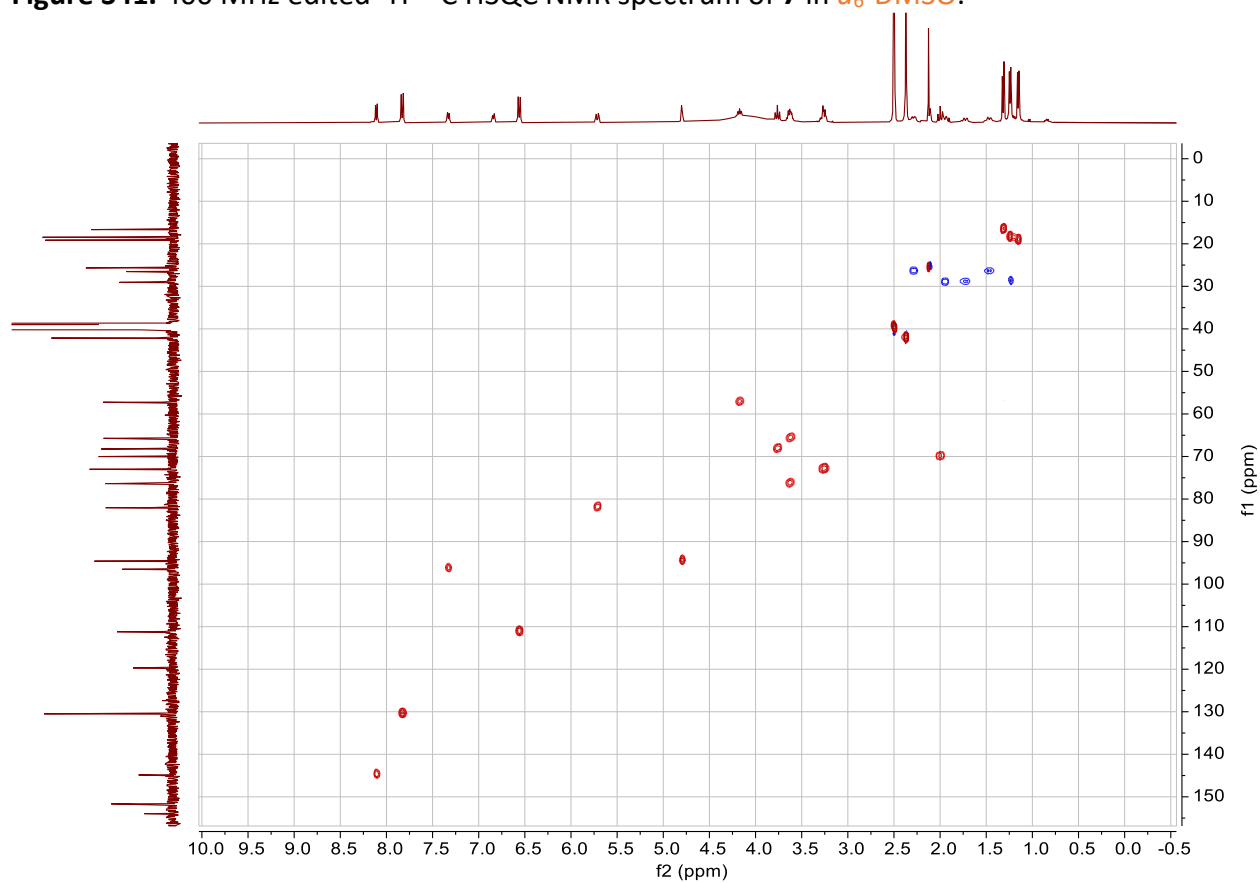


Figure S42. 400 MHz ^1H - ^1H COSY NMR spectrum of cytosaminomycin G (**7**) in d_6 -DMSO.

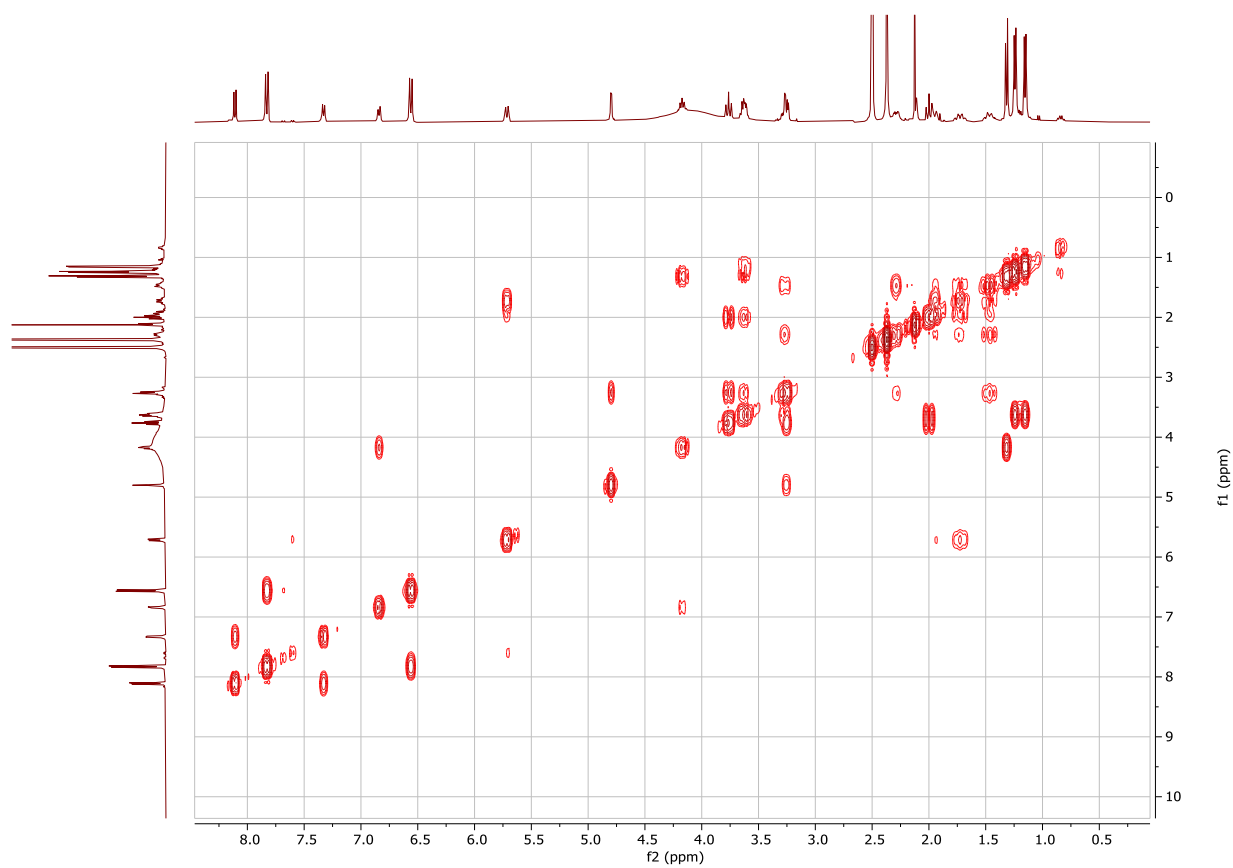


Figure S43. 400 MHz ^1H - ^{13}C HSQC-TOCSY NMR spectrum of **7** in d_6 -DMSO.

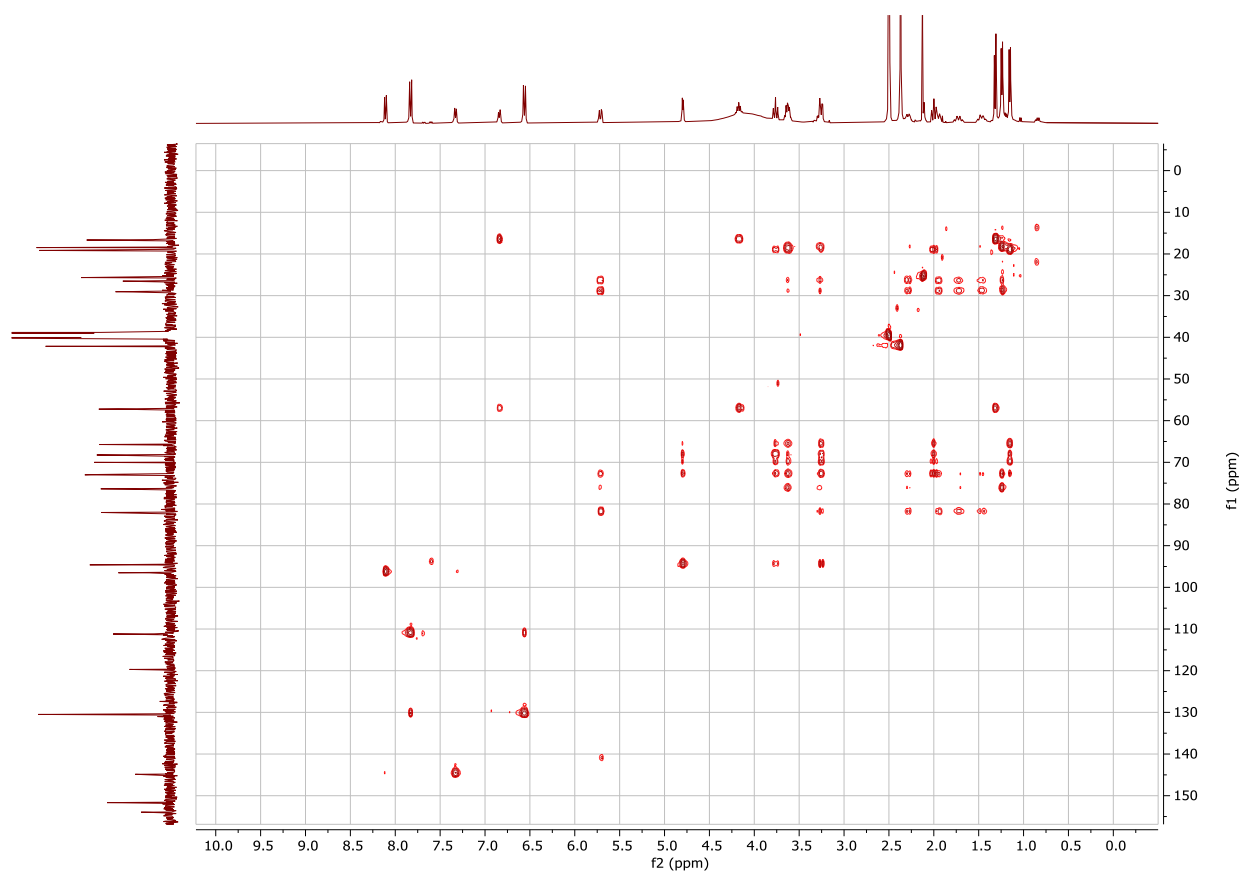


Figure S44. 400 MHz ^1H - ^{13}C HMBC NMR spectrum of cytosaminomycin G (**7**) in d_6 -DMSO.

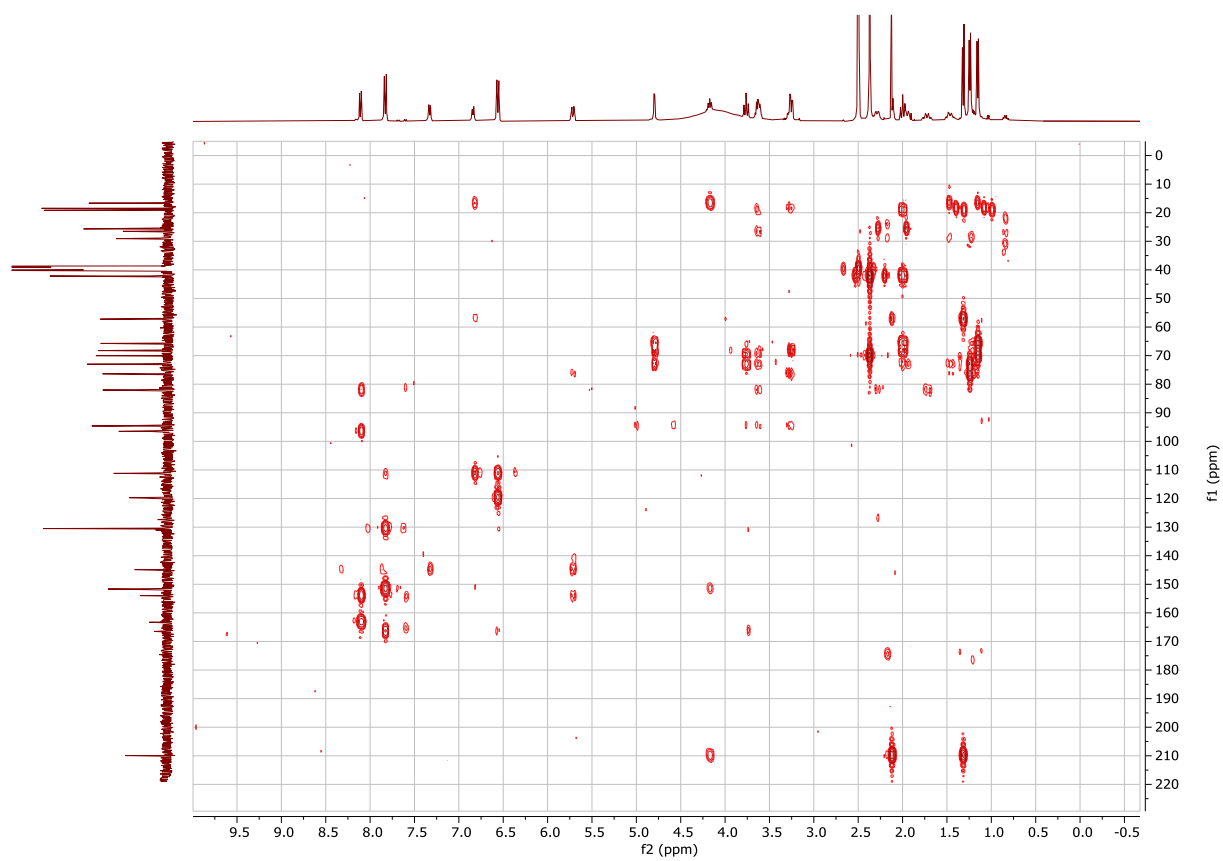


Figure S45. 400 MHz ^1H - ^{15}N HSQC NMR spectrum of cytosaminomycin G (**7**) in d_6 -DMSO.

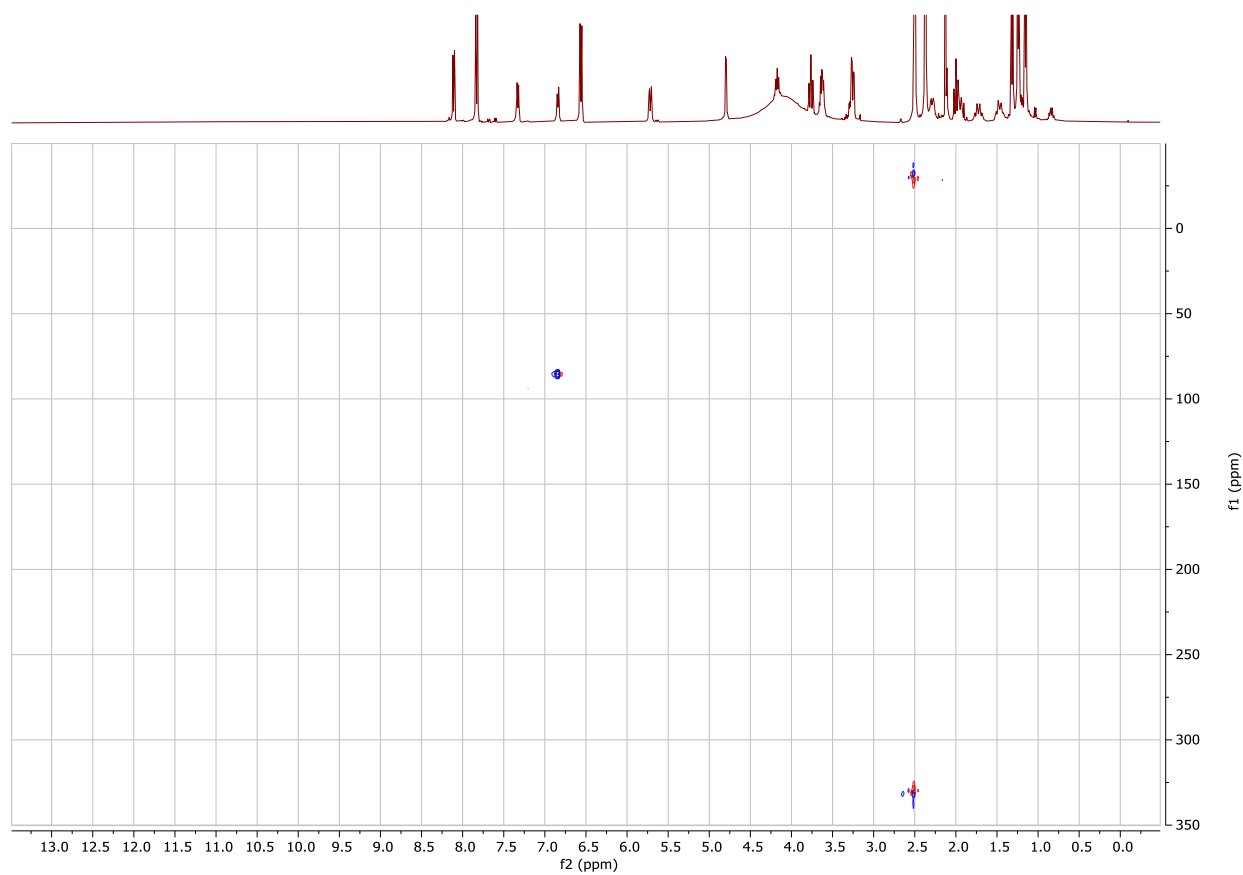


Figure S46. 400 MHz ^1H - ^{15}N HMBC NMR spectrum of cytosaminomycin G (**7**) in d_6 -DMSO.

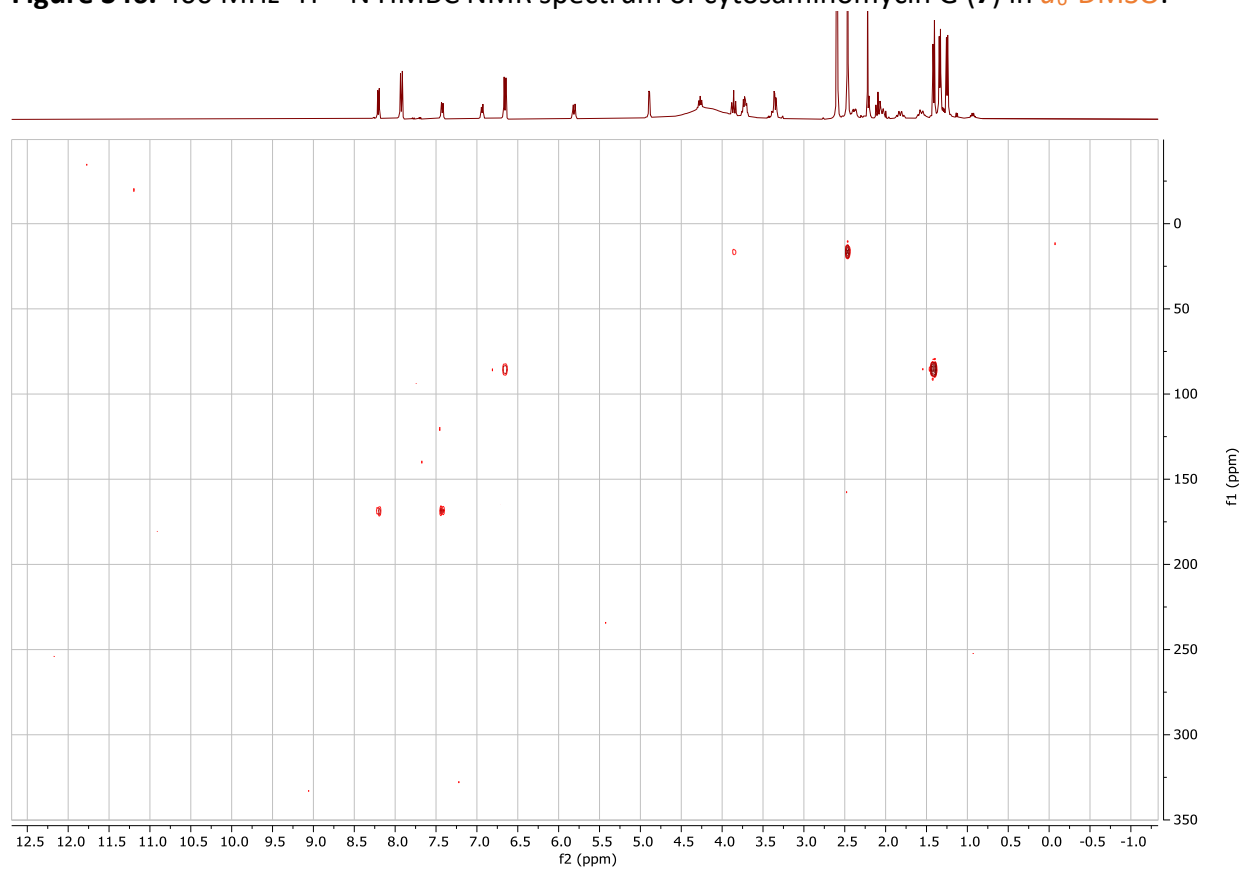


Table S6. ^1H and ^{13}C NMR data of cytosaminomycin G (**7**) in d_6 -DMSO.

moiety	no.	δ_{H}	$\delta_{\text{C,N}}$
cytosine	2		163.3, qC
	4		154.0, qC
	5	7.33, d (7.5)	96.5, CH
	6	8.11, d (7.5)	144.9, CH
	7	10.79, brs	NH
side chain	8		166.5, qC
	9		119.7, qC
	10	7.83, d (8.9)	130.5, CH
	11	6.56, d (8.9)	111.2, CH
	12		151.7, qC
	13	6.56, d (8.9)	111.2, CH
	14	7.83, d (8.9)	130.5, CH
	15	6.84, d (7.3)	85.4, NH
	16	4.17, dq (7.1, 7.3)	57.2, CH
	17		209.9, qC
	18	2.13, s	25.7, CH ₃
19	1.32, d (7.1)	16.7, CH ₃	
amicetose	1'	5.71 dd (10.6, 1.9)	82.0, CH
	2'	1.73, m	29.1, CH ₂
		1.95, m	
	3'	1.47, m	26.5, CH ₂
		2.28, m	
	4'	3.24, m	73.0, CH
	5'	3.63, m	76.4, CH
6'	1.24, d (6.1)	18.5, CH ₃	
amosamine	1''	4.80, d (3.7)	94.6, CH
	2''	3.26, m	72.9, CH
	3''	3.76, t (9.6)	68.2, CH
	4''	2.00, t (10.1)	70.0, CH
	5''	3.62, m	65.7, CH
	6''	1.15, d (6.1)	19.2, CH ₃
	7''	2.37, s	42.2, CH ₃
	8''	2.37, s	42.2, CH ₃

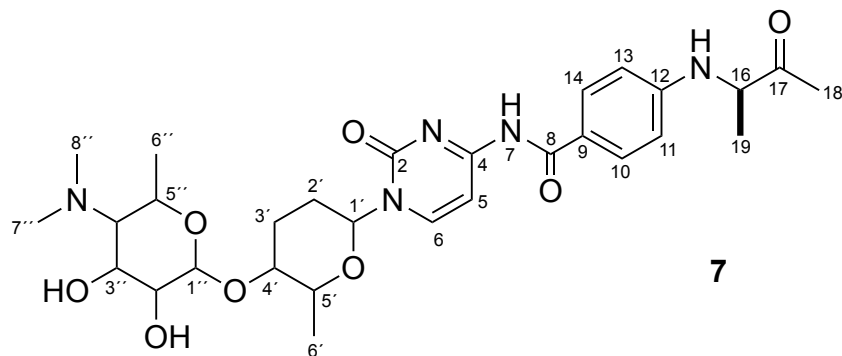


Figure S47. FT-IR spectrum of cytosaminomycin G (7)

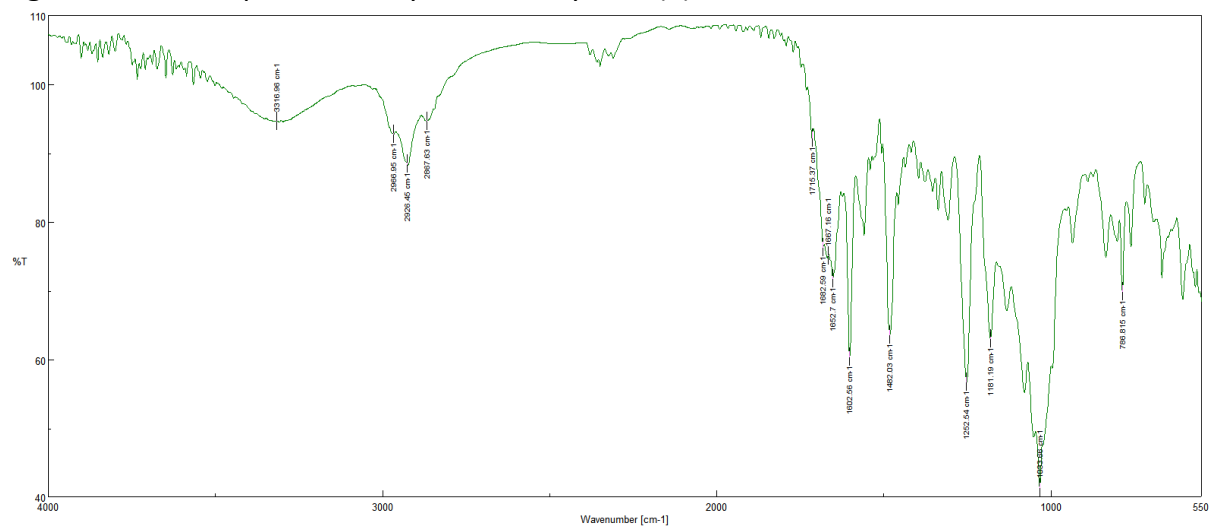


Figure S48. 400 MHz ^1H NMR spectrum of streptcytosine D (**8**) in d_6 -DMSO.

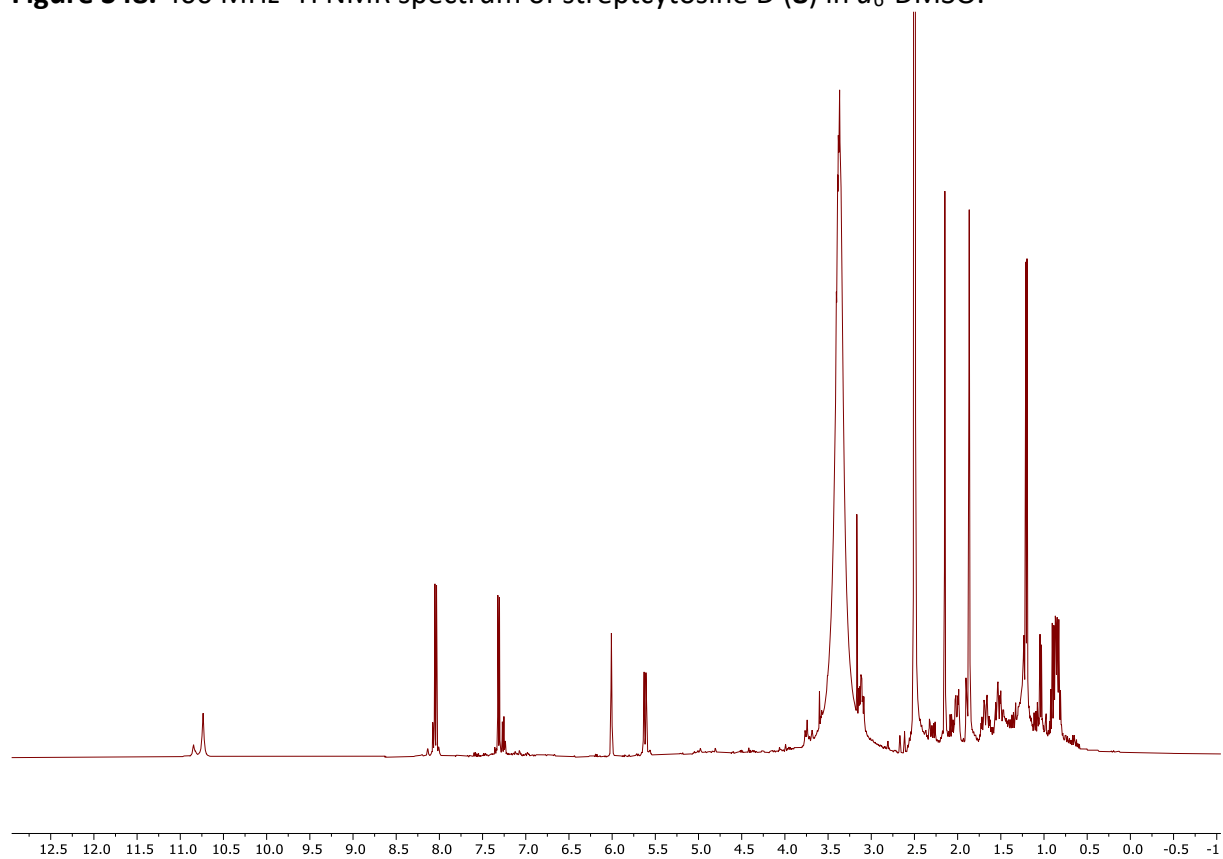


Figure S49. 100 MHz ^{13}C NMR spectrum of streptcytosine D (**8**) in d_6 -DMSO.

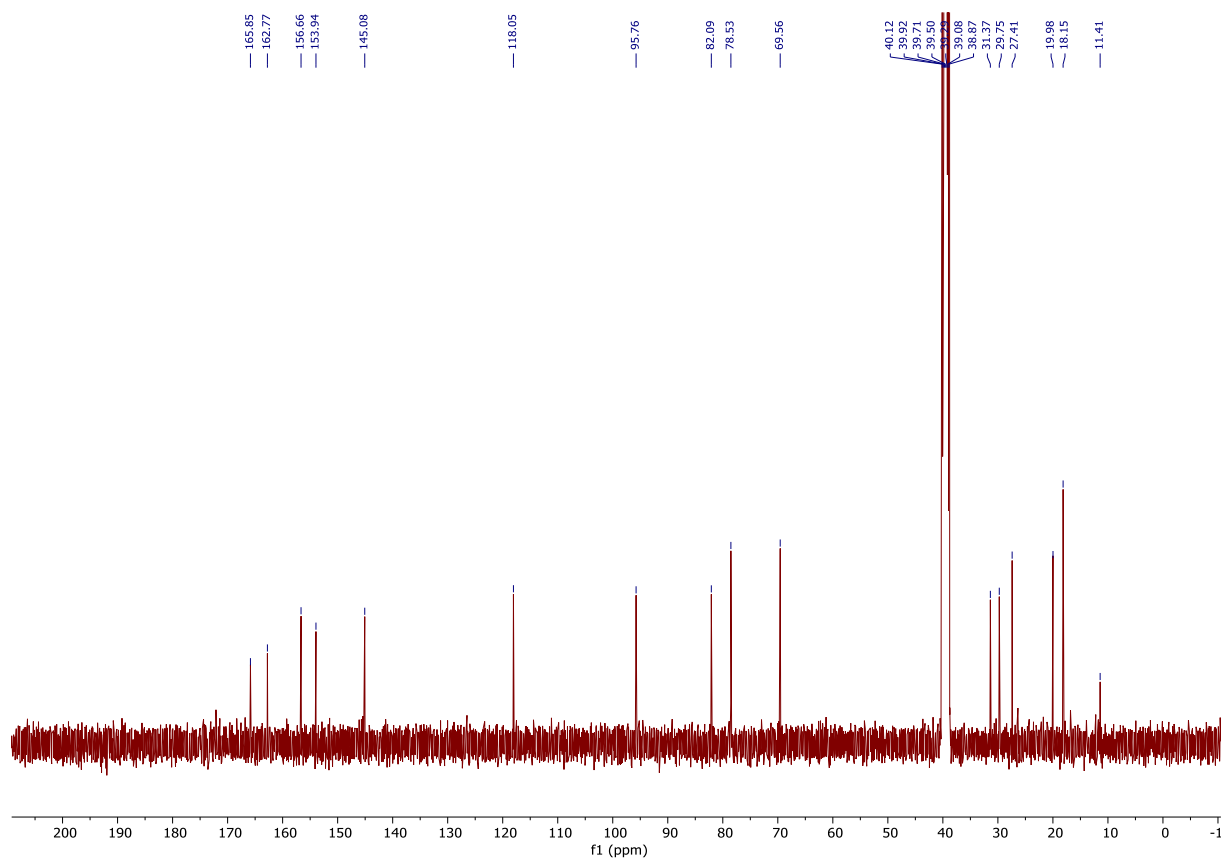


Table S7. ^1H and ^{13}C NMR data of streptcytosine D (**8**), recorded in d_6 -DMSO.

moiety	no.	δ_{H}	δ_{C}
cytosine	2		153.9, qC
	4		162.8, qC
	5	7.31, d (7.4)	95.8, CH
	6	8.04, d (7.4)	145.1, CH
	7	10.74, s	
side chain	8		165.9, qC
	9	6.01, t (1.4)	118.1, CH
	10		156.7, qC
	11	1.87, d (1.4)	27.4, CH ₃
	12	2.15, d (1.4)	20.0, CH ₃
amicetose	1'	5.62, dd (10.6, 2.0)	82.1, CH
	2'	1.68, m	29.8, CH ₂
		1.88, m	
	3'	1.52, m	31.4, CH ₂
		2.01, m	
	4'	3.11, m	69.6, CH
5'	3.38, m	78.5, CH	
6'	1.20, d (6.2)	18.2, CH ₃	

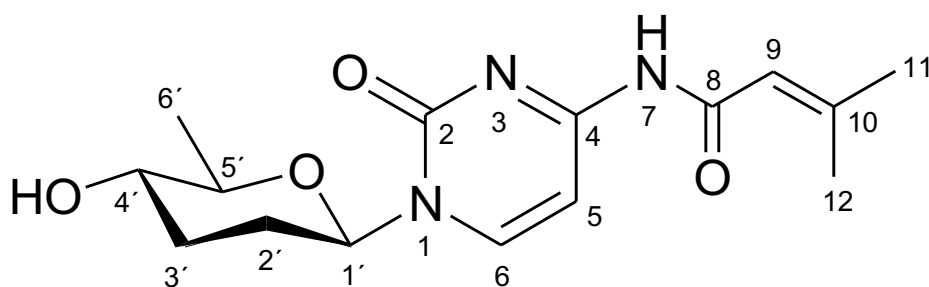


Figure S50. FT-IR spectrum of streptcytosine D (**8**).

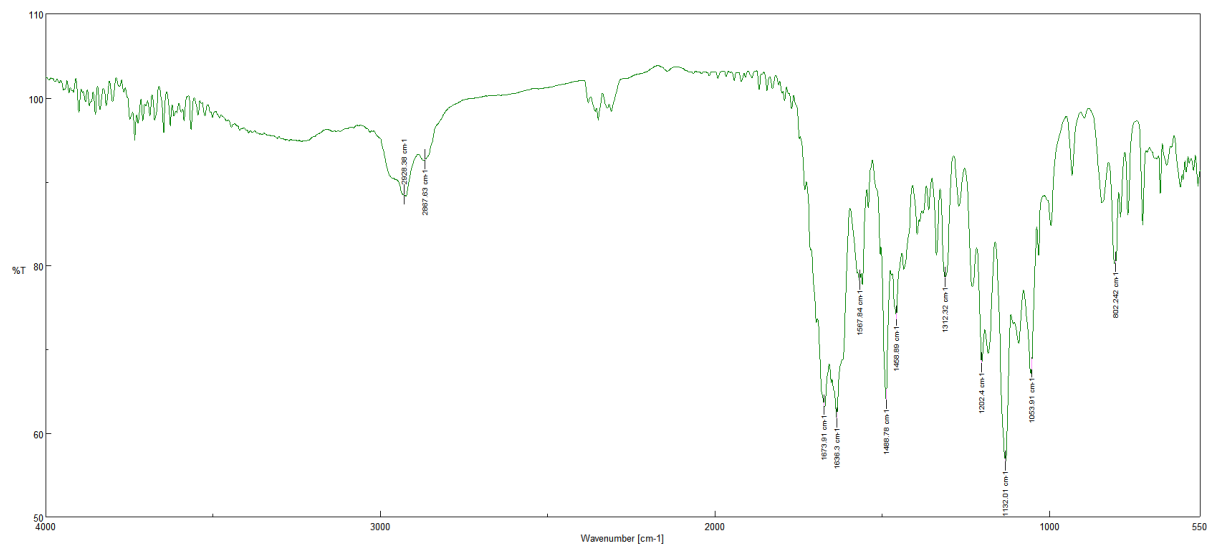


Figure S51. 400 MHz ^1H NMR spectrum of streptocytosine E (**9**), recorded in d_6 -DMSO.

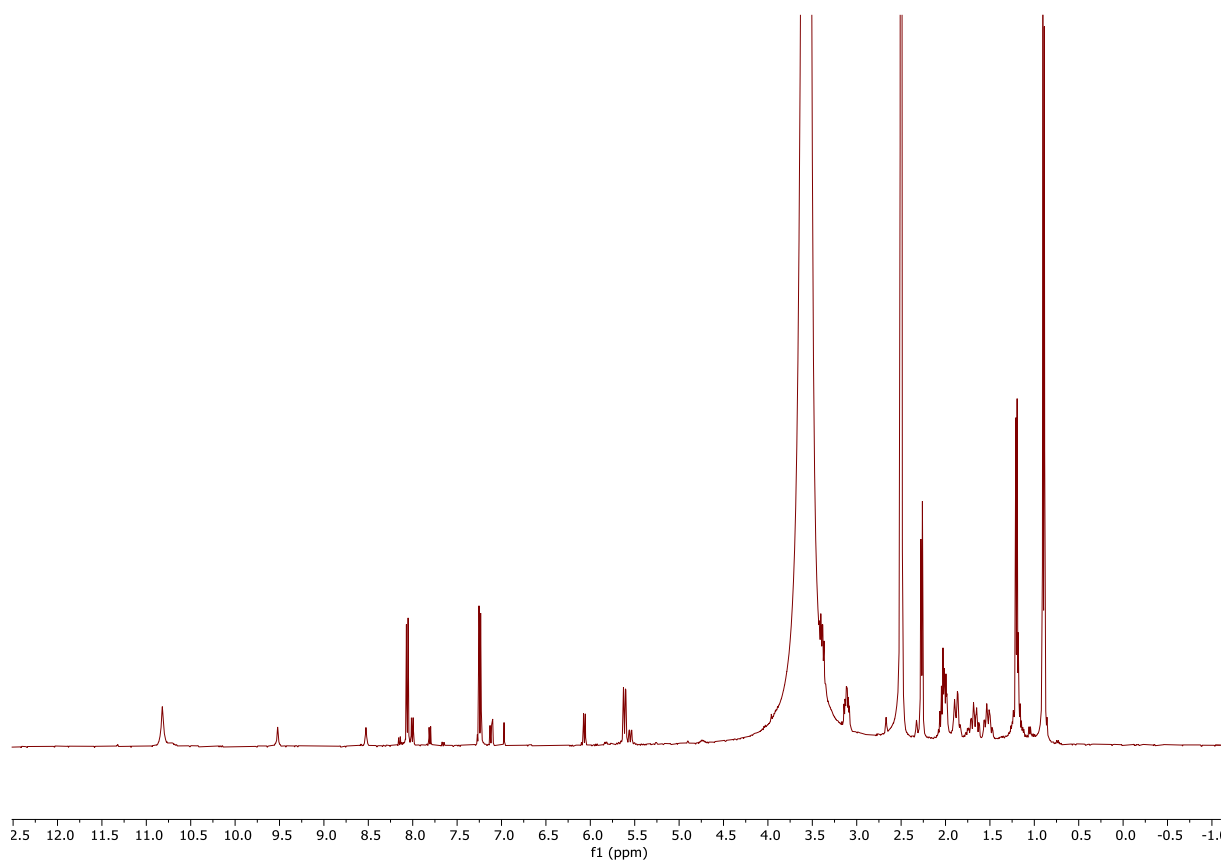


Figure S52. 100 MHz ^{13}C NMR spectrum of streptocytosine E (**9**), recorded in d_6 -DMSO.

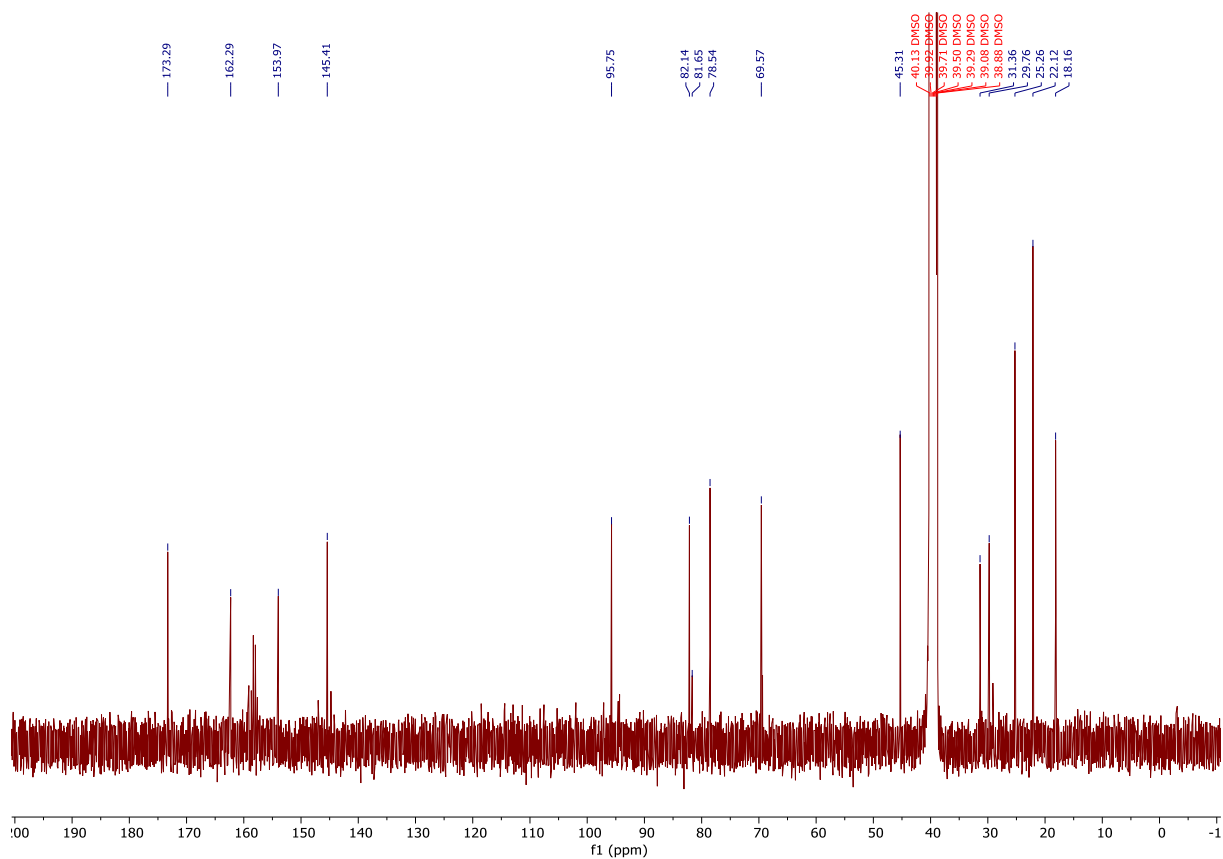


Table S8. ^1H and ^{13}C NMR data of streptcytosine E (**9**), recorded in d_6 -DMSO.

moiety	no.	δ_{H}	δ_{C}
cytosine	2		154.0, qC
	4		162.3, qC
	5	7.24, d (7.5)	95.8, CH
	6	8.06, d (7.5)	145.4, CH
	7	10.82, s	
side chain	8		173.3, qC
	9	2.27, d (7.0)	45.3, CH ₂
	10	2.04, m	25.3, CH
	11	0.90, d (6.6)	22.1, CH ₃
	12	0.90, d (6.6)	22.1, CH ₃
amicetose	1'	5.62, dd (10.5, 1.8)	82.1, CH
	2'	1.68, m	29.8, CH ₂
		1.88, m	
	3'	1.52, m	31.4, CH ₂
		2.00, m	
	4'	3.11, m	69.6, CH
5'	3.39, m	78.5, CH	
6'	1.20, d (6.1)	18.2, CH ₃	

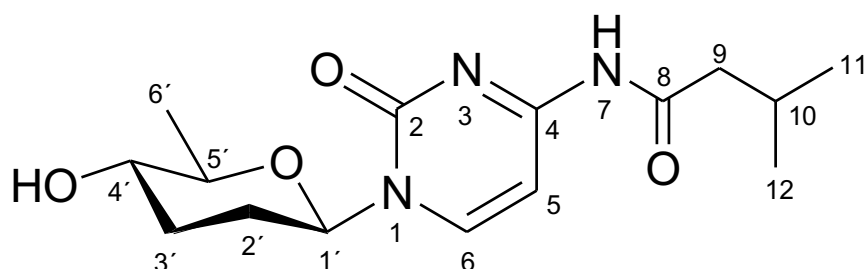


Figure S53. 400 MHz ^1H NMR spectrum of streptcytosine P (**10**) in d_4 -MeOH.

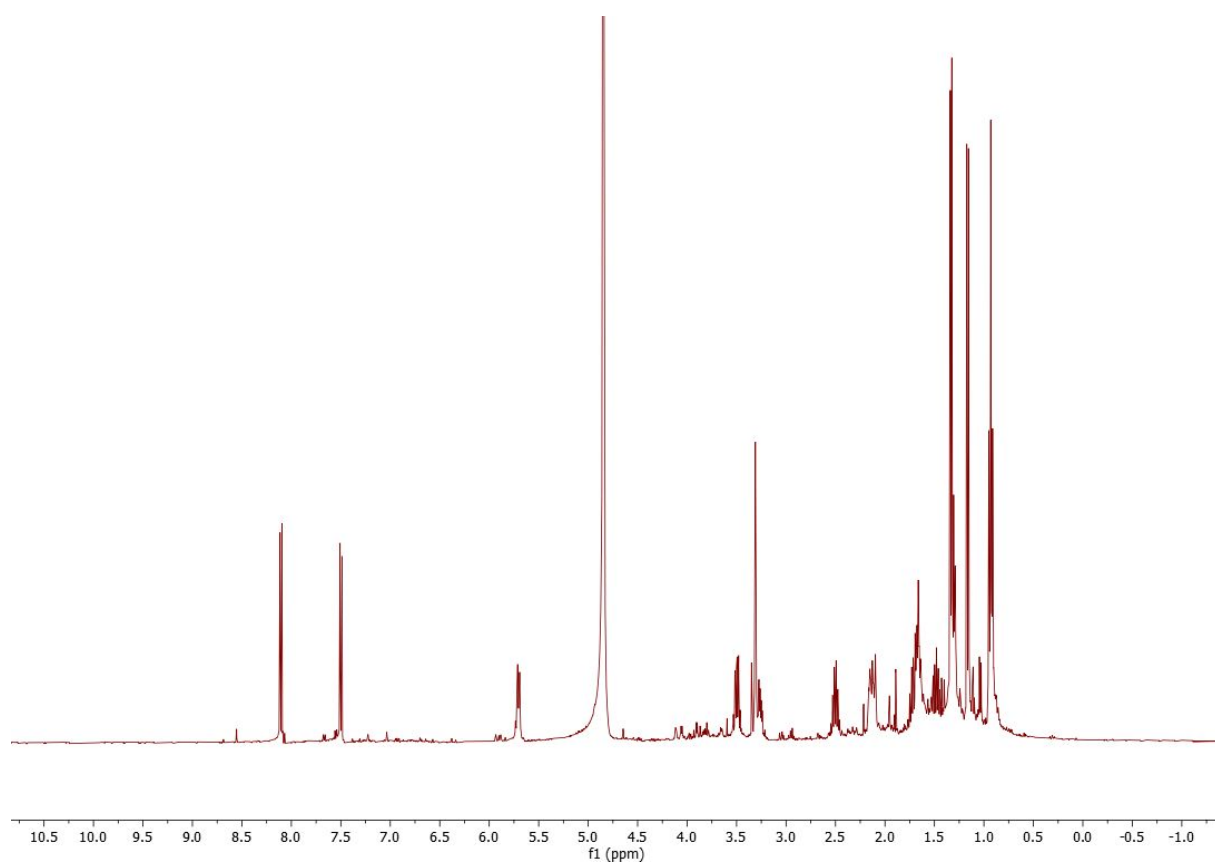


Figure S54. 100 MHz ^{13}C NMR spectrum of streptcytosine P (**10**) in d_4 -MeOH.

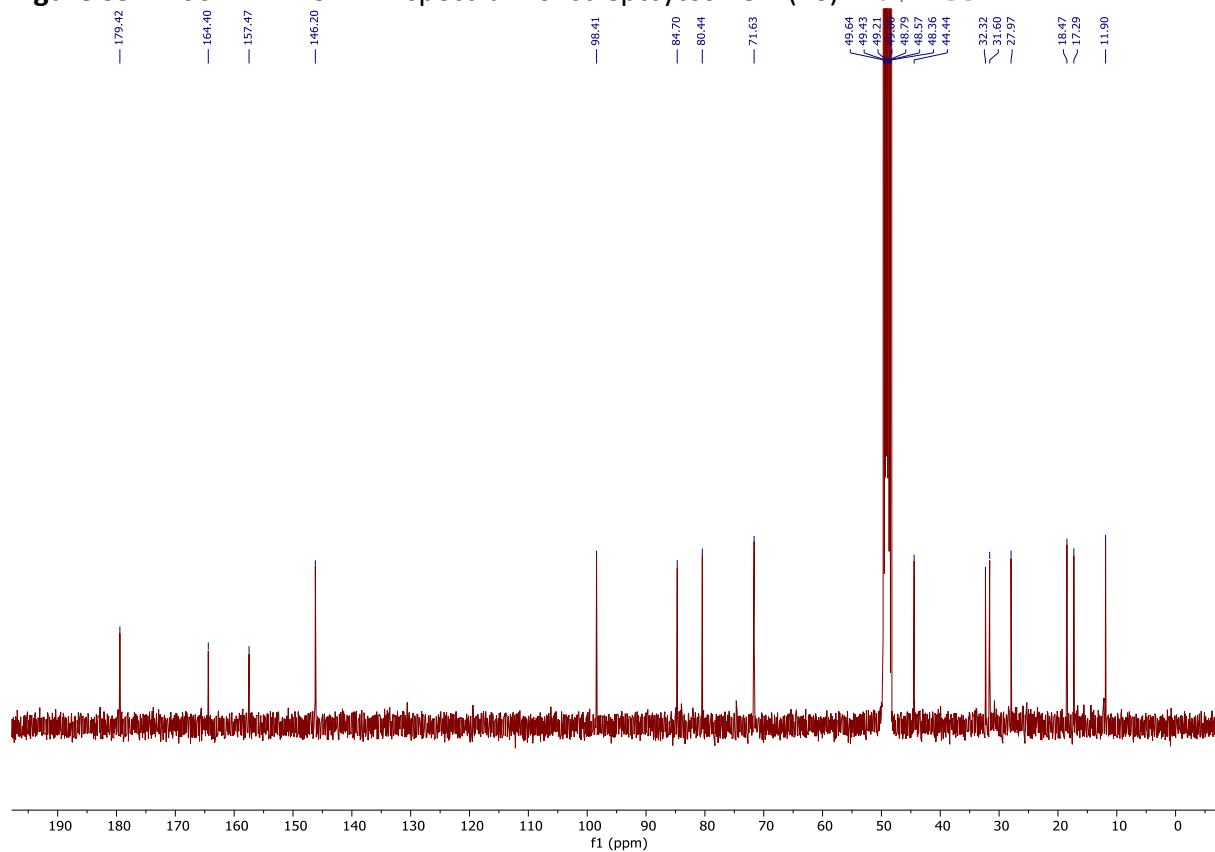


Figure S55. 400 MHz DEPT135 NMR spectrum (top) and 100 MHz ^{13}C NMR spectrum (bottom) of streptcytosine P (**10**) in d_4 -MeOH.

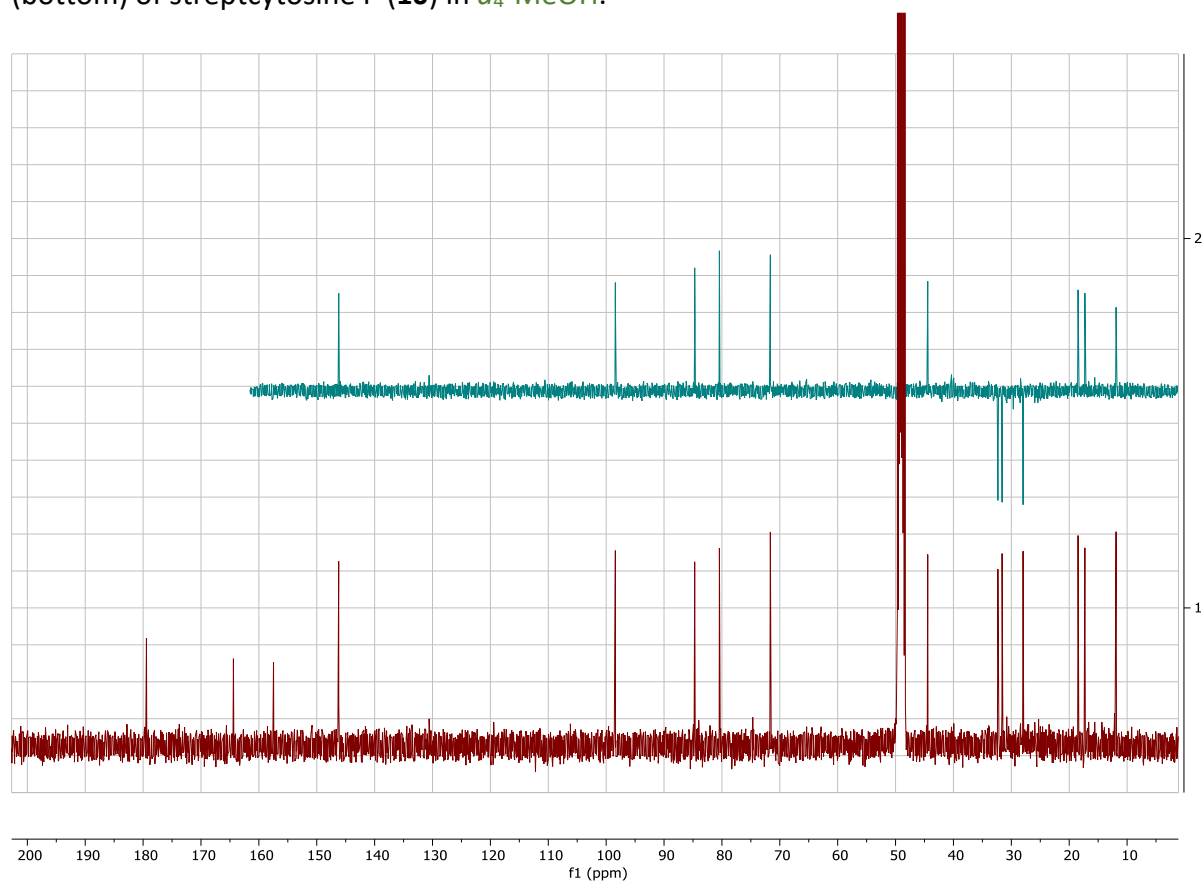


Figure S56. 400 MHz edited ^1H - ^{13}C HSQC NMR spectrum of streptcytosine P (**10**) in d_4 -MeOH.

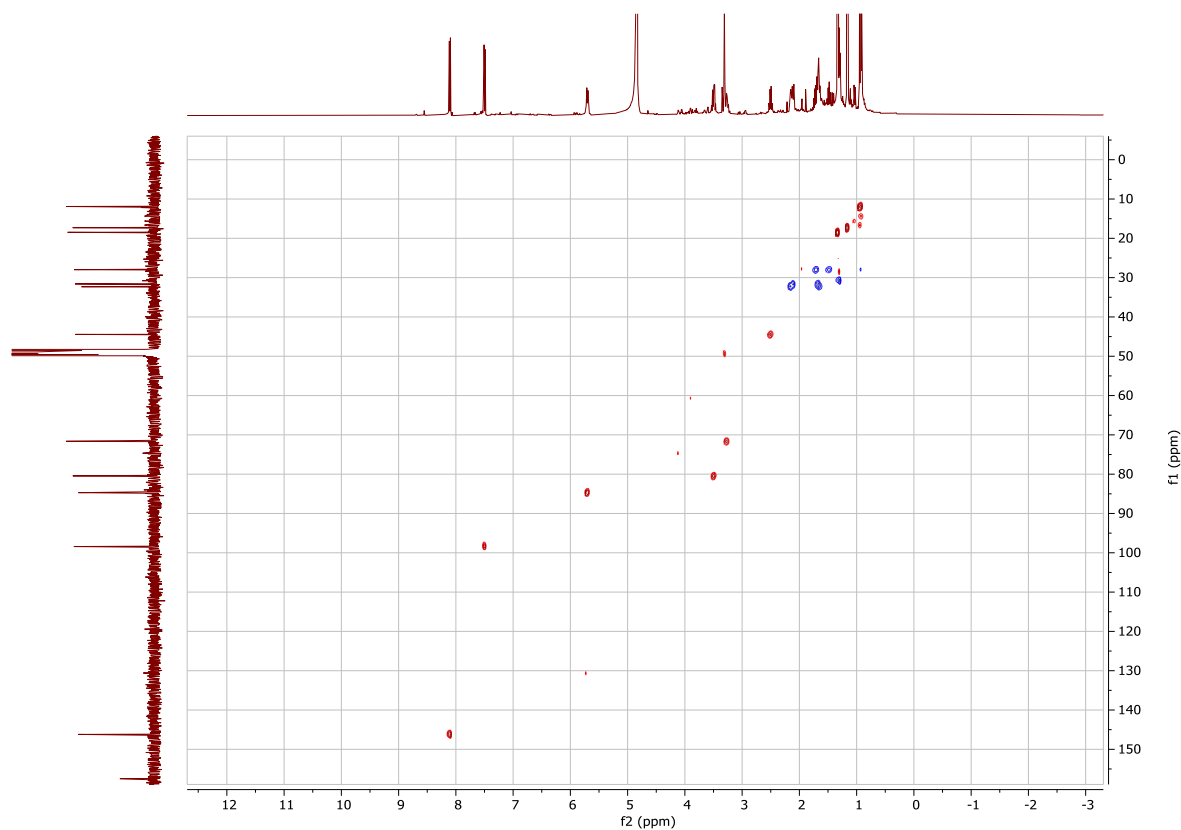


Figure S57. 400 MHz ^1H - ^1H COSY NMR spectrum of streptcytosine P (**10**) in d_4 -MeOH.

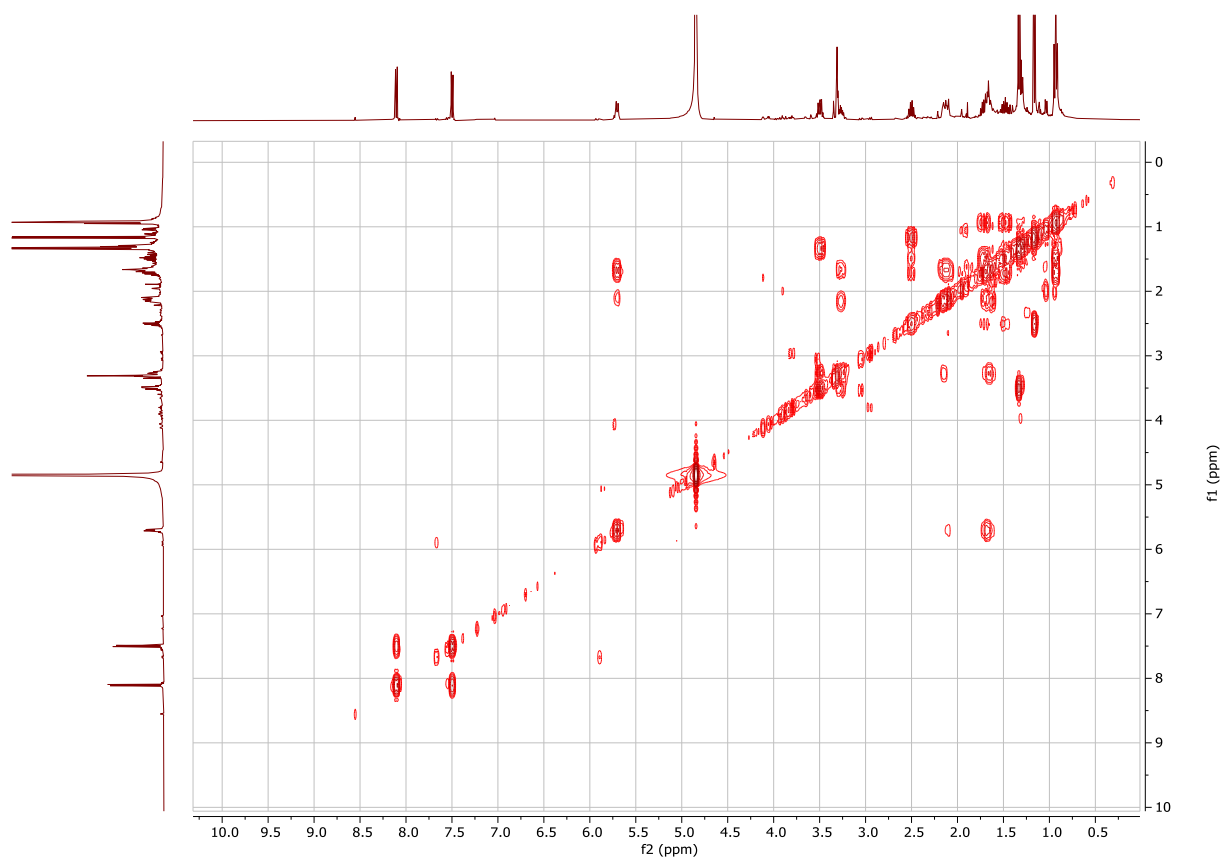


Figure S58. 400 MHz ^1H - ^{13}C HSQC-TOCSY NMR spectrum of **10** in d_4 -MeOH.



Figure S59. 400 MHz ^1H - ^{13}C HMBC NMR spectrum of streptcytosine P (**10**) in d_4 -MeOH.

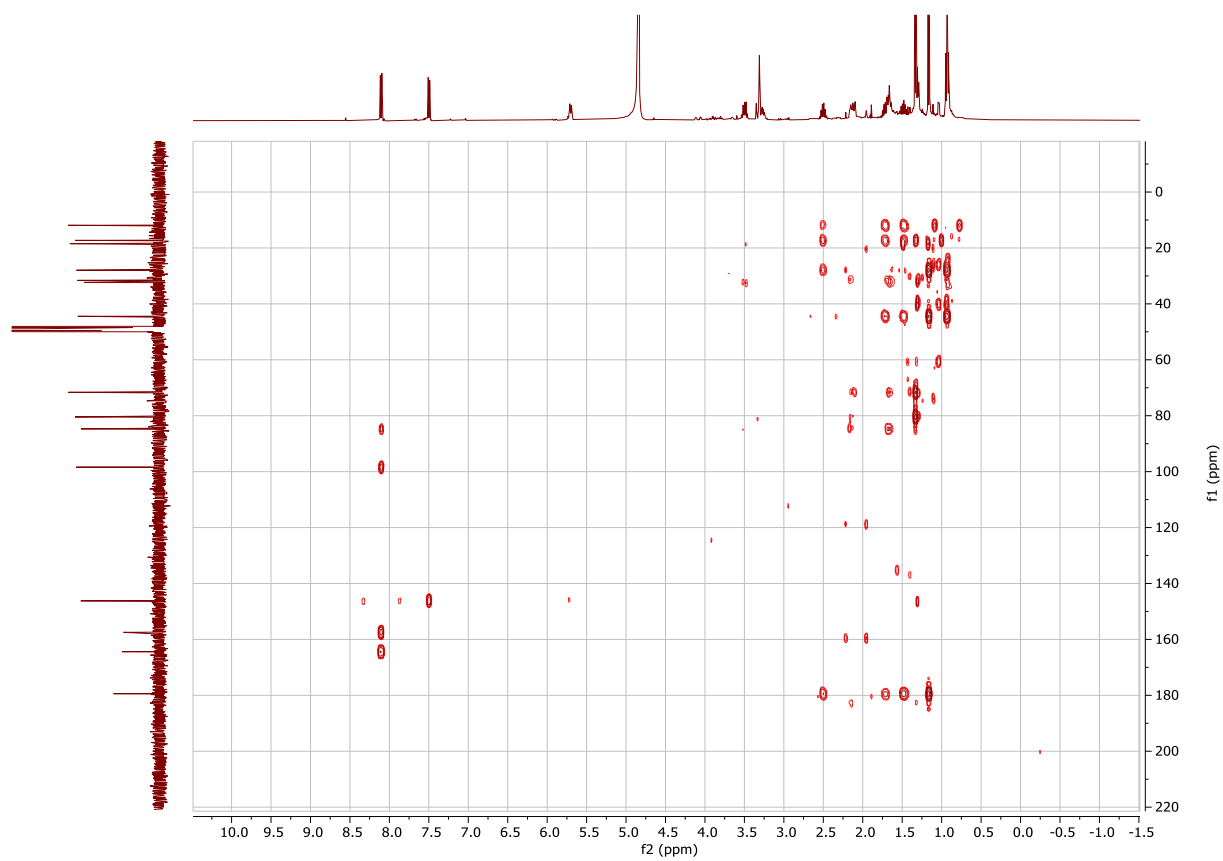


Table S9. ^1H and ^{13}C NMR data of streptcytosine P (**10**), recorded in $d_4\text{-MeOH}$.

moiety	no.	δ_{H}	δ_{C}
cytosine	2		157.5, qC
	4		164.4, qC
	5	7.50, d (7.5)	98.4, CH
	6	8.10, d (7.5)	146.2, CH
side chain	8		179.4, qC
	9	2.50, m	44.4, CH
	10	1.48, m	28.0, CH ₂
		1.71, m	
	11	0.93, t (7.4)	11.9, CH ₃
	12	1.16, d (6.9)	17.3, CH ₃
amicetose	1'	5.70, dd (10.2, 1.9)	84.7, CH
	2'	1.66 m	31.6 CH ₂
		2.11, m	
	3'	1.66, m	32.3, CH ₂
		2.16, m	
	4'	3.27, m	71.6, CH
5'	3.50, m	80.4, CH	
6'	1.33, d (6.1)	18.5, CH ₃	

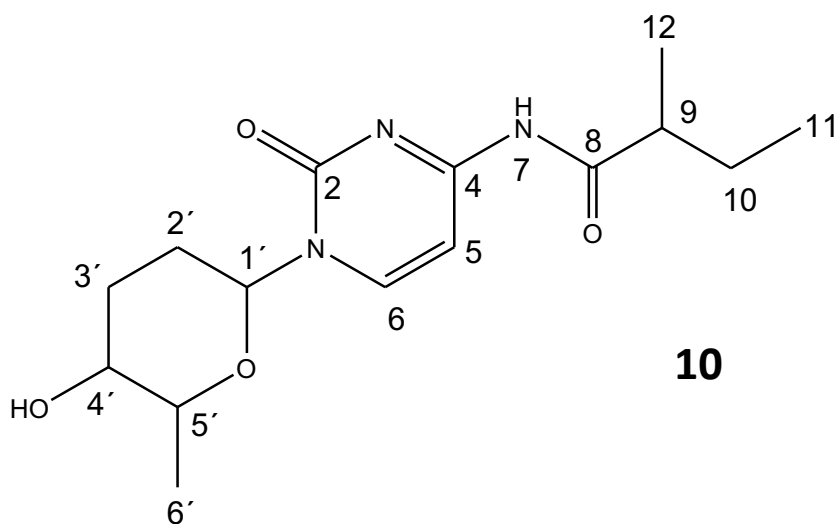


Figure S60. 700 MHz ^1H NMR spectrum of streptcytosine P (**10**) in d_6 -DMSO.

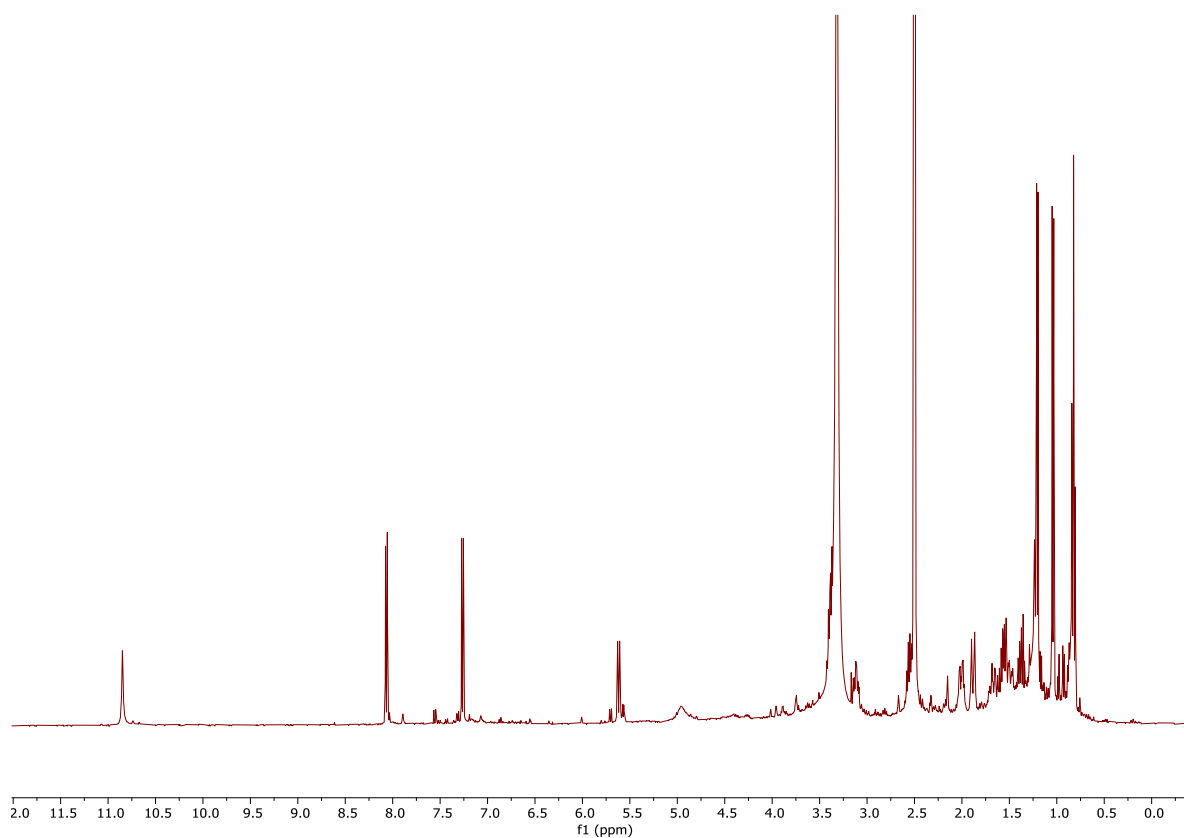


Figure S61. 175 MHz ^{13}C NMR spectrum of streptcytosine P (**10**) in d_6 -DMSO.

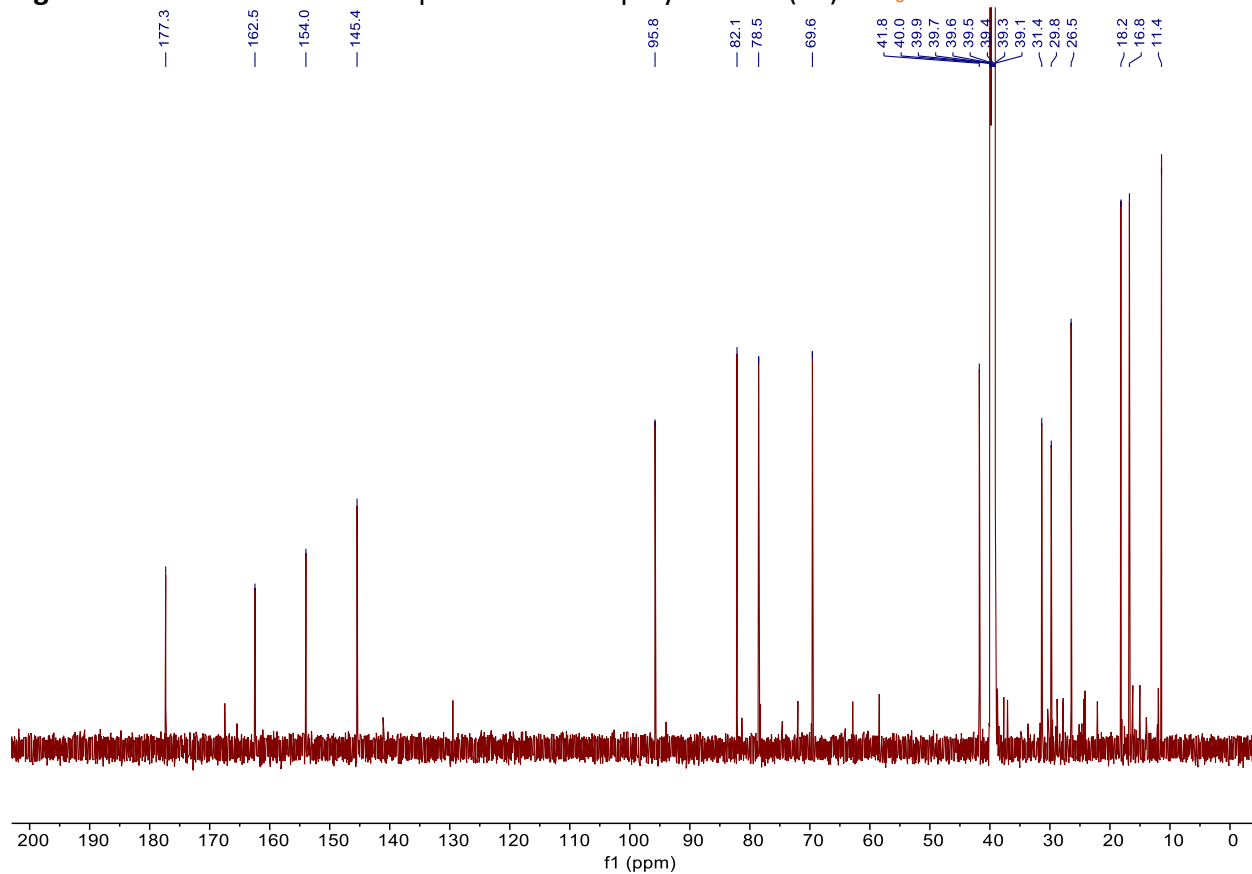


Figure S62. 700 MHz edited ^1H - ^{13}C HSQC NMR spectrum of streptocytosine P (**10**) in d_6 -DMSO.

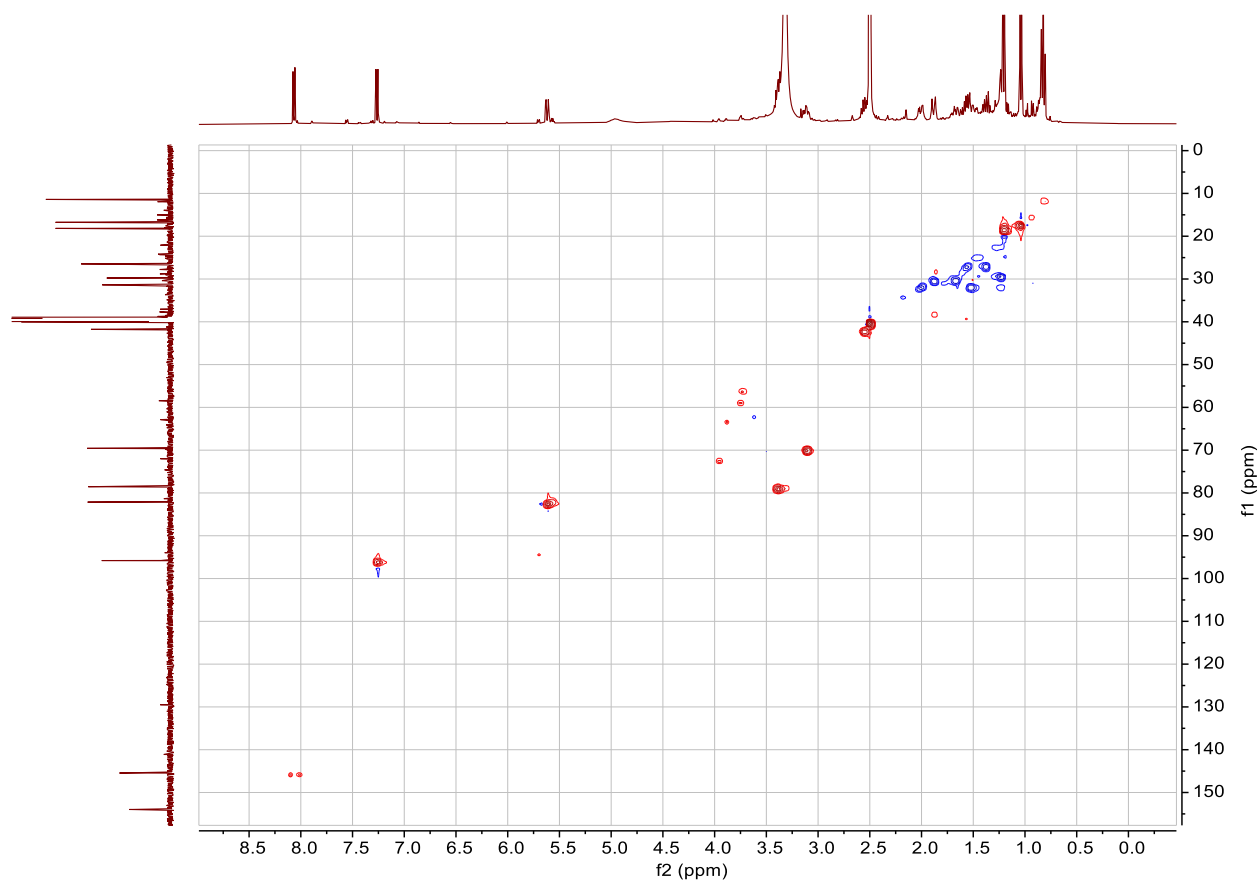


Figure S63. 700 MHz ^1H - ^{15}N HSQC NMR spectrum of streptocytosine P (**10**) in d_6 -DMSO.

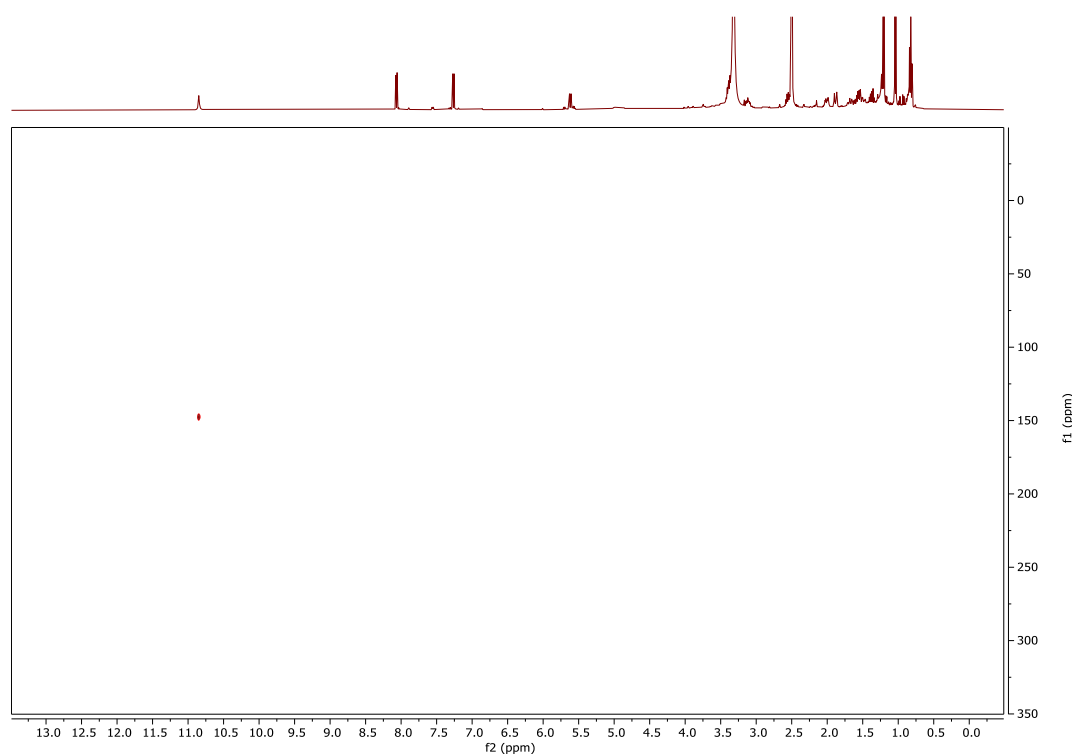


Figure S64. 700 MHz ^1H - ^1H COSY NMR spectrum of streptcytosine P (**10**) in d_6 -DMSO.

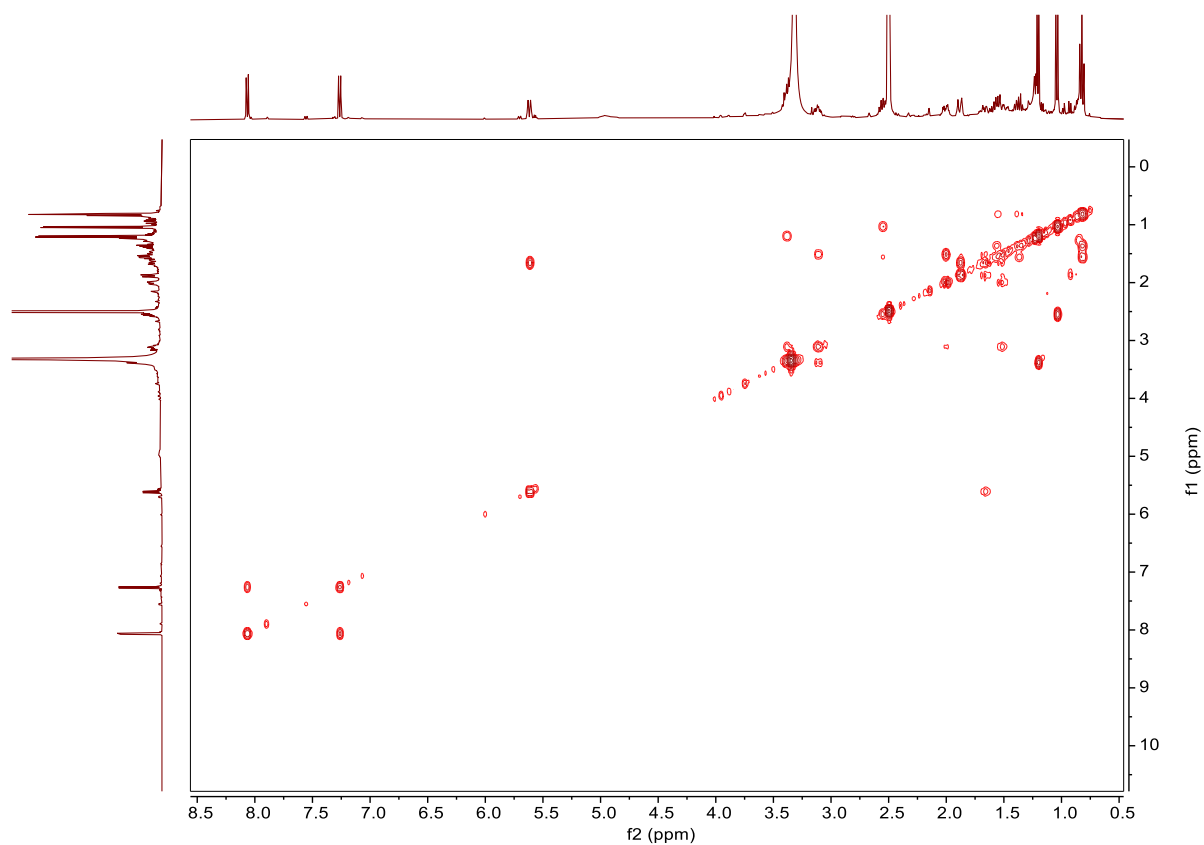


Figure S65. 700 MHz ^1H - ^{13}C HMBC NMR spectrum of streptcytosine P (**10**) in d_6 -DMSO.

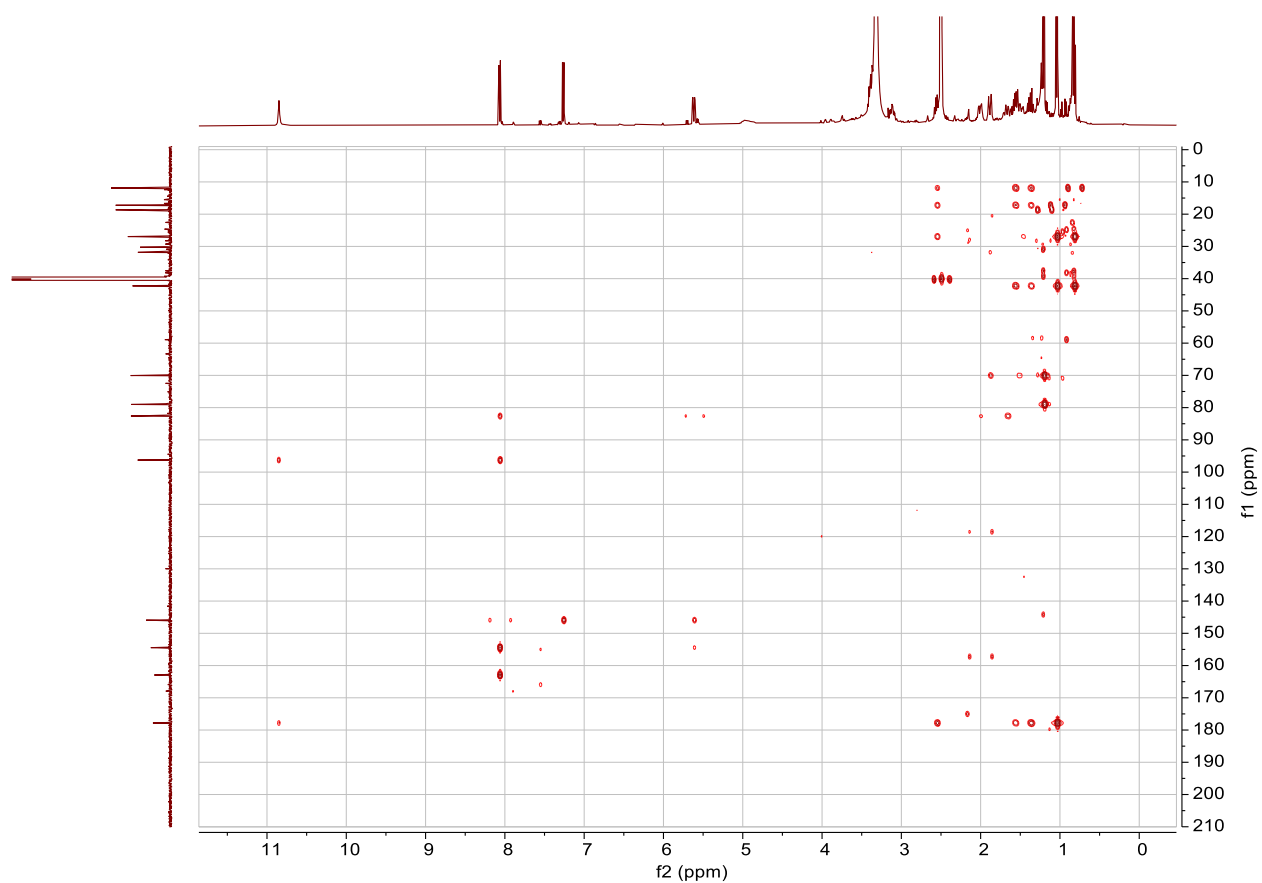


Figure S66. 700 MHz ^1H - ^1H NOESY NMR spectrum of streptcytosine P (**10**) in d_6 -DMSO.

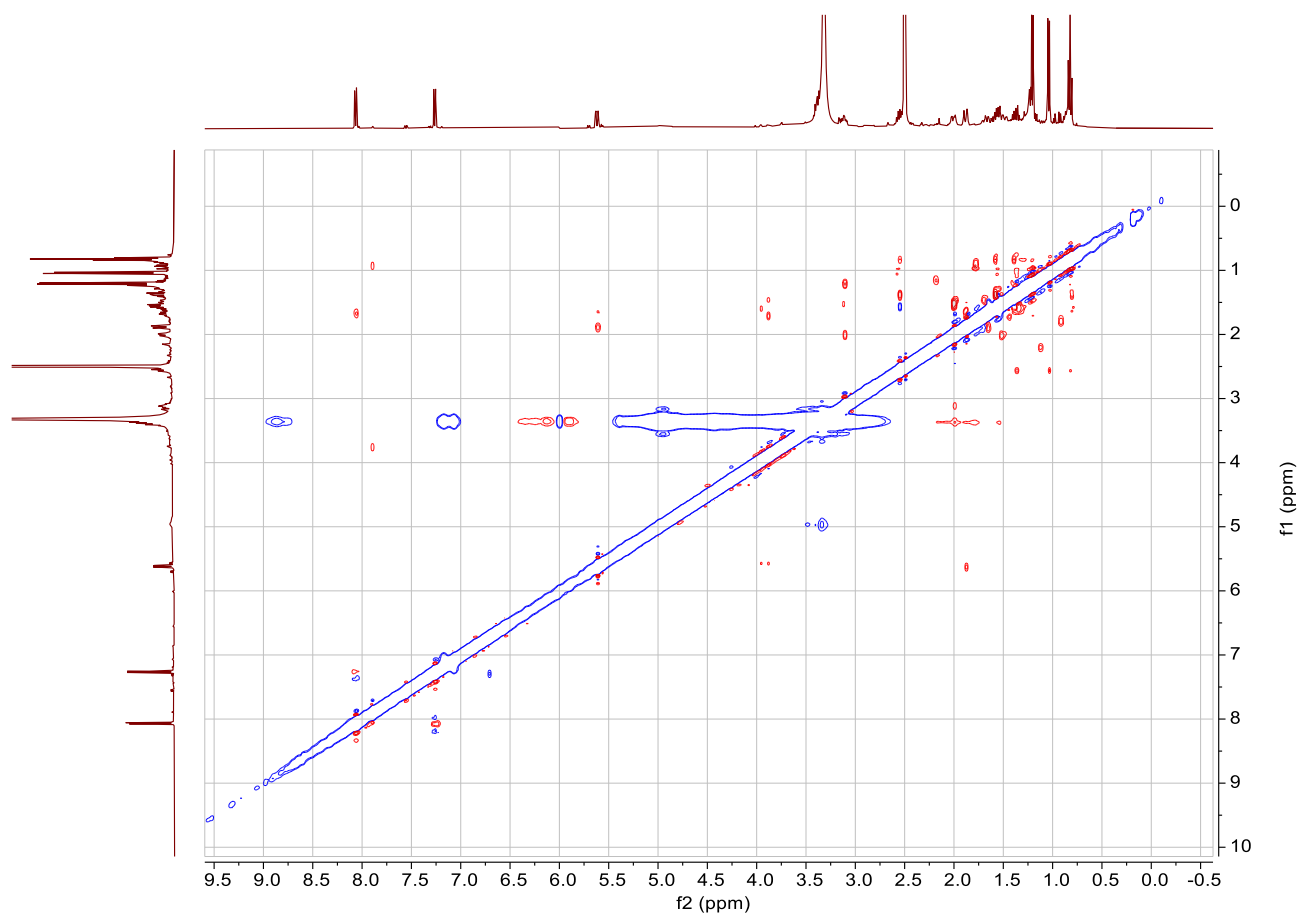


Figure S67. Interpretation of the NOESY correlations. Shown are minimized 3D structures of compound **10** from two different perspectives. The upper one highlights the through space interactions (as dashed lines) of amicitose and cytosine, while the one at the bottom visualizes the NOE contacts given in the side chain.

Color Code: **Yellow:** NOEs at the upper face of the sugar moiety
Orange: NOEs at the lower face of the sugar moiety
Blue: NOE's of the cytosine portion and the sidechain

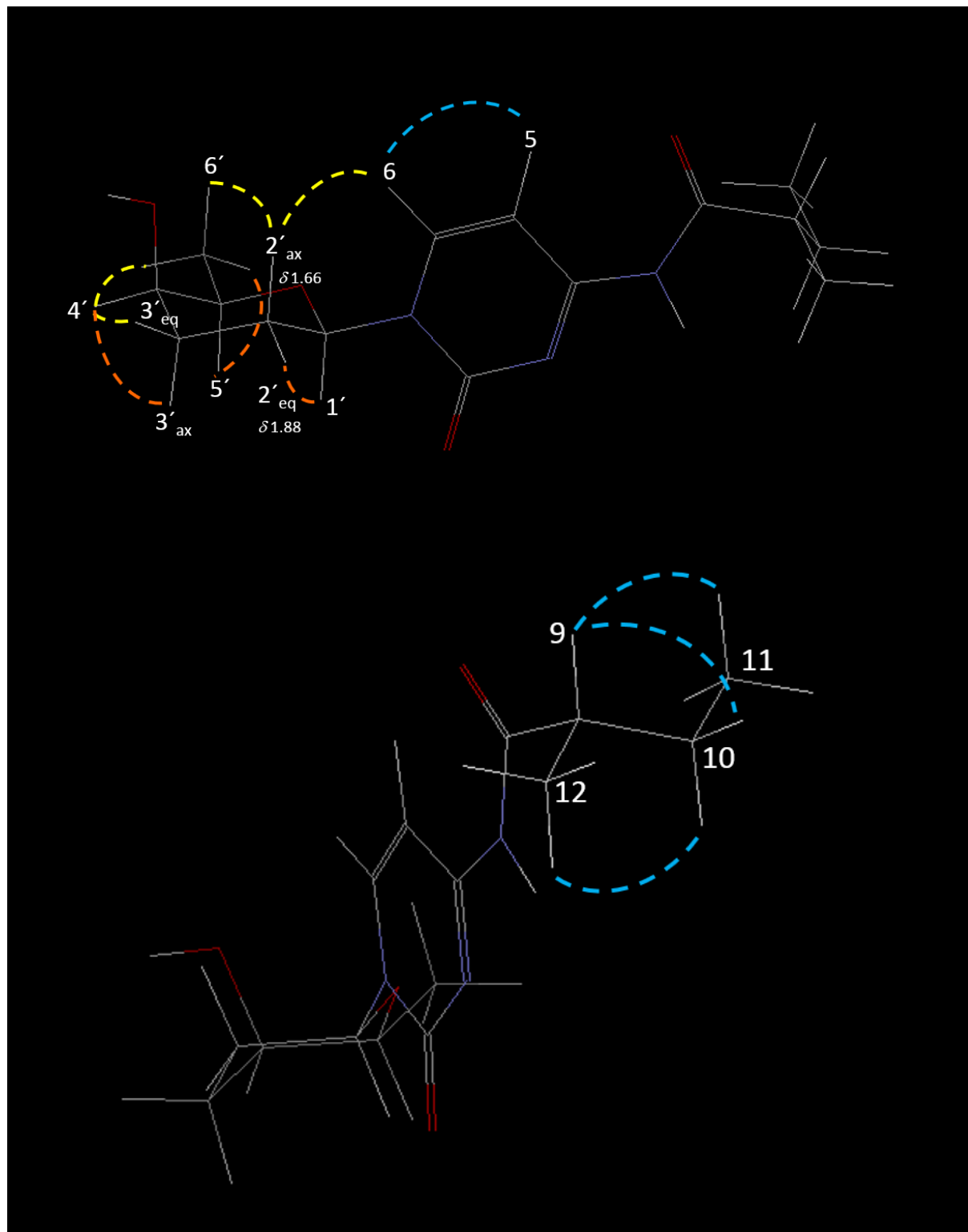


Figure S68. FT-IR spectrum of streptocytosine E (**10**).

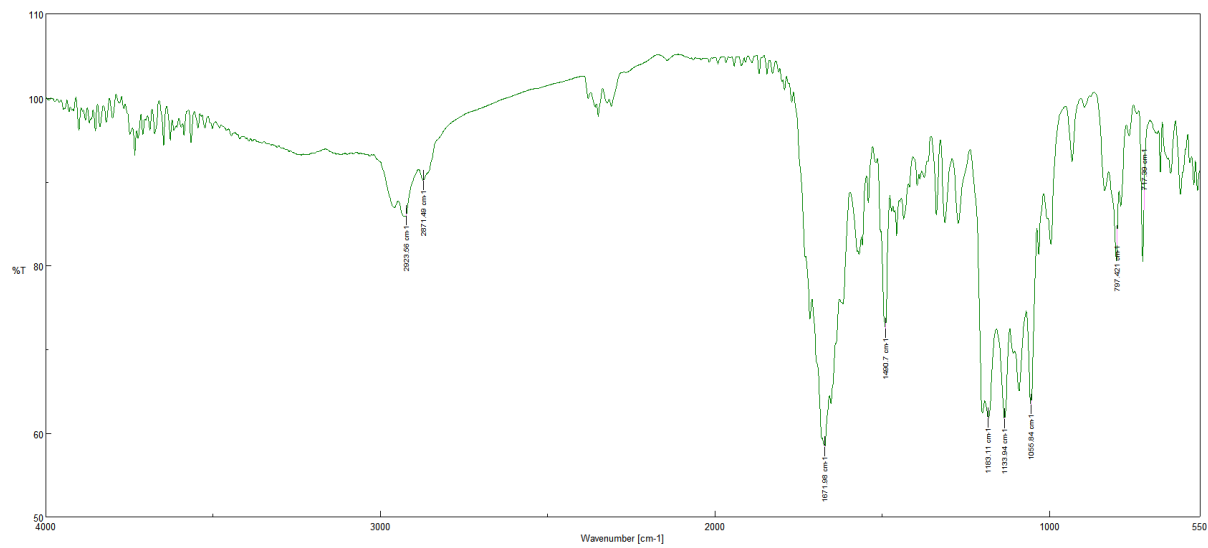


Figure S69. CD spectrum of **10** in MeOH (conc = 0.2 mg/mL)

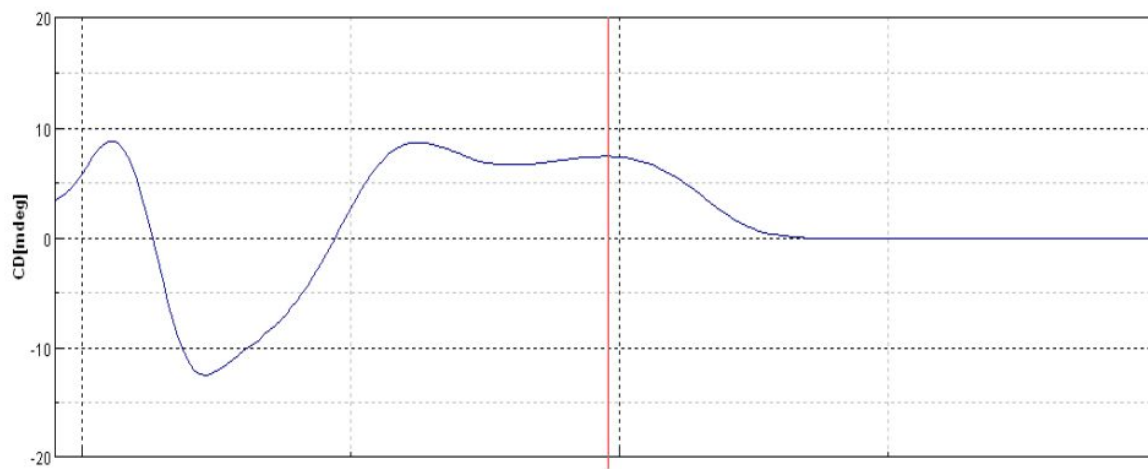


Figure S70. 400 MHz ^1H NMR spectrum of 12F-plicacetin (**11**) in d_4 -MeOH. X indicates resonances, generated by a lipid impurity.

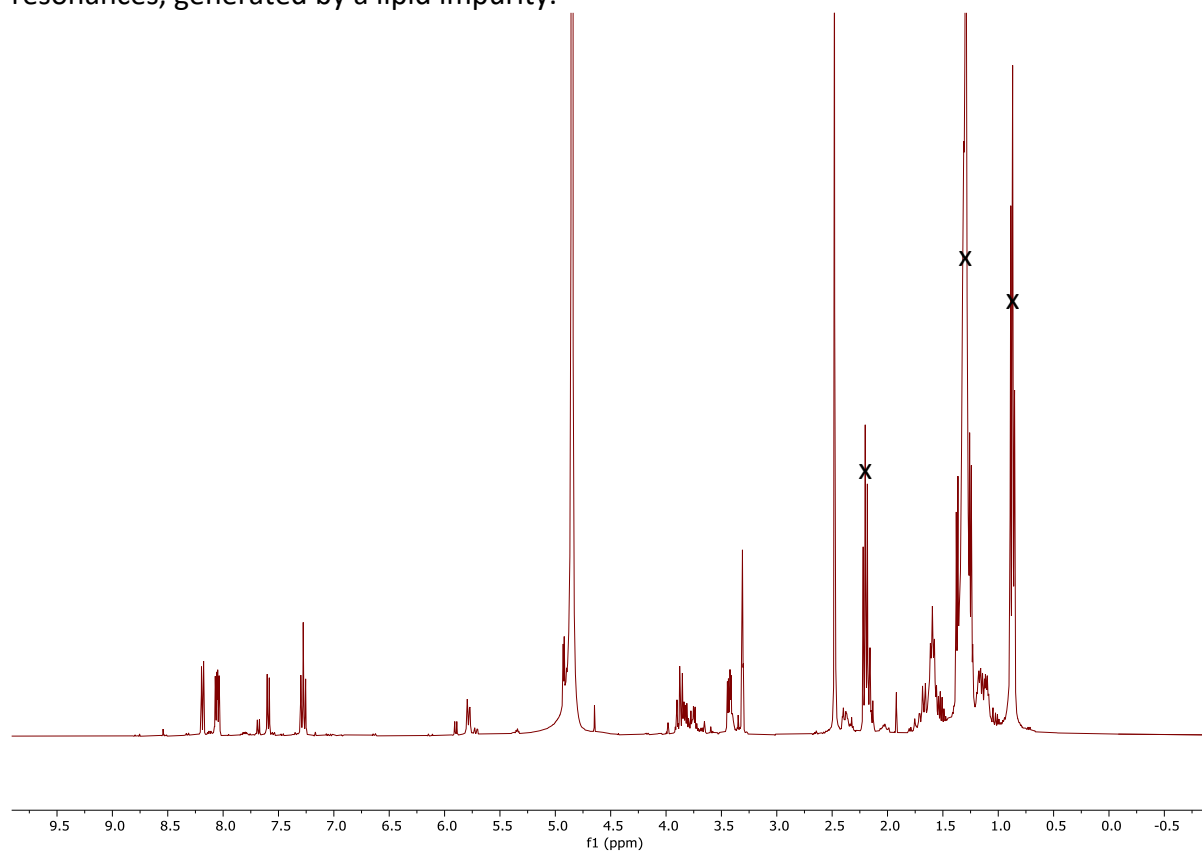


Figure S71. 100 MHz ^{13}C NMR spectrum of 12F-plicacetin (**11**) in d_4 -MeOH. X indicates resonances, generated by a lipid impurity.

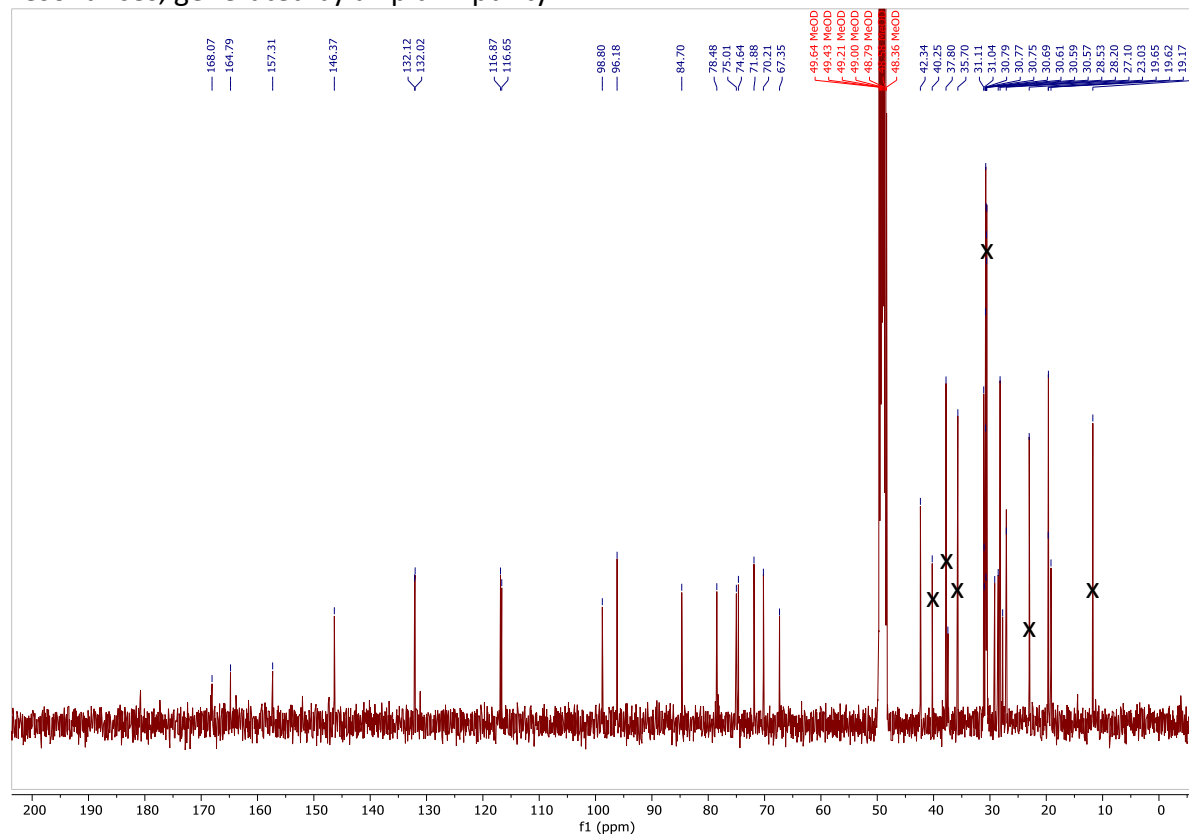


Figure S72. Superimposed ^{13}C NMR spectra of **12F-plicacetin (11)** and **plicacetin (2)** in d_4 -MeOH.

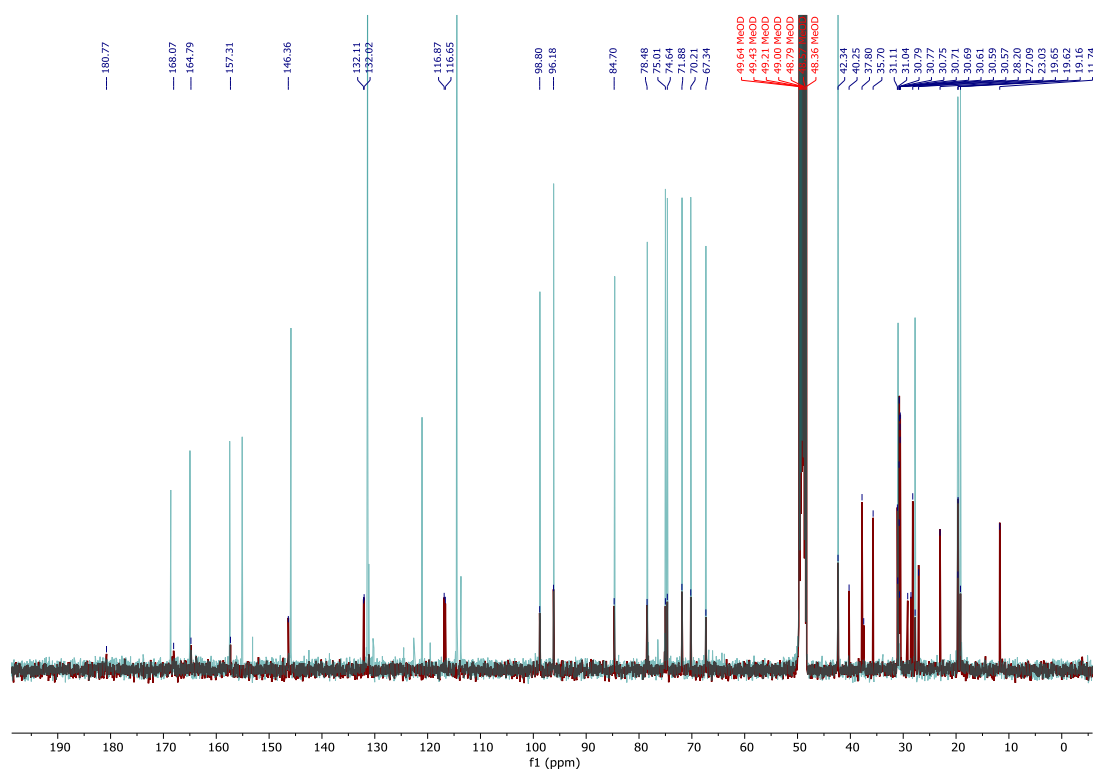


Figure S73. 400 MHz edited ^1H - ^{13}C -HSQC NMR spectrum of **12F-plicacetin (11)** in d_4 -MeOH.

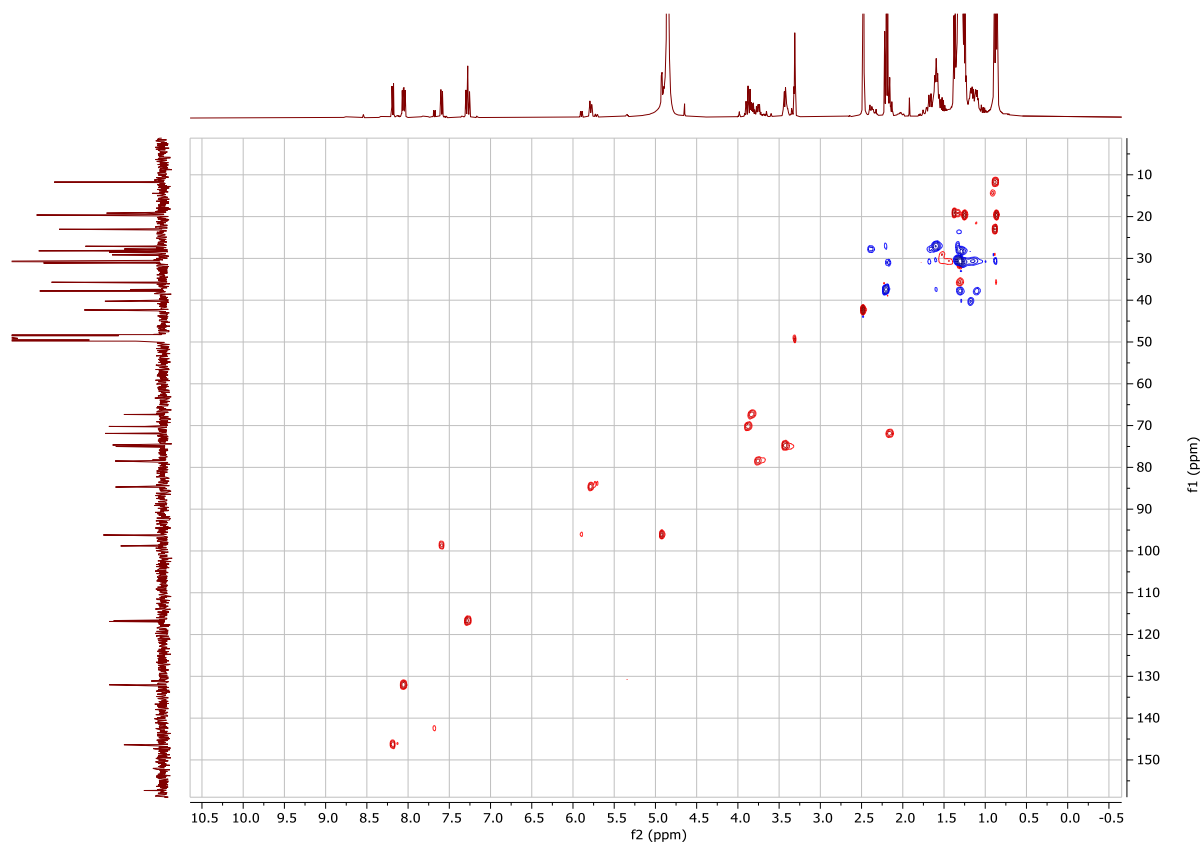


Figure S74. 400 MHz ^1H - ^1H -COSY NMR spectrum of 12F-plicacetin (**11**) in d_4 -MeOH.

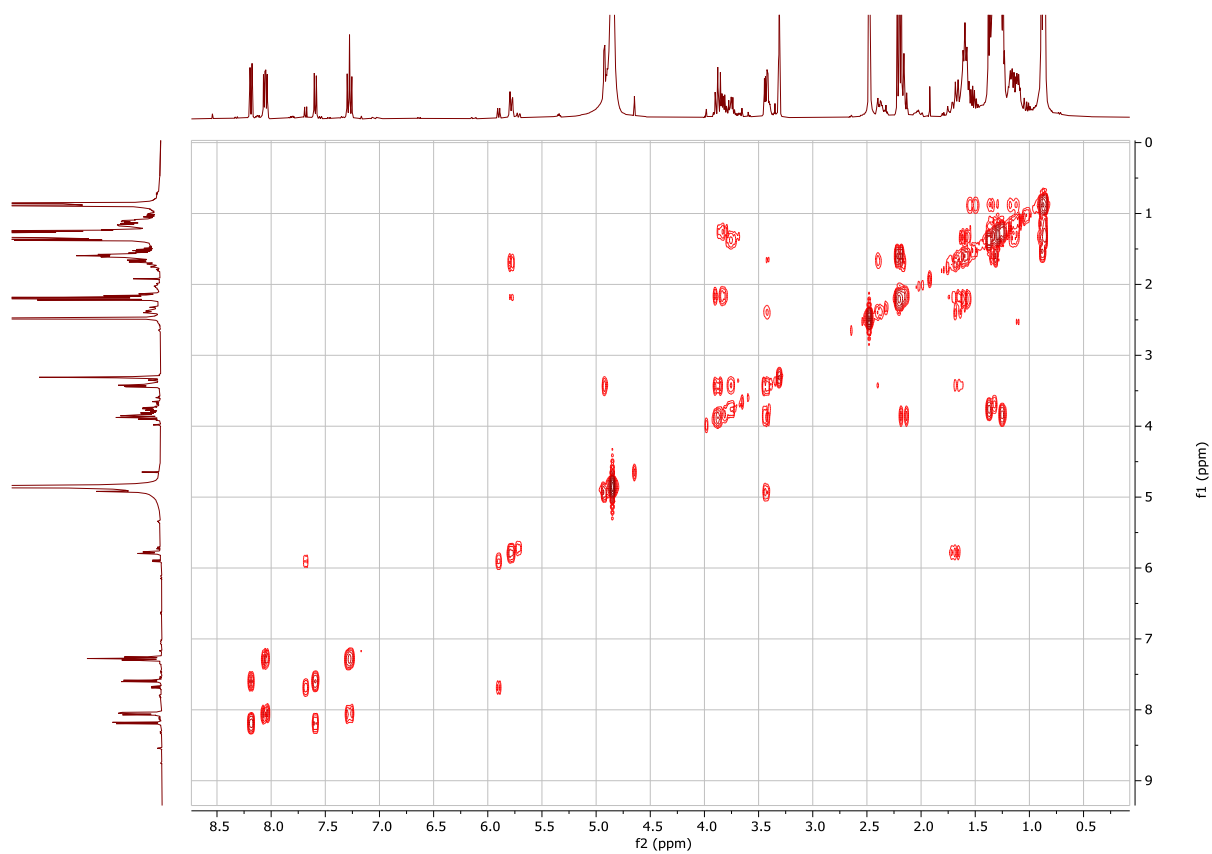


Figure S75. 400 MHz ^1H - ^{13}C -HSQC-TOCSY NMR spectrum of 12F-plicacetin (**11**) in d_4 -MeOH.

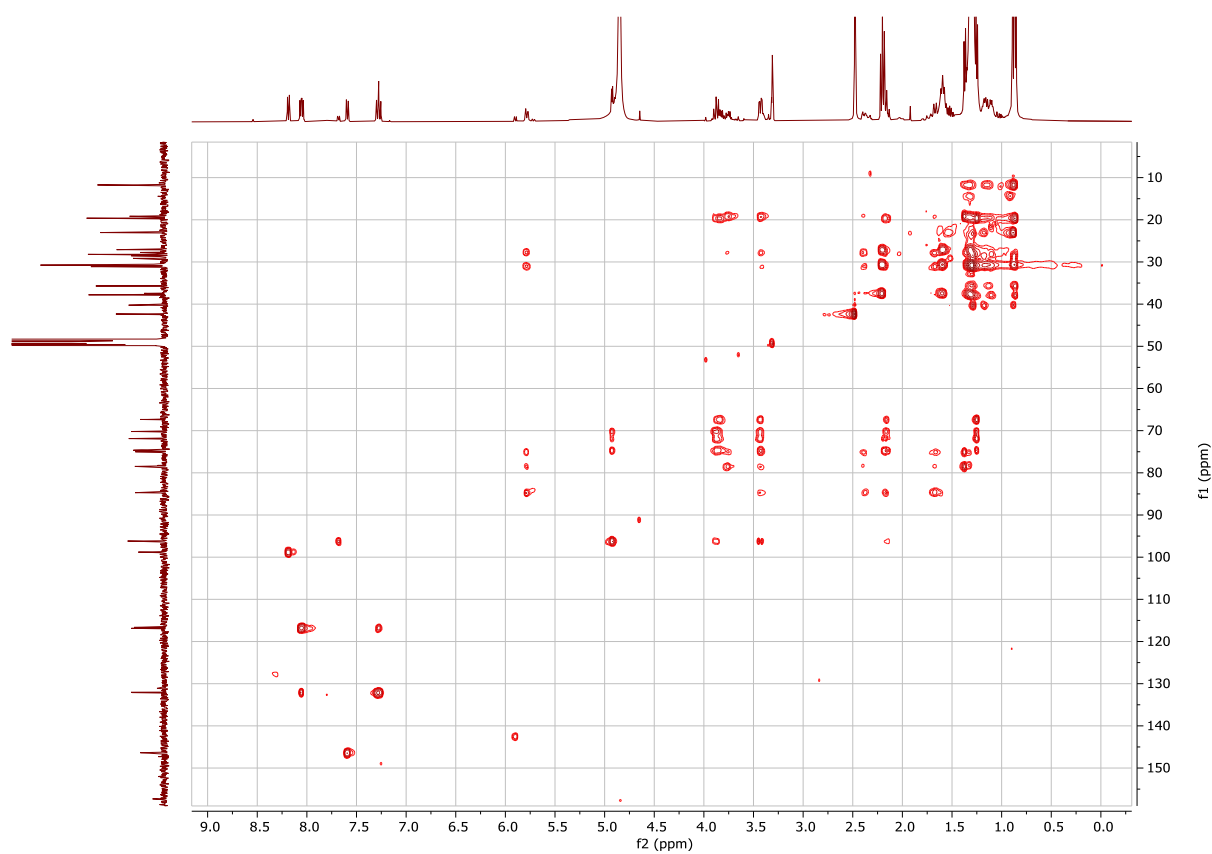


Figure S76. 400 MHz ^1H - ^{13}C -HMBC NMR spectrum of 12F-plicacetin (**11**) in d_4 -MeOH.

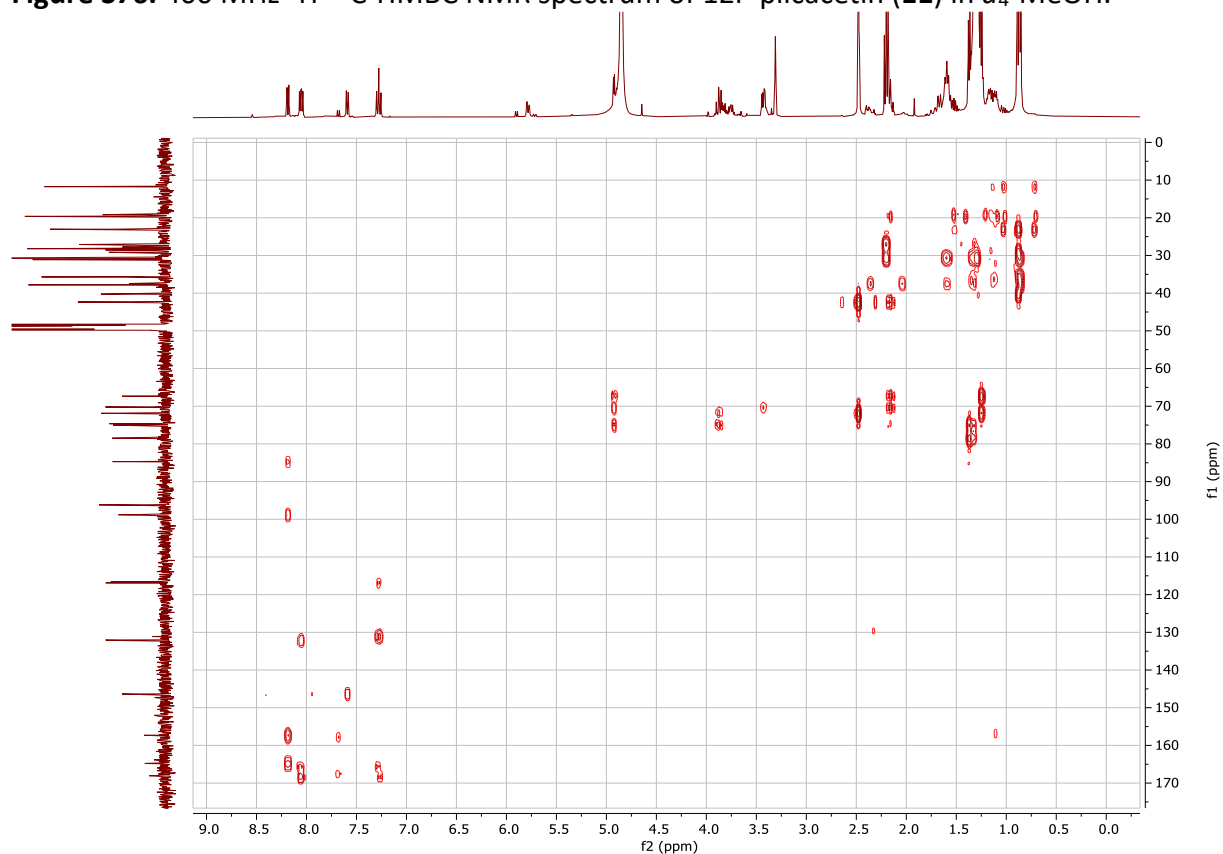


Figure S77. 376.5 MHz ^{19}F -NMR spectrum of 12F-plicacetin (**11**) in d_4 -MeOH. Trifluoro-acetic acid represents the internal calibration standard (-76.55 ppm).

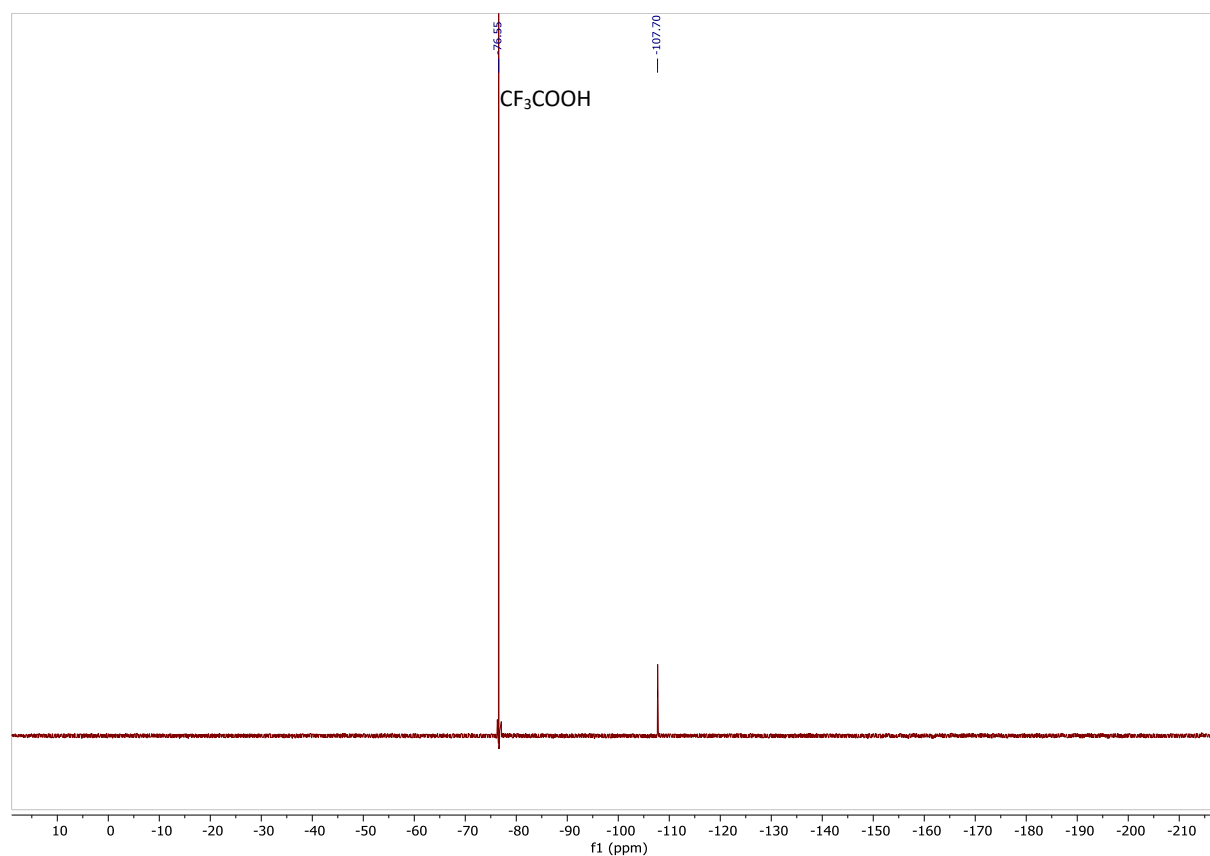


Figure S78. FT-IR spectrum of 12F-plicacetin (**11**).

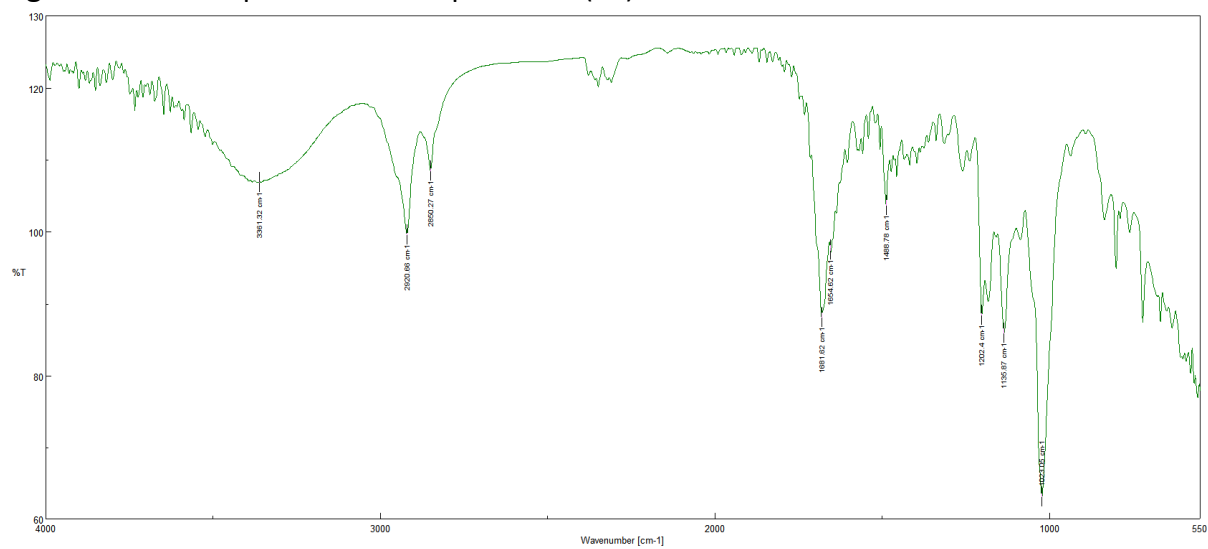


Figure S79. HPLC-UV enantiomer separation of **4-methylhexanoic acid** obtained by hydrolysis of compound **6** and subsequent precolumn derivatization with 1-naphthylamine (a) (from bottom to top: *R*-enantiomer, *S*-enantiomer, racemate, (b) sample hydrolysate, sample hydrolysate spiked with racemate) on Chiralpak IH-U in reversed phase elution mode. After spiking of real sample to the racemate, the ratio changed from 1:1 to 45:55 (*R*:*S*), indicating that the absolute configuration of the real sample is *S*. * is indicating a reagent peak. The following gradient was applied: 0 min 20% B, 30 min 90% B, 30.01 min 20% B, 36 min 20% B.

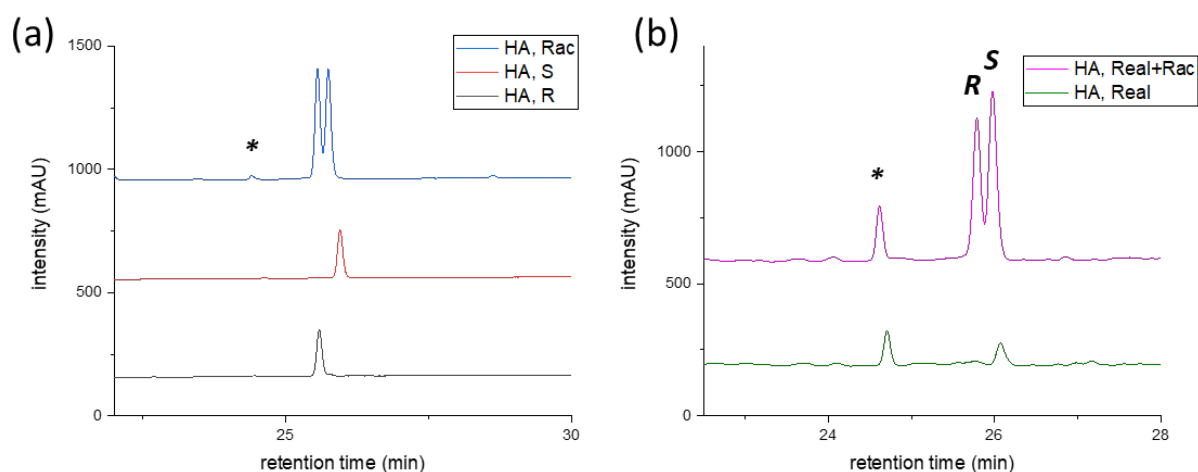


Figure S80. HPLC-MS enantiomer separation of **4-methylhexanoic acid** obtained by hydrolysis of compound **6** after precolumn derivatization with 1-naphthylamine on Chiralpak IH-U in reversed phase elution mode. From bottom to top: *R*-enantiomer, *S*-enantiomer, racemate, sample hydrolysate. The following gradient was applied: 0 min 20% B, 37.50 min 90% B, 37.51 min 20% B, 45 min 20% B.

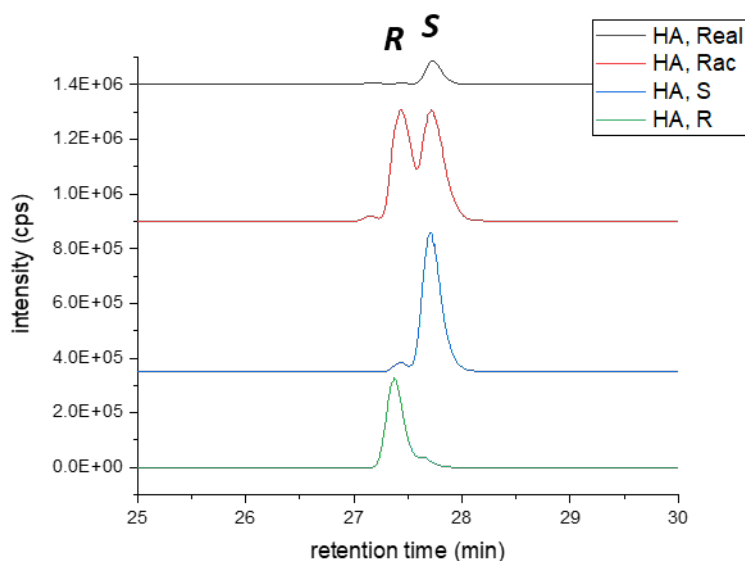


Figure S81. HPLC-MS enantiomer separation of **2-methylbutyric acid** obtained by hydrolysis of **10** and subsequent precolumn derivatization with 1-naphthylamine (a), of *R* + sample, *S* + sample, racemic standard + sample as well as sample (b) on Chiralpak IB-U in reversed phase elution mode. Analysis was carried out under isocratic conditions (water + 0.1% FA/ACN + 0.1% FA, 45/55). A slight racemization of the real sample might have occurred under the harsh hydrolysis conditions, explaining the second eluting peak in the real sample.

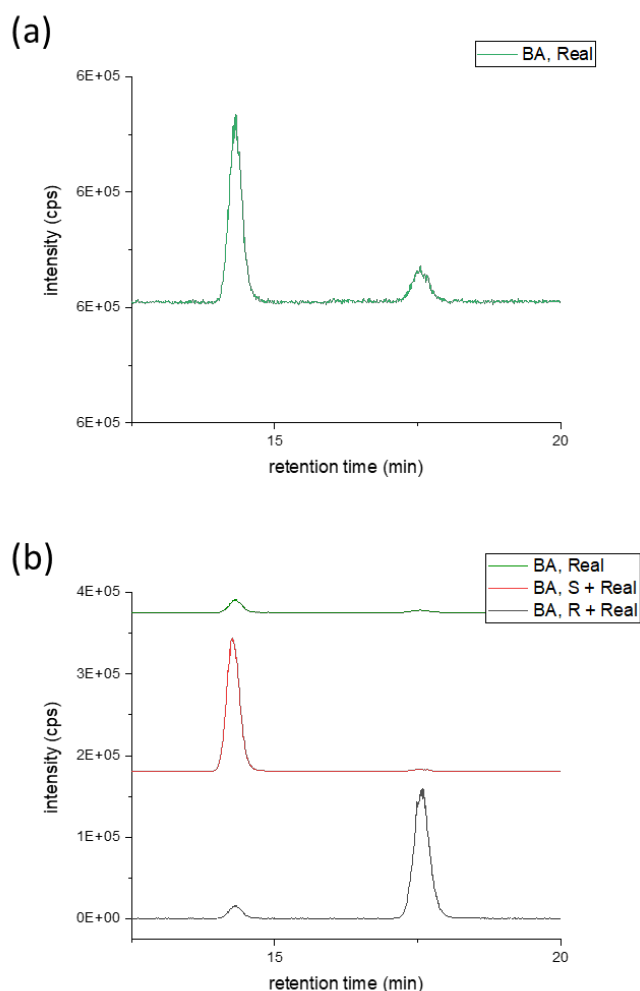


Table S10. Chromatographic parameters obtained for **6** and **10** with different columns.

Compound	Column	Flow rate [mL/min]	t_0 [min]	t_{R1} [min]	t_{R2} [min]	R_s
(rac)-2-Methylbutyric acid	IB-U, isocratic, NP	1.0	0.58	7.60	9.50	1.55
(rac)-2-Methylbutyric acid	IB-U, gradient, RP (MS)	0.2	2.51	14.28	17.58	5.64
(rac)-4-Methylhexanoic acid	IH-U, gradient, RP (LC)	0.2	2.98	25.56	25.75	1.04

Figure S82. Synteny analysis of the amicetin biosynthetic gene cluster of strain *Streptomyces* sp. SHP 22-7 with the *ami* locus reported from *Streptomyces vinaceusdrappus* NRRL 2363.

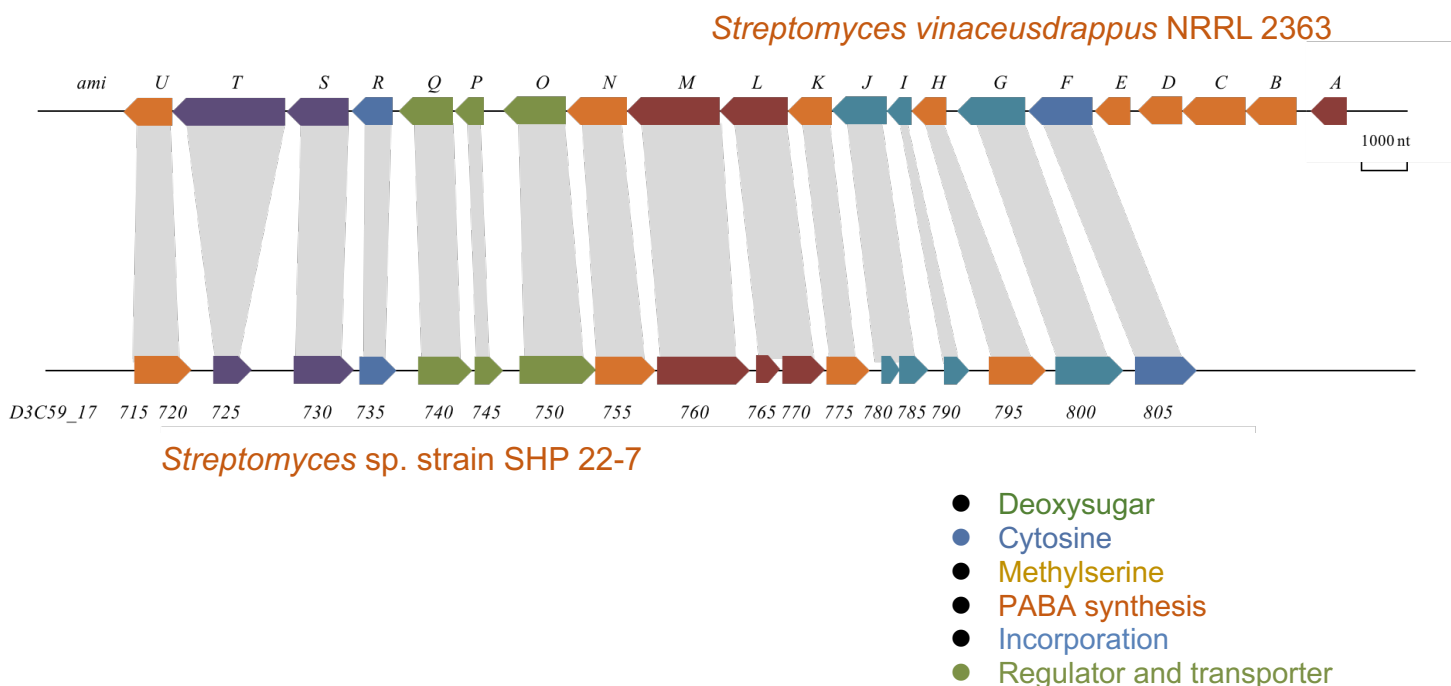
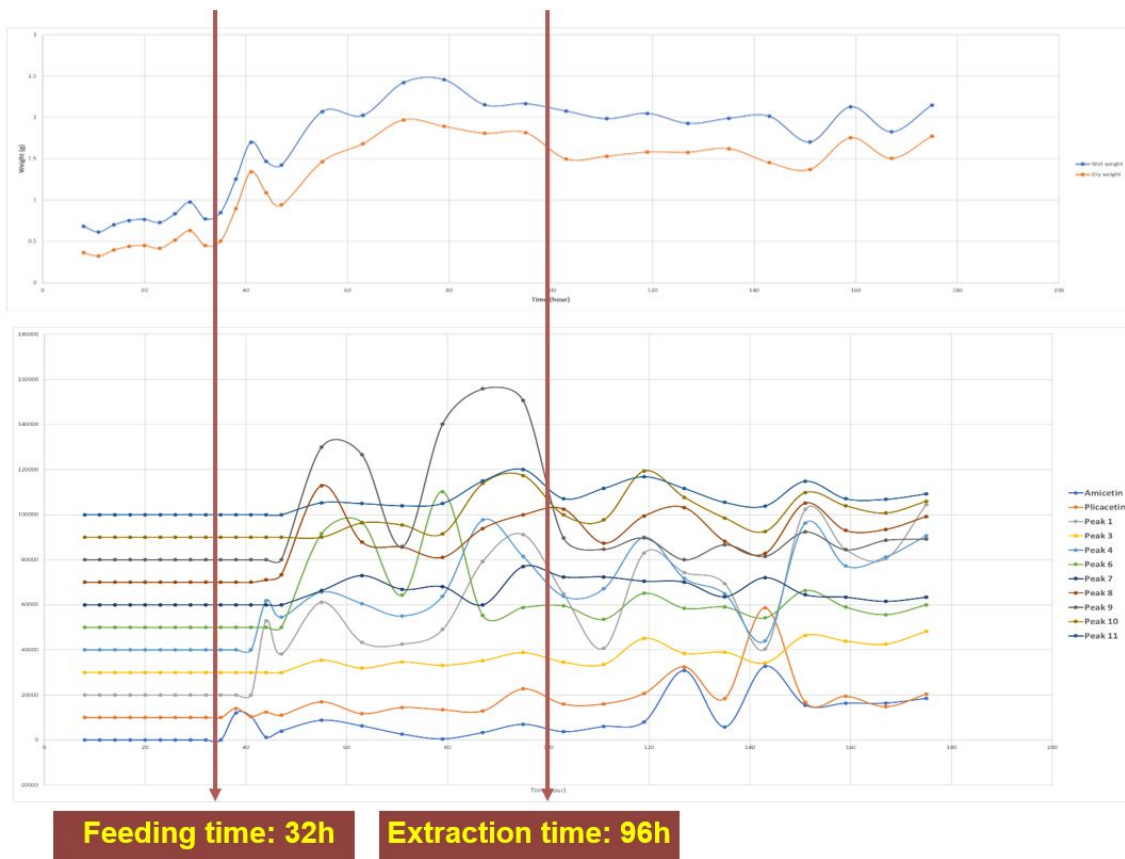


Table S11. Detailed overview about the *ami* locus in strain SHP 22-7. The blue boxes indicate the genes encoding enzymes, responsible for amide bond formation in the amicetin biosynthetic pathway.

Gene of SHP 22-7	Size (nt)	Putative function	Identity (%)	Gene from NRRL 2363	Size (nt)
D3C59_17715	735	NAD-dependent epimerase/dehydratase family protein	99.86	<i>amiU</i>	1065
D3C59_17720	528	NAD-dependent epimerase/dehydratase family protein	99.81		
D3C59_17725	864	Nonribosomal peptide synthetase (A-PCP)	99.88	<i>amiT</i>	2466
D3C59_17730	1317	serine hydroxymethyltransferase	99.92	<i>amiS</i>	1359
D3C59_17735	810	Malonyl CoA-acyl carrier protein transacylase	99.88	<i>amiR</i>	900
D3C59_17740	1192	MFS transporter	99.66	<i>amiQ</i>	1194
D3C59_17745	633	TetR family transcriptional regulator	98.90	<i>amiP</i>	639
D3C59_17750	1679	ABC transporter ATP-binding protein	99.94	<i>amiO</i>	1680
D3C59_17755	1318	lipopolysaccharide biosynthesis protein RfbH	99.85	<i>amiN</i>	1320
D3C59_17760	2034	aminodeoxychorismate synthase component I	99.95	<i>amiM</i>	2034
D3C59_17765	543	Benzoate-CoA synthase	99.82	<i>amiL</i>	1497
D3C59_17770	942	Benzoate-CoA synthase	99.89		
D3C59_17775	957	NAD(P)-dependent oxidoreductase	99.90	<i>amiK</i>	948
D3C59_17780	405	Cytosylglucuronic acid synthase/glycosyltransferase	100	<i>amiJ</i>	1212
D3C59_17785	636	Cytosylglucuronic acid synthase/glycosyltransferase	99.69		
D3C59_17790	549	(Deoxy)cytidine deoxyribosyltransferase	100	<i>amiI</i>	549
D3C59_17795	1254	methyltransferase domain-containing protein	100	<i>amiH</i>	750
D3C59_17800	1488	glycosyltransferase family 1 protein	100	<i>amiG</i>	1488
D3C59_17805	1359	GNAT family N-acetyltransferase	99.93	<i>amiF</i>	1407
/	/	Glucose-1-phosphate thymidyltransferase	/	<i>amiE</i>	774
/	/	NDP-hexose 3-ketoreductase	/	<i>amiD</i>	969
/	/	NDP-hexose 2,3-dehydratase	/	<i>amiC</i>	1377
/	/	NDP-sugar aminotransferase	/	<i>amiB</i>	1119
/	/	Putative 4-amino-4-deoxychorismate lyase	/	<i>amiA</i>	795

Figure S83. Top: growth curve; blue trace represents the wet weight, while orange represents the dry weight. Bottom: Production curve regarding plicacetin (**2**) and analogs.



Precursor directed biosynthesis feeding study

Comparative LC-MS TIC chromatograms of crude extracts (in positive mode).

Red trace: sample fed with the respective precursor

(Blue arrow marks the peak of the resultant compound)

Blue trace: media control

Figure S84. Precursor directed biosynthesis feeding study with precursor **1a**.

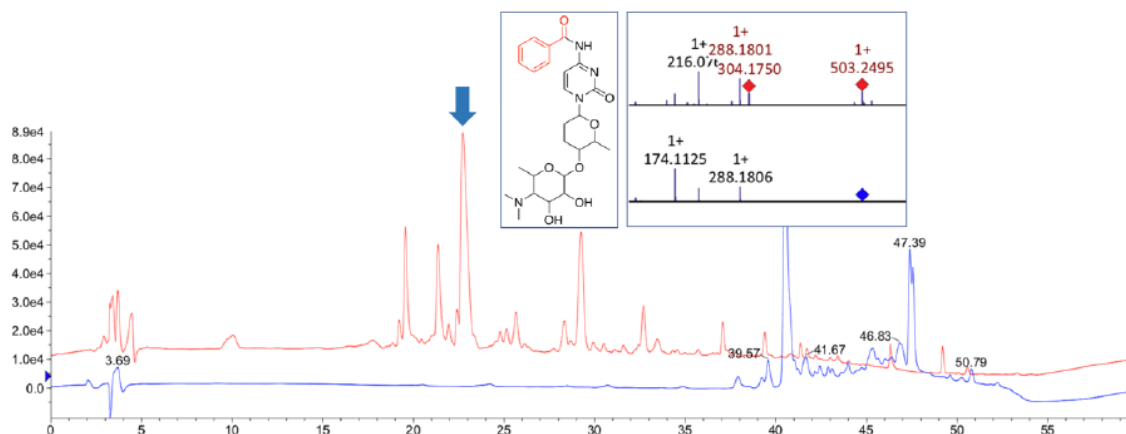


Figure S85. Precursor directed biosynthesis feeding study with precursor **2c**.

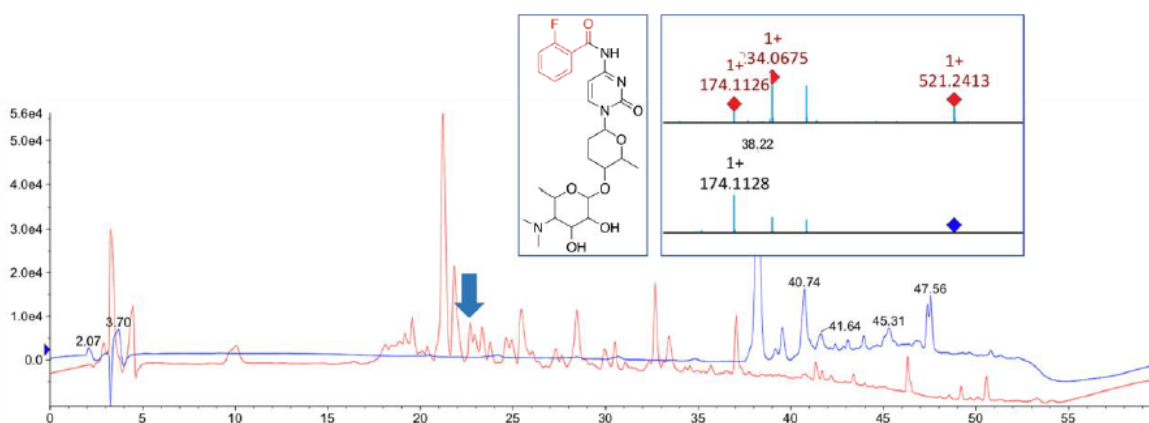


Figure S86. Precursor directed biosynthesis feeding study with precursor **3c**.

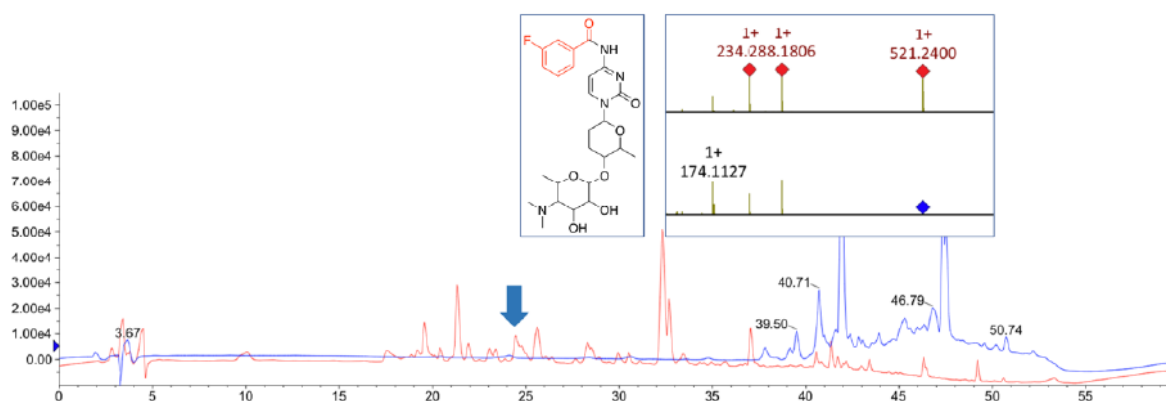


Figure S87. Precursor directed biosynthesis feeding study with precursor 4c.

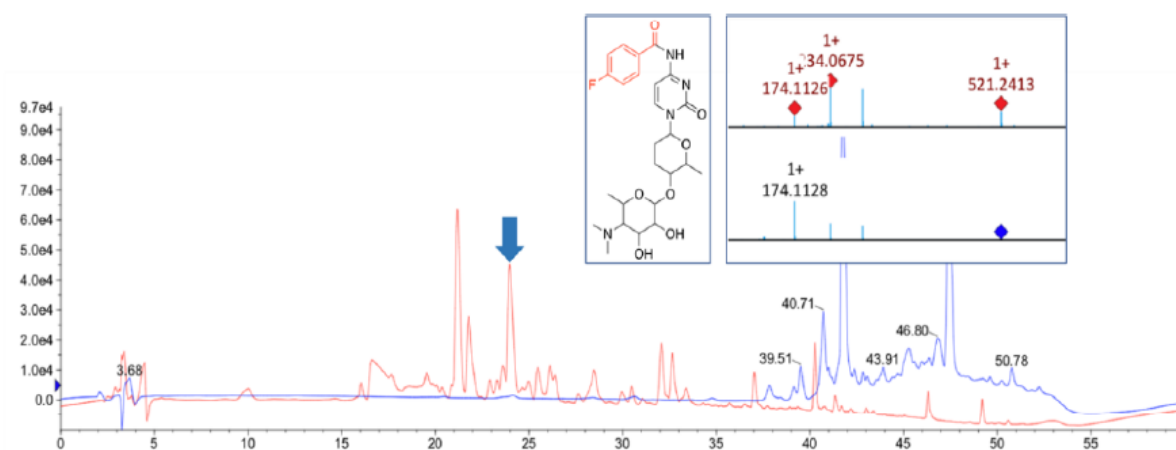


Figure S88. Precursor directed biosynthesis feeding study with precursor 4d.

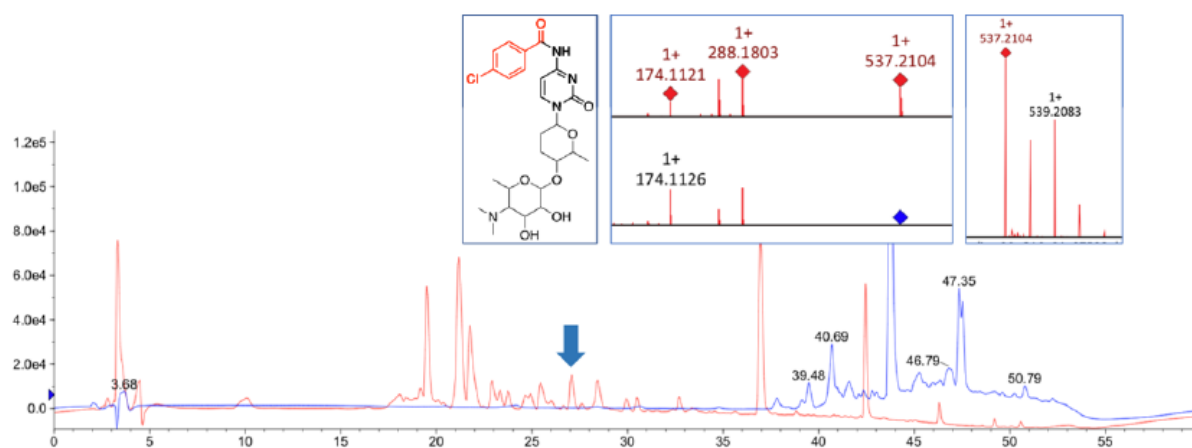


Figure S89. Precursor directed biosynthesis feeding study with precursor 4e.

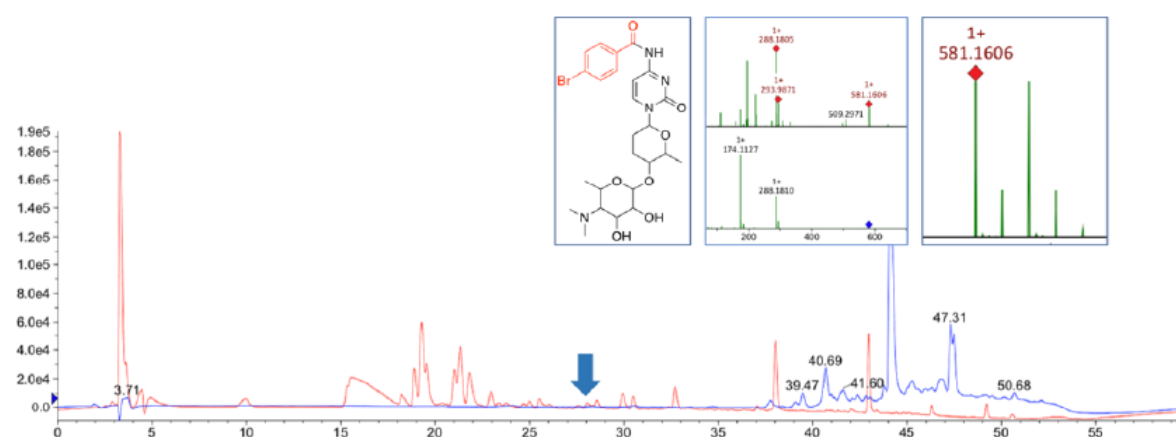


Figure S90. Precursor directed biosynthesis feeding study with precursor 5c.

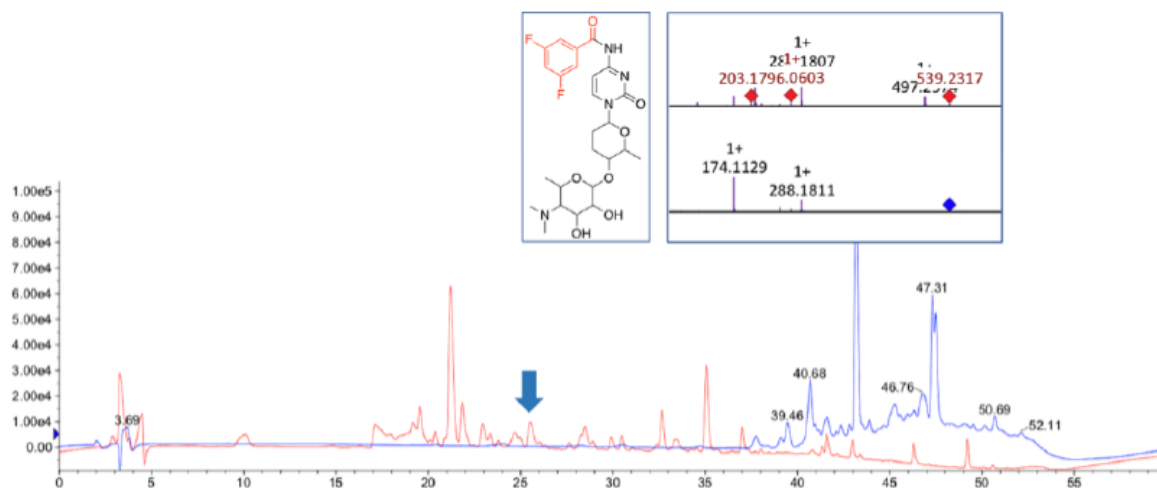


Figure S91. Precursor directed biosynthesis feeding study with precursor 5d.

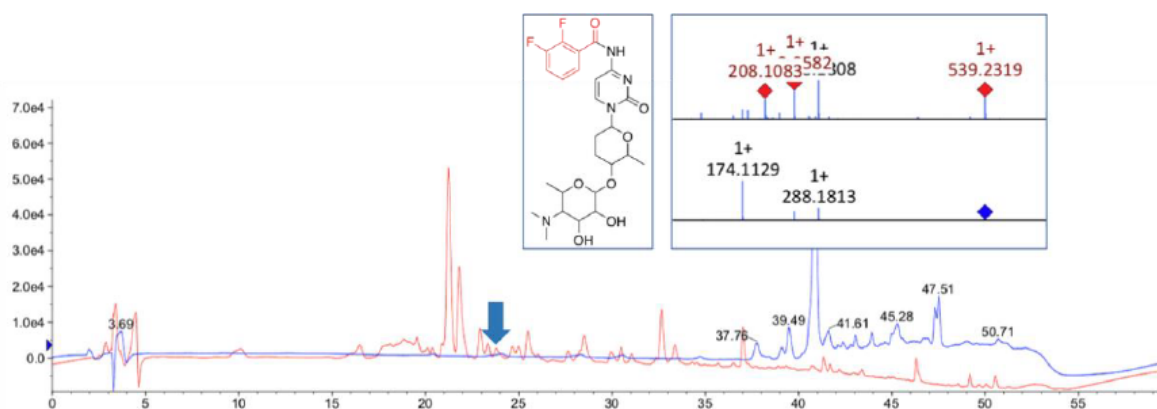


Figure S92. Precursor directed biosynthesis feeding study with precursor 5e.

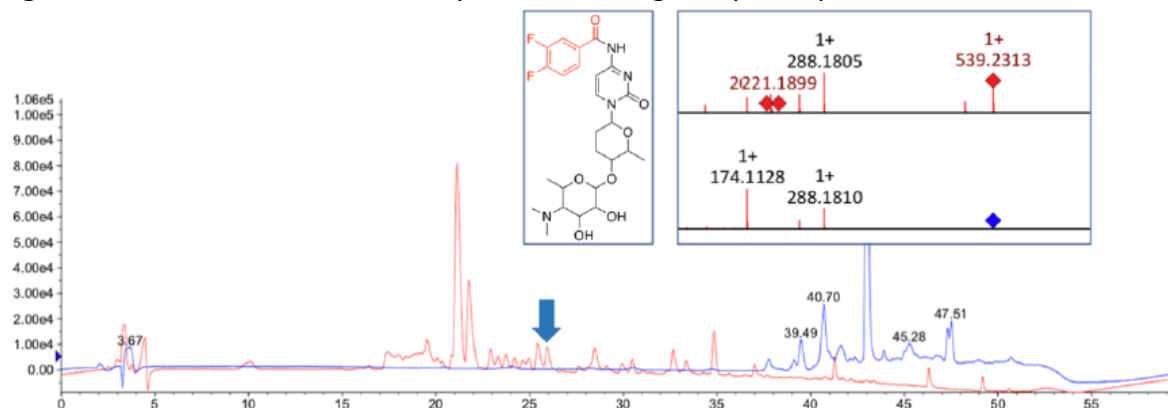


Figure S93. Precursor directed biosynthesis feeding study with precursor **5h**.

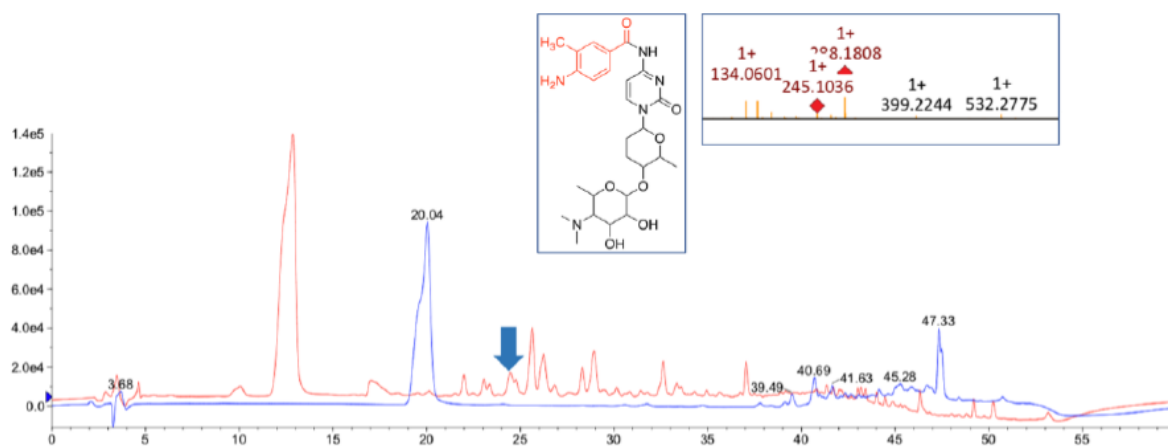
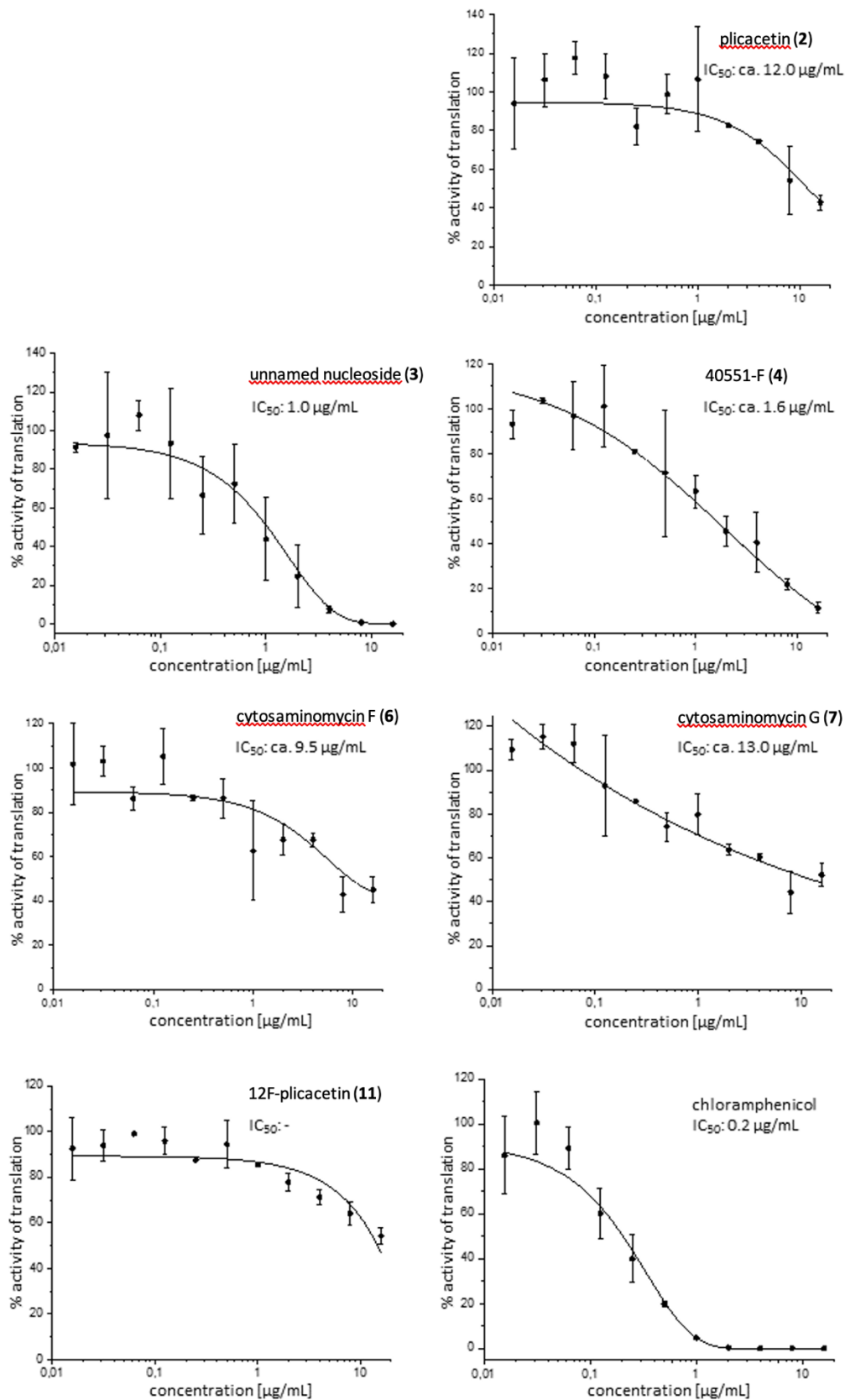


Figure S94. Cell-free assay specific for bacterial translation inhibitors. Translation is conducted by the translation machinery contained in an *E. coli* S30 extract. Curves depict means of two independent replicates and standard deviations. IC₅₀, reduction of the translation activity of an untreated control reaction by 50%. IC₅₀ curves were calculated by OriginPro.



3.2.3 Publication VII: **DoE Optimization Empowers the Automated Preparation of Enantiomerically Pure [¹⁸F]Talazoparib and its *In Vivo* Evaluation as a PARP Radiotracer**

Gregory D. Bowden^{†,‡,‡}, Sophie Stotz^{†,‡,‡}, Johannes Kinzler[†], Christian Geibel[§],
Michael Lämmerhofer[§], Bernd J. Pichler^{†,‡}, and Andreas Maurer^{†,‡,*}

[†] Werner Siemens Imaging Center, Department of Preclinical Imaging and Radiopharmacy, Eberhard Karls University, Tuebingen, Germany

[#] Cluster of Excellence iFIT (EXC 2180) "Image-Guided and Functionally Instructed Tumor Therapies", Eberhard Karls University, Tuebingen, Germany

[§] Institute of Pharmaceutical Sciences, Department of Pharmaceutical (Bio-)Analysis, Eberhard Karls University, Auf der Morgenstelle 8, 72076 Tuebingen, Germany

[‡] These authors contributed equally

* Corresponding author. E-mail address: andreas.maurer@med.uni-tuebingen.de (A. Maurer)

Reprinted with permission from *Journal of Medicinal Chemistry* **2021**, *64*, 21, 15690-15701. DOI: 10.1021/acs.jmedchem.1c00903

Copyright 2022 American Chemical Society.

DoE Optimization Empowers the Automated Preparation of Enantiomerically Pure [¹⁸F]Talazoparib and its *In Vivo* Evaluation as a PARP Radiotracer

Gregory D. Bowden, Sophie Stotz, Johannes Kinzler, Christian Geibel, Michael Lämmerhofer, Bernd J. Pichler, and Andreas Maurer*

Cite This: *J. Med. Chem.* 2021, 64, 15690–15701

Read Online

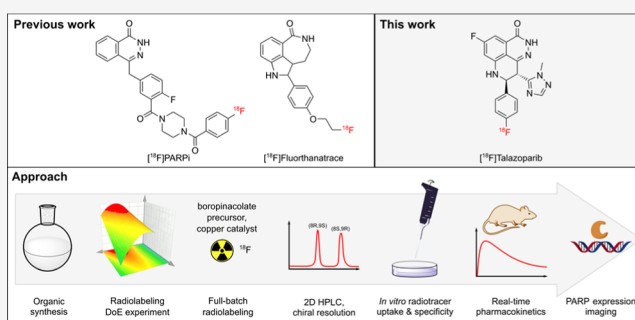
ACCESS |

Metrics & More

Article Recommendations

Supporting Information

ABSTRACT: Given the clinical potential of poly(ADP-ribose) polymerases (PARP) imaging for the detection and stratification of various cancers, the development of novel PARP imaging probes with improved pharmacological profiles over established PARP imaging agents is warranted. Here, we present a novel ¹⁸F-labeled PARP radiotracer based on the clinically superior PARP inhibitor talazoparib. An automated radiosynthesis of [¹⁸F]talazoparib (RCY: 13 ± 3.4%; *n* = 4) was achieved using a “design of experiments” (DoE) optimized copper-mediated radiofluorination reaction. The chiral product was isolated from the reaction mixture using 2D reversed-phase/chiral radio-HPLC (>99% ee). (8*S*,9*R*)-[¹⁸F]Talazoparib demonstrated PARP binding in HCC1937 cells *in vitro* and showed an excellent tumor-to-blood ratio in xenograft-bearing mice (10.2 ± 1.5). Additionally, a favorable pharmacological profile in terms of excretion, metabolism, and target engagement was observed. This synthesis of [¹⁸F]talazoparib exemplifies how DoE can enable the radiosyntheses of synthetically challenging radiolabeled compounds of high interest to the imaging community.



INTRODUCTION

Poly(ADP-ribose) polymerases (PARP) have become important targets for personalized cancer treatment, and this has spurred the development of several highly potent PARP inhibitors. PARP inhibitors induce synthetic lethality in malignant tumors that lack the homologous recombination (HR) DNA repair pathway.^{1,2} PARP overexpression in several tumor entities has also made the enzyme a valuable biomarker for optical and nuclear imaging techniques to detect malignant lesions and aid surgical excision of difficult-to-detect cancers.³ Non-invasive imaging techniques such as positron emission tomography (PET) are used to track the fate and quantify the uptake of a radioactively labeled molecule *in vivo*; thus, aiding diagnosis and therapy surveillance. PARP expression levels are thought to be predictive of tumor malignancy as its overexpression is correlated with a poor clinical prognosis.^{4–6}

The PARP enzyme family consists of 17 members, of which PARP1 is the most abundant and best-characterized. It senses DNA single-strand breaks (SSBs) with its zinc finger domains and initiates their repair upon auto poly(ADP-ribosylation) (PARylation), which recruits repair enzymes.^{7–9} PARP1, PARP2, and PARP5a and b (tankyrase 1 and 2) are capable of PAR chain formation, while the remaining PARP enzymes can perform mono(ADP-ribosylation) (MARylation) or are enzymatically inactive.^{10,11}

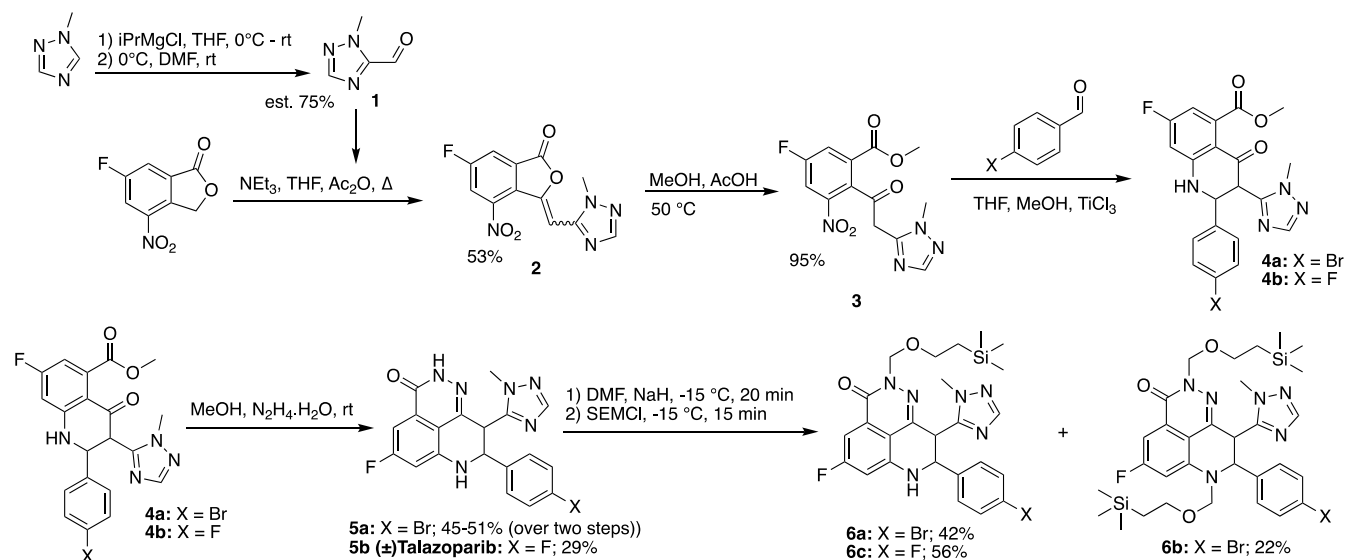
The catalytic domains of PARP enzymes use nicotinamide adenine dinucleotide (NAD⁺) as the substrate for PARylation.^{12,13} PARP inhibitors structurally mimic NAD⁺, thus blocking the catalytic domain and escalating the SSBs to double-strand breaks that can only be repaired by alternative DNA repair mechanisms like HR.¹⁴ In addition to their catalytic inhibition, some PARP inhibitors are (to various extents) able to trap the PARP enzyme on the damaged DNA site, leading to replication fork collapse and ultimately cell death.¹⁵

Within the last decade, numerous PARP inhibitors with various levels of cytotoxic efficacy have been approved by the U.S. Food and Drug Administration (FDA): olaparib (2014), rucaparib (2016), niraparib (2017), and talazoparib (2018).^{16–19} These inhibitors are mainly used in combination with DNA damaging agents like cisplatin in HR-deficient cancer entities or for maintenance therapy. Several ongoing

Received: May 19, 2021

Published: October 21, 2021



Scheme 1. Synthesis of Advanced Intermediates for [¹⁸F]Talazoparib Precursor Synthesis

studies are also exploring the potential of PARP inhibitors for monotherapy in HR-potent tumors.²⁰ It is commonly agreed that the substantial differences in the cytotoxic efficacies of the known PARP inhibitors are explained by the differences in their abilities to trap PARP1 on damaged DNA and not necessarily by their binding affinities alone.²¹

Talazoparib is considered the most potent of the known PARP1 inhibitors and the best PARP trapping agent.^{21–23} The molecule possesses two distinct chiral centers. Of the four possible stereoisomers, the *trans* enantiomers are present as the two dominant diastereomers. The (8*S*,9*R*)-diastereomer (talazoparib) is an excellent PARP inhibitor, while its enantiomer [(8*R*,9*S*) LT-674] is less active by several orders of magnitude, along with the other diastereomers.²⁴ It has been proposed that the bulky structure and stereochemistry of talazoparib contribute to its high potency, although the exact nature of the molecular interaction remains elusive.²⁵

PARP imaging has proven its exceptional clinical merit in several scenarios, specifically for the detection and delineation of oral, brain, pancreatic, and liver cancers, as well as target engagement imaging of different PARP inhibitors.^{26–32} Several PARP1-targeted imaging probes have been developed, with the most prominent among these being PARPi-FL, a fluorescently labeled olaparib analogue; [¹⁸F]PARPi, PARPi-FL's radioactive sibling; [¹⁸F]olaparib, isotopically radiolabeled olaparib; and [¹⁸F]FTT, the first clinically applied PARP radiotracer based on rucaparib.³³ To fully exploit PARP as an imaging biomarker, the development of novel PARP imaging probes with further improved pharmacological profiles is warranted. The high interest in the preparation of [¹⁸F]talazoparib is emphasized by the very recent disclosure of an elegant yet complex early-stage manual radiolabeling of the molecule.³⁴ This 2-step 2-pot approach makes use of harsh reagents (such as TiCl₃ and hydrazine) and conditions that would make automated production for eventual clinical use very difficult. To our knowledge, no efficient automated late-stage radiolabeling of talazoparib has been published till date.

Given the short half-life of ¹⁸F-fluorine (109.8 min), the synthesis of enantiomerically pure and isotopically radiolabeled [¹⁸F]talazoparib represents a complex radiosynthetic challenge. An accessible radiosynthesis of [¹⁸F]talazoparib has become

possible because of the recent advances in radiochemical methodology research, such as the development of copper-mediated radiofluorination (CMRF) chemistry.^{35–38} Our previous studies have explored this methodology by using the “design of experiments” (DoE) approach to reaction optimization, and this has helped us lay the foundation of a DoE-based radiotracer development pipeline using CMRF chemistry.^{39,40} DoE aids in establishing reliable and robust radiosyntheses from the onset of the tracer development process and, in combination with the “de-risking” strategies described by Taylor *et al.*, this approach can be used to expedite the development of novel radiotracers.⁴¹ In this work, we successfully applied a refined DoE-based tracer development workflow to the challenging radiosynthetic problem of [¹⁸F]talazoparib. Here, we present an efficient automated radiosynthesis and subsequent enantiomeric resolution of [¹⁸F]talazoparib as a potential next-generation PARP radiotracer together with a preliminary *in vitro* evaluation and pilot *in vivo* study of the tracer in mice.

RESULTS AND DISCUSSION

The late-stage radiosynthesis of chiral [¹⁸F]talazoparib can be achieved *via* two possible approaches. The most obvious approach would be to employ an enantiomerically pure precursor in the radiosynthesis. However, for an uncharacterized radiotracer, chiral separation of the precursor would be costly and time-consuming, with a risk of product racemization during the synthesis. We thus decided to pursue an approach that first involves the production and purification of the racemic radiotracer, followed by enantiomeric resolution, isolation, and formulation of the active enantiomer. Therefore, as the radiochemical yield would be reduced by half (assuming a 1:1 ratio of enantiomers), the radiosynthesis would need to be carefully optimized for maximum radiochemical yield to ensure an adequate and reliable synthesis output for biological studies. The two possible sites for late-stage isotopic ¹⁸F radiolabeling are both situated on electron-rich or electron-neutral aromatic rings. This excludes the use of traditional S_NAr radiofluorination in favor of more recently developed methodologies such as CMRF chemistry. However, the proposed radiotracer contains multiple heteroaromatic nitro-

gen atoms that have been shown to have detrimental effects on CMRF-based radiosyntheses.⁴¹ These moieties are thought to complex with the copper mediator, forming unreactive copper species that inhibit the radiosynthesis performance. For this reason, we set out to develop a protecting group strategy that would allow for maximal radiosynthetic performance while still affording an easily accessible, convenient to use, and shelf-stable precursor.

Chemistry. We adapted the synthesis of the precursor from the synthetic route employed by Wang *et al.* for the synthesis of talazoparib (Scheme 1).²⁴ 1-Methyl-1*H*-1,2,4-triazole was formylated to **1** via the published procedure.⁴² **1** was then condensed with commercially available 6-fluoro-4-nitroisobenzofuran-1(3*H*)-one in tetrahydrofuran (THF) in the presence of NEt₃ and Ac₂O to afford **2** in a 53% yield. The resulting lactone **2** was opened to give the keto-ester derivative **3** by warming in methanol with a catalytic amount of acetic acid. As in the original synthesis by Wang *et al.*,²⁴ **3** was then reacted with 4-fluorobenzaldehyde in THF and methanol via reductive cyclization driven by TiCl₃ to afford **4b**. This intermediate was then cyclized with hydrazine monohydrate to afford (±)-talazoparib (**5b**) as a non-radioactive reference compound. Performing the same two-step procedure with **3** and 4-bromobenzaldehyde afforded the derivatizable bromide **5a**. The presence of corresponding *cis*-diastereomers was not detected by either HPLC or NMR, suggesting the route to exclusively favor the formation of the desired *trans*-diastereomers.

A protecting group strategy using the trimethylsilyloxyethyl (SEM) ether protecting group was successfully employed by Wilson *et al.* for the “de-risked” radiosynthesis of [¹⁸F]olaparib, a PARP tracer structurally related to talazoparib.^{41,43,44} We thus applied the same protecting group strategy to compounds **5a** and **5b**, which were protected with SEM-Cl using sodium hydride in *N,N*-dimethylformamide (DMF) at 0 °C. These conditions afforded both the mono- (**6a**) and di-SEM (**6b**) protected bromide derivatives in an approximate 2:1 ratio. **5b** was exclusively converted to the mono-protected fluoride derivative **6c** for use as a non-radioactive reference compound.

Compounds **6a** and **6b** were then further derivatized to yield several potential precursors for radiolabeling. Compounds **6a** and **6b** were converted to their corresponding boronic acid pinacol esters under Miyaura borylation conditions in DMF with KOAc, bis(pinacolato)diboron, and Pd(dppf)Cl₂ as the catalyst (Scheme 2). This afforded the compounds **7a** and **7b** in good to excellent yields. **7a** was purified through recrystallization as a shelf-stable and convenient-to-handle white crystalline solid. **7b** was purified through chromatography and was much harder to obtain in the high purities required for reliable radiochemistry. Despite being of high

chromatographic purity (HPLC-MS), samples of **7b** displayed a complex NMR spectrum, indicative of multiple conformational isomers. Moreover, **7b** was found to degrade to the more stable **7a** over time. CMRF chemistry has also been well established with aryl stannane precursors, and we have investigated this variation of the CMRF reaction extensively in our previous work.³⁹ Thus, the analogous stannylation of **6a** was carried out with bis tributyltin to afford the stannyl precursor **7c** as an amorphous glass.

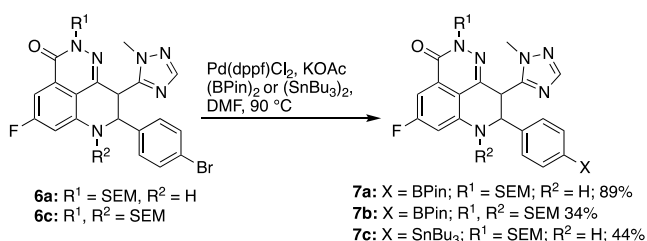
Optimal chiral HPLC conditions were screened using racemic (±)talazoparib (**5b**) in combination with commercially obtained authentic samples of talazoparib and LT-674. CHIRALPAK IA-U, IB-U, IC-U, and IG-U columns (1.6 μm particle diameter, DAIKEL Chiral Technologies, France) were tested for their abilities to resolve the two enantiomers under reversed-phase conditions (Figure S6). CHIRALPAK IB packing material was found to provide good enantiomeric resolution at a relatively low retention time (Figure S7). CHIRALPAK IB-N5 (5 μm) columns run under reversed-phase conditions (water with 0.1% TFA/acetonitrile) would thus be used for both semipreparative enantiomeric resolution of [¹⁸F]talazoparib and [¹⁸F]LT-674 and for chiral radio-HPLC for quality control (QC) analysis.

Radiochemistry and DoE Optimization. With the precursors **7a–c** in hand, we set out to evaluate which precursor would provide the best radiosynthesis performance while still being relatively easy to produce, shelf-stable, and convenient to handle. A series of pilot experiments carried out using each precursor under a small set of arbitrarily chosen unoptimized reaction conditions determined that compounds **7b** and **7c** displayed a marginally better reaction performance (17 and 19% respectively, data not shown) than **7a** (8–15% RCY). As expected, the di-SEM protected derivative **7b** offered the best overall reaction performance under unoptimized conditions; however, as **7a** proved easier to synthesize, purify, and characterize, as well as being shelf-stable, it was chosen as the preferred precursor for further development and optimization.

We have previously explored the use of DoE to solve complex radiochemical optimization problems and have developed a workflow and ¹⁸F processing method that is compatible with both small-scale DoE radiochemical experiments and large-scale automated tracer productions.⁴⁰ We applied this workflow to a computer-generated D-optimal DoE study designed to investigate the effects of precursor load (*Pre*, 5–30 μmol), copper-mediator load (*Cop*, 5–40 μmol), pyridine load (*Py*, 20–500 μmol), and concentration of *n*-BuOH co-solvent (*Bu*, 0–75%) in DMA, on the reaction performance (Figure 1A). The study consisted of 24 experiments (including centerpoints) and was conducted over 5 days (5 runs/day) using [¹⁸F]fluoride from cyclotron target washes (Table S1). Each run was carried out for 20 min at 120 °C before evaluation by radioTLC. Analysis of the data revealed the presence of one outlier (Table S1, exp 21), which was excluded from the final regression model. The remaining data (*n* = 23) was used to fit a regression model with R² = 0.946 (goodness of model fit) and Q² = 0.855 (goodness of model prediction), suggesting the model to be valid and predictive (Figure S1).

The use of larger amounts of the precursor was found to positively affect the reaction performance, while smaller quantities of the copper mediator (Cu(OTf)₂) were beneficial (Figure 1B). A small amount of *n*-BuOH (5–10%) was also

Scheme 2. Synthesis of [¹⁸F]Talazoparib Precursors



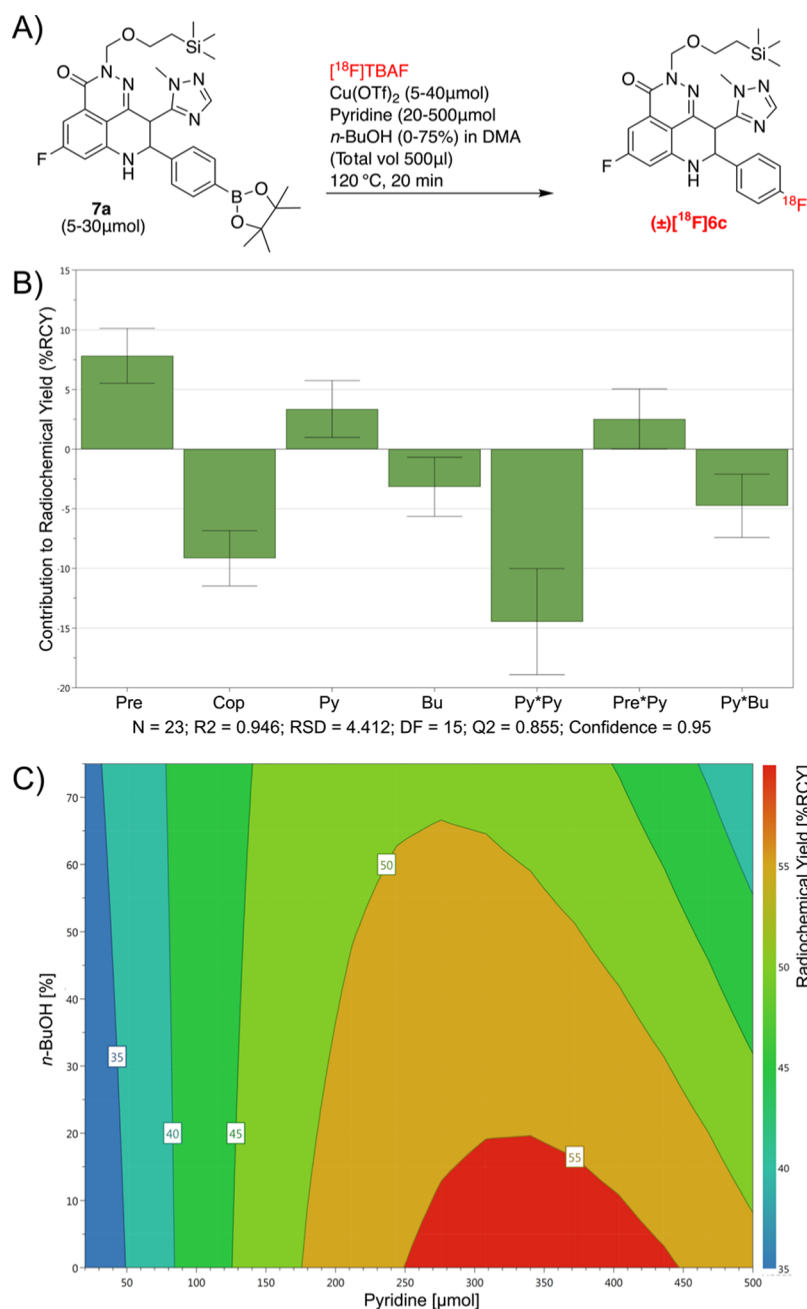


Figure 1. (A) D-optimal DoE study was used to optimize the radiolabeling of **7a**. (B) Scaled and centered regression coefficients were calculated from the results of the D-optimal response surface modeling study of the radiosynthesis of [¹⁸F]**6c**. Large bars represent factors with a large contribution to the response (%RCY). A positive number denotes a positive influence on the response. A negative number indicates a diminishing effect on the response. If a factor's regression coefficient is smaller than the associated error bars, it is probable (at the 95% confidence interval) then that factor is not significant. (C) Section of the response surface calculated from the regression model. Variables not shown: *Cop* = 5 μmol, *Pre* = 30 μmol (see Figure S3 for the entire 4D response surface plot.).

found to provide a small increase in the reaction performance. It is thought that *n*-BuOH increases the rate of the CMRF transmetalation step.⁴⁵ Factor interactions (where the setting of one factor affects the behavior of another) were found between pyridine and the precursor amount as well as pyridine and *n*-BuOH. The effect of pyridine on the reaction performance was found to possess strong quadratic (*Py*Py*, curved) behavior. Optimal reaction conditions of 30 μmol **7a**, 300 μmol pyridine, and 5 μmol Cu(OTf)₂ in DMA with 10% *n*-BuOH were chosen from the response surface plot generated from the regression model (Figure 1C). These conditions were

validated manually using full batches of processed [¹⁸F]TBAF and were able to produce protected (±)[¹⁸F]**6c** with 57 ± 7.5 %RCY (*n* = 6) (compound identity was verified using the non-radioactive standard **6c**). These results align with the DoE model (predicted yield = 56%) and afford the product in yields acceptable for establishment as an automated radiosynthesis featuring enantiomeric resolution. Quantitative deprotection to (±)[¹⁸F]talazoparib (>95% conversion according to HPLC) was achieved with 6 M HCl at 120 °C for 15 min (compound identity was verified against the non-radioactive standard **5b**).

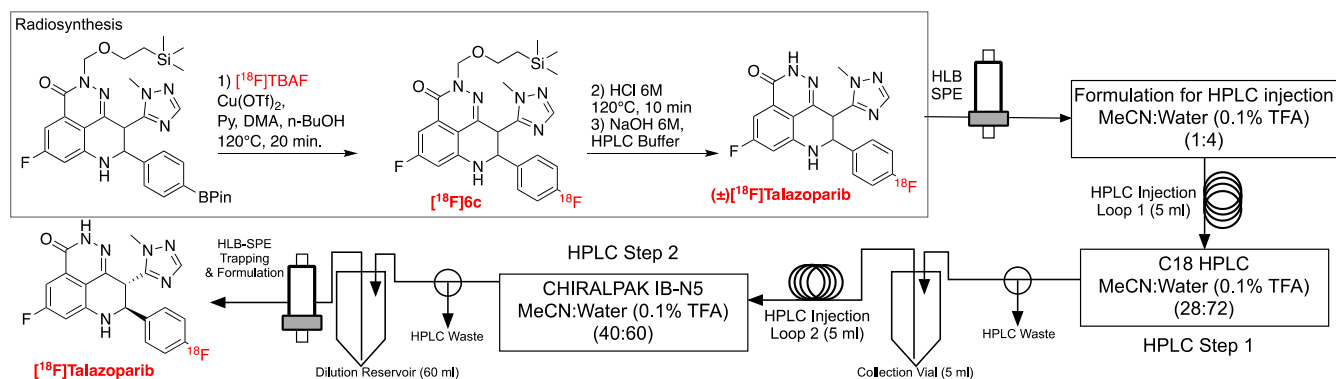


Figure 2. General automated procedure for the radiosynthesis, HLB-SPE clean-up, 2D HPLC purification, and chiral resolution, and product concentration and formulation of [^{18}F]talazoparib.

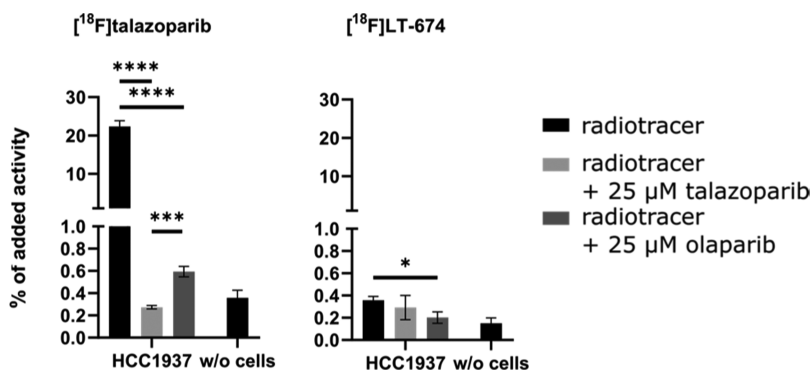


Figure 3. Uptake of [^{18}F]talazoparib (left) and the inactive enantiomer [^{18}F]LT-674 (right) in HCC1937 cells, blocked with olaparib or talazoparib. *: $p < 0.05$, ***: $p < 0.001$, and ****: $p < 0.0001$.

Automated Radiochemistry. The optimized CMRF radiosynthesis was translated onto two different synthesis platforms: an ELIXYS Flex/Chem automated radiosynthesizer coupled to a PURE/FORM purification and formulation module (Sofie Biosciences, USA) and an FX N Pro (GE Healthcare, Sweden). The ELIXYS Flex/Chem platform is a cassette-based system (up to three reactors) and can perform complex multi-reactor radiosyntheses. The PURE/FORM module is equipped with two semipreparative HPLC injection loops (5 mL each) and up to three selectable HPLC columns. Therefore, this setup would allow for the sequential HPLC-based purification and enantiomeric resolution required for the synthesis of [^{18}F]talazoparib. The TRACERlab FX N Pro is a fixed fluid path system with a single HPLC injection loop and column. The purified product racemate must, therefore, be transferred to a secondary external HPLC system (in this case, an ELIXYS PURE/FORM) for enantiomeric resolution. While the exact technical details differ between the two synthesis modules (the radiosynthesis using both systems is described in detail in the [Supporting Information](#)), the automated synthesis of [^{18}F]talazoparib follows the same general procedure irrespective of which module is used ([Figure 2](#)).

The DoE-optimized reaction mixture was added to the processed [^{18}F]TBAF and reacted at 120 °C for 20 min. This was followed by the removal of the SEM protecting group with 6 M HCl at 120 °C for 15 min. The pH of the reaction mixture was then adjusted to pH 5–7 with the addition of ammonium formate solution (25 mM, 5–10 mL, dependent on the automated system used) containing NaOH (6 M, 600 μL). The diluted reaction mixture was passed over an HLB SPE cartridge (Waters, USA), trapping the product (\pm) [^{18}F]-

talazoparib and removing the DMA, residual salts, and unreacted [^{18}F]fluoride. While some product is lost, especially when lower dilution volumes are used, this step is important to ensure efficient HPLC purification. The product was then eluted from the HLB cartridge with acetonitrile (1 mL) and reformulated with HPLC buffer (4 mL) for injection onto the first HPLC column. The reaction mixture was then subjected to purification *via* C18 reversed-phase HPLC to separate the product racemate from the remaining precursor and other CMRF reaction byproducts. The product HPLC peak was isolated (≈ 5 mL), and this solution was then transferred to a second HPLC injection loop for enantiomeric resolution using a semipreparative CHIRALPAK IB-N5 (5 μm , 10 \times 250 mm) column operating under reversed-phase conditions. The desired enantiomer, either [^{18}F]talazoparib or [^{18}F]LT-674, was then isolated, diluted, and trapped on a second HLB cartridge. The product was then eluted from the cartridge and formulated for injection with ethanol and phosphate-buffered saline (PBS, final ethanol content 5%). This procedure yielded enantiomerically pure (>99% ee) [^{18}F]talazoparib (or [^{18}F]LT-674) with $13 \pm 3.4\%$ RCY ($n = 4$) [radioactivity yield (%AY) = 4–8% over 120 min; molar radioactivity = 52–176 GBq/ μmol]. Product identity, chemical and radiochemical purity, and molar activity were determined using CHIRALPAK IB-N5 (5 μm , 4.6 \times 150 mm) analytical HPLC against the commercially available non-radioactive standard compounds. This synthesis produced both [^{18}F]talazoparib and [^{18}F]LT-674 in good yields, chemical and radiochemical purities, and molar activities for both *in vitro* and *in vivo* preclinical evaluation.

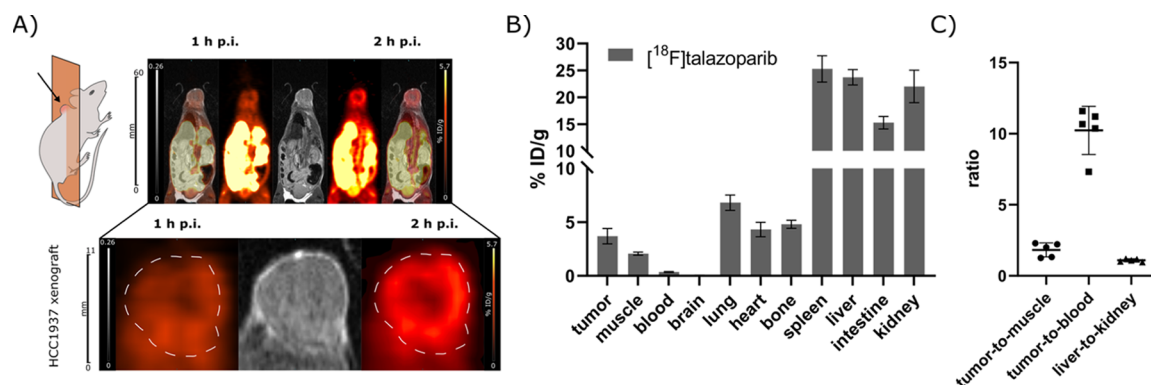


Figure 4. (A) Representative PET images of 1 mouse 1 h p.i. (Left, Last 10 min of a 1 h dynamic scan) and 2 h p.i. (right, 10 min static scan) with the corresponding MR image. The respective xenograft is displayed enlarged underneath. A scheme to depict the image plane is provided at the left side with a black arrow indicating the xenograft position. Images of the transverse plane are shown in Figure S20. (B) Biodistribution of $[^{18}\text{F}]$ talazoparib in various organs 2.5 h p.i. ($n = 5$). (C) TMR, TBR, and LKR of mice injected with $[^{18}\text{F}]$ talazoparib ($n = 5$) 2.5 h p.i.

In Vitro Evaluation. The stability of $[^{18}\text{F}]$ talazoparib was evaluated in mouse and human serum before the *in vivo* experiments, and the radiotracer was found to be stable over a time course of 240 min (Figure S19). Additionally, no significant degradation of the tracer was observed when incubated in the presence of human liver microsomes (Figures S21–23). $[^{18}\text{F}]$ Talazoparib demonstrated a high uptake in human breast cancer cells (HCC1937), while, as expected, the inactive enantiomer $[^{18}\text{F}]$ LT-674 showed only very low radiotracer uptake (Figure 3). The $[^{18}\text{F}]$ Talazoparib signal was blockable to baseline with excesses of both olaparib and talazoparib. Olaparib was found to be less effective at blocking the $[^{18}\text{F}]$ talazoparib signal than talazoparib. This effect was confirmed using a concentration-dependent blocking assay, revealing IC_{50} values of 14.51 and 23.77 nM for talazoparib and olaparib, respectively (Figure S16). As talazoparib blocked the amount of bound $[^{18}\text{F}]$ talazoparib to a significantly greater extent than olaparib, we theorize that this difference represents talazoparib's ability to bind a wider array of other PARP isoforms, an effect that we plan to investigate further.^{22,46}

In Vivo Evaluation. $[^{18}\text{F}]$ Talazoparib was further characterized *in vivo* in HCC1937 xenograft-bearing mice. PET imaging showed substantial tracer uptake in the abdominal tissues as well as in bone and muscle (Figure 4A), data that are in line with the literature published blockable uptake of other established PARP radiotracers in these organs.^{47,48} These findings were further confirmed by *ex vivo* biodistribution analysis after 2.5 h post-injection (p.i.) (Figure 4B). PARP1 expression in the xenograft tissue was verified *ex vivo* by PARP1 immunofluorescence microscopy (Figure S18).

$[^{18}\text{F}]$ Talazoparib showed an elevated uptake in the tumor xenografts at 1 h p.i. relative to reference tissues. The specific uptake was found to further intensify up to the 2 h p.i. timepoint. *Ex vivo* biodistribution data showed the absolute xenograft uptake to be 3.7 ± 0.7 %ID/g with a mean tumor-to-muscle ratio (TMR) of 1.8 ± 0.4 (Figure 4C). The TMR was comparable to the reported TMR (1.9, 60 min p.i.) of the PARP tracer $[^{18}\text{F}]$ FTT in the same xenograft model.³⁰ The tumor-to-blood ratio (TBR) of $[^{18}\text{F}]$ talazoparib is exceptionally high (10.2 ± 1.5) and exceeds the TMR by a factor of 5.6. In the context of our *in vitro* data, we hypothesize that the high muscle uptake observed in this animal model may be caused by the binding of $[^{18}\text{F}]$ talazoparib to other PARP enzymes or an as-of-yet unidentified protein target. These questions will be the subject of future investigations using this novel radiotracer.

$[^{18}\text{F}]$ Talazoparib exhibited balanced clearance between both renal and hepatobiliary pathways with a mean liver-to-kidney ratio (LKR) of 1.1 ± 0.1 , a finding which was confirmed by the time–activity curves (TAC) obtained from dynamic PET imaging (Figure S17). While no tracer uptake was observed in the *ex vivo* biodistribution data, the brain TAC shows an initial perfusion peak (SUV_{peak} 2.4) with complete tracer washout occurring rapidly thereafter ($\text{SUV}_{60\text{min}}$ 0.5). Thus, $[^{18}\text{F}]$ -talazoparib uptake could be examined in glioblastoma models, a setting in which the observed high muscle uptake would only play a minor role. Fast blood clearance with a calculated blood half-life of 3.3 min was determined.

CONCLUSIONS

Fluorine is present in many clinically relevant drug-like molecules that may serve as candidates for novel imaging probes. PET imaging is also becoming more important as a valuable research tool to assess the *in vivo* pharmacological properties of promising drug candidates in real-time. The synthesis and evaluation of enantiomerically pure $[^{18}\text{F}]$ -talazoparib discussed here serves as an example of how an efficient DoE-based tracer development pipeline can be used to aid in the establishment of procedurally complex ^{18}F based radiosyntheses. Given the time constraints of ^{18}F radiochemistry, our decision to perform enantiomeric resolution after the radiolabeling step meant that our synthesis needed to be optimized for radiochemical efficiency from the outset. Using information from previous radiosynthesis “de-risking” studies,^{41,43,44} we were able to rapidly identify and test a suitable protecting group strategy and identify a focused set of precursor candidates. After selecting a precursor that was shelf-stable, easy to obtain, and handle, although not necessarily chemically optimal, we used DoE to discover a set of reaction conditions that would produce (\pm) $[^{18}\text{F}]$ talazoparib in yields sufficient for enantiomeric resolution, product formulation, and subsequent delivery for preclinical evaluation.

While $[^{18}\text{F}]$ talazoparib was found to target PARP1 expression in an established tumor model effectively, the *in vitro* and *in vivo* results of this work highlight the importance of the further exploration of $[^{18}\text{F}]$ talazoparib as a PARP imaging agent for alternative indications. In particular, the use of $[^{18}\text{F}]$ talazoparib to quantify PARP isoforms beyond PARP1/2 may be of clinical merit. $[^{18}\text{F}]$ Talazoparib may thus allow us to study the PARP family of proteins from a new angle.

EXPERIMENTAL SECTION

General. All chemicals, reagents, catalysts, and solvents were purchased from either Sigma-Aldrich (Steinheim, Germany), Merck (Darmstadt, Germany), abcr GmbH (Karlsruhe, Germany), and Carl Roth (Karlsruhe, Germany) and were used without any additional purification unless otherwise stated. QMA, SPE, and SEP-PAK cartridges were obtained from Waters (Milford, Massachusetts, USA) unless otherwise stated. Reactions were monitored using thin-layer chromatography (TLC) on 0.20 mm POLYGRAM SIL G/UV₂₅₄ (silica gel 60) TLC plates and were developed with an appropriate running buffer/solvent mixture. Spots were visualized with UV light (254 or 366 nm). Preparative flash chromatography was performed using pre-packed silica gel columns [SNAP KP-Sil or SNAP Ultra (25 μ m HP-Sphere), 10, 25, 50, or 100 g, (Biotage, Uppsala, Sweden)] on an automated chromatography system (Isolera 4, Biotage) which featured a UV detector and fraction collector. Unless otherwise stated, all columns were dry loaded by absorption onto either silica gel or diatomaceous earth packing material (Isolute, Biotage). ¹H and ¹³C NMR spectra were obtained at 300 K using an Avance III AV 600 (¹H: 600.13 MHz and ¹³C: 150.61 MHz) spectrometer (Bruker Biospin, Ettlingen, Germany). All chemical shifts (δ) are reported in parts per million, and all *J* values are reported in Hz. The following abbreviations are used to describe multiplicities: s (singlet), d (doublet), t (triplet), q (quartet), m (multiplet), and brs (broad singlet). All compounds were dissolved in chloroform (CDCl₃) unless otherwise stated. All chemical shifts were referenced to residual chloroform ($\delta_{\text{H}} = 7.24$ and $\delta_{\text{C}} = 77.00$) or DMSO ($\delta_{\text{H}} = 2.50$ and $\delta_{\text{C}} = 39.52$). Analytical HPLC-MS data were collected using a 1200 series HPLC machine coupled to quadrupole 6120 series MS detector in the ESI mode (Agilent, Santa Clara, California, USA) under the following conditions: Column: Luna 5 μ m C18 (2) 100 \AA , 50 \times 2 mm; solvent A: H₂O + formic acid (0.1%); solvent B: acetonitrile; gradient: 0–7.60 min (0–100% B), 7.60–7.80 min (100% B), 7.80–8.30 min (100–0% B), 8.30–12.0 min (0% B). High-resolution mass spectroscopy (HRMS) was acquired using a maXis 4G mass spectrometer (Bruker Daltonics, Bremen, Germany) operating using electron spray ionization time-of-flight. Deviation from the calculated mass was found to be <2.00 ppm for all measured compounds.

Chemical Synthesis. *1-Methyl-1H-1,2,4-triazole-5-carbaldehyde (1)*. 1-Methyl-1H-1,2,4-triazole (10 g, 120 mmol) was dissolved in THF (60 mL) in a dry argon purged two-neck reaction flask fitted with a rubber septum, and the resulting solution was then cooled to 0 °C. A solution of 2 M isopropyl magnesium chloride (66 mL, 132 mmol) was then added dropwise through the septum *via* a syringe over 15 min. The reaction mixture was then allowed to warm slowly to room temperature and stir for 1.5 h. The reaction vessel was again cooled to 0 °C, after which DMF (14 mL, 180.5 mmol) was added dropwise *via* a syringe. The reaction mixture was once more allowed to slowly warm to room temperature and stirred overnight. The next morning, the reaction was quenched by the slow addition of HCl (2 M) until pH 2, and the resulting mixture was diluted with DCM (100 mL). The phases were separated with a separating funnel, and the aqueous phase was neutralized with saturated aqueous sodium bicarbonate (NaHCO₃) and extracted with DCM (2 \times 80 mL). The organic fractions were combined, washed once with brine, dried with magnesium sulfate (MgSO₄), and concentrated under reduced pressure to remove the DCM. Product **1** is a volatile oil (\approx 60 °C) and was thus not purified further. The compound was used, in excess, directly in the next step without further analysis, assuming a synthesis yield of 75% (presented in the previous literature).⁴²

6-Fluoro-3-((1-methyl-1H-1,2,4-triazol-5-yl)methylene)-4-nitroisobenzofuran-1(3H)-one (2). Commercially available 6-fluoro-4-nitroisobenzofuran-1(3H)-one (9.8 g, 50 mmol), a solution of **1** in THF (*ca.* 100 mmol, assuming 75% conversion in the previous step), and triethylamine (21 mL, 150 mmol) were dissolved in dry THF (150 mL) in an argon-filled two-neck reaction flask fitted with a reflux condenser. Acetic anhydride (35 mL) was then added dropwise to the reaction mixture over 3 min, and the resulting mixture was then heated to reflux for 1 h. The mixture was then removed from the heat and concentrated under reduced pressure to a volume of

approximately (10 mL) until a green/yellow precipitate is formed. The resulting slurry was then cooled in a freezer to –5 °C, and the solid was collected through vacuum filtration. The resulting cake was washed with cold ethyl acetate, and the residue was then dried under high vacuum for 4 h to afford **2** as a gray-green solid (7.34 g, 50%). The analytical data are in agreement with the literature.²⁴

¹H NMR (600 MHz, DMSO): δ 7.74 (dd, *J* = 8.7, 2.3 Hz, 1H, Ar), 7.56 (dd, *J* = 6.4, 2.4 Hz, 1H, Ar), 7.25 (s, 1H, TzH), 6.32 (s, 1H, C=CH), 3.09 (s, 3H, Me).

Methyl 5-Fluoro-2-(2-(1-methyl-1H-1,2,4-triazol-5-yl)acetyl)-3-nitrobenzoate (3). Compound **2** (7.34 g, 25.2 mmol) was suspended in methanol (204 mL), and acetic acid (0.5 mL) was added to the resulting solution. The mixture was then warmed to 50 °C until HPLC-MS confirmed complete consumption of the starting material (4–12 h). The solvents were then removed under high vacuum to afford **3** as a yellow solid in nearly a quantitative yield (8.1 g, 99%). The product was used directly in the next step without further purification. The analytical data are in agreement with the literature.²⁴

¹H NMR (600 MHz, DMSO): δ 8.52 (dd, *J* = 8.2, 2.6 Hz, 1H, Ar), 8.26 (dd, *J* = 8.3, 2.6 Hz, 1H, Ar), 7.85 (s, 1H, TzH), 4.59 (s, 2H, CH₂), 3.91 (s, 3H, Me), 3.88 (s, 3H, Me); ¹³C NMR (151 MHz, DMSO): δ 195.48, 163.48, 161.21 (d, *J* = 252.6 Hz), 150.18, 148.75, 147.10 (d, *J* = 8.8 Hz), 133.58, 131.24 (d, *J* = 7.7 Hz), 123.63, 117.09 (d, *J* = 26.9 Hz), 53.71, 40.55, 35.34.

8-(4-Bromophenyl)-5-fluoro-9-(1-methyl-1H-1,2,4-triazol-5-yl)-2,7,8,9-tetrahydro-3H-pyrido[4,3,2-de]phthalazin-3-one (5a) and 5-Fluoro-8-(4-fluorophenyl)-9-(1-methyl-1H-1,2,4-triazol-5-yl)-2,7,8,9-tetrahydro-3H-pyrido[4,3,2-de]phthalazin-3-one (5b). **5a**. Compound **3** (8.1 g, 25.2 mmol) and 4-bromobenzaldehyde (8.9 g, 50.5 mmol) were suspended in THF (50 mL) and MeOH (10 mL). To the resulting mixture was added titanium(III) chloride solution [20% wt solution in HCl (2 M), 130 mL, 6 equiv] in dropwise fashion over 30 min at room temperature. The reaction temperature was maintained between 30 and 50 °C for 2 h, after which it was quenched by the slow addition of water (260 mL). The reaction mixture was then poured into a separating funnel and extracted with ethyl acetate (4 \times 140 mL). The organic fractions were pooled and washed with NaHCO₃ (3 \times 60 mL) and NaHSO₃ (3 \times 100 mL), dried with sodium sulfate (Na₂SO₄), and concentrated under reduced pressure to afford a thick yellow syrup, which was carefully washed with aliquots of diethyl ether (3 \times 10 mL). The resulting yellow syrup was then dried under high vacuum to afford the crude intermediate **4** as a yellow amorphous solid (11.3 g, 98%) that was used in the next step without any further purification.

Intermediate **4** (11.3 g, 24.6 mmol) was dissolved in methanol (30 mL) at room temperature, and to the resulting solution was added hydrazine monohydrate (7.7 mL). The reaction mixture was then left to stir overnight at room temperature. The next morning the resulting white precipitate was collected *via* vacuum filtration to afford compound **5** as an off-white solid (4.9 g, 45% over two steps).

5a. ¹H NMR (600 MHz, DMSO): δ 12.35 (s, 1H, NH), 7.81 (s, 1H, TzH), 7.72 (s, 1H, NH), 7.55–7.50 (m, 2H, Ar), 7.43–7.39 (m, 2H, Ar), 7.07 (dd, *J* = 9.0, 2.4 Hz, 1H, Ar), 6.91 (dd, *J* = 11.1, 2.5 Hz, 1H, Ar), 5.00 (m, 2H, CH, CH), 3.68 (s, 3H, Me); ¹³C NMR (151 MHz, DMSO): δ 165.40 (d, *J* = 248.2 Hz), 159.37 (d, *J* = 3.5 Hz), 152.36, 150.77, 148.78 (t, *J* = 12.7 Hz), 141.38, 139.03, 131.77, 130.74, 130.35 (d, *J* = 11.1 Hz), 121.96, 111.76, 103.33 (d, *J* = 26.7 Hz), 99.08 (d, *J* = 24.7 Hz), 59.14, 42.85, 35.40; HRMS (ESI): *m/z* calcd for C₁₉H₁₅BrFN₆O [M + H]⁺, 441.04693; found, 441.04736.

5b. To synthesize **5b**, the same general procedure was followed using compound **3** (800 mg, 2.5 mmol), 4-fluorobenzaldehyde (462 mg, 3.7 mmol), and titanium(III) chloride solution [20% wt solution in HCl (2 M), 9.4 mL, 6 equiv]. The resulting intermediate **4b** was treated with hydrazine monohydrate (1.5 mL) to afford **5b** (274 mg, 29%). Spectral analysis agreed with the published data.²⁴ **5b talazoparib**: ¹H NMR (600 MHz, DMSO): δ 12.35 (s, 1H, NH), 7.81 (s, 1H, TzH), 7.73 (s, 1H, NH), 7.52–7.47 (m, 2H, Ar), 7.20–7.13 (m, 2H, Ar), 7.08 (dd, *J* = 8.9, 2.5 Hz, 1H, Ar), 6.93 (dd, *J* = 11.2, 2.5 Hz, 1H, Ar), 5.01 (m, 2H, CH, CH), 3.67 (s, 3H, Me).

8-(4-Bromophenyl)-5-fluoro-9-(1-methyl-1H-1,2,4-triazol-5-yl)-2-((2-(trimethylsilyl)ethoxy)methyl)-2,7,8,9-tetrahydro-3H-pyrido[4,3,2-de]phthalazin-3-one (**6a**), 8-(4-Bromophenyl)-5-fluoro-9-(1-methyl-1H-1,2,4-triazol-5-yl)-2,7-bis((2-(trimethylsilyl)ethoxy)methyl)-2,7,8,9-tetrahydro-3H-pyrido[4,3,2-de]phthalazin-3-one (**6b**), and 5-Fluoro-8-(4-fluorophenyl)-9-(1-methyl-1H-1,2,4-triazol-5-yl)-2-((2-(trimethylsilyl)ethoxy)methyl)-2,7,8,9-tetrahydro-3H-pyrido[4,3,2-de]phthalazin-3-one (**6c**). **6a** and **6b**. Sodium hydride (60% in mineral oil, 181 mg, 4.53 mmol) was suspended in DMF (10 mL) in a dry, argon-filled flask, and the resulting solution was then cooled to 0 °C. Compound **5a** (1 g, 2.27 mmol) was added to the NaH suspension in small portions, and DMF (2 mL) was used to wash any compound off the vessel walls. The deep red/purple solution was allowed to stir for 15 min, whereupon a solution of (trimethylsilyl)ethoxymethyl chloride (752 mg, 4.53 mmol) in DMF (2 mL) was added dropwise through a rubber septum over 5 min. Throughout the addition, the solution turned clear and light orange and was allowed to stir for a further 20 min before being quenched with sat. aq. NH₄Cl (10 mL). The reaction mixture was diluted with water (250 mL) and transferred to a separating funnel, where it was extracted with ethyl acetate (3 × 50 mL). The organic fractions were pooled, dried with MgSO₄, and evaporated to dryness. The crude product residue was then purified using flash chromatography (40% EtOAc in hexanes) to afford compounds **6a** and **6b** as crystalline solids (**6a**: 547 mg, 42%; **6b**: 347 mg, 22%). Despite the presence of several minor impurities, both compounds were used in the next step without further purification. **6a**: ¹H NMR (600 MHz, CDCl₃): δ 7.80 (s, 1H, TzH), 7.39 (d, J = 8.5 Hz, 2H, Ar), 7.32 (dd, J = 8.5, 2.3 Hz, 1H, Ar), 7.24 (d, J = 8.5 Hz, 2H, Ar), 6.75 (dd, J = 10.0, 2.3 Hz, 1H, Ar), 5.36 (d, J_{gem} = 9.9 Hz, 1H, CH₂), 5.31 (s, 1H, NH), 5.21 (d, J_{gem} = 9.9 Hz, 1H, CH₂), 5.13 (d, J = 11.1 Hz, 1H, CH), 4.43 (d, J = 11.0 Hz, 1H, CH), 3.64 (s, 3H, Me), 3.60–3.48 (m, 2H, CH₂), 0.90–0.81 (m, 2H, CH₂), –0.06 (s, 9H); ¹³C NMR (151 MHz, CDCl₃): δ 167.05 (d, J = 253.1 Hz), 160.49 (d, J = 3.4 Hz), 152.80, 151.64, 148.17 (d, J = 11.8 Hz), 141.07, 139.07, 133.46, 131.69 (d, J = 11.0 Hz), 130.55, 124.42, 112.90, 105.77 (d, J = 26.8 Hz), 104.08 (d, J = 24.6 Hz), 80.91, 68.78, 61.15, 46.06, 36.69, 19.46, 0.00; HRMS (ESI): m/z calcd for C₂₃H₂₈BrFN₆O₂SiNa [M + Na]⁺, 593.11026; found, 593.11030.

6b. ¹H NMR (600 MHz, CDCl₃): δ 7.72 (s, 1H, TzH), 7.43 (dd, J = 8.5, 2.3 Hz, 1H, Ar), 7.39 (d, J = 8.5 Hz, 2H, Ar), 7.10 (dd, J = 11.4, 2.3 Hz, 1H, Ar), 7.07 (d, J = 8.5 Hz, 2H, Ar), 5.40 (d, J = 9.9 Hz, 1H, CH₂), 5.36 (d, J = 9.9 Hz, 1H, CH₂), 5.21 (d, J = 3.9 Hz, 1H, CH), 4.87 (d, J = 11.2 Hz, 1H, CH₂), 4.78 (d, J = 11.2 Hz, 1H, CH₂), 4.53 (d, J = 3.9 Hz, 1H, CH), 3.93 (s, 3H, Me), 3.61–3.56 (m, 2H, CH₂), 3.45–3.38 (m, 1H, CH₂), 3.38–3.21 (m, 1H, CH₂), 0.90–0.78 (m, 4H, CH₂), –0.08 (s, 9H, SiMe₃), –0.09 (s, 9H, SiMe₃); ¹³C NMR (151 MHz, CDCl₃): δ 167.80 (d, J = 252.9 Hz), 160.77 (d, J = 3.6 Hz), 154.13, 151.87, 147.34 (d, J = 11.8 Hz), 139.40, 139.11, 133.67, 131.67 (d, J = 11.8 Hz), 129.99, 123.86, 113.46, 105.98 (d, J = 28.2 Hz), 104.17 (d, J = 24.6 Hz), 84.26, 80.44, 68.72, 67.45, 66.12, 44.67, 37.61, 19.49, 19.44, 0.00; HRMS (ESI): m/z calcd for C₃₁H₄₂BrFN₆O₃Si₂Na [M + Na]⁺, 723.19165; found, 723.19109.

6c. The same general procedure was followed using compound **5b** (200 mg, 0.53 mmol), sodium hydride (60% in mineral oil, 46 mg, 1.16 mmol), and (trimethylsilyl)ethoxymethyl chloride (192 mg, 1.16 mmol) in DMF (4 mL). These conditions afforded the non-radioactive reference compound **6c** (139 mg, 52%). ¹H NMR (600 MHz, CDCl₃): δ 7.86 (s, 1H, TzH), 7.45–7.37 (m, 3H, Ar), 7.02 (t, J = 8.5 Hz, 2H, Ar), 6.80 (dd, J = 10.0, 2.3 Hz, 1H, Ar), 5.42 (d, J_{gem} = 9.9 Hz, 1H, CH₂), 5.28 (d, J_{gem} = 9.9 Hz, 1H, CH₂), 5.28 (s, 1H, NH), 5.20 (d, J = 11.1 Hz, 1H, CH), 4.50 (d, J = 11.1 Hz, 1H, CH), 3.68 (s, 3H, Me), 3.67–3.56 (m, 2H, CH₂), 0.95–0.86 (m, 2H, CH₂), 0.00 (s, 9H, SiMe₃); ¹³C NMR (151 MHz, CDCl₃): δ 167.07 (d, J = 253.0 Hz), 164.22 (d, J = 248.8 Hz), 160.51 (d, J = 3.5 Hz), 152.90 (151.58, 148.21 (d, J = 11.7 Hz), 141.18, 135.79 (d, J = 3.2 Hz), 131.75 (d, J = 11.1 Hz), 130.63 (d, J = 8.2 Hz), 117.33 (d, J = 21.5 Hz), 112.96, 105.70 (d, J = 26.9 Hz), 104.11 (d, J = 24.5 Hz), 80.90, 68.79, 61.12, 46.33, 36.66, 31.09, 19.47, 15.52; HRMS (ESI): m/z

calcd for C₂₅H₂₈F₂N₆O₂SiNa [M + Na]⁺, 533.19033; found, 533.19021.

General Procedure for the Synthesis of Compounds 7a–c. The corresponding bromide (**6a** or **6b**), bis(pinacolato)diboron (2.2 equiv), and potassium acetate (3 equiv) were suspended in DMF in a dry argon-filled reaction flask fitted with a reflux condenser. [1,1'-bis(Diphenylphosphino)ferrocene]dichloropalladium(II) [Pd(dppf)-Cl₂, 20 mol %] was added to the reaction mixture, and a small portion of DMF was used to wash the catalyst of the vessel walls. The reaction flask was purged with argon, and the reaction was heated to 90 °C for 2–6 h until HPLC-MS showed conversion of the starting material into the desired product. The reaction mixture was diluted with ethyl acetate (80 mL) and passed through a tightly packed plug of Celite under vacuum. The filtrate was collected and transferred to a separating funnel, where it was washed with water (200 mL). The aqueous layer was further extracted with ethyl acetate (3 × 80 mL), after which the organic fractions were pooled, washed with brine, dried with MgSO₄, and concentrated under reduced pressure to afford the desired product racemate.

5-Fluoro-9-(1-methyl-1H-1,2,4-triazol-5-yl)-8-(4-(4,4,5,5-tetra-methyl-1,3,2-dioxaborolan-2-yl)phenyl)-2-((2-(trimethylsilyl)ethoxy)methyl)-2,7,8,9-tetrahydro-3H-pyrido[4,3,2-de]phthalazin-3-one (**7a**). The general procedure described above was applied using compound **6a** (1.448 g, 2.534 mmol), bis(pinacolato)diboron (1.415 g, 5.574 mmol), potassium acetate (746 mg, 7.602 mmol), and Pd(dppf)Cl₂ (371 mg, 0.507 mmol, 20 mol %) in DMF (22 mL + 3 mL wash). After 4 h, these conditions afforded the desired product racemate (**7a**) as an off-white solid (1.391 g, 89%). For radiochemical experiments, the product (515 mg) was further purified by recrystallization. The product was dissolved completely in a hot mixture of acetone and acetonitrile (1:1), and deionized water was then added dropwise until the solution became turbid. The solution was again slightly heated until the solution was nearly transparent, and it was then allowed to slowly cool to the ambient temperature, after which the recrystallization vessel was placed in a refrigerator at 4 °C and allowed to sit overnight. The next day the pure product was collected via vacuum filtration to afford a pure racemic mixture of **7a** as a white crystalline solid (361 mg, 70% recovery). ¹H NMR (600 MHz, CDCl₃): δ 7.78 (s, 1H, TzH), 7.69 (d, J = 7.8 Hz, 2H, Ar), 7.34 (dd, J = 8.8, 2.3 Hz, 1H, Ar), 7.30 (d, J = 7.8 Hz, 2H, Ar), 6.72 (dd, J = 10.0, 2.3 Hz, 1H, Ar), 5.37 (d, J_{gem} = 9.9 Hz, 1H, CH₂), 5.28 (s, 1H, NH), 5.22 (d, J_{gem} = 9.9 Hz, 1H), 5.06 (d, J = 11.1 Hz, 1H, CH), 4.47 (d, J = 11.1 Hz, 1H, CH), 3.62–3.50 (m, 5H, CH, Me), 1.31 (s, 12H, BPin), 0.85 (dd, J = 9.1, 7.5 Hz, 2H, CH₂), 0.06 (s, 9H, SiMe₃); ¹³C NMR (151 MHz, CDCl₃): δ 167.07 (d, J = 252.7 Hz), 160.58 (t, J = 3.5 Hz), 153.04, 151.67, 148.31 (d, J = 11.8 Hz), 142.85, 141.35, 136.73, 131.74 (d, J = 11.0 Hz), 128.07, 112.97, 105.60 (d, J = 26.5 Hz), 103.93 (q, J = 24.6 Hz), 85.47, 80.86, 68.74, 61.94, 46.06, 36.55, 26.26 (d, J = 4.9 Hz), 19.45, 0.00; HRMS (ESI): m/z calcd for C₃₁H₄₀BFN₆O₄SiNa [M + Na]⁺, 641.28554; found, 641.28497.

5-Fluoro-9-(1-methyl-1H-1,2,4-triazol-5-yl)-8-(4-(4,4,5,5-tetra-methyl-1,3,2-dioxaborolan-2-yl)phenyl)-2,7-bis((2-(trimethylsilyl)ethoxy)methyl)-2,7,8,9-tetrahydro-3H-pyrido[4,3,2-de]phthalazin-3-one (**7b**). The same general procedure was used to synthesize compound **7b** using compound **6b** (253 mg, 0.36 mmol), bis(pinacolato)diboron (201 mg, 0.79 mmol), potassium acetate (106 mg, 1.08 mmol), and Pd(dppf)Cl₂ (52 mg, 0.07 mmol, 20 mol %) in DMF (4 mL + 1 mL wash). The reaction was stirred at 90 °C for 2 h. This afforded the desired product as an off yellow solid (92 mg, 34%). ¹H NMR showed a complex spectrum which suggested the presence of conformational isomers (denoted *): ¹H NMR (600 MHz, CDCl₃): δ 7.80 (s, 1H, TzH), 7.75 (s, 1H, TzH*), 7.73–7.69 (m, 2H, Ar, Ar*), 7.45 (dd, J = 8.5, 2.3 Hz, 1H, Ar), 7.36 (dd, J = 8.5, 2.3 Hz, 1H, Ar*), 7.19 (d, J = 7.9 Hz, 2H, Ar), 7.17–7.08 (m, 3H, Ar, Ar*), 5.54–5.48 (m, 1H, CH), 5.45 (d, J = 10 Hz, 1H, CH), 5.41–5.36 (m, 2H, CH₂), 5.34 (d, J = 9.7 Hz, 1H, CH₂), 5.25 (d, J = 4.8 Hz, 1H, CH), 4.97 (d, J = 11.0 Hz, 1H, CH₂), 4.86 (d, J = 11.2 Hz, 1H, CH₂), 4.70 (d, J = 11.2 Hz, 1H, CH₂), 4.62 (d, J = 4.7 Hz, 1H, CH), 4.56 (d, J = 1.6 Hz, 1H, CH), 4.10 (s, 3H, Me*), 3.89 (s, 3H, Me*), 3.77–3.71 (m, 2H, CH₂), 3.63–3.56 (m, 4H, CH₂, CH₂*)

3.41–3.34 (m, 1H, CH₂), 3.34–3.27 (m, 1H, CH₂), 1.32–1.28 (m, 12H, BPin, BPin*), 0.99–0.93 (m, 2H, CH₂), 0.90–0.83 (m, 2H, CH₂), 0.02 (s, 24H, SiMe₃), –0.08 (s, 24H, SiMe₃); HRMS (ESI): *m/z* calcd for C₃₇H₅₄BFN₆O₅Si₂Na [M + Na]⁺, 771.36705; found, 771.36681.

5-Fluoro-9-(1-methyl-1H-1,2,4-triazol-5-yl)-8-(4-(tributylstannyl)phenyl)-2-((2-(trimethylsilyl)ethoxy)methyl)-2,7,8,9-tetrahydro-3H-pyrido[4,3,2-de]phthalazin-3-one (7c). The same general procedure was used to synthesize compound **7a** using compound **6a** (100 mg, 0.18 mmol), bis(tributyltin) (203 mg, 0.35 mmol), potassium acetate (98 mg, 0.525 mmol), and Pd(dppf)Cl₂ (13 mg, 0.02 mmol, 20 mol %) in DMF (3 mL). This afforded **7c** as an amorphous glass (60 mg, 44%). ¹H NMR (600 MHz, CDCl₃): δ 7.81 (s, 1H), 7.45–7.38 (m, 3H), 7.28–7.23 (m, 2H), 6.70 (dd, *J* = 9.9, 2.4 Hz, 1H), 5.43 (d, *J* = 9.9 Hz, 1H), 5.25 (d, *J* = 9.9 Hz, 1H), 5.08 (d, *J* = 10.9 Hz, 1H), 4.93 (s, 1H), 4.49 (d, *J* = 10.9 Hz, 1H), 3.66–3.53 (m, 5H), 1.56–1.47 (m, 6H), 1.38–1.24 (m, 10H), 1.11–0.96 (m, 6H), 0.96–0.84 (m, 13H), –0.04 (s, 9H); ¹³C NMR (151 MHz, CDCl₃): δ 165.82 (d, *J* = 252.1 Hz), 159.31, 152.10, 150.73, 146.98 (d, *J* = 12.2 Hz), 143.91, 140.14, 138.27, 137.15, 130.57, 126.79, 111.84, 104.26 (d, *J* = 27.5 Hz), 102.84 (d, *J* = 25.0 Hz), 79.64, 67.48, 60.78, 44.86, 35.18, 29.18, 27.44, 18.21, 13.80, 9.74, –1.25; HRMS (ESI): *m/z* calcd for C₃₇H₅₅FN₆O₂SiSnNa [M + Na]⁺, 805.30607; found, 805.30523.

Radiochemistry. All radiochemical reactions and experiments were carried out behind appropriate shielding as per the rules and guidelines laid out in the German act on radiation protection (Strahlenschutzverordnung, StrlSchV). Radionuclides were produced using a PETtrace 890 (16 MeV protons) cyclotron (GE Healthcare, Uppsala, Sweden). ¹⁸F was produced *via* the bombardment of [¹⁸O]H₂O with the ¹⁸O(p,n)¹⁸F nuclear reaction and was delivered either as a target wash in H₂O (1.5–2.5 mL, 0.5–2 GBq/mL) for manual radiochemical experiments or in [¹⁸O]H₂O (1.5–2.5 mL) through direct delivery from the cyclotron for automated synthesis [activity concentration is dependent on bombardment time and beam current (10 min ≈ 34 GBq at 80 μA)]. Automated ¹⁸F tracer syntheses were performed on a either a GE FX N Pro synthesis module (GE Healthcare, Muenster, Germany) running the TRACERlab (GE) control and user–interface software or with an ELIXYS FLEX/CHEM radiosynthesizer coupled to an ELIXYS PURE/FORM purification and formulation module (Sofie Biosciences, Los Angeles, California, CA, USA) using proprietary ELIXYS FLEX/CHEM control software. Manual radiochemical experiments were performed using sealable single-use borosilicate glass reaction tubes (Pyrex 9 mL, corning, New York, NY, USA) with screw-top poly-(tetrafluoroethylene)-lined caps. All reactions were stirred using either Teflon- or glass-coated micro stirrer bars.

The radiochemical reaction performance was monitored using radioTLC on 0.20 mm Polygram SIL G/UV₂₅₄ (silica gel 60) TLC plates. RadioTLC plates were developed with an appropriate running buffer/solvent mixture. RadioTLC data were acquired using a Cyclone Plus storage phosphor imaging system (PerkinElmer, Waltham, Massachusetts, USA). Analytical radioHPLC data were collected using an Agilent HPLC (1260 Infinity series with an automated sample injector) coupled to an inline radiation detector [NaI(Tl)]. In all cases, analytical radioHPLC data were obtained under the following general conditions unless otherwise stated: column: Luna 5 μm C18 (2) 100 Å column (250 × 4.6 mm). The following gradient was run in all instances: solvent A: H₂O + 0.1% TFA; solvent B: MeCN; 0–2 min: (5% B); 0–17 min: (5–100% B); 17–23 min: (100% B); and 23–28 min: (100–5% B).

For all radiochemical experiments, reagents, solvents, QMA eluents, reaction mixtures, and buffers were freshly prepared and dispensed directly before use unless otherwise stated.

¹⁸F Processing. ¹⁸F processing was carried out using a previously developed procedure:⁴⁰ cyclotron-produced aqueous [¹⁸F]fluoride was trapped on a QMA cartridge conditioned with aqueous KOTf (90 mg/mL). Residual water was blown off the cartridge using a stream of argon. ¹⁸F was then eluted as [¹⁸F]TBAF, using a solution of 10 mg of TBAOTf in methanol (1 mL). The resulting methanolic [¹⁸F]TBAF solution was transferred to a reactor vessel, either aliquoted for DoE

optimization experiments or full batch tracer productions. This was followed by evaporation of the methanol under a stream of argon gas to afford dry [¹⁸F]TBAF without the need for azeotropic drying.

General Procedure. To dry [¹⁸F]TBAF in a single-use glass reactor vessel was added a premade solution containing the required quantities of the precursor for radiolabeling (**7a–c**), Cu(OTf)₂, pyridine, DMA, and *n*-BuOH (total reaction volume of 700 μL). The reaction mixture was then stirred at 120 °C for 10 min before being quenched with HCl (0.25 M, 700 μL) or reacted further with 6 M HCl. The reaction performance was evaluated using radioTLC, which was read out using a Cyclone Plus storage phosphor imaging system (PerkinElmer, Waltham, Massachusetts, USA). Compound identity was confirmed by analytical radioHPLC against the non-radioactive standard compound.

DoE Studies and Validation. A computer-generated D-optimal DoE study was designed and analyzed using MODDE Go 12 (Sartorius, Göttingen, Germany). The D-optimal DoE study was performed to maximize the radiochemical yield of the CMRF step of the [¹⁸F]talazoparib radiosynthesis across four experimental factors: the precursor load (*Pre*, 5–30 μmol), the copper-mediator load (*Cop*, 5–40 μmol), the pyridine load (*Py*, 20–500 μmol), and the % of *n*-BuOH co-solvent (*Bu*, 0–75%). The resulting worksheet table (Table S1) was used to calculate the required reactants, reagents, and solvents for each experiment, and the study was performed over 4 days using four cyclotron target washes. All DoE experiments were carried out in a randomized order. All reactions (tests and tracer productions) were carried out using a racemic mixture of protected (**7a**) precursor. In all cases, [¹⁸F]fluoride was processed into [¹⁸F]TBAF *via* the general procedure described above. The response (*Y*) was the %RCY of the labeling reaction and was measured by radioTLC (100% ethyl acetate development solvent). Selected runs were analyzed *via* radioHPLC against a non-radioactive standard (**6c**) to confirm the compound identity.

Automated Radiosynthesis. The detailed automated radiosynthesis of [¹⁸F]talazoparib, using both the ELIXYS and FX N Pro systems, is described in the Supporting Information. The general procedure is as follows:

[¹⁸F]Fluoride in [¹⁸O]water was delivered into the module directly from the cyclotron, where it was trapped on a QMA cartridge (OTf-form). The [¹⁸O]water was collected for recycling. The ¹⁸F was then eluted with a solution of tetrabutylammonium triflate (TBAOTf) in methanol (1 mL), which was evaporated to dryness under a stream of argon to afford base-free [¹⁸F]TBAF.⁴⁰ The DoE-optimized reaction mixture, consisting of **7a** (19 mg, 30 μmol), Cu(OTf)₂ (3 mg, 5 μmol), and pyridine (24 μL, 300 μmol) in 700 μL DMA with *n*-BuOH (10%), was then added to the [¹⁸F]TBAF and reacted at 120 °C for 20 min. After cooling the reactor vessel to ambient temperature, HCl (6 M, 700 μL) was added to the mixture and reacted at 120 °C for 15 min. The reaction vessel was again cooled, and the reaction was quenched with the addition of ammonium formate solution (25 mM, 5–10 mL dependent on the reactor vessel volume) containing NaOH (6 M, 600 μL). The mixture was then passed over an HLB SPE cartridge, trapping the product. The product was then eluted into a 5 mL vessel with acetonitrile (1 mL) and HPLC buffer (4 mL), and this solution was transferred to the first HPLC injection loop (5 mL). The product racemate was then isolated (retention time = 12–13 min) from the reaction mixture using reversed-phase HPLC [C18 Luna (10 μm, 10 × 250 mm)] *via* an isocratic method using water (0.1% TFA)/acetonitrile (72:28) at a flow rate of 6 mL/min at room temperature. The radioactive fraction was collected in a sealed v-vial that was subsequently pressurized to load the solution onto a second HPLC injection loop. The purified racemic product was then injected onto a semipreparative CHIRALPAK IB-N5 (5 μm, 10 × 250 mm) HPLC column for enantiomeric resolution [water (0.1% TFA)/acetonitrile (60:40); 5 mL/min, room temperature]. The radioactive fraction corresponding to [¹⁸F]talazoparib (retention time ≈ 12–13 min) or [¹⁸F]LT-674 (retention time ≈ 14–15 min) was collected in a dilution reservoir, and the contents of which were subsequently passed over an HLB cartridge. The product [¹⁸F]talazoparib (or [¹⁸F]LT-674) was eluted

from the cartridge with ethanol (0.5 mL) and reconstituted with PBS (4.5 mL).

Quality Control. Product identity was confirmed with analytical CHIRALPAK IB-NS (5 μ m, 4.6 \times 150 mm) HPLC [water (0.1% TFA)/acetonitrile (60:40); 1 mL/min, room temperature] against commercially acquired non-radioactive standard samples of talazoparib and its biologically inactive enantiomer LT-674. The radiochemical purity of each compound was found to be >98%. The molar activity of the radiotracer was calculated from the analytical HPLC UV signal using a calibration curve generated from the serial dilution of a standard sample of talazoparib.

In Vitro Uptake Studies. Cell Culture. Human breast carcinoma cells (HCC1937 and ACC513) were purchased from the German Collection of Microorganisms and Cell Cultures (DSMZ GmbH, Braunschweig, Germany) and cultured in Roswell Park Memorial Institute (RPMI) 1640 medium supplemented with 16% fetal calf serum, 100 U/mL penicillin, and 100 μ g/mL streptomycin at 37 °C under a humid 5% CO₂ atmosphere. The absence of the mycoplasma infection was confirmed by PCR analysis in monthly intervals.

In Vitro Radiotracer Uptake. HCC1937 cells (0.2 \times 10⁶) were incubated in 96-well filter plates (MADVN6550, Merck Millipore, Darmstadt, Germany) with 60 μ L of a 0.4 MBq/mL radiotracer solution containing either 2.5 μ L DMSO as vehicle, 2.5 μ L 10 mM olaparib, or 2.5 μ L talazoparib to a final concentration of 25 μ M for blocking. After 30 min of incubation at 37 °C, the cells were washed by vacuum filtration of the medium through the plate (2 \times 100 μ L followed by 2 \times 200 μ L), the filters were transferred into tubes using a commercial punch kit (MAMP09608, Merck) and measured in a gamma counter (Wizard 2, PerkinElmer, Waltham, MA, USA). Experiments were performed in triplicates, and the uptake was quantified as percent of added activity.

Competition Assays. HCC1937 cells (0.2 \times 10⁶) were incubated in 96-well filter plates (MADVN6550, Merck Millipore, Darmstadt, Germany) with 40 μ L of a 0.4 MBq/mL radiotracer and 20 μ L of a 1:2 serial dilution of either talazoparib or olaparib starting with a final concentration of 1 μ M. After 30 min of incubation at 37 °C, the cells were washed by vacuum filtration of the medium through the plate (2 \times 100 μ L followed by 2 \times 200 μ L); the filters were transferred into tubes using a commercial punch kit (MAMP09608, Merck) and measured in a gamma counter (Wizard 2, PerkinElmer). Experiments were performed in triplicates, and the uptake was quantified as percent of added activity.

In Vivo Evaluation. PET and MR Imaging. All animal experiments were performed according to the German animal welfare act and approved by the local authorities (Regierungspraesidium Tuebingen, R3/18). Animals were housed in individually ventilated cages (IVCs, five mice per cage) with bedding and enrichment, and food and water provided *ad libitum*. Animals were kept under isoflurane anesthesia (1.5% in medical oxygen, 1.5 L/min) during all experiments. 1 \times 10⁷ cells in 1:1 ice-cold Matrigel (Thermo Scientific)/PBS were injected subcutaneously in the right shoulder area of 7 weeks old female NOD.CB17-Prkdc^{scid}/J mice ($n = 5$). After the xenografts reached a suitable size (215.1 \pm 72.8 mm³), mice were injected with 13.12 \pm 0.71 MBq [¹⁸F]talazoparib and subjected to 1 h dynamic PET imaging (Inveon D-PET, Siemens, Knoxville, TN, USA) with subsequent MR anatomical scans using a 7 Tesla Biospec 70/30 USR (ClinScan, Bruker BioSpin) and a spin-echo sequence. The mice underwent a second, 10 min static PET scan 2 h post-injection (p.i.). Mice were sacrificed by cervical dislocation. The collected organs were weighed, the tissue uptake was determined by gamma-counting (Wizard 2, PerkinElmer) and quantified as % of injected dose per gram (%ID/g). PET image reconstruction and correlation with the corresponding MR image were performed with Inveon Acquisition Workplace and Inveon Research Workplace, respectively, using a user-defined dynamic framing and an ordered subset expectation maximization (OSEM3D) algorithm. Regions of interest (ROIs) were drawn according to the acquired MR images and co-registered with the PET data to obtain TACs.

Ex Vivo. Immunofluorescence. Immunofluorescence staining was performed by the Department of Dermatology at the University

Hospital Tuebingen, Germany. Sections of paraffin-embedded xenografts were blocked with donkey serum for 30 min and incubated with primary antibody overnight [rabbit anti-PARP (1:50, ab74290, Abcam, Cambridge, UK)]. After washing, the sections were incubated for 1 h at room temperature with a secondary antibody [donkey anti-mouse IgG Cy3 (1:250, 715-166-151) Dianova, Hamburg, Germany]. Nuclei were stained with YO-PRO-1 iodide solution (Y3603, Thermo Scientific) for 5 min; the samples were subsequently mounted with Mowiol (Sigma-Aldrich) and imaged on an LSM 800 microscope (Carl Zeiss, Oberkochen, Germany).

Blood Half-Life Calculation. Blood half-life was calculated using the blood TACs and a two-phase decay fit in GraphPad Prism 9 (GraphPad, La Jolla, CA, USA).

Statistical Analyses. Statistical analyses were performed with GraphPad Prism 9 using nonparametric *t*-tests and are represented as mean value \pm standard deviation. *P*-values < 0.05 were considered statistically significant according to the software (*: *p* < 0.05, **: *p* < 0.01, ***: *p* < 0.001, and ****: *p* < 0.0001).

■ ASSOCIATED CONTENT

Supporting Information

The Supporting Information is available free of charge at <https://pubs.acs.org/doi/10.1021/acs.jmedchem.1c00903>.

DoE results and statistical analysis, compound NMR spectra, radiochemistry, radiochemistry HPLC data, biological analysis, and metabolite analysis (PDF)

Molecular formula strings (CSV)

■ AUTHOR INFORMATION

Corresponding Author

Andreas Maurer – Werner Siemens Imaging Center, Department of Preclinical Imaging and Radiopharmacy, Eberhard Karls University, 72076 Tuebingen, Germany; Cluster of Excellence iFIT (EXC 2180) “Image-Guided and Functionally Instructed Tumor Therapies”, Eberhard Karls University, 72076 Tuebingen, Germany; orcid.org/0000-0003-2412-5361; Email: andreas.maurer@med.uni-tuebingen.de

Authors

Gregory D. Bowden – Werner Siemens Imaging Center, Department of Preclinical Imaging and Radiopharmacy, Eberhard Karls University, 72076 Tuebingen, Germany; Cluster of Excellence iFIT (EXC 2180) “Image-Guided and Functionally Instructed Tumor Therapies”, Eberhard Karls University, 72076 Tuebingen, Germany; orcid.org/0000-0003-2274-6738

Sophie Stotz – Werner Siemens Imaging Center, Department of Preclinical Imaging and Radiopharmacy, Eberhard Karls University, 72076 Tuebingen, Germany; Cluster of Excellence iFIT (EXC 2180) “Image-Guided and Functionally Instructed Tumor Therapies”, Eberhard Karls University, 72076 Tuebingen, Germany; orcid.org/0000-0003-4020-1088

Johannes Kinzler – Werner Siemens Imaging Center, Department of Preclinical Imaging and Radiopharmacy, Eberhard Karls University, 72076 Tuebingen, Germany

Christian Geibel – Institute of Pharmaceutical Sciences, Department of Pharmaceutical (Bio-)Analysis, Eberhard Karls University, 72076 Tuebingen, Germany

Michael Lämmerhofer – Institute of Pharmaceutical Sciences, Department of Pharmaceutical (Bio-)Analysis, Eberhard Karls University, 72076 Tuebingen, Germany; orcid.org/0000-0002-1318-0974

Bernd J. Pichler – Werner Siemens Imaging Center, Department of Preclinical Imaging and Radiopharmacy, Eberhard Karls University, 72076 Tuebingen, Germany; Cluster of Excellence iFIT (EXC 2180) “Image-Guided and Functionally Instructed Tumor Therapies”, Eberhard Karls University, 72076 Tuebingen, Germany; German Cancer Research Center, German Cancer Consortium DKTK, Partner Site Tuebingen, 72076 Tuebingen, Germany

Complete contact information is available at:

<https://pubs.acs.org/10.1021/acs.jmedchem.1c00903>

Author Contributions

G.D.B. and S.S. contributed equally. The study was designed by A.M., B.J.P., G.D.B., and S.S. Organic synthesis, radiosynthesis, and the analysis of the (radio)chemical DoE data were performed by G.D.B. M.L. and C.G. established the protocol for the chiral separation. *In vitro* and *in vivo* experiments and data analysis were performed by S.S. G.D.B., S.S., and A.M. wrote the first draft of the manuscript. All authors commented on previous versions of the manuscript. All authors read and approved the final version of the manuscript.

Funding

This work was supported by the Werner Siemens Foundation (WSS), and parts of this work were funded by the Deutsche Forschungsgemeinschaft (DFG, German Research Foundation) under Germany's Excellence Strategy—EXC 2180—390900677.

Notes

The authors declare the following competing financial interest(s): The matter of the manuscript is subject to priority patent applications (European patent application 21 173 663.2 and 21 173 674.9)

ACKNOWLEDGMENTS

The authors want to thank Birgit Fehrenbacher and her team from the Department of Dermatology for IF staining, Ramona Stremme for assistance with the radiosyntheses, as well as Siaoan Huang and Karl Mau for assistance with the animal studies. We would also like to thank Dr. Dorothee Wistuba and her colleagues at the mass spectroscopy core facility at the University of Tübingen, Germany. We would also like to thank Dr. Gerald Reischl and colleagues in the radiopharmacy at the Werner Siemens Imaging Center for the delivery of [¹⁸F] fluoride and for technical support.

ABBREVIATIONS

CMRF, copper-mediated radiofluorination; DoE, design of experiment; DSB, double-strand break; HLB, hydrophilic lipophilic balance; HR, homologous recombination; ID, injected dose; i.v., intravenous; LKR, liver-to-kidney ratio; MAR, mono(ADP-ribose); OSEM, ordered subset expectation maximization; PAR, poly(ADP-ribose); PARP, poly(ADP-ribosyl)polymerase; p.i., post injection; QC, quality control; QMA, quaternary methyl ammonium; RCY, radiochemical yield; ROI, region of interest; SEM, trimethylsilyloxyethyl; SSB, single-strand break; SPE, solid-phase extraction; TAC, time–activity curve; TBR, tumor-to-blood ratio; TMR, tumor-to-muscle ratio

REFERENCES

(1) Bryant, H. E.; Schultz, N.; Thomas, H. D.; Parker, K. M.; Flower, D.; Lopez, E.; Kyle, S.; Meuth, M.; Curtin, N. J.; Helleday, T. Specific

killing of BRCA2-deficient tumours with inhibitors of poly(ADP-ribose) polymerase. *Nature* **2005**, *434*, 913–917.

(2) Farmer, H.; McCabe, N.; Lord, C. J.; Tutt, A. N. J.; Johnson, D. A.; Richardson, T. B.; Santarosa, M.; Dillon, K. J.; Hickson, I.; Knights, C.; Martin, N. M. B.; Jackson, S. P.; Smith, G. C. M.; Ashworth, A. Targeting the DNA repair defect in BRCA mutant cells as a therapeutic strategy. *Nature* **2005**, *434*, 917–921.

(3) Schöder, H.; França, P. D. D. S.; Nakajima, R.; Burnazi, E.; Roberts, S.; Brand, C.; Grkovski, M.; Mauguen, A.; Dunphy, M. P.; Ghossein, R. A.; Lyashchenko, S. K.; Lewis, J. S.; O'Donoghue, J. A.; Ganly, I.; Patel, S. G.; Lee, N. Y.; Reiner, T. Safety and feasibility of PARP1/2 imaging with ¹⁸F-PARPi in patients with head and neck cancer. *Clin. Cancer Res.* **2020**, *26*, 3110–3116.

(4) Siraj, A. K.; Pratheeshkumar, P.; Parvathareddy, S. K.; Divya, S. P.; Al-Dayel, F.; Tulbah, A.; Ajarim, D.; Al-Kuraya, K. S. Overexpression of PARP is an independent prognostic marker for poor survival in Middle Eastern breast cancer and its inhibition can be enhanced with embelin co-treatment. *Oncotarget* **2018**, *9*, 37319–37332.

(5) Li, X.; Li, C.; Jin, J.; Wang, J.; Huang, J.; Ma, Z.; Huang, X.; He, X.; Zhou, Y.; Xu, Y.; Yu, M.; Huang, S.; Yan, X.; Li, F.; Pan, J.; Wang, Y.; Yu, Y.; Jin, J. High PARP-1 expression predicts poor survival in acute myeloid leukemia and PARP-1 inhibitor and SAHA-bendamustine hybrid inhibitor combination treatment synergistically enhances anti-tumor effects. *EBioMedicine* **2018**, *38*, 47–56.

(6) Bertucci, F.; Finetti, P.; Monneur, A.; Perrot, D.; Chevreau, C.; Le Cesne, A.; Blay, J. Y.; Mir, O.; Birnbaum, D. PARP1 expression in soft tissue sarcomas is a poor-prognosis factor and a new potential therapeutic target. *Mol. Oncol.* **2019**, *13*, 1577–1588.

(7) Gradwohl, G.; Menissier de Murcia, J. M.; Molinete, M.; Simonin, F.; Koken, M.; Hoeijmakers, J. H.; de Murcia, G. The second zinc-finger domain of poly(ADP-ribose) polymerase determines specificity for single-stranded breaks in DNA. *Proc. Natl. Acad. Sci. U. S. A.* **1990**, *87*, 2990–2994.

(8) Langelier, M.-F.; Planck, J. L.; Roy, S.; Pascal, J. M. Structural basis for DNA damage-dependent poly(ADP-ribosylation) by human PARP-1. *Science* **2012**, *336*, 728–732.

(9) Rouleau, M.; Patel, A.; Hendzel, M. J.; Kaufmann, S. H.; Poirier, G. G. PARP inhibition: PARP1 and beyond. *Nat. Rev. Cancer* **2010**, *10*, 293–301.

(10) Langelier, M.-F.; Eisemann, T.; Riccio, A. A.; Pascal, J. M. PARP family enzymes: regulation and catalysis of the poly(ADP-ribose) posttranslational modification. *Curr. Opin. Struct. Biol.* **2018**, *53*, 187–198.

(11) Vyas, S.; Matic, I.; Uchima, L.; Rood, J.; Zaja, R.; Hay, R. T.; Ahel, I.; Chang, P. Family-wide analysis of poly(ADP-ribose) polymerase activity. *Nat. Commun.* **2014**, *5*, 4426.

(12) Eisemann, T.; Pascal, J. M. Poly(ADP-ribose) polymerase enzymes and the maintenance of genome integrity. *Cell. Mol. Life Sci.* **2020**, *77*, 19–33.

(13) Langelier, M.-F.; Zandarashvili, L.; Aguiar, P. M.; Black, B. E.; Pascal, J. M. NAD(+) analog reveals PARP-1 substrate-blocking mechanism and allosteric communication from catalytic center to DNA-binding domains. *Nat. Commun.* **2018**, *9*, 844.

(14) Javle, M.; Curtin, N. J. The role of PARP in DNA repair and its therapeutic exploitation. *Br. J. Cancer* **2011**, *105*, 1114–1122.

(15) Francica, P.; Rottenberg, S. Mechanisms of PARP inhibitor resistance in cancer and insights into the DNA damage response. *Genome Med.* **2018**, *10*, 101.

(16) Kim, G.; Ison, G.; McKee, A. E.; Zhang, H.; Tang, S.; Gwise, T.; Sridhara, R.; Lee, E.; Tzou, A.; Philip, R.; Chiu, H.-J.; Ricks, T. K.; Palmby, T.; Russell, A. M.; Ladouceur, G.; Pfuma, E.; Li, H.; Zhao, L.; Liu, Q.; Venugopal, R.; Ibrahim, A.; Pazdur, R. FDA approval summary: Olaparib monotherapy in patients with deleterious germline BRCA-mutated advanced ovarian cancer treated with three or more lines of chemotherapy. *Clin. Cancer Res.* **2015**, *21*, 4257–4261.

- (17) Dockery, L.; Gunderson, C.; Moore, K. Rucaparib: the past, present, and future of a newly approved PARP inhibitor for ovarian cancer. *OncoTargets Ther.* **2017**, *10*, 3029–3037.
- (18) Scott, L. J. Niraparib: First global approval. *Drugs* **2017**, *77*, 1029–1034.
- (19) Hoy, S. M. Talazoparib: First global approval. *Drugs* **2018**, *78*, 1939–1946.
- (20) Keung, M. Y.; Wu, Y.; Badar, F.; Vadgama, J. V. Response of breast cancer cells to PARP inhibitors is independent of BRCA status. *J. Clin. Med.* **2020**, *9*, 940.
- (21) Lord, C. J.; Ashworth, A. PARP inhibitors: Synthetic lethality in the clinic. *Science* **2017**, *355*, 1152–1158.
- (22) Carney, B.; Kossatz, S.; Lok, B. H.; Schneeberger, V.; Gangangari, K. K.; Pillarsetty, N. V. K.; Weber, W. A.; Rudin, C. M.; Poirier, J. T.; Reiner, T. Target engagement imaging of PARP inhibitors in small-cell lung cancer. *Nat. Commun.* **2018**, *9*, 176.
- (23) Shen, Y.; Rehman, F. L.; Feng, Y.; Boshuizen, J.; Bajrami, I.; Elliott, R.; Wang, B.; Lord, C. J.; Post, L. E.; Ashworth, A. BMN 673, a novel and highly potent PARP1/2 inhibitor for the treatment of human cancers with DNA repair deficiency. *Clin. Cancer Res.* **2013**, *19*, 5003–5015.
- (24) Wang, B.; Chu, D.; Feng, Y.; Shen, Y.; Aoyagi-Scharber, M.; Post, L. E. Discovery and characterization of (8S,9R)-5-fluoro-8-(4-fluorophenyl)-9-(1-methyl-1H-1,2,4-triazol-5-yl)-2,7,8,9-tetrahydro-3H-pyrido[4,3,2-de]phthalazin-3-one (BMN 673, talazoparib), a novel, highly potent, and orally efficacious poly(ADP-ribose) polymerase-1/2 inhibitor, as an anticancer agent. *J. Med. Chem.* **2016**, *59*, 335–357.
- (25) Pommier, Y.; O'Connor, M. J.; de Bono, J. Laying a trap to kill cancer cells: PARP inhibitors and their mechanisms of action. *Sci. Transl. Med.* **2016**, *8*, 362ps17.
- (26) Carlucci, G.; Carney, B.; Brand, C.; Kossatz, S.; Irwin, C. P.; Carlin, S. D.; Keliher, E. J.; Weber, W.; Reiner, T. Dual-modality optical/PET imaging of PARP1 in glioblastoma. *Mol. Imag. Biol.* **2015**, *17*, 848–855.
- (27) Kossatz, S.; Brand, C.; Gutiontov, S.; Liu, J. T. C.; Lee, N. Y.; Gönen, M.; Weber, W. A.; Reiner, T. Detection and delineation of oral cancer with a PARP1 targeted optical imaging agent. *Sci. Rep.* **2016**, *6*, 21371.
- (28) Kossatz, S.; Pirovano, G.; Demétrio De Souza França, P.; Strome, A. L.; Sunny, S. P.; Zanoni, D. K.; Mauguen, A.; Carney, B.; Brand, C.; Shah, V.; Ramanajinappa, R. D.; Hedne, N.; Birur, P.; Sihag, S.; Ghossein, R. A.; Gönen, M.; Strome, M.; Suresh, A.; Molena, D.; Ganly, I.; Kuriakose, M. A.; Patel, S. G.; Reiner, T. Validation of the use of a fluorescent PARP1 inhibitor for the detection of oral, oropharyngeal and oesophageal epithelial cancers. *Nat. Biomed. Eng.* **2020**, *4*, 272–285.
- (29) Michel, L. S.; Dyroff, S.; Brooks, F. J.; Spayd, K. J.; Lim, S.; Engle, J. T.; Phillips, S.; Tan, B.; Wang-Gillam, A.; Bogner, C.; Chu, W.; Zhou, D.; Mach, R. H.; Laforest, R.; Chen, D. L. PET of poly(ADP-ribose) polymerase activity in cancer: preclinical assessment and first in-human studies. *Radiology* **2017**, *282*, 453–463.
- (30) Edmonds, C. E.; Makvandi, M.; Lieberman, B. P.; Xu, K.; Zeng, C.; Li, S.; Hou, C.; Lee, H.; Greenberg, R. A.; Mankoff, D. A.; Mach, R. H. [¹⁸F]FluorThanatrace uptake as a marker of PARP1 expression and activity in breast cancer. *Am. J. Nucl. Med. Mol. Imaging* **2016**, *6*, 94–101.
- (31) Young, R. J.; Demétrio De Souza Franca, P.; Pirovano, G.; Piotrowski, A. F.; Nicklin, P. J.; Riedl, C. C.; Schwartz, J.; Bale, T. A.; Donabedian, P. L.; Kossatz, S.; Burnazi, E. M.; Roberts, S.; Lyashchenko, S. K.; Miller, A. M.; Moss, N. S.; Fiasconaro, M.; Zhang, Z.; Mauguen, A.; Reiner, T.; Dunphy, M. P. Preclinical and first-in-human-brain-cancer applications of [¹⁸F]poly(ADP-ribose) polymerase inhibitor PET/MR. *Neurooncol. Adv.* **2020**, *2*, vdaa119.
- (32) Kossatz, S.; Carney, B.; Farley, C.; Weber, W. A.; Drain, C. M.; Reiner, T. Direct imaging of drug distribution and target engagement of the PARP inhibitor rucaparib. *J. Nucl. Med.* **2018**, *59*, 1316–1320.
- (33) Carney, B.; Kossatz, S.; Reiner, T. Molecular imaging of PARP. *J. Nucl. Med.* **2017**, *58*, 1025–1030.
- (34) Zhou, D.; Chen, H.; Mpoy, C.; Afrin, S.; Rogers, B. E.; Garbow, J. R.; Katzenellenbogen, J. A.; Xu, J. Radiosynthesis and evaluation of talazoparib and its derivatives as PARP-1-targeting agents. *Bio-medicines* **2021**, *9*, S65.
- (35) Wright, J. S.; Kaur, T.; Preshlock, S.; Tanzey, S. S.; Winton, W. P.; Sharninghausen, L. S.; Wiesner, N.; Brooks, A. F.; Sanford, M. S.; Scott, P. J. H. Copper-mediated late-stage radiofluorination: Five years of impact on pre-clinical and clinical PET imaging. *Clin. Transl. Imaging* **2020**, *8*, 167–206.
- (36) Tredwell, M.; Preshlock, S. M.; Taylor, N. J.; Gruber, S.; Huiban, M.; Passchier, J.; Mercier, J.; Génicot, C.; Gouverneur, V. A general copper-mediated nucleophilic 18F fluorination of arenes. *Angew. Chem., Int. Ed. Engl.* **2014**, *53*, 7751–7755.
- (37) Makaravage, K. J.; Brooks, A. F.; Mossine, A. V.; Sanford, M. S.; Scott, P. J. H. Copper-mediated radiofluorination of arylstannanes with [¹⁸F]KF. *Org. Lett.* **2016**, *18*, 5440–5443.
- (38) Mossine, A. V.; Brooks, A. F.; Makaravage, K. J.; Miller, J. M.; Ichiishi, N.; Sanford, M. S.; Scott, P. J. H. Synthesis of [¹⁸F]arenes via the copper-mediated [¹⁸F]fluorination of boronic acids. *Org. Lett.* **2015**, *17*, 5780–5783.
- (39) Bowden, G. D.; Pichler, B. J.; Maurer, A. A Design of Experiments (DoE) approach accelerates the optimization of copper-mediated ¹⁸F-fluorination reactions of arylstannanes. *Sci. Rep.* **2019**, *9*, 11370.
- (40) Bowden, G. D.; Chailangar, N.; Pichler, B. J.; Maurer, A. Scalable ¹⁸F processing conditions for copper-mediated radiofluorination chemistry facilitate DoE optimization studies and afford an improved synthesis of [¹⁸F]olaparib. *Org. Biomol. Chem.* **2021**, *19*, 6995–7000.
- (41) Taylor, N. J.; Emer, E.; Preshlock, S.; Schedler, M.; Tredwell, M.; Verhoog, S.; Mercier, J.; Genicot, C.; Gouverneur, V. Derisking the Cu-mediated ¹⁸F-fluorination of heterocyclic positron emission tomography radioligands. *J. Am. Chem. Soc.* **2017**, *139*, 8267–8276.
- (42) Albrecht, B. K.; Bauer, D.; Bellon, S.; Bode, C. M.; Booker, S.; Boezio, A.; Choquette, D.; D'Amico, D.; Harmange, J.-C.; Hirai, S.; Hungate, R. W.; Kim, T.-S.; Lewis, R. T.; Liu, L.; Lohman, J.; Norman, M. H.; Potashman, M.; Siegmund, A. C.; Springer, S. K.; Stec, M.; Xi, N.; Yang, K. Fused heterocyclic derivatives and methods of use as c-met inhibitors. WO 2009091374 A3, 2009.
- (43) Wilson, T. C.; Xavier, M.-A.; Knight, J.; Verhoog, S.; Torres, J. B.; Mosley, M.; Hopkins, S. L.; Wallington, S.; Allen, P. D.; Kersemans, V.; Hueting, R.; Smart, S.; Gouverneur, V.; Cornelissen, B. PET imaging of PARP expression using ¹⁸F-olaparib. *J. Nucl. Med.* **2019**, *60*, 504–510.
- (44) Guibbal, F.; Isenegger, P. G.; Wilson, T. C.; Pacelli, A.; Mahaut, D.; Sap, J. B. I.; Taylor, N. J.; Verhoog, S.; Preshlock, S.; Hueting, R.; Cornelissen, B.; Gouverneur, V. Manual and automated Cu-mediated radiosynthesis of the PARP inhibitor [¹⁸F]olaparib. *Nat. Protoc.* **2020**, *15*, 1525–1541.
- (45) Zischler, J.; Kolks, N.; Modemann, D.; Neumaier, B.; Zlatopolskiy, B. D. Alcohol-enhanced Cu-mediated radiofluorination. *Chemistry* **2017**, *23*, 3251–3256.
- (46) Ryan, K.; Bolaños, B.; Smith, M.; Palde, P. B.; Cuenca, P. D.; VanArsdale, T. L.; Niessen, S.; Zhang, L.; Behenna, D.; Ornelas, M. A.; Tran, K. T.; Kaiser, S.; Lum, L.; Stewart, A.; Gajiwala, K. S. Dissecting the molecular determinants of clinical PARP1 inhibitor selectivity for tankyrase1. *J. Biol. Chem.* **2021**, *296*, 100251.
- (47) Carney, B.; Carlucci, G.; Salinas, B.; Di Galleonardo, V.; Kossatz, S.; Vansteene, A.; Longo, V. A.; Bolaender, A.; Chiosis, G.; Keshari, K. R.; Weber, W. A.; Reiner, T. Non-invasive PET imaging of PARP1 expression in glioblastoma models. *Mol. Imag. Biol.* **2016**, *18*, 386–392.
- (48) Oláh, G.; Szczesny, B.; Brunyánszki, A.; López-García, I. A.; Gerö, D.; Radák, Z.; Szabo, C. Differentiation-associated down-regulation of poly(ADP-ribose) polymerase-1 expression in myoblasts serves to increase their resistance to oxidative stress. *PLoS One* **2015**, *10*, No. e0134227.

Supporting Information

DoE Optimization Empowers the Automated Preparation of Enantiomerically Pure [¹⁸F]Talazoparib and its *In Vivo* Evaluation as a PARP Radiotracer.

Gregory D. Bowden^{†,‡,¶}, Sophie Stotz^{†,‡,¶}, Johannes Kinzler[†], Christian Geibel[§], Michael Lämmerhofer[§], Bernd J. Pichler^{†,‡,^}, and Andreas Maurer^{†,‡,*}

[†]Werner Siemens Imaging Center, Department of Preclinical Imaging and Radiopharmacy, Eberhard Karls University, Roentgenweg 15, 72076 Tuebingen, Germany

[‡]Cluster of Excellence iFIT (EXC 2180) "Image-Guided and Functionally Instructed Tumor Therapies", Eberhard Karls University, Roentgenweg 13, 72076 Tuebingen, Germany

[§]Institute of Pharmaceutical Sciences, Department of Pharmaceutical (Bio-)Analysis, Eberhard Karls University, Auf der Morgenstelle 8, 72076 Tuebingen, Germany

[^]German Cancer Research Center, German Cancer Consortium DKTK, Partner Site Tuebingen, Roentgenweg 13, 72076 Tuebingen, Germany

* Corresponding author: andreas.maurer@med.uni-tuebingen.de

Table of Contents

1. DoE Results and Statistical Analysis	S2
2. Compound NMR Spectra	S4
3. Radiochemistry	S29
3.1. General Information	S29
3.2. Fully Automated Radiosynthesis of [¹⁸ F]Talazoparib using the Elixys Radiosynthesis System	S29
3.3. Semi-Automated Radiosynthesis of [¹⁸ F]Talazoparib using a GE FX N Pro Radiosynthesis System and Elixys PURE/FORM Module	S32
4. Radiochemistry HPLC Data	S35
4.1. Rational for Column Selection	S35
4.2. UV HPLC of Non-radioactive Standard Compounds	S37
4.3. Representative HPLC data from Manual CMRF Radiochemical Experiments	S39
4.4. Representative Semipreparative HPLC Purification of [¹⁸ F]Talazoparib	S41
4.5. Analytical Quality Control (QC) HPLC of [¹⁸ F]Talazoparib	S43
5. Biological Supplementary Information	S45
6. Metabolite analysis	S47

1. DoE Results and Statistical Analysis.

Table S1: The DoE Worksheet table. Experiments were performed in randomized order and are listed in the order in which they were carried out.

Exp No	Run Order	Precursor Loading (μmol)	Precursor (mg)	Cu(OTf) ₂ (μmol)	Cu(OTf) ₂ (mg)	Pyridine Loading (μmol)	Pyridine (mg)	Pyridine (μl)	n-BuOH %	n-BuOH (μl)	RXN Vol (μl)	RCC (%)
4	1	5	3	40	14	500	39.55	40.4	0	0	500	10.4
18	2	13.3333	8	5	2	500	39.55	40.4	75	375	500	13.7
16	3	30	19	28.3333	10	500	39.55	40.4	75	375	500	25.6
21	4	17.5	11	22.5	8	20	1.582	1.6	37.5	187.5	500	36.3
13	5	30	19	5	2	180	14.238	14.6	75	375	500	47.1
9	6	5	3	5	2	500	39.55	40.4	25	125	500	26.4
20	7	17.5	11	40	14	260	20.566	21.0	37.5	187.5	500	27.2
14	8	30	19	40	14	500	39.55	40.4	25	125	500	26
1	9	5	3	5	2	20	1.582	1.6	0	0	500	15.9
17	10	21.6667	13	5	2	500	39.55	40.4	0	0	500	48.3
10	11	30	19	5	2	20	1.582	1.6	25	125	500	35.7
5	12	5	3	5	2	20	1.582	1.6	75	375	500	27.5
19	13	5	3	22.5	8	260	20.566	21.0	37.5	187.5	500	22.3
3	14	30	19	40	14	20	1.582	1.6	0	0	500	11
24	15	17.5	11	22.5	8	260	20.566	21.0	37.5	187.5	500	32.7
23	16	17.5	11	22.5	8	260	20.566	21.0	37.5	187.5	500	38.9
7	17	30	19	40	14	20	1.582	1.6	75	375	500	10.9
22	18	17.5	11	22.5	8	260	20.566	21.0	37.5	187.5	500	38.7
15	19	30	19	16.6667	6	500	39.55	40.4	0	0	500	45.5
11	20	30	19	5	2	500	39.55	40.4	50	250	500	40.5
12	21	30	19	5	2	340	26.894	27.5	0	0	500	57.8
2	22	5	3	40	14	20	1.582	1.6	0	0	500	3.7
8	23	5	3	40	14	500	39.55	40.4	75	375	500	4.3
6	24	5	3	40	14	20	1.582	1.6	75	375	500	3.3

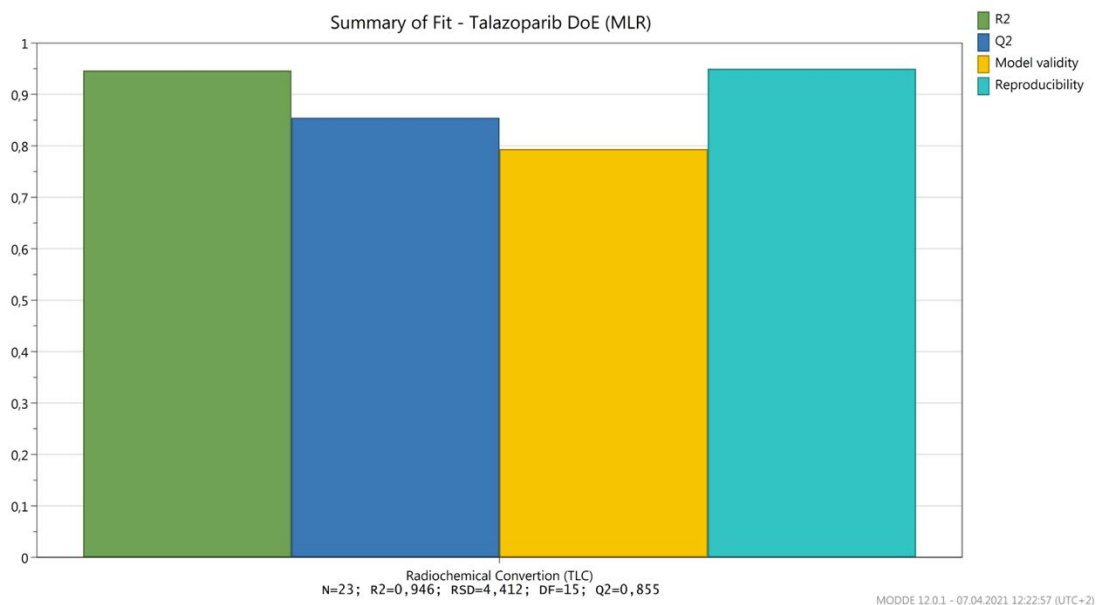


Figure S1: Summary statistics for D-Optimal DoE for CMRF of [¹⁸F]talazoparib. R² represents the goodness of regression model fit. Q² represents the goodness of model prediction. "Reproducibility" is calculated from the standard deviation in replicate (centerpoint) experiment results. These statistics represent a valid and predictive regression model.

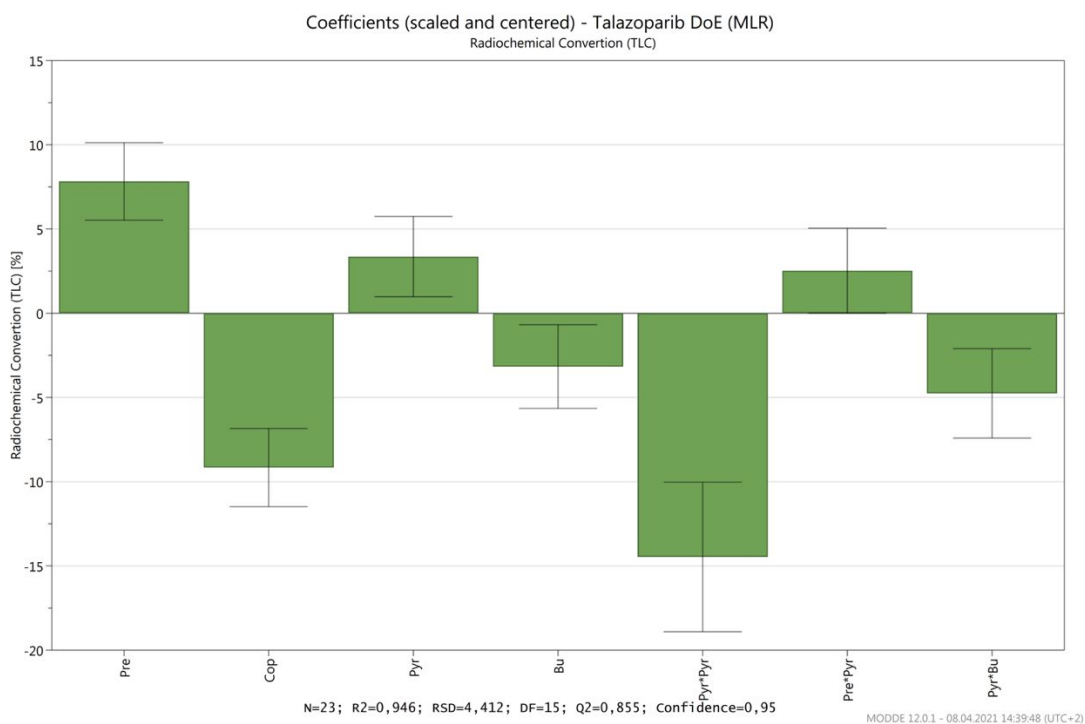


Figure S2: The scaled and centered regression coefficient calculated from the results of D-optimal response surface modeling DoE of the radiosynthesis of [^{18}F]talazoparib. Large bars represent factors with a large contribution to the response (%RCY). A positive number denotes a positive influence on the response. A negative number indicates a diminishing effect on the response. If a factor's regression coefficient is smaller than the associated error bars, it is probable (at the 95% confidence interval) then that factor is not significant.

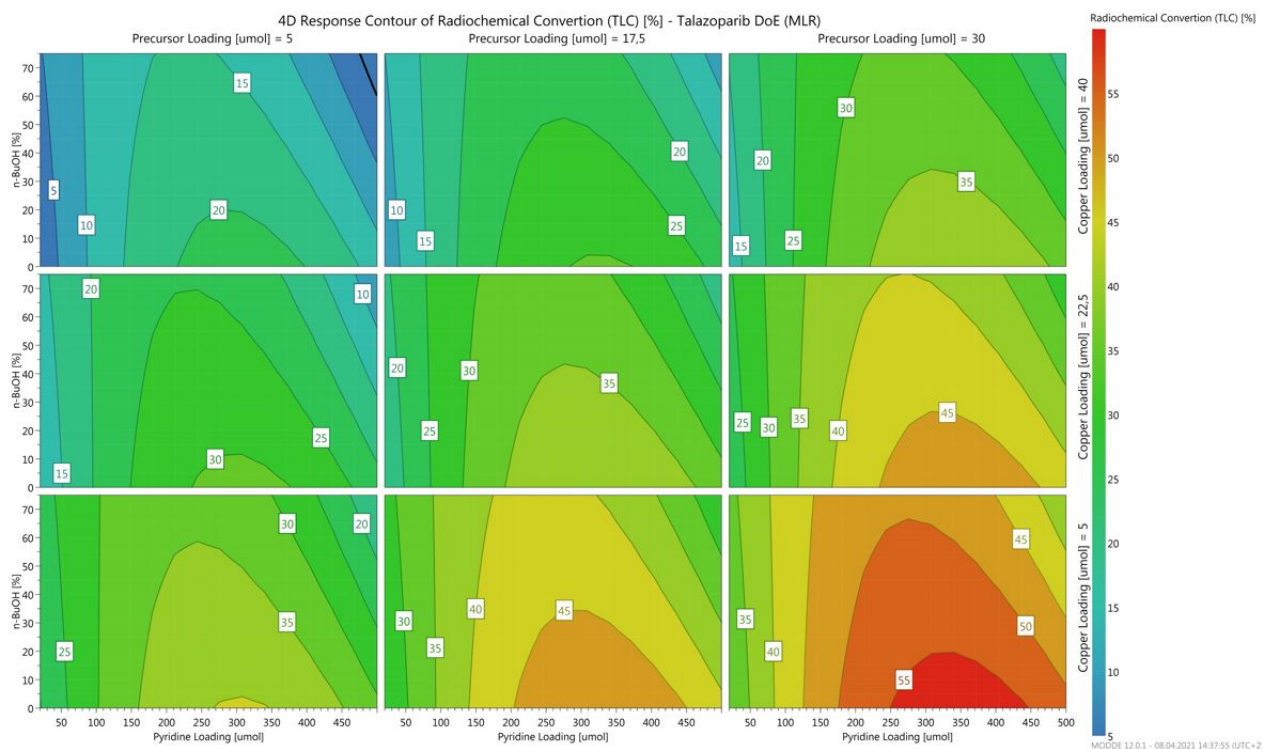
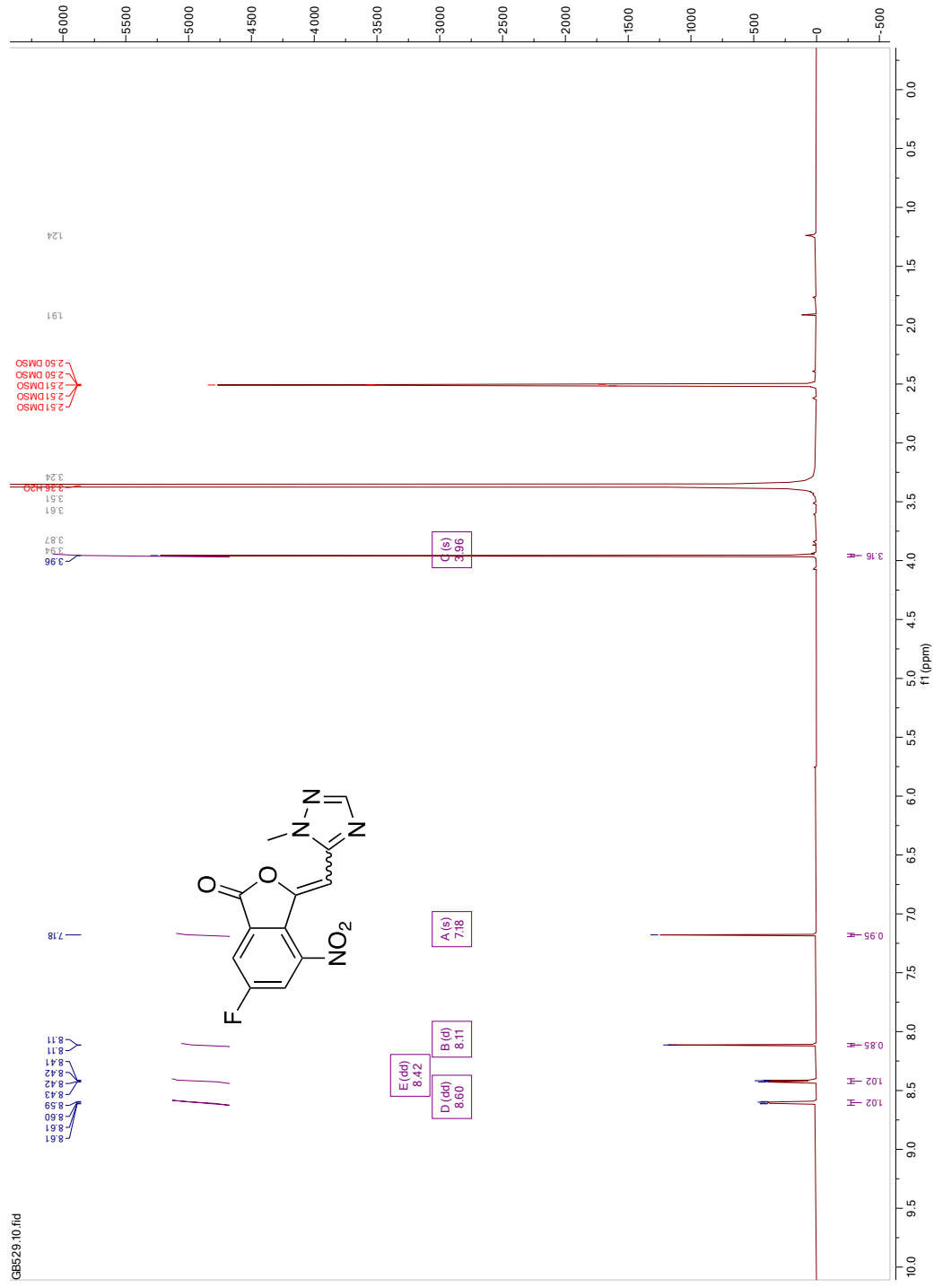


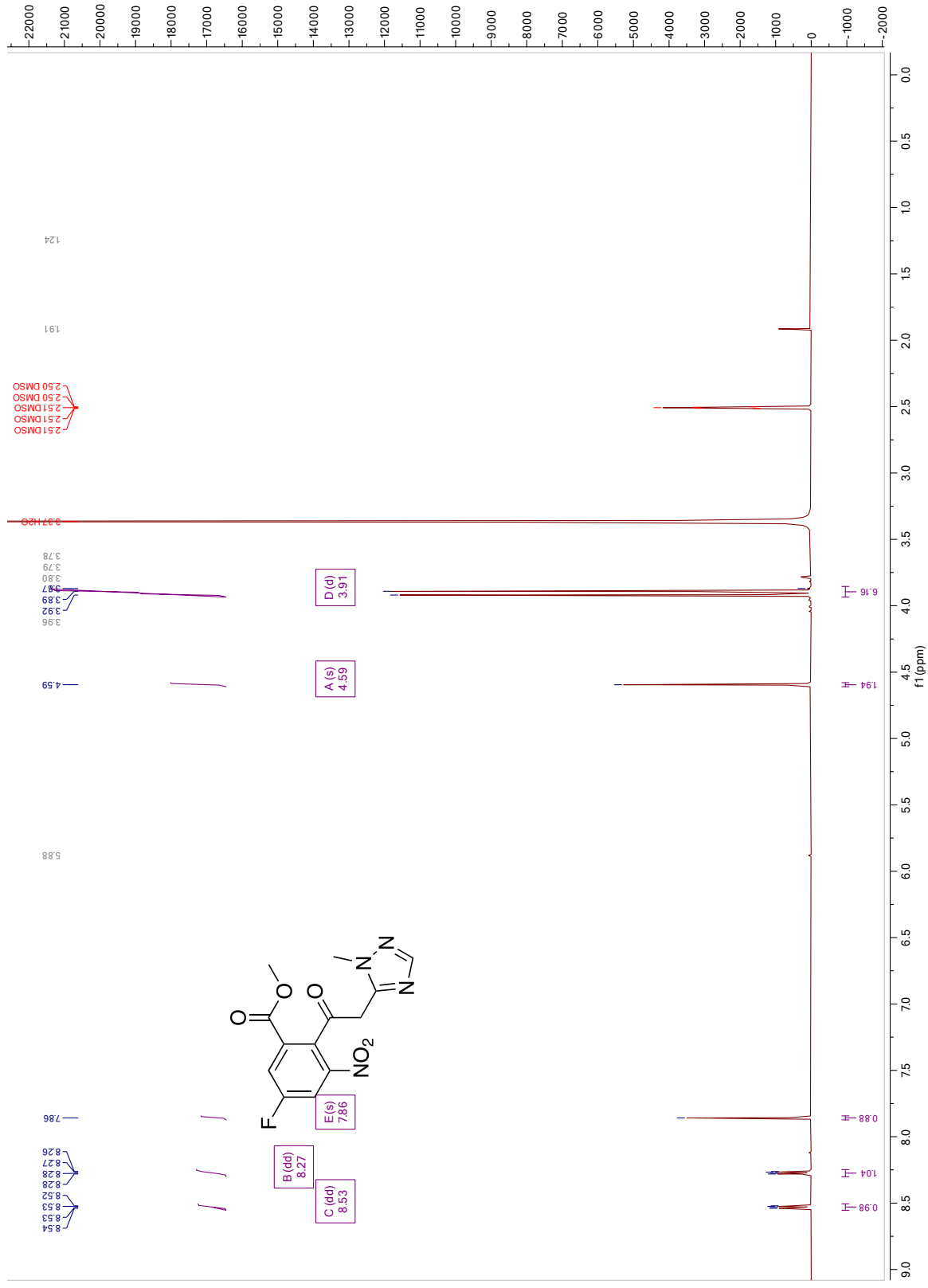
Figure S3: 4D response surface plot generated from the regression model.

2. Compound NMR Spectra

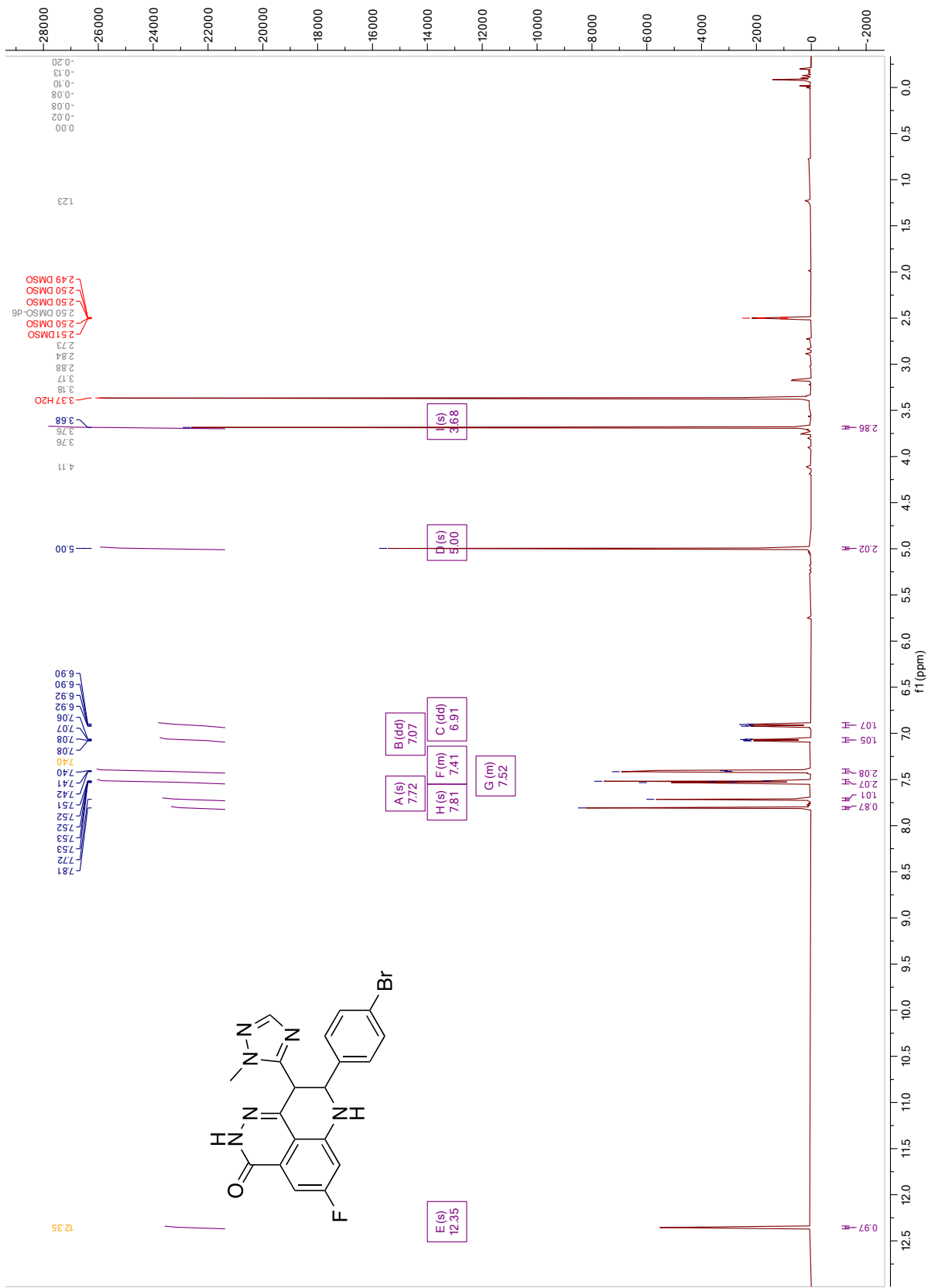
¹H NMR: 6-Fluoro-3-(1-methyl-1H-1,2,4-triazol-5-yl)methylene)-4-nitroisobenzofuran-1(3H)-one (2)



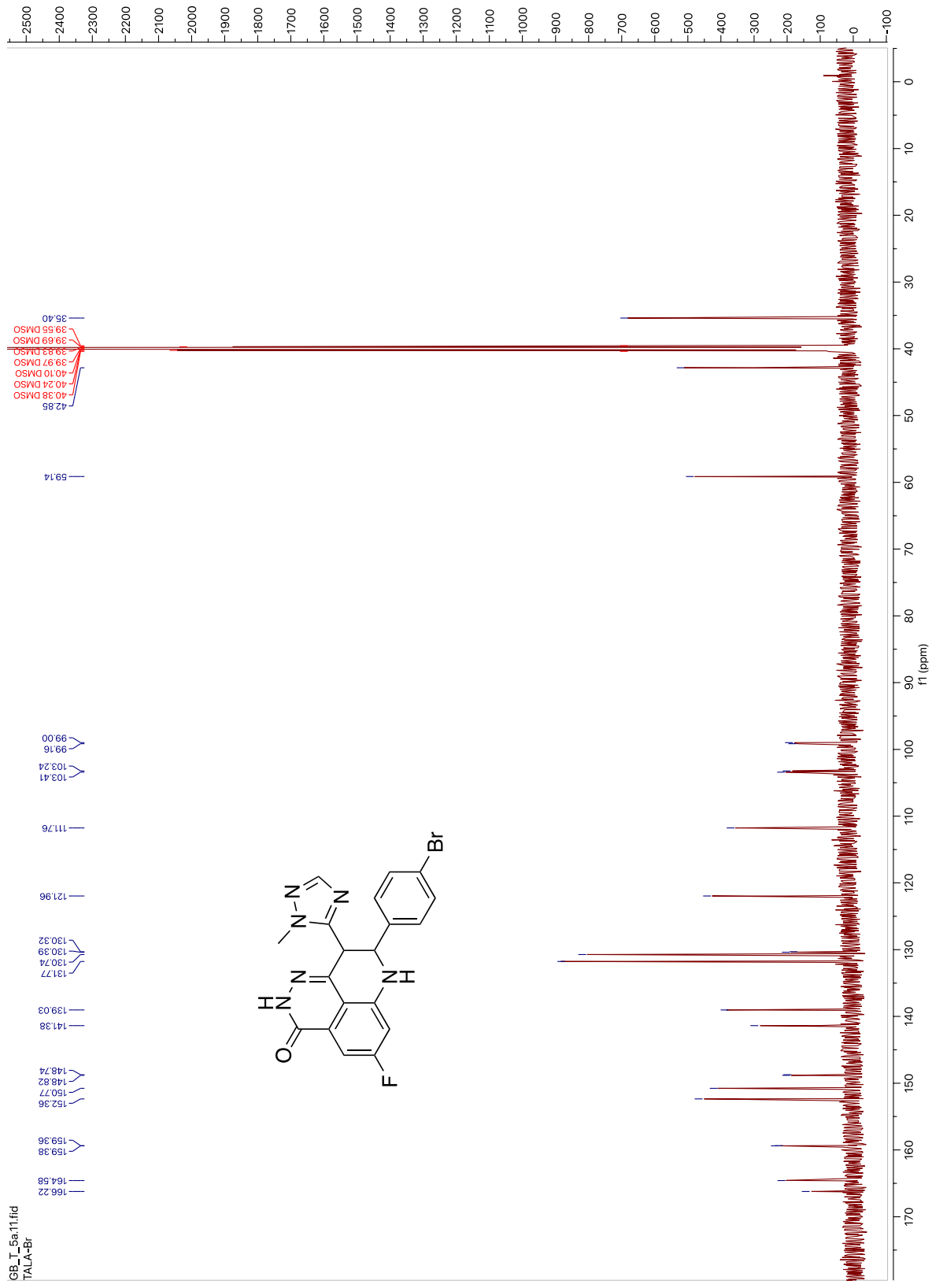
¹H NMR: Methyl 5-fluoro-2-(2-(1-methyl-1H-1,2,4-triazol-5-yl)acetyl)-3-nitrobenzoate (3)



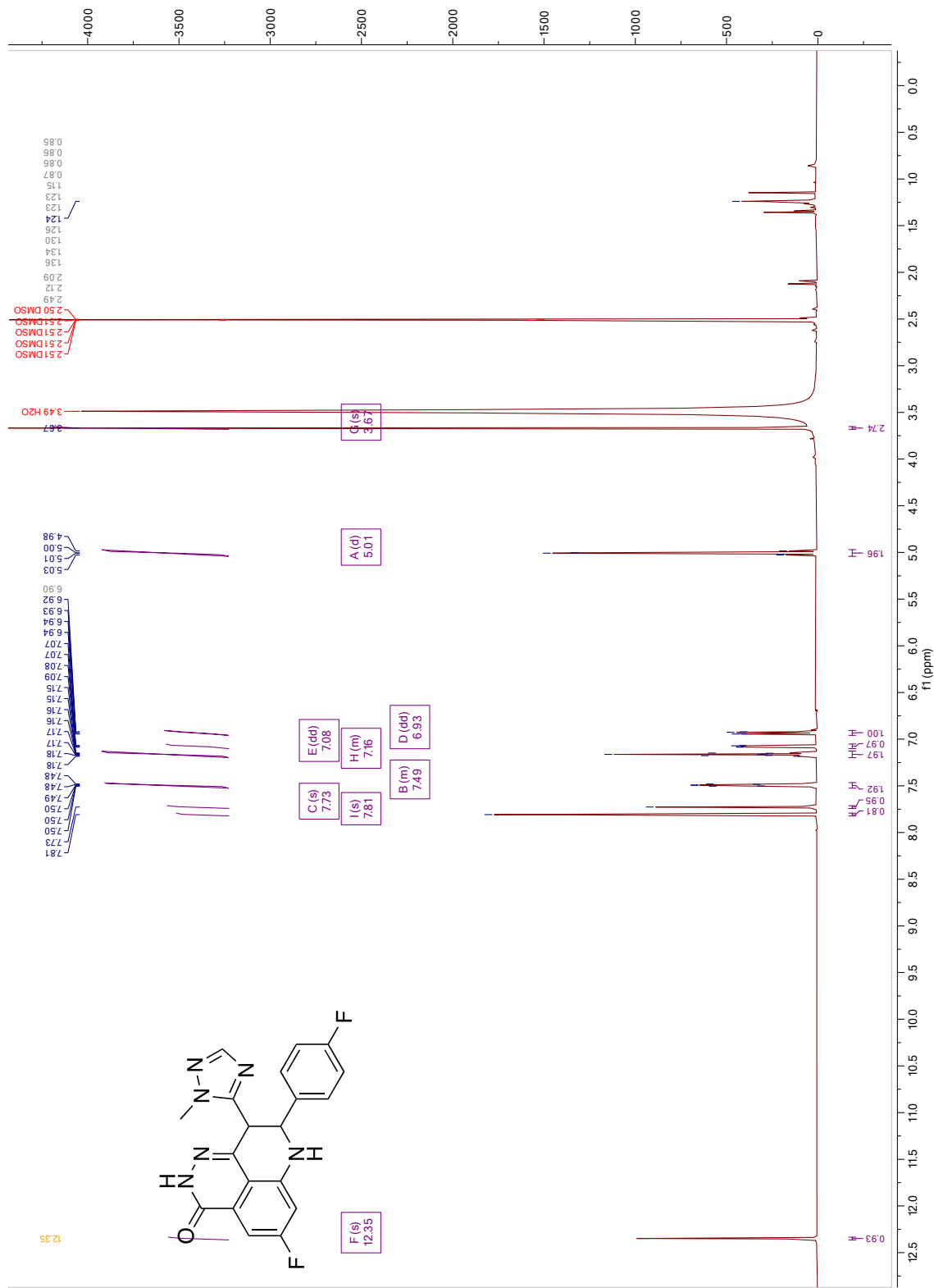
¹H NMR: 8-(4-Bromophenyl)-5-fluoro-9-(1-methyl-1H-1,2,4-triazol-5-yl)-2,7,8,9-tetrahydro-3H-pyrido[4,3,2-de]phthalazin-3-one (5a)



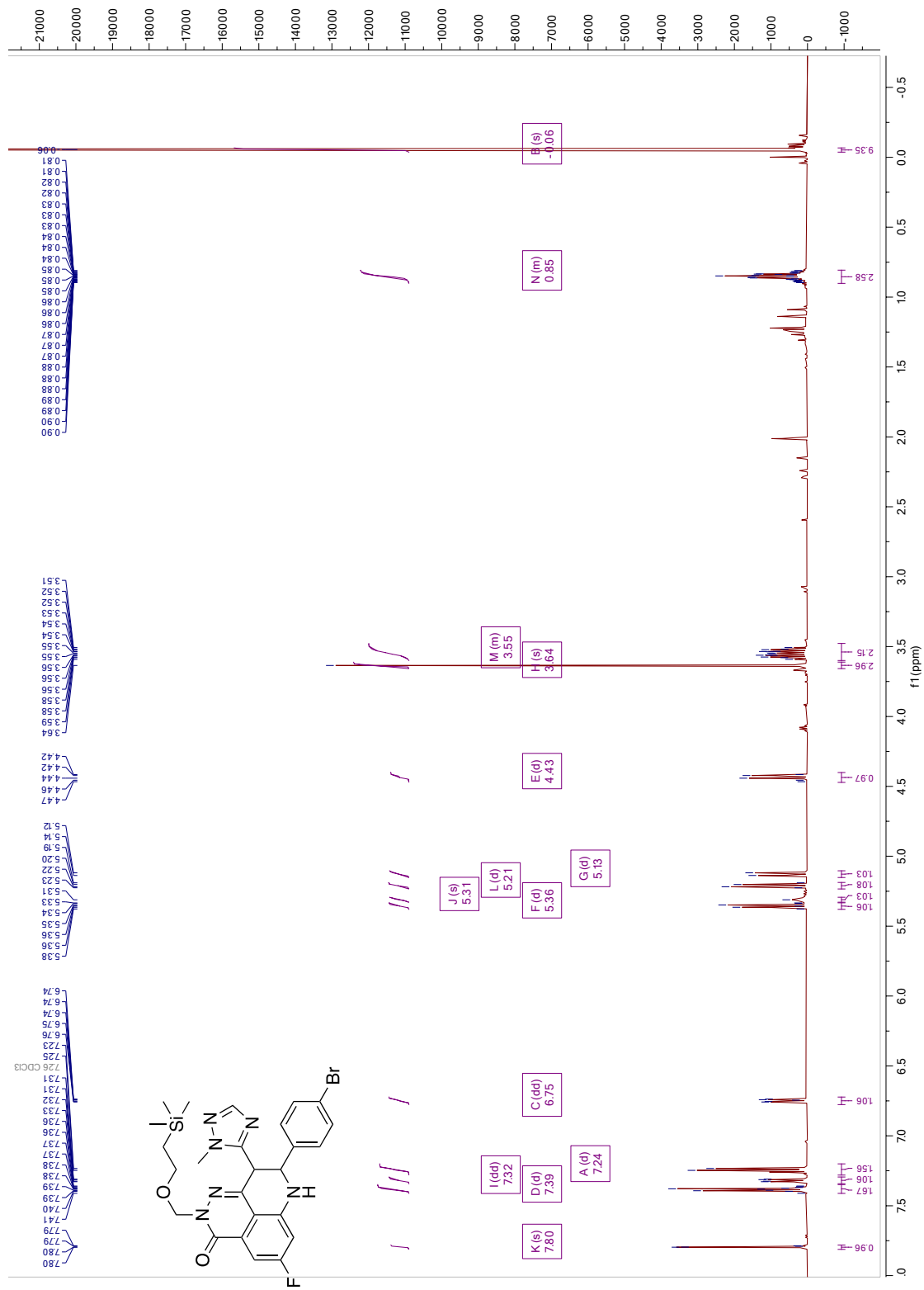
¹³C NMR: 8-(4-Bromophenyl)-5-fluoro-9-(1-methyl-1H-1,2,4-triazol-5-yl)-2,7,8,9-tetrahydro-3H-pyrido[4,3,2-de]phthalazin-3-one (5a)



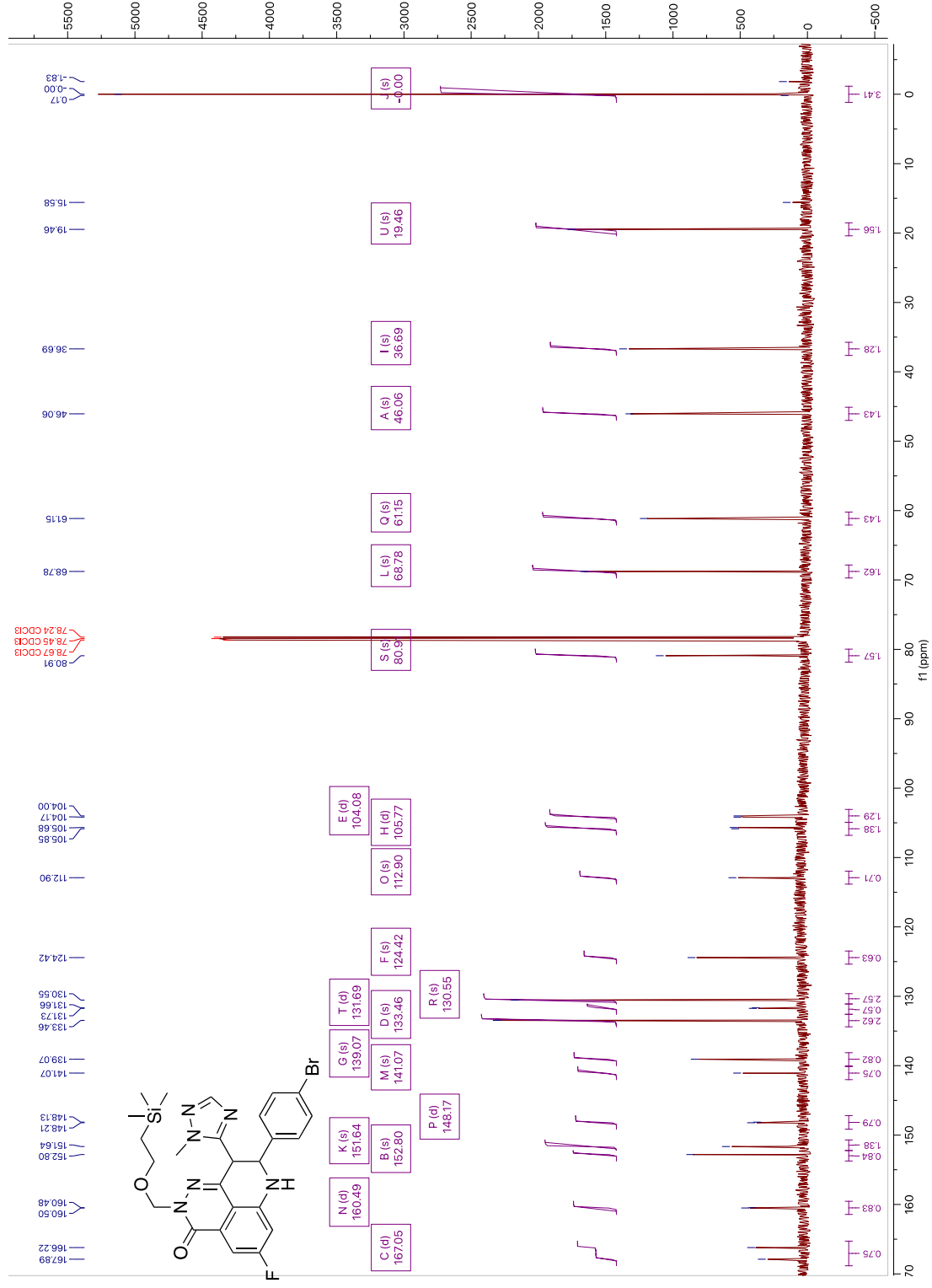
¹H NMR: 5-fluoro-8-(4-fluorophenyl)-9-(1-methyl-1H-1,2,4-triazol-5-yl)-2,7,8,9-tetrahydro-3H-pyrido[4,3,2-de]phthalazin-3-one (5b)



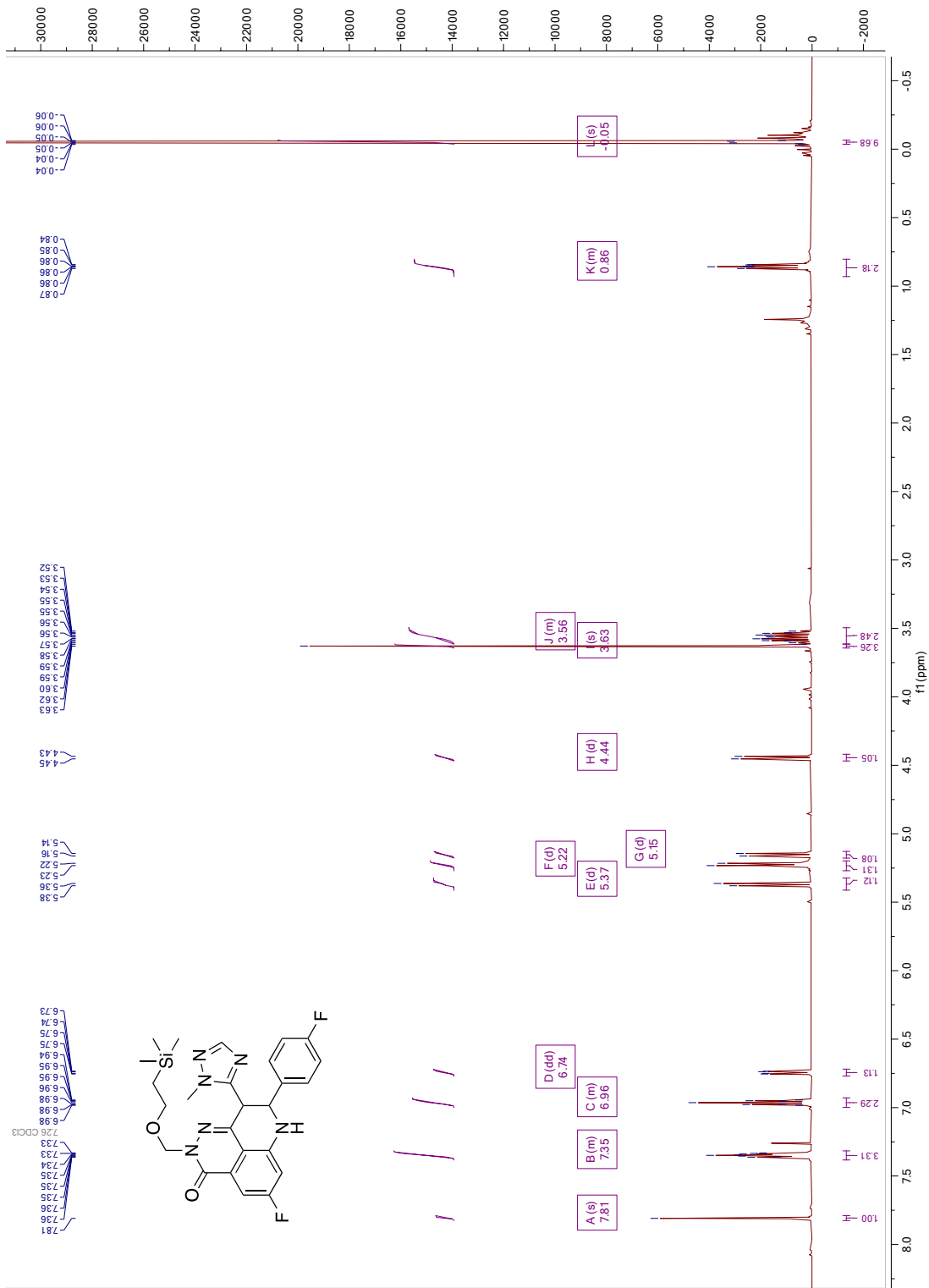
¹H NMR: 8-(4-Bromophenyl)-5-fluoro-9-(1-methyl-1H-1,2,4-triazol-5-yl)-2-((2-(trimethylsilyl)ethoxy)methyl)-7,8,9-tetrahydro-3H-pyrido[4,3,2-de]phthalazin-3-one (6a)



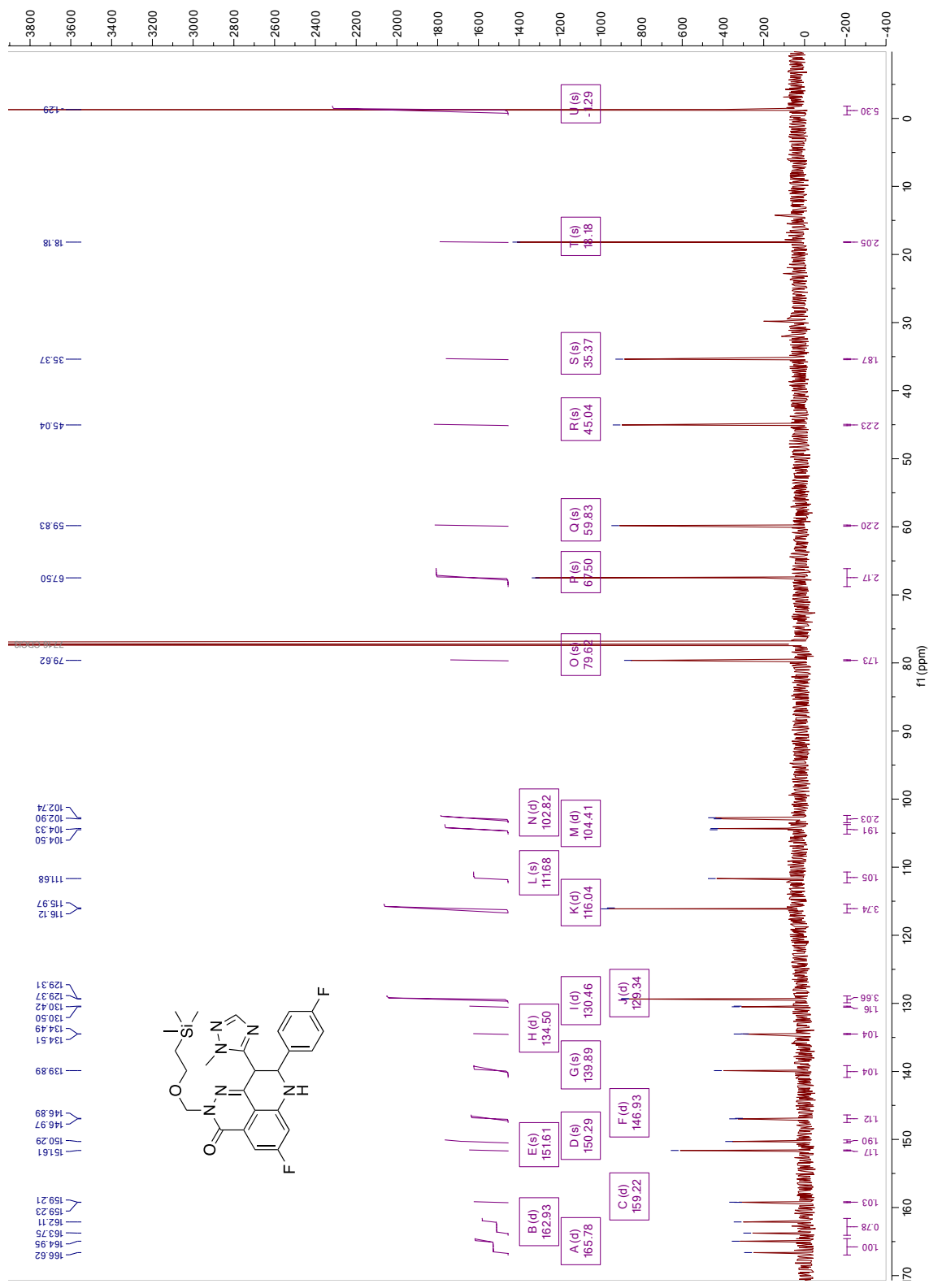
¹³C NMR: 8-(4-Bromophenyl)-5-fluoro-9-(1-methyl-1H-1,2,4-triazol-5-yl)-2-(2-(trimethylsilyl)ethoxy)methyl)-2,7,8,9-tetrahydro-3H-pyrido[4,3,2-de]phthalazin-3-one (6a)



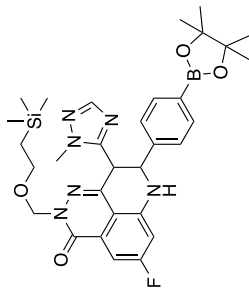
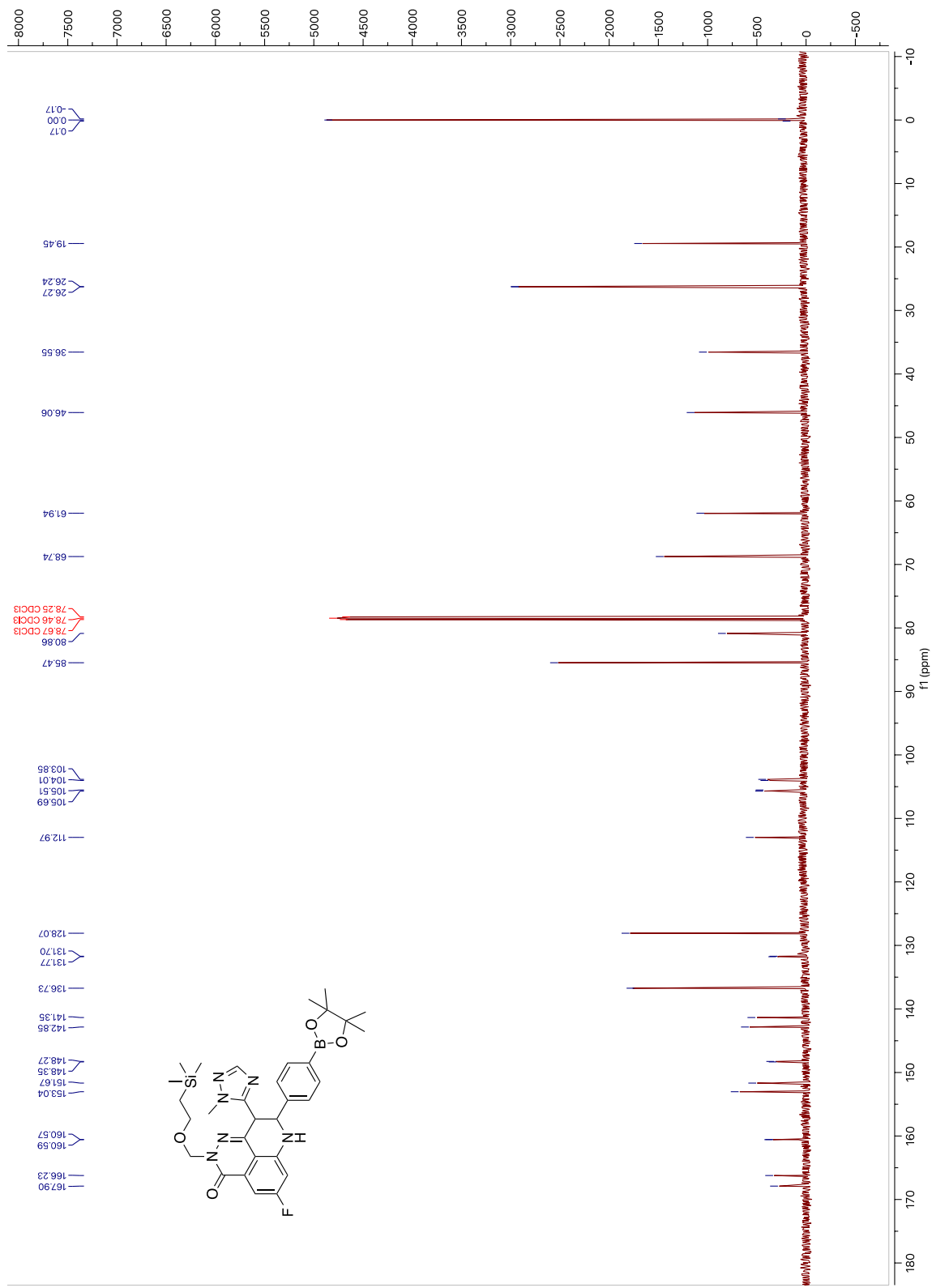
¹H NMR: 5-fluoro-8-(4-fluorophenyl)-9-(1-methyl-1H-1,2,4-triazol-5-yl)-2-((2-(trimethylsilyl)ethoxy) methyl)-2,7,8,9-tetrahydro-3H-pyrido[4,3,2-de]phthalazin-3-one (6c)



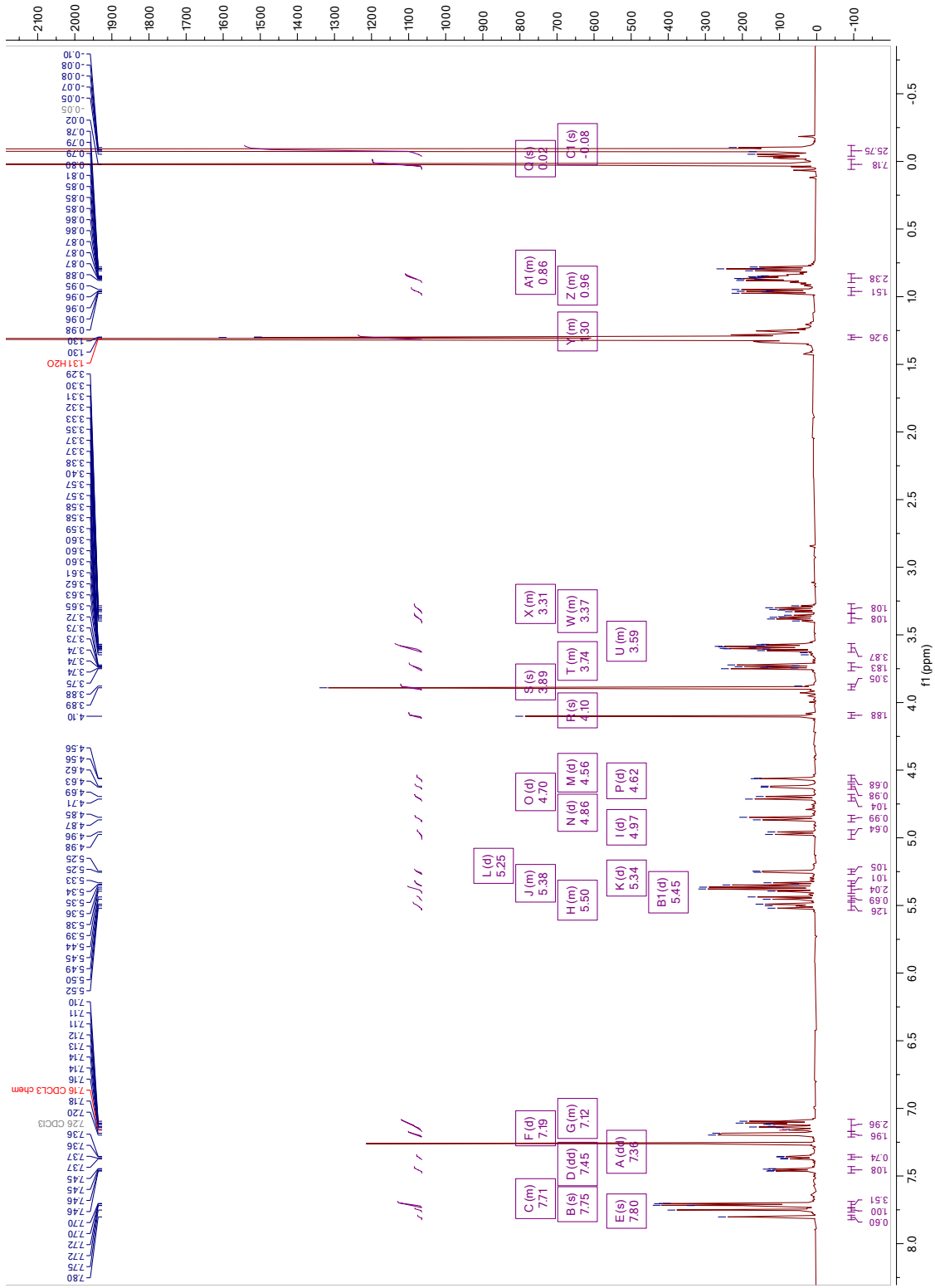
¹H NMR: 5-fluoro-8-(4-fluorophenyl)-9-(1-methyl-1H-1,2,4-triazol-5-yl)-2-((2-(trimethylsilyl)ethoxy) methyl)-2,7,8,9-tetrahydro-3H-pyrido[4,3,2-de]phthalazin-3-one (6c)



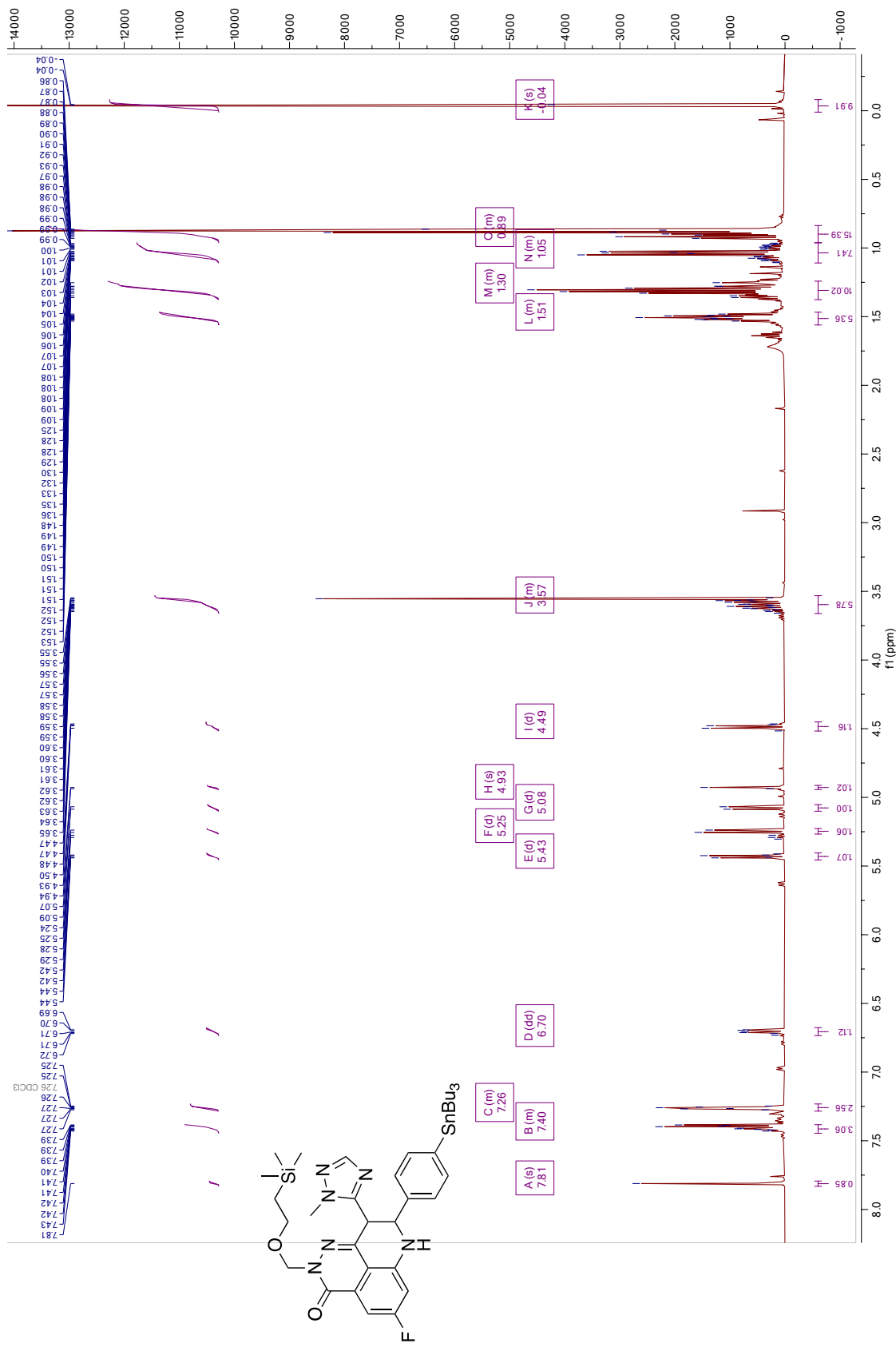
¹³C NMR: 5-fluoro-9-(1-methyl-1H-1,2,4-triazol-5-yl)-8-(4-(4,4,5,5-tetramethyl-1,3,2-dioxaborolan-2-yl)phenyl)-2-((2-(trimethylsilyl)ethoxy)methyl)-2,7,8,9-tetrahydro-3H-pyrido[4,3,2-de]phthalazin-3-one (7a)



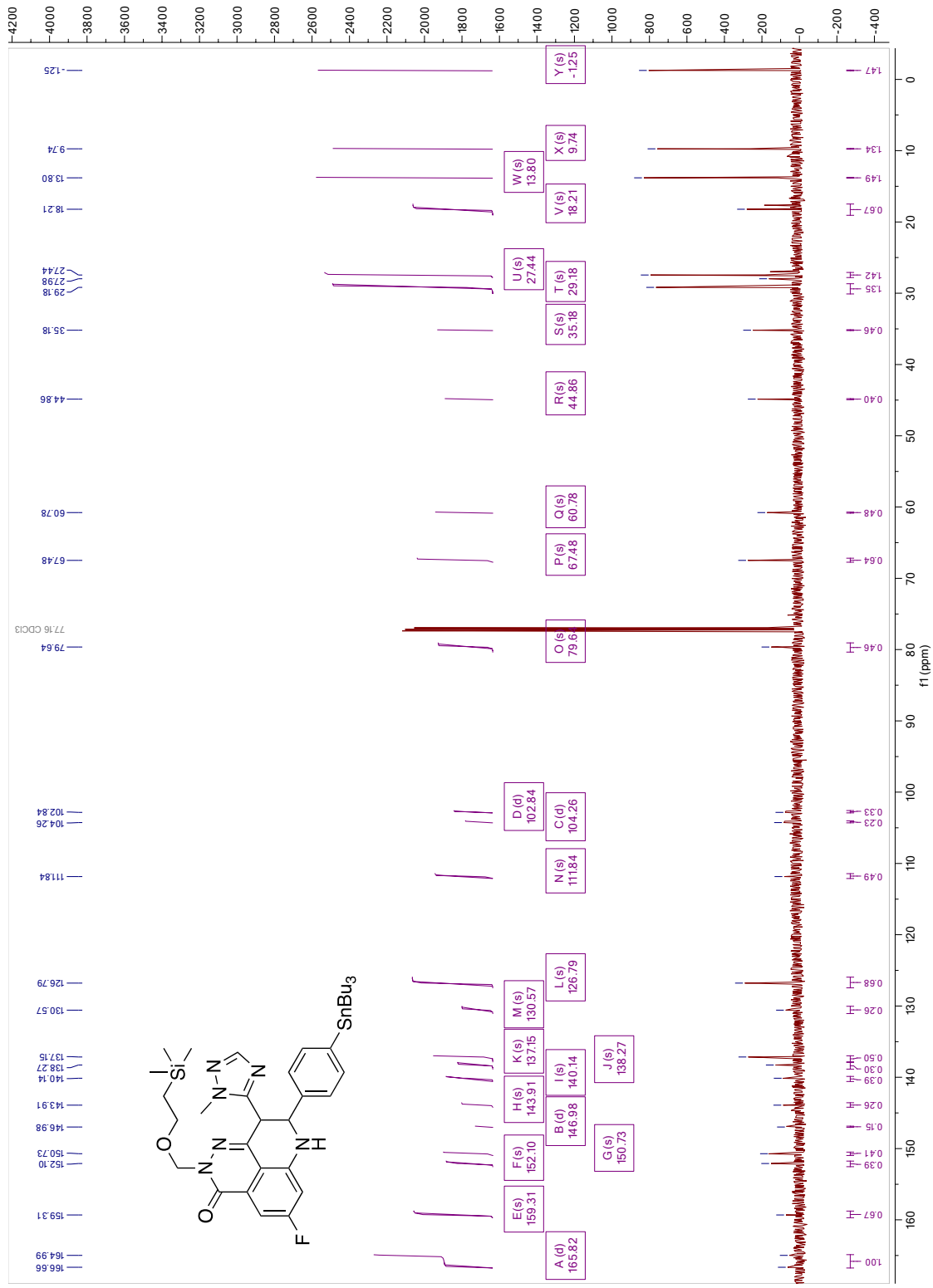
¹H NMR: 5-fluoro-9-(1-methyl-1H-1,2,4-triazol-5-yl)-8-(4-(4,4,5,5-tetra-methyl-1,3,2-dioxaborolan-2-yl)phenyl)-2,7-bis((2-(trimethylsilyl)ethoxy)methyl)-2,7,8,9-tetrahydro-3H-pyrido[4,3,2-de]phthalazin-3-one (7b)



¹H NMR: 5-fluoro-9-(1-methyl-1H-1,2,4-triazol-5-yl)-8-(4-(tributylstanny) phenyl)-2-((2-(trimethylsilyl)ethoxy)methyl)-2,7,8,9-tetrahydro-3H-pyrido[4,3,2-de]phthalazin-3-one (7c)



¹³C NMR: 5-fluoro-9-(1-methyl-1H-1,2,4-triazol-5-yl)-8-(4-(tributylstanny) phenyl)-2-((2-(trimethylsilyl)ethoxy)methyl)-2,7,8,9-tetrahydro-3H-pyrido[4,3,2-de]phthalazin-3-one (7c)



3. Radiochemistry

3.1. General Information

The Radiosynthesis described in this work features 4 distinct process steps: 1) The radiosynthesis of (\pm)[^{18}F]talazoparib. 2) Semi-preparative HPLC of (\pm)[^{18}F]talazoparib. 3) Enantiomeric separation of [^{18}F]talazoparib and [^{18}F]LT-674 via semi-preparative Chiral-PAK HPLC. 4) Tracer concentration and formulation. All four steps could be performed using an Elixys FLEX/CHEM synthesizer coupled to a PURE/FORM concentration and formulation module. Alternatively, steps 1) and 2) could be performed using a FX N Pro (GE), after which the compound was transferred to an external purification and Formulation module for steps 3) and 4).

3.2. Fully Automated Radiosynthesis of [^{18}F]Talazoparib using the Elixys Radiosynthesis System.

The radiosynthesis of [^{18}F]talazoparib was performed using an Elixys FLEX/CHEM with three Elixys cassettes and three 5 ml v-vial reactor vessels. Each cassette was loaded with prefilled reagent vials in accordance with the table below (Table S2). The cassettes were set up and connected as shown below (Figure S4). The PURE/FORM syringe pump was primed before each synthesis.

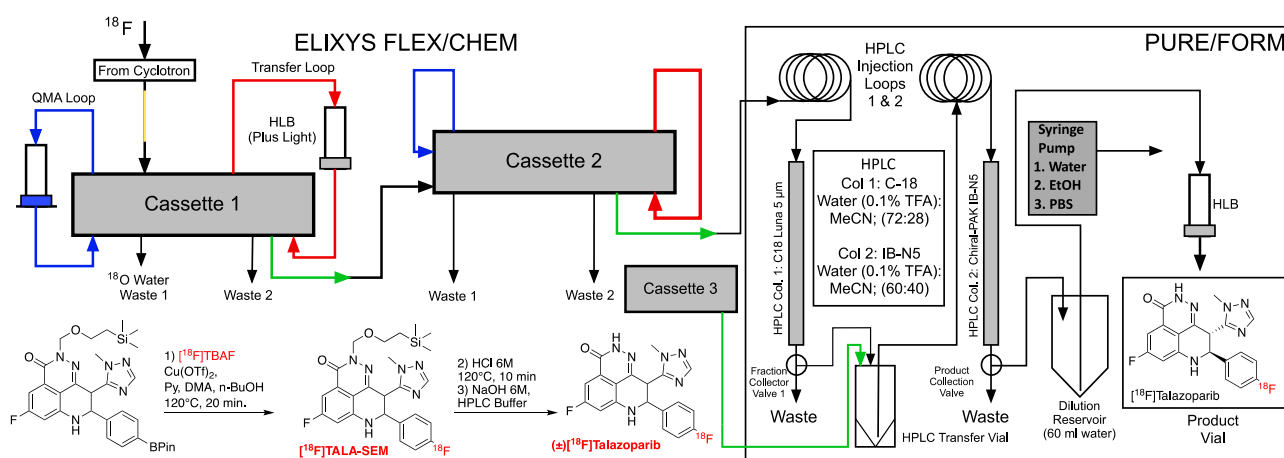


Figure S4: Connection schematic for the fully automated [^{18}F]talazoparib radiosynthesis using an Elixys FLEX/CHEM radiosynthesizer coupled to a PURE/FORM formulation and purification module. Yellow is the cassette activity-in line. Blue is cassette cartridge loop one (cassette one = QMA; cassette two = HLB). Red is cassette cartridge loop two (no cartridge). Green is the cassette activity-out line.

Table S2: Synthesis reagents, cartridges, and eluents, and their corresponding cassette positions

Cassette and Reagent Position	Reagent
Cassette 1; Position 1: QMA Eluent	TBAOTf in Methanol (10 mg/ml) 1 ml
Cassette 1; Position 2: Reaction Mixture	7a (19 mg); Cu(OTf)₂ (3 mg); Pyridine (24 µl); DMA (606 µl); n - BuOH (70 µl)
Cassette 1; Position 3	HCl 6M (700 µl)
Cassette 1; Position 4	Ammonium Formate Buffer (25 mM, 1.5 ml) + NaOH (6M, 300 µl)
Cassette 1; Position 5	Ammonium Formate Buffer (25 mM, 1.5 ml) + NaOH (6M, 300 µl)
Cassette 1; Position 6	Acetonitrile (1 ml)
Cassette 2; Position 1	Water (0.1% TFA) (2 ml)
Cassette 2; Position 2	Water (0.1% TFA) (2 ml)
Dilution Reservoir 2 (PURE/FORM)	Water (60 ml)
Cassette 1; Cartridge Loop 1 (BLUE)	QMA (KOTf Preconditioned)
Cassette 1; Cartridge Loop 2 (RED)	HLB (Conditioned EtOH (2 ml), water (2 ml))
PURE/FORM SPE Loop	HLB (Conditioned EtOH (2 ml), water (2 ml))
HPLC Eluent A	Water (0.1% TFA)
HPLC Eluent B	Acetonitrile
HPLC Column 1	C-18 Luna (10 µm, 10 mm x 250 mm)
HPLC Column 2	CHIRALPAK IB-N5 (5 µm, 10 mm x 250 mm)
PURE/FORM Syringe Pump "water"	Water (40 ml)
PURE/FORM Syringe Pump "Ethanol"	Ethanol (20 ml)
PURE/FORM Syringe Pump "Saline"	PBS (40 ml)

The Elixys sequence for the radiosynthesis of [¹⁸F]talazoparib (listed as Elixys unit operations) is as follows:

- Step 1: Trap Isotope (¹⁸F delivered directly from the cyclotron, over the QMA cartridge in Position A)
- Step 2: Elute Isotope (Cassette 1: Position 1: QMA Eluent)
- Step 3: Evaporate (100 °C, 4-7 minutes or until no liquid is observed through reactor camera)
- Step 4: Add Reagent (Cassette 1: Position 2: Reaction Mixture)
- Step 5: Move Reactor (Blow 20 ml of air into the reactor vessel with a syringe fitted with a long needle)
- Step 6: React (120 °C, 20 min)
- Step 7: Add Reagent (Cassette 1: Position 3: HCl (700 µl))
- Step 8: React (120 °C, 15 min)
- Step 9: Add Reagent (Cassette 1: Position 4: Ammonium Formate (25 mM, 1.5 ml) + NaOH (6M, 300 µl))
- Step 10: Add Reagent (Cassette 1: Position 5: Ammonium Formate (25 mM, 1.5 ml) + NaOH (6M, 300 µl))
- Step 11: Transfer to reactor 2 (Mode: "Trap" to reactor 2).
- Step 12: Add Reagent (Cassette 1: Position 6: Acetonitrile (1 ml)).
- Step 13: Transfer to reactor 2 (Mode: "Elute" to reactor 2).
- Step 14 and 15: Add Reagent (Cassette 2: Positions 2 & 3: HPLC Aqueous phase (4 ml))
- Step 16: Transfer (Cassette 2 to PURE/FORM Loop 1 (manual injection))

When the transfer is complete (fluid detector reads "No Fluid"), trigger HPLC injection manually.

Step 17: Semiprep HPLC 1

Column: C-18 luna (10 μ m, 10 x 250 mm)

HPLC Eluent (Isocratic): 28 % Acetonitrile; 72 % Water (w/ 0.1% TFA); 6 ml/min.

The product radio peak elutes at approximately 10:30-13 min and is cut into a sealed v-vial (10 ml) fitted with a vent, a connection to cassette 3, and long needle pushed to bottom of the vial for transfer to HPLC loop 2.

Prompt 18: After the radioactive fraction has been collected, remove the vent needle from the HPLC transfer vial.

Step 19: Transfer (Cassette 3 (only provides gas pressure) to PURE/FORM Loop 1 (manual injection))

Step 20: Semiprep HPLC 2

Column: CHIRALPAK IB-N5 (5 μ m, 10 x 250 mm) fitted with CHIRALPAK IB-N5 (5 μ m, 10 x 20mm) column guard

HPLC Eluent (Isocratic): 40 % Acetonitrile; 60 % Water (w/ 0.1% TFA); 5 ml/min.

The product enantiomer peak elutes at approximately 12:30-13:30 min (see attached HPLC Trace) and is cut into the PURE/FORM Dilution reservoir (Containing 60 ml water) for SPE reformulation. The Inactive enantiomer elutes at 14:30-15:30 min and can be isolated using the Elixys fraction collector if need be.

Step 21: Formulation

The dilution reservoir contents are passed over an HLB cartridge, trapping the purified [18 F]talazoparib. Ethanol (0.5 ml) is then used to elute the radiotracer into a product vial. PBS (4.5 ml) is then used to reconstitute the tracer in the product vial.

3.3. Semi-Automated Radiosynthesis of [¹⁸F]Talizoparib using a GE FX N Pro Radiosynthesis System and Elixys PURE/FORM Module.

The FX N Pro was set up as depicted in the diagram (Figure S5). Reagent vials were filled as described in the table below (

Table S3: Synthesis reagents, cartridges, and eluents and their corresponding positions.).

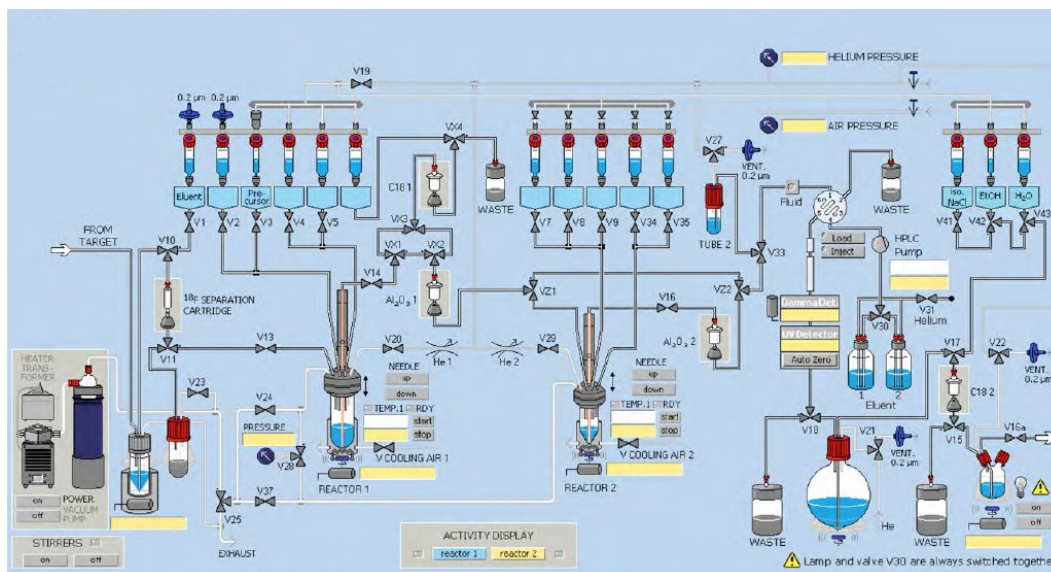


Figure S5: Schematic diagram of the fixed fluid path system used by the FX N pro.

Table S3: Synthesis reagents, cartridges, and eluents and their corresponding positions.

Reagent Position	Reagent
Vial 1: QMA Eluent	TBAOTf in Methanol (10 mg/ml) 1 ml
Vial 2: Reaction Mixture	7a (19 mg); Cu(OTf) ₂ (3 mg); Pyridine (24 µl); DMA (606 µl); n-BuOH (70 µl)
Vial 3:	HCl 6M (600 µl)
Vial 4:	Ammonium Formate Buffer (25 mM, 10 ml) + NaOH (6M, 600 µl)
Vial 5:	Methanol Wash (0.5 ml)
Vial 6:	Acetonitrile (1 ml)
Tube 2: For HPLC injection	Water (0.1% TFA) (3.5 ml)
Vial 12: Formulation	PBS (4.5 ml)
Vial 13: Formulation	EtOH (0.5 ml)
Vial 14: Formulation	Water (4 ml)
Dilution Reservoir (Crystal Ball)	Water (60 ml)
QMA Cartridge Slot: QMA	QMA (KOTf Preconditioned)
C-18 Cartridge Slot 1: HLB	HLB (Conditioned EtOH (2 ml), water (2 ml))
C-18 Cartridge Slot 2: HLB	HLB (Conditioned EtOH (2 ml), water (2 ml))
PURE/FORM SPE Loop	HLB (Conditioned EtOH (2 ml), water (2 ml))
FXN Pro HPLC Eluent A: (For purification)	Water (TFA 0.1%): Acetonitrile (72:28)
FXN Pro HPLC Eluent B: (For column flush)	Acetonitrile
HPLC Column 1	C-18 Luna (10 µm, 10 mm x 250 mm)
Elixys HPLC Eluent A	Water (0.1% TFA)
Elixys HPLC Eluent B	Acetonitrile
PURE/FORM HPLC Column 2	CHIRALPAK IB-N5 (5 µm, 10 mm x 250 mm)
PURE/FORM Syringe Pump "water"	Water (40 ml)
PURE/FORM Syringe Pump "Ethanol"	Ethanol (20 ml)
PURE/FORM Syringe Pump "Saline"	PBS (40 ml)

Synthesis Protocol:

At the end of bombardment (EOB), ¹⁸F was delivered from the cyclotron into a delivery vial contained within the FX N pro. The contents of the vial were then drawn over the QMA cartridge by vacuum, and the [¹⁸O]water was collected in a separate waste vial for recycling. The ¹⁸F was then eluted from the QMA with TBAOTf (10 mg) in methanol (1 ml) into the reactor. The walls of the reaction vessel were then washed with methanol (0.5 ml) from vial 5, and the methanol was removed by evaporation at 100 °C for 6 minutes under vacuum and a stream of helium. The reaction mixture was drawn into the reaction vessel with vacuum from vial 2. As vial 2 was open to the air, air was thus also drawn into the reaction vessel over 1 minute. The reactor was sealed, and the temperature was raised to 120 °C for 20 minutes. After cooling to 45 °C, the contents of vial 3 (HCl 6M, 600 µl) were pushed into the reactor. The reactor was then again heated to 120 °C for 15 minutes, resulting in the deprotection of the racemic [¹⁸F]talazoparib. 10 ml of 25 mM ammonium formate buffer containing NaOH (6M, 600 µl) was added to the reaction mixture with stirring from vial 4. The reactor needle was lowered to the bottom of the reactor, and the contents were pushed over the first HLB cartridge. The crude product racemate was then eluted with acetonitrile (1 ml, from vial 6) into tube 2 (containing water (0.1% TFA), 3.5 ml).

The contents of tube 2 were then loaded onto the HPLC injection loop (5 ml) and injected onto the HPLC column for purification using eluent A (Water (0.1%) . The product radio peak appeared at 12-13 minutes and was cut into the large dilution reservoir. The contents of the dilution reservoir were then stirred and passed over the second HLB cartridge into the waste. The product, which was trapped on the HLB cartridge, was washed with water (4 ml, from vial 14), after which it was eluted with acetonitrile (1 ml) and diluted with water (0.1 % TFA) into a 10 ml v-vial. This afforded (\pm)[^{18}F]talazoparib (15 ± 3.2 %AY; 28 ± 5.0 %RCY; synthesis time 90 min).

The racemic product solution was transferred to a separate semipreparative HPLC system (Elixys PURE/FORM) for enantiomeric resolution using a CHIRALPAK IB-N5 (5 μm , 10 x 250 mm) column fitted with CHIRALPAK IB-N5 (5 μm , 10 x 20mm) column guard. An isocratic HPLC method (40 % Acetonitrile; 60 % Water (w/ 0.1% TFA); 5 ml/min) was able to separate the two enantiomers [^{18}F]talazoparib (retention time \approx 12:30-13:30 min) and [^{18}F]LT-674 (retention time \approx 14:30-15:30 min). The desired HPLC product peak was diverted into a dilution reservoir (water, 60 ml), the contents of which was passed over and HLB SEP cartridge, trapping the product. The product was eluted with ethanol (0.5 ml) and reconstituted with PBS (4.5).

4. Radiochemistry HPLC Data

4.1. Rationale for Column Selection

For the chiral analysis of talazoparib, four different polysaccharide phases were screened. Columns Chiralpak IA-U, IB-U, IC-U and IG-U (all: 100 mm l. x 3 mm i.d., sub-2 μ m, IA-U and IG-U: amylose based, IB-U and IC-U: cellulose based) were tested in gradient mode (mobile phase A: ACN/water (50/50) + 20 mM NH₄HCO₃, mobile phase B: water + 20 mM NH₄HCO₃, 0.00 min: 0% B, 2.00 min 0% B, 12.00 min 100% B, 15.00 min 100% B, 15.01 0% B, temperature: 25°C). While IA-U showed no baseline separation, IB-U and IC-U showed the most promising results (Figure S6). For this reason, further experiments were conducted on cellulose-based columns IB-U and IC-U. In a mobile phase screening, ammonium bicarbonate was replaced by trifluoroacetate. In this way, the analysis time could be shortened from 12 to 9 min in IB-U and from 12 to 11 min in IC-U under the chosen conditions. When switching from gradient to isocratic mode (water + 0.1% TFA/ACN (70/30, v/v), IB-U showed baseline separation in shorter time than IC-U (8 min for IB-U, 14 min for IC-U at a flowrate of 0.5 mL/min, Figure S7). To further improve the separation, a stationary phase optimized for basic compounds, as recommended by the manufacturer, Chiralpak IB-N (containing an updated version of the Chiralpak IB packing material) was finally selected as chiral stationary phase. It shows less peak tailing for basic compounds, and according to the manufactures could be used for several applications beyond the work discussed here. For semipreparative applications, the manufactures also suggested using relatively pure racemic mixtures to maximize the efficiency of the enantiomeric resolution and prolong the column life span. This ultimately led to our decision to perform standard reverse-phase HPLC before the enantiomeric separation.

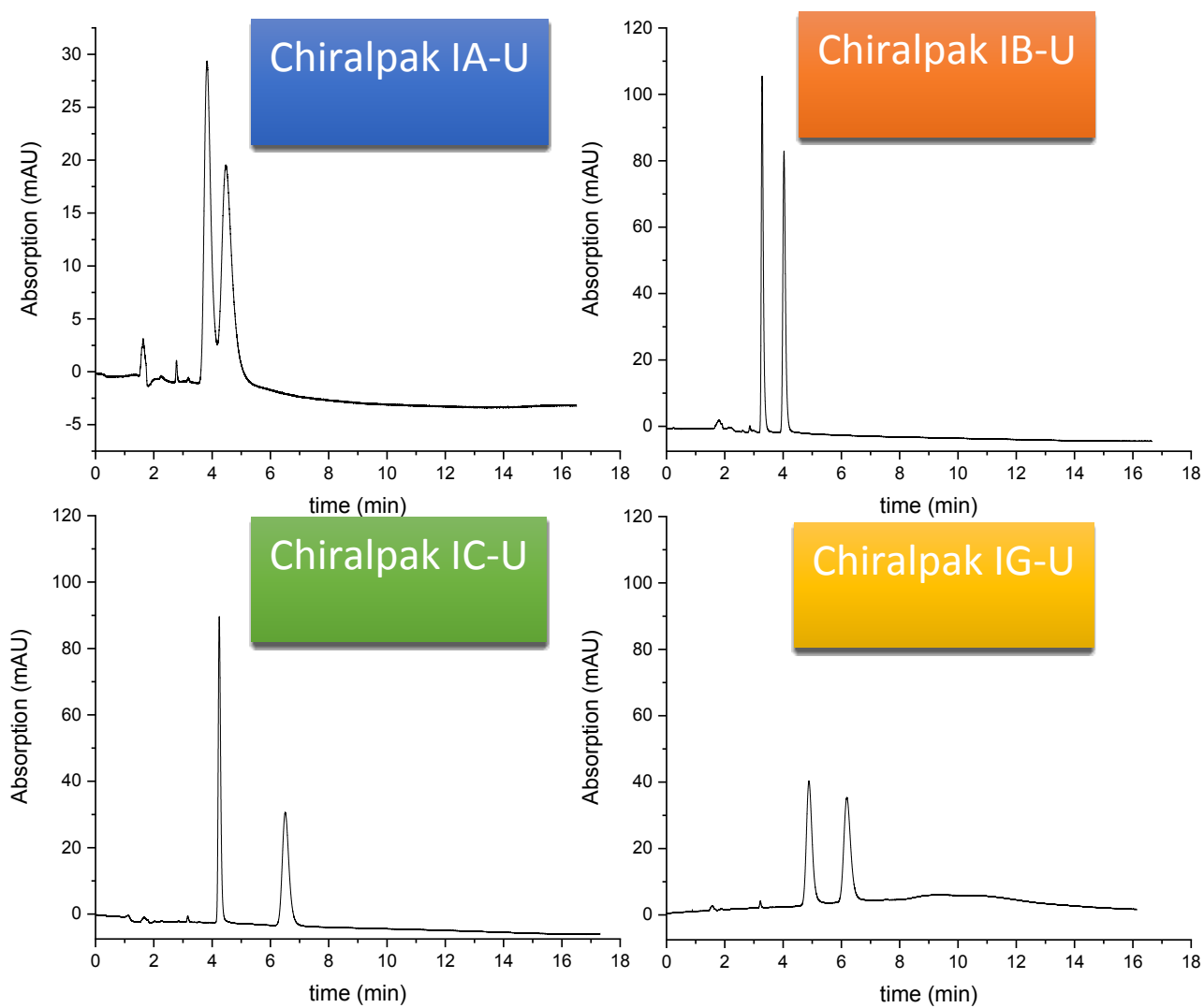


Figure S6: Column screening of racemic talazoparib. Conditions.

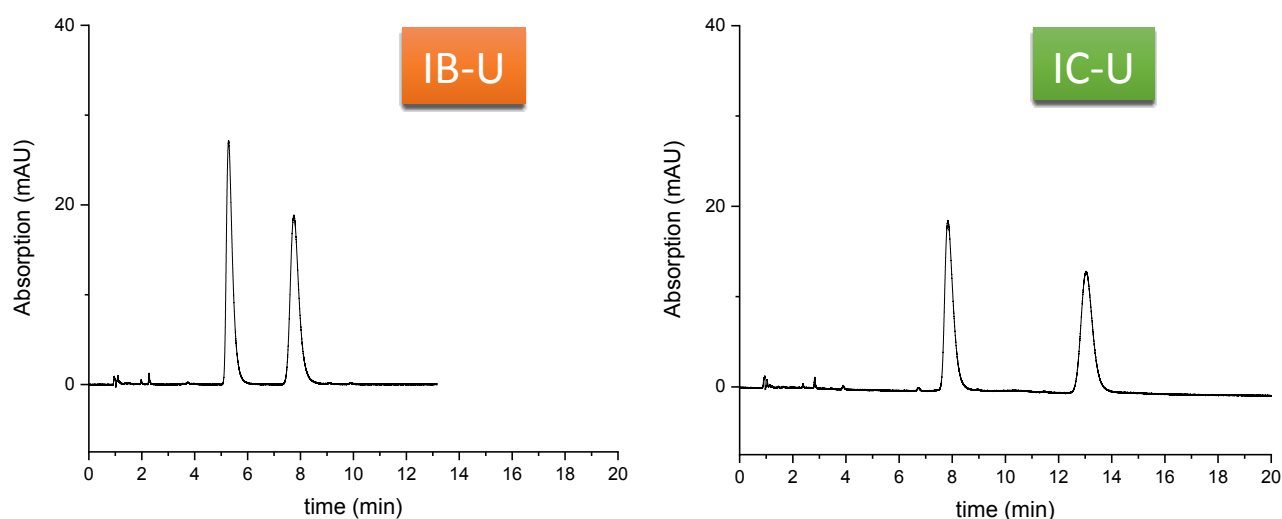


Figure S7: Isocratic separation of racemic talazoparib on IB-U (left) and IC-U (right). Conditions: mobile phase: water + 0.1% TFA/ACN (70/30; v/v), flow rate: 0.5 mL/min, temperature: 25°C, detection wavelength: 254 nm

4.2. UV HPLC of Non-radioactive Standard Compounds

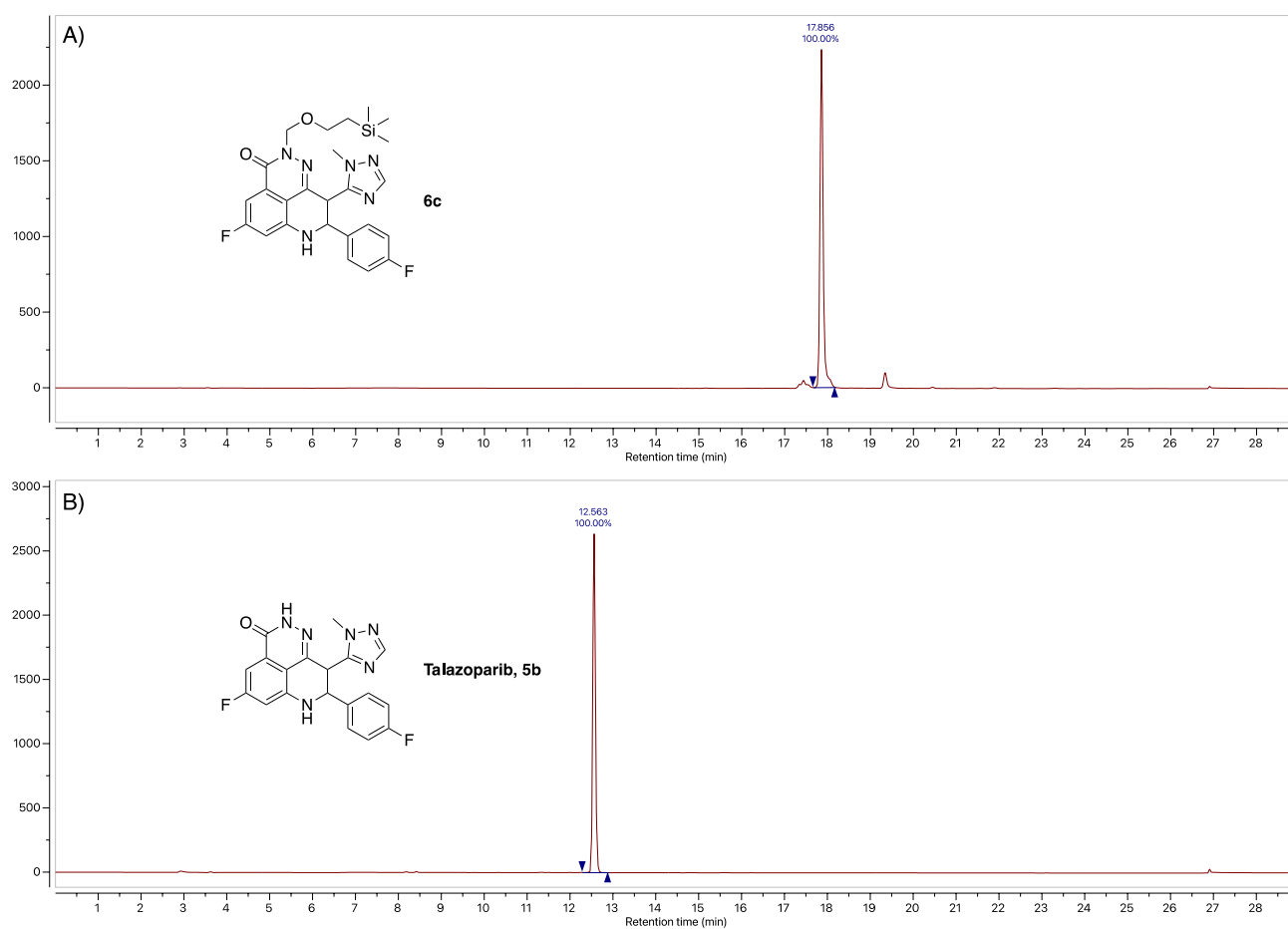


Figure S8: UV HPLC (254 nm) tracers of the non-radioactive reference samples of A) **6c** and B) **5b** (\pm)talazoparib). These samples used to verify compound identity in radio chemical experiments. Data was acquired using the following conditions: Column: Luna 5 μ m C18 (2) 100 Å column (4.6 x 250 mm). Solvent A: water + 0.1% TFA; Solvent B: acetonitrile; 0 - 2 min: (5% B); 0-17 min: (5 - 100% B); 17 - 23 min: (100% B); 23-28 min: (100-5% B); Flowrate: 1 ml/min.

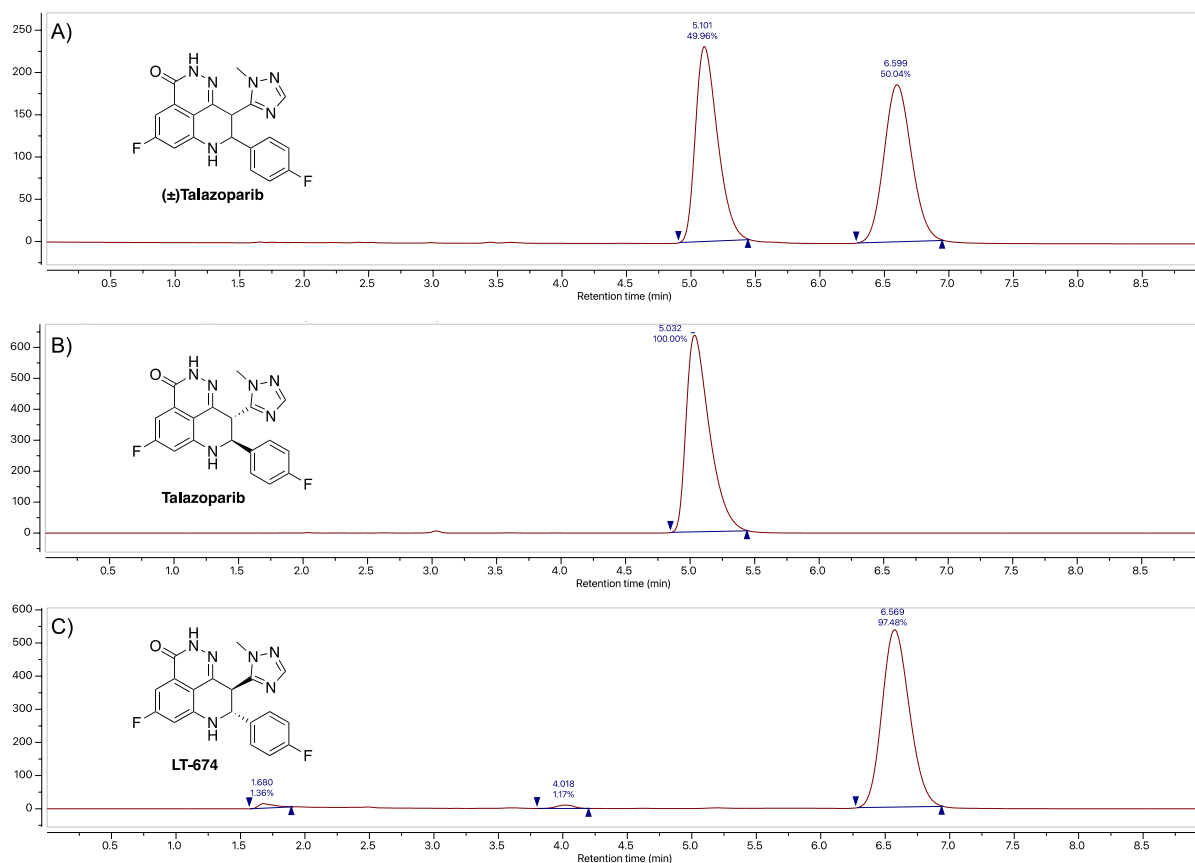


Figure S9: Chiral HPLC (UV 254 nm) tracers of the non-radioactive reference sample of: A) talazoparib racemic mixture (compound **5b**), B) commercially obtained talazoparib, and C) commercially obtained LT-674. These samples were used to resolve the talazoparib enantiomers and verify the enantiomeric purity of the final product radio tracer [^{18}F]talazoparib. Data was acquired using the following conditions: Column: CHIRALPAK IB-N5 (5 μm , 4.6 X 150 mm); Isocratic HPLC method: Water + 0.1% TFA: Acetonitrile (60:40); Flowrate: 1 ml/min.

4.3. Representative HPLC data from Manual CMRF Radiochemical Experiments

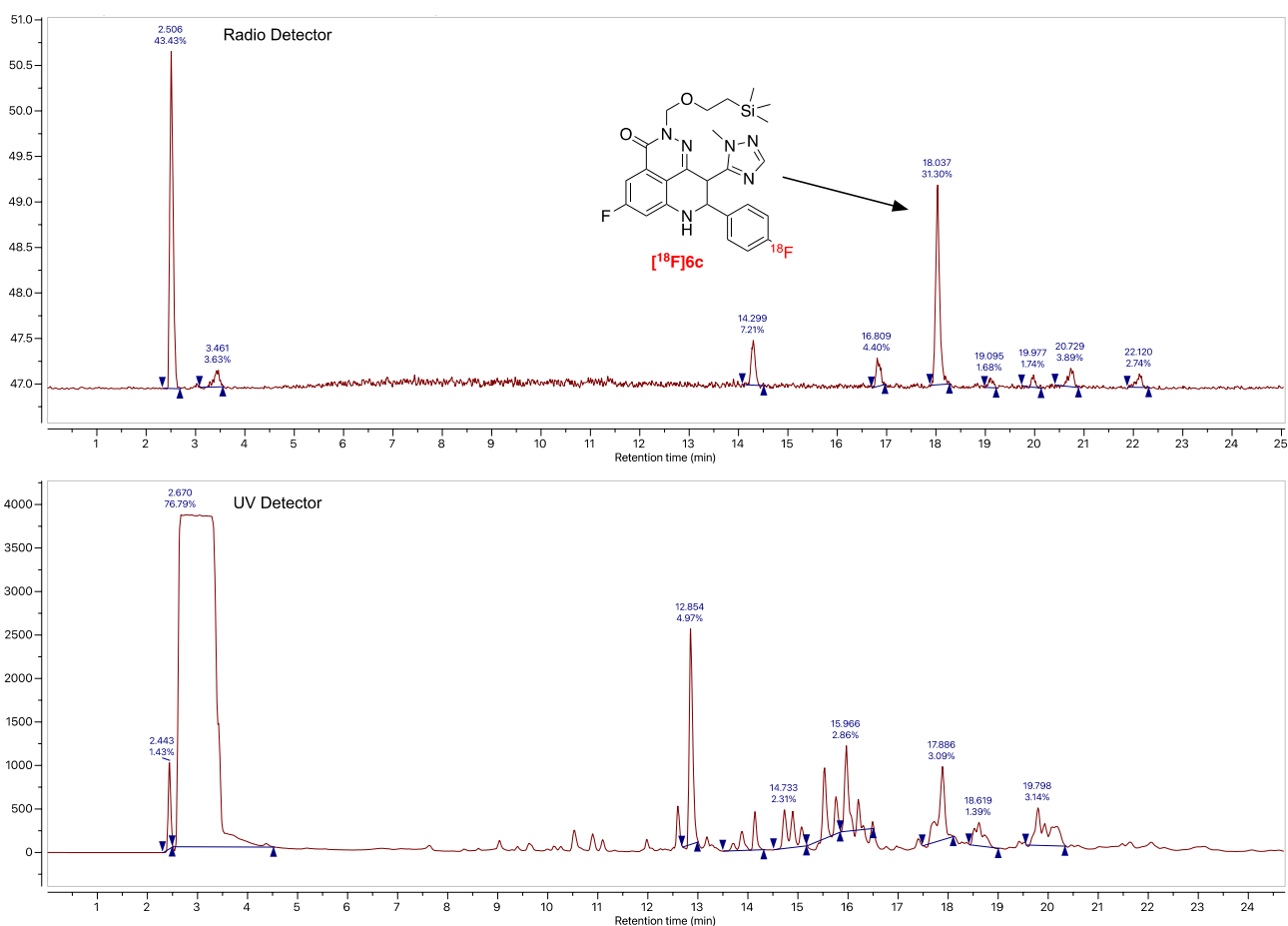


Figure S10: Representative UV and Radio-detector traces for the copper-mediated radiofluorination of compound **7a** to $[^{18}\text{F}]\mathbf{6c}$. Product retention time corresponds to that of the non-radioactive standard displayed in Figure S6. Data was acquired using the following conditions: Column: Luna 5 μm C18 (2) 100 \AA column (4.6 x 250 mm). Solvent A: water + 0.1% TFA; Solvent B: acetonitrile; 0 - 2 min: (5% B); 0-17 min: (5 - 100% B); 17 - 23 min: (100% B); 23-28 min: (100-5% B); Flowrate: 1 ml/min.

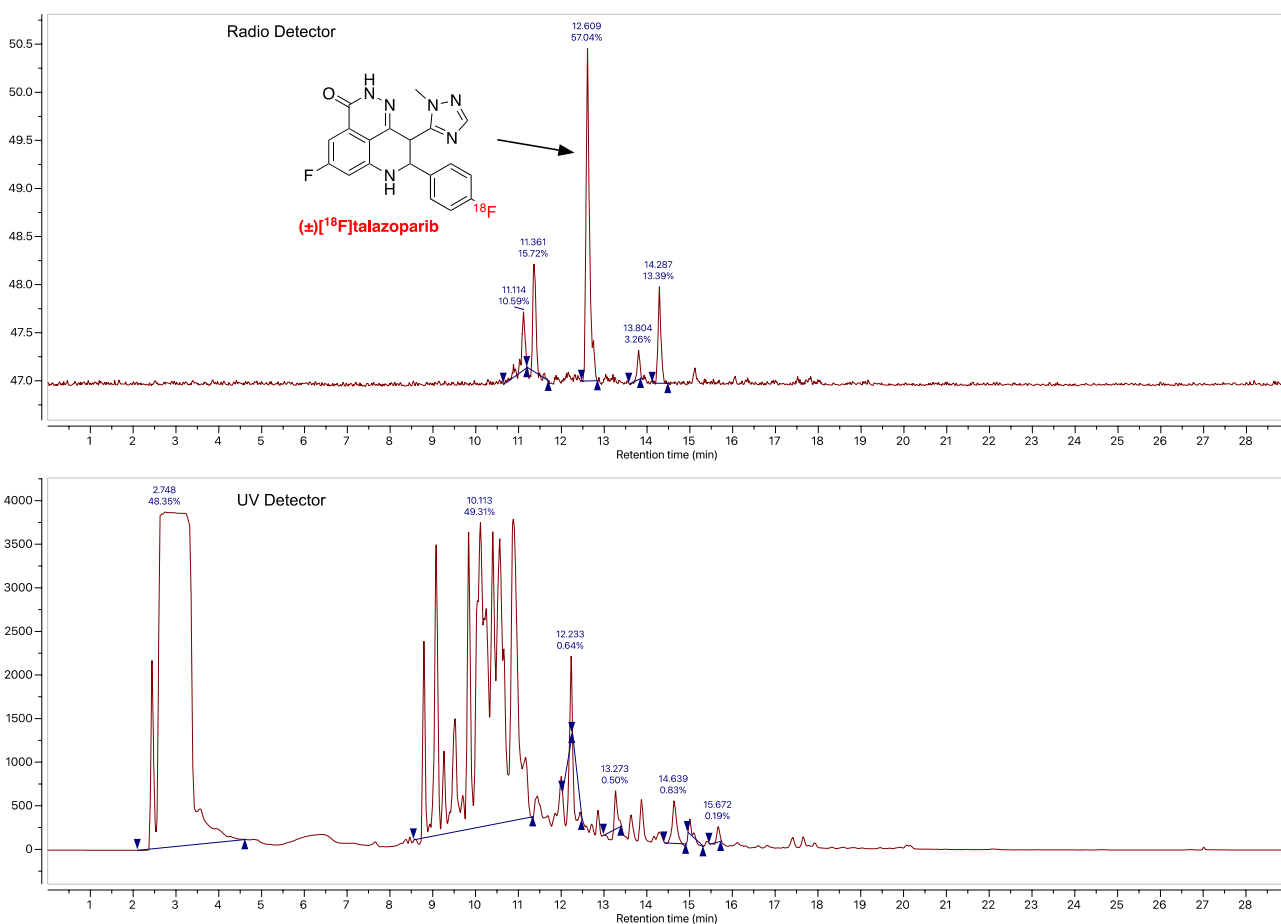


Figure S11: Representative UV and Radio-detector traces for the acid driven deprotection of compound [¹⁸F]6c to (±)[¹⁸F]talazoparib. Product retention time corresponds to that of the non-radioactive standard displayed in Figure S6. Data was acquired using the following conditions: Column: Luna 5 μm C18 (2) 100 Å column (4.6 x 250 mm). Solvent A: water + 0.1% TFA; Solvent B: acetonitrile; 0 - 2 min: (5% B); 0-17 min: (5 - 100% B); 17 - 23 min: (100% B); 23-28 min: (100-5% B); Flowrate: 1 ml/min.

4.4. Representative Semipreparative HPLC Purification of [^{18}F]Talazoparib

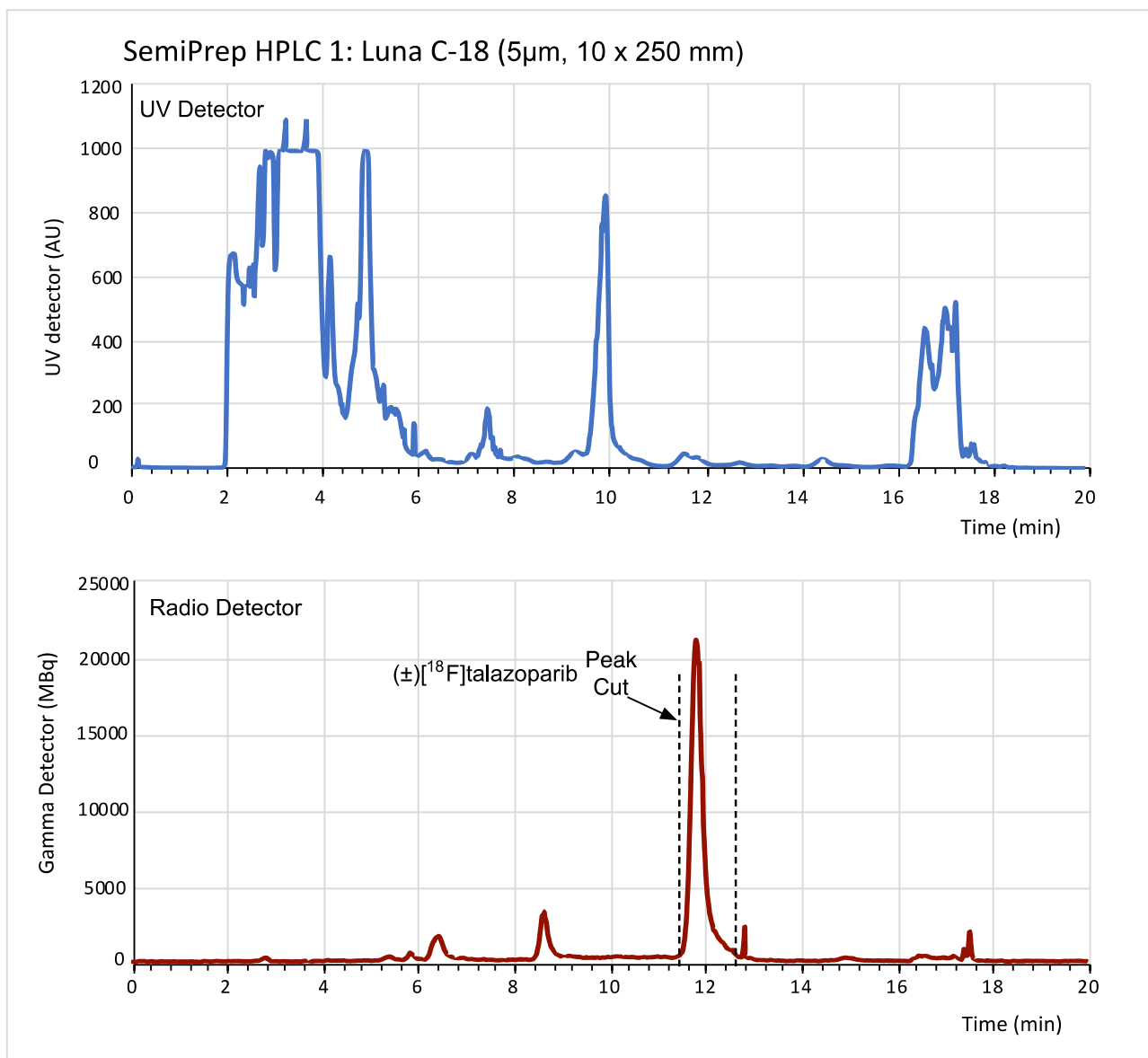


Figure S12: Semipreparative C18 HPLC purification of the crude reaction mixture. The radioactive fraction corresponding to (\pm) ^{18}F]talazoparib was isolated into a collection vessel for enantiomeric resolution. Data was obtained using the semi-preparative HPLC system build into the FX N Pro operating with the following parameters: Column: Luna 10 μm C18 (2) 100 \AA column (10 x 250 mm); Isocratic HPLC method: Water + 0.1% TFA: Acetonitrile (72:28); Flowrate: 6 ml/min.

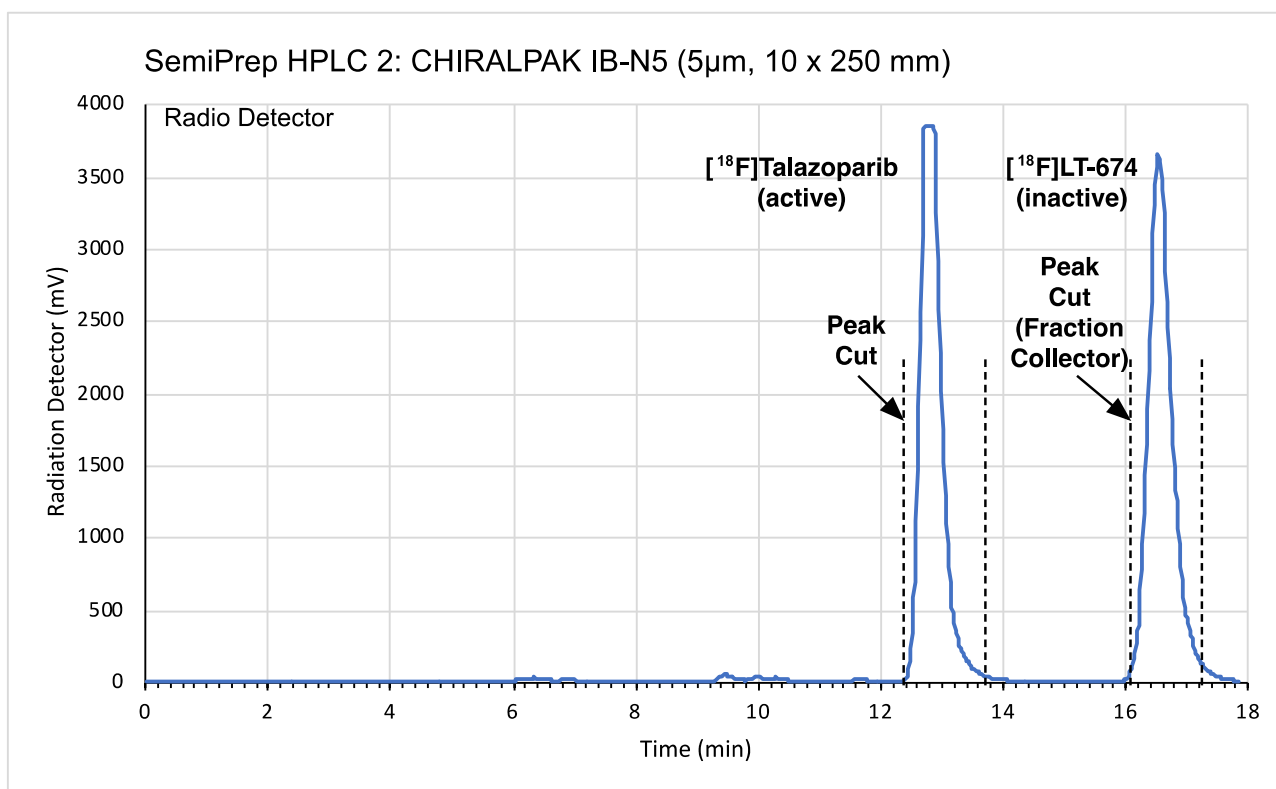


Figure S13: Semipreparative HPLC-based enantiomeric resolution of purified (\pm)[¹⁸F]talazoparib. The radioactive fraction corresponding to either enantiomerically pure [¹⁸F]talazoparib or [¹⁸F]LT-674 was isolated into a collection vessel product concentration and formulation. Data was obtained using an Elixys PURE/FORM purification and formulation system operating with the following parameters: CHIRALPAK IB-N5 (5 μ m, 10 X 250 mm); Isocratic HPLC method: Water + 0.1% TFA: Acetonitrile (60:40); Flowrate: 5 ml/min.

4.5. Analytical Quality Control (QC) HPLC of [¹⁸F]Talazoparib

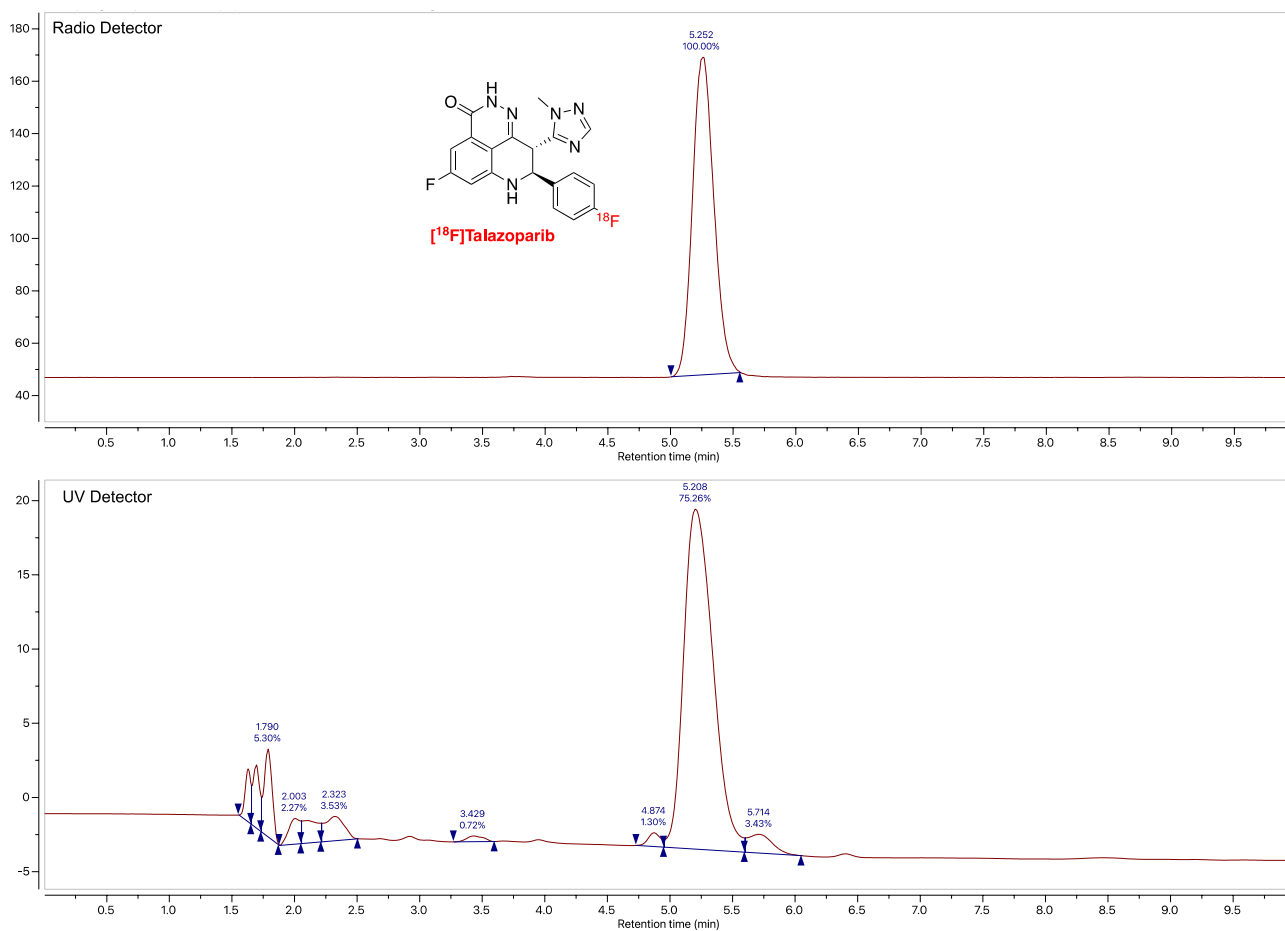


Figure S14: Chiral reversed-phase HPLC analysis of [¹⁸F]talazoparib to verify enantiomeric identity and enantiomeric purity. HPLC Data was acquired using the following conditions: Column: CHIRALPAK IB-N5 (5 μ m, 4.6 X 150 mm); Isocratic HPLC method: Water + 0.1% TFA: Acetonitrile (60:40); Flow rate: 1 ml/min; Injected volume = 25 μ l.

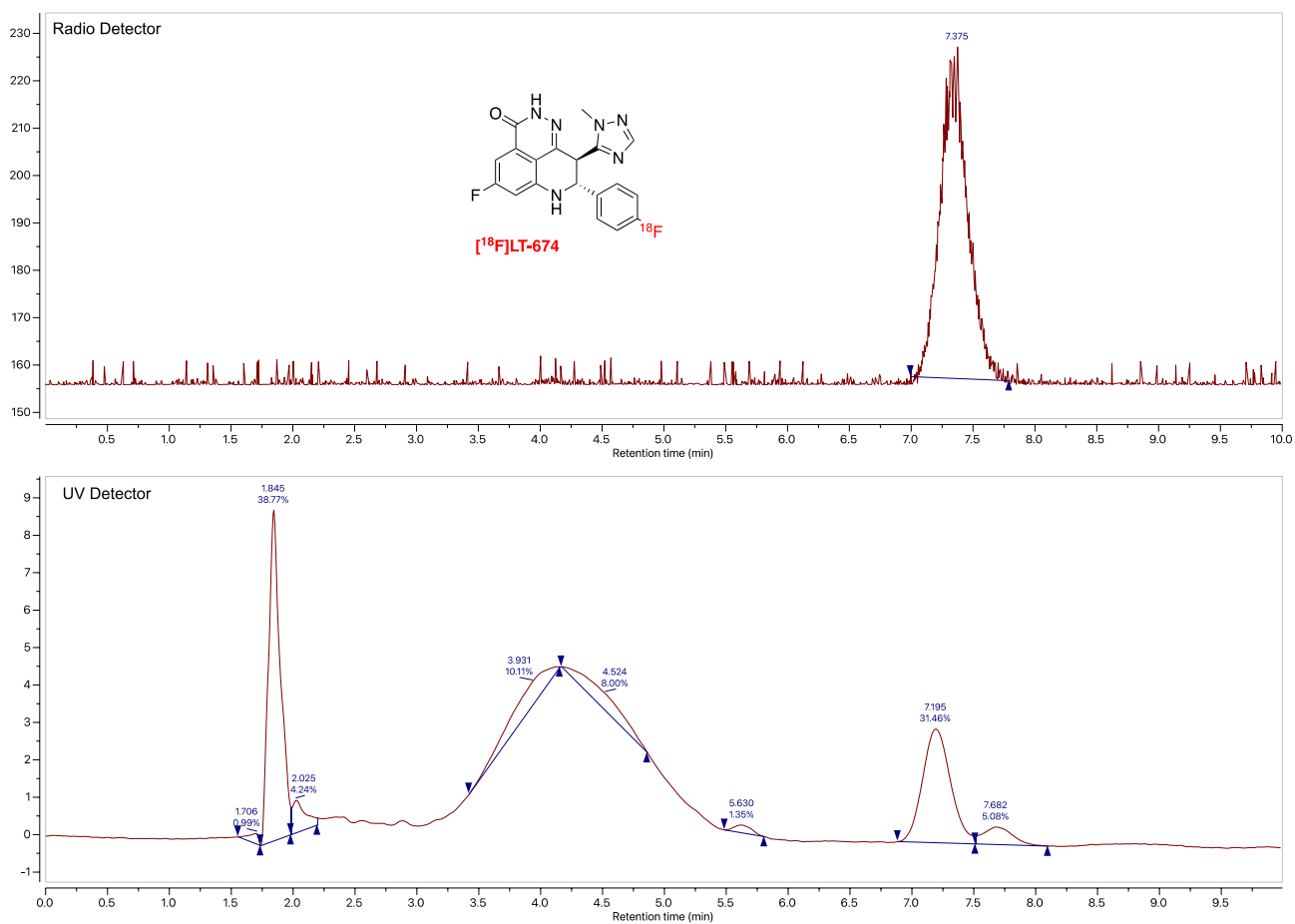


Figure S15: Chiral reversed-phase HPLC analysis of [¹⁸F]LT-674 to verify enantiomeric identity and enantiomeric purity. HPLC Data was acquired using the following conditions: Column: CHIRALPAK IB-N5 (5 μm, 4.6 X 150 mm); Isocratic HPLC method: Water + 0.1% TFA: Acetonitrile (60:40); Flowrate: 1 ml/min; Injected volume = 100 μl.

5. Biological Supplementary Information

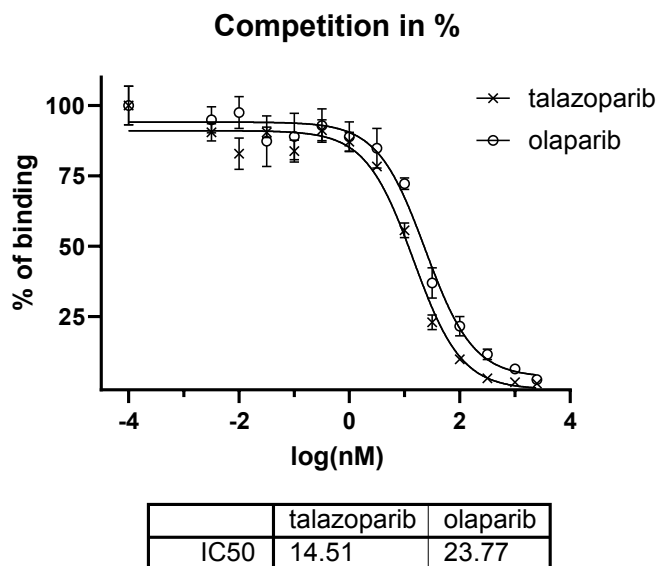


Figure S16: Uptake of [¹⁸F]talazoparib in HCC1937 cells, blocked with different concentrations of olaparib or talazoparib.

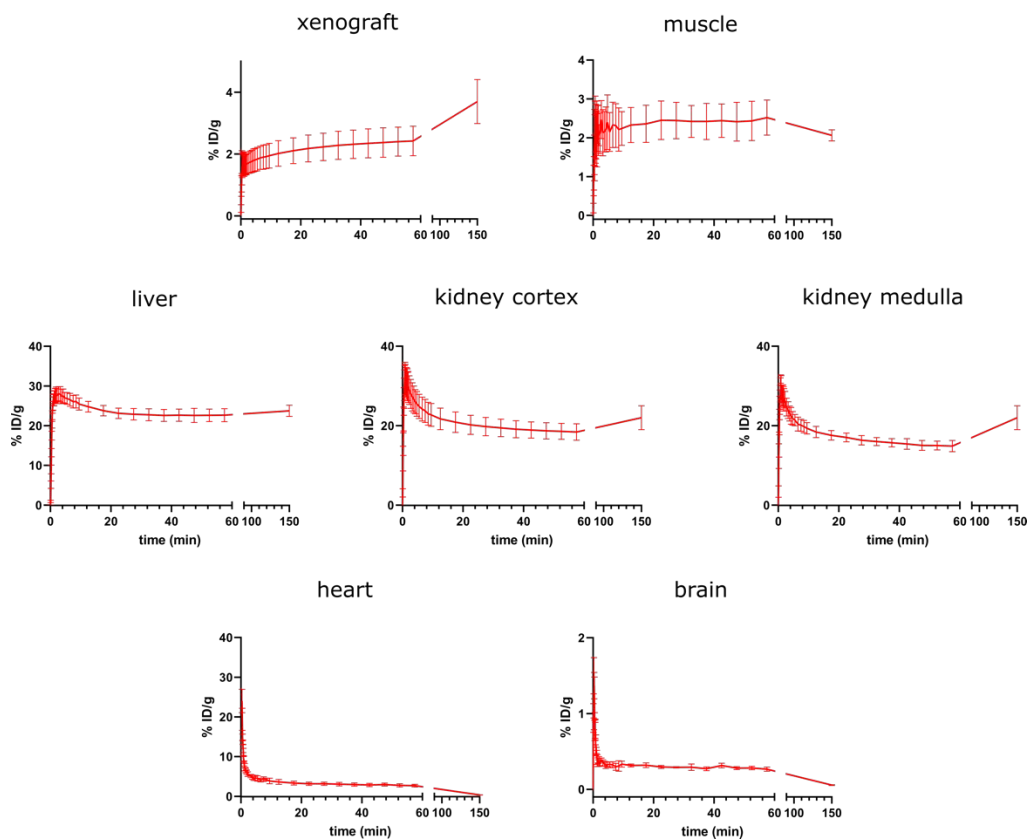


Figure S17: TACs displaying the uptake in the different organs dynamically over a time course of 1 h after injection of [¹⁸F]talazoparib.

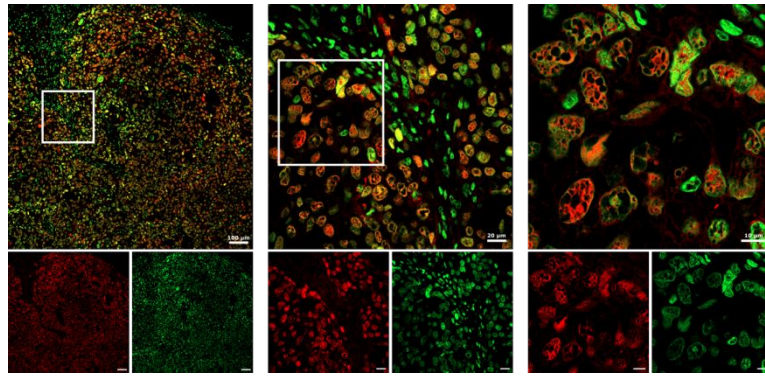


Figure S18: Representative Immunofluorescence Images of HCC1937 xenograft tissue. PARP1 is displayed in red and nuclei are stained in green. Scale bars represent 100 μm (left image), 20 μm (middle image) and 10 μm (right image)

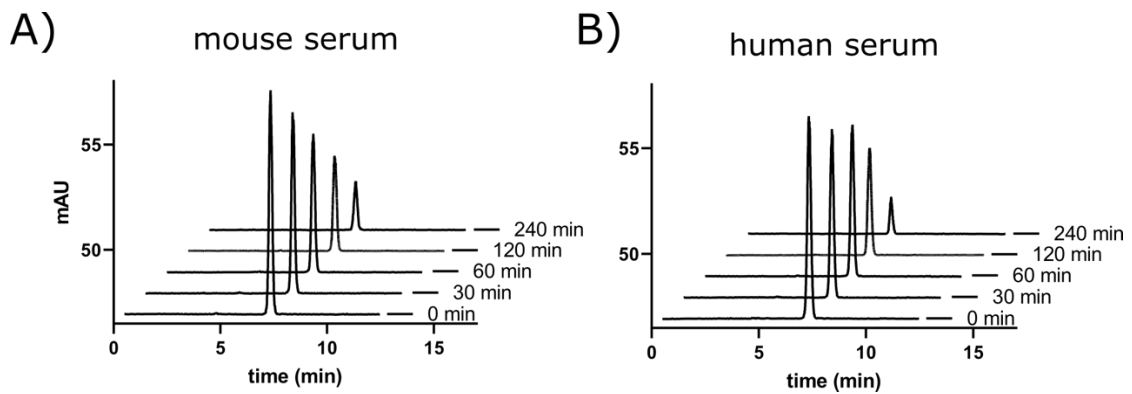


Figure S19: Serum stability of [^{18}F]talazoparib over 240 minutes in A) mouse and B) human serum.

1 h p.i.

2 h p.i.

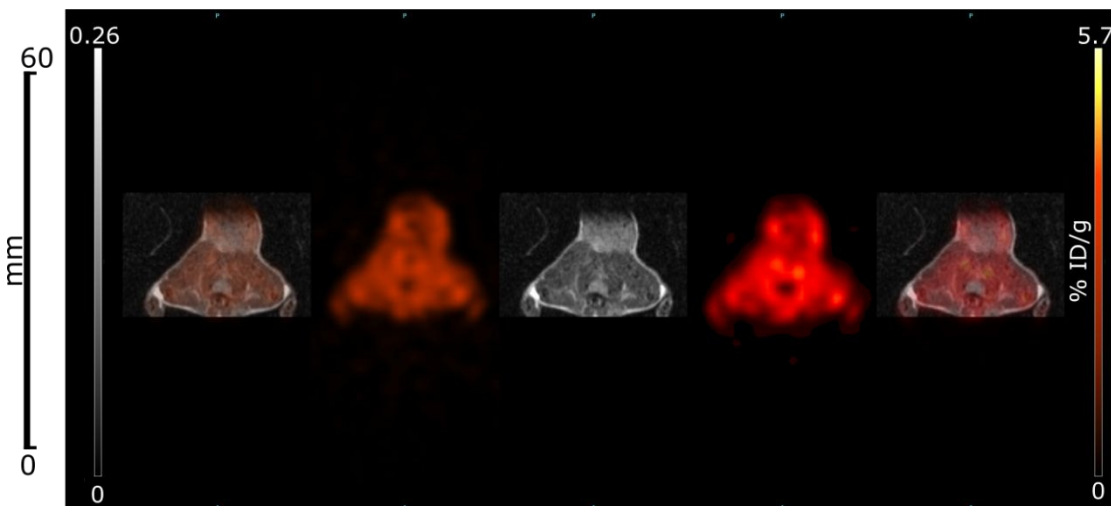


Figure S20: Transverse plane of the animal in Fig. 4 A through the xenograft.

6. Metabolite analysis

To monitor the metabolization of talazoparib, a sample of both talazoparib and propranolol as positive control was incubated with pooled human liver microsomes (Sigma-Aldrich M0567). To do so, microsomes were suspended in phosphate buffer (100 mM, pH 7.4). After the addition of 1.3 mM NADP, a NADPH regenerating system (0.4 U/mL isocitrate dehydrogenase, 3.3 mM isocitrate) and 3.3 mM MgCl₂ as cofactor, 3 μM non-radioactive drug (talazoparib, or propranolol) or 0.4 μM [¹⁸F]talazoparib (37 MBq/ml) were added. Incubation was performed at 37°C at 200 rpm on a thermoshaker. After 0, 5, 15, 30, 60, 90 and 180 min (120 min for the radiotracer), the reaction was quenched by adding the double amount of methanol and subsequent vortexing. Subsequently, samples were centrifuged, and the supernatant was analyzed by LC-MS (for non-radioactive assays) and radio-HPLC (for radioactive experiments).

LC-ESI-MS/MS analysis was performed by a TripleTOF 5600+ (Sciex, Framingham, MA, USA) with DuoSpray Ion Source coupled to a1290 Infinity UHPLC system (Agilent Technologies, Waldbronn, Germany) equipped with PAL HTC-xt autosampler (CTC Analytics, Zwingen, Switzerland). TOF-MS full scan experiment for precursor ion detection was performed in the mass range of *m/z* 100 – 2,000 with an accumulation time of 250 ms. MS/MS experiments were performed in Information Dependent Acquisition mode (high sensitivity mode) with top 6 most abundant precursor ions selected for fragmentation with accumulation time 100 ms. The analytical system was controlled by Analyst TF 1.8.1 (Sciex). Data processing was performed with PeakView 2.2 and MetabolitePilot 1.5 (both Sciex).

As negative control, heat inactivated microsomes (60°C for 45 min) were incubated with talazoparib for 180 min. Negative controls showed no metabolites. Propranolol, a positive control for the CYP1A2, CYP2B6, CYP2C9, CYP2C19 and CYP2D6 enzymes, showed fast transformation into hydroxypropranolol confirming the microsomes to be active under these conditions. In contrast, talazoparib showed high metabolic stability under these conditions, with no significant amounts of monohydroxy-talazoparib formed within 3 h. Similarly, no metabolites were detected in the radioactive experiment.

The high stability is in line with the literature data from the FDA label of Talzenna stating that the majority of the compound is excreted without metabolic modification. When [¹⁴C]talazoparib was administered, 68.7% (54.6% unchanged) were excreted in urine, and 19.7% (13.6% unchanged) was recovered in feces (Talzenna [package insert]. Pfizer Laboratories Div Pfizer Inc. 2018).

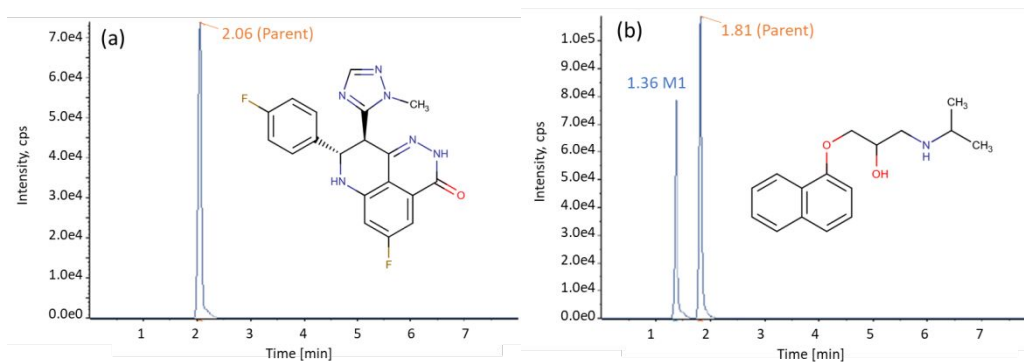


Figure S21: Representative chromatograms of microsomal metabolic stability assay of talazoparib (a) and (b) the positive control propranolol after 180 min. (a) No metabolite was found by MetabolitePilot 1.5 (Sciex) and manual extraction of EIC of monohydroxy-talazoparib (m/z 397.1220 \pm 0.001). m/z (Talazoparib) 381.1330 \pm 0.001. (b) Besides the parent propranolol MetabolitePilot also found hydroxymetabolite (M1) after 180 min. HPLC method: Kinetex C18 (2.6 μ m, 50 x 2.1 mm, Phenomenex); A: water + 0.1% acetic acid; B: acetonitrile + 0.1% acetic acid. 0.00 min: 10% B, 4.00 min: 80% B, 4.50 min: 100% B, 6.00 min: 100% B, 6.01 min: 10% B. Injection volume: 5 μ L; flow rate: 0.35 mL/min.

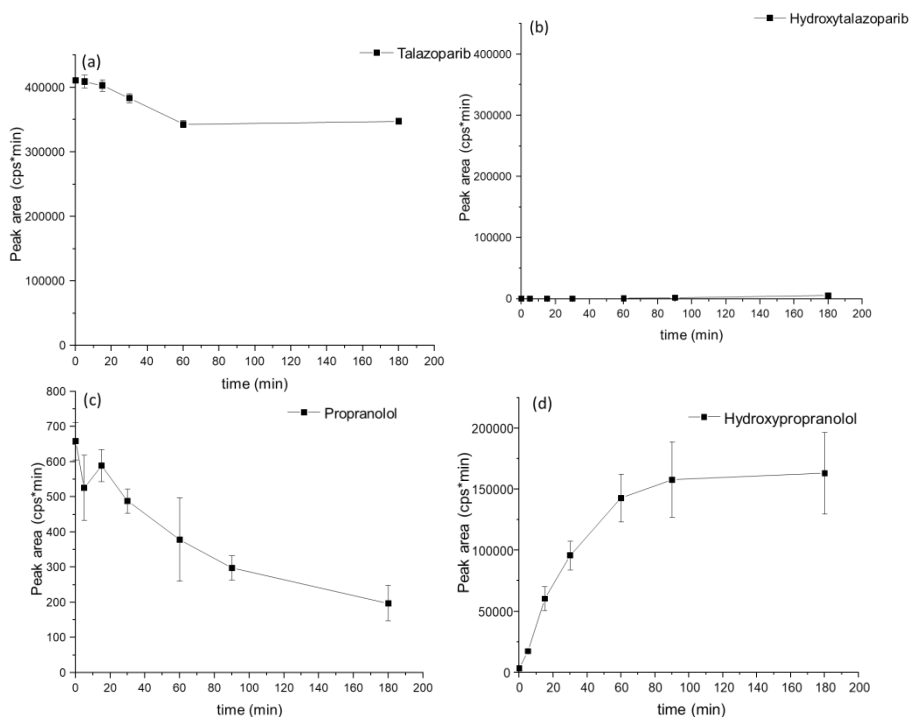


Figure S22: *In vitro* phase I pharmacokinetics documenting metabolic stability of talazoparib by microsomal incubation: (a) talazoparib, (b) monohydroxy-talazoparib, (c) propranolol, (d) hydroxyl-propranolol under different incubation times.

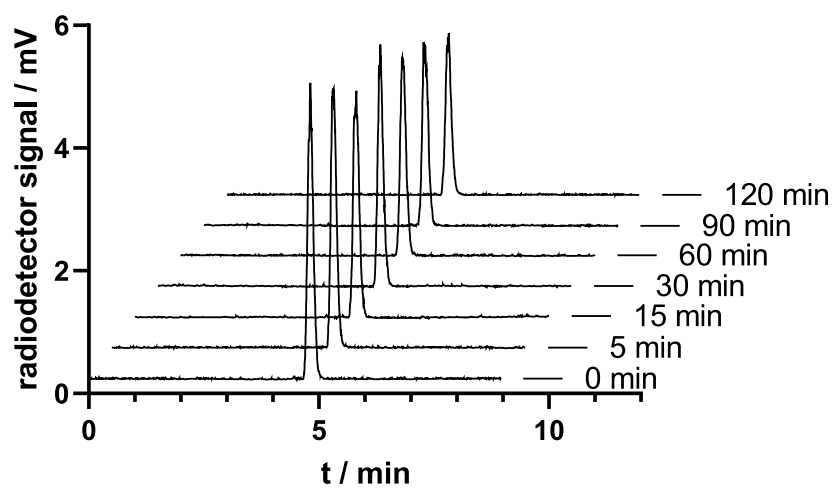


Figure S23: The stability of [^{18}F]talazoparib in the presence of human liver microsomes. No degradation of the tracer was observed. HPLC method: Kinetex C18 (2.6 μm , 50 x 2.1 mm, Phenomenex); A: water + 0.1% TFA; B: acetonitrile. 0.00 min: 5% B, 5.00 min: 100% B, 5.50 min: 100% B, 5.51 min: 5% B. Injection volume: 25 μL ; flow rate: 0.35 mL/min.

3.2.4 Publication VIII: **Discovery and Evaluation of Enantiopure 9H-pyrindo[4,5-b]indoles as Nanomolar GSK-3 β Inhibitors with Improved Metabolic Stability**

Stanislav Andreev¹, Tatu Patsar^{1,2}, Ahmed El-Gokha^{1,3}, Francesco Ansideri¹, Mark Kudolo¹, Débora Bublitz Anton⁴, Giulia Sita⁵, Jenny Romasco⁶, Christian Geibel⁷, Michael Lämmerhofer⁷, Márcia Ines Goettert⁴, Andrea Tarozzi⁶, Stefan A. Laufer¹ and Pierre Koch^{1,8,*}

¹ Institute of Pharmaceutical Sciences, Department of Medicinal and Pharmaceutical Chemistry, Eberhard Karls University Tübingen, Auf der Morgenstelle 8, 72076 Tübingen, Germany

² School of Pharmacy, University of Eastern Finland, P.O. Box 1627, 70211 Kuopio, Finland

³ Menoufia University, Chemistry Department, Faculty of Science, Menoufia, Egypt

⁴ Cell Culture Laboratory, Postgraduate Program in Biotechnology, University of Vale do Taquari (Univates), Lajeado, Brazil

⁵ Department of Pharmacy and Biotechnology, Alma Mater Studiorum-University of Bologna, Via Irnerio, 48, 40126 Bologna, Italy

⁶ Department for Life Quality Studies, Alma Mater Studiorum-University of Bologna, Corso D'Augusto, 237, 47921 Rimini, Italy

⁷ Institute of Pharmaceutical Sciences, Department of Pharmaceutical (Bio-)Analysis, Eberhard Karls University Tübingen, Auf der Morgenstelle 8, 72076 Tübingen, Germany

⁸ Department of Pharmaceutical / Medicinal Chemistry II, Institute of Pharmacy, University of Regensburg, Universitätsstraße 31, 93053 Regensburg, Germany

* Corresponding author. E-mail address: pierre.koch@uni-tuebingen.de, pierre.koch@ur.de (P. Koch)

International Journal of Molecular Sciences **2020**, *21*(21), 7823.

DOI: 10.3390/ijms21217823

© This is an open access article distributed under the Creative Commons Attribution License which permits unrestricted use, distribution, and reproduction in any medium, provided the original work is properly cited. 2020 MDPI.



Article

Discovery and Evaluation of Enantiopure 9H-pyrimido[4,5-*b*]indoles as Nanomolar GSK-3 β Inhibitors with Improved Metabolic Stability

Stanislav Andreev ¹, Tatu Pantsar ^{1,2}, Ahmed El-Gokha ^{1,3}, Francesco Ansideri ¹, Mark Kudolo ¹, Débora Bublitz Anton ⁴, Giulia Sita ⁵ , Jenny Romasco ⁶, Christian Geibel ⁷, Michael Lämmerhofer ⁷ , Márcia Ines Goettert ⁴, Andrea Tarozzi ⁶ , Stefan A. Laufer ¹ and Pierre Koch ^{1,8,*}

¹ Institute of Pharmaceutical Sciences, Department of Medicinal and Pharmaceutical Chemistry, Eberhard Karls University Tübingen, Auf der Morgenstelle 8, 72076 Tübingen, Germany; stanislav.andreev@uni-tuebingen.de (S.A.); tatu.pantsar@uni-tuebingen.de (T.P.); ahmed.abdelaleem@science.menofia.edu.eg (A.E.-G.); francesco.ansideri@uni-tuebingen.de (F.A.); mark.kudolo@uni-tuebingen.de (M.K.); stefan.laufer@uni-tuebingen.de (S.A.L.)

² School of Pharmacy, Faculty of Health Sciences, University of Eastern Finland, P.O. Box 1627, 70211 Kuopio, Finland

³ Chemistry Department, Faculty of Science, Menoufia University, Gamal Abdel-Nasser Street, Shebin El-Kom 32511, Egypt

⁴ Cell Culture Laboratory, Postgraduate Program in Biotechnology, University of Vale do Taquari (Univates), Lajeado 95914-014, Brazil; debora.anton@univates.br (D.B.A.); marcia.goettert@univates.br (M.I.G.)

⁵ Department of Pharmacy and Biotechnology, Alma Mater Studiorum, University of Bologna, Via Irnerio, 48, 40126 Bologna, Italy; giulia.sita2@unibo.it

⁶ Department for Life Quality Studies, Alma Mater Studiorum, University of Bologna, Corso D'Augusto, 237, 47921 Rimini, Italy; jenny.romasco@unibo.it (J.R.); andrea.tarozzi@unibo.it (A.T.)

⁷ Institute of Pharmaceutical Sciences, Department of Pharmaceutical (Bio-)Analysis, Eberhard Karls University Tübingen, Auf der Morgenstelle 8, 72076 Tübingen, Germany; christian.geibel@uni-tuebingen.de (C.G.); michael.laemmerhofer@uni-tuebingen.de (M.L.)

⁸ Department of Pharmaceutical/Medicinal Chemistry II, Institute of Pharmacy, University of Regensburg, Universitätsstraße 31, 93053 Regensburg, Germany

* Correspondence: pierre.koch@uni-tuebingen.de; Tel.: +49-(941)-943-2847

Received: 10 September 2020; Accepted: 16 October 2020; Published: 22 October 2020



Abstract: Glycogen synthase kinase-3 β (GSK-3 β) is a potential target in the field of Alzheimer's disease drug discovery. We recently reported a new class of 9H-pyrimido[4,5-*b*]indole-based GSK-3 β inhibitors, of which 3-(3-((7-chloro-9H-pyrimido[4,5-*b*]indol-4-yl)(methyl)amino)piperidin-1-yl)propanenitrile (**1**) demonstrated promising inhibitory potency. However, this compound underwent rapid degradation by human liver microsomes. Starting from **1**, we prepared a series of amide-based derivatives and studied their structure–activity relationships against GSK-3 β supported by 1 μ s molecular dynamics simulations. The biological potency of this series was substantially enhanced by identifying the eutomer configuration at the stereocenter. Moreover, the introduction of an amide bond proved to be an effective strategy to eliminate the metabolic hotspot. The most potent compounds, (*R*)-3-(3-((7-chloro-9H-pyrimido[4,5-*b*]indol-4-yl)(methyl)amino)piperidin-1-yl)-3-oxopropanenitrile ((*R*)-**2**) and (*R*)-1-(3-((7-bromo-9H-pyrimido[4,5-*b*]indol-4-yl)(methyl)amino)piperidin-1-yl)propan-1-one ((*R*)-**28**), exhibited IC₅₀ values of 480 nM and 360 nM, respectively, and displayed improved metabolic stability. Their favorable biological profile is complemented by minimal cytotoxicity and neuroprotective properties.

Keywords: protein kinase; kinase inhibitor; 9H-pyrimido[4,5-*b*]indole; glycogen synthase kinase-3 β ; metabolic stability

1. Introduction

Glycogen synthase kinase-3 (GSK-3) is a ubiquitously expressed protein existing in two highly related isoforms, GSK-3 α and GSK-3 β [1]. This serine/threonine kinase is involved in several signal cascades and is assumed to phosphorylate more than 30 different substrates, highlighting its multifaceted role in intracellular processes [1,2]. Under physiological conditions, complex mechanisms ensure a strict regulation and proper functionality of this highly multitasking enzyme. In turn, aberrant activity of GSK-3 is assumed to be a critical factor for the development of diverse pathologies, including diabetes, cancer, bipolar disorder, and especially Alzheimer's disease (AD) [3]. In particular, GSK-3 β is implicated in crucial mechanisms associated with AD pathology. These include tau hyperphosphorylation and A β generation, the two major histopathological hallmarks of the disease [4]. Therefore, GSK-3 β is a potential target for novel disease-modifying AD therapeutics motivating drug discovery efforts in the field of small molecule kinase inhibitors.

Recently, we reported on the optimization of a novel class of 7-chloro-9*H*-pyrimido[4,5-*b*]indole-based glycogen synthase kinase-3 β (GSK-3 β) inhibitors, including compound **1** (Figure 1a) [5]. This tertiary alicyclic amine with a promising biological activity on the target enzyme, however, suffered from poor metabolic stability when exposed to human liver microsomes (HLMs). In the HLM stability assay, inhibitor **1** underwent rapid biotransformation, resulting in a limited half-life of approximately 30 min (Figure 1b).

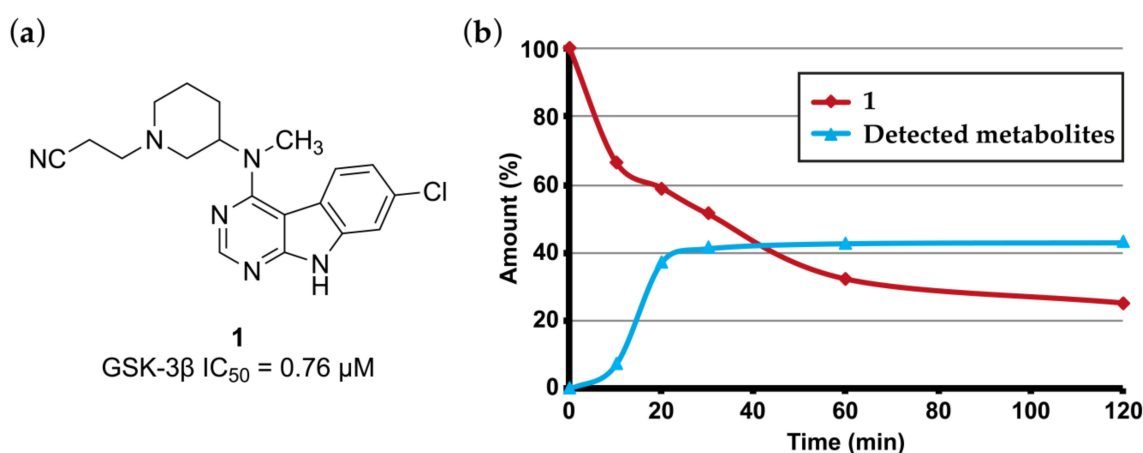
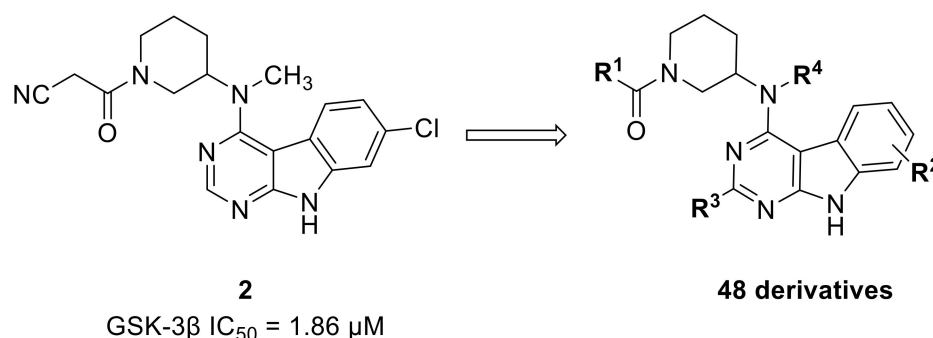


Figure 1. (a) Structure and biological activity of compound **1**; (b) metabolic degradation and formation of detected metabolites of **1**.

Tertiary alicyclic amines represent common yet metabolically vulnerable motifs in pharmaceutical agents. Their oxidative metabolization typically includes chemical modifications such as α -carbonyl introduction and ring opening as well as oxygenation or dealkylation of the nitrogen atom [6]. Correspondingly, the observed metabolic lability of **1** can be ascribed to the (2-cyanoethyl)piperidine substructure of the molecule. The mass spectrometry-based profiling of the metabolites formed from **1** in the HLM experiment indicated an extensive elimination of the cyanoethyl substituent through C–N bond cleavage. However, we found this moiety to be of utmost importance for the biochemical activity of **1** in our preliminary optimization study. This suggests that its removal would compromise the activity of this compound.

Herein, we present a strategy to improve the metabolic stability of this class of 9*H*-pyrimido[4,5-*b*]indole-based GSK-3 β inhibitors while maintaining the biological activity. We hypothesized that the introduction of an acyl substituent on the piperidine nitrogen was a suitable approach to eliminate the potential metabolic hotspot. To this end, we refocused our attention on the reported

amide derivative **2**, which was 2.5-fold less active than **1** [5]. We used this compound as a template in order to design and optimize a series of novel amide-based GSK-3 β inhibitors by applying a variety of structural modifications (Scheme 1). The obtained biological data established structure–activity relationships (SARs), which were substantiated by *in silico* approaches. The most promising candidates were assessed for their metabolic stability in the HLM experiment and further were characterized in cellular assays.



Scheme 1. Development of novel amide-based Glycogen synthase kinase-3 β (GSK-3 β) inhibitors; IC₅₀: halfmaximal inhibitory concentration.

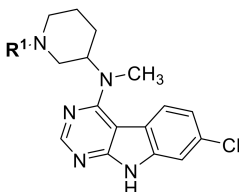
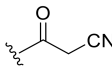
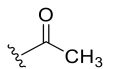
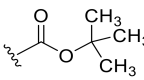
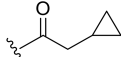
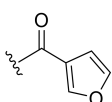
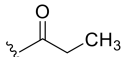
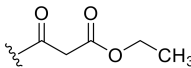
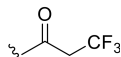
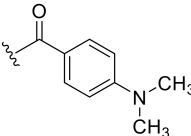
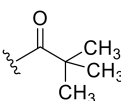
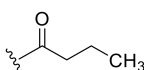
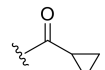
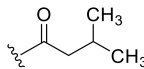
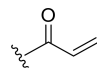
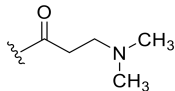
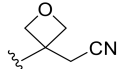
2. Results and Discussion

2.1. Biological Evaluation

In our initial attempts to optimize **2** for GSK-3 β inhibition, we focused on the piperidine nitrogen substituent and evaluated its effect on the compound potency (Table 1). The application of bulky moieties including aromatic rings (**8** and **10**), an ethyl ester function (**9**), or a *tert*-butyloxy group (**6c**) led to inactive compounds. Analogs carrying substituents with longer aliphatic moieties such as butanoyl- (**11**), isovaleryl- (**12**), or cyclopropylacetyl- (**15**) were inactive or exhibited significantly higher IC₅₀ values than **2**. Derivatives with shorter hydrocarbon chains, i.e., cyclopropanoyl- (**39**), acryloyl- (**40**), 3-(dimethylamino)propanoyl- (**13**), and *tert*-butanoyl- (**38**), were found to retain moderate biological activity. In agreement with this trend, a slight potency improvement was seen with the acetyl- and propanoyl-substituted compounds **14** and **16** compared to their cyanoacetyl counterpart. Perhaps surprisingly, the 3,3,3-trifluoropropanoyl derivative **17** was clearly less active than its propanoyl congener **16**. This dramatical difference in potency can be rationalized by the larger van der Waals volume of the CF₃ group as compared to a CH₃ group [7]. These results indicate that only short-chained substituents such as acetyl-, cyanoacetyl-, or propanoyl- are tolerated in this position.

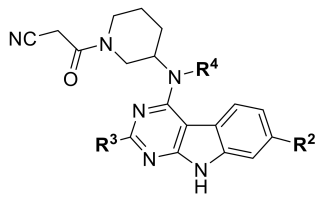
To assess the effect of the carbonyl group functionality, we replaced it with an oxetane ring (**41**). This four-membered heterocyclic motif has been successfully applied in medicinal chemistry programs in order to improve the metabolic stability of drug candidates [8]. The resulting compound **41**, however, displayed a 4-fold higher IC₅₀ value than **2**. An oxetane is considered to form weaker hydrogen bonds than an amide carbonyl group [9]. Thus, we ascertain that carbonyl group-mediated interactions are important for the binding affinity of **2**.

Table 1. Structures and biological activities of compounds **2**, **6c**, **8–17**, and **38–41**.

					
Cpd.	R ¹	IC ₅₀ (μM) Mean ± SEM GSK-3β ^a	Cpd.	R ¹	IC ₅₀ (μM) Mean ± SEM GSK-3β ^a
2		1.86 ± 0.11 ^b	14		1.57 ± 0.30
6c		≥10	15		≥10
8		5.46 ± 1.03	16		1.71 ± 0.52
9		≥10	17		≥10
10		≥10	38		4.39 ± 0.09
11		7.07 ± 1.03	39		3.49 ± 0.66
12		≥10	40		3.92 ± 0.56
13		3.83 ± 0.08	41		6.70 ^c

^a IC₅₀ values were determined in an ADP Glo™ Kinase assay [10,11] (for details, see the Supplementary Materials) and are the means of at least two independent experiments; ^b data taken from [5]; ^c *n* = 1.

The results obtained from the piperidine substituent series highlighted the suitability of both the cyanoacetyl and propanoyl substituent in this position. Based on these results, we elected to maintain both moieties for further optimization and shifted our focus to other positions of the scaffold that are amenable to modification (Table 2).

Table 2. Structures and biological activities of compounds **2**, **18–24**, and **45–50**.


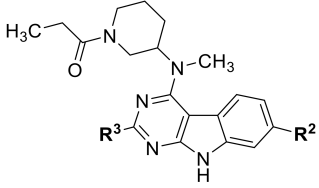
Cpd.	R ²	R ³	R ⁴	IC ₅₀ (μM) Mean ± SEM GSK-3β ^a
18 45	-H	-H	-CH ₃ -H	1.73 ± 0.03 2.17 ± 0.02
19 46	-F	-H	-CH ₃ -H	1.79 ± 0.18 ≥10
2 47	-Cl	-H	-CH ₃ -H	1.86 ± 0.11 ^b 1.29 ± 0.27
20 48	-Br	-H	-CH ₃ -H	1.42 ± 0.16 1.94 ± 0.72
21	-I	-H	-CH ₃	0.94 ± 0.17
22 49	-OCH ₃	-H	-CH ₃ -H	≥10 ≥10
23 50	-CF ₃	-H	-CH ₃ -H	≥10 ≥10
24	-Cl	-CH ₃	-CH ₃	≥10

^a IC₅₀ values were determined in an ADP Glo™ Kinase assay and are the means of at least two independent experiments; ^b data taken from [5].

Replacement of the chlorine atom in the 7-position of the tricyclic core (R² in Table 2) with different halides, i.e., fluorine (**19**), bromine (**20**), and iodine (**21**), as well as removal of this substituent (**18**) was well tolerated. In fact, the inhibitory potency within these compounds marginally increased alongside the van der Waals radii of the halogens. In contrast, the introduction of a methoxy (**22**) or CF₃ (**23**) group in this position gave inactive derivatives, presumably due to a steric clash at the target binding site. Similarly, the addition of a methyl group in the 2-position of the 7-chloro-9H-pyrimido[4,5-*b*]indole (**24**) resulted in a substantial loss in potency. Within this series, the removal of the *N*-methyl group (R⁴ in Table 2) typically proved unfavorable to the activity (**45–50**), which prompted us to maintain this substituent.


Accordingly, the activity trend observed for the halogen series in Table 2 was maintained with the propionamides (Table 3). The only exception was the iodine derivative (**29**), which exhibited a 5-fold reduced potency compared to its bromine counterpart **28**. Unfortunately, no inhibition data could be generated for the methylated propionamide **27** due to insufficient aqueous solubility.

The relocation of the R² substituent to the adjacent 6-position retained potency in the case of chlorine (**30** and **34**) and bromine (**31** and **35**) (Table 4). In contrast to compound **22**, the methoxy substituent was also tolerated in this position (**32** and **36**). However, compounds **33** and **37** carrying chlorine in the 5-position of the tricyclic scaffold suffered from a decrease in activity relative to their regioisomers **2** and **15**.

Table 3. Structures and biological activities of compounds **16** and **25–29**.


Cpd.	R ²	R ³	IC ₅₀ (μM) Mean ± SEM GSK-3β ^a
25	–H	–H	4.58 ± 0.74
26	–F	–H	4.81 ± 0.61
16	–Cl	–H	1.71 ± 0.52
27	–Cl	–CH ₃	n.d. ^b
28	–Br	–H	0.71 ± 0.02
29	–I	–H	3.75 ± 0.65

^a IC₅₀ values were determined in an ADP Glo™ Kinase assay and are the means of at least two independent experiments; ^b not determined.

Table 4. Structure and biological activities of compounds **16** and **30–37** as well as **2**, **20**, and **28** and their enantiopure analogs.


Cpd.	R ²	IC ₅₀ (μM) Mean ± SEM GSK-3β ^a	Cpd.	R ²	IC ₅₀ (μM) Mean ± SEM GSK-3β ^a
2		1.86 ± 0.11 ^b			
(R)-2	7-Cl	0.48 ± 0.04	16	7-Cl	1.71 ± 0.52
(S)-2		≥10			
20		1.42 ± 0.16	28		0.71 ± 0.02
(R)-20	7-Br	0.84 ± 0.07	(R)-28	7-Br	0.36 ± 0.05
(S)-20		≥10	(S)-28		n.d. ^c
30	6-Cl	2.30 ± 0.07	34	6-Cl	1.25 ± 0.03
31	6-Br	2.01 ± 0.20	35	6-Br	1.27 ± 0.47
32	6-OCH ₃	2.54 ± 0.11	36	6-OCH ₃	1.18 ± 0.03
33	5-Cl	8.20 ± 1.27	37	5-Cl	≥10

^a IC₅₀ values were determined in an ADP Glo™ Kinase assay and are the means of at least two independent experiments; ^b data taken from [5]; ^c not determined.

As observed in several instances [12,13], the bioactivity of enantiomers may be strikingly different. The compounds presented in this work have a stereocenter in the 3-position of the piperidine ring. We expected the conformations of the different enantiomers to be unidentical, which motivated us to examine the influence of stereochemistry on the compound activity. To this end, we prepared the enantiopure analogs *(R)*-**2**/*(S)*-**2** and *(R)*-**20**/*(S)*-**20** of inhibitors **2** and **20**, respectively, and determined their IC₅₀ values. Within these two matched pairs, the respective *(S)*-configured enantiomers showed a dramatic loss in activity, while their *(R)*-configured stereoisomers displayed IC₅₀ values in the nanomolar

range. Having identified the eutomer configuration, we also prepared (*R*)-**28**, which followed the same trend and exhibited an improved IC₅₀ value of 360 nM. These findings demonstrated that only the (*R*)-enantiomer displays GSK3β inhibition among these compounds.

2.2. Molecular Modeling

To gain insight into the binding interactions of these amide-based compounds within the ATP site of GSK-3β, we performed 1 μs molecular dynamics (MD) simulations for the most potent inhibitors (*R*)-**2** and (*R*)-**28**. The observed binding modes for (*R*)-**2** and (*R*)-**28** are highly similar and provide plausible explanations for structure–activity relationships of the compound series (Figure 2a,b). Both compounds display extremely stable hydrogen bonding interactions to the hinge region residues Asp133 and Val135 (>95% frequency, Figure S1). The halogen substituent in the 7-position of the tricyclic scaffold (chlorine in (*R*)-**2** and bromine in (*R*)-**28**) is pointing towards the hydrophobic region I of the kinase. Furthermore, the observed low values of ligand root-mean-square deviation (RMSD) highlight the stable binding conformation of both ligands.

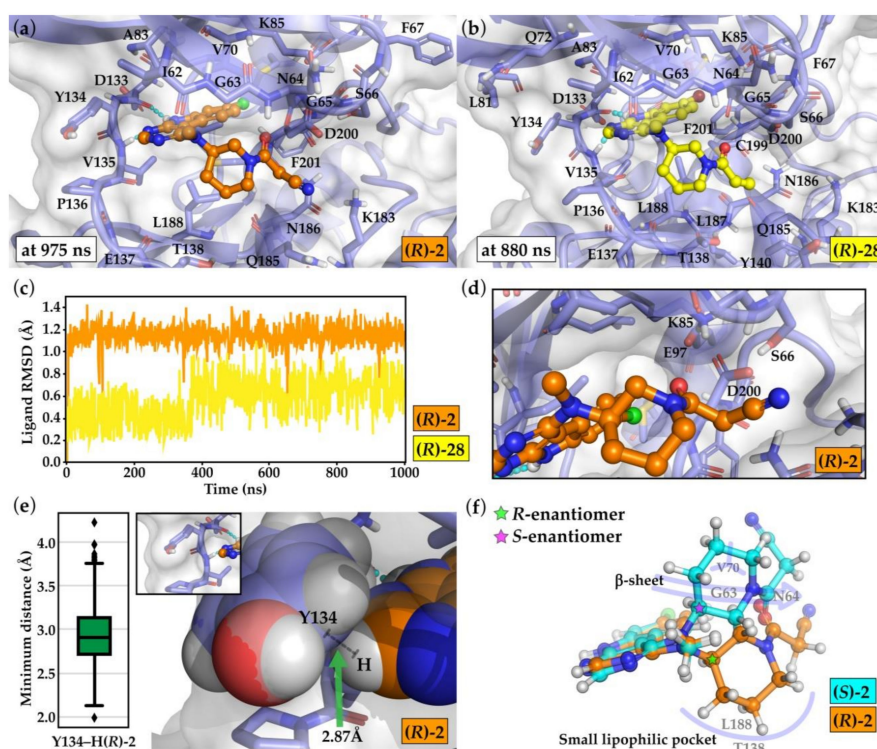


Figure 2. Putative binding mode of the described GSK3β inhibitors: (a) representative snapshot of the (*R*)-**2** binding conformation during the 1 μs molecular dynamics (MD) simulation. All residues located within 4 Å of the ligand during the simulation are shown as sticks. Hydrogen bonds are depicted with cyan dashed lines; (b) representative snapshot of the (*R*)-**28** binding conformation during the 1 μs MD simulation; (c) the ligands appear extremely stable in the shown conformation throughout the simulations as demonstrated by their root-mean-square deviation (RMSD) values; (d) the carbonyl oxygen points towards the polar residues Asp200, Lys85, Ser66, and Glu97 but does not form any specific direct interactions with GSK-3β; (e) the proton in the 2-position of the pyrimidine ring is in close proximity to the side chain of Tyr134. Here, the conformation of (a) is illustrated, where the distance is 2.87 Å. The (*R*)-**2** and Tyr134 atoms are shown as spheres representing their van der Waals radius; and (f) comparison of the preferred quantum mechanics (QM)-derived conformations of the different enantiomers of **2**. (*S*)-**2** is unable to obtain the binding conformation as observed for (*R*)-**2**. In the preferred (*S*)-**2** conformation, the piperidine ring would clash with the β-sheet and Val70 and would not occupy the small lipophilic pocket formed by Leu188 and Thr138.

The carbonyl oxygen, which points towards the polar residues Asp200, Lys85, Ser66, and Glu87, does not form any direct interactions to any residues of GSK3 β throughout the simulations (Figure 2d). Nevertheless, water-mediated interactions are evident for the carbonyl group (Figure S1), which might explain the enhanced activity of **2** compared to its oxetane bioisoster **41**.

The piperidine ring of both compounds occupies a small lipophilic pocket formed by Leu188 (and Thr138) in the bottom of the binding site (Figure 2a,b). The amide substituent on the piperidine nitrogen atom is oriented towards the solvent interface with polar residues, e.g., Lys183. We postulate that this space, which does not present any suitable binding sites for accommodation, especially of bulkier lipophilic substituents, provides an explanation for the observed activity trends in Table 1.

The proton in the 2-position of the pyrimidine ring is in close proximity and in contact with the side chain of hinge residue Tyr134 (Figure 2e). This observation offers an explanation for the inactivity of 2-methyl derivative **24**, as this substitution would result in a steric clash with the side chain of Tyr134.

The remarkable activity difference among the stereoisomers can be realized via the comparison of the preferred quantum mechanics (QM)-derived conformations of (*R*)-**2** and (*S*)-**2** (Figure 2f). The superimposition of the enantiomers clearly demonstrates that a favorable configuration of the piperidine is not possible for (*S*)-**2**. This enantiomer not only would be unable to occupy the small lipophilic pocket but also would clash with the β -sheet next to the G-loop (Figure 2f).

2.3. Microsomal Stability

As our initial aim was to improve the metabolic stability of the compounds, we evaluated the most potent enantiomers (*R*)-**2** and (*R*)-**28** in our in-house microsomal stability assay. To this end, the compounds were incubated with pooled male and female HLM for 120 min, and the compound degradation as well as the formation of metabolites was monitored by liquid chromatography-mass spectrometry (LC-MS) analysis.

In contrast to the labile tertiary amine **1**, the enantiopure cyanoacetamide compound (*R*)-**2** displayed a favorable metabolic profile in the microsomal stability assay (Figure 3a). The metabolization of this inhibitor was characterized by a slower degradation rate and consequently a larger fraction of intact compound after the time span of 120 min. Some metabolites with an *m/z* ratio of 399 were detected in the LC-MS analysis and likely result from monooxygenation of the parent compound. However, no elimination of the piperidine nitrogen substituent was seen, which supports our initial hypothesis concerning stability of the amide bond.

The propanoyl analog (*R*)-**28** even showed a slightly enhanced stability compared to its cyanoacetamide counterpart. Nearly 70% of unchanged inhibitors was detected after the incubation time of 120 min (Figure 3b). We assume that this noticeable decrease in decomposition can be attributed to the lack of the metabolically vulnerable nitrile group. Similar to (*R*)-**2**, the LC-MS-based metabolite profiling indicates formation of oxygenated derivatives of (*R*)-**28** yet no cleavage of the piperidine amide bond.

2.4. Cell Data

To extend the biological profile of inhibitor (*R*)-**28**, we evaluated the in vitro cytotoxic potential of this compound on a variety of cell lines. These included two wild-type cell lines (human lung fibroblast cell line MRC-5 and Chinese hamster ovary cell line CHO-K1) as well as three cancer cell lines (hepatocellular carcinoma cell line HepG2, human breast adenocarcinoma cell line MCF-7, and human neuroblastoma cell line SH-SY5Y). The cells were treated with different concentrations of (*R*)-**28**, and their viability was assessed by the 3-(4,5-dimethylthiazol-2-yl)-2,5-diphenyltetrazolium bromide (MTT) colorimetric assay (for details, see Supplementary Materials). Even at the highest tested concentration of 10 μ M, minimal to no cytotoxic effects were seen for (*R*)-**28** on all cell lines, demonstrating a highly favorable cytotoxicity profile (Figures S2 and S3).

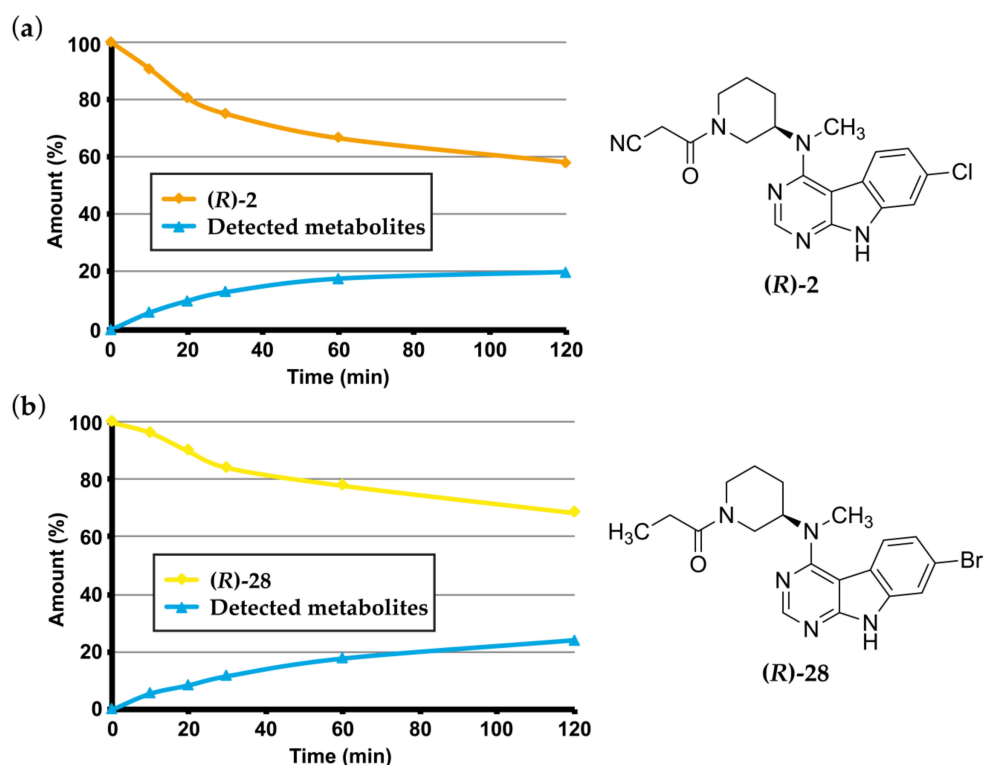


Figure 3. Microsomal degradation and formation of detected metabolites of (a) (R)-2 and (b) (R)-28 during the incubation time of 120 min.

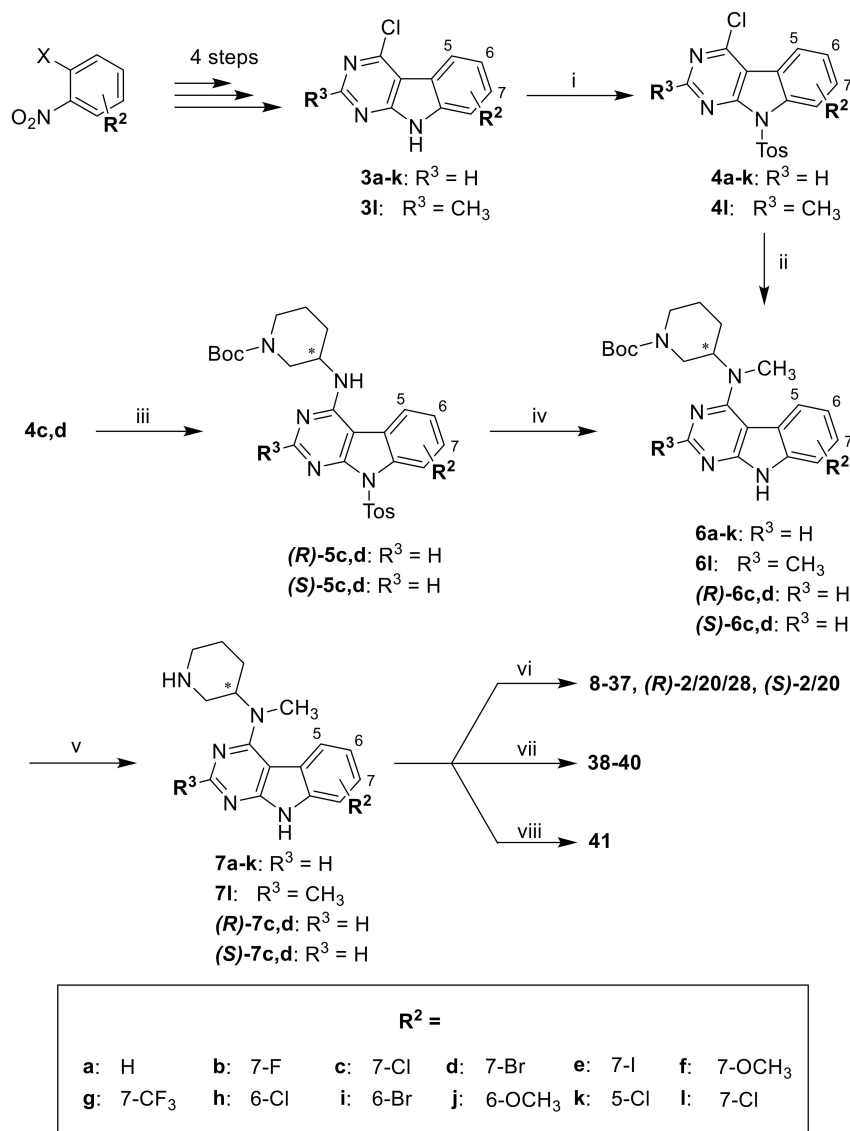
These results motivated us to further characterize compound (R)-28 by its ability to inhibit GSK-3 β and to exert neuroprotective effects in neuronal SH-SY5Y cells (for details, see Supplementary Materials). Initially, we determined the concentrations of (R)-28 not associated to neurotoxicity by the MTT assay [14]. Therefore, concentrations of 1 and 5 μ M were selected for the assays in SH-SY5Y cells, which were performed according to previously described protocols [15–17]. At the tested concentration of 1 μ M, (R)-28 inhibited GSK3 β activity in terms of inactive phospho-GSK3 α/β (Ser21/9) increase and active phospho-GSK3 α/β (Tyr279/Tyr216) decrease after 1 h of treatment in neuronal SH-SY5Y cells (Figure S4).

Next, we investigated the neuroprotective effects of (R)-28 in SH-SY5Y cells against the neurotoxicity induced by neurotoxins. These included hydrogen peroxide (H₂O₂, 100 μ M) and amyloid- β 1–42 oligomers (OA β _{1–42}, 10 μ M), that mimic general oxidative stress and Alzheimer's disease (AD), respectively. In these experiments, the concomitant treatment of 5 μ M (R)-28 with neurotoxins significantly decreased the neurotoxicity elicited by H₂O₂ but not OA β _{1–42} (Figure S5). Still, these neuroprotective effects against the oxidative stress underline the potential usefulness of inhibitor (R)-28 in the AD therapeutic area.

2.5. Chemistry

We previously reported a synthetic route for the preparation of compound 2 [5]. This strategy demonstrated broad applicability within the herein presented study, as it provided access to the majority of final compounds with only minor alterations in the experimental protocols (Scheme 2). 4-Chloro-9H-pyrimido[4,5-b]indoles 3a–l were prepared in four steps from commercially available *o*-halonitrobenzenes according to modified literature procedures (for details, see Supplementary Materials) [5,18–20]. These tricyclic intermediates were protected by a tosyl group on the indole nitrogen, resulting in 4a–l. The aliphatic side chain was then introduced by treatment of 4a–l with appropriate amines under basic conditions. In the case of 6a–l, we used racemic 1-Boc-3-(methylamino)piperidine, which was prepared as described previously [5]. For the synthesis of

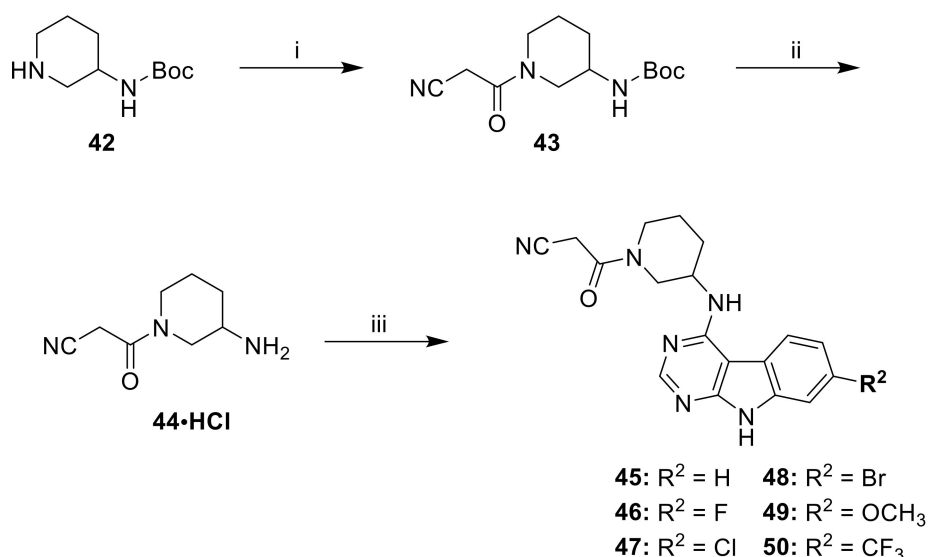
analogues (*R*)-5c,d and (*S*)-5c,d, enantiopure 1-Boc-3-aminopiperidine building blocks were utilized. This demanded an additional methylation step, which was carried out with methyl iodide under strictly anhydrous, basic conditions [21]. Subsequent cleavage of the orthogonal protecting groups furnished precursors 7a–l, (*R*)-7c,d, and (*S*)-7c,d, which were acylated on the piperidine nitrogen to access the final compounds.



Scheme 2. Synthetic route to final compounds 8–41, (*R*)-2/20/28, and (*S*)-2/20 listed with their structures in Tables 1–4. Reagents and conditions: (i) *p*-toluenesulfonyl chloride, NaH, THF, rt (82%-quant.); (ii) (1) 1-Boc-3-(methylamino)piperidine, DIPEA, DMF, 70 °C, (2) *K*tBuO or Na*t*BuO, THF or DMF, rt (43–74% over two steps); (iii) (*R*)-1-Boc-3-aminopiperidine in case of (*R*)-5c,d or (*S*)-1-Boc-3-aminopiperidine in case of (*S*)-5c,d, DIPEA, DMF, 70 °C (62–80%); (iv) (1) methyl iodide, NaH, DMF, –10 °C to rt, (2) *K*tBuO, THF, rt (24–70% over two steps); (v) TFA, DCM, rt (76%-quant.); (vi) corresponding carboxylic acid, appropriate amide coupling reagent, DIPEA or TEA, DCM, rt (22–83%); and (vii) 7c, corresponding acid chloride, DIPEA, THF or DCM, 0 °C to rt (47–76%); (viii) 7c, 2-(oxetan-3-ylidene)acetonitrile, EtOH, 70 °C (76%). Abbreviations: THF: tetrahydrofuran; DMF: dimethylformamide; DIPEA: *N,N*-diisopropylethylamine; TFA: trifluoroacetic acid; DCM: dichloromethane; DCC: *N,N'*-dicyclohexylcarbodiimide; TEA: triethylamine; rt: room temperature.

Searching for a generally applicable and regioselective amide coupling procedure, various reagents including 3-(ethyliminomethylideneamino)-*N,N*-dimethyl-propan-1-amine (EDCI), benzotriazol-1-yl-oxytripyrrolidinophosphonium hexafluorophosphate (PyBOP), and *O*-(benzotriazol-1-yl)-*N,N,N',N'*-tetramethyluronium tetrafluoroborate (TBTU) were tested. The application of EDCI suffered from a slow and inefficient conversion, while utilizing PyBOP required a laborious separation of the liberated tri(pyrrolidin-1-yl)phosphine oxide. In contrast, the use of TBTU conveniently provided the final compounds in short reaction times and high purity and thus became the method of choice in the course of the project. In addition, compounds **38**, **39**, and **40** were prepared using commercially available acid chlorides applying common procedures. Compound **41** was accessible via Michael reaction of **7c** with 2-(oxetan-3-ylidene)acetonitrile (synthesized from (triphenylphosphoranylidene)acetonitrile [22] and oxetan-3-one according to the literature [9]) [23].

For convenient access to the *N*-desmethyl analogs **45–50**, a 3-aminopiperidine building block with a preinstalled cyanoacetyl substituent (**44**) was synthesized (Scheme 3). Following a published protocol, 3-(Boc-amino)piperidine (**42**) was coupled with cyanoacetic acid in the presence of *N,N'*-dicyclohexylcarbodiimide (DCC) furnishing **43**, which was Boc-protected with HCl in dioxane to afford the hydrochloride salt of **44** [21]. This precursor was reacted with the appropriate 4-chloro-9-tosyl-9*H*-pyrimido[4,5-*b*]indoles (**4a–d** and **4f,g**), and the resulting S_NAr products were finally detosylated to obtain **45–50**.



Scheme 3. Synthetic route to final compounds **45–50** listed with their structures in Table 2. Reagents and conditions: (i) cyanoacetic acid, DCC, DCM, 0 °C to rt (71%); (ii) 4*N* HCl in dioxane, THF, rt (96%); and (iii) (1) corresponding 4-chloro-9-tosyl-9*H*-pyrimido[4,5-*b*]indole (**4a–d** and **4f–g**), DIPEA, DMF, 70 °C and (2) *K*tBuO or *Na*tBuO, THF or DMF, rt (7–53% over two steps). Abbreviations: THF: tetrahydrofuran; DMF: dimethylformamide; DIPEA: *N,N*-diisopropylethylamine; TFA: trifluoroacetic acid; DCM: dichloromethane; DCC: *N,N'*-dicyclohexylcarbodiimide; TEA: triethylamine; rt: room temperature.

2.6. Conclusion

We used the moderately potent 9*H*-pyrimido[4,5-*b*]indole **2** as a lead structure to design a series of novel amide-based GSK-3 β inhibitors. The newly synthesized compounds were evaluated for their biological activity on the targeted kinase in an ADP Glo™ assay. Compounds **2** and **28** demonstrated an optimized scaffold decoration pattern for GSK-3 β inhibition. Remarkably, we observed a strong influence of the stereoconfiguration on the activity of this compound series. The (*R*)-enantiomers were found to be nanomolar inhibitors of GSK-3 β , while a substantial loss in activity was seen with the (*S*)-configured counterparts. Furthermore, the most potent nanomolar inhibitors (**R**)-**2** and (**R**)-**28** and

their binding modes were examined by 1 μ s molecular dynamics simulations, rationalizing the SARs of the series. Most importantly, these inhibitors exhibited enhanced stability in the HLM assay as well as a minimal toxicity along with neuroprotective effects in a cellular context. The favorable properties of these compounds motivate additional studies to further assess the biological effects of this class of GSK-3 β inhibitors and to finally elucidate the binding mode to the target enzyme.

3. Materials and Methods

3.1. Molecular Modelling

All in silico work was conducted with Maestro (Schrödinger Release 2019-3/4: Maestro, Schrödinger, LLC, New York, NY, USA, 2019) using OPLS3e force field [24]. Illustrations were made with PyMOL (The PyMOL Molecular Graphics System, Version 2.2.3 Schrödinger, LLC, New York, NY, USA, 2020). First, we prepared the ligands (**R**)-**2** and (**R**)-**28** with LigPrep (Schrödinger, LLC) and then optimized their conformations with the QM Conformer & Tautomer Predictor tool (Schrödinger, LLC), which utilizes Jaguar [25]. In short, this tool optimizes conformations of the compounds with increasing levels of theory, starting with semiempirical method and using density functional theory (DFT) with M06-2X/cc-pVTZ(-f) in the final step. For more detailed description of the QM Conformer & Tautomer Predictor protocol, see the supplementary information in [26]. Next, the ligand of the Protein preparation wizard [27] prepared and energy-minimized GSK-3 β structure (PDB ID: 4PTC) [28] was manually replaced with the lowest energy QM-derived structure of (**R**)-**2** or (**R**)-**28**. After this, the new complex was prepared for simulations with the Protein preparation wizard [27]. For MD simulations, we used Desmond [29]. The systems were solvated in the cubic box with the minimum distance to the edges of 13 Å from the protein and neutralized with Cl⁻ ions, adding a total of 0.15 M KCl salt. The water molecules were described with the TIP3P water model [30]. The production simulations of 1000 ns were run with NpT ensemble ($T = 310$ K, Nosé–Hoover method; $p = 1.01325$ bar, Martyna–Tobias–Klein method) with the default Desmond settings as described previously [5]. Before the actual production run, the default Desmond relaxation protocol was applied for both systems. For the conformation comparison of different enantiomers of **2** (in Figure 2f), (**S**)-**2** was also prepared with the QM Conformer & Tautomer Predictor tool with the same default settings as (**R**)-**2**, and they were superimposed by their hinge binding moieties.

3.2. Chemistry

3.2.1. General Information

All solvents and reagents were purchased from commercial sources and used without further purification, if not stated otherwise. Organic solvents used for analytical chromatography were generally of HPLC grade.

High performance liquid chromatography (HPLC) was performed on a Hewlett Packard HP1090 series II HPLC system (Hewlett-Packard, Palo Alto, CA, USA) or an Agilent 1100 series HPLC system (Agilent, Santa Clara, CA, USA) equipped with a diode array detector detecting at 230 nm and 254 nm. Method A consisted of elution using mobile phase A (MeOH) and mobile phase B (aqueous 0.01 M KH₂PO₄ buffer, pH 2.3) in a flow of 1.5 mL/min on a Phenomenex Luna 5 μ m C8(2) 100 Å RP column (150 \times 4.6 mm) (Phenomenex, Torrance, CA, USA) and the gradient as follows: mobile phase A 40% to 85% during 8 min, mobile phase A 85% constant for 5 min, mobile phase A 85% to 40% during 1 min, mobile phase A 40% constant for 2 min; complete run time 16 min; injection volume 5 μ L. Method B consisted of elution using the same mobile phases in a flow of 1.5 mL/min on an XBridge C18 5 μ m RP column (150 \times 4.6 mm) (Waters, Milford, MA, USA) and the gradient as follows: mobile phase A 45% to 85% during 10 min, mobile phase A constant for 6 min; complete run time 16 min; injection volume 10 μ L. The purity of the final compounds was determined at 254 nm and was >95%.

Final compounds (**R**)-2/(**S**)-2, (**R**)-20/(**S**)-20, and (**R**)-28 were evaluated for their enantiomeric purity by chiral chromatography, which was performed on an Agilent 1290 Infinity series LC system (Agilent, Santa Clara, CA, USA) consisting of a binary pump, a thermostatted column compartment, an autosampler, and a diode array detector. The system was provided with an ultralow dispersion kit (including a Max-Light ultralow dispersion cartridge flow cell with an inner volume of 0.6 μ L, an ultralow dispersion needle seat, and capillaries with 0.075-mm inner diameter from autosampler to column compartment (350 mm length) and from column compartment to DAD (220 mm length)) to minimize extra column volume. The method consisted of elution using the mobile phase (64% n-heptane/36% isopropanol) in a flow of 0.4 mL/min on a Chiralpak IA-U 1.6 μ m column (100 \times 3.0 mm) (Daicel, Osaka/Tokyo, Japan); injection volume was 5 μ L. Samples of the stereoisomers and racemates were prepared by diluting 10 mM aliquotes in dimethyl sulfoxide (DMSO) by the factor 10 with the mobile phase to a total concentration of 1 mM. The purity was determined at 254 nm. The enantiomeric excess (ee) was >98% in all cases.

Thin layer chromatography—electrospray ionization—mass spectrometry coupled analysis (TLC-ESI-MS) was performed on an Advion expression^s CMS coupling system (Advion, Ithaca, NY, USA). The parameters of the ESI+ mode were as follows: capillary temperature 250 °C, capillary voltage 180 V, source gas temperature 250 °C, and ESI voltage 3500 V. The parameters of the ESI- mode were as follows: capillary temperature 250 °C, capillary voltage 180 V, source gas temperature 250 °C, and ESI voltage 2500 V. The compounds were eluted from the TLC plate with MeOH.

Flash column chromatography was performed on an Interchim puriflash 430 or XS 420 (Interchim, Montluçon, France) on Grace Davison Discovery Sciences DAVISIL Chromatographic Silica Media LC60A (20–45 μ m) (Grace Davison Discovery Sciences, MD, USA) or Interchim puriflash prepac silica columns (SIHP-JP, 30 μ m) (Interchim, Montluçon, France). For preparation of pre-columns, Merck Geduran Si60 63–200 μ m silica gel (Merck, Darmstadt, Germany) was used. Mobile phases for each compound were described in the respective experimental procedure.

¹H and ¹³C Nuclear magnetic resonance (NMR) analysis was performed on 200, 300, and 400 MHz Bruker Avance and 400 MHz Bruker Ascend spectrometers (Bruker, Billerica, MA, USA). Spectra were calibrated to residual peaks of the utilized deuterated solvents. Chemical shifts were reported in parts per million (ppm) relative to tetramethylsilane ($\delta = 0$). NMR spectra of compounds with acyl substituents on the piperidine nitrogen frequently showed mixtures of amide bond rotamers resulting in complex reports. The ratio of rotamers was estimated from the respective integrals in the ¹H-NMR spectra.

Thin layer chromatography (TLC) was performed on silica gel coated aluminum sheets (Merck TLC Silica gel F₂₅₄, Merck, Darmstadt, Germany or Macherey-Nagel Alugram Sil G/UV₂₅₄, Macherey-Nagel, Düren, Germany), detected under UV light (254 nm).

3.2.2. General Procedures

(1) General Procedure A

The appropriate intermediate (**3a,b** and **3d-1**) was suspended in dry tetrahydrofuran (THF). NaH was added, and the mixture was stirred at room temperature (rt) and under N₂ atmosphere for 15–30 min. *p*-Toluenesulfonyl chloride was added, and the mixture was stirred at rt and under N₂ atmosphere until reaction control by TLC indicated complete consumption of the starting material. The reaction mixture was poured into ice-cold, water and saturated NH₄Cl solution was added. The precipitate was filtered off, rinsed with fresh demineralized water, and dried over P₂O₅ in vacuo. The crude product was used in the next step without further purification.

(2) General Procedure B

The appropriate intermediate (**4a-1**) was suspended in dry dimethylformamide (DMF). *N,N*-diisopropylethylamine (DIPEA) and the appropriate Boc protected secondary amine were added,

and the mixture was stirred at 70–80 °C until reaction control by HPLC indicated sufficient consumption of the starting material. After cooling down to rt, the mixture was poured into ice-cold water and saturated NH₄Cl solution was added. The resulting precipitate was filtered off, rinsed with fresh demineralized water, and dried over P₂O₅ in vacuo. The crude product was used in the next step without further purification, if not stated otherwise.

(3) General Procedure C

A solution of the appropriate intermediate ((**R**)-**5c,d** and (**S**)-**5c,d**) in dry DMF was stirred in a flame-dried Schlenk tube under Ar atmosphere and ice-cooling. NaH was added, and the mixture was left to stir for 30 min for deprotonation. Cooling was then switched to a MeOH ice bath prior to adding methyl iodide. The mixture was left to warm to 0 °C and then to rt and stirred under Ar atmosphere until HPLC indicated sufficient consumption of the starting material. The mixture was then poured into ice-cold saturated NH₄Cl solution. The resulting precipitate was filtered off, washed with demineralized, and dried over P₂O₅ in vacuo. The crude product was used in the next step without further purification, if not stated otherwise.

(4) General Procedure D

The appropriate intermediate was dissolved in THF (dry or HPLC grade). *K*tBuO was added, and the mixture was stirred at rt and under N₂ atmosphere until reaction control by HPLC indicated complete consumption of the starting material. Saturated NH₄Cl solution and ethyl acetate (EtOAc) were added to the reaction mixture, and phases were separated. The aqueous layer was extracted with EtOAc (2–3×). Combined organic layers were dried over Na₂SO₄ and concentrated under reduced pressure. The residue was purified by flash column chromatography.

(5) General Procedure E

The appropriate intermediate (**6a,b**, **6d-l**, (**R**)-**6c,d**, and (**S**)-**6c,d**) was stirred in a 17% (*v/v*) mixture of dry dichloromethane (DCM) and trifluoroacetic acid (TFA) at rt and under N₂ atmosphere until reaction control by HPLC indicated complete consumption of the starting material. The mixture was concentrated under reduced pressure, and saturated NaHCO₃ solution was added to neutralize residual TFA. The mixture was then extracted repeatedly with EtOAc. MeOH was added to improve the solubility of the product in the organic layer. Combined organic layers were washed with saturated NaHCO₃ solution (3×), dried over Na₂SO₄, and evaporated to dryness. The crude product was used in the next step without further purification, if not stated otherwise.

(6) General Procedure F

The appropriate carboxylic acid and PyBOP or TBTU were stirred in dry DCM for 15–30 min at rt and under N₂ atmosphere. A mixture of the appropriate intermediate (**7a-l**, (**R**)-**7c,d**, and (**S**)-**7c,d**) and DIPEA in dry DCM was added to the activated carboxylic acids and the reaction mixture stirred at rt and under N₂ atmosphere until reaction control by HPLC indicated complete consumption of the starting material. The mixture was diluted with DCM, washed with saturated NaHCO₃ solution (2–3×) and saturated NH₄Cl solution (2–3×), dried over Na₂SO₄, and concentrated under reduced pressure. The residue was purified by flash column chromatography.

(7) General Procedure G

The appropriate intermediate (**4a-d** and **4f,g**), **44-HCl**, and DIPEA were stirred in dry DMF at 70 °C overnight. After cooling down to rt, Na*t*BuO was added and the mixture was stirred at rt overnight. Saturated NH₄Cl solution was added, and the mixture was extracted thrice with EtOAc. Combined organic layers were dried over Na₂SO₄ and concentrated under reduced pressure. The residue was purified by flash column chromatography.

3.2.3. Detailed Procedures

(1) Detailed Procedures for the Preparation of Intermediates **4a–l**

4-Chloro-9-tosyl-9H-pyrimido[4,5-*b*]indole (**4a**)

The title compound was prepared from **3a** (500.0 mg, 2.45 mmol), *p*-toluenesulfonyl chloride (585.0 mg, 3.07 mmol), and NaH (147.3 mg of a 60% in mineral oil, 3.68 mmol) in dry THF (16 mL) according to general procedure A (reaction time 2 h); 753 mg of a yellow solid was yielded (82% crude yield) and used in the next step without further purification. ESI-MS: (*m/z*) 380.3 [M + Na]⁺, 356.3 [M – H][–].

4-Chloro-7-fluoro-9-tosyl-9H-pyrimido[4,5-*b*]indole (**4b**)

The title compound was prepared from **3b** (250.0 mg, 2.05 mmol), *p*-toluenesulfonyl chloride (268.8 mg, 1.41 mmol), and NaH (67.7 mg of a 60% dispersion in mineral oil, 1.69 mmol) in dry THF (7.5 mL) according to general procedure A (reaction time 1.5 h); 412 mg of a yellow solid was yielded (97% crude yield) and used in the next step without further purification. ESI-MS: (*m/z*) 398.2 [M + Na]⁺, 374.1 [M – H][–].

4,7-Dichloro-9-tosyl-9H-pyrimido[4,5-*b*]indole (**4c**)

The title compound was prepared from **3c** as described previously [5].

7-Bromo-4-chloro-9-tosyl-9H-pyrimido[4,5-*b*]indole (**4d**)

The title compound was prepared from **3d** (560.0 mg, 1.98 mmol), *p*-toluenesulfonyl chloride (472.4 mg, 2.48 mmol), and sodium hydride (118.9 mg of a 60% dispersion in mineral oil, 2.97 mmol) in dry THF (15 mL) according to general procedure A (reaction time 20 min); 834 mg of a yellow solid was yielded (96% crude yield) and used in the next step without further purification. ESI-MS: (*m/z*) 457.8 [M + Na]⁺, 433.9 [M – H][–].

4-Chloro-7-iodo-9-tosyl-9H-pyrimido[4,5-*b*]indole (**4e**)

The title compound was prepared from **3e** (421.0 mg, 1.35 mmol), *p*-toluenesulfonyl chloride (322.5 mg, 1.69 mmol), and sodium hydride (81.2 mg of a 60% dispersion in mineral oil, 2.03 mmol) in dry THF (10 mL) according to general procedure A (reaction time 1 h); 606 mg of a dark yellow solid was yielded (93% crude yield) and used in the next step without further purification. ESI-MS: (*m/z*) 506.3 [M + Na]⁺; 482.4 [M – H][–].

4-Chloro-7-methoxy-9-tosyl-9H-pyrimido[4,5-*b*]indole (**4f**)

The title compound was prepared from **3f** (710.0 mg, 3.03 mmol) and NaH (182.3 mg of a 60% dispersion in mineral oil, 4.56 mmol) in dry THF (10 mL) according to general procedure A (reaction time 30 min). *p*-Toluenesulfonyl chloride (695.1 mg, 3.65 mmol) was added as solution in THF (2 mL); 1.15 g was yielded (98% yield) and used in the next step without further purification.

4-Chloro-9-tosyl-7-(trifluoromethyl)-9H-pyrimido[4,5-*b*]indole (**4g**)

NaH (176.7 mg of a 60% dispersion in mineral oil, 4.42 mmol) was added portion-wise to an ice-cooled stirring suspension of **3g** (800.0 mg, 2.95 mmol) in dry THF (10 mL). The mixture was stirred under ice-cooling for 30 min. A solution of *p*-toluenesulfonyl chloride (673.8 mg, 3.53 mmol) in dry THF (2 mL) was drop-added, while the mixture was left to warm to rt and stirring continued at rt for 30 min. The mixture was poured into saturated NH₄Cl solution (100 mL). The resulting precipitate was filtered off, washed with demineralized water, and dried over P₂O₅ in vacuo; 1.2 g was yielded (96% crude yield) and used in the next step without further purification. ESI-MS: (*m/z*) 448.0 [M + H]⁺, 424.0 [M – H][–].

4,6-Dichloro-9-tosyl-9H-pyrimido[4,5-b]indole (4h)

The title compound was prepared from **3h** (550.0 mg, 2.31 mmol), *p*-toluenesulfonyl chloride (550.2 mg, 2.89 mmol), and NaH (138.6 mg of a 60% dispersion in mineral oil, 3.47 mmol) in dry THF (18 mL) according to general procedure A (reaction time 40 min); 890 mg of a yellow solid was yielded (98% crude yield) and used in the next step without further purification. ESI-MS: (*m/z*) 413.9 [M + Na]⁺, 390.0 [M – H][–].

6-Bromo-4-chloro-9-tosyl-9H-pyrimido[4,5-b]indole (4i)

The title compound was prepared from **3i** (740.0 mg, 2.62 mmol), *p*-toluenesulfonyl chloride (624.2 mg, 3.27 mmol), and NaH (157.2 mg of a 60% dispersion in mineral oil, 3.93 mmol) in dry THF (33 mL) according to general procedure A (reaction time 1.5 h); 1.1 g was yielded (96% crude yield) and used in the next step without further purification. ESI-MS: (*m/z*) 457.7 [M + Na]⁺, 433.8 [M – H][–].

4-Chloro-6-methoxy-9-tosyl-9H-pyrimido[4,5-b]indole (4j)

The title compound was prepared from **3j** (480.0 mg, 2.05 mmol), *p*-toluenesulfonyl chloride (489.6 mg, 2.57 mmol), and sodium hydride (123.3 mg of a 60% dispersion in mineral oil, 3.08 mmol) in dry THF (16 mL) according to general procedure A in a (reaction time 30 min); 750 mg of a brown solid was yielded (94% crude yield) and used in the next step without further purification. ESI-MS: (*m/z*) 410.7 [M + Na]⁺, 386.7 [M – H][–].

4,5-Dichloro-9-tosyl-9H-pyrimido[4,5-b]indole (4k)

3k (600.0 mg, 2.52 mmol) was suspended in dry THF (20 mL), and NaH (151.2 mg of a 60% dispersion in mineral oil, 3.78 mmol) was added. The mixture was stirred at rt and under N₂ atmosphere for 15 min. *p*-Toluenesulfonyl chloride (600.6 mg, 3.15 mmol) was added and the mixture stirred at rt and under N₂ atmosphere for 40 min. Saturated NH₄Cl solution (50 mL), EtOAc (30 mL), and some MeOH were added, and phases were separated. The aqueous layer was extracted with DCM (4 × 30 mL). Combined organic layers were dried over Na₂SO₄. Volatiles were removed under reduced pressure to yield 1.1 g of a brown solid (>100% crude yield), which contained excessive *p*-toluenesulfonyl chloride. The crude product was used in the next step without further purification. ESI-MS: (*m/z*) 414.7 [M + Na]⁺, 390.7 [M – H][–].

4,7-Dichloro-2-methyl-9-tosyl-9H-pyrimido[4,5-b]indole (4l)

The title compound was prepared from **3l** (470.0 mg, 1.86 mmol), *p*-toluenesulfonyl chloride (444.3 mg, 2.33 mmol), and NaH (111.9 mg of a 60% dispersion in mineral oil, 2.80 mmol) in dry THF (16 mL) according to general procedure A (reaction time 20 min); 759 mg of a beige solid was yielded (100% crude yield) and used in the next step without further purification.

(2) Detailed Procedures for the Preparation of Enantiopure Intermediates (R)-5c,d and (S)-5c,d***tert*-Butyl (R)-3-((7-chloro-9-tosyl-9H-pyrimido[4,5-b]indol-4-yl)amino)piperidine-1-carboxylate ((R)-5c)**

The title compound was prepared from **4c** (465.0 mg, 1.19 mmol), (*R*)-1-Boc-3-aminopiperidine (284.9 mg, 1.42 mmol), and DIPEA (444.3 mg, 3.44 mmol) in dry DMF (11 mL) according to general procedure B (reaction time 16 h). Purification by flash column chromatography (SiO₂, hexane–EtOAc–MeOH 60:38:2) gave 462 mg of a pale yellow solid (69% yield). ¹H-NMR (300 MHz, CDCl₃) δ 8.60 (s, 1H), 8.49 (s, 1H), 8.05 (d, *J* = 7.9 Hz, 2H), 7.68 (s, 1H), 7.35 (d, *J* = 7.5 Hz, 1H), 7.25 (d, *J* = 8.9 Hz, 2H, overlap with CHCl₃ signal), 6.44–4.91 (m, 1H), 4.55–4.31 (m, 1H), 4.23–3.66 (m, 2H), 3.54–2.97 (m, 2H), 2.46–2.01 (m, 4H), 1.97–1.79 (m, 1H), 1.75–1.30 (m, 11H); ESI-MS: (*m/z*) 578.0 [M + Na]⁺, 553.9 [M – H][–]; HPLC method A: *t*_r = 10.118 min.

***tert*-Butyl (R)-3-((7-bromo-9-tosyl-9H-pyrimido[4,5-b]indol-4-yl)amino)piperidine-1-carboxylate ((R)-5d)**

The title compound was prepared from **4d** (465.0 mg, 1.07 mmol), (*R*)-1-Boc-3-aminopiperidine (277.2 mg, 1.38 mmol), and DIPEA (412.9 mg, 3.19 mmol) in dry DMF (12 mL) according to general procedure B (reaction time 7 h). Purification by flash column chromatography (SiO₂, hexane–EtOAc–MeOH 67:31.5:1.5) gave 400 mg of a light yellow solid (62% yield). ESI-MS: (*m/z*) 599.8 [M + H]⁺, 621.7 [M + Na]⁺, 597.7 [M – H][–]; HPLC method A: *t_r* = 10.848 min.

tert-Butyl (*S*)-3-((7-chloro-9-tosyl-9*H*-pyrimido[4,5-*b*]indol-4-yl)amino)piperidine-1-carboxylate ((**S**)-**5c**)

The title compound was prepared from **4c** (460.0 mg, 1.17 mmol), (*S*)-1-Boc-3-aminopiperidine (305.3 mg, 1.53 mmol), and DIPEA (444.8 mg, 3.44 mmol) in dry DMF (11 mL) according to general procedure B (reaction time 9 h). Purification by flash column chromatography (SiO₂, DCM–MeOH 97.5:2.5) gave 523 mg of a yellow solid (80% yield). ESI-MS: (*m/z*) 578.8 [M + Na]⁺, 554.8 [M – H][–]; HPLC method A: *t_r* = 10.577 min.

tert-Butyl (*S*)-3-((7-bromo-9-tosyl-9*H*-pyrimido[4,5-*b*]indol-4-yl)amino)piperidine-1-carboxylate ((**S**)-**5d**)

The title compound was prepared from **4d** (510.0 mg, 1.17 mmol), (*S*)-1-Boc-3-aminopiperidine (315.8 mg, 1.58 mmol), and DIPEA (452.9 mg, 3.50 mmol) in dry DMF (14 mL) according to general procedure B (reaction time 6 h). Purification by flash column chromatography (SiO₂, hexane–EtOAc–MeOH 67:31.5:1.5) gave 462 mg of a light yellow solid (66% yield). ¹H-NMR (300 MHz, CDCl₃) δ 8.67 (s, 1H), 8.60 (s, 1H), 8.06 (d, *J* = 8.4 Hz, 2H), 7.62 (br s, 1H), 7.49 (dd, *J* = 8.1, 1.3 Hz, 1H), 7.25 (d, 2H, overlap with CHCl₃ signal), 6.14–5.03 (m, 1H), 4.45–4.32 (m, 1H), 4.20–3.72 (m, 2H), 3.47–2.98 (m, 2H), 2.42–2.02 (m, 4H), 1.92–1.78 (m, 1H), 1.75–1.32 (m, 11H); ESI-MS: (*m/z*) 599.8 [M + H]⁺, 621.8 [M + Na]⁺, 597.9 [M – H][–]; HPLC method A: *t_r* = 10.767 min.

(3) Detailed Procedures for the Preparation of Intermediates **6a,b** and **6d–l**

tert-Butyl 3-(methyl(9*H*-pyrimido[4,5-*b*]indol-4-yl)amino)piperidine-1-carboxylate (**6a**)

The title compound was prepared by a two-step procedure. In the first step, **4a** (100.0 mg, 0.28 mmol), 1-Boc-3-(methylamino)piperidine (71.9 mg, 0.34 mmol), and DIPEA (108.4 mg, 0.84 mmol) were reacted in dry DMF (3 mL) according to general procedure B (reaction time 16 h) to afford 145 mg of crude *tert*-butyl 3-(methyl(9-tosyl-9*H*-pyrimido[4,5-*b*]indol-4-yl)amino)piperidine-1-carboxylate (97% crude yield), used in the second step without further purification. ESI-MS: (*m/z*) 558.1 [M + Na]⁺, 533.9 [M – H][–]; HPLC method B: 10.875 min. The crude material obtained from the first step was reacted with Na*t*BuO (182.1 mg, 1.89 mmol) in dry THF (5 mL) according to general procedure D (reaction time 1 h). Purification by flash column chromatography (SiO₂, DCM–EtOH 95:5) gave 60 mg of the title compound (58% yield). ¹H-NMR (300 MHz, DMSO-*d*₆) δ 12.10 (s, 1H), 8.42 (s, 1H), 7.76 (br s, 1H), 7.50 (d, *J* = 7.7 Hz, 1H), 7.43–7.35 (m, 1H), 7.25 (t, *J* = 7.4 Hz, 1H), 4.30–3.72 (m, 3H), 3.20–3.04 (m, 4H), 2.79–2.60 (m, 1H), 2.09–1.71 (m, 3H), 1.51–0.99 (m, 10H); HPLC method B: *t_r* = 8.335 min.

tert-Butyl 3-((7-fluoro-9*H*-pyrimido[4,5-*b*]indol-4-yl)(methyl)amino)piperidine-1-carboxylate (**6b**)

The title compound was prepared by a two-step procedure. In the first step, **4b** (420.0 mg, 1.12 mmol), 1-Boc-3-(methylamino)piperidine (287.4 mg, 1.34 mmol), and DIPEA (433.0 mg, 3.35 mmol) were reacted in dry DMF (15 mL) according to general procedure B (reaction time 16 h) to afford 549 mg of crude *tert*-butyl 3-((7-fluoro-9-tosyl-9*H*-pyrimido[4,5-*b*]indol-4-yl)(methyl)amino)piperidine-1-carboxylate as a yellow solid (89% crude yield), used in the second step without further purification. Purification of a small portion for analytical purposes was performed by flash column chromatography (SiO₂, petroleum ether–EtOAc gradient elution from 2:1 to 1:1). ¹H-NMR (400 MHz, CDCl₃) δ 8.63 (s, 1H), 8.26 (dd, *J* = 10.2, 2.4 Hz, 1H), 8.10 (d, *J* = 8.4 Hz, 2H), 7.65 (s, 1H), 7.26 (d, *J* = 8.2 Hz, 2H, overlap with CHCl₃ signal), 7.17 (td, *J* = 8.7, 2.4 Hz, 1H), 4.49–3.89 (m, 3H), 3.13 (s, 3H), 3.11–3.02 (m, 1H), 2.76–2.65 (m, 1H), 1.99–1.70 (m, 3H), 1.67–1.29 (m, 10H); ESI-MS: (*m/z*) 554.7 [M + H]⁺, 576.7 [M + Na]⁺, 552.7 [M – H][–]; HPLC method A: *t_r* = 10.806 min.

The crude material obtained from the first step was reacted with *Kt*BuO (780.0 mg, 6.95 mmol) in HPLC grade THF (28 mL) according to general procedure D. Purification by flash column chromatography (SiO₂, DCM–MeOH gradient elution from 97.5:2.5 to 93:7) gave 191 mg of a beige solid (48% yield). ¹H-NMR (400 MHz, CDCl₃) δ 11.48 (s, 1H), 8.54 (s, 1H), 7.79–7.69 (m, 1H), 7.24 (dd, *J* = 8.9, 2.3 Hz, 1H), 7.05 (td, *J* = 9.1, 2.4 Hz, 1H), 4.59–3.98 (m, 3H), 3.27 (s, 3H), 3.12–3.02 (m, 1H), 2.77–2.60 (m, 1H), 2.08–1.77 (m, 3H), 1.69–1.54 (m, 1H), 1.43 (s, 9H); ESI-MS: (*m/z*) 422.5 [M + Na]⁺, 398.5 [M – H][–]; HPLC method A: *t*_r = 9.140 min.

tert-Butyl 3-((7-bromo-9*H*-pyrimido[4,5-*b*]indol-4-yl)(methyl)amino)piperidine-1-carboxylate (**6d**)

The title compound was prepared by a two-step procedure. In the first step, **4d** (752.0 mg, 1.73 mmol), 1-Boc-3-(methylamino)piperidine (479.4 mg, 2.23 mmol), and DIPEA (667.4 mg, 5.17 mmol) were reacted in dry DMF (22 mL) according to general procedure B (reaction time 6 h) to afford 1.2 g of crude *tert*-butyl 3-((7-bromo-9-tosyl-9*H*-pyrimido[4,5-*b*]indol-4-yl)(methyl)amino)piperidine-1-carboxylate as a yellow solid (>100% crude yield), used in the second step without further purification. A small portion was purified for analytical purposes by flash column purification (SiO₂; DCM–EtOH 97.5:2.5). ¹H-NMR (300 MHz, CDCl₃) δ 8.75–8.55 (m, 2H), 8.17–8.03 (m, 2H), 7.61–7.46 (m, 2H), 7.31–7.21 (m, 2H, overlap with CHCl₃ signal), 4.46–3.93 (m, 3H), 3.20–2.95 (m, 4H), 2.75–2.61 (m, 1H), 2.37 (s, 3H), 2.00–1.71 (m, 3H), 1.62–1.32 (m, 10H); ¹³C NMR (50 MHz, CDCl₃) δ 160.5, 157.2, 154.8, 154.3, 145.8, 136.3, 135.4, 129.8, 128.2, 127.3, 123.7, 120.7, 120.5, 117.5, 101.2, 80.0, 55.6, 46.7, 44.0 (br), 33.7 (br), 28.5, 28.0, 24.8, 21.8; ESI-MS: (*m/z*) 636.1 [M + Na]⁺, 612.2 [M – H][–]; HPLC method A: *t*_r = 11.296 min. The crude material obtained from the first step was reacted with *Kt*BuO (1.4 g, 12.05 mmol) in dry THF (50 mL) according to general procedure D (reaction time 1 h). Purification by flash column chromatography (SiO₂, DCM:MeOH gradient elution from 97.5:2.5 to 93:7) gave 488 mg of a light brown solid (62% yield). ¹H-NMR (300 MHz, CDCl₃) δ 11.46 (br s, 1H), 8.56 (s, 1H), 7.71–7.62 (m, 2H), 7.40 (dd, *J* = 8.6, 1.8 Hz, 1H), 4.52–4.01 (m, 3H), 3.27 (s, 3H), 3.13–3.01 (m, 1H), 2.77–2.62 (m, 1H), 2.09–1.77 (m, 3H), 1.72–1.56 (m, 1H), 1.43 (s, 9H); ESI-MS: (*m/z*) 481.9 [M + Na]⁺, 458.0 [M – H][–]; HPLC method A: *t*_r = 9.546 min.

tert-Butyl 3-((7-iodo-9*H*-pyrimido[4,5-*b*]indol-4-yl)(methyl)amino)piperidine-1-carboxylate (**6e**)

The title compound was prepared by a two-step procedure. In the first step, **4e** (590.0 mg, 1.22 mmol), 1-Boc-3-(methylamino)piperidine (339.8 mg, 1.59 mmol), and DIPEA (473.0 mg, 3.66 mmol) were reacted in dry DMF (16 mL) according to general procedure B. Dissident from the general procedure, the mixture was stirred at 60 °C for 2 h; 779 mg of crude *tert*-butyl 3-((7-iodo-9-tosyl-9*H*-pyrimido[4,5-*b*]indol-4-yl)(methyl)amino)piperidine-1-carboxylate as a beige solid (97% crude yield) was used in the second step without further purification. Purification of a small portion for analytical purposes was performed by flash column chromatography (SiO₂, petroleum ether–EtOAc gradient elution from 3:2 to 1:1). ¹H-NMR (300 MHz, CDCl₃) δ 8.86 (d, *J* = 1.4 Hz, 1H), 8.62 (s, 1H), 8.09 (d, *J* = 8.4 Hz, 2H), 7.74 (dd, *J* = 8.4, 1.4 Hz, 1H), 7.41 (d, *J* = 7.9 Hz, 1H), 7.27 (d, *J* = 8.1 Hz, 2H; overlap with CHCl₃ signal), 4.47–3.90 (m, 3H), 3.11 (s, 3H), 3.08–2.98 (m, 1H), 2.77–2.60 (m, 1H), 2.37 (s, 3H), 2.01–1.71 (m, 3H), 1.64–1.29 (m, 10H); ¹³C NMR (50 MHz, CDCl₃) δ 160.5, 157.0, 154.8, 154.4, 145.8, 136.4, 135.4, 133.2, 129.8, 128.2, 124.0, 123.1, 121.3, 101.2, 91.3, 80.0, 55.6 (br), 46.7, 44.1 (br), 33.7 (br), 28.5, 28.1, 24.8, 21.8; ESI-MS: (*m/z*) 684.7 [M + Na]⁺, 660.8 [M – H][–]; HPLC method A: *t*_r = 10.993 min.

The crude material obtained from the first step was reacted with *Kt*BuO (807.4 mg, 7.2 mmol) in dry THF (30 mL) according to general procedure D (reaction time 1 h). Purification twice by flash column chromatography (SiO₂, DCM–MeOH 95:5 and SiO₂, DCM–MeOH gradient elution from 97.5:2.5 to 93:7) gave 292 mg of a beige solid (56% yield). ¹H-NMR (300 MHz, CDCl₃) δ 11.30 (s, 1H), 8.52 (s, 1H), 7.92 (d, *J* = 1.1 Hz, 1H), 7.61 (dd, *J* = 8.5, 1.4 Hz, 1H), 7.53 (d, *J* = 8.5 Hz, 1H), 4.55–4.04 (m, 3H), 3.29 (s, 3H), 3.11–2.98 (m, 1H), 2.78–2.61 (m, 1H), 2.10–1.76 (m, 3H), 1.74–1.30 (m, 10H); ESI-MS: (*m/z*) 530.6 [M + Na]⁺, 506.6 [M – H][–]; HPLC method A: *t*_r = 9.541 min.

tert-Butyl 3-((7-methoxy-9*H*-pyrimido[4,5-*b*]indol-4-yl)(methylamino)piperidine-1-carboxylate (**6f**)

4f (250.0 mg, 0.64 mmol), 1-Boc-3-(methylamino)piperidine (165.8, 0.77 mmol), and DIPEA (249.5 mg, 1.93 mmol) were stirred in dry DMF (10 mL) at 70 °C overnight. After cooling down to rt, Na*t*BuO (433.6 mg, 4.51 mmol) was added and stirring continued at rt for 1 h. Saturated NH₄Cl solution (150 mL) was added. The resulting precipitate was filtered off, washed with water, and dried over P₂O₅ in vacuo. Purification by flash column chromatography (SiO₂, DCM–EtOH 97:3) gave 172 mg (64% yield). ¹H-NMR (300 MHz, DMSO-*d*₆) δ 12.00 (s, 1H), 8.37 (s, 1H), 7.64 (br s, 1H), 6.98 (d, *J* = 2.3 Hz, 1H), 6.85 (dd, *J* = 8.7, 1.6 Hz, 1H), 4.24–3.80 (m, 6H), 3.19–3.03 (m, 4H), 2.79–2.60 (m, 1H), 2.05–1.70 (m, 3H), 1.47–1.02 (m, 10H); ESI-MS: (*m/z*) 412.0 [M + H]⁺, 433.9 [M + Na]⁺, 410.1 [M – H][–]; HPLC method B: *t*_r = 8.342 min.

tert-Butyl 3-(methyl(7-(trifluoromethyl)-9*H*-pyrimido[4,5-*b*]indol-4-yl)amino)piperidine-1-carboxylate (**6g**)

4g (600.0 mg, 1.41 mmol), 1-Boc-3-(methylamino)piperidine (362.4 mg, 1.69 mmol), and DIPEA (546.7 mg, 4.23 mmol) were stirred in dry DMF (20 mL) at 70 °C overnight. After cooling down to rt, Na*t*BuO (947.9 mg, 9.86 mmol) was added and stirring continued at rt for 1 h. Saturated NH₄Cl solution (200 mL) was added. The resulting precipitate was filtered off, washed with water, and dried over P₂O₅ in vacuo. Purification by flash column chromatography (SiO₂, DCM–EtOH 97:3) gave 280 mg (44% yield). ¹H-NMR (300 MHz, DMSO-*d*₆) δ 12.48 (s, 1H), 8.47 (s, 1H), 7.97 (br s, 1H), 7.75 (s, 1H), 7.54 (d, *J* = 8.3 Hz, 1H), 4.39–3.83 (m, 3H), 3.21 (s, 3H), 3.18–3.06 (m, 1H), 2.81–2.61 (m, 1H), 2.12–1.71 (m, 3H), 1.53–1.01 (m, 10H); HPLC method B: *t*_r = 10.213 min.

tert-butyl 3-((6-chloro-9*H*-pyrimido[4,5-*b*]indol-4-yl)(methylamino)piperidine-1-carboxylate (**6h**)

The title compound was prepared by a two-step procedure. In the first step, **4h** (450.0 mg, 1.15 mmol), 1-Boc-3-(methylamino)piperidine (368.8 mg, 1.72 mmol), and DIPEA (444.7 mg, 3.44 mmol) were reacted in dry DMF (17 mL) according to general procedure B (reaction time 14 h) to afford 682 mg of crude *tert*-butyl 3-((6-chloro-9-tosyl-9*H*-pyrimido[4,5-*b*]indol-4-yl)(methylamino)piperidine-1-carboxylate as a beige solid (>100% crude yield), used in the second step without further purification. Purification of a small portion for analytical purposes was performed by flash column chromatography (SiO₂, petroleum ether–EtOAc gradient elution from 65:35 to 1:1). ¹H-NMR (300 MHz, CDCl₃) δ 8.61 (s, 1H), 8.43 (d, *J* = 9.0 Hz, 1H), 8.05 (d, *J* = 8.4 Hz, 2H), 7.58 (d, *J* = 2.0 Hz, 1H), 7.46 (dd, *J* = 9.0, 2.1 Hz, 1H), 7.24 (d, *J* = 9.2 Hz, 2H; overlapping with CHCl₃ signal), 4.30–3.94 (m, 3H), 3.13 (s, 3H), 3.07–2.94 (m, 1H), 2.75–2.61 (m, 1H), 2.35 (s, 3H), 2.16–2.04 (m, 1H), 1.98–1.78 (m, 2H), 1.74–1.55 (m, 1H), 1.38 (s, 9H); ESI-MS: (*m/z*) 592.0 [M + Na]⁺, 568.1 [M – H][–]; HPLC method A: *t*_r = 10.903 min.

The crude material obtained from the first step was reacted with K*t*BuO (774.5 mg, 6.91 mmol) in HPLC grade THF (29 mL) according to general procedure D (reaction time 2.5 h). Purification by flash column chromatography (SiO₂, DCM–MeOH gradient elution from 97.5:2.5 to 93:7) gave 252 mg of a yellow solid (61% yield). ¹H-NMR (300 MHz, CDCl₃) δ 11.46 (br s, 1H), 8.54 (s, 1H), 7.73 (d, *J* = 1.6 Hz, 1H), 7.45 (d, *J* = 8.5 Hz, 1H), 7.38 (dd, *J* = 8.6, 1.8 Hz, 1H), 4.54–4.40 (m, 1H), 4.38–4.01 (m, 2H), 3.30 (s, 3H), 3.10–2.97 (m, 1H), 2.77–2.62 (m, 1H), 2.22–2.11 (m, 1H), 2.03–1.84 (m, 2H), 1.81–1.63 (m, 1H), 1.40 (s, 9H); ESI-MS: (*m/z*) 416.1 [M + H]⁺, 438.1 [M + Na]⁺, 414.1 [M – H][–]; HPLC method A: *t*_r = 9.385 min.

tert-Butyl 3-((6-bromo-9*H*-pyrimido[4,5-*b*]indol-4-yl)(methylamino)piperidine-1-carboxylate (**6i**)

The title compound was prepared by a two-step procedure. In the first step, **4i** (650 mg, 1.49 mmol), 1-Boc-3-(methylamino)piperidine (415.1 mg, 1.94 mmol), and DIPEA (576.5 mg, 4.46 mmol) were reacted in dry DMF (20 mL) according to procedure B (reaction time 5 h) to yield 871 mg of crude *tert*-butyl 3-((6-bromo-9-tosyl-9*H*-pyrimido[4,5-*b*]indol-4-yl)(methylamino)piperidine-1-carboxylate as a dark yellow solid (95% crude yield), used in the second step without further purification. Purification of a small portion for analytical purposes was performed by flash column chromatography (SiO₂,

petroleum ether–EtOAc gradient elution from 2:1 to 1:1). ¹H-NMR (300 MHz, CDCl₃) δ 8.61 (s, 1H), 8.39 (d, *J* = 9.0 Hz, 1H), 8.05 (d, *J* = 8.3 Hz, 2H), 7.73 (d, *J* = 1.9 Hz, 1H), 7.60 (dd, *J* = 9.0, 1.9 Hz, 1H), 7.25 (d, *J* = 8.4 Hz, 2H, overlap with CHCl₃ signal), 4.30–3.96 (m, 3H), 3.13 (s, 3H), 3.06–2.93 (m, 1H), 2.75–2.60 (m, 1H), 2.36 (s, 3H), 2.16–2.07 (m, 1H), 1.98–1.80 (m, 2H), 1.75–1.58 (m, 1H), 1.37 (s, 9H); ¹³C NMR (50 MHz, CDCl₃) δ 160.6, 157.5, 155.0, 154.6, 145.7, 135.4, 134.4, 129.8, 129.4, 128.0, 125.3, 123.7, 117.3, 115.8, 100.5, 79.9, 55.2, 46.4 (br), 44.0 (br), 34.3, 28.4, 28.1, 24.8, 21.8; ESI-MS: (*m/z*) 614.2 [M + H]⁺, 636.1 [M + Na]⁺, 612.2 [M – H][–]; HPLC method A: *t_r* = 11.194 min.

The crude material obtained from the first step was reacted with *K*tBuO (976.5 mg, 8.70 mmol) in dry THF (36 mL) according to general procedure D (reaction time 1 h). Purification by flash column chromatography (SiO₂, DCM–MeOH gradient elution from 97.5:2.5 to 93:7) gave 364 mg of a beige solid (64% yield). ¹H-NMR (300 MHz, CDCl₃) δ 11.26 (br s, 1H), 8.53 (s, 1H), 7.87 (d, *J* = 0.8 Hz, 1H), 7.52 (dd, *J* = 8.5, 1.6 Hz, 1H), 7.40 (d, *J* = 8.5 Hz, 1H), 4.54–4.40 (m, 1H), 4.35–4.03 (m, 2H), 3.30 (s, 3H), 3.09–2.96 (m, 1H), 2.77–2.63 (m, 1H), 2.24–2.13 (m, 1H), 2.04–1.67 (m, 3H), 1.40 (s, 9H); ¹³C NMR (50 MHz, CDCl₃) δ 160.2, 157.1, 155.1, 152.8, 135.5, 127.8, 125.4, 121.9, 113.7, 112.8, 98.0, 79.9, 54.8, 46.6 (br), 44.1 (br), 33.8, 28.5, 28.3, 24.9; ESI-MS: (*m/z*) 482.3 [M + Na]⁺, 458.3 [M – H][–]; HPLC method A: *t_r* = 9.550 min.

tert-Butyl 3-((6-methoxy-9*H*-pyrimido[4,5-*b*]indol-4-yl)(methylamino)piperidine-1-carboxylate (6j)

The title compound was prepared by a two-step procedure. In the first step, **4j** (730.0 mg, 1.88 mmol), 1-Boc-3-(methylamino)piperidine (524.4 mg, 2.45 mmol), and DIPEA (729.8 mg, 5.65 mmol) were reacted in dry DMF (22 mL) according to general procedure B (reaction time 6.5 h) to afford 975 mg of crude *tert*-butyl 3-((6-methoxy-9-tosyl-9*H*-pyrimido[4,5-*b*]indol-4-yl)(methylamino)piperidine-1-carboxylate as a beige solid (92% crude yield), used in the next step without further purification. Purification of a small portion for analytical purposes was performed by flash column chromatography (SiO₂). ¹H-NMR (400 MHz, CDCl₃) δ 8.63 (s, 1H), 8.40 (d, *J* = 9.0 Hz, 1H), 8.03 (d, *J* = 7.8 Hz, 2H), 7.22 (d, *J* = 7.9 Hz, 2H), 7.16–7.07 (m, 2H), 4.24–3.98 (m, 3H), 3.89 (s, 3H), 3.14 (s, 3H), 3.08–2.99 (m, 1H), 2.75–2.64 (m, 1H), 2.34 (s, 3H), 2.10–2.02 (m, 1H), 1.95–1.76 (m, 2H), 1.69–1.57 (m, 1H), 1.45–1.22 (m, 9H); ESI-MS: (*m/z*) 588.5 [M + Na]⁺, 564.6 [M – H][–]; HPLC method A: *t_r* = 10.013 min.

The crude material obtained from the first step was reacted with *K*tBuO (1180.2 mg, 10.52 mmol) in dry THF (45 mL) according to general procedure D (reaction time 30 min). Purification by flash column chromatography (SiO₂, DCM–MeOH gradient elution from 97.5:2.5 to 93:7) gave 369 mg of a beige solid (60% yield). ¹H-NMR (400 MHz, DMSO-*d*₆) δ 11.95 (s, 1H), 8.40 (s, 1H), 7.41 (d, *J* = 8.7 Hz, 1H), 7.19 (s, 1H), 7.06 (dd, *J* = 8.8, 2.4 Hz, 1H), 4.25–4.15 (m, 1H), 4.06–3.57 (m, 5H), 3.15 (s, 3H), 3.11–3.01 (m, 1H), 2.80–2.61 (m, 1H), 2.20–1.89 (m, 2H), 1.87–1.77 (m, 1H), 1.55–1.43 (m, 1H), 1.39–0.91 (m, 9H); ESI-MS: (*m/z*) 412.4 [M + H]⁺, 434.5 [M + Na]⁺, 410.4 [M – H][–]; HPLC method A: *t_r* = 8.549 min.

tert-Butyl 3-((5-chloro-9*H*-pyrimido[4,5-*b*]indol-4-yl)(methylamino)piperidine-1-carboxylate (6k)

The title compound was prepared by a two-step procedure. In the first step, **4k** (675.0 mg, 1.72 mmol), 1-Boc-3-(methylamino)piperidine (516.3 mg, 2.41 mmol), and DIPEA (667.3 mg, 5.16 mmol) were reacted in dry DMF (25 mL) according to general procedure B. Purification of a small portion for analytical purposes was performed by flash column chromatography (SiO₂; DCM–MeOH gradient elution from 96.5:3.5 to 92.5:7.5). ¹H-NMR (300 MHz, CDCl₃) δ 8.51 (s, 1H), 8.38 (d, *J* = 7.8 Hz, 1H), 8.08 (d, *J* = 6.6 Hz, 2H), 7.45–7.30 (m, 2H), 7.25 (d, 2H, overlap with CHCl₃ signal), 4.60–3.88 (m, 3H), 3.25–2.55 (m, 5H), 2.36 (s, 3H), 2.19–1.62 (m, 4H), 1.42 (s, 9H); ESI-MS: (*m/z*) 592.1 [M + Na]⁺, 568.1 [M – H][–]; HPLC method A: 10.604 min. The crude material obtained from the first step was reacted with *K*tBuO (1.2 g, 10.71 mmol) in HPLC grade THF (45 mL) according to general procedure D (reaction time 2 h). Purification by flash column chromatography (SiO₂, DCM–MeOH gradient elution from 96.5:3.5 to 92.5:7.5) gave 379 mg of a beige solid (53% yield over two steps). ¹H-NMR (400 MHz, DMSO-*d*₆) δ 12.35 (s, 1H), 8.41 (s, 1H), 7.44 (d, *J* = 7.5 Hz, 1H), 7.38 (t, *J* = 7.8 Hz, 1H), 7.28 (d, *J* = 7.5 Hz, 1H), 4.35–3.65 (m, 3H), 3.09–2.87 (m, 4H), 2.84–2.63 (m, 1H), 2.18–1.66 (m, 3H), 1.50–1.09 (m, 10H); ESI-MS: (*m/z*) 438.1 [M + Na]⁺, 414.1 [M – H][–]; HPLC method A: *t_r* = 9.317 min.

tert-Butyl 3-((7-chloro-2-methyl-9H-pyrimido[4,5-*b*]indol-4-yl)(methyl)amino)piperidine-1-carboxylate (**6l**)

The title compound was prepared by a two-step procedure. In the first step, **4l** (535.0 mg, 1.32 mmol), 1-Boc-3-(methylamino)piperidine (423.3 mg, 1.98 mmol), and DIPEA (510.6 mg, 3.95 mmol) were reacted in dry DMF (20 mL) according to general procedure B (reaction time 6.5 h) to afford 750 mg of crude *tert*-butyl 3-((7-chloro-2-methyl-9H-tosyl-9H-pyrimido[4,5-*b*]indol-4-yl)(methyl)amino)piperidine-1-carboxylate as a beige solid (98% crude yield), used in the next step without further purification. Purification of a small portion for analytical purposes was performed by flash column chromatography (SiO₂, petroleum ether–EtOAc gradient elution from 7:3 to 3:7). ¹H-NMR (300 MHz, CDCl₃) δ 8.52 (d, *J* = 1.8 Hz, 1H), 8.12 (d, *J* = 8.3 Hz, 2H), 7.55 (d, *J* = 8.2 Hz, 1H), 7.35 (dd, *J* = 8.5, 1.9 Hz, 1H), 7.26 (d, *J* = 8.1 Hz, 2H, overlap with CHCl₃ signal), 4.45–3.91 (m, 3H), 3.15–2.96 (m, 4H), 2.75–2.59 (m, 4H), 2.37 (s, 3H), 1.98–1.70 (m, 3H), 1.64–1.31 (m, 10H); ESI-MS: (*m/z*) 606.5 [M + Na]⁺, 582.5 [M – H][–]; HPLC method A: *t_r* = 12.593 min.

The crude material obtained from the first step was reacted with *Kt*BuO (874.0 mg, 7.79 mmol) in dry THF (32 mL) according to general procedure D (reaction time 2.5 h). Purification by flash column chromatography (SiO₂, DCM–MeOH gradient elution from 97.5:2.5 to 93:7) gave 358 mg of a light yellow solid (75% yield). ¹H-NMR (400 MHz, DMSO-*d*₆) δ 12.03 (s, 1H), 7.78–7.60 (m, 1H), 7.45 (d, *J* = 1.8 Hz, 1H), 7.26–7.13 (m, 1H), 4.30–3.78 (m, 3H), 3.12 (s, 3H), 3.09–3.01 (m, 1H), 2.80–2.57 (m, 1H), 2.50 (s, 3H, overlap with DMSO-*d*₅ signal), 2.08–1.68 (m, 3H), 1.54–0.99 (m, 10H); ¹³C NMR (101 MHz, DMSO-*d*₆) δ 162.5, 159.6, 158.4, 153.9, 137.4, 128.8, 123.3, 120.2, 118.6, 110.8, 95.2, 78.7, 54.5, 46.0 (br), 43.3 (br), 32.5, 27.8, 27.4, 25.8, 24.6; ESI-MS: (*m/z*) 430.5 [M + H]⁺, 452.5 [M + Na]⁺; 428.6 [M – H][–]; HPLC method A: *t_r* = 10.332 min.

(4) Detailed Procedures for the Preparation of Enantiopure Intermediates (**R**)-**6c,d** and (**S**)-**6c,d***tert*-Butyl (*R*)-3-((7-chloro-9H-pyrimido[4,5-*b*]indol-4-yl)(methyl)amino)piperidine-1-carboxylate ((**R**)-**6c**)

The title compound was prepared by a two-step procedure. In the first step, (**R**)-**5c** (350.0 mg, 0.63 mmol), methyl iodide (134.0 mg, 0.94 mmol), and NaH (37.7 mg of a 60% dispersion in mineral oil, 0.94 mmol) were reacted in dry DMF (15 mL) according to general procedure C (reaction time of 3 h) to afford 346 mg of crude *tert*-butyl (*R*)-3-((7-chloro-9H-tosyl-9H-pyrimido[4,5-*b*]indol-4-yl)(methyl)amino)piperidine-1-carboxylate as an off-white solid (96% crude yield), used in the next step without further purification. Purification for analytical purposes was performed by flash column chromatography (SiO₂, DCM–MeOH gradient elution from 98:2 to 97.5:2.5). ¹H-NMR (200 MHz, CDCl₃) δ 8.61 (s, 1H), 8.52 (d, *J* = 1.6 Hz, 1H), 8.09 (d, *J* = 8.2 Hz, 2H), 7.60 (d, *J* = 8.6 Hz, 1H), 7.38 (dd, *J* = 8.5, 1.6 Hz, 1H), 7.26 (d, *J* = 8.1 Hz, 2H, overlap with CHCl₃ signal), 4.56–3.88 (m, 3H), 3.18–2.94 (m, 4H), 2.79–2.57 (m, 1H), 2.35 (s, 3H), 2.07–1.68 (m, 3H), 1.66–1.51 (m, 1H), 1.40 (s, 9H); ¹³C NMR (50 MHz, CDCl₃) δ 160.2, 157.3, 154.8, 154.0, 145.8, 136.2, 135.4, 132.8, 129.8, 128.2, 124.6, 123.4, 120.2, 114.7, 101.2, 80.0, 55.7, 46.7, 44.0 (br), 33.8, 28.5, 28.1, 24.8, 21.8; ESI-MS: (*m/z*) 591.8 [M + Na]⁺, 567.7 [M – H][–]; HPLC method A: *t_r* = 10.548 min.

The crude material obtained from the first step was reacted with *Kt*BuO (476.7 mg, 4.25 mmol) in dry THF (19 mL) according to general procedure D (reaction time 1 h). Purification by flash column chromatography (DCM–MeOH gradient elution from 96.5:3.5 to 93:7) gave 183 mg of an off-white solid (73% yield). ¹H-NMR (200 MHz, CDCl₃) δ 11.91 (br s, 1H), 8.53 (s, 1H), 7.65 (d, *J* = 8.6 Hz, 1H), 7.46 (s, 1H), 7.21 (d, *J* = 8.3 Hz, 1H, overlap with CHCl₃ signal), 4.75–3.89 (m, 3H), 3.24 (s, 3H), 3.15–2.95 (m, 1H), 2.82–2.53 (m, 1H), 2.21–1.59 (m, 4H), 1.51 (s, 9H); ¹³C NMR (50 MHz, CDCl₃) δ 160.1, 156.8, 154.9, 152.1, 137.5, 131.1, 123.6, 121.5, 118.7, 111.7, 98.6, 80.0, 55.1, 46.8 (br), 44.0 (br), 33.4, 28.5, 28.2, 24.9; ESI-MS: (*m/z*) 416.0 [M + H]⁺, 437.9 [M + Na]⁺, 413.8 [M – H][–]; HPLC method A: *t_r* = 9.052 min.

tert-Butyl (*R*)-3-((7-bromo-9H-pyrimido[4,5-*b*]indol-4-yl)(methyl)amino)piperidine-1-carboxylate ((**R**)-**6d**)

The title compound was prepared by a two-step procedure. In the first step, (**R**)-**5d** (400.0 mg, 0.67 mmol), methyl iodide (141.8 mg, 1.0 mmol), and NaH (40.0 mg of a 60% dispersion in mineral

oil, 1.0 mmol) were reacted in dry DMF (14 mL) according to general procedure C (reaction time 2.5 h) to afford 382 mg of crude *tert*-butyl (*R*)-3-((7-bromo-9-tosyl-9*H*-pyrimido[4,5-*b*]indol-4-yl)(methyl)amino)piperidine-1-carboxylate as an off-white solid (93% crude yield), used in the next without further purification. Purification of a small portion for analytical purposes was performed by flash column chromatography (SiO₂, hexane–EtOAc 3:2). ¹H-NMR (300 MHz, CDCl₃) δ 8.68 (s, 1H), 8.62 (s, 1H), 8.10 (d, *J* = 8.4 Hz, 2H), 7.60–7.48 (m, 2H), 7.27 (d, *J* = 8.0 Hz, 2H, overlap with CHCl₃ signal), 4.45–3.97 (m, 3H), 3.11 (s, 3H), 3.09–2.98 (m, 1H), 2.75–2.61 (m, 1H), 2.37 (s, 3H), 1.95–1.72 (m, 3H), 1.59–1.31 (m, 10H); ¹³C NMR (75 MHz, CDCl₃) δ 160.41, 157.10, 154.69, 154.23, 145.69, 136.14, 135.26, 129.70, 128.02, 127.23, 123.66, 120.65, 120.32, 117.28, 101.06, 79.80, 55.48, 46.56, 43.99 (br), 33.71 (br), 28.36, 27.93, 24.75, 21.68. ESI-MS: (*m/z*) 635.9 [M + Na]⁺, 612.1 [M – H][–]; HPLC method A: *t_r* = 11.342 min.

The crude material obtained from the first step was reacted with *Kt*BuO (488.0 mg, 4.35 mmol) in dry THF (20 mL) according to general procedure D (reaction time 45 min). Purification by flash column chromatography (SiO₂, DCM–MeOH 96:4) gave 175 mg of a white solid (61% yield). ¹H-NMR (300 MHz, CDCl₃) δ 11.59 (br s, 1H), 8.58 (s, 1H), 7.72–7.62 (m, 2H), 7.40 (dd, *J* = 8.6, 1.8 Hz, 1H), 4.48–4.02 (m, 3H), 3.26 (s, 3H), 3.14–3.00 (m, 1H), 2.77–2.61 (m, 1H), 2.11–1.75 (m, 3H), 1.70–1.54 (m, 1H), 1.43 (s, 9H); ESI-MS: (*m/z*) 482.0 [M + Na]⁺, 458.2 [M – H][–]; HPLC method A: *t_r* = 9.693 min.

tert-Butyl (*S*)-3-((7-chloro-9*H*-pyrimido[4,5-*b*]indol-4-yl)(methyl)amino)piperidine-1-carboxylate ((*S*)-**6c**)

The title compound was prepared by a two-step procedure. In the first step, (*S*)-**5c** (465.0 mg, 0.84 mmol), methyl iodide (178.0 mg, 1.25 mmol), and NaH (50.2 mg of a 60% dispersion in mineral oil, 1.25 mmol) were reacted in dry DMF (15 mL) according to general procedure C (reaction time 3.5 h) to afford 440 mg of crude *tert*-butyl (*S*)-3-((7-chloro-9-tosyl-9*H*-pyrimido[4,5-*b*]indol-4-yl)(methyl)amino)piperidine-1-carboxylate as a yellow solid (92% crude yield), used in the next step without further purification. ESI-MS: (*m/z*) 591.8 [M + Na]⁺, 567.7 [M – H][–]; HPLC method A: *t_r* = 11.053 min.

The crude material obtained from the first step was reacted with *Kt*BuO (606.2 mg, 5.40 mmol) in dry THF (24 mL) according to general procedure D (reaction time 1 h). Purification by flash column chromatography (SiO₂, DCM–MeOH gradient elution from 96.5:3.5 to 92.5:7.5) gave 203 mg of a white solid (63% yield). ¹H-NMR (300 MHz, CDCl₃) δ 11.71 (br s, 1H), 8.57 (s, 1H), 7.71 (d, *J* = 8.6 Hz, 1H), 7.53 (d, *J* = 1.7 Hz, 1H), 7.26 (dd, *J* = 8.6, 1.9 Hz, 1H, overlap with CHCl₃ signal), 4.59–3.97 (m, 3H), 3.27 (s, 3H), 3.16–2.99 (m, 1H), 2.83–2.58 (m, 1H), 2.11–1.54 (m, 4H), 1.43 (s, 9H); ESI-MS: (*m/z*) 437.9 [M + Na]⁺, 413.8 [M – H][–]; HPLC method A: *t_r* = 9.451 min.

tert-Butyl (*S*)-3-((7-bromo-9*H*-pyrimido[4,5-*b*]indol-4-yl)(methyl)amino)piperidine-1-carboxylate ((*S*)-**6d**)

The title compound was prepared by a two-step procedure. In the first step, (*S*)-**5d** (585.0 mg, 0.97 mmol), NaH (58.4 mg of a 60% dispersion in mineral oil, 1.46 mmol), and methyl iodide (207.4 mg, 1.46 mmol) were reacted in dry DMF (10 mL) according to general procedure C (reaction time 3 h) to afford 578 mg of crude *tert*-butyl (*S*)-3-((7-bromo-9-tosyl-9*H*-pyrimido[4,5-*b*]indol-4-yl)(methyl)amino)piperidine-1-carboxylate as a light yellow solid (96% crude yield), used in the next step without further purification.

The crude material obtained from the first step was reacted with *Kt*BuO (639.1 mg, 5.70 mmol) in dry THF (25 mL) according to general procedure D (reaction time 2 h). Purification by flash column chromatography (SiO₂, DCM–MeOH 96:4) gave 214 mg of a white solid (57% yield). ¹H-NMR (400 MHz, CDCl₃) δ 12.09 (s, 1H), 8.56 (s, 1H), 7.66 (d, *J* = 1.6 Hz, 1H), 7.64 (d, *J* = 8.6 Hz, 1H), 7.38 (dd, *J* = 8.6, 1.8 Hz, 1H), 4.61–3.96 (m, 1H), 3.26 (s, 1H), 3.11–3.01 (m, 1H), 2.78–2.61 (m, 1H), 2.09–1.75 (m, 1H), 1.72–1.55 (m, 1H), 1.44 (s, 1H).

(5) Detailed Procedures for the Preparation of Intermediates **7a–I**

N-methyl-*N*-(piperidin-3-yl)-9*H*-pyrimido[4,5-*b*]indol-4-amine (**7a**)

The title compound was prepared from **6a** (60.0 mg, 0.16 mmol) in dry DCM (1 mL) and TFA (0.2 mL) according to general procedure E (reaction time 1.5 h); 36 mg of a light brown solid was yielded (81% crude yield) and used in the next step without further purification. ¹H-NMR (400 MHz, MeOD) δ 8.36 (s, 1H), 7.84 (d, *J* = 8.0 Hz, 1H), 7.52 (d, *J* = 8.0 Hz, 1H), 7.41 (td, *J* = 7.7, 1.0 Hz, 1H), 7.34–7.27 (m, 1H), 3.30–3.23 (m, 4H), 3.14–3.07 (m, 1H), 3.07–3.00 (m, 1H), 2.72–2.63 (m, 1H), 2.20–1.94 (m, 3H), 1.83–1.70 (m, 1H); ESI-MS: (*m/z*) 282.3 [M + H]⁺, 280.3 [M – H][–]; HPLC method A: *t_r* = 2.232 min.

7-Fluoro-*N*-methyl-*N*-(piperidin-3-yl)-9*H*-pyrimido[4,5-*b*]indol-4-amine (**7b**)

The title compound was prepared from **6b** (170.0 mg, 0.43 mmol) in dry DCM (5 mL) and TFA (1 mL) according to general procedure E (reaction time 1.5 h); 119 mg of a beige solid was yielded (93% crude yield) and used in the next step without further purification. ¹H-NMR (200 MHz, MeOD) δ 8.33 (s, 1H), 7.78 (dd, *J* = 8.8, 5.2 Hz, 1H), 7.22 (dd, *J* = 9.3, 2.4 Hz, 1H), 7.06 (td, *J* = 9.3, 2.5 Hz, 1H), 4.54–4.37 (m, 1H), 3.24 (s, 3H), 3.17–2.83 (m, 3H), 2.62–2.45 (m, 1H), 2.16–1.55 (m, 4H); ESI-MS: (*m/z*) 300.3 [M + H]⁺, 298.3 [M – H][–]; HPLC method A: *t_r* = 3.036 min.

7-Chloro-*N*-methyl-*N*-(piperidin-3-yl)-9*H*-pyrimido[4,5-*b*]indol-4-amine (**7c**)

The title compound was prepared as described previously [5].

7-Bromo-*N*-methyl-*N*-(piperidin-3-yl)-9*H*-pyrimido[4,5-*b*]indol-4-amine (**7d**)

6d (425.0 mg, 0.92 mmol) was stirred in dry DCM (9 mL) and TFA (1.5 mL) at rt for 1 h. The mixture was concentrated under reduced pressure. Residual TFA was neutralized by addition of saturated NaHCO₃ solution, resulting in a precipitate which was filtered off and washed with saturated NaHCO₃ solution and demineralized water and was then dried over P₂O₅ in vacuo; 285 mg of an off-white solid was yielded (86% crude yield) and used in the next step without further purification. ¹H-NMR (300 MHz, MeOD) δ 8.35 (s, 1H), 7.70 (d, *J* = 8.6 Hz, 1H), 7.65 (d, *J* = 1.7 Hz, 1H), 7.40 (dd, *J* = 8.6, 1.9 Hz, 1H), 4.55–4.37 (m, 1H), 3.24 (s, 3H), 3.15–3.06 (m, 1H), 3.02–2.95 (m, 1H), 2.95–2.85 (m, 1H), 2.61–2.48 (m, 1H), 2.15–1.84 (m, 3H), 1.78–1.60 (m, 1H); ¹³C NMR (75 MHz, DMSO-*d*₆) δ 159.6, 157.3, 153.8, 137.7, 124.1, 123.1, 118.9, 117.2, 113.7, 97.1, 55.9, 48.7, 45.5, 32.7, 28.3, 26.5; ESI-MS: (*m/z*) 360.1 [M + H]⁺, 358.1 [M – H][–]; HPLC method A: *t_r* = 4.033 min.

7-Iodo-*N*-methyl-*N*-(piperidin-3-yl)-9*H*-pyrimido[4,5-*b*]indol-4-amine (**7e**)

6e (240.0 mg, 0.473 mmol) was suspended in dry DCM (7 mL), and TFA was added (1.5 mL). The mixture was stirred at rt for 30 min and then concentrated under reduced pressure. Residual TFA was neutralized by addition of saturated NaHCO₃ solution (30 mL), which resulted in a precipitate. The precipitate was filtered off, washed with saturated NaHCO₃ solution and demineralized water, and dried over P₂O₅ in vacuo; 199 mg of a beige solid was yielded (>100% crude yield) and used in the next step without further purification. ¹H-NMR (300 MHz, MeOD) δ 8.35 (s, 1H), 7.86 (s, 1H), 7.65–7.52 (m, 2H), 4.55–4.40 (m, 1H), 3.24 (s, 3H), 3.14–3.05 (m, 1H), 3.02–2.84 (m, 2H), 2.60–2.47 (m, 1H), 2.15–1.84 (m, 3H), 1.77–1.59 (m, 1H); ESI-MS: (*m/z*) 408.3 [M + H]⁺, 406.3 [M – H][–]; HPLC method A: *t_r* = 4.563 min.

7-methoxy-*N*-methyl-*N*-(piperidin-3-yl)-9*H*-pyrimido[4,5-*b*]indol-4-amine (**7f**)

TFA (0.4 mL) was added to a solution of **6f** (126.0 mg, 0.31 mmol) in dry DCM (10 mL). The mixture was stirred at rt for 1.5 h and then concentrated under reduced pressure. Saturated NaHCO₃ solution was added to the residue, and the mixture was extracted with EtOAc (3 × 20 mL). Combined organic layers were dried over Na₂SO₄ and evaporated to dryness to afford 90 mg (95% crude yield). ¹H-NMR (300 MHz, DMSO-*d*₆) δ 11.95 (s, 1H), 8.33 (s, 1H), 7.68 (d, *J* = 8.8 Hz, 1H), 6.97 (d, *J* = 2.4 Hz, 1H), 6.88 (dd, *J* = 8.8, 2.4 Hz, 1H), 4.40–4.26 (m, 1H), 3.84 (s, 3H), 3.13 (s, 3H), 3.06–2.80 (m, 3H), 2.51–2.41 (m, 1H, overlap with DMSO-*d*₅ signal), 2.00–1.71 (m, 3H), 1.60–1.39 (m, 1H); ESI-MS: (*m/z*) 312.0 [M + H]⁺, 310.1 [M – H][–]; HPLC method B: *t_r* = 2.684 min.

N-Methyl-N-(piperidin-3-yl)-7-(trifluoromethyl)-9H-pyrimido[4,5-*b*]indol-4-amine (7g)

TFA (1 mL) was added to a solution of **6g** (237.0 mg, 0.53 mmol) in dry DCM (10 mL). The mixture was stirred at rt for 2 h and then concentrated under reduced pressure. Saturated NaHCO₃ solution was added to the residue, and the mixture was then extracted with EtOAc (3 × 20 mL). Combined organic layers were dried over Na₂SO₄ and evaporated to dryness; 194 mg was yielded (100% crude yield) and used in the next step without further purification. ¹H-NMR (300 MHz, DMSO-*d*₆) δ 12.30 (br s, 1H), 8.44 (s, 1H), 8.01 (d, *J* = 8.5 Hz, 1H), 7.74 (s, 1H), 7.56 (dd, *J* = 8.5, 1.2 Hz, 1H), 4.54–4.40 (m, 1H), 3.22 (s, 3H), 3.12–3.05 (m, 1H), 3.01–2.86 (m, 2H), 2.58–2.49 (m, 1H, overlap with DMSO-*d*₅ signal), 2.01–1.75 (m, 3H), 1.66–1.49 (m, 1H); HPLC method B: *t*_r = 4.956 min.

6-Chloro-N-methyl-N-(piperidin-3-yl)-9H-pyrimido[4,5-*b*]indol-4-amine (7h)

The title compound was prepared from **6h** (215.0 mg, 0.52 mmol) in dry DCM (5.6 mL) and TFA (1.1 mL) according to general procedure E (reaction time 1 h); 163 mg of a yellow solid (100% crude yield) was yielded, used in the next step without further purification. ¹H-NMR (300 MHz, MeOD) δ 8.35 (s, 1H), 7.76 (d, *J* = 1.8 Hz, 1H), 7.48 (d, *J* = 8.6 Hz, 1H), 7.38 (dd, *J* = 8.6, 2.0 Hz, 1H), 4.54–4.39 (m, 1H), 3.25 (s, 3H), 3.11–2.95 (m, 2H), 2.95–2.85 (m, 1H), 2.63–2.49 (m, 1H), 2.23–1.88 (m, 3H), 1.83–1.65 (m, 1H); ¹³C NMR (101 MHz, DMSO-*d*₆) δ 159.6, 157.5, 153.9, 135.1, 124.6, 124.3, 121.6, 120.9, 112.5, 96.8, 55.8, 48.8, 45.5, 32.5, 28.4, 26.3; ESI-MS: (*m/z*) 316.1 [M + H]⁺, 314.0 [M – H][–]; HPLC method A: *t*_r = 4.102 min.

6-Bromo-N-methyl-N-(piperidin-3-yl)-9H-pyrimido[4,5-*b*]indol-4-amine (7i)

The title compound was prepared from **6i** in dry DCM (6.3 mL) and TFA (1 mL) according to general procedure E (reaction time 1 h). Purification by flash column chromatography (SiO₂, DCM–(2N NH₃ in MeOH) 9:1) gave 218 mg of a beige solid (93% yield). ¹H-NMR (300 MHz, MeOD) δ 8.35 (s, 1H), 7.91 (d, *J* = 1.6 Hz, 1H), 7.52 (dd, *J* = 8.6, 1.8 Hz, 1H), 7.43 (d, *J* = 8.6 Hz, 1H), 4.51–4.40 (m, 1H), 3.24 (s, 3H), 3.08–2.95 (m, 2H), 2.94–2.85 (m, 1H), 2.61–2.48 (m, 1H), 2.22–1.89 (m, 3H), 1.84–1.66 (m, 1H); ¹³C NMR (75 MHz, DMSO-*d*₆) δ 159.6, 157.4, 154.0, 135.4, 127.1, 124.6, 121.6, 113.1, 112.5, 96.7, 56.0, 48.9, 45.5, 32.5, 28.6, 26.5; ESI-MS: (*m/z*) 360.1 [M + H]⁺, 358.1 [M – H][–]; HPLC method A: *t*_r = 4.058 min.

6-Methoxy-N-methyl-N-(piperidin-3-yl)-9H-pyrimido[4,5-*b*]indol-4-amine (7j)

The title compound was prepared from **6j** (325.0 mg, 0.78 mmol) in dry DCM (10 mL) and TFA (2 mL) according to general procedure E (reaction time 2 h); 207 mg of a beige solid (84% yield) was yielded. ¹H-NMR (200 MHz, MeOD) δ 8.32 (s, 1H), 7.43 (d, *J* = 8.8 Hz, 1H), 7.29 (d, *J* = 2.4 Hz, 1H), 7.07 (dd, *J* = 8.9, 2.3 Hz, 1H), 4.48–4.29 (m, 1H), 3.89 (s, 3H), 3.22 (s, 3H), 3.13–2.81 (m, 3H), 2.60–2.44 (m, 1H), 2.23–1.84 (m, 3H), 1.82–1.58 (m, 1H); ESI-MS: (*m/z*) 312.2 [M + H]⁺, 310.2 [M – H][–]; HPLC method A: *t*_r = 2.084 min.

5-Chloro-N-methyl-N-(piperidin-3-yl)-9H-pyrimido[4,5-*b*]indol-4-amine (7k)

The title compound was prepared from **6k** (340.0 mg, 0.82 mmol) in dry DCM (9 mL) and TFA (1.8 mL) according to general procedure E (reaction time 2 h); 244 mg of a beige solid (95% crude yield) was yielded, used in the next step without further purification. ¹H-NMR (300 MHz, MeOD) δ 8.31 (s, 1H), 7.43 (dd, *J* = 7.9, 1.2 Hz, 1H), 7.35 (t, *J* = 7.8 Hz, 1H), 7.26 (dd, *J* = 7.7, 1.2 Hz, 1H), 4.52–4.33 (m, 1H), 3.19–2.90 (m, 5H), 2.89–2.68 (m, 1H), 2.57–2.41 (m, 1H), 2.20–1.97 (m, 1H), 1.96–1.74 (m, 2H), 1.73–1.56 (m, 1H); ESI-MS: (*m/z*) 316.1 [M + H]⁺, 314.1 [M – H][–]; HPLC method A: *t*_r = 3.814 min.

7-Chloro-N,2-dimethyl-N-(piperidin-3-yl)-9H-pyrimido[4,5-*b*]indol-4-amine (7l)

The title compound was prepared from **6l** (310.0 mg, 0.72 mmol) in TFA (2 mL) and dry DCM (10 mL) according to general procedure E (reaction time 2.5 h); 239 mg of a yellow solid (100% crude yield) was yielded, used in the next step without further purification. ¹H-NMR (300 MHz, MeOD)

δ 7.70 (d, $J = 8.6$ Hz, 1H), 7.46 (d, $J = 1.9$ Hz, 1H), 7.22 (dd, $J = 8.6, 2.0$ Hz, 1H), 4.57–4.44 (m, 1H), 3.23 (s, 3H), 3.15–3.06 (m, 1H), 3.02–2.93 (m, 1H), 2.93–2.84 (m, 1H), 2.59–2.47 (m, 4H), 2.13–1.84 (m, 3H), 1.77–1.59 (m, 1H); ^{13}C NMR (101 MHz, DMSO- d_6) δ 162.5, 159.6, 158.4, 137.3, 128.6, 123.3, 120.2, 118.8, 110.7, 94.9, 55.8, 48.8, 45.5, 32.4, 28.3, 26.4, 25.9; ESI-MS: (m/z) 330.1 [$\text{M} + \text{H}$] $^+$, 328.1 [$\text{M} - \text{H}$] $^-$; HPLC method A: $t_r = 4.602$ min.

(6) Detailed Procedures for the Preparation of Enantiopure Intermediates (**R**)-**7c,d** and (**S**)-**7c,d**

(**R**)-7-Chloro-*N*-methyl-*N*-(piperidin-3-yl)-9*H*-pyrimido[4,5-*b*]indol-4-amine ((**R**)-**7c**)

The title compound was prepared from (**R**)-**6c** (160.0 mg, 0.39 mmol) in dry DCM (5 mL) and TFA (1 mL) according to general procedure E (reaction time 45 min); 120 mg of a yellow solid (99% crude yield) was yielded, used in the next step without further purification. ^1H -NMR (400 MHz, MeOD) δ 8.35 (s, 1H), 7.78 (d, $J = 8.6$ Hz, 1H), 7.50 (d, $J = 1.9$ Hz, 1H), 7.28 (dd, $J = 8.6, 2.0$ Hz, 1H), 4.56–4.47 (m, 1H), 3.26 (s, 3H), 3.20–3.13 (m, 1H), 3.06–3.00 (m, 1H), 2.99–2.92 (m, 1H), 2.64–2.55 (m, 1H), 2.16–1.90 (m, 3H), 1.78–1.65 (m, 1H); ESI-MS: (m/z) 316.0 [$\text{M} + \text{H}$] $^+$, 338.0 [$\text{M} + \text{Na}$] $^+$, 313.9 [$\text{M} - \text{H}$] $^-$; HPLC method A: $t_r = 3.411$ min.

(**R**)-7-Bromo-*N*-methyl-*N*-(piperidin-3-yl)-9*H*-pyrimido[4,5-*b*]indol-4-amine ((**R**)-**7d**)

The title compound was prepared from (**R**)-**6d** (175.0 mg, 0.38 mmol) in dry DCM (5 mL) and TFA (1 mL) according to general procedure E (reaction time 2.5 h); 135 mg of a beige solid (99% crude yield) was yielded, used in the next step without further purification. ^1H -NMR (300 MHz, MeOD) δ 8.35 (s, 1H), 7.70 (d, $J = 8.6$ Hz, 1H), 7.65 (d, $J = 1.8$ Hz, 1H), 7.40 (dd, $J = 8.6, 1.9$ Hz, 1H), 4.54–4.41 (m, 1H), 3.24 (s, 3H), 3.15–3.06 (m, 1H), 3.02–2.95 (m, 1H), 2.94–2.84 (m, 1H), 2.61–2.48 (m, 1H), 2.15–1.85 (m, 3H), 1.77–1.60 (m, 1H); ESI-MS: (m/z) 360.0 [$\text{M} + \text{H}$] $^+$, 358.1 [$\text{M} - \text{H}$] $^-$; HPLC method A: $t_r = 3.985$ min.

(**S**)-7-Chloro-*N*-methyl-*N*-(piperidin-3-yl)-9*H*-pyrimido[4,5-*b*]indol-4-amine ((**S**)-**7c**)

The title compound was prepared from (**S**)-**6c** (180.0 mg, 0.43 mmol) in dry DCM (5 mL) and TFA (1 mL) according to general procedure E (reaction time 1.5 h); 142 mg of a beige solid (>100% crude yield) was yielded, used in the next step without further purification. ^1H -NMR (300 MHz, MeOD) δ 8.34 (s, 1H), 7.76 (d, $J = 8.6$ Hz, 1H), 7.49 (d, $J = 1.9$ Hz, 1H), 7.27 (dd, $J = 8.6, 2.0$ Hz, 1H), 4.58–4.41 (m, 1H), 3.25 (s, 3H), 3.19–3.09 (m, 1H), 3.05–2.97 (m, 1H), 2.97–2.86 (m, 1H), 2.64–2.50 (m, 1H), 2.19–1.83 (m, 3H), 1.80–1.59 (m, 1H); ESI-MS: (m/z) 316.0 [$\text{M} + \text{H}$] $^+$, 338.0 [$\text{M} + \text{Na}$] $^+$, 313.9 [$\text{M} - \text{H}$] $^-$; HPLC method A: $t_r = 3.897$ min.

(**S**)-7-Bromo-*N*-methyl-*N*-(piperidin-3-yl)-9*H*-pyrimido[4,5-*b*]indol-4-amine ((**S**)-**7d**)

The title compound was prepared from (**S**)-**6d** (190.0 mg, 0.41 mmol) in dry DCM (5 mL) and TFA (1 mL) according to general procedure E (reaction time 1 h); 141 mg of a beige solid (95% crude yield) was yielded, used in the next step without further purification. ^1H -NMR (400 MHz, MeOD) δ 8.35 (s, 1H), 7.69 (d, $J = 8.6$ Hz, 1H), 7.65 (d, $J = 1.8$ Hz, 1H), 7.40 (dd, $J = 8.6, 1.9$ Hz, 1H), 4.53–4.43 (m, 1H), 3.24 (s, 3H), 3.14–3.08 (m, 1H), 3.02–2.95 (m, 1H), 2.95–2.87 (m, 1H), 2.59–2.50 (m, 1H), 2.12–1.86 (m, 3H), 1.75–1.62 (m, 1H); ESI-MS: (m/z) 360.2 [$\text{M} + \text{H}$] $^+$, 358.2 [$\text{M} - \text{H}$] $^-$; HPLC method A: $t_r = 4.025$ min.

(7) Detailed Procedures for the Preparation of Final Compounds 8–41

3-((7-Chloro-9*H*-pyrimido[4,5-*b*]indol-4-yl)(methylamino)piperidin-1-yl)(furan-3-yl)methanone (**8**)

The title compound was prepared from **7c** (64.0 mg, 0.20 mmol), 3-furoic acid (27.3 mg, 0.24 mmol), PyBOP (130.8 mg, 0.24 mmol), and DIPEA (78.6 mg, 0.61 mmol) in dry DCM (total amount 10 mL) according to general procedure F (reaction time 1.5 h). Purification by flash column chromatography (SiO_2 , DCM–MeOH gradient elution from 96.5:3.5 to 93.5:6.5) gave 50 mg of a white solid (60% yield). ^1H -NMR (400 MHz, DMSO- d_6) δ 12.25 (s, 1H), 8.38 (s, 1H), 8.26–7.97 (m, 1H), 7.92–7.77 (m, 1H),

7.73 (t, $J = 1.7$ Hz, 1H), 7.48 (d, $J = 2.0$ Hz, 1H), 7.24 (dd, $J = 8.6, 2.1$ Hz, 1H), 6.85–6.58 (m, 1H), 4.81–3.79 (m, 3H), 3.30–2.56 (m, 5H), 2.15–1.94 (m, 2H), 1.94–1.74 (m, 1H), 1.63–1.47 (m, 1H); ESI-MS: (m/z) 410.0 $[M + H]^+$, 432.0 $[M + Na]^+$, 407.9 $[M - H]^-$; HPLC method A: $t_r = 7.624$ min.

Ethyl 3-(3-((7-chloro-9H-pyrimido[4,5-*b*]indol-4-yl)(methylamino)piperidin-1-yl)-3-oxopropanoate (9)

The title compound was prepared from **7c** (70.0 mg, 0.22 mmol), ethyl potassium malonate (45.3 mg, 0.27 mmol), PyBOP (138.4 mg, 0.27 mmol), and DIPEA (86.0 mg, 0.67 mmol) in dry DCM (total amount 10 mL) according to general procedure F. Additional ethyl potassium malonate (5.7 mg, 0.03 mmol) and PyBOP (17.3 mg, 0.03 mmol) were added after a reaction time of 2.5 h, and then stirring continued for 1 h. Purification twice by flash column chromatography (SiO₂, DCM–MeOH gradient elution from 97.5:2.5 to 93.5:6.5 and SiO₂, DCM–EtOH gradient elution from 95:5 to 93:7) gave 50 mg of a white solid (53% yield). ¹H-NMR shows a 3:2 mixture of amide bond rotamers. ¹H-NMR (400 MHz, DMSO-*d*₆) δ 12.32–12.14 (m, 1H), 8.46–8.34 (m, 1H), 7.86–7.77 (m, 1H), 7.52–7.44 (m, 1H), 7.32–7.16 (m, 1H), 4.61–4.50 (m, 0.6H), 4.42–4.34 (m, 0.4H), 4.33–4.16 (m, 1H), 4.10–3.95 (m, 2H), 3.95–3.90 (m, 0.4H), 3.79–3.68 (m, 0.6H), 3.64–3.47 (m, 2H), 3.33–3.28 (m, 0.4H, overlap with water signal), 3.28–3.15 (m, 3H), 3.08–2.95 (m, 1.2H), 2.63–2.54 (m, 0.4H), 2.10–1.74 (m, 3H), 1.58–1.40 (m, 1H), 1.17–1.08 (m, 3H); ¹³C NMR (101 MHz, DMSO-*d*₆) δ 167.7, 167.6, 164.5, 164.4, 159.43, 159.40, 157.51, 157.48, 153.7, 153.6, 137.44, 137.40, 129.3, 124.03, 123.97, 120.5, 120.4, 118.4, 118.3, 110.83, 110.81, 97.4, 97.2, 60.5, 60.4, 54.7, 54.5, 47.6, 45.7, 44.0, 41.5, 40.9, 40.8, 33.9, 32.6, 27.2, 27.1, 24.8, 24.3, 13.89, 13.86; ESI-MS: (m/z) 430.0 $[M + H]^+$, 451.9 $[M + Na]^+$, 427.8 $[M - H]^-$; HPLC method A: $t_r = 7.274$ min.

(3-((7-Chloro-9H-pyrimido[4,5-*b*]indol-4-yl)(methylamino)piperidin-1-yl)(4-(dimethylamino)phenyl) methanone (10)

The title compound was prepared from **7c** (60.0 mg, 0.19 mmol), 4-(dimethylamino) benzoic acid (37.7 mg, 0.22 mmol), PyBOP (118.6 mg, 0.22 mmol), and DIPEA (73.7 mg, 0.57 mmol) in dry DCM (total amount 7 mL) according to general procedure F (reaction time 40 min). Purification by flash column chromatography (SiO₂, DCM–MeOH gradient elution from 95.5:4.5 to 93.5:6.5) gave 70 mg of an off-white solid (80% yield). ¹H-NMR (400 MHz, DMSO-*d*₆) δ 12.25 (s, 1H), 8.39 (s, 1H), 7.80 (d, $J = 8.0$ Hz, 1H), 7.50 (d, $J = 1.9$ Hz, 1H), 7.25 (dd, $J = 8.6, 2.0$ Hz, 1H), 7.17 (d, $J = 7.8$ Hz, 2H), 6.60 (d, $J = 7.4$ Hz, 2H), 4.50–3.85 (m, 3H), 3.28–3.13 (m, 4H), 3.04–2.78 (m, 7H), 2.12–1.99 (m, 2H), 1.93–1.76 (m, 1H), 1.65–1.46 (m, 1H); ESI-MS: (m/z) 463.9 $[M + H]^+$, 485.9 $[M + Na]^+$, 461.8 $[M - H]^-$; HPLC method A: $t_r = 8.928$ min.

1-(3-((7-Chloro-9H-pyrimido[4,5-*b*]indol-4-yl)(methylamino)piperidin-1-yl)butan-1-one (11)

The title compound was prepared from **7c** (60.0 mg, 0.19 mmol), butyric acid (20.9 mg, 0.24 mmol), TBTU (76.3 mg, 0.24 mmol), and DIPEA (73.7 mg, 0.57 mmol) in dry DCM (total amount 10 mL) according to general procedure F (reaction time 1 h). Purification by flash column chromatography (SiO₂, DCM–MeOH 94.5:5.5) gave 54 mg of a white solid (74% yield). ¹H-NMR shows a 5:4 mixture of amide bond rotamers. ¹H-NMR (400 MHz, CDCl₃) δ 12.42 (br s, 1H), 8.58–8.42 (m, 1H), 7.74–7.59 (m, 1H), 7.51–7.38 (m, 1H), 7.25–7.16 (m, 1H), 5.05–4.86 (m, 0.45H), 4.81–4.65 (m, 0.55H), 4.53–4.29 (m, 1H), 4.28–4.16 (m, 0.55H), 3.97–3.81 (m, 0.45H), 3.37–3.19 (m, 3H), 3.19–3.10 (m, 0.55H), 3.05–2.89 (m, 0.9H), 2.57–2.30 (m, 2.55H), 2.22–1.85 (m, 3H), 1.82–1.53 (m, 3H), 0.98 (t, $J = 7.3$ Hz, 3H); ¹³C NMR (101 MHz, CDCl₃) δ 172.4, 171.9, 160.1, 157.7, 157.3, 152.8, 152.6, 137.6, 137.5, 131.2, 131.1, 123.8, 123.7, 121.5, 121.4, 118.7, 111.7, 111.5, 98.8, 98.5, 55.3, 55.2, 47.8, 46.0, 45.0, 42.2, 35.7, 34.4, 33.4, 28.8, 28.0, 25.6, 25.0, 19.0, 14.3, 14.2; ESI-MS: (m/z) 408.3 $[M + Na]^+$, 384.3 $[M - H]^-$; HPLC method A: $t_r = 8.285$ min.

1-(3-((7-Chloro-9H-pyrimido[4,5-*b*]indol-4-yl)(methylamino)piperidin-1-yl)-3-methylbutan-1-one (12)

The title compound was prepared from **7c** (60.0 mg, 0.19 mmol), isovaleric acid (22.3 mg, 0.22 mmol), TBTU (76.3 mg, 0.24 mmol), and DIPEA (73.7 mg, 0.57 mmol) in dry DCM (total amount 10 mL) according to general procedure F (reaction time 1 h). Purification by flash column chromatography

(SiO₂, DCM–MeOH 95:5) gave 61 mg of a white solid (80% yield). ¹H-NMR shows a 5:4 mixture of amide bond rotamers. ¹H-NMR (400 MHz, CDCl₃) δ 12.30 (br s, 1H), 8.56–8.47 (m, 1H), 7.73–7.63 (m, 1H), 7.50–7.41 (m, 1H), 7.25–7.19 (m, 1H), 5.04–4.93 (m, 0.45H), 4.80–4.70 (m, 0.55H), 4.52–4.29 (m, 1H), 4.28–4.20 (m, 0.55H), 3.97–3.85 (m, 0.45H), 3.34–3.20 (m, 3H), 3.18–3.10 (m, 0.55H), 3.05–2.91 (m, 0.9H), 2.55–2.46 (m, 0.55H), 2.45–2.24 (m, 2H), 2.23–1.86 (m, 4H), 1.75–1.54 (m, 1H), 1.01–0.93 (m, 6H); ¹³C NMR (101 MHz, CDCl₃) δ 171.9, 171.4, 160.1, 157.7, 157.3, 152.8, 152.6, 137.6, 137.5, 131.22, 131.15, 123.8, 123.7, 121.6, 121.4, 118.7, 111.7, 111.5, 98.9, 98.6, 55.4, 55.3, 48.0, 46.2, 45.1, 42.5, 42.3, 34.4, 33.4, 28.8, 28.0, 26.0, 25.9, 25.7, 25.0, 22.93, 22.89; ESI-MS: (*m/z*) 422.3 [M + Na]⁺, 398.3 [M – H][–]; HPLC method A: t_r = 8.646 min.

1-(3-((7-Chloro-9*H*-pyrimido[4,5-*b*]indol-4-yl)(methyl)amino)piperidin-1-yl)-3-(dimethylamino)propan-1-one (**13**)

The title compound was prepared from **7c** (75.0 mg, 0.24 mmol), 3-(dimethylamino) propionic acid hydrochloride (47.4 mg, 0.31 mmol), PyBOP (160.7 mg, 0.31 mmol), and TEA (72.1 mg, 0.71 mmol) in dry DCM (total amount 10 mL) according to general procedure F (reaction time 1.5 h). During the extractive work-up the organic layer was not washed with saturated NH₄Cl solution due to the basic amino function of the introduced substituent. Purification twice by flash column chromatography (SiO₂, DCM–(2N NH₃ in MeOH) gradient elution from 95:5 to 9:1 and SiO₂, DCM:(2N NH₃ in MeOH) gradient elution from 92.5:7.5 to 9:1) gave 60 mg of a white solid (61% yield). ¹H-NMR shows a 3:2 mixture of amide bond rotamers. ¹H-NMR (400 MHz, CDCl₃) δ 13.05–12.30 (m, 1H), 8.52–8.41 (m, 1H), 7.65–7.56 (m, 1H), 7.44–7.36 (m, 1H), 7.21–7.11 (m, 1H), 4.96–4.83 (m, 0.4H), 4.76–4.62 (m, 0.6H), 4.47–4.20 (m, 1.6H), 3.95–3.84 (m, 0.4H), 3.32–3.17 (m, 3H), 3.17–3.08 (m, 0.6H), 3.03–2.95 (m, 0.4H), 2.93–2.86 (m, 0.4H), 2.85–2.57 (m, 4H), 2.55–2.45 (m, 0.6H), 2.32 (s, 6H), 2.18–1.83 (m, 3H), 1.73–1.52 (m, 1H); ¹³C NMR (101 MHz, CDCl₃) δ 170.7, 170.2, 160.1, 160.0, 157.8, 157.7, 153.0, 137.7, 137.6, 131.0, 130.9, 123.7, 123.6, 121.22, 121.15, 118.7, 118.6, 111.6, 111.4, 98.8, 98.5, 55.3, 55.2, 54.9, 47.6, 46.0, 45.4, 45.3, 44.9, 42.3, 34.4, 33.4, 31.8, 31.5, 28.7, 27.9, 25.5, 24.8; ESI-MS: (*m/z*) 415.4 [M + H]⁺, 413.2 [M – H][–]; HPLC method A: t_r = 4.833 min.

1-(3-((7-Chloro-9*H*-pyrimido[4,5-*b*]indol-4-yl)(methyl)amino)piperidin-1-yl)ethan-1-one (**14**)

The title compound was prepared from **7c** (70.0 mg, 0.22 mmol), acetic acid (20.0 mg, 0.33 mmol), PyBOP (144.4 mg, 0.28 mmol), and DIPEA (86.1 mg, 0.67 mmol) in dry DCM (total amount 12 mL) according to general procedure F (reaction time 1.5 h). Purification twice by flash column chromatography (SiO₂, DCM–MeOH gradient elution from 96:4 to 93.5:6.5 and SiO₂, EtOAc/MeOH 9:1) gave 44 mg of an off-white solid (55% yield). ¹H-NMR shows a 5:4 mixture of amide bond rotamers. ¹H-NMR (300 MHz, DMSO-*d*₆) δ 12.30–12.14 (m, 1H), 8.41 (s, 1H), 7.87–7.78 (m, 1H), 7.51–7.44 (m, 1H), 7.30–7.17 (m, 1H), 4.57–4.47 (m, 0.55H), 4.43–4.12 (m, 1.45H), 4.07–3.95 (m, 0.45H), 3.84–3.72 (m, 0.55H), 3.33–3.16 (m, 3.45H), 3.07–2.85 (m, 1.1H), 2.57–2.44 (m, 0.45H, overlap with DMSO-*d*₅ signal), 2.10–1.86 (m, 5H), 1.86–1.73 (m, 1H), 1.58–1.35 (m, 1H); ¹³C NMR (101 MHz, DMSO-*d*₆) δ 168.3, 168.2, 159.5, 159.4, 157.50, 157.47, 153.7, 153.6, 137.4, 129.2, 124.0, 123.9, 120.4, 120.3, 118.4, 118.3, 110.8, 97.4, 97.1, 54.7, 54.5, 47.6, 45.7, 43.6, 41.0, 33.8, 32.6, 27.3, 27.1, 25.1, 24.4, 21.3; ESI-MS: (*m/z*) 380.4 [M + Na]⁺, 356.5 [M – H][–]; HPLC method A: t_r = 6.993 min.

1-(3-((7-Chloro-9*H*-pyrimido[4,5-*b*]indol-4-yl)(methyl)amino)piperidin-1-yl)-2-cyclopropylethan-1-one (**15**)

The title compound was prepared from **7c** (50.0 mg, 0.16 mmol), 2-cyclopropylacetic acid (19.8 mg, 0.20 mmol), TBTU (63.6 mg, 0.20 mmol), and DIPEA (61.4 mg, 0.48 mmol) in dry DCM (total amount 10 mL) according to general procedure F (reaction time 1.5 h). Purification by flash column chromatography (SiO₂, DCM–MeOH gradient elution from 96:4 to 93.5:6.5) gave 52 mg of a beige solid (83% yield). ¹H-NMR shows a 5:4 mixture of amide bond rotamers. ¹H-NMR (300 MHz, CDCl₃) δ 12.20 (br s, 1H), 8.72–8.27 (m, 1H), 7.79–7.59 (m, 1H), 7.56–7.39 (m, 1H), 7.29–7.17 (m, 1H, overlap with CHCl₃ signal), 5.07–4.88 (m, 0.45H), 4.81–4.66 (m, 0.55H), 4.58–4.30 (m, 1H), 4.27–4.12

(m, 0.55H), 3.94–3.79 (m, 0.45H), 3.38–2.91 (m, 4.55H), 2.60–2.29 (m, 2.45H), 2.25–1.83 (m, 3H), 1.81–1.52 (m, 1H), 1.18–0.96 (m, 1H), 0.65–0.40 (m, 2H), 0.34–0.08 (m, 2H); ^{13}C NMR (101 MHz, CDCl_3) δ 172.0, 171.5, 160.0, 157.6, 157.0, 152.7, 152.4, 137.6, 131.2, 123.9, 123.6, 121.6, 121.4, 118.7, 111.7, 98.8, 55.3, 55.2, 47.9, 46.2, 45.1, 42.2, 38.9, 38.8, 34.4, 33.5, 28.8, 28.0, 25.6, 24.9, 7.5, 4.70, 4.66; ESI-MS: (m/z) 398.3 $[\text{M} + \text{H}]^+$, 420.3 $[\text{M} + \text{Na}]^+$, 396.3 $[\text{M} - \text{H}]^-$; HPLC method A: t_r = 8.031 min.

1-(3-((7-Chloro-9H-pyrimido[4,5-*b*]indol-4-yl)(methyl)amino)piperidin-1-yl)propan-1-one (16)

The title compound was prepared from **7c** (60.0 mg, 0.17 mmol), propionic acid (16.9 mg, 0.23 mmol), PyBOP (118.6 mg, 0.23 mmol), and DIPEA (73.7 mg, 0.57 mmol) in dry DCM (total amount 10 mL) according to general procedure F (reaction time 40 min). Purification by flash column chromatography (SiO_2 , DCM–MeOH gradient elution from 96:4 to 93.5:6.5) gave 38 mg of a white solid (54% yield). ^1H -NMR shows a 5:4 mixture of amide bond rotamers. ^1H -NMR (400 MHz, CDCl_3) δ 12.58 (br s, 1H), 8.59–8.37 (m, 1H), 7.74–7.58 (m, 1H), 7.52–7.40 (m, 1H), 7.24–7.15 (m, 1H), 5.02–4.88 (m, 0.45H), 4.81–4.67 (m, 0.55H), 4.52–4.30 (m, 1H), 4.29–4.18 (m, 0.55H), 3.95–3.81 (m, 0.45H), 3.37–3.19 (m, 3H), 3.19–3.07 (m, 0.55H), 3.07–2.85 (m, 1H), 2.65–2.34 (m, 2.45H), 2.21–1.83 (m, 3H), 1.76–1.54 (m, 1H), 1.26–1.12 (m, 3H); ^{13}C NMR (101 MHz, CDCl_3) δ 173.2, 172.7, 159.92, 159.88, 157.2, 156.5, 152.4, 151.8, 137.6, 137.5, 131.1, 123.8, 123.6, 121.5, 121.3, 118.6, 111.72, 111.68, 98.5, 98.4, 55.2, 55.1, 47.5, 45.8, 44.9, 42.2, 34.5, 33.5, 28.7, 28.0, 26.9, 26.8, 25.5, 24.9, 9.8; ESI-MS: (m/z) 393.9 $[\text{M} + \text{Na}]^+$, 369.8 $[\text{M} - \text{H}]^-$; HPLC method A: t_r = 7.599 min.

1-(3-((7-Chloro-9H-pyrimido[4,5-*b*]indol-4-yl)(methyl)amino)piperidin-1-yl)-3,3,3-trifluoropropan-1-one (17)

The title compound was prepared from **7c** (65.0 mg, 0.21 mmol), trifluoropropionic acid (33.0 mg, 0.26 mmol), TBTU (82.6 mg, 0.26 mmol), and DIPEA (79.8 mg, 0.62 mmol) in dry DCM (total amount 10 mL) according to general procedure F (reaction time 2 h). Purification by flash column chromatography (SiO_2 , DCM–MeOH 95:5) gave 44 mg of a light yellow solid (50% yield). ^1H -NMR shows a 3:2 mixture of amide bond rotamers. ^1H -NMR (300 MHz, $\text{DMSO}-d_6$) δ 12.23 (s, 1H), 8.44–8.33 (m, 1H), 7.89–7.76 (m, 1H), 7.54–7.44 (m, 1H), 7.30–7.16 (m, 1H), 4.65–4.52 (m, 0.6H), 4.43–4.16 (m, 1.4H), 4.05–3.95 (m, 0.4H), 3.84–3.62 (m, 2.6H), 3.34–3.17 (m, 3.4H), 3.08–2.93 (m, 1.2H), 2.68–2.54 (m, 0.4H), 2.11–1.72 (m, 3H), 1.62–1.40 (m, 1H); ESI-MS: (m/z) 447.8 $[\text{M} + \text{Na}]^+$, 423.8 $[\text{M} - \text{H}]^-$; HPLC method A: t_r = 8.124 min.

1-(3-((7-chloro-9H-pyrimido[4,5-*b*]indol-4-yl)(methyl)amino)piperidin-1-yl)-2,2-dimethylpropan-1-one (38)

7c (60.0 mg, 0.19 mmol), pivalic acid (24.3 mg, 0.24 mmol), TBTU (70.3 mg, 0.24 mmol), and DIPEA (73.7 mg, 0.57 mmol) were stirred in dry DCM (10 mL) at rt and under N_2 atmosphere, but no conversion was observed. Therefore, the stirring mixture was cooled down to 0 °C, and pivaloyl chloride (237 μL of a freshly prepared 1-M solution in dry DCM, 0.24 mmol) was added. The cooling was removed, and the mixture was stirred for 45 min under N_2 atmosphere. Saturated NH_4Cl solution (20 mL) was added, and the mixture was diluted with DCM. Phases were separated, and the organic layer was washed with saturated NH_4Cl solution (20 mL) and saturated NaHCO_3 solution (2 \times 20 mL), then dried over Na_2SO_4 , and concentrated under reduced pressure. Purification of the residue by flash column chromatography (DCM–MeOH 95:5) gave 36 mg of a white solid (47% yield). ^1H -NMR (300 MHz, CDCl_3) δ 12.39 (br s, 1H), 8.49 (s, 1H), 7.67 (d, J = 8.5 Hz, 1H), 7.46 (s, 1H), 7.21 (d, J = 8.3 Hz, 1H), 4.85–4.68 (m, 1H), 4.59–4.37 (m, 2H), 3.29 (s, 3H), 3.12–3.00 (m, 1H), 2.82–2.67 (m, 1H), 2.17–1.85 (m, 3H), 1.75–1.57 (m, 1H), 1.31 (s, 9H); ^{13}C NMR (101 MHz, CDCl_3) δ 177.0, 160.0, 157.4, 152.5, 137.6, 131.1, 123.7, 121.3, 118.7, 111.6, 98.6, 55.2, 47.8, 45.7, 39.0, 33.9, 28.6, 28.5, 25.2; ESI-MS: (m/z) 400.5 $[\text{M} + \text{H}]^+$, 422.5 $[\text{M} + \text{Na}]^+$, 398.5 $[\text{M} - \text{H}]^-$; HPLC method A: t_r = 8.748 min.

(3-((7-chloro-9H-pyrimido[4,5-*b*]indol-4-yl)(methyl)amino)piperidin-1-yl)(cyclopropyl)methanone (39)

Cyclopropanecarbonyl chloride (190 μL of a freshly prepared 1M solution in dry THF, 0.19 mmol) was slowly added to an ice-cooled stirring solution of **7c** (50.0 mg, 0.16 mmol) and TEA (32.0 mg,

0.32 mmol) in dry THF (10 mL) under N₂ atmosphere. The mixture was left to warm to rt and stirred under N₂ atmosphere. Additional cyclopropanecarbonyl chloride solution was added after 1 h (79 µL, 0.08 mmol) and 2 h (158 µL, 0.16 mmol) after cooling down the mixture each time; however, full consumption of the starting material was not achieved. The mixture was evaporated to dryness. Purification of the residue by flash column chromatography (DCM–MeOH 95:5) gave 46 mg of a white solid (76% yield). ¹H-NMR shows a 5:4 mixture of amide bond rotamers. ¹H-NMR (400 MHz, DMSO-*d*₆) δ 12.23 (s, 1H), 8.41 (s, 1H), 7.86–7.76 (m, 1H), 7.48 (s, 1H), 7.32–7.14 (m, 1H), 4.63–4.48 (m, 0.55H), 4.44–4.14 (m, 2.45H), 3.30–3.14 (m, 3H), 3.12–2.92 (m, 1H), 2.64–2.54 (m, 0.45H), 2.12–1.74 (m, 4H), 1.56–1.38 (m, 1H), 0.78–0.55 (m, 4H), missing 0.45H below water signal; ¹³C NMR (101 MHz, CDCl₃) δ 172.5, 160.1, 157.2 (br), 152.5 (br), 137.6, 131.1, 123.7, 121.4, 118.7, 111.6, 98.7, 55.3, 47.9 (br), 45.9 (br), 42.9 (br), 34.2 (br), 28.7 (br), 24.9 (br), 11.4, 7.6, 7.4; ESI-MS: (*m/z*) 384.2 [M + H]⁺, 406.2 [M + Na]⁺, 382.2 [M – H][–]; HPLC method A: t_r = 7.837 min.

1-(3-((7-Chloro-9*H*-pyrimido[4,5-*b*]indol-4-yl)(methyl)amino)piperidin-1-yl)prop-2-en-1-one (40)

Acryloyl chloride (228 µL of a freshly prepared 1M solution in dry THF, 0.23 mmol) was slowly added to a stirring solution of **7c** (60.0 mg, 0.19 mmol) and TEA (38.5 mg, 0.38 mmol) in dry THF (10 mL) under N₂ atmosphere and ice/MeOH cooling. The mixture was left to warm to rt and stirred until reaction control indicated sufficient conversion. Extractive work-up followed by flash column chromatography (DCM–MeOH 95:5) gave 50 mg of a white solid (71% yield). ¹H-NMR shows a 5:4 mixture of amide bond rotamers. ¹H-NMR (400 MHz, DMSO-*d*₆) δ 12.23 (s, 1H), 8.41 (s, 1H), 7.88–7.75 (m, 1H), 7.48 (d, *J* = 1.8 Hz, 1H), 7.22 (d, *J* = 8.3 Hz, 1H), 6.94–6.74 (m, 1H), 6.15–6.03 (m, 1H), 5.74–5.62 (m, 1H), 4.65–4.54 (m, 0.55H), 4.50–4.38 (m, 0.45H), 4.34–4.19 (m, 1.45H), 4.10–3.98 (m, 0.55H), 3.29–3.16 (m, 3H), 3.10–2.97 (m, 1.1H), 2.70–2.58 (m, 0.45H), 2.10–1.78 (m, 3H), 1.53–1.37 (m, 1H), missing 0.45H below water signal; ¹³C NMR (101 MHz, DMSO-*d*₆) δ 164.49, 159.40, 157.45, 153.58, 137.40, 129.23, 128.45, 126.98, 123.91, 120.33, 118.34, 110.81, 97.33, 55.07, 54.43, 47.22, 45.09, 44.16, 41.65, 33.63, 32.67, 27.22, 25.37, 24.31; ESI-MS: (*m/z*) 370.1 [M + H]⁺, 392.2 [M + Na]⁺, 368.1 [M – H][–]; HPLC method A: t_r = 7.384 min.

2-(3-(3-((7-Chloro-9*H*-pyrimido[4,5-*b*]indol-4-yl)(methyl)amino)piperidin-1-yl)oxetan-3-yl)acetonitrile (41)

7c (60.0 mg, 0.19 mmol) and 2-(oxetan-3-ylidene)acetonitrile (36.1 mg, 0.38 mmol) were stirred in EtOH at 70 °C for 6 d. The mixture was concentrated under reduced pressure. Purification of the residue by flash column chromatography (SiO₂, DCM–MeOH gradient elution from 96:4 to 93.5:6.5) gave 59 mg of a beige solid (76% yield). ¹H-NMR (400 MHz, DMSO-*d*₆) δ 12.21 (s, 1H), 8.41 (s, 1H), 7.79 (d, *J* = 8.6 Hz, 1H), 7.48 (d, *J* = 1.5 Hz, 1H), 7.27 (dd, *J* = 8.6, 1.6 Hz, 1H), 4.52–4.31 (m, 5H), 3.17 (s, 3H), 3.01 (s, 2H), 2.82–2.73 (m, 1H), 2.61–2.54 (m, 1H), 2.49–2.44 (m, 1H, overlap with DMSO-*d*₅ signal), 2.18–2.06 (m, 1H), 1.93–1.69 (m, 3H), 1.60–1.47 (m, 1H); ¹³C NMR (50 MHz, DMSO-*d*₆) δ 159.5, 157.5, 153.8, 137.4, 129.2, 123.8, 120.3, 119.3, 118.5, 110.9, 97.1, 78.1, 61.0, 55.1, 48.0, 45.0, 33.1, 27.3, 24.7, 17.4; ESI-MS: (*m/z*) 411.0 [M + H]⁺, 433.0 [M + Na]⁺, 409.0 [M – H][–]; HPLC method A: t_r = 7.888 min.

3-(3-(methyl(9*H*-pyrimido[4,5-*b*]indol-4-yl)amino)piperidin-1-yl)-3-oxopropanenitrile (18)

Cyanoacetic acid (36.7 mg, 0.31 mmol) and PyBOP (179.8 mg, 0.34 mmol) were stirred in dry DCM (3 mL) at rt for 20 min. A solution of **7a** (80.4 mg, 0.29 mmol) and DIPEA (43.9 mg, 0.34 mmol) in dry DCM (2 mL) was drop-added. The mixture was stirred at rt for 2 h and then concentrated under reduced pressure. Saturated NaHCO₃ solution was added to the residue, and the mixture was extracted with EtOAc (3 × 10 mL). Combined organic layers were dried over Na₂SO₄ and concentrated under reduced pressure. Purification of the residue by flash column chromatography (SiO₂, DCM–EtOH gradient elution from 98:2 to 9:1) gave 55 mg (55% yield). ¹H-NMR shows a 3:2 mixture of amide bond rotamers: (300 MHz, DMSO-*d*₆) δ 12.19–11.99 (m, 1H), 8.47–8.36 (m, 1H), 7.90–7.78 (m, 1H), 7.54–7.45 (m, 1H), 7.44–7.34 (m, 1H), 7.31–7.19 (m, 1H), 4.55–4.43 (m, 0.6H), 4.39–4.21 (m, 1.4H), 4.18–3.97 (m, 2H), 3.94–3.84 (m, 0.4H), 3.69–3.56 (m, 0.6H), 3.31–3.14 (m, 3.4H), 3.10–2.93 (m, 1.2H), 2.70–2.56 (m, 0.4H),

2.10–1.74 (m, 3H), 1.66–1.42 (m, 1H); ^{13}C NMR (101 MHz, $\text{DMSO-}d_6$) δ 161.6, 161.4, 159.6, 159.5, 157.0, 153.3, 136.7, 124.8, 122.7, 122.6, 120.4, 120.3, 119.32, 119.28, 116.1, 116.0, 111.2, 97.9, 97.7, 54.6, 54.2, 47.4, 45.5, 44.2, 42.1, 34.0, 32.7, 27.1, 26.9, 24.8, 24.7, 24.1; ESI-MS: (m/z) 370.9 [$\text{M} + \text{Na}$] $^+$, 346.9 [$\text{M} - \text{H}$] $^-$; HPLC method B: t_r = 3.316 min.

3-(3-((7-Fluoro-9H-pyrimido[4,5-*b*]indol-4-yl)(methyl)amino)piperidin-1-yl)-3-oxopropanenitrile (19)

7b (80.0 mg, 0.27 mmol) and DIPEA (51.7 mg, 0.40 mmol) were stirred in dry DCM (3 mL). A suspension of cyanoacetic acid (25.0 mg, 0.29 mmol) and PyBOP (166.9 mg, 0.32 mmol) in dry DCM (3 mL) was drop-added. The mixture was stirred at rt for 2 h and then concentrated under reduced pressure. Saturated NaHCO_3 solution (10 mL) was added to the residue, and the mixture was extracted with EtOAc (3×10 mL). Combined organic layers were dried over Na_2SO_4 and concentrated under reduced pressure. Purification of the residue by flash column chromatography (SiO_2 , DCM–EtOH gradient elution from 98:2 to 90:10 (twice)) gave 28 mg (29% yield); $^1\text{H-NMR}$ shows a 5:4 mixture of amide bond rotamers. $^1\text{H-NMR}$ (300 MHz, $\text{DMSO-}d_6$) δ 12.28–12.15 (m, 1H), 8.45–8.37 (m, 1H), 7.90–7.77 (m, 1H), 7.30–7.21 (m, 1H), 7.16–7.01 (m, 1H), 4.53–4.44 (m, 0.55H), 4.40–4.17 (m, 1.45H), 4.15–3.98 (m, 2H), 3.92–3.84 (m, 0.45H), 3.66–3.58 (m, 0.55H), 3.30–3.16 (m, 3H), 3.09–2.96 (m, 1.1H), 2.69–2.57 (m, 0.45H), 2.09–1.89 (m, 2H), 1.88–1.75 (m, 1H), 1.67–1.41 (m, 1H), missing 0.45H below water signal; ESI-MS: (m/z) 389.2 [$\text{M} + \text{Na}$] $^+$, 365.1 [$\text{M} - \text{H}$] $^-$; HPLC method B: t_r = 4.514 min.

3-(3-((7-bromo-9H-pyrimido[4,5-*b*]indol-4-yl)(methyl)amino)piperidin-1-yl)-3-oxopropanenitrile (20)

Cyanoacetic acid (31.8 mg, 0.37 mmol) and PyBOP (213.3 mg, 0.4 mmol) were stirred in dry DCM (5 mL) at rt. A suspension of **7d** (120.0 mg, 0.33 mmol) and DIPEA (66.0 mg, 0.5 mmol) in dry DCM (5 mL) was added. The mixture was stirred at rt for 2 h and then concentrated under reduced pressure. Saturated NaHCO_3 solution was added to the residue, and the mixture was extracted with EtOAc (3×10 mL). Combined organic layers were dried over Na_2SO_4 and concentrated under reduced pressure. Purification of the residue by flash column chromatography (SiO_2 , DCM–EtOH gradient elution from 98:2 to 9:1) gave 72 mg (51% yield). $^1\text{H-NMR}$ shows a 5:4 mixture of amide bond rotamers. $^1\text{H-NMR}$ (300 MHz, $\text{DMSO-}d_6$) δ 12.29–12.17 (m, 1H), 8.47–8.38 (m, 1H), 7.82–7.73 (m, 1H), 7.65–7.59 (m, 1H), 7.43–7.33 (m, 1H), 4.54–4.45 (m, 0.55H), 4.40–4.18 (m, 1.45H), 4.14–3.98 (m, 2H), 3.92–3.82 (m, 0.45H), 3.68–3.57 (m, 0.55H), 3.29–3.17 (m, 3H), 3.09–2.95 (m, 1.1H), 2.70–2.57 (m, 0.45H), 2.08–1.74 (m, 3H), 1.67–1.41 (m, 1H), missing 0.45H below water signal; ESI-MS: (m/z) 448.9 [$\text{M} + \text{Na}$] $^+$, 424.8 [$\text{M} - \text{H}$] $^-$; HPLC method B: t_r = 6.305 min.

3-(3-((7-Iodo-9H-pyrimido[4,5-*b*]indol-4-yl)(methyl)amino)piperidin-1-yl)-3-oxopropanenitrile (21)

The title compound was prepared from **7e** (75 mg, 0.18 mmol), cyanoacetic acid (19.6 mg, 0.23 mmol), TBTU (73.9 mg, 0.23 mmol), and DIPEA (71.4 mg, 0.55 mmol) in dry DCM (total amount 12 mL) according to general procedure F (reaction time 2 h). Purification by flash column chromatography (SiO_2 , DCM–MeOH 96:4) gave 61 mg of a white solid (70% yield); $^1\text{H-NMR}$ shows a 3:2 mixture of amide bond rotamers. $^1\text{H-NMR}$ (400 MHz, $\text{DMSO-}d_6$) δ 12.24–12.12 (m, 1H), 8.47–8.38 (m, 1H), 7.79 (s, 1H), 7.68–7.59 (m, 1H), 7.58–7.47 (m, 1H), 4.55–4.42 (m, 0.6H), 4.40–4.19 (m, 1.4H), 4.19–3.98 (m, 2H), 3.92–3.82 (m, 0.4H), 3.69–3.56 (m, 0.6H), 3.32–3.13 (m, 3H), 3.09–2.95 (m, 1.2H), 2.68–2.57 (m, 0.4H), 2.09–1.89 (m, 2H), 1.89–1.75 (m, 1H), 1.67–1.44 (m, 1H), missing 0.4H below water signal; ^{13}C NMR (101 MHz, $\text{DMSO-}d_6$) δ 161.6, 161.5, 159.5, 159.4, 156.9, 153.8, 138.0, 128.8, 128.7, 124.6, 124.5, 119.6, 119.02, 118.96, 116.1, 116.0, 97.4, 97.2, 89.5, 89.4, 54.6, 54.2, 47.3, 45.5, 44.1, 42.0, 34.0, 32.7, 27.0, 26.9, 24.8, 24.6, 24.1. ESI-MS: (m/z) 497.2 [$\text{M} + \text{Na}$] $^+$, 473.2 [$\text{M} - \text{H}$] $^-$; HPLC method A: t_r = 7.258 min.

3-(3-((7-methoxy-9H-pyrimido[4,5-*b*]indol-4-yl)(methyl)amino)piperidin-1-yl)-3-oxopropanenitrile (22)

7f (120.0 mg, 0.39 mmol) and DIPEA (99.6 mg, 0.77 mmol) were stirred in dry DCM (5 mL) at rt. A suspension of cyanoacetic acid (36.1 mg, 0.42 mmol) and PyBOP (240.7 mg, 0.46 mmol) in dry DCM

(5 mL) was drop-added. The mixture was stirred at rt for 2 h and then concentrated under reduced pressure. Saturated NaHCO₃ solution (10 mL) was added to the residue, and the mixture was extracted with EtOAc (3 × 10 mL). Combined organic layers were dried over Na₂SO₄ and concentrated under reduced pressure. Purification of the residue by flash column chromatography (SiO₂, DCM–EtOH gradient elution from 98:2 to 9:1 (twice)) gave 62 mg (43% yield). ¹H-NMR shows a 3:2 mixture of amide bond rotamers. ¹H-NMR (300 MHz, DMSO-*d*₆) δ 12.05–11.88 (m, 1H), 8.43–8.28 (m, 1H), 7.79–7.61 (m, 1H), 7.02–6.92 (m, 1H), 6.92–6.79 (m, 1H), 4.52–4.40 (m, 0.6H), 4.38–4.16 (m, 1.4H), 4.15–3.97 (m, 2H), 3.93–3.77 (m, 3.4H), 3.68–3.56 (m, 0.6H), 3.27–3.12 (m, 3H), 3.08–2.93 (m, 1.2H), 2.69–2.58 (m, 0.4H), 2.10–1.74 (m, 3H), 1.65–1.41 (m, 1H), missing 0.4H below water signal; ESI-MS: (*m/z*) 379.0 [M + H]⁺, 400.9 [M + Na]⁺, 378.0 [M – H][–]; HPLC method B: t_r = 3.635 min.

3-(3-(Methyl(7-(trifluoromethyl)-9H-pyrimido[4,5-*b*]indol-4-yl)amino)piperidin-1-yl)-3-oxopropanenitrile (23)

7g (100.0 mg, 0.29 mmol) and DIPEA (54.3 mg, 0.42 mmol) were stirred in dry DCM (5 mL) at rt. A suspension of cyanoacetic acid (26.8 mg, 0.31 mmol) and PyBOP (178.7 mg, 0.36 mmol) in dry DCM (5 mL) was drop-added. The mixture was stirred at rt for 2 h and then concentrated under reduced pressure. Saturated NaHCO₃ solution (10 mL) was added to the residue, and the mixture was extracted with EtOAc (3 × 10 mL). Combined organic layers were dried over Na₂SO₄ and concentrated under reduced pressure. Purification of the residue twice by flash column chromatography (SiO₂, DCM–EtOH gradient elution from 97:3 to 4:1 and SiO₂, DCM–(2N NH₃ in MeOH) gradient elution from 99:1 to 92:8) gave 28 mg (23% yield); ¹H-NMR shows a 3:2 mixture of amide bond rotamers. ¹H-NMR (300 MHz, DMSO-*d*₆) δ 12.45 (s, 1H), 8.50–8.43 (m, 1H), 8.09–7.99 (m, 1H), 7.74 (s, 1H), 7.59–7.48 (m, 1H), 4.58–4.49 (m, 0.6H), 4.41–4.27 (m, 1.4H), 4.16–4.00 (m, 2H), 3.93–3.84 (m, 0.4H), 3.71–3.60 (m, 0.6H), 3.33–3.21 (m, 3.4H), 3.10–2.95 (m, 1.2H), 2.69–2.58 (m, 0.4H), 2.11–1.76 (m, 3H), 1.70–1.45 (m, 1H); ESI-MS: (*m/z*) 438.9 [M + Na]⁺, 415.0 [M – H][–]; HPLC method B: t_r = 6.640 min.

3-(3-((7-Chloro-2-methyl-9H-pyrimido[4,5-*b*]indol-4-yl)(methyl)amino)piperidin-1-yl)-3-oxopropanenitrile (24)

The title compound was prepared from **71** (65.0 mg, 0.20 mmol), cyanoacetic acid (21.0 mg, 0.25 mmol), TBTU (79.1 mg, 0.25 mmol), and DIPEA (76.4 mg, 0.59 mmol) in dry DCM (total amount 10 mL) according to general procedure F (reaction time 2 h). Purification by flash column chromatography (SiO₂, DCM–MeOH gradient elution from 95.5:4.5 to 93:7) gave 48 mg of a grey-yellow solid (61% yield). ¹H-NMR shows a 1:1 mixture of amide bond rotamers. ¹H-NMR (300 MHz, DMSO-*d*₆) δ 12.02 (s, 1H), 7.84–7.71 (m, 1H), 7.45 (d, *J* = 2.0 Hz, 1H), 7.28–7.15 (m, 1H), 4.57–4.48 (m, 0.5H), 4.39–4.30 (m, 0.5H), 4.29–3.97 (m, 3H), 3.95–3.86 (m, 0.5H), 3.67–3.58 (m, 0.5H), 3.34–3.27 (m, 0.5H), 3.26–3.14 (m, 3H), 3.08–2.92 (m, 1H), 2.70–2.58 (m, 0.5H), 2.53–2.47 (m, 3H, overlap with DMSO-*d*₅ signal), 2.13–1.72 (m, 3H), 1.67–1.43 (m, 1H); ¹³C NMR (101 MHz, DMSO-*d*₆) δ 162.6, 162.5, 161.7, 161.5, 159.5, 159.4, 158.5, 158.4, 137.5, 137.4, 128.8, 123.7, 123.5, 120.3, 118.6, 118.5, 116.2, 116.0, 110.8, 95.2, 95.0, 54.5, 54.3, 47.2, 45.6, 44.1, 42.3, 34.2, 32.7, 27.4, 27.0, 25.8, 25.7, 25.0, 24.9, 24.7, 24.3; ESI-MS: (*m/z*) 396.9 [M + H]⁺, 418.9 [M + Na]⁺, 394.9 [M – H][–]; HPLC method A: t_r = 7.427 min.

1-(3-(methyl(9H-pyrimido[4,5-*b*]indol-4-yl)amino)piperidin-1-yl)propan-1-one (25)

The title compound was prepared from **7a** (60.0 mg, 0.21 mmol), propionic acid (19.8 mg, 0.27 mmol), TBTU (85.6 mg, 0.27 mmol), and DIPEA (82.7 mg, 0.64 mmol) in dry DCM (total amount 10 mL) according to general procedure F (reaction time 1 h). Purification by flash column chromatography (SiO₂; DCM–MeOH 94:6) gave 45 mg of a beige solid (63% yield). ¹H-NMR shows a 5:4 mixture of amide bond rotamers. ¹H-NMR (400 MHz, DMSO-*d*₆) δ 12.08 (s, 1H), 8.43–8.36 (m, 1H), 7.88–7.78 (m, 1H), 7.52–7.45 (m, 1H), 7.43–7.35 (m, 1H), 7.30–7.17 (m, 1H), 4.62–4.49 (m, 0.55H), 4.45–4.37 (m, 0.45H), 4.35–4.27 (m, 0.45H), 4.26–4.16 (m, 0.55H), 4.08–4.00 (m, 0.45H), 3.88–3.75 (m, 0.55H), 3.29–3.15 (m, 3.45H), 3.02–2.87 (m, 1.1H), 2.56–2.46 (m, 0.45H, overlap with DMSO-*d*₆ signal), 2.46–2.26

(m, 2H), 2.07–1.87 (m, 2H), 1.85–1.75 (m, 1H), 1.52–1.37 (m, 1H), 1.02–0.92 (m, 3H); ESI-MS: (*m/z*) 338.7 [M + H]⁺, 360.7 [M + Na]⁺, 336.7 [M – H][–]; HPLC method A: *t_r* = 6.107 min.

1-(3-((7-Fluoro-9*H*-pyrimido[4,5-*b*]indol-4-yl)(methyl)amino)piperidin-1-yl)propan-1-one (26)

The title compound was prepared from **7b** (50.0 mg, 0.17 mmol), propionic acid (15.5 mg, 0.21 mmol), TBTU (67.5 mg, 0.21 mmol), and DIPEA (64.8 mg, 0.50 mmol) in dry DCM (total amount 15 mL) according to general procedure F (reaction time 45 min). Purification by flash column chromatography (SiO₂; DCM–MeOH 95:5) gave 50 mg of a white solid (84% yield). ¹H-NMR (400 MHz, DMSO-*d*₆) δ 12.28–12.14 (m, 1H), 8.44–8.34 (m, 1H), 7.86–7.76 (m, 1H), 7.30–7.20 (m, 1H), 7.13–6.99 (m, 1H), 4.60–4.51 (m, 0.55H), 4.45–4.36 (m, 0.45H), 4.32–4.23 (m, 0.45H), 4.21–4.11 (m, 0.55H), 4.08–3.98 (m, 0.45H), 3.87–3.74 (m, 0.55H), 3.28–3.14 (m, 3.45H), 3.00–2.85 (m, 1.1H), 2.54–2.46 (m, 0.45H, overlap with DMSO-*d*₅ signal), 2.44–2.26 (m, 2H), 2.05–1.86 (m, 2H), 1.83–1.75 (m, 1H), 1.52–1.37 (m, 1H), 1.03–0.92 (m, 3H); ¹³C NMR (101 MHz, DMSO-*d*₆) δ 171.54, 171.37, 160.25 (d, *J* = 240.1 Hz), 159.33, 159.21, 157.72, 153.12, 153.03, 137.47 (d, *J* = 12.5 Hz), 124.14–123.87 (m), 116.17, 108.07 (d, *J* = 23.5 Hz), 97.80 (d, *J* = 26.1 Hz), 54.80, 54.55, 46.74, 44.79, 43.87, 41.22, 33.75, 32.55, 27.52, 27.24, 25.65, 25.15, 24.46, 9.43. ESI-MS: (*m/z*) 378.3 [M + Na]⁺, 354.4 [M – H][–]; HPLC method B: *t_r* = 7.075 min.

1-(3-((7-Chloro-2-methyl-9*H*-pyrimido[4,5-*b*]indol-4-yl)(methyl)amino)piperidin-1-yl)propan-1-one (27)

The title compound was prepared from **7i** (28.0 mg, 0.09 mmol), propionic acid (7.9 mg, 0.11 mmol), TBTU (34.1 mg, 0.11 mmol), and DIPEA (32.9 mg, 0.26 mmol) in dry DCM (total amount 5 mL) according to general procedure F (reaction time 2 h). Purification by flash column chromatography (SiO₂, DCM–MeOH gradient elution from 96:4 to 94:6) gave 20 mg of a beige solid (61% yield). ¹H-NMR shows a 3:2 mixture of amide bond rotamers. ¹H-NMR (400 MHz, DMSO-*d*₆) δ 12.02 (s, 1H), 7.85–7.71 (m, 1H), 7.48–7.40 (m, 1H), 7.29–7.13 (m, 1H), 4.64–4.53 (m, 0.4H), 4.49–4.37 (m, 0.6H), 4.34–4.23 (m, 0.6H), 4.20–4.06 (m, 1H), 3.89–3.77 (m, 0.4H), 3.29–3.14 (m, 3.6H), 3.02–2.86 (m, 0.8H), 2.63–2.54 (m, 0.6H), 2.47–2.29 (m, 2H), 2.10–1.75 (m, 3H), 1.54–1.39 (m, 1H), 1.08–0.92 (m, 3H); ESI-MS: (*m/z*) 408.2 [M + Na]⁺, 384.2 [M – H][–]; HPLC method A: *t_r* = 7.761 min.

1-(3-((7-Bromo-9*H*-pyrimido[4,5-*b*]indol-4-yl)(methyl)amino)piperidin-1-yl)propan-1-one (28)

The title compound was prepared from **7d** (115.0 mg, 0.32 mmol), propionic acid (29.6 mg, 0.40 mmol), TBTU (128.1 mg, 0.40 mmol), and DIPEA (123.8 mg, 0.96 mmol) in dry DCM (total amount 15 mL) according to general procedure F (reaction time 30 min). Purification by flash column chromatography (SiO₂, DCM–MeOH 94:6) gave 48 mg of an off-white solid (36% yield). ¹H-NMR shows a 5:4 mixture of amide bond rotamers. ¹H-NMR (400 MHz, CDCl₃) δ 12.75–12.17 (m, 1H), 8.58–8.47 (m, 1H), 7.67–7.53 (m, 2H), 7.40–7.30 (m, 1H), 5.01–4.90 (m, 0.45H), 4.80–4.68 (m, 0.55H), 4.54–4.40 (m, 0.55H), 4.38–4.29 (m, 0.45H), 4.28–4.20 (m, 0.55H), 3.95–3.82 (m, 0.45H), 3.36–3.20 (m, 3H), 3.19–3.09 (m, 0.55H), 3.05–2.88 (m, 0.9H), 2.67–2.36 (m, 2.55H), 2.21–1.86 (m, 3H), 1.76–1.56 (m, 1H), 1.28–1.13 (m, 3H); ¹³C NMR (101 MHz, CDCl₃) δ 173.2, 172.6, 160.1, 160.0, 157.54, 157.46, 153.0, 137.9, 124.0, 123.92, 123.88, 119.1, 119.0, 118.73, 118.68, 114.6, 114.4, 98.4, 55.2, 55.0, 47.5, 45.8, 45.0, 42.2, 34.4, 33.4, 28.8, 28.0, 26.9, 26.8, 25.6, 24.9, 9.8; ESI-MS: (*m/z*) 438.0 [M + Na]⁺, 414.0 [M – H][–]; HPLC method A: *t_r* = 8.212 min.

1-(3-((7-Iodo-9*H*-pyrimido[4,5-*b*]indol-4-yl)(methyl)amino)piperidin-1-yl)propan-1-one (29)

The title compound was prepared from **7e** (43.0 mg, 0.11 mmol), propionic acid (9.8 mg, 0.13 mmol), TBTU (42.4 mg, 0.13 mmol), and DIPEA (40.9 mg, 0.32 mmol) in dry DCM (total amount 8 mL) according to general procedure F (reaction time 2 h). Purification by flash column chromatography (SiO₂, DCM–MeOH 95:5) gave 25 mg of an off-white solid (51% yield). ¹H-NMR shows a 1:1 mixture of amide bond rotamers. ¹H-NMR (400 MHz, DMSO-*d*₆) δ 12.20–12.11 (m, 1H), 8.43–8.37 (m, 1H), 7.82–7.76 (m, 1H), 7.67–7.60 (m, 1H), 7.56–7.47 (m, 1H), 4.59–4.52 (m, 0.5H), 4.44–4.37 (m, 0.5H), 4.35–4.26 (m, 0.5H), 4.23–4.14 (m, 0.5H), 4.07–3.98 (m, 0.5H), 3.85–3.79 (m, 0.5H), 3.26–3.15 (m, 3.5H), 3.01–2.87

(m, 1H), 2.54–2.46 (m, 0.5H, overlap with DMSO- d_5 signal), 2.45–2.25 (m, 2H), 2.05–1.75 (m, 3H), 1.53–1.37 (m, 1H), 1.02–0.93 (m, 3H); ESI-MS: (m/z) 464.9 [M + H]⁺, 486.9 [M + Na]⁺, 462.8 [M – H][–]; HPLC method A: t_r = 8.443 min.

3-(3-((6-Chloro-9H-pyrimido[4,5-*b*]indol-4-yl)(methyl)amino)piperidin-1-yl)-3-oxopropanenitrile (30)

Cyanoacetic acid (16.8 mg, 0.20 mmol) and TBTU (63.5 mg, 0.20 mmol) were stirred in dry DCM (5 mL) at rt and under N₂ atmosphere for 15 min. A suspension of **7h** (50.0 mg, 0.16 mmol) and DIPEA (61.4 mg, 0.48 mmol) in dry DCM (5 mL) was added to the activated acid, and the mixture was stirred at rt and under N₂ atmosphere for 2.5 h. A precipitate formed. The mixture was diluted with DCM, and MeOH was added to dissolve the precipitate. The solution was washed with saturated NaHCO₃ solution (2 × 20 mL) and saturated NH₄Cl solution (2 × 20 mL). The organic layer was dried over Na₂SO₄ and concentrated under reduced pressure. Purification of the residue by flash column chromatography (SiO₂, DCM–MeOH gradient elution from 95:5 to 92:8) gave 34 mg of a white solid (56% yield); ¹H-NMR shows a 5:4 mixture of amide rotamers. ¹H-NMR (400 MHz, DMSO- d_6) δ 12.32–12.18 (m, 1H), 8.46–8.36 (m, 1H), 7.83–7.73 (m, 1H), 7.53–7.45 (m, 1H), 7.44–7.36 (m, 1H), 4.51–4.42 (m, 0.55H), 4.40–4.25 (m, 1.45H), 4.17–3.99 (m, 2H), 3.93–3.85 (m, 0.45H), 3.69–3.60 (m, 0.55H), 3.29–3.19 (m, 3H), 3.07–2.91 (m, 1.1H), 2.68–2.57 (m, 0.45H), 2.10–1.94 (m, 2H), 1.89–1.79 (m, 1H), 1.71–1.42 (m, 1H), missing 0.45H below water signal; ¹³C NMR (101 MHz, DMSO- d_6) δ 161.6, 161.5, 159.5, 157.5, 153.8, 135.20, 135.18, 124.7, 124.6, 121.8, 121.7, 120.72, 120.71, 116.02, 115.97, 112.6, 97.0, 96.9, 54.6, 53.8, 47.4, 45.4, 43.9, 42.0, 34.1, 33.1, 27.0, 26.9, 24.9, 24.6, 24.1; ESI-MS: (m/z) 405.4 [M + Na]⁺, 381.4 [M – H][–]; HPLC method A: t_r = 6.666 min.

3-(3-((6-Bromo-9H-pyrimido[4,5-*b*]indol-4-yl)(methyl)amino)piperidin-1-yl)-3-oxopropanenitrile (31)

A mixture of cyanoacetic acid (21.3 mg, 0.25 mmol) and EDCI·HCl (47.9 mg, 0.25 mmol) was stirred in dry DCM (6 mL) at rt and under N₂ atmosphere for 20 min. A suspension of **7i** (60.0 mg, 0.17 mmol) and DIPEA (64.6 mg, 0.51 mmol) in dry DCM (4 mL) was added, and the mixture was stirred at rt and under N₂ atmosphere. Due to slow conversion, reactants were added repeatedly: EDCI·HCl (47.9 mg, 0.25 mmol) after 3 h of stirring, cyanoacetic acid (21.3 mg, 0.25 mmol) after 5 h of stirring, and again EDCI·HCl (63.9 mg, 0.33 mmol) after 20 h of stirring. Sufficient conversion was achieved after a reaction time of 2 days. The mixture was diluted with DCM, washed with saturated NH₄Cl solution and saturated NaHCO₃ solution, dried over Na₂SO₄, and concentrated under reduced pressure. Purification of the residue by flash column chromatography (SiO₂, DCM–MeOH 95:5) gave 16 mg of an off-white solid (22% yield). ¹H-NMR shows a 5:4 mixture of amide bond rotamers. ¹H-NMR (400 MHz, DMSO- d_6) δ 12.34–12.22 (m, 1H), 8.44 (s, 0.45H), 8.40 (s, 0.55H), 7.96–7.87 (m, 1H), 7.57–7.50 (m, 1H), 7.48–7.41 (m, 1H), 4.49–4.41 (m, 0.55H), 4.40–4.24 (m, 1.45H), 4.15–3.99 (m, 2H), 3.92–3.84 (m, 0.45H), 3.70–3.60 (m, 0.55H), 3.29–3.19 (m, 3H), 3.07–2.92 (m, 1.1H), 2.69–2.57 (m, 0.45H), 2.11–1.95 (m, 2H), 1.90–1.80 (m, 1H), 1.72–1.43 (m, 1H), missing 0.45H below water signal; ¹³C NMR (101 MHz, DMSO- d_6) δ 161.6, 161.5, 159.5, 159.4, 157.4, 153.9, 135.5, 127.3, 127.2, 124.7, 124.6, 121.4, 121.3, 116.1, 116.0, 113.1, 112.5, 112.4, 96.8, 96.8, 54.7, 53.9, 47.4, 45.4, 43.9, 42.0, 34.0, 33.1, 27.0, 26.9, 24.9, 24.6, 24.1. ESI-MS: (m/z) 449.4 [M + Na]⁺, 425.5 [M – H][–]; HPLC method A: t_r = 6.749 min.

3-(3-((6-Methoxy-9H-pyrimido[4,5-*b*]indol-4-yl)(methyl)amino)piperidin-1-yl)-3-oxopropanenitrile (32)

The title compound was prepared from **7j** (60.0 mg, 0.19 mmol), cyanoacetic acid (20.5 mg, 0.24 mmol), TBTU (77.3 mg, 0.24 mmol), and DIPEA (74.7 mg, 0.58 mmol) in dry DCM (total amount 10 mL) according to general procedure F (reaction time 0.5 h). Purification by flash column chromatography (SiO₂; DCM–MeOH 95:5) gave 38 mg of a beige solid (52% yield). ¹H-NMR shows a 5:4 mixture of amide bond rotamers. ¹H-NMR (400 MHz, DMSO- d_6) δ 12.00–11.87 (m, 1H), 8.43–8.36 (m, 1H), 7.44–7.37 (m, 1H), 7.34–7.20 (m, 1H), 7.09–7.01 (m, 1H), 4.40–3.97 (m, 4H), 3.92–3.80 (m, 3.45H), 3.65–3.57 (m, 0.55H), 3.30–3.17 (m, 3H), 3.06–2.92 (m, 1.1H), 2.69–2.57 (m, 0.4H), 2.15–1.98 (m, 2H), 1.90–1.79 (m, 1H), 1.71–1.44 (m, 1H), missing 0.45H below water signal; ¹³C NMR (101 MHz, DMSO- d_6)

δ 161.6, 161.4, 159.9, 159.6, 157.3, 157.2, 154.0, 153.9, 153.1, 131.4, 131.3, 119.9, 119.7, 116.00, 115.96, 113.6, 112.9, 111.9, 111.8, 106.8, 106.0, 98.3, 97.9, 55.6, 55.5, 54.7, 54.3, 47.4, 45.4, 44.0, 42.0, 34.0, 32.7, 27.2, 27.1, 24.9, 24.8, 24.6, 24.1; ESI-MS: (m/z) 379.1 [M + H]⁺, 401.2 [M + Na]⁺, 377.2 [M – H][–]; HPLC method A: t_r = 4.053 min.

3-(3-((5-Chloro-9H-pyrimido[4,5-*b*]indol-4-yl)(methyl)amino)piperidin-1-yl)-3-oxopropanenitrile (33)

The title compound was prepared from **7k** (55.0 mg, 0.17 mmol), cyanoacetic acid (18.5 mg, 0.22 mmol), TBTU (69.9 mg, 0.22 mmol), and DIPEA (67.5 mg, 0.52 mmol) in dry DCM (total amount 10 mL) according to general procedure F (reaction time 1 h). A precipitate formed during the reaction and was dissolved by adding DCM and MeOH prior to the extractive work-up. Repeated purification by flash column chromatography (SiO₂, DCM–MeOH 94:6; SiO₂, DCM–MeOH gradient elution from 96:4 to 92:8; SiO₂, DCM–MeOH gradient elution from 96:4 to 92:8; and SiO₂, DCM–EtOH 95:5) gave 35 mg of a beige solid (52% yield). ¹H-NMR shows a 1:1 mixture of amide bond rotamers. ¹H-NMR (300 MHz, DMSO-*d*₆) δ 12.35 (s, 1H), 8.50–8.32 (m, 1H), 7.50–7.34 (m, 2H), 7.33–7.25 (m, 1H), 4.42–3.95 (m, 4H), 3.92–3.80 (m, 0.5H), 3.66–3.55 (m, 0.5H), 3.09–2.89 (m, 4H), 2.71–2.58 (m, 0.5H), 2.07–1.73 (m, 3H), 1.71–1.42 (m, 1H), missing 0.5H below water signal; ESI-MS: (m/z) 405.4 [M + Na]⁺, 381.3 [M – H][–]; HPLC method A: t_r = 6.396 min.

1-(3-((6-Chloro-9H-pyrimido[4,5-*b*]indol-4-yl)(methyl)amino)piperidin-1-yl)propan-1-one (34)

The title compound was prepared from **7h** (50.0 mg, 0.16 mmol), propionic acid (14.7 mg, 0.20 mmol), TBTU (63.5 mg, 0.20 mmol), and DIPEA (61.4 mg, 0.48 mmol) in dry DCM (10 mL) according to general procedure F (reaction time 45 min). Purification by flash column chromatography (SiO₂, DCM–MeOH gradient elution from 96.5:3.5 to 92.5: 7.5) gave 42 mg of an off-white solid (71% yield); ¹H-NMR shows a 1:1 mixture of amide bond rotamers. ¹H-NMR (400 MHz, DMSO-*d*₆) δ 12.25 (s, 1H), 8.39 (s, 1H), 7.84–7.69 (m, 1H), 7.52–7.45 (m, 1H), 7.43–7.37 (m, 1H), 4.55–4.46 (m, 0.5H), 4.46–4.38 (m, 0.5H), 4.35–4.19 (m, 1H), 4.12–4.00 (m, 0.5H), 3.89–3.77 (m, 0.5H), 3.31–3.18 (m, 3.5H), 3.02–2.92 (m, 0.5H), 2.92–2.83 (m, 0.5H), 2.55–2.26 (m, 2.5H, overlap with DMSO-*d*₅ signal), 2.08–1.93 (m, 2H), 1.90–1.75 (m, 1H), 1.60–1.35 (m, 1H), 1.04–0.91 (m, 3H); ¹³C NMR (101 MHz, DMSO-*d*₆) δ 171.5, 171.4, 159.5, 157.5, 153.8, 153.8, 135.2, 124.7, 124.6, 124.5, 121.8, 121.6, 120.7, 112.6, 96.9, 96.8, 54.8, 54.1, 46.8, 44.7, 43.6, 41.1, 33.8, 32.9, 27.4, 27.2, 25.6, 25.0, 24.4, 9.3; ESI-MS: (m/z) 394.4 [M + Na]⁺, 370.4 [M – H][–]; HPLC method A: t_r = 7.789 min.

1-(3-((6-Bromo-9H-pyrimido[4,5-*b*]indol-4-yl)(methyl)amino)piperidin-1-yl)propan-1-one (35)

Propionic acid (16.7 mg, 0.23 mmol) and TBTU (72.4 mg, 0.23 mmol) were stirred in dry DCM (4 mL) at rt and under N₂ atmosphere for 15 min. A suspension of **7i** (65.0 mg, 0.18 mmol) in dry DCM (8 mL) was added to the activated acid, followed by addition of DIPEA (70.0 mg, 0.54 mmol). The mixture was stirred at rt and under N₂ atmosphere for 50 min; then diluted with DCM; and washed with saturated NaHCO₃ solution (2 × 25 mL), saturated NH₄Cl solution (2 × 25 mL), and saturated NaCl solution (25 mL). The organic layer was dried over Na₂SO₄ and concentrated under reduced pressure. Purification of the residue by flash column chromatography (DCM–MeOH 95:5) gave 24 mg of an off-white solid (32% yield); ¹H-NMR shows a 1:1 mixture of amide bond rotamers. ¹H-NMR (400 MHz, DMSO-*d*₆) δ 12.26 (s, 1H), 8.39 (s, 1H), 7.96–7.81 (m, 1H), 7.56–7.48 (m, 1H), 7.48–7.40 (m, 1H), 4.50–4.36 (m, 1H), 4.34–4.16 (m, 1H), 4.08–4.01 (m, 0.5H), 3.87–3.77 (m, 0.5H), 3.31–3.18 (m, 3.5H), 3.02–2.92 (m, 0.5H), 2.92–2.82 (m, 0.5H), 2.54–2.26 (m, 2.5H, overlap with DMSO-*d*₅ signal), 2.09–1.96 (m, 2H), 1.92–1.76 (m, 1H), 1.60–1.36 (m, 1H), 1.02–0.90 (m, 3H); ¹³C NMR (101 MHz, DMSO-*d*₆) δ 171.6, 171.5, 159.5, 157.4, 153.9, 153.8, 135.5, 127.3, 124.7, 124.5, 121.4, 113.2, 112.5, 96.8, 96.7, 54.9, 54.1, 46.9, 44.7, 43.7, 41.2, 33.8, 32.9, 27.4, 27.3, 25.7, 25.1, 24.4, 9.4; ESI-MS: (m/z) 438.0 [M + Na]⁺, 414.0 [M – H][–]; HPLC method A: t_r = 8.360 min.

1-(3-((6-Methoxy-9H-pyrimido[4,5-*b*]indol-4-yl)(methyl)amino)piperidin-1-yl)propan-1-one (36)

The title compound was prepared from **7j** (60.0 mg, 0.19 mmol), cyanoacetic acid (17.9 mg, 0.24 mmol), TBTU (77.3 mg, 0.24 mmol), and DIPEA (74.7 mg, 0.58 mmol) in dry DCM (total amount 10 mL) according to general procedure F (reaction time 2 h). Purification by flash column chromatography (SiO₂; DCM–MeOH 95:5) gave 43 mg of a beige solid (61% yield). ¹H-NMR (300 MHz, DMSO-*d*₆) δ 12.03–11.84 (m, 1H), 8.45–8.31 (m, 1H), 7.46–7.36 (m, 1H), 7.33–7.19 (m, 1H), 7.12–6.99 (m, 1H), 4.50–4.34 (m, 1H), 4.33–4.09 (m, 1H), 4.06–3.96 (m, 0.45H), 3.90–3.74 (m, 3.55H), 3.30–3.14 (m, 3.45H), 3.03–2.81 (m, 1.1H), 2.57–2.44 (m, 0.45H, overlap with DMSO-*d*₅ signal), 2.41–2.23 (m, 2H), 2.12–1.77 (m, 3H), 1.62–1.37 (m, 1H), 1.01–0.86 (m, 3H); ¹³C NMR (101 MHz, DMSO-*d*₆) δ 171.42, 171.38, 159.9, 159.6, 157.3, 157.2, 154.0, 153.9, 153.1, 131.3, 119.8, 119.8, 113.5, 113.0, 111.9, 111.8, 106.7, 105.9, 98.3, 97.8, 55.6, 55.5, 54.9, 54.5, 46.8, 44.6, 43.6, 41.2, 33.6, 32.6, 27.6, 27.3, 25.6, 25.1, 24.4, 9.3; ESI-MS: (*m/z*) 390.2 [M + Na]⁺, 366.2 [M – H][–]; HPLC method A: t_r = 5.463 min.

1-(3-((5-Chloro-9*H*-pyrimido[4,5-*b*]indol-4-yl)(methyl)amino)piperidin-1-yl)propan-1-one (**37**)

The title compound was prepared from **7k** (55.0 mg, 0.17 mmol), propionic acid (16.2 mg, 0.22 mmol), TBTU (69.9 mg, 0.22 mmol), and DIPEA (67.5 mg, 0.52 mmol) in dry DCM (total amount 10 mL) according to general procedure F (reaction time 2 h). Purification by flash column chromatography (SiO₂, DCM–MeOH 94:6) gave 46 mg of a light beige solid (71% yield). NMR shows a 5:4 mixture of amide rotamers. ¹H-NMR (300 MHz, Pyr-*d*₅) δ 14.06–13.63 (m, 1H), 8.88–8.80 (m, 1H), 7.70–7.61 (m, 1H), 7.50–7.36 (m, 2H), 4.87–4.77 (m, 0.55H), 4.69–4.55 (m, 0.45H), 4.55–4.42 (m, 0.55H), 4.27–4.15 (m, 0.55H), 3.73–3.58 (m, 0.45H), 3.23–2.95 (m, 4H), 2.95–2.78 (m, 0.45H), 2.72–2.22 (m, 2.55H), 2.17–1.96 (m, 1H), 1.95–1.42 (m, 3H), 1.31–1.11 (m, 3H), missing 0.45H below water signal; ESI-MS: (*m/z*) 372.3 [M + H]⁺, 394.4 [M + Na]⁺, 370.3 [M – H][–]; HPLC method A: t_r = 7.646 min.

(8) Detailed Procedures for the Preparation of Enantiopure Final Compounds (**R**)-**2**, (**R**)-**20** and (**R**)-**28**

(**R**)-3-(3-((7-Chloro-9*H*-pyrimido[4,5-*b*]indol-4-yl)(methyl)amino)piperidin-1-yl)-3-oxopropanenitrile ((**R**)-**2**)

The title compound was prepared from (**R**)-**7c** (50.0 mg, 0.16 mmol), cyanoacetic acid (16.2 mg, 0.19 mmol), PyBOP (98.9 mg, 0.19 mmol), and DIPEA (61.4 mg, 0.48 mmol) in dry DCM (total amount 10 mL) according to general procedure F (reaction time 2 h). Purification twice by flash column chromatography (SiO₂, DCM–MeOH gradient elution from 1:0 to 92:8 and SiO₂, DCM–EtOH gradient elution from 96.5:3.5 to 92:8) gave 33 mg of a white solid (54% yield). ¹H-NMR shows a 3:2 mixture of amide bond rotamers. ¹H-NMR (400 MHz, DMSO-*d*₆) δ 12.33–12.17 (m, 1H), 8.48–8.36 (m, 1H), 7.90–7.77 (m, 1H), 7.53–7.45 (m, 1H), 7.31–7.18 (m, 1H), 4.55–4.46 (m, 0.6H), 4.39–4.20 (m, 1.4H), 4.18–4.00 (m, 2H), 3.94–3.83 (m, 0.4H), 3.69–3.58 (m, 0.6H), 3.29–3.17 (m, 3H), 3.09–2.97 (m, 1.2H), 2.70–2.58 (m, 0.4H), 2.12–1.74 (m, 3H), 1.68–1.43 (m, 1H), missing 0.4H below water signal; ¹³C NMR (101 MHz, DMSO-*d*₆) δ 161.6, 161.5, 159.4, 159.3, 157.5, 153.7, 137.4, 129.3, 129.2, 124.1, 124.0, 120.4, 118.4, 118.3, 116.14, 116.08, 110.8, 97.3, 97.2, 54.6, 54.2, 47.3, 45.5, 44.1, 42.0, 34.1, 32.8, 27.0, 26.9, 24.9, 24.7, 24.2; ESI-MS: (*m/z*) 404.9 [M + Na]⁺, 380.8 [M – H][–]; HPLC method A: t_r = 6.644 min.

(**R**)-3-(3-((7-Bromo-9*H*-pyrimido[4,5-*b*]indol-4-yl)(methyl)amino)piperidin-1-yl)-3-oxopropanenitrile ((**R**)-**20**)

The title compound was prepared from (**R**)-**7d** (70.0 mg, 0.19 mmol), cyanoacetic acid (20.7 mg, 0.24 mmol), TBTU (78.0 mg, 0.24 mmol), and DIPEA (75.3 mg, 0.58 mmol) in dry DCM (total amount 12 mL) according to general procedure F (reaction time 30 min). Purification by flash column chromatography (SiO₂, DCM–MeOH 94.5:5.5) gave 63 mg of a white solid (76% yield); ¹H-NMR shows a 3:2 mixture of amide bond rotamers. ¹H-NMR (300 MHz, DMSO-*d*₆) δ 12.30–12.14 (m, 1H), 8.49–8.37 (m, 1H), 7.82–7.72 (m, 1H), 7.66–7.58 (m, 1H), 7.44–7.31 (m, 1H), 4.55–4.44 (m, 0.6H), 4.40–4.19 (m, 1.4H), 4.16–3.98 (m, 2H), 3.93–3.82 (m, 0.4H), 3.68–3.57 (m, 0.6H), 3.28–3.14 (m, 3.4H), 3.09–2.94 (m, 1.2H), 2.70–2.56 (m, 0.4H), 2.09–1.74 (m, 3H), 1.67–1.41 (m, 1H); ¹³C NMR (101 MHz, DMSO-*d*₆) δ 161.6, 161.4, 159.44, 159.36, 157.3, 153.7, 137.7, 124.4, 124.2, 123.1, 123.0, 118.7, 118.6, 117.38, 117.35, 116.1, 116.0,

113.7, 97.3, 97.2, 54.6, 54.2, 47.3, 45.5, 44.1, 42.0, 34.0, 32.8, 27.0, 26.9, 24.8, 24.6, 24.1; ESI-MS: (m/z) 449.4 $[M + Na]^+$, 425.5 $[M - H]^-$; HPLC method A: t_r = 6.672 min.

(*R*)-1-(3-((7-bromo-9*H*-pyrimido[4,5-*b*]indol-4-yl)(methyl)amino)piperidin-1-yl)propan-1-one ((*R*)-**28**)

The title compound was prepared from (*R*)-**7d** (45.0 mg, 0.13 mmol), propionic acid (11.6 mg, 0.16 mmol), TBTU (50.1 mg, 0.16 mmol), and DIPEA (48.4 mg, 0.38 mmol) in dry DCM (total amount 10 mL) according to general procedure F (reaction time 40 min). Purification by flash column chromatography (SiO₂, DCM–MeOH gradient elution from 96:4 to 92:8) gave 28 mg (54% yield). ¹H-NMR shows a 5:4 mixture of amide bond rotamers. ¹H-NMR (400 MHz, CDCl₃) δ 12.89–12.09 (m, 1H), 8.52 (s, 1H), 7.73–7.55 (m, 2H), 7.43–7.29 (m, 1H), 5.01–4.88 (m, 0.45H), 4.80–4.67 (m, 0.55H), 4.55–4.41 (m, 0.55H), 4.39–4.29 (m, 0.45H), 4.28–4.18 (m, 0.55H), 3.94–3.80 (m, 0.45H), 3.35–3.19 (m, 3H), 3.18–3.09 (m, 0.55H), 3.04–2.87 (m, 0.9H), 2.64–2.35 (m, 2.55H), 2.20–1.84 (m, 3H), 1.75–1.54 (m, 1H), 1.26–1.17 (m, 3H); ¹³C NMR (101 MHz, CDCl₃) δ 173.2, 172.6, 160.1, 157.6, 157.4, 153.0, 137.84, 137.76, 124.1, 124.03, 123.96, 119.2, 119.1, 118.84, 118.79, 114.6, 114.4, 98.8, 98.5, 55.2, 55.1, 47.5, 45.8, 45.0, 42.3, 34.5, 33.4, 29.8, 28.8, 28.0, 26.9, 25.6, 24.9, 9.8; ESI-MS: (m/z) 416.0 $[M + H]^+$, 438.0 $[M + Na]^+$, 414.0 $[M - H]^-$; HPLC method A: t_r = 8.046 min.

(9) Detailed Procedures for the Preparation of Enantiopure Final Compounds (*S*)-**2** and (*S*)-**20**

(*S*)-3-(3-((7-Chloro-9*H*-pyrimido[4,5-*b*]indol-4-yl)(methyl)amino)piperidin-1-yl)-3-oxopropanenitrile ((*S*)-**2**)

The title compound was prepared from (*S*)-**7c** (64.0 mg, 0.20 mmol), cyanoacetic acid (20.7 mg, 0.24 mmol), PyBOP (126.6 mg, 0.24 mmol), and DIPEA (78.6 mg, 0.61 mmol) in dry DCM (total amount 10 mL) according to general procedure F (reaction time 3 h). Purification by flash column chromatography (SiO₂, DCM–MeOH gradient elution from 95.5:4.5 to 92:8) gave 54 mg of a white solid (70% yield). ¹H-NMR shows a 3:2 mixture of amide bond rotamers: (300 MHz, DMSO-*d*₆) δ 12.31–12.16 (m, 1H), 8.48–8.37 (m, 1H), 7.89–7.77 (m, 1H), 7.53–7.43 (m, 1H), 7.32–7.18 (m, 1H), 4.58–4.44 (m, 0.6H), 4.41–4.19 (m, 1.4H), 4.16–3.98 (m, 2H), 3.93–3.81 (m, 0.4H), 3.71–3.56 (m, 0.6H), 3.29–3.17 (m, 3H), 3.10–2.94 (m, 1.2H), 2.70–2.56 (m, 0.4H), 2.10–1.73 (m, 3H), 1.68–1.42 (m, 1H), missing 0.4H below water signal; ESI-MS: (m/z) 405.1 $[M + Na]^+$, 380.9 $[M - H]^-$; HPLC method A: t_r = 6.679 min.

(*S*)-3-(3-((7-Bromo-9*H*-pyrimido[4,5-*b*]indol-4-yl)(methyl)amino)piperidin-1-yl)-3-oxopropanenitrile ((*S*)-**20**)

The title compound was prepared from (*S*)-**7d** (65.0 mg, 0.18 mmol), cyanoacetic acid (19.2 mg, 0.23 mmol), TBTU (72.4 mg, 0.23 mmol), and DIPEA (70.0 mg, 0.54 mmol) in dry DCM (total amount 12 mL) according to general procedure F (reaction time 30 min). Purification by flash column chromatography (SiO₂, DCM–MeOH 94.5:5.5) gave 48 mg of an off-white solid (62% yield). ¹H-NMR shows a 3:2 mixture of amide bond rotamers. ¹H-NMR (300 MHz, DMSO-*d*₆) δ 12.32–12.12 (m, 1H), 8.49–8.37 (m, 1H), 7.83–7.72 (m, 1H), 7.67–7.57 (m, 1H), 7.44–7.30 (m, 1H), 4.56–4.44 (m, 0.6H), 4.41–4.19 (m, 1.4H), 4.17–3.99 (m, 2H), 3.93–3.81 (m, 0.4H), 3.69–3.58 (m, 0.6H), 3.32–3.14 (m, 3.4H), 3.11–2.95 (m, 1.2H), 2.70–2.56 (m, 0.4H), 2.10–1.73 (m, 3H), 1.67–1.41 (m, 1H); ESI-MS: (m/z) 449.3 $[M + Na]^+$, 425.3 $[M - H]^-$; HPLC method A: t_r = 6.649 min.

(10) Detailed Procedures for the Preparation of Intermediates **43** and **44·HCl**

tert-Butyl (1-(2-cyanoacetyl)piperidin-3-yl)carbamate (**43**)

tert-Butyl piperidin-3-yl-carbamate (**42**) (1.0 g, 4.99 mmol) and cyanoacetic acid (470.0 mg, 5.49 mmol) were stirred in dry DCM (15 mL) at 0°C and under N₂ atmosphere. A solution of DCC (1.1 g, 5.49 mmol) in dry DCM (11 mL) was drop-added. The mixture was stirred at rt overnight and then filtered rinsing the residue with fresh DCM. The filtrate was concentrated under reduced pressure. Purification of the residue by flash column chromatography (SiO₂, DCM–EtOAc 7:3) gave 942 mg (71% yield); ¹H-NMR shows a 3:2 mixture of amide bond rotamers. ¹H-NMR (300 MHz, DMSO-*d*₆) δ 7.08–6.49 (m, 1H), 4.10–3.88 (m, 2.6H), 3.81–3.67 (m, 0.4H), 3.53–3.19 (m, 2H, overlap with water signal), 3.06–2.91 (m, 1.4H), 2.69–2.58 (m, 0.6H), 1.85–1.36 (m, 13H).

1-(2-Cyanoacetyl)piperidin-3-amine hydrochloride (44·HCl)

4N HCl in dioxane (2.1 mL) was added to a solution of **43** (200.0 mg, 0.75 mmol) in dry THF (2 mL). The mixture was stirred at rt overnight. The resulting precipitate was filtered off, washed with Et₂O, and dried under reduced pressure. The yield was 130 mg (96% crude yield), used in the next step without further purification. ¹H-NMR shows a 3:2 mixture of amide bond rotamers. ¹H-NMR (400 MHz, DMSO-*d*₆) δ 8.61–8.25 (m, 3H), 4.26–3.95 (m, 2.4H), 3.70–3.64 (m, 0.6H), 3.55–3.50 (m, 0.4H), 3.45–3.36 (m, 1H), 3.31–3.04 (m, 2.6H), 2.03–1.89 (m, 1H), 1.77–1.62 (m, 2H), 1.54–1.36 (m, 1H); ¹³C NMR (101 MHz, DMSO-*d*₆) δ 162.1, 161.7, 116.2, 116.1, 47.7, 46.1, 46.0, 45.3, 43.9, 41.6, 27.4, 27.1, 25.3, 25.2, 25.1, 22.0, 21.1.

(11) Detailed Procedures for the Preparation of Final Compounds 45–50**3-(3-((9H-Pyrimido[4,5-*b*]indol-4-yl)amino)piperidin-1-yl)-3-oxopropanenitrile (45)**

The title compound was prepared from **4a** (100.0 mg, 0.27 mmol), **44·HCl** (113.8 mg, 0.56 mmol), DIPEA (181.0 mg, 1.40 mmol), and Na^tBuO (188.0 mg, 1.96 mmol) in dry DMF (5 mL) according to general procedure G. Purification by flash column chromatography (SiO₂, DCM–EtOH gradient elution from 97:3 to 85:15) gave 34 mg (36% yield). ¹H-NMR shows a 5:4 mixture of amide bond rotamers. ¹H-NMR (300 MHz, DMSO-*d*₆) δ 11.98–11.84 (m, 1H), 8.42–8.34 (m, 1H), 8.33–8.26 (m, 2H), 7.50–7.43 (m, 1H), 7.42–7.33 (m, 1H), 7.29–7.20 (m, 1H), 6.86–6.63 (m, 1H), 4.51–4.23 (m, 2H), 4.16–3.98 (m, 2H), 3.93–3.83 (m, 0.45H), 3.69–3.57 (m, 0.55H), 3.21–3.11 (m, 0.45H), 3.08–2.97 (m, 0.55H), 2.94–2.84 (m, 0.55H), 2.73–2.60 (m, 0.45H), 2.13–1.97 (m, 1H), 1.92–1.72 (m, 2H), 1.69–1.42 (m, 1H); ESI-MS: (*m/z*) 335.1 [M + H]⁺, 357.0 [M + Na]⁺, 332.9 [M – H][–]; HPLC method B: t_r = 2.649 min.

3-(3-((7-Fluoro-9H-pyrimido[4,5-*b*]indol-4-yl)amino)piperidin-1-yl)-3-oxopropanenitrile (46)

The title compound was prepared from **4b** (100.0 mg, 0.27 mmol), **44·HCl** (81.3 mg, 0.40 mmol), DIPEA (171.9 mg, 1.33 mmol), and Na^tBuO (179.0 mg, 1.86 mmol) in dry DMF (5 mL) according to general procedure G. The precipitate formed upon addition of saturated NH₄Cl solution was not extracted with EtOAc but instead filtered off, washed with water, and dried over P₂O₅ in vacuo. Purification by flash column chromatography (SiO₂, DCM–EtOH gradient elution from 94:6 to 9:1) gave 29 mg (31% yield). ¹H-NMR shows a 5:4 mixture of amide bond rotamers. ¹H-NMR (300 MHz, DMSO-*d*₆) δ 12.14–11.96 (m, 1H), 8.41–8.27 (m, 2H), 7.26–7.18 (m, 1H), 7.17–7.06 (m, 1H), 6.92–6.73 (m, 1H), 4.49–4.23 (m, 2H), 4.16–3.97 (m, 2H), 3.93–3.83 (m, 0.45H), 3.70–3.59 (m, 0.55H), 3.20–3.08 (m, 0.45H), 3.08–2.95 (m, 0.55H), 2.90–2.80 (m, 0.55H), 2.72–2.61 (m, 0.45H), 2.13–1.95 (m, 1H), 1.88–1.74 (m, 2H), 1.68–1.42 (m, 1H); ¹³C NMR (101 MHz, DMSO-*d*₆) δ 161.59, 161.56, 161.5, 161.4, 159.1, 159.1, 156.1, 155.6, 155.6, 154.4, 154.4, 137.1, 137.0, 122.9, 122.83, 122.80, 122.7, 116.2, 116.1, 116.02, 115.99, 107.9, 107.6, 97.9, 97.6, 95.7, 95.5, 50.0, 47.5, 46.4, 46.3, 45.8, 42.2, 29.83, 29.75, 24.94, 24.86, 24.3, 23.7; ESI-MS: (*m/z*) 375.3 [M + Na]⁺, 351.1 [M – H][–]; HPLC method B: t_r = 3.525 min.

3-(3-((7-Chloro-9H-pyrimido[4,5-*b*]indol-4-yl)amino)piperidin-1-yl)-3-oxopropanenitrile (47)

The title compound was prepared by a two-step procedure.

In the first step **4c** (200.0 mg, 0.51 mmol), **44·HCl** (135.0 mg, 0.66 mmol), and DIPEA (197.7 mg, 1.53 mmol) were reacted in dry DMF (3.5 mL) at 70 °C for 19 h. Additional **44·HCl** (26.0 mg, 0.128 mmol) was added, and stirring at 70 °C continued for 6 h. After cooling down to rt, the mixture was poured into ice-cold water and saturated NH₄Cl solution was added (30 mL). The resulting precipitate was filtered off, washed with water, and dried over P₂O₅ in vacuo. Purification by flash column chromatography (SiO₂, DCM–MeOH 96.5:3.5) gave 104 mg of 3-(3-((7-Chloro-9H-pyrimido[4,5-*b*]indol-4-yl)amino)piperidin-1-yl)-3-oxopropanenitrile as a pale yellow solid (39% yield). ¹H-NMR shows a 5:4 mixture of amide bond rotamers. ¹H-NMR (300 MHz, DMSO-*d*₆) δ 8.55–8.44 (m, 1H), 8.42–8.30 (m, 2H), 8.00 (d, *J* = 8.4 Hz, 2H), 7.64–7.52 (m, 1H), 7.39 (d, *J* = 8.3 Hz, 2H), 7.22–7.05 (m, 1H), 4.44–4.19 (m, 2H), 4.15–3.92 (m, 2H), 3.84–3.74

(m, 0.45H), 3.67–3.57 (m, 0.55H), 3.16–3.06 (m, 0.45H), 3.05–2.92 (m, 0.55H), 2.87–2.75 (m, 0.55H), 2.70–2.55 (m, 0.45H), 2.32 (s, 3H), 2.07–1.90 (m, 1H), 1.90–1.68 (m, 2H), 1.68–1.35 (m, 1H); ESI-MS: (*m/z*) 544.8 [M + Na]⁺, 520.7 [M – H][–]; HPLC method A: *t_r* = 8.439 min.

The purified material obtained from the first step (91.0 mg, 0.17 mmol) was reacted with *Kt*BuO (136.7 mg, 1.22 mmol) in dry THF (10 mL) according to general procedure D (reaction time 2 h). Purification by flash column chromatography (SiO₂, DCM–MeOH gradient elution from 95:5 to 92:8) gave 41 mg of a white solid (64% yield). ¹H-NMR shows a 5:4 mixture of amide bond rotamers. ¹H-NMR (300 MHz, DMSO-*d*₆) δ 12.07 (s, 1H), 8.49–8.26 (m, 2H), 7.54–7.41 (m, 1H), 7.36–7.21 (m, 1H), 6.99–6.78 (m, 1H), 4.51–4.24 (m, 2H), 4.17–3.97 (m, 2H), 3.93–3.82 (m, 0.45H), 3.72–3.57 (m, 0.55H), 3.20–3.09 (m, 0.45H), 3.08–2.95 (m, 0.55H), 2.90–2.79 (m, 0.55H), 2.74–2.59 (m, 0.45H), 2.15–1.96 (m, 1H), 1.91–1.72 (m, 2H), 1.71–1.38 (m, 1H); ¹³C NMR (101 MHz, DMSO-*d*₆) δ 161.6, 161.4, 155.90, 155.85, 155.8, 155.03, 154.99, 137.0, 129.1, 129.0, 122.9, 122.8, 120.0, 118.22, 118.18, 116.2, 116.1, 110.7, 95.6, 95.4, 49.9, 47.5, 46.5, 46.2, 45.8, 42.2, 29.8, 29.7, 24.94, 24.86, 24.3, 23.7; ESI-MS: (*m/z*) 391.0 [M + Na]⁺, 366.9 [M – H][–]; HPLC method A: *t_r* = 6.023 min.

3-(3-((7-Bromo-9*H*-pyrimido[4,5-*b*]indol-4-yl)amino)piperidin-1-yl)-3-oxopropanenitrile (48)

4d (50.0 mg, 0.11 mmol), **44·HCl** (35.0 mg, 0.17 mmol), and DIPEA (73.7 mg, 0.57 mmol) were stirred in a solvent mixture of dry dioxane (1 mL) and dry DMF (0.1 mL) at 70 °C overnight. Additional **44·HCl** (35.0 mg, 0.17 mmol) and DIPEA (73.7 mg, 0.57 mmol) were added, and stirring at 70 °C continued overnight. The mixture was concentrated under reduced pressure, the residue diluted with dry THF (4 mL). *Nat*BuO (77.0 mg, 0.80 mmol) was added, and the mixture was stirred at rt for 1 h. Saturated NH₄Cl solution (30 mL) was added, and the mixture was extracted with EtOAc (3 × 20 mL). Combined organic layers were dried over Na₂SO₄ and concentrated under reduced pressure. Purification of the residue by flash column chromatography (SiO₂, DCM–EtOH gradient elution from 97:3 to 4:1) gave 25 mg (53% yield). ¹H-NMR shows a 5:4 mixture of amide bond rotamers. ¹H-NMR (400 MHz, DMSO-*d*₆) δ 12.11–12.03 (m, 1H), 8.43–8.34 (m, 1H), 8.33–8.26 (m, 1H), 7.60 (s, 1H), 7.45–7.38 (m, 1H), 6.99–6.80 (m, 1H), 4.49–4.41 (m, 0.55H), 4.39–4.26 (m, 1.45H), 4.15–3.99 (m, 2H), 3.90–3.83 (m, 0.45H), 3.68–3.61 (m, 0.55H), 3.19–3.10 (m, 0.45H), 3.05–2.96 (m, 0.55H), 2.87–2.79 (m, 0.55H), 2.70–2.61 (m, 0.45H), 2.12–1.97 (m, 1H), 1.87–1.75 (m, 2H), 1.67–1.40 (m, 1H); ¹³C NMR (101 MHz, DMSO-*d*₆) δ 161.5, 161.4, 155.9, 155.8, 155.7, 155.13, 155.09, 137.3, 123.2, 123.1, 122.7, 118.51, 118.47, 117.2, 117.1, 116.2, 116.1, 113.6, 95.6, 95.4, 49.9, 47.5, 46.5, 46.2, 45.8, 42.2, 29.8, 29.7, 24.9, 24.9, 24.3, 23.7; ESI-MS: (*m/z*) 434.8 [M + Na]⁺, 410.7 [M – H][–]; HPLC method B: *t_r* = 5.144 min.

3-(3-((7-Methoxy-9*H*-pyrimido[4,5-*b*]indol-4-yl)amino)piperidin-1-yl)-3-oxopropanenitrile (49)

The title compound was prepared from **4f** (496.0 mg, 1.28 mmol), **44·HCl** (392.2 mg, 1.92 mmol), DIPEA (828.5 mg, 6.41 mmol), and *Nat*BuO (863.7 mg, 8.97 mmol) in dry DMF (20 mL) according to general procedure G but was stirred at rt for 3 d after addition of *Nat*BuO. Purification by flash column chromatography (SiO₂, DCM–EtOH gradient elution from 97:3 to 4:1) gave 70 mg (15% yield). ¹H-NMR shows a 5:4 mixture of amide bond rotamers. ¹H-NMR (400 MHz, DMSO-*d*₆) δ 11.88–11.77 (m, 1H), 8.37–8.27 (m, 1H), 8.22–8.16 (m, 1H), 6.98–6.94 (m, 1H), 6.90–6.84 (m, 1H), 6.74–6.57 (m, 1H), 4.48–4.24 (m, 2H), 4.15–4.00 (m, 2H), 3.91–3.81 (m, 3.45H), 3.67–3.59 (m, 0.55H), 3.18–3.09 (m, 0.45H), 3.06–2.96 (m, 0.55H), 2.89–2.82 (m, 0.55H), 2.71–2.61 (m, 0.45H), 2.11–1.98 (m, 1H), 1.88–1.74 (m, 2H), 1.66–1.40 (m, 1H); ¹³C NMR (101 MHz, DMSO-*d*₆) δ 161.5, 161.4, 157.7, 157.6, 155.4, 155.2, 155.1, 153.5, 153.4, 137.7, 122.4, 122.2, 116.2, 116.1, 112.9, 112.8, 108.8, 96.1, 95.9, 95.0, 55.3, 50.1, 47.5, 46.3, 45.8, 42.2, 29.84, 29.76, 24.9, 24.8, 24.2, 23.7; ESI-MS: (*m/z*) 387.0 [M + Na]⁺, 363.1 [M – H][–]; HPLC method B: *t_r* = 2.768 min.

3-Oxo-3-(3-((7-(trifluoromethyl)-9*H*-pyrimido[4,5-*b*]indol-4-yl)amino)piperidin-1-yl)propanenitrile (50)

The title compound was prepared from **4g** (180.0 mg, 0.42 mmol), **44·HCl** (129.1 mg, 0.63 mmol), DIPEA (272.7 mg, 2.11 mmol), and *Nat*BuO (284.4 mg, 2.96 mmol) in dry DMF (10 mL) according

to general procedure G. Purification by flash column chromatography (SiO₂, 1.DCM–EtOH gradient elution from 97:3 to 4:1, 2.DCM–(2N NH₃ in MeOH) gradient elution from 99:1 to 92:8) gave 12 mg (7% yield). ¹H-NMR shows a 5:4 mixture of amide bond rotamers. ¹H-NMR (300 MHz, DMSO-*d*₆) δ 12.31 (s, 1H), 8.60–8.51 (m, 1H), 8.50–8.39 (m, 1H), 7.73 (s, 1H), 7.62–7.53 (m, 1H), 7.17–6.98 (m, 1H), 4.52–4.24 (m, 2H), 4.16–3.97 (m, 2H), 3.93–3.83 (m, 1H), 3.71–3.61 (m, 1H), 3.22–3.12 (m, 1H), 3.08–2.96 (m, 1H), 2.92–2.82 (m, 1H), 2.73–2.62 (m, 1H), 2.15–1.97 (m, 1H), 1.92–1.74 (m, 2H), 1.70–1.40 (m, 1H); ESI-MS: (*m/z*) 424.9 [M + Na]⁺, 401.0 [M – H][–]; HPLC method B: t_r = 5.880 min.

Supplementary Materials: The following are available online at <http://www.mdpi.com/1422-0067/21/21/7823/s1>: the ADP Glo™ assay protocol; additional data for inhibitors (**R**)-**2** and (**R**)-**28** including interaction frequencies of 1 μs molecular dynamics simulations, microsomal stability assay, cell toxicity data on five different cell lines, cellular GSK-3α/β inhibition, neuroprotective effects, and MD movies as well as preparation of 4-chloro-9H-pyrimido[4,5-*b*]indoles **3a–l**. Figure S1: Observed interactions of (**R**)-**2** and (**R**)-**28** in the MD simulations; Figure S2: Evaluation of the cytotoxic potential of (**R**)-**28** cell lines; Figure S3: Evaluation of the cytotoxic potential of (**R**)-**28** on cancer cell lines; Figure S4: Compound (**R**)-**28** inhibits GSK-3β activity in neuronal SH-SY5Y cells; Figure S5: Neuroprotective effects of (**R**)-**28** against the neurotoxicity induced by H₂O₂ and OAβ_{1–42} in neuronal SH-SY5Y cells; Table S1: Chromatographic gradient for separation of metabolism analytes. Scheme S1: Synthetic route to 4-chloro-9H-pyrimido[4,5-*b*]indoles **3a–l**. The QM output conformations and full raw trajectories are freely available at <https://doi.org/10.5281/zenodo.3973296>.

Author Contributions: S.A., A.E.-G., T.P., F.A., M.K., D.B.A., G.S., J.R., C.G., M.L., M.I.G., A.T., S.A.L., and P.K. conceived and designed the experiments; S.A. and A.E.-G. performed synthesis; T.P. performed molecular modelling; F.A., M.K., D.B.A., G.S., and J.R. performed biological assays; C.G. performed chiral chromatography; S.A., T.P., and P.K. analyzed the data; and S.A., T.P., and P.K. wrote the paper. All authors have read and agreed to the published version of the manuscript.

Funding: This study was supported by the Federal Ministry of Education and Research (BMBF) within the BioPharma—Neuroallianz consortium (Neuro-T8B project). P.K. gratefully acknowledges funding from the DPhG-Stiftung (Horst-Böhme-Stiftung). T.P. acknowledges funding from the European Union’s Horizon 2020 research and innovation programme under the Marie Skłodowska-Curie Grant agreement No 839230 and Orion Research Foundation sr.

Acknowledgments: The authors acknowledge Jens Strobach for the biological assays of some synthesized compounds, Michael Forster for fruitful scientific discussion, and the CSC-IT Center for Science Ltd. (Espoo, Finland) for computational resources. The authors thank Kristine Schmidt for proof reading (language) of the manuscript.

Conflicts of Interest: The authors declare no conflict of interest.

References

1. Kaidanovich-Beilin, O.; Woodgett, J. GSK-3: Functional Insights from Cell Biology and Animal Models. *Front. Mol. Neurosci.* **2011**, *4*, 40. [[CrossRef](#)]
2. Sutherland, C. What are the bona fide GSK3 Substrates? *Int. J. Alzheimer’s Dis.* **2011**, *2011*, 23.
3. Beurel, E.; Grieco, S.F.; Jope, R.S. Glycogen synthase kinase-3 (GSK3): Regulation, actions, and diseases. *Pharmacol. Ther.* **2015**, *148*, 114–131. [[CrossRef](#)]
4. Lauretti, E.; Dincer, O.; Praticò, D. Glycogen synthase kinase-3 signaling in Alzheimer’s disease. *Biochim. Biophys. Acta* **2020**, *1867*, 118664. [[CrossRef](#)] [[PubMed](#)]
5. Andreev, S.; Pantsar, T.; Ansideri, F.; Kudolo, M.; Forster, M.; Schollmeyer, D.; Laufer, S.A.; Koch, P. Design, Synthesis and Biological Evaluation of 7-Chloro-9H-pyrimido[4,5-*b*]indole-based Glycogen Synthase Kinase-3β Inhibitors. *Molecules* **2019**, *24*, 2331. [[CrossRef](#)] [[PubMed](#)]
6. Gorrod, J.W.; Aislaitner, G. The metabolism of alicyclic amines to reactive iminium ion intermediates. *Eur. J. Drug Metab. Pharmacokinet.* **1994**, *19*, 209–217. [[CrossRef](#)]
7. Meanwell, N.A. Fluorine and Fluorinated Motifs in the Design and Application of Bioisosteres for Drug Design. *J. Med. Chem.* **2018**, *61*, 5822–5880. [[CrossRef](#)]
8. Bull, J.A.; Croft, R.A.; Davis, O.A.; Doran, R.; Morgan, K.F. Oxetanes: Recent Advances in Synthesis, Reactivity, and Medicinal Chemistry. *Chem. Rev.* **2016**, *116*, 12150–12233. [[CrossRef](#)]
9. Wuitschik, G.; Carreira, E.M.; Wagner, B.; Fischer, H.; Parrilla, I.; Schuler, F.; Rogers-Evans, M.; Müller, K. Oxetanes in Drug Discovery: Structural and Synthetic Insights. *J. Med. Chem.* **2010**, *53*, 3227–3246. [[CrossRef](#)]

10. Heider, F.; Ansideri, F.; Tesch, R.; Pantsar, T.; Haun, U.; Döring, E.; Kudolo, M.; Poso, A.; Albrecht, W.; Laufer, S.A.; et al. Pyridinylimidazoles as dual glycogen synthase kinase 3 β /p38 α mitogen-activated protein kinase inhibitors. *Eur. J. Med. Chem.* **2019**, *175*, 309–329. [[CrossRef](#)]
11. Zegzouti, H.; Zdanovskaia, M.; Hsiao, K.; Goueli, S.A. ADP-Glo: A Bioluminescent and Homogeneous ADP Monitoring Assay for Kinases. *Assay Drug Dev. Technol.* **2009**, *7*, 560–572. [[CrossRef](#)] [[PubMed](#)]
12. Pantsar, T.; Singha, P.; Nevalainen, T.J.; Koshevoy, I.; Leppänen, J.; Poso, A.; Niskanen, J.M.A.; Pasonen-Seppänen, S.; Savinainen, J.R.; Laitinen, T.; et al. Design, synthesis, and biological evaluation of 2,4-dihydropyrano[2,3-c]pyrazole derivatives as autotaxin inhibitors. *Eur. J. Pharm. Sci.* **2017**, *107*, 97–111. [[CrossRef](#)] [[PubMed](#)]
13. Laufer, S.A.; Hauser, D.R.J.; Domeyer, D.M.; Kinkel, K.; Liedtke, A.J. Design, Synthesis, and Biological Evaluation of Novel Tri- and Tetrasubstituted Imidazoles as Highly Potent and Specific ATP-Mimetic Inhibitors of p38 MAP Kinase: Focus on Optimized Interactions with the Enzyme's Surface-Exposed Front Region. *J. Med. Chem.* **2008**, *51*, 4122–4149. [[CrossRef](#)] [[PubMed](#)]
14. Di Martino, R.M.C.; Pruccoli, L.; Bisi, A.; Gobbi, S.; Rampa, A.; Martinez, A.; Pérez, C.; Martinez-Gonzalez, L.; Paglione, M.; Di Schiavi, E.; et al. Novel Curcumin-Diethyl Fumarate Hybrid as a Dualistic GSK-3 β Inhibitor/Nrf2 Inducer for the Treatment of Parkinson's Disease. *ACS Chem. Neurosci.* **2020**, *11*, 2728–2740. [[CrossRef](#)] [[PubMed](#)]
15. Tarozzi, A.; Morroni, F.; Merlicco, A.; Hrelia, S.; Angeloni, C.; Cantelli-Forti, G.; Hrelia, P. Sulforaphane as an inducer of glutathione prevents oxidative stress-induced cell death in a dopaminergic-like neuroblastoma cell line. *J. Neurochem.* **2009**, *111*, 1161–1171. [[CrossRef](#)] [[PubMed](#)]
16. Tarozzi, A.; Bartolini, M.; Piazzzi, L.; Valgimigli, L.; Amorati, R.; Bolondi, C.; Djemil, A.; Mancini, F.; Andrisano, V.; Rampa, A. From the dual function lead AP2238 to AP2469, a multi-target-directed ligand for the treatment of Alzheimer's disease. *Pharmacol. Res. Perspect.* **2014**, *2*, e00023. [[CrossRef](#)]
17. Pruccoli, L.; Morroni, F.; Sita, G.; Hrelia, P.; Tarozzi, A. Esculetin as a Bifunctional Antioxidant Prevents and Counteracts the Oxidative Stress and Neuronal Death Induced by Amyloid Protein in SH-SY5Y Cells. *Antioxidants* **2020**, *9*, 551. [[CrossRef](#)]
18. Showalter, H.D.H.; Bridges, A.J.; Zhou, H.; Sercel, A.D.; McMichael, A.; Fry, D.W. Tyrosine Kinase Inhibitors. 16. 6,5,6-Tricyclic Benzothieno[3,2-d]pyrimidines and Pyrimido[5,4-b]- and -[4,5-b]indoles as Potent Inhibitors of the Epidermal Growth Factor Receptor Tyrosine Kinase. *J. Med. Chem.* **1999**, *42*, 5464–5474. [[CrossRef](#)]
19. Tichý, M.; Pohl, R.; Xu, H.Y.; Chen, Y.-L.; Yokokawa, F.; Shi, P.-Y.; Hocek, M. Synthesis and antiviral activity of 4,6-disubstituted pyrimido[4,5-b]indole ribonucleosides. *Bioorganic Med. Chem.* **2012**, *20*, 6123–6133. [[CrossRef](#)]
20. Tichý, M.; Pohl, R.; Tloušťová, E.; Weber, J.; Bahador, G.; Lee, Y.-J.; Hocek, M. Synthesis and biological activity of benzo-fused 7-deazaadenosine analogues. 5- and 6-substituted 4-amino- or 4-alkylpyrimido[4,5-b]indole ribonucleosides. *Bioorganic Med. Chem.* **2013**, *21*, 5362–5372.
21. Gehringer, M.; Forster, M.; Pfaffenrot, E.; Bauer, S.M.; Laufer, S.A. Novel Hinge-Binding Motifs for Janus Kinase 3 Inhibitors: A Comprehensive Structure–Activity Relationship Study on Tofacitinib Bioisosteres. *ChemMedChem* **2014**, *9*, 2516–2527. [[CrossRef](#)] [[PubMed](#)]
22. Manley, D.W.; McBurney, R.T.; Miller, P.; Walton, J.C.; Mills, A.; O'Rourke, C. Titania-Promoted Carboxylic Acid Alkylations of Alkenes and Cascade Addition–Cyclizations. *J. Org. Chem.* **2014**, *79*, 1386–1398. [[CrossRef](#)] [[PubMed](#)]
23. Gehringer, M.; Pfaffenrot, E.; Bauer, S.; Laufer, S.A. Design and Synthesis of Tricyclic JAK3 Inhibitors with Picomolar Affinities as Novel Molecular Probes. *ChemMedChem* **2014**, *9*, 277–281. [[CrossRef](#)] [[PubMed](#)]
24. Roos, K.; Wu, C.; Damm, W.; Reboul, M.; Stevenson, J.M.; Lu, C.; Dahlgren, M.K.; Mondal, S.; Chen, W.; Wang, L.; et al. OPLS3e: Extending Force Field Coverage for Drug-Like Small Molecules. *J. Chem. Theory Comput.* **2019**, *15*, 1863–1874. [[CrossRef](#)]
25. Bochevarov, A.D.; Harder, E.; Hughes, T.F.; Greenwood, J.R.; Braden, D.A.; Philipp, D.M.; Rinaldo, D.; Halls, M.D.; Zhang, J.; Friesner, R.A. Jaguar: A high-performance quantum chemistry software program with strengths in life and materials sciences. *Int. J. Quantum Chem.* **2013**, *113*, 2110–2142. [[CrossRef](#)]
26. Heider, F.; Pantsar, T.; Kudolo, M.; Ansideri, F.; De Simone, A.; Pruccoli, L.; Schneider, T.; Goettert, M.I.; Tarozzi, A.; Andrisano, V.; et al. Pyridinylimidazoles as GSK3 β Inhibitors: The Impact of Tautomerism on Compound Activity via Water Networks. *ACS Med. Chem. Lett.* **2019**, *10*, 1407–1414. [[CrossRef](#)]

27. Madhavi Sastry, G.; Adzhigirey, M.; Day, T.; Annabhimoju, R.; Sherman, W. Protein and ligand preparation: Parameters, protocols, and influence on virtual screening enrichments. *J. Comput. Aided Mol. Des.* **2013**, *27*, 221–234. [[CrossRef](#)]
28. Sivaprakasam, P.; Han, X.; Civiello, R.L.; Jacutin-Porte, S.; Kish, K.; Pokross, M.; Lewis, H.A.; Ahmed, N.; Szapiel, N.; Newitt, J.A.; et al. Discovery of new acylaminopyridines as GSK-3 inhibitors by a structure guided in-depth exploration of chemical space around a pyrrolopyridinone core. *Bioorg. Med. Chem. Lett.* **2015**, *25*, 1856–1863. [[CrossRef](#)]
29. Bowers, K.J.; Chow, E.; Xu, H.; Dror, R.O.; Eastwood, M.P.; Gregersen, B.A.; Klepeis, J.L.; Kolossvary, I.; Moraes, M.A.; Sacerdoti, F.D.; et al. *Scalable Algorithms for Molecular Dynamics Simulations on Commodity Clusters, Proceedings of the 2006 ACM/IEEE Conference on Supercomputing, Tampa, FL, USA, 11–17 November 2006*; ACM: Tampa, FL, USA, 2006; p. 84.
30. Jorgensen, W.L.; Chandrasekhar, J.; Madura, J.D.; Impey, R.W.; Klein, M.L. Comparison of simple potential functions for simulating liquid water. *J. Chem. Phys.* **1983**, *79*, 926–935. [[CrossRef](#)]

Publisher’s Note: MDPI stays neutral with regard to jurisdictional claims in published maps and institutional affiliations.



© 2020 by the authors. Licensee MDPI, Basel, Switzerland. This article is an open access article distributed under the terms and conditions of the Creative Commons Attribution (CC BY) license (<http://creativecommons.org/licenses/by/4.0/>).



Supplementary Materials

Discovery and Evaluation of Enantiopure 9H-pyrimido[4,5-*b*]indoles as Nanomolar GSK-3 β Inhibitors with Improved Metabolic Stability

Stanislav Andreev ¹, Tatu Pantsar ^{1,2}, Ahmed El-Gokha ^{1,3}, Francesco Ansideri ¹, Mark Kudolo ¹, Débora Bublitz Anton ⁴, Giulia Sita ⁵, Jenny Romasco ⁶, Christian Geibel ⁷, Michael Lämmerhofer ⁷, Márcia Ines Goettert ⁴, Andrea Tarozzi ⁶, Stefan A. Laufer ¹ and Pierre Koch ^{1,8,*}

- ¹ Institute of Pharmaceutical Sciences, Department of Medicinal and Pharmaceutical Chemistry, Eberhard Karls University Tübingen, Auf der Morgenstelle 8, 72076 Tübingen, Germany; stanislav.andreev@uni-tuebingen.de (S.A.); tatu.pantsar@uni-tuebingen.de (T.P.); ahmed.abdelaleem@science.menofia.edu.eg (A.E.-G.); francesco.ansideri@uni-tuebingen.de (F.A.); mark.kudolo@uni-tuebingen.de (M.K.); stefan.laufer@uni-tuebingen.de (S.L.)
 - ² School of Pharmacy, Faculty of Health Sciences, University of Eastern Finland, P.O. Box 1627, 70211 Kuopio, Finland
 - ³ Chemistry Department, Faculty of Science, Menoufia University, 32511 Shebin El-Kom, Egypt
 - ⁴ Cell Culture Laboratory, Postgraduate Program in Biotechnology, University of Vale do Taquari (Univates), 95914-014 Lajeado, Brazil; debora.anton@univates.br (D.B.A.); marcia.goettert@univates.br (M.I.)
 - ⁵ Department of Pharmacy and Biotechnology, Alma Mater Studiorum, University of Bologna, Via Irnerio, 48, 40126 Bologna, Italy; giulia.sita2@unibo.it
 - ⁶ Department for Life Quality Studies, Alma Mater Studiorum, University of Bologna, Corso D'Augusto, 237, 47921 Rimini, Italy; jenny.romasco@unibo.it (J.R.); andrea.tarozzi@unibo.it (A.T.)
 - ⁷ Institute of Pharmaceutical Sciences, Department of Pharmaceutical (Bio-)Analysis, Eberhard Karls University Tübingen, Auf der Morgenstelle 8, 72076 Tübingen, Germany; christian.geibel@uni-tuebingen.de (C.G.); michael.laemmerhofer@uni-tuebingen.de (M.L.)
 - ⁸ Department of Pharmaceutical/Medicinal Chemistry II, Institute of Pharmacy, University of Regensburg, Universitätsstraße 31, 93053 Regensburg, Germany
- * Correspondence: pierre.koch@uni-tuebingen.de; Tel.: +49-(941)-943-2847

Received: 10 September 2020; Accepted: 16 October 2020; Published: 22 October 2020

Table of Contents

1. ADP Glo™ Kinase assay	3
2. Interaction Frequencies of (<i>R</i>)- 2 and (<i>R</i>)- 28 in the 1 μ s Molecular Dynamics Simulations	3
3. Microsomal Stability Assay	3
4. Investigation of Cell Toxicity of (<i>R</i>)- 28 on Five Different Cell Lines	4
5. Investigation of Cellular GSK-3 α / β Inhibition by (<i>R</i>)- 28 and Its Neuroprotective Effects	7
6. Preparation of 4-chloro-9 <i>H</i> -pyrimido[4,5- <i>b</i>]indoles 3a-1	9

1. ADP Glo™ Kinase Assay

The inhibitory activity of the final compounds on GSK-3 β was determined by the Promega ADP-Glo™ Kinase assay (Promega Corporation, Madison, WI 53711, USA), which was performed in white, non-treated 384-well plates (Corning). The experiments were carried out as quadruplicates using a concentration of 0.58 ng/ μ L of recombinant human GSK-3 β , 0.2 μ g/ μ L GSK-3 substrate G50-58 (sequence: YRRAAVPPSPSLSRHSSPHQ(pS)EDEEE) and 25 μ M ATP in the presence of serial dilutions of the final compounds. In addition, two control experiments with uninhibited kinase and two blank experiments with ATP/substrate solution were performed.

In detail, the kinase was pre-incubated with the final compounds for 10 min at rt. Then substrate/ATP was added to start the reaction, which was run for 1 h at rt. The next steps consisted of addition of ADP-Glo™ reagent (5 μ L, then 1 h incubation) and Kinase detection reagent (10 μ L, then 30 min incubation). Finally, the luminescence was measured on a FilterMax F5 microplate reader (Molecular Devices) (integration time 500 ms). GraphPad Prism v. 7.03. was used to normalize the raw data to the values of the control and blank experiments and generate absolute IC₅₀ values.

2. Interaction Frequencies of (R)-2 and (R)-28 in the 1 μ s Molecular Dynamics Simulations

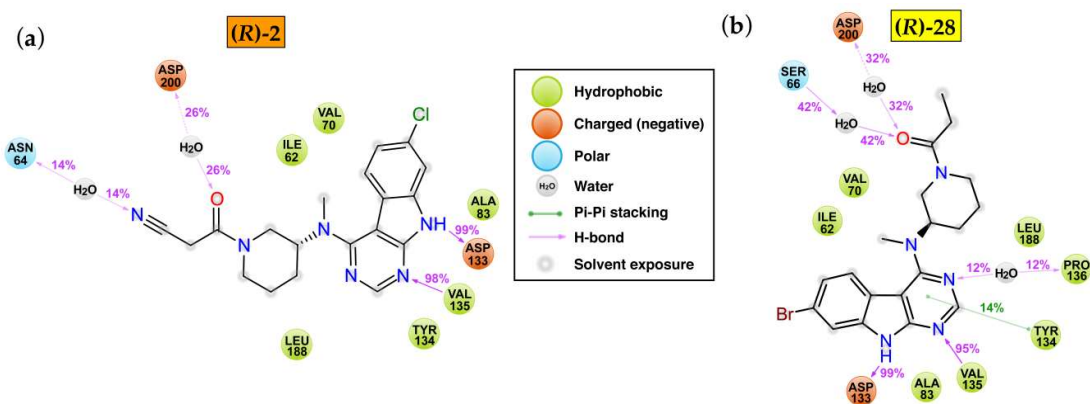


Figure S1. Observed interactions of (R)-2 (a) and (R)-28 (b) in the MD simulations. Both ligands demonstrate stable hinge binding (95–99% Asp133 and Val135 interactions). The carbonyl group mediates water-bridged interactions to Asp200 or Ser66. Interactions with >10% frequency are shown.

3. Microsomal Stability Assay

Pooled male and female human liver microsomes (HLMs) (Lot: SLBQ7487V) were purchased from Merck (Schnelldorf, Germany). The compounds ((R)-2 and (R)-28, respectively) (100 μ M), 4 mM MgCl₂·6 H₂O in 0.1 M Tris buffer (pH 7.4) and an NADPH-regenerating system (5 mM glucose-6-phosphate, 5 U/mL glucose-6-phosphate dehydrogenase and 1 mM NADP⁺) were preincubated for 5 min at 37 °C and 750× rpm on a shaker. The HLMs were added to start the reaction. The reaction mixture was then split into triplicates of 50 μ L. The reaction was quenched at six time points (0, 10, 20, 30, 60 and 120 min) by addition of 100 μ L internal standard (30 μ M in MeCN). The samples were vortexed for 30 s and centrifuged (19,800 relative centrifugal force/4 °C/10 min). The obtained supernatant was directly used for LC-MS analysis. A limit of 1% organic solvent was not exceeded.

Positive control: Propranolol

Negative control: Heat inactivated microsomes

The metabolite formation was analyzed with an Alliance 2695 Separations Module (Waters GmbH, Eschborn).

Sample temperature: 4 °C

Column: Phenomenex Kinetex C18 column (100 × 3 mm; 2.6 μ m; 100 Å)

Column temperature: 40 °C

Injection volume: 5 μ L

Flow rate: 0.6 mL/min

Gradient: see Table below

Table S1. Chromatographic gradient for separation of metabolism analytes.

Time (min)	Solvent A (%)	Solvent B (%)
	(90% H ₂ O, 10% MeCN, 0.1% formic acid)	(MeCN, 0.1% formic acid)
0	90	10
2.5	90	10
10	45	55
12	45	55
12.01	90	10
15	90	10

The detection was performed on a Micromass Quattro micro triple quadrupole mass spectrometer (Waters GmbH, Eschborn).

Ionization mode: Electrospray ionization, positive mode

Spray voltage: 4.5 kV

Desolvation temperature: 250 °C

Desolvation gas flow: 600 L/h

4. Investigation of Cell Toxicity on Five Different Cell Lines

4.1. Maintenance of Cell Culture

The experiments were performed in an *in vitro* model of cell cytotoxicity analyses on hepatocellular carcinoma (HepG2), human breast adenocarcinoma (MCF-7), human neuroblastoma (SH-SY5Y), human lung fibroblast (MRC-5) and chinese hamster ovary (CHO-K1). The cells lines were cultured in appropriate medium, supplemented with 10% (*v/v*) of fetal bovine serum (FBS) and 1% antibiotic/antimycotic solution. For subculture, cells were dissociated with trypsin-EDTA (Cultilab), split into a 1:3 ratio and subcultured into Petri dishes with 25 cm² growth area. Culture medium was replaced every 2 days until the cells reached the total confluence after 4–5 days of initial seeding. Cells were maintained in the following controlled conditions: 95% of humidified atmosphere, 5% of CO₂ and constant temperature of 37 °C.

4.2. Cytotoxicity

The assessment of cell viability was performed according to the MTT colorimetric assay. The cytotoxicity of the compounds was assessed on 5 different cell lines. Cells (5×10^3 /well) in 200 μ L appropriate medium containing 10% FBS were seeded on 96-well plates and incubated overnight. These cells were subsequently treated with different concentrations of compound (**R**)-**28** for 48 h. The effects were estimated by colorimetric assay based on the conversion of tetrazolium salts (MTT) after 3 h of incubation to a blue formazan product by active mitochondria. The absorbance was read at 570 nm using a Spectramax i5 microplate reader. Results were expressed as percentage of control.

Cell Lines

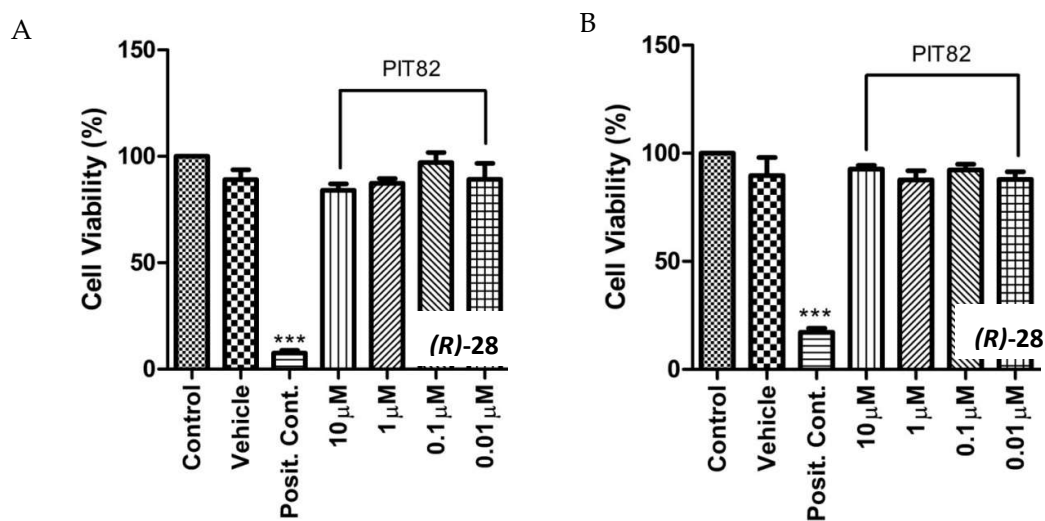


Figure S2. Evaluation of the cytotoxic potential of (R)-28 on cell lines. (A) Human lung fibroblast cell line MRC-5 and (B) chinese hamster ovary cell line CHO-K1. Cell viability was evaluated by MTT assay, after 48 h treatment with (R)-28. Mean values \pm SEM of three independent experiments are shown. *** $p < 0.001$ compared with control. (R)-28; Vehicle (DMSO); Positive Control (hydrogen peroxide).

Cancer Cell Lines

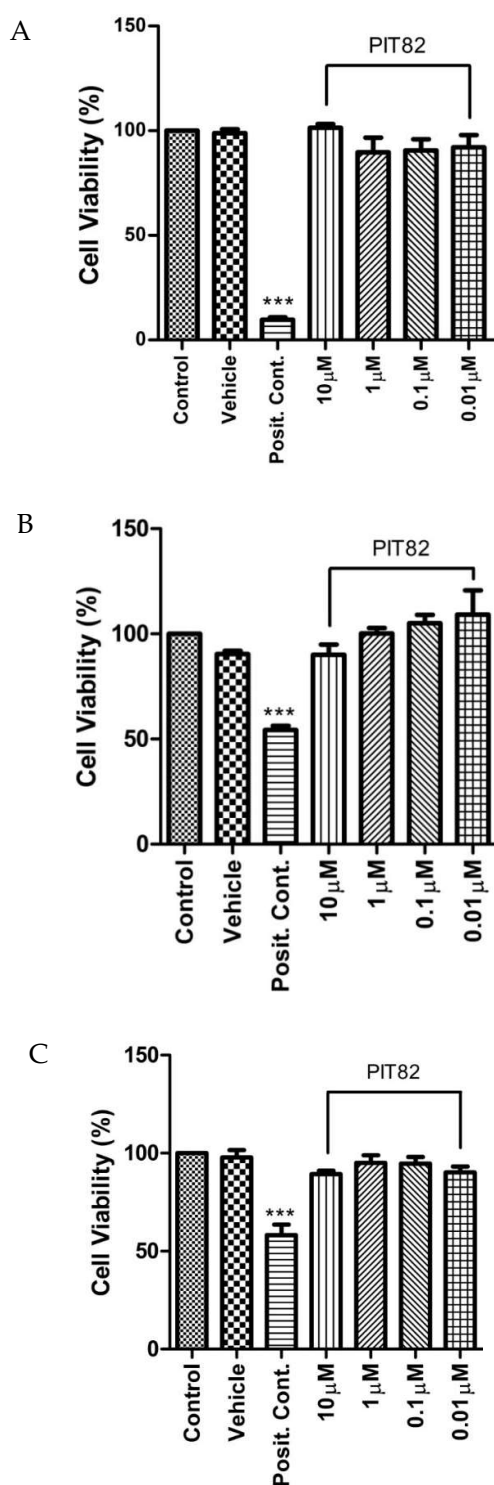


Figure S3. Evaluation of the cytotoxic potential of (*R*)-28 on cancer cell lines. (A) Hepatocellular carcinoma cell line HepG2, (B) human breast adenocarcinoma cell line MCF-7 and (C) human neuroblastoma cell line SH-SY5Y. Cell viability was evaluated by MTT assay, after 48 h treatment with (*R*)-28. Mean values \pm SEM of three independent experiments are shown. *** $p < 0.001$ compared with control. (*R*)-28; Vehicle (DMSO); Positive Control (hydrogen peroxide).

5. Investigation of Cellular GSK-3 α/β Inhibition by (R)-28 and Its Neuroprotective Effects

5.1. Cell Cultures

Human neuronal SH-SY5Y cells (Sigma Aldrich, St. Louis, MO, USA) were routinely grown in Dulbecco's modified Eagle's Medium supplemented with 10% fetal bovine serum, 2 mM L-glutamine, 50 U/mL penicillin and 50 $\mu\text{g/mL}$ streptomycin at 37 °C in a humidified incubator with 5% CO₂.

5.2. Neuronal Viability

SH-SY5Y cells were seeded in a 96-well plate at 2×10^4 cells/well, incubated for 24 h and then treated with various concentrations (1.25–40 μM) of (R)-28 for 24 h. Cell viability, in terms of mitochondrial activity, was evaluated by MTT assay, as previously described [14].

5.3. Neuroprotective Activity toward H₂O₂

SH-SY5Y cells were seeded in a 96-well plate at 2×10^4 cells/well, incubated for 24 h and subsequently treated with (R)-28 (5 μM) and H₂O₂ (100 μM) for 1 h. Then, cells were starved in complete medium for 22 h. The neuroprotective activity was measured by using the MTT assay as previously described [15]. Data are expressed as a percentage of neurotoxicity versus untreated cells.

5.4. OA β_{1-42} Preparation for the Determination of Neuroprotective Activity

A β_{1-42} peptide (AnaSpec, Fremont, CA, USA) was first dissolved in 1,1,1,3,3,3-hexafluoroisopropanol to 1 mg/mL, sonicated, incubated at rt for 24 h, and lyophilised to obtain an unaggregated A β_{1-42} peptide film that was solubilised with DMSO and stored at –20 °C until use. The aggregation of A β_{1-42} peptide into oligomers was performed as previously described [16].

5.5. Neuroprotective Activity toward OA β_{1-42}

SH-SY5Y cells were seeded in a 96-well plate at 3×10^4 cells/well, incubated for 24 h, and subsequently treated with (R)-28 (5 μM) and OA β_{1-42} (10 μM) for 4 h. The neuroprotective activity was measured by using the MTT assay as previously described [17]. Data are expressed as a percentage of neurotoxicity versus untreated cells.

5.6. Western Blotting

SH-SY5Y cells were seeded in 60 mm dishes at 2×10^6 cells/dish, incubated for 24 h and subsequently treated with (R)-28 (1 μM) for 1 h at 37 °C in 5% CO₂. At the end of incubation, cells were trypsinized and the cellular pellet was resuspended in complete lysis buffer containing leupeptin (2 $\mu\text{g/mL}$), PMSF (100 $\mu\text{g/mL}$) and cocktail of protease/phosphatase inhibitors (100 \times). Small amounts were removed for the determination of the protein concentration using the Bradford method. The samples (30 μg proteins) were run on 4–15% SDS polyacrylamide gels (Bio-rad Laboratories S.r.L., Hercules, CA, USA) and electroblotted onto 0.45 μm nitrocellulose membranes. The membranes were incubated at 4 °C overnight with primary antibody recognizing phospho-GSK3 α/β (Ser21/9), (1:1000; Cell Signaling Technology Inc, Danvers, MA, USA), or anti-phospho-GSK3(Tyr279/Tyr216), (1:1000; EMD Millipore, Darmstadt, Germany). After washing with TBS-T (TBS +0.05% Tween20), the membranes were incubated with secondary antibodies (1:2000; GE Healthcare). Enhanced chemiluminescence was used to visualize the bands (ECL; Bio-rad Laboratories). The membranes were then reprobated with GSK3 α/β , (1:1000; Cell Signaling Technology Inc.). The data were analyzed by densitometry, using Quantity One software (Bio-Rad Laboratories® S.r.L.). The values were normalized and expressed as mean \pm SD of densitometry in each experimental group.

5.7. Statistical Analysis

Results are shown as mean \pm standard deviation (SD) of three independent experiments. Statistical analysis was performed using Student's t-test. Differences were considered significant at $p < 0.05$. Analyses were performed using GraphPad PRISM software (v. 5.0; GraphPad Software, La Jolla, CA, USA) on a Windows platform.

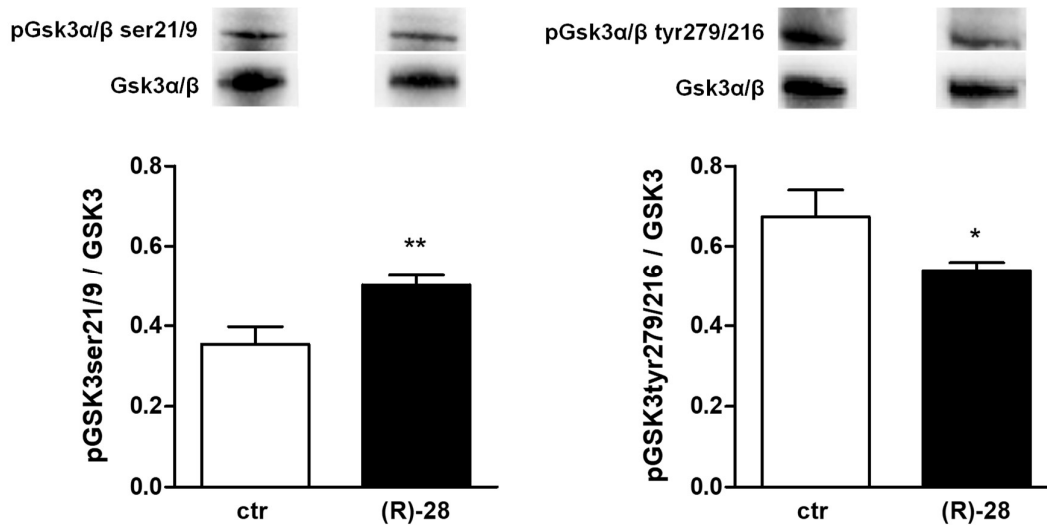


Figure S4. Compound (R)-28 inhibits the GSK-3 β activity in neuronal SH-SY5Y cells. Cells were incubated with (R)-28 (1 μ M) for 1 h. At the end of incubation, the phosphorylation of GSK-3 α/β (Ser21/9) (inactive GSK-3 α/β form) and GSK-3 α/β (Tyr279/Tyr216) (active GSK-3 α/β form) was determined by western blotting. Data are expressed as ratio between phospho-GSK-3 α/β and total GSK-3 β levels normalized against β -Actin. Mean values \pm SD of at least three independent experiments are shown (* $p < 0.05$ and ** $p < 0.01$ vs untreated cells).

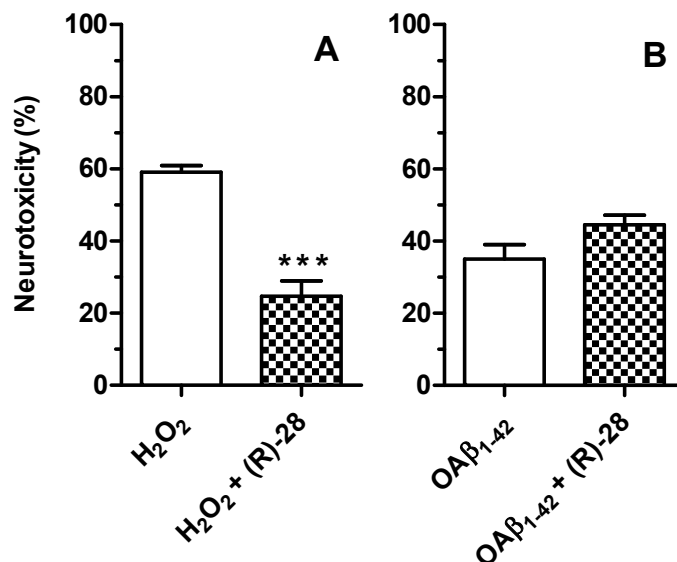
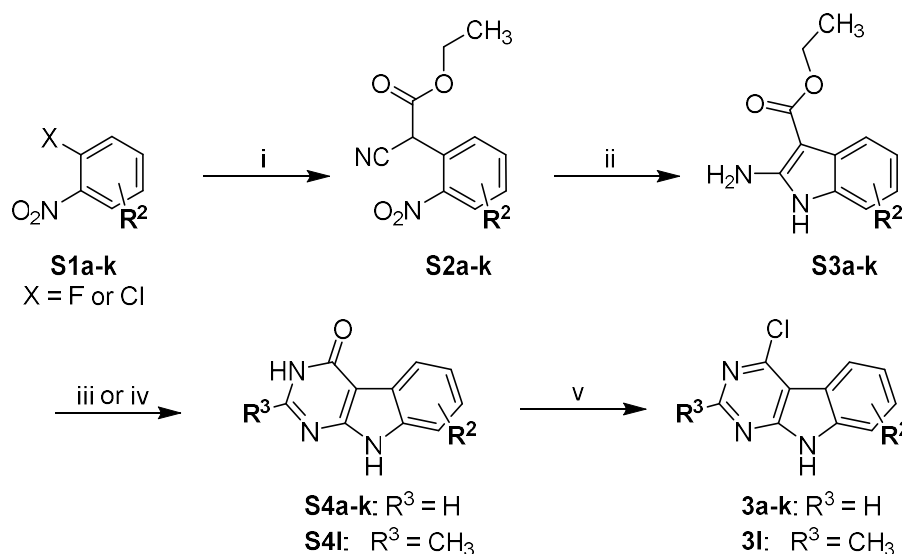


Figure S5. Neuroprotective effects of (R)-28 against the neurotoxicity induced by H₂O₂ and OAβ₁₋₄₂ in SH-SY5Y cells. **(A)** Cells were incubated with (R)-28 (5 μM) and H₂O₂ (100 μM) for 1 h and then starved in complete medium for 22 h. **(B)** Cells were incubated with (R)-28 (5 μM) and OAβ₁₋₄₂ (10 μM) for 4 h. The neurotoxicity was evaluated by MTT assay as described above. Data are expressed as percentages of neurotoxicity versus untreated cells. Mean values ± SD of three independent experiments are shown (***) $p < 0.001$ vs cells treated with H₂O₂).

6. Preparation of 4-chloro-9H-pyrimido[4,5-*b*]indoles 3a–l

The substitution pattern of the non-aromatic ring in the 9H-pyrimido[4,5-*b*]indole core was defined by utilizing appropriate *o*-halonitrobenzenes (**S1a–k**) in the first step of the synthetic route (Scheme S1). These commercially available starting materials were reacted with ethyl cyanoacetate under highly basic conditions giving substitution products **S2a–k**. Reductive ring closure was then effected with elemental zinc in acetic acid and typically generated 2-aminoindoles **S3a–k** along with characteristic by-products, which presumably are the corresponding 1-hydroxy-2-aminoindoles [18]. However, a purification of these mixtures was unnecessary in most cases, as the following condensation with formamide predominantly afforded the desired 3,9-dihydro-4H-pyrimido[4,5-*b*]indol-4-ones **S1a–k**. The introduction of a methyl group in the 2-position of the pyrimidine ring of **S4l** was achieved applying a protocol modified from Showalter et al. [18]. To this end, **S3c** was converted to an amidine intermediate with acetonitrile, which was then cyclized to **S4l** with aqueous NaOH in EtOH. The reaction of **S4a–l** with POCl₃ finally delivered 4-chloro-9H-pyrimido[4,5-*b*]indoles **3a–l**.



Scheme S1. Synthetic route to 4-chloro-9H-pyrido[4,5-b]indoles **3a-l**. For the definition of R² see Scheme 1 in the main manuscript. Reagents and conditions: (i) ethyl cyanoacetate, NaH, DMF, 0 °C to rt or 75 °C in case of **S2a-g** or ethyl cyanoacetate, K^tBuO, THF, 0 °C to 60 °C in case of **S2h-k** (ii) Zn⁰, AcOH, 90 °C; (iii) NH₄HCOO, formamide, 160 °C in case of **S4a-d** and **S4h-k** or formamide, 160–190 °C in case of **S4e-g**; (iv) (1) **S3c**, HCl, MeCN, rt to reflux, (2) NaOH_(aq), EtOH, reflux (in case of **S4l**); (v) POCl₃, DIPEA, chlorobenzene, rt to 80–100 °C in case of **3a**, **3c-e**, **3h,i** and **3k,l** or DIPEA, POCl₃ (neat), rt to 80 °C in case of **3b**, **3f** and **3j** or POCl₃ (neat), rt to 80 °C in case of **3g**.

6.1. General Procedure H

The appropriate intermediate was dissolved in glacial AcOH. The solution was heated to 80–90 °C and zinc powder was added in portions. The suspension was stirred at 80–90 °C until reaction control by HPLC indicated complete consumption of the starting material. The suspension was left to cool down to rt and filtered rinsing the residue with glacial AcOH or EtOAc. The filtrate was concentrated under reduced pressure to leave a residue of AcOH which was neutralized by addition of saturated NaHCO₃ solution. The resulting precipitate was filtered off, washed with demineralised water and dried over P₂O₅ in vacuo. The crude material isolated from these reactions typically consisted of a mixture of the title compounds and the corresponding 1-hydroxyindoles. These crude mixtures were used in the next step without further purification.

6.2. General Procedure I

The appropriate intermediate was suspended in formamide and ammonium formate was added. The mixture was stirred at 160 °C until reaction control by HPLC indicated complete consumption of the starting material. The suspension was left to cool down to rt and poured into ice-cold water. The resulting precipitate was filtered off, rinsed thoroughly with demineralised water and dried over P₂O₅ in vacuo. The crude product was used in the next step without further purification.

6.3. General Procedure J

The appropriate intermediate was suspended in chlorobenzene. DIPEA was added followed by careful addition of POCl₃ (used in stoichiometric amounts or as co-solvent). The mixture was stirred at 80–100 °C until reaction control by HPLC indicated complete consumption of the starting material. After cooling down to rt the mixture was carefully transferred into stirring demineralised water of rt. The highly acidic aqueous mixture was neutralized with aqueous NaOH solution. The resulting precipitate was filtered off, rinsed thoroughly with demineralised water and dried over P₂O₅ in

vacuo. If not stated otherwise, the crude material was purified by hot filtration from toluene as described previously [5].

Detailed Procedures for the Preparation of Intermediates S3a–k.

Ethyl 2-amino-1*H*-indole-3-carboxylate (S3a)

The title compound was prepared by a two-step procedure. In the first step ethyl cyanoacetate (32.1 g, 283.79 mmol) was drop-added to an ice-cooled stirring suspension of NaH (11.4 g of a 60% dispersion in mineral oil, 283.79 mmol) in dry DMF (20 mL) under N₂ atmosphere. The mixture was left to warm to rt for 30 min. A solution of 1-fluoro-2-nitrobenzene (S1a) (20.0 g, 141.74 mmol) in dry DMF (10 mL) was drop-added at 0 °C. The mixture was left to warm to rt for 30 min and then heated to 75 °C for 3 h. After cooling down to rt, 10% HCl_(aq) (80 mL) was added to acidify the mixture, which was then extracted with EtOAc (3 × 80 mL). Combined organic layers were washed with saturated NaCl solution (2 × 100 mL), dried over Na₂SO₄ and concentrated under reduced pressure. The oily residue contained ethyl 2-cyano-2-(2-nitrophenyl)acetate (S2a), as well as the excessive ethyl cyanoacetate and was used in the next step without further purification; ESI-MS: (*m/z*) 257.0 [M + Na]⁺, 232.9 [M – H][–]; HPLC method B: *t_r* = 3.399 min.

The crude material obtained from the first step was reacted with zinc powder (111.2 g, 1.70 mol) in glacial AcOH (50 mL) according to general procedure H (reaction time 2 h, after complete addition of zinc). The precipitate obtained during the aqueous work-up was not filtered off, but extracted repeatedly with EtOAc. Combined organic layers were dried over Na₂SO₄ and evaporated to dryness. 26.7 g of the crude product were yielded (92% crude yield over two steps) and used in the next step without further purification; HPLC method B: *t_r* = 5.176 min.

Ethyl 2-amino-6-fluoro-1*H*-indole-3-carboxylate (S3b)

The title compound was prepared by a two-step procedure. In the first step ethyl cyanoacetate (6.0 g, 52.80 mmol) was drop-added to an ice-cooled stirring suspension of NaH (2.1 g of a 60% dispersion in mineral oil, 52.80 mmol) in dry DMF (4 mL) under N₂ atmosphere. The mixture was left to warm to rt for 30 min. A solution of 1,4-difluoro-2-nitrobenzene (S1b) (4.0 g, 25.14 mmol) in dry DMF (4 mL) was drop-added and the mixture stirred at rt for 30 min and then heated to 75 °C for another 30 min. After cooling down to rt, 10% HCl_(aq) (20 mL) was added to acidify the mixture, which was then extracted with EtOAc (3 × 20 mL). Combined organic layers were washed with saturated NaCl solution (2 × 40 mL), dried over Na₂SO₄ and concentrated under reduced pressure. The oily residue contained ethyl 2-cyano-2-(4-fluoro-2-nitrophenyl)acetate (S2b), as well as excessive ethyl cyanoacetate and was used in the next step without further purification.

The crude material obtained from the first step was reacted with zinc powder (19.7 g, 301.31 mmol) in glacial AcOH (50 mL) according to general procedure H (reaction time 1.5 h). 4.6 g of the crude product were yielded (82% crude yield over two steps) and used in the next step without further purification; ¹H NMR (300 MHz, DMSO-*d*₆) δ 10.70 (s, 1H), 7.48 (dd, *J* = 8.5, 5.6 Hz, 1H), 6.94 (dd, *J* = 9.7, 2.4 Hz, 1H), 6.78 (ddd, *J* = 10.2, 8.5, 2.5 Hz, 1H), 6.71 (s, 2H), 4.22 (q, *J* = 7.1 Hz, 2H), 1.31 (t, *J* = 7.1 Hz, 3H).

Ethyl 2-amino-6-bromo-1*H*-indole-3-carboxylate (S3d)

The title compound was prepared by a two-step procedure. In the first step ethyl cyanoacetate (8.1 g, 71.59 mmol) was drop-added to an ice-cooled stirring suspension of NaH (2.9 g of a 60% dispersion in mineral oil, 71.59 mmol) in dry DMF (15 mL) under N₂ atmosphere. The dropping funnel was purged with additional dry DMF (3 mL) and the mixture left to warm to rt for 10 min. A solution of 4-bromo-1-fluoro-2-nitrobenzene (S1d) (7.5 g, 34.01 mmol) in dry DMF (7.5 mL) was then drop-added to the stirring suspension. Again, the dropping funnel was purged with additional dry DMF (5 mL). The mixture was stirred at rt for 45 min. 10% HCl_(aq) (40 mL) was added to acidify the mixture, which was then extracted with EtOAc (3 × 30 mL). Combined organic layers were washed

with saturated NaCl solution (5 × 30 mL), dried over Na₂SO₄ and concentrated under reduced pressure. The liquid residue was treated with ice-cold water resulting in a precipitate, which was filtered off and dried over P₂O₅ in vacuo. 10.7 g of crude ethyl 2-(4-bromo-2-nitrophenyl)-2-cyanoacetate (**S2d**) as a yellow solid (100% crude yield) were yielded and used in the next step without further purification. ¹H NMR (300 MHz, DMSO-*d*₆) δ 8.44 (d, *J* = 2.0 Hz, 1H), 8.13 (dd, *J* = 8.3, 2.1 Hz, 1H), 7.70 (d, *J* = 8.3 Hz, 1H), 6.25 (s, 1H), 4.22 (q, *J* = 7.1 Hz, 2H), 1.19 (t, *J* = 7.1 Hz, 3H); ¹³C NMR (75 MHz, DMSO-*d*₆) δ 163.7, 147.4, 137.9, 134.7, 128.7, 124.9, 123.3, 115.0, 63.1, 40.8, 13.8; ESI-MS: (*m/z*) 310.8 [M – H][–]; HPLC method A: *t*_r = 6.985 min.

The crude material obtained from the first step (10.3 g, 32.81 mmol) was reacted with zinc powder (12.9 g, 196.83 mmol) in glacial AcOH (80 mL) according to general procedure H (reaction time 2.5 h). 9.4 g of the crude product as a grey-red solid were yielded (98% crude yield over two steps) and used in the next step without further purification.

Ethyl 2-amino-6-iodo-1*H*-indole-3-carboxylate (**S3e**)

The title compound was prepared by a two-step procedure. In the first step a solution of ethyl cyanoacetate (4.2 g, 36.97 mmol) in dry DMF (4 mL) was drop-added to an ice-cooled stirring suspension of NaH (1.48 g of a 60% dispersion in mineral oil, 36.97 mmol) in dry DMF (13 mL) under N₂ atmosphere. The dropping funnel was purged with additional dry DMF (2 mL) and the mixture left to warm to rt. A solution of 1-fluoro-4-iodo-2-nitrobenzene (**S1e**) (4.7 g, 17.60 mmol) in dry DMF (7 mL) was then drop-added to the stirring suspension during 15 min. The mixture was left stirring for 30 min at rt. 10% HCl_(aq) (50 mL) was added to acidify the mixture, which was then extracted with EtOAc (3 × 60 mL). Combined organic layers were washed with saturated NaCl solution (3 × 60 mL), dried over Na₂SO₄ and concentrated under reduced pressure. The oily residue was treated with ice-cold water resulting in a yellow precipitate, which was filtered off and dried over P₂O₅ in vacuo. 6.5 g of crude ethyl 2-cyano-2-(4-iodo-2-nitrophenyl)acetate (**S2e**) as a yellow solid were yielded (>100% crude yield) and used in the next step without further purification; ¹H NMR (300 MHz, DMSO-*d*₆) δ 8.53 (d, *J* = 1.7 Hz, 1H), 8.27 (dd, *J* = 8.1, 1.7 Hz, 1H), 7.50 (d, *J* = 8.1 Hz, 1H), 6.21 (s, 1H), 4.22 (q, *J* = 7.1 Hz, 2H), 1.19 (t, *J* = 7.1 Hz, 3H); ¹³C NMR (75 MHz, DMSO-*d*₆) δ 163.7, 147.1, 143.7, 134.5, 134.0, 125.1, 115.0, 96.5, 63.1, 40.9, 13.8. ESI-MS: (*m/z*) 359.2 [M – H][–]; HPLC method A: *t*_r = 6.970 min.

The crude material obtained from the first step (3.3 g, 9.08 mmol) was dissolved in glacial acetic acid (22 mL). Pronounced dehalogenation was observed when applying the general procedure H, therefore zinc powder (3.3 g, 49.94 mmol) was added in portions at rt and the mixture was then stirred at 80 °C for 30 min. The suspension was left to cool down to rt and filtered rinsing the residue with EtOAc. The filtrate was concentrated under reduced pressure to leave a residue of AcOH, which was neutralized by addition of saturated NaHCO₃ solution. The resulting precipitate was filtered off and washed with demineralised water. It was then redissolved in EtOAc and the solution was dried over Na₂SO₄ and evaporated to dryness. 2.5 g of the crude product as a black foam were yielded (85% crude yield over two steps) and used in the next step without further purification.

Ethyl 2-amino-6-methoxy-1*H*-indole-3-carboxylate (**S3f**)

The title compound was prepared by a two-step procedure. In the first step ethyl cyanoacetate (6.3 g, 55.98 mmol) was drop-added to an ice-cooled stirring suspension of NaH (2.2 g, 55.98 mmol) in dry DMF (35 mL) under N₂ atmosphere. The mixture was left to warm to rt for 30 min. A solution of 1-chloro-4-methoxy-2-nitrobenzene (**S1f**) (5.0 g, 26.66 mmol) in dry DMF (7 mL) was drop-added and the mixture stirred at rt for 30 min and then heated to 75 °C for 5 h. After cooling down to rt, 5N HCl_(aq) was added to acidify the mixture followed by DCM (150 mL) and saturated NaCl solution (100 mL). The mixture was stirred at rt for 30 min and phases were separated. The aqueous layer was extracted with DCM (50 mL). Combined organic layers were dried over Na₂SO₄ and concentrated under reduced pressure. Purification of the residue by flash column chromatography (SiO₂, hexane:EtOAc gradient elution from 1:0 to 3:2) gave 4.3 g of ethyl 2-cyano-2-(4-methoxy-2-nitrophenyl)acetate (**S2f**); ¹H NMR (300 MHz, DMSO-*d*₆) δ 7.76 (d, *J* = 2.7 Hz, 1H), 7.65 (d, *J* = 8.7 Hz,

1H), 7.46 (dd, $J = 8.6, 2.8$ Hz, 1H), 6.13 (s, 1H), 4.21 (q, $J = 7.0$ Hz, 2H), 1.19 (t, $J = 7.1$ Hz, 3H); ESI-MS: (m/z) 287.3 [M + Na]⁺, 263.1 [M - H]⁻; HPLC method B: $t_r = 4.414$ min.

The purified material from the first step (4.3 g, 16.27 mmol) was reacted with zinc powder (12.8 g, 195.8 mmol) in glacial AcOH (50 mL) according to general procedure H (reaction time 1.5 h). Purification by flash column chromatography (SiO₂, hexane:EtOAc gradient elution from 1:0 to 3:2) gave 1.6 g of the title compound (26% yield over two steps); ¹H NMR (300 MHz, DMSO-*d*₆) δ 10.49 (s, 1H), 7.40 (d, $J = 8.4$ Hz, 1H), 6.73 (d, $J = 2.3$ Hz, 1H), 6.62–6.46 (m, 3H), 4.20 (q, $J = 7.1$ Hz, 2H), 1.30 (t, $J = 7.1$ Hz, 3H); ESI-MS: (m/z) 234.3 [M + H]⁺, 257.3 [M + Na]⁺, 233.1 [M - H]⁻; HPLC method B: $t_r = 4.805$ min.

Ethyl 2-amino-6-(trifluoromethyl)-1*H*-indole-3-carboxylate (**S3g**)

The title compound was prepared by a two-step procedure. In the first step ethyl cyanoacetate (5.3 g, 46.55 mmol) was drop-added to an ice-cooled stirring suspension of NaH (1.9 g of a 60% dispersion in mineral oil, 46.55 mmol) in dry DMF (30 mL) under N₂ atmosphere. The mixture was left to warm to rt for 30 min. A solution of 1-chloro-2-nitro-4-(trifluoromethyl)benzene (**S1g**) (5.0 g, 22.17 mmol) in dry DMF (10 mL) was drop-added and the mixture stirred at rt for 30 min and then heated to 70 °C for 2 h. After cooling down to rt, 10% HCl_(aq) was added to acidify the mixture, which was then extracted with EtOAc (3 × 50 mL). Combined organic layers were dried over Na₂SO₄ and concentrated under reduced pressure. The oily residue contained ethyl 2-cyano-2-(2-nitro-4-(trifluoromethyl)phenyl)acetate (**S2g**), as well as excessive ethyl cyanoacetate and was used in the next step without further purification; ESI-MS: (m/z) 301.1 [M - H]⁻; HPLC method B: 6.395 min.

The crude material obtained from the first step was reacted with zinc powder (17.4 g, 266.04 mmol) in glacial AcOH (50 mL) according to general procedure G (reaction time 1.5 h). 6.8 g of the crude product were yielded (>100% crude yield over two steps) and used in the next step without further purification; ¹H NMR (300 MHz, DMSO-*d*₆) δ 10.91 (s, 1H), 7.67 (d, $J = 8.2$ Hz, 1H), 7.42 (d, $J = 1.0$ Hz, 1H), 7.26 (dd, $J = 8.2, 1.0$ Hz, 1H), 6.97 (br s, 2H), 4.24 (q, $J = 7.1$ Hz, 2H), 1.32 (t, $J = 7.1$ Hz, 3H); ESI-MS: (m/z) 270.9 [M - H]⁻; HPLC method B: $t_r = 8.259$ min.

Ethyl 2-amino-5-chloro-1*H*-indole-3-carboxylate (**S3h**)

The title compound was prepared by a two-step procedure. In the first step a solution of ethyl cyanoacetate (6.2 g, 54.69 mmol) in dry THF (35 mL) was drop-added to an ice-cooled stirring suspension of *K*tBuO (6.1 g, 54.69 mmol) in dry THF (115 mL) under N₂ atmosphere. The mixture was left to warm to rt and a solution of 2,4-dichloro-1-nitrobenzene (**S1h**) (5.0 g, 26.04 mmol) in dry THF (30 mL) was drop-added. The mixture was stirred at 60 °C for 20 h. After cooling down to rt, 10% HCl_(aq) (50 mL) was added and the mixture extracted with EtOAc (3 × 30 mL). Combined organic layers were dried over Na₂SO₄ and concentrated under reduced pressure. The oily residue contained ethyl 2-(5-chloro-2-nitrophenyl)-2-cyanoacetate (**S2h**), as well as excessive ethyl cyanoacetate and was used in the next step without further purification. Purification of a small portion for analytical purposes was performed by flash column chromatography (SiO₂; petroleum ether:EtOAc gradient elution from 4:1 to 3:1); ¹H NMR (300 MHz, DMSO-*d*₆) δ 8.36–8.25 (m, 1H), 7.92–7.79 (m, 2H), 6.18 (s, 1H), 4.22 (q, $J = 7.0$ Hz, 2H), 1.19 (t, $J = 7.1$ Hz, 3H); ¹³C NMR (75 MHz, DMSO-*d*₆) δ 163.7, 145.5, 139.8, 133.2, 131.3, 128.2, 127.8, 115.0, 63.3, 41.1, 13.9. ESI-MS: (m/z) 266.8 [M - H]⁻; HPLC method A: $t_r = 6.130$ min.

The crude material obtained from the first step was reacted with zinc powder (10.0 g, 152.32 mmol) in glacial AcOH (60 mL) according to general procedure G (reaction time 2 h). 7.0 g of the crude product as a dark red solid were yielded (>100% crude yield over two steps) and used in the next step without further purification.

Ethyl 2-amino-5-bromo-1*H*-indole-3-carboxylate (**S3i**)

The title compound was prepared by a two-step procedure. In the first step a solution of ethyl cyanoacetate (5.4 g, 47.73 mmol) in dry THF (30 mL) was drop-added to an ice-cooled stirring suspension of *Kt*BuO (5.4 g, 47.73 mmol) in dry THF (100 mL) under N₂ atmosphere. The dropping funnel was purged with additional dry THF and the mixture left to warm to rt. A solution of 4-bromo-2-fluoro-1-nitrobenzene (**S1i**) (5.0 g, 22.73 mmol) in dry THF was then drop-added to the stirring suspension. The mixture was heated to reflux for 1.5 h. After cooling down to rt, 10% HCl_(aq) (40 mL) was added followed by EtOAc (40 mL). Phases were separated and the aqueous layer was extracted with EtOAc (2 × 30 mL). Combined organic layers were dried over Na₂SO₄ and concentrated under reduced pressure. The oily residue contained ethyl 2-(5-bromo-2-nitrophenyl)-2-cyanoacetate (**S2i**), as well as the excessive ethyl cyanoacetate and was used in the next step without further purification. Purification of a small portion for analytical purposes was performed by flash column chromatography (SiO₂, petroleum ether:(EtOAc + MeOH 95+5) 3:1); ¹H NMR (300 MHz, DMSO-*d*₆) δ 8.25–8.17 (m, 1H), 8.05–7.96 (m, 2H), 6.19 (s, 1H), 4.23 (q, *J* = 7.1 Hz, 2H), 1.19 (t, *J* = 7.1 Hz, 3H); ¹³C NMR (75 MHz, DMSO-*d*₆) δ 163.6, 145.8, 136.0, 134.2, 128.7, 128.0, 127.7, 114.9, 63.2, 40.9, 13.8; ESI-MS: (*m/z*) 311.0 [M – H][–]; HPLC method A: *t*_r = 6.437 min.

The crude material obtained from the first step was reacted with zinc powder (8.9 g, 136.38 mmol) in glacial AcOH (55 mL) according to general procedure H. Heat was applied after the complete addition of the zinc powder. After a reaction time of 2 h HPLC indicated incomplete conversion, therefore additional zinc powder was added (1.5 g, 22.73 mmol) and stirring continued for 1.5 h. 7.1 g of the crude product were yielded (>100% crude yield over two steps) and used in the next step without further purification; HPLC method A: *t*_r = 8.042 min.

Ethyl 2-amino-5-methoxy-1*H*-indole-3-carboxylate (**S3j**)

The title compound was prepared by a two-step procedure. In the first step a solution of ethyl cyanoacetate (6.9 g, 61.32 mmol) in dry THF (40 mL) was drop-added to an ice-cooled stirring suspension of *Kt*BuO (6.87 g, 61.32 mmol) in dry THF (120 mL) under N₂ atmosphere. The mixture was left to warm to rt and a solution of 2-fluoro-4-methoxy-1-nitrobenzene (**S1j**) (5.0 g, 29.20 mmol) in dry THF (10 mL) was then drop-added to the stirring suspension. The mixture was heated to reflux for 5 h. After cooling down to rt, 10% HCl_(aq) (50 mL) was added and the mixture extracted with EtOAc (2 × 30 mL). Combined organic layers were dried over Na₂SO₄ and concentrated under reduced pressure. The oily residue contained ethyl 2-cyano-2-(5-methoxy-2-nitrophenyl)acetate (**S2j**), as well as the excessive ethyl cyanoacetate and was used in the next step without further purification. Purification of a small portion for analytical purposes was performed by flash column chromatography (SiO₂, petroleum ether:EtOAc gradient elution from 3:1 to 3:2); ¹H NMR (200 MHz, DMSO-*d*₆) δ 8.39–8.29 (m, 1H), 7.34–7.22 (m, 2H), 6.14 (s, 1H), 4.21 (qd, *J* = 7.0, 0.8 Hz, 2H), 3.93 (s, 3H), 1.19 (t, *J* = 7.1 Hz, 3H); ¹³C NMR (50 MHz, DMSO-*d*₆) δ 163.9, 139.2, 129.0, 128.7, 119.4, 115.3, 115.0, 62.8, 56.5, 41.8, 13.8; ESI-MS: (*m/z*) 286.9 [M + Na]⁺, 262.9 [M – H][–]; HPLC method A: *t*_r = 6.002 min.

The crude material obtained from the first step was reacted with zinc powder (11.5 g, 175.0 mmol) in glacial AcOH (66 mL) according to general procedure H (reaction time 3 h). 5.6 g of the crude product as a red-brown solid were yielded (82% crude yield over two steps) and used in the next step without further purification. Purification of a small portion for analytical purposes was performed by flash column chromatography (SiO₂, DCM:MeOH 97:3); ¹H NMR (200 MHz, DMSO-*d*₆) δ 10.45 (s, 1H), 7.13 (d, *J* = 2.4 Hz, 1H), 6.99 (d, *J* = 8.5 Hz, 1H), 6.60 (br s, 2H), 6.49 (dd, *J* = 8.5, 2.5 Hz, 1H), 4.21 (q, *J* = 7.1 Hz, 2H), 3.71 (s, 3H), 1.32 (t, *J* = 7.1 Hz, 3H); ¹³C NMR (50 MHz, DMSO-*d*₆) δ 165.8, 154.5, 153.9, 127.7, 127.3, 110.0, 106.4, 103.0, 84.0, 58.0, 55.2, 14.7; ESI-MS: (*m/z*) 233.2 [M – H][–]; HPLC method A: *t*_r = 5.545 min.

Ethyl 2-amino-4-chloro-1*H*-indole-3-carboxylate (**S3k**)

The title compound was prepared by a two-step procedure. In the first step a solution of ethyl cyanoacetate (8.6 g, 76.56 mmol) in dry THF (48 mL) was drop-added to an ice-cooled stirring suspension of *Kt*BuO (8.6 g, 76.56 mmol) in dry THF (160 mL). The stirring suspension was left to warm to rt and a solution of 1,2-dichloro-3-nitrobenzene (**S1k**) (7.0 g, 36.46 mmol) in dry THF (44 mL) was drop-added. The mixture was stirred at 60 °C for 43 h, when additional *Kt*BuO (1.6 g, 14.58 mmol) was added and stirring at 60 °C continued for another 34 h. After cooling down to rt, 10% HCl_(aq) (70 mL) was added and the mixture extracted with EtOAc (3 × 30 mL). Combined organic layers were dried over Na₂SO₄ and concentrated under reduced pressure. The oily residue contained ethyl 2-(2-chloro-6-nitrophenyl)-2-cyanoacetate (**S2k**), as well as excessive ethyl cyanoacetate and was used in the next step without further purification. Purification of a small portion for analytical purposes was performed by flash column chromatography (SiO₂, petroleum ether:EtOAc gradient elution from 4:1 to 1:1); ¹H NMR (300 MHz, DMSO-*d*₆) δ 8.15 (dd, *J* = 8.2, 1.2 Hz, 1H), 8.06 (dd, *J* = 8.2, 1.2 Hz, 1H), 7.79 (t, *J* = 8.2 Hz, 1H), 6.37 (s, 1H), 4.23 (q, *J* = 6.9 Hz, 2H), 1.21 (t, *J* = 7.1 Hz, 3H), ¹³C NMR (75 MHz, DMSO-*d*₆) δ 163.2, 149.7, 136.1, 135.5, 132.0, 124.8, 123.4, 114.3, 63.2, 38.2, 13.7; ESI-MS: (*m/z*) 266.9 [M – H][–]; HPLC method A: *t*_r = 5.470 min.

The crude material obtained from the first step was reacted with zinc powder (14.1 g, 215.3 mmol) in glacial AcOH (87 mL) according to general procedure H (reaction time 1.5 h). 7.6 g of the crude product as a brown solid were yielded (87% crude yield over two steps) and used in the next step without further purification; HPLC method A: *t*_r = 7.689 min.

Detailed Procedures for the Preparation of Intermediates **S4a,b** and **S4d–l**.

3,9-Dihydro-4*H*-pyrimido[4,5-*b*]indol-4-one (**S4a**)

S3a (26.7 g, 130.7 mmol) and ammonium formate (9.1 g, 144.3 mmol) were stirred in formamide (140 mL) at 170 °C for 18 h. After cooling down to rt, MeOH (150 mL) was added. The resulting precipitate was filtered off, washed with MeOH and dried under reduced pressure. 7.4 g of the crude product were yielded (30% crude yield) and used in the next step without further purification; ¹H NMR (300 MHz, DMSO-*d*₆) δ 12.31–12.04 (m, 2H), 8.12 (s, 1H), 7.98 (d, *J* = 7.7 Hz, 1H), 7.47 (d, *J* = 8.0 Hz, 1H), 7.36–7.29 (m, 1H), 7.23 (td, *J* = 7.6, 1.1 Hz, 1H); ESI-MS: (*m/z*) 183.8 [M – H][–]; HPLC method B: *t*_r = 2.066 min.

7-Fluoro-3,9-dihydro-4*H*-pyrimido[4,5-*b*]indol-4-one (**S4b**)

The title compound was prepared from **S3b** (4.0 g, 18.00 mmol) and ammonium formate (1.3 g, 20.70 mmol) in formamide (40 mL) according to general procedure I (reaction time 28 h). 3.2 g of the crude product were yielded (86% crude yield) and used in the next step without further purification; ESI-MS: (*m/z*) 201.9 [M – H][–].

7-Bromo-3,9-dihydro-4*H*-pyrimido[4,5-*b*]indol-4-one (**S4d**)

The title compound was prepared from **S3d** (9.0 g, 31.79 mmol) and ammonium formate (2.3 g, 36.56 mmol) in formamide (65 mL) according to general procedure I (reaction time 22 h). 8.7 g of the crude product as a brown solid were yielded (>100% crude yield) and used in the next step without further purification; ESI-MS: (*m/z*) 261.8 [M – H][–]; HPLC method B: *t*_r = 4.027 min.

7-Iodo-3,9-dihydro-4H-pyrimido[4,5-*b*]indol-4-one (S4e)

The title compound was prepared from **S3e** (2.5 g, 6.83 mmol) in formamide (17 mL) according to general procedure I (reaction time 29 h). No ammonium formate was used for this reaction. 1.7 g of the crude product as a brown solid were yielded (73% crude yield) and used in the next step without further purification. Purification of a small portion for analytical purposes was performed by flash column chromatography (SiO₂, DCM:MeOH 9:1); ¹H NMR (200 MHz, DMSO-*d*₆) δ 12.37–12.16 (m, 2H), 8.16 (s, 1H), 7.84–7.73 (m, 2H), 7.58–7.49 (m, 1H); ¹³C NMR (50 MHz, DMSO-*d*₆) δ 158.1, 153.8, 148.2, 136.7, 129.6, 122.4, 121.5, 120.0, 100.1, 88.3; ESI-MS: (*m/z*) 310.2 [M – H][–]; HPLC method A: t_r = 5.770 min.

7-Methoxy-3,9-dihydro-4H-pyrimido[4,5-*b*]indol-4-one (S4f)

The title compound was prepared from **S3f** (1.6 g, 6.83 mmol) in formamide (40 mL) according to general procedure I (reaction time 16 h). No ammonium formate was used for this reaction. 1.5 g of the crude product were yielded (97% crude yield) and used in the next step without further purification; ¹H NMR (300 MHz, DMSO-*d*₆) δ 12.15 (s, 1H), 12.04 (s, 1H), 8.05 (s, 1H), 7.84 (d, *J* = 8.6 Hz, 1H), 6.96 (d, *J* = 2.2 Hz, 1H), 6.86 (dd, *J* = 8.6, 2.3 Hz, 1H), 3.81 (s, 3H); ESI-MS: (*m/z*) 213.9 [M – H][–].

7-(Trifluoromethyl)-3,9-dihydro-4H-pyrimido[4,5-*b*]indol-4-one (S4g)

A suspension of **S3g** (4.5 g, 16.53 mmol) in formamide (75 mL) was stirred at 190 °C for 3 h. After cooling down to rt, MeOH (700 mL) was added and stirring continued at rt overnight. The mixture was filtered rinsing with fresh MeOH. The filtrate was concentrated under reduced pressure to the half and the resulting precipitate filtered off. The filtrate was then concentrated under reduced pressure to afford a dark brown oil. Water (300 mL) was added and the mixture stirred at rt for 1 h resulting in a precipitate, which was filtered off, washed with water and dried over P₂O₅ in vacuo. 1 g of the crude product were yielded (24% crude yield) and used in the next step without further purification; ESI-MS: (*m/z*) 251.9 [M – H][–]; HPLC method B: t_r = 5.113 min.

6-Chloro-3,9-dihydro-4H-pyrimido[4,5-*b*]indol-4-one (S4h)

The title compound was immediately converted into **3h** (see the detailed procedure for the preparation of **3h**).

6-Bromo-3,9-dihydro-4H-pyrimido[4,5-*b*]indol-4-one (S4i)

The title compound was prepared from **S3i** (7.1 g, 25.2 mmol) and ammonium formate (1.6 g, 25.9 mmol) in formamide (65 mL) according to general procedure I (reaction time 24 h). 7.3 g of the crude product as a brown solid were yielded (>100% crude yield) and used in the next step without further purification. Purification of a small portion by flash column chromatography for analytical purposes (SiO₂, petroleum ether:(EtOAc + MeOH 95+5) gradient elution from 3:2 to 1:4); ¹H NMR (300 MHz, DMSO-*d*₆) δ 12.49–12.19 (m, 2H), 8.16 (s, 1H), 8.06 (s, 1H), 7.54–7.36 (m, 2H); ¹³C NMR (50 MHz, DMSO-*d*₆) δ 158.1, 154.3, 148.3, 134.2, 126.7, 123.9, 122.5, 113.8, 113.4, 99.6; HPLC method A: t_r = 5.689 min.

6-Methoxy-3,9-dihydro-4H-pyrimido[4,5-*b*]indol-4-one (S4j)

The title compound was prepared from **S3j** (5.3 g, 22.62 mmol) and ammonium formate (1.6 g, 26.02 mmol) in formamide (46 mL) according to general procedure I. Purification of a small portion for analytical purposes was performed by flash column chromatography (SiO₂, DCM:MeOH 9:1). 3.9 g of the crude product were yielded (80% crude yield) and used in the next step without further purification; ¹H NMR (200 MHz, DMSO-*d*₆) δ 12.16 (s, 1H), 12.04 (s, 1H), 8.08 (s, 1H), 7.48 (d, *J* = 2.4 Hz, 1H), 7.38 (d, *J* = 8.8 Hz, 1H), 6.95 (dd, *J* = 8.9, 2.6 Hz, 1H), 3.80 (s, 3H); ¹³C NMR (50 MHz, DMSO-

d_6) δ 158.5, 154.7, 153.8, 147.2, 130.0, 122.7, 113.6, 112.5, 102.8, 100.2, 55.4; ESI-MS: (m/z) 214.1 [M – H]⁻; HPLC method A: t_r = 3.430 min.

5-Chloro-3,9-dihydro-4*H*-pyrimido[4,5-*b*]indol-4-one (**S4k**)

The title compound was prepared from **S3k** (7.0 g, 29.33 mmol) and ammonium formate (2.4 g, 38.13 mmol) in formamide (60 mL) according to general procedure I (reaction time 24 h). 5.5 g of the crude product as a brown solid were yielded (85% crude yield) and used in the next step without further purification. Purification of a small portion for analytical purposes was performed by flash column chromatography (SiO₂, DCM:MeOH 9:1). ¹H NMR (200 MHz, DMSO- d_6) δ 12.49 (s, 1H), 12.16 (s, 1H), 8.13 (s, 1H), 7.40 (dd, J = 7.4, 1.7 Hz, 1H), 7.35–7.18 (m, 2H); ¹³C NMR (50 MHz, DMSO- d_6) δ 156.9, 154.3, 148.4, 136.9, 125.7, 125.0, 122.3, 120.7, 110.4, 99.4. ESI-MS: (m/z) 242.0 [M + Na]⁺, 218.0 [M – H]⁻; HPLC method A: t_r = 4.214 min.

7-Chloro-2-methyl-3,9-dihydro-4*H*-pyrimido[4,5-*b*]indol-4-one (**S4l**)

Ethyl 2-amino-6-chloro-1*H*-indole-3-carboxylate (**S3c**) was prepared by a two-step procedure from 1,4-dichloro-2-nitrobenzene (**S1c**) as described previously [5] and purified by flash column chromatography (SiO₂, DCM:MeOH 97.5:2.5). Purified **S3c** (400.0 mg, 1.68 mmol) was dissolved in dry acetonitrile (22 mL). The stirring solution was treated with hydrogen chloride gas at rt for 45 min and then refluxed for 2.5 h. After cooling the mixture overnight the formed precipitate was filtered off, washed with cold acetonitrile and dried under reduced pressure to yield 240 mg of the amidine intermediate. EtOH (50 mL) and 10% NaOH_(aq) (5 mL) were added and the suspension refluxed for 3.5 h. After cooling down to rt the mixture was concentrated under reduced pressure. 10% HCl_(aq) (5 mL) was added to the aqueous residue. The resulting precipitate was filtered off, washed with demineralised water and dried under reduced pressure. 127 mg of a white solid were yielded (32% crude yield) and used in the next step without further purification; ¹H NMR (300 MHz, DMSO- d_6) δ 12.20 (s, 1H), 12.12 (s, 1H), 7.90 (d, J = 8.3 Hz, 1H), 7.44 (d, J = 1.7 Hz, 1H), 7.22 (dd, J = 8.3, 1.9 Hz, 1H), 2.40 (s, 3H); ESI-MS: (m/z) 232.0 [M – H]⁻.

Detailed Procedures for the Preparation of Intermediates 3a–l.

4-Chloro-9*H*-pyrimido[4,5-*b*]indole (**3a**)

The title compound was prepared from **S4a** (2.2 g, 11.61 mmol), DIPEA (2.3 g, 17.40 mmol) in POCl₃ (11 mL) and chlorobenzene (24 mL) according to general procedure J (reaction time 20 h at a temperature of 100°C). 1.8 g of the crude product as a brown solid were obtained (76% crude yield) and purified by hot filtration from toluene to yield 524 mg of a dark yellow solid; ¹H NMR (400 MHz, DMSO- d_6) δ 12.76 (s, 1H), 8.78 (s, 1H), 8.28 (d, J = 7.9 Hz, 1H), 7.68–7.60 (m, 2H), 7.46–7.40 (m, 1H); ESI-MS: (m/z) 202.0 [M – H]⁻; HPLC method A: t_r = 7.570 min.

4-Chloro-7-fluoro-9*H*-pyrimido[4,5-*b*]indole (**3b**)

The title compound was prepared from **S4b** (1.5 g, 7.38 mmol) and DIPEA (1.9 g, 14.77 mmol) according to general procedure J (reaction time 4 h), but using POCl₃ (20 mL) as only solvent. 1.6 g of the crude product were obtained (98% crude yield) and purified by hot filtration from toluene in portions; ¹H NMR (300 MHz, DMSO- d_6) δ 12.91 (s, 1H), 8.78 (s, 1H), 8.27 (dd, J = 8.7, 5.4 Hz, 1H), 7.42 (dd, J = 9.5, 2.3 Hz, 1H), 7.33–7.22 (m, 1H); ¹³C NMR (50 MHz, DMSO- d_6) δ 162.1 (d, J = 243.7 Hz), 156.5 (d, J = 1.2 Hz), 153.6, 150.8 (d, J = 1.4 Hz), 139.5 (d, J = 13.2 Hz), 124.0 (d, J = 10.7 Hz), 114.3 (d, J = 1.2 Hz), 110.8, 109.9 (d, J = 24.3 Hz), 99.1 (d, J = 26.6 Hz); ESI-MS: (m/z) 219.8 [M – H]⁻; HPLC method B: t_r = 7.001 min.

4,7-Dichloro-9H-pyrimido[4,5-*b*]indole (3c)

The title compound was prepared in four steps from 1,4-dichloro-2-nitrobenzene (**S1c**) as described previously [5].

7-Bromo-4-chloro-9H-pyrimido[4,5-*b*]indole (3d)

The title compound was prepared from **S4d** (8.0 g, 30.3 mmol) and DIPEA (5.9 g, 45.44 mmol) in POCl₃ (24 mL) and chlorobenzene (60 mL) according to general procedure J (reaction time 7 h). 6.9 g of the crude product as a brown solid were obtained (81% crude yield) and purified by hot filtration in toluene in portions; ¹H NMR (200 MHz, DMSO-*d*₆) δ 12.86 (s, 1H), 8.78 (s, 1H), 8.09 (d, *J* = 8.5 Hz, 1H), 7.73 (d, *J* = 1.2 Hz, 1H), 7.51 (dd, *J* = 8.5, 1.5 Hz, 1H); ¹³C NMR (50 MHz, DMSO-*d*₆) δ 156.1, 154.3, 151.4, 139.3, 124.6, 123.9, 121.1, 116.8, 114.9, 110.7; ESI-MS: (*m/z*) 280.0 [M – H][–]; HPLC method A: *t*_r = 8.804 min.

4-Chloro-7-iodo-9H-pyrimido[4,5-*b*]indole (3e)

S4e (1.8 g, 5.82 mmol) was suspended in chlorobenzene (12 mL) and POCl₃ (5 mL) was added carefully. DIPEA (1.1 g, 8.73 mmol) was added portionwise to the stirring suspension and the mixture then stirred at 80 °C for 7 h. The mixture was stirred at rt overnight and then carefully transferred into stirring demineralised water of rt. The stirring mixture was cooled by ice and neutralized with 50% NaOH_(aq). The brown precipitate was filtered off and stirred in hot toluene (600 mL) for 1 h. The hot suspension was filtered rinsing with additional hot toluene. The filtrate was concentrated under reduced pressure resulting in a precipitate. The suspension was cooled by ice and filtered off rinsing with cold toluene. The residue was dried under reduced pressure. 843 mg of a brown solid were obtained (44% yield); ¹H NMR (200 MHz, DMSO-*d*₆) δ 12.82 (s, 1H), 8.79 (s, 1H), 7.99 (d, *J* = 8.3 Hz, 1H), 7.94 (d, *J* = 1.0 Hz, 1H), 7.70 (dd, *J* = 8.3, 1.5 Hz, 1H); ¹³C NMR (50 MHz, DMSO-*d*₆) δ 155.9, 154.5, 151.5, 139.5, 130.4, 124.0, 120.8, 117.2, 110.9, 94.0; ESI-MS: (*m/z*) 328.0 [M – H][–]; HPLC method A: *t*_r = 9.375 min.

4-Chloro-7-methoxy-9H-pyrimido[4,5-*b*]indole (3f)

The title compound was prepared from **S4f** (1.4 g, 5.99 mmol) and DIPEA (1.8 g, 13.70 mmol) according to general procedure J (reaction time 5 h), but using POCl₃ (25 mL) as only solvent. 1.3 g of the crude product were obtained (87% crude yield) and purified by hot filtration in toluene; ¹H NMR (300 MHz, DMSO-*d*₆) δ 12.65 (s, 1H), 8.69 (s, 1H), 8.11 (d, *J* = 8.7 Hz, 1H), 7.08 (d, *J* = 2.2 Hz, 1H), 7.02 (dd, *J* = 8.7, 2.3 Hz, 1H), 3.89 (s, 3H); ESI-MS: (*m/z*) 231.9 [M – H][–]; HPLC method B: *t*_r = 6.760 min.

4-Chloro-7-(trifluoromethyl)-9H-pyrimido[4,5-*b*]indole (3g)

A suspension of **S4g** (1.0 g, 3.95 mmol) in POCl₃ (50 mL) was stirred at 80°C for 6 h. After cooling down to rt, the mixture was carefully transferred into stirring water of rt and then neutralized with 50% NaOH_{aq}. The precipitate was filtered off, washed with water and dried over P₂O₅ in vacuo. 845 mg of the crude product were obtained (79% crude yield). The crude material was not purified by hot filtration from toluene, but used in the next step without further purification; ¹H NMR (300 MHz, DMSO-*d*₆) δ 13.13 (s, 1H), 8.85 (s, 1H), 8.39 (d, *J* = 8.3 Hz, 1H), 7.87 (s, 1H), 7.69 (dd, *J* = 8.3, 1.0 Hz, 1H); ESI-MS: (*m/z*) 269.9 [M – H][–]; HPLC method B: *t*_r = 9.071 min.

4,6-Dichloro-9H-pyrimido[4,5-*b*]indole (3h)

The title compound was prepared by a two-step procedure. In the first step crude **S3h** (5.8 g) was reacted with ammonium formate (4.2 g, 66.19 mmol) in formamide (50 mL) according to general procedure I (reaction time 35 h). The solvent was replenished in between, as the reaction had dried out. Drying procedures gave 9.5 g of 6-chloro-3,9-dihydro-4H-pyrimido[4,5-*b*]indol-4-one (**S4h**) as a crude brown material with residual formamide. Purification of a small portion for analytical purposes was performed by flash column chromatography (SiO₂, DCM:MeOH 9:1); ¹H NMR (300

MHz, DMSO- d_6) δ 12.49–12.21 (m, 2H), 8.16 (s, 1H), 7.91 (d, $J = 2.0$ Hz, 1H), 7.49 (d, $J = 8.6$ Hz, 1H), 7.34 (dd, $J = 8.6, 2.1$ Hz, 1H); ESI-MS: (m/z) 218.0 [M – H][–]; HPLC method A: $t_r = 5.251$ min. The crude material obtained from the first step (4.4 g) was reacted with DIPEA (3.8 g, 30.05 mmol) and POCl₃ (17 mL) in chlorobenzene (40 mL) according to general procedure J (reaction time 24 h). The reaction mixture was additionally stirred at rt overnight. The reaction seized at 85% conversion as calculated by HPLC and was therefore worked up according to the general procedure. 4.4 g of a brown solid were obtained and purified by hot filtration from toluene in portions to yield a total 600 mg of a dark yellow solid (25% yield over 4 steps); ¹H NMR (300 MHz, DMSO- d_6) δ 12.91 (s, 1H), 8.80 (s, 1H), 8.21–8.14 (m, 1H), 7.63 (d, $J = 1.3$ Hz, 2H); ESI-MS: (m/z) 235.9 [M – H][–]; HPLC method A: $t_r = 8.583$ min.

6-Bromo-4-chloro-9H-pyrimido[4,5-*b*]indole (3i)

The title compound was prepared from **S4i** (4.6 g, 17.42 mmol) and DIPEA (3.4 g, 26.13 mmol) in chlorobenzene (35 mL) and POCl₃ (15 mL) according to general procedure J (reaction time 20 h). 3.7 g of the crude product as a brown solid were obtained (75% crude yield) and purified by hot filtration from toluene in portions; ¹H NMR (300 MHz, DMSO- d_6) δ 12.91 (s, 1H), 8.79 (s, 1H), 8.29 (d, $J = 2.0$ Hz, 1H), 7.73 (dd, $J = 8.7, 2.0$ Hz, 1H), 7.61–7.53 (m, 1H); ¹³C NMR (50 MHz, DMSO- d_6) δ 156.1, 154.5, 151.8, 137.3, 130.9, 124.4, 119.5, 114.4, 113.7, 110.3; ESI-MS: (m/z) 280.0 [M – H][–]; HPLC method A: $t_r = 8.963$ min.

4-Chloro-6-methoxy-9H-pyrimido[4,5-*b*]indole (3j)

The title compound was prepared from **S4j** (2.0 g, 9.29 mmol) and DIPEA (1.8 g, 13.93 mmol) according to general procedure J, but using POCl₃ (17.5 mL) as only solvent. 1.7 g of a brown solid were obtained (80% crude yield) and purified by hot filtration from toluene in portions; ¹H NMR (200 MHz, DMSO- d_6) δ 12.58 (s, 1H), 8.71 (s, 1H), 7.65 (d, $J = 2.4$ Hz, 1H), 7.52 (d, $J = 8.8$ Hz, 1H), 7.22 (dd, $J = 8.8, 2.5$ Hz, 1H), 3.85 (s, 3H); ¹³C NMR (50 MHz, DMSO- d_6) δ 155.9, 154.7, 153.6, 151.2, 132.9, 118.2, 117.4, 113.1, 111.0, 104.8, 55.6; ESI-MS: (m/z) 231.8 [M – H][–]; HPLC method A: $t_r = 7.566$ min.

4,5-Dichloro-9H-pyrimido[4,5-*b*]indole (3k)

The title compound was prepared from **S4k** (5.2 g, 23.68 mmol), DIPEA (4.6 g, 35.5 mmol) and POCl₃ (20 mL) in chlorobenzene (47 mL) according to general procedure J (reaction time 24 h). The wet crude material obtained was directly purified by hot filtration from toluene to yield 2.4 g (43% yield); ¹H NMR (400 MHz, DMSO- d_6) δ 13.12 (s, 1H), 8.77 (s, 1H), 7.57–7.55 (m, 2H), 7.40 (dd, $J = 5.1, 3.7$ Hz, 1H); ¹³C NMR (101 MHz, DMSO- d_6) δ 156.2, 153.9, 151.3, 140.2, 129.2, 127.0, 123.6, 115.5, 111.2, 110.2; ESI-MS: (m/z) 236.0 [M – H][–]; HPLC method A: $t_r = 8.664$ min.

4,7-Dichloro-2-methyl-9H-pyrimido[4,5-*b*]indole (3l)

The title compound was prepared from **S4l** (810.0 mg, 3.51 mmol), DIPEA (680.0 mg, 5.26 mmol) and POCl₃ (3 mL) in chlorobenzene (7 mL) according to general procedure J. The reaction mixture was left to stir at rt overnight after heating to 80°C for 6 h. The wet crude material obtained was directly purified by hot filtration in toluene to yield 512 mg of a beige solid (59% yield); ¹H NMR (400 MHz, DMSO- d_6) δ 12.62 (s, 1H), 8.15–8.09 (m, 1H), 7.56 (dd, $J = 1.9, 0.4$ Hz, 1H), 7.37 (dd, $J = 8.4, 1.9$ Hz, 1H), 2.67 (s, 3H); ¹³C NMR (101 MHz, DMSO- d_6) δ 164.0, 157.1, 151.1, 139.0, 132.1, 123.2, 121.7, 116.7, 111.9, 108.1, 25.5; ESI-MS: (m/z) 251.8 [M + H]⁺, 249.8 [M – H][–]; HPLC method A: $t_r = 9.012$ min.

3.2.5 Publication IX: **Addressing a Trapped High-Energy Water: Design and Synthesis of Highly Potent Pyrimidoindole-Based Glycogen Synthase Kinase-3 β Inhibitors**

Stanislav Andreev^{1,‡}, Tatu Pantsar^{1,2,‡}, Roberta Tesch^{3,4}, Niclas Kahlke¹, Ahmed El-Gokha^{1,5}, Francesco Ansideri¹, Lukas Grätz⁶, Jenny Romasco⁷, Giulia Sita⁸, Christian Geibel⁹, Michael Lämmerhofer⁹, Andrea Tarrozzi⁸, Stefan Knapp^{3,4}, Stefan A. Laufer^{1,10} and Pierre Koch^{1,6,*}

¹ Institute of Pharmaceutical Sciences, Department of Medicinal and Pharmaceutical Chemistry, Eberhard Karls University Tübingen, Auf der Morgenstelle 8, 72076 Tübingen, Germany

² School of Pharmacy, Faculty of Health Sciences, University of Eastern Finland, P.O. Box 1627, 70211 Kuopio, Finland

³ Institute for Pharmaceutical Chemistry, Johann Wolfgang Goethe-University, Max-von-Laue-Str. 9, 60438 Frankfurt am Main, Germany

⁴ Structural Genomics Consortium, Buchmann Institute for Life Sciences, Johann Wolfgang Goethe-University, Max-von-Laue-Str. 15, 60438 Frankfurt am Main, Germany

⁵ Chemistry Department, Faculty of Science, Menoufia University, Gamal Abdel-Nasser Street, 32511 Shebin El-Kom, Egypt

⁶ Department of Pharmaceutical/Medicinal Chemistry II, Institute of Pharmacy, University of Regensburg, Universitätsstraße 31, 93053 Regensburg, Germany

⁷ Department for Life Quality Studies, Alma Mater Studiorum, University of Bologna, Corso D'Augusto, 237, 47921 Rimini, Italy

⁸ Department of Pharmacy and Biotechnology, Alma Mater Studiorum, University of Bologna, Via Irnerio, 48, 40126 Bologna, Italy

⁹ Institute of Pharmaceutical Sciences, Department of Pharmaceutical (Bio-)Analysis, Eberhard Karls University Tübingen, Auf der Morgenstelle 8, 72076 Tübingen, Germany

¹⁰ Tübingen Center for Academic Drug Discovery (TüCAD2), Auf der Morgenstelle 8, 72076 Tübingen, Germany

‡ These authors contributed equally

* Corresponding author. E-mail address: pierre.koch@uni-tuebingen.de, pierre.koch@ur.de (P. Koch)

Reprinted with permission from *Journal of Medicinal Chemistry* **2022**, 65, 2, 1283-1301. DOI: 10.1021/acs.jmedchem.0c02146
Copyright 2022 American Chemical Society.

Addressing a Trapped High-Energy Water: Design and Synthesis of Highly Potent Pyrimidoindole-Based Glycogen Synthase Kinase-3 β InhibitorsStanislav Andreev,[◆] Tatu Pantsar,[◆] Roberta Tesch, Niclas Kahlke, Ahmed El-Gokha, Francesco Ansideri, Lukas Grätz, Jenny Romasco, Giulia Sita, Christian Geibel, Michael Lämmerhofer, Andrea Tarozzi, Stefan Knapp, Stefan A. Laufer, and Pierre Koch*Cite This: *J. Med. Chem.* 2022, 65, 1283–1301

Read Online

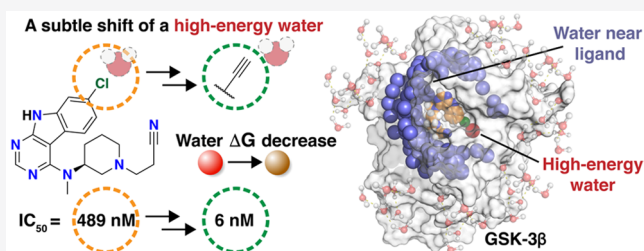
ACCESS |

Metrics & More

Article Recommendations

Supporting Information

ABSTRACT: In small molecule binding, water is not a passive bystander but rather takes an active role in the binding site, which may be decisive for the potency of the inhibitor. Here, by addressing a high-energy water, we improved the IC₅₀ value of our co-crystallized glycogen synthase kinase-3 β (GSK-3 β) inhibitor by nearly two orders of magnitude. Surprisingly, our results demonstrate that this high-energy water was not displaced by our potent inhibitor (*S*)-3-(3-((7-ethynyl-9*H*-pyrimido[4,5-*b*]indol-4-yl)(methyl)amino)piperidin-1-yl)propanenitrile ((*S*)-15, IC₅₀ value of 6 nM). Instead, only a subtle shift in the location of this water molecule resulted in a dramatic decrease in the energy of this high-energy hydration site, as shown by the WaterMap analysis combined with microsecond timescale molecular dynamics simulations. (*S*)-15 demonstrated both a favorable kinome selectivity profile and target engagement in a cellular environment and reduced GSK-3 autophosphorylation in neuronal SH-SY5Y cells. Overall, our findings highlight that even a slight adjustment in the location of a high-energy water can be decisive for ligand binding.



INTRODUCTION

Protein kinases are important regulators in the cellular signaling machinery.¹ Aberrations in their activity can lead to disease, and they are considered to be potential drug targets in many therapeutic areas, including cancer, degenerative disorders, and autoimmune and inflammatory diseases.² Therefore, perhaps unsurprisingly, protein kinases are currently the most pursued drug targets in the pharmaceutical industry.³

Over the last decades, glycogen synthase kinase-3 β (GSK-3 β) in particular has received extensive attention both from academia and industry.^{4–7} This serine/threonine kinase is a highly multitasking enzyme that contributes to several signaling pathways in cells.⁸ GSK-3 β dysregulation has been associated with various pathologies, such as type II diabetes mellitus, various types of cancer, and Alzheimer's disease.^{9–11} Therefore, determined efforts are ongoing to develop selective inhibitors against GSK-3 β .

We recently reported the optimization of a novel class of 7-chloro-9*H*-pyrimido[4,5-*b*]indole-based inhibitors of GSK-3 β .¹² In this study, we revealed that the cyanoethyl-substituted piperidine moiety present in compound **1** is essential for the compound activity, which was further improved by a rigidification approach (**2**) (Scheme 1). Having identified the optimal structural features for the aliphatic side chain of the

molecules, we herein pursued the optimization of decorations at the 9*H*-pyrimido[4,5-*b*]indole core.

Water is a vital component in the biological matrix and plays various important roles in molecular biology.¹³ This is especially true at the protein interface, as water is pivotal in ligand binding thermodynamics.^{14–19} As solvent organization may be decisive for the binding affinity,^{20,21} exploiting water offers an excellent opportunity to optimize ligand binding. However, not all waters are equal at the protein interface. While the displacement of an energetically favorable water molecule from the binding site by the ligand has a negative impact on the binding affinity, it is highly beneficial in the case of energetically unfavorable water molecules. Therefore, it is essential to estimate the energies of these molecules before aiming to displace them. There is a rising number of computational methods that aim to predict hydration site energies and thereby guide the decision for beneficial water molecule displacement.^{22,23} One such method is Water-

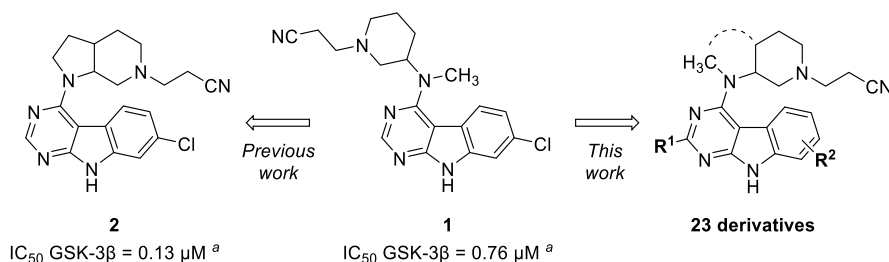
Special Issue: New Horizons in Drug Discovery - Understanding and Advancing Kinase Inhibitors

Received: December 11, 2020

Published: July 2, 2021



Scheme 1. Previously Reported Optimization of the Aliphatic Side Chain



^aData taken from Andreev et al.¹².

Table 1. Structures and Biological Activities of Halogen-Substituted Compounds

No.	R ¹	R ²	GSK-3β IC ₅₀ ± SEM [μM] ^a	pIC ₅₀	clogP ^c	LLE ^d
5a	H	H	0.480 ± 0.076	6.3	2.6	3.7
5b	H	F	0.973 ± 0.276	6.0	2.8	3.2
1 (= rac-5c)	H	Cl	0.764 ± 0.203 ^b	6.1	3.3	2.9
(R)-5c	H	Cl	0.712 ± 0.176	6.1	3.3	2.9
(S)-5c	H	Cl	0.489 ± 0.119	6.3	3.3	3.0
5d	H	Br	0.388 ± 0.080	6.4	3.3	3.1
(R)-5d	H	Br	0.408 ± 0.099	6.4	3.3	3.1
(S)-5d	H	Br	0.319 ± 0.066	6.5	3.3	3.2
11	H	I	1.382 ± 0.394	5.9	3.2	2.7
5g	H	Cl	3.811 ± 0.118	5.4	3.2	2.2
5h	H	Br	6.096 ± 0.654	5.2	3.3	1.9
5i	H	Cl	8.042 ± 0.617	5.1	3.2	1.9
5j	CH ₃	Cl	>10	-	3.2	-

^aIC₅₀ values were determined in an ADP Glo kinase assay (for details, see the Supporting Information).³⁶ The reported data are mean values ± the SEM from at least two independent experiments. ^bData were taken from Andreev et al.¹² ^cclogP was calculated with Canvas (Schrödinger LLC).³⁷ ^dLipophilic ligand efficiency (LLE) = pIC₅₀ - clogP.³⁸

Map,^{24,25} which evaluates the hydration site energies based on a short molecular dynamics (MD) simulation where non-solvent heavy atoms are restrained. This method has been successfully applied in several instances related to protein kinases, such as with platelet-derived growth factor receptor-β (PDGF-Rβ),²⁶ p38α MAP kinase,²⁷ dual-specificity tyrosine phosphorylation-regulated kinase (DYRK),²⁸ kinase inhibitor selectivity among four kinases,²⁹ inhibitor selectivity among phosphoinositide 3-kinases (PI3Ks),³⁰ cyclin G-associated kinase (GAK),³¹ Janus kinases (JAKs),³² and interleukin-1 receptor-associated kinase 4 (IRAK4).³³

Here we applied a water-guided ligand design approach to the development of highly potent inhibitors of GSK-3β. By exploiting a new co-crystal structure (PDB 7B6F) in combination with WaterMap and MD simulations, we were able to improve the potency of our 9H-pyrimido[4,5-*b*]indole-based compounds by almost two orders of magnitude, resulting in single-digit nanomolar IC₅₀ values. Remarkably, our results

demonstrate how a small shift in the location of a high-energy water molecule by the ligand is highly beneficial. This strategy of inducing a subtle shift for an isolated high-energy water molecule in a lipophilic environment introduces a new tool for water-targeted ligand design in addition to canonical solvent displacement, replacement, or interaction.³⁴

RESULTS

Our initial structural modifications on the tricyclic scaffold of **1** were mainly focused on the non-heteroaromatic ring of the 9H-pyrimido[4,5-*b*]indole tricycle (Table 1). The exchange of the chlorine atom in the 7-position with either fluorine or bromine and its complete removal were well tolerated, generally providing triple-digit nanomolar GSK-3β inhibitors (**5a–d**). Only the corresponding 7-iodine derivative (**11**) displayed a diminished activity. In contrast, the relocation of the chlorine or bromine substituent to the 6-position (**5g** and **5h**) or the 5-position (**5i**) was associated with a substantial (5–10-fold)

decrease in potency. Furthermore, the introduction of a methyl group in the pyrimidine 2-position of parent compound **1** afforded an inactive derivative (**5j**, IC_{50} value $>10 \mu M$). As we recently observed a strong influence of the stereoconfiguration on the bioactivity of structurally related GSK-3 β inhibitors,³⁵ we also decided to evaluate the activity of enantiopure compounds within this series. Here, however, this effect was less pronounced. Nevertheless, respective (*S*)-enantiomers of **1** (*rac*-**5c**) and **5d** displayed a slight trend of improved IC_{50} values (1.5- and 1.3-fold, respectively).

Considering these results, we next set out to resolve the binding mode of the eutomer (*S*)-**5c** to GSK-3 β by X-ray crystallography (PDB 7B6F). As we anticipated, the crystal structure confirmed interactions of the 9*H*-pyrimido[4,5-*b*]indole core with the hinge region of the kinase (Figure 1).

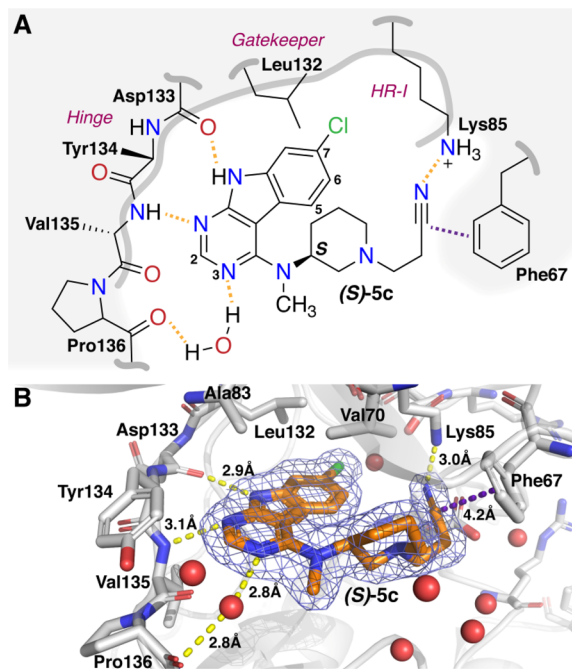


Figure 1. Co-crystal structure of (*S*)-**5c** in complex with GSK-3 β (PDB 7B6F). (A) 2D depiction of the binding mode observed in the crystal structure. (B) The hinge binder of (*S*)-**5c** is stabilized by two direct interactions and one water-bridged interaction to the protein. The chlorine atom is located near the gatekeeper residue Leu132, and the nitrile group is in close proximity to Lys85. GSK-3 β residues that make close contacts with (*S*)-**5c** are shown in the stick representation, and water molecules are displayed as red spheres. The blue mesh surface on the ligand displays a $2F_o - F_c$ map contoured at 1σ . Hydrogen bonds are indicated by yellow dashed lines, and the distance from the Phe67 aromatic ring center to the carbon of the nitrile group is depicted as a purple dashed line.

In particular, two hydrogen bonds were formed with the backbone of the hinge residues Asp133 and Val135. Moreover, a water bridge was observed between the N-3 atom of the pyrimidine ring and Pro136, which was also suggested by our earlier MD simulations.¹² The third aromatic ring of the tricyclic core is located deeper in the pocket, the chlorine substituent is oriented toward hydrophobic region I (HR-I) of the kinase, and the piperidine ring is accommodated in the sugar pocket. This allows the flexible cyanoethyl substituent to obtain a folded conformation under Phe67. The nitrile group displays a hydrogen bond to the side chain of Lys85. Notably, the

obtained conformation of the inhibitor would be disturbed by larger substituents in the 5- or 6-position of the 9*H*-pyrimido[4,5-*b*]indole core, explaining the decreased activities of **5g–i**. The inactivity of **5j** is evident from the apparent clash with the protein caused by the methyl group in the 2-position of the pyrimidine.

During a closer examination of the crystal structure, we noticed that a single water molecule is trapped in HR-I and the chlorine atom of the ligand points toward it (Figure 2A). Intrigued by this finding, we decided to evaluate the solvent organization near the ligand using WaterMap.^{24,25} This analysis, which provides an estimate of the hydration sites and their energies, revealed both low- and high-energy hydration sites (Figure 2B and C). The hydration site related to the water bridge located between the N-3 atom of the pyrimidine ring and GSK-3 β was characterized as a low-energy site (+0.13 kcal/mol). Importantly, we noticed that the trapped water molecule in HR-I was indeed identified as a high-energy hydration site (+6.71 kcal/mol). Therefore, our subsequent ligand design aimed for the displacement of this high-energy water molecule. To this end, we installed a variety of substituents at the 7-position of the 9*H*-pyrimido[4,5-*b*]indole core. Our initial efforts toward introducing considerably bulkier residues (**5k** and **5l**) or a methoxy group (**5e**) resulted in compounds with decreased activities (Table 2). Also, perhaps surprisingly, the trifluoromethyl derivative (**5f**) appeared to be inactive. Notably, the radius of the trifluoromethyl group is substantially bulkier compared to that of chlorine (Figure S1A). Therefore, we ascertained a clear limitation on the substituent's radius in this area, which is most likely caused by the steric hindrance of the gatekeeper residue Leu132 (Figure 2D). We speculate that this also applies to the observed slight decrease in activity seen for derivative **1l**, which carries the considerably larger iodine substituent (Figure S1A). Based on these initial results, addressing this high-energy water required a long and narrow substituent. Correspondingly, we next tested a nitrile derivative (**5m**), as the use of this moiety was previously demonstrated to be a successful approach to displace a water molecule in the design of the autotaxin inhibitor GLPG1690 and Hsp90 inhibitors.^{39,40} The nitrile group is comparable to the chlorine substituent in terms of its van der Waals radius but is longer and reaches deeper toward HR-I (Figure S1B). Unfortunately, in this case this approach was unsuccessful, as **5m** displayed even lower activity than the parent compound **5c**. Next, we introduced an ethynyl substituent (**15**), which is even longer than the nitrile group but maintains a similar radius (Figure S1B). To our astonishment, **15** displayed a remarkable increase in activity, with an IC_{50} value of 23 nM. Since we initially identified a trend toward (*S*)-**5c** and (*S*)-**5d** being the eutomers, we assumed that a higher activity would be observed for the corresponding stereoisomer of **15**. Indeed, compound (*S*)-**15** displayed an improved IC_{50} value of 6 nM.

We were puzzled about the remarkable activity difference between the ethynyl (**15**) and the nitrile (**5m**) derivative. To further rationalize this finding, we ran additional WaterMap analyses for both compounds using them as ligands in the simulations. Interestingly, the high-energy hydration site appeared at the same location with the nitrile (**5m**) as with (*S*)-**5c**, whereas this hydration site was shifted with the highly active ethynyl analog (*S*)-**15** (Figure S2). These results demonstrated that an adequate length of the ethynyl substituent was required to push the water, with the nitrile group being “too short” in this case. The evaluated energy of this hydration site in

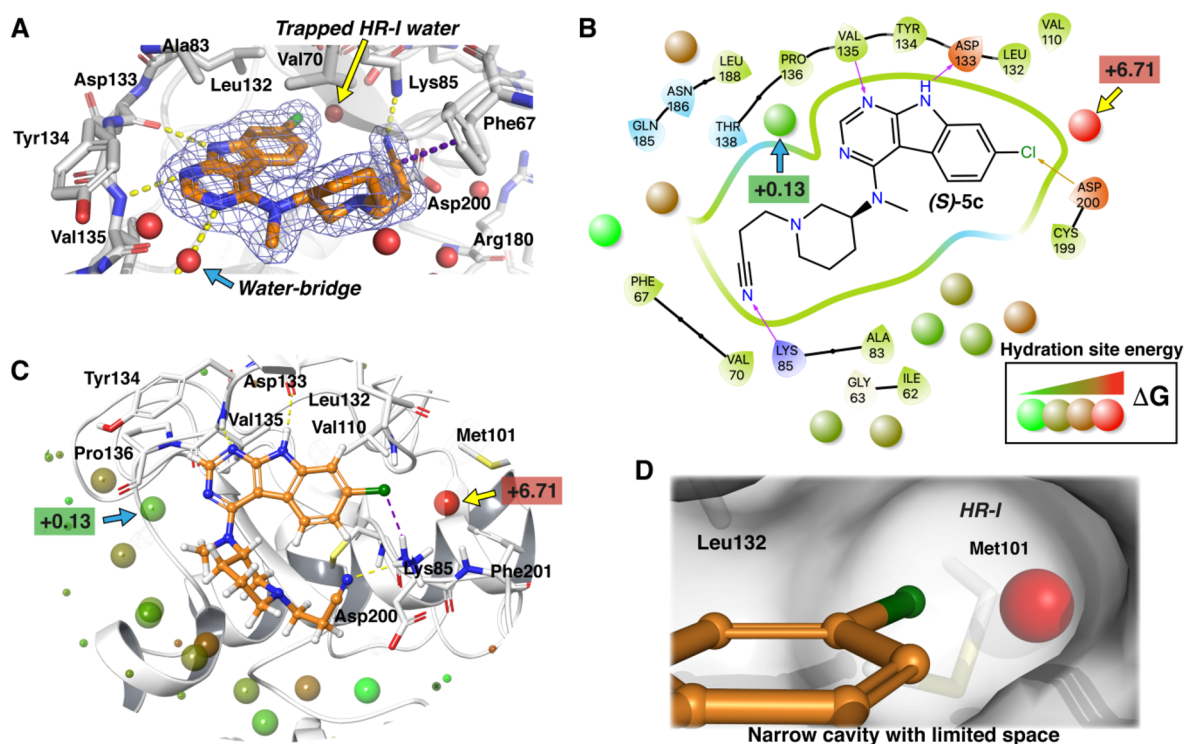


Figure 2. The WaterMap analysis of the GSK-3 β –(S)-5c crystal structure revealed a high-energy water in HR-I. (A) In the crystal structure, a trapped water molecule was found in HR-I (indicated by a yellow arrow). The water molecule that forms the water bridge is indicated by a blue arrow. (B) 2D and (C) 3D depictions of the WaterMap analysis. The hydration site related to the water bridge was identified as a low-energy site (+0.13 kcal/mol), whereas the estimated free energy for the trapped water molecule in HR-I is high (+6.71 kcal/mol). All other hydration sites near the ligand located in the solvent interface displayed low- or medium-energy values. (D) The chlorine atom of (S)-5c points toward HR-I where the high-energy water molecule is located. The gatekeeper residue Leu132 sterically restricts the ligand's access to HR-I.

Table 2. Structures and Biological Activities of Compounds Addressing the High-Energy Water Molecule

No.	R ²	GSK-3 β IC ₅₀ ± SEM [μ M] ^a	pIC ₅₀	clogP ^b	LLE ^c
5k		5.112 ± 0.270	5.3	4.1	1.2
5l		5.299 ± 0.145	5.3	3.3	2.0
5e		8.690 ± 0.057	5.1	2.6	2.5
5f		> 10	-	3.5	-
5m		1.204 ± 0.146	5.9	2.5	3.4
15		0.023 ± 0.008	7.6	3.7	3.9
(S)-15		0.006 ± 0.003	8.2	3.7	4.5

^aIC₅₀ values were determined in an ADP Glo kinase assay.³⁶ The reported data are mean values ± the SEM from at least two independent experiments. ^bclogP was calculated with Canvas (Schrödinger LLC).³⁷ ^cLLE = pIC₅₀ – clogP.³⁸

the case of **5m** (+6.21 kcal/mol, which was calculated for the (S)-enantiomer) was comparable with that of chlorine-substituted (S)-5c (+6.71 kcal/mol). Even though the electrostatic potentials among these compounds were notably different in their high-energy water-facing apical site (Figure S3), no interactions between the water molecule and the ligand were

observed. Therefore, the decreased biological activity of **5m** most likely arose from its lower lipophilicity (see the LLE value in Table 2). For the shifted hydration site with (S)-15, however, an even higher energy (+7.97 kcal/mol) was estimated by the WaterMap analysis. Therefore, this approach failed to provide us a further rationale for the remarkable activity of (S)-15.

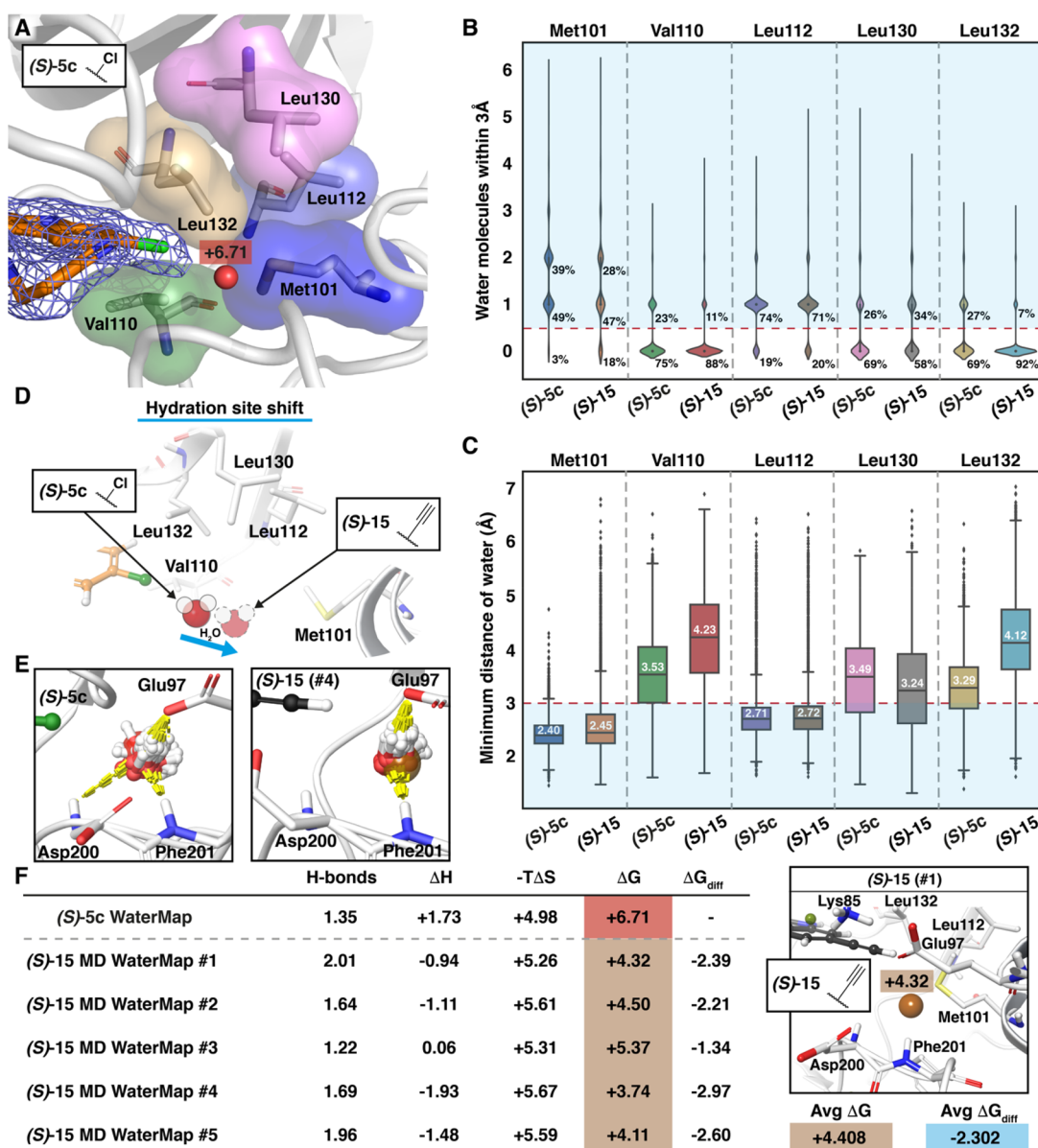
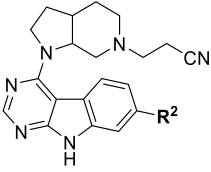


Figure 3. Molecular dynamics simulations reveal the high-energy hydration site shift that is accompanied by decreased energy. (A) Lipophilic residues Met101, Val110, Leu112, Leu130, and Leu132 flank the high-energy water in HR-I. (B) Quantitation of the number of observed water molecules within 3 Å of the side chains of the selected lipophilic residues during the simulations (a total simulation time of 10 μ s for each ligand). The light blue-shaded area indicates the water exposure of the lipophilic side chains. (C) Observed minimum distance of the water to the side chain of the selected lipophilic residues during the simulations. The light blue-shaded area indicates the water exposure of the lipophilic side chains. In the boxplots, the box indicates quartiles of the data set (25–75%), and whiskers indicate the rest of the data within 1.5 \times the interquartile range (IQR) (outliers are shown with black diamonds). Median values are provided as horizontal lines in the boxes. (D) Schematic depiction of the hydration site movement based on the data in panels B and C. (E) Based on WaterMap simulations, the subtle shift of the water molecule's location induces alterations in the hydrogen bond network of the high-energy water molecule (see also Figure S5). (F) The WaterMap analysis of the MD simulation output structures for five replicas of (S)-15 demonstrates that the shifted hydration site has a lower energy compared to that of (S)-5c.

To further investigate the water molecule's behavior in the high-energy site, we conducted $10 \times 1 \mu$ s MD simulations for both compounds, i.e., (S)-5c and (S)-15, in complex with GSK-3 β . Throughout the simulations, the two inhibitors displayed nearly identical interaction patterns, demonstrating that the ethynyl substituent does not affect the direct interactions of the ligand with GSK-3 β (Figure S4). Comprehensive protein side chain conformational sampling occurs within a microsecond timescale;⁴¹ therefore, these simulations would be expected to reveal the putative water displacement if it occurred. Interestingly, these longer simulations agreed with the notably

shorter (2 ns) WaterMap simulations - the water molecule was slightly shifted but not displaced from the HR-I site. We further evaluated the water location and the solvent exposure of the lipophilic residue side chains in this region. A total of five lipophilic residues were found in this area: gatekeeper Leu132 and Val110, which were in close contact with the ligand; Leu112 and Leu130, which were located deep in the pocket; and Met101, which protruded from the α C-helix (Figure 3A). Leu132 was almost fully shielded from the solvent exposure by (S)-15, which clearly pushed the water molecule away from the gatekeeper (Figure 3B and C). A similar trend was also evident

Table 3. Structures and Biological Activities of Rigid Compounds



No.	R ²	GSK-3β IC ₅₀ ± SEM [μM] ^a	(IC ₅₀ nonrigid)	pIC ₅₀	clogP ^d	LLE ^e
19	F	2.668 ± 1.488	(0.973)	5.6	2.7	2.9
2	Cl	0.130 ± 0.008 ^b	(0.764 ^b)	6.9	3.2	3.7
20	Br	0.066 ± 0.015	(0.388)	7.2	3.2	3.9
21	I	0.132 ± 0.036	(1.382)	6.9	3.1	3.8
22	≡	0.002 ± 0.000	(0.023)	8.7	3.6	5.1

^aIC₅₀ values were determined in an ADP Glo kinase assay.³⁶ The reported data are mean values ± the SEM from at least two independent experiments. ^bData were taken from Andreev et al.¹² ^cIC₅₀ values of the corresponding non-rigid compounds from Tables 1 and 2. ^dlogP was calculated with Canvas (Schrödinger LLC).³⁷ ^eLLE = pIC₅₀ - clogP.³⁸

in the case of Val110, while only marginal changes were observed for the other lipophilic residues. There was virtually no change in the water exposure of Leu112 with (S)-15. Met101 appeared to be somewhat less exposed to water with (S)-15, whereas a slight increase in the water exposure of Leu130 was observed. These findings clearly demonstrated that the hydration site was shifted away from the gatekeeper Leu132, but the water molecule remained in HR-I (Figure 3D). Next, we wanted to re-evaluate the energy of this shifted high-energy hydration site. To this end, we selected five conformations (at 1 μs) of the (S)-15 MD simulations. Of note, one should always use caution when applying WaterMap for an MD simulation-derived structure as the method was originally developed to be applied for crystal structures and is highly sensitive to changes in side chain conformations. In other words, the thermodynamic quantities calculated by WaterMap only apply to the input conformation. Intriguingly, even though the slightly shifted water molecule was still trapped in the hydrophobic environment, WaterMap now demonstrated a significantly decreased energy of this hydration site, which was mainly enthalpy-driven (Figure 3F). We noticed that the subtle shift in the position of the water molecule resulted in altered hydrogen bond interactions with the protein (specifically the loss of the hydrogen bond to Asp200) (Figures 3E and S5). As a consequence, this shift appeared to improve the hydrogen bonding with Phe201 and Glu97, providing an explanation for the observed decrease in the hydration site energy. The estimated hydration site energy (average difference of 2.302 kcal/mol compared to that of (S)-5c) was in line with the observed biological activities, as a free energy difference of 2.6 kcal/mol would be expected in their binding affinities (80-fold difference).

To examine if our earlier successful rigidification approach on this compound series also applied here (Scheme 1), we evaluated a set of rigidified congeners (Table 3). Indeed, most of these compounds displayed enhanced IC₅₀ values compared to those of their nonrigid counterparts. Importantly, the ethynyl derivative 22 exhibited an outstanding potency (IC₅₀ value of 2 nM), confirming the highly beneficial effect of this substituent. We also observed a clear trend of enhanced activities alongside the increasing sizes of the halogens (2 and 19-21). The results of this rigidified compound set imply an impact of the substituent

in the 7-position on the high-energy hydration site similar to that observed with the non-rigid analogs.

Next, we set out to evaluate the cellular target engagement of (S)-5c, (S)-15, 20, and 22. In a NanoBRET assay, these inhibitors generally demonstrated GSK-3β binding affinities in the single-digit micromolar range (for details, see the Supporting Information and Table S1). Importantly, these data correlate well with the IC₅₀ values determined in the kinase activity assay, with (S)-15 and 22 displaying the highest affinity to GSK-3β in cells.

These results motivated us to further characterize (S)-15 and 20 in terms of their intracellular GSK-3 inhibition and neuroprotective effects in neuronal SH-SY5Y cells. The treatment of SH-SY5Y cells with (S)-15 and 20 at concentrations lower than 10 μM and 20 μM, respectively, did not affect cell viability (3-(4,5-dimethylthiazol-2-yl)-2,5-diphenyltetrazolium bromide (MTT) assay) (Figure S6).⁴² Therefore, we selected the concentration of 5 μM to perform an immunoblotting assay to monitor the phosphorylation status of GSK-3 in the presence of the inhibitors. While both (S)-15 and 20 increased the amount of phospho-GSK-3α/β (Ser21/9) (inactive GSK-3α/β form), only (S)-15 decreased the amount of phospho-GSK-3α/β (Tyr279/Tyr216) (the active GSK-3α/β form) after 3 h of treatment in neuronal SH-SY5Y cells (Figure S7). As Tyr279 and Tyr216 are the autophosphorylation sites of GSK-3α and GSK-3β, respectively, the phosphorylation status of these residues reflects the enzymatic activity of the kinase.⁴³⁻⁴⁵ Accordingly, these results demonstrate that (S)-15 inhibits GSK-3 activity in cells, targeting the ATP binding pocket of both GSK-3α and GSK-3β and rendering its inhibition selective and persistent. Furthermore, we investigated the neuroprotective effects of (S)-15 and 20 against the neurotoxicity induced by hydrogen peroxide (H₂O₂, 100 μM), which mimics general oxidative stress.⁴⁶ The concomitant treatment of the SH-SY5Y cells with H₂O₂ and the compounds (5 μM) significantly decreased the neurotoxicity elicited by oxidative stress on a neuronal level (Figure S8). Interestingly, the neuroprotective effect of (S)-15 was significantly higher than of 20, corroborating the ability of (S)-15 to promote neuronal survival through the strong inhibition of GSK-3β.

Finally, to assess the kinase selectivity of the inhibitors (S)-15 and 22, we evaluated their biological activities on a subset of

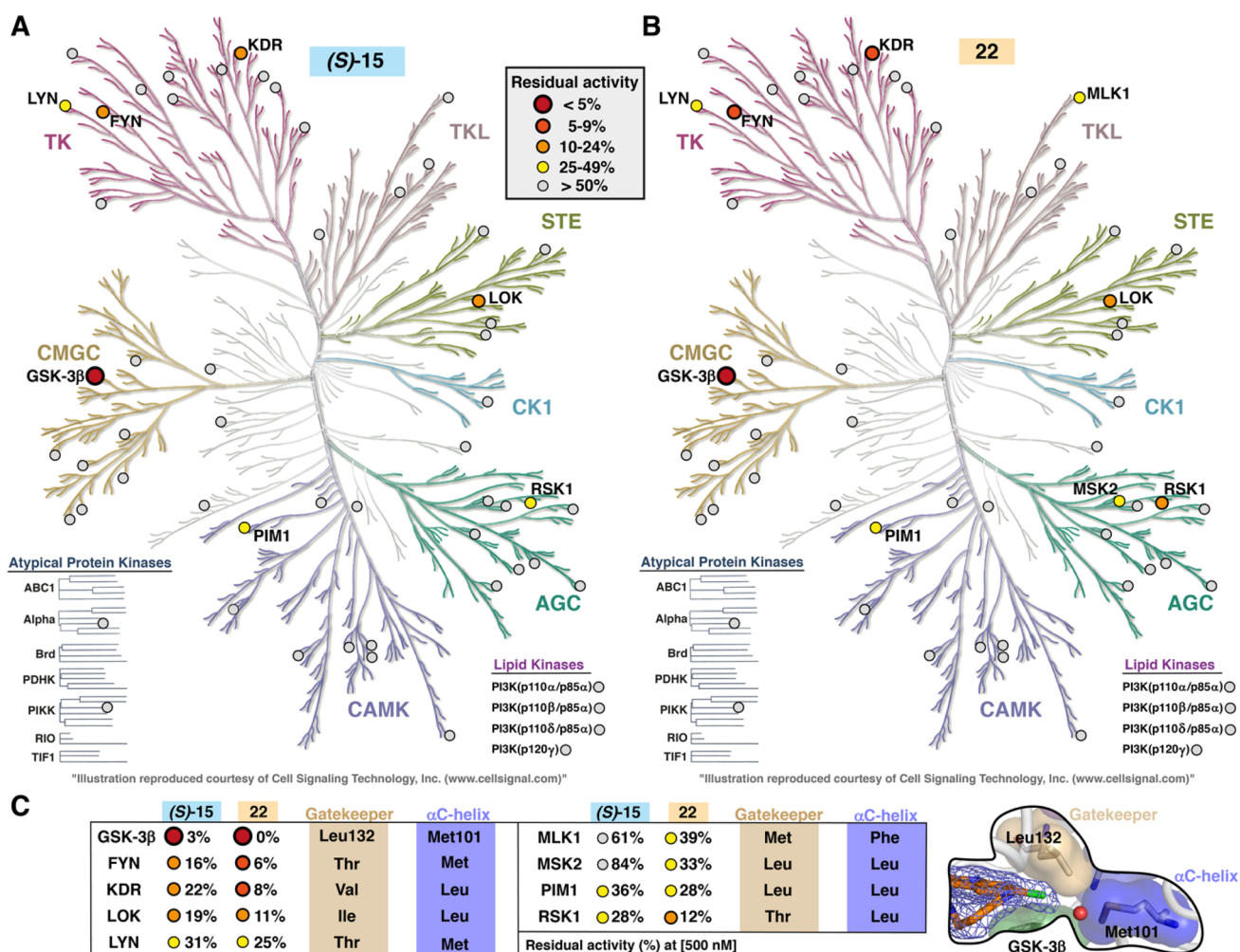
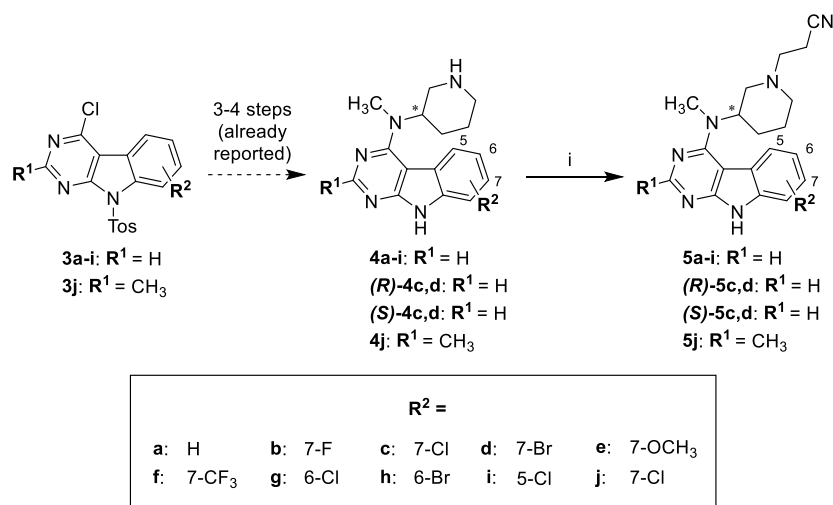


Figure 4. Selectivity of (S)-15 and 22 within the human kinome. (A) Selectivity of compound (S)-15. All tested kinases are highlighted with circles and colored according to their residual activity at a 500 nM inhibitor concentration. (B) Selectivity of compound 22. (C) The residual activities of the off-targets, which display <50% residual activity for either (S)-15 or 22. The corresponding gatekeeper and α C-helix residues are listed for each kinase. Panels A and B were generated with the help of the KinMap tool.⁴⁷

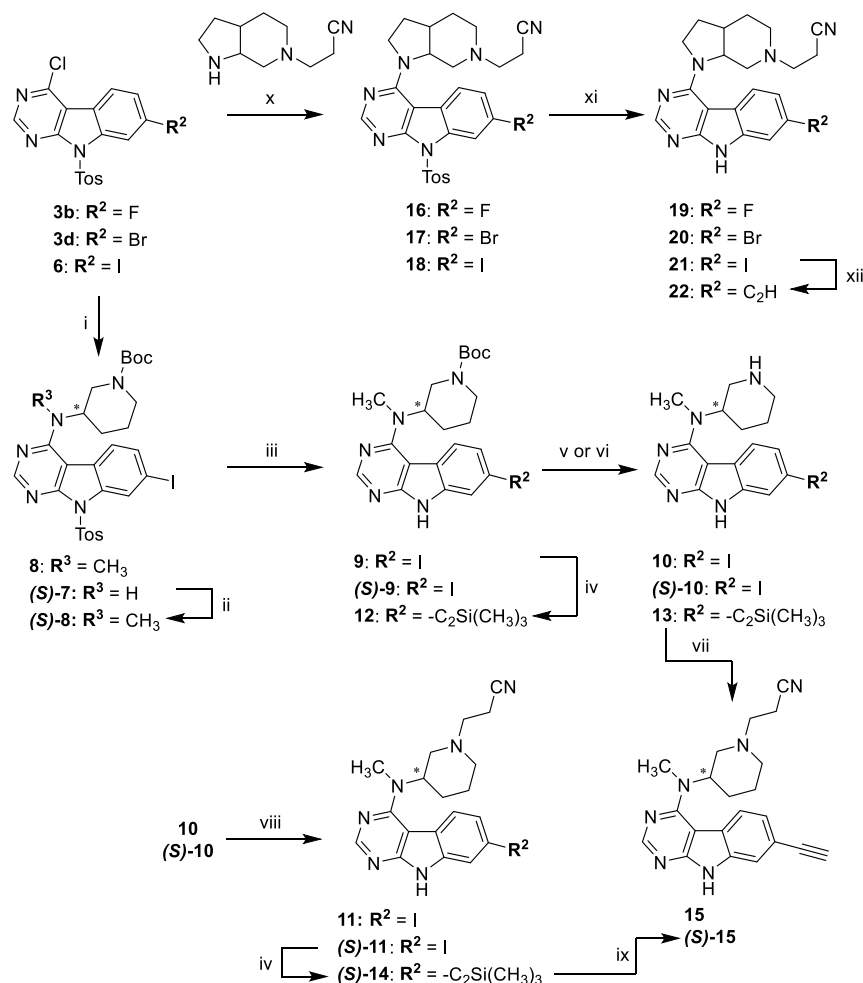
Scheme 2. Synthetic Route Towards Compounds 5a–j and the Enantiopure Analogs (R)-5c,d and (S)-5c,d^a



^aListed in Tables 1 and 2. Reagents and conditions are as follows: (i) acrylonitrile, MeOH, rt (37–84%).

57 kinases. At an inhibitor concentration of 500 nM, only a few kinases were substantially inhibited by (S)-15 and 22 (Figure 4;

see the full list in Table S2). These data suggested a similar off-target profile for the two compounds. Notably, the more potent

Scheme 3. Synthetic Route Towards Compounds 11, 15, (S)-15 and 19-21^a

^aListed in Tables 2 and 3. Reagents and conditions are as follows: (i) **6**, DIPEA, DMF, 70 °C (54% for (S)-7); (ii) iodomethane, NaH, DMF, -10 °C to rt (5); (iii) *t*BuO⁻, THF, rt (54-58% over two steps); (iv) TMS-acetylene, Pd(PPh₃)₄ or PdCl₂(PPh₃)₂, CuI, TEA, DMF, rt or 50 °C (86-96%); (v) **9** or (S)-**9**, TFA, DCM, rt (quant.); (vi) **12**, 4 N HCl in 1,4-dioxane, rt (42%); (vii) (1) acrylonitrile, MeOH, rt, (2) K₂CO₃, MeOH, rt (41% over two steps); (viii) acrylonitrile, MeOH, rt (44-74%); (ix) K₂CO₃, MeOH, rt (68%); (x) DIPEA, DMF, 70 °C (41-62%); (xi) *t*BuO⁻, THF, rt (40-62%); (xii) (1) TMS-acetylene, PdCl₂(PPh₃)₂, CuI, TEA, DMF, rt, (2) K₂CO₃, MeOH, rt (41% over two steps).

rigid inhibitor **22** consistently exhibited the stronger inhibition on all off-target kinases compared to that of its non-rigid counterpart (S)-**15**. Even though the off-targets appeared to be only remotely related, they shared structural similarities in residues near the HR-I site that participate in the accommodation of the ethynyl substituent in the 7-position of the 9H-pyrimido[4,5-*b*]indole core (Figure 4C). In particular, they mostly harbor a branched gatekeeper residue (Ile, Leu, Thr, and Val) and a large lipophilic amino acid protruding from the αC helix (Met, Leu, and Phe). Thus, we anticipate that these residues together with a suitable overall binding site topology allow the binding of (S)-**15** or **22**, offering a putative explanation for the observed off-target activity.

Chemistry. We recently reported the synthetic preparation of piperidines **4a-j** and the enantiopure analogs (R)-**4c**, (R)-**4d**, (S)-**4c**, and (S)-**4d** from 9-tosyl-9H-pyrimido[4,5-*b*]indoles **3a-j** (Scheme 2).³⁵ These piperidine intermediates display diverse substitution patterns of the tricyclic core and served as precursors to prepare the final compounds **5a-j**, (R)-**5c**, (R)-**5d**, (S)-**5c**, and (S)-**5d** within the herein reported study. As previously described in the synthesis of inhibitor **1**, the

cianoethyl substituent was installed on the piperidine nitrogen by a Michael reaction with acrylonitrile.¹²

Moreover, our established synthetic methodologies were successfully applied to the corresponding 7-iodo derivatives (Scheme 3).³⁵ In detail, previously reported 7-iodo-9-tosyl-9H-pyrimido[4,5-*b*]indole (**6**) was reacted with *N*-Boc-3-(methylamino)piperidine in a nucleophilic aromatic substitution (S_NAr) to yield intermediate **8**. In the case of the enantiopure analog (S)-**8**, commercially available (S)-*N*-Boc-3-aminopiperidine was used in the S_NAr resulting in (S)-**7**, which was subsequently methylated with iodomethane under strictly anhydrous basic conditions. Intermediates **8** and (S)-**8** were then subjected to deprotection procedures to generate piperidines **10** and (S)-**10**, respectively, which were similarly reacted with acrylonitrile to form final compound **11** and the intermediate (S)-**11**.

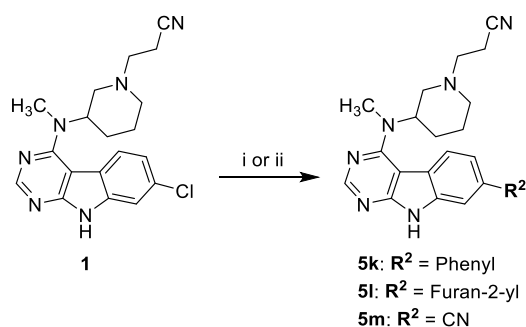
For the synthesis of the racemic ethynyl derivative **15**, a Sonogashira cross coupling reaction was initially performed with the Boc-protected intermediate **9** and trimethylsilylacetylene (TMS-acetylene) following a modified literature protocol (Scheme 3).⁴⁸ The treatment of the Sonogashira product **12** with TFA in DCM, however, resulted in simultaneous Boc and

TMS deprotection as well as in pronounced by-product formation. While the application of 4 N HCl in 1,4-dioxane allowed for selective Boc cleavage, the reaction still suffered from a poor yield in the synthesis of **13**. Nevertheless, this intermediate was converted to the racemic final compound **15** in a one-pot two-step reaction, including the introduction of the cyanoethyl substituent and TMS deprotection with K_2CO_3 .

To avoid an acidic Boc deprotection in the presence of the alkyne substituent in the synthesis of the (*S*)-configured analog (*S*)-**15**, the Pd-catalyzed alkynylation was instead carried out with (*S*)-**11**. The TMS protecting group of (*S*)-**14** was then smoothly cleaved with K_2CO_3 to obtain (*S*)-**15** in a 2.5-fold higher yield over four steps compared to the initial approach.

Compounds **5k–m** bearing a nitrile substituent or aryl moieties in the 7-position of the 9*H*-pyrimido[4,5-*b*]indole core were prepared by cross coupling reactions from the already reported compound **1** (Scheme 4). In the case of **5m**, precursor

Scheme 4. Synthetic Route Towards Compounds **5k–m**^a



^aListed in Table 2. Reagents and conditions are as follows: (i) $K_4[Fe(CN)_6] \cdot 3H_2O$, BrettPhos Pd G3, BrettPhos, KOAc, 1,4-dioxane/ H_2O (1:1, v/v), 100 °C (26%); (ii) appropriate aryl boronic acid, XPhos Pd G3, K_3PO_4 , 1,4-dioxane/ H_2O (4:1, v/v), 100 °C (60–66%).

1 was subjected to a palladium-catalyzed cyanation procedure using $K_4[Fe(CN)_6]$ as the cyanide source,⁴⁹ whereas **5k** and **5l** were synthesized via Suzuki coupling with the appropriate aryl boronic acids by applying common procedures.

The rigidized compounds **19–21** were accessible by a two-step synthetic route that started from the corresponding 9-tosyl-9*H*-pyrimido[4,5-*b*]indoles **3b**, **3d**, and **6** (Scheme 3). The required 3-(octahydro-6*H*-pyrrolo[2,3-*c*]pyridin-6-yl)propanenitrile building block was prepared as described previously and introduced under S_NAr conditions.¹² The application of the tosyl deprotection protocol on intermediates **16–18** eventually furnished **19–21**, respectively. In addition, the iodine derivative **21** was subjected to the established methodology to introduce the ethynyl substituent to afford inhibitor **22**. We previously resolved the molecular structure of **2** by X-ray crystallography, confirming the protocols for the preparation of the 3-(octahydro-6*H*-pyrrolo[2,3-*c*]pyridin-6-yl)propanenitrile building block and its use in the subsequent steps deliver a mixture of the (3*aR*, 7*aS*)- and (3*aS*, 7*aR*)-enantiomers of the respective final compound.¹²

CONCLUSION

We utilized the newly obtained co-crystal structure of the moderately potent GSK-3 β inhibitor (*S*)-**5c** to identify highly potent compounds. The binding affinities of these compounds were improved by addressing a trapped high-energy water

molecule in the HR-I site. Here, the ethynyl substituent proved highly beneficial, affording an up to 80-fold increase in potency. The improved inhibitory activity of (*S*)-**15** toward GSK-3 β (IC_{50} value of 6 nM) also translated to a cellular context, as the target engagement was demonstrated in a NanoBRET assay together with neuroprotective effects against H_2O_2 and the reduced autophosphorylation of GSK-3 in neuronal SH-SY5Y cells. In addition, the ethynyl-substituted compounds displayed favorable kinome selectivity profiles.

Based on our MD simulations and a WaterMap analysis, this ethynyl substituent induced only a subtle shift in the position of the trapped water molecule, which resulted in the lower energy of the hydration site that is in line with the observed biological activity. This decrease in energy was mainly driven by enthalpy, arising from alterations in the protein–water hydrogen bond network. The nearly identical interactions of (*S*)-**5c** and (*S*)-**15** toward GSK-3 β and the improved LLE values of the ethynyl derivatives suggested that it is mainly the subtle change in location of the the high-energy hydration site that influences the ligand binding. To the best of our knowledge, these results demonstrate for the first time that a high-energy water does not necessarily need to be fully displaced, replaced, or interacted with by the ligand to alter its energy in a manner beneficial for ligand binding. In the location where the high-energy water molecule was found, protein kinases harbor conserved water molecules, which are commonly interacted with by type I inhibitors.⁵⁰ This also applies to human GSK-3 β based on our analysis of the high-resolution crystal structures currently available in the Protein Data Bank in Europe (PDBe) (for a full list, see the Supporting Information). Interestingly, we observed in a completely different compound series that stabilizing a dynamic water network and avoiding unfavorable water exposure related to the HR-I site of GSK-3 β is also crucial for the inhibitor activity.⁵¹

We noted that a combination of longer (μs) MD simulations with the short (ns) and restrained WaterMap simulations was required for a more accurate analysis of the energy evaluation of a shifted hydration site (see the workflow of the combination approach in Figure S9). To note, there are always limitations and inaccuracies that are associated with in silico techniques, especially related to the description of the solvent; nevertheless, the herein-applied methodology proved to be highly efficient, substantiating the relevance of water-guided in silico approaches for the ligand design process. Overall, these results highlight the importance of considering even subtle changes of hydration site positions in the ligand design process.

EXPERIMENTAL SECTION

General Information. All solvents and reagents were obtained from commercial sources and utilized without additional purification. Solvents used for analytical chromatography were of HPLC grade. 3-(Octahydro-6*H*-pyrrolo[2,3-*c*]pyridin-6-yl)propanenitrile was prepared according to modified reported procedures and obtained as a free base or TFA salt.¹² High-performance liquid chromatography (HPLC) was carried out on either an HP1090 series II HPLC system from Hewlett-Packard (Palo Alto, CA) or an 1100 series HPLC system from Agilent Technologies (Santa Clara, CA). The systems consisted of a binary pump, a column compartment equipped with a Luna C8(2) 100 Å RP column (4.6 mm inner diameter \times 150 mm length, 5 μm particle size) from Phenomenex (Torrance, CA), an autosampler, and a diode array detector (DAD) (the purity of test compounds was determined at 254 nm). Mobile phases A (MeOH) and B (aqueous 0.01 M KH_2PO_4 buffer, pH 2.3) were used in the following gradient: mobile phase A 40% to 85% over 8 min, mobile phase A 85% constant

for 5 min, mobile phase A 85% to 40% over 1 min, and mobile phase A 40% constant for 2 min. The complete run time was 16 min, the flow rate was 1.5 mL/min, and the sample injection volume was 5 μ L.

The chiral chromatographic analysis was performed on a 1290 Infinity series LC system from Agilent Technologies (Santa Clara, CA). The system consisted of a binary pump, a thermostated column compartment equipped with a Chiralpak IB-U column (3.0 mm inner diameter \times 100 mm length, 1.6 μ m particle size) from Daicel (Osaka and Tokyo, Japan), an autosampler, and a DAD (the chiral purity of test compounds was determined at 254 nm). To minimize the extra column volume, the system was provided with an ultralow dispersion kit (including a Max-Light ultralow dispersion cartridge flow cell with an inner volume of 0.6 μ L, an ultralow dispersion needle seat, and capillaries with a 0.075 mm inner diameter from the autosampler to the column compartment (350 mm length) and from the column compartment to the DAD (220 mm length)). The mobile phase was composed of 90% *n*-heptane, 10% isopropanol, and 0.1% diethylamine. The flow rate was 0.15 mL/min. Samples were prepared by diluting 10 mM aliquots in DMSO by a factor of 10 with the mobile phase to a total concentration of 1 mM and were injected with a volume of 5 μ L. The enantiomeric excess (ee) of the enantiopure final compounds was >98% in all cases.

Thin-layer chromatography (TLC) was carried out on either TLC Silica gel F254 sheets from Merck (Darmstadt, Germany) or Alugram Sil G/UV254 sheets from Macherey-Nagel (Düren, Germany). Bands were visualized under UV light at 254 nm.

Electrospray ionization mass spectrometry (ESI-MS) was performed on an Advion expressions CMS TLC-ESI-MS coupling system from Advion (Ithaca, NY) that operated in the positive ESI mode (capillary temperature of 250 $^{\circ}$ C, capillary voltage of 180 V, source gas temperature of 250 $^{\circ}$ C, and ESI voltage of 3500 V) and the negative ESI mode (capillary temperature of 250 $^{\circ}$ C, capillary voltage of 180 V, source gas temperature of 250 $^{\circ}$ C, and ESI voltage of 2500 V). Elution occurred with LCMS-grade MeOH.

Flash column chromatography was performed on a Puriflash 430 or XS 420 system from Interchim (Montluçon, France) on Davisil Chromatographic silica media LC60A (20–45 μ m) from Grace Davison Discovery Sciences (Columbia, MD) or Interchim Puriflash preppacked silica columns (SIHP-JP, 30 μ m) from Interchim (Montluçon, France) and Geduran Si60 63200 μ m silica gel from Merck (Darmstadt, Germany) for precolumn preparation. Mobile phases are described in the detailed procedures for each purified compound.

Nuclear magnetic resonance (NMR) analysis was carried out on 200, 300, and 400 MHz Avance and 400 MHz Ascend spectrometers from Bruker (Billerica, MA). Spectra were calibrated to the residual peaks of the utilized solvents. The chemical shifts are reported in parts per million (ppm) relative to tetramethylsilane (δ 0).

Experimental Procedures. General Procedure A for the Preparation of Final Compounds 5a, 5b, and 5d–j and the Enantiopure Analogs (R)-5c, (R)-5d, (S)-5c, and (S)-5d. The appropriate secondary amine intermediate was dissolved in MeOH (HPLC grade or dry). To the mixture was added acrylonitrile. The mixture was stirred at rt under a N₂ atmosphere for 16 h and concentrated under reduced pressure. The residue was purified by flash column chromatography.

Detailed Procedures for the Preparation of Final Compounds 5a, 5b, and 5d–j and the Enantiopure Analogs (R)-5c, (R)-5d, (S)-5c, and (S)-5d. 3-(3-(Methyl(9H-pyrimido[4,5-*b*]indol-4-yl)amino)piperidin-1-yl)propanenitrile (**5a**). The title compound was prepared from *N*-methyl-*N*-(piperidin-3-yl)-9H-pyrimido[4,5-*b*]indol-4-amine (36.0 mg, 0.13 mmol) and acrylonitrile (10.1 mg, 0.19 mmol) in dry MeOH (5 mL) according to general procedure A. Purification by flash column chromatography (SiO₂; DCM/EtOH gradient elution from 98:2 to 9:1) gave 26 mg of the product (61% yield). ¹H NMR (400 MHz, DMSO-*d*₆) δ 12.07 (s, 1H), 8.39 (s, 1H), 7.80 (d, *J* = 8.0 Hz, 1H), 7.48 (d, *J* = 7.8 Hz, 1H), 7.39 (t, *J* = 7.5 Hz, 1H), 7.33–7.27 (m, 1H), 4.52–4.41 (m, 1H), 3.15 (s, 3H), 3.07–2.99 (m, 1H), 2.90–2.80 (m, 1H), 2.73–2.66 (m, 2H), 2.65–2.58 (m, 2H), 2.41–2.34 (m, 1H), 1.99–1.90 (m, 1H), 1.86–1.67 (m, 3H), 1.57–1.44 (m, 1H); ¹³C

NMR (101 MHz, DMSO-*d*₆) δ 159.6, 157.0, 153.4, 136.6, 124.7, 122.5, 120.5, 120.0, 119.5, 111.2, 97.6, 55.7, 54.8, 53.0, 52.2, 32.5, 27.3, 24.4, 14.9; ESI-MS (*m/z*) 335.1 [M + H]⁺, 357.0 [M + Na]⁺, 333.0 [M – H][–]; HPLC method B *t*_r = 2.391 min.

3-(3-(7-Fluoro-9H-pyrimido[4,5-*b*]indol-4-yl)(methylamino)piperidin-1-yl)propanenitrile (**5b**). The title compound was prepared from 7-fluoro-*N*-methyl-*N*-(piperidin-3-yl)-9H-pyrimido[4,5-*b*]indol-4-amine (80.0 mg, 0.27 mmol) and acrylonitrile (28.1 mg, 0.53 mmol) in dry MeOH (7 mL) according to general procedure A. Purification by flash column chromatography (SiO₂, DCM/EtOH gradient elution from 98:2 to 9:1) gave 44 mg of the product (47% yield). ¹H NMR (400 MHz, DMSO-*d*₆) δ 12.21 (s, 1H), 8.38 (s, 1H), 7.78 (dd, *J* = 8.8, 5.3 Hz, 1H), 7.24 (dd, *J* = 9.4, 2.4 Hz, 1H), 7.15 (td, *J* = 9.4, 2.4 Hz, 1H), 4.50–4.35 (m, 1H), 3.13 (s, 3H), 3.09–3.02 (m, 1H), 2.90–2.81 (m, 1H), 2.74–2.66 (m, 2H), 2.65–2.58 (m, 2H), 2.42–2.33 (m, 1H), 1.99–1.89 (m, 1H), 1.81–1.65 (m, 3H), 1.55–1.42 (m, 1H); ¹³C NMR (101 MHz, DMSO-*d*₆) δ 160.2 (d, *J* = 239.8 Hz), 159.3, 157.6, 153.2, 137.4 (d, *J* = 12.6 Hz), 123.9 (d, *J* = 10.0 Hz), 120.0, 116.3, 108.3 (d, *J* = 23.5 Hz), 97.7 (d, *J* = 26.0 Hz), 97.3, 55.7, 54.8, 53.0, 52.2, 32.5, 27.2, 24.3, 15.0; ESI-MS (*m/z*) 353.2 [M + H]⁺, 375.2 [M + Na]⁺, 351.1 [M – H][–]; HPLC method B *t*_r = 2.804 min.

(*R*)-3-(3-(7-Chloro-9H-pyrimido[4,5-*b*]indol-4-yl)(methylamino)piperidin-1-yl)propanenitrile (**(R)-5c**). (*R*)-7-Chloro-*N*-methyl-*N*-(piperidin-3-yl)-9H-pyrimido[4,5-*b*]indol-4-amine (50.0 mg, 0.16 mmol) and acrylonitrile (12.6 mg, 0.24 mmol) were stirred in dry MeOH (15 mL) at rt under a N₂ atmosphere for 6 h. To the mixture was added DIPEA (24.6 mg, 0.19 mmol) to promote conversion, and stirring continued overnight. The mixture was concentrated under reduced pressure. The residue was dissolved in DCM. The solution was washed with a saturated NH₄Cl solution (3 \times 10 mL), dried over Na₂SO₄, and concentrated under reduced pressure. Purification of the residue twice by flash column chromatography (SiO₂, DCM/MeOH gradient elution from 1:0 to 93:7) gave 30 mg of a white solid (51% yield). ¹H NMR (400 MHz, DMSO-*d*₆) δ 12.22 (s, 1H), 8.40 (s, 1H), 7.78 (d, *J* = 8.7 Hz, 1H), 7.48 (d, *J* = 2.0 Hz, 1H), 7.34 (dd, *J* = 8.6, 2.0 Hz, 1H), 4.52–4.40 (m, 1H), 3.14 (s, 3H), 3.11–3.03 (m, 1H), 2.91–2.82 (m, 1H), 2.76–2.69 (m, 2H), 2.66–2.59 (m, 2H), 2.43–2.34 (m, 1H), 2.02–1.89 (m, 1H), 1.82–1.66 (m, 3H), 1.57–1.42 (m, 1H); ¹³C NMR (101 MHz, DMSO-*d*₆) δ 159.4, 157.4, 153.8, 137.4, 129.2, 123.9, 120.7, 120.1, 118.6, 110.8, 97.0, 55.7, 54.8, 53.1, 52.3, 32.6, 27.3, 24.4, 15.1; ESI-MS (*m/z*) 369.0 [M + H]⁺, 390.9 [M + Na]⁺, 366.8 [M – H][–]; HPLC method A *t*_r = 4.329 min.

(*S*)-3-(3-(7-Chloro-9H-pyrimido[4,5-*b*]indol-4-yl)(methylamino)piperidin-1-yl)propanenitrile (**(S)-5c**). The title compound was prepared from (*S*)-7-chloro-*N*-methyl-*N*-(piperidin-3-yl)-9H-pyrimido[4,5-*b*]indol-4-amine (65.0 mg, 0.21 mmol) and acrylonitrile (21.8 mg, 0.41 mmol) in dry MeOH (20 mL) according to general procedure A. Purification by flash column chromatography (SiO₂, DCM/MeOH gradient elution from 95.5:4.5 to 93.5:6.5) gave 53 mg of a white solid (70% yield). ¹H NMR (200 MHz, DMSO-*d*₆) δ 12.21 (s, 1H), 8.40 (d, *J* = 0.4 Hz, 1H), 7.78 (d, *J* = 8.7 Hz, 1H), 7.47 (d, *J* = 2.0 Hz, 1H), 7.34 (dd, *J* = 8.7, 1.8 Hz, 1H), 4.57–4.36 (m, 1H), 3.15 (s, 3H), 3.12–3.01 (m, 1H), 2.94–2.80 (m, 1H), 2.78–2.68 (m, 2H), 2.67–2.57 (m, 2H), 2.46–2.30 (m, 1H), 2.05–1.86 (m, 1H), 1.85–1.37 (m, 4H); ¹³C NMR (50 MHz, DMSO-*d*₆) δ 159.4, 157.4, 153.8, 137.3, 129.1, 123.9, 120.6, 120.1, 118.5, 110.8, 97.0, 55.7, 54.8, 53.0, 52.2, 32.6, 27.2, 24.3, 15.0; ESI-MS (*m/z*) 369.1 [M + H]⁺, 391.0 [M + Na]⁺, 366.9 [M – H][–]; HPLC method A *t*_r = 4.724 min.

3-(3-(7-Bromo-9H-pyrimido[4,5-*b*]indol-4-yl)(methylamino)piperidin-1-yl)propanenitrile (**5d**). The title compound was prepared from 7-bromo-*N*-methyl-*N*-(piperidin-3-yl)-9H-pyrimido[4,5-*b*]indol-4-amine (120.0 mg, 0.33 mmol) and acrylonitrile (26.5 mg, 0.50 mmol) in dry MeOH (10 mL) according to general procedure A. Purification by flash column chromatography (SiO₂, DCM/EtOH gradient elution from 98:2 to 9:1) gave 90 mg of the product (65% yield). ¹H NMR (300 MHz, DMSO-*d*₆) δ 12.20 (s, 1H), 8.40 (s, 1H), 7.73 (d, *J* = 8.7 Hz, 1H), 7.61 (d, *J* = 1.9 Hz, 1H), 7.46 (dd, *J* = 8.6, 1.9 Hz, 1H), 4.51–4.39 (m, 1H), 3.14 (s, 3H), 3.10–3.03 (m, 1H), 2.90–2.81 (m, 1H), 2.76–2.67 (m, 2H), 2.67–2.58 (m, 2H), 2.44–2.33 (m, 1H), 2.01–1.88 (m, 1H),

1.80–1.64 (m, 3H), 1.58–1.41 (m, 1H); ESI-MS (m/z) 412.9 [M + H]⁺, 434.9 [M + Na]⁺, 410.7 [M – H][–]; HPLC method B t_r = 5.272 min.

(R)-3-(3-((7-Bromo-9H-pyrimido[4,5-b]indol-4-yl)(methylamino)piperidin-1-yl)propanenitrile ((R)-5d). The title compound was prepared from (R)-7-bromo-N-methyl-N-(piperidin-3-yl)-9H-pyrimido[4,5-b]indol-4-amine (65.0 mg, 0.18 mmol) and acrylonitrile (21.1 mg, 0.4 mmol) in HPLC-grade MeOH (30 mL) according to general procedure A. Purification by flash column chromatography (SiO₂, DCM/MeOH 95:5) gave 65 mg of a white solid (87% yield). ¹H NMR (300 MHz, DMSO-*d*₆) δ 12.20 (s, 1H), 8.40 (s, 1H), 7.73 (d, *J* = 8.7 Hz, 1H), 7.61 (d, *J* = 1.9 Hz, 1H), 7.46 (dd, *J* = 8.6, 1.9 Hz, 1H), 4.52–4.39 (m, 1H), 3.14 (s, 3H), 3.11–3.04 (m, 1H), 2.91–2.81 (m, 1H), 2.76–2.68 (m, 2H), 2.67–2.59 (m, 2H), 2.44–2.33 (m, 1H), 2.02–1.89 (m, 1H), 1.82–1.64 (m, 3H), 1.58–1.40 (m, 1H); ESI-MS (m/z) 413.5 [M + H]⁺, 435.5 [M + Na]⁺, 411.5 [M – H][–]; HPLC method A t_r = 4.038 min.

(S)-3-(3-((7-Bromo-9H-pyrimido[4,5-b]indol-4-yl)(methylamino)piperidin-1-yl)propanenitrile ((S)-5d). The title compound was prepared from (S)-7-bromo-N-methyl-N-(piperidin-3-yl)-9H-pyrimido[4,5-b]indol-4-amine (55.0 mg, 0.15 mmol) and acrylonitrile (17.8 mg, 0.34 mmol) in HPLC-grade MeOH (25 mL) according to general procedure A. Purification by flash column chromatography (SiO₂, DCM/MeOH 95:5) gave 28 mg of a white solid (44% yield). ¹H NMR (300 MHz, DMSO-*d*₆) δ 12.20 (s, 1H), 8.40 (s, 1H), 7.73 (d, *J* = 8.7 Hz, 1H), 7.61 (d, *J* = 1.9 Hz, 1H), 7.46 (dd, *J* = 8.6, 1.9 Hz, 1H), 4.52–4.38 (m, 1H), 3.14 (s, 3H), 3.11–3.02 (m, 1H), 2.92–2.81 (m, 1H), 2.76–2.68 (m, 2H), 2.68–2.57 (m, 2H), 2.45–2.31 (m, 1H), 2.03–1.88 (m, 1H), 1.83–1.63 (m, 3H), 1.60–1.40 (m, 1H); ESI-MS (m/z) 413.3 [M + H]⁺, 435.3 [M + Na]⁺, 411.3 [M – H][–]; HPLC method A t_r = 4.099 min.

3-(3-((7-Methoxy-9H-pyrimido[4,5-b]indol-4-yl)(methylamino)piperidin-1-yl)propanenitrile (5e). The title compound was prepared from 7-methoxy-N-methyl-N-(piperidin-3-yl)-9H-pyrimido[4,5-b]indol-4-amine (90.0 mg, 0.29 mmol) and acrylonitrile (23.0 mg, 0.43 mmol) in dry MeOH (7 mL) according to general procedure A. Purification by flash column chromatography (SiO₂, DCM/EtOH gradient elution from 98:2 to 9:1) gave 60 mg of the product (57% yield). ¹H NMR (300 MHz, DMSO-*d*₆) δ 11.96 (s, 1H), 8.34 (s, 1H), 7.67 (d, *J* = 8.7 Hz, 1H), 7.01–6.89 (m, 1H), 4.52–4.35 (m, 1H), 3.83 (s, 3H), 3.11 (s, 3H), 3.06–2.98 (m, 1H), 2.90–2.81 (m, 1H), 2.76–2.57 (m, 4H), 2.43–2.32 (m, 1H), 2.00–1.87 (m, 1H), 1.83–1.63 (m, 3H), 1.59–1.40 (m, 1H); ¹³C NMR (101 MHz, DMSO-*d*₆) δ 158.8, 157.6, 157.0, 152.3, 138.0, 123.3, 119.9, 113.1, 109.2, 97.9, 95.1, 55.7, 55.2, 54.5, 53.0, 52.2, 32.2, 27.2, 24.3, 14.9; ESI-MS (m/z) 365.0 [M + H]⁺, 387.0 [M + Na]⁺, 363.1 [M – H][–]; HPLC method B t_r = 2.744 min.

3-(3-(Methyl(7-(trifluoromethyl)-9H-pyrimido[4,5-b]indol-4-yl)amino)piperidin-1-yl)propanenitrile (5f). The title compound was prepared from N-methyl-N-(piperidin-3-yl)-7-(trifluoromethyl)-9H-pyrimido[4,5-b]indol-4-amine (85.0 mg, 0.24 mmol) and acrylonitrile (19.1 mg, 0.36 mmol) in dry MeOH (3 mL) according to general procedure A. Purification twice by flash column chromatography (SiO₂, DCM/EtOH gradient elution from 97:3 to 4:1 and SiO₂, DCM/(2 N NH₃ in MeOH) gradient elution from 99:1 to 92:8) gave 36 mg of the product (37% yield). ¹H NMR (300 MHz, DMSO-*d*₆) δ 12.44 (s, 1H), 8.44 (s, 1H), 8.00 (d, *J* = 8.5 Hz, 1H), 7.74 (s, 1H), 7.64 (d, *J* = 8.5 Hz, 1H), 4.59–4.45 (m, 1H), 3.19 (s, 3H), 3.15–3.07 (m, 1H), 2.92–2.83 (m, 1H), 2.77–2.69 (m, 2H), 2.68–2.60 (m, 2H), 2.46–2.35 (m, 1H), 2.02–1.91 (m, 1H), 1.84–1.66 (m, 3H), 1.60–1.42 (m, 1H); ESI-MS (m/z) 403.1 [M + H]⁺, 425.0 [M + Na]⁺, 401.0 [M – H][–]; HPLC method B t_r = 5.218 min.

3-(3-((6-Chloro-9H-pyrimido[4,5-b]indol-4-yl)(methylamino)piperidin-1-yl)propanenitrile (5g). The title compound was prepared from 6-chloro-N-methyl-N-(piperidin-3-yl)-9H-pyrimido[4,5-b]indol-4-amine (45.0 mg, 0.14 mmol) and acrylonitrile (16.6 mg, 0.31 mmol) in HPLC-grade MeOH (13 mL) according to general procedure A. Purification by flash column chromatography (SiO₂, DCM/MeOH gradient elution from 95.5:4.5 to 93.5:6.5) gave 44 mg of a white solid (84% yield). ¹H NMR (400 MHz, DMSO-*d*₆) δ 12.23 (s, 1H), 8.40 (s,

1H), 7.73 (d, *J* = 1.4 Hz, 1H), 7.49 (d, *J* = 8.6 Hz, 1H), 7.41 (dd, *J* = 8.5, 1.5 Hz, 1H), 4.48–4.36 (m, 1H), 3.17 (s, 3H), 3.03–2.94 (m, 1H), 2.90–2.81 (m, 1H), 2.72–2.61 (m, 4H), 2.43–2.34 (m, 1H), 2.05–1.94 (m, 1H), 1.92–1.70 (m, 3H), 1.63–1.49 (m, 1H); ¹³C NMR (101 MHz, DMSO-*d*₆) δ 159.5, 157.5, 153.9, 135.1, 124.6, 124.4, 121.6, 120.8, 119.8, 112.6, 96.8, 55.4, 54.7, 52.9, 51.9, 32.8, 27.2, 24.3, 14.7; ESI-MS (m/z) 369.4 [M + H]⁺, 391.4 [M + Na]⁺, 367.4 [M – H][–]; HPLC method A t_r = 6.421 min.

3-(3-((6-Bromo-9H-pyrimido[4,5-b]indol-4-yl)(methylamino)piperidin-1-yl)propanenitrile (5h). The title compound was prepared from 6-bromo-N-methyl-N-(piperidin-3-yl)-9H-pyrimido[4,5-b]indol-4-amine (55.0 mg, 0.15 mmol) and acrylonitrile (17.8 mg, 0.34 mmol) in HPLC-grade MeOH (25 mL) according to general procedure A. Purification by flash column chromatography (SiO₂, DCM/MeOH gradient elution from 95.5:4.5 to 93.5:6.5) gave 48 mg of a white solid (76% yield). ¹H NMR (300 MHz, DMSO-*d*₆) δ 12.25 (s, 1H), 8.40 (s, 1H), 7.86 (d, *J* = 1.5 Hz, 1H), 7.53 (dd, *J* = 8.6, 1.7 Hz, 1H), 7.44 (d, *J* = 8.5 Hz, 1H), 4.48–4.35 (m, 1H), 3.16 (s, 3H), 3.02–2.91 (m, 1H), 2.91–2.81 (m, 1H), 2.75–2.59 (m, 4H), 2.46–2.34 (m, 1H), 2.05–1.70 (m, 4H), 1.65–1.49 (m, 1H); ¹³C NMR (101 MHz, DMSO-*d*₆) δ 159.5, 157.3, 154.0, 135.4, 127.1, 124.5, 121.4, 119.9, 113.1, 112.5, 96.7, 55.4, 54.8, 52.9, 51.9, 32.7, 27.3, 24.3, 14.7; ESI-MS (m/z) 413.1 [M + H]⁺, 435.0 [M + Na]⁺, 411.1 [M – H][–]; HPLC method A t_r = 4.195 min.

3-(3-((5-Chloro-9H-pyrimido[4,5-b]indol-4-yl)(methylamino)piperidin-1-yl)propanenitrile (5i). The title compound was prepared from 5-chloro-N-methyl-N-(piperidin-3-yl)-9H-pyrimido[4,5-b]indol-4-amine (47.0 mg, 0.15 mmol) and acrylonitrile (17.4 mg, 0.33 mmol) in HPLC grade MeOH (13.5 mL) according to general procedure A (reaction time 20 h). Purification by flash column chromatography (SiO₂, DCM/MeOH 94.5:5.5) gave 38 mg of a white solid. ¹H NMR (400 MHz, DMSO-*d*₆) δ 12.26 (s, 1H), 8.37 (s, 1H), 7.45–7.34 (m, 2H), 7.27 (dd, *J* = 7.5, 0.8 Hz, 1H), 4.49–4.33 (m, 1H), 3.03–2.76 (m, 5H), 2.71–2.54 (m, 4H), 2.37–2.19 (m, 1H), 2.01–1.46 (m, 5H); ESI-MS (m/z) 369.3 [M + H]⁺, 391.3 [M + Na]⁺, 367.3 [M – H][–]; HPLC method A t_r = 3.343 min.

3-(3-((7-Chloro-2-methyl-9H-pyrimido[4,5-b]indol-4-yl)(methylamino)piperidin-1-yl)propanenitrile (5j). The title compound was prepared from 7-chloro-N-2-dimethyl-N-(piperidin-3-yl)-9H-pyrimido[4,5-b]indol-4-amine (60.0 mg, 0.18 mmol) and acrylonitrile (21.2 mg, 0.40 mmol) in HPLC-grade MeOH (17 mL) according to general procedure A. Purification by flash column chromatography (SiO₂, DCM/MeOH gradient elution from 96:4 to 94:6) gave 55 mg of a beige solid (79% yield). ¹H NMR (300 MHz, DMSO-*d*₆) δ 11.99 (s, 1H), 7.72 (d, *J* = 8.7 Hz, 1H), 7.44 (d, *J* = 2.0 Hz, 1H), 7.30 (dd, *J* = 8.6, 2.1 Hz, 1H), 4.49–4.35 (m, 1H), 3.11 (s, 3H), 3.09–3.02 (m, 1H), 2.90–2.80 (m, 1H), 2.75–2.67 (m, 2H), 2.66–2.55 (m, 2H), 2.48 (s, 3H), 2.41–2.29 (m, 1H), 2.02–1.89 (m, 1H), 1.82–1.63 (m, 3H), 1.58–1.43 (m, 1H); ¹³C NMR (50 MHz, DMSO-*d*₆) δ 162.6, 159.4, 158.4, 137.4, 128.7, 123.5, 120.5, 120.2, 118.8, 110.8, 94.8, 55.6, 54.8, 53.1, 52.5, 32.4, 27.4, 25.9, 24.4, 15.1; ESI-MS (m/z) 382.9 [M + H]⁺, 404.9 [M + Na]⁺, 380.9 [M – H][–]; HPLC method A t_r = 5.951 min.

Detailed Procedures for the Preparation of Final Compound 11. *tert*-Butyl 3-((7-Iodo-9H-pyrimido[4,5-b]indol-4-yl)(methylamino)piperidine-1-carboxylate (9). The title compound was prepared by a two-step procedure. In the first step, 4-chloro-7-iodo-9-tosyl-9H-pyrimido[4,5-b]indole (6) (590.0 mg, 1.22 mmol), *N*-Boc-3-(methylamino)piperidine (339.8 mg, 1.59 mmol), and DIPEA (473.0 mg, 3.66 mmol) were stirred in dry DMF (16 mL) at 60 °C for 2 h. After cooling to rt, the mixture was poured into ice-cold water, and a saturated NH₄Cl solution (50 mL) was added. The resulting precipitate was filtered off and dried over P₂O₅ in vacuo to yield 779 mg of crude *tert*-butyl 3-((7-iodo-9-tosyl-9H-pyrimido[4,5-b]indol-4-yl)(methylamino)piperidine-1-carboxylate (8) as a beige solid (97% crude yield), which was used in the second step without further purification. A small portion was purified by flash column chromatography for analytical purposes (SiO₂, petroleum ether/EtOAc gradient elution from 3:2 to 1:1). ¹H NMR (300 MHz, CDCl₃) δ 8.86 (d, *J* = 1.4 Hz, 1H), 8.62 (s, 1H), 8.09 (d, *J* = 8.4 Hz, 2H), 7.74 (dd, *J* = 8.4, 1.4 Hz, 1H), 7.41 (d, *J* = 7.9 Hz, 1H), 7.27 (d, *J* = 8.1 Hz, 2H; overlap with the

CHCl₃ signal), 4.47–3.90 (m, 3H), 3.11 (s, 3H), 3.08–2.98 (m, 1H), 2.77–2.60 (m, 1H), 2.37 (s, 3H), 2.01–1.71 (m, 3H), 1.64–1.29 (m, 10H); ¹³C NMR (50 MHz, CDCl₃) δ 160.5, 157.0, 154.8, 154.4, 145.8, 136.4, 135.4, 133.2, 129.8, 128.2, 124.0, 123.1, 121.3, 101.2, 91.3, 80.0, 55.6 (br), 46.7, 44.1 (br), 33.7 (br), 28.5, 28.1, 24.8, 21.8; ESI-MS (*m/z*) 684.7 [M + Na]⁺, 660.8 [M – H][–]; HPLC method A *t_r* = 10.993 min.

Crude *tert*-butyl 3-((7-iodo-9-tosyl-9H-pyrimido[4,5-*b*]indol-4-yl)-(methyl)amino)piperidine-1-carboxylate (**8**) (680 mg) was dissolved in dry THF (30 mL). To the mixture was added *Kt*BuO (807.4 mg, 7.2 mmol), and the mixture was stirred at rt for 1 h. A saturated NH₄Cl solution (50 mL) was added, and the mixture was extracted with EtOAc (3 × 30 mL). Combined organic layers were dried over Na₂SO₄ and concentrated under reduced pressure. Purification of the residue twice by flash column chromatography (SiO₂, DCM/MeOH 95:5 and SiO₂, DCM/MeOH gradient elution from 97.5:2.5 to 93:7) gave 292 mg of a beige solid (56% yield). ¹H NMR (300 MHz, CDCl₃) δ 11.30 (s, 1H), 8.52 (s, 1H), 7.92 (d, *J* = 1.1 Hz, 1H), 7.61 (dd, *J* = 8.5, 1.4 Hz, 1H), 7.53 (d, *J* = 8.5 Hz, 1H), 4.55–4.04 (m, 3H), 3.29 (s, 3H), 3.11–2.98 (m, 1H), 2.78–2.61 (m, 1H), 2.10–1.76 (m, 3H), 1.74–1.30 (m, 10H); ESI-MS (*m/z*) 530.6 [M + Na]⁺, 506.6 [M – H][–]; HPLC method A *t_r* = 9.541 min.

7-Iodo-N-methyl-N-(piperidin-3-yl)-9H-pyrimido[4,5-*b*]indol-4-amine (10). *tert*-Butyl 3-((7-iodo-9H-pyrimido[4,5-*b*]indol-4-yl)-(methyl)amino)piperidine-1-carboxylate (**9**) (240.0 mg, 0.473 mmol) was suspended in dry DCM (7 mL). Then, TFA (1.5 mL) was added to the mixture. The mixture was stirred at rt for 30 min and then concentrated under reduced pressure. Residual TFA was neutralized by the addition of a saturated NaHCO₃ solution (30 mL), which resulted in a precipitate. The precipitate was filtered off, washed with a saturated NaHCO₃ solution and demineralized water, and dried over P₂O₅ in vacuo to yield 199 mg of a beige solid (>100% crude yield), which was used in the next step without further purification. ¹H NMR (300 MHz, MeOD) δ 8.35 (s, 1H), 7.86 (s, 1H), 7.65–7.52 (m, 2H), 4.55–4.40 (m, 1H), 3.24 (s, 3H), 3.14–3.05 (m, 1H), 3.02–2.84 (m, 2H), 2.60–2.47 (m, 1H), 2.15–1.84 (m, 3H), 1.77–1.59 (m, 1H); ESI-MS (*m/z*) 408.3 [M + H]⁺, 406.3 [M – H][–]; HPLC method A *t_r* = 4.563 min.

3-(3-((7-Iodo-9H-pyrimido[4,5-*b*]indol-4-yl)(methyl)amino)piperidin-1-yl)propanenitrile (11). The title compound was prepared from 7-iodo-*N*-methyl-*N*-(piperidin-3-yl)-9H-pyrimido[4,5-*b*]indol-4-amine (**10**) (70.0 mg, 0.17 mmol) and acrylonitrile (20.1 mg, 0.38 mmol) in HPLC-grade MeOH (30 mL) according to general procedure A. Purification by flash column chromatography (SiO₂, DCM/MeOH 95:5) gave 35 mg of a white solid (44% yield). ¹H NMR (400 MHz, DMSO-*d*₆) δ 12.15 (s, 1H), 8.40 (s, 1H), 7.79 (s, 1H), 7.67–7.53 (m, 2H), 4.51–4.37 (m, 1H), 3.13 (s, 3H), 3.09–3.01 (m, 1H), 2.90–2.80 (m, 1H), 2.76–2.67 (m, 2H), 2.67–2.58 (m, 2H), 2.42–2.31 (m, 1H), 2.01–1.89 (m, 1H), 1.82–1.63 (m, 3H), 1.58–1.41 (m, 1H); ¹³C NMR (101 MHz, DMSO-*d*₆) δ 159.5, 156.9, 153.9, 137.9, 128.9, 124.4, 120.0, 119.5, 119.2, 97.1, 89.3, 55.6, 54.7, 53.0, 52.2, 32.5, 27.2, 24.3, 15.0; ESI-MS (*m/z*) 461.2 [M + H]⁺, 483.2 [M + Na]⁺, 459.2 [M – H][–]; HPLC method A *t_r* = 5.555 min.

Detailed Procedures for the Preparation of Final Compound 15. *tert*-Butyl 3-(Methyl(7-((trimethylsilyl)ethynyl)-9H-pyrimido[4,5-*b*]indol-4-yl)amino)piperidine-1-carboxylate (**12**). A mixture of *tert*-butyl 3-((7-iodo-9H-pyrimido[4,5-*b*]indol-4-yl)(methyl)amino)piperidine-1-carboxylate (**9**) (310.0 mg, 0.61 mmol), CuI (23.3 mg, 0.12 mmol), and Pd(PPh₃)₄ (70.6 mg, 0.06 mmol) in dry DMF was degassed under reduced pressure by sonication and subsequently set under an Ar atmosphere. To the mixture were added TMS-acetylene (180.0 mg, 1.83 mmol) and TEA (123.0 mg, 1.22 mmol), and the mixture was stirred at 50 °C under an Ar atmosphere overnight. After cooling to rt, a saturated NH₄Cl solution (3 mL) was added, and the mixture was extracted with EtOAc (5 × 3 mL). Combined organic layers were washed with a saturated NaCl solution (4 × 7 mL), dried over Na₂SO₄, and concentrated under reduced pressure. Purification of the residue by flash column chromatography (SiO₂, DCM/MeOH gradient elution from 30:1 to 93:7) gave 280 mg of a brown solid (96% yield) that contained approximately 10% of an impurity, which was detected in the ¹H NMR spectra and assumed to be triphenylphosphine

oxide. ¹H NMR (400 MHz, CDCl₃) δ 11.81 (s, 1H), 8.61 (s, 1H), 7.72 (d, *J* = 8.3 Hz, 1H), 7.64 (s, 1H), 7.39 (dd, *J* = 8.3, 1.4 Hz, 1H), 4.55–4.02 (m, 3H), 3.28 (s, 3H), 3.11–3.00 (m, 1H), 2.75–2.60 (m, 1H), 2.11–2.04 (m, 1H), 1.97–1.77 (m, 2H), 1.70–1.57 (m, 1H), 1.42 (s, 9H), 0.29 (s, 9H); ESI-MS (*m/z*) 500.4 [M + Na]⁺, 476.5 [M – H][–]; HPLC method A *t_r* = 11.448 min.

***N*-Methyl-*N*-(piperidin-3-yl)-7-((trimethylsilyl)ethynyl)-9H-pyrimido[4,5-*b*]indol-4-amine (13).** *tert*-Butyl 3-((trimethylsilyl)ethynyl)-9H-pyrimido[4,5-*b*]indol-4-yl)amino)piperidine-1-carboxylate (**12**) (115.2 mg, 0.24 mmol) was suspended in dry 4 N HCl in 1,4-dioxane (6 mL). The mixture was stirred at rt for 20 min (the reaction time was strictly kept short to prevent by-product formation). A saturated NaHCO₃ solution (20 mL) was added for neutralization, and the mixture was extracted with EtOAc (10 × 20 mL). Combined organic layers were dried over Na₂SO₄ and concentrated under reduced pressure. Purification of the residue by flash column chromatography (SiO₂, DCM/(2 N NH₃ in MeOH) 9:1) gave 38 mg of a solid (42% yield). ¹H NMR (400 MHz, MeOD) δ 8.33 (s, 1H), 7.76 (d, *J* = 8.4 Hz, 1H), 7.56 (s, 1H), 7.35 (d, *J* = 8.3 Hz, 1H), 4.54–4.45 (m, 1H), 3.26 (s, 3H), 3.13–3.07 (m, 1H), 3.02–2.95 (m, 1H), 2.94–2.86 (m, 1H), 2.59–2.49 (m, 1H), 2.14–1.87 (m, 3H), 1.76–1.63 (m, 1H), 0.26 (s, 9H); HPLC method A *t_r* = 7.008 min.

3-(3-((7-Ethynyl-9H-pyrimido[4,5-*b*]indol-4-yl)(methyl)amino)piperidin-1-yl)propanenitrile (15). Acrylonitrile (8.0 mg, 0.15 mmol) and TEA (15.3 mg, 0.15 mmol) were added to a stirring solution of *N*-methyl-*N*-(piperidin-3-yl)-7-((trimethylsilyl)ethynyl)-9H-pyrimido[4,5-*b*]indol-4-amine (**13**) in HPLC-grade MeOH (20 mL), and the mixture was stirred at rt under a N₂ atmosphere. Due to the slow conversion, reactants were added repeatedly as follows: acrylonitrile (8.0 mg, 0.15 mmol) and TEA (15.3 mg, 0.15 mmol) after 3 h of stirring, and additional acrylonitrile (4.0 mg, 0.08 mmol) and TEA (7.7 mg, 0.08 mmol) after 6 h of stirring. After stirring at rt under a N₂ atmosphere overnight, K₂CO₃ (16.7 mg, 0.12 mmol) was added to the mixture to initiate the TMS deprotection, and stirring continued. Additional K₂CO₃ (10.0 mg, 0.07 mmol) was added to the mixture, and stirring continued for two days. The mixture was concentrated under reduced pressure, and the residue was purified three times by flash column chromatography (SiO₂, DCM/MeOH 95:5; SiO₂, DCM/(2 N NH₃ in MeOH) gradient elution from 96.5:3.5 to 93:7; and SiO₂, DCM/MeOH gradient elution from 96.5:3.5 to 93:7) to yield 15 mg of a light beige solid (41% yield). ¹H NMR (400 MHz, DMSO-*d*₆) δ 12.18 (s, 1H), 8.39 (s, 1H), 7.79 (d, *J* = 8.4 Hz, 1H), 7.54 (d, *J* = 1.1 Hz, 1H), 7.40 (dd, *J* = 8.3, 1.4 Hz, 1H), 4.56–4.41 (m, 1H), 4.19 (s, 1H), 3.16 (s, 3H), 3.13–3.06 (m, 1H), 2.94–2.84 (m, 1H), 2.80–2.59 (m, 4H), 2.47–2.35 (m, 1H), 2.06–1.90 (m, 1H), 1.89–1.67 (m, 3H), 1.60–1.45 (m, 1H); ¹³C NMR (101 MHz, DMSO-*d*₆) δ 159.5, 157.6, 153.9, 136.2, 124.0, 122.7, 120.1, 117.4, 114.3, 97.2, 84.2, 80.4, 55.6, 54.6, 53.0, 52.2, 32.7, 27.1, 24.2, 14.9; ESI-MS (*m/z*) 359.1 [M + H]⁺, 381.1 [M + Na]⁺, 357.0 [M – H][–]; HPLC method A *t_r* = 3.865 min.

Detailed Procedures for the Preparation of Final Compound (S)-15. *tert*-Butyl (S)-3-((7-iodo-9-tosyl-9H-pyrimido[4,5-*b*]indol-4-yl)amino)piperidine-1-carboxylate ((S)-7). 4-Chloro-7-iodo-9-tosyl-9H-pyrimido[4,5-*b*]indole (**6**) (500.0 mg, 1.03 mmol), (S)-*N*-Boc-3-aminopiperidine (288.8 mg, 1.45 mmol), and DIPEA (399.3 mg, 3.09 mmol) were stirred in dry DMF (14 mL) at 80 °C for 16 h. After cooling to rt, the mixture was poured into ice-cold water, and a saturated NH₄Cl solution (75 mL) was added. The mixture was extracted twice with EtOAc (175 and 25 mL). Combined organic layers were washed with a saturated NaCl solution (3 × 30 mL), dried over Na₂SO₄, and concentrated under reduced pressure. Purification of the residue by flash column chromatography (SiO₂, petroleum ether/(EtOAc/MeOH 95:5) 2:1) gave 360 mg of a yellow solid (54% yield). ESI-MS 671.0 [M + Na]⁺, 646.9 [M – H][–]; HPLC method A *t_r* = 11.182 min.

***tert*-Butyl (S)-3-((7-Iodo-9H-pyrimido[4,5-*b*]indol-4-yl)(methyl)amino)piperidine-1-carboxylate ((S)-9).** The title compound was prepared by a two-step procedure. In the first step, a solution of *tert*-butyl (S)-3-((7-iodo-9-tosyl-9H-pyrimido[4,5-*b*]indol-4-yl)amino)piperidine-1-carboxylate ((S)-7) (342.0 mg, 0.53 mmol) in dry DMF (6 mL) was stirred in a flame-dried Schlenk tube under an Ar

atmosphere and then cooled to 0 °C. NaH (31.0 mg of a 60% dispersion in mineral oil, 0.752 mmol) was added, and the mixture was stirred for 30 min for deprotonation. The mixture was then cooled by a bath of MeOH and ice before the addition of iodomethane (112.5 mg, 0.79 mmol). Stirring continued under an Ar atmosphere for 2.5 h, and the mixture was left to warm to rt. A saturated NH₄Cl solution (5 mL) was added, and the mixture was poured into ice-cold water, which was then extracted with EtOAc (3 × 50 mL). Combined organic layers were dried over Na₂SO₄ and concentrated under reduced pressure to afford 368 mg of crude (S)-3-((7-iodo-9-tosyl-9H-pyrimido[4,5-*b*]indol-4-yl)(methylamino)piperidine-1-carboxylate ((S)-8), which was used in the second step without further purification. The crude material was dissolved in dry THF (15 mL). K₂BuO (414.7 mg, 3.70 mmol) was added, and the mixture was stirred at rt for 2.5 h. A saturated NH₄Cl solution (20 mL) was added, and the mixture was extracted with EtOAc (3 × 20 mL). Combined organic layers were dried over Na₂SO₄ and concentrated under reduced pressure. Purification of the residue by flash column chromatography (SiO₂, DCM/MeOH gradient elution from 97.5:2.5 to 96.5:3.5) gave 157 mg of a white solid (59% yield). ¹H NMR (400 MHz, CDCl₃) δ 11.58 (br s, 1H), 8.55 (s, 1H), 7.89 (s, 1H), 7.59 (dd, *J* = 8.5, 1.3 Hz, 1H), 7.53 (d, *J* = 8.5 Hz, 1H), 4.52–4.00 (m, 3H), 3.27 (s, 3H), 3.10–3.00 (m, 1H), 2.76–2.60 (m, 1H), 2.10–1.77 (m, 3H), 1.71–1.56 (m, 1H), 1.43 (s, 9H); ESI-MS 508.9 [M + H]⁺, 530.9 [M + Na]⁺, 506.9 [M – H][–]; HPLC method A *t*_r = 10.246 min.

(S)-7-Iodo-N-methyl-N-(piperidin-3-yl)-9H-pyrimido[4,5-*b*]indol-4-amine ((S)-10). *tert*-Butyl (S)-3-((7-iodo-9H-pyrimido[4,5-*b*]indol-4-yl)(methylamino)piperidine-1-carboxylate ((S)-9) (140.0 mg, 0.28 mmol) was stirred in a mixture of dry DCM (4 mL) and TFA (0.8 mL) at rt for 1 h. The mixture was concentrated under reduced pressure, and residual TFA was neutralized by the addition of a saturated NaHCO₃ solution (30 mL). The mixture was then extracted with EtOAc (3 × 25 mL), and MeOH was added to improve the solubility of the product in the organic layer. Combined organic layers were washed with a saturated NaHCO₃ solution (3 × 30 mL), dried over Na₂SO₄, and evaporated to dryness to afford 113 mg of a beige solid (100% yield). ¹H NMR (400 MHz, MeOD) δ 8.35 (s, 1H), 7.85 (s, 1H), 7.61–7.54 (m, 2H), 4.53–4.44 (m, 1H), 3.24 (s, 3H), 3.15–3.08 (m, 1H), 3.03–2.96 (m, 1H), 2.95–2.87 (m, 1H), 2.61–2.50 (m, 1H), 2.13–1.86 (m, 3H), 1.76–1.63 (m, 1H); ESI-MS (*m/z*) 408.5 [M + H]⁺, 406.5 [M – H][–]; HPLC method A *t*_r = 5.134 min.

(S)-3-((7-Iodo-9H-pyrimido[4,5-*b*]indol-4-yl)(methylamino)piperidin-1-yl)propanenitrile ((S)-11). Acrylonitrile (16.6 mg, 0.31 mmol) and triethylamine (26.5 mg, 0.26 mmol) were added to a stirring solution of (S)-7-iodo-N-methyl-N-(piperidin-3-yl)-9H-pyrimido[4,5-*b*]indol-4-amine ((S)-10) (107.0 mg, 0.26 mmol) in HPLC-grade MeOH (45 mL). The mixture was stirred at rt for 16 h and then concentrated under reduced pressure. Purification of the residue by flash column chromatography (SiO₂, DCM/MeOH gradient elution from 95:5 to 92.5:7.5) gave 89 mg of a white solid (74% yield). ¹H NMR (400 MHz, DMSO-*d*₆) δ 12.15 (s, 1H), 8.40 (s, 1H), 7.79 (d, *J* = 1.2 Hz, 1H), 7.62 (dd, *J* = 8.5, 1.5 Hz, 1H), 7.58 (d, *J* = 8.5 Hz, 1H), 4.51–4.38 (m, 1H), 3.13 (s, 3H), 3.09–3.02 (m, 1H), 2.89–2.81 (m, 1H), 2.75–2.67 (m, 2H), 2.67–2.58 (m, 2H), 2.41–2.32 (m, 1H), 2.00–1.88 (m, 1H), 1.81–1.65 (m, 3H), 1.56–1.42 (m, 1H); ¹³C NMR (101 MHz, DMSO-*d*₆) δ 159.5, 156.9, 154.0, 137.9, 129.0, 124.4, 120.1, 119.6, 119.2, 97.1, 89.4, 55.7, 54.8, 53.0, 52.2, 32.6, 27.3, 24.3, 15.0.

(S)-3-((7-((Trimethylsilyl)ethynyl)-9H-pyrimido[4,5-*b*]indol-4-yl)amino)piperidin-1-yl)propanenitrile ((S)-14). A solution of (S)-3-((7-iodo-9H-pyrimido[4,5-*b*]indol-4-yl)(methylamino)piperidin-1-yl)propanenitrile ((S)-11) (40.0 mg, 0.09 mmol) and CuI (1.65 mg, 0.009 mmol) in dry DMF (1.5 mL) was degassed and stirred in a Schlenk tube under an Ar atmosphere. To the mixture were added triethylamine (17.6 mg, 0.17 mmol) and trimethylsilylacetylene (25.6 mg, 0.26 mmol) under an Ar flow, followed by a small amount of bis(triphenylphosphine)palladium(II) dichloride (5 mg, 0.007 mmol). The mixture was stirred at rt for 2 h, then diluted with EtOAc and washed with a saturated NaHCO₃ solution (2 × 10 mL). The organic layer was dried over Na₂SO₄ and concentrated under reduced pressure. Purification of the residue by flash column chromatography (SiO₂,

DCM/MeOH 95:5) gave 32 mg of a yellow solid (86% yield). ¹H NMR (400 MHz, CDCl₃) δ 12.49 (br s, 1H), 8.59 (br s, 1H), 7.69 (d, *J* = 8.4 Hz, 1H), 7.63 (s, 1H), 7.40 (dd, *J* = 8.3, 0.8 Hz, 1H), 4.71–4.58 (m, 1H), 3.27 (s, 3H), 3.19–3.12 (m, 1H), 2.98–2.91 (m, 1H), 2.85–2.74 (m, 2H), 2.58 (t, *J* = 7.0 Hz, 2H), 2.50–2.41 (m, 1H), 2.15–2.07 (m, 1H), 2.03–1.94 (m, 1H), 1.90–1.71 (m, 3H), 0.35–0.21 (m, 9H); ¹³C NMR (101 MHz, CDCl₃) δ 160.2, 157.8, 153.0, 136.4, 124.9, 122.6, 120.5, 119.5, 118.8, 115.0, 105.8, 98.8, 94.5, 56.1, 55.1, 53.8, 53.1, 33.6, 27.9, 24.6, 16.0, 0.2; ESI-MS (*m/z*) 431.7 [M + H]⁺, 453.7 [M + Na]⁺, 429.7 [M – H][–]; HPLC method A *t*_r = 7.262 min.

(S)-3-((7-((Trimethylsilyl)ethynyl)-9H-pyrimido[4,5-*b*]indol-4-yl)amino)piperidin-1-yl)propanenitrile ((S)-15). (S)-3-((Methyl(7-((trimethylsilyl)ethynyl)-9H-pyrimido[4,5-*b*]indol-4-yl)amino)piperidin-1-yl)propanenitrile ((S)-14) (32.0 mg, 0.07 mmol) and K₂CO₃ (12.0 mg, 0.09 mmol) were stirred in HPLC-grade MeOH (4 mL) at rt under a N₂ atmosphere for 3 h. The mixture was concentrated under reduced pressure, and the residue was redissolved in EtOAc. The solution was washed with a saturated NaHCO₃ solution (2 × 15 mL), dried over Na₂SO₄, and concentrated under reduced pressure. Purification of the residue by flash column chromatography (SiO₂, DCM/MeOH 95:5) gave 18 mg of a white solid (68% yield). ¹H NMR (400 MHz, DMSO-*d*₆) δ 12.18 (s, 1H), 8.39 (s, 1H), 7.79 (d, *J* = 8.4 Hz, 1H), 7.54 (s, 1H), 7.40 (dd, *J* = 8.3, 1.1 Hz, 1H), 4.53–4.43 (m, 1H), 4.19 (s, 1H), 3.16 (s, 3H), 3.11–3.04 (m, 1H), 2.90–2.83 (m, 1H), 2.76–2.68 (m, 2H), 2.67–2.58 (m, 2H), 2.43–2.33 (m, 1H), 2.01–1.90 (m, 1H), 1.83–1.66 (m, 3H), 1.60–1.43 (m, 1H); ¹³C NMR (101 MHz, DMSO-*d*₆) δ 159.5, 157.6, 153.8, 136.2, 124.0, 122.6, 120.0, 119.9, 117.3, 114.2, 97.2, 84.1, 80.2, 55.6, 54.7, 53.0, 52.2, 32.6, 27.2, 24.3, 15.0; ESI-MS (*m/z*) 359.9 [M + H]⁺, 381.9 [M + Na]⁺, 357.8 [M – H][–]; HPLC method A *t*_r = 3.237 min.

Detailed Procedures for the Preparation of Final Compounds 5k–m. 3-((7-((Methyl(7-phenyl-9H-pyrimido[4,5-*b*]indol-4-yl)amino)piperidin-1-yl)propanenitrile (5k). Degassed dry dioxane (4 mL) and a degassed 0.5 M aq. K₃PO₄ solution (1 mL) were added to 3-((7-chloro-9H-pyrimido[4,5-*b*]indol-4-yl)(methylamino)piperidin-1-yl)propanenitrile (1) (60.0 mg, 0.16 mmol), phenylboronic acid (31.7 mg, 0.26 mmol), and XPhos Pd G3 (4.1 mg, 0.005 mmol) under an Ar atmosphere. The mixture was stirred at 100 °C for 3 h. After cooling the mixture to rt, a saturated NaCl solution (3 mL) was added, and the mixture was extracted with EtOAc (5 × 3 mL). To the mixture were added DCM and MeOH to improve the solubility of the product in the organic layer. Combined organic layers were washed with a saturated NaHCO₃ solution (3 × 20 mL), dried over Na₂SO₄, and concentrated under reduced pressure. Purification of the residue by flash column chromatography (SiO₂, DCM/MeOH gradient elution from 95:5 to 92.5:7.5) gave 40 mg of an off-white solid (60% yield). ¹H NMR (300 MHz, DMSO-*d*₆) δ 12.18 (s, 1H), 8.40 (s, 1H), 7.88 (d, *J* = 8.5 Hz, 1H), 7.78–7.68 (m, 3H), 7.64 (dd, *J* = 8.4, 1.5 Hz, 1H), 7.54–7.45 (m, 2H), 7.42–7.34 (m, 1H), 4.60–4.46 (m, 1H), 3.17 (s, 3H), 3.13–3.05 (m, 1H), 2.93–2.83 (m, 1H), 2.77–2.58 (m, 4H), 2.46–2.34 (m, 1H), 2.03–1.89 (m, 1H), 1.86–1.66 (m, 3H), 1.63–1.42 (m, 1H); ¹³C NMR (101 MHz, DMSO-*d*₆) δ 159.4, 157.4, 153.4, 140.4, 137.3, 136.8, 129.0, 127.2, 126.7, 122.9, 120.0, 119.6, 118.9, 108.9, 97.4, 55.7, 54.7, 53.0, 52.2, 32.5, 27.3, 24.3, 15.0; ESI-MS (*m/z*) 411.1 [M + H]⁺, 433.1 [M + Na]⁺, 409.2 [M – H][–]; HPLC method A *t*_r = 5.034 min.

3-((7-((Furan-2-yl)-9H-pyrimido[4,5-*b*]indol-4-yl)(methylamino)piperidin-1-yl)propanenitrile (5l). Degassed dry dioxane (4 mL) and a degassed 0.5 M aq. K₃PO₄ solution (1 mL) were added to 3-((7-chloro-9H-pyrimido[4,5-*b*]indol-4-yl)(methylamino)piperidin-1-yl)propanenitrile (1) (60.0 mg, 0.16 mmol), 2-furanylboronic acid (29.1 mg, 0.26 mmol), and XPhos Pd G3 (4.1 mg, 0.005 mmol) in a reaction tube. The tube was sealed, and the mixture was stirred at 100 °C for 3 h. After cooling the mixture to rt, a saturated NaCl solution (3 mL) was added, and the mixture was extracted with EtOAc (5 × 3 mL). To the mixture were added DCM and MeOH to improve the solubility of the product in the organic layer. Combined organic layers were washed with a saturated NaHCO₃ solution. The combined NaHCO₃ solution layers were extracted once more with DCM. The organic layers were unified, dried over Na₂SO₄, and

concentrated under reduced pressure. Purification of the residue by flash column chromatography (SiO₂, DCM/MeOH gradient elution from 96:4 to 93:7) gave 43 mg of a beige solid (66% yield). ¹H NMR (400 MHz, DMSO-*d*₆) δ 12.17 (s, 1H), 8.39 (s, 1H), 7.82 (d, *J* = 8.5 Hz, 1H), 7.79–7.72 (m, 2H), 7.68 (dd, *J* = 8.4, 1.1 Hz, 1H), 6.96 (d, *J* = 3.2 Hz, 1H), 6.62 (dd, *J* = 3.2, 1.7 Hz, 1H), 4.56–4.43 (m, 1H), 3.16 (s, 3H), 3.11–3.02 (m, 1H), 2.92–2.82 (m, 1H), 2.78–2.58 (m, 4H), 2.45–2.34 (m, 1H), 2.03–1.90 (m, 1H), 1.86–1.68 (m, 3H), 1.60–1.45 (m, 1H); ¹³C NMR (101 MHz, DMSO-*d*₆) δ 159.3, 157.5, 153.5, 153.4, 142.8, 137.0, 126.9, 122.9, 120.0, 118.8, 116.7, 112.1, 105.6, 105.5, 97.5, 55.6, 54.7, 53.0, 52.1, 32.5, 27.2, 24.3, 14.9; ESI-MS (*m/z*) 401.1 [M + H]⁺, 423.1 [M + Na]⁺, 399.1 [M – H][–]; HPLC method A *t*_r = 4.069 min.

4-((1-(2-Cyanoethyl)piperidin-3-yl)(methylamino)-9H-pyrimido[4,5-*b*]indole-7-carbonitrile (5m). Degassed dry 1,4-dioxane (2 mL) and a degassed 0.01 M aq. KOAc solution (2 mL) were added to 3-(3-((7-chloro-9H-pyrimido[4,5-*b*]indol-4-yl)(methylamino)piperidin-1-yl)propanenitrile (1) (60.0 mg, 0.16 mmol), K₄[Fe(CN)₆]·3H₂O (41.2 mg, 0.10 mmol), BrettPhos Pd G3 (5.2 mg, 0.006 mmol), and BrettPhos (3.1 mg, 0.006 mmol) under an Ar atmosphere. The mixture was stirred at 100 °C under an Ar atmosphere for 2.5 h. To the mixture were added additional BrettPhos Pd G3 and BrettPhos catalysts (1.0 mg each) to promote conversion, and stirring continued at 100 °C for 2 h; however, the conversion seized at ~85%. After cooling the mixture to rt, a saturated NaCl solution (3 mL) was added, and the mixture was extracted with EtOAc (6 × 3 mL). Combined organic layers were dried over Na₂SO₄ and concentrated under reduced pressure. Purification of the residue twice by flash column chromatography (SiO₂, petroleum ether/(EtOAc/MeOH 95:5) gradient elution from 1:1 to 0:1 and SiO₂, DCM/MeOH gradient elution from 95.5:4.5 to 93.5:6.5) gave 15 mg of an off-white solid (26% yield). ¹H NMR (400 MHz, DMSO-*d*₆) δ 12.50 (s, 1H), 8.44 (s, 1H), 7.95 (d, *J* = 8.4 Hz, 1H), 7.88 (s, 1H), 7.67 (dd, *J* = 8.4, 1.2 Hz, 1H), 4.58–4.41 (m, 1H), 3.19 (s, 3H), 3.14–3.06 (m, 1H), 2.96–2.82 (m, 1H), 2.79–2.56 (m, 4H), 2.47–2.31 (m, 1H), 2.06–1.89 (m, 1H), 1.87–1.65 (m, 3H), 1.61–1.47 (m, 1H); ¹³C NMR (101 MHz, DMSO-*d*₆) δ 159.8, 158.2, 154.7, 135.8, 123.5, 123.4, 123.3, 119.6, 114.9, 105.9, 96.8, 55.4, 54.8, 52.9, 52.1, 32.9, 27.0, 24.2, 15.0; ESI-MS (*m/z*) 360.1 [M + H]⁺, 382.1 [M + Na]⁺, 358.1 [M – H][–]; HPLC method A *t*_r = 3.062 min.

Detailed Procedures for the Preparation of Intermediates 16–18.
3-(1-(7-Fluoro-9-tosyl-9H-pyrimido[4,5-*b*]indol-4-yl)octahydro-6H-pyrrolo[2,3-*c*]pyridin-6-yl)propanenitrile (16). 4-Chloro-7-fluoro-9-tosyl-9H-pyrimido[4,5-*b*]indole (3b) (200.0 mg, 0.53 mmol), 3-(octahydro-6H-pyrrolo[2,3-*c*]pyridin-6-yl)propanenitrile (used as a TFA salt and calculated to 37.2 mg of the free base, 0.21 mmol), and DIPEA (275.3 mg, 2.13 mmol) were stirred in dry DMF (6 mL) at 70 °C for 2.5 h. To the mixture were added additional 3-(octahydro-6H-pyrrolo[2,3-*c*]pyridin-6-yl)propanenitrile (used as TFA salt and calculated to 71.0 mg of the free base, 0.40 mmol) and DIPEA (137.7 mg, 1.07 mmol), and stirring at 70 °C continued for 5 h. After cooling the mixture to rt, a saturated NaCl solution (15 mL) was added, and the mixture was extracted with EtOAc (3 × 25 mL). Combined organic layers were washed with a saturated NaCl solution (3 × 25 mL), dried over Na₂SO₄, and concentrated under reduced pressure. Purification of the residue by flash column chromatography (SiO₂, petroleum ether/(EtOAc/MeOH 95:5) gradient elution from 2:1 to 1:3) gave 113 mg of a solid (41% yield). ¹H NMR (400 MHz, CDCl₃) δ 8.51 (s, 1H), 8.22 (d, *J* = 9.8 Hz, 1H), 8.10 (d, *J* = 8.4 Hz, 2H), 7.82 (br s, 1H), 7.26 (d, *J* = 8.2 Hz, 2H, overlap with CHCl₃ signal), 7.14 (td, *J* = 8.7, 2.0 Hz, 1H), 4.67–4.50 (m, 1H), 4.28–4.08 (m, 1H), 3.50–3.41 (m, 1H), 3.19–2.98 (m, 1H), 2.91–2.53 (m, 4H), 2.52–2.13 (m, 7H), 1.99–1.81 (m, 3H), 1.69–1.56 (m, 1H); ESI-MS (*m/z*) 519.5 [M + H]⁺, 541.5 [M + Na]⁺, 517.6 [M – H][–]; HPLC method A *t*_r = 6.594 min.

3-(1-(7-Bromo-9-tosyl-9H-pyrimido[4,5-*b*]indol-4-yl)octahydro-6H-pyrrolo[2,3-*c*]pyridin-6-yl)propanenitrile (17). 7-Bromo-4-chloro-9-tosyl-9H-pyrimido[4,5-*b*]indole (3d) (92.0 mg, 0.21 mmol), 3-(octahydro-6H-pyrrolo[2,3-*c*]pyridin-6-yl)propanenitrile (41.5 mg of the free base, 0.23 mmol), and DIPEA (81.7 mg, 0.63 mmol) were stirred in dry DMF (2.5 mL) at 75 °C for 1.5 h. To the mixture was

added additional 3-(octahydro-6H-pyrrolo[2,3-*c*]pyridin-6-yl)propanenitrile (10.0 mg of the free base, 0.06 mmol), and stirring at 75 °C continued for 3 h. A saturated NaCl solution (10 mL) was added, and the mixture was extracted with EtOAc (3 × 20 mL). Combined organic layers were washed with a saturated NaCl solution (3 × 20 mL), dried over Na₂SO₄, and concentrated under reduced pressure. Purification of the residue by flash column chromatography (SiO₂, petroleum ether/(EtOAc/MeOH 95:5) gradient elution from 2:1 to 1:3) gave 66 mg of an off-white solid (54% yield). ESI-MS 579.7 [M + H]⁺, 601.7 [M + Na]⁺; HPLC method A *t*_r = 7.363 min.

3-(1-(7-Iodo-9-tosyl-9H-pyrimido[4,5-*b*]indol-4-yl)octahydro-6H-pyrrolo[2,3-*c*]pyridin-6-yl)propanenitrile (18). 4-Chloro-7-iodo-9-tosyl-9H-pyrimido[4,5-*b*]indole (6) (200.0 mg, 0.41 mmol), 3-(octahydro-6H-pyrrolo[2,3-*c*]pyridin-6-yl)propanenitrile (used as TFA salt and calculated to 83.8 mg of the free base, 0.47 mmol), and DIPEA (213.7 mg, 1.65 mmol) were stirred in dry DMF (6 mL) at 75 °C for 2.5 h. After cooling the mixture to rt, a saturated NaCl solution (15 mL) was added, and the mixture was extracted with EtOAc (3 × 25 mL). Combined organic layers were washed with a saturated NaCl solution (3 × 20 mL), dried over Na₂SO₄, and concentrated under reduced pressure. Purification of the residue by flash column chromatography (SiO₂, petroleum ether/(EtOAc/MeOH 95:5) gradient elution from 2:1 to 1:3) gave 158 mg of a solid (61% yield). ¹H NMR (400 MHz, CDCl₃) δ 8.84 (s, 1H), 8.53 (s, 1H), 8.09 (d, *J* = 8.4 Hz, 2H), 7.69 (d, 1H), 7.66–7.51 (br s, 1H), 7.27 (d, *J* = 7.3 Hz, 2H, overlap with CHCl₃ signal), 4.62–4.45 (m, 1H), 4.29–4.02 (m, 1H), 3.49–3.41 (m, 1H), 3.21–3.00 (m, 1H), 2.81–2.48 (m, 4H), 2.47–2.23 (m, 7H), 1.95–1.80 (m, 3H), 1.72–1.61 (m, 1H); ESI-MS (*m/z*) 627.2 [M + H]⁺, 649.2 [M + Na]⁺, 625.0 [M – H][–]; HPLC method A *t*_r = 7.423 min.

Detailed Procedures for the Preparation of Final Compounds 19–22.
3-(1-(7-Fluoro-9H-pyrimido[4,5-*b*]indol-4-yl)octahydro-6H-pyrrolo[2,3-*c*]pyridin-6-yl)propanenitrile (19). The title compound was prepared from 3-(1-(7-fluoro-9-tosyl-9H-pyrimido[4,5-*b*]indol-4-yl)octahydro-6H-pyrrolo[2,3-*c*]pyridin-6-yl)propanenitrile (16) (100.0 mg, 0.19 mmol) and K_tBuO (151.4 mg, 1.35 mmol), which were stirred in HPLC-grade THF (10 mL) at rt for 1.5 h. A saturated NaCl solution (10 mL) was added, and the mixture was extracted with EtOAc (4 × 25 mL). Combined organic layers were dried over Na₂SO₄ and concentrated under reduced pressure. Purification of the residue by flash column chromatography (SiO₂, DCM/MeOH gradient elution from 95:5 to 91.5:8.5) gave 43 mg of a solid (61% yield). ¹H NMR (400 MHz, DMSO-*d*₆) δ 12.12 (s, 1H), 8.28 (s, 1H), 8.04 (dd, *J* = 9.0, 5.3 Hz, 1H), 7.19 (dd, *J* = 9.3, 2.6 Hz, 1H), 7.05 (td, *J* = 9.3, 2.6 Hz, 1H), 4.66–4.58 (m, 1H), 4.21–4.11 (m, 1H), 3.86–3.77 (m, 1H), 2.94–2.84 (m, 1H), 2.67–2.46 (m, 6H, overlap with DMSO-*d*₆ signal), 2.44–2.32 (m, 2H), 2.03–1.82 (m, 3H), 1.77–1.68 (m, 1H); ¹³C NMR (101 MHz, DMSO-*d*₆) δ 159.9 (d, *J* = 239.5 Hz), 157.1, 156.4, 153.3, 137.3 (d, *J* = 12.5 Hz), 123.8 (d, *J* = 9.8 Hz), 119.9, 116.3, 107.9 (d, *J* = 23.2 Hz), 97.5 (d, *J* = 25.8 Hz), 96.2, 56.5, 53.2, 52.9, 49.1, 48.5, 34.1, 26.7, 25.5, 14.8; ESI-MS (*m/z*) 387.0 [M + Na]⁺, 363.0 [M – H][–]; HPLC method A *t*_r = 3.053 min.

3-(1-(7-Bromo-9H-pyrimido[4,5-*b*]indol-4-yl)octahydro-6H-pyrrolo[2,3-*c*]pyridin-6-yl)propanenitrile (20). The title compound was prepared from 3-(1-(7-bromo-9-tosyl-9H-pyrimido[4,5-*b*]indol-4-yl)octahydro-6H-pyrrolo[2,3-*c*]pyridin-6-yl)propanenitrile (17) (66.0 mg, 0.11 mmol) and K_tBuO (89.5 mg, 0.80 mmol), which were stirred in HPLC-grade THF (4 mL) for 2 h. A saturated NH₄Cl solution (25 mL) was added, and the mixture was extracted with EtOAc (3 × 25 mL). Combined organic layers were dried over Na₂SO₄ and concentrated under reduced pressure. Purification of the residue by flash column chromatography (SiO₂, DCM/MeOH 95.5:4.5) gave 19 mg of a beige solid (40% yield). ¹H NMR (400 MHz, DMSO-*d*₆) δ 12.13 (s, 1H), 8.30 (s, 1H), 7.99 (d, *J* = 8.8 Hz, 1H), 7.57 (d, *J* = 2.0 Hz, 1H), 7.35 (dd, *J* = 8.7, 2.0 Hz, 1H), 4.68–4.58 (m, 1H), 4.21–4.10 (m, 1H), 3.89–3.77 (m, 1H), 2.96–2.86 (m, 1H), 2.66–2.48 (m, 6H, overlap with DMSO-*d*₆ signal), 2.44–2.33 (m, 2H), 2.07–1.84 (m, 3H), 1.77–1.69 (m, 1H); ¹³C NMR (101 MHz, DMSO-*d*₆) δ 156.8, 156.6, 154.0, 137.6, 124.2, 123.0, 120.0, 118.9, 116.8, 113.6, 96.0, 56.7, 53.2, 52.9, 49.1, 48.5, 34.1, 26.7, 25.5, 14.9. ESI-MS (*m/z*) 425.5 [M +

H⁺, 447.5 [M + Na]⁺, 423.4 [M - H]⁻; HPLC method A *t_r* = 3.996 min.

3-(1-(7-Iodo-9H-pyrimido[4,5-*b*]indol-4-yl)octahydro-6H-pyrrolo[2,3-*c*]pyridin-6-yl)propanenitrile (21). 3-(1-(7-Iodo-9H-pyrimido[4,5-*b*]indol-4-yl)octahydro-6H-pyrrolo[2,3-*c*]pyridin-6-yl)propanenitrile (18) (100.0 mg, 0.16 mmol) and K₂CO₃ (125.4 mg, 1.11 mmol) were stirred in HPLC-grade THF (10 mL) at rt for 2 h. A saturated NaCl solution (10 mL) was added, and the mixture was extracted with EtOAc (4 × 20 mL). Combined organic layers were dried over Na₂SO₄ and concentrated under reduced pressure. Purification of the residue by flash column chromatography (SiO₂, DCM/MeOH gradient elution from 95:5 to 91.5:8.5) gave 47 mg of a light beige solid (62% yield). ¹H NMR (400 MHz, DMSO-*d*₆) δ 12.07 (s, 1H), 8.30 (s, 1H), 7.86 (d, *J* = 8.7 Hz, 1H), 7.74 (d, *J* = 1.4 Hz, 1H), 7.51 (dd, *J* = 8.6, 1.4 Hz, 1H), 4.66–4.58 (m, 1H), 4.20–4.10 (m, 1H), 3.87–3.77 (m, 1H), 2.95–2.86 (m, 1H), 2.68–2.47 (m, 6H, overlap with DMSO-*d*₆ signal), 2.43–2.33 (m, 2H), 2.06–1.83 (m, 3H), 1.78–1.69 (m, 1H). ESI-MS (*m/z*) 473.2 [M + H]⁺, 495.1 [M + Na]⁺, 471.1 [M - H]⁻; HPLC method A *t_r* = 4.747 min.

3-(1-(7-Ethynyl-9H-pyrimido[4,5-*b*]indol-4-yl)octahydro-6H-pyrrolo[2,3-*c*]pyridin-6-yl)propanenitrile (22). A solution of 3-(1-(7-iodo-9H-pyrimido[4,5-*b*]indol-4-yl)octahydro-6H-pyrrolo[2,3-*c*]pyridin-6-yl)propanenitrile (21) (22.0 mg, 0.05 mmol), triethylamine (11.9 mg, 0.12 mmol), and CuI (0.89 mg, 0.005 mmol) in dry DMF (1.5 mL) was degassed and stirred in a Schlenk tube under an Ar atmosphere. To the mixture were added more triethylamine (11.9 mg, 0.12 mmol) and trimethylsilylacetylene (13.8 mg, 0.14 mmol) under an Ar flow, followed by a small amount of bis(triphenylphosphine)-palladium(II) dichloride (<5 mg). The mixture was stirred at rt under an Ar atmosphere for 2 h, then diluted with EtOAc (40 mL) and washed with a saturated NaHCO₃ solution (2 × 10 mL). The combined aqueous layers were re-extracted with EtOAc (25 mL). The combined organic layers were dried over Na₂SO₄ and concentrated under reduced pressure. The residual DMF was removed under an oil pump vacuum. The brown oily residue was mixed with HPLC-grade MeOH (5 mL), and to the mixture was added K₂CO₃ (7.8 mg, 0.06 mmol). The mixture was stirred at rt under a N₂ atmosphere for 3 h and then concentrated under reduced pressure. The residue was dissolved in EtOAc (40 mL), and the solution was washed with a saturated NaHCO₃ solution (2 × 15 mL), dried over Na₂SO₄, and concentrated under reduced pressure. Purification of the residue by flash column chromatography (SiO₂, DCM/MeOH gradient elution from 95:5 to 92.5:7.5) gave 7 mg of a beige solid (41% yield). ¹H NMR (400 MHz, DMSO-*d*₆) δ 12.10 (s, 1H), 8.30 (s, 1H), 8.06 (d, *J* = 8.5 Hz, 1H), 7.50 (d, *J* = 1.5 Hz, 1H), 7.32 (dd, *J* = 8.5, 1.5 Hz, 1H), 4.70–4.62 (m, 1H), 4.23–4.14 (m, 2H), 3.90–3.81 (m, 1H), 2.96–2.88 (m, 1H), 2.67–2.51 (m, 6H, overlap with DMSO-*d*₆ signal), 2.46–2.36 (m, 2H), 2.08–1.98 (m, 1H), 1.96–1.85 (m, 2H), 1.79–1.70 (m, 1H); ¹³C NMR (101 MHz, DMSO-*d*₆) δ 157.1, 156.7, 154.1, 136.2, 123.8, 122.7, 120.1, 120.4, 117.0, 114.3, 96.2, 84.2, 80.3, 56.7, 53.2, 52.9, 49.2, 48.5, 34.2, 26.7, 25.5, 14.9; ESI-MS (*m/z*) 393.8 [M + Na]⁺; HPLC method A *t_r* = 3.014 min.

Protein Expression and Purification. GSK-3β was expressed using a construct (pNIC-CH vector) that contained residues 26–383 followed by a C-terminal hexahistidine tag. The construct was transformed into BL21(D3)-R3-pRARE2. The colonies were inoculated into a 2X LB medium that contained 50 μg/mL kanamycin and 34 μg/mL chloramphenicol and cultured overnight at 37 °C. Then, 10–12 mL of the overnight culture were inoculated in 1 L of a TB medium that contained 50 μg/mL kanamycin, and cultures were grown at 37 °C with shaking until an OD₆₀₀ value of 1.5–1.8 was reached. After the temperature was reduced to 18 °C, IPTG was added to the cultures at a final concentration of 0.5 mM, and the cultures were left overnight. The cells were harvested the next day by centrifugation at 5000 rpm for 10 min, and the pellet was collected for the purification steps.

The pellet was resuspended in a lysis buffer that contained 50 mM HEPES pH 7.5, 500 mM NaCl, 30 mM imidazole, 5% glycerol, and 0.5 mM TCEP. A protease inhibitor cocktail (Sigma) was added to the mixture to a dilution of 1:5000. The resuspended cells were lysed by sonication and cleared of DNA by the addition of 0.15% polyethylenimine, followed by centrifugation at 23000 rpm for 30

min. The supernatant was added to a gravity column containing 5 mL of a 50% Ni-NTA slurry (Qiagen) that was previously equilibrated with 40 mL of the lysis buffer. Subsequently, 100 mL of the lysis buffer were used to wash the column, and GSK-3β was eluted with lysis buffer containing 50, 100, 200, and 300 mM imidazole. The eluted fractions that contained the protein were pulled together and concentrated using a 10 kDa cutoff ultrafiltration unit until a volume of 5 mL was reached and further purified by fractionation via size exclusion chromatography (SEC) using a Hiloal 16/600 Superdex 200 column, which was pre-equilibrated with SEC buffer that contained 25 mM HEPES pH 7.5, 200 mM NaCl, 5% glycerol, and 0.5 mM TCEP. The purified protein was concentrated to 12 mg/mL and snap frozen into liquid nitrogen. The protein identity was confirmed by electrospray ionization mass spectrometry (expected 41550.9 Da, observed 41552.0 Da).

Crystallization and Structure Determination. The inhibitors were added at a final concentration of 1 mM to 10 mg/mL protein (diluted from 12 mg/mL stock using SEC buffer) that was incubated for minimum 1 h at 4 °C. The protein/inhibitor mixture was centrifuged to separate any insoluble material, and crystals were obtained by the sitting drop vapor diffusion method at 20 °C using 12% PEG 8000, 1 mM MgCl₂, 0.5 M NaCl, and 0.1 M Tris pH 8.0 into a 300 nL drop, mixing the protein and precipitant at a 2:1 volume ratio. The crystals were cryoprotected with a solution of the precipitant and 20% ethylene glycol and then flash cooled to 100 K. Diffraction data were collected at the Swiss Light Source station PXI-X06SA. The data were processed with the XDS package⁵² and AIMLESS⁵³ and solved by molecular replacement using the program PHASER,⁵⁴ which was implemented in the CCP4 suite,⁵⁵ and the structure of GSK-3β (PDB ID 6GN1) was used as the searching model.⁵⁶ The asymmetric unit contained one molecule, and the electron density on the ATP binding site was clearly detected. The structure was further refined upon the insertion of water molecules and the ligand using REFMACS,⁵⁷ PHENIX,⁵⁸ COOT,⁵⁹ and MOLPROBITY⁶⁰ for the model validation. Data collection and refinement statistics are summarized in Table 4.

Molecular Modeling. All modeling was conducted with Maestro ver. 2020-2 (Schrödinger LLC, New York, NY) using the OPLS3e force field,⁶¹ unless otherwise stated.

For WaterMap^{24,25} calculations, the crystal structure was first prepared with Protein Preparation Wizard,⁶² where hydrogen bonds, for example, were optimized and the structure was energy minimized (a

Table 4. Data Collection and Refinement Statistics for GSK-3β and Compound (S)-5c (PDB 7B6F)

data collection	
resolution range (Å) ^a	42.41–2.05 (2.11–2.05)
space group	P121
cell dimensions <i>a</i> (Å), <i>b</i> (Å), <i>c</i> (Å), α (°), β (°), γ (°)	57.7, 63.1, 132.2, 90.0, 97.4, 90.0
no. of unique observations ^a	28973 (2204)
completeness (%) ^a	97.7 (96.8)
mean (<i>I</i>)/σ(<i>I</i>) ^a	11.1 (2.2)
<i>R</i> _{pim} ^a	0.036 (0.373)
mean CC (1/2) ^a	0.998 (0.713)
multiplicity ^a	2.7 (2.5)
refinement	
no. of atoms in refinement	2928
average B factor (Å ²)	43.0
<i>R</i> _{work} (%)	17.4
<i>R</i> _{free} (%)	20.9
r.m.s. deviation from the ideal bond length (Å)	0.86
r.m.s. deviation from the ideal bond angle (deg)	0.008
MolProbity Ramachandran	
favoured (%)	97
outliers (%)	0

^aValues within parentheses refer to the highest-resolution shell.

RMSD restrain of 0.3 Å was applied for heavy atoms convergence). For calculations with (S)-15 and (S)-5m, the co-crystallized ligand (S)-5c was first replaced with the aligned ligands that were prepared with LigPrep (Schrödinger LLC). Then, the obtained protein–ligand structure was prepared with the Protein Preparation Wizard (as above). Water molecules within 10 Å of the retained ligand were included in the WaterMap analysis. Existing crystal structure water molecules were treated as part of the explicit solvent, and a simulation time of 2.0 ns was used in the WaterMap simulation where water was described with the TIP4P water model and non-solvent heavy atoms were restrained. The WaterMap analysis for the MD-derived structures were run with the same settings, and the protein–ligand complexes were taken from final frames (at 1000 ns) of five MD simulation replicas where ions and water molecules (except water within 4 Å from the ligand) were deleted before system preparation with the Protein Preparation Wizard.

QM calculations were conducted with the Jaguar program.⁶³ Geometry optimization was done for the aligned ligands, which were prepared with the LigPrep program using B3LYP-D3 theory with the 6-31G** basis set in the gas phase (except LACVP** for (S)-11 with iodine). Atomic electrostatic potential (ESP) charges were calculated for the optimized geometries using 6-31G**+, with the PBF water as solvent model.

MD simulations were run in the NPT ensemble (310 K; 1.01325 bar) using the Desmond engine.⁶⁴ Simulation settings were the same as those described earlier.⁶⁵ Protein Preparation Wizard prepared GSK-3β–(S)-15 complexes that were solvated in a cubic box (minimum distance of 15 Å from the protein to the box edges), and K⁺ and Cl[−] ions were included in a 0.15 M concentration with a neutral net charge for the final system. The water was described with the TIP3P model.⁶⁶ Final systems consisted of 76 109 atoms. Ten replica simulations were run, using a different seed for each simulation. A default Desmond relaxation protocol was applied before the 1000 ns production simulations. Water distances and locations were analyzed with the trajectory_asl_monitor.py script (Schrödinger LLC). Maestro and the PyMOL molecular graphics system (ver. 2.2.3 Schrödinger, LLC) were used for visualization.

■ ASSOCIATED CONTENT

SI Supporting Information

The Supporting Information is available free of charge at <https://pubs.acs.org/doi/10.1021/acs.jmedchem.0c02146>.

ADP Glo kinase assay protocol; NanoBRET target engagement assay protocol and results; materials and methods for cellular assays in neuronal SH-SY5Y cells; kinome screening data for compounds (S)-15 and 22; and ¹H and ¹³C NMR spectra and HPLC chromatograms of compounds (S)-5c, (S)-15, 20, and 22 (PDF)
SMILES strings of tested compounds (CSV)
Analysis of the HR-I conserved water residues in high-resolution GSK-3β crystal structures (CSV)

■ AUTHOR INFORMATION

Corresponding Author

Pierre Koch – Institute of Pharmaceutical Sciences, Department of Medicinal and Pharmaceutical Chemistry, Eberhard Karls University Tübingen, 72076 Tübingen, Germany; Department of Pharmaceutical/Medicinal Chemistry II, Institute of Pharmacy, University of Regensburg, 93053 Regensburg, Germany; orcid.org/0000-0003-4620-4650; Phone: +49 941 943 4827; Email: pierre.koch@uni-tuebingen.de, pierre.koch@ur.de

Authors

Stanislav Andreev – Institute of Pharmaceutical Sciences, Department of Medicinal and Pharmaceutical Chemistry,

Eberhard Karls University Tübingen, 72076 Tübingen, Germany

Tatu Patsar – Institute of Pharmaceutical Sciences, Department of Medicinal and Pharmaceutical Chemistry, Eberhard Karls University Tübingen, 72076 Tübingen, Germany; School of Pharmacy, Faculty of Health Sciences, University of Eastern Finland, 70211 Kuopio, Finland; orcid.org/0000-0002-0369-2909

Roberta Tesch – Institute for Pharmaceutical Chemistry, Goethe University, 60438 Frankfurt am Main, Germany; Structural Genomics Consortium, Buchmann Institute for Life Sciences, Goethe University, 60438 Frankfurt am Main, Germany; orcid.org/0000-0003-3347-2111

Niclas Kahlke – Institute of Pharmaceutical Sciences, Department of Medicinal and Pharmaceutical Chemistry, Eberhard Karls University Tübingen, 72076 Tübingen, Germany

Ahmed El-Gokha – Institute of Pharmaceutical Sciences, Department of Medicinal and Pharmaceutical Chemistry, Eberhard Karls University Tübingen, 72076 Tübingen, Germany; Chemistry Department, Faculty of Science, Menoufia University, 32511 Shebin El-Kom, Egypt

Francesco Ansideri – Institute of Pharmaceutical Sciences, Department of Medicinal and Pharmaceutical Chemistry, Eberhard Karls University Tübingen, 72076 Tübingen, Germany

Lukas Grätz – Department of Pharmaceutical/Medicinal Chemistry II, Institute of Pharmacy, University of Regensburg, 93053 Regensburg, Germany

Jenny Romasco – Department for Life Quality Studies, Alma Mater Studiorum, University of Bologna, 47921 Rimini, Italy

Giulia Sita – Department of Pharmacy and Biotechnology, University of Bologna, 40126 Bologna, Italy

Christian Geibel – Institute of Pharmaceutical Sciences, Department of Pharmaceutical (Bio-)Analysis, Eberhard Karls University Tübingen, 72076 Tübingen, Germany

Michael Lämmerhofer – Institute of Pharmaceutical Sciences, Department of Pharmaceutical (Bio-)Analysis, Eberhard Karls University Tübingen, 72076 Tübingen, Germany; orcid.org/0000-0002-1318-0974

Andrea Tarozzi – Department for Life Quality Studies, Alma Mater Studiorum, University of Bologna, 47921 Rimini, Italy; orcid.org/0000-0001-7983-8575

Stefan Knapp – Institute for Pharmaceutical Chemistry, Goethe University, 60438 Frankfurt am Main, Germany; Structural Genomics Consortium, Buchmann Institute for Life Sciences, Goethe University, 60438 Frankfurt am Main, Germany; orcid.org/0000-0001-5995-6494

Stefan A. Laufer – Institute of Pharmaceutical Sciences, Department of Medicinal and Pharmaceutical Chemistry, Eberhard Karls University Tübingen, 72076 Tübingen, Germany; Tübingen Center for Academic Drug Discovery (TüCAD2), 72076 Tübingen, Germany; orcid.org/0000-0001-6952-1486

Complete contact information is available at: <https://pubs.acs.org/doi/10.1021/acs.jmedchem.0c02146>

Author Contributions

◆ These authors contributed equally.

Notes

The authors declare no competing financial interest.

The raw concatenated trajectories of the MD simulations of compounds (S)-5c and (S)-15 and the WaterMap-output files are freely available at <https://doi.org/10.5281/zenodo.4646862>.

ACKNOWLEDGMENTS

The authors acknowledge CSC—IT Center for Science, Finland, for computational resources. T.P. acknowledges funding from the European Union's Horizon 2020 research and innovation program under the Marie Skłodowska-Curie Grant 839230 and Orion Research Foundation sr. R.T. was supported by the German Research Foundation (DFG) Grant 397659447. The data collection at the Swiss Light Source (SLS) was supported by funding from the European Union's Horizon 2020 research and innovation program Grant 730872, project CALIPSOplus. The Structural Genomics Consortium (SGC) is a registered charity (no. 1097737) that receives funds from AbbVie, Bayer AG, Boehringer Ingelheim, the Canada Foundation for Innovation, the Eshelman Institute for Innovation, Genentech, the Genome Canada through Ontario Genomics Institute (OGI-196), EU/EFPIA/OICR/McGill/KTH/Diamond, Innovative Medicines Initiative 2 Joint Undertaking (EUBOPEN Grant 875510), Janssen, Merck KGaA (aka EMD in Canada and US), Merck & Co (also known as MSD outside Canada and the US), Pfizer, São Paulo Research Foundation-FAPESP, Takeda and Wellcome (106169/ZZ14/Z). The authors thank Jens Strobach and Maria Beer-Krön for their excellent assistance with the GSK-3 β ADP Glo and NanoBRET assays, respectively. We thank the staff at beamline X06SA of the Swiss Light Source for assistance during data collection.

ABBREVIATIONS USED

BRET, bioluminescence resonance energy transfer; GSK-3 β , glycogen synthase kinase-3 β ; HPLC, high-performance liquid chromatography; HR-I, hydrophobic region I; MS, mass spectrometry; MD, molecular dynamics; N_NAr, nucleophilic aromatic substitution

REFERENCES

- (1) Taylor, S. S.; Meharena, H. S.; Kornev, A. P. Evolution of a dynamic molecular switch. *IUBMB Life* **2019**, *71*, 672–684.
- (2) Ferguson, F. M.; Gray, N. S. Kinase inhibitors: the road ahead. *Nat. Rev. Drug Discovery* **2018**, *17*, 353–377.
- (3) Shih, H.-P.; Zhang, X.; Aronov, A. M. Drug discovery effectiveness from the standpoint of therapeutic mechanisms and indications. *Nat. Rev. Drug Discovery* **2018**, *17*, 19–33.
- (4) Liu, S.-K.; Xie, H.-X.; Ge, Y.-X.; Zhang, J.; Jiang, C.-S. An updated research of glycogen synthase kinase-3 β inhibitors: a review. *Monatsh. Chem.* **2021**, *152*, 19–33.
- (5) Rippin, I.; Eldar-Finkelman, H. Mechanisms and therapeutic implications of GSK-3 in treating neurodegeneration. *Cells* **2021**, *10*, 262.
- (6) Roca, C.; Campillo, N. E. Glycogen synthase kinase 3 (GSK-3) inhibitors: a patent update (2016–2019). *Expert Opin. Ther. Pat.* **2020**, *30*, 863–872.
- (7) De Simone, A.; Tumiatti, V.; Andrisano, V.; Milelli, A. Glycogen synthase kinase 3 β : a new gold rush in anti-Alzheimer's disease multitarget drug discovery? *J. Med. Chem.* **2021**, *64*, 26–41.
- (8) Patel, P.; Woodgett, J. R. Chapter eight - glycogen synthase kinase 3: A kinase for all pathways? *Curr. Top. Dev. Biol.* **2017**, *123*, 277–302.
- (9) Phukan, S.; Babu, V.; Kannoji, A.; Hariharan, R.; Balaji, V. GSK3 β : role in therapeutic landscape and development of modulators. *Br. J. Pharmacol.* **2010**, *160*, 1–19.
- (10) Lauretti, E.; Dincer, O.; Praticò, D. Glycogen synthase kinase-3 signaling in Alzheimer's disease. *Biochim. Biophys. Acta, Mol. Cell Res.* **2020**, *1867*, 118664.
- (11) Ding, L.; Billadeau, D. D. Glycogen synthase kinase-3 β : a novel therapeutic target for pancreatic cancer. *Expert Opin. Ther. Targets* **2020**, *24*, 417–426.
- (12) Andreev, S.; Pantsar, T.; Ansideri, F.; Kudolo, M.; Forster, M.; Schollmeyer, D.; Laufer, S. A.; Koch, P. Design, synthesis and biological evaluation of 7-chloro-9H-pyrimido[4,5-b]indole-based glycogen synthase kinase-3 β Inhibitors. *Molecules* **2019**, *24*, 2331.
- (13) Ball, P. Water is an active matrix of life for cell and molecular biology. *Proc. Natl. Acad. Sci. U. S. A.* **2017**, *114*, 13327–13335.
- (14) Snyder, P. W.; Mecinović, J.; Moustakas, D. T.; Thomas, S. W.; Harder, M.; Mack, E. T.; Lockett, M. R.; Héroux, A.; Sherman, W.; Whitesides, G. M. Mechanism of the hydrophobic effect in the biomolecular recognition of arylsulfonamides by carbonic anhydrase. *Proc. Natl. Acad. Sci. U. S. A.* **2011**, *108*, 17889–17894.
- (15) Breiten, B.; Lockett, M. R.; Sherman, W.; Fujita, S.; Al-Sayah, M.; Lange, H.; Bowers, C. M.; Héroux, A.; Krilov, G.; Whitesides, G. M. Water networks contribute to enthalpy/entropy compensation in protein–ligand binding. *J. Am. Chem. Soc.* **2013**, *135*, 15579–15584.
- (16) Michel, J.; Tirado-Rives, J.; Jorgensen, W. L. Energetics of displacing water molecules from protein binding sites: consequences for ligand optimization. *J. Am. Chem. Soc.* **2009**, *131*, 15403–15411.
- (17) Spyraakis, F.; Ahmed, M. H.; Bayden, A. S.; Cozzini, P.; Mozzarelli, A.; Kellogg, G. E. The roles of water in the protein matrix: A largely untapped resource for drug discovery. *J. Med. Chem.* **2017**, *60*, 6781–6827.
- (18) Ladbury, J. E. Just add water! The effect of water on the specificity of protein–ligand binding sites and its potential application to drug design. *Chem. Biol. (Oxford, U. K.)* **1996**, *3*, 973–980.
- (19) Maurer, M.; Oostenbrink, C. Water in protein hydration and ligand recognition. *J. Mol. Recognit.* **2019**, *32*, e2810.
- (20) Darby, J. F.; Hopkins, A. P.; Shimizu, S.; Roberts, S. M.; Brannigan, J. A.; Turkenburg, J. P.; Thomas, G. H.; Hubbard, R. E.; Fischer, M. Water networks can determine the affinity of ligand binding to proteins. *J. Am. Chem. Soc.* **2019**, *141*, 15818–15826.
- (21) Krimmer, S. G.; Cramer, J.; Betz, M.; Fridh, V.; Karlsson, R.; Heine, A.; Klebe, G. Rational design of thermodynamic and kinetic binding profiles by optimizing surface water networks coating protein-bound ligands. *J. Med. Chem.* **2016**, *59*, 10530–10548.
- (22) Nittinger, E.; Gibbons, P.; Eigenbrot, C.; Davies, D. R.; Maurer, B.; Yu, C. L.; Kiefer, J. R.; Kuglstatter, A.; Murray, J.; Ortwine, D. F.; Tang, Y.; Tsui, V. Water molecules in protein–ligand interfaces. Evaluation of software tools and SAR comparison. *J. Comput.-Aided Mol. Des.* **2019**, *33*, 307–330.
- (23) Bucher, D.; Stouten, P.; Triballeau, N. Shedding light on important waters for drug design: simulations versus grid-based methods. *J. Chem. Inf. Model.* **2018**, *58*, 692–699.
- (24) Abel, R.; Young, T.; Farid, R.; Berne, B. J.; Friesner, R. A. Role of the active-site solvent in the thermodynamics of factor Xa ligand binding. *J. Am. Chem. Soc.* **2008**, *130*, 2817–2831.
- (25) Young, T.; Abel, R.; Kim, B.; Berne, B. J.; Friesner, R. A. Motifs for molecular recognition exploiting hydrophobic enclosure in protein–ligand binding. *Proc. Natl. Acad. Sci. U. S. A.* **2007**, *104*, 808–813.
- (26) Horbert, R.; Pinchuk, B.; Johannes, E.; Schlosser, J.; Schmidt, D.; Cappel, D.; Totzke, F.; Schächtele, C.; Peifer, C. Optimization of potent DFG-in inhibitors of platelet derived growth factor receptor β (PDGFR β) guided by water thermodynamics. *J. Med. Chem.* **2015**, *58*, 170–182.
- (27) Pearlstein, R. A.; Sherman, W.; Abel, R. Contributions of water transfer energy to protein–ligand association and dissociation barriers: Watermap analysis of a series of p38 α MAP kinase inhibitors. *Proteins: Struct., Funct., Genet.* **2013**, *81*, 1509–1526.
- (28) Myrianthopoulos, V.; Kritsanida, M.; Gaboriaud-Kolar, N.; Magiatis, P.; Ferandin, Y.; Durieu, E.; Lozach, O.; Cappel, D.; Soundararajan, M.; Filippakopoulos, P.; Sherman, W.; Knapp, S.; Meijer, L.; Mikros, E.; Skaltsounis, A.-L. Novel inverse binding mode of

indirubin derivatives yields improved selectivity for DYRK kinases. *ACS Med. Chem. Lett.* **2013**, *4*, 22–26.

(29) Robinson, D. D.; Sherman, W.; Farid, R. Understanding kinase selectivity through energetic analysis of binding site waters. *ChemMedChem* **2010**, *5*, 618–627.

(30) Robinson, D.; Bertrand, T.; Carry, J.-C.; Halley, F.; Karlsson, A.; Mathieu, M.; Minoux, H.; Perrin, M.-A.; Robert, B.; Schio, L.; Sherman, W. Differential water thermodynamics determine PI3K-beta/delta selectivity for solvent-exposed ligand modifications. *J. Chem. Inf. Model.* **2016**, *56*, 886–894.

(31) Asquith, C. R. M.; Tizzard, G. J.; Bennett, J. M.; Wells, C. I.; Elkins, J. M.; Willson, T. M.; Poso, A.; Laitinen, T. Targeting the water network in cyclin G-associated kinase (GAK) with 4-anilino-quin(az)-oline Inhibitors. *ChemMedChem* **2020**, *15*, 1200–1215.

(32) Hamaguchi, H.; Amano, Y.; Moritomo, A.; Shirakami, S.; Nakajima, Y.; Nakai, K.; Nomura, N.; Ito, M.; Higashi, Y.; Inoue, T. Discovery and structural characterization of peficitinib (ASP015K) as a novel and potent JAK inhibitor. *Bioorg. Med. Chem.* **2018**, *26*, 4971–4983.

(33) Lee, K. L.; Ambler, C. M.; Anderson, D. R.; Boscoe, B. P.; Bree, A. G.; Brodfuehrer, J. L.; Chang, J. S.; Choi, C.; Chung, S.; Curran, K. J.; Day, J. E.; Dehnhardt, C. M.; Dower, K.; Drozda, S. E.; Frisbie, R. K.; Gavrin, L. K.; Goldberg, J. A.; Han, S.; Hegen, M.; Hepworth, D.; Hope, H. R.; Kamtekar, S.; Kilty, I. C.; Lee, A.; Lin, L.-L.; Lovering, F. E.; Lowe, M. D.; Mathias, J. P.; Morgan, H. M.; Murphy, E. A.; Papaioannou, N.; Patny, A.; Pierce, B. S.; Rao, V. R.; Saiah, E.; Samardjiev, I. J.; Samas, B. M.; Shen, M. W. H.; Shin, J. H.; Soutter, H. H.; Strohbach, J. W.; Symanowicz, P. T.; Thomason, J. R.; Trzuppek, J. D.; Vargas, R.; Vincent, F.; Yan, J.; Zapf, C. W.; Wright, S. W. Discovery of clinical candidate 1-[[[(2S,3S,4S)-3-Ethyl-4-fluoro-5-oxopyrrolidin-2-yl]methoxy]-7-methoxyisoquinoline-6-carboxamide (PF-06650833), a potent, selective inhibitor of interleukin-1 receptor associated kinase 4 (IRAK4), by fragment-based drug design. *J. Med. Chem.* **2017**, *60*, 5521–5542.

(34) Matricon, P.; Suresh, R. R.; Gao, Z.-G.; Panel, N.; Jacobson, K. A.; Carlsson, J. Ligand design by targeting a binding site water. *Chem. Sci.* **2021**, *12*, 960–968.

(35) Andreev, S.; Pantsar, T.; El-Gokha, A.; Ansideri, F.; Kudolo, M.; Anton, D. B.; Sita, G.; Romasco, J.; Geibel, C.; Lämmerhofer, M.; Goettert, M. I.; Tarozzi, A.; Laufer, S. A.; Koch, P. Discovery and evaluation of enantiopure 9H-pyrimido[4,5-b]indoles as nanomolar GSK-3 β inhibitors with improved metabolic stability. *Int. J. Mol. Sci.* **2020**, *21*, 7823.

(36) Zegzouti, H.; Zdanovskaia, M.; Hsiao, K.; Goueli, S. A. ADP-glo: A bioluminescent and homogeneous ADP monitoring assay for kinases. *Assay Drug Dev. Technol.* **2009**, *7*, 560–572.

(37) Ghose, A. K.; Viswanadhan, V. N.; Wendoloski, J. J. Prediction of hydrophobic (lipophilic) properties of small organic molecules using fragmental methods: an analysis of ALOGP and CLOGP methods. *J. Phys. Chem. A* **1998**, *102*, 3762–3772.

(38) Hopkins, A. L.; Keserü, G. M.; Leeson, P. D.; Rees, D. C.; Reynolds, C. H. The role of ligand efficiency metrics in drug discovery. *Nat. Rev. Drug Discovery* **2014**, *13*, 105–121.

(39) Desroy, N.; Housseman, C.; Bock, X.; Joncour, A.; Bienvenu, N.; Cherel, L.; Labeguere, V.; Rondet, E.; Peixoto, C.; Grassot, J.-M.; Picolet, O.; Annot, D.; Triballeau, N.; Monjardet, A.; Wakselman, E.; Roncoroni, V.; Le Tallec, S.; Blaque, R.; Cottreaux, C.; Vandervoort, N.; Christophe, T.; Mollat, P.; Lamers, M.; Auberval, M.; Hrvacic, B.; Ralic, J.; Oste, L.; van der Aar, E.; Brys, R.; Heckmann, B. Discovery of 2-[[[2-ethyl-6-[4-[2-(3-hydroxyazetididin-1-yl)-2-oxoethyl]piperazin-1-yl]-8-methylimidazo[1,2-a]pyridin-3-yl]methylamino]-4-(4-fluorophenyl)thiazole-5-carbonitrile (GLPG1690), a first-in-class autotaxin inhibitor undergoing clinical evaluation for the treatment of idiopathic pulmonary fibrosis. *J. Med. Chem.* **2017**, *60*, 3580–3590.

(40) Kung, P.-P.; Sinnema, P.-J.; Richardson, P.; Hickey, M. J.; Gajiwala, K. S.; Wang, F.; Huang, B.; McClellan, G.; Wang, J.; Maegeley, K.; Bergqvist, S.; Mehta, P. P.; Kania, R. Design strategies to target crystallographic waters applied to the Hsp90 molecular chaperone. *Bioorg. Med. Chem. Lett.* **2011**, *21*, 3557–3562.

(41) Henzler-Wildman, K.; Kern, D. Dynamic personalities of proteins. *Nature* **2007**, *450*, 964–972.

(42) Pruccoli, L.; Morroni, F.; Sita, G.; Hrelia, P.; Tarozzi, A. Esculetin as a bifunctional antioxidant prevents and counteracts the oxidative stress and neuronal death induced by amyloid protein in SH-SY5Y cells. *Antioxidants* **2020**, *9*, 551.

(43) Lochhead, P. A.; Kinstrie, R.; Sibbet, G.; Rawjee, T.; Morrice, N.; Cleghon, V. A chaperone-dependent GSK3 β transitional intermediate mediates activation-loop autophosphorylation. *Mol. Cell* **2006**, *24*, 627–633.

(44) Cole, A.; Frame, S.; Cohen, P. Further evidence that the tyrosine phosphorylation of glycogen synthase kinase-3 (GSK3) in mammalian cells is an autophosphorylation event. *Biochem. J.* **2004**, *377*, 249–255.

(45) Wagner, F. F.; Benajiba, L.; Campbell, A. J.; Weüwer, M.; Sacher, J. R.; Gale, J. P.; Ross, L.; Puissant, A.; Alex, G.; Conway, A.; Back, M.; Pikman, Y.; Galinsky, I.; DeAngelo, D. J.; Stone, R. M.; Kaya, T.; Shi, X.; Robers, M. B.; Machleidt, T.; Wilkinson, J.; Hermine, O.; Kung, A.; Stein, A. J.; Lakshminarasimhan, D.; Hemann, M. T.; Scolnick, E.; Zhang, Y.-L.; Pan, J. Q.; Stegmaier, K.; Holson, E. B. Exploiting an Asp-Glu “switch” in glycogen synthase kinase 3 to design paralog-selective inhibitors for use in acute myeloid leukemia. *Sci. Transl. Med.* **2018**, *10*, eaam8460.

(46) Tarozzi, A.; Morroni, F.; Merlicco, A.; Hrelia, S.; Angeloni, C.; Cantelli-Forti, G.; Hrelia, P. Sulforaphane as an inducer of glutathione prevents oxidative stress-induced cell death in a dopaminergic-like neuroblastoma cell line. *J. Neurochem.* **2009**, *111*, 1161–1171.

(47) Eid, S.; Turk, S.; Volkamer, A.; Rippmann, F.; Fulle, S. KinMap: a web-based tool for interactive navigation through human kinome data. *BMC Bioinf.* **2017**, *18*, 16.

(48) Young, J. R.; Lim, J.; Machacek, M. R.; Taoka, B. M.; Otte, R. D. Inhibitors of Janus Kinases. WO 2009075830 A1, 2009.

(49) Senecal, T. D.; Shu, W.; Buchwald, S. L. A general, practical palladium-catalyzed cyanation of (hetero)aryl chlorides and bromides. *Angew. Chem., Int. Ed.* **2013**, *52*, 10035–10039.

(50) Levinson, N. M.; Boxer, S. G. A conserved water-mediated hydrogen bond network defines bosutinib's kinase selectivity. *Nat. Chem. Biol.* **2014**, *10*, 127–32.

(51) Heider, F.; Pantsar, T.; Kudolo, M.; Ansideri, F.; De Simone, A.; Pruccoli, L.; Schneider, T.; Goettert, M. I.; Tarozzi, A.; Andrisano, V.; Laufer, S. A.; Koch, P. Pyridinylimidazoles as GSK3 β inhibitors: the impact of tautomerism on compound activity via water networks. *ACS Med. Chem. Lett.* **2019**, *10*, 1407–1414.

(52) Kabsch, W. XDS. *Acta Crystallogr., Sect. D: Biol. Crystallogr.* **2010**, *66*, 125–132.

(53) Evans, P. An introduction to data reduction: space-group determination, scaling and intensity statistics. *Acta Crystallogr., Sect. D: Biol. Crystallogr.* **2011**, *67*, 282–292.

(54) McCoy, A. J.; Grosse-Kunstleve, R. W.; Adams, P. D.; Winn, M. D.; Storoni, L. C.; Read, R. J. Phaser crystallographic software. *J. Appl. Crystallogr.* **2007**, *40*, 658–674.

(55) Winn, M. D.; Ballard, C. C.; Cowtan, K. D.; Dodson, E. J.; Emsley, P.; Evans, P. R.; Keegan, R. M.; Krissinel, E. B.; Leslie, A. G. W.; McCoy, A.; McNicholas, S. J.; Murshudov, G. N.; Pannu, N. S.; Potterton, E. A.; Powell, H. R.; Read, R. J.; Vagin, A.; Wilson, K. S. Overview of the CCP4 suite and current developments. *Acta Crystallogr., Sect. D: Biol. Crystallogr.* **2011**, *67*, 235–242.

(56) Tesch, R.; Becker, C.; Müller, M. P.; Beck, M. E.; Quambusch, L.; Getlik, M.; Lategahn, J.; Uhlenbrock, N.; Costa, F. N.; Polêto, M. D.; Pinheiro, P. d. S. M.; Rodrigues, D. A.; Sant'Anna, C. M. R.; Ferreira, F. F.; Verli, H.; Fraga, C. A. M.; Rauh, D. An unusual intramolecular halogen bond guides conformational selection. *Angew. Chem., Int. Ed.* **2018**, *57*, 9970–9975.

(57) Murshudov, G. N.; Skubak, P.; Lebedev, A. A.; Pannu, N. S.; Steiner, R. A.; Nicholls, R. A.; Winn, M. D.; Long, F.; Vagin, A. A. REFMAC5 for the refinement of macromolecular crystal structures. *Acta Crystallogr., Sect. D: Biol. Crystallogr.* **2011**, *67*, 355–367.

(58) Liebschner, D.; Afonine, P. V.; Baker, M. L.; Bunkoczi, G.; Chen, V. B.; Croll, T. I.; Hintze, B.; Hung, L. W.; Jain, S.; McCoy, A. J.; Moriarty, N. W.; Oeffner, R. D.; Poon, B. K.; Prisant, M. G.; Read, R. J.;

Richardson, J. S.; Richardson, D. C.; Sammito, M. D.; Sobolev, O. V.; Stockwell, D. H.; Terwilliger, T. C.; Urzhumtsev, A. G.; Videau, L. L.; Williams, C. J.; Adams, P. D. Macromolecular structure determination using X-rays, neutrons and electrons: recent developments in Phenix. *Acta Crystallogr. Sect. D: Biol. Crystallogr.* **2019**, *75*, 861–877.

(59) Emsley, P.; Lohkamp, B.; Scott, W. G.; Cowtan, K. Features and development of Coot. *Acta Crystallogr., Sect. D: Biol. Crystallogr.* **2010**, *66*, 486–501.

(60) Chen, V. B.; Arendall, W. B., III; Headd, J. J.; Keedy, D. A.; Immormino, R. M.; Kapral, G. J.; Murray, L. W.; Richardson, J. S.; Richardson, D. C. MolProbity: all-atom structure validation for macromolecular crystallography. *Acta Crystallogr., Sect. D: Biol. Crystallogr.* **2010**, *66*, 12–21.

(61) Roos, K.; Wu, C.; Damm, W.; Reboul, M.; Stevenson, J. M.; Lu, C.; Dahlgren, M. K.; Mondal, S.; Chen, W.; Wang, L.; Abel, R.; Friesner, R. A.; Harder, E. D. OPLS3e: Extending force field coverage for drug-like small molecules. *J. Chem. Theory Comput.* **2019**, *15*, 1863–1874.

(62) Madhavi Sastry, G.; Adzhigirey, M.; Day, T.; Annabhimoju, R.; Sherman, W. Protein and ligand preparation: parameters, protocols, and influence on virtual screening enrichments. *J. Comput.-Aided Mol. Des.* **2013**, *27*, 221–234.

(63) Bochevarov, A. D.; Watson, M. A.; Greenwood, J. R.; Philipp, D. M. Multiconformation, density functional theory-based pKa prediction in application to large, flexible organic molecules with diverse functional groups. *J. Chem. Theory Comput.* **2016**, *12*, 6001–6019.

(64) Bowers, K. J.; Chow, E.; Xu, H.; Dror, R. O.; Eastwood, M. P.; Gregersen, B. A.; Klepeis, J. L.; Kolossvary, I.; Moraes, M. A.; Sacerdoti, F. D.; Salmon, J. K.; Shan, Y.; Shaw, D. E., Scalable algorithms for molecular dynamics simulations on commodity clusters. In *Proceedings of the 2006 ACM/IEEE conference on Supercomputing*; ACM: Tampa, FL, 2006; p 84.

(65) Pantsar, T. KRAS(G12C)–AMG 510 interaction dynamics revealed by all-atom molecular dynamics simulations. *Sci. Rep.* **2020**, *10*, 11992.

(66) Jorgensen, W. L.; Chandrasekhar, J.; Madura, J. D.; Impey, R. W.; Klein, M. L. Comparison of simple potential functions for simulating liquid water. *J. Chem. Phys.* **1983**, *79*, 926–935.

Supporting Information

Addressing a Trapped High-Energy Water: Design and Synthesis of Highly Potent Pyrimidoindole-based GSK-3 β inhibitors

Stanislav Andreev,^{1,‡} Tatu Pantsar,^{1,2,‡} Roberta Tesch,^{3,4} Niclas Kahlke,¹ Ahmed El-Gokha,^{1,5} Francesco Ansideri,¹ Lukas Grätz,⁶ Jenny Romasco,⁷ Giulia Sita,⁸ Christian Geibel,⁹ Michael Lämmerhofer,⁹ Andrea Tarozzi,⁷ Stefan Knapp,^{3,4} Stefan A. Laufer^{1,10} and Pierre Koch^{1,6,*}

¹ Institute of Pharmaceutical Sciences, Department of Medicinal and Pharmaceutical Chemistry, Eberhard Karls University Tübingen, Auf der Morgenstelle 8, 72076 Tübingen, Germany

² School of Pharmacy, Faculty of Health Sciences, University of Eastern Finland, P.O. Box 1627, 70211 Kuopio, Finland

³ Institute for Pharmaceutical Chemistry, Johann Wolfgang Goethe-University, Max-von-Laue-Str. 9, 60438 Frankfurt am Main, Germany

⁴ Structural Genomics Consortium, Buchmann Institute for Life Sciences, Johann Wolfgang Goethe-University, Max-von-Laue-Str. 15, 60438 Frankfurt am Main, Germany

⁵ Chemistry Department, Faculty of Science, Menoufia University, Gamal Abdel-Nasser Street, 32511 Shebin El-Kom, Egypt

⁶ Department of Pharmaceutical/Medicinal Chemistry II, Institute of Pharmacy, University of Regensburg, Universitätsstraße 31, 93053 Regensburg, Germany

⁷ Department for Life Quality Studies, Alma Mater Studiorum, University of Bologna, Corso D'Augusto 237, 47921 Rimini, Italy

⁸ Department of Pharmacy and Biotechnology, Alma Mater Studiorum, University of Bologna, Via Irnerio 48, 40126 Bologna, Italy

⁹ Institute of Pharmaceutical Sciences, Department of Pharmaceutical (Bio-)Analysis, Eberhard Karls University Tübingen, Auf der Morgenstelle 8, 72076 Tübingen, Germany

¹⁰ Tübingen Center for Academic Drug Discovery (TüCAD2), Auf der Morgenstelle 8, 72076 Tübingen, Germany

‡ These authors contributed equally.

* Correspondence: pierre.koch@uni-tuebingen.de, pierre.koch@ur.de; Tel.: +49 941 943-2847.

Table of Contents

ADP GloTM Kinase Assay Protocol	S3
Figure S1. Comparison of molecular surface areas among selected compounds (<i>S</i> -isomers) based on Jaguar-optimized geometries.	S4
Figure S2. Comparison of the electrostatic potential and electron density of (<i>S</i>)- 5c , (<i>S</i>)- 15 and (<i>S</i>)- 5m .	S5
Figure S3. WaterMap analysis of (<i>S</i>)- 5m and (<i>S</i>)- 15 based on the (<i>S</i>)- 5c crystal structure.	S6
Figure S4. Molecular dynamics simulations of (<i>S</i>)- 5c and (<i>S</i>)- 15 suggest no shift in interactions with GSK-3 β among these compounds.	S7
Figure S5. The orientation and hydrogen bond interactions of the high-energy water molecule observed in the WaterMap simulations of (<i>S</i>)- 5c and (<i>S</i>)- 15 .	S8
NanoBRET target engagement assay	S9
Figure S6. Cytotoxicity of 20 and (<i>S</i>)- 15 in neuronal SH-SY5Y cells.	S11
Figure S7. Effects of 20 and (<i>S</i>)- 15 on the GSK-3 activity in neuronal SH-SY5Y cells.	S12
Figure S8. Neuroprotective effects of 20 and (<i>S</i>)- 15 against the neurotoxicity induced by H ₂ O ₂ in neuronal SH-SY5Y cells.	S13
Materials and Methods for cellular assays in neuronal SH-SY5Y cells	S14
Kinome screening data for (<i>S</i>)-15 and 22	S16
Figure S9. Workflow of combining molecular dynamics simulations with WaterMap while evaluating new ligand designs.	S18
¹H and ¹³C NMR spectra of (<i>S</i>)-5c, (<i>S</i>)-15, 20 and 22	S19
HPLC chromatograms of (<i>S</i>)-5c, (<i>S</i>)-15, 20 and 22	S23
References	S27

ADP Glo™ Kinase Assay Protocol

The IC₅₀ values of the final compounds for GSK-3β were determined in an ADP Glo™ kinase assay from Promega (Madison, WI, USA).

The assay was carried out in white, non-treated 384-well plates from Corning (Corning, NY, USA). The experiments were carried out as duplicates or quadruplicates using a concentration of 0.58 ng/μL of recombinant human GSK-3β, 0.2 μg/μL GSK-3 substrate G50-58 (sequence: YRRAAVPPSPSLSRHSSPHQ(pS)EDEEE) and 25 μM ATP in the presence of serial dilutions of the final compounds (six 1:3 or 1:4 dilution steps starting from 10 μM). Two control experiments with uninhibited kinase and blank experiments with ATP/substrate solution were performed and their results were used for the normalization of the raw data.

In detail, GSK-3β was pre-incubated with the final compounds for 10 min at rt. Then substrate/ATP was added to start the reaction, which was run for 1 h at rt. ADP Glo™ reagent (5 μL, then 1 h incubation) and Kinase detection reagent (10 μL, then 30 min incubation) were subsequently added. The luminescence was finally measured on a FilterMax F5 microplate reader from Molecular Devices LLC (San José, CA, USA) (integration time 500 ms). The raw data was normalized and absolute IC₅₀ values were generated with PRISM v.7.03. from GraphPad Software (San Diego, CA, USA).

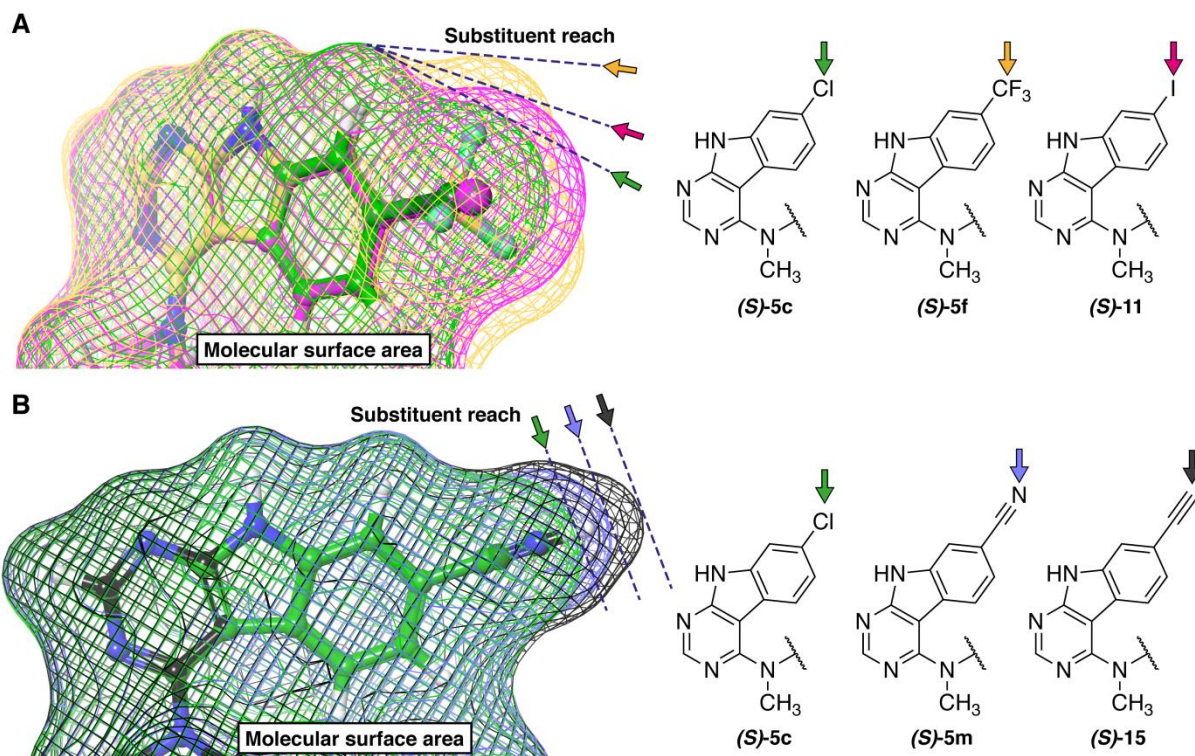


Figure S1. Comparison of molecular surface areas among selected compounds (*S*-isomers) based on Jaguar-optimized geometries. **(A)** Compared to *(S)*-**5c**, the substituents of *(S)*-**5f** and *(S)*-**11** have considerably larger radii, which will most likely result in a clash with the gatekeeper residue Leu132. **(B)** Compared to *(S)*-**5c**, the substituents of *(S)*-**5m** and *(S)*-**15** reach deeper towards the HR-I but do not significantly increase the molecular radius (compare to *(S)*-**5f** and *(S)*-**11** in **A**). Molecular surfaces were generated by Maestro (Schrodinger LLC).

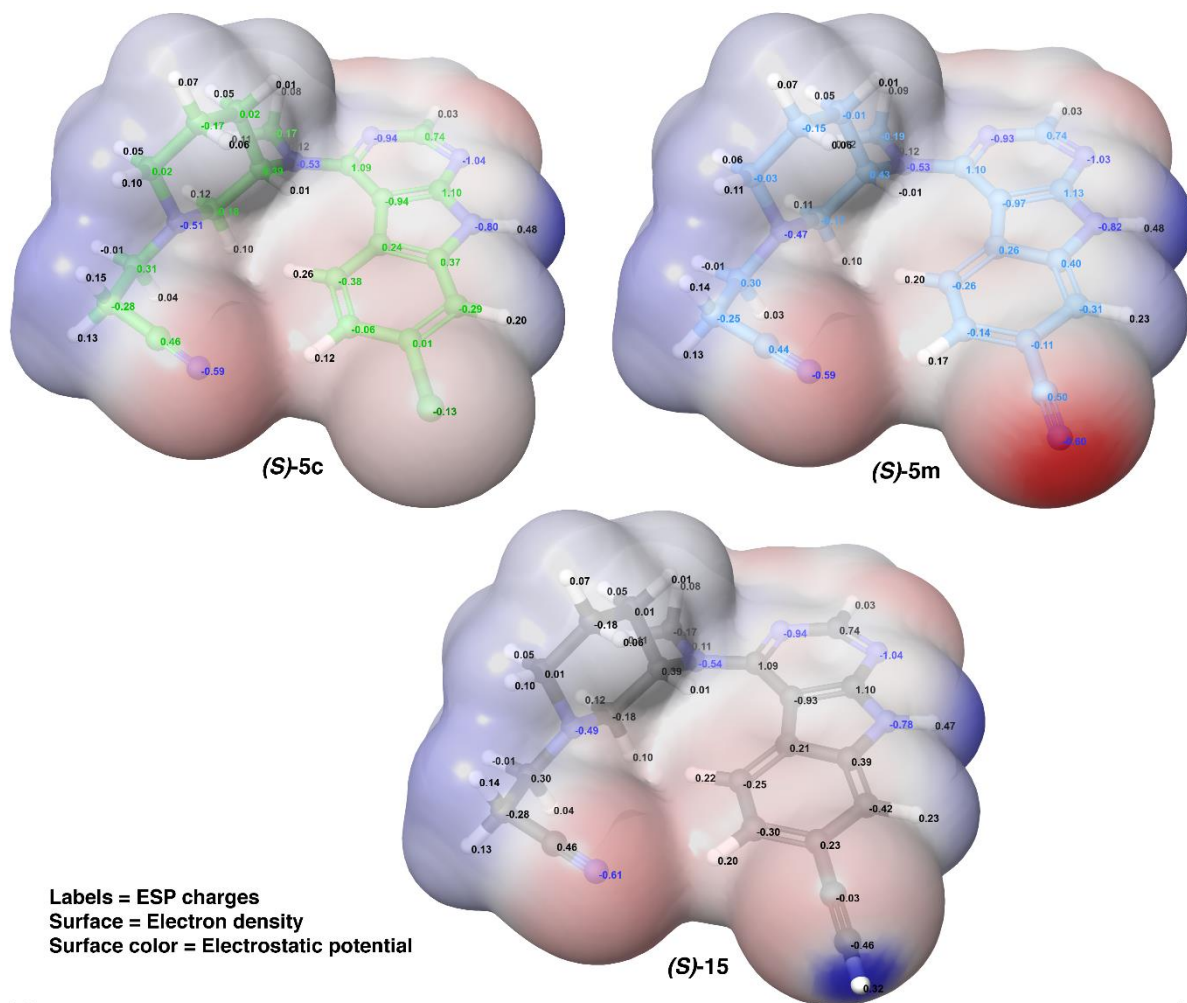


Figure S2. Comparison of the electrostatic potential and electron density of (S)-5c, (S)-5m and (S)-15. Atomic electrostatic potential (ESP) charges were calculated with Jaguar (6-31G**+, PBF water solvent model).

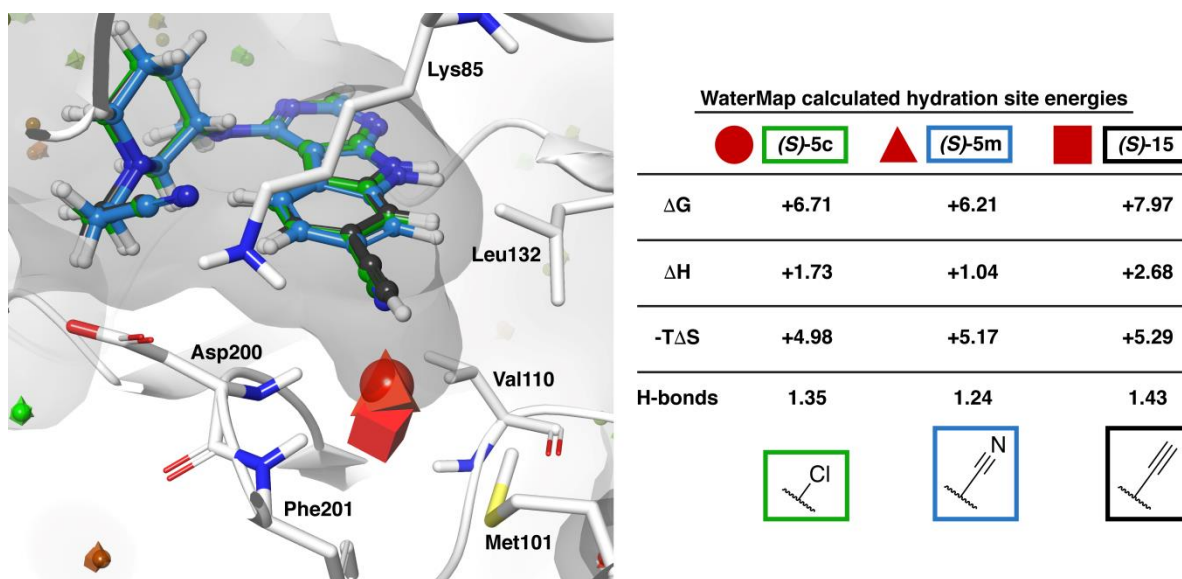


Figure S3. WaterMap analysis of (*S*)-**5m** and (*S*)-**15** based on the (*S*)-**5c** crystal structure. No shift of the high-energy hydration site is observed with (*S*)-**5m** (pyramid) compared to (*S*)-**5c** (sphere), whereas (*S*)-**15** clearly shifts the hydration site position (cube). A slightly lower free energy value is observed with (*S*)-**5m** compared to (*S*)-**5c**. The shifted hydration site of (*S*)-**15** displays an extremely high free energy value.

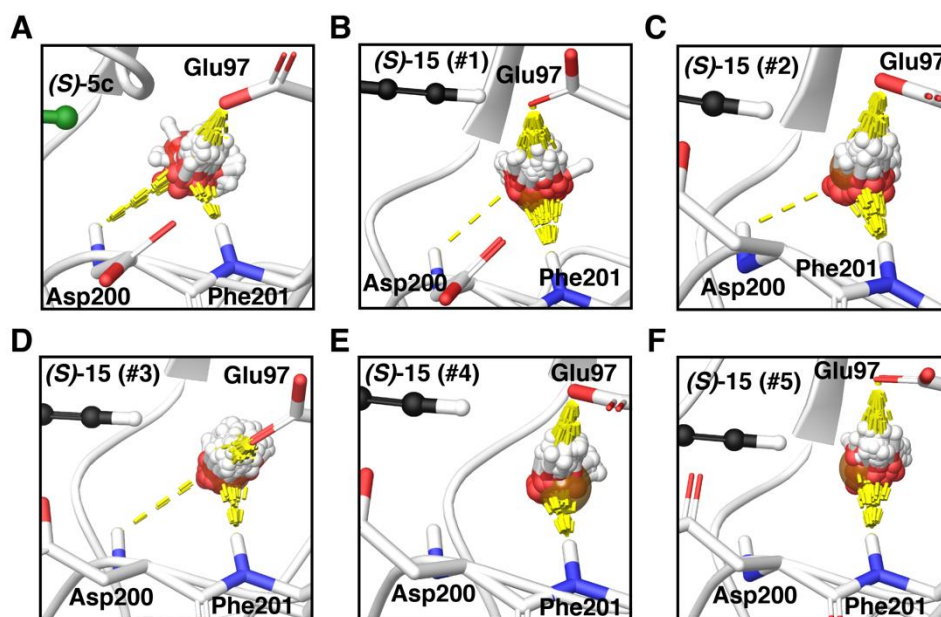


Figure S5. The orientation and hydrogen bond interactions of the high-energy water molecule observed in the WaterMap simulations of (*S*)-**5c** and (*S*)-**15**. In the case of (*S*)-**15**, the slight shift in the position of the water molecule results in the loss of the hydrogen bond to Asp200 along with improved hydrogen bonding with Phe201 and Glu97 (**B–F**). This shift in the position and altered hydrogen bonding correlate with the enthalpic gain (decrease in energy): the biggest benefit in gain in enthalpy is observed with (**E**) #4 (-1.93 kcal/mol) and (**F**) #5 (-1.48 kcal/mol), where all water molecule conformations display interactions solely to Phe201 and Glu97. Lowest gain in enthalpy is observed with (**D**) #3 (0.06 kcal/mol), where in two conformations the hydrogen bond to Asp200 still exists.

NanoBRET target engagement assay

HEK293T cells (kind gift from Prof. Dr. Wulf Schneider, Institute for Medical Microbiology and Hygiene, University Hospital Regensburg, Germany) were routinely maintained in DMEM (Dulbecco's Modified Eagle's Medium, Sigma-Aldrich, Munich, Germany), supplemented with 10% FCS (Sigma-Aldrich, Munich, Germany), at 37 °C in a water-saturated atmosphere (5% CO₂). All cells were routinely checked for mycoplasma infection using the Venor GeM Mycoplasma Detection Kit (Minerva Biolabs, Berlin, Germany).

HEK293T cells stably expressing NLuc-GSK3 β were generated according to a described procedure with the exception that the amount of transfected cDNA was reduced to 1 μ g.¹ The cDNA encoding NLuc-GSK3 β was kindly provided by Promega (Mannheim, Germany). Stably transfected cells were selected in the presence of 1 mg/mL G418 (Fisher Scientific, Nidderau, Germany). For further cultivation of the stable transfectants, the concentration of G418 was reduced to 600 μ g/mL.

After reaching \approx 80-90% confluency, the stably transfected cells were detached with trypsin/EDTA (0.05%/0.02%, Biochrom, Berlin, Germany) and centrifuged (500 g, 5 min). The cell pellet was resuspended in Leibovitz' L-15 medium (L-15, Fisher Scientific, Nidderau, Germany), supplemented with 5% FCS and 10 mM HEPES (Sigma-Aldrich, Munich, Germany). After adjusting the cell density to 6.25 x 10⁵ cells/mL, 80 μ L of the cell suspension were added to each well of a white 96-well plate (Brand, Wertheim, Germany) and incubated overnight at 37 °C (no additional CO₂).

On the day of the experiment, serial dilutions of the test compounds (10-fold more concentrated than the final assay concentration) were prepared in L-15 + 10 mM HEPES. The fluorescent tracer K-8 (Promega, Mannheim, Germany) was diluted in DMSO to a concentration of 4 μ M (100-fold more concentrated than the final assay concentration). This was further diluted 10-fold using the Tracer Dilution Buffer (Promega, Mannheim, Germany) yielding a dilution, which was 10-fold concentrated to the final assay concentration. Next, 10 μ L of the final fluorescent tracer dilution were added to the cells (final concentration of K-8 in the assay: 0.04 μ M) and the plate was shaken for 10 seconds (orbital, 250 rpm). After adding 10 μ L of the serial dilutions of the respective test compounds, the plate was shaken again for 10 seconds (orbital, 250 rpm). A solvent control (0%) and a positive control, which contained solely the fluorescent tracer K-8 but no test compound, were included in each experiment. After incubating the plate at 37 °C for 2 h, the plate was equilibrated to room temperature for 15 min.

Next, 10 μL of the detection reagent (consisting of 1192 μL L-15 + 6 μL NanoBRET NanoGlo Substrate + 2 μL Extracellular NanoLuc Inhibitor; substrate and inhibitor were purchased from Promega, Mannheim, Germany) were added to each well on the plate and the measurement was started. All measurements were performed at room temperature using a TECAN InfiniteLumi plate reader (TECAN Austria GmbH, Grödig, Austria). The bioluminescence of NLuc was detected using a 460/35 nm band-pass filter. The fluorescence of the fluorescent tracer K-8 was detected using a 610 nm long-pass filter. Integration times were set to 1000 ms for both channels. The raw BRET ratio was calculated by dividing the emission of the fluorescent acceptor (measured with the 610 nm long-pass filter) by the donor luminescence (measured with the 460/35 nm band-pass filter). The obtained data were analyzed by a four-parameter logistic equation (GraphPad Prism 8.0, GraphPad Software Inc., San Diego, CA, USA) yielding IC_{50} values, for which means and the SEM were calculated.

Table S1. Cellular target engagement of compounds *(S)*-**5c**, *(S)*-**15**, **20** and **22** determined by a nanoBRET assay (n = 3).

Compound	<i>(S)</i>-5c	<i>(S)</i>-15	20	22
$\text{IC}_{50} \pm \text{SEM}$ [μM]	10.31 \pm 1.53	2.51 \pm 0.16	5.27 \pm 0.24	2.40 \pm 0.017

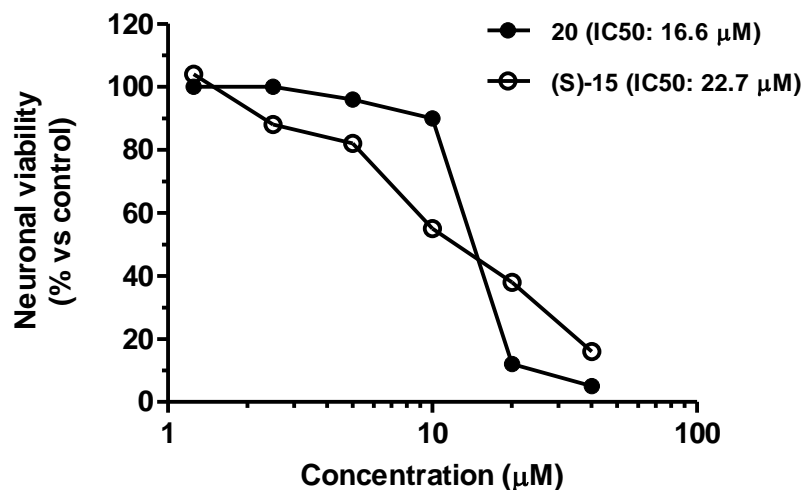


Figure S6. Cytotoxicity of **20** and (*S*)-**15** in SH-SY5Y cells. Cells were incubated for 24 h with different concentrations of the studied compounds [1.25 - 40 µM]. At the end of incubation, the neuronal viability was measured using MTT assay. Data are expressed as percentage of neuronal viability versus untreated cells and reported as mean of two independent experiments. IC₅₀ value: concentration resulting in 50% inhibition of neuronal viability.

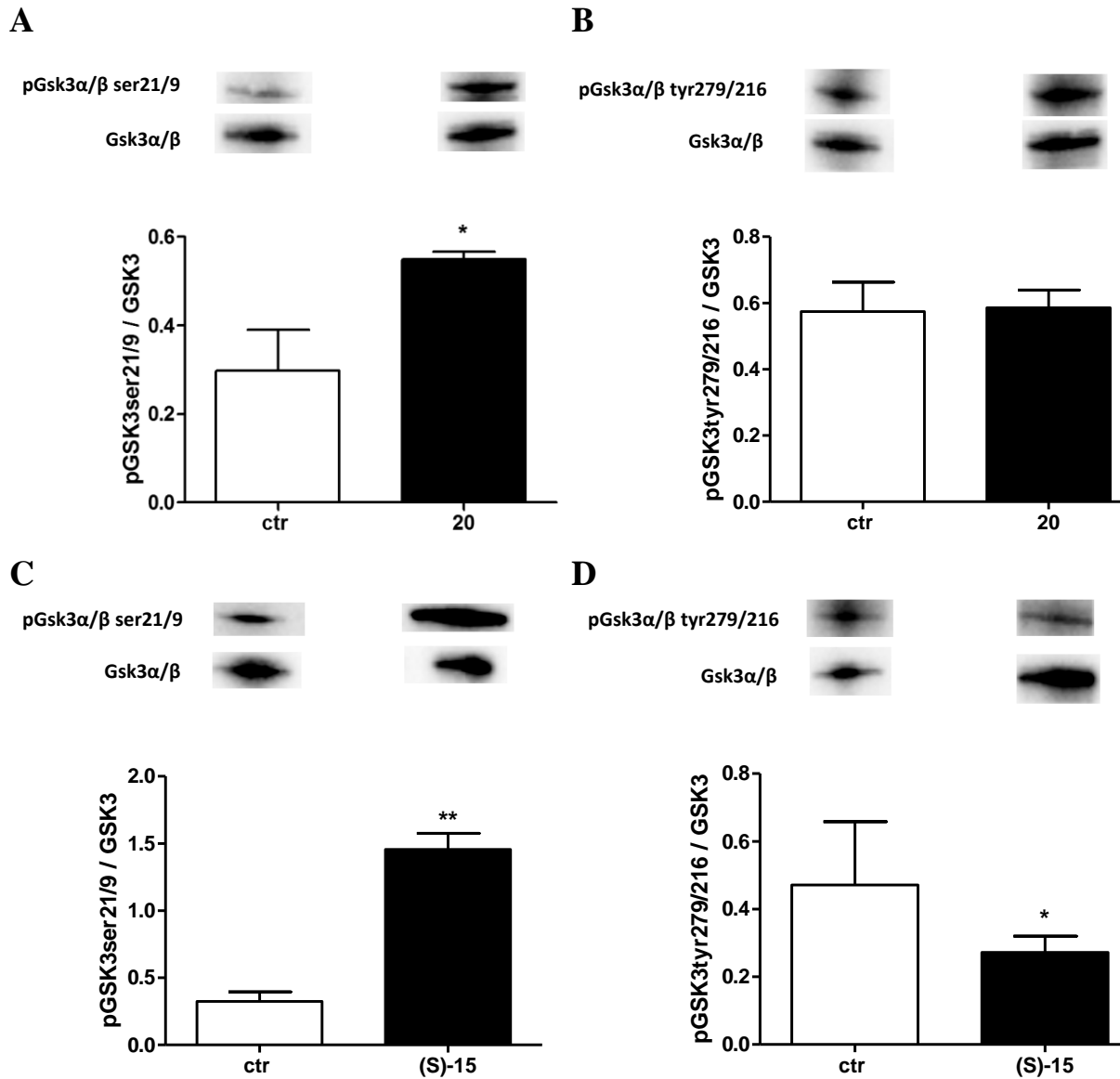


Figure S7. Effects of **20** and **(S)-15** on the GSK-3 activity in neuronal SH-SY5Y cells. Cells were incubated with **20** and **(S)-15** (5 μ M) for 3 h. At the end of incubation, the phosphorylation of GSK3 α/β on Ser21/9 (inactive GSK3 α/β form) (**A** for **20**, **C** for **(S)-15**) and on Tyr279/Tyr216 (active GSK3 α/β form) (**B** for **20**, **D** for **(S)-15**), respectively, was determined by western blotting. Data are expressed as ratio between phospho-GSK3 α/β and total GSK-3 levels normalized against β -Actin and reported as mean \pm SD of at least three independent experiments (* $p < 0.05$ and ** $p < 0.01$ vs untreated cells).

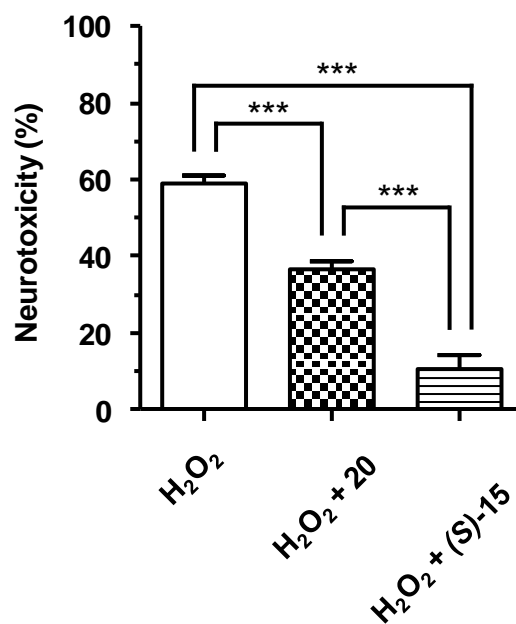


Figure S8. Neuroprotective effects of **20** and *(S)*-**15** against the neurotoxicity induced by H₂O₂ in neuronal SH-SY5Y cells. Cells were incubated with **20** and *(S)*-**15** (5 μM) and H₂O₂ (100 μM) for 1 h and then starved in complete medium for 22 h. The neurotoxicity was then evaluated by MTT assay as reported in materials and methods section. Data are expressed as percentages of neurotoxicity versus untreated cells and reported as mean ± SD of three independent experiments (***p < 0.001).

Materials and methods for cellular assays in neuronal SH-SY5Y cells

Cell cultures

Human neuronal SH-SY5Y cells (Sigma Aldrich, St. Louis, MO, USA) were routinely grown in Dulbecco's modified Eagle's Medium supplemented with 10 % fetal bovine serum, 2 mM L-glutamine, 50 U/mL penicillin and 50 µg/mL streptomycin at 37 °C in a humidified incubator with 5 % CO₂.

Neuronal viability

SH-SY5Y cells were seeded in a 96-well plate at 2×10^4 cells/well, incubated for 24 h and then treated with various concentrations (1.25-40 µM) of **20** and (*S*)-**15** for 24 h. Cell viability, in terms of mitochondrial activity, was evaluated by MTT assay, as previously described.²

Neuroprotective activity toward H₂O₂

SH-SY5Y cells were seeded in a 96-well plate at 2×10^4 cells/well, incubated for 24 h and subsequently treated with **20** and (*S*)-**15** (5 µM) and H₂O₂ (100 µM) for 1 h. Then, cells were starved in complete medium for 22 h. The neuroprotective activity was measured by using the MTT assay as previously described.³ Data are expressed as a percentage of neurotoxicity versus untreated cells.

Western blotting

SH-SY5Y cells were seeded in 60 mm dishes at 2×10^6 cells/dish, incubated for 24 h and subsequently treated with **20** and (*S*)-**15** (5 µM) for 3 h at 37°C in 5% CO₂. At the end of incubation, cells were trypsinized and the cellular pellet was resuspended in complete lysis buffer containing leupeptin (2µg/mL), PMSF (100µg/mL) and cocktail of protease/phosphatase inhibitors (100×). Small amounts were removed for the determination of the protein concentration using the Bradford method. The samples (30 µg proteins) were run on 4-15% SDS polyacrylamide gels (Bio-rad Laboratories S.r.L., Hercules, CA, USA) and electroblotted onto 0.45 µm nitrocellulose membranes. The membranes were incubated at 4 °C overnight with primary antibody recognizing phospho-GSK3α/β (Ser21/9), (1:1000; Cell Signaling Technology Inc, Danvers, MA, USA), or anti-phospho-GSK3(Tyr279/Tyr216), (1:1000; EMD Millipore, Darmstadt, Germany). After washing with TBS-T (TBS +0.05% Tween20), the membranes were incubated with secondary antibodies (1:2000; GE Healthcare). Enhanced chemiluminescence was used to visualize the bands (ECL; Bio-rad Laboratories). The

membranes were then reprobred with GSK3 α/β , (1:1000; Cell Signaling Technology Inc.). The data were analyzed by densitometry, using Quantity One software (Bio-Rad Laboratories® S.r.L.). The values were normalized and expressed as mean \pm SD of densitometry in each experimental group.

Statistical Analysis. Results are shown as mean \pm standard deviation (SD) of three independent experiments. Statistical analysis was performed using Student's t-test and One-way ANOVA (post-hoc Bonferroni test). Differences were considered significant at $p < 0.05$. Analyses were performed using GraphPad PRISM software (version 5.0; GraphPad Software, La Jolla, CA, USA) on a Windows platform.

Kinome screening data for inhibitors (S)-15 and 22

The selectivity of inhibitors (S)-15 and 22 was evaluated by the Eurofins KinaseProfiler™ (Eurofins Cerep, Celle l'Evescault, France) on 57 human kinases. The percentage residual activity of each kinase at an inhibitor concentration of 500 nM was determined and is reported in Table S2.

Table S2. Selectivity data of (S)-15 and 22 on 57 human kinases. Residual kinase activity is reported in percentage. Values below 50% are highlighted in red.

	(S)-15	22
Abl(h)	79	82
ALK(h)	71	90
AMPK α 1(h)	103	95
ASK1(h)	94	122
Aurora-A(h)	80	97
CaMKI(h)	86	94
CDK1/cyclinB(h)	113	85
CDK2/cyclinA(h)	77	79
CDK6/cyclinD3(h)	100	85
CDK7/cyclinH/MAT1(h)	86	80
CDK9/cyclin T1(h)	75	76
CHK1(h)	86	99
CK1 γ 1(h)	123	115
CK2 α 2(h)	97	105
c-RAF(h)	80	98
DRAK1(h)	85	100
eEF-2K(h)	90	77
EGFR(h)	94	101
EphA5(h)	90	57
EphB4(h)	94	97
Fyn(h)	16	6
GSK3 β (h)	3	-5
IGF-1R(h)	99	104
IKK α (h)	103	111
IRAK4(h)	97	118
JAK2(h)	129	79
KDR(h)	22	8
LOK(h)	19	11
Lyn(h)	31	25
MAPKAP-K2(h)	71	111
MEK1(h)	85	77
MLK1(h)	61	39
Mnk2(h)	82	92
MSK2(h)	84	33
MST1(h)	72	67

Table S2. continued.

	(S)-15	22
mTOR(h)	93	103
NEK2(h)	94	92
p70S6K(h)	99	79
PAK2(h)	77	83
PDGFR β (h)	67	72
Pim-1(h)	36	28
PKA(h)	87	89
PKB α (h)	91	94
PKC α (h)	99	87
PKC θ (h)	82	75
PKG1 α (h)	84	75
Plk3(h)	109	113
PRAK(h)	91	99
ROCK-I(h)	84	90
Rse(h)	99	78
Rsk1(h)	28	12
SAPK2a(h)	107	126
SRPK1(h)	109	121
TAK1(h)	53	88
PI3 Kinase (p110 β /p85 α)(h)	98	100
PI3 Kinase (p120 γ)(h)	95	99
PI3 Kinase (p110 δ /p85 α)(h)	68	97
PI3 Kinase (p110 α /p85 α)(h)	96	100

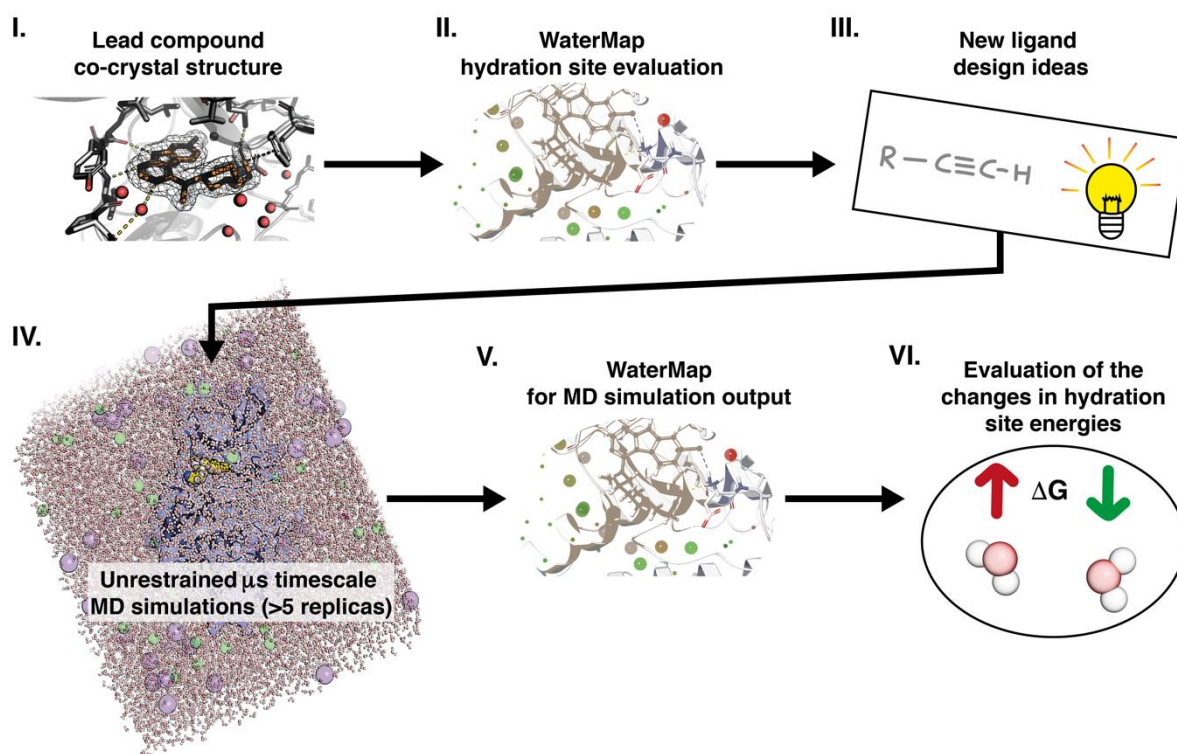
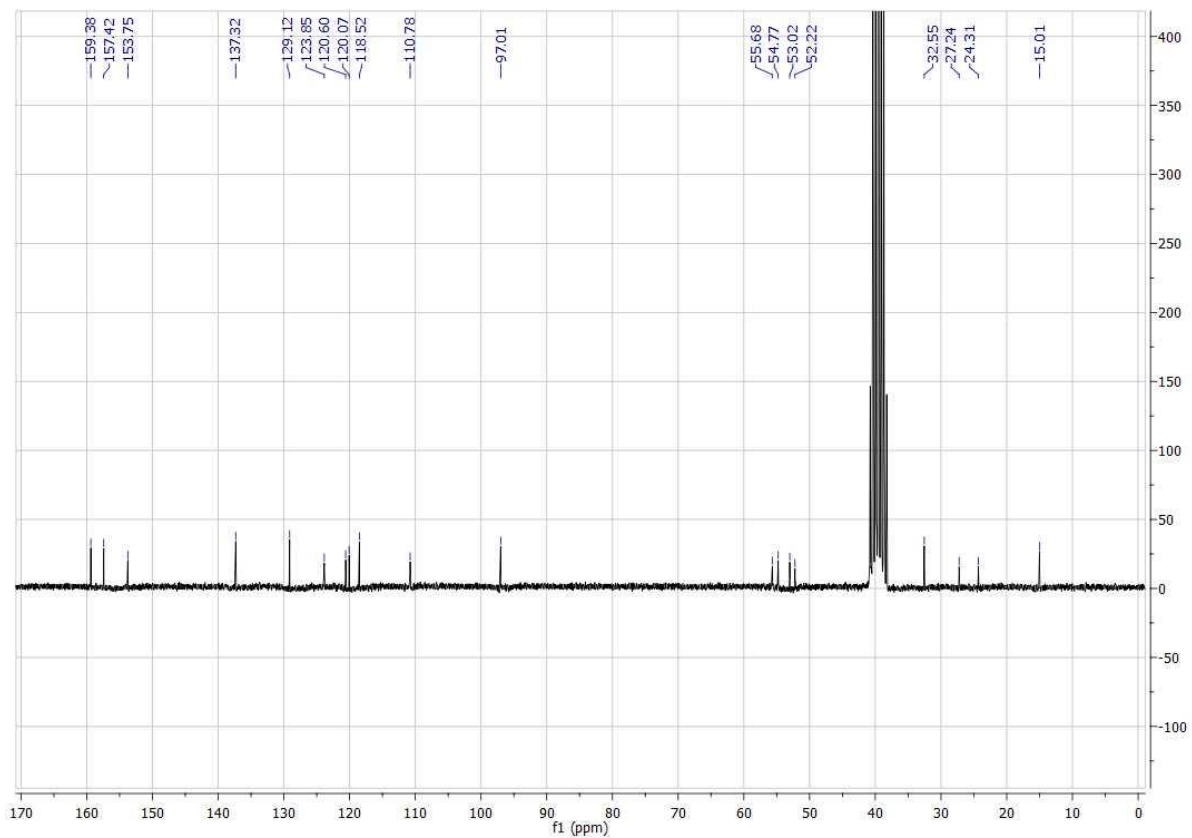
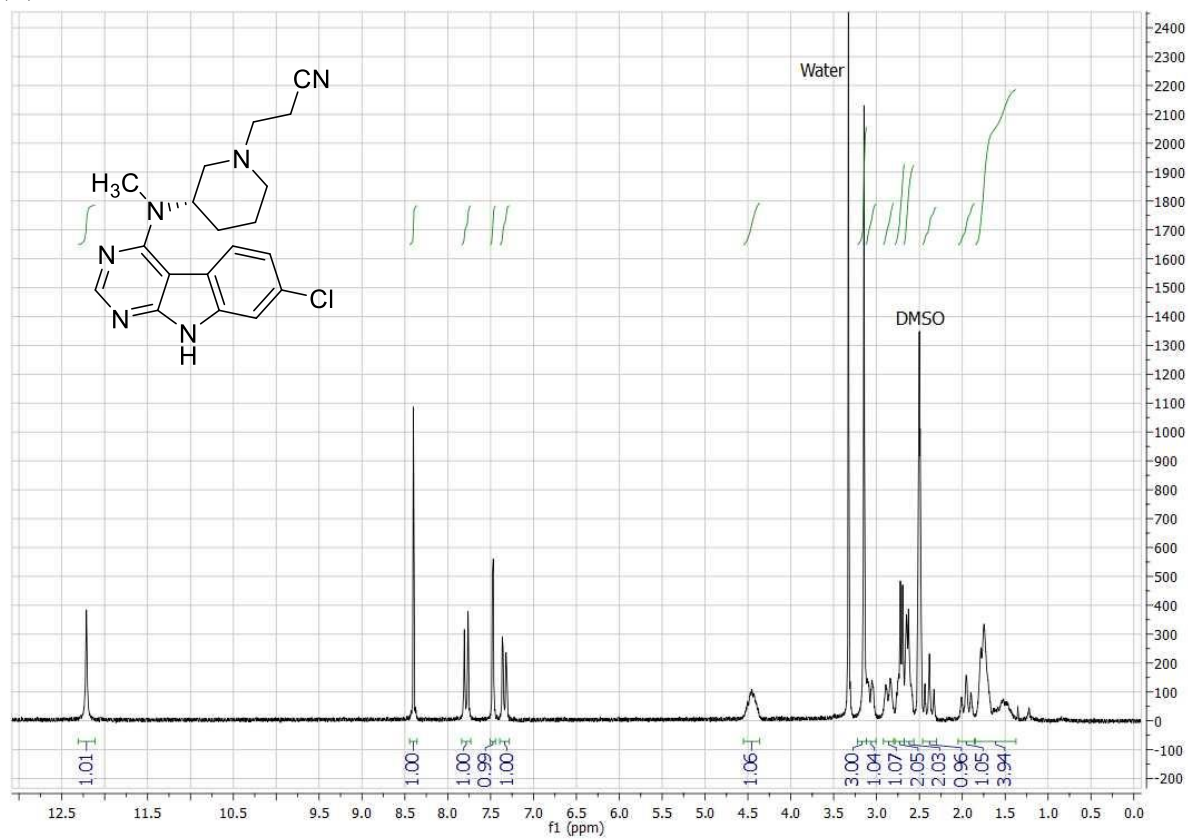


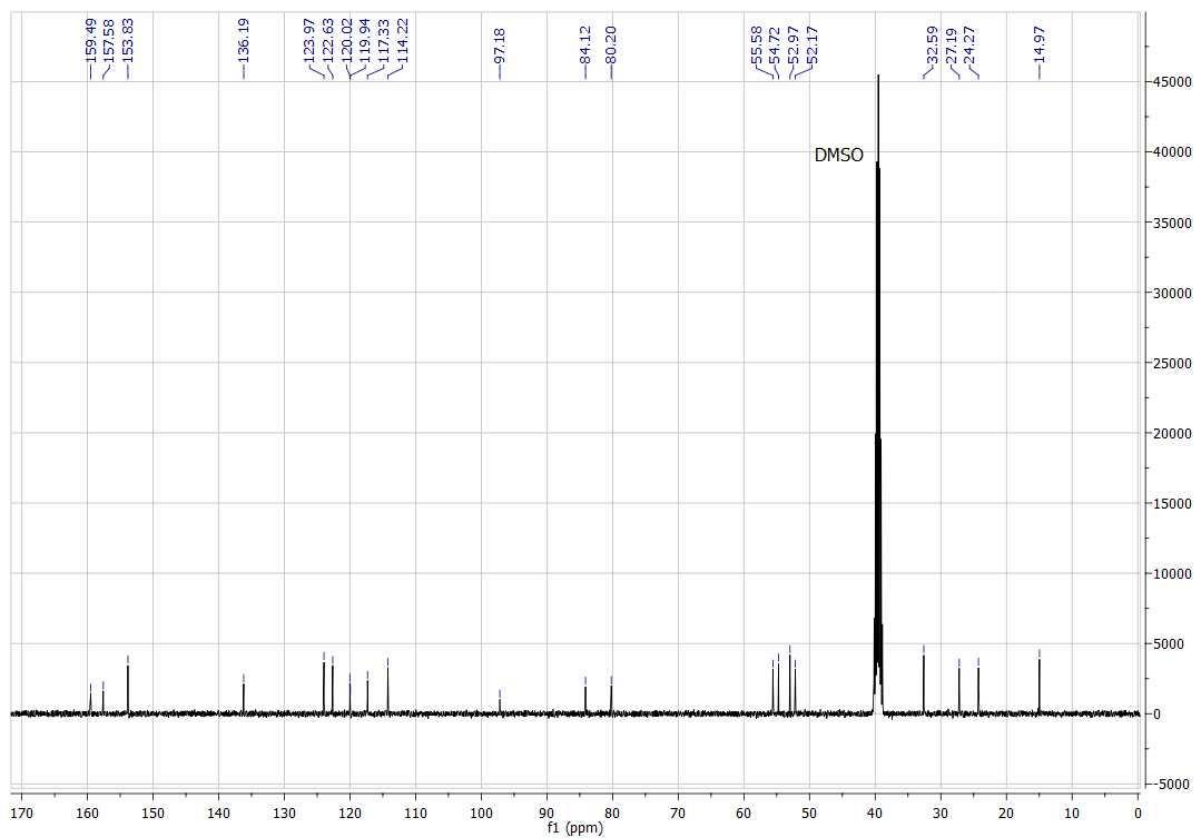
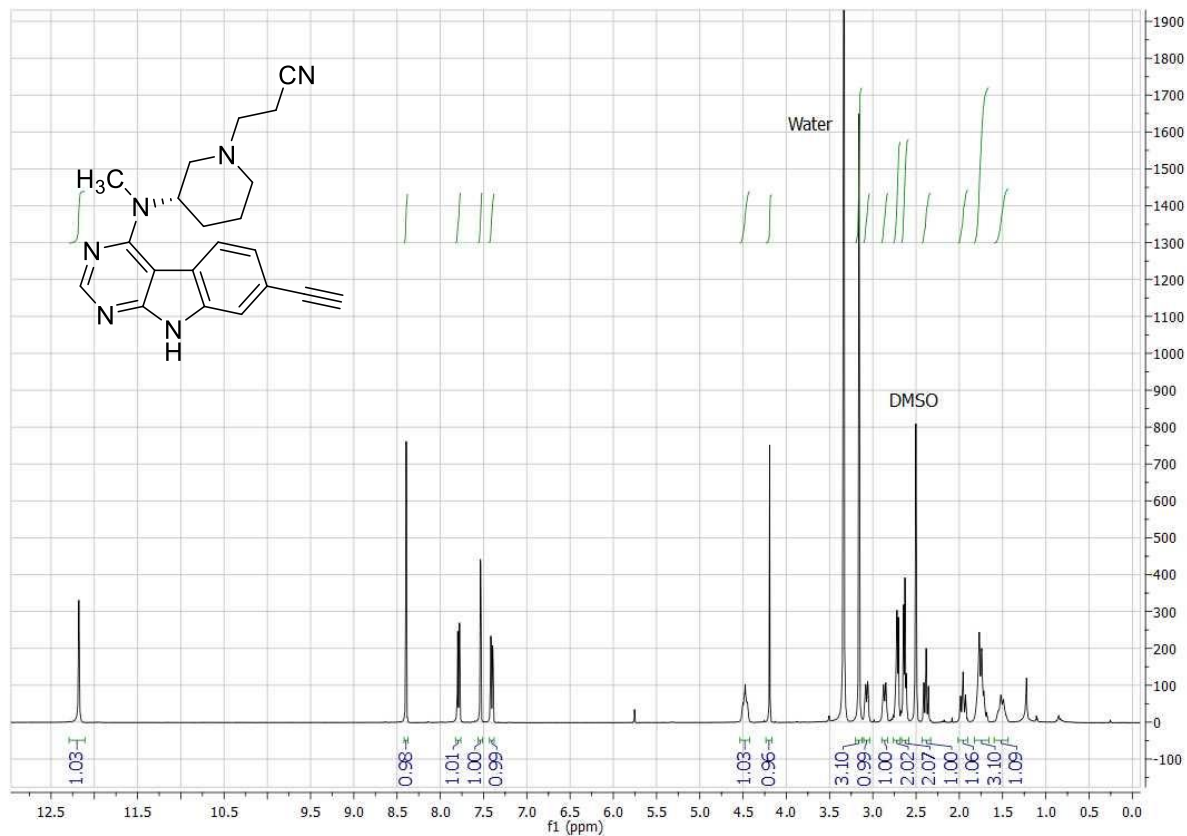
Figure S9. Workflow of combining molecular dynamics simulations with WaterMap while evaluating new ligand designs. **(I.)** Obtain/use crystal structure with reasonable resolution with the lead structure. **(II.)** Evaluate the hydration site energies to find out potential hydration sites to target. **(III.)** Design new ligands based on the potential high-energy hydration sites. **(IV.)** Run classical MD simulations to relax the new protein-ligand system. Note that it is obligatory to include several replicas to limit the random bias in the results. **(V.)** Run WaterMap for the MD simulation output structures (include several replicas). **(VI.)** Based on the WaterMap results, evaluate if the new design is beneficial or not in the context of shifted hydration site energies.

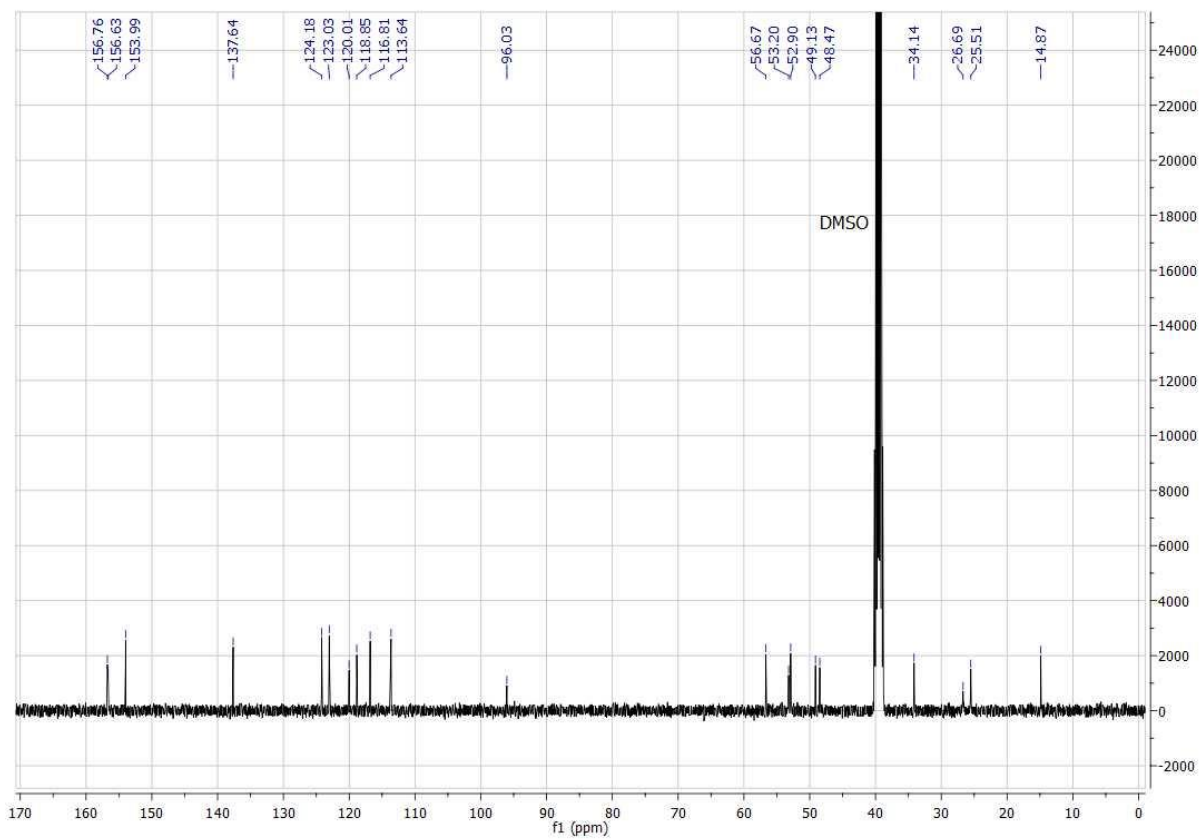
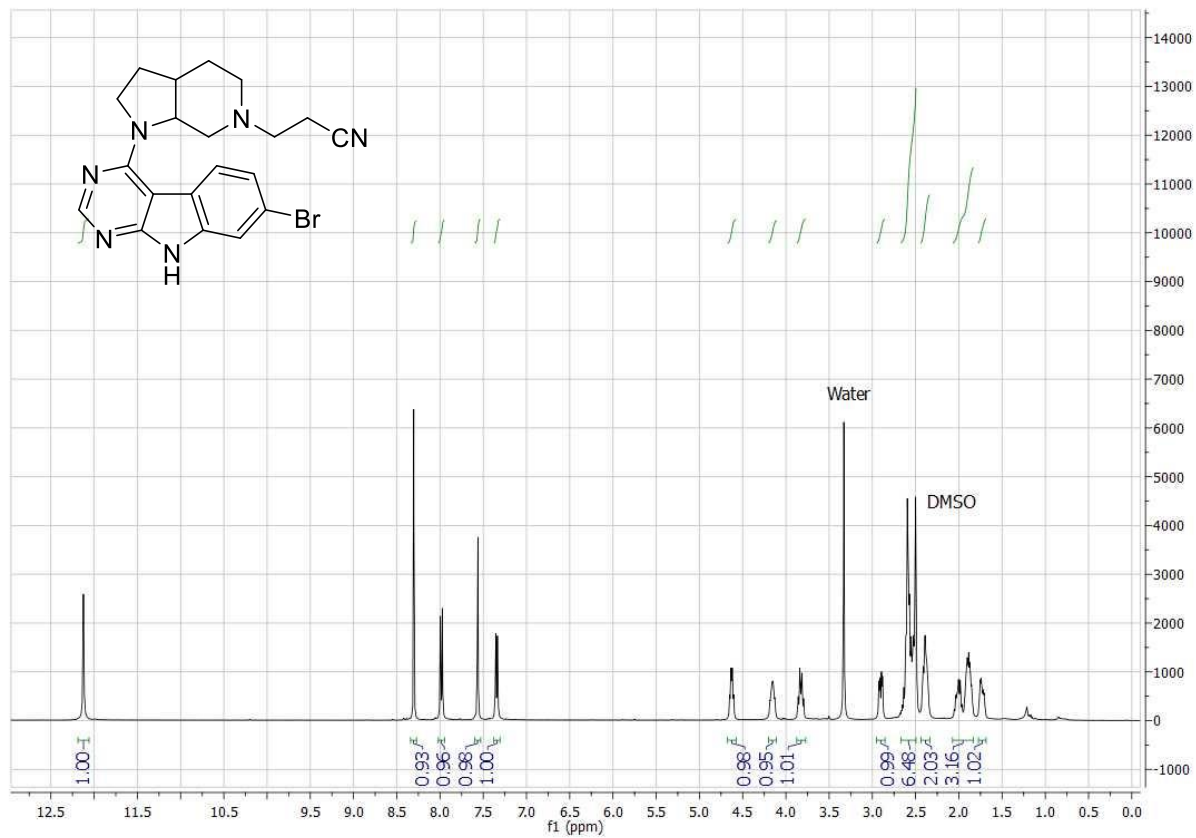
^1H and ^{13}C NMR spectra of (S)-5c, (S)-15, 20 and 22

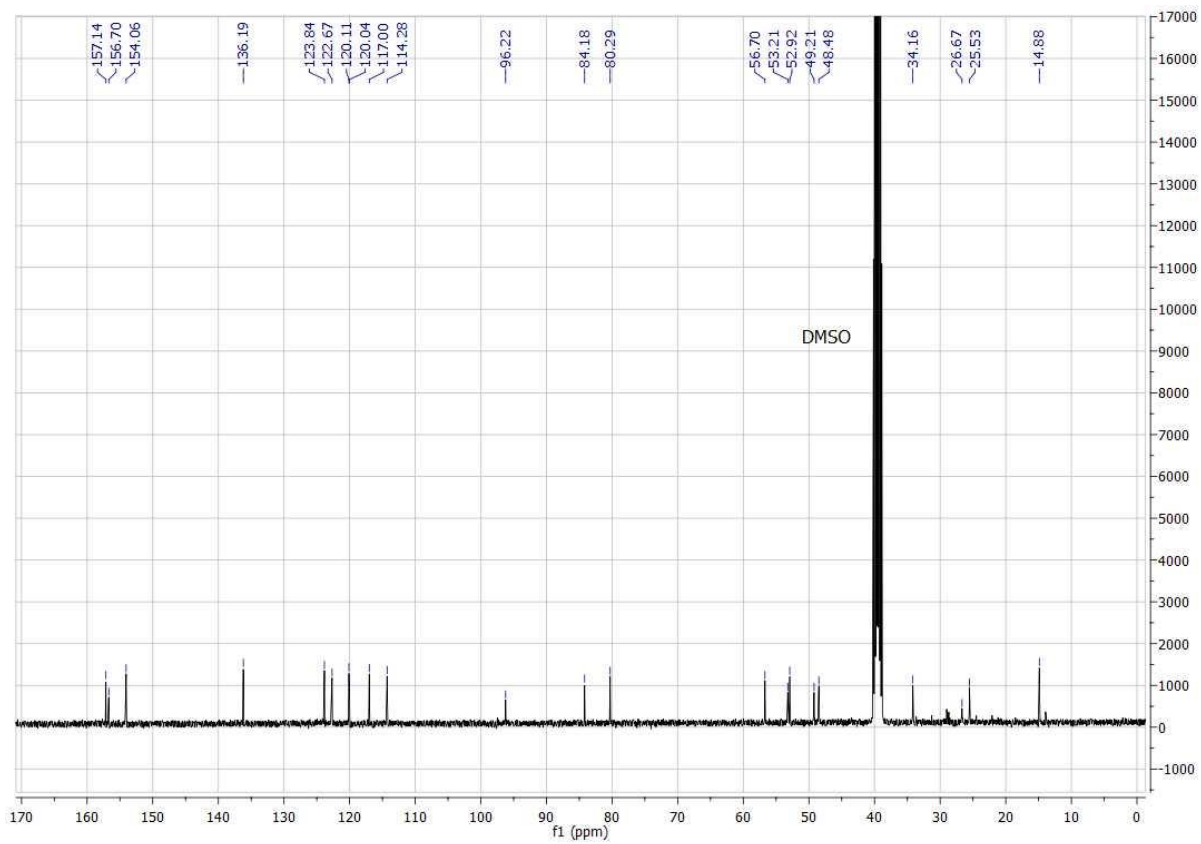
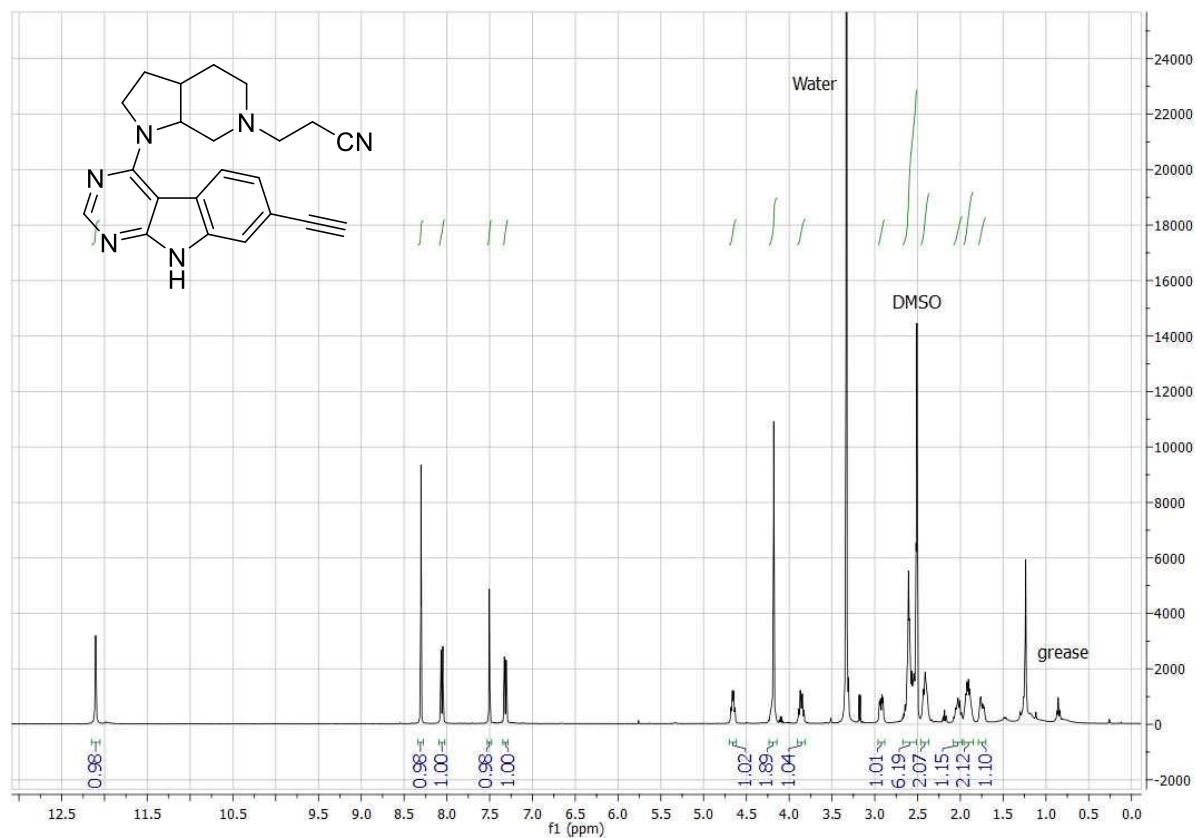
(S)-5c



(S)-15

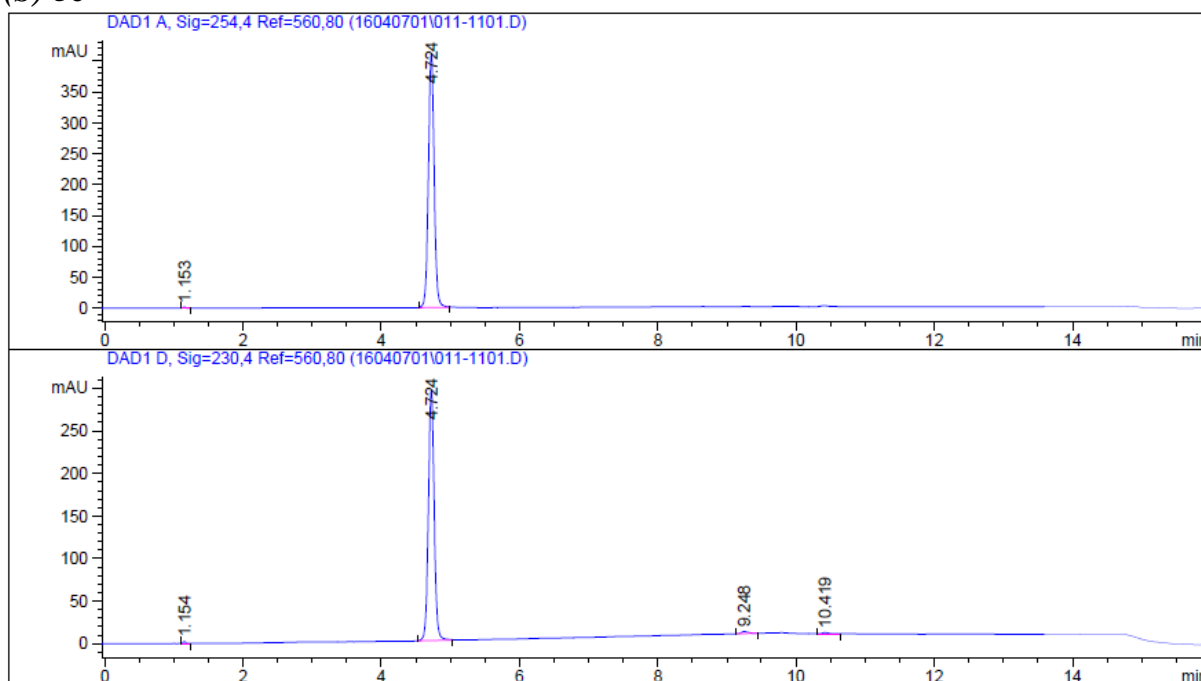






HPLC chromatograms of (S)-5c, (S)-15, 20 and 22

(S)-5c



Area Percent Report

```
Sorted By           :      Signal
Multiplier          :      1.0000
Dilution            :      1.0000
Use Multiplier & Dilution Factor with ISTDs
```

Signal 1: DAD1 A, Sig=254,4 Ref=560,80

Peak #	RetTime [min]	Type	Width [min]	Area [mAU*s]	Height [mAU]	Area %
1	1.153	BP	0.0389	4.10806	1.78100	0.1717
2	4.724	BB	0.0897	2388.50879	411.59946	99.8283

Totals : 2392.61685 413.38045

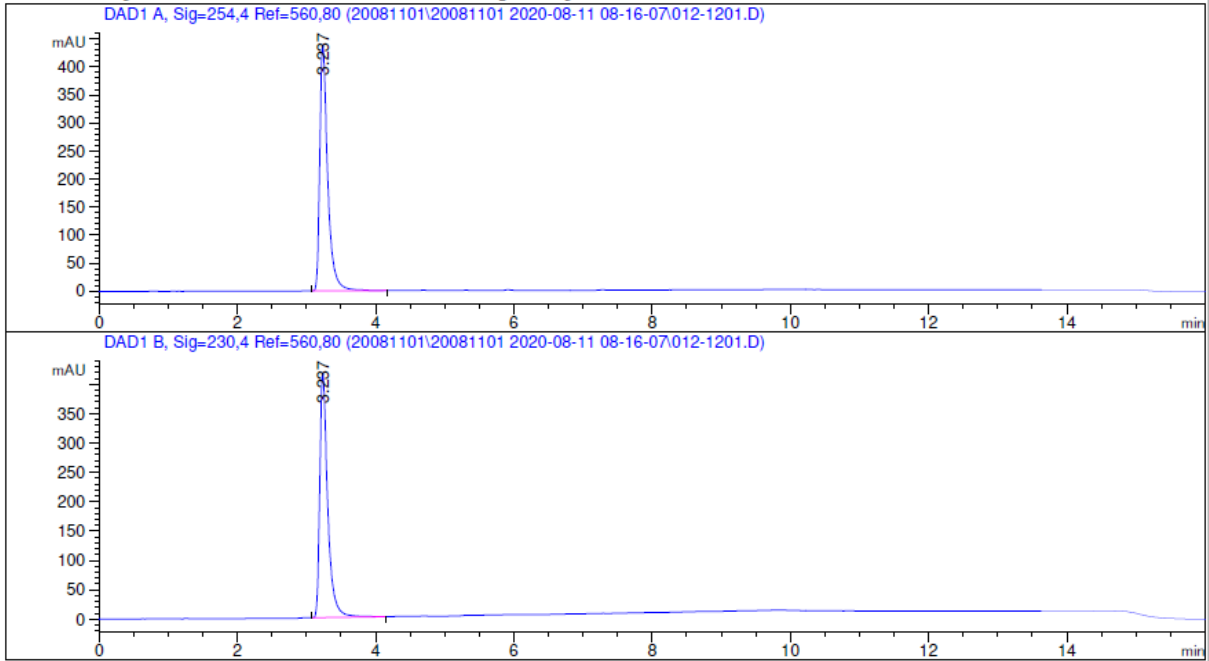
Results obtained with enhanced integrator!

Signal 2: DAD1 D, Sig=230,4 Ref=560,80

Peak #	RetTime [min]	Type	Width [min]	Area [mAU*s]	Height [mAU]	Area %
1	1.154	BP	0.0408	5.73826	2.32211	0.3290
2	4.724	BB	0.0898	1712.81812	294.86554	98.1915
3	9.248	BP	0.0974	16.50928	2.42639	0.9464
4	10.419	PB	0.0965	9.29896	1.41834	0.5331

Totals : 1744.36462 301.03238

(S)-15



=====
Area Percent Report
=====

Sorted By : Signal
Multiplier: : 1.0000
Dilution: : 1.0000
Use Multiplier & Dilution Factor with ISTDs

Signal 1: DAD1 A, Sig=254,4 Ref=560,80

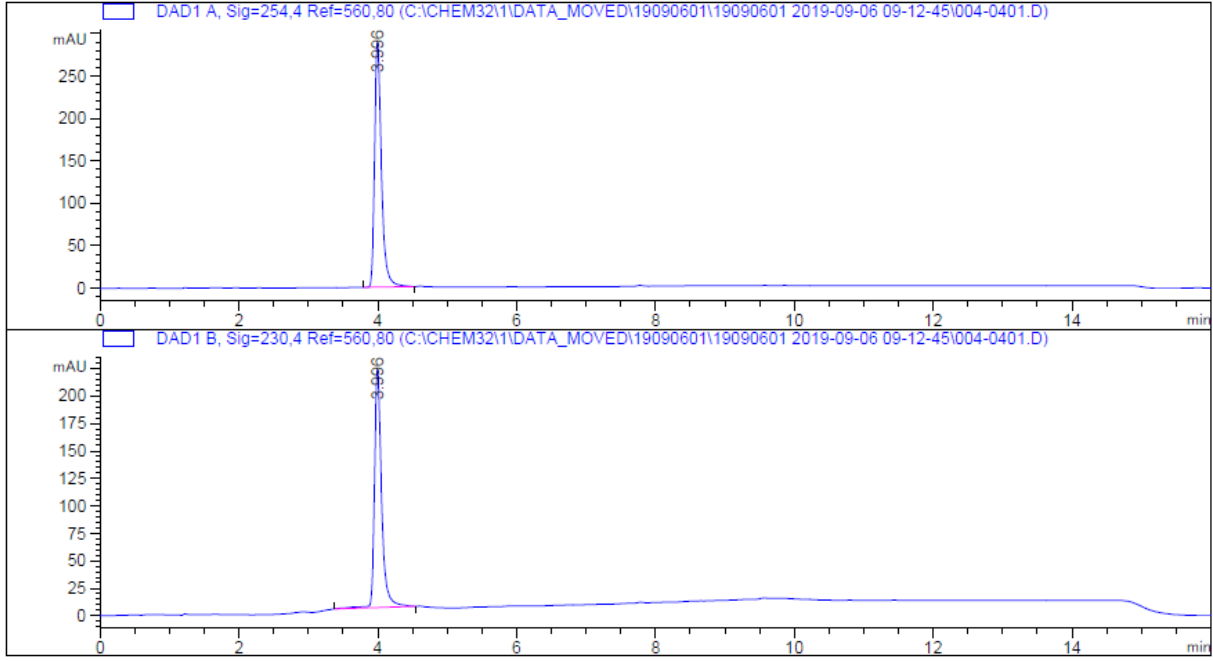
Peak #	RetTime [min]	Type	Width [min]	Area [mAU*s]	Height [mAU]	Area %
1	3.237	BB	0.1168	3502.43384	440.36560	100.0000

Totals : 3502.43384 440.36560

Signal 2: DAD1 B, Sig=230,4 Ref=560,80

Peak #	RetTime [min]	Type	Width [min]	Area [mAU*s]	Height [mAU]	Area %
1	3.237	BB	0.1168	3324.89258	418.22137	100.0000

Totals : 3324.89258 418.22137



=====
 Area Percent Report
 =====

Sorted By : Signal
 Multiplier: : 1.0000
 Dilution: : 1.0000
 Use Multiplier & Dilution Factor with ISTDs

Signal 1: DAD1 A, Sig=254,4 Ref=560,80

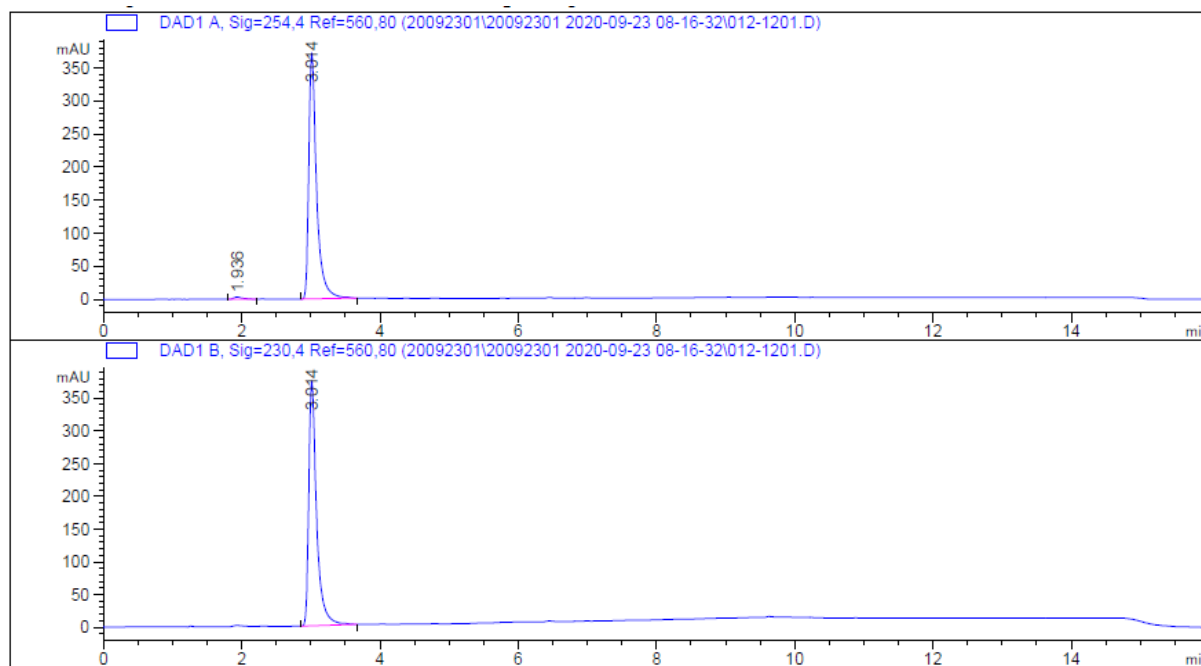
Peak #	RetTime [min]	Type	Width [min]	Area [mAU*s]	Height [mAU]	Area %
1	3.996	BB	0.1040	1979.62488	288.86835	100.0000

Totals : 1979.62488 288.86835

Signal 2: DAD1 B, Sig=230,4 Ref=560,80

Peak #	RetTime [min]	Type	Width [min]	Area [mAU*s]	Height [mAU]	Area %
1	3.996	BB	0.1068	1539.44324	216.92783	100.0000

Totals : 1539.44324 216.92783



=====
 Area Percent Report
 =====

Sorted By : Signal
 Multiplier: : 1.0000
 Dilution: : 1.0000
 Use Multiplier & Dilution Factor with ISTDs

Signal 1: DAD1 A, Sig=254,4 Ref=560,80

Peak #	RetTime [min]	Type	Width [min]	Area [mAU*s]	Height [mAU]	Area %
1	1.936	BB	0.1352	28.03933	3.10950	0.9500
2	3.014	BB	0.1158	2923.41162	371.68216	99.0500

Totals : 2951.45095 374.79166

Signal 2: DAD1 B, Sig=230,4 Ref=560,80

Peak #	RetTime [min]	Type	Width [min]	Area [mAU*s]	Height [mAU]	Area %
1	3.014	BB	0.1157	2942.89551	374.27606	100.0000

Totals : 2942.89551 374.27606

References

1. Bartole, E., Grätz, L., Littmann, T., Wifling, D., Seibel, U., Buschauer, A., Bernhardt, G. UR-DEBa242: a Py-5-labeled fluorescent multipurpose probe for investigations on the histamine H₃ and H₄ receptors. *J. Med. Chem.* **2020**, *63*, 5297-5311.
2. Pruccoli, L., Morroni, F., Sita, G., Hrelia, P., Tarozzi, A. Esculetin as a bifunctional antioxidant prevents and counteracts the oxidative stress and neuronal death induced by amyloid protein in SH-SY5Y cells. *Antioxidants* **2020**, *9*, 551.
3. Tarozzi, A., Morroni, F., Merlicco, A., Hrelia, S., Angeloni, C., Cantelli-Forti, G., Hrelia P. Sulforaphane as an inducer of glutathione prevents oxidative stress-induced cell death in a dopaminergic-like neuroblastoma cell line. *J. Neurochem.* **2009**, *5*, 1161-1171.

Danksagung

Ich möchte mich sehr herzlich bei allen Menschen bedanken, die mich in den letzten Jahren begleitet und auf meinem Weg durch die Dissertation unterstützt haben.

Für die Möglichkeit meine Dissertation in seinem Arbeitskreis zu schreiben und mich in die Welt der Forschung einzuführen, möchte ich Herrn Prof. Dr. Michael Lämmerhofer danken. Vielen Dank für die Unterstützung, Beratung und wissenschaftlichen Diskussionen in den vergangenen Jahren!

Allen ehemaligen und aktuellen Doktorand*innen, Mitarbeiter*innen und Student*innen des AK Prof. Lämmerhofer sei gedankt, für viele anregende Gespräche, für Hilfe, für's gemeinsam Aufregen und Rumblödeln und für das gemeinsame Lösen (oder Finden - oder auch Kreieren) von Problemen.

Ein besonderer Dank gilt meinem DAB-Team Dr. Stefanie Bäurer, Dr. Ulrich Woiwode, Marc Wolter und Kristina Dittrich, die mich bei der Lehre unterstützt haben sowie meinen ehemaligen und aktuellen Bürokolleg*innen Ece Aydin, Dr. Ryan Karongo, Dr. Adrian Sievers-Engler (danke an der Stelle auch für reichlich MS-Expertise und die vielen Ohrwürmer), Kristian Serafimov, Dr. Carlos Calderón Castro und Dr. Malgorzata Cebo. Vielen Dank auch an meine restlichen Kolleg*innen, an Matthias Olfert, Peng Li, Xiaoqing Fu, Simon Jaag, Feiyang Li, Dr. Stefan Neubauer, Cornelius Knappe, Adrian Brun, Mirna Maalouf, Min Su, Dr. Jörg Schlotterbeck, Dr. Bernhard Drotleff, Dr. Jeannie Horak und Dr. Corinna Sanwald.

Herzlichen Dank auch an die CTAs, mit denen ich arbeiten durfte und ohne die die Laborarbeit und -organisation fast nicht möglich gewesen wäre. Danke an Mike Kaupert, Karolin Handke und Franz Fießinger. Ebenso möchte ich den Sekretärinnen des Arbeitskreises Eveline Wachendorfer, Ingrid Straub und Michaela Friedrichs für ihre Unterstützung bei jeglichen Fragen danken.

Einen herzlichen Dank auch an Herrn Jun.-Prof. Dr. Matthias Gehringer für das Übernehmen des Zweitgutachtens dieser Arbeit.

Ebenfalls möchte ich Herrn Prof. Dr. Harald Groß und Herrn Prof. Dr. Stefan Laufer und sämtlichen Mitgliedern beider Arbeitsgruppen für die enge und freundschaftliche Zusammenarbeit bei diversen Projekten danken.

In meinem privaten Umfeld möchte ich vor allem meinen Eltern, Michaela und Thomas, für die konstante Unterstützung danken. Danke, dass ihr immer für mich da seid! Das gleiche gilt für meine Schwester Natascha, die mich konstant unterstützt hat. Danke auch an meine Omas Irmgard und Lydia!

Antonia sei ein besonderer Dank ausgerichtet, dafür dass sie immer an meiner Seite war und meine Stimmung auch an schlechten Tagen ausgehalten hat, die mir bei allen Problemen und Fragen geholfen hat und mir über die vergangenen Jahre eine enorme Stütze war.

Für die intensive Unterstützung, besonders in der Endphase der Dissertation, sei neben Antonia auch Andi, Dennis und Daniel gedankt! Ihr habt die Schreibearbeit deutlich angenehmer gemacht!

Zu guter Letzt sei all den Menschen gedankt, die in den letzten Jahren mit mir Musik gemacht, gehört oder über Musik gesprochen haben. Danke an all meine Freunde und Freundinnen, an Alex, Jannik, Kevin, Marci, Lorenz, Juli, Max, Philipp, Adri, Laura, Vera, Max, Claudi, Paddi, Dr. Steff, Fredi, Anna-Lena, Beate, Antonia, Andi, Dennis, Daniel, Marc, Thomas, Matthias, Kim, Sven, Sina, Antje, Anki, Toschi und ganz viele Menschen mehr! Vielen Dank für die Unterstützung!